SP-721
October 2013

21st ESA Symposium

European Rocket & Balloon Programmes and Related Research

9–13 June 2013
Thun, Switzerland

Sponsored by
Hochschule Luzern
Swiss Space Office
Business Development Nidwalden

European Space Agency
Agence spatiale européenne

Programme Committee

Chair: M. Egli, HSLU

Members: K. Boen, Andoya Rocket Range
S. Kemi, SSC Esrange
F.-J. Lübken, IAP Kühlungsborn
J. Moen, University of Oslo
J. Urban, Chalmers University
A. Verga, ESA
B. Zappoli, CNES

Symposium Organising Committee

Chair: M. Cogoli, Zero-g LifeTec

Co-chair: M-P. Havinga, ESA

Members: I. Hutzli, Wirk
F. Ille, HSLU
S. Richard, HSLU
S. Tanner, HSLU
J. Wirz, Wirk

Publication	Proc. '21st ESA Symposium on European Rocket & Balloon Programmes and Related Research', Thun, Switzerland (ESA SP-721, October 2013)
Edited by	L. Ouwehand ESA Communications
Published and distributed by	ESA Communications ESTEC, Noordwijk, The Netherlands
Price	€ 60
ISBN *ISSN*	978-92-9092-285-8 0379-6566

Copyright © 2013 European Space Agency

CONTENTS

Foreword 11

National Reports

Chair: M. Cogoli

National Report – Germany 15
Sounding Rocket and Balloon Research Activities Supported by the German Space Programme in 2011 – 2013
R. Kuhl, C. Gritzner & D. Friedrichs

National Report – Norway 23
Norwegian National Report - Arctic Access to Space
P. Brekke

National Report – Sweden 33
Swedish Space Activities – An Overview with a Focus on Balloons and Rockets
K. Dannenberg

National Report – Switzerland 37
Sounding Rocket and Balloon Activities and Related Research in Switzerland 2011 – 2013
M. Egli

National Report – Japan 43
Recent Activities of Japanese Sounding Rocket Experiments
A. Takumi & I. Nobuaki

Invited Lectures

Space Education in Norway 49
A.H. Hansen, S.V. Mathisen, F.F. Nicolaisen et al.

Ranges

Chair: A. Verga

An UAV to Scan Rocket Impact Area for Safety Procedures 57
J.V.A. Tavares, R.C.A. Sousa, M.T.A.B. Segundo et al.

The Facilities at Chinese Hainan Sounding Rocket Launch Site 65
C. Liu & X. Jiang

The Use of WRF Mesoscale Model to Derive the Winds to Support Launchings at the Brazilian Space Center 69
G. Fisch, A.F. Gomes da Siva & P.G. Iriart

Ionosphere

Chair: O. Havnes

Bonus Results from Ion Probes 75
M. Friedrich, K. Torkar, S. Robertson & S. Dickson

Power Spectral Analysis of High Latitude F-Region Small-Scale Irregularities 81
A. Spicher, W.J. Miloch & J.I. Moen

Error Estimates for In Situ Probe Systems and Wave Detections 87
H. Sato, H. Pécseli & J.K. Trulsen

Troposphere, Stratophere & Climate

Chairs: J. Urban, H. Oelhaf & J.-P. Pommereau

Balloon-Borne Measurements of Ice Particle Shape and Ice Water Content in the Upper Troposphere over Northern Sweden 93
T. Kuhn, A.J. Heymsfield & S.A. Buehler

Boudary Layer Pressurized Balloons Deployed in the Mediterranean 99
A. Doerenbecher, C. Basdevant, F. Bernard et al.

MISSUS Experiment Onboard BEXUS 15: An Innovative Integrated Sensors Suite for Meteorologic Measurements in Low Pressure Environments and for Attitude Reconstruction 107
F. Cucciarrè, S. Chiodini, C. Palla et al.

Projects & Missions for Rockets

Chairs: A. Verga, A. Blix Dahle, E. Thrane, W. Jung & K. Dannenberg

ARES Rockets Demonstraters of French Space Agency Perseus Project 117
C. Dupont, S. Pernon & J. Oswald

Technical Aspects of the Brazilian Sounding Rockets 125
F. de Azevedo Corrêa Junior & A.W. da Silva Mello Junior

The System Design of the Sounding Rocket KUNPENG-1 of the Chinese Meridian Project 133
X. Jiang & A. Xu

SHEFEX II Vehicle and Subsystem Design, Flight Performance and their Application to Future Hypersonic Missions 137
J. Turner, J. Ettl. M. Hörschgen-Eggers et al.

Sounding Rockets for Entry Research: SHEFEX Flight Test Program 143
H. Weihs

REDEMPTION: An Experiment on Sounding Rocket to Test a System for Actival Debris Removal – REXUS12 153
M. Valdatta, F. Romei, A. Spadanuda et al.

Sounding Rocket System of China 'Meridian Spaceweather Monitoring Project' 161
Q.S. Peng. Q.B. Ren & Y. Jun

MASER-12 Sounding Rocket: A Hot Mission in Cold Environment 167
G. Florin, M. Abrahamson, P. Holm et al.

Swedish Sounding Rocket Projects 175
C. Lockowandt, K. Sjölander, S. Kemi & K. Löth

Material Physics Rockets MAPHEUS-3/4: Flights and Developments 179
M. Siegl, F. Kargl, F. Scheuerpflug et al.

Space Sailors: Experimental Deployment of a Dragsail in a Sounding Rocket 185
C. Fiebig, W. Bauer, P. Gerding et al.

Developing Technological Knowledge in Microgravity Missions by Matching Partners Expertise 193
A. La Neve & F. de Azevedo Corrêa Junior

Data Logging a Water Rocket with Arduino 201
T. Joris, J.-H. Thysen, M. De Roeve et al.

Multi-Disciplinary Conception Approach for a Reentry Platform 207
T.H. Matos de Carvalho, L.E. Vergueiro Loures da Costa & M.L. Gregori

Projects & Missions for Balloons

Chairs: P. Cocquerez & C. Lockowandt

Requirements Versus Constraints in Designing Stratospheric Platforms for Multi-User Payloads: The Large-Scale Polarization Explorer (LSPE) Experiment 217
L. Fiorineschi, A. Boscaleri, P. Rissone & M. Baldi

VEXREDUS: A Student High Altitude Glider Project to Demonstrate the Capabilities of a Blended Wing Body Concept 225
D. Steenari, T. Kuhn & S. Wlach

Small Whiskbroom Imager for Atmospheric Composition Monitoring (SWING) from an Unmanned Aerial Vehicle (UAV) 233
A. Merlaud, D.-E. Constantin, E. Mingireanu et al.

Station-Keeping Control Strategies Analysis for Stratospheric Airship 241
L. Zhang, Z. Wang, K. Zhao & X. Yang

Superheat Simulation of the High Altitude Scientific Balloon During Floating Flight 247
K. Zhao, X. Yang, Z. Hou et al.

NOSYCA: A New Standard for Balloon Operations, Flight Proven 2013 255
T. Moule, J. Mongis, P. Dezen & C. Chatain

Ballooning in Spain: Zero2Infinity Develops New Launch Capability for Medium to Heavy Payloads on Stratospheric Balloons 265
J.M. López-Urdiales & A. Schoenmaker

Life & Physical Science

Chairs: B. Zappoli, Y. Houltz, M. Egli & M. Cogoli

The XRMON-GF Microgravity Experiment Module on MASER 12 and its Continuation 275
Y. Houltz, J. Li, H. Nguyen-Thi et al.

Results from Low-Gravity and Normal Gravity Experiment ”Trace+” on Dendritic Growth and the Columnar-Equiaxed Transition in the Transparent Alloy System NPG-DC 285
L. Sturz, M. Hamacher & G. Zimmermann

CaRu: An Investigation of Capillary Action Under Low Gravity Conditions Through Runge Instabilities 293
et al.

Design, Operational Aspects and Flight Results of a Propellant Management Device (PMD) Experiment on a TEXUS Sounding Rocket 301
B. Schmitz, P. Behruzi & A. Schütte

CoCoRAD and TechDose Cosmic Radiation Experiments on Board BEXUS Stratospheric Research Balloons 307
B. Zábori, I. Apáthy, A. Csöke et al.

Continuous Measurement of the Biological Effects of Stratospheric UV Radiation – BioDos Experiment, BEXUS-15 315
V. Grósz, V. Gorócz, A. Futó et al.

Cytosolic Calcium, Hydrogen Peroxide, and Related Gene Expression and Protein Modulation in *Arabidopsis Thaliana* Cell Cultures Respond Immediately to Altered Gravitation: A Holistic View 321
M. Neef, S. Fengler, N. Hausmann et al.

Lessons Learned from REXUS-12’s Suiaineadh Experiment: Spinning Deployment of a Space Web in Milli Gravity 329
T. Sinn, M. McRobb, A. Wujek et al.

New Techniques for Rockets

Chairs: S. Kemi, J. Ettl, P. Turner, A. Schütte, G. Florin & H. Steinau

Experimental In-Flight Model-Analysis of a Sounding Rocket Structure 341
A. Gierse, S. Krämer, D.J. Daab et al.

Companders for High Frequency and High Dynamic Range Measurements on Sounding Rockets and Launch Vehicles 347
H.A.C. Procopio & M. Barbosa Lucks

Research on Sounding Rocket Boom Deploying Technology in Meridian Project 351
X. Yang, H. Yang, X. Jiang et al.

Flight Control of SHEFEX II 357
F. Scheuerpflug & A. Kallenbach

Active Falling Sphere for High-Resolution Measurements of Density, Temperature, and Horizontal Winds in the Middle Atmosphere 361
Q. Li, B.Strelnikov, M. Rapp et al.

UV-Cleaned Langmuir Probe 367
C.T. Steigies & A. Barjatya

Sounding Rocket Guidance, Navigation and Control and Anticipated Next Generation Developments 371
L. Ljunge

High Precision Drag Deceleration Measurement System to Use Onboard Active Falling Spheres 377
J.B. Schumacher, H. Ewald, S. Finke et al.

Navigation and Cold Gas Control Systems Flown on SHEFEX II 383
J. Ettl & J. Turner

Measurements of the D-Region Plasma Using Active Falling Plasma Probes 393
C. Baumann, H. Asmus, J. Schumacher et al.

Development of the Aerospace Parachute System (ASPS) Operating at Altitude Range of 60-150 km for Salvation of the First Stages of Launch Vehicles and Propulsion Systems 399

Development and Flight-Testing of a System to Isolate Vibrations for Microgravity Experiments on Sounding Rockets 405
S. Krämer, D.J. Daab, B. Müller et al.

Gravity Gradient Earth Sensor Experiment on REXUS 11 413
K. Ghose, S. Dandavino, H. Meyer et al.

Deployment and Characterisation of a Telescopic Boom for Sounding Rockets: REXUS-11 419
D. Vather, P. Duffy, S. Curran & J. Keegan

StrathSat-R: Deploying Inflatable Structures from CubeSats in Milli Gravity 425
I. Dolan, T. Sinn, R. Clark et al.

Results of the GPS Experiment on the VS-30 V08 Sounding Rocket 433
F. Mota, F. Spina, T. Luna & F. Miranda

A Mathematical Model to Simulate Rocket Exhaust Clouds in Alcântara Launch Center 437
D. Moreira, E. Nascimento, T. Albuquerque et al.

ICON, A Mass Analyser for the Ice Content of NLC/PMSE Particles 441
O. Havnes, T. Antonsen, A. Frederiksen et al.

Constant Flow Under Free Fall – Ensuring Conditions for Applied Research in Space 445
H. Steinau

New Developments on Rocket Propulsion with Gelled Propellants 451
K.-W. Naumann, J. Ramsel, K, Schmid et al.

TLM-Net: An Ethernet Based Telemetry Data Distribution System 459
A. de O. Moraes, G.A.Wanderson, M.B. Lucks & S. Fugivara

Providing a Standard Support Bus for Sounding Rockets Experiments with the CERESS Experiment 461
A. Schmitt, D. Bugger, C. Friedl & S. Althapp

PoleCATS – A Plasma Instrumentation Technology Demonstration for REXUS-14 469
A. Lee, R. Bedington, L. Comandar et al.

Development of INPE 13 and INPE 14 Payloads 473
E.D. Roda, M.A.B.H. Rizol, M.B. Lucks & A.O. Moraes

New Generation DVS for Future Sounding Rocket Missions 475
G. Capuano, D. Titomanlio & M. Severi

Mesosphere

Chairs: F.-J. Lübken, M. Friedrich, J. Urban & J. Moen

In Situ Density, Temperature, and Turbulence Measurements in the Middle Atmosphere During PHOCUS 2011 485
A. Szewczyk, B. Strelnikov & M. Rapp

In Situ Measurements of Charged Mesospheric Ice Particles During the PHOCUS 2011 Campaign and Comparison of the Results with a Microphysical Model 489
H. Asmus, B. Strelnikov & M. Rapp

Collision Fragments from Impacting NLC/PMSE Particles: Are the Fragments Mainly Meteoric Smoke Particles? 495
O. Havnes, J. Gumbel, C. La Hoz & J. Hedin

Multi-Radar Observations of Polar Mesosphere Summer Echoes During the PHOCUS Campaign on 21 July 2011 499
E. Belova, S. Kirkwood, M. Zecha et al.

Sounding Rocket Experiments with Ejectable Payloads KTH 503
N. Ivchenko & G. Tibert

Preliminary Results from the Rain Mesospheric and Stratospheric Aerosol Particle Collection Experiment Launched on REXUS-11 511
P. Magnusson, W. Reid, P. Achtert et al.

Rocket-Borne Experiment for the Measurement of the Variation in Electric Conductivity with Altitude (Gekko Experiment - REXUS14) 519
Z. Váradi, O. Botond Lőrinczi, G. Balassa & P. Bencze

Application of Rocket Related Luminocity Signatures to Study the Upper Atmosphere 527
S.A. Chernouss, Yu.V. Platov & M.V. Uspensky

The Role of Wake Effects in Experiments by Sounding Rockets and other Spacecrafts 535
W.J. Miloch

Space-Related Education

Chairs: N. Callens, A. Stamminger & E. Zumbrunnen

Building Research Competences in Secondary School Students Through Hands-On Earth and Space Science Education Projects 541
E. de Schrijver

CanSat Teacher Training Course 547
T. Gansmoe & J. Grande

CanSat, Science in a Sodacan 551
M. Uitendaal

STERN – A Rocket Programme for German Students 555
A. Stamminger, H. Ciezki, W. Kitsche et al.

REXUS/BEXUS – Rocket and Balloon Experiments for University Students 561
N. Callens, A. Kinnaird, K. Dannenberg et al.

Soldering Alloys in Reduced Gravity – Solar 569
A. Svedevall

MUSCAT Experiment: Active Free Falling Units for *In Situ* Measurements of Temperature and Density in the Middle Atmosphere 575
M.T. Bordogna, L. Fidjeland, M. Fjällid et al.

CAESAR –Capillarity-Based Experiment for Spatial Advanced Research on REXUS-14 583
E. Zumbrunnen & D. Strobino

Scientific – Educational Microsatellite «CONDOR» 589
O.M. Brekhov

The Norwegian Student Satellite Program – Status Update 593
J. Grande

ASGARD-II, III and III-b Balloon Flights: Growing a Worldwide Hands-On Space Education Project for Secondary School Students 597
E. de Schrijver & R. Van Malderen

SP.ACE 2011-2013: Exploring New Approaches in Hands-On Space Education for Secondary Schools Including Balloon, UAV and Antarctic Science Projects 603
et al.

Odyssée-S2, A France-Japan Experimental Rocket Project 609
H. Charrier & M. Martin-Lagarde

An Unmanned High Speed Glider for Weather Data Gathering 617

Development of Drop Test System for Pretesting of REXUS/BEXUS Experiments 627
P. Pongsuwan, M. Fittock, A. Schmidt et al.

Astrophysics

Chairs: M. Wiedner & S. Kemi

Radiation Measurement on a Stratospheric Balloon BEXUS13 637
T. Möller, B. Ehresmann, J. Labrenz & L. Panitzsch

Autonomous Payload Function: The PoGOLite Software 641
M.S. Jackson for the PoGOLite Collaboration

Measurement with a Phoswich Detector on a Stratospheric Balloon 647
E. Scharrenberg, E.M. Dönsdorf, P. Kühl et al.

CIDRE – A Small Astronimical Balloon Experiment at Far Infrared Wavelengths (2.7 THZ) 651
M. Wiedner, L. Pagani, C. Berthod et al.

Discovery and Research of Cosmic Rays on Balloons 655
L. Dorman

A New Paradigm in Space Based Experiments Using Rubber Balloons 663
S.K. Chakrabarti, D. Bhowmick, S. Palit et al.

On Different Internal Earth's Magnetic Field Models in Dependence on Satellite Altitudes and their Geophysical Properties 671
W.A. Webers

New Techniques for Balloons

Chairs: M. Zell & A. Cogoli

Compact Telemetry System for Small Satellites Ejected from Sounding Rockets and Balloons 681
S. Finke, R. Pohlmann, Q. Li et al.

Accuracy Estimation of the Global Analytical Models of the Main Magnetic Field by Means of the Gradient Magnetic Survey on Stratospheric Balloons 685
Y. Tsvetkov, O. Brekhov, S. Filippov et al.

Calibration of the Pilot Photometer 689
R. Misawa, J.-P. Bernard and the PILOT Team

Addressing the Goals in the Planetary Science Decadal Survey from a Balloon-Borne Platform 695
E.F. Young, T. Kremic, C.A. Hibbitts et al.

Balloon Magnetometric Complex 703
O.M. Brekhov & Y. Tsevtkov

List of Participants 711

Foreword

21st ESA Symposium on Sounding Rockets and Balloons and Related Research

Dear PAC Delegates, dear Participants, dear Colleagues and Friends

The 21st ESA Symposium on "European Rocket & Balloon Programmes and related Research" has closed its doors. To me, an intense and exciting week came to an end. During the symposium days, we were listening to inspiring talks, discussing new projects with colleagues and had ideas exchanged with the exhibitors on-site. I hope you have enjoyed participating in the symposium similarly like me.

From 9 – 13 June, more than 260 participants from 21 different countries were present in Thun. This represents a record in the history of the symposium. There have never been such a variety of nationalities registered yet. Among the participants, there were also about 80 students that indicates the large interest of the next generation of engineers and scientists in the sounding rocket and balloon activities.

Besides the symposium, we were able to enjoy leisure moments at picturesque villages, on the Lake of Thun or the magnificent view from the mountains nearby. The high point of the excursion was certainly the visit of the Jungfraujoch, at close to 3'500 m above sea level.

As chairman of the 21st ESA Symposium on "European Rocket and Balloon Programmes and Related Research" I would like to thank the attendees for their numerous appearance. The smooth conduction of the symposium we all enjoyed was possible thanks to the hard work of many people behind the scenes like Marie-Pierre Havinga and Antonio Verga from ESA as well as the members of the local organizing committee, chaired by Marianne Cogoli. I would also like to thank the people from KKThun who did an excellent work in supporting us. Last but not least, I would like to acknowledge the extensive work of the scientific committee who managed to fit more than 170 presentations into three parallel sessions.

I am now looking forward to the next meeting that will take place in Norway 2015 and I hope to meet you all there again.

Marcel Egli
Chairman, Lucerne University of Applied Sciences and Arts

Proc. '21st ESA Symposium European Rocket & Balloon Programmes and Related Research',
9–13 June 2013, Thun, Switzerland (ESA SP-721, October 2013)

National Reports

Chair: M. Cogoli

SOUNDING ROCKET AND BALLOON RESEARCH ACTIVITIES SUPPORTED BY THE GERMAN SPACE PROGRAMME in 2011 - 2013

R. Kuhl, C. Gritzner, D. Friedrichs

DLR, German Aerospace Center, Space Administration
Koenigswinterer Str. 524, D-53227 Bonn, Germany
fax.: +49-228-447-735, tel.: +49-228-447-0
e-mail: Rainer.Kuhl@dlr.de, Christian.Gritzner@dlr.de, Dietmar.Friedrichs@dlr.de

ABSTRACT

Mainly sounding rockets but also stratospheric balloons have played a crucial role in implementing the German Space Programme since many years. Research activities were conducted in the fields of Microgravity, Space Sciences, Earth Observation, Space Technology Development, Education, and Outreach.

Currently, in the field of Space Science the mesosphere and ionosphere of the Earth as well as the solar photosphere and chromosphere are in the focus of research. In Microgravity Research the disciplines of life and physical sciences benefit from ballistic rocket flights. Balloon-borne measurements are conducted to investigate the chemistry of our stratosphere. Student activities are mainly supported under the auspices of the Swedish-German programme REXUS/BEXUS.

1. INTRODUCTION

The disciplines Space Science, Microgravity Research, Earth Observation, and Space Technology Development are core elements of the German Space Programme. Both, sounding rockets and balloons represent cost-effective research tools for in-situ measurements in the Earth's atmosphere. On the other side experiments in nearly weightlessness can be performed on a free fall trajectory of sounding rockets. A hypersonic re-entry can be tested by rockets on special trajectories. Rockets and balloons are also very suitable for the education and training of young scientists in space projects.

In order to conduct space and atmospheric research with rockets and balloons German scientists of more than 20 research institutions currently benefit from the launch sites Andøya Rocket Range - ARR (Norway) - and the Esrange Space Center (Sweden) in established European autonomy.

At Esrange most of the flight campaigns are conducted by EUROLAUNCH. This is a joint venture of the entity DLR-MORABA (Mobile Rocket Base) and the Swedish Space Corporation (SSC).

The paper reports on activities supported by the German Space Programme and implemented by the DLR Space Management in the period June 2011 to June 2013.

2. SPACE SCIENCE

2.1 Aeronomy

2.1.1. WADIS project

The project WADIS (Wellenausbreitung und Dissipation in der Mittleren Atmosphäre; wave propagation and dissipation in the middle atmosphere) was initiated in 2011 by the Leibniz-Institute for Atmospheric Physics (IAP) in Kühlungsborn (PIs: F.-J. Lübken, M. Rapp). Its main goals are the analysis of gravity-wave dynamics in the middle atmosphere and in-situ measurements of atomic oxygen.

For the gravity-wave studies the already flown and well proven CONE sensors will be used. For the atomic oxygen measurement two new instruments - FIPEX and PHLUX - are to be supplied by the Institute of Space Systems (IRS), University of Stuttgart. The FIPEX sensor was already successfully flown on the International Space Station, while the PHLUX sensor originnally was developed to be launched into space aboard the re-entry capsule EXPERT by ESA. In the meantime, both instruments were optimized for the WADIS sounding rocket campaigns.

There will be an instrument set of all three sensors (CONE, FIPEX and PHLUX) on each end of the rocket payload section. This allows for measurements during the ascent and decent phase of the flown parabolic trajectory while the longitudinal rocket axis is inertially stabilized. The measurement phase will cover the altitude range of about 70 km to 134 km. The horizontal distance of the flown parabola will be about 50 km at an altitude of 80 km.

It is intended to conduct two WADIS launch campaigns that are planned for July 2013 and January 2014. Both rocket campaigns will be accompanied by atmospheric measurements at the ALOMAR ground station at ARR. This concerns two instruments: the lidar investigation DORIS (Doppler Rayleigh Iodine System) and the radar study MAARSY (Middle Atmosphere ALOMAR Radar System).

DLR-MORABA will prepare and conduct the WADIS launches from Andøya. Each campaign consists of one

Proc. '21st ESA Symposium European Rocket & Balloon Programmes and Related Research', 9–13 June 2013, Thun, Switzerland (ESA SP-721, October 2013)

VS 30 rocket flight together with twelve meteorological rocket launches. The last ones are provided by NASA in the frame of a cooperation.

2.1.2 TURB3D project

TURB3D (Dreidimensionale Struktur mesosphärischer Turbulenz; three-dimensional structure of mesospheric turbulence) is a technology preparation project initiated by IAP and DLR. The scientific aspects are handled by IAP (PI: F.-J. Lübken) while the technological tasks are performed by IAP together with the midsize company Von Hoerner & Sulger GmbH, Schwetzingen.

With TURB3D the scientific objectives of the WADIS project will be extended towards a 3-dimensional measurement. This will be achieved by flying four identical instrument units in a swarm formation. After reaching the apogee at about 120 km a separation mechanism will be activated releasing three CONE experiment units from a rotating payload section. The fourth unit (another CONE instrument and possibly the FIPEX and PHLUX sensors) stays attached to the payload section. The three separated units will reach a distance in the mesosphere of about 250 metres from the payload section within a minute. The separation mechanism, communication lines, and the tracking are still to be studied. The first TURB3D campaign is expected in the next 2-3 years.

2.2 Solar Physics

SUNRISE (Fig. 1) is a balloon-borne solar telescope working in the ultraviolet spectral region down to 214 nm. Due to the disturbances of the Earth atmosphere measured data of the solar atmosphere in this region are not accessible from the ground. The instrument is able to produce spectral and polarimetric images of the solar photosphere and chromosphere with very high temporal and spatial resolution. The main objective of the project is to understand the formation of magnetic structures in the solar atmosphere and to study their interaction with plasma processes in the sun.

SUNRISE represents a joint project of German, US, and Spanish groups led by the Max Planck Institute for Solar System Research (MPS). The project is managed by P. Barthol and the PI is S. K. Solanki, both working at MPS. The one meter aperture telescope was built by the German company Kayser-Threde, under the scientific responsibility of MPS.

The instrumentation consists of a filter imager built by MPS and a magnetograph provided by the Instituto de Astrofisica de Canarias, Spain. The Kiepenheuer Institute for Solar Physics, Freiburg, was responsible for the image stabilisation system and the correlation wavefront sensor. The balloon gondola, equipped with the power supply and the pointing and telemetry system, was built under the responsibility of the High Altitude Observatory in Boulder, USA. The launch services for this mission are provided by the NASA Columbia Scientific Balloon Facility, Palestine.

On 8 June 2009 the SUNRISE 1 mission was launched from Esrange. On the way up to the stratosphere the balloon diameter increased to more than 100 meters carrying more than two tons of scientific equipment. Flying at heights up to 37 km the gondola left 99% of the Earth atmosphere below. During its travel beyond the Arctic Circle the telescope had an untarnished and continuous sun view for more than five days. The telescope worked flawlessly and was recovered without damage after a perfect parachute landing of the gondola on 13 June 2009 in the north of Canada.

Figure 1: SUNRISE 1 solar telescope during launch preparations at Esrange. Credit: MPS

Due to the high resolution of the instruments small-scale plasma structures, i. e. bright spots in the photosphere, below 100 km latitude could be characterized for the first time. In these spots the magnetic field is up to three thousand times as strong as that of the Earth. The brightness of the spots could be measured in the far UV spectral region. It could be confirmed in detail that the brightness fluctuations of the photosphere immediately reflect the temperature distributions at the sun surface. Until now, the excellent results of this mission could be published in more than twenty scientific papers.

The second SUNRISE mission is planned in the period June-July 2013. The scientific payload will be nearly identical to the one flown in 2009 but slightly changed filters in the filter imager.

While the images taken in 2009 revealed the atmosphere of an extremely quiet sun in the solar minimum, a much higher solar activity is expected in 2013. Therefore, the main mission objective is now to investigate very active regions at the solar surface.

3. MICROGRAVITY RESEARCH: LIFE AND PHYSICAL SCIENCES

3.1 TEXUS and MAPHEUS flights

To investigate the effect of gravity on physical, chemical, and biological processes numerous German scientists participated during the period of this report in three sounding rocket missions TEXUS with eleven experiments (Tab. 1) and one MAPHEUS mission with four experiments. The microgravity flight phases amounted to about 3 min for the MAPHEUS flight and 6 min for TEXUS. The TEXUS rockets were powered by the Brazilian 2-stage motor VSB-30 and MAPHEUS by the Nike-Improved Orion.

ESA and DLR jointly tested on TEXUS 48 a new way of handling propellants on Europe's future rockets. ESA is working on a cryogenic upper stage that is restartable. To ensure engine ignition after a long coast in microgravity the propellant must be held ready at the tank's outlet using capillary forces. Two Propellant Management Devices were used to mimic the handling of supercold liquid hydrogen and oxygen propellants. To ease cost and safety constraints, and simplify the thermal design liquid nitrogen represented in this experiment the cryogenic propellants. TEXUS 48 was launched on 27 November 2011 and supported by ESA's Cryogenic Upper Stage Technologies Project. A team of Astrium engineers in Bremen led this project.

A third experiment investigated the orientation ability of fish larvae under microgravity. Specifically, the calcium uptake of inner ear stones of fish was measured. The motivation for this topic is given by finding causes for motion sickness. The DLR Space Agency supported scientists of the University of Stuttgart-Hohenheim to investigate cichlid fish under microgravity conditions provided by the ballistic rocket flight (10^{-4}g) as well as under more slightly reduced gravity conditions (0.01g) generated by an onboard centrifuge. A precursor experiment was already successfully performed by DLR on TEXUS 45 in 2008.

The anniversary flight of TEXUS 50 took place on 12 April 2013 from Esrange conducted by the DLR Space Agency. For the fifth time the EML module (Electromagnetic Levitator) was exploited. This facility (Fig. 2) enables containerless processing of metallic melts with low levitation forces. Under such conditions the thermophysical properties of an alloy melt and its solidification dynamics can precisely be studied. Data of the viscosity, surface tension, specific heat, electrical conductivity, and thermal expansion of reactive metallic melts can be contactless measured. The data are needed by the metallurgical industry for improved computer modelling to carry out more efficient casting processes. In ground experiments such data are not achievable with the required precision.

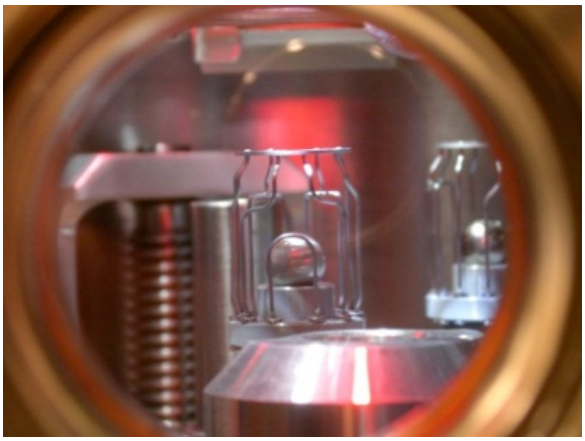

Figure 2: Two spherical metallic samples in the EML facility before processing. Credit: Astrium

The two EML experiments on TEXUS 50 were led by scientists of the DLR Institute of Materials Physics in Space. In the first one, the viscosity of a Zr-Ni alloy should be measured in a large temperature region. For the chosen alloy composition a lot of data exists from ground-based research, molecular dynamic simulations, and theory. The experiment on the TEXUS flight should offer reliable reference data. The second EML sample was a Ni-Al alloy, which crystallisation kinetics as function of undercooling of the melt should be studied. The chosen alloy reveals at a specific composition a very unusual behaviour. The dendritic growth velocity is decreasing with increasing undercooling. During two previous TEXUS missions several data points for the undercooling could be recorded. To further clarify the underlying physical mechanisms additional data at large undercooling temperatures of the melt were required. Unfortunately, due to a malfunction of the electronic subsystem of EML both experiments could not be processed as planned.

Two biological experiment modules were also flown on TEXUS 50. Scientists of the University of Freiburg investigated the molecular responses of plant cells upon changes in gravity. This reaction results in an immediate

change in the expression of specific genes. Therefore, such genes and signal networks should be identified.

Table 1: German microgravity experiments on sounding rockets TEXUS (June 2011 - June 2013)

Principal Investigator	Experiment	Mission
P. Behruzi Astrium	Validation of the LH_2 PMD Concept	TEXUS 48
P.Behruzi Astrium	Validation of the LOX PMD Concept	TEXUS 48
R. Hilbig Univ. Hohenheim	Calcium Biomineralisation of Fish Otholiths	TEXUS 48
A. Meyer DLR-MP, Cologne	Viscosity of a Zr-Ni Melt in Dependence on Temperature	TEXUS 50
D. Herlach DLR-MP Cologne	Dendrite Growth Velocity as Function of Undercooling in a Ni-Al Alloy	TEXUS 50
K. Palme Univ. Freiburg	Gravity-related Changes in Gene Network Organization	TEXUS 50
P. Galland W. Schmidt Univ. Marburg	Fast Gravitropic Primary Reactions in Fungi	TEXUS 50
J. Friedrich IISB, Erlangen	Critical Capture Velocity of SiC Particles During Solar Silicon Growth	TEXUS 51
G. Zimmermann ACCESS, Aachen	Columnar-to-Equiaxed Transition in Transparent Melt Solidification	TEXUS 51
R. Holzwarth T. W. Hänsch MPQ, Munich	Test of a Fiberlaser-based Optical-Frequency Comb	TEXUS 51
O. Ullrich Univ. Magdeburg	Signal Transduction in Cells of the Immune System	TEXUS 51

Seeds of the Arabidopsis thaliana **plant were exposed to microgravity as well as for comparison to a 1-g onboard centrifuge during the flight.**

In the second biological module the gravitropism of fungi was studied. This is the phenomenon how fungi sense the Earth gravitational field and orient themselves in space. The goal was the characterization of the nearly instantaneous gravitational reactions. These so-called primary responses were measured by applying the fast in-vivo spectroscopy. In addition to the microgravity data, a build-in centrifuge allowed for determining the gravity threshold of the primary responses by a stepwise variation of the acceleration level acting on the fungi.

Four research modules were accommodated on TEXUS 51. In the materials sciences experiment PARSIWAL the critical growth rate for particle incorporation during the directional solidification of so-called solar silicon is investigated. In the photovoltaics industry most of the solar cells are made from multicrystalline silicon, which is grown by directional solidification. During the growth process, the silicon melt is in contact with a crucible, which walls have to be coated with silicon nitride. In addition, the real furnace atmosphere contains carbon monoxide. The dissolution of the coating as well as the carbon bearing gas leads to the precipitation of silicon carbide and nitride. Such particles of up to several hundred micrometers in diameter lead to severe problems during the industrial sawing process for wafering the ingots. SiC particles can act as a shunt, circuiting parts of the solar cell. In industrial processing the incorporation of such particles needs to be avoided.

There is a critical growth velocity below which particles are pushed in front of the solid-liquid interface. In contrast to theoretical predictions, which state that only mm-sized particles are incorporated, the reality shows the presence of µm-sized particles in grown Si crystals. The microgravity experiment should therefore offer the opportunity to study the incorporation only as function of the growth rate and particle size. This experiment will help to improve the quality and efficiency of future solar cells.

Another materials sciences module called TRACE-3 is also aboard TEXUS 51. This facility was already flown on TEXUS 47 and 49. Scientists of the ACCESS group in Aachen investigated the columnar-to-equiaxed transition of the microstructure pattern during solidifying a transparent model alloy. This effect represents a transition from a directional (columnar) to a nondirectional (equiaxed) solidification morphology and determines optimization data of an industrial casting. Because the alloy melt is neither affected by sedimentation nor by convection in microgravity these undisturbed data can be used for calibration purposes and improvements of numerical models for industrial casting processes. The development of the solidification morphology of the melt is recorded by video cameras in addition to the measurement of the solidification velocity.

In the field of Fundamental Physics the FOKUS module serves as a technology demonstrator for the readiness

level of a so-called frequency comb for future sounding rocket or satellite missions. The corresponding technology was invented at the Max-Planck-Institute of Quantum Optics (MPQ) in 1999 and is now commercially available. T. W. Hänsch at MPQ was awarded the Nobel Prize for this development in 2005.

A frequency comb is a highly pulsed laser that can be used, for instance, for precision spectroscopy or when building extremely accurate atomic clocks. Its most helpful feature is to facilitate the measurement of optical frequencies, i. e. frequencies at which light waves are oscillating. Future applications in space could concern the study of trace gases in the atmosphere or the next generation atomic clocks for research and navigation. A team of MPQ and the German company MenloSystems developed a miniaturized and robust instrument (Fig. 3) for operation on the TEXUS mission. This approach was a major challenge because of the new technologies required to reduce volume, mass, and the electric power consumption significantly.

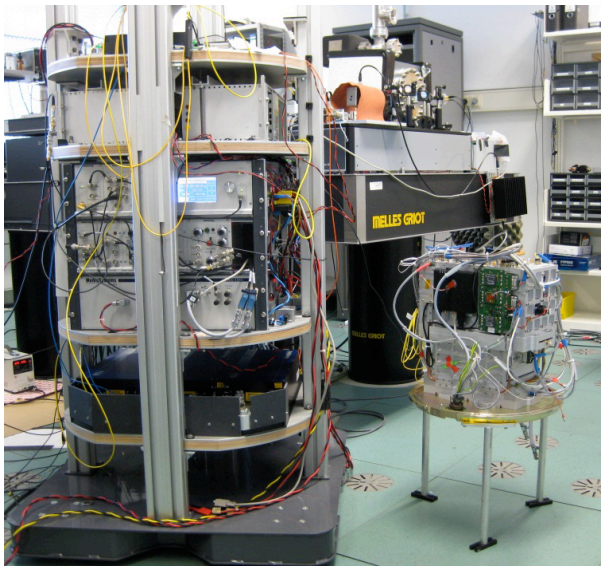

Figure 3: Comparison of the differences in size of an Optical Frequency Comb (OFC) payload. Left: OFC as used in Drop Tower Bremen experiments Right: FOKUS-OFC of TEXUS 51 rocket Credit: MPQ, MenloSystems

For the purpose of a frequency comparison with an atomic clock working in the optical domain a team of the Humboldt University, the Ferdinand-Braun-Institute in Berlin, and the University of Hamburg integrated a compact diode laser system in the FOKUS module. This innovation shall become the first spectroscopy test of Rb atoms in space.

In the fourth module of the TEXUS 51 payload the signal transduction in cells of the immune system shall be investigated by a team of the Universities of Magdeburg and Zurich. It is well known that the activity of cells of the immune system is severely affected in microgravity but the underlying molecular mechanisms are far from being understood. The objective of the experiment is to achieve a more systematic overview of gravity-related gene expressions in cells of the immune system. The hypothesis is to be tested that a specific kind of cell proteins is responsible for the interplay of gravity changes and cellular response.

TEXUS 51 was planned to be launched by DLR on 19 April 2013. According to a decision of the Swedish range safety board the flight had to be postponed during the ongoing campaign due to technical reasons of the launching facility at Esrange.

On 25 November 2012 the third sounding rocket mission MAPHEUS took place. This was a DLR internal R&D activity of the Institute of Materials Physics in Space, Cologne, in cooperation with DLR-MORABA and the Institute of Space Systems, Bremen. The 2-stage Nike-Improved Orion rocket reached an altitude of 140 km with a 100 kg scientific payload and offered more than 3 min of microgravity conditions. Four scientific modules were flown on MAPHEUS 3. The ATLAS-M module allowed precise measurements of liquid diffusion coefficients in Al-rich alloys. The demixing of Cu-Co melts at different compositions was studied in the DEMIX module. This process is of interest to industry to test current numerical models. The MEGRAMA module permitted studies on the dynamics of granular matter. Specifically, magnets were used to excite paramagnetic particles in a gas. The subsequent “cooling” by losing energy due to collisions with one another leads to compaction of the particles. This process was analysed by video recording. The rocket also carried a newly developed furnace that is transparent to X-rays. This approach enables the direct study of the changes in the composition and structure taking place in the interior of six melted metallic alloy samples.

4. EDUCATION

4.1 REXUS / BEXUS flights

REXUS and BEXUS (Rocket/Balloon EXperiments for University Students) are a German-Swedish student programme to acquire practical experience in real space projects on a regular basis. By annual calls for proposals the flight experiments are selected after evaluation by the agencies DLR and SNSB. The ESA education office cooperates with SNSB to fly other European payloads on the Swedish share. All campaigns are conducted by the launch provider EUROLAUNCH.

The sounding rocket missions REXUS 11, 12, 13, and 14 were performed during the last two years. Altogether

six payloads developed by German students were flown. The 1-stage Improved Orion rocket was used resulting in altitudes of about 85 km and providing 1 min µg.

On 19 March 2012 REXUS 12 was launched with the German modules SPACE and SOMID. In the first case a student team of the University of Braunschweig investigated the collision and aggregation of mm-sized dust particles. Such a process of mutual collisions between dust grains and dust aggregates is assumed to play an important role in the first phase of planet formations. The results were compared with a mathematical model that predicts the outcome of collisions between protoplanetary dust aggregates.

The SOMID module conducted sound measurements during the flight that stem from vibrations of the rocket structure. Such an individual behaviour can indicate defect structural elements. This technology experiment was prepared by students of the Universität der Bundeswehr, Munich. Due to experimental concept and quality of the results the team was awarded the Herman Oberth medal for graduate students at the IAF congress in 2012.

Two German payloads flew on REXUS 11 on 12 Nov. 2012. Students of the Aachen University of Applied Sciences tested the advanced isolation platform ADIOS. The purpose was to decouple microgravity sensitive experiments from vibrations induced by the rocket structure or other experimental equipment. This module is an advanced development of the VIBRADAMP experiment flown on REXUS 7 in 2007. In the second module CARU students of the Technical University in Dresden investigated the behaviour of two chemically reacting liquids driven by a capillarity effect.

An extendable experiment support bus called CERESS was successfully flown on REXUS 13 on 9 May 2013. This universal system for providing regulated electrical power, on board data handling, command and control of individual REXUS experiments, and the standard communication with the ground station was developed by students of the Technical University of Munich.

REXUS 14 was already launched on 7 May 2013. The German experiment SpaceSailors tested the deployment of a dragsail under microgravity. The increasing amount of space debris in low Earth orbit represents a major problem for current and future satellite missions. To develop new de-orbit technologies for satellites at the end of their active lifetime the aerodynamic drag of the atmosphere can be increased by using a thin foil sail at the spacecraft that causes an accelerated re-entry of the whole ensemble. The deployment mechanism (Fig. 4) of a 2 m^2 polyamide sail was successfully monitored by cameras during the microgravity phase. Students of the RWTH Aachen University developed this module.

Figure 4: Students are testing the SpaceSailors dragsail set-up on REXUS 14. Credit: RWTH Aachen

In the period from June 2011 until June 2013 the four balloon missions BEXUS 12, 13, 14, and 15 were conducted from Esrange. Typical float times of the balloons were 3-4 hours at an altitude of 25 km.

BEXUS 12 was launched on 27 September 2011 with the LITOS module. Students of University of Rostock as well as the University of Applied Sciences Hamburg investigated fine-scale turbulences in the stratosphere. The instrument allowed for high resolution wind turbulence soundings up to 35 km altitude. On BEXUS 13 students of the University of Kiel flew the RETA experiment and measured the radiation dose of charged and neutral particles in dependence on the altitude. The balloon was launched on 28 September 2011.

During this flight also a glider called VEXREDUS of students of the University of Stuttgart was tested. The aerodynamic behaviour of a vehicle with a shaped wing body was investigated in the low density atmospheric layers by dropping it from an altitude of 10 km.

BEXUS 14 and 15 were launched on September 24 and 25, 2012, respectively. Students of the University of Kiel measured with the MONSTA module the neutron flux in the atmosphere in dependence on the altitude. Such neutrons originate from galactic cosmic rays after interaction with the molecules and atoms of the Earth atmosphere. The solar spectral changes in layers of the atmosphere with various gas compositions and aerosols were measured on BEXUS 15. Students of the University of Oldenburg designed a spectrometer called SOLSPECTRE which is sensitive in the 300-950 nm range. For the second time, the VEXREDUS atmospheric glider was released from a balloon and autonomously glided back to the landing site.

5. HYPERSONIC FLIGHT TECHNOLOGY

5.1 SHEFEX / HIFIRE / SCRAMSPACE flights

The re-entry vehicle SHEFEX II (Sharp Edge Flight Experiment) was successfully launched from ARR on 22 June 2012. The main objective of this German flight experiment was to correlate numerical analysis data with real flight data in terms of aerodynamic effects and to test a new structural design concept of the thermal protection system. This included an active cooling of the ceramic heat shield by nitrogen gas. It was a further step towards the demonstration that sharp leading edge configurations are qualified for a hypersonic re-entry vehicle. Moreover, facetted thermal protection systems are also assumed to reduce the manufacturing and maintenance cost compared to traditional systems.

In contrast to the ballistic trajectory of the first re-entry mission in 2005 SHEFEX II (Fig. 5) demonstrated a hypersonic re-entry with a fully aerodynamically controlled vehicle. A powerful Brazilian rocket motor combination S40/S44 together with a suppressed trajectory of the burning second stage allowed an available experiment time of about 45 sec at a speed of Mach 10 to 11. Data from more than 300 sensors were recorded.

Figure 5: SHEFEX II re-entry vehicle in the integration hall at ARR. Credit: DLR-MORABA

Besides the facetted ceramic thermal protection system, ceramic based aerodynamic control elements (canards), also a new automatic flight control unit was implemented. Different inertial platforms and a star tracker sensor provided accurate data related to position and orientation of the vehicle. Altogether eight DLR entities cooperated in this project under the lead of the Institute of Structures and Design. External partners from Brazil, Australia, Germany, USA, and ESA were also involved.

Another project of collaboration to advance the science and technology of hypersonic flight is called HIFIRE (Hypersonic International Flight Research Experimentation). This project with altogether nine consecutive flight experiments and associated flight vehicles is led by US and Australian institutions. Its objective is to gather fundamental scientific data in the hypersonic flight regime that are difficult or impossible to obtain through ground testing alone. The project started in 2006 as a bilateral one and after that several German research institutes joined the collaboration.

DLR-MORABA provided the launch services at ARR for the HIFIRE 5 and 3 missions in April and September 2012. In September 2013 the HIFIRE 7 rocket will also be launched by MORABA as well as HIFIRE 4 in 2014.

For the HIFIRE 5 flight the DLR Institute of Structures and Design, Stuttgart, developed a ceramic fin (FinEx) to test the performance of new structures with sharp leading edges during hypersonic flight. The analysis of the thermal performance of this fin is conducted by in-depth mounted thermocouples protocolling temperatures during flight. In cooperation with the Institute for Space Systems, University of Stuttgart, the thermal behaviour is studied and numerically modeled. The DLR Institute of Aerodynamics and Flow Technology, Braunschweig, currently develops a numerical generation of a flush air data system for the hypersonic flight of HIFIRE 7.

The international project SCRAMSPACE (Scramjet-based Access-to-Space Systems) is led by the University of Queensland, Australia. The first launch will be provided by DLR-MORABA from ARR in September 2013. Its main objective is to test a vehicle powered by a supersonic combustion airbreathing engine. The DLR Institutes of Structures and Design, as well as of Aerodynamics and Flow Technology supply the control fins of the test vehicle and provide aerodynamic simulations.

6. CONCLUSION

As part of the German Space Programme sounding rockets are important for research of the middle Earth atmosphere, for medium-duration microgravity experiments, and for hypersonic flight technology tests. In the fields of Space Science and Earth Observation stratospheric balloons complement ground-based and satellite investigations. Both research tools are very beneficially for the education and training of students and young scientists. Also in the upcoming years the DLR Space Agency will provide its relevant support.

ACKNOWLEGEMENT

The authors thank all DLR colleagues, who contributed to the mentioned activities as well as the scientists from universities und other research entities in Germany for the provision of information material used in this paper. The activities were funded by the German Ministry of Economics and Technology, according to a resolution of the German parliament.

NORWEGIAN NATIONAL REPORT – ARCTIC ACCESS TO SPACE

Pål Brekke[(1)]

[(1)] *Norwegian Space Centre, Norway, paal.brekke@spacecentre.no*

ABSTRACT

Norway has long traditions as a space nation, much due to our northern latitude. Our space science activities are concentrated into relatively few areas. This concentration is necessary due to limited resources, both in funding and personnel. The main scientific activities are within Solar-terrestrial physics and cosmology.

The first field has been a priority since before the space age and is still the major priority. The usage of the ground infrastructure in Northern Norway and on Svalbard is essential in studying the middle and upper atmosphere and the interaction with the Sun. This includes the utilization of sounding rockets, both small and large, and ground based installations like radars, lidars and other optical instrumentation. The planned use of Svalbard as a launch site for large stratospheric balloons may allow the cosmology community access to our northern infrastructure. The solar physics community is also heavily involved in the HINODE and IRIS missions and Norway is supporting downlink of data via the Svalbard Station for these missions.

The sounding rocket program is in close collaboration with many countries like Germany, USA, France, Canada and Japan. Two scientific sounding rocket programs are currently being pursued: The ICI series (from Svalbard) and MaxiDusty (from Andøya). A series of scientific publications have recently appeared from the ECOMA campaign a few years ago.

A significant improvement of today's polar and ionospheric research infrastructure in Northern Norway and Svalbard has recently been put on the ESFRI roadmap for European research infrastructure through the SIOS and EISCAT 3D initiatives. The Norwegian government has recently decided to upgrade the VLBI facilities at Svalbard.

1. HISTORIC PERSPECTIVES

Norway has a long tradition as a space nation, in no small measure due to its northern position on the globe. Kristian Birkeland's famous Terrella experiment in 1896 in which he created synthetic northern lights can be seen as the start of modern space activities. He understood that it was the sun that caused the aurora borealis and that particles from the sun interact with Earth's magnetic field and atmosphere. Thus the aurora and solar research led to the establishment of the rocket range on the island of Andøya in North Norway, where the first Norwegian research rocket was launched in 1962. Researchers from numerous countries now utilize this rocket range in their studies of the northern lights and the Earth's atmosphere and the facility is NASA´s most important launch facility for sounding rockets outside USA. More than 1000 rockets have been launched since 1962, the biggest being NASA's 15 meter long Black Brant XII, with an apogee of up to 1500 km.

The solar observatory at Harestua north of Oslo was opened in 1957 and included several optical and radio telescopes. One telescope was dedicated to tracking satellites passing across the sky. These observations were made on a request from the US Air Force and this was Norway's first connection to satellites.

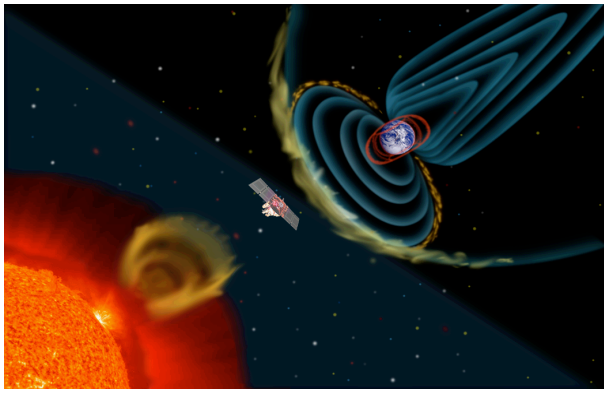

Figure 1: The Sun-Earth connection has a long tradition in Norway (S.Hill/NASA).

Norwegian scientists participated in the solar telescope HRTS (High Resolution Telescope and Spectrograph) that flew on the space shuttle Challenger in 1985 and several times on sounding rockets. More recently they played a central role in the successful SOHO mission - a large satellite based solar observatory including 12 different telescopes and instruments launched in 1995, which is still operating. SOHO is a collaboration between ESA and NASA in which Norwegian industry provided equipment and services to the tune of 80 million Norwegian kroner.

Scientists at the Norwegian Defence Research Establishment (FFI) participated on Spacelab 1 flying

Proc. '21st ESA Symposium European Rocket & Balloon Programmes and Related Research', 9–13 June 2013, Thun, Switzerland (ESA SP-721, October 2013)

onboard the space shuttle Challenger in 1983. They built the electron accelerator, which produced artificial aurora in space. Later Norwegian institutes participated in the European Space Agency's Cluster mission, a «space fleet» of four identical satellites flying in formation through the Earth's magnetosphere. The University of Oslo (UiO), The University of Bergen (UiB) and NDRE all delivered electronics and parts to three different instruments on Cluster.

NASA's Polar satellite, launched in 1996, studied the aurora from space. UiB delivered important electronics to the PIXIE instrument taking images of the X-rays from the aurora. Scientists at UiB were also involved in data analysis and recently their results made the front page of the journal Nature.

2. OVERALL SPACE SCIENCE PRIORITIES

Due to its size and the resulting limited resources, Norway needs to concentrate efforts to compete with other space nations. Space related science in Norway can be divided into three major fields: research OF space, research FROM space and research IN space.

- "OF space"
  - Solar-Terrestrial physics (about 80%)
  - Cosmology
- "FROM space"
  - Ocean monitoring
  - Polar and climate research
  - Science leading to needed applications
- "IN space"
  - Plant physiology
  - Human psychology
  - Technology demonstrators

In this article the main focus is science OF space and the other fields will just be mentioned briefly. Science OF space includes space physics with the emphasis on the magnetospheric/-ionospheric physics and processes in the neutral middle atmosphere at high latitudes. Solar physics and cosmology and life sciences with a focus on plant physiology are also included.

Norway is participating in ESAs Space Situational Awareness program. The Norwegian Mapping Autority is contributing to monitoring space weather effects on the ionosphere and degradation of positioning systems. Tromsø Geophysical Observatory is monitoring deviations in the Earth's magnetic field. Kongsberg Spacetec is involved in the Phase A Study for Space Weather part of the SSA program. They have a contract related to the architectural design of the Space Weather system, with responsibilities related to ground based sensors, services and the overall system architectural design.

3. SOUNDING ROCKET PROGRAM

3.1 Andøya Rocket Range

Andøya Rocket Range (ARR) provides sounding rocket and balloon operations from Norway. ARR was established in the 1960s and more than a thousand sounding rockets have been launched from Andøya since the first lift-off in 1962. The sophisticated infrastructure includes a cluster of ground-based state-of-the-art instruments. The Norwegian Institute for Air Research (NILU), the Institute of Atmospheric Physics (IAP Kühlungsborn), ARR, the Norwegian Defence Research Establishment (FFI), University of Oslo, and eight other science groups from outside Norway run their instruments at ALOMAR (Arctic Lidar Observatory for Middle Atmosphere Research) and contribute to the running costs of the observatory. The instruments include four lidars, four atmospheric radars, and a number of passive instruments, such as an imaging riometer, all-sky camera, several spectrometers, microwave radiometers, and others. ARR has operated the observatory since 1994.

Figure 2. Andøya Rocket Range (ARS).

ARR offers the scientists the opportunity for in-depth studies of the Arctic atmosphere and ionosphere by both short- and long-term monitoring techniques which can be combined with in-situ measurements from rocket and/or balloons. The User Science Operator Centre (USOC) provides real-time monitoring of scientific parameters and other phenomena during operational campaigns. The latest contribution to the infrastructure at ARR is the building of a new powerful VHF-radar consisting of 433 Yagi antennas and Unmanned Aircraft System (UAS) operations. The high latitude location of ARR (69^{0}N), north of the Arctic Circle, is favourable because it is close to the southern boundary of the Polar Vortex and lies within the nightside auroral oval. The

infrastructure gives the scientists the opportunity to exploit these advantages; the physics, chemistry and dynamics in all atmospheric layers can be investigated, thus both climate change and space weather parameters can be monitored.

In the context of Space Weather Services, there are several relevant ground-based instruments located at Andøya. In particular, the Imaging riometer (IRIS) is important because it can monitor the ionosphere and its response to particle precipitation. An All-sky camera will monitor the aurora and the cluster of radars have the capability to monitor the mesosphere and lower ionosphere and provide information on electron density, meteors, turbulence, wind field and tides.

The ALOMAR observatory provides measurements of the troposphere to the lower thermosphere and includes profiles of temperature, total density, wind speed and direction, certain trace constituents such as Na and O_3, atmospheric gravity waves and their momentum flux. Several of the scientific parameters that are monitored play an important role regarding the space weather. ARR also has the knowledge and expertise to build sounding rocket payloads, which can be used to study parameters relevant to the understanding of space weather phenomena.

Sounding rockets could either be launched from Ny Ålesund (78.92°N, 11.93°E) on Svalbard (SVALRAK) or at Andøya (69.28°N, 16.01°E). At Andøya two launchers are capable of launching large rockets such as Black Brant XII up to more than 1600 km in altitude. At Ny Ålesund the launcher can launch rockets to altitudes above 1100 km while from Longyearbyen (78.25°N, 15.47°E) long duration balloons are launched up to altitudes between 30 and 40 km.

One recent extensive rocket campaign was the ECOMA programme. The ECOMA project (Existence and Charge state Of Meteoric smoke particles in the middle Atmosphere) aims to measure in-situ the number densities of both charged and uncharged aerosol particles in the mesosphere and lower thermosphere. The experiment a collaboration between IAP Kühlungsborn in Germany and the Defence Research Establishment in Norway. The ECOMA campaigns in 2006, 2008 and 2010 included important ground-based contributions using many ALOMAR instruments and EISCAT and sometimes even from satellites. An MoU between University of Oslo, University of Tromsø, IAP and DLR was signed during the 21st ESA PAC meeting in Thun to enhance the Norway-German collaboration on middle atmospheric research. The collaboration is motivated by the desire to unravel the role of the middle atmosphere in coupling space to Earth, likely hidden in multi-scale coupled processes and chemistry. Sounding rockets are the only feasible approach to study the small scale processes.

3.2 ICI Rocket Programme

The ICI-series of rockets is a space weather mission. There is an increasing demand for scintillation forecasts in the polar caps. For Norway this is due to an increasing amount of activities in the high north relying on communication and high precision GNSS signals (offshore and opening of the northern sea route). With the ICI-series of rockets, the University of Oslo aims to study instability processes in connection with auroras, high speed plasma flow channels and polar cap patches, and in particular to quantify growth rates and to characterize electron plasma structures associated with these instabilities. The ICI-rocket program delivers building blocks for space weather scintillation models.

The ICI rocket program takes advantage of the total Hotel payload services developed Andøya Rocket Range where the scientists only take care of preparing their own instruments and tell when science conditions are met for launch. This is cost effective approach that increases the chance to revive a sustainable Norwegian sounding rocket program. The ICI payload is optimised to perform high resolution measurements of the electron plasma structures, down to meter scale, and it is equipped with an electron particle spectrometer that can resolve the thickness of magnetic field-aligned electron beams down to ~meter resolution, i.e. down to an electron gyro radius which is thinnest thinkable structure which has not been measured before!

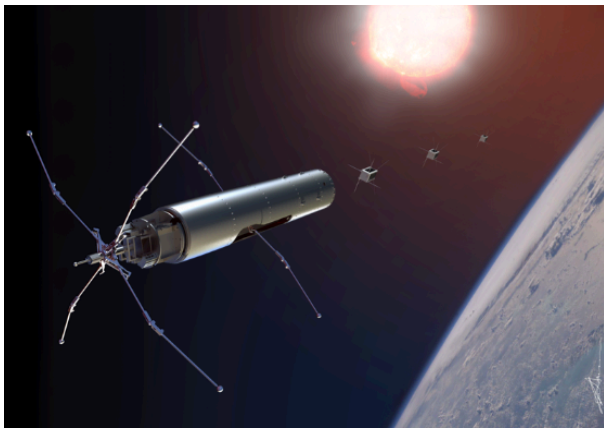

Figure 3. Artist concept of future ICI missions with a combination of rocket and release of 3 Cubesat format sub-payloads (T. Abrahamsen, ARS)

ICI-2 was successfully launched from Ny-Ålesund in 5 December, 2008. It intersected 3 regions of HF radar backscatter targets. With UiO's new concept Langmuir probe system it measured absolute electron density at 5.7 kHz resolution, and for the first time it resolved decametre HF backscatter irregularities.

ICI-3 was launched from Ny-Ålesund in December 2011. The ICI-3 payload consisted of several instruments with contributions from University of Oslo (UiO), Japan Aerospace Exploration Agency/Institute of Space and Astronautical Science (ISAS/JAXA) and Laboratoire de Physique des Plasmas (LPP). University of Alberta, Canada contributes to the payload instrumentation of ICI-4 that will be launched in December 2013As illustrated in Figure 3 the ICI-5 rocket planned for December 2016 will include three or more sub payloads.

3.3 MAXIDUSTY Rocket Programme.

The aim of the MAXIDUSTY (MXD) programme at the University of Tromsø, in cooperation with the University of Oslo, is to enhance our understanding of key physical and chemical processes in the Earth's mesosphere and of its coupling to other atmospheric regions. The project represent a continuation of the Norwegian rocket programme on the mesosphere, including the rocket projects TURBO, TURBO/DUSTY, MINIDUSTY, MIDAS, ROMA, and ECOMA. The MXD project has a particularly strong emphasis on the investigation of dust and aerosol particles, their structure and composition, compared to earlier mesosphere projects. The investigations will involve the launch of rocket payloads from Andøya Rocket Range, Norway. The first payload MXD-I is planned to be launched on July 2014. This payload will include several recently developed dust probes and plasma probes. It will also carry a new dust probe ICON, a mass spectrometer which will mass analyze the evaporation gas from captured icy NLC/PMSE cloud particles.

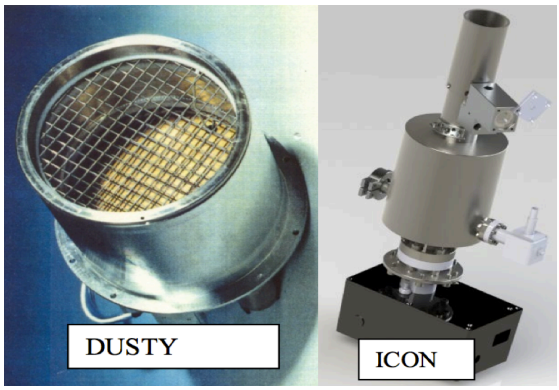

Figure 4. From left to right we show the dust probe DUSTY which in 1994 for the first time detected mesospheric charged dust particles. The mass spectrometer ICON is intended to mass analyze the vapour from the ice of the NLC particles. ICON is planned to be launched for the first time on MXD-I in 2014.

The launch will be supported by the EISCAT UHF and VHF radars, the EISCAT Heating Facility, and the MORRO 56 MHz radar at the EISCAT site, by all relevant ground-based instrumentation at Andøya Rocket Range, and by satellite observations. The MXD payloads will also carry daughter payloads to be ejected in the mesosphere to conduct 3D measurements of vital parameters such as the plasma density and possibly the dust charge density. There will also be instrument contributions from University of Colorado (Boulder), University of Stockholm (MISU) and Technical University Graz.

The major goals of the MAXIDUSTY investigations are to reveal the chemical content of the icy noctilucent cloud/polar mesospheric cloud (NLC/PMC) particles by: in situ mass spectroscopy, weighing collision fragments from impacting ice particles, find the secondary charging effects, mass analyze the incoming primary dust particles, and analyze smoke particles brought back by a "Meteoric Smoke Sampler" (MESS) probe on the planned MXD-II payload. The MESS probe, will collect many NLC/PMSE particles, each of which should contain a large number of meteoric smoke particles which will remain in the collection chamber after the NLC/PMSE ice evaporates. MXD-II is planned to be recovered.

4. AURORA RESEARCH

The old Aurora Station in Adventdalen at Svalbard was built in 1978 but was in recent years outdated and hampered by increasing light pollution from Longyearbyen. The new Kjell Henriksen Observatory was opened in 2008 and is the largest of its kind with a gross total area of approximately 700 square meters, which includes a service section of approximately 200 square meters floor space.

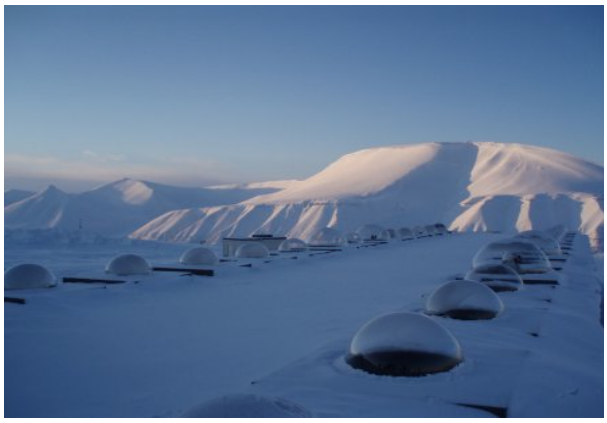

Figure 5. Kjell Henriksen Observatory at Svalbard was opened in 2008 (KHO

The instrument section contains 30 instrument rooms with domes. Even prior to the opening the observatory was fully operative with 24 instruments from different groups around the world.

In addition, prior to the opening, KHO was used as scientific command centre for the SCIFER 2 (Sounding of the Cusp Ion Fountain Energization Region) rocket campaign. The main task of KHO is in general to study processes associated with the Magnetospheric cusp and its connection to the Sun-Earth environment. The dayside aurora gives an open window to processes on the Sun and how they interact with our upper atmosphere. Studies of phenomena such as airglow and aurora are therefore essential for understanding of how energy is transported into the Magnetospheric Clefts down the whole vertical column of the atmosphere, and how it on a larger scale contributes to the climate.

Each instrument at KHO has its own scientific task and objective listed at the observatory's own home page: http://kho.unis.no.

5. GEOMAGNETIC RESEARCH

Tromsø Geophysical Observatory (TGO), University of Tromsø, is operating a network of 14 magnetometers in Norway and Norwegian areas in the Arctic [picture from Hopen magnetometer attached]. Three of them - Bear Island, Tromsø and Dombås - are geomagnetic observatories, the remaining are stable variometers with less accurate absolute calibration aimed to serve ionosphere physics and monitoring magnetic field variations during directional drilling operation by the oil industry at the Norwegian continental shelf. Most of the stations are included in the IMAGE database.

Near real time data can be found at http://flux.phys.uit.no/geomag.html where they are displayed along with corresponding data from Finland, Denmark, Greenland, Alaska and Russia. TGO is also an Expert Center withing the ESAs Space Situational Awareness (SSA).

Additionally, TGO is operating an ionsonde near Tromsø, meteoradars (jointly with Japanese institutions) at Tromsø, Bear Island and Longyearbyen, a HF radar (with Japan and Canada) at Tromsø, the SOUSY radar and an imaging riometer (with Denmark) in Longyearbyen.

SuperMAG is a worldwide collaboration of organizations and national agencies that currently operate more than 300 ground based magnetometers. The purpose is to help scientists, teachers, students and the general public easy access to measurements of variations in the Earth's magnetic field. Through the ESA PRODEX programme, a mirror server for the global SuperMAG network of magnetometer data has been established in Bergen.

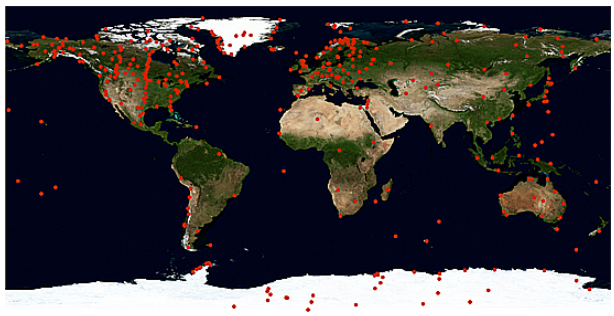

Figure 6. SuperMag – The Global Ground Magnetometer Initiative is located at the University of Bergen, Norway.

6. BIRKELAND CENTRE FOR SPACE SCIENCE

The Birkeland Centre for Space Science (BCSS) is a centre of excellence that was established in 2012 to tackle a broad range of scientific topics. It is located at the University of Bergen in collaboration with NTNU and UNIS. It will strengthen the international position of the Norwegian space physics community by making significant progress on compelling science questions. The primary objective for the centre is to understand *How is the Earth coupled to Space?* This includes understanding when and why the aurora in the two hemispheres are asymmetric, better understanding of the ionosphere, the effects of particle precipitation on the atmospheric system, and the role of energetic particles from thunderstorms in geospace.

BCSS will maximize the utilization of existing Norwegian infrastructure at Svalbard, Northern Norway as well as our large investments in Cluster and ASIM. It will also strengthen and expand UiB's capability to develop and build state-of-the-art instrumentation for space. Furthermore it will contribute to educate and position the next generation of Norwegian space physics scientists through an ambitious educational and public outreach components.

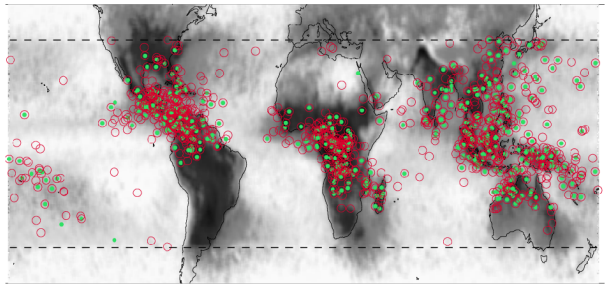

Fig. 7. *The new map of TGFs after re-searching the RHESSI data: 3 times more TGFs (Gjesteland et al., 2012)*

7. GEODETIC RESEARCH

The Space Geodetic Research Facility of the Norwegian Mapping Authority in Ny Ålesund, Svalbard, is part of an international network of stations, which is crucial for society's satellite-based infrastructure and provides the basis for accurate climate monitoring in the far north. The observatory is the northernmost facility of its kind, and maps movements in the Earth's surface, planetary rotation, and the Earth's position in space. The Norwegian government appropriated funds for a new geodetic observatory with new technology in its revised national planning budget for 2012. The new observatory is due to be completed in 2018.

Figure 8. The VLBI antenna in Ny Ålesund, Svalbard.

The upgraded observatory will combine several geodetic measuring techniques - very long baseline interferometry (VLBI), satellite laser ranging (SLR), global navigation satellite systems (GNSS) – including GPS – and doppler orbitography and radio positioning integrated by satellite (Doris), based on the standard set by the global geodetic network. Norway's Uninett group is preparing to lay fibreoptic cables along the seabed between Longyearbyen and Ny-Ålesund. This link will be important for the research community at the latter site. Plans call for cable to be laid in the summer of 2014. With this fibreoptic link, the Norwegian Mapping Authority will be able to transmit real time data from its new observatory to such recipients as NASA in the USA and the international geodetic research network.

8. SOLAR RESEARCH

The solar research environment blossomed early in Norway and today Norway has one of the strongest solar research groups in the world. Today observations of the sun are carried out from large international observatories as well as from satellites. Norway is currently involved in the SOHO mission and the Japanese solar satellite Hinode. Data from the satellite are downloaded at the Svalbard archipelago and a European data centre at the University of Oslo is processing the raw material making it accessible for the entire European science community.

In addition Norwegian scientist are involved in NASA's Solar Dynamics Observatory (SDO) launched in 2010. SDO is a super-telescope taking images with four times higher resolution than HD-TV quality every 10 seconds, transmitting 1500 Gb of data every single day. The NASA solar mission IRIS (Interface Region Imaging Spectrograph) was launched in June 2013 with a significant Norwegian contribution in modeling of the solar atmosphere as well as providing downlink of data via the Svalbard Satellite Station.

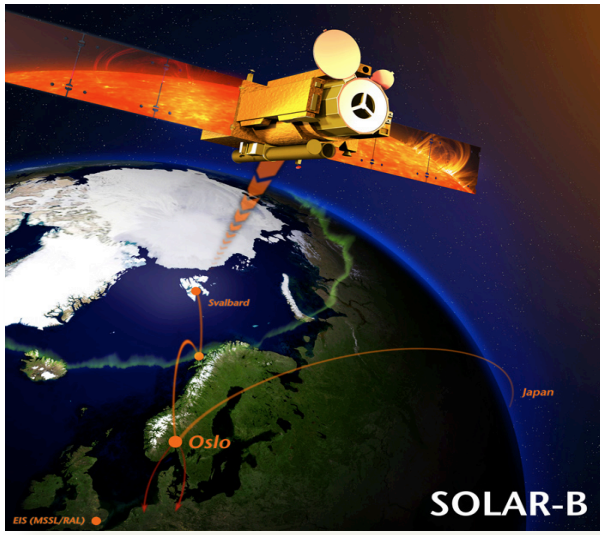

Figure 9. The data from HINODE is downloaded to Svalbard and Troll (T. Abrahamsen).

What has become increasingly clear is that a proper utilization of high quality satellite data requires extensive numerical modelling. This is needed in order to make the connection between observed quantities such as spectral lines and the physical conditions in the radiating atmosphere. The solar physics group in Norway has built up a considerable expertise in this area and is now, as one of the first groups in the world, producing three-dimensional models of the solar atmosphere, from the convection zone to the corona. These models include enough of the relevant physics so that synthetic observations from them can be compared directly with observations.

9. COSMOLOGY AND ASTRONOMY

A small cosmology group has existed at the University of Oslo since the 1960's, but in the last decade it has grown to become an internationally leading research group. Presently the most important research subject is the Cosmic Microwave Background, the group

emphasizes the closest interaction between analysis of data from experiments and fundamental theory to further the understanding of the Universe.

The last decade has seen an enormous growth in cosmology, making it a leading branch of both astronomy and physics. While cosmology until one or two decades ago was a data-starved science, the opposite is the case today. The wealth of new data coming out of new large space- and ground-based experiments has made cosmology a data-rich science where one poses detailed questions and where simplified models are no longer sufficient. Already with NASA's Wilkinson Microwave Anisotropy Probe (WMAP), large classes of cosmological models are today ruled out, and a concordance model has been established.

The cosmology group concentrates its activities on The cosmology group concentrates its activities on studies of the cosmic microwave background through ESA's Planck mission and until recently the ground based QUIET experiment, and theoretical cosmology, concentrating on inflationary physics and on models that can explain the mysterious observed acceleration of the expansion of the Universe. The group's studies of large-scale anisotropies in the cosmic microwave background have caught world-wide attention. About 20 people at the University of Oslo have been involved in analyzing the first results from Planck. The initial cosmological results from Planck were released in May 2013, and the UiO group had contributed strongly to separation of components, estimation of power spectrum, measurements of gaussianity of the fluctuations and of large-scale anisotropies.

10. SPACE EXPLORATION

Svalbard offers a unique variety of geological sites in an Arctic dessert environment perfectly suited for planetary exploration. Mars analogue activities have been ongoing since 1997 when rocks in the Bockfjord Volcanic Complex (BVC) were discovered to be identical to the Martian meteorite ALH84001. The Arctic Mars Analog Svalbard Expedition project (AMASE) was initiated by Norway in 2003 and is funded by ESA and NASA to develop and test instruments onboard "Search for Life" missions to Mars including Mars Science Laboratory, ExoMars and Mars Sample Return. AMASE also provides training for mission scientists and engineers as well as field-testing of astronaut suites and robotic platforms and plays an important role in fostering collaboration between ESA and NASA teams.

Fig. 10. NASA's Mars rover and space suits being tested at Svalbard (AMASE)

The Norwegian Defence Research Establishment (FFI) is developing a ground penetrating radar (WISDOM) as part of the ExoMars payload. WISDOM will chart ice, water and rocks to a depth of three meters on Mars and is being field tested on AMASE. FFI was also responsible for the CAPS instrument designed to study plasma processes onboard the Cassini mission. The University of Bergen delivered components to the SIR-2 infrared spectrometer on the Indian Chandrayaan-1 lunar mission.

11. INTERNATIONAL SPACE STATION

The International Space Station (ISS) also contains a mini-greenhouse (EMCS - European Modular Cultivation System) with a number of plant cultivation chambers developed by Prototech in Bergen in collaboration with the Plant Biocentre at the Norwegian University of Technology and Sciences (NTNU) in Trondheim. They cost 500,000 NOK apiece and can safely be said to be Norway's most expensive flowerpots. All experiments in this mini-greenhouse are controlled and operated from the Norwegian User Support and Operation Centre at the Plant Biocentre. Everything - water, nutrients, light, temperature - are controlled by commands from this center. The first Norwegian experiment on the ISS called MULTIGEN-1 was performed in 2007 and the scientists are very satisfied with the results. One of the major results obtained solved a problem that has been a challenge since Charles Darwin asked the question about gravity and plant movements as they grow; Are circumnutations in plants dependent on gravity or will internal control mechanisms in plants also participate? The results from the ISS show clearly that both factors are required.

The next Norwegian plant experiment (MULTIGEN-2) from the same scientific Project Team has been

postponed due to the phasing out of the NASA Space Shuttle. The capacity of science sample return from ISS to Earth is therefore a limiting factor for performing experiments like MULTIGEN-2. In a new ESA contract between the Project Team and an industrial partner (Prototech a.s., Bergen, Norway) an alternative approach for the sample return from ISS has been implemented as a consequence of this. Using the same model plant (*Arabidopsis thaliana*) as for MULTIGEN-1, gene expression (microarray) under microgravity is now in focus but the total mass of plant sample, which originally was planned to return, will now be reduced to a minimum.

Figure 11. The Norwegian User and Operation Centre for plant research on the International Space Station.

The Oslo branch of the research and technology group SINTEF has developed the Multi-Comcponent Trace Gas Monitor (ANITA) to monitor air quality on the International Space Station (ISS). The instrument was launched in 2007 on the space shuttle to detect whether the air might contain gases potentially hazardous to the astronauts. The instrument can trace gasses no other previous systems on ISS could detect. Only ANITA detected a leak in the cooling system in 2007.

The University of Bergen is one of the key participants in the ASIM instrument currently being built for the International Space Station for observation of transient effects such as sprites, elves and blue jets. ASIM (Atmosphere- Space Interaction Monitor) is scheduled for launched in 2016/2017.

12. ACCESS TO SATELLITE DATA

On Svalbard, Norway has the world's biggest station for satellites in polar orbits. The satellite station is operated by Kongsberg Satellite Services (KSAT), which also has antennae in Tromsø, Grimstad and at the Troll Station in Antarctica. KSAT is expanding by building antennas in Dubai, Singapore, Bangalore (India), and South Africa. This makes them the world leader in retrieval of satellite data from polar orbiting satellites. This includes ESA, NASA and JAXA science missions and ensures easy access to high quality science data for Norwegian scientists.

In 2004 a 20 Gbit/s capacity fiber-optical highway between Svalbard and the Norwegian mainland was inaugurated. The cable is owned by Norsk Romsenter Eiendom AS and was built as a cooperation between NASA and NOAA, the Norwegian Space Centre and Kongsberg Satellite Services. The cable also makes it easy for scientists around the world to remotely operate science instruments at Svalbard and get easy access to data in real time.

Norway is therefore a big operational user of remote sensing data from satellites, and Norwegian scientists are involved in many of ESA's Explorer satellites for earth observation research. We will not go into the details in this article.

12.1. Ship Detection from Space

In July 2010 Norway's first satellite for ship traffic monitoring was launched. AISSat-1 has been a big success, and a copy AISSat-2 is being launced in 2013. A Norwegian built AIS receiver has also been placed on the ISS and is being used for anti-piracy operations in the Indian Ocean. Combined with the oil spill detection from radar satellites, the space based AIS system is a unique system to detect and identify illegal release of oil or illegal fishing and even support monitoring of pirates. The AISSat-1 was reprogrammed to support the Japanese government in monitoring ships around their coast in the aftermath of the devastating earthquake and tsunami.

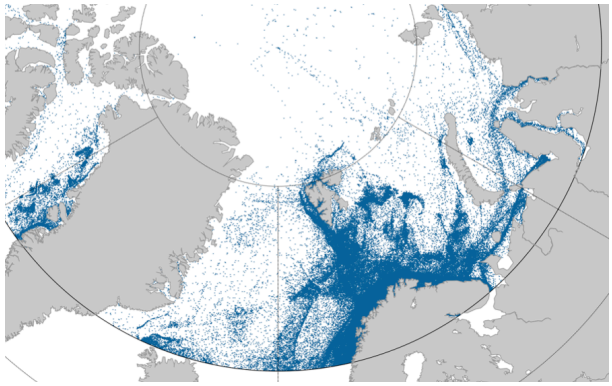

Figure 12. AISSat-1 has for the first time monitored all ship traffic in the Arctic and it is obvious that mots traffic is within Norwegian territories.

Norway is now building a small satellite called NORSAT-1 to be launched in 2015. The payload will consist of a new generation Solar Total Irradiance monitor delivered by PMOC/WRC in Switzerland and will provide important data for the Sun-climate

connection. A Mini-Langmuir probe from the University of Oslo will provide space weather measurements while a new AIS receiver will be tested out.

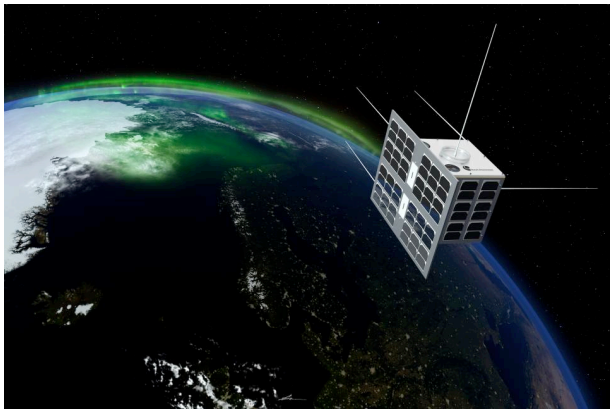

Figure 13. NORSAT-1 will be launched in 2015 and will provide Sun-Earth connection observations as well monitoring ship traffic.

13. EDUCATION AND PUBLIC OUTREACH

NAROM (Norwegian Centre for Space-related Education), partly funded by the Norwegian Government, offers educational programmes for teachers and students at many different levels to promote appreciation for the benefits of space activities, to facilitate recruitment in the space industry, and to stimulate an interest in science in general.
NAROM is co-located with Andøya Rocket Range (ARR). The close proximity to the facilities and personnel at ARR provides important advantages with respect to educational activities, and NAROM uses the unique technical facilities at ARR to provide an exciting educational experience. The European Space Educational Resource Office *ESERO in Norway* is established at ARR by NAROM . The office provides five different courses for teachers in upper secondary schools.

13.1 Student Satellite Program

NSC is actively sponsoring a student satellite programme i Norway, which is implemented together with NAROM and ARR. Currently three student satellites are under construction at the universities in Oslo and Trondheim and at Narvik University College. Almost 100 students are involved in this program. The aim is to plan, build and launch nano satellites built by students, the first one hopefully in 2012.

13.2 CaNoRock – a Canadian Norwegian Student Exchange & Rocket Programme

The Canada-Norway Student Sounding Rocket (CaNoRock) exchange program is a partnership between the Universities of Alberta, Calgary and Saskatchewan, the University of Oslo, University of Tromsø, Andøya Rocket Range and NAROM (Norwegian Center for Space Related Education) in Norway. The University of Bergen and University Centre in Svalbard (UNIS) in Norway are currently working to be included in the program. To further enhance the educational benefits and cooperation between students in the two countries a student satellite program – CaNoSat will be developed to run in parallel and coordinated with the sounding rocket activities. Funding for the necessary student activities like travel and subsistence will be covered by CaNoRock STEP, funded by Norwegian Centre for International Cooperation in Education (SIU) for 2012-2016.

13.3 European Space Camp

Each year a group of students (17-19 years old) meet at Andøya Rocket Range to learn more about the Sun, the atmosphere, and the aurora. After a week they are among the few that can call themselves real rocket scientists.

The goal of Space Camp is to let the students take part in real science. They get to work with the same tools as real rocket scientists. Tutors from Norway, the European Space Agency (ESA), and NASA guide the students while they construct their own instruments to take measurements in the atmosphere. The highlight is launching their instruments on a self-built rocket.

Figure14: European Space Camp at Andøya

14.4 Public Outreach

The Norwegian Space Centre is focusing on outreach and media activities to increase the interest in science and technology among young people and the general audience.

Our web site, romsenter.no and the English "light version" spacecentre.no, is our main access to the target groups. In 2010 there were 220 000 unique visitors to the sites. We publish stories on astronomy, industrial policy, ESA activities and space activities in general, all with a Norwegian hook or commented by the staff at the space centre.

This pays off in media, last year the NSC was cited more than 1000 times in papers, magazines, websites, TV and radio.

In 2009 we launched a Facebook page to inform students about ongoing activities, courses and funding. The Twitter feed is followed by quite a few journalists and is an efficient way of communicating with media.

Presentations for schools, students and the general public are a priority as well. The staff of 32 employees makes more than 200 presentations a year.

14. THE NORWEGIAN SPACE CENTRE

The Norwegian Space Centre (NSC) is a government agency under the Ministry of Trade and Industry. NSC works according to five main objectives. These are to contribute to growth in national, high-tech industry, meet societal needs, ensure that Norway plays a leading role in the global market for space-related ground structure, contribute to Norwegian research attaining prominent international positions in space research and ensure that the public is well aware of Norwegian space activities. In the 2010 Norwegian national budget, NOK 775 million (€93.3 million) was allocated for space activities.

Membership in the European Space Agency (ESA) is instrumental in attaining these objectives. About 85% of the Ministry of Trade and Industry's appropriations for the Norwegian Space Centre are for ESA participation. The Norwegian Space Centre oversees the Norwegian interests in ESA and coordinates national space activities.

Norway is also participating in ESA´s Space Situational Awareness program with a strong focus on the space weather elements. In particular to utilize, and further develop the arctic space infrastructure.

14.1 Organization of space activities.

Norwegian Space Centre and the Research Council in Norway are reporting to two different ministries. There also is a clear division of responsibility, as the ESA membership is funded through NSC and Ph.D and Post-doc grants are funded through RCN. Sounding rocket projects typically receive funding from NSC for the rocket itself, and funding from RCN for the scientific instrument and analysis.

SWEDISH SPACE ACTIVITIES – AN OVERVIEW WITH A FOCUS ON BALLOONS AND ROCKETS

Kristine Dannenberg

Swedish National Space Board, Box 4006, SE 171 04 Solna, Sweden
Email: dannenberg@snsb.se

ABSTRACT

The paper gives a brief overview of Swedish space activities with a focus on balloon and rocket projects, within the Swedish national balloon and rocket programme and/or within international collaboration; launched or scheduled for launch in the near future from Esrange Space Center. Several on-going national balloon and rocket projects are described in brief. Sweden is also a major player in sounding rocket activities within the ESA Elips programme as provider of launch services and developer of modules for microgravity experiments. Another important activity, described below, is the student programme REXUS / BEXUS, carried out within the framework of bilateral agreement between DLR and SNSB, in collaboration with ESA. It should also be noted that a considerable number of other balloons and rockets have been launched from Esrange Space Center during the reporting period. The present paper focuses, however, on the projects led by Swedish Principal Investigators and activities with a major involvement of Swedish scientists and engineers.

INTRODUCTION

Swedish space research comprises many different fields, such as astronomy, space physics, astrobiology, Earth observation, atmospheric research, space physiology, space radiation and microgravity research. The major part of Swedish space research activities is supported by SNSB (Swedish National Space Board), within its national programme for space research and Earth observation. The annual budget available for these activities is around 10 M€, enabling support to approximately 65 research projects at Swedish universities and research institutes. Most projects utilise flights offered by the European Space Agency (ESA) programmes and/or data provided by ESA satellites and other international space missions.

This year, a dedicated national programme for balloon and rocket programmes was established in order to allow Swedish scientists to utilise balloon and rocket flights from Esrange on regular basis. National activities within this field are of high value as they provide unique opportunity of combining basic science with instrument development as well as possibility to use a custom-made platform for the experiment. In addition, the smaller scale of the balloon and rocket projects allows close cooperation between the research groups, technicians and industry. Another advantage is the fact that the time-frame from the start of the project to publishing the results is relatively short, which is especially attractive for young researchers and PhD students.

The establishment of the new national balloon and rocket programme will allow issuing regular calls for balloon and rocket projects. Swedish national balloon and rocket programme programme is also open for projects carried out in international collaboration.

The balloons and rockets are launched from Esrange Space Center, a unique Swedish and European facility, situated above the polar circle 40 km East of Kiruna at lat. 67° 53'N, long. 21° 04'E, with a rocket impact area of 5600 km^2. Landing sites for short duration balloons include northern Scandinavia whereas long duration balloons usually land in northwest Canada.

Figure 1. Esrange Space Center in early summer (photo: Kristine Dannenberg)

1. SWEDISH NATIONAL BALLOON AND ROCKET PROGRAMME

Currently, two nationally led balloon projects are on-going and two new rocket projects have recently been kicked-off within the national balloon and rocket programme.

One of the balloon projects, PoGOLite, deals with studies of polarisation of gamma-rays from extreme astrophysical objects, such as Crab Nebula. PoGOLite project is led by Mark Pearce from KTH (Royal Insti-

Proc. '21st ESA Symposium European Rocket & Balloon Programmes and Related Research', 9–13 June 2013, Thun, Switzerland (ESA SP-721, October 2013)

tute of Technology), in cooperation with scientists from USA and Japan as well as Russia. PoGOLite is planned to be launched from Esrange in July 2013 by a 1 000 000 m^3 balloon.

Another balloon project within the Swedish national programme is In-situ IWC (In-situ Ice Water Content), led by Thomas Kuhn from Luleå Tehnical University. This project deals with ice clouds and studies of ice water content. The aim of the project is to improve remote sensing measurements of ice clouds and to refine parameterizations of cloud ice to be used in radiative transfer models. Several balloon launches have taken place already and more are foreseen in near future in order to study ice clouds at different atmospheric conditions. The volume of the balloons carrying experiments is 500 m^3, enabling several launches during each campaign.

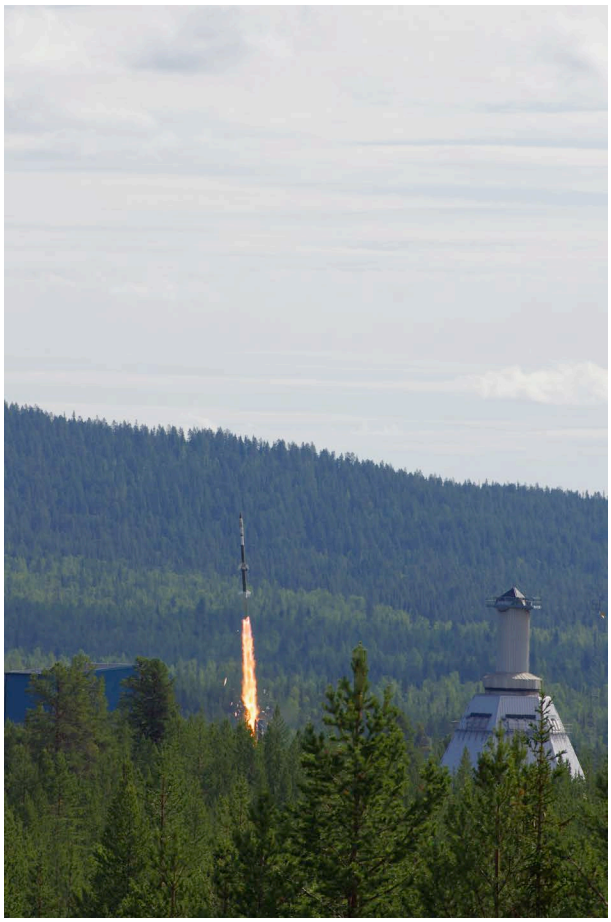

Figure 2. Launch of PHOCUS from Esrange in 2011 (photo: Mikhail Khaplanov, SU)

Two new rocket projects have been kicked-off in 2013. One of the rocket projects, SPIDER (Small Payloads for Investigation of Disturbances in Electrojet by Rockets), deals with the study of turbulence in the auroral electrojets. PI of SPIDER project is Nickolay Ivchenko from KTH (Royal Institute of Technology). During the flight of SPIDER, several autonomous free-flying payloads will be released, based on the technology previously studied within several student projects supervised by SPIDER PI Nickolay Ivchenko. This is also a very good illustration of synergies between student projects and projects carried out by senior scientists. The launch of the SPIDER rocket is planned in early 2015.

Another rocket project, O-States (Oxygen Species and Thermospheric Airglow in The Earth's Sky), is led by Jörg Gumbel from Stockholm University and deals with the studies of the lower thermosphere using O_2 atmospheric band emissions. O-States will provide information about atomic oxygen and temperature at altitudes 100-250 km by means of dayglow emission spectra of O_2. Two rocket launches at different atmospheric conditions are planned within O-States project in summer 2015.

Jörg Gumbel, PI of O-States, has led another successful rocket project, PHOCUS, launched from Esrange Space Center on July 21, 2011 in presence of noctilucent clouds observed by Esrange lidar. The payload, consisted of 17 instruments, developed by 8 research groups in Sweden, Norway, Germany, Austria and USA. The PHOCUS rocket reached an apogee of about 108 km and was successfully recovered after the landing. The results obtained from data collected during the PHOCUS flight were highlighted in numerous presentations during the current 21st ESA Symposium on European Rocket and Balloon Programmes.

2. PARTICIPATION IN ESA ELIPS PROGRAMME

Besides national activities, Sweden contributes to several of ESA programmes. ELIPS is one of the major optional programmes with Swedish participation, and Swedish industrial activities are mainly focused on MASER and MAXUS sounding rockets.

One of the sounding rocket modules, XRMON, has been developed by SSC, enabling generation of metal foam *in situ* at temperatures up to 700-900 °C, to be studied by means of X-ray technique in order to characterise various parameters and mechanisms of metallic foam formation, diffusion and solidification of metals.

Currently, development of MAXUS-9 and MASER-13 is on-going, to be launched within the framework of ELIPS-4. In addition to ESA microgravity rockets, several German microgravity rockets (e. g. TEXUS) are also launched from Esrange, within the framework of German national programmes.

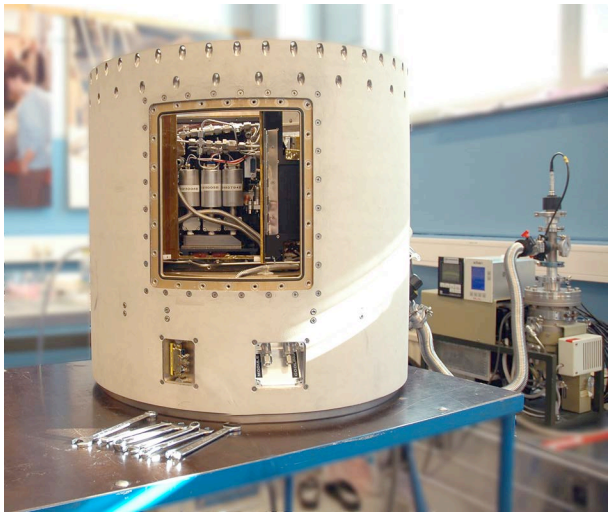

Figure 3. Sounding rocket module XRMON, developed by SSC (photo: ESA)

3. REXUS AND BEXUS PROGRAMME

Sweden takes an active part in the student rocket and balloon programme REXUS/BEXUS (Rocket and Balloon Experiments for University Students). The project is a joint undertaking of DLR (German Aerospace Center) and SNSB in collaboration with ESA. Two REXUS rockets and two BEXUS balloons are launched from Esrange every year.

Figure 4. Beautiful surroundings of Esrange in early summer (photo: Kristine Dannenberg)

An annual call for proposals is being issued each autumn, offering an opportunity to carry out European student experiments on real rockets and balloons.

The duration of the BEXUS balloon flights is 2-3 hours at 26-30 km altitude. The REXUS rockets reach altitudes of around 90 km. More than 400 students from various European countries have participated in REXUS/BEXUS programme since the start of the joint programme in 2006. During the current ESA Symposium on European Rocket and Balloon Programmes, around 40 students from 24 teams participated in its various sessions, giving 25 presentations on the results obtained in REXUS and BEXUS experiments during last two years.

The next call for new proposals will open in September 2013 and students from ESA member states and cooperating states are invited to submit their proposals. Similarly to previous years, the proposals will be evaluated by experts during autumn and the selection of the new student teams will be finalised in December.

Figure 5. BEXUS 14 launch from Esrange Space Center in September 2012 (photo: Kristine Dannenberg)

SOUNDING ROCKET AND BALLOON ACTIVITIES AND RELATED RESEARCH IN SWITZERLAND 2011 - 2013

Marcel Egli

Lucerne University of Applied Sciences and Arts, CC Aerospace Biomedical Science & Technology, "Space Biology Group", CH-6052 Hergiswil, Switzerland
Email: marcel.egli@hslu.ch

ABSTRACT

Swiss scientists working in the field of high altitude research were particularly active during the reporting period from 2011 to 2013. As in other years, their research included platforms such as sounding rockets, stratospheric balloons, and two high altitude stations, "Jungfraujoch" and "Gornergrat", which are located in the heart of the Swiss Alps. The intensified research activity of these scientists led to numerous publications in various disciplines, such as physics, astrophysics, meteorology, and biology/medicine.
Several Swiss experiments were carried out on sounding rockets, such as "STIM", which was installed in a MASER rocket and launched in Sweden. The goal of the investigations was to further examine the mechanism of activation of human blood cells under microgravity conditions. Students from École Polytechnique Fédérale de Lausanne (EPFL) were able to participate in another sounding rocket project called REXUS. The aim of their experiment was to test a new sensor technology designed to measure the altitude of satellites.
There was also an increase in research activity at the high altitude research stations, which was primarily the result of two large medical examinations that started in the reporting period. The "Gornergrat" station underwent a transition into a public outreach center during the last few years. It is now open for educational projects in astrophysics at the high school level. A very short summary of a few Swiss projects within the framework of sounding rocket and balloon activities and related research carried out between 2011 and 2013 is provided in the following paragraphs.

1. INTRODUCTION

During the many years that Switzerland has participated in the Esrange Andoya Special Projects (EASP) program, numerous Swiss researchers have conducted high altitude balloon or sounding rocket campaigns. During the period 2011 to 2013 there were two research groups involved in sounding rocket missions for example. Among these is the team of the Zero-g LifeTec Company that coordinated a sounding rocket project on the effects of microgravity on immune cells. The same topic was investigated by the other research group of the University of Zurich, Institute of Anatomy.

The high altitude research stations Jungfraujoch and Gornergrat, located in the heart of the Swiss Alps offer researchers additional platforms for investigations. These stations provide infrastructure and support for scientific research that has to be carried out at an altitude of 3'000 – 3'500 meters above sea level. Scientists from institutions of the member countries as well as from other countries are eligible to conduct research there. But also commercial companies are using the harsh environment of these high altitude research stations to test their outdoor products.

Some of the research projects carried out in the framework of "Sounding rocket and balloon activities and related research" during the years 2011 – 2013 by Swiss institutes are presented here. A compilation of their abstracts can be found below.
Additional information on Swiss activities in high altitude or space can be found under the following web links: http://www.sbfi.admin.ch/themen/ or http://www.hfsjg.ch/.

2. SOUNDING ROCKET EXPERIMENT: "STIM" (SIGNAL TRANSDUCTION IN MICROGRAVITY)

Collaboration between Zero-g LifeTec Zurich, University of Zurich and University of Sassari

The goal of the experiment was to investigate the influence of altered gravity on key proteins of T cell activation during the MASER-12 ballistic suborbital rocket mission of the European Space Agency (ESA) and the Swedish Space Cooperation (SSC) at ESRANGE Space Center (Kiruna, Sweden). Components of the T cell receptor, the membrane proximal signaling, MAPK-signaling, IL-2R, histone modifications and the cytoskeleton in non-activated and in ConA/CD28-activated primary human T lymphocytes were quantified. The hypergravity phase during the launch resulted in a down regulation of the IL-2 and CD3 receptor and reduction of tyrosine

Proc. '21st ESA Symposium European Rocket & Balloon Programmes and Related Research', 9–13 June 2013, Thun, Switzerland (ESA SP-721, October 2013)

phosphorylation, p44/42-MAPK phosphorylation and histone H3 acetylation, whereas LAT phosphorylation was increased. Compared to the baseline situation at the point of entry into the microgravity phase, CD3 and IL-2 receptor expression at the surface of non-activated T cells were reduced. Importantly, p44/42-MAPK-phosphorylation was also reduced after 6 minutes of microgravity (µg) compared to the 1g ground controls, but also in direct comparison between the in-flight µg and the 1g group. In activated T cells, the reduced CD3 and IL-2 receptor expression at the baseline situation recovered significantly during in-flight 1g conditions, but not during microgravity conditions. Beta-tubulin increased significantly after onset of microgravity until the end of the microgravity phase, but not in the in-flight 1g condition.

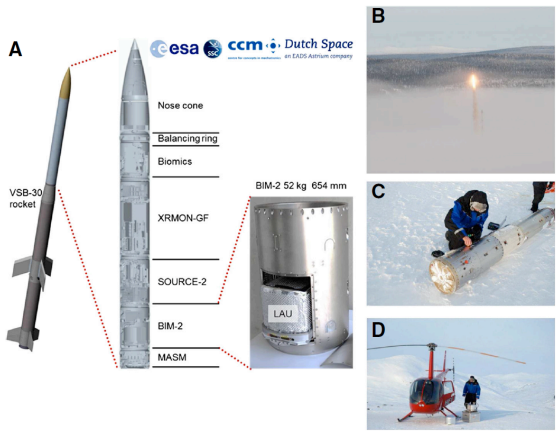

Figure 1. Payload configuration of MASER-12, launch and recovery. (A) MASER-12 consisting of a VSB-30 motor and of the payload (B) MASER-12 launch, February 13th 2012 (C) BIM-2 module disassembly (D) transport of the "Late Access Unit"

The results of the study suggest that key proteins of T cell signal modules are not severely disturbed in microgravity. Instead, it can be assumed that the strong T cell inhibiting signal occurs downstream from membrane proximal signaling, such as at the transcriptional level as described recently. However, the MASER-12 experiment could identify signal molecules, which are sensitive to altered gravity.

3. SOUNDING ROCKET EXPERIMENT: DNA STABILITY AND INTEGRITY AFTER SPACE FLIGHT AND RE-ENTRY

University of Zurich and Astrium Space Transportation, Bremen, Germany

Desoxyribonucleic acid (DNA) plays a unique role in storage and transmission of the genetic information of all living organisms on Earth and represents a valuable biomarker to detect life. The massive bombardment in the early stage of the Earth's history represents a possibility to explain the hypothetical interplanetary transport of matrix-bound DNA to Earth. In this scenario, the DNA would have to withstand the hostile conditions in space as well as the extreme conditions during atmospheric-entry. In the experiment the hypothesis was tested whether the DNA molecule withstands the Earth atmosphere entry-conditions prevailing during a ballistic rocket flight and whether it retains its biological activity. Therefore, the stability and functionality of artificial plasmid DNA during atmospheric re-entry conditions was investigated. During the TEXUS-49 sounding rocket mission small amounts of DNA at 15 different positions on the outer surface of the payload were exposed to the harsh re-entry conditions of the sounding rocket. The apogee of the TEXUS-49 flight was 264km. On the inside of the recovery module, temperatures of more than 130°C were measured while at the sample application locations, temperatures of more than 1'000°C were estimated. Directly after retrieval and back transport of the payload, DNA samples were recovered. The recovery rate was around 4.9 - 27.3%. Representative samples were analyzed to determine the DNA integrity by transformation in bacteria. Subsequently to incubation, bacterial growth was detected due to the incorporated plasmid antibiotic resistance. This indicates that at least a fraction of the plasmid DNA was intact after recovery. A second functionality test was performed by transfecting the DNA into mouse fibroblast cells to analyze the integrity of the fluorescent marker. Finally, DNA mutation and degradation was analyzed. We were able to show that plasmid DNA bound to a matrix can withstand a time period in space and the re-entry conditions into the Earth atmosphere.

4. SOUNDING ROCKET EXPERIMENT: CONCEPT OF AN UNMANNED SUPERSONIC GLIDER FOR WEATHER DATA GATHERING

Interdisciplinary Aerodynamics Group, École Polytechnique Fédérale de Lausanne (EPFL)

Sounding the upper tropopause and the stratosphere is a challenging enterprise. This delicate zone of the atmosphere traps significant pollutants that can influence the weather; not only NO_x and CO_2 but also H_2O and particulates for instance are critical catalysers for weather perturbation and the influence on the ozone layer. Atmospheric emissions directly concern an assessment on climate impact such as contrails and cirrus cloud formations. Contrails are functions of atmospheric conditions and may give rise to formation

of cirrus clouds that can affect the balance of energy absorption and radiation through the atmosphere. This contributes to radiative forcing and hence to climate change. The transition zone to the troposphere, the tropopause is fragile and requires precise sounding; the role of stratospheric ozone depletion by NO_x and sulfur compounds is critical, high altitude thin clouds have an impact on the climate.

Atmospheric sounding is usually performed by balloons; however, these devices tend to be lost, become untraceable, or are destroyed. An attractive alternative is to monitor and collect data via unmanned air vehicles (UAV). The system devised here is an UAV capable of behaving as a lifting body in high altitude ranges, and be able to fly back to a single destination as a glider. The proposed system uses an innovative design shape, with a built in health monitoring system of the aircraft capable of controlling and reacting to the aircraft's flight stages during descent. The UAV is designed to be ultra-lightweight and released from a sounding balloon at 35-40km. The aircraft will then return to ground within a reasonable area, pre-designed by the onboard flight controller and its associated functional engineering simulator that can account for the modifying aerodynamics of the vehicle along the flight path. The success of such missions will provide solutions for ulterior families of such concepts that can be then equipped with emission capture data.

Figure 2. CAD model of the UAV "Glider Smart Fish"

The atmospheric sounding glider UAV is based on an innovative design. It is equipped with a health monitoring system (HMS) that reacts to the vehicles aircraft performance during its whole mission from high altitude (above 35km) to ground landing.

5. EXPERIMENT OF HIGH ALTITUDE RESEARCH STATIONS: THE GLOBAL ATMOSPHERE WATCH (GAW) AEROSOL PROGRAM AT JUNGFRAUJOCH

Laboratory of Atmospheric Chemistry, Paul Scherrer Institute

Airborne aerosols affect our climate primarily by influencing the atmospheric energy budget through direct and indirect effects. Direct effects refer to the scattering and absorption of radiation and their influence on the planetary albedo and the climate system. Indirect effects refer to the increase in available cloud condensation nuclei due to an increase in anthropogenic aerosol concentration. This leads to an increase in cloud droplet number concentration and a decrease in cloud droplet effective radius, when the cloud liquid water content remains constant. The resulting cloud droplet spectrum leads to reduced precipitation and increased cloud lifetime. The overall result in the global atmosphere would be an increase in cloud albedo which cools the Earth's climate. Despite the uncertainty it is believed that in regions with high anthropogenic aerosol concentrations, aerosol forcing may be of the same magnitude but opposite in sign compared to the combined effect of all greenhouse gases.

The Global Atmosphere Watch (GAW) program is an activity overseen by the World Meteorological Organization (WMO). It is the goal of GAW to ensure long-term measurements in order to detect trends and to develop an understanding of these trends. With respect to aerosols the objective of GAW is to determine the spatio-temporal distribution of aerosol properties related to climate forcing and air quality up to multi-decadal time scales. Since the atmospheric residence time of aerosol particles is relatively short, a large number of measuring stations are needed.

The GAW monitoring network consists of 27 global and about 300 regional stations (including the Jungfraujoch). While global stations are expected to measure as many of the key variables as possible, the regional stations generally carry out a smaller set of observations. The Jungfraujoch aerosol program is among the most complete ones worldwide. By the end of 2012 it has reached 18 years of continuous measurements.

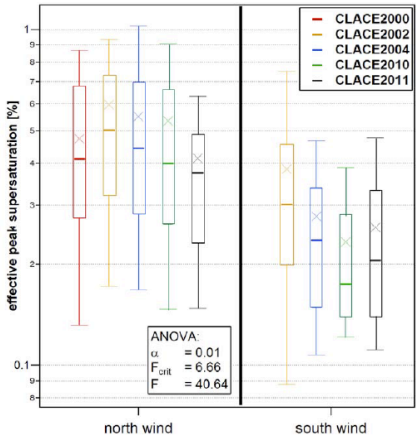

Figure 3. Effective peak supersaturations for the two main wind fields present at the Jungfraujoch during several CLACE campaigns

6. EXPERIMENT OF HIGH ALTITUDE RESEARCH STATIONS: CLOUD CLIMATOLOGY AND SURFACE RADIATIVE FORCING OVER SWITZERLAND (CLASS)

Physikalisch-Meteorologisches Observatorium Davos, World Radiation Center (PMOD/WRC)

The CLASS project aims at quantifying changes in the short-wave and long-wave radiative fluxes and the effect of clouds on the surface radiation budget by differentiating between cloud types and cloud coverage using ancillary instrumentation and datasets. In order to discriminate between different cloud types and to calculate fractional cloud cover more precisely, hemispherical sky cameras were deployed at four stations across Switzerland. The systems at Davos, Payerne and Zimmerwald were already installed in 2010 and 2011. At Jungfraujoch, the installation was delayed due to technical problems with the camera system and the particular requirements at the high alpine station. Finally in July 2012, we were also able to successfully deploy a camera at this. The camera delivers images from the sky during the daytime with a 1-minute cadence. The camera has been operational without any technical difficulties so far and data availability is at 100%. Pictures from any particular day are stored for 10 days on the PMOD/WRC FTP server.
The camera system allows the fractional cloud cover to be calculated on a routine basis. This is accomplished by calculating the ratios of the blue to the green channel and blue to the red channel for each pixel, which are then compared to a reference value. If the calculated value is higher than the reference value due to an atmosphere with no clouds which scatters more blue than red light, the pixel is classified as cloud-free. On the other hand, if the value is below the reference value due to clouds which scatter more red light compared to a cloud-free sky, the pixel is classified as cloudy (see Figure 4). The validation of our results, however, is not trivial because alternative surface-based observations of the fractional cloud cover are limited at these stations. Therefore, we plan to compare our results to fractional cloud cover derived from Meteosat in the upcoming year.

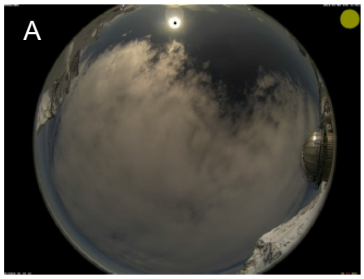

Figure 4. Original image of the sky over Jungfraujoch taken January 5 2013 at 11:42. The cloud cover algorithm produces a simplified image (B) from the actual situation (A) in which the cloud-free and cloudy sky is represented by blue and white pixels, respectively

Besides calculating fractional cloud cover, we have developed and tested an algorithm to classify the images into seven different cloud classes like cirrus-cirrostratus (ci-cs), cirrocumulusaltocumulus (cc-ac), stratus-altostratus (st-as), cumulus (cu), stratocumulus (sc), cumulonimbusnimbostratus (cb-ns) and cloud-free (cf). The cloud type classification algorithm is based on a set of statistical features describing the color and the texture of an image. For the actual classification of an image, the k-nearest-neighbor classifier is used.
We are currently adapting the algorithm to the atmospheric conditions at Jungfraujoch. Indeed, clouds with a low cloud base such as stratus, stratocumulus, cumulus, cumulonimbus and nimbostratus no longer occur above but below the station due to its high altitude at 3’580 meters above sea level. In addition, when the station is within these clouds their type cannot be discriminated. Therefore, a separate training set may be required for Jungfraujoch and the number of cloud classes has to be reduced.

7. EXPERIMENT OF HIGH ALTITUDE RESEARCH STATIONS: AEROSOL CHEMICAL SPECIATION MONITOR (ACSM) MEASUREMENTS ON THE JUNGFRAUJOCH (EU project ACTRIS)

Laboratory of Atmospheric Chemistry, Paul Scherrer Institute

The project is comprised of two main goals: First, the augmentation of knowledge about the aerosol present in the high-alpine atmosphere by monitoring its chemical composition over a period of at least one year. Embedded in the framework of the ACTRIS (Aerosols, Clouds, and Trace Gases Research Infrastructure Network) which encompasses about a dozen similar measurement stations all over Europe, these measurements are to contribute to a unique, chemically resolved dataset of the European aerosol. The second

goal is the validation of a prototype of a new time of flight instrument (ToF-ACSM, see Figure 5) suitable to monitor the chemical composition of the non-refractory, submicron aerosol with lower detection limits than the current quadrupole version (Q-ACSM).
The specific conditions on the Jungfraujoch in terms of aerosol concentrations which are mostly very low but can still be highly variable in summer, provide an ideal proving ground for both detection limits and temporal resolution of the instrument. Additionally, the infrastructure and the large number of complementary measurements at the Sphinx Research Station allow for sanity tests of the recorded data and the testing of the prototype's remote control capability.
The work on the project was started in late June 2012. From the beginning of August until mid-November 2012 the ToF-ACSM prototype was operated in parallel with the current Q-ACSM version, which has already been validated and available on the market for about three years. The inter-comparison of the time series of the individual chemical species (organics, sulfate, nitrate, ammonium and chloride) recorded with the two instruments showed very good agreement in absolute concentrations as well as in capturing the variability. Furthermore, an inter-comparison of the ToF-ACSM to a co-located instrument employing an optical method to estimate aerosol mass also showed a very good qualitative agreement. These results are a very important step towards proving the validity of the ToF-ACSM data and therefore suitability for the market. A further comparison to the high-end aerosol mass spectrometer (AMS) during the CLACE campaign in the first quarter of 2013 will complete the validation and will be published soon.

Figure 6. V Sketch of ToF-ACSM

8. ACKNOWLEDGEMENT

I would like to thank all the contributors from the different institutions for providing the input necessary to write this report. Furthermore, I gratefully acknowledge the support of the Swiss Space Office SSO, Federal Department of Home Affairs FDHA, State Secretariat for Education and Research SER.

RECENT ACTIVITIES OF JAPANESE SOUNDING ROCKET EXPERIMENTS

Takumi Abe[(1)], Nobuaki Ishii[(2)]

[(1)] Japan Aerospace Exploration Agency, 3-1-1, Yoshinodai, Chuo-ku, Sagamihara 252-5210, Japan, E-mail: abe.takumi@jaxa.jp
[(2)] Japan Aerospace Exploration Agency, 3-1-1, Yoshinodai, Chuo-ku, Sagamihara 252-5210, Japan, E-mail: ishii@isas.jaxa.jp

ABSTRACT

The sounding rockets are used for various objectives such as studies of thermospheric, ionospheric, magnetospheric physics, astrophysics, microgravity experiment, demonstration of various instrument and technique, and advanced engineering experiments. Japanese sounding rockets have been launched from not only in a domestic site but also in overseas range for such purposes for more than four decades. In the period from 2011 to 2012, a total of four sounding rockets were launched in Japan. We give a brief introduction on these experiments by describing the objectives and the main result of each experiment and on a development of avionics system for the sounding rocket.

1. INTRODUCTION

In Japan, the Institute of Space and Astronautical Science (ISAS) of Japan Aerospace Exploration Agency (JAXA) has been continuing sounding rockets experiments for various objectives. In these years, we are operating three different types of the rocket; S-310, S-520, and SS-520. As shown in Tab. 1, one S-310 rocket was launched for a purpose of the ionospheric study in 2011, while two S-520 and one S-310 rockets were launched for the thermospheric physics, engineering demonstration, and microgravity experiment in 2012. We present the recent activity with Japanese rockets during 2011-2012 and a near-future plan of our rocket experiments.

Table 1. List of Japanese rocket experiments during 2011-2012.

Rocket	Objective	Launch Date
S-310-40	Ionospheric physics	Dec 19, 2011
S-520-26	Thermospheric physics	Jan 12, 2012
S-310-41	Engineering demonstration	Aug 7, 2012
S-520-28	Micro-gravity experiment	Dec 17, 2012

2. S-310-40 ROCKET EXPERIMENT (DECEMBER, 2011)

It is well-known that the ionospheric D region disappears at nighttime because the ionization process decays. Then, long-distance propagation of the medium frequency (MF) radio waves becomes possible. However, recent observations suggest that the long-distance propagation is sometimes interfered at night probably due to unexpected enhancement of the electron density in the D and/or E region. S-310-40 rocket experiment was planned to elucidate a generation mechanism of high plasma density layer which can cause unexpected absorption and/or scattering of MF radio wave propagation at nighttime. In December 2011, we conducted S-310-40 experiment in Uchinoura, which is a domestic launch site for the sounding rocket located in the southwestern part of Japan. This experiment is named SPIDER, which comes from SPoradic layer in the nighttime Ionospheric D or E Region. A total of five instruments; receiver of MF/VLF waves, impedance probe, Langmuir probe, fixed bias probe, magnetometer, and horizon sensor were installed on the rocket.

The MF/VLF receiver detects waves from three stations; 873 kHz from Kumamoto (north-west), 666 kHz from Osaka (north-east), and 405 kHz from Minami-Daito (south from rocket), and it is possible to estimate the electron density distribution in the respective direction. The detailed analysis of the received waves suggests that the altitude profile of the electron density has the local peaks at ~100 km in the north-west direction and at ~92 km in the north-east direction. On the other hand, the density peaks of 6×10^3 cm^{-3} was observed at 105 km altitude by the impedance probe. The difference among these density profiles may be caused by the spatial structure of the plasma density distribution. From the comparison, we suppose that the high density layer has inclined to the north or north-east direction at the time of the rocket launch. Further investigation will be made to understand the spatial structure of the electron density in the lower ionosphere.

3. S-520-26 ROCKET EXPERIMENT (JANUARY, 2012)

In January 2012, S-520-26 rocket was launched from Uchinoura to study a coupling process between neutral particles and charged particles (plasma) in the mid-latitude lower thermosphere. Another purpose of this experiment was to get important parameters to understand a generation mechanism of the large scale traveling ionospheric disturbance (LS-TID). This experiment was named "WIND-2" (Wind measurement for Ionized and Neutral atmospheric Dynamics study -2), and is the second mission of the successful WIND

Proc. '21st ESA Symposium European Rocket & Balloon Programmes and Related Research', 9–13 June 2013, Thun, Switzerland (ESA SP-721, October 2013)

campaign in September 2007. In this experiment, Lithium vapor was released from the rocket during its flight so that we can get information on the neutral wind by taking continuous images of Lithium emission which was caused by resonant scattering due to the sunlight in the wavelength of 670 nm. In order to get Lithium images on the better condition, it was necessary to launch the rocket just before the local sunrise because the Lithium should be illuminated by the sun light but elevation angle of the sun on the ground should be less than 0°. For the plasma observation, in-situ measurements of the electric field, magnetic field, and electron density and temperature in the rocket position have been made by several instruments during the rocket flight.

Fig.1 shows pictures of Lithium emission images taken from the ground-based observation site near Uchinoura. As the time sequence, Lithium vapor was released from its canister on the rocket at 05:59 local time (LT), and thereafter Lithium had spread due to the ambient neutral wind. However, it is remarkable that it had spread like a wheel. This means that the neutral wind was blowing in a different direction depending on the altitude. From this information, it is possible to estimate the neutral wind direction and speed in this altitude range. As a result, it is confirmed that there existed the wind shear in the east-west component at 113 km altitude; eastward above and westward below this altitude. The detailed discussion on the observed data will be reported in the other papers.

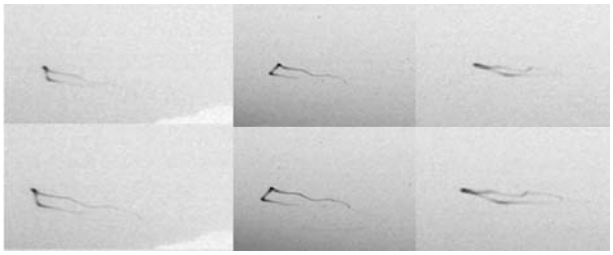

Figure 1. Lithium images taken at 6:05 (upper) and 6:06 (lower) LT from the three ground-based sites. (Photo credit: Hokkaido Univ. and Kochi Univ. of Technology)

4. S-310-41 ROCKET EXPERIMENT (AUGUST 2012)

An inflatable aeroshell attracts attention as an innovative atmospheric-entry system. In JAXA, the experimental vehicle with an inflatable aeroshell was developed for the sounding rocket experiment, and was practically launched on S-310-41 rocket in August 2012, to demonstrate its flight performance for the atmospheric-reentry.

Objectives of this atmospheric entry flight are:

1) To demonstrate a deceleratin g performance of the flare-type membrane aeroshell sustained by the inflatable torus.
2) To demonstrate a deploy ment of the inflatable aeroshell under micro-gravity and vacuum condition.
3) To acquire the aerodynamic characteristics and aerodynamic heating of the vehicle in supersonic free flight.

After the nose cone of the rocket was opened at 60 sec from the lift-off, the payload system released aero-shell cover from the inflatable capsule and subsequently started injecting gas at 95 sec. The capsule was separated from the launch vehicle at 100 sec. Various monitoring data such as temperature, pressure, acceleration, and attitude as well as images of flying capsule were obtained for about 20 min. Thus, the time sequences were executed without delay, and all of the flight performance including the aeroshell image, were successfully obtained by telemetry system.

According to the flight data, the inflatable aeroshell has completely kept intact during its reentry. The experimental vehicle started decelerating at 70 km altitude due to the aerodynamic force. It was confirmed that the actual decelerating trend is consistent with the simulation result. Thus, the aeroshell made a good performance as we expected.

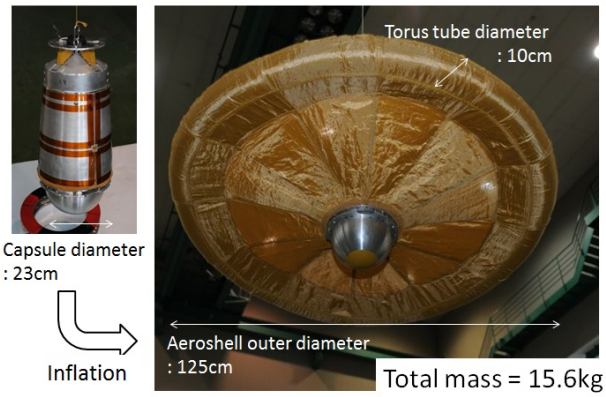

Figure 2. Experimental vehicle with inflatable aeroshell for S-310-41 rocket.

5. S-520-28 ROCKET EXPERIMENT (DECEMBER 2012)

In December 2012, S-520-28 rocket was launched to conduct two nucleation experiments under microgravity; 1) in-situ visualization of nucleation environment in gas phase, and 2) electrical detection of the nucleation event of calcium carbonate. The main subject was to observe formation of cosmic dust and calcium carbonate nucleus. These experiments were carried out during ballistic flight of the rocket. The objective of this experiment was to better understand the homogeneous nucleation mechanism by onboard measurements under microgravity environment. This experiment is a joint project between Tohoku University, Tokai University and JAXA.

In the first experiment to observe nucleation formation of cosmic dust, temperature and concentration of evaporated material, such as iron, at the nucleation were observed directly using interferometer, and the process was elucidated. This is the experiment leading to know how the building blocks of Earth were formed.
In the second experiment of homogeneous nucleation mechanism of calcium carbonate, homogeneous nucleation rate of $CaCO_3$ crystals as a function of supersaturation was measured after mixing two solutions containing carbonate and calcium ions. This is a part of Japan-U.S. joint research to understand crystallization speed of $CaCO_3$ underground for carbon sequestration.

6. NEAR-FUTURE EXPERIMENTS

In summer of 2013, we will conduct two consecutive launches by using S-310-42 and S-520-27 rockets during a short time interval with a particular interest in the electromagnetic interaction of the nighttime ionospheric disturbance between the E and F regions. The objective of this experiment is to elucidate the electromagnetic interaction and neutral-plasma interaction occurring in the ionosphere. For this purpose, we will conduct a comprehensive measurement of plasma, neutrals, electric and magnetic fields in the ionospheric E and F regions with a multiple rocket launches. The ground-based instruments will also be operated to monitor the latest condition of the plasma disturbance in the mid-latitude ionosphere.
Also in this experiment, Lithium vapor is going to be released from the rocket to get information on the neutral wind in the lower ionosphere. Unlike the case of the last Lithium release experiments in which the sunlight scattering by Lithium vapor was taken to images, we will make use of the moonlight scattering in this experiment. We are going to launch two rockets on the full moon condition under active electron density disturbance in July 2013. The special feature of this experiment is in our strategy that we observe the ionospheric E region by S-310 rocket and F region by S-520 rocket.

7. DEVELOPMENT OF NEW AVIONICS SYSTEM

We would like to give a brief description on our development of new avionics system.
In the past, we had many common instruments such as timer-, igniter-, power control-, and telemetry-subsystems which need to accept minor changes according to the respective experimental requirement. To improve applicability and scalability of the common instruments, we decided to carry out modulization and integration of the instruments. Our development of the new avionics system based on such motivation was finally completed in 2011, and now these units were integrated in one unit. The system has been installed for the first time on the S-310-40 rocket in 2011.
We realized that the new avionics system brings a lot of advantages, once an integration of control and signal processing devices is finished. For example, it will decrease a cost of manufacturing and operation. Second, it will make it easier to extend and to exchange each element. Moreover, it is expected to simplify cables and to improve efficiency in the integration and outfitting.
As an example of benefit brought from this system, we could replace malfunctioning avionics in one experiment with the normal one which was supposed to install on the next rocket. Thus, it could save a time very much because we did not have a time to fix or to rebuild the unit in the schedule.

8. SUMMARY

In the period from 2011 to 2012, the ISAS of JAXA conducted the four sounding rocket experiments; 1) ionospheric physics experiment, 2) thermospheric physics experiment, 3) engineering demonstration experiment, and 4) micro-gravity experiment. In 2013, we are planning to launch three sounding rockets.
We would like to promote the international collaboration in our sounding rocket activity, expecting more fruitful science result. The ISAS will continue the sounding rocket activity with the current level.

Invited Lectures

SPACE EDUCATION IN NORWAY

Arne Hjalmar Hansen [(1)], Stian Vik Mathisen [(2)], Filip Ferris Nicolaisen [(3)], Thomas Gansmoe [(4)], Birgit Strømsholm [(5)], Jøran Grande [(6)]

[(1)] Norwegian Centre for Space-related Education, P.O. Box 54, 8483 Andenes, Norway, arne-hjalmar@rocketrange.no
[(2)] Norwegian Centre for Space-related Education, P.O. Box 54, 8483 Andenes, Norway, stian@rocketrange.no
[(3)] Norwegian Centre for Space-related Education, P.O. Box 54, 8483 Andenes, Norway, filip@rocketrange.no
[(4)] Norwegian Centre for Space-related Education, P.O. Box 54, 8483 Andenes, Norway, thomasg@rocketrange.no
[(5)] Norwegian Centre for Space-related Education, P.O. Box 54, 8483 Andenes, Norway, birgit@rocketrange.no
[(6)] Norwegian Centre for Space-related Education, P.O. Box 54, 8483 Andenes, Norway, joran@rocketrange.no

ABSTRACT

NAROM (Norwegian Centre for Space-related Education) offers educational programmes for teachers and students at many different levels to promote appreciation for the benefits of space activities, to facilitate recruitment in the space industry, and to stimulate an interest in science in general.

NAROM has a student rocket program where students learn to build and launch their own instruments on-board a rocket.

NAROM offers a satellite program for university students, as well a CanSat program for students and teachers by enabling them to carry out a full space project, involving design, construction, programing, testing, rocket launch, telemetry and data handling.

In 2014 NAROM will open a new visitor- and education-center at ARR; the Spaceship Aurora. It will have classical facilities for space-education, such as classrooms and auditoriums and displays of space and space technology.

ESERO (European space education resource office), is an education project of ESA and represents ESA's major initiative in the field of primary and secondary education. The ESERO Norway was established at NAROM in 2009, and in cooperation with Nordic space and education partners, the ESERO Norway will have Nordic teachers as target group in the period 2013-2015.

1. INTRODUCTION

NAROM was founded in 2000 and is partly funded by the Norwegian Government. NAROM is co-located with Andøya Rocket Range (ARR). The close proximity to the facilities and personnel at ARR provides important advantages with respect to educational activities, and NAROM uses the unique technical facilities at ARR to provide an exciting educational experience.

This paper deals with some of the activities NAROM is running; the student rocket program, the student satellite program, the CanSat program, Spaceship Aurora and ESERO activities.

2. THE STUDENT ROCKET PROGRAM

The Student rocket program aims to be a first hands-on experience with rocketry. The main focus is to build simple sensors, integrate them into the rocket payload, perform the rocket launch operation, tracking the sounding rocket and analyzing data from the instruments on-board. All this is normally done during one week where the students live and work at ARR.

NAROM offers the student rocket program to Space Camps, several Universities and University Colleges courses and the Space Technology Program at Andøya secondary school. The Space Technology Program at Andøya secondary school is a one year course for Norwegian high school students. Within this course they have the opportunity to launch their own sounding rocket. The students get tasks to create and manufacture instruments that will be on-board the rocket. The

Proc. '21st ESA Symposium European Rocket & Balloon Programmes and Related Research', 9–13 June 2013, Thun, Switzerland (ESA SP-721, October 2013)

duration of this construction is over couple of months.

For university and university college students, most of them come without any rocket experience to Andøya and within a week get to know how it is to be a rocket scientist. The students attend lectures about rockets and how they work. The sensor-board that the students integrate into the rocket measures temperature,pressure, accelerometer, magnetometer and light intensity.
The student rocket that NAROM is using is the Mongoose 98, provided by Rebel Space in the Netherlands. The rocket motor is Pro 98 6G from Cesaroni. It has a burn time of 5.38 seconds and with the current configuration reach about 8 km. The body is made from carbon-fiber, weight 16.3 kg and is 2.64 meter long.

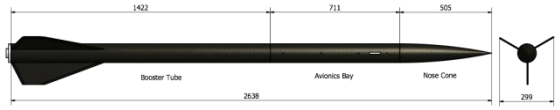

Figure 1. The student rocket Mongoose 98

One thing that is common for all student rockets is the launch procedure. The students are using the same procedures that are used during a real scientific sounding rocket. With all launches there is a pre-flight meeting involving all relevant personnel to ensure all stations are ready and learn what we can expect during the countdown. The most critical launching condition of student rockets is wind condition. The countdown is usually set to be one hour. The students go through the necessary testing and procedures during the countdown, under supervision of the ARR and NAROM staff. The students operate all the stations, which gives them a unique hands-on experience.

After launch, the students start analyzing the retrieved data. The students case assignments, so they have to analyze the data and explain the rocket performance. In the end, the students give a presentation of their work and analysis of the data.

NAROM also offers the student rocket program to the CaNoRock program, a 10 year sounding rocket program with Norwegian and Canadian universities. Currently the University of Oslo, Tromsø together with the Universities of Alberta, Calgary and Saskatchewan are a part of this program. In addition to the student rocket program, the CaNoRock program includes the possibility for students to participate in larger scientific sounding rockets. The next sounding rockets that will include student involvement from CaNoRock are; MAXI Dusty(2014) and ICI-4(2013). Other sounding rockets that are proposed are MAXI Dusty 2(2015/2016) and ICI-5(2015/2016).

3.THE STUDENT SATELLITE PROGRAM

NAROM, ARR and the Norwegian Space Center initiated the program, which is planned to go from 2007 – 2014. This includes the development and launch of three student satellites. So far more than 140 students has participated in the program and produced over 4000 credits at Bachelor, Master and PhD level.

The student satellite program has the intention to stimulate cooperation between educational institutions in Norway and with industry, and also to give the students experience in team work and hands-on training. The program also aims to increase the interest for science and technology in lower educational levels to secure future recruitment to higher education.

The program has three participating universities; Narvik University College, University of Oslo and the Norwegian University of Science and Technology. The first satellite, HiNCube has an imaging camera as main payload. The second satellite, CubeStar is a technological demonstration of a scientific instrument for space weather developed by the University of Oslo. The third and last satellite is called NUTS were the main payload is an infrared camera that will try to take pictures of gravity waves.

HiNCube has been ready for launch since September 2012. The launch arrangement is covered by Innovative Solutions In Space B.V. (ISIS) from Yasny, Russia with Dnepr. The launch date was initially set to Q4 2012 but is now delayed with no fixed date at the moment.

The students involved in the second satellite CubeSTAR are currently finishing the design of the engineering model. The main scientific payload has been successfully tested and flown on several sounding rockets and has also been selected as payload for QB50.

The third satellite NUTS has some new concept designs that most likely haven’t been tried on a CubeSat before. The structure itself consists of Carbon fiber, resulting in a much lower weight compared to the traditional aluminum structure. The main board design is similar to CubeSTAR, as a back plane instead of the traditional stack plane. This gives several advantages in terms of design and testing of the subsystems but makes it difficult to buy any ready made subsystems.

Through the program there has been much student activity in terms of design reviews, workshops and conferences. The aim of the workshops is to give the institutions that are working on these projects a

chance to come together and discuss their ideas on design and solutions and to exchange valued experience. ANSAT will continue to offer students the possibilities to attend workshops and conferences, both international and national arranged.

4. THE CANSAT PROGRAM

A CanSat is the combination of the complex world of satellite design into a small and easy to understand project. For the last decade, students of Secondary Schools and University Students all over the world have been building CanSats. In Norway, NAROM is running teacher training courses and national competitions for pupils at Upper Secondary Schools.

The CanSat concept was first introduced in the late 1990s by the American professor Robert Twiggs. It provides an affordable way to introduce students to the many challenges in building a satellite. Students design and build a small electronic payload that can fit inside a 330ml soda can. The CanSat is launched and ejected from a rocket or a balloon. By the use of a parachute, the CanSat slowly descends back to the ground performing its mission while transmitting telemetry to a ground station.

Norway was one of the first European countries to establish their own national CanSat competition for high school students. The first national CanSat competition in Norway was organized by NAROM in 2009. With an exception for 2012, NAROM has organized national CanSat competitions every year since the start in 2009.

Figure 2. The winning team from the Norwegian CanSat competition 2009.

In April 2014, NAROM will expand from a national competition to a Nordic competition, which will include Norway, Sweden, Denmark and Finland.

NAROM and ARR have also in collaboration with ESA Education (European Space Agency) hosted the ESA European CanSat competition in 2010 and 2012 with respectively 11 and 14 different nationalities participating in the competitions.

During a CanSat competition the CanSat are brought up to an altitude of approximately 1000 meters above ground by a rocket. The rocket has a payload capability for two CanSats. With a maximum speed of above 500 km/h, the rocket use about 15 seconds to reach apogee where a small explosive charge ejects the nose cone of the rocket and the two CanSats. After ejection from the rocket, the CanSats will use up to 120 seconds to descend back to the ground. During this time, the teams receive live data from the CanSats and hopefully complete their mission before the CanSats are safely back on the ground.

In addition to using rockets to transport the CanSat, which is both expensive and time consuming, NAROM has had good experience using tethered balloons with a remotely controlled release mechanism to drop the CanSats. This is also the methods used during training courses for teachers at NAROM.

Figure 3. CanSat drop from tethered balloon.

NAROM is also looking into other methods of launching CanSats. One method, which will be less expensive and time consuming, is to use small UAVs to drop CanSats. The UAVs also gives the big advantage of being able to better control the landing area of the CanSats.

NAROM will this year arrange two CanSat teacher-training courses. During these courses, the teachers will get theoretical and practical knowledge of how to design, build, program and take measurements with a CanSat kit. The teachers will also get suggestions and ideas for how they can use space technology in subject like physics, science etc.

5. SPACESHIP AURORA

The Spaceship Aurora is a new visitor- and education-center at ARR. It will have classical facilities for space-education, such as classrooms and auditoriums and displays of space and space technology. More special; it will host a virtual space center, where visitors will participate in a scientific mission. Such missions can contain launches of rockets, balloons and unmanned aircraft, use of remote sensing equipment and design and implementation of space electronics. There will also be a spaceship, the "Aurora", in which the participants can take virtual trips to important destinations such as the magnetospheric rim, the moon and other planets, the photosphere and beyond. The center will open for students and the public in 2014, and the project is currently valued at € 4.000.000.

The most important target group for the spaceship is primary education. This has been chosen firstly since we have under-prioritized this group until now. It has also become obvious that unless we have a strong focus on this group, we will neglect the largest recruiting opportunity in the school system.

Figure 4. Spaceship Aurora will open in 2014

The curricular content of levels 5 and 8 in the Norwegian school system has therefore been important guidelines in deciding the learning goals of the missions. Among others, the following are important:

- Scientific method and reasoning
- The solar system
- Magnetism and electricity
- Gases, fluids and solids

The first mission is to investigate a solar storm. After a large eruption on the sun, a coronal mass ejection, plasma is hurdles towards Earth at large speeds. The team needs to launch a sounding rocket, based on the ICI-program, to investigate the effect it has on Earth's magnetosphere.

The different groups involved in the mission are:

- Mission Control (controlling the operation)
- Telemetry (communication with the sounding rocket, and other airborne objects)
- Payload (construct the instruments that go into the rocket)
- ALOMAR (handling a laser-based measuring device)
- Science (communicate with scientists from around the world)

After first launching a sounding rocket, the group now has to board a spaceship to do further investigations in space, seen from above the planet.

The following groups are involved in this mission:

- Pilot and navigation (self-explanatory)
- Communication (communicating with Earth)
- Solar observation (mission specialist, investigating what is happening with the sun)
- Control systems (responsible for all the life-support systems on the spaceship)
- Earth Observation (mission specialist, investigating what is happening with Earth)

It is of vital importance that the missions fit into the school curriculum, both to get teachers to embrace the concept, but most importantly to optimize learning. We therefore have a structure that looks like the following:

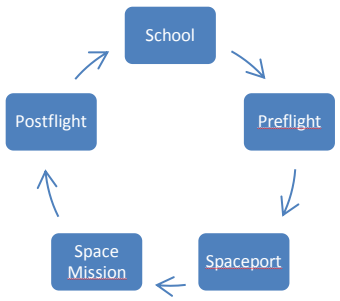

Figure 5. Learning strategy Spaceship Aurora

1. The students are presented with the material in school, to get a basic theoretic understanding of the concepts. It is important at this level to introduce the Spaceship as where the information will be utilized.

2. At Andøya, the students are taken into a preflight-meeting, where they are introduced with the mission of the day.
3. They then conduct the mission(s).
4. After the mission, they are immediately taken into postflight-meeting, where the analyze and discuss the results of the mission.
5. Back at school, they continue the analysis of the missions. They are to extrapolate them to "the real world" of space, and to prepare presentations for each other and/or other school groups.

6. ESERO (EUROPEAN SPACE EDUCATION RESOURCE OFFICE)

The ESERO Norway was established at NAROM in 2009. ESERO is an education project of ESA and represents ESA's major initiative in the field of primary and secondary education.

NAROM has developed and performed different web based and field based teacher training courses as formal competence. At the end of 2012 a total of 680 teachers at secondary level have participated in the 33 training courses offered by ESERO Norway.

ESA has taken steps for the future of the ESERO activities for primary and secondary education to cover the timeframe 2013 to 2015.With positive experience running ESERO Norway for four years, NAROM invited Denmark, Finland and Sweden to cooperate within a Nordic ESERO.

Nordic ESERO was established January 2013,- is based at Andøya Rocket Range (ARR) and operated by NAROM.

The main space and educational Nordic partners are the Swedish National Space Board, Norwegian Space Centre, the Swedish National Agency for Education, National Board of Education in Finland, the Danish Agency for Science and Innovation, Ministry of Education in Denmark, national and local education authorities on Nordic level. In addition, there are established close and formal relationships with different national Centre for Science Education, Science Centre, Universities and Science networks.

A key objective of ESA's ESERO project is to help with teacher training courses based on space-related resources. This is achieved either by introducing ESA material to existing courses or by developing and delivering original courses.
In cooperation with Nordic partners and the University of Nordland, Nordic ESERO Norway will every year in the period 2013-2015 develop and perform 8-12 web based including field based formal teacher training courses.

Each course gives a formal competence with 10 credits. The aims of the courses are to improve teachers' qualification within science and geography areas, and also to generate teacher enthusiasm in using space-related resources in the classroom. The field based activities will be set up in different areas of Norway and in the other Nordic countries.

In addition there will be at least 8 in-formal trainings each year. The target group will be both upper primary and secondary teachers in the Nordic countries. Every year Nordic ESERO will offer a total of minimum 160-240 teachers formal trainings and minimum 160 teachers expect to attend the in-formal trainings each year.

In 2013 Nordic ESERO will offer the following formal teacher trainings as original courses (developed and performed by Nordic ESERO): "Climate Research in the Polar Landscape", "Space and classroom", "Geology in schools" and "Below the polar sky". The office will also take part in existing formal trainings with activities and space resources.

Figure 6. Teachers at traing course

Example of in-formal trainings will be CanSat teacher trainings held in Norway and Denmark, Northern lights and Space Weather in Finland, Rocket physics and Nordic Teacher Space Camp in Norway.

Figure 7. Northern lights above ARR

The teacher trainings will be the main activities for the Nordic ESERO in the period 2013-2015. But in addition the office will offer workshops and events within different space areas and take part in educational conferences with lectures and exhibitions, and give support to different school projects.

Related to the different trainings and projects, there will be developed, adapted and published relevant content/ activities at the space education website www.sarepta.org. The different content will be developed in cooperation with Nordic space specialists/science experts and teachers at various levels. The cooperation with the teacher networks of evaluators is very important to secure that the resources are based on pedagogical concepts and didactical methods that are well proven. At the same time, ICT resources should stimulate the development of new concepts and methods for learning.

Resources offered by ESA will also be important for the different trainings, e.g. classical material and online material. In addition we will also introduce access to real space data sets, e.g. use of Earth Observation data in monitoring climate change and its effect. Some of these will be space data based on ESA projects and expertise. The scientific data will be adapted for the elaboration of teaching and learning activities.

Ranges

Chair: A. Verga

AN UAV TO SCAN ROCKET IMPACT AREA FOR SAFETY PROCEDURES

João V. A. Tavares[1], Ricardo C. A. Sousa[1], Marcos T. A. B. Segundo[1], Guilherme P. M. Bertelli[1], Luiz F. Q. Silveira[1], Gutemberg S. Santiago[1], Pablo J. Alsina[1], Albanisa F. Santos[2], J. B. Dolvim Dantas[2], Márcia D. Senna[2], and Glauberto L. A. Albuquerque[2]

[1]*Federal University of Rio Grande do Norte, Natal-RN, Brazil, pablo@dca.ufrn.br*
[2]*Barreira do Inferno Launching Center, Natal-RN, Brazil, leilsonglaa@clbi.cta.br*

ABSTRACT

This paper presents the outline and some preliminary results of the development of an UAV to be used in sounding rockets operations. The aim of this UAV is to scan impact points of this rockets searching for unexpeced boats for secutiry reasons. This project requires an multidisciplinary team including image recognition, robotics, space operations and telecomunications experts. This paper shows the main concepts used to develop all this areas for this project.

Key words: Sounding Rocket; Impact Points; Safety Procedures; Robotics; UAV; Telecomunications.

1. INTRODUCTION

Like many other Rocket Ranges around the world the Brazilian ones, Barreira do Inferno and Alcântara are installed on the coast and, in order to minimize the concerns about flight safety, the impact point for the rockets are offshore. Despite the fact there is a Defined Safety Envelope where planes and boats cannot trespass, sometimes unexpected situations occurs and invasions, especially with small boats. Thus, tactical and logistic supports are provided to assure there is no unaccepted risk of injuries for any people at the moment of launching. This support includes airplanes, helicopters, boats and others facilities provided by other organizations apart the rocket ranges. Depending on the mission profile, the launch timeline could have many hours or could be repeated many days. This increases costs as well as the dependence on external organizations.

In the other hand, due to the fact that Unmanned Aerial Vehicles (UAVs) applications have become more common, this study intends to develop an UAV (or even an UAV squad) capable to scan the sea surface and identify possible unexpected boats. In a second phase of project, the UAV will be used to transmit warnings to these boats and keep the registry of the violation for legal purposes. Project directives includes: At least eight hours of flight time, flight range of hundreds of kilometers, operation at any time of the day, customization to different missions profiles, secure communications and control links.

The next sections will discuss the main concept and projects decisions for the UAV development in the following areas: image processing, path planning, interface and communication. The team involved in this project includes several researchers of different areas, both of Barreira do Inferno Launching Center and Federal University of Rio Grande do Norte.

2. IMAGE PROCESSING

Remote sensing of images has been increasing over the past decades and is becoming a very useful method to identify targets in the industry and the military. On the other hand, the application Unmanned Aerial Vehicles (UAVs) have also become more common, and the features of lightweight digital cameras, like flexibility and high resolution, have enabled more affordable UAV-systems, and remote-sensing platforms better conceived.

In this way, this section of the paper intends to present one of the possible solutions for the problem. It will present the attributes needed for a good target perception, such as camera stabilization; and the heuristic used to recognize the objects and how to merge these images, as well as the results obtained.

2.1. Camera Stabilization

Due to the initial state of the project and one of its objectives, which is to create a low cost system, it will not be afforded a proper camera mechanical stabilization system. However, a good software stabilization system is being developed. The software stabilization is based on an image registration with a transformation model as in [1] and a good image stabilization proposed by [2]. Thus, it is possible to detect an image perfectly, although the mechanical stabilization system of the camera is not one of the best.

Proc. '21st ESA Symposium European Rocket & Balloon Programmes and Related Research', 9–13 June 2013, Thun, Switzerland (ESA SP-721, October 2013)

Although the mechanical stabilization is not focused, a simple one will be developed based on a controlled gyrocompass. Therefore, a damping system will involve the camera, smoothing the noise and vibration of the avionics.

2.2. Target Recognition Heuristic

The heuristic used is based on a shape detection, so it is possible to identify the targets and compare them with a database. It can be separated into two parts: the recognition of the target; and how to merge all the images obtained during the flight in order to compose a mosaic using the images.

2.2.1. Recognition

The main objective of the target recognition is to identify boats in the water that eventually invade the restricted impact area of the rocket fall. In this way, the techniques used to do the image processing are image threshold and shape recognition.

The first step of the heuristic is filtering the image noise, so a smooth filter is applied as a low-pass filter. The second step is to pass from color image to grayscale image for for further image processing. The last step is the application of the threshold filter. This last filter allows the identification of the shapes of the different elements on the image. Some shapes are boats, others shapes are water foam or a reflection of the sun. To distinguish these three possibilities, other heuristic is applied. As the images shows basically water, then different elements are categorized as possible targets. In addition to this, the average RGB color of the image is calculated and compared with the pixels next to the contour of the shapes identified: if the color of these pixels matches with the average value, this possible target could not be a real target, it could just be sea water foam or a reflection of the sun. However, if the value next to the shape contour is different from the average value, this classifies a possible target, considering that the boat is a different color to the water. Another important point is to compare the images with a database of boat shapes. However, this can only be done after some real pictures have been taken from the aircraft.

In Figure 1 it is possible to see how the threshold filter acts on the image, and after this, the contours of the detected objects are identified. As it is possible to see in the images, it is clear how the shapes are identified. It is worth mentioning that at least one of the boats must be recognized, because after recognition the images go to the ground station operator, who can make the subsequent decision to send the coast-guard using the specific coordinates sent by the UAV.

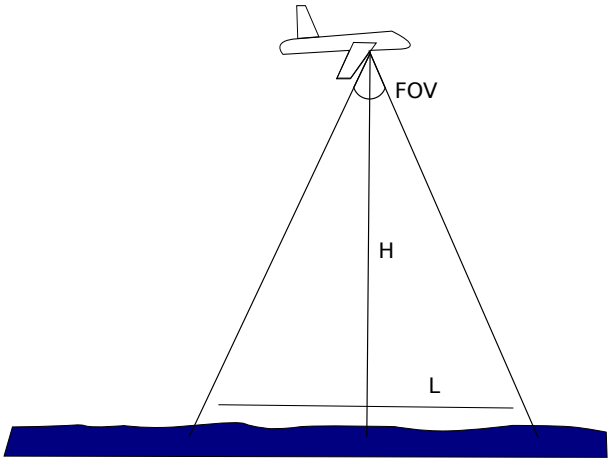

Figure 2. Schema of the height by the FOV of the camera

2.2.2. Merged Images

Another objective of the image processing is to produce large images with the mosaic of all the images obtained during the flight. This mosaic is a composition of images generated by the spatial position of the airplane and the size of the images. Other applications of the mosaic images are observed in [3], where a landslide investigation is made. The difference between landslide and ocean surveillance is that the ocean is always changing because of the waves, while the landslide does not have big differences between the frames of the camera.

In this case a simple mosaic will be made with the images. The position and the direction of the UAV is provided upon request and the distances on the water can be calculated by the FOV (Field of View), along with the height, which can also be accessed upon request. In the Figure 2, it is possible to take the simple trigonometry function of the linear space of the water by the height of the UAV through the Equation (1), where L is the width of the observed area and H the height.

$$\tan\left(\frac{FOV}{2}\right) = \frac{L}{2 \cdot H} \tag{1}$$

Therefore, once the value of the width of the observed area is obtained, it is possible to relate to it the resolution of the camera and count how many pixels are needed for 1 meter, which allows the calculation of any area or distances between pixels.

3. PATH PLANNING

Due to autonomy restrictions, one of the main goals when the trajectory of a UAV is planned is to make it able to identify the targets, covering the largest distance in the shortest possible time. Besides, the path that the airplane

(a) the original image

(b) the processed image

Figure 1. The application of the threshold filter. Image obtained by Google maps (maps.google.com)

is going to perform will be directly linked with the field of view of the camera used in image processing, the height of the flight and with the airplane velocity. In this way, it is possible to see how important is to create a good trajectory.

To solve the path planning problem there are two main search algorithms in convex areas: Spiral and Back and Forth [4, 5]. The idea of the Spiral method is start searching on the outer perimeter, and go to the center of the area in spiral pattern (Figure 3). In the method Back and Forth, the search is made by going back and forth in parallel and turning at the perimeter of the area (Figure 4).

Therefore, for the UAV path planning be performed, this following variables are needed: the area to be investigated, the coordinate of the rocket target and the covered area by one frame of the embedded camera in the aircraft (Figure 5). Initially, it was decided to choose a simple algorithm based on the spiral to obtain the trajectory of the airplane, however the starting point, the center of the spiral, will be chosen near one of the previous calculated impact points (the closer to the impact areas). This method was chosen since it starts to cover the main impact points areas first. Once occurs the time to investigate is shorter than expected, the main impact point area has already been covered.

The idea is to perform a spiral described in [6] with the center on the impact area. The distances between the turns must be the width of the observed area of the camera used to the surveillance. Thus, using the parametric equations of the spiral, it be possible to create an algorithm to provide us the (x, y) coordinates of the vertices of the spiral path in the Cartesian plane. It is worth mentioning, for the stop condition of the algorithm, that the radius of the spiral should reach up to 2x the radius of possible rocket impact area for increase the security.

According to these specifications, the path planning algorithm is given by:

Algorithm 1 Spiral Method Algorithm

01: $C_x = X$ of center spiral;
02: $C_y = Y$ of center spiral;
03: $l =$ width of the observed area;
04: $r_{max} =$ diameter of possible rocket impact area;
05: $r = 0 : l/4 : r_{max} \cdot 2.0$;
06: $t = 0 : \pi/4 : (length(r) - 1) \cdot \pi/4$;
07: $x = C_x + r \cdot \cos(t)$;
08: $y = C_y + r \cdot \sin(t)$;

Assuming that the camera can cover 192m wide by photo, the rocket has the impact point coordinate 05° 57.97 'S / 034° 30.1' W and has a radius of 3km as a possible area of impact, the following result shown in Figure 6 was obtained. It must be remember that is necessary to convert the coordinate system in degrees, minutes and seconds for the Universal Transverse Mercator (UTM) system. For our application, the location is the 25M zone.

4. GROUND STATION INTERFACE

The human-machine interface of the ground station was divided in two different screens, one to be used by the pilot, while the other is used by the sensor operator, in charged of the operation's security. The decision of separating the interface in two screens was to maintain the

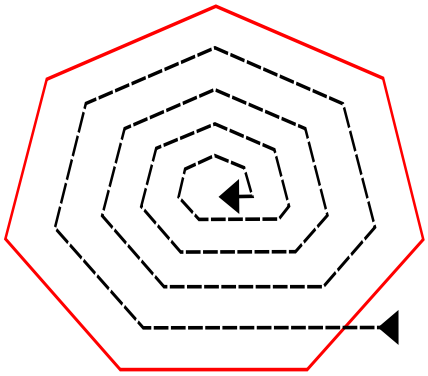

Figure 3. Spiral Method

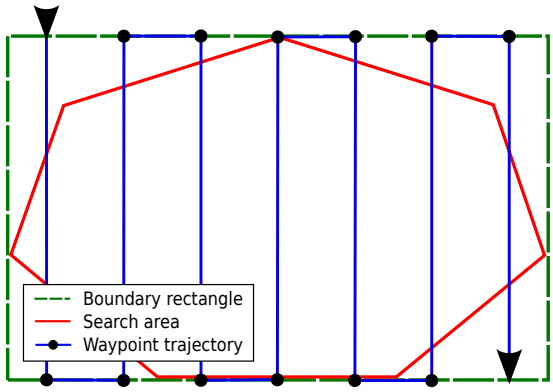

Figure 4. Back and Forth Method

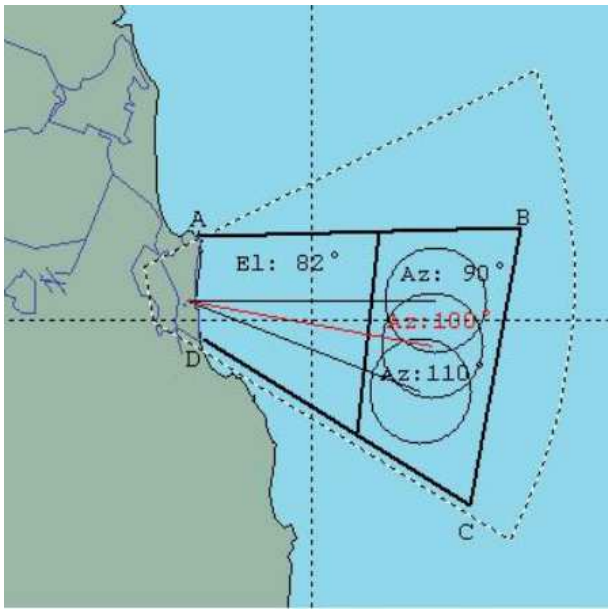

Figure 5. Area under investigation

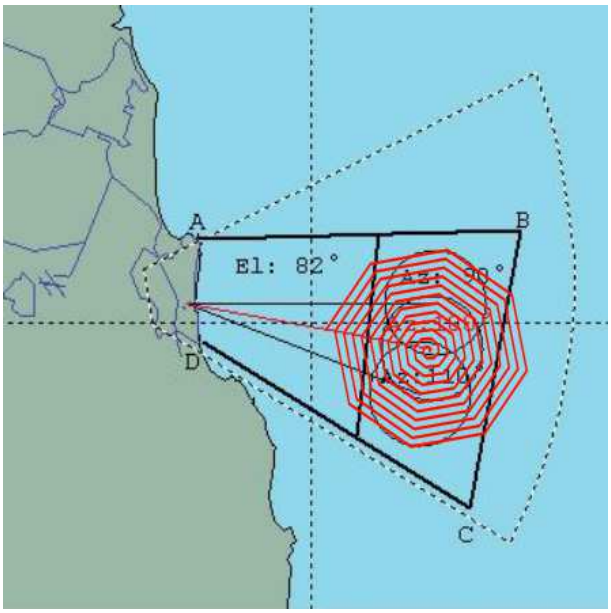

Figure 6. Algorithm applied to the area to be investigated

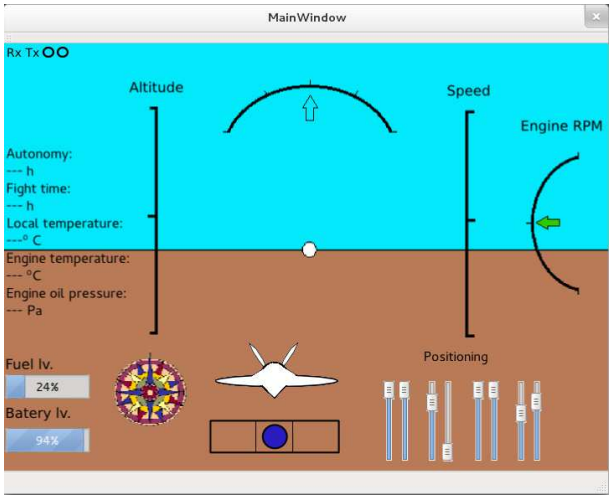

Figure 8. Pilot's screen

pilot's attention on guiding the VANT, not needing him to focus on the camera's image.

The sensor operator's screen can be seen in Figure 7. The mission map shows the origin point, the VANT's desired trajectory and it's current position. There is also a numeric representation of the location, in latitude and longitude. The processed camera image shows the filtered image of the VANT's camera, already identifying possible boats surrounding the impact area.

Figure 8 shows the interface to be used by the pilot. All the important and relevant information for the pilot to monitor the flight as well as assume manual command are show in it: autonomy, flight time, engine temperature, local temperature, engine's oil pressure, fuel level, battery voltage, compass, slide angle indicator, speed, altitude, engine's rotation per minute, positioning of servos and flaps, as well as an indication of the horizon line and roll. The angle positioning for servos and flaps is important for the pilot to verify that his commands are activating the correct devices, while the slide angle indicator shows the difference between the VANT's longitudinal axis vector and the speed vector, so it's possible to verify if the vehicle is moving towards the same direction the camera is observing.

5. COMMUNICATION LINK

The main purpose of link budget is to ensure that the data transmition error rate and the average time of system unavailability meets the needs of the application [7]. In order to achieve this goal, it is essential that the channel effects over the transmitted signal to be properly modeled.

Propagation through the atmosphere and near Earth's surface can cause different effects over the RF signal, such as absorption, reflection, diffraction or scattering. The wireless channel characteristics clearly generate degradation in the quality of the communication link.

When the distance between the transmitter and receiver is of the order of tenth of kilometers, the atmospheric absorption effects on RF signals transmitted in line of sight is given by the Friis Equation [8],

$$P_r = \frac{P_t G_t G_r \lambda^2}{(4\pi)^2 d^2 L} \tag{2}$$

where P_r is the received power, P_t is the transmitted power, G_t is the gain of the transmitting antenna, G_r is the gain of the receiving antenna, λ is the wavelength of the transmitted signal, d is the distance between the transmitter and receptor and L is the attenuation due to the losses in the transmission and reception circuits.

The attenuation of the signal, measured in dB, is defined as the difference between the effectively transmitted power and received power, as expressed by:

$$\begin{aligned} P_{t(\text{dBm})} - P_{r(\text{dBm})} &= 32,4 + 20\log f_{(\text{MHz})} \\ &+ 20\log d_{(\text{km})} \\ &+ L_{(\text{dB})} \\ &- G_{t(\text{dB})} - G_{r(\text{dB})}. \end{aligned} \tag{3}$$

From Equation 3, it can be observed that as higher are the frequency of the radio signal and the distance between transmitter and receiver, the greater will be the attenuation of the signal in the receiving antenna.

In addition to the absorption effects on the transmitted signals, some wireless channels, such as that considered in this work, can cause time-variant fluctuations in the signal received amplitude. The model based on the Friis equation cannot explain this phenomenon, which is called *multipath fading*. The presence of multiple propagation paths is due to factors such as atmospheric refraction and diffraction, or reflections on planes surfaces. In this communication environment, the signals that arrive from different paths will have different delays and attenuations. Moreover, the paths can be continuously altered with the change of the channel geometry or the relative movement between the antennas. These phenomena affect the signal in a random manner and cause time-variant attenuation and dispersion [8, 9, 10].

The multipath fading can be taken into account in the link analysis through the concept of *fading margin*, which is the difference between the nominal received power (in the absence of any multipath fading), denoted by P_r, and receiver threshold power P_{th}, that depends on the reception sensitivity of the radio equipment:

$$FM_{(\text{dB})} = P_{r(\text{dBm})} - P_{th(\text{dBm})}. \tag{4}$$

The fading margin must be large enough to accommodate the random fluctuations of the signal caused by the multipath fading. Thus, the probability of unavailability of the communication link should decrease when the fading

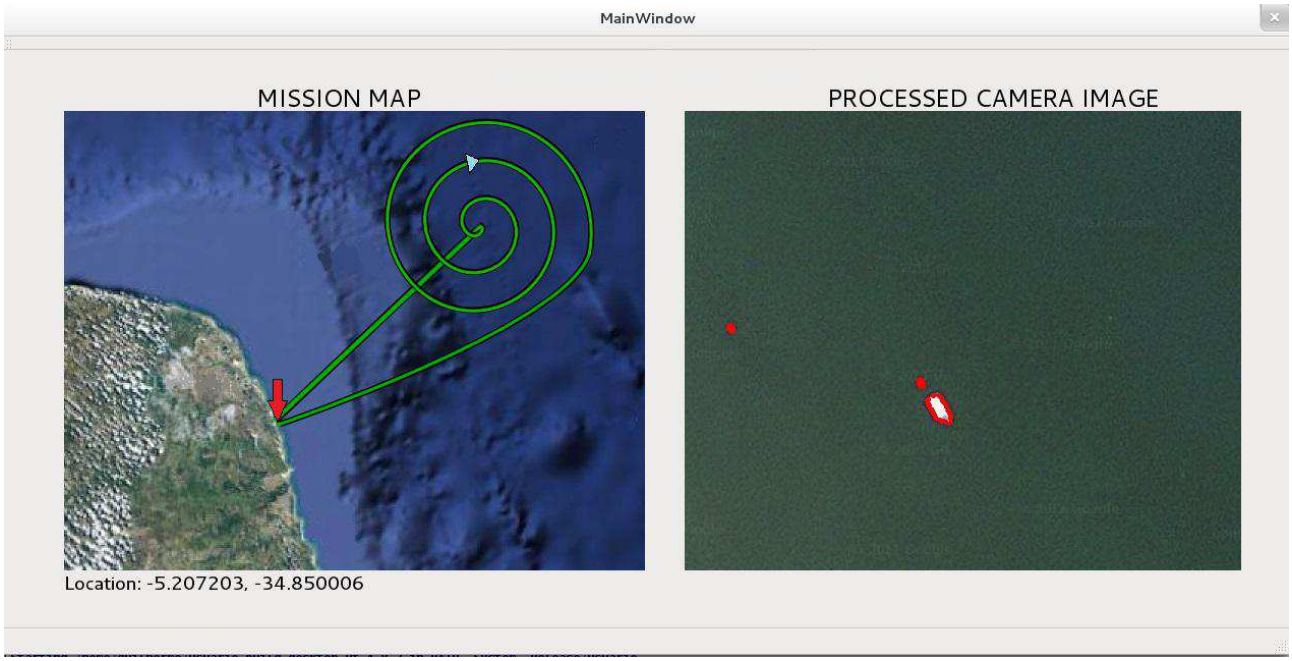

Figure 7. Sensor operator screen

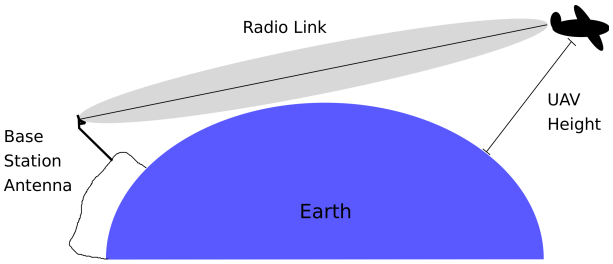

Figure 9. The earth curvature and the mobility of the airplane can affect the radio link.

margin is increased. According to the Barnett-Vigants model, the probability of a fade of depth FM (dB), which leads to an interruption of the radio link, is given by [11]:

$$P_F = 6 \times 10^{-7} C f d^3 10^{-0,1FM} \quad (5)$$

where P_F is the probability of a fade as a fraction of time, d is the path length in kilometers, f is the frequency in gigahertz, FM is the fading margin in dB and C is selected based on the basis of the type of environment in which the link is to operate. In humid regions, the factor C is approximately equal to 6 [11].

The project of long distance radio links for UAVs with operations in sea areas should also consider issues related to the earth curvature and mobility of the airplane. The earth curvature can result in the absence of the line of sight between the transmitter and receiver antennas. On the other hand, the UAV can move outside of the coverage area of the base station antenna (Figure 9).

The link budget developed in this work took into account all the characteristics of the communication environment previously presented to define the system parameters used in the communication with the UAV. These parameters are presented in the Table 1.

Table 1. System Parameters

Maximum Path Length	160 km
Average Height of Overflight	500 m
RF Power Output (Base Station)	50 W
RF Power Output (UAV)	5 W
RF sensitivity, 1ppm BER	-90 dBm
Base Station Antenna Gain	43 dBi
UAV Antenna Gain	6 dBi
UAV Antenna Beamwidth	80°
Height of Base Station Antenna	70 m

From Table 1, considering a circuit loss of 2.5 dB in the transmission and reception circuits, the power of the signal received by the UAV on the uplink can be calculated from the Equation 2, being equal to -22.56 dBm for a path length of 160 km, whereas the received power at the base station on the downlink is approximately equal to -55.35 dBm.

From Equation 4, the fading margin in the uplink is equal to 67.44 dB, which leads to an unavailability probability approximately equals to $P_F = 9.88 \times 10^{-6}\%$. In the downlink, the fading margin is equal to 34.65 dB with an unavailability probability approximately equals to $P_F = 0.259\%$.

6. RESULTS

First results obtained in the project includes: image recognition for boats, optimized path planning for mission profile, airplane software interface for missions and the development of the communication link.

The image processing results obtained were acceptable. An experimental test considering 10 different images with boats was performed, and all the image elements was identified. Next step in development is match the type of boat. Actually this is not a problem since it is only necessary to identify one boat in the image for the ground operator to send to the coast guard.

A spiral algorithm for path planning was developed and applied in a simulation using real data. The results show the simulated airplane was capable to scan the interested area from a given previous calculated impact point. Next step in development is to implement other methods to compare the algorithms, analyzing the distance to be traveled and the path easier for the plane.

A human-machine interface to manage the UAV was developed for the ground station using two different screens, one to be used by the pilot, and the other to be used by the sensor operator, in charge of the operation's security.

A radio system was specified in order to ensure reliable communication with the UAV. The values obtained for the fading margins of the system indicate a very low unavailability probability, approximately equal to 3 seconds per year in the uplink (control link) and 23 hours per year in the downlink (data link).

7. CONCLUSIONS

The Brazilian rocket range Barreira do Inferno operates with sounding rockets in order to make many different scientific experiments like micro-gravity physics and meteorological researches, and develops an UAV to scan impact points of this rockets, searching for unexpeced boats for secutiry reasons. The results of the project will possible modify Brazilian launch procedures and safety rules. The project has started in December 2011 and the first flight of the prototype is scheduled for 2013.

ACKNOWLEDGMENTS

Funds are provided by AEB (Brazilian Space Agency) and CNPq (National Counsel of Technological and Scientific Development).

REFERENCES

[1] Brian P. Jackson and Arthur A. Goshtasby. Image registration for a video stabilization and motion detection. In *WorldComp*, Las Vegas, Nevada, 2011.

[2] Carlos Guestrin, Fabio Cozman, and Eric Krotkov. Fast software image stabilization with color registration. In *IEEE/RSJ International Conference on Intelligent Robots and Systems (IROS)*, 1998.

[3] U. Niethammer, S. Rothmund, U. Schwaderer, J. Zeman, and M. Joswig. Open source image-processing tools for low-cost uav-based landslide investigations. *ISPRS - International Archives of the Photogrammetry, Remote Sensing and Spatial Information Sciences*, XXXVIII-1/C22, 2011. doi: 10.5194/isprsarchives-XXXVIII-1-C22-161-2011.

[4] Gustav Öst. *Search path generation with UAV applications using approximate convex decomposition*. PhD thesis, Linköping, 2012.

[5] Yu-Song Jiao, Xin-Min Wang, Hai Chen, and Yan Li. Research on the coverage path planning of uavs for polygon areas. In *The 5th IEEE Conference on Industrial Electronics and Applications (ICIEA)*, pages 1467–1472. IEEE, 2010.

[6] Petruševski Ljiljana, Dabić Milana, and Devetaković Mirjana. Parametric curves and surfaces: Mathematica demonstrations as a tool in exploration of architectural form. *Spatium*, 2010.

[7] Bernard Sklar. *Digital Communications: Fundamentals and Applications*. Prentice-Hall, Inc., Upper Saddle River, NJ, USA, 1988. ISBN 0-13-211939-0.

[8] Theodore Rappaport. *Wireless Communications: Principles and Practice*. Prentice Hall PTR, Upper Saddle River, NJ, USA, 2nd edition, 2001. ISBN 0130422320.

[9] Bernard Sklar. Rayleigh fading channels in mobile digital communication systems - Part I: Characterization. *Communications Magazine, IEEE*, 35(7):90–100, 1997. ISSN 0163-6804. doi: 10.1109/35.601747.

[10] Bernard Sklar. Rayleigh fading channels in mobile digital communication systems - Part II: Mitigation. *Communications Magazine, IEEE*, 35 (9):148–155, 1997. ISSN 0163-6804. doi: 10.1109/MCOM.1997.621038.

[11] Harry R. Anderson. *Fixed Broadband Wireless System Design*. Wiley, West Sussex, England, New York, 2003. ISBN 0-470-84438-8.

THE FACILITIES AT CHINESE HAINAN SOUNDING ROCKET LAUNCH SITE

Liu Cheng[(1)], Jiang Xiujie[(2)]

(1)National Space Scince Center, CAS, P.R.China，No.1 Nanertiao, Zhongguancun, Haidian district, Beijing,China, Liucheng@nssc.ac.cn

(2)National Space Scince Center, CAS, P.R.China，No.1 Nanertiao, Zhongguancun, Haidian district, Beijing,China, Jiangxj@nssc.ac.cn

ABSTRACT

Hainan sounding rocket launch site is a non-military site built in 1980s by Chinese Academy of Sciences. The geographic location in Chinese low-latitude area makes it to be a unique and important observation of the space environment in China by sounding rocket or ground-based instruments. This paper introduces the location, infrastructure, facilities and observation instruments of the site. The site is still in developing phase, the planning of new facilities and range expansion is involved.

1. INTRODUCTION

The Chinese Hainan sounding rocket launch site (19º30′N, 109º8′E) is located in the Fuke town, northwestern of Chinese Hainan Island, 12 km southeast to the Beibu gulf, and 140km to the Meilan airport. The site was established in 1985 to utilize sounding rockets to detect low-latitude space environment, by National Space Science Center (NSSC), Chinese Academy of Sciences, formerly known as Center for Space Science and Applied Research (CSSAR).

Also, its geographic location near equator makes it to be a unique and important observation of the space environment in China. Now, the site has the capability of launching sounding rockets, and deploys about ten ground-based observational instruments. About 7 rockets have been launched in the site. And, it has been appointed as a Chinese national field research station for space weather in the low latitude area.

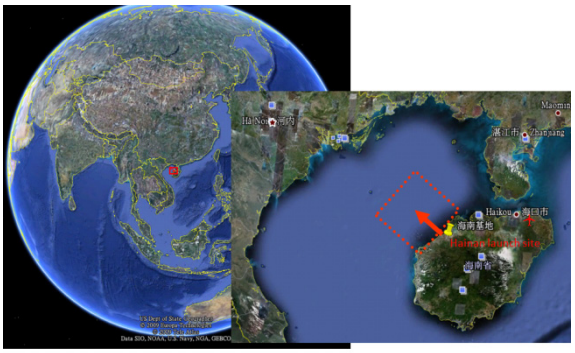

Figure 1. Geographic position of the Chinese Hainan launch site

2. INFRASTRUCTURE

After the launch site was established and ZN-3 sounding rockets launched in 1991, no sounding rocket mission was carried out in the site during 1991 to 2010[1]. And, no financial support was obtained for the facilities maintenance and repair, until the Meridian Project started in 2008.

Meridian Space Weather Monitoring Project (Meridian Project) developed the rocket sounding subsystem in the site[2]. After limited rehabilitation and reconstruction, the site regains the capacity of assembling, launching and tracking sounding rockets.

Therefore, the site is still in its true developing phase, with limited technical facilities. The impact area is the Beibu gulf near the Hainan island. Till now, the site has no recovery system, or no TC facilities. All the rockets launched here were non-recovery.

The site is divided into 3 zones: the main zone, the assembly zone and launch zone. The internal communications in the site are implemented by a Cisco IP communications platform based on the local fiber

Proc. '21st ESA Symposium European Rocket & Balloon Programmes and Related Research', 9–13 June 2013, Thun, Switzerland (ESA SP-721, October 2013)

LAN, with more than 20 IP phones.

The main zone covers an area of nearly 20 acres, comprising the main building, the commanding hall, the meeting room, scientific ground-based observation instruments, hotels, apartment houses, and a restaurant. It can accommodate nearly 50 people. The 40 people meeting room is close to the commanding hall. The restaurant is generally open for breakfast, lunch and dinner during campaigns.

Figure 2. The commanding hall

The assembly zone covers an area of nearly 8 acres, located 1.5 km west of the main part, including a assembly workshop and a storage. The assembly zone is 300 square meters large, deployed a 3-ton hoist, where the payloads and rockets are assembled. The launch zone includes a launcher pad and a blockhouse.

3. WEATHER

Hainan Sounding Rocket launch site has a tropical monsoon climate, mild climate. Its annual average sunshine is more than 2000 hours, with annual average temperature 23~24 ℃. In January average temperature is 16.9 ℃, while mean temperature in the month of July is 28.3 ℃. Annual rainfall is nearly 1800 mm. It is the rainy season from May to October, throughout which rainfall accounts for 85% of the year. Situated in northwest of the Hainan island, the site is less affected by the typhoon. Every year there are nearly 3 times strong winds. The annual average of wind speed is 3.5 m/s. As the site is near the Beibu gulf, the daily average air humidity is above 70%RH. At nights or rainy days, the air humidity is often above 90%. Moisture-proof design is necessary for payloads onboard and instruments on ground.

It is suitable for launching activities in Hainan sounding rocket site from November to April of the next year.

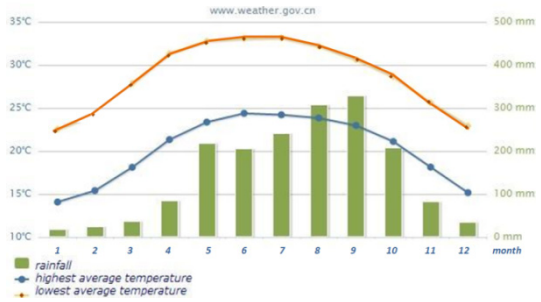

Figure 3. The monthly average temperature and rainfall in Hainan sounding launch site [3]

4. FACILITIES

4.1. Launcher

The launcher is rated as a 1.5 tons maximum design load launcher, with one 7 meter long rail. The azimuth angle is fixed, with the northwest direction. Launcher is suitable for rockets of TY-3 or TY-4 type, developed by China Aerospace Science and Technology (CAST).

Figure 4. Launcher

4.2. Telemetry

Two mobile telemetry stations, supporting S band 2.3 GHz RF downlink, are situated on the seacoast of the Beibu gulf. One locates in the Haiwei town nearly 40km west of the launch site, while the other is in the Eman town 40km northeast. For the Kunpeng-1 sounding rocket with a 4W RF transmitter and antenna, tracking

near the 200km altitude range is guaranteed.

1) Operating frequency: S-band (nom. 2300MHz);

2) Modulation mode: BPSK;

3) Antenna diameter 3m, parabolic;

4) Gain: 60dB;

5) Demodulation sensitivity: -99.5dBm;

6) Tracking modes：manual, auto, program;

7) Maximum tracking velocity：10°/s.

Figure 5. Telemetry station in Haiwei

4.3. Meteorological facilities

For sounding rockets without guidance and navigation control, it is very import to confirm that the wind speed meets the launch criterion. Usually, the wind is 2~4 class in the site. Meteorological facilities of the site include a ground-base automatic meteorological monitor and a balloon radiosounding system.

Measure altitude range of balloon radiosounding system is 0~30km. Measure items are wind speed and direction, temperature, pressure. Automatic meteorological monitor on ground, WMAS-600, measures wind speed and direction, temperature, pressure, humidity and rainfall.

4.4. Observational instruments

As a national field research station, ground-based observational instruments of space environment are listed below [4].

1) Digital ionosonde DPS-4D: To investigate electron density profiles and plasma drift.

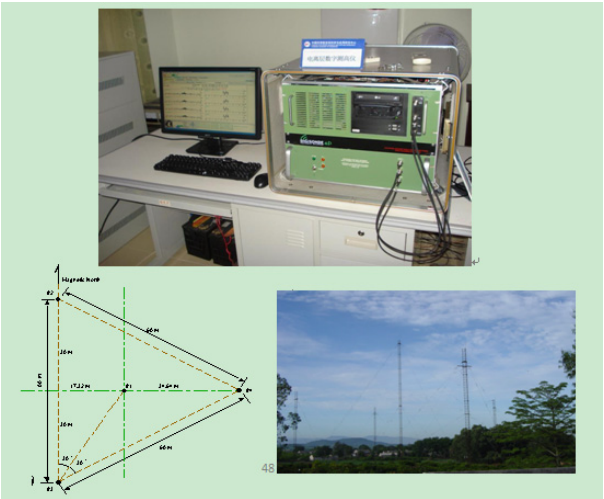

Figure 6. Digital ionosonde DPS-4D

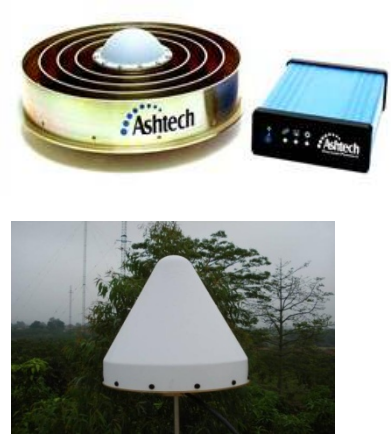

Figure 7. UZ-CGRSGPSReceiver and antenna

2) GPS-TEC Monitor, Ashtech uZ-CGRS GPS receiver: To monitor the total electron content of ionosphere on global scale.

3) GPS scintillation monitor: To monitor ionospheric scintillation by the means of GPS radio signal.

4) Very high frequency radar: To detect ionospheric irregularities structure and electrical field in the ionospheric E layer, and the intensity and drift of the spread F layer.

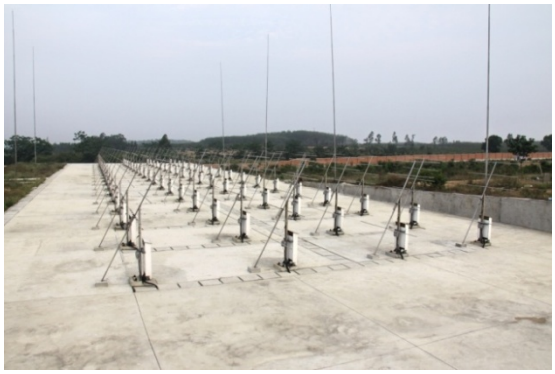

Figure 8. Very high frequency radar

5) All-sky meteor radar: To detect the wind field and diffusive coefficient of the atmosphere, the flux, position and velocity of the meteors between 70~110 km by tracing the meteors.

6) All-sky airglow imager: To detect the horizontal structure and transmitting feature of gravity waves.

7) Lidar: To detect temperature and density profiles of the middle atmosphere

8) Atmospheric electric field instrument: To monitor atmospheric electric field.

9) CHIMAG fluxgate magnetometers: To detect variations in the earth's magnetic field.

5. New infrastructure and facilities

In 2011, Chinese Strategic Pioneer Program on Space Sciences Satellite initiated. NSSC reconstructs the Hainan launch range, and proposes to use sounding rocket to support space science mission.

The Hainan sounding rocket site will construct a new hotel building with more than 20 double rooms. A new ground-based instruments observation building has been constructed recently.

The fixed station of telemetry and recovery system is being built now on the beach of Eman town, with nearly 5 acres area. New infrastructure includes a boat dock, a recovery workshop and a lodging building. The new fix telemetry station will be equipped to tracking sounding rockets above 300 km altitude.

And, a new launcher is going to be developed, with a 12m length beam, 2000kg load. Its elevation and azimuth would both be adjusted automatically.

Currently, an enlargement plan is under consideration, to make the assembly part and the launch pad to be one zone. And a new modern assemble hall, at least 10 meter high and 1000 square meters area, will be built.

6. CONCLUSION

Hainan sounding rocket launch site is a quit new launch site in Chinese low-latitude area. And it has the elementary capacities of assembling, launching and tracking sounding rockets, with altitude range up to 200km. Also, it was a comprehensive ground-based observation for space environment in Chinese low latitude.

About 7 rockets have been launched in Hainan sounding rocket launch site, such as ZNs, Haiyan-1, Kunpeng-1 and Kenpeng-1A. In the future, with more infrastructure and facilities developed, more sounding rockets would be conducted in Hainan launch site. International co-operations in jointed detections or launch services are welcome.

7. REFERENCE

1. Jiang Xiujie, Liu Bo, Yu Shiqiang, etc. Development Status and Trend of Sounding Rocket. Science & Technology Review. 27(23), 2009.
2. The Meridian Project Management Office. Proposal of the Meridian Space Weather Monitoring Project. 2005.
3. The forecast and climate of Danzhou in Hainan. http://www.nmc.gov.cn/publish/forecast/AHI/danzhou.html. (Visited in 18th Jun, 2013).
4. Wu Ji, Wang Chi, Fan Quanlin. Introduction to Meridian Space Weather Monitoring Project. J. Space Sci., 2006, 26(supp): 17~24.
5. Li Dayao. The development of Chinese first generation sounding rocket. Carrier rocket and Recovery Technology. 1992(03).

THE USE OF WRF MESOSCALE MODEL TO DERIVE THE WINDS TO SUPPORT LAUNCHINGS AT THE BRAZILIAN SPACE CENTER

Gilberto Fisch[(1)], Adaiana Francisca Gomes da Silva[(2)], Paulo Geovani Iriart [(1)]

[(1)] *Institute of Aeronautics and Space, Praça Marechal Eduardo Gomes, 50, CEP 12228-904, São José dos Campos, Brazil, Email: fisch.gilberto@gmail.com, pgiriart@gmail.com*
[(2)] *Institute of Aeronautical Technology,* Praça Marechal Eduardo Gomes, 50 *CEP 12228-904, São José dos Campos, Brazil, Email:adaiana1@yahoo.com.br*

ABSTRACT

The determination of the winds (both at surface and upper air) at a Space Launching Center is crucial for the safety in a rocket launching. The wind profile can be used for the determination of the flight trajectory as well as to predict the dispersion of the plume released by the gases exhausted during the lift-off. The mesoscale model WRF (Weather Research and Forecasting) is the state-of-art in terms of atmospheric model and it can be used to forecast all the climatic elements, specially the winds. So, the goal of this paper is to investigate the use of the model WRF at the Centro de Lançamento de Alcântara (CLA), which is the Brazilian access to the space, to provide forecast winds information to the Operational Flight Coordinator. The validation was made through out comparisons between outputs of the model and wind measurements. The observations were made at CLA by rawinsoundings released each 6 hours during 10 days period in the dry season 2008 and wet season 2010. The model WRF-ARW (version 3.2.1) was tested for a domain centered at the CLA. The configuration of the runs was 3 grid nested with a resolution of 9, 3 and 1 km, respectively and 40 vertical levels. The wind forecast for 72 hours were made with initial data-set from GFS (Global Forecasting System, which is the operational analysis from NCEP), starting at 00 and 12 UTC for both periods. The statistical metrics used were Wilmott indexes; bias and square mean error, computing from the differences between the outputs from the model and observations up to a height of 5000 m (ballistic winds). From the boundary layer parameterizations tested (ACM2, MYNN2,5, ETA and YSU), the ACM2 and MYNN2,5 gave the best results for the dry and wet season, respectively. The model WRF was able to represented, reasonable and within the limit of 1 m/s, the wind profile up to 36 hour, for both periods (dry and wet). Also, there is no difference if the simulation started at 00 or 12 UTC. In order to verify the influence of the initial input data, 4 simulations (2 for each season) were made with GFS (analysis) and FNL (re-analysis). The results did not show any significant difference, concluding that it is possible to use the GFS (which is operational) for the simulations during a launching operation. In summary, the model WRF was proved to be useful for a rocket flight providing winds in advance.

1. INTRODUCTION

The Alcântara Space Center (CLA) is the Brazilian gate to the space. From this Center, it is launched the guided rocket as Satelite Vehicle Launcher (VLS) and unguided sounding rockets (like VSB30). Especially for the sounding rockets, the winds are very important to determine the flight trajectory and it is computed as a sum of the internal (characteristics of the rocket) and external (winds) forces involved [1].

Consequently, the wind determination is a key parameter for the successful of the mission. During the countdown, the wind profile is determined using different techniques (including rawinsoundings and/or wind profiler). However, for future determination, only numerical models can do it based on the prognostic Navier-Stokes equations.

The wind regime at CLA is very complex as it is a superposition of the trade winds and the sea breeze developed due to the thermal contrast between ocean and continent [2]. Following the reference [3], the rainfall regime at CLA is governed by the position of the Intertropical Convergence Zone, which follows the relative position between Earth and Sun.

The objective this work is to compare the outputs from a numerical mesoscale model with the observations collected at the Alcantara Space Center. The better boundary layer parametrization (which distributes the momentum within the atmosphere) was also determined for the tropical conditions.

2. DATA SET AND METHODOLOGY

The ASC is located along the coast at the latitude 2° 19' S and the longitude 44° 22' W and 40 m above sea-level (Figure 1). The climate presents a precipitation regime divided in wet period (from January up to June) being March and April the peak of the rain (higher than 300 mm/month) and a dry period (from July up to December) with precipitation lower than15 mm/month (Figure 2). The wind regime possesses a distinct behavior between the rainy and dry season. During the wet period the surface winds are weaker (typically around 4.0 – 5.0 m/s) than during the dry season (winds

Proc. '21st ESA Symposium European Rocket & Balloon Programmes and Related Research', 9–13 June 2013, Thun, Switzerland (ESA SP-721, October 2013)

around 7.0 – 9.0 m/s). This is due to intensification of the sea breeze that presents its maximum influence during this time (particularly from September until November). The wind direction is from the NE at both periods.

Two observational data-sets made by radiosondes have been used to compare with the numerical outputs. The rawinsounding system used was from Vaisala Oy (Helsinki, Finland) MW11 using a sonde RS80-15G (with GPS capabilities). During the ascension phase, the GPS sensor sampled the balloon positions at 2 s and an average winds for 50 m height interval were processed as the averaged wind profile for the layer. The data-set used were obtained from an intensive field campaign from September 15 until 30, 2008 (representing the dry season) and from March 19 up to 25, 2010 (representing the wet season).

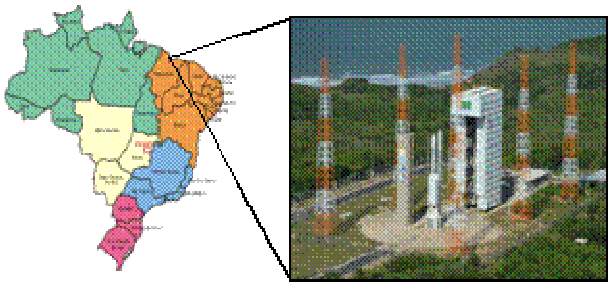

Figure 1. Geographic Localization of the ASC and a view of the launching pad

For this work the mesoscale model named WRF –ARW (*Weather Research and Forecasting - Advanced Research WRF*) version 3.2.1 was used as it is the "state-of-art" for regional models [4].It is also an open code, friendly user and has several parametrizations for radiation, boundary layer, convection, etc that can be easily tested and changed to be locally adapted. Especifically for the boundary layer parameterizations, the following schemes were tested and compared with the measurements (rawinsoundings): ACM2, MYNN2.5, ETA and YSU. This software is relatively easy to install and operate it at the range center [5].

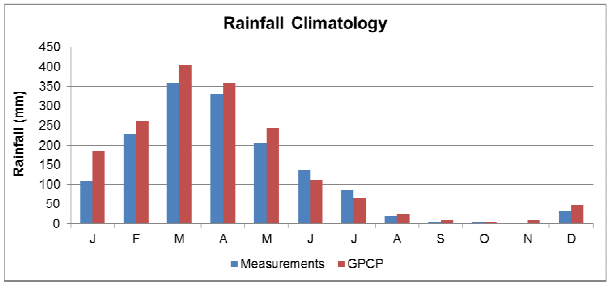

Figure 2. The rainfall climatology for ASC.

In general, the statistics metrics used to compare the observations and the numerical outputs are bias, root-mean-square. For this study, the Willmott indexes were also used to identify which boundary layer parameterization are better [6].

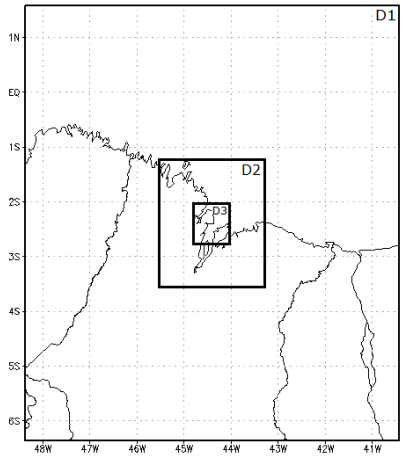

Figure 3. The 3 domains used for the numerical simulations.

3. RESULTS

The data used to initialize the model was the meteorological field from National Center of Atmospheric Research (NCEP) named GFS, with spatial resolution of 0.5° x 0.5° (approximately 55 x 55 km). The land use – land cover data was obtained at United States Geological Survey (USGS) (available at http://www.mmm.ucar.edu/wrf/src/wps_files/geog.tar.gz), with spatial resolution 30". All the simulations were made with 42 vertical levels at the 3 nested grids centered at CLA (Figure 3). The spatial resolution was 9, 3 and 1 km for the inner grid. The simulation was started at 12 UTC, with a forecast of 72 hours (3 days) and a spin-up of 6 hours.

The Figure 4 presents the time series of the windspeed (ballistic winds) for all simulations (2008 and 2010). It can be observed that the either the intensification (case for 2008) or reduction (case for 2010) of the measured winds was simulated by the model. The differences are within the range of 0.5 – 1.0 m/s which is absolutely negligible for trajectory determination. The temporal variation is much more important for the operational perspectives.

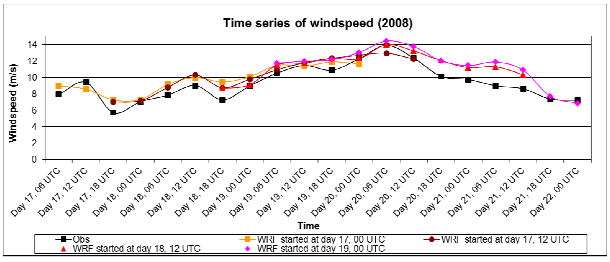

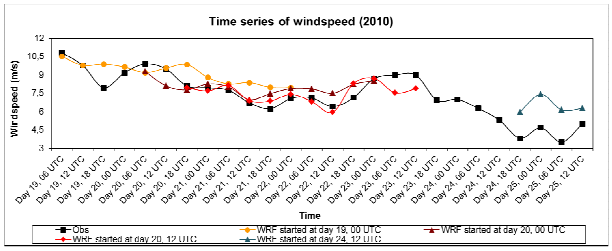

Figure 4. Time series of the windspeed: observations and numerical outputs for 2008 and 2010.

At Fig. 5, it is presented the time series for the wind direction for the dry and wet periods. Again, the direction of the winds was very well represented (for both cases 2008 and 2010), although the results for the dry season is slightly better. A diurnal oscillation of the wind direction (probably due to the sea breeze) was also captured by the model.

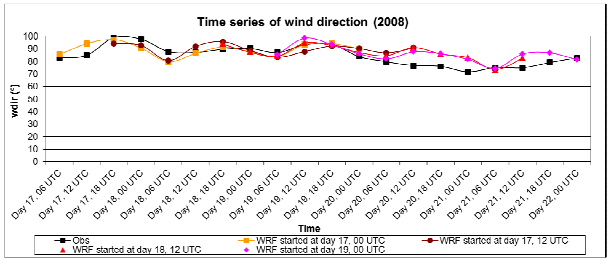

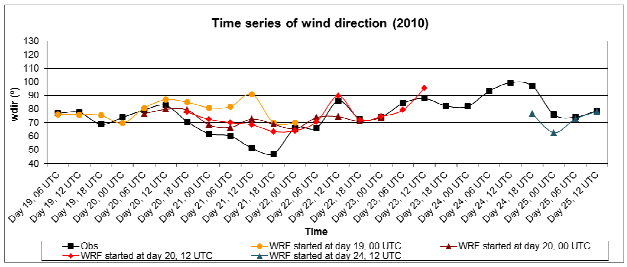

Figure 5. Time series of the direction: observations and numerical outputs for2008 and 2010.

Finally, the initial data assimilation (GFL or FNL) was tested. It should be mentioned that the GFL is a operational scheme (e.g., there are outputs from a larger model each 6 hours) and FNL is a better description of the meteorological fields, but it is not available rapidly. The results are presented at Figure 6 and there is no significant different between the 2 initial data-sets.

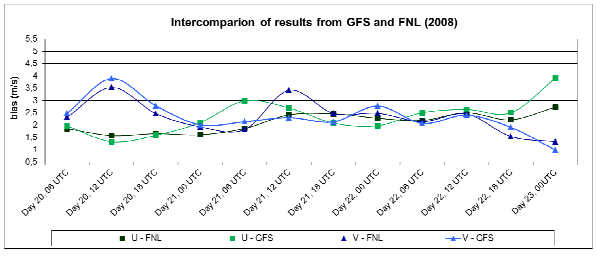

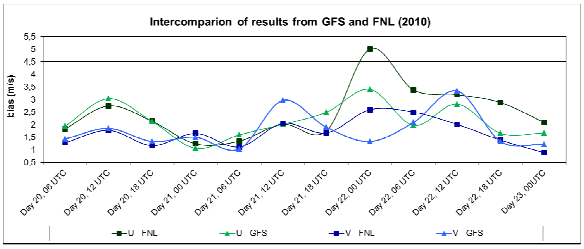

Figure 6. Time series of the windspeed for the numerical outputs for different initialization (GFS and FNL) for 2008 and 2010.

4. CONCLUDING REMARKS

The differences amongst the 4 parametrizations used were very small and the best parameterizations that can be used for the tropical region is either ACM2 (better results for dry season) or MYNN2.5 (better results for wet season). The differences between them are negligible. The WRF model was able to represent very well the wind profile at CLA up to 2 days in advance and this information is very useful for the launching operations. Another important result is that the use of FNL does not represent an improvement of the results and the initial data from GFS can be used.

5. ACKNOWLEDGMENTS

The authors would like to thanks the financial support from the Brazilian Organizations: AEB – Brazilian Space Agency (contract number 559949/2010-3) and CNPq - National Council for Research (303720/2010-7). This work is part of the Master of Science Dissertation from Adaiana Francisca Gomes da Silva presented at INPE in Feb 2013.

6. REFERENCES

1. Palmério, A.F. (2006*). Introdução a Engenharia de Foguetes*, ITA Mestrado Profissionalizante, São José dos Campos, Brazil, 142 p.
2. Fisch, G. (2010). *J. Aerosp. Technol. Manag*., **2**(1), 105-110.
3. Barros, S.S. & Oyama, M.D. (2010). *Revista Brasileira de Meteorologia*, 25(3), 333-344.
4. Smararock, W.C., Klemp, J.B. & Dudhia, J. (2008). A description of the Advanced Research WRF – version 3, 113 p.
5. Wang, C., Hu, J., Feng, S., Jin, S., Zhang, F. & Liu, C. (2011). Comparing different boundary layer schemes of WRF by simulation the low-level wind over complex terrain. In: INTERNATIONAL CONFERENCE ON ARTIFICIAL INTELIGENCE, MANAGEMENT SCIENCE AND ELECTRONIC COMMERCE Zhengzhou, China (p 6183-6188.).
6. Willmott, C.J. (1981). *Physical Geography*, **2**, 184-194.

Ionosphere

Chair: O. Havnes

BONUS RESULTS FROM ION PROBES

Martin Friedrich[(1)], **Klaus Torkar**[(2)], **Scott Robertson**[(3)], **Shannon Dickson**[(3)]

[(1)] *Graz University of Technology, Graz, Austria, Email: martin.friedrich@tugraz.at*
[(2)] *Space Research Institute, Austrian Academy of Sciences, Graz, Austria, Email: klaus.torkar@oeaw.ac.at*
[(3)] *University of Colorado, Boulder, CO 80304, USA, Email: scott.robertson@colorado.edu*

ABSTRACT

The two CHAMPS rocket payloads were attitude controlled to maintain (almost) zero angles between rocket axis and velocity vector. Each payload carried two positive ion probes on hinged booms opposite to each other. With such an arrangement no spin modulation of the measured current is expected; however the currents measured by the two probes were slightly modulated with the spin frequency and clearly in antiphase. The hitherto best explanation for this unexpected phenomenon is that winds perpendicular to the rocket axis led to an effective misalignment of the otherwise almost perfectly attitude controlled flights.

1. THE USUAL ARRANGEMENT

Electrostatic probes to measure the number density of ions have been used by the rocket community for decades. The basic idea is that a gridded sphere, sweeping through stationary plasma, collects an ion current primarily determined by the (relative) velocity and the probe's effective cross section. The current to a stationary probe is due to the ions' thermal velocity v_{th}, but the main contribution is due to the velocity of the probe relative to the plasma [1]. For realistic rocket trajectories (apogees >100 km) the (assumed) thermal velocity considered in these calculations only contributes a minor uncertainty near apogee when the rocket velocity is lowest and of the same order as v_{th}. Fortunately at altitudes above 90 km the ions' mass is known (30 or 32 amu) and the assumptions concerning their mass and temperature are not critical; at low altitudes on the other hand, the rocket velocity by far exceeds v_{th}. The usual location of positive ion probes (PIP) is on a boom deployed sideways, whereas the central location is only rarely available for this instrument (Fig. 1). The length of the boom ideally positions the probe outside the shock cone which is developed by the forward instrumentation, thus the probe samples the undisturbed ionosphere. The Rexus payload flown in October 2004 provides a good example of such a scenario. In Fig. 2 the ion current near 85 km is shown. In this particular flight at that height the angle of attack exceeds 4° and apparently the probe moves in and out of the shock cone. Fig. 3 shows the measured current of the whole flight. The general practice is to assume that only the maxima in each spin period represent the undisturbed ionosphere. The ion density thus based on only one value per spin period is depicted in the right panel of Fig. 3. The good agreement between up- and downleg confirms the validity of the procedure of relying on the highest value in a spin period.

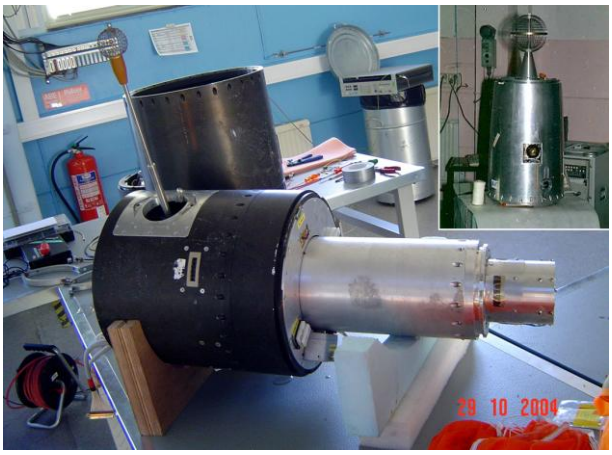

Figure 1. Location of the ion probe (PIP) on the REXUS payload. The configuration in the insert is preferable, but a very exceptional case (payload NLTE-91).

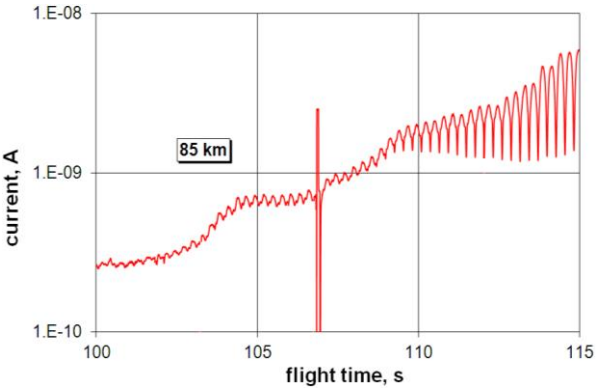

Figure 2. Ion current measured near 85 km on upleg. For angles of attack beyond 4° the PIP only reaches outside the shock-cone once in a spin period.

2. THE SPECIAL CASE OF CHAMPS

CHAMPS were two sounding rocket payloads designated to investigate charged dust particles by means of a dedicated mass spectrometer. As outlined above, one generally expects only one current value per spin period representing the true ion density. Primarily in order to improve the height resolution two (largely) identical ion probes were flown on the CHAMPS payloads 180° to each other (Fig. 4, left panel), notably since these payloads had a very low spin rate of only 2 s^{-1}.

Proc. '21st ESA Symposium European Rocket & Balloon Programmes and Related Research', 9–13 June 2013, Thun, Switzerland (ESA SP-721, October 2013)

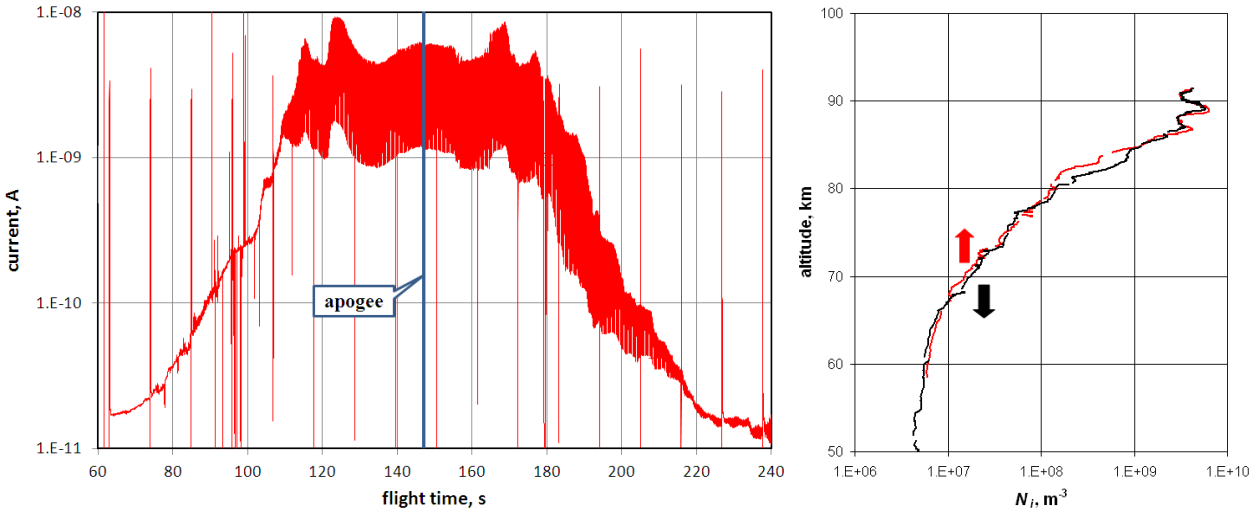

Figure 3. Ion current of the whole flight (left) and the resulting ion density profile (up- and downleg) using only the maxima in a spin period (right).

The instrument MASS (= Mesospheric Aerosol Sampling Spectrometer) required attitude stabilised flights of the payloads to ensure unimpeded direct flow into the detector, both on up- and downleg. These NASA rockets, which were flown from the Andøya Rocket Range, were therefore actively controlled to maintain an angle of attack of less than 1.3°. One rocket was flown in darkness (41.094, 2011-10-11, 21:15 UT, at a solar zenith angle of $\chi = 116°$), the other in daylight (41.093, 2011-10-13, 13:45 UT, $\chi = 83°$). The region of the main interest was 70 to 90 km, *i.e.* where charged meteoric dust is expected; the DSMC (= Direct Simulation Monte Carlo) simulation for that height shows that the booms are long enough that the probes sample the undisturbed ionosphere ([2]; Fig. 4, right panel). Fig. 5 shows the current measured by the PIPs as a function of flight time (night flight 41.094). As one would expect the currents measured by the two PIPs

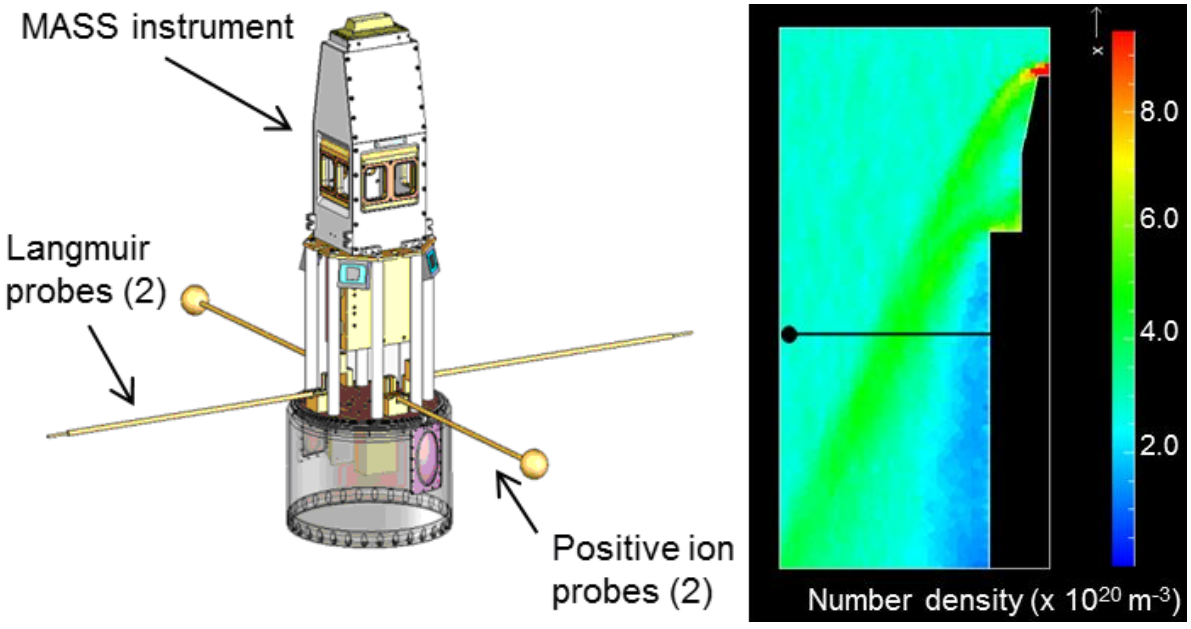

Figure 4. Forward instrumentation of the CHAMPS payloads (left), and DSMC simulation of the neutral number density at 80 km: note that the probes appears to be well outside the shock cone [3].

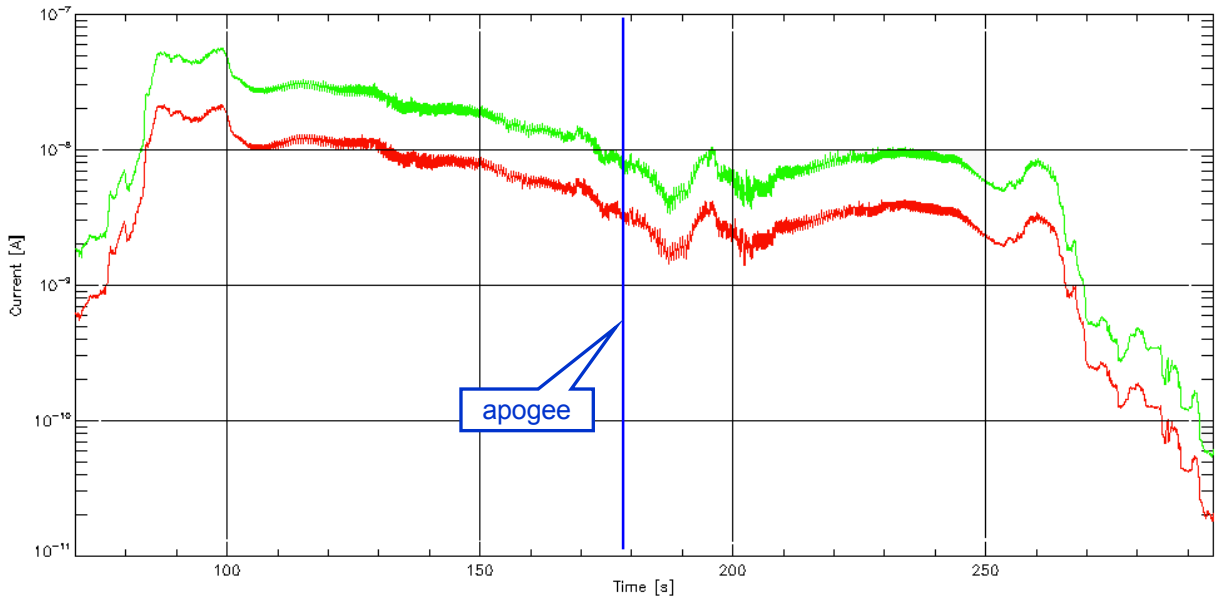

Figure 5. Ion currents measured by the two PIPs (night flight 41.094). Green: HV (-4 V bias), red: LV (-2.5 V bias). The curves are separated for graphical reasons.

show no obvious spin modulation; contrary to the Rexus flight the ion densities on up- and downleg are very different which is confirmed by the data from other instruments aboard the payload. Fig. 6 shows the blow-up of the currents of the two PIPs. The large signal dips are due to the firings of the attitude control and are removed in the further processing. Upon close inspection the currents are modulated with the spin frequency at 180° between the two probes. The sinusoidal spin modulation is less than 10% compared to a factor of four or even more in the case of the Rexus flight. In addition there are also small, anti-correlated rapid ripples on the current (less than 2%; not shown). We now determine the amplitude (in % of the current, Fig. 7 left panel). For the phase we add 180° to data of the PIP with -4 V and form the mean of the two probes (right panel). To allay all arguments that the observations might be due to instrumental effects, Fig. 8 shows the corresponding diagrams with the data of the daytime flight (41.093).

For the spin modulation we can at this stage propose a number of explanations:

(1) The attitude control assures that the rocket axis is aligned with the nominal velocity vector (the tangent of the trajectory). A wind across the rocket axis is equivalent to an alignment error. In such a situation the radial distance of the probes from the shock cone will vary at the spin frequency. According to the DSMC simulation (Fig. 4) and the resolution in that figure a misalignment of >20° should bring the probes in and out of the shock cone.

(2) We have so far always conveniently ignored the fact that the probe spinning with payload moves at a velocity at right angle to the vehicle's velocity. In the case of the

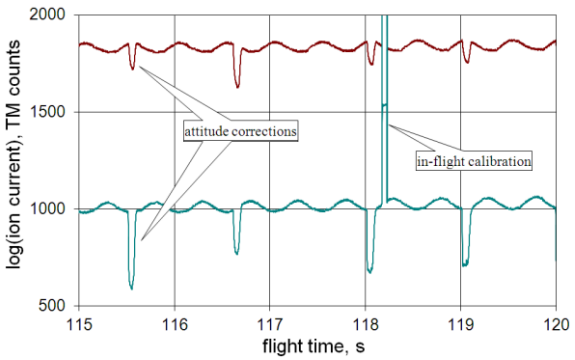

Figure 6. Expanded view of the ion currents measured by the two PIPs (night flight 41.094) clearly displaying anti-correlation between the two probes. The signatures of the attitude corrections and the in-flight calibrations are removed in the further analysis.

CHAMPS payloads this velocity is about 8 m s^{-1} contributing to the total velocity; this has to be compared to the vehicle's velocity of between 200 and 1100 m s^{-1}. Neglecting this contribution leads to an error of the total velocity of between 0.08 to 0.002%. A horizontal wind has to be added or subtracted from the tangential velocity of 8 m s^{-1}, or in other words, the horizontal wind effective for the total velocity "seen" by the probes, will be spin-modulated by ±8 m s^{-1}. In that scenario the currents will indeed be spin-modulated and in anti-phase, but the effect is orders of magnitude too small to explain the observations.

(3) A typical thermal velocity of 400 m s^{-1} leads to a gyro radius of 2.5 m (for an ion of 30 amu); the payload may therefore at times obstruct the ions' motion of such a radius. The fact that the phase of the spin modulation is very different between the flights makes this scenario unlikely.

(4) The attitude control system only has a finite accuracy and there is a residual misalignment. The fact that the phase is not random, but appears similar on up- and downleg, rules out this explanation.

(5) The payload charge varies within a spin period due to, *e.g.* different work functions on the payload surface. In that case the spin modulation of the two probes should be *in phase*.

Of the above suggestions only the first seems plausible. The fact that the modulation increases with altitude (with decreasing velocity) can qualitatively be explained by a widening of the shock cone which brings it closer to the probes. Any misalignment due to cross winds leads to a spin related movement of the probes towards and away from the shock cone. The relation between the expected modulation depth as a function of misalignment angle, rocket velocity and background density is too complex to draw conclusions pertaining to the velocity of the cross wind. The phase of the modulation, however, provides clues to the direction of the displaced shock cone and in consequence the wind direction.

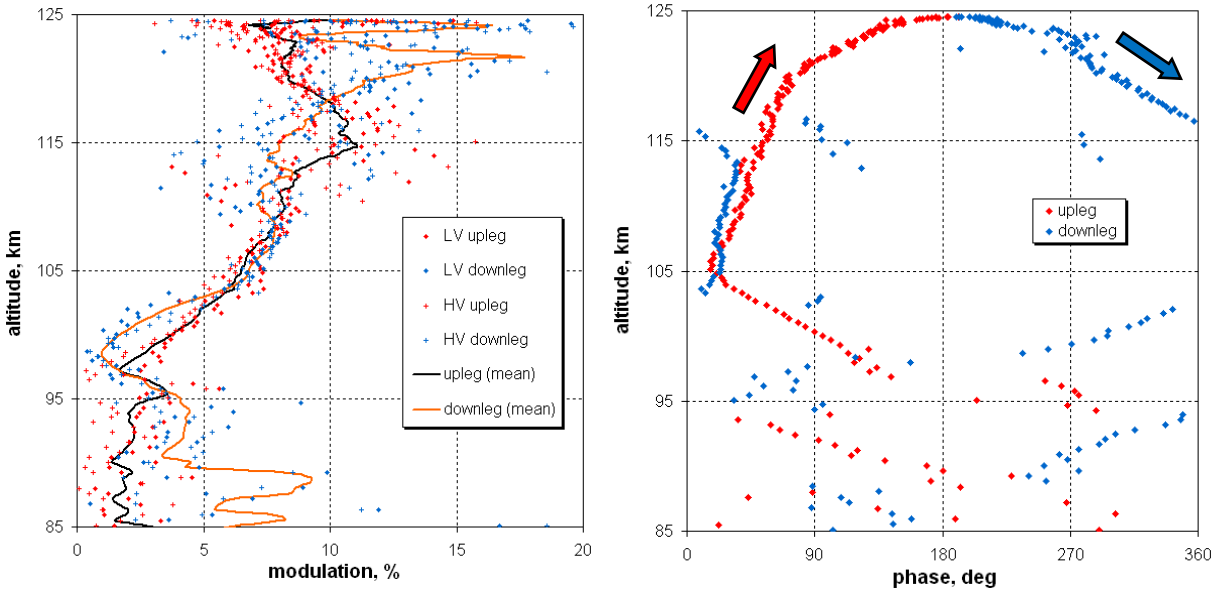

Figure 7. Amplitude and phase of the spin modulation of the ion current; 180° are added to the phase of the HV probe (night flight 41.094).

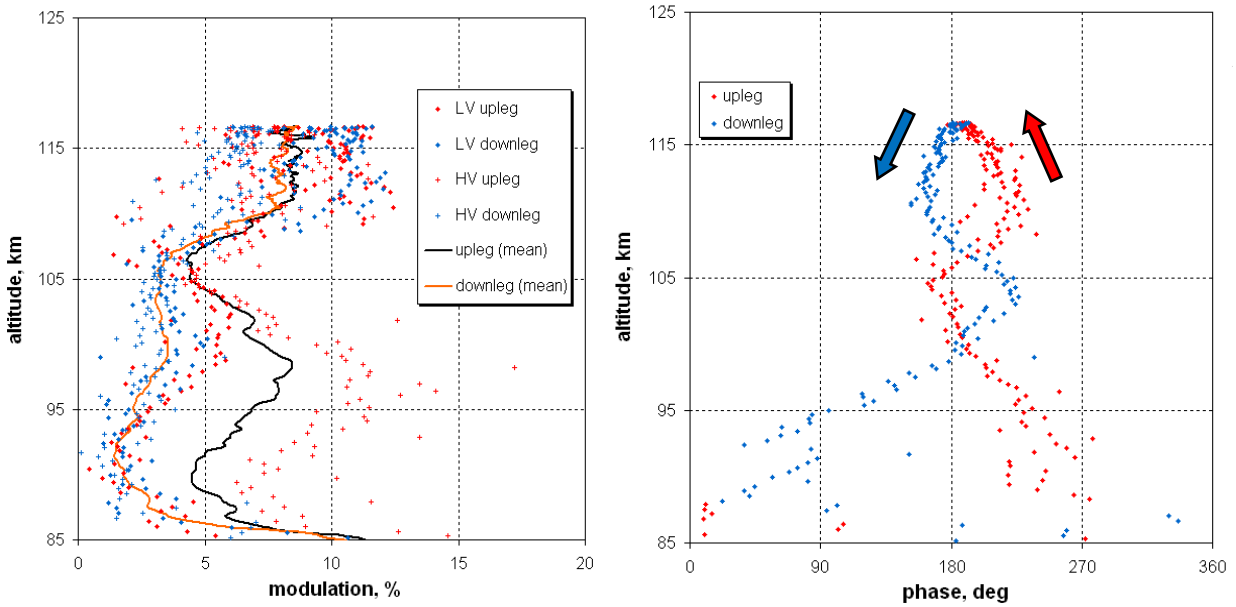

Figure 8. As Figure 7, but for the dayflight 41.093.

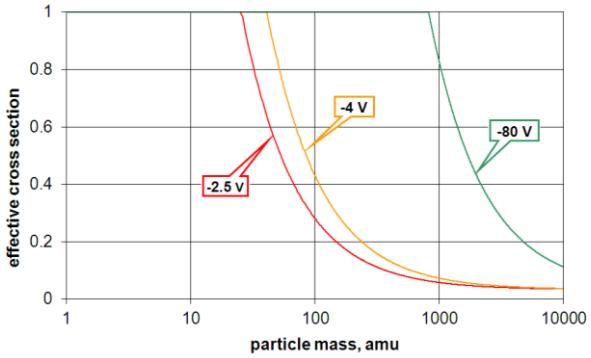

Figure 9. Collection efficiency of a PIP for different bias voltages as function of particle mass. The calculation is for 97 km and a velocity of 800 m s^{-1}.

3. THE EXPECTED BONUS

The CHAMPS payloads were dedicated to the detection of charged aerosols in four mass ranges covering 500 to 20,000 amu, *i.e.* significantly heavier than any known ions. The general assumption underlying the operation of PIPs is that the path of any positively charged "thing" (ion, aerosol) once inside the gridded sphere will be sufficiently deflected to end at the negatively biased inner collector. A typical velocity in the height region where charged dust is expected (70 to 90 km) is 1 km s^{-1}. This translates to an energy of 0.2 eV for a light ion, but up to 50 eV for the heaviest expected charged aerosol. A bias of a few Volts will therefore not suffice to collect all positive matter. Figure 9 shows the expected mass discrimination for a positive ion probe as flown on the CHAMPS payloads [4]. The effective cross section varies from that of the outer grid (small masses) to that of the inner collector (for [infinitely] heavy masses); a large bias, *e.g.* -80 V, would collect heavier masses, but poses the risk of secondary electrons being emitted by the collector when hit by accelerated particles. The diameter of the outer grid and the inner collector were 44 and 8 mm, respectively. Hence too low a bias will in case of extremely heavy particles only measure a current reduced by a factor of $(8/44)^2 = 0.033$. As stated before, the primary reason for using two positive ion probes was to improve the height resolution. The two probes were almost identical, only the biases were different, namely LV (-2.5 V) and HV (-4.0 V). The anticipation was that the HV probe would measure a somewhat larger current in the height region where the positive "things" are heavier than ions. Figs. 10 and 11 show the ratios HV/LV-currents of the up- and downleg, of the night and daytime flights. As expected, below 75 km the HV probe measures more current than the LV probe, In that height region the mass spectrometer detected charged positive dust particles which are only incompletely sampled by the positive ion probes with relatively low bias voltages. More pronounced, however, is the HV/LV-ratio near 85 km. Why and how the charged negative particles detected by the mass spectrometer could produce this effect is not obvious.

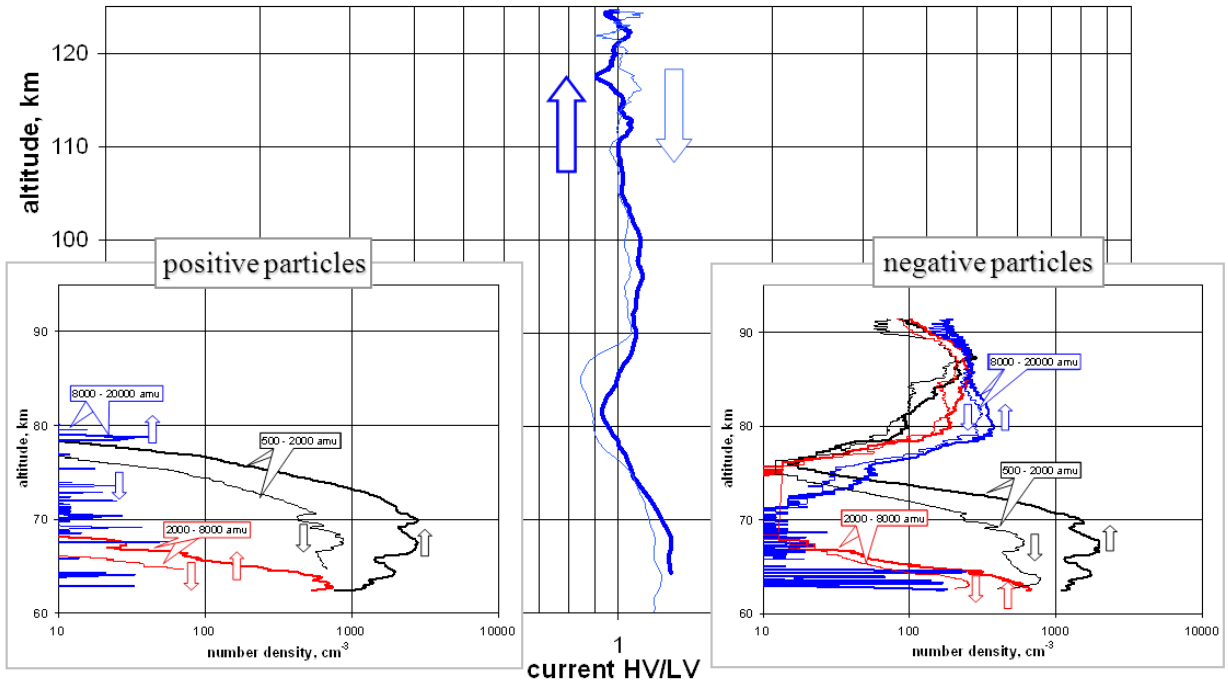

Figure 10. Current ratio of the HV/LV probes as a function of altitude (night flight 41.094) together with the charged particle data of the mass spectrometer. Bold lines: upleg, thin lines: downleg.

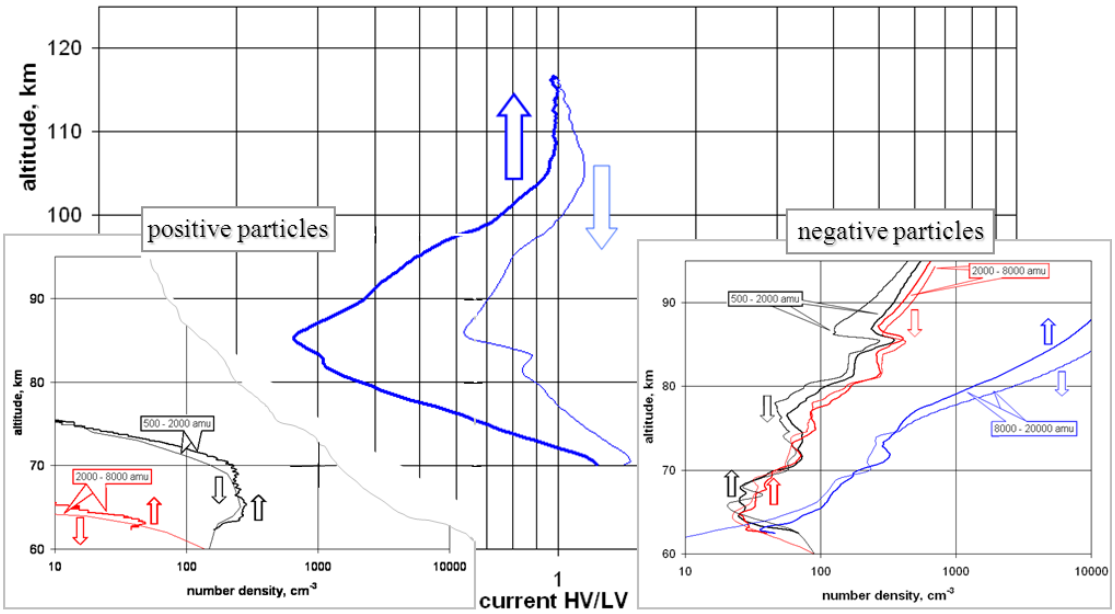

Figure 11. As Figure 10, but for the day flight 41.093.

4. CONCLUSIONS

The necessary assumptions underlying the positive ion probes are simple and plausible, *i.e.* the current is proportional to the rocket velocity and the ions are embedded in the neutrals. The present unique cases of fully attitude controlled rocket flights revealed unexpected features which can best be explained by winds transverse to the rocket axis. The probe with the somewhat larger bias indeed measured a larger current in the height region where the mass spectrometer detected positively charged dust. Why, however, near 85 km the current ratios are consistently reversed, remains to be understood.

5. ACKNOWLEDGEMENTS

The CHAMPS flights were supported by the NASA Low Cost Access to Space programme. The Austrian participation was made possible by Grant P23100-N23 of the Austrian Science Fund (FWF).

6. REFERENCES

1. Folkestad, K. (1970). Ionospheric Studies by *in situ* Measurements in Sounding Rockets. Internal NDRE Report 59 (and PhD Thesis University of Oslo).

2. Knappmiller, S., Robertson, S., Sternovsky, Z. & . Friedrich, M. (2008). A Rocket-Borne Mass Analyzer for Charged Aerosol Particles. *Rev. Sci. Instr*. **79**, 104502.

3. Robertson, S., Dickson, S. Horány, M., Sternovsky, Z., Friedrich, M., Janches, D., Megner, L. & Williams, B. (2013). Detection of Meteoric Smoke Particles in the Mesosphere by a Rocket-Borne Mass Spectrometer. *J. atmos. Solar terr. Phys*., submitted.

4. Pürstl, F. (2000). MARIPROBE-D a 3D-Ion-Spectrometer for *in-situ* Investigation of Cold Ions in the Martian Ionosphere. PhD Thesis, Graz University of Technology.

POWER SPECTRAL ANALYSIS OF HIGH LATITUDE F-REGION SMALL-SCALE IRREGULARITIES

A. Spicher[(1)], W. J. Miloch[(1)], J. I. Moen[(1)]

[(1)] Department of Physics, University of Oslo, Box 1048, 0316 Oslo, Norway
andres.spicher@fys.uio.no, w.j.miloch@fys.uio.no, j.i.moen@fys.uio.no

ABSTRACT

The Investigation of Cusp Irregularities-2 (ICI-2) sounding rocket was launched into the cusp ionosphere in December 2008 from Ny-Ålesund, Norway. Its main objectives were to resolve irregularity structures at meter-scales and to quantify the gradient drift instability process. The rocket intersected instability regions in connection with both particle precipitation and density enhancements. In this paper we analyze the spectral characteristics of electron density fluctuations associated with the encountered plasma structures and present the power laws of the irregularity spectra. The power spectra of the strong density fluctuations exhibit characteristic dual-power law behavior with a steeper slope at high frequencies.

1. INTRODUCTION

Electron density irregularities are common phenomena in the F-region high latitude ionosphere [17]. These irregularities have spatial scales ranging from tens of kilometres to a few meters and may have negative effects on communication and navigation systems [5]. They might distort radio signals and cause backscatter at HF frequencies [13]. High latitude ionospheric irregularities are thus of particular interest for mitigation/circumvention of consequences to satellite communication, Global Positioning System (GPS) navigation and HF communications.

When the interplanetary magnetic field (IMF) is directed southward, the irregularities located on the dayside are closely related to the density gradients associated with electron density enhancements and/or polar cap patches [15]. The irregularities have been observed to populate patches and electron density enhancements entirely [15], but the strongest irregularities are often located on their trailing edges [18]. Many mechanisms have been proposed for the generation of these irregularities [11]. Nowadays, two macroinstabilities are believed to be dominant mechanisms for the production of irregularities in the high-latitude F-region [9][17]; the gradient-drift instability (GDI) and the Kelvin-Helmoltz (KH) instability.

The GDI is due to the difference in the drift velocities of ions and electrons perpendicular to a density gradient [17]. The GDI has a preferred direction, meaning that it is unstable if the $\boldsymbol{E} \times \boldsymbol{B}$-polarization drift produced by the charge separation is parallel to the preexisting density gradient.

The KH plasma instability is accredited to strong velocity shear flows perpendicular to the magnetic field [10]. It was argued that velocity shears were inherent polar cap patch formation, implying that the KH instability was likely to be the first mechanism to structure the patches [3][4]. The GDI would then operate as a secondary process breaking down the structures into smaller-scales. However, work still remains to be done on the quantification and the characterization of F-region irregularities.

Ground-based radars are not well adapted to resolve precisely irregularity structures at decametre-scales. This implies an ultimate need for in-situ measurements in order characterize irregularities at small-scales and to assess the role of different instability mechanisms.

In this study, the high-resolution electron density data obtained from the measurements made by the Investigation of Cusp Irregularities 2 (ICI-2) sounding rocket is analysed. The main objectives of the ICI-2 sounding rocket were the resolution of meter-scale irregularities and the quantification of the gradient drift instability mechanism.

We have carried out a spectral analysis of the electron density fluctuation data at various segments of cusp/polar cap activities associated with different plasma structures such as particle precipitations or density gradients.

Previous satellites and rocket experiments showed that, in the high-latitude ionosphere, the density fluctuations exhibited power law spectra [6] [1]. Thus, the main objective here is to determine whether different power-laws can be associated with different plasma structures.

This paper is divided into two parts. The first part describes the rocket experiment and the second presents the observations and the results,

2. EXPERIMENT

The Investigation of Cusps Irregularities 2 sounding rocket was launched from Ny-Ålesund, Svalbard, Norway (78.9°N, 11.9°E geographic coordinates) at 1035 Universal Time (UT) on the 5th of December

Proc. '21st ESA Symposium European Rocket & Balloon Programmes and Related Research', 9–13 June 2013, Thun, Switzerland (ESA SP-721, October 2013)

2008. Ny-Ålesund is located below the cusp region and the inclination angle of the Earth's magnetic field was 82.1° on launch-day. The rocket was launched almost parallel to the magnetic field lines (less than 21°) with an azimuth angle of 204° from the North direction, meaning that it flew towards South-West. The ICI-2 rocket reached apogee after t = 302 s of flight at an altitude h = 328.7 km and was located in the F-region ionosphere during approximately 400 s.
The total rocket measured 9278 mm. It comprised a two Stages Motor and a payload (see Fig. 1) hosting the following instruments.

- An AC/DC Electric field and wave experiment. The AC and DC electric field are measured in two frequency ranges. The DC electric field data had a sampling frequency Fs = 180 Hz.
- Two types of Langmuir probes for the electron density measurements; a fixed bias Langmuir probe mounted in the front of the rocket and four cylindrical fixed bias Langmuir probes mounted in the middle of the E-field booms, symmetrically around the spin axis of the rocket. The latter instruments is referred to as the m-NLP and provided the electron density data analysed in this study, with a sampling frequency Fs = 5787 Hz. The probes were biased at 2.5, 4, 5.5 and 10 V, had a length l = 25 mm and a diameter d = 0.51 mm. A complete description of the m-NLP system is given in Bekkeng et al. [2].
- A low-energy electron spectrometer (LEP) for an energy range between 10 eV and 10 keV and a time resolution of 16 ms. This instrument was used to measure the electron precipitation during the flight. The data available from the LEP device start at approximately t = 200 s, corresponding to an altitude of h = 283 km.
- A solid-state spectrometer for ions and electrons measuring energies above 20 keV.
- An altitude determination system and sun sensors.

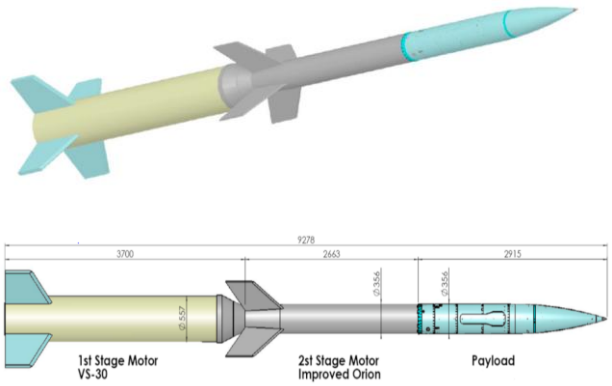

Figure 1. Illustration of the ICI-2 sounding rocket.

3. OBSERVATIONS AND RESULTS

3.1. Plasma Flow conditions

A detailed overview of the solar wind and auroral conditions during the launch of the rocket in the morning hours of Dec. 5, 2008 is presented in Lorentzen et al. [12]. A few important features are nevertheless recalled here.
The solar wind speed was about 390 km/s before launch and increased slightly later. While the IMF Bx was fluctuating around $Bx \approx 0$ nT, the IMF Bz was steady negative $Bz \approx -6$ nT and the IMF By was steady positive with values about 4−5 nT. Due to the long-lasting negative IMF Bz component, magnetic reconnection occurred on the dayside equatorward of the cusp, allowing direct entry of plasma from the solar wind into the cusps. Several poleward moving auroral forms were observed into the polar cap.
The electric field measured by the rocket provides precise information concerning the direction of the plasma flow encountered by the rocket. Using the magnetic field data from the International Geomagnetic Reference Field (IGRF) model and assuming B to be perpendicular to the ground over Svalbard, one can compute the $\mathbf{E}\times\mathbf{B}/\mathbf{B}^2$ velocity. Fig. 2 a) shows the magnitude and the components perpendicular to the magnetic field of the $\mathbf{E}\times\mathbf{B}/\mathbf{B}^2$ velocity in an Earth-fixed coordinate system North-East-Down (NED), using the value $Bz \approx -5 \cdot 10^{-5}$ T. The velocity does not exhibit much features, except between $t \approx 170$ s and $t \approx 230$ s of flight, where it shows a wave-like pattern. The flow was directed westward during the entire flight and pointed slightly northward until t = 370 s. The direction of the plasma flow can be better appreciated in Fig. 2 b) showing the velocity vector with respect to the azimuth angle.

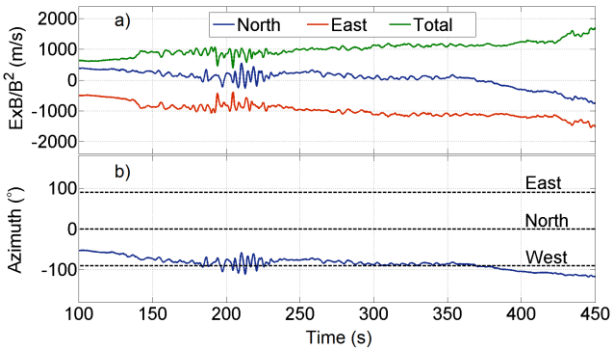

Figure 2. a) Norm (green), northward (blue) and eastward (red) components of the $\mathbf{E}\times\mathbf{B}/\mathbf{B}^2$ velocity in an Earth-fixed reference frame (NED). b) The direction of the plasma flow with regard to the azimuth angle.

3.2. Overview of the electron density measured by the ICI-2 sounding rocket

From the currents measured by the 4-needle Langmuir probes on the ICI-2 sounding rocket, the raw electron density was calculated using the following equation

$$n_e = \sqrt{\frac{m_e}{2q(2qrl)^2}\frac{\Delta(I_c)^2}{\Delta V}}\ , \qquad (1)$$

where r and l give the dimensions of the probes, m_e the electron mass, q the charge, ΔI_c the current difference measured by two probes with potential difference ΔV.
Fig. 3 a) shows the raw electron density data between t = 100 s and t = 450 s of flight, corresponding to the altitudes h = 148.28 km and h = 232.25 km, respectively. This altitude range is well located in the F-region ionosphere. The data appears very noisy due to the spinning of the rocket at the frequency fs = 3.25 Hz. The measurements were thus filtered using band-reject filters to remove the spin frequency and the three following harmonics (2nd, 3rd and 4th harmonics). The filtering process is explained in more details in Jacobsen et al. [8]. The processed electron density measured with respect to the time of flight t and the altitude h is shown in Fig. 3 b).
Four large regions of density enhancements with respect to the density background can be seen in Fig. 3. They are labelled A, B, C and D. As a consequence of the westward motion of the plasma presented in sec. 3.1, one can assume that the left-hand sides of these density enhancements match the leading edges of the plasma structures, while their right-hand sides correspond to their trailing edges. Note that since the motion of the plasma was not exactly in the same direction as the rocket, zonal flows cannot be completely excluded.

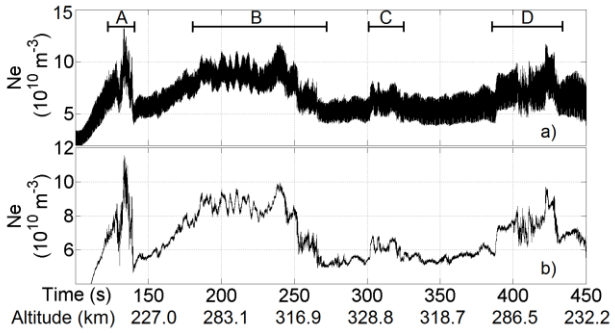

Figure 3. a) Raw electron density measured by the 4 Needle Langmuir Probes on the ICI- 2 sounding rocket. The data is dominated by the spin rotation of the rocket. b) Processed electron density. Four large-scale density enhancements with respect to the background density are visible. They are labelled A, B, C and D.

The four regions abovementioned are

- **Region A**: The first density enhancement crossed the path of the rocket on the up-leg between approximately t = 120 s and t = 140 s. It coincides with the bottom of an intense F-region plasma patch that has been traveling from lower latitudes, as described in Lorentzen et al. [12] and Oksavik et al. [16]. The density reached the maximum of $Ne = 11.5 \cdot 10^{10}$ m^{-3} at t = 135 s, corresponding to h = 205 km. This value was also the maximum density encountered during the entire ICI-2 flight. On the trailing edge of the patch, the density decreased abruptly from $Ne = 9.8 \cdot 10^{10}$ m^{-3} to $Ne = 5 \cdot 10^{10}$ m^{-3} in $t \approx 6$ s. Using the horizontal velocity $v_{rel} \approx 1200$ m/s, the density gradient is $\Delta Ne/\Delta x \approx -6.7 \cdot 109$ m^{-3}/km and contains strong fluctuations, implying that some irregularity might be taking place.
- **Region B**: The second density enhancement was also encountered by the rocket on the up-leg, between $t \approx 180$ s and $t \approx 270$ s of flight. This region is much broader than the first one. On the top of the structure, between $t \approx 200$ s and $t \approx 225$ s, the electron density exhibits a wave pattern at about $Ne \approx 9 \cdot 10^{10}$ m^{-3} with frequency $fs \approx 0.25$ Hz. The trailing edge of the density enhancement exhibits sawtooth-like structures with strong fluctuations between approximately t = 250 s and t = 270 s of flight. The strong fluctuations might imply that some irregularity process is developing. Note indeed that Hysell et al. [7] described density structures with similar shape in the equatorial region and associated them with plasma irregularities.
- **Region C**: The rocket encountered an increase in density around apogee, between $t \approx 300$ s and t ≈ 320 s (apogee was reached after t = 302 s of flight). The density increment is approximately $1.8 \cdot 10^{10}$ m^{-3} above the background. Note that in contrast to region A and B, this density enhancement is correlated with particle precipitations [14].
- **Region D**: On the down-leg, the ICI-2 sounding rocket intersected an electron density enhancement at t = 387 s of flight corresponding to h = 297 km altitude. This region matches a cusp electron precipitation region and is believed to be a spatial structure modulated by particle precipitation [14].

3.3. Spectral analysis using the windowed FFT

In order to compute the power spectra, the filtered electron density data were detrended and windowed using a Hann window. The relative electron density fluctuations are given by $\Delta Ne/Ne \equiv Ne/Ne_{tr} - 1$, where

Ne_{tr} corresponds to average electron density. Also, all the structures are assumed to be frozen in turbulences, meaning that the phase velocity of the plasma structures is much smaller than the relative velocity between the plasma and the rocket. This assumption is based on the Doppler spectra from HF backscatter radars associated with small-scale irregularities. Indeed, they indicate that these irregularities are low frequency processes, with small phase velocities compared to the convection velocities [17].

The frozen in turbulences assumption allows the transformation from time domain (in frequencies) into spatial domain (wavenumbers). However, knowing the ambiguity of such assumption, wavelengths are given as simple indications of length-scales and should not be considered as being exact.

The spectral components of the density fluctuations can be obtained computing a spectrogram, as in Fig. 4. The top panel of Fig. 4 presents the electron density data, as already shown in Fig. 3, and the lower panel presents the spectrogram, providing the power spectral density (PSD) in color-coded versus the time of flight and frequency. This figure was produced using the sample frequency of the rocket, i.e. Fs = 5787 Hz, a Hann window of 6000 data points (corresponding to approximately one second) and an overlap of half a second. Several regions with strong irregularity power can be observed. The most intense is visible between approximately t = 120 s and t = 140 s of flight. The power extends to frequencies of about fs = 90 Hz, which correspond to spatial scales of tens of meters. This result is similar to the one obtained by Oksavik et al. [16]. Two other regions with strong PSD can be identified. The first around t = 260 s and the other from t = 400 s of flight. Note that the increase in power occurs at almost all frequencies below approximately 100 Hz and that these regions can be associated with strong electron density perturbations matching with density gradients.

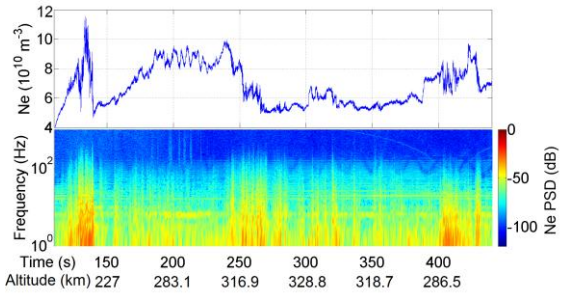

Figure 4. (top) Electron density between t = 100 s and t = 440 s of fligth. (bottom) Power spectral density of the entire flight. The spectrogram was performed using one second intervals, a Hann window and half a second overlapping.

To regions of the flight exhibiting strong fluctuations have been selected for a more detailed presentation: the first one containing particle precipitations and the second one without particle precipitations.

The first interval is located in **region C,** just after apogee. The relative electron density fluctuation measured between t = 317.5 s and t = 321.5 s of flight is shown in the top panel of Fig. 5. This corresponds to altitudes h = 327.7 km and h = 327.1 km, respectively. The fluctuations are ranging between -4 % and 5 % and the corresponding power spectrum is shown in the bottom panel of Fig. 5, with logarithmic axis. Since power spectra at low frequencies are dependent on the detrending process, the figure is only shown from the frequency fs = 1 Hz. In addition, the depletion in power at $fs \approx 3.3$ Hz is due to the removal of the spin and has not been taken into account for the fitting process. From $fs \approx 350$ Hz (corresponding to 3.5 m), the quantization noise level is reached, which is detectable in Fig. 5 as the flat portion at high frequencies, similar to the spectrum of a white noise.

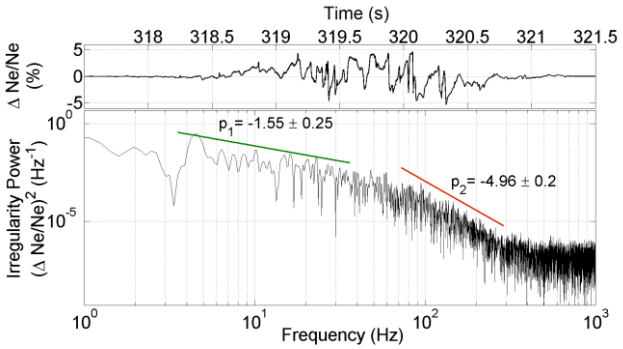

Figure 5. (top) Relative electron density fluctuation between t = 317.5 s and t = 321.5 s of flight, which corresponds to h = 327.7 km and h = 327.1 km altitude, respectively. (bottom) Power spectrum of this interval. The slopes are $p_1 = -1.55 \pm 0.25$ at low frequencies and $p_2 = -4.96 \pm 0.2$ at high frequencies. The spectral knee occurs at about 25 m.

The power spectrum shown in Figure 5 exhibits two different linear regimes in the frequency interval $fs \approx [2, 300]$ Hz: one for low frequencies and one for high frequencies. Both ranges join at a break frequency $f_{sb} \approx 45$ Hz, corresponding to about 25 m. The two slopes are $p_1 = -1.55 \pm 0.25$ and $p_2 = -4.96 \pm 0.2$, implying that the slope at high frequencies is steeper than the slope at lower frequencies.

The other interval considered is located in **region B,** i.e. between t = 250 s and t = 254 s, which is on the up-leg in the altitude range h = [316.9, 318.7] km. The windowed relative electron density fluctuations are shown in the top panel of Fig. 6. The fluctuations are ranging between -9 % and 10 %, which is two times higher than the interval considered before.

The lower panel of Fig. 6 displays the power spectrum of the abovementioned density fluctuations with logarithmic axis. The figure is, again, only shown from fs = 1 Hz because of the detrending process and the depletion at $fs \approx 3.3$ Hz is due to the spin removal. From $fs \approx 300$ Hz the noise level is reached. The power spectrum exhibits two linear regimes that merge at about fs = 40 Hz, or equivalently approximately 30 m. The slope at low frequencies is $p_1 = -1.7 \pm 0.25$ and the slope at high frequencies is $p_2 = -4.6 \pm 0.2$. Despite the fact that the density fluctuation profiles are different between both intervals investigated, the slopes of their power spectra (compare Fig. 5 and Fig. 6) are very similar: both spectra exhibit a dual slope power spectrum with a knee at about 30 m, a slope in low frequency range $p_1 \approx -1.6$ and a slope $p_2 \approx -4.7$ at higher frequencies.

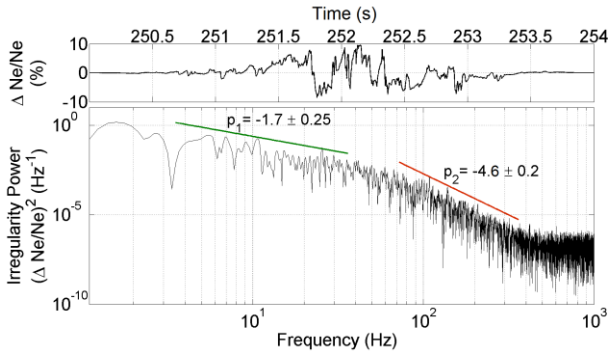

Figure 6. (top) Relative electron density fluctuation between t = 250 s and t = 254 s of flight, corresponding to altitudes h=316.9 km and h=318.7 km, respectively. (bottom) Power spectrum of this interval. The slopes are $p_1 = -1.7 \pm 0.25$ and $p_2 = -4.6 \pm 0.2$. The spectral knee occurs at about 31 m.

Acknowledgements: The authors thank Tore André Bekkeng and Espen Trondsen for the discussions concercning the rocket instruments. We thank also Dr. Lasse Clausen for providing the electric field data.

References

1. Basu, S., S. Basu, E. Mackenzie, W. R. Coley, J. R. Sharber, and W. R. Hoegy (1990). Journal of Geophysical Research-Space Physics 95 (A6), 7799–7818.
2. Bekkeng, T. A., K. S. Jacobsen, J. K. Bekkeng, A. Pedersen, T. Lindem, J.-P. Lebreton, and J. I. Moen (2010). Measurement Science & Technology 21 (8), 085903.
3. Carlson, H. C., T. Pedersen, S. Basu, M. Keskinen, and J. Moen (2007). Journal of Geophysical Research-Space Physics (A11), A11304.
4. Carlson, H. C., K. Oksavik, and J. Moen (2008). Annales Geophysicae 26 (9), 2871–2885.
5. Carlson, H. C. (2012). Radio Science 47, RS0L21.
6. Dyson, P. L., J. P. McClure, and W. B. Hanson (1974). Journal of Geophysical Research 79 (10), 1497–1502.
7. Hysell, D. L., M. C. Kelley, W. E. Swartz, R. F. Pfaff, and C. M. Swenson (1994). Journal of Geophysical Research-Space Physics 99 (A5), 8827–8840.
8. Jacobsen, K. S., A. Pedersen, J. I. Moen, and T. A. Bekkeng (2010). Measurement Science & Technology 21 (8), 085902.
9. Keskinen, M. J. and S. L. Ossakow (1983). Radio Science 18 (6), 1077–1091.
10. Keskinen, M. J., H. G. Mitchell, J. A. Fedder, P. Satyanarayana, S. T. Zalesak, and J. D. Huba (1988). Journal of Geophysical Research: Space Physics 93 (A1), 137–152.
11. Kintner, P. M. and C. E. Seyler (1985). Space Science Reviews 41 (1-2), 91–129.
12. Lorentzen, D. A., J. Moen, K. Oksavik, F. Sigernes, Y. Saito, and M. G. Johnsen (2010). Journal of Geophysical Research-Space Physics 115, A12323.
13. Moen, J., H. C. Carlson, S. E. Milan, N. Shumilov, B. Lybekk, P. E. Sandholt, and M. Lester (2000). Annales Geophysicae 18 (12), 1531–1549.
14. Moen, J., K. Oksavik, T. Abe, M. Lester, Y. Saito, T. A. Bekkeng, and K. S. Jacobsen (2012). Geophysical Research Letters 39, L07104.
15. Moen, J., K. Oksavik, L. Alfonsi, Y. Daabakk, V. Romano, and L. Spogli (2013). Journal of Space Weather and Space Climate 3 (26), A02.
16. Oksavik, K., J. Moen, M. Lester, T. A. Bekkeng, and J. K. Bekkeng (2012). Journal of Geophysical Research-Space Physics 117, A11301.
17. Tsunoda, R. T. (1988). Reviews of Geophysics 26 (4), 719–760.
18. Weber, E. J., J. Buchau, J. G. Moore, J. R. Sharber, R. C. Livingston, J. D. Winningham, and B. W. Reinisch (1984). Journal of Geophysical Research: Space Physics 89 (A3), 1683–1694.

ERROR ESTIMATES FOR IN SITU PROBE SYSTEMS AND WAVE DETECTIONS

H. Sato[(1),(2)] , H. Pécseli[(1)], J. K. Trulsen[(3)]

[(1)] *University of Oslo, Physics Department, Box 1048 Blindern, N-0316 Oslo, Norway*

[(2)] *Deutsches Zentrum für Luft- und Raumfahrt (DLR), Institut für Kommunikation und Navigation, Kalkhorstweg Neustrelitz, Germany.*

[(2)] *University of Oslo, Physics Department, Box 1048 Blindern, N-0316 Oslo, Norway*

ABSTRACT

Data from the ionospheric plasma would be best studied by probe configurations having scale sizes small compared to the characteristic scales of the plasma disturbances. This condition makes it possible to effectively treat the results as originating from a point measurement. Unfortunately, such a condition is only rarely fulfilled. Aim of our study is to illustrate the problems related to finite probe separations on the rocket.

INTRODUCTION

Ionosphere is rich source for plasma waves and instabilities and sounding rocket experiment has provided plasma parameters along with ground based radar measurements. The electric field magnitude and direction estimated from the probe measurements will generally be different from the true values, and we discuss these errors. These discussions will have a general nature, and the conclusions will be relevant for other similar probe configuration. In order to exemplify the general idea of error analysis, we use the data obtained by four spherical probes placed at two booms from Rose rocket [1]. By this construction, the probes can give information of all three vector components of electric fields in the ionosphere.

PROBE COMBINATIONS

We use a combination of Langmuir probes to approximate the three components of the electric fields. The potential differences between the selected two probes and spatial distance will give approximated component of the field signals. It is expected that these signals would exactly recover the field-components for constant electric fields.

In the case of wavelengths longer than the probe separations, we assume this probe combination to give a good approximation for the magnitude and direction of the fluctuating electrostatic field.

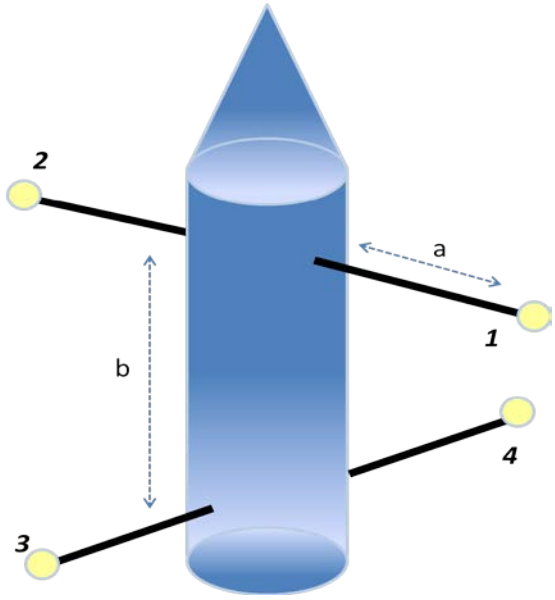

Figure 1. Schematic diagram for positioning of the four probe system. Probes are mounted on two pair of booms which gives probe separation 2a. The separation along the rocket axis is denoted by b.

Proc. '21st ESA Symposium European Rocket & Balloon Programmes and Related Research', 9–13 June 2013, Thun, Switzerland (ESA SP-721, October 2013)

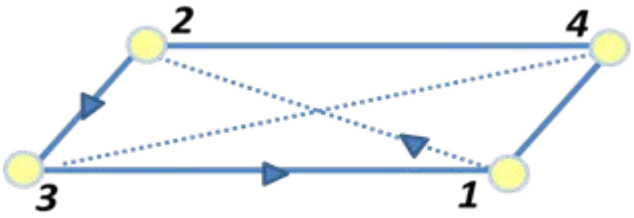

Figure2. An illustration of graphical understanding of closed loops of probes. All the four probes from Fig.1 are mapped to corners of a rectangle.

Figure 1 shows our simple model of sounding rocked with two-boom system where the each probes are separated vertically along the rocket body. The boom length *a* and the separation distance *b* determine effective rocket size as point measurement. We obtain electric potential value ϕ for each probe with respect to a suitably defined common ground. We analyse the fluctuating signals $U6(t) = \phi1(t) - \phi2(t)$; $U5(t) = \phi4(t) - \phi3(t)$; $U4(t) = \phi1(t) - \phi4(t)$; $U3(t) = \phi2(t) - \phi3(t)$; $U2(t) = \phi1(t) - \phi3(t)$; and $U1(t) = \phi2(t) - \phi4(t)$, where $\phi j(t)$ for $j = 1, 2, 3, 4$ denotes *j*-th probe potential.

Many basic tests can be carried out to determine the reliability of the data. The one of the simplest analysis consists of basic check sums: inspection of Figure 1 shows that sums of selected signals should ideally vanish such as, for instance, $U6(t) + U3(t) - U2(t) = 0$. The number of vanishing signal selection can be obtained by making closed loop of probes.

The idea of vanishing sum is easily illustrated when the probes are mapped to 2D plane as shown in Figure 2 where four probes create corners of a rectangle. The arrows denote an example of closed loop for the selection mentioned above. This mapping and loop selection can be valid when the number of probes is increased.

We compare values of single probe signal and closed loop form Rose rocket experiment. One data example is shown in Fig3. It shows a fluctuating potential signal values are reasonably vanished at selected sum. We have made these checks and find them to be satisfied within 3% accuracy. The deviations have no correlations with the amplitudes of the probe signals.

With configuration of rocket boom system in Fig.1, our electric field estimates are based on the following probe combinations: $Ex = - U6/2a$, $Ey = - U5/2a$. Ideally, we could use $Ez = -(U3 + U4)/2b$ just as well as $Ez = -(U1 + U2)/2b$, the two signals being identical. However, due to imperfections in the setup there can be small differences up to at most a few presence , so we here use the average value $Ez = -(U3 + U4 + U1 + U2)/4b$, with the z axis being along the rocket axis. These combinations would give the exact result for a constant electric field (like the ambient electric field) in an arbitrary direction.

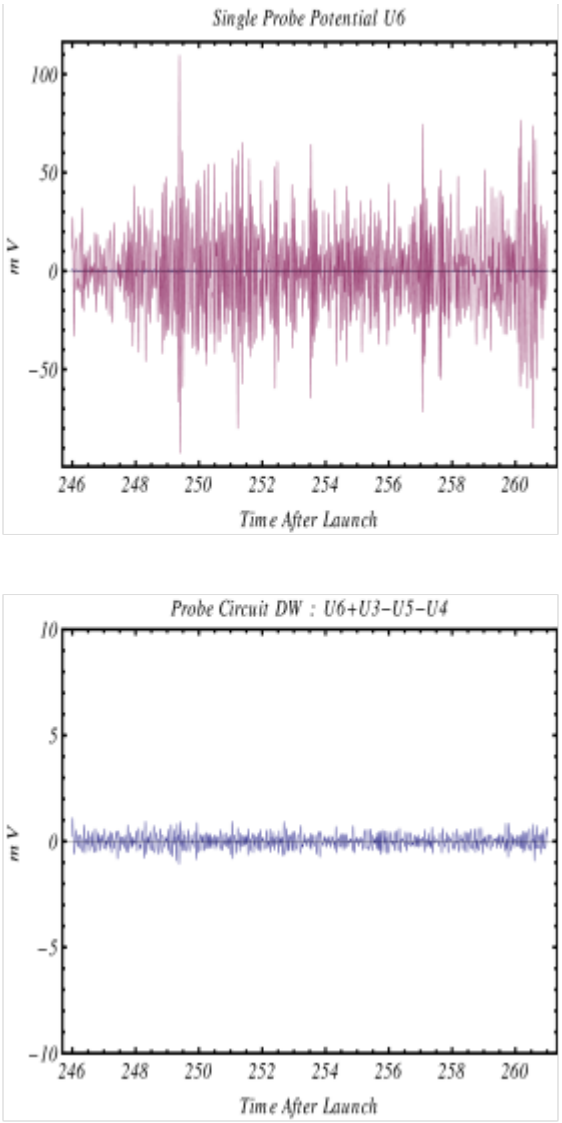

Figure 3. Comparison of signals from fluctuating single probe potential and a closed loop including the same probe from ROSE rocket. The rocket has the same probe system as Figure 1

PLANE WAVE ASSUMPTION

Ionospheric waves are in many cases propagating in the direction approximately perpendicular to the local magnetic field, i.e., $k \perp B_0$. Thus numbers of rocket experiments have been designed to place the rocket body parallel to the magnetic field either for up leg or down leg flight part. For a general mathematical model of a wavefield composed of many plane electrostatic waves, we have

$$\mathbf{E}(\mathbf{r},\mathrm{t}) = \int\int\int_{-\infty}^{\infty} \mathrm{E}(\mathbf{k})\frac{\mathbf{k}}{k} e^{-i(\omega(\mathbf{k})t-\mathbf{k}\cdot\mathbf{r})} \qquad (1)$$

and the dispersion relation $\omega = \omega(\mathbf{k})$ is assumed to be known. The integral gives the weighted average of the electric field vector at a space-time position (r,t) and at the same time also a correspondingly averaged direction of propagation, where $(E)k$ enters as a weight function for the direction of the unit vector $k//k$.

The local Boltzmann equilibrium is justified for long wavelengths and low frequencies [2]. Our assumption thus is $n_0 + \tilde{n} \approx n_0 \exp(e\tilde{\phi}/T_e)$ which implies $\tilde{E} \sim kn$ for this limit.

ERROR ESTIMATE FOR PROPAGATION DIRECTION

We now apply the assumption of electric field propagation (1) to corresponding potential variation which will be observed by rocket probes. The model for the electric static potential in arbitrary direction can be written as

$$\varphi(\mathrm{x},\mathrm{y},\mathrm{z},\mathrm{t}) = \mathrm{A}\cos(\mathrm{k}_x\mathrm{x}+\mathrm{k}_y\,y+\mathrm{k}_z\mathrm{z}-\omega t-\psi) \qquad (2)$$

where ψ is a phase. The total phase addition to $\mathbf{k}\cdot\mathbf{r}$ is $-\omega t+\psi$, which allows us to take $t=0$ and let Ψ represents all of the phase without loss of generality. Inserting position of the all the four probes to spatial variables, we obtain all three components of estimated electric field.

$$E_i = \frac{A}{a}\sin(\frac{\mathrm{k}_z b}{2}\pm\psi)\sin(\mathrm{k}_i\mathrm{a}) \qquad \mathrm{i} = \mathrm{x},\mathrm{y}$$

$$E_z = \frac{A}{a}\left(\cos(\frac{\mathrm{k}_z b}{2}-\psi)\cos(\mathrm{k}_y\mathrm{a}) - \cos(\frac{\mathrm{k}_z b}{2}+\psi)\cos(\mathrm{k}_z\mathrm{a})\right) \qquad (3)$$

By the definitions in (3) we effectively consider the rocket as a point probe. The information regarding phase differences from the probe sets giving U_1 and U_2 is lost. Similarly, they are lost for the probe sets giving U_3 and U_4. This phase information can be, when available, utilized to estimate the components of the propagation velocity that is perpendicular to the rocket axis.

ERROR ESTIMATE FOR PROPAGATION DIRECTION

The plane wave model (1) gives components $E^t_{x,y,z} = A\,k_{x,\mathrm{y},\mathrm{z}}\sin(\mathbf{k}\cdot\mathbf{r}+\psi)$, which can be named as the true electric field. The propagation direction is given by the k vector. At the rocket reference position (the geometrical center of the probes) we have $E^t_{x,y,z} = A\,k_{x,\mathrm{y},\mathrm{z}}\sin(\psi)$. It is easily seen that the differences between the two fields E and E_t vanish in the limit where $a \to 0$ and $b \to 0$. Since an arbitrary electric field variation can be described by a superposition of plane waves, we can use this single wave as an adequate model. In particular, we can give results for the error that we make concerning the electric field direction and magnitude by using the estimates (3) instead of the true electric field. We here define the error inn direction by the angle $\arccos(\mathbf{E}^t\cdot\mathbf{E}^t/|E^t|\cdot|E|)$.

Figure 4 shows the average error in the direction of propagation when using (3) to represent the true electrostatic electric field E_t.The model is applied to the boom systems of ROSE rocket where boom length is 180cm and the vertical separation is 185cm. The sphere corresponds to one wave number, here wavelength 17.5 m or frequency 20Hz by use of a characteristic phase velocity of 350 m/s with an averaging over all ψ. A point on the spheres correspond to a direction for the wave propagation given by k and the color coding gives an indication of the error, with scales given by the color bar. In general case, it should be noted that the frequencies need to be within the range of band pass filter for particular waves of interest for individual experiments.

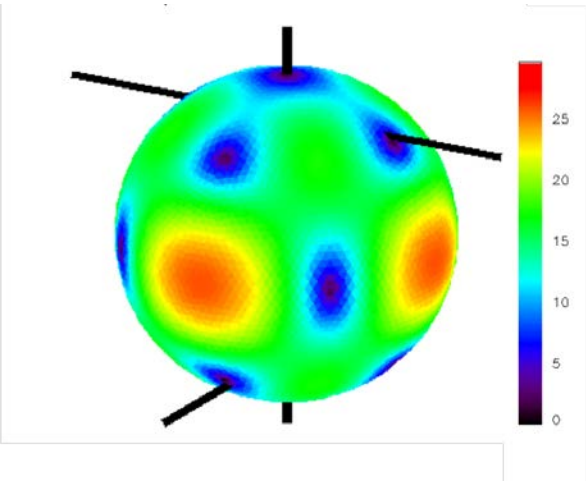

Figure 4. Error estimate for direction of propagation for one wavelength17.5m. The black lines indicate the relative positions of the boom and probes in Rose rocket system where a=180cm and b=185cm.The color scale represents degree.

The results in Fig.4 give the average over all phases for a particular wavelength. The variation of error estimate and its dependence in frequency are obtained by applying different frequencies in the range concerned for the analysis. The error can be larger for individual phase values. It is particularly seen when the phase approaches to 0. For vanishing electric fields the field direction is thus undefined and the error becomes large which may lead to experience that a local small can be detected as A017242.

having the opposite direction. The further analysis of the same data and errors in amplitude are seen in [3].

SUMMARY AND OUTLOOK

In present study we analyzed the error estimate for rocket measurement of three dimensional wave fields. By assuming propagation of plane waves, the errors in propagation directions are shown. The future study will include further development of general idea to variation of in-situ probe combinations and design to detect selective wave phenomena.

ACKNOWLEDGEMENT

We thank to UNIFOR from University of Oslo for their support for this work and travel to the symposium.

REFERENCE

1. Rose, G., et al. (1992), The ROSE project—Scientific objectives and discussion of 1st results, J. Atmos. Terr. Phys., 54, 657–667.
2. Krane, B., H. L. Pécseli, J. Trulsen, and F. Primdahl (2000), Spectral properties of low-frequency electrostatic waves in the ionospheric E region, J. Geophys. Res., 105, 10,585–10,601.
3. Sato, H., H. L. Pécseli, and J. Trulsen (2012), Fluctuations in the direction of propagation of intermittent low-frequency ionospheric waves, J. Geophys. Res., 117, A03329, doi:10.1029/2011J

Troposphere, Stratophere & Climate

Chairs: J. Urban, H. Oelhaf & J.-P. Pommereau

BALLOON-BORNE MEASUREMENTS OF ICE PARTICLE SHAPE AND ICE WATER CONTENT IN THE UPPER TROPOSPHERE OVER NORTHERN SWEDEN

Thomas Kuhn[1], **Andrew J. Heymsfield**[2], **and Stefan A. Buehler**[1]

[1]*Luleå University of Technology, Department of Computer Science, Electrical and Space Engineering, Division of Space Technology, 98128 Kiruna, Sweden*
[2]*National Center for Atmospheric Research, Boulder, Colorado, USA*

ABSTRACT

Ice clouds play an important role in the energy budget of the atmosphere. They are at high altitudes, absorb longwave radiation from below and, as they are cold, emit little infrared radiation. This greenhouse effect warms the Earth-atmosphere system. On the other hand, ice clouds have a cooling effect by reflecting incoming solar short wave radiation. The net effect is crucial for the atmosphere, but will depend highly on the cloud's horizontal extent, vertical position, ice water content (IWC), and ice particle microphysical properties such as size and shape.

Targeting these upper-tropospheric, cold ice clouds, a series of in-situ balloon-borne experiments has been started at Kiruna, Sweden, which is located at 68°N. Fewer measurements exist at these high latitudes compared to mid- or tropical latitudes. Also temperatures in the upper troposphere can be around -60 °C, a temperature range under-represented in available in-situ data. Experiments are launched from Esrange Space Center. Ice particles are collected with a balloon-borne replicator and also imaged in-situ, and measurements are complemented by a radiosonde added to the instrument. Particle shape and size as well as IWC are determined from the replicas and images. The data are analysed to reveal relationships between IWC and other measurements such as temperature and volume extinction coefficient. Such relationships can be used for validation and improvement of satellite retrievals of IWC from, for example, thin cirrus measurements with satellite-borne lidar, such as on the future EarthCARE mission.

Key words: IWC; ice clouds; lidar; ice particles; in-situ.

1. INTRODUCTION

To better assess the influence of ice clouds on the radiative balance of the atmosphere, and therefore on climate, it is essential to know more about the properties of ice clouds. While satellite measurements are very promising and have the advantage of good spatial and temporal coverage, in-situ measurements of properties of single ice particles are still very important. They support apriori knowledge required for retrievals of ice cloud properties from satellite data. For example, knowledge of both particle size and shape distributions are required for retrieval of cirrus properties [1, 2].

Thin ice clouds occur mostly in the colder parts of the troposphere, in the upper few kilometers of the troposphere, where clouds are detected remotely only by space-borne lidar, not by other instruments such as radar. Ice clouds in this region influence the radiative budget by trapping longwave radiation from Earth and reflecting incoming shortwave radiation from the sun. In order to use lidar to measure ice clouds, relationships between volume extinction coefficient (σ), as measured by the lidar, and ice water content (IWC), an important variable in climate models, have been studied [3, 4]. However, for cold clouds (T <-50 °C) direct measurements of IWC are limited and more cold-temperature comparisons are needed [4]. In particular, measured vertical profiles, as can be acquired by balloon, are needed for comparison with space-borne lidar, an active instrument sampling ice clouds vertically. Hence, an accurate IWC for thin ice clouds cannot be retrieved from satellite data; but it is needed for this important class of clouds.

Here, we describe a balloon-borne measurement campaign that has the primary goal to find a relationship between IWC and σ by using direct measurements of these two quantities in thin and cold ice clouds.

2. BALLOON CAMPAIGN

We have started a series of balloon-borne experiments targeting upper-tropospheric, cold ice clouds in the north of Sweden. In these experiments we are sampling individual ice particles and measuring their properties to determine, for ensemble of particles, σ and IWC. The balloon launches are carried out at Esrange Space Center (67.9°N 21.1°E) located about 30 km east of Kiruna. To lift the payload, which currently weighs about 5 kg, a 500-m^3 plastic balloon is used, as can be seen in Fig. 1. The ascent speed is approximately 4 m s^{-1}. Measurements are

Proc. '21st ESA Symposium European Rocket & Balloon Programmes and Related Research', 9–13 June 2013, Thun, Switzerland (ESA SP-721, October 2013)

performed during ascent, which is terminated at an altitude of 14 km by the E-TAG system from SSC (Esrange Space Center, Sweden). The E-TAG transmits its GPS coordinates to a ground station at Esrange Space Center and is used for tracking the trajectory in real time and to find the payload during recovery. The recovery of the payload is performed by helicopter immediately after the descent on a parachute. Attached to each payload are a Vaisala radiosonde (RS92) to measure atmospheric temperature and humidity and a video camera looking at the clouds (see Fig. 2).

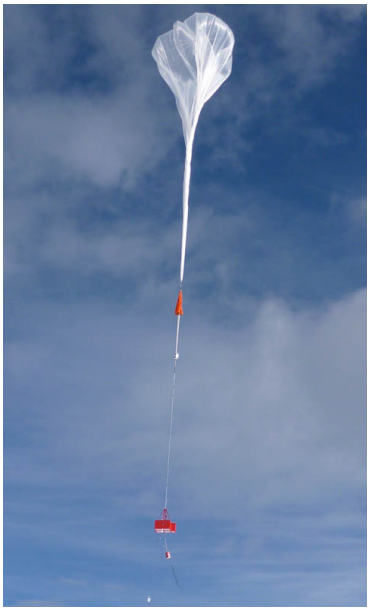

Figure 1. Balloon and payload just after launch.

The first launch was carried out in February 2012; since then four more launches have been performed until spring 2013, and more are planned during the next few winters. All launches happened during winter-spring period with completely snow-covered ground. This allowed for relatively soft landings of the payload. Hence, so far no major damage occurred, so that the instrument could easily be re-used. This is one reason why also the future experiments are being planned during this colder season. The other reason is the usually colder upper-troposphere during this period allowing us to measure in these colder temperatures according to our original aim.

3. EXPERIMENTAL METHOD

To determine IWC and σ in the experiments a combination of sampling and imaging of ice particles is used. Ice particles are collected by impaction of particles on a film strip (transparent leader of movie film). Two instruments are being used to do this. One is the NCAR ice crystal replicator, which uses a film strip coated with polyvinyl formal (Formvar) to collect ice particles with a high collection efficiency down to 10- µm particles [5].

Figure 2. Picture of clouds during experiment on 2012-04-04 taken with the video camera mounted on the instrument.

The film is advanced at a constant speed, so that the section exposed to atmospheric air containing ice particles in clouds, beneath the inlet, changes as the balloon ascends. In this way ice particle properties can be studied as a function of atmospheric conditions encountered at different altitudes. The Formvar coating is softened by dispensing chloroform immediately prior to exposing the film to ice particles underneath the inlet. Impacting particles sink into the Formvar and, after the Formvar has hardened again, create replicas that are later imaged in the laboratory to reveal size and shape.

The other instrument is similar to the NCAR ice crystal replicator using a film strip with thin oil coating, on which impacting particles will stick. This requires an almost immediate analysis before the particles are exposed to changing atmospheric conditions, which is achieved by imaging the particles on the film shortly after collection with an imaging system attached above the film as close to the inlet as possible. The imaging system consists of a microscope objective, a tube lens, and a CCD camera. A typical image of sampled ice particles on the oil-coated film strip can be seen in Fig. 3. Half of the original image width is shown, and part of the perforation, used to transport the film, can be seen at the top right of the image. The column on the image is 77 µm long. The imaging system used here resulted in a pixel resolution of 1.65 µm, so that the smallest particle that can be resolved properly is on the order of 10 µm (i.e. with more than 5 pixels across).

After imaging the ice particle, it will be melted and the resulting droplet, attached to the oil-coated film, will be imaged again to determine the volume of the droplet and, hence, the ice particle mass. The IWC will then be determined by the sum (per unit volume of sampled air) of the ice particle masses. A silicone-type oil is used, which does not harden at low temperatures and has a known contact angle for attached water droplets. Both instruments are used together, mounted side-by-side in the balloon payload, so that more data can be collected, and the results will be compared and combined.

The projected cross-sectional area of each ice particle will be determined from the images. Hence, σ, given by

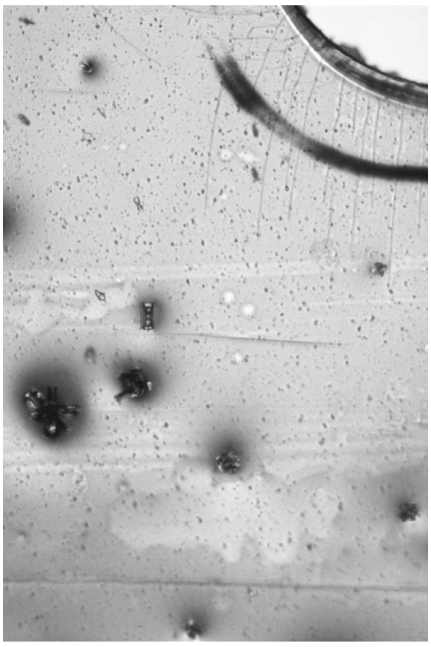

Figure 3. Typical image from the first CCD camera. The column on the image is 77 µm long. Half of the original width is shown. Part of the perforation can be seen at the top right of the image.

twice the cross section of the ice particle population per unit volume, will be determined directly from the images.

4. PRELIMINARY RESULTS

Fig. 4 shows profiles from the radiosonde measurements of temperature and relative humidity (RH: with respect to liquid water; RH_{ice}: with respect to ice) during the experiment on 2012-04-04. At a lower altitude of around 2 km a liquid layer was detected, corresponding with elevated relative humidity. A second layer of hydrometeors contained only ice particles. This ice layer consisted of two thin ice clouds, vertically separated only by a short particle-free region. Temperature inside the ice layer was

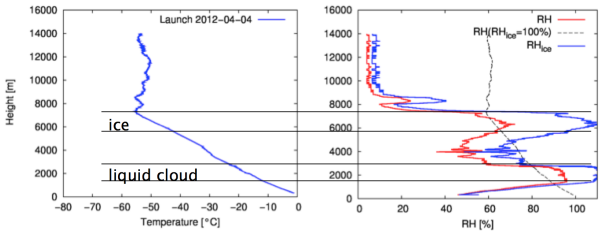

Figure 4. Radiosonde profiles from flight on 2012-04-04. The temperature is shown in the left panel, the relative humidity in the right panel as red line. The black dashed line indicates the relative humidity at which the measured water vapour was in equilibrium with ice. The relative humidity with respect to ice is shown in blue.

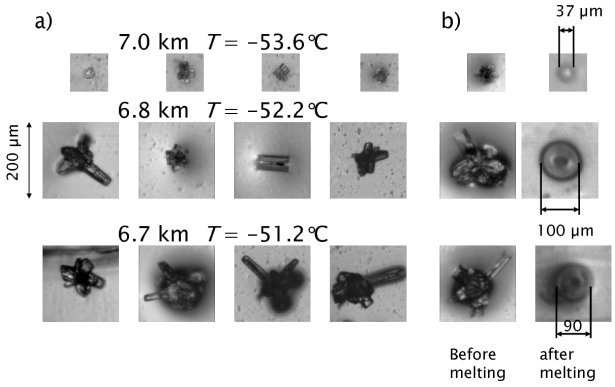

Figure 5. Ice particles from an ice cloud detected during the balloon launch on 2012-04-04. Panel a): Bottom row: particles from approximately 6.7 km altitude; middle row: particles from 6.8 km; top row: particles from 7.0 km. From cloud bottom to cloud top temperatures decreased from 51 °C to 55 °C. Panel b): particles before and after melting (explanation in the text).

between about -45 °C and -55 °C, and, apart from the top of the higher ice cloud, humidity was slightly supersaturated with respect to ice.

As atmospheric conditions change while the balloon is ascending through the cloud, size and shape of ice particles vary with altitude, as is indicated in Fig. 5 by showing typical images from three consecutive altitude ranges (representing bottom, middle and top of the higher of the two ice clouds). Most ice particles had bullet-rosette shapes with sizes on the order of 100 µm. Near the cloud top particles were much smaller (see top row in Fig. 5a). For three ice particles the corresponding droplets after melting to determine particle mass are shown in Fig. 5b).

In addition to size and shape, also the particle number concentration varied as a function of atmospheric conditions. For the high ice cloud on 2012-04-04 it increased from 0.006 to 0.2 cm^{-3} with decreasing temperature, i.e. the smaller particles towards the colder cloud top were encountered at higher concentrations. This resulted in similar values for σ throughout the ice cloud, approximately 0.2 km^{-1}, which yields an optical depth of about 0.1 for this thin ice cloud.

To evaluate size distributions of particles, the maximum dimension was determined for each particle by finding the diameter of the smallest circle that completely encloses the particle on the image. Size distributions of the particles analysed so far from three layers of the investigated ice cloud from 2012-04-04 are shown in Fig 6 by the number of particles falling in equally spaced size bins. For comparison, the figure also shows a size distribution from a new parameterization published in [6]. It agrees well with the combined size distribution determined from all particles of the cloud.

As a simple proxy for shape, the area ratio of particles can be determined as the ratio of the particle cross-sectional

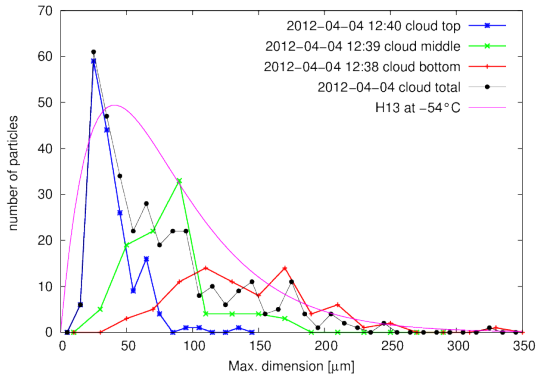

Figure 6. Size distribution of ice particles from the cloud detected during the balloon launch on 2012-04-04. Histograms with equally spaced bins are shown for particles at cloud top, middle, and bottom, respectively, as well as for the whole cloud (total). For comparison, a size distribution from the new parameterizations published by [6] is shown (indicated as H13).

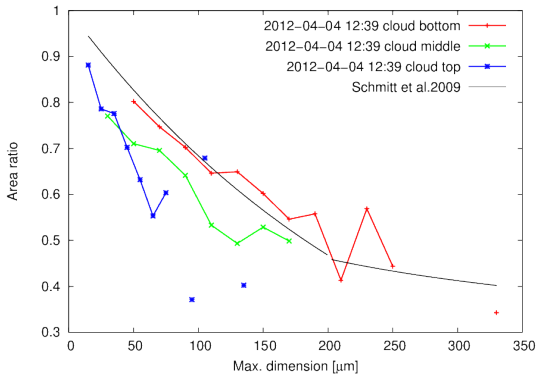

Figure 7. Averaged area ratios from the ice cloud on 2012-04-04. (Where the number of particles in a size bin was not sufficient to get a good average, data points are not connected by lines.)

area on the image to the area of the circle with the maximum dimension as diameter. Fig. 7 shows the area ratios as function of maximum dimension, averaged in size bins. For comparison, area ratios published in [7] are shown, which agree best with the larger ice particles encountered at the cloud bottom.

5. CONCLUSIONS AND FURTHER PLANS

A measurement campaign with an extended series of balloon-borne measurements of ice particles that has recently started has been described here. The preliminary data presented shows the great potential of the campaign to acquire vertical profiles of directly measured IWC and σ, useful for satellite remote sensing retrievals. Analysis of the data collected so far is continuing. All particles need to be analysed and more data is required to improve the statistical sample size and to investigate a greater variety of atmospheric conditions. Also more properties need to be studied, in particular ice particle mass to start evaluating the IWC–σ relation, which is the main goal of the campaign.

As many of the planned measurements as possible shall be accompanied by ground-based lidar measurements. Two lidar systems available for these measurements are the lidar at Esrange Space Center (operated by Prof. Gumbel, MISU, Stockholm University) and the lidar located 1 km from LTU's space campus just outside Kiruna (operated by the Swedish Institute of Space Physics, IRF). Before and during part of the measurement time of two balloon launches in February 2013 the two lidars were operated for the first time during the campaign. Such lidar measurements will be very useful both for describing better the atmospheric conditions encountered by the balloon-borne in-situ measurements, as well as for testing of the IWC–σ relation. The latter will be particularly interesting since the IWC–σ relationship to be determined will be used to retrieve IWC from satellite-borne lidars. For further validating this relationship, some of the future balloon launches will be performed at the same time as close-by overpasses of satellite-borne lidar instruments, such as on CALIPSO or on the future EarthCARE mission.

Polarization of the scattered light measured by lidar depends on the shape of ice particles. Hence, it is possible to use lidar depolarization ratios to determine dominant shape habits. Therefore, our in-situ measurements, which provide particle shape directly, collocated with lidar measurements, either space-borne or ground-based, can be used to confirm or calibrate such habit information from lidar.

The data analysis for cold, thin high latitude clouds presented in this paper showed the possibility to study parameterizations of ice particle size, shape, area ratio, and mass. More data being collected in the future measurements of the balloon campaign will provide the unique opportunity to improve such parameterizations for the temperature range typically encountered at our high latitude location. In addition, the small particle sizes together with the good image quality, allow more data to be collected of properties such as area ratio below 200-µm size than during previous measurements in the literature.

ACKNOWLEDGMENTS

We thank Swedish National Space Board for funding this balloon campaign and National Center for Atmospheric Research (NCAR, USA) for supporting a visiting period of T. Kuhn at NCAR during which data analysis has been started.

REFERENCES

[1] B. A. Baum, P. Yang, A. J. Heymsfield, C. G. Schmitt, Y. Xie, A. Bansemer, Y. X. Hu, and Z. Zhang. Improvements in shortwave bulk scattering and absorption models for the remote sensing of ice clouds. *J. Appl. Meteorol. Clim.*, 50:1037–1056, 2011.

[2] P. Eriksson, M. Ekström, B. Rydberg, and D. Murtagh. First Odin sub-mm retrievals in the tropical upper troposphere: ice cloud properties. *Atmos. Chem. Phys.*, 7:471–483, 2007.

[3] J. Delanoë and R. J. Hogan. A variational scheme for retrieving ice cloud properties from combined radar, lidar, and infrared radiometer. *J. Geophys. Res.*, 113, 2008.

[4] M. A. Avery, D. M. M. Winker, A. J. Heymsfield, M. A. Vaughan, S. A. Young, Y. Hu, and C. R. Trepte. Cloud ice water content retrieved from the CALIOP space-based lidar. *Geophys. Res. Lett.*, 39, 2012.

[5] L. M. Miloshevich and A. J. Heymsfield. A balloon-borne continuous cloud particle replicator for measuring vertical profiles of cloud microphysical properties: Instrument design, performance, and collection efficiency analysis. *J. Atmos. Oceanic Technol.*, 14(4):753–768, 1997.

[6] A. Heymsfield, C. Schmitt, and A. Bansemer. Ice cloud particle size distributions and pressure-dependent terminal velocities from in situ observations at temperatures from 0 to -86 C. *J. Atmos. Sci.*, 2013.

[7] C. G. Schmitt and A. J. Heymsfield. The size distribution and mass-weighted terminal velocity of low-latitude tropopause cirrus crystal populations. *J. Atmos. Sci.*, 66(7):2013–2028, 2009.

BOUNDARY LAYER PRESSURIZED BALLOONS DEPLOYED IN THE MEDITERRANEAN

Alexis Doerenbecher[1], Claude Basdevant[2], Fabien Bernard[2], Philippe Cocquerez[3], Nicolas Verdier[3], and Pierre Durand[3]

[1]*Météo-France, CNRM-GAME, 42 Av. G. Coriolis, 31057 Toulouse Cedex, France.*
alex.doerenbecher@meteo.fr
[2]*IPSL/LMD, École Polytechnique, 91128 Palaiseau, France.*
[3]*CNES, 18 Av. E. Belin, 31401 Toulouse Cedex 4, France.*
[4]*Laboratoire d'Aérologie, O.M.P. 14 Av. E. Belin, 31400 Toulouse, France.*

ABSTRACT

Boundary Layer Pressurized Balloons (BLPBs) from the CNES are small and light balloons equipped with sensors to monitor air thermodynamics and chemistry.

Between June 2012 and August 2013, these balloons have been deployed in the North-West Mediterranean, during three successive campaigns: TRAQA, HYMEX and CHARMEX, split in five observing periods, successively. All together, these campaigns comprise 70 balloons (5, 35 and 30 planned by time of writing). Various configurations of BLPB have been implemented. The simplest instrumental set consists in sensors for pressure, relative humidity and temperature, all *in-situ* and fitted inside a specifically designed shelter on top of the balloon. For CHARMEX, this basic instrumentation was enhanced with ozone sensors (also in TRAQA), solar flux measurements and aerosols counters (LOAC).

The data were collected at high rate and were transmitted via an Iridium communication system. The collected data were exploited in near real-time and also assimilated in weather prediction models such as AROME-WESTMED.

During these campaigns, the scientific missions of the BLPB always consisted in the monitoring of air masses, the physical characteristics of which were measured all along their travel above the Mediterranean Sea. However, the very different scientific objectives of the campaigns lead to a variety of flight conditions. Also, the BLPBs were part of a larger observing system that was activated on alert during intensive observing period and the launch/flights were coordinated with other observing platforms such as research aircraft.

In this short paper, we describe the BLPB platform, the programmatic context for the deployments and the types of missions, that range from pollution monitoring (ozone and aerosols) to humidity transport and evaporation. Then we present preliminary results about the use of balloon derived meteorological observations in numerical weather prediction (NWP) models.

Key words: balloons; boundary layer; meteorology; HYMEX.

1. PROJECTS: HYMEX, CHARMEX, BAMED.

The deployments of Boundary Layer Pressurized Balloons (BLPBs) by the CNES in the Mediterranean region during the last 12 months were operated in the framework of various field campaigns all dedicated to the observation and understanding of the Mediterranean environment. This field campaigns are part of three projects: TRAQA (long distance TRAnsport and Air Quality), HYMEX (Hydrological Cycle in the

Proc. '21st ESA Symposium European Rocket & Balloon Programmes and Related Research', 9–13 June 2013, Thun, Switzerland (ESA SP-721, October 2013)

Mediterranean Experiment) and CHARMEX (Chemistry-Aerosol Mediterranean Experiment). Both HYMEX and CHARMEX projects are funded by MISTRALS (Mediterranean Integrated STudies at Regional And Local Scales) a French initiative managed by CNRS and IRD with the participation of various institutions (http://www.mistrals-home.org).

TRAQA took place during Summer (June-July) 2012, followed by the two HYMEX SOPS (Special Observing Periods) during Autumn 2012 and Winter 2013, respectively. In June 2013, the first SOP of CHARMEX started. The second SOP of CHARMEX is planned to start mid-July 2013.

The BAMED project (Balloons in the Mediterranean) funded by CNES and INSU started in 2008. In this project CNES is partner of three laboratories LMD, OMP/LA and CNRM-GAME. This project aimed at preparing the aerostats to be deployed in the field campaigns of TRAQA, HYMEX and CHARMEX and at preparing all the scientific strategies and data exploitation. The figure 1 illustrates the "in-between" and "upstream" position of BAMED with respect to the two other major projects.

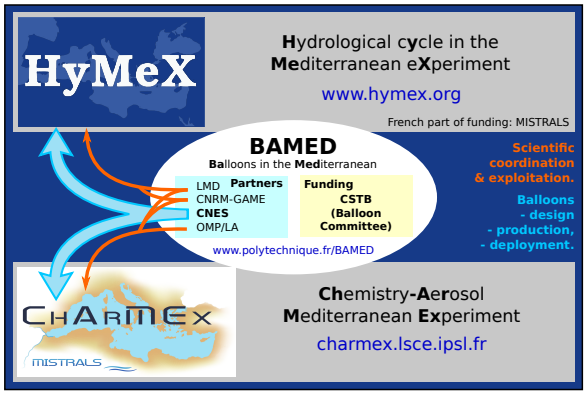

Figure 1. Relations between the projects HYMEX, CHARMEX *and the* BAMED *project that aimed at preparing the balloons for these field campaigns.*

1.1. A focus on HyMeX

The HYMEX project (Ducrocq and coauthors (2013)) focuses on the water cycle in the Mediterranean at various scales, from small scales with short but intense events to larger scales (e.g. the basin) at the seasonal or decadal scales. HYMEX is a multi-disciplinary initiative. Many scientific communities work together to understand the interactions between environmental compartments that participate to the water cycle: ocean, atmosphere, surface and hydrology... The scientific activity of HYMEX is organized in five working groups tackling the following issues: The water budget of the Mediterranean Sea (WG1); The continental hydrological cycle and related water resources (WG2); Heavy rainfalls, flash-floods and floods (WG3); Intense sea-atmosphere interactions (WG4); Societal and economic impacts (WG5).

The observation strategy of HYMEX consists in nested periods of decreasing length with varying objectives but increasing observing efforts. The longest period (LOP) lasts 10 years and is dedicated to WG1. The LOP started in 2010. Two special observing periods (SOPS) have been implemented in 2012 and 2013 to tackle the heavy rainfalls, flash-floods (WG3) and the intense sea-atmosphere interactions (WG4). The SOPS aimed at a better understanding of relatively small scale features with a very dense and flexible observing system. As the phenomena of interest could occur in many places of the North-Western Mediterranean basin, specific target areas have been designed to manage many spots with very high observation density.

The table 1 lists the name of the targets areas for HYMEX SOP1 which are mapped on figure 3. SOP1 started on the 5th of September 2012 and finished on the 6th of November 2012. For SOP2 (1st of February 2013 - 15th of March 2013), the main target area is the so-called dense water formation area (shown on figure 4).

For the purpose of both HYMEX SOPS, a specific modelling system has been implemented at Météo-France to encompass all the Western Mediterranean: AROME-WESTMED (Ducrocq and coauthors (2013)). This 2.5km non-hydrostatic limited-area model was the keystone for all NWP-derived products and decisions. For instance, AROME-WESTMED forecasts were used to predict balloons trajectories, on a daily basis.

Name and symbols for SOP1 target areas.	
CV	Cévennes-Vivarais (France)
CO	Corsica (France)
BA	Balearic (Spain)
CA	Catalonia(Spain)
VA	Valencia (Spain)
NEI	North-East Italy
CI	Central Italy

Table 1. HYMEX *target areas during* SOP1.

2. INTRODUCTION: WHAT IS A BLPB ?

Boundary Layer Pressurized Balloons (BLPBS) are small (between 2 and 3 meters in diameter) drifting aerostats designed to fly at constant density in the lower levels of the atmosphere. The balloons described here have been designed, produced and operated by CNES. The former conception of the BLPBS that were deployed in past field campaigns such as VASCO (2007, Indian Ocean, Duvel et al. (2009); Vialard and coauthors (2009)) or AMMA (2006, Western Africa, Redelsperger et al. (2006)), among others, has been revised to improve the capability of the aerostat to fulfil its scientific missions in the Mediterranean and precipitation context. The diagram shown on figure 2 describes the main characteristics of the new BLPB.

The scientific instrumentation has been gathered in a dedicated and aired shelter at the top of the balloon. This shelter aims at protecting the sensors from the rain or any other kind of contact. The shelter position on the balloon ("Sky pole") helps preventing any contact with sea water in case of *sea-landing*. In this case, the scientific payload is not piggy-pack, but fully included in the balloon. As a consequence, this payload has been designed and produced by CNES, together with the housekeeping gondola which is located inside the envelope at the "Earth pole" of the balloon.

Heavy rain can load BLPBS substantially and sufficiently to counteract the Archimedes force and bring the balloon to sea level. To minimize the mass increase due to rain or simply condensation, the BLPBS were coated with an hydrophobic substance and fitted with drop deflector preventing any raindrop to leak on the southern hemisphere of the balloon.

The data collected (every 30 seconds) by the scientific gondola are radio-transmitted to the housekeeping gondola which manages the communications with the "ground-segment" of the flight system. These communications are frequent (every 2 minutes), thanks to the Iridium link. The basic instrumentation does not include wind. Indeed, under the hypothesis of Lagrangian behaviour of the aerostat, one can deduce the wind (speed and direction) from the successive locations of the aerostat. These locations are given by a GPS system.

During CHARMEX (Durand et al. (2012)) additional instrumentation is added to the basic configuration described above. An additional payload is added below the balloon, as it is done generally. Indeed, the rain issue does not apply to CHARMEX (flights within dry conditions) so the *sea-landing* should not occur before the end of flight. The two payloads in question are: an ozone sensor and a particle counter LOAC (Light Optical Aerosol Counter, see paper A-4 by J.-B. Renard *et al.* in the present proceedings). And finally, some radiative flux sensors are added on these CHARMEX' BLPBS.

3. SCIENTIFIC MISSIONS

In HYMEX SOP1, the scientific mission of the BLPBS was to collect information on the moistening of air parcels above the sea. It has been shown (Duffourg and Ducrocq (2011)) that a significant part of the water that fall in convective cells during heavy precipitation events comes from the Mediterranean Sea, which surface is still warm during Fall. Hence, the sea is an energy reservoir for the HPES. We know also that air parcels in the boundary layer have a greater capacity to bring humidity in areas of convergence where convection is triggered. So, to monitor this process, BLPBS had to be placed in the low level flow as early as possible, i.e. before the air parcels have gained too much humidity, and as low as possible to get information on the transports in the boundary layer, which is quite thin (compared to land), even above a warm sea. Considering the advection process, early means upstream. That's why the selected launch site is not in a continental target area, but on an island. The figure 3 illustrates

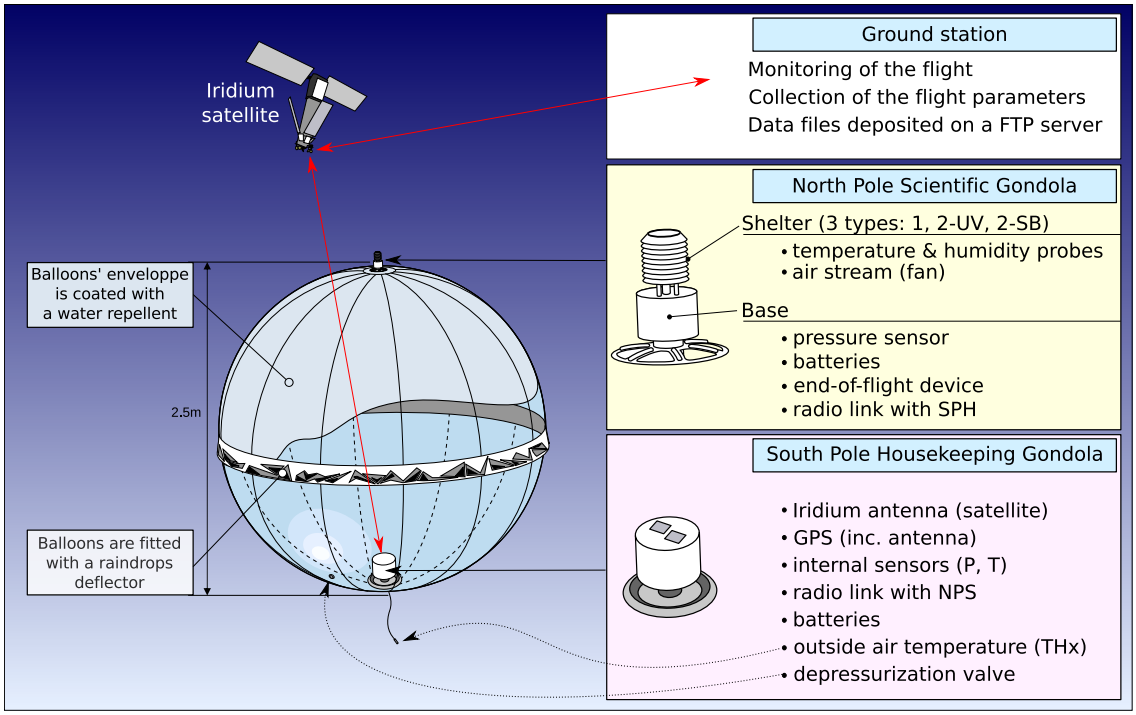

Figure 2. This diagram shows most of the BLPB *functional features. But it is not exhaustive. On the left is a general view of the balloon with its gondolas. On the right, the 3 functional blocks of the system, including the ground segment (not drawn on that picture).*

the situation. The fact that the site coincides with the "BA" target area is pure chance. The BLPBs have been launched in advance with respect to the occurrence of the HPEs, in order to let them enough time to drift in the flow and reach the continental target areas right on time.

During HYMEX SOP2, the mission was to collect a quite similar information but in a physical process that works in the opposite direction: here the cold and dry air masses coming from the continent extract heat and water from the sea, the surface of which gets colder and more salted, hence denser. This surface dense water, eventually sinks during so-called oceanic convection events (Candela (2001)). The BLPBs have been launched in the heart of Mistral and Tramontana episodes, during which air-sea surface fluxes are extremely intense. The balloons flew very fast, describing with great details the wind events above the sea, in coordination with research aircraft that documented surface waves and fluxes. The figure 4 shows the configuration for the SOP2 flights.

For TRAQA and CHARMEX, the BLPBs are used for chemistry missions. In TRAQA, the BLPBs played the role of tracers for air masses allowing the research aircraft ATR42 to sample them several times for studying the ageing process on chemical species. During CHARMEX, the flights aim at sampling (Saharan) dust and (continental) pollution episodes.

4. HYMEX **FLIGHTS AND DATA.**

The figure 5 shows the trajectories of the flights made during the SOP1 of HYMEX. Most of the flights were successful, only 2 of them underwent unexpected problems (partial-loss of communications). This panel of trajectories shows that Minorca was the right choice as a launch site. BLPBs have been able to reach most of the target areas, or at least those which were contiguous with the authorized flight domain. Thus the **CI** target area was out of reach, and the **NEI** only partially.

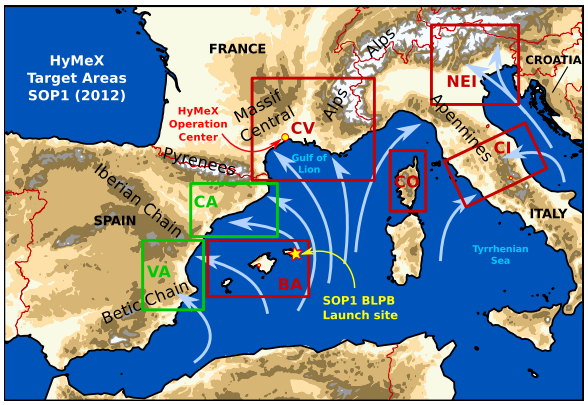

Figure 3. Geographical distribution of the HyMeX *target areas for* Sop1*, i.e. regions where* HPEs *were expected and instrumentation available. The red squares show areas where a dedicated and enhanced observing system was deployed. The green squares correspond to areas with little* HyMeX*-specific observing systems. Refer to the table 1 for the name of target areas. The sky-blue arrows show the classical low-level air flow that produces humidity convergence against coastal elevated land which is a key ingredient for the deep convection. The star shows the* Blpb *launch site. The* HyMeX *Operation Centre (*Hoc*) was in La Grande Motte (France).*

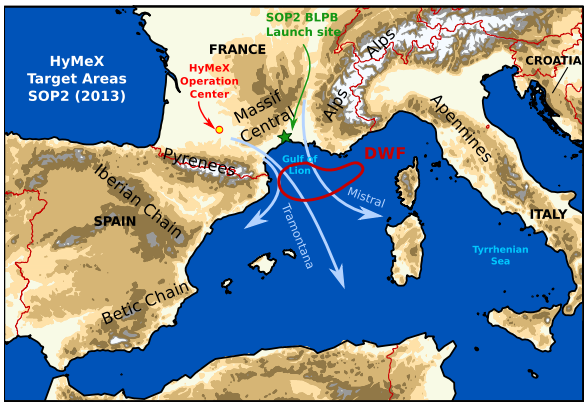

Figure 4. Configuration of the low level flow above the Gulf of Lion, in case of Tramontana and Mistral. These strong dry and cold winds (winter) trigger the increase of the sea surface water density (Dense Water Formation, Dwf *on the map). This process persists until the surface water sinks down to the sea bottom, producing oceanic convection. The balloons were launched from Candillargues. The* Hoc *was in Toulouse (France).*

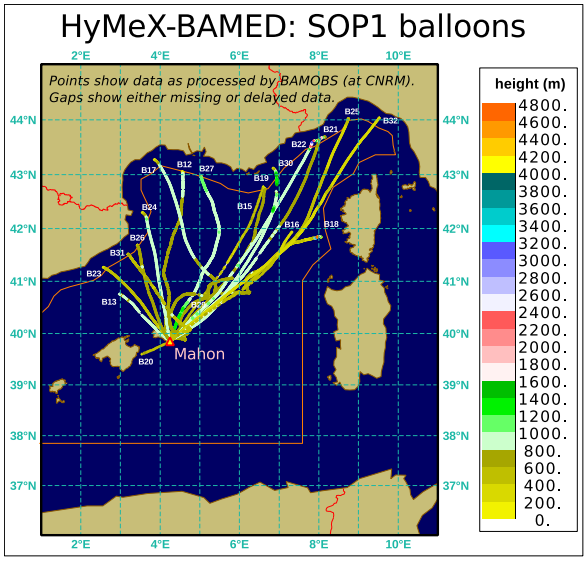

Figure 5. Trajectories of the 19 balloons deployed from Minorca during Sop1*. The colour of the trajectories show the flight altitude, following the rule shown on the legend on the right hand side. The orange line on the picture shows the limit of the balloon flight domain.*

The Cnes team made a special effort to tune the flight level as low as possible to match the scientific objectives (to fly within the boundary layer). The flights were generally quite stable (at about 500m and even lower: 300m), except when they encountered the convective systems they aimed at. B18, B21 and B22 reached up to 3500m within convective systems. These ascents triggered the end of flight, but these flights are considered as successful anyway.

The figure 6 shows the trajectories of the flights made during the Sop2 of HyMeX. In that case, the trajectories are very similar from one flight to another and all passed above the Dwf (Dense Water Formation) target area.

The figure 7 shows an example of *Quick-look* (QL) for the flight B41. Such QL were displayed on the Hoc (HyMeX Operation Centre) website in order to allow the scientists to follow the flights. The QL gathers the information on parameters that are relevant for the meteorology. Refer to the caption on figure 7 for more details on this QL in particular.

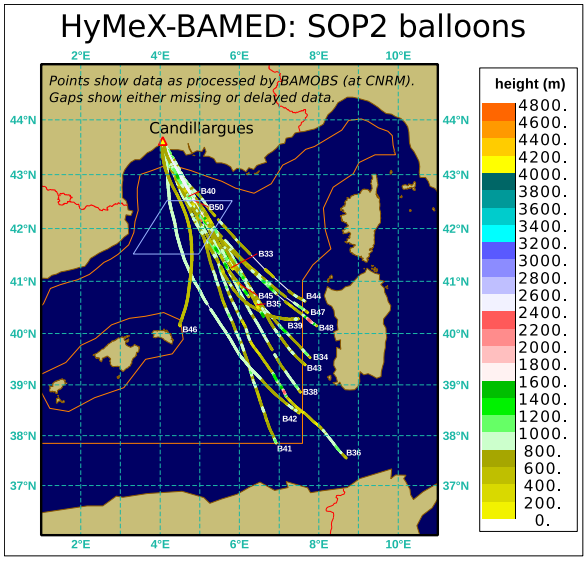

Figure 6. Trajectories of the 16 balloons deployed from Candillargues during SOP2. *The colour of the trajectories show the flight altitude, following the rule shown on the legend on the right hand side. The flights were generally very shaky (at about 800m) as the trajectories went in the Mistral-Tramontana convergence area.*

5. DATA QUALITY ISSUES

The data collected were processed in near real-time at both LMD and CNRM-GAME. At CNRM-GAME in the BAMOBS observation processing, the wind was derived and the stability of the flight checked. When a short (but long enough) portion of flight was detected, an observation *report* was built (filtering). Here, the observation *report* is a piece of information which is representative of what a numerical weather prediction system is able to describe. This information can be used to fit the model state with the reality. These reports were then introduced in Météo-France operational database. From that database, the data were used in the data assimilation computation for ARPÈGE, AROME-FRANCE and AROME-WESTMED.

The examination of the BLPBs data showed a bias on the air temperature when the flight is quite calm and the weather sunny. As the BLPB is a Lagrangian drifting object, there's no relative wind, and the whole balloon can get warmed up by the sun. Despite a sufficient airing of the scientific gondola, a warm air chimney may set in the vicinity of the scientific gondola. Thus, the temperature measurements may not be fully representative of the ambient air.

As a by-product of the data assimilation, it was easy to compare the measurement with the model values. However, to get a clean check of the observations, we have to use a model, which had not assimilated the BAMOBS data. Thus the statistical non-dependency is guaranteed. So to perform this data sanity check we use the IFS (ECMWF) model. Here the model is used as a reference, because we suppose that it is less biased than the data. However, the model is not the truth and some uncertainty is associated to it. This should not be forgotten when examining the results.

The figure 8 shows the statistics on the BAMOBS data with respect to the IFS data at observation points. Several subset of data are compared. We distinguish between daytime and night-time and we also distinguish between SOPs. Indeed, the flight conditions were so different and two new versions of the meteorological shelter have been tested during SOP2. The figure 8 shows clearly the discordance between the model and the observations by daytime. The discrepancy is stronger during SOP1. We suggest that the improvement between SOP1 and SOP2 may be due to the revision of the meteorological shelter but also due to the very high level of turbulence in the strong winds, with small scale air movements that may have prevented the warm chimney phenomena to settle on the balloon. The temperature by night-time looks of good quality.

Humidity is not the best described parameter in NWP models. Indeed, this parameter has very high spatial variability and in-situ observations are quite rare above oceans. That's why the data collected by the BLPB's are so important. However, we attempted a sanity check of these measurements, to make up our mind on a possible contamination of these data by the temperature bias. Naturally, one should check the mass of water (specific humidity or mixing ratio), not the relative humidity which is a function of the (biased) air temperature. Again, we have used various models, but here we show the results with IFS on figure 9. The day-night variation does not appear in that case. The data is free of diurnal bias. The quality looks quite good with an overall RMS of 1 g/kg. The reason for the difference between

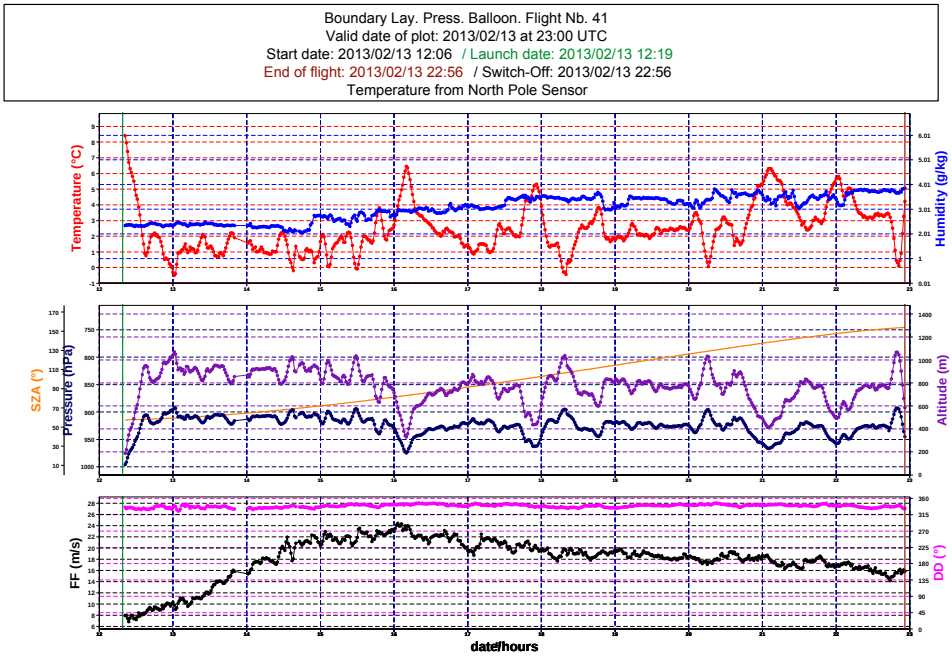

Figure 7. Example of Quick-look (QL) diagram built in near real-time and displayed on the HOC *website. The top frame contains the air temperature (°C, red curve) and the specific humidity (g/kg, blue curve). On the middle frame, the purple curve depicts the GPS altitude (m) and the dark blue curve gives the air pressure (hPa). The lower frame shows wind, the direction (°, magenta curve) and the speed (m/s, black curve). In this case, the balloon B42 was deployed during* SOP2. *One can notice how shaky the flight was: the altitude curve isn't flat whatever the flight phase. The wind speed reached its maximum 25 m/s, 4 hours after launch. The increase of moisture during the flight is 25 % from 3 to 4 g/kg between Gulf of Lion and Algerian sea (on fig. 6).*

SOP1 and SOP2 may be due to the very different air masses that have been sampled. In SOP1, the air was warm and moist (with about 12 g/kg), when in SOP2 the air was cold and dry with generally about 5 g/kg and even less: B42 sampled an air parcel with less than 0.5 g/kg !

6. CONCLUSIONS

During HYMEX SOP1, the BLPBS drifted in the converging low-level air flow above the Mediterranean Sea that controls the localisation and the intensity of the HPES. The moisture extracted from the sea feeds the precipitations on-shore. In that respect, the BLPBS were sampling in the key-process. In this flow, very few routine observations are available: the closeness of the surface allows very limited satellite data and the weather radars only collect data in coastal areas. The BLPBS nicely complemented the research aircraft (ATR + Falcon) and radiosoundings.

For SOP2, the campaign focussed on regional winds such as Mistral and Tramontana that influence (conditioning and triggering) dense water formation in the Gulf of Lion. This DWF process mixes water on the entire water column. Very limited in-situ observation of these winds exist above the ocean. The BLPBS allowed a high resolution description of the wind dynamics (small scales) and their variability. The BLPBS were coordinated with ATR flights and radiosoundings.

The data have been treated in near real-time to allow NWP models to take advantage of this uncommon information source and get a better representation of what occurs just above the Mediterranean sea and is not sampled by any other observation means. This immediate use of the BLPBS

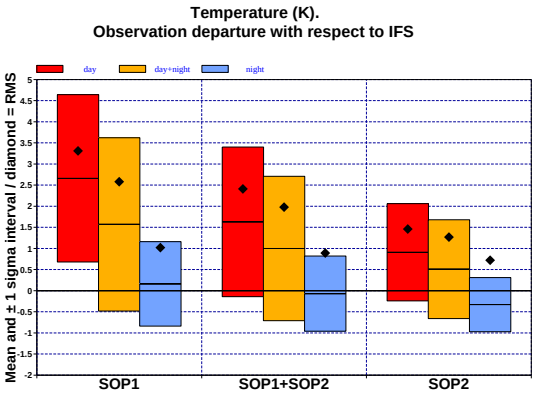

Figure 8. Root mean square error (diamond), bias and standard deviation of measured temperature with respect to the IFS *model.*

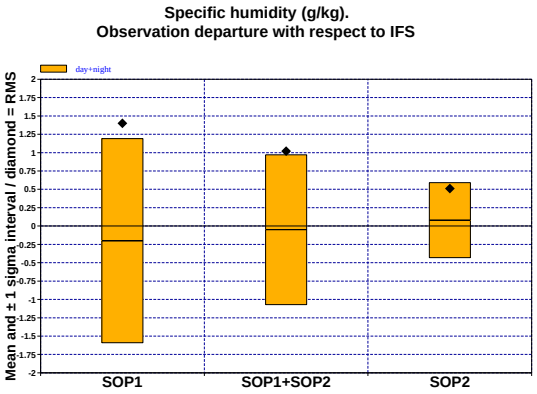

Figure 9. Root mean square error (diamond), bias and standard deviation of measured specific humidity with respect to the IFS *model.*

in the model allowed to get a rapid insight on temperature problem by daytime. In that respect, the scientists in BAMED helped CNES in a continuous improvement of the observing platform.

The data collected during CHARMEX, especially the radiative flux data will help us to consider rule to remove the temperature bias of all the HYMEX and CHARMEX data. By the time of writing, this has nor been done yet, but only the daytime temperature data have to be used with care: humidity, pressure, wind and night-time temperature are fine and are available by the PIs of BAMED and the HYMEX database.

7. ACKNOWLEDGEMENTS

Raw data were obtained through observing platforms integrated into Boundary Layer Pressurized Balloons (BLPB) operated by CNES under the agreement between CNES and CNRS/INSU in the BAMED project. Raw and processed data are available thanks to HYMEX program, sponsored by grants CNES-CNRS/BAMED and MISTRALS/HYMEX.

REFERENCES

Candela J. (2001). Ocean Circulation and Climate., chapter Mediterranean water and global circulation. Academic Press, San Diego, CA.

Ducrocq V. & coauthors (2013). Hymex-sop1, the field campaign dedicated to heavy precipitation and flash-flooding in northwestern mediterranean. *Bull. Amer. Meteor. Soc.*, **submitted**.

Duffourg F. & Ducrocq V. (2011). Origin of the moisture feeding the heavy precipitating systems over southeastern france. *Nat. Haz. Earth Sys. Sci.*, **11**, 1163–1178.

Durand P., Attié J.-L., Basdevant C., Bernard F., Dulac F., Gheusi F., Lohou F., Lothon M., Mallet M., Renard J.-B. & Verdier N. (2012). Boundary-layer drifting balloons for chemistry-dynamics studies in the mediterranean region. In 20th Symposium on Boundary Layer Turbulence, Boston, MA.

Duvel J.-P., Basdevant C., Bellenger H., Reverdin G., Vialard J. & Vargas A. (2009). The aeroclipper: A new device to explore convective systems and cyclones. *Bull. Amer. Meteor. Soc.*, **90**, 63–71.

Redelsperger J.-L., Thorncroft C., Diedhiou A., Lebel T., Parker D. & Polcher J. (2006). African monsoon multidisciplinary analysis (amma): An international research project and field campaign. *Bull. Amer. Meteor. Soc.*, **87**, 1739–1746.

Vialard J. & coauthors (2009). A field experiment in the southwestern indian ocean provides new insights into ocean–atmosphere interactions in a key climatic region. *Bull. Amer. Meteor. Soc.*, **90**, 45–61.

MISSUS EXPERIMENT ONBOARD BEXUS 15: AN INNOVATIVE INTEGRATED SENSORS SUITE FOR METEOROLOGICAL MEASUREMENTS IN LOW PRESSURE ENVIRONMENTS AND FOR ATTITUDE RECONSTRUCTION

F. Cucciarrè [(1)], S. Chiodini [(2)], C. Palla [(2)], G. Tovo [(2)], I. Vidali [(2)], D. Bettio [(2)], D. Cornale [(2)], V. Botti [(2)], E. De Villa Bais [(2)], M. Didonè [(2)], G. Colombatti [(1)], S. Debei [(1)]

[(1)] CISAS "G.Colombo", Via Venezia 15, 35131 Padova (ITALY), E-mail: francesca.cucciarre@unipd.it
[(2)] University of Padova, Via Venezia 15, 35131 Padova (ITALY), E-mail: missus.exp@gmail.com

ABSTRACT

This paper describes the MISSUS experiment (Meteorological Integrated Sensor SUite for Stratospheric Analysis), developed at CISAS (Center for Studies and Activities for Space "G.Colombo") with the aim to characterize the most significant environmental parameters of thin atmospheres and fully reconstruct attitude and trajectory. MISSUS flew onboard the BEXUS15 ESA/SSC/DLR stratospheric balloon in September 2012 and it has been designed to collect meteorological and attitude data and validate the atmospheric models during the ascent, cruise and descent phases. The flight provided an unique opportunity for testing the onboard innovative instrumentation, which has been designed basing on CISAS previous know-how on balloon flights and space missions. In particular, MISSUS temperature sensor is the prototype of the MarsTem, the instrument which will be part of the DREAMS suite (Dust characterization, Risk assessment, and Environment Analyser on the Martian Surface) onboard ESA Mission Exomars 2016.
The design and the results are presented.

1. INTRODUCTION

The role of meteorological instrumentation is central for planning a surface mission on a planet because the study of the atmosphere allows to go deeply into the dynamics of the atmosphere formation and to investigate the evolution processes of the whole Solar System. The recent ESA programs have focused on Mars for 2012-2016 and beyond, to investigate the environment of the planet, in particular on the research of present and past life traces and demonstrate new technologies for future missions and landings.
From this starting point the need of realizing a meteorological package conceived for applications in Mars-like environments arose. MISSUS experiment, composed of several sensors for the measurement of temperature, pressure, humidity, velocity, magnetic field and attitude, gives a useful contribution in the development of integrated multi-sensors packages for harsh atmospheres exploration. At an altitude of 20-30 km, Earth atmosphere is similar to Mars ground environment concerning the pressure and the thermal exchange mechanisms, whereas differences respect to Mars atmosphere are related to the thermal conductivity and thermal capacity of Carbon Dioxide and the presence of dust [1].
At the moment, CISAS is involved in the design and realization of DREAMS package, which will be part of the payload on Exomars 2016 Mission [2].
MISSUS results constitute a useful input for the mission: the innovative temperature sensor onboard is the prototype of the sensor which will be used to directly measure the temperature profile of Mars atmosphere on the Entry Descent and Landing Demonstrator Module (EDM, Exomars 2016). From the detailed analysis of the acquired data and the sensor behavior during flight, some useful improvement and modifications have been introduced in the design of the Flight Model of the sensor.
In addition, thanks to the collected data during flight, the BEXUS gondola attitude and trajectory (not presented here) have been determined and atmospheric models have been validated.

2. MAIN OBJECTIVES

MISSUS planned to reach both scientific and technical goals.
The scientific goals are:

- Characterization of the environment up to 20-30 km altitude.
- Validation of the atmospheric mathematical models, thanks to the data acquired by the sensors onboard.

Proc. '21st ESA Symposium European Rocket & Balloon Programmes and Related Research', 9–13 June 2013, Thun, Switzerland (ESA SP-721, October 2013)

- Comparison between Earth thin atmosphere at 20-30 km altitude and Mars atmosphere on ground (this objective will be reached once data from Mars will be available).
- Reconstruction of the attitude and the trajectory of the gondola, on which MISSUS is mounted.

Strictly related to the previous scientific goals, the technical goals consist of:

- Design and realization of an integrated multi-sensors scientific payload.
- Design, development, calibration and test of an innovative temperature sensor, able to measure fast temperature fluctuations.
- Design and development of a system for the impact detection of the gondola with ground.

3. EXPERIMENT DESCRIPTION

As described above, MISSUS experiment is able to provide both meteorological measurements and attitude and trajectory measurements.

The innovation of the experiment is based on the integration of all the sensors and on data-fusion, which has been managed in post-processing: every measurement has been cross-correlated with the others to increase the accuracy of the results, based on a synergic approach.

The experiment is split in two parts: some sensors have been placed outside the gondola, on a 1.2 meter length Aluminum mast attached to the gondola rails, for the meteorological measurements; the other sensors have been placed inside the gondola, together with the electronics, which controlled the sensors, the batteries and the PC104, for the data-sampling, data-handling and transmission to ground station. Power supply for all the sensors has been provided by two Lithium - ion batteries through the electronics. Data conditioning and telemetry subsystem collected data coming from sensors and sent part of them to the ground station through BEXUS E-link unit, while the whole data volume has been stored in a solid state memory.

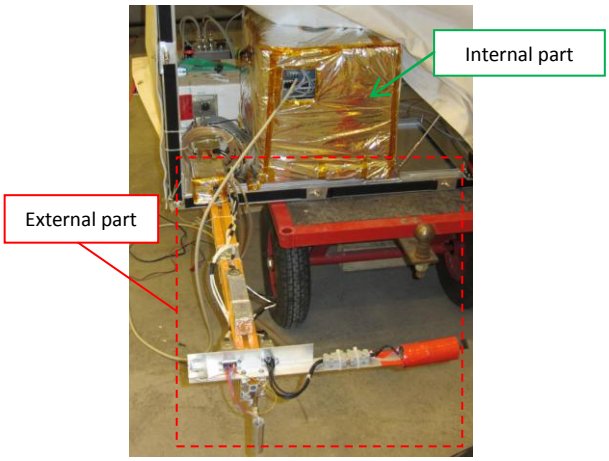

Figure 1. MISSUS experiment onboard the gondola

All internal components (sensors, electronics and batteries) have been mounted inside an edged box, (380x360x364) mm^3 volume, close to the external side of the gondola, easily accessible (in order to recharge batteries) and close to the boom (in order to minimize the length of the external cables).

The experiment has been provided with the following sensors:

- An innovative resistance temperature sensor, placed on the tip of the external mast, on an Aluminum support, in order to get the temperature of the external environment as a function of the altitude. This sensor is a home-made platinum resistance thermometer with a thin platinum wire wrapped around a PEEK support.
- A second temperature sensor (a Resistance Temperature Device commercial sensor), used as a reference sensor for the innovative temperature sensor and for redundancy reasons; it has been placed near to the innovative temperature sensor.
- A humidity sensor (Honeywell HIH-4000 series), placed on the mast, used for the measurement of humidity during the ascending and descending phases.
- Two USB cameras (Logitech), for the monitoring of the experiment (e.g. to assess the position of the Sun by the observation of the shadows) and for public outreach contribution.
- A fluxgate tri-axial magnetometer (Bartington Mag-03MS1000) for the measurement of Earth magnetic field; it has been placed on the mast, far from the gondola in order to minimize spurious effects due to the magnetic field of the gondola and its subsystems: it gave a contribution to completely reconstruct the gondola attitude.
- An absolute pressure sensors (Freescale MPX-2200 series) and a gage pressure sensor (Honeywell 060MG), placed inside the gondola, near to the electronics, to get the absolute pressure as a function of the altitude.
- A differential pressure sensor (Vaisala PDT101), placed inside the gondola, and connected to the external Pitot tube, placed on the tip of the mast, in order to obtain the descending velocity measurements by the measure of the differential pressure.
- An IMU (XSENS MTi-G), provided with GPS receiver, in order to reconstruct the gondola attitude and trajectory;
- A tri-axial accelerometer (Dytran7523A5), specific for shock measurements.

Combining the signals provided by the tri-axial accelerometer, able to measure shocks, and the absolute pressure sensor, a system has been developed to detect the probe impact with the ground. The aim of the system was to demonstrate the feasibility of this technology since one of the most critical issues in

stratospheric balloon missions is the separation of the payload from the parachute after probe landing, considering that parachute may drag the payload for long distances before being recovered, with consequent damage of the instrumentation. The absolute pressure sensor signal is fundamental to measure absolute pressure on ground, avoiding accidental separation during the flight (e.g. when parachute is deployed).
A housekeeping system (e.g. additional temperature sensor) and active thermal control system have been used in order to monitor and control the experiment respectively.
Fig. 2 and Fig. 3 show the internal and the external parts of MISSUS with all the sensors integrated.

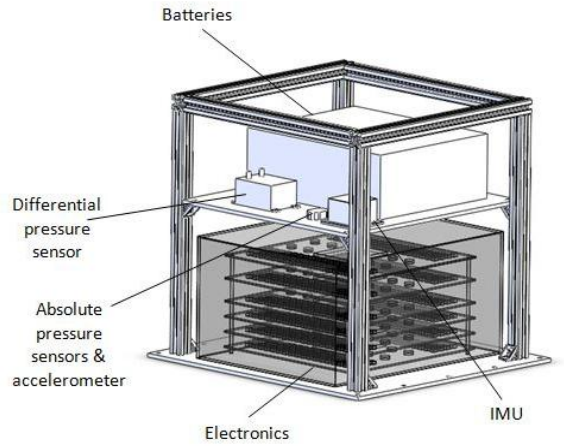

Figure 2. Internal components of MISSUS experiment

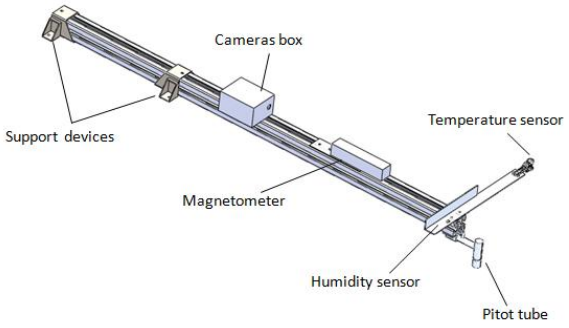

Figure 3. External components of MISSUS experiment

3.1 The Innovative Sensors

MISSUS is equipped with two innovative sensors, entirely designed, developed, calibrated and tested at the University of Padova: the temperature sensor and the Pitot tube.
The temperature sensor, which constitutes the prototype of the sensor that will land on Mars ground in 2016 (MarsTem), has been conceived to measure fast temperature fluctuations and has been placed on the tip of the experiment boom.

The main structure of the sensor consists of two titanium arms internally hollow in order to accommodate and shield the electric cables. At the tips of the arms two rings support 3 PolyEther Ether Ketone (PEEK) bars (450GL30); the platinum sensitive wire is wrapped around them and fixed thanks to glue (resistant at low temperatures). The edges of the structure are smoothed, in order to reduce fluid perturbations due to the stem. Two holes per ring allow the connections between the sensitive platinum wire with the electric cables.
Thanks to the platinum net, the exchange surface between the wire itself and the air flux is maximized. Conductive thermal exchange between sensitive element and Titanium structure is negligible considering PEEK insulating properties.
Fig. 4 shows the innovative temperature sensor and the coarse temperature sensor attached on the titanium structure.

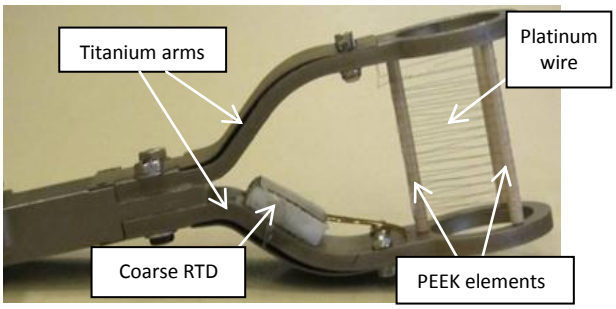

Figure 4. Innovative temperature sensor

The Pitot tube, realized in Aluminum Alloy (AA 6061-T6), has been designed to detect the flow velocity of the gondola during the descending phase: it can be estimated once the static pressure and the total pressure on the Pitot tube are measured by the differential pressure transducer (Bernoulli law, Eq.1).

$$v = k\sqrt{\frac{2(p_{tot} - p_s)}{\rho}} \qquad (1)$$

v is the flow velocity, coefficient k has been estimated by the calibration process, p_{tot} and p_s are the total pressure and the static pressure respectively, ρ is the air density obtained by the atmospheric models.
The Pitot tube has been placed on the tip of the external boom, not far from the temperature sensor, and connected to the internal differential pressure sensor through plastic tubes. The special configuration has been conceived in order to avoid possible issues arising from the misalignment between total pressure probe axis and flow direction. The total pressure probe is inside a cylindrical cover, which consists of a tube with a convergent-divergent section.

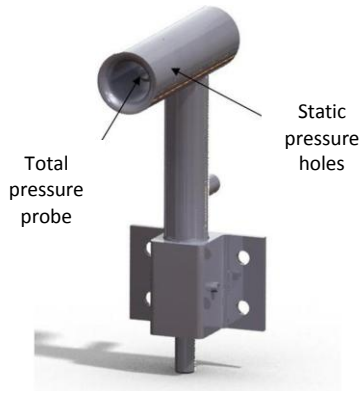

Figure 5. Pitot tube

The static holds are around the external cylinder and their position has been optimized thanks to fluid-dynamics analysis in order to compensate the overpressure due to the stem by the depression due to the leading edge of the tube.

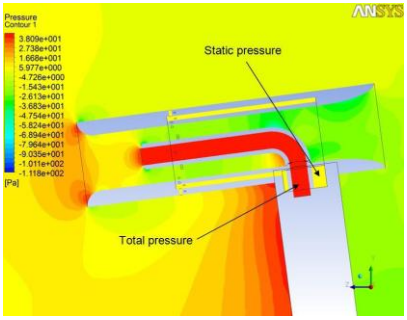

Figure 6. Pitot tube, CFD analysis

3.2 Mechanical Design

MISSUS mechanical structure has been designed in order to withstand the worst static load condition (-10 g in the vertical direction, ±5 g in the horizontal direction), according to BEXUS user manual. Starting from analytical considerations, in the earlier stages of the project, then the design process focused on FEM verification, which has been extended on the main structure and on all home-made elements (temperature sensor and Pitot tube).
A minimum safety factor of 2 has been guaranteed.

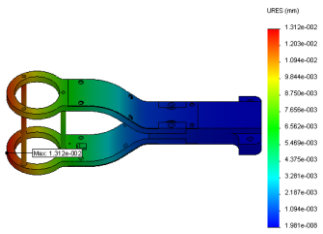

Figure 7. Temperature sensor, FEM analysis

In order to reduce the weight of the experiment and maintain an acceptable cost, aluminum has been extensively used where possible. The boom, the box structure, support plates of the internal systems and the Pitot tube have been realized in Aluminum 6061-T6, whereas the support devices which fix the boom to the gondola structure have been realized in AISI304 steel. The temperature sensor, being the prototype of DREAMS temperature sensor, has been realized in the same material, titanium.

3.3 Thermal Design

A detailed thermal model has been developed in order to estimate the temperature of components and eventually implement thermal control techniques (passive and active) on the experiment. All environmental thermal fluxes (solar, albedo, planetary flux) and internal generation (electronics and batteries self-heating) have been considered; the external temperature of the atmosphere has been treated as a boundary condition. Fig. 8 shows the temperature of sensitive components as a function of time, as a result of the thermal model.

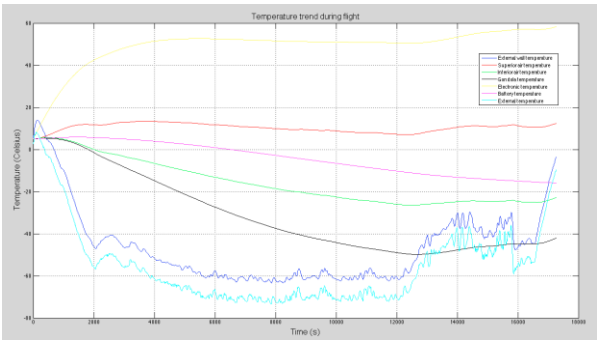

Figure 8. Temperature of MISSUS components

In order to keep the temperature of the internal units and sensors within their operative limits, polyurethane-foam walls and MLI have been used to cover MISSUS box; in addition heaters have been placed on the batteries and on Pitot tube, with the aim to avoid ice formation inside the static pressure holes during flight.

3.4 Electronics

The experiment main electronics has been designed to acquire, supply sensors and heaters, detect impact with ground. All electronics boards have been mounted inside a rack placed on MISSUS box, inside the gondola.
Main electronics is composed of the following elements:

- A logical unit (PC104) which provides: (1) experiment monitoring; (2) data acquisition management; (3) telemetry management by means of Ethernet bus; (4) data storage (IDE Solid State Disc – 32 GB memory).
- Signal sampling (ADC) unit.

- Two Power management boards, provided with DC/DC converters (one to supply power at 5V, the other one at ±15 V).
- One power digital board to activate heaters, provided with 8 configurable digital channels.
- Four analog conditioning boards, with 6 analog channels for each board. Only 21 channels of the conditioning boards are used.
- One additional board, also called separation system simulation board, devoted to the impact detection system and implementing vector sum of 3 acceleration components and critical parameters (acceleration and pressure) threshold setup.

The following figure is a representation of the electronics functional overview.

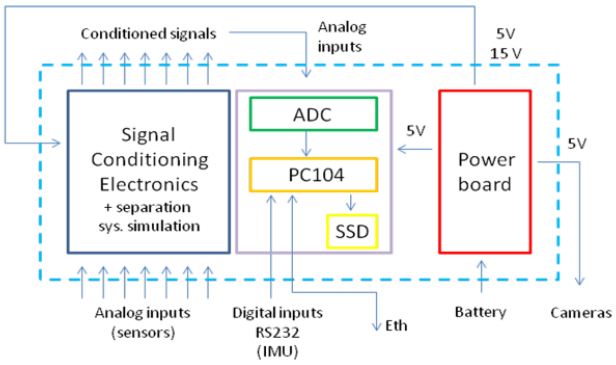

Figure 9. Electronics functional diagram

Fig. 10 shows electronics rack assembled.

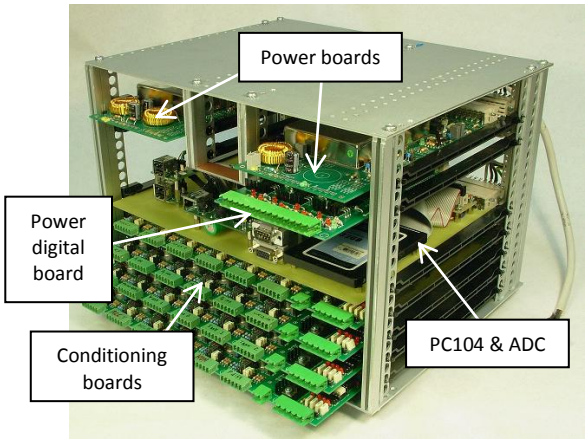

Figure 10. Electronics rack

3.5 Software Design

MISSUS on board software has been designed to record data sampled from the ADC continuously during flight, save data and transmit a subset of the sampled data through the ethernet interface. Software is real time (every function has to be run within a fixed amount of time) and has been designed to run on a Unix-like operating system (Linux), in order to increase both reliability and performance. It is subdivided in 2 different layers: operating system layer (Linux layer) and MISSUS layer (data logging, telemetry management, monitoring, power management); all software has been written in C++.

The onboard software is able to send data to the Ground Support Equipment (GSE) using UDP through BEXUS E-link system to the GSE. Every data packet contains start and end codes (0x0010, 0x9000). The start code is followed by a sequence number, a timestamp and all the sampled data. In case of packet loss from gondola to ground, the packet is not retransmitted.

The Ground Support Equipment is a GUI client program that allows to: (1) log data received from the MISSUS board, (2) display sensors data during flight, (3) display house-keeping data (temperature of the batteries and electronics, batteries voltage and current), (4) switch on and off the sensors, (5) send telecommands onboard (e.g. to activate heaters). The client has been written in C++, using Qt4.8 and KDE marble library, and runs on Linux.

Experiment status has been monitored by the GSE thanks to dedicated control packets; in addition onboard software was able to accept commands packets from the GSE using UDP and consequently to send an acknowledgment packet as reply to every command.

4. CALIBRATION

Both innovative temperature sensor and Pitot tube have been calibrated at University of Padova premises.

4.1 Temperature Sensor Calibration

Using an Ethanol thermal bath (Ultra Low Temperature Bath 7380, Hart Scientific) at controlled temperature, the output of the secondary sensor (to be calibrated), in other words the resistance of Platinum wire, has been compared with that of a primary calibrated sensor. Given the resistance of the sensors as a function of the temperature of the bath (that is an input), interpolating curves, which represent resistance as a function of temperature, have been obtained within the calibration range (from -80°C up to +40°C). Interpolation laws are reported in Eq. 2 and Eq. 3.

$$T = AR^3 + BR^2 + CR + D, T < 0 \quad (2)$$

$$T = AR^2 + BR + C, T > 0 \quad (3)$$

Calibration coefficients *A*, *B*, *C*, *D* have been experimentally estimated.

The result of the calibration is reported in Fig.11, which represents the correlation between resistance (x axis) and the temperature (y axis), both for the reference sensor (blue curve) and for the innovative sensor (red curve).

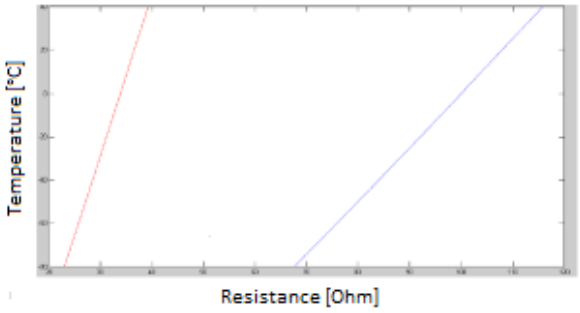

Figure 11. Temperature sensors calibration curves

4.2 Pitot Tube Calibration

The calibration process allowed to estimate *k* coefficient (see Eq. 1). The Pitot tube has been mounted inside a wind gallery (a duct of constant section) by means of a devoted flange (Fig. 12) and has been subjected to a flow of known velocity.

Figure 12. Pitot tube calibration set-up

The flow speed inside the duct has been regulated by means of a fan (UNI 10531) and the stable mass flow (stabilized thanks to a honeycomb structure) has been measured by means of an orifice plate. Then, known the velocity of the flow, the relative pressure has been measured by means of MISSUS relative pressure sensor. Several measurements have been performed, in order to evaluate the dependence of the output as a function of the attack angle: in particular yaw and pitch angles have been varied thanks to the gimbaled support of the Pitot tube flange. Fig. 13 represents the result of the calibration, the flow velocity as a function of relative pressure variation.

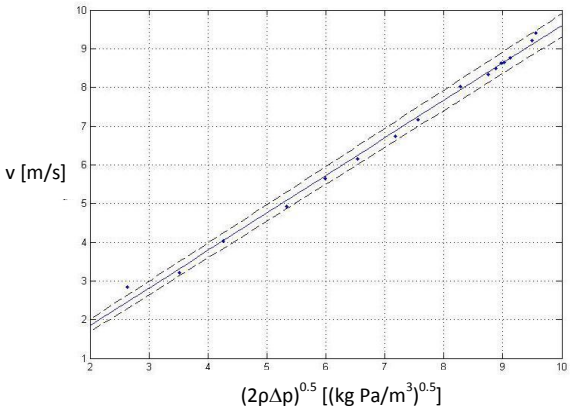

Figure 13. Pitot tube calibration curve

5. VERIFICATION AND TEST

Test campaign involved all the system and different subsystem, during the development of the experiment and at qualification/acceptance level, in order to guarantee the performance of the experiment in space-like environment, assessing readiness for flight.
Development tests involved electronics and software: (1) debug procedures have been implemented on the flight software, step by step at first, verifying different functionalities separately, and then on the whole software; (2) electronics have been extensively tested using oscilloscopes, spectrum analyzers, signal generators (each board has been tested separately, then the whole system has been verified). Qualification tests have been performed on the whole experiment: (1) Thermal vacuum tests have been performed on mechanical and electronics components, in extreme pressure and temperature conditions (from -80°C up to +40°C) for 6 hours continuously (that is the nominal duration of the flight); (2) Vibration tests have been performed on the experiment, subjecting the structure on random vibrations; (3) Some mechanical parts (e.g. sensors for detection of impact with ground) have been subjected to shocks.
At the end, functional tests have been performed to verify the general behavior of the system after all other tests, both in Padova and during launch campaign preparation at Esrange, before final integration on the gondola.
In general all test results have been successful and all experiment requirements have been fulfilled.

6. LAUNCH CAMPAIGN

MISSUS has been launched onboard BEXUS15 on 25th September 2012 from Esrange base in Kiruna, after 5 days of preparation activities, such as: check of components integrity and functionality (electronics and sensors check out), mechanical assembly, calibration and synchronization operations (for IMU and magnetometer), software and communication functional tests, radio frequency interference tests.
PC104 seemed to be defective before launch, provided that sometimes the communication between the experiment and the ground station had failed and MISSUS could not be switched on remotely. Problems seemed to be fixed before launch, MISSUS worked properly and, once switched on, the experiment logged data continuously as expected until 4 hours and 6 minutes after launch, when suddenly the ground station lost contact with MISSUS. After the recovery a detailed investigation has been performed in order to asses motivations which caused the lost of connection: the experiment has been carefully isolated from the gondola and each sub-system has been analyzed one by one. A preliminary data-analysis demonstrated no anomalies in the behavior of the components: as an example, voltage, current and temperature levels of

sensitive items (such as batteries or DC/DC) have been considered; all values appeared normal, without peaks or discontinuities. In this phase the experiment has been completely rebuilt, finding out that it was still alive and properly working. During flight not only the connection had been lost but the PC104 did completely stop working, causing the lost of the data on the descending phase: both Pitot tube data and sensors system for impact detection data have not been acquired. However a great amount of data has been collected during the ascent and floating phase; such data have been then analyzed in detail and cross-correlated. In addition the prototype of the MarsTem has been successfully tested; the sensor resulted undamaged after impact with ground and is still available for further investigations.

7. RESULTS

The main objectives of the data analysis are here summarized: (1) BEXUS gondola attitude and trajectory reconstruction; (2) Meteorological data collection; (3) Atmospheric models validation.
First of all, it has been noticed that all analogical signals were affected by a systematic disturbance: peaks of 0.05 V were present in all analog channels signals with a non-constant frequency (from 1 Hz up to 256 Hz). Therefore some preliminary elaborations of the signals resulted necessary: Discrete Wavelet Transforms (DWT) have been applied to sampled signals; the noise has been mitigated, with a negligible phase delay. Fig. 14 shows the noise isolated from the signal, whereas Fig. 15 represents the temperature signal (V) as a function of time, acquired by the innovative thermometer, before (blue curve) and after (red curve) de-noising procedure.

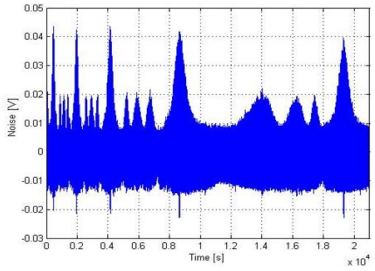

Figure 14. Noise isolated from the signal

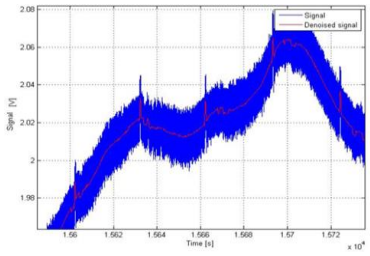

Figure 15. Temperature sensor signal before and after de-noising

After de-noising, analog signals resulted appropriate to be analyzed.
The attitude of the gondola have been reconstructed, basing on the GPS data and on the gravity vector and on the magnetic vector respectively. The following graphs show the resulting Euler angles (yaw, pitch and roll) in the North-East-Down frame.

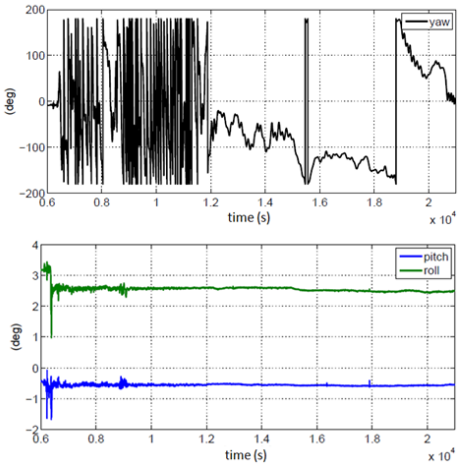

Figure 16. Euler angles as a function of time

Once Euler angles have been obtained, the yaw angle has been cross-correlated with the temperature signal provided by the thermometer, in order to deeply understand the influence of the direct solar radiation on the measurement at high altitudes, when heat exchange by convection is negligible. A thermal model has been developed, and, by the comparison between the yaw angle, the temperature provided by measurements and by the model, it resulted that the platinum wire is highly sensitive to the solar radiation: as the gondola turns and the thermometer is subjected to the direct solar flux, an increase of the measured temperature of about 30°C occurs. The understanding of this effect led to some original improvements and modifications on the design of the Flight Model of the MarsTem, which has been provided with special shields to prevent the direct illumination of the sensitive element.
In addition atmospheric models have been validated. As an example, Fig. 17 shows the temperature sensor signal (black curve), compared with the temperature curves provided by ISA standard atmospheric model from ICAO 1964 [3](red curve) and by NRLMSISE-00 model [4] (green curve). It can be seen that: (1) during the ascending phase the mean trends are compatible; (2) a temperature drop of about 10°C at 10-13 km occurs; (3) in the tropo-pause, over 12 km, an unexpected positive lapse rate takes place; (4) the measurement in the stratosphere layer is compatible with the models. In order to explain these anomalies, the atmosphere stability has been analyzed, taking into account the cloud profiles provided by CALIPSO

satellite, buoyancy and potential temperature, revealing that the unexpected local variations are due to the presence of strong winds or cold layers.

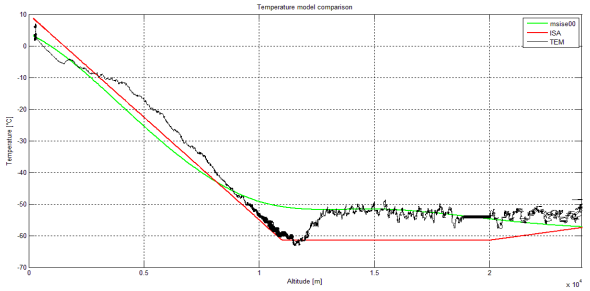

Figure 17. Measured and calculated temperature

8. CONCLUSIONS

Concluding, an integrated sensor suite for meteorological measurements and attitude and trajectory reconstruction has been conceived, designed and realized at University of Padova.
All primary scientific goals have been achieved, thanks to the great amount of data collected, available for the ascending and cruise phase: trajectory and attitude have been reconstructed and atmospheric models have been validated.
The prototype of the MarsTem onboard, the RTD which will fly on the EDM of ESA Exomars 2016 mission, has been developed and successfully tested during the flight; the acquired data allowed CISAS team to improve the design of the Flight Model of the sensor for the future planetary mission.
Since the temperature sensor resulted undamaged and undivided after impact with ground and perfectly operating, further tests will be performed in the near future to compare the thermal behavior of the prototype which flew on MISSUS and the Flight Model of the sensor. In particular thermal vacuum tests with solar simulator will take place at CISAS premises, in order to evaluate the effect of the direct solar illumination in vacuum conditions on the sensitive elements of the different sensors.

9. ACKNOWLEDGEMENTS

The experiment realization was possible thanks to the support by CISAS "G. Colombo", Borgoverde S.r.L., Rotary Club International Valle dell'Agno and Ca' Da Mosto S.p.A, Federmanager Venezia, which provided the team with funds needed to manufacture the experiment. In particular University of Padova provided also the facilities and premises needed for the realization and the verification. Professor Massimo Masi made available his expertise and the wind gallery for the calibration of the Pitot tube, whereas Alessio Aboudan and Michele Cesaro gave their constant and effective contribution in the software conception and development.
Antonio Selmo, electronics engineer and professor, designed, manufactured and tested the electronics board and the rack, making available his workshop and supervisioning the last phases of the experiment realization, also during the launch campaign.
Our gratitude goes to all ESA, SSC, SNSB, DLR staff for the great support during milestones and the launch campaign.

10. ABBREVIATIONS AND ACRONYMS

MISSUS	Meteorological Integrated Sensor SUite for Stratospheric Analysis
CISAS	Centro Interdipartimentale Studi e Attività Spaziali
ESA	European Space Agency
SSC	Swedish Space Corporation
SNSB	Swedish National Space Board
DLR	Deutsches Zentrum fur Luft-und Raumfahrt
DREAMS	Dust characterization, Risk assessment, and Environment Analyser on the Martian Surface
EDM	Entry Descent and Landing Demonstrator Module
PEEK	PolyEther Ether Ketone
RTD	Resistance Temperature Device
IMU	Inertial Measurement Unit
FEM	Finite Element Method
MLI	Multi Layer Insulation
ADC	Analogical Digital Converter
GSE	Ground Support Equipment
GUI	Graphical User Interface
DWT	Discret Wavelet Transform
GPS	Global Positioning System
ISA	International Standard Atmosphere
ICAO	International Civil Aviation Organization
CALIPSO	Cloud-Aerosol Lidar and Infrared Pathfinder Satellite Observations

11. REFERENCES

1. A.Spiga (2011), Elements of comparison between Martian and terrestrial mesoscale meteorological phenomena: Katabatic winds and boundary layer convection, *Planetary and Space Science*, vol.59, pp.915-922.
2. F.Esposito, M.Montmessin, S.Debei and International Team (2011), The DREAMS scientific package for the Exomars Entry Descent and Landing Demonstrator Module, EPSC-DPS Joint Meeting 2011.
3. L. Trainelli (2008), *Lezioni di Meccanica del Volo 2 – Modello dell'atmosfera*.
4. ModelWeb catalogue and Archive, Atmosphere models (2012): http://ccmc.gsfc.nasa.gov/modelweb/atmos/nrlmsise00.html.

Projects & Missions for Rockets

Chairs: A. Verga, A. Blix Dahle, E. Thrane, W. Jung & K. Dannenberg

ARES ROCKETS DEMONSTRATORS OF FRENCH SPACE AGENCY PERSEUS PROJECT

Cédric DUPONT[(1)], Sylvain PERNON[(2)], Jean OSWALD[(3)]

[(1)]BERTIN TECHNOLOGIES, 10 avenue Ampère 78180 MONTIGNY-LE-BRETONNEUX, Email: cedric.dupont@bertin.fr
[(2)]IPSA, 7-9 rue Maurice Grandcoing 94200 IVRY-SUR-SEINE FRANCE, Email: sylvain_pernon@yahoo.fr
[(3)]CNES - Direction des lanceurs, 52 rue Jacques Hillairet, 75612 PARIS CEDEX, Email: jean.oswald@yahoo.fr

ABSTRACT

ARES (Advanced Rockets for Experimental Studies) macro-project is part of the PERSEUS (Projet Etudiant de Recherche Spatiale Européen Universitaire Et Scientifique) initiative set up by the French Space Agency (CNES – Centre National d'Etudes Spatiales).

ARES main objective is to build small modular rocket demonstrators in order to study supersonic flight domain (SERA), two-stage flight configuration, airborne launch from a dedicated unmanned carrier EOLE, and to be used as PERSEUS flying test-bed for rocket engine demonstrator, liquid Oxygen – Ethanol bi-liquid engine for instance. Its final goal is to build a suborbital rocket with a culmination above 100 km.

The project is based on an organization with students associations, school projects and research laboratories, working on the innovating ARES modular architecture.

1. PERSEUS PROJECT

1.1. Presentation

Launched during the 2005 Paris Air Show [3] & [5], PERSEUS (Projet Etudiant de Recherche Spatiale Européen Universitaire Et Scientifique) initiative was set up by the French Space Agency (CNES). As part of the forward-planning efforts of its Launch Vehicles Directorate, this project is looking to spur innovative technical solutions in all areas related to launchers, aimed chiefly at students in higher education level.

To achieve this objective, PERSEUS is pursuing an original approach in which postgraduate students, university space club members and lecturers/researchers are coordinating their efforts to build technology demonstrators. The long-term goal is a detailed preliminary project of a small launch vehicle able to put 10-kilogram nanosatellites in low-Earth orbit [4]. A step-by-step approach is the best way to succeed, with managements and procedures derived from the aerospace industry where it is widely used. PERSEUS is a project which is able to delete barriers between education, training and research.

Work is coordinated together with different partners (Bertin Technologies, GAREF Aérospatial, MI-GSO, ONERA (the French Aerospace Lab – Office National d'Etudes et de Recherches Aérospatiales), Planète Sciences, Roxel France and the University of Evry-Val d'Essonne). In the last five years, the PERSEUS university network has attracted regularly about 250 students per year, spread on 80 projects, and some studies extend now beyond France, reaching students, researchers and space industries from different places in Europe.

1.2. Management

Project management is a major task for projects in cooperation. It also corresponds to the "launchers" culture and to the foundation of every big aerospace project. Finally, it presents an educational interest for the young people attracted by space technologies.

PERSEUS' management specifications have been adapted from the CNES' simplified normative guide and the practical experience in management of some of our student projects.

The principles of PERSEUS rules are:

- Management by phases with associated reviews, taking into account the different aspects of human, financial and calendar resources. The management of documentation, the traceability of the projects is included in this project management.
- The application of PERSEUS management specifications is adapted to each project: realizations, duration, investment costs, relation with other projects,…
- At least 5 milestones spread out all along the activity of each project: annual objective review, preliminary design review, critical design review, ground or flight tests, exploitation review.

The first use of these management specifications was applied on macro-projects: organization notes, functional specifications, road map,… Two documents describe the specifications which have been defined, and a documentary basis is proposed to the projects. The

Proc. '21st ESA Symposium European Rocket & Balloon Programmes and Related Research', 9–13 June 2013, Thun, Switzerland (ESA SP-721, October 2013)

requirement documentation is more rigorous for demonstrator projects.

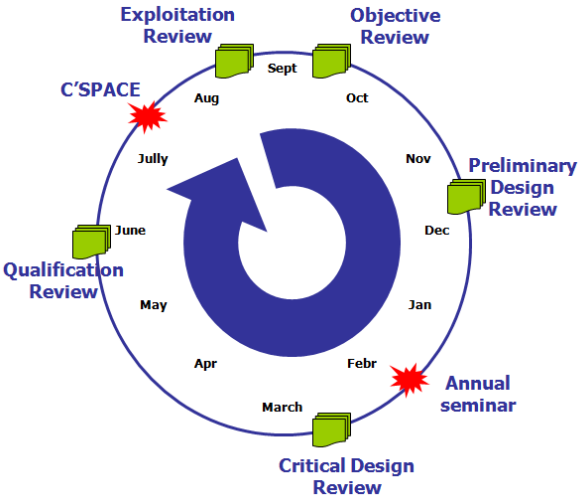

Figure 1. Typical year organization

1.3. Flight Demonstrators

Flight demonstrators are important stakes in PERSEUS. Two categories of flight demonstrators are studied:

- Ground launch demonstrators
- Airborne launch demonstrators

Ground launch demonstrators are rockets launched from different places depending on the performance of the rocket [**Erreur ! Source du renvoi introuvable.**]. Main objectives are to prepare more powerful rockets and test technologies suitable for very small launch vehicle. This paper deals particularly with these demonstrators.

Airborne launch demonstrators are rockets launch under an automatic and reusable carrier developed inside PERSEUS project. The carrier, EOLE [2], drops the rocket at about 4 000 m. The objectives of these demonstrators are to evaluate different drop out sequences.

Figure 2. PERSEUS flight demonstrators program

2. ARES ROCKET

2.1. ARES Objectives

ARES objective is to study and build small modular rocket demonstrators in order to:

- be used as flying test-bed for technologies developed in other PERSEUS macro-projects, for instance Hybrid rocket engine.
- qualify PERSEUS procedure for atmospheric dimensioning test cases of a future launcher : transonic flight and maximum of dynamic pressure
- finalize a two-stage flight configuration
- study airborne launch

It focuses on innovation and modularity. A particular study concerns mass optimization of structures and electrical systems.

All ARES rockets are defined around a common basis:

- Ø 160mm body Outside Diameter
- Recovery system by axial separation
- External support structure made of composite tubes
- Easy assembly/removable light fins
- Use of PERSEUS launcher (for launches operated from ground)

Some combinations can be performed.
In short terms, one of the performance objectives, is to reach max speeds around Mach 1.5 with culmination altitude close to 12km in a two-stage configuration.

2.2. Organization

As all PERSEUS Macro Project, ARES is coordinated by a project manager. In this case, a specific link is guaranteed between the Mechatronics Laboratory of IPSA (Institut Polytechnique des Sciences Avancées) and the PERSEUS project team.Project manager assumes coordination between different participants and manages the macro-project organization.

The macro-project is principally based on student teams which work as part of their school year projects, on specific ARES developments and studies, or on student associations' team members who work on rocket conception.

School research laboratories also take part in technology developments of the macro-project and in students project supervision.

2.3. Developed technologies

There are many technological developments for ARES demonstrators. The small size of the rockets doesn't often allow the use of existent technologies or systems at affordable price or sufficient light weight.

ARES modular architecture is divided into several parts. Each of these parts is the subject of specific studies (support structure, fins, nosecone, recovery system, motor section, electronic bay, roll control system, etc…).
Next subsections present three main studies of ARES macro-project.

2.3.1. Innovating composites structures

The Mechatronics Research Laboratory of IPSA works on an innovative manufacturing process of ARES composite structure. The main goal is to improve structural factor.

Because of the "small size" of ARES demonstrators, we can reduce mass by reducing the carbon layer thickness of the support structure. There is, however, an impact on tubes rigidity and technological limits.

The solution is the use of sandwich technology. This technology allows to increase rigidity while reducing the final mass. But it is not so easy to produce according to a constant quality without industrial capacities. One of our main objectives is to be innovative. To this end, we developed a cheap and "easy" full "cold process" used to manufacture our sandwich carbon composites with core made "in-situ".

Heaviest parts of a sandwich composite are carbon layers. We decided to reduce as possible the carbon thickness and worked on a complex optimized core which presents many functions (reinforcement, vibrations absorption, etc...).

The laboratory is developing, with IPSA students, a dedicated 4 axis mill machine that allows to manufacture 3 continuous meters of ARES composite tubes (Ø160mm) and presents a capacity to produce 3m tubes for the future ARCADIA (Ø250mm) and even bigger (max Ø500mm). This machine is modular: it gives the possibility to increase the tube length capacity, depending on the internal mandrels rigidity.

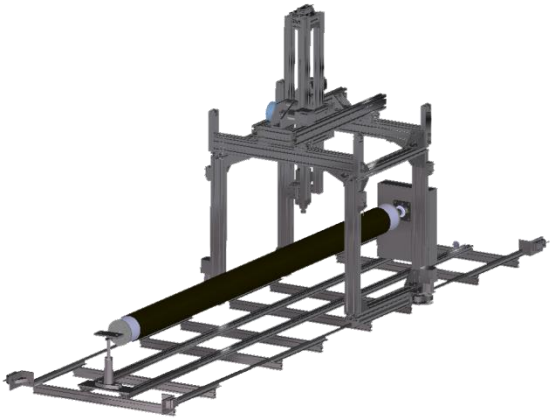

Figure 3. IPSA 4 axis dedicated mill machine

On each tube we can choose the number of layers, the fibres orientation, and the core thickness and complexity. The process per rocket goes relatively quickly (between 1 and 1.5 weeks) and we can ensure an excellent final external aspect and geometric fidelity.

2.3.2. Supersonic composite fins

ISAE students are working, during their school projects, on supersonic capability composites fins.

Since 2010 student teams of ISAE (Institut Supérieur de l'Aéronautique et de l'Espace) has made a first differential approach between two different stability systems, fins and a "rear skirt" during transonic and supersonic flight. A more complete study has been realized on fins solution and students have worked on a process derived from SICOMIN technologies (French composite formulator) which are applied to boats.

This technology of manufacturing has been first tested in flight in 2010 on the Ares-α prototype in subsonic speed and since confirmed on all Ares rockets. It led to a reduction of 50% of the mass of fins, compared with aluminum fins traditionally used on small experimental rockets. It has especially demonstrated very good mechanical characteristics and robustness in regard to its light weight.

These students determined, in two optimization loops, an adapted geometry to ensure stability of the future ARES supersonic rocket, and then, made a first estimation of material thickness, number of carbon layers, reinforcement zones and mounting system.

The two loops designs have been tested for different speeds, flight incidence and structural configuration in loads simulations and structural static and dynamic analysis.

Testing on samples and fin prototypes has been conducted in order to verify the potential differences with simulation models.

Figure 4. Composite sample testing

A first operational test in flight will occur in 2014 on Ares11S-SERA1 rocket.

2.3.3. Electrical integrated systems

This thematic is studied in coordination with the AETNA macro-project, macro-project dedicated to electrical system studies. Its main goal is to define modular electrical architecture and electronic systems adapted to every ARES demonstrators needs. It also has to anticipate next size demonstrators' needs.

There is two ways of specification for ARES electrical systems. The first concerns hardware specifications like:
- using validated boxes
- connector types
- components package

All those characteristics are defined around common ambient values measured on previous PERSEUS launch and in literature.

The other specification is about a common electrical architecture of each demonstrator. One of the objectives is to reduce as maximum cables weight by using communication buses derived from industry or automobile domains.

Ground connectivity takes also part of this specification with a common mechanical interface, a ground station, energy and batteries management, etc...

GAREF Aerospatial, is developing a S-Band telemetry system with 1Mbits of data transfer capacity. It uses a commercial 2200MHz 1W emitter and is studying a patch antenna that could be mounted around the rocket.

This telemetry allows us to use conventional telemetry receiving system of many international launch sites for future ARES demonstrators.

Students of ESIEE (Ecole Supérieure d'Ingénieurs en Electronique et Electrotechnique) are working on a IMU. This module is based on Mems technology (Micro Electro-Mechnical System). It includes: accelerometers, gyroscopes, 3 axis-magetometers, and temperature sensor. Integrated to IMUs are different sensors: absolute analogical pressure, numerical pressure, differential analogical pressure (to measure dynamic pressure from Pitot tube), and GPS (Global Positionning System).

First objective is to restore precisely by means of hybridizing methods, the rocket trajectory in three dimensions and the rocket attitudes and flight environment. A second objective is to anticipate future trajectory control system for future advanced ARES rockets.

In order to compare the measurements, an IMU made by SYSNAV Corporation, a French start-up issued from l'Ecole des Mines de Paris, is embedded on each flight demonstrator as a black box.

After data restore, comparison is done between the two IMU systems and as possible with launch site external measurement systems. It gives very interesting results: we obtain correct attitude, velocity and height estimations, which are coherent to visual observations and data obtained from other sensors.

It is a good way to guarantee the integrity of attitude and velocity parameters, necessary for safety during separation and ignition of a second stage. Nevertheless, inertial navigation is deviating by nature. For longer flight, it will be necessary to use sensors of better quality or to use readjustments by hybridization.

Vibration tests will be systematically realized on all developed modules in order to qualify the hardware. Tests are made with domain's experts to be sure of the results availability.

2.4. Launches

At this day, twenty PERSEUS rocket demonstrators have been successfully launched during the annual French National Campaigns since 2007.

Ten ARES rockets have been developped and sucesfully launched. Three are in preparation the first PERSEUS supersonic demonstrator SERA1 and two rockets that will be launched this summer during the French National Campaign at DGA-EM in Biscarrosse, Ares12-MasterLeia and Ares13-EVE5.

Ares12-MasterLeia will conduct tests on an active roll control system. ISAE-Supaero students are developing this demonstrator in the continuity of two previous ARES rockets launched in 2010 and 2011 with an embedded passive roll control system.

Ares13-EVE5 developed by Evry University students will be an opportunity to flight test some technology modules destined to future ARES supersonic demonstrators. Two major sub-systems will be tested, a dual-parachute recovery system and a special nose cap made by laser fusion that integrates pressure measurement for speed and incidence restitution.

The airborne launched rocket, Ares10Eole, is in preparation and will hopefully fly in 2014. It will be embedded under Eole carrier and will be dropped at 4000m of altitude on a 45° ramp. A ingnition sequence will be tested on a small Pro54-5G solid motor and culmination point should be 8000m.

Figure 5. Ares rocket under Eole Carrier

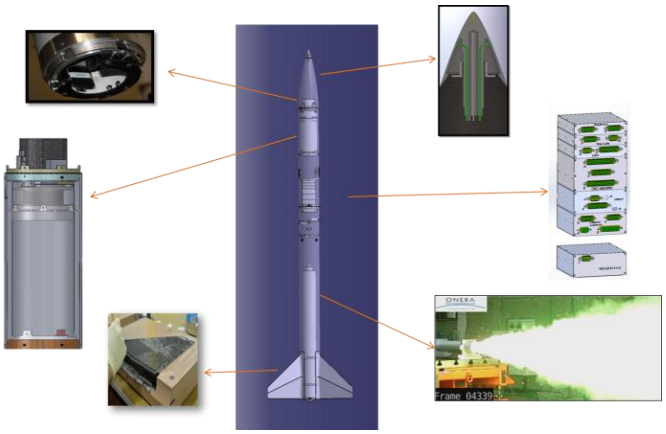

Figure 6. Ares technological decomposition

3. SERA1 Rocket

3.1. Overview

In order to achieve the 100km suborbital flight goal, a new series of rockets are currently under development. These rockets, called SERA (Supersonic Experimental Rocket ARES) are supersonic rocket developed inside ARES macro-project that can't be launched from metropolitan France due to the higher altitude expected. The main objective is to validate technologies that allow flights at supersonic speed and altitudes greater than 5 km.

SERA1 is part of the EASP initiative (Esrange Andoya Special Project) and will be launch in May 2014 from Esrange (Kiruna, Sweden).

SERA1 will be the first French supersonic rocket developed by students since 1998 and the 20th rocket developed inside PERSEUS.

The particularity and the interest of this project is the strong implication of students in the design, development, realization and operations associated with a multidisciplinary PERSEUS project team to ensure the good realization of the project.
Two students' teams are primary involved in SERA1 and are in charge of the conception, the development and a part of the operations of the rocket:

- S3, non-profit students association inside the "Institut supérieur de l'aéronautique et de l'espace" (ISAE)
- OCTAVE, non-profit students association inside University of Evry Val d'Essonne

In addition, several projects are made in different university to help the definition of the rocket.

3.2. Technical characteristics

SERA1 is characterized by:

- Off-the-shell engine : CESARONI PRO98 6G Green 3
- Lightweight rocket (full composites materials)
- Complete restitution of the trajectory
- Use of past experience and elements developed in previous ARES Rockets

Figure 7. SERA1 external layout

PRELIMINARY MASS BUDGET	
Fairing	0,6 kg
Carbon fiber tubes	2,2 kg
Fins	1,8 kg
Electrical systems	2,9 kg
Recovery system	1,7 kg
Separation system	0.8 kg
Propulsion system	13,5 kg
Payload (experience)	0,5 kg
Margin	1 kg
Lift-off Mass	**25 kg**

3.3. Measurements plan

In order to ensure the validation of technologies, SERA1 will be fully instrumented:

- two different inertial unit measurements,
- one vibration sensor in the fairing,
- 5 pressure sensors: 3 in the fairing, one on the side of the rocket and one at the aft end.
- two video cameras, one that films the top and the other the bottom.

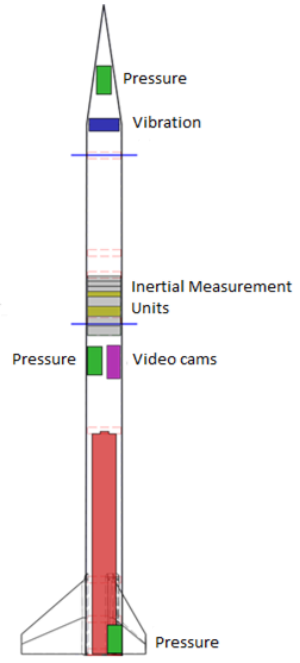

Figure 8. SERA1 measurement plan

3.4. Expected performance

Performance and design of the rocket have been made using PERSEUS home-made tools, to simulate rocket trajectory.

Main results are shown below.

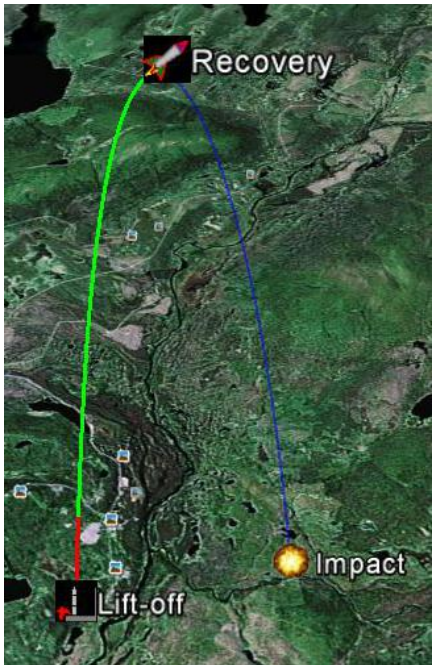

Figure 9. SERA1 GoogleEarth™ Trajectory

Mach Max	1.26	
Culmination	5 280	m
Max longitudinal acceleration	10.4	g
Max Dynamic Pressure	88.80	kPa
Max thermal flux Flux	37.26	MW/m²
Time to culmination	31.2	s
Exit launcher velocity	32.6	m/s

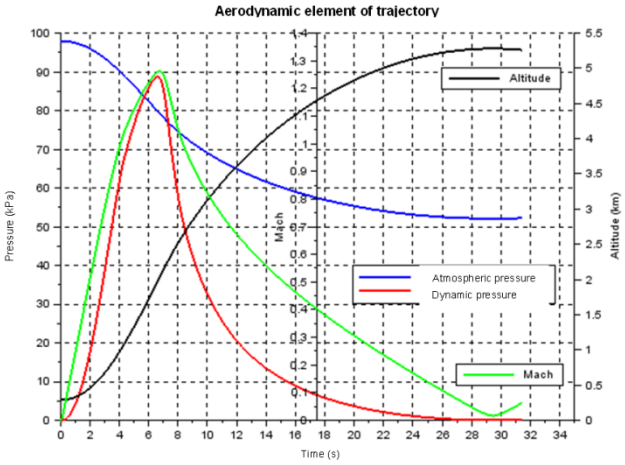

Figure 10. SERA1 expected performance graph

3.5. Status of the project

The Critical design review has been made in June 2013. First elements are under fabrication. Critical elements will be tested during the French launch campaign in August 2013 and a test campaign will occur at the end of the year.

3.6. Next Steps

The Next step is the development of a supersonic two-stage rocket for 2015. In parallel, a development of a liquid rocket engine is under progress. The objective is to integrate this engine in a SERA rocket in order to reach higher altitude and speed.

4. CONCLUSION

A significant step has been taken with the development of SERA1 rocket enabling to reach transonic and supersonic flow regime and the use of a professional launch site, Esrange.
This tremendous progression is mainly due to the maturity level both in structures and electrical architecture demonstrate by ARES demonstrators. In the same time, SERA gives the opportunity of new scientific studies for students and laboratories.

Finally, with the development of SERA1 rocket, PERSEUS proposes a unique initiative to work on an supersonic rocket,

PERSEUS is always looking for motivated students' team conduct by scholar supervisor to work on these projects.

Contact: perseus@cnes.fr

5. REFERENCES

1. S. Pernon, J. Oswald, R. Bec, H. Hingre, *ARES Rocket Demonstrators of French Space Agency Project PERSEUS*, 20th ESA Symposium on European Rocket and Balloon Programmes and Related Research, Hyère, France, 22-26 May 2011.

2. J. Ledogar, J. Hermetz, H. Sohier, J. Oswald, E. Rantet, *EOLE, an innovative flying test scale demonstrator for air-launch-to-orbit autonomous systems*, 28th ICAS International Congress of the Aeronautical Sciences, Brisbane, Australia, 23-28 September 2012

3. J.M. Astorg, R. Bec, C. Bernard-Lepine, K. de Groote, F. Amouroux, PERSEUS - *A Nanosatellite Launch System Project Focusing on Innovation and Education*, 58th International Astronautic Congress, Hyderabad, India September 2007.

4. J. Kohlenberg, C. Dupont, Prospectives studies on Nano Satellites in Telecommunications Economics and Marketing domains in the context of PERSEUS project, 1st International Conference on Small Satellites Systems (CSSS2011), Paris, France.

5. L. de Botton, R. Bec, C. Bernard-Lepine, K. de Groote, *CNES EXPRESSO and PERSEUS: Student-led Innovation in Space Systems' projects*, 59th International Astronautic Congress, Glasgow, Scotland 2008.

TECHNICAL ASPECTS OF THE BRAZILIAN SOUNDING ROCKETS

Flávio de Azevedo Corrêa Junior[(1)], Alberto Walter da Silva Mello Junior[(2)]

[(1)] Instituto de Aeronáutica e Espaço - Pça. Eduardo Gomes,50- S. José dos Campos - SP- Brazil - ZIP Code:12228-904, Space Project Coordination Group, flaviofacj@iae.cta.br
[(2)] Instituto de Aeronáutica e Espaço - Pça. Eduardo Gomes,50- S. José dos Campos - SP- Brazil - ZIP Code:12228-904, Space Project Coordination Group, albertoawsmj@iae.cta.br

ABSTRACT

This paper presents a piece of information about the Brazilian sounding rockets manufactured and operated by the *Instituto de Aeronáutica e Espaço* (DCTA/IAE), a governmental institution established for developing scientific and technological solutions to strengthen the Brazilian aerospace knowledge, through the research, development, innovation, launch operations and technology services in aeronautical and space systems.

In the past, Brazilian sounding rockets were traditionally applied in local researches of high atmosphere layers and ionosphere. The continuous development of knowledge demanded new mission scopes promoting an institutional interest of DCTA/IAE to fulfill these new lines of application.

Resulting from this scenario, the sounding rockets VS-30, VSB-30 and VS-40 started to be successful used for Brazilian and foreign institutions performing a wide range of important technological and scientific aerospace missions.

1. INTRODUCTION

Traditionally Brazilian sounding rockets have been used for decades to carry out local studies, such as researches on high atmosphere layers and ionosphere. The continuous development of knowledge demanded new mission scopes promoting an institutional interest of DCTA/IAE to fulfill these new lines of application So that, new sounding rockets were developed to better fit and fulfill those missions, bringing as a result an expansion of DCTA/IAE´s opportunities.

Nowadays, overcoming frontiers, our sounding rockets are being used by international partners and friendly countries in a wide range of peaceful technological and scientific missions.

At this point we would like to remark our long term cooperation with *Deutsches Zentrum für Luft- und Raumfahrt e. V.* (DLR/MORABA), a team whose expertise and confidence were responsible for the development of new technological concepts such as the SHEFEX project, a remarkable event of success and a true demonstration of excellence.

Regarding our operational sounding rockets, DCTA/IAE has actually three main operational vehicles: the VS-30, the VSB-30 and the VS-40. As a matter of fact, inside our cooperation with DLR/MORABA, we developed a hybrid vehicle named VS-30/ ORION, whose second stage motor ORION is provided by DLR/MORABA and the first stage S30 is provided by DCTA/IAE. As this vehicle that is not entirely Brazilian - regarding the foreigner motor dependency - this vehicle is not considered in the DCTA/IAE´s folders, however some of its characteristics will be also shown in this paper.

2. SONDA III AND RELATED ROCKETS

In 1969, DCTA/IAE developed the two-stage sounding rocket SONDA III (Fig. 1). The SONDA III was a sounding rocket capable of transporting in a ballistic trajectory a scientific or technological payload of 60 kg to 600 km or 140 kg to 200 km. The rocket had a S30 solid motor for the first stage and a S20 solid motor for the second one. Later, a version defined as SONDA III M1 was developed. This version was designed to transport prolonged payloads adopting a shorter solid motor (S23) in the second stage in order to keep the original vehicle's length.

The rocket payload had a complete onboard instrumentation for onboard data acquisition with telemetry and tele-destruction. The stage separation and the ignition system of the second stage were both autonomous systems. The first prototype flew on 26th of February 1976.

Some of the SONDA III general technical characteristics were:

- Overall length: 6.717 m
- Maximum diameter: 0.557 m
- Number of stages: 2
- Total weight: 1,615 kg
- Max. payload mass: 140 kg
- Apogee: 700 km

Proc. '21st ESA Symposium European Rocket & Balloon Programmes and Related Research', 9–13 June 2013, Thun, Switzerland (ESA SP-721, October 2013)

Figure 1. Sounding rocket SONDA III.

After 31 fruitful flights, the sounding rocket had its manufactured officially discontinued in 2005.

The sounding rockets VS-30, VS-30/ ORION and the VSB-30 are important spinoffs of the SONDA III technology.

2.1. Sounding rockets VS-30, VS-30 ORION and VSB-30

The sounding rockets VS-30, VS-30 ORION and VSB-30 (Fig. 2) use the solid motor S30 from the first stage of SONDA III rocket.

Figure 2. VS-30, VS-30 ORION and VSB-30 vehicles.

In 1996, the *Deutsches Zentrum für Luft- und Raumfahrt* (DLR/MORABA) proposed to the *Departamento de Ciência e Tecnologia Aeroespacial* (DCTA) to launch a MINI-TEXUS payload with a S30 solid motor, this new vehicle was known as VS-30.

The VS-30 (Fig. 3) is a single stage, unguided and fin stabilized vehicle capable of transporting payloads with mass up to 230 kg during, at least, 220 seconds of ballistic flight above 110 km. Its length is 3,303 m from the S31 nozzle to the S30 motor / cone adapter's mechanical interface. This length does not take into account the payload's length. Also, in this particular vehicle, the cone adaptor and the payload are considered a customer's responsibility and their jointed mass should be computed as the payload mass.

Figure 3. VS-30 vehicle.

Tab. 1 provides a relation of the VS-30 missions with its apogees.

Table 1. VS-30 missions and related apogees.

Flight Designation	Mission Designation	Date	Apogee (km)
VS-30 XV-01	*Santana* (Qualification flight)	28th April 1997	128
VS-30 XV-02	Ronald (Aeronomy mission)	12th October 1997	120
VS-30 XV-03	Ronald 2 (Aeronomy mission)	31st January 1998	120
VS-30 XV-04	*São Marcos* (Microgravity mission)	15th March 1999	128
VS-30 XV-05	*Lençóis Maranhenses* (Microgravity mission)	6th February 2000	148
VS-30 XV-06	*Cumã* (Microgravity mission)	1st December 2002	145
VS-30 V07	*Angicos* (GPS technology mission and test of the Argentinean payload CU-VS30)	16th December 2007	120
VS-30 V08	*Brasil-Alemanha* / (GPS technology mission)	2nd December 2011	139

The success of the VS-30 boosted a new sounding rocket project, the VS-30/ ORION. Initially development for microgravity purposes, the vehicle VS-30/ ORION is also an interesting option for high atmosphere & low ionosphere studies. It is appropriate to mention that the ORION motor considered in this paper refers to its 'IMPROVED' version.

The VS-30/ ORION (Fig. 4) is a two-stage, unguided and fin stabilized vehicle, capable of transporting a payload of 238 kg in a ballistic flight to an apogee of 295 km. Its length is 6,357 m, considered from the nozzle to the ORION / payload's mechanical interface. This length does not take in account the payload's length.

Tab. 2 provides a relation of the VS-30/ ORION missions and its related apogees.

Table 2. VS-30/ ORION missions and apogees.

Flight Designation	Mission Designation	Date	Apogee (km)
VS-30/ ORION V01	*Baronesa* (Microgravity mission)	21st August 2000	315
VS-30/ ORION V02	*Pirapema* (Ionosphere mission)	23rd November 2002	434
VS-30/ ORION V03	SHEFEX Re-entry vehicle test	27th October 2005	211
VS-30/ ORION V04	ARR HotPay-2	31st January 2008	381
VS-30/ ORION V05	ARR ICI-2	5th December 2008	330
VS-30/ ORION V06	HIFIRE 3	13th September 2012	345
VS-30/ ORION V07	HIFIRE 5	25th April 2012	Orion ignition failure
VS-30/ ORION V08	ARR ICI-3	3rd December 2011	350
VS-30/ ORION V10	*Iguaíba* (GPS technology mission)	8th December 2012	428

A brand-new agreement between DLR and DCTA was established in 2001, when the 'Unified Microgravity Program for Sounding Rockets' proposed the development of a boosted version of the VS-30 to the DCTA. The European main objective was to find a substitute for the Skylark 7 vehicle, used into both TEXUS and MASER programs. The Skylark 7 was a two-stage solid fuel vehicle motor that had its production stopped a few years ago. On 2nd May 2005, the ESA last remaining Skylark 7 vehicle was launched from the Swedish Launch Range Esrange carrying a MASER platform (MASER 10).

Figure 4. VS-30 ORION vehicle.

The VSB-30 (Fig. 5) is a two-stage vehicle unguided and fin stabilized, capable of transporting payloads with mass up to 400 kg during at least 360 seconds in a ballistic flight above 110 km for microgravity missions. The first flight was done in the *ALCANTARA* Launching Center in *Maranhão*, Brazil, on 23th October 2004.

Its length is 7,403 m, considered from the S31 nozzle to the mechanical payload separation interface in the second stage. This length does not take in account the payload's length.

Figure 5. VSB-30 vehicle.

Tab. 3 provides a relation of the VSB-30 missions and its related apogees.

Table 3. VSB-30 missions and apogees.

Flight Designation	Mission Designation	Date	Apogee (km)
VSB-30 XV-01	*Cajuana* (Qualification flight)	23th October 2004	240
VSB-30 V02	TEXUS 42 (EML-1 Microgravity mission)	1st December 2005	263
VSB-30 V03	TEXUS 43 (Microgravity mission)	10th May 2006	237
VSB-30 V04	*Cumã II* (MICROG 1 Microgravity mission)	19th July 2007	242
VSB-30 V05	DLR TEXUS 44 (EML-2)	7th February 2008	264
VSB-30 V06	DLR TEXUS 45	21st February 2008	270
VSB-30 V08	MASER 11	15th May 2008	252
VSB-30 V09	TEXUS 46	22nd November 2009	252
VSB-30 V10	TEXUS 47	29th November 2009	264
VSB-30 V07	*Maracati II* (MICROG 1A Microgravity mission)	12th December 2010	242
VSB-30 V15	TEXUS 49	29th March 2011	268
VSB-30 V14	TEXUS 48	29th March 2011	268
VSB-30 V16	MASER 12	13th February 2012	259
VSB-30 V17	TEXUS 50	12th April 2013	268

Tab. 4 shows some of the motor characteristics of the sounding rockets VS-30, VS-30 ORION and VSB-30.

Table 4. VS-30, VS-30/ ORION and VSB-30 Motor Characteristics

	Rocket Stage Characteristics				
Rocket	VS-30	VSB-30		VS-30/ ORION	
Stage	-	1st	2nd	1st	2nd
Rocket Motor	S30	S31	S30	S30	Orion
Manufacturer	BRA	BRA	BRA	BRA	NA(1)
Provider	BRA	BRA	BRA	BRA	DEU
Length (mm)	4094	3310	4094	3700	2657
External diameter (mm)	557				356
Propellant mass (kg)	875	670	875	875	290
Structural mass (kg)	308	325	361(2)	291	134.5
Propellant type	HTPB/AP/Al				NA
Average thrust (kN)	108.0 ± 5.0 (3)	136.5 ± 5.0 (3)	108.0 ± 5.0 (3)	108.0 ± 5.0 (3)	22.1 (4)
Burning time 20°C (s)	19.0 ± 1.0	12.0 ± 1.0	19.0 ± 1.0	19.0 ± 1.0	22.0
Action time (s)	27.9 ± 1.0	17.8 ± 1.0	27.9 ± 1.0	27.9 ± 1.0	26.0
Specific Impulse in vacuum (N.s/kg)	2,590 ± 50 (3)	2,551 ± 50 (3)	2,590 ± 50 (3)	2,590 ± 50 (3)	2,000 (4)
Total impulse in vacuum (kN.s)	2,280 ± 23 (3)	1,720 ± 33 (3)	2,280 ± 23 (3)	2,280 ± 23 (3)	575.7 (4)

NOTES: (1) Not available
(2) Payload/Motor Adapter mass included
(3) In vacuum
(4) Sea level

3. SOUNDING ROCKET VS-40

In late 80's, the VS-40 sounding rocket (Fig. 6) was idealized in order to gather in-flight propulsive data from the fourth stage motor (S44) of the Brazilian Satellite Launching Vehicle (VLS-1). In addition, the vehicle was intended to test the VLS-1 upper separation systems and the VLS-1 first stage nose cone. It flew on 2nd April 1993 achieving an apogee of 950 km and a ground range of 2,680 km with a payload mass of 197 kg at 81.8 degree launch elevation.

The VS-40 is a two-stage, unguided and fin stabilized vehicle that uses a S40 solid motor in the 1st stage and the S44 solid motor in the 2nd stage. Due to its high performance some variations in its configuration could be done in accordance with the mission, allowing for example the inactivation of the 2nd stage (S44 envelope) for shorter range missions.

Its length is 6, 824 m from the S40 nozzle to the S44/ payload mechanical interface. This length does not take in account the payload's length.

A design modification regarding the mechanical interfaces, the internal thermal protections, the skirt interfaces, the propellant and the implementation of a mechanical safety device was done to update on the 1st stage of the VS-40 vehicle. The final vehicle named VS-40M has not difference in its performance from the former VS-40, in fact, the modifications was done mainly to bring the old S40 motor of the SONDA IV to a VLS-1 configuration.

Figure 6. VS-40 vehicle.

Tab. 5 shows some of the motor characteristics.

Table 5. Motor Characteristics

	Rocket Stage Characteristics	
Rocket	VS-40	
Stage	1st	2nd
Rocket Motor	S40	S44
Manufacturer	BRA	BRA
Provider	BRA	BRA
Length (mm)	5,680	1,710
External diameter (mm)	1,007	1,009
Propellant mass (kg)	4,244	810
Structural mass (kg)	1,194	156
Propellant type	HTPB/AP/Al	
Average thrust in vacuum (kN)	254	35.68
Burning time 20°C (s)	37.0	58.0
Action time (s)	50	62
Specific Impulse in vacuum (N.s/kg)	2,642	2,770
Total impulse in vacuum (kN.s)	11,400	2,250

Tab. 6 names the missions carried out by this vehicle.

Table 6. VS-40 missions and related apogees

Flight Designation	Mission Designation	Date	Apogee (km)
VS-40 PT-01	*Santa Maria* (Qualification flight)	2nd April 1993	950
VS-40 PT-02	*Livramento* (VAP-1 payload - Fokker)	21st March 1998	355(1)
VS-40M	*SHEFEX (Sharp Edge Flight Experiment) II* payload	22nd June 2012	270

OBS.: (1) Nose cone structural failure.

3.1. Vehicle SHEFEX II

The reentry experiment SHEFEX II (Sharp Edge Flight Experiment) was a technological demonstrator built by DLR/MORABA for testing novel aerodynamic concepts and the advanced materials needed to implement them.

Figure 7. SHEFEX II vehicle.

In order to transport the SHEFEX II, a Brazilian VS-40 motor system was used. With focus on the experiment phase for the SHEFEX II experimental vehicle, the conventional parabolic trajectory for unguided sounding rockets was modified with respect to lower apogee but longer re-entry and atmospheric flight sequence, maximizing the vehicle`s Mach regime.

SHEFEX II was launched from *Andøya* Rocket Range in Norway in 22nd June 2012, having an apogee of about 177 km. The vehicle achieved flight velocities up to 2,790 m/s corresponding to Mach numbers up to 9.3.

4. VEHICLES' PERFORMANCE

Figures 8 and 9 show the nominal performance of the operational rockets regarding the apogee (Fig. 8) and the elapsed time above 110 km (Fig. 9), being assumed an 85-degree lift-off elevation for both diagrams.

Observe that the payload mass concerns to the payload and the motor adaptor for the VS-30 vehicle, while it means only payload for the VS-30/ ORION, VSB-30 and VS-40 sounding rockets.

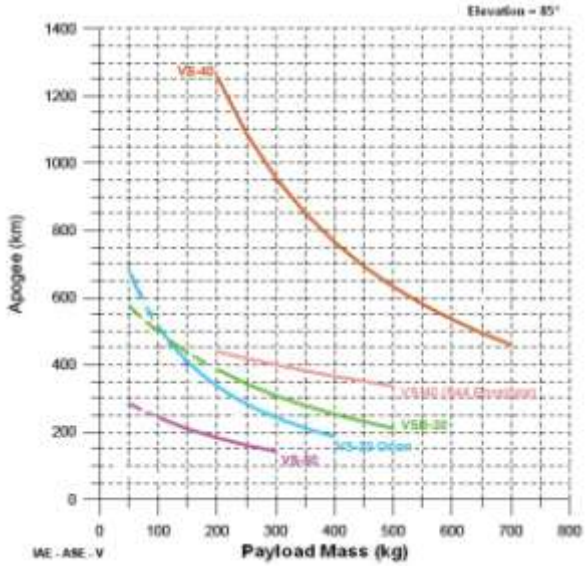

Figure 8. Vehicle performance.

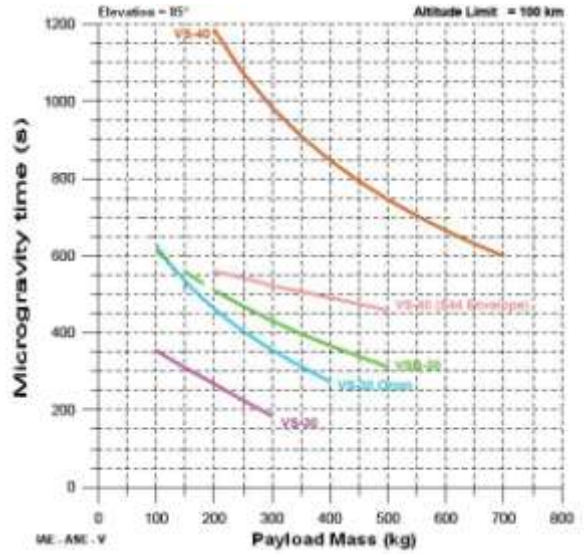

Figure 9. Elapsed time above 110 km.

5. FINAL REMARKS

The present article presented some technical characteristics of the Brazilian sounding rockets showing the vehicles` performance, applications and a bit of their history.

Regarding its institutional mission, DCTA/IAE aims to support the Brazilian scientific community not only performing sounding rockets launches missions but also developing new vehicles to meet new scientific challenges. Nevertheless, DCTA/IAE is always open to receive proposals regarding international scientific cooperation.

6. ACKNOWLEDGEMENTS

The authors would like to express their special gratitude to **FUNCATE** (Space Science, Applications and Technology Foundation, Brazil) for the financial support that enables the participation in the 21st ESA Symposium on European Rocket and Balloon Programmes and Related Research in Thun, Switzerland.

7. REFERENCES

1. Moen, J., Haugen, E., Hansen, G. and Dragϕy, P, *Flight Requirement Plan, ICI-1*, Document number: ARR (03) 5, *Andøya* Rocket Range, SvalRak; Norway, 2003.
2. Palmerio, A. F., Da Silva, J. P. C. P., Turner, P. and Jung W., *The Development of the VSB-30 Sounding Rocket Vehicle*, 16th ESA Symposium on European Rocket and Balloon Programmes and Related Research, ESA SP-530, St. Gallen, Switzerland, 2003.
3. Palmerio, A. F., Roda, E. D., Turner, P. and Jung W., *Results from the first flight of the VSB-30 Sounding Rocket*, 17th ESA Symposium on European Rocket and Balloon Programmes and Related Research, ESA SP-590, pp. 345-349, Sandefjörd, Norway, 2003.
4. Kemi, S.; Norberg; O. et Turner, P.; *Eurolaunch– A Cooperation between DLR, German Aerospace Center and SSC, Swedish Space Corporation in sounding rocket launches*, AIAA: IAC-04-IAF-J.5.05, 55th International Astronautical Congress, Vancouver, Canada, 2004.
5. Corrêa Jr, F. de A., et al., *Brazilian microgravity program: challenges and perspectives*, 17th ESA Symposium on European Rocket and Balloon Programmes and Related Research, ESA SP-590, pp. 509-514, Sandefjörd, Norway, 2005.
6. Gülhan, A., Siebe, F., et al., *Instrumentation of the SHEFEX-II flight experiment and selected flight data*, 18th AIAA / 3 AF International Space Planes and Hypersonic Systems and Technologies Conference, AIAA 2012-5819, Tours, France, 2012.
7. AEB, *Relatório do I workshop brasileiro sobre microgravidade*, pp. 35-45, São José dos Campos, SP, Brazil, 1999.
8. DLR, *40 jahre deutsch-brasilianische Zusammenarbeit in der Luft- und Raumfahrt*, pp. 28-30, DLR, Köln, Germany, 2011.

9. Palmerio, A. F., Del Monaco, L. R., Furlan, B. M. P. and Yoshino, T., *Definição da missão e da configuração do sistema VS-40*, 587-0000/B1002, IAE, São José dos Campos, Brazil, 1989.
10. Yamanaka, S. S. and Moraes Jr, P., *Avaliação da Carteira de Foguetes de Sondagem do IAE*, ASE-RT-009-2005, IAE, São José dos Campos, Brazil, 2005.

THE SYSTEM DESIGN OF THE SOUNDING ROCKET KUNPENG-1 OF THE CHINESE MERIDIAN PROJECT

Jiang Xiujie，Xu An

National Space Science Center, Chinese Academy of Sciences,
No.1 Nanertiao, Zhongguancun, Haidian district, Beijing, 100190, China
Email: jiangxj@nssc.ac.cn; xuan@nssc.ac.cn

ABSTRACT

Meridian Space Weather Monitoring Project (for short, Meridian Project) is a Chinese multi-station chain along 120°E longitude to monitor space environment. The Sounding Rocket Mission KUNPENG-1 given by this paper is an important part of the Meridian Project. On May 7th, 2011, the sounding rocket KUNPENG-1 was successfully launched from the Hainan Sounding Rocket Launch Site, China，which located in low latitude area. The orbit of KUNPENG-1 has an apogee of 196.5km from the earth. KUNPENG-1 carried three scientific payloads, which are Langmiur probe, Electric field detector and Atmospheric micro-constitutes sonde. Many kinds of the in-situ detection parameters were obtained，including electron density, ion density, electric field strength in the ionosphere, and O_3 and NO_2 density in the middle and high layers of the atmosphere. This paper gives the scientific objectives, the system design, the mission profile and the flight results of the sounding rocket KUNPENG-1.

Key words: Sounding Rocket KUNPENG-1; Chinese Meridian Project; in-situ measurement.

1. INTRODUCTION

Sounding rockets provide a cost-effective way of 50km to 1500 km above the near-earth environment. For many years, sounding rockets have played an important role in addressing scientific and technical problems in space-based investigations, including in-situ detection of near space, microgravity scientific experiment and flight-test of new technologies and techniques. Sounding rockets offer a unique approach for in-situ measurements to cover the altitude regime between 50km and 300 km above the Earth surface, which is not accessible by other spacecrafts, such as balloons and satellites [1]. Flight times of the sounding rockets are typically 5 to 20 minutes in duration [2]. In addition, the smaller sounding rockets are suitable tools for the education of students and the training of young scientists and engineers in space projects.

The Meridian Space Weather Monitoring Project (for short, Meridian Project) is a national key scientific and technological program, which established the chains of 15 ground-based observatories located roughly along 120°E longitude and 30°N latitude [3]. It is a large-scale ground monitoring system to continuously monitor the space environment over China, which is the country's first space weather monitoring project, coordinated by the National Space Science Center (NSSC) of Chinese Academy of sciences (CAS), with participation of several other research institutes and universities in China. The Meridian Project started in 2008 and was completed by 2012. The sounding rocket KUNPENG-1 is the important mission in the Meridian Project.

2. SCIENTIFIC OBJECTIVES AND PERFORM -ANCES

Scientific Objectives: The flight experiment of the sounding rocket KUNPENG-1 was designed to provide in-situ measurements for investigating the distributions of the key parameters of geo-space environment in low latitudes and calibration for ground-based remote-sensing observational facility. The key space parameters up to 200km include space electron density, ion density, electric field strength, and the atmospheric micro-constitutes etc.

Performances of the system：

- Apogee: 196.5km
- Detection range: from 30km to 196.5km
- Downlink rate: 2Mbps
- Electric field strength range: 0~±1V/m
- Electron density range: 5×10^2～$5\times10^6 cm^{-3}$
- Ion density range: 5×10^2～$5\times10^6 cm^{-3}$
- Atmospheric element: NO_2, O_3

3. MISSION PROFILE

To achieve the scientific objectives, the mission profile was designed as shown in Tab.1.

Table 1 Key events of the Mission Profile

No.	Time	Height	Key events
1	0s	0m	Rocket launch, devices onboard reset time
2	16.6s	14.4km	Engine off
3	43s	59.6km	Head-body separate and Electric booms expand； start detecting electric field
4	46s	64.4km	Rocket hood outstripped

Proc. '21st ESA Symposium European Rocket & Balloon Programmes and Related Research',
9–13 June 2013, Thun, Switzerland (ESA SP-721, October 2013)

5	47s	66km	Unlock and expand electronic booms, start detecting space electron density and ion density
6	215s	196.5km	Rocket reach the apogee
7	601s	0.8km	Signal miss

4. SYSTEM DESIGN

4.1 System Constitutes

The sounding rocket KUNPENG-1 contains five systems, namely carrier system, payload system, telemetry ground station, data processing system, and launch site system (Fig.1). The onboard data flow diagram of the sounding rocket in Meridian Project is shown in Fig.2.

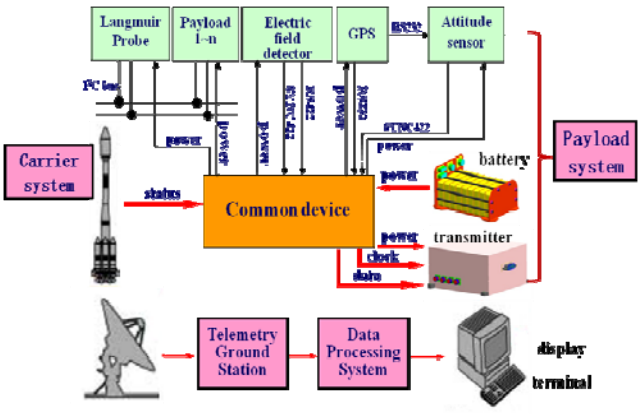

Figure 1 System Constitutes of KUNPENG-1

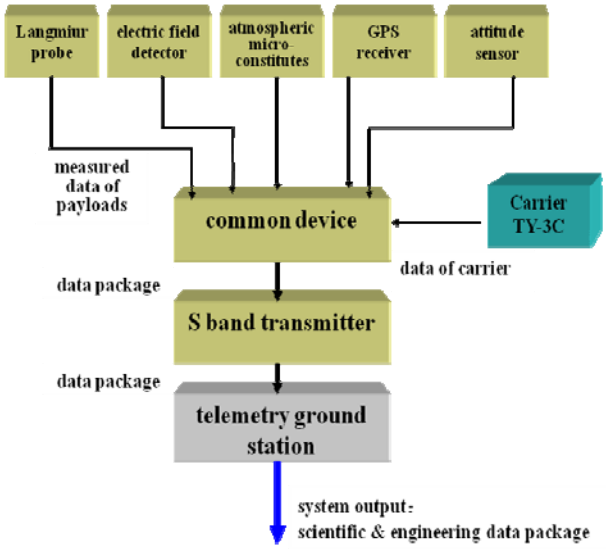

Figure 2 Onboard data flow diagram

Carrier system: The carrier TY-3C is an uncontrolled rocket with 6700mm at height and ϕ400mm in diameter. It carries all the devices onboard in the ten-minute flight.

Payload system: During the flight, the payload system obtained the scientific parameters and engineering data in space and sent the onboard data package to the ground.

Telemetry ground station: The telemetry ground stations received the downlink onboard data and send them by network to the data processing system at the command hall of the launch site.

Data processing system: Data processing system provided data storage, preprocessing, management, and real-time shown on the display screen.

Launch site system: Launch site system provided all the supports on the ground.

4.2 Payload System

The sounding rocket KUNPENG-1 carries eight devices of the payload system, including five common service devices and three scientific payloads (Fig.3). The common devices contain a common device, an S-band transmitter with an antenna, a GPS receiver with an antenna, a battery and an attitude sensor.

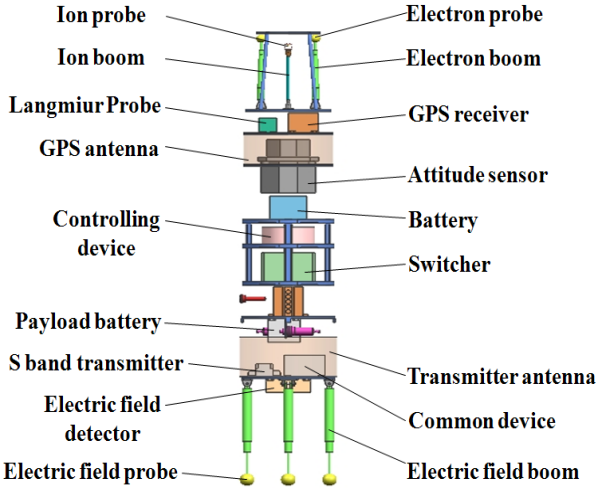

Figure 3 Layout of the payload system

The science payloads (Tab.2) consist of a Langmuir probe (Fig.4) with one ion probe and two electric probes to determine the vertical distribution of the electrons and ions, an electric field detector (Fig.5) with four probes to detect the vertical distribution of the space electric field, and an atmospheric micro-constitutes sonde (Fig.6) to measure O_3 and NO_2 density in the atmosphere. There are 7 booms extended in flight as shown in Fig.7.

Table 2 Three scientific payloads

Payload	Detection Object	Development Department
Langmiur probe	Electron density Ion density	NSSC of China /Austria
Electric field detector	electric field strength	NSSC of China
Atmospheric micro-constitutes sonde	O_3 and NO_2 density in the atmosphere	NSSC of China

During the flight, the scientific payloads made in-situ observations to obtain the scientific parameters in space. At the same time, the common service devices provided many kinds of powers, time tagging, GPS data and attitude information, and sampled all the onboard data including scientific and engineering data, which were transmitted as data package through the S-band transmitter to the ground.

Figure 4 Langmuir probe

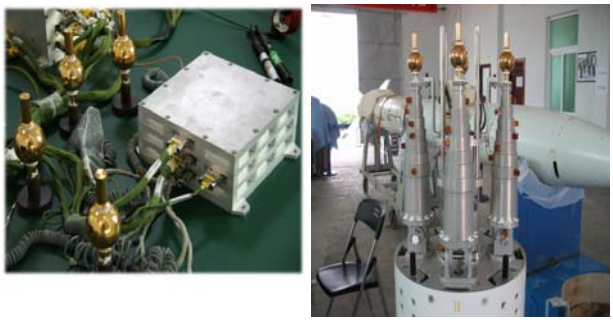

Figure 5 Electric field detector

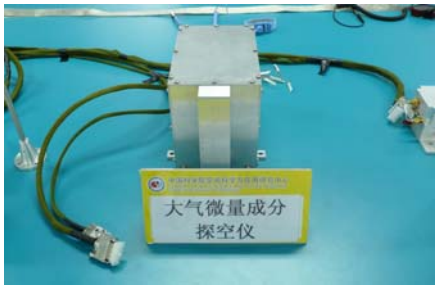

Figure 6 Atmospheric micro-constitutes sonde

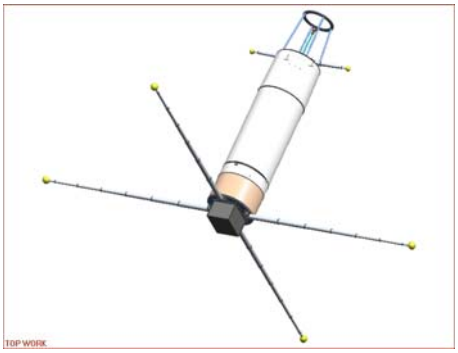

Figure 7 Booms extended in flight

4.3 **Data Processing System**

Data processing system received and verified onboard data package from different telemetry ground stations through the network, provided data storage, preprocessing, management, and real-time shown on the display screen in the command hall of the launch site. All the downlink data were stored in data base for further processing (Fig.8).

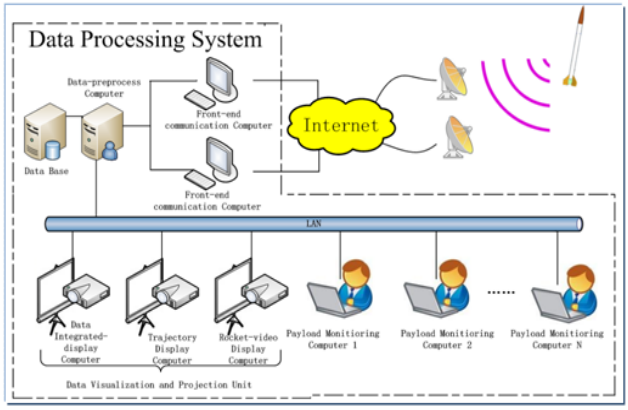

Figure 8 Data processing system

4.4 Launch site in Hainan of China

The Hainan Sounding Rocket Launch Site was set up in 1986 on the outskirts of Danzhou City, Hainan Province of China. It has the capability of launching sounding rockets, and deploys more than ten ground-based space environment observational instruments. Its geographic location near equator makes the space environment observations important in the world (Fig.9).

Figure 9 Launch site and telemetry ground stations

5. THE PRELIMINARY FLIGHT RESULTS

With the successful launch, KUNPENG-1 achieved the scientific objectives and acquired many engineering data during the flight.

Fig.10 shows that the electron density profile and the ion density profile during the ascent stage and descent stage of the rocket are basically identical and the trend is basically consistent with the results of DPS-4 digital

altimeter on ground and International reference ionosphere model IRI-2007.

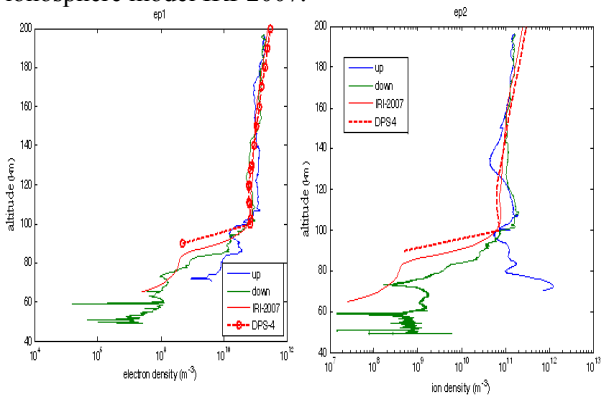

Figure 10 Electron density profile & ion density profile

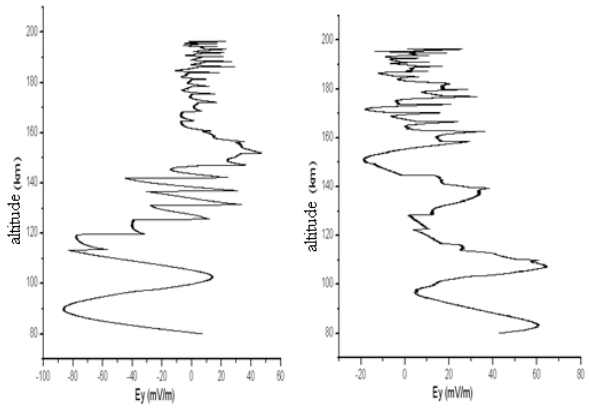

Figure 11 Electric field data of one channel

The spatial electric field data (Fig.11) at the altitude of 60km to 200km in low latitudes of China was obtained for the first time. The theory of detecting spatial electric field by the double-boom electric field instrument was verified.

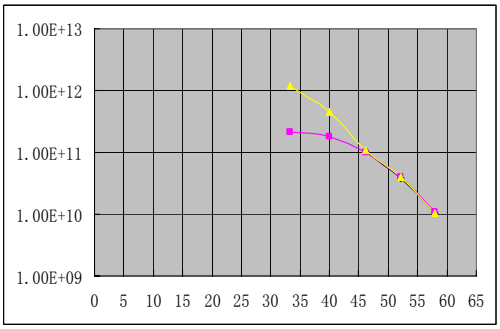

Figure 12 Distribution curve of O_3 concentration

Fig.12 shows the distribution curve of O_3 concentration. The red line is the detection result of this test and the yellow line is the detection result of French Guiana rocket.

6. CONCLUSION

The sounding rocket KUNPENG-1 of the Meridian Project was successfully launched on May 7th, 2011, and made the in-situ measurements of key space parameters up to 200km including space electron density, ion density, electric field, and the atmospheric micro-constitutes etc. In this paper, we show and discuss the system design and the flight results. The success of the sounding rocket in the Meridian Project marks the new beginning for China's sounding rockets career.

Figure 12 Sounding rocket KUNPENG-1 launch

7. ACKNOWLEDGEMENTS

The sounding rocket mission is funded by the Chinese Meridian Project. We acknowledge the use of data from the Chinese Meridian Project. We would like to thank all persons who participated in this mission.

8. REFERENCES

1. Jiang xiujie, Liu Bo, etc. Development Status and Trend of Sounding Rocket, *Science and Technology Review*, Vol.27(23),102-110,2009
2. P.J.Eberspeaker, D.D.Gregory, An Overview of the NASA Sounding Rockers and Balloon Programs, *Proceedings of 19th ESA Symposium on European Rocket and Balloon Programmes and Related Research*, ESA SP-671, Germany, 27-34 June 2009
3. WANG Chi, REN Liwen. Recent Development and Preliminary Results of Chinese Meridian Project [J]. *Chinese Journal of Space Science*, Vol.33(1),1-5,2013
4. Wang C. New Chains of Space Weather Monitoring Stations in China, Space Weather, 2010,8,S08001,doi:10.1029/2010SW000603

SHEFEX II VEHICLE AND SUBSYSTEM DESIGN, FLIGHT PERFORMANCE AND THEIR APPLICATION TO FUTURE HYPERSONIC MISSIONS

John Turner[1], Josef Ettl[2], Marcus Hörschgen-Eggers[2], Peter Turner[2], Wolfgang Jung[2]

1) TwIG, contracted by Deutsches Zentrum für Luft- und Raumfahrt e.V. (DLR), RB-MR D-82234 Oberpfaffenhofen, Germany, Email: john.turner@dlr.de

2) Deutsches Zentrum für Luft- und Raumfahrt (DLR) e.V., RB-MR, D-82234 Oberpfaffenhofen, Germany josef.ettl@dlr.de, marcus.hoerschgen-eggers@dlr.de, peter.turner@dlr.de, wolfgang.jung@dlr.de,

ABSTRACT

The purpose of the Sharp Edge Flight Experiment program (SHEFEX), is to investigate the aerodynamic behavior and thermal problems of unconventional shapes for re-entry vehicles comprising multi-facetted surfaces with sharp edges. The main object of these experiments is the correlation of numerical analysis with real flight data, with respect to the aerodynamic effects and structural concept for the thermal protection system (TPS).

The SHEFEX II vehicle was launched on the 22nd of June 2012 from the Andoya Rocket Range, Norway on a two stage VS40 motor system. It comprised a symmetrical forebody and canards to investigate dynamic control parameters at hypersonic velocities. This vehicle also included repointing of the second stage motor and payload prior to ignition, to provide a flatter re-entry trajectory and reduce dispersion.

The Mobile Rocket Base of the German Aerospace Centre (DLR), was responsible for the development, test and qualification of the payload, service systems and the complete vehicle and their operation during flight. This presentation describes the techniques used for attitude control, the design and performance of the SHEFEX II vehicle and sub-systems and their application to future hypersonic missions.

1. PAYLOAD AND MISSION DESCRIPTION

The SHEFEX experiment program was conceived to investigate the aerodynamic behaviour and thermal protection characteristics of new materials and unconventional shapes for re-entry vehicles comprising multi-facetted surfaces with sharp edges. The main object of these experiments is the correlation of numerical analysis with real flight data in terms of the aerodynamic effects and structural concept of the thermal protection system. SHEFEX I, launched on the 27th October 2005, comprised an asymmetrical forebody and passive reentry at Mach 6-7.

The SHEFEX II experiments comprised a symmetrical forebody, a hybrid navigation system and active canard control during reentry at a velocity in the region of Mach 10. The Mobile Rocket Base MORABA, of the German Aerospace Centre (DLR), was responsible for the development and test flight of SHEFEX II on a two-stage solid propellant sounding rocket. After separation from the first stage motor and prior to ignition, the second stage motor and payload was actively re-pointed while spinning, by a cold gas precession attitude control system, to provide a reduced apogee but greater horizontal velocity and flatter re-entry trajectory. This in turn, lead to a longer experiment period during the atmospheric re-entry between the altitudes of 100 and 20 kilometres, at a velocity in the order of Mach 10.

A digital miniature attitude reference system, (DMARS) inertial platform, which was part of the autonomous service module, measured the attitude, velocity and acceleration, derived the instantaneous position and provided the rate and attitude control signals for the cold gas thrusters. As the experiment performance analysis was dependent on the accuracy of measurement of the angle of attack to the flight vector, GPS data was also used to provide independent accurate real time trajectory data during the experiment phase. In addition, subsequent to the two stage motor burn phase and separation of the payload from the second stage motor, a three axis pointing manoeuvre was performed so that a star camera could obtain an independent measurement of the inertial attitude and determination of any accumulated absolute pointing drift of the control and experiment platforms. The same attitude control system then realigned the payload to the re-entry vector and provided rate control to damp out aerodynamic stabilization oscillation during the re-entry phase.

2. VEHICLE AND SYSTEM DEVELOPMENTS

Although MORABA has been involved in the design, development, construction and launch of sounding

Proc. '21st ESA Symposium European Rocket & Balloon Programmes and Related Research', 9–13 June 2013, Thun, Switzerland (ESA SP-721, October 2013)

rockets to fulfill the particular requirements of space research experiments for aeronomy, magnetospherics, astronomy and microgravity for over 40 years, the unique requirements of SHEFEX II and particularly our increasing involvement with hypersonic reentry and scramjet research experiments, necessitated the development of a variety of new subsystems and operational capabilities. The most significant of these developments which were deter mined by the requirements of the SHEFEX II vehicle and experiment, are described in the following:

3. THE VS40 ROCKET MOTOR SYSTEM

The Brazilian VS40 rocket motor system comprises a steel case S40 first stage and a Kevlar S44 second stage. Because of the requirement for use as a first stage, with an atmospheric burn, the S40 motor was modified to include a new aft closure and nozzle and required a requalification static firing. The existing tailcan, interstage and separation system were used, but the stability requirements of the complete vehicle during the first stage burn, necessitated the design, construction and qualification of the largest fins yet produced by MORABA. A new hydraulic trolley was also procured and adapted for the S40 motor transport to and installation on, the Norwegian launcher.

The Kevlar S44 motor case, was load tested with 40 tons of compression and 5 tons of tension to ensure that the motor and its adapters could withstand the extreme bending loads which could be produced by the long and heavy SHEFEX II payload in the case of high shear winds. As the second stage motor and payload was to include two axis active control for repointing, before ignition and duri ng the burn phase, a flight termination system (FTS) was mandatory. The standard S44 destruct charges were suitable for this purpose.

The motor - payload adapter module was designed and constructed by MORABA for this vehicle. It comprised a one metre diameter section adapting the S44 motor to the 600 mm diameter aft interface of the reentry payload. This module contained the forward vehicle launch lug, the FTS with command receivers and antennas, and pyrotechnic ignition systems for the interstage adapter between both motors, ignition of the S44 motor and payload separation. To prevent aerodynamic destabilization of the complete vehicle by the payload fins, which were forward of the centre of gr avity of the complete vehicle, a composite split fairing was constructed to cover these fins at least during the ascent through the atmosphere. The fairing was held to the motor adapter via a six segment manacle ring at the aft end and to the payload at the forward end with two shells and a four segment manacle ring. The fairing was released after burnout of the second stage motor and YO-YO despin and immediately before payload separation from the burnt out S44 motor.

4. THE PAYLOAD

The main re-entry payload with a masss of 580 kg is shown in Fig. 1 and comprised the SHEFEX forebody with 140 sensors, the canard experiment module, six 500 mm diameter sections containing the precession gas thruster system, a watertight service module, main recovery system, YO-YO despin and payload split system, ignition and forward fairing release system and the aft gas tank supplies for the three axis and spin rate control systems. The aft end of the payload comprised a stabilizing flare module with the three a xis thruster system, roll spin rate solenoid valves and four composite payload fins. All payload modules except the SHEFEX forebody, were coated with zirconium oxide for thermal protection

Because of the considerably larger dimensions and complexity of t he SHEFEX II vehicle and payload, compared with the systems usually constructed and launched by MORABA, all of these components required detailed analysis, design and qualification as well as the c onstruction of new mechanical ground support equipment (MGSE).

5. SERVICE SYSTEMS

The precession gas system, with three 6.9 litre tanks and three radial mounted 100 Newton thrusters, was mounted between the service and the canard modules for maximum moment arm during control of the S44 and payload configuration. This gas system was also used to cool one of the experiment thermal tiles during re-entry. The star camera was also mounted in this module with a

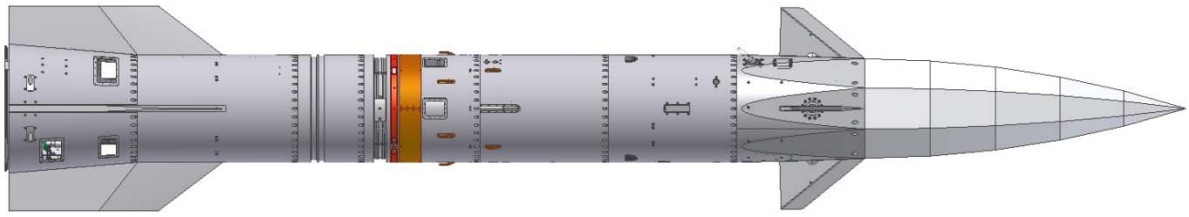

Fig. 1. SHEFEX II Re-entry Payload

complex sunlight baffle and an ejectable door, together with two aft pointing video cameras.

The main service system comprised a watertight module which contained the DMARS inertial platform, the main electronics for payload, rate and attitude control systems, telemetry and telecommand processing and power distribution, as well as telemetry, TV and telecommand transmitters, and receivers, radar transponder, GPS receiver, four video recorders and redundant battery supplies. Also contained in this module were the experimental hybrid navigation system and the canard control computer. In the aft section of this module were the main umbilical and all antennas except the GPS wrap around antenna which was mounted on the main recovery system and the redundant telemetry tran smitter and patch antennas which were mounted in the SHEFEX forebody.

The main recovery system was mounted on the aft end of the service module and contained the forward ignition system, the complete pyrotechnic data acquisition, as well as a TV camera to record parachute deployment. To reduce the payload velocity prior to deployment of the recovery heatshield and parachute, it was planned to split the stable payload into two unstable sections which would then tumble and provide additional aerodynamic braking. Both payload sections were constructed with recovery systems but later, experimental requirements on the location of the centre of gravity, resulted in the removal of the aft parachute system. The combined payload split separation and YO-YO despin section were connected to the main recovery system by a four segment manacle ring.

The forward fairing release module contained the second ignition system for aft recovery and the operation of the forward and aft fairing pyrotechnic release. This was followed by the aft gas module containing four 6.9 litre tanks which provided gas to the three axis and spin rate control system thrusters in the aft flare. The aft flare contained a dual level regulator and eight thrusters for the three axis system as well as a separate regulator and two solenoid valves for the spin rate control. These two valves were mounted on the aft flange and connected by slip release couplings to the motor payload adapter spin rate th ruster blocks on the adapter skin, for maximum moment arm. These thrusters provided a torque of +/-40 Nm about the roll axis. Two forward looking video cameras were also mounted on the flare.

6. VEHICLE - PAYLOAD CONFIGURATIONS

The three main flight system configurations of the SHEFEX II vehicle are shown in Fig. 2. The configuration at lift-off comprised a passively stabilized vehicle with canted fins to provide a nominal spin rate of 1.5 Hz. The fairing at the aft end of the

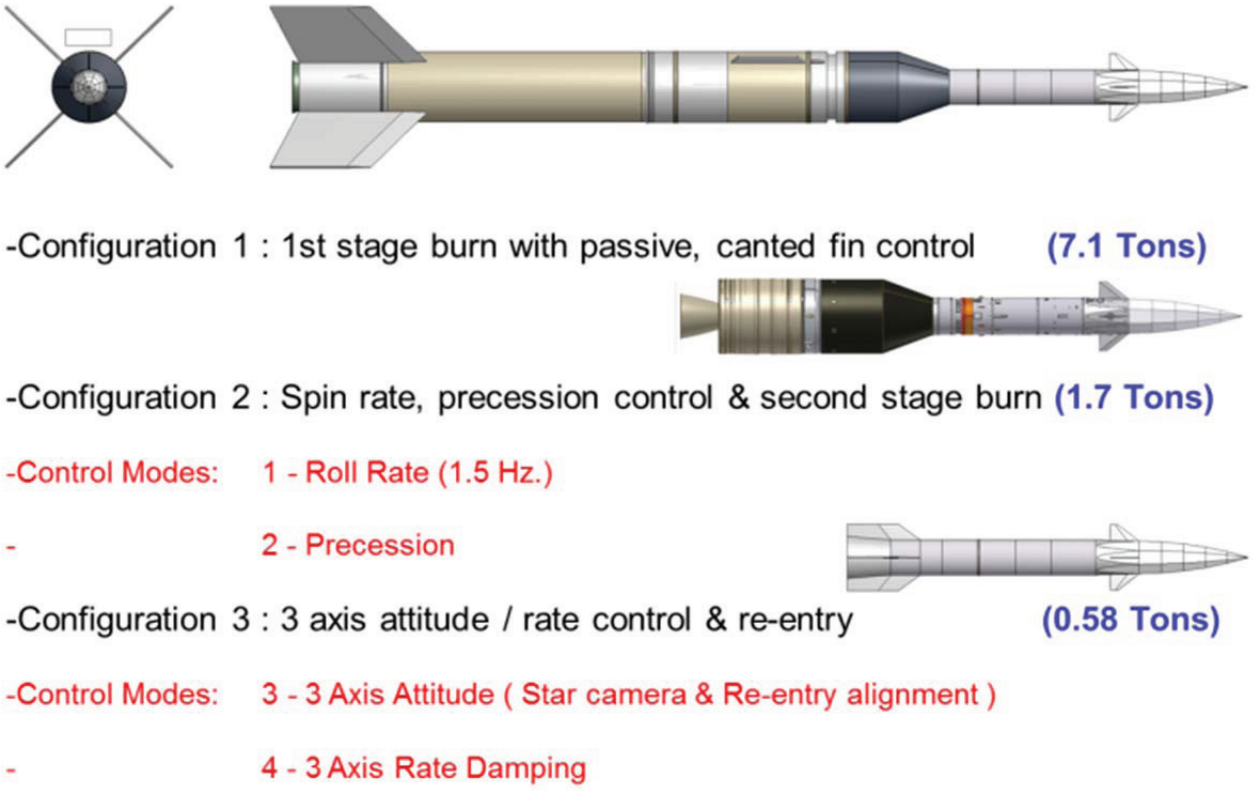

Fig. 2. SHEFEX II flight configurations

payload was to prevent any aerodynamic destabilizing effect of the payload fins on the complete vehicle. Separation of the first and second stage motors was timed for an altitude of 80 Km so that the spinning second stage and payload, shown in configuration 2, would not be subjected to significant aerodynamic disturbing torques. This configuration contained the roll rate control system to correct the first stage canted fin induced spin rate to 1.5 Hz, and a precession control system to repoint the vehicle to the desired attitude for the second stage burn. The nominal flight vector for the second stage motor could be stored in the control system before lift-off and then corrected during flight according to the measured dispersion of the first stage trajectory. After burnout of the S44 motor, the vehicle was despun with the YO-YO system, then the fairings released and the payload as shown in configuration 3, separated from the S44 motor. The payload was then attitude controlled in three axes such that the star camera was pointed upwards and subsequently, the payload was repointed to the re-entry vector. At 100 Km on the descent, the three axis system was switched to rate control mode.

7. TRAJECTORY CONTROL

Provided no obvious catastrophic disturbance occur**ed** during the first stage burn, the vehicle would, prior to second stage ignition, fly on the trajectory generated by the S40 thrust phase. This means that even after the precession manoeuvre and prior to S44 ignition, trajectory data from the radar, GPS and the navigation output of the DMARS would not provide any indication whether or not, the conditions were safe for ignition of the S44. This meant that the attitude data from the DMARS was the only indication whether or not the pointing attitude was within the limits required for safe S44 ignition. For this reason, a signal was provided via the command destruct system to enable ignition of the S44 **only** when the precession manoeuvre was complete and successful. Because of the safety relevance, it was decided to perform this enable function on the ground, where radar, GPS and DMARS data were available, rather than on-board, which would have entailed a considerable effort in test and qualification for an automatic system.

The correct pointing of the second stage and payload vehicle for an impact on the aiming point is also significantly affected by the trajectory parameters generated by the first stage motor, which can de viate from the nominal due to variations in high altitude winds, thrust profile and thrust vector misalignment which can considerably affect the dis persion. As the precession manoeuvre was expected to be com plete by around 150 seconds after lift off, this time was available to analyse th e velocity and position errors to the nominal values generated during the S40 thrust phase, and determine the corrections to the S44 ignition vector, as corrections to the pitch and yaw target attitude could be transmitted during the precession manoeuvre. This operation requires a competent operations team with real time graphical data display of all available trajectory data and any indication of anomalies in the DMARS or control system operation. In case of short duration telemetry reception problems and provided that the radar transponder and tracking are operational, the ignition enable signal could be transmitted at the appropriate time and the flight termination performed in case of an unacceptable deviation of the post S44 ignition trajectory from the safe limits.

Independent of which condition leads to the ignition of the second stage, once the S44 has ignited, radar, GPS and the DMARS navigation will provide realtime information on the new trajectory and permit instantaneous impact prediction. A flight termination system was provided to terminate the thrust of the second stage motor in case of problems resulting in an inacceptable deviation of the flight trajectory.

8. FLIGHT PERFORMANCE

All of the control system functions could be selected by buttons on the main service module EGSE. The rate control system spin rate was programmed to 1.5 Hz. with a hysteresis of 0.1 Hz. A box manoeuvre of 10° by 10° with an elevated launcher was performed to calibrate the ground trajectory computer. Shortly before lift-off, the nominal precession vector for the S44 burn was loaded in the DMARS as an Euler angle. From lift-off, the colleague operating the trajectory computer monitored the position of the vehicle and calculated the required corrections for the second stage burn.

On reaching the 80 km first stage separation, the roll spin command would have been activated to correct the rate required for the precession manoeuvre, however, as the canted fin induced spin rate was well within the acceptable tolerance for the manoeuvre, the precession control system was imme diately activated and the payload and S44 motor precessed towards the target which had been loaded before launch. Shortly after, the trajectory computer operater provided a corrected vector which compensated the offset drift of the passive stabilized first stage burn and this was sent to the DMARS, which then precessed to the corrected target. The nominal and actual flight trajectories are shown in Fig. 3 . The correction resulted in a slightly lower trajectory than planned, but an impact within 8 km of the predicted point at a range of 800 km.

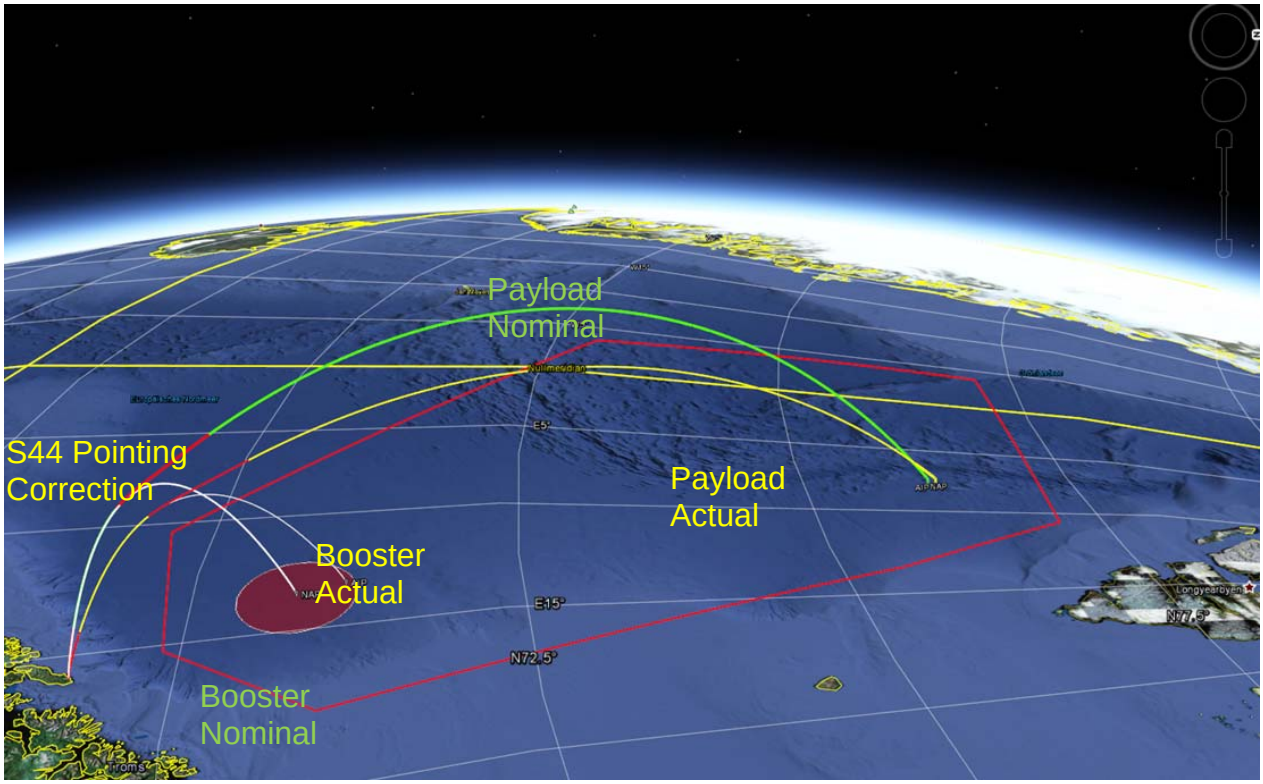

Fig. 3. Comparison of Nominal and Actual Trajectory

It was not intended to control the vehicle during the S44 burn phase, as this is more complex due to the rapidly changing physical characteristics during the expulsion of 870 Kg of propellant, however, as the control function showed no instability, it was left active for most of the burn phase and disabled only a few seconds prior to burnout and demonstrated its usefulness by correcting a slight coning tendency due to a thrust misalignment offset in the motor.

9. APPLICATIONS IN FUTURE MISSIONS

A number of sub-systems and procedures which were developed for and flight proven on, the SHEFEX II vehicle, have obvious potential for use in future missions, particularly those involving larger payloads for hypersonic re-entry and scramjet development tests.

The VS40 two stage motor provides a significant improvement in apogee or range for heavier and larger diameter payloads and with the addition of multi-purpose cold gas attitude and rate control systems can provide experiment optimised trajectories and together with real time flight analysis and pointing correction, drastic reduction of impact dispersion. Such a vehicle and payload required the design and construction of new electronic and mechanical flight systems, real time in-flight data display and command input and operational procedures and also more complex electrical and mechanical ground support equipment.

Recent and current projects which have a requirement for technology and systems developed for the SHEFEX program include HEXAFLY, HIFiRE 8 and SHEFEX III and a number of future missions under consideration in the HIFiRE and SCRAMSPACE programs. Most of these projects involve hypersonic flight bodies with scramjet engines, and require a vehicle diameter of at least one m etre for the payload and a suppressed or at least unconventional trajectory to provide hypersonic velocities at altitudes in the range of 30 km.

10. CONCLUSION

The design, development, qualification and launch of the SHEFEX II payload and vehicle was a complex, demanding and rewarding experience and has increased the qualifications of the DLR MORABA for the challenges presented by the new fields of hypersonic vehicle tests and guided vehicles.

11. ACKNOWLEDGEMENT

The development, construction, qualification and successful flight of the SH EFEX II vehicle was only possible with the enthusiastic and competent support of the DLR MORABA team, colleagues from the other DLR institutes and experimenter groups who participated in the mission. Also much appreciation is due to our cooperation partners from DCTA/IAE in Brazil for the rocket motors and the Andoya Rocket Range, for their support. Last but not least, special thanks are due to the DLR Space System Integration Group, SHEFEX project manager Hendrik Weihs.

12. REFERENCES

Turner. J., Hörschgen, M. Turner, P. Ettl, J. Jung, W. Stamminger, A. (2005) *SHEFEX – The Vehicle and Sub-Systems for a Hypersonic Re-entry Flight Experiment.* 17th ESA Symposium on European Rocket and Balloon Programmes and Related Research, Sandefjord, Norway, 31.Mai – 4.Juni 2005. Volltext nicht online.

John Turner, Wolfgang Jung, Andreas Stamminger, Peter Turner, et al. *SHEFEX – Hypersonic Re-entry Flight Experiment Vehicle and Subsystem Design, Flight Performance and Prospects* in 14th AIAAAHI Space Planes and Hypersonic Systems and Technologies Conference (2006)

J. Turner et al. *SHEFEX 2 - The Vehicle, Subsystems and Mission Concept for a Hypersonic Re-entry Flight Experiment* 18th ESA Symposium on European Rocket and Balloon Programmes and Related Research 3–7 June 2007 Visby, Sweden

Eggers, Th., Longo, J.M.A., Gülhan, A. Hörschgen, M. Stamminger, A., Turner, J. (2006) *Preliminary Post-Flight Data Analysis of the SHEFEX Experiment.* In: 1st International ARA Days, "Atmospheric Reentry Systems, Missions and Vehicles". 2006-07-03 - 2006-07-05, Arcachon.

Longo, José Maria, Turner John, Weihs Hendrik (2008) *SHEFEX II - Aerodynamic Re-Entry Controlled Sharp Edge Flight Experiment.* 6th European Symposium on Aerothermodynamics for Space Vehicles, 2008-11-03 - 2 008-11-06, Versailles (France).

John Turner, Marcus Hörschgen, Wolfgang Jung, Andreas Stamminger, Peter Turner (2006) *SHEFEX - Hypersonic Re-entry Fllight Experiment - Vehicle and Subsystem Design, Flight Performance and Prospects.* In: Proceedings AIAA 14th Spaceplane Systems and Technologies Conference. 14th Spaceplane Systems and Technologies Conference, 2006-11-08, Canberra, Australia.

Hendrik Weihs, John Turner, José Maria Longo (2008) *The Sharp Edge Flight Experiment SHEFEX II, a Mission Overview and Status.* AIAA International Space Planes and Hypersonic Systems nad Technologies Conference, 2008-04-28 - 2008-05-01, Dayton, OH (USA).

John Turner(1), Marcus Hörschgen(2), Josef Ettl(2), Wolfgang Jung(2), Peter Turner(2) *SHEFEX 2 - DEVELOPMENT STATUS OF THE VEHICLE AND SUB-SYSTEMS FOR A HYPERSONIC RE-ENTRY FLIGHT EXPERIMENT* Proc. '19th ESA Symposium on European Rocket and Balloon Programmes and Related Research, Bad Reichenhall, Germany, 7–11 June 2009 (ESA SP-671, September 2009)

Josef Ettl, John Turner *Navigation and Cold Gas Control Systems flown on SHEFEX II* Proc. '20th ESA Symposium on European Rocket and Balloon Programmes and Related Research, Thun, Switzerland

Frank Scheuerpflug, Alexander Kallenbach *THE FLIGHT CONTROL OF SHEFEX II* Proc. '20th ESA Symposium on European Rocket and Balloon Programmes and Related Research, Thun, Switzerland

SHEFEX II System Specifications, by John Turner 16th March 2010

Precession Manoeuvre, by Josef Ettl, 3rd March 2009

SHEFEX II Post Flight Report, Flight Safety, by Frank Scheuerpflug, 6th July 2012

SOUNDING ROCKETS FOR ENTRY RESEARCH: SHEFEX FLIGHT TEST PROGRAM

Hendrik Weihs

German Aerospace Center, DLR
Pfaffenwaldring 38-40, D-70569 Stuttgart, Germany
Hendrik.weihs@dlr.de, phone +49-711-6862-625 /fax -227

*

Abstract

Within research for space vehicles with Re-entry capability and hypersonic airplane development in the last decade sounding rocket systems became a major and important test bed. This paper will present an overview of the national development and flight test program SHEFEX (SHARP EDGE FLIGHT EXPERIMENT) of the German Aerospace Center DLR. After 2 successful flight campaigns in 2005 and 2012 DLR is now preparing the next test vehicle SHEFEX III, which is planned for launch in 2016. The paper will focus on the strategic test approach and scientific experiments on board in interaction and possibilities of the sounding rocket system. Also some spin off effects will be prescribed which will enhance the performance of the rocket system also outside re-entry research.

Main goal of re-entry experiments is to verify technologies and simulation tools regarding hypersonic gas flow and structural response. A full scale re-entry test flight is expensive and needs in general a launch system with orbital capacity. To simplify and to reduce costs a step by step approach seems to be practicable and less risky. Thus, sounding rockets are a very attractive vehicle to perform related research. Even, they do not cover the whole performance to accelerate the entry vehicle to real re-entry conditions; they allow generating interesting flight conditions to verify aerodynamic simulation tools.

Within SHEFEX the step by step development results in stepwise increasing velocity and test duration. SHEFEX I performs a Mach 6 flight for 20 Seconds. SHEFEX II reaches Mach 10-11 for 45 Seconds. SHEFEX III is aimed to reach Mach 20 for 15 minutes, a significant and

Proc. '21st ESA Symposium European Rocket & Balloon Programmes and Related Research', 9–13 June 2013, Thun, Switzerland (ESA SP-721, October 2013)

ambitious step which require a big sounding rocket which is currently not available, but under development in Brasil.

In the field of hypersonic aircraft and air breathing propulsion development the SHEFEX launch systems could be a standard rocket family for flight tests. The improvement in high temperature stable stabilizers, huge lift fairings to cover complex vehicles and high accurate pointing and control systems are applicable especially to such kinds of flight tests, which partially is already done within the HiFire and Scramspace Programs.

Introduction

One key technology for returnable space transport vehicles, hypersonic aircraft or winged first stage of a space transportation system is the structural design of hot structures at exposed locations of the vehicle (e.g. nose, wing leading edges, control flaps, air intake etc.) and the overall fuselage design considering the thermal loads. Besides high temperature resistant materials, also structures or single components cooled by special physical effects are candidates for extremely exposed locations at the fuselage and the engine. For the fuselage and wing design different design solutions are possible. In addition to the classic variants like TPS protected conventional structures or hot skin structures, the basic shape approach may influence the system performance and cost frame of the vehicle.

Another key technology is simulation and prediction of aerodynamic and aerothermodynamic phenomena and effects occurring during atmospheric re-entry. Thus accuracy and reliability of simulation tools and ground testing facilities control margin policy and safety of vehicle lay out and mission success.

In addition, GNC technology, autonomous aerodynamic control during re-entry and final approach using moveable rudders, flaps or fins is an essential technology for future re-entry vehicles.

A lot of development effort can be done on ground or using ground based test facilities. However, a flight test is extremely important to set a reasonable development step forward. The challenge to deliver flight hardware which has to operate in a very reliable way during the mission speeds up development process and supports learning curve significantly. However, a rather complex test vehicle or demonstrator requires a reasonable time frame and financial resources. Thus, an optimal

Figure 2: S 40 Launcher system for SHEFEX II and payload configuration

compromise is to reduce size and complexity of the test vehicle, to simplify trajectory requirements and to use a cheap launcher system and existing ground support.

After demonstration within the SHEFEX I mission sounding rocket systems are suitable to perform re-entry related flight experiments. Having the SHEFEX I in a "passive" re-entry configuration only stabilized by a conic tail and fins, the SHEFEX II payload was provided by an active aerodynamic control system.

Lay Out of the Launcher

After a trade off of different launcher configurations and examination of each possible performance and related trajectory, a final 2 stage configuration was chosen considering Brazilian solid rocket boosters derived from the S 40 family. Within table 1 the basic characteristics of both configurations are summarised.

	SHEFEX I	SHEFEX II
Payload	250 kg	500 kg
Apogee	210 km	180 km
Downrange	230 km	800 km
Max. Speed	Ma 6.5	Ma 10-11
Stages	2	2
Experiment time	20 sec	45 sec
Re-Entry angle	84 °	35°

Table 1: main characteristics of the SHEFEX I and II launcher configurations

As a rocket vehicle to fulfil the demands on payload capacity and re-entry velocity, the two-stage Brazilian VS-40 sounding rocket was considered.. The S-40 motor is part of the VLS vehicle operating as the third stage. The S-44 motor and also the interstage adapters are lightweight structures built of Kevlar composites. The VS-40 was first launched successfully in April 1993 achieving an apogee of 950 km and a ground range of 2680 km with a payload mass of 197 kg and 81.8 deg of launch elevation. Up to now, two flights are recorded, both successful.

Description of the SHEFEX II Test Vehicle

In the opposite to SHEFEX I the shape of the test article was chosen to create a facetted symmetric re-entry body stabilized by tail fins and 4 movable small canards

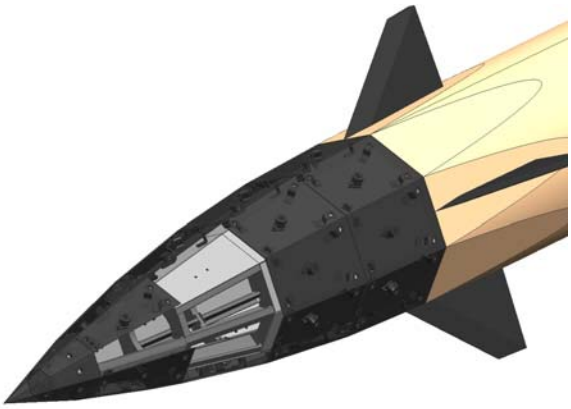

Figure 3: Detail of the payload Tip including TPS (dark grey) inner Alu substructure (light grey) and actuator module.

near the front area of the cylindrical pay load segments. Within the cylindrical segments all necessary subsystems like navigation platform, power cells, RCS- unit, data acquisition, parachute and recovery system, telemetry, etc. are integrated.

Mounted on top of the second stage the payload was separated before re-entry to begin an autonomous flight till final breaking manoeuvre and parachute deployment.

Including the payload the overall length of the system was 12, 7m. The overall mass of the system was 6,7 tons.

The flight envelope enabled a max. Mach number during entry up to Ma 10 (approx. 2.8 km/sec) for 45 seconds. This high Mach number caused extreme heat fluxes at the payload tip and sharp leading edges at the canards and stabilizers. So temperatures above 1800 °C occured at these exposed locations. The dynamic pressure increased up to 4 bar at the end of entry trajectory at 20 km.

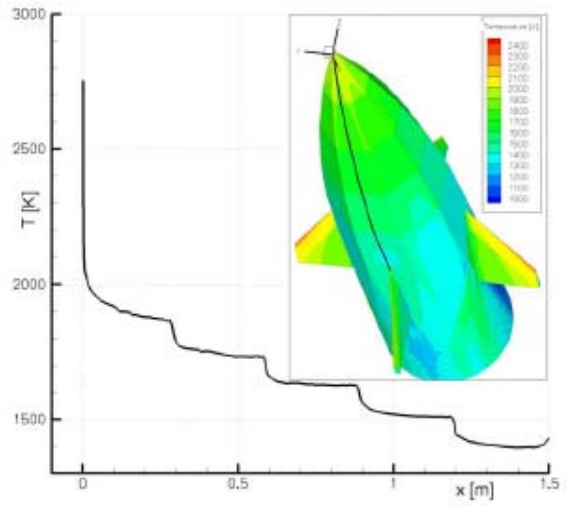

Figure 4: predicted temperature distribution at radiation adiabatic boundary conditions

Key Experiments

The primary substructure of the payload tip is similar to the SHEFEX I concept and consists of a aluminium frame created by stiff booms and spares. The free space is closed by flat aluminium panels, which create an inner mould line (IML). The panels are also used for mounting the TPS facets and experiments. Inside the frame, some measurement equipment is integrated. These items are boxes for thermocouple connection and compensation, pressure transducers, a pyrometer system, data processing boxes and subsystems for passenger experiments.

The tip geometry is symmetrically divided into 8 identical facets in circular direction and consists of 5 segments along the tip to the actuator module interface. Thus, the payload tip houses 40 single flat areas. 32 of them were available for different experiment positions.

As shown in figure 5 with exception of the forward tip area, the heat fluxes have individual nearly constant values at each segment. The heat flux decreases from segment to segment in rearward direction. Thus, each segment is suitable for different TPS concepts and materials due to their specific limit temperature.

Flush Air Data System (FADS)

Within the nose cone tip some special arrangement of 8 pressure sensors were implemented to investigate possibility of a flush air data system, which may be useful for vehicle control (pitch and yaw) against gas flow direction during hypersonic flight. However, this was a passive experiment with no interaction of SHEFEX II active control. But pressure data assessment shall allow a comparison of vehicle orientation data got by GNC platform and advanced algorithms for pressure data processing. From a structural point of view, the integration of pressure holes and tubing within the hottest area of the vehicle was a challenging issue.

Thermal protection systems TPS

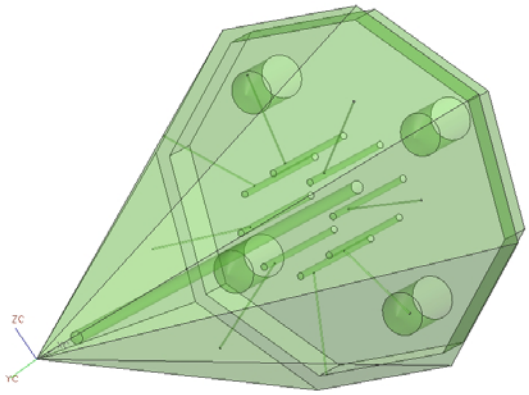

Figure 5: CMC Nose with integral pressure sensor holes for the FADS

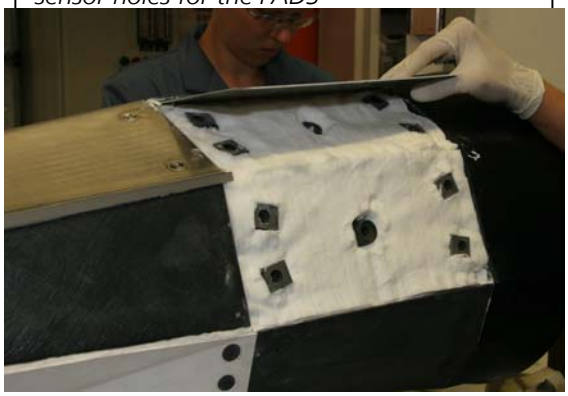

Figure 6: C/C-SiC standard TPS as mounted on SHEFEX I

The second section includes 8 single TPS or material experiments designed very similar to those, which are flown already on SHEFEX I. Main element of the concept is a fiber ceramic cover plate, supported in all directions by a so called central post and flexible stand offs at the corners. Thus, the thermal expansion will be not suppressed. Beneath the cover plate a lightweight fibrous ceramic insulation felt is inserted. Key element of this TPS concept is a ceramic fastener, used for the connection of the panel to the CMC stand off and central post.

A new approach was performed within the SHEFEX project. Within DLR an oxide ceramic based CMC material was developed during the last years. The so called WHIPOX material can be used as an oxidation stable alternative to carbon based CMCs. However, temperature stability is limited and a special coating is necessary to improve emissivity and catalytic behaviour. Nevertheless, this material provides a flexible intermediate state during the manufacturing process. Thus, it is possible to shape a component (in case of SHEFEX the rigid seal) during assembly. Hardening will occur during operation.

Using this property, it is possible to shape and cut all required seal components from one uniform unfired WHIPOX tape. A typical seal interface was tested within a plasma wind tunnel and handling procedure, seal performance and temperature stability could be demonstrated successfully.

Besides DLR`s C/C-SiC material for the cover panels, 3 facets of the second segment are covered by passengers on SHEFEX II, two different C/SiC materials developed by EADS ASTRIUM and one C/SiC Panel developed by MT-Aerospace.

4 TPS-elements of the third segment are provided with patch antennas behind. This is to demonstrate functionality of “hot” antennas which are able to be integrated within a heat shield of a re-entry vehicle. The cover panels are made from DLR`s WHIPOX oxide based ceramics to take benefit from their electromagnetic permeability.

This technology enters also usage for standard hook antennas which were covered by a small WHIPOX fairing. Thus, also useable for standard Sounding rocket applications this is a direct spin off from the SHEFEX program.

Within the 4th and 5th segment a number of passengers and standard TPS elements are located. Besides the surface protected

flexible insulation SPFI 2 metallic TPS elements from EADS ASTRIUM are integrated. Additional Experiments from, AFRL (USA) were also integrated

Actively cooled TPS AKTIV

At DLR an actively cooled TPS concept is under investigation. Based on the very good experience got during development of an effusion cooled ceramic rocket engine burning chamber, it seems to be possible to transfer this technology for the design of extremely loaded sharp leading edges or flat TPS elements exposed to heat fluxes beyond materials temperature limits. First screening tests of different porous ceramic materials and cooling gases showed a promising potential for this technique. Significant cooling effects at rather low gas consumption could be demonstrated within a plasma channel test sequence at hypersonic gas flow conditions. However, a large effort has to be invested to investigate and understand the responsible parameters for an optimal cooling effect considering the thermal conductivity and interactions between the surrounding gas flow and boundary layer.

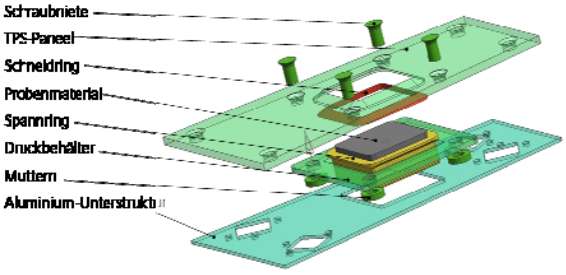

Active cooling systems are of special interest for use in severe thermal environments where the passive systems are inadequate. The transpiration cooling experiment uses a porous ceramic material at the outer surface through which a coolant flows into the boundary layer. Thus, transpiration cooling is effected by two physical phenomena, as there are the porous structure being convection cooled by the coolant and the coolant layer on the outer, hot surface, lowering the heat transfer from the high-enthalpy environment to the vehicle surface.

The flight results showed a very high cooling efficiency in comparison to the uncooled reference set up.

Active aerodynamic control

The first cylindrical part behind the facetted payload tip includes the aerodynamic flight control unit. The active part is an actuator system to move the 4 canards. Interaction with the RCS system at altitudes above 70 km and continuously changing aerodynamic sensitivity till payload split at 20 km require challenging advanced control algorithms and high speed actuators.

The canards themselves are highly thermomechanically loaded structures. Due to limited shaft diameter and very high bending loads, a CMC/metallic hybrid structure was chosen for structural design. The leading edge structure is made from C/C-SiC fiber ceramic to withstand the expected high temperatures of 1700°C at the leading edge. The canard main structure is made from a Titanium alloy to carry bending loads and to transfer torsion from the actuators. Special attention has to be paid for the attachment design between Titanium and CMC to balance thermal expansion mismatch.

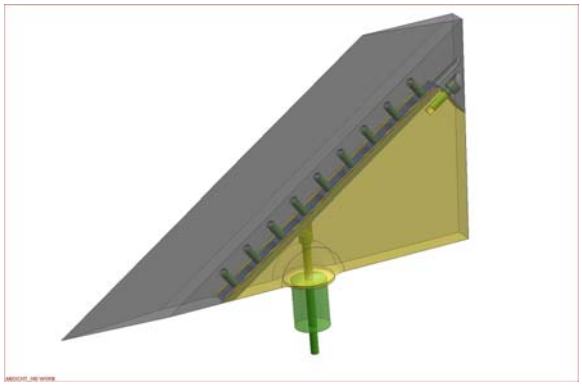

Figure 8: Hybrid CMC (grey) and metallic (yellow) canard structure

Instrumentation

The whole tip structure was instrumented with up to 60 thermocouples, 1 pyrometer, 24 pressure sensors and 8 heat flux sensors. Special care was applied to the integration of the pressure and heat flux sensors within the TPS elements. This is to minimize secondary gas flow effects at the sensor/ceramic interface at the outer surface. Otherwise, the heat flux signal may be disturbed by local turbulence or stagnation areas. All signals were processed and send to the data storage and telemetry system by special multi function cards also integrated within the payload tip. Lessons learnt from SHEFEX I and parallel on ground testing and calibration promises a high quality of flight data, which will allow optimisation and calibration of CFD tools for further reliable aerothermodynamic vehicle lay out.

The uncovered tip allowed also aerodynamic measurement during the up leg of trajectory which is a valuable data base to estimate heat and aerodynamic loading of standard sounding rocket missions.

The University of Stuttgart provides additional instrumentation in terms of fiber optic sensor and a pyrometer and radiometer sensor combination respectively.

Mounted on top of the second stage the payload was separated before re-entry to begin an autonomous flight till final breaking manoeuvre and parachute deployment.

Secondary structural developments

The VS 40 launch system needed some modifications to meet the SHEFEX mission requirements. Especially the stabilizer fin leading edges and fairing structure were specially developed for SHEFEX II. During SHEFEX I the stainless steel leading edge structures of the second stage aluminium stabilizers showed a thermal buckling effect during ascent and re-entry which was caused by a thermal expansion mismatch of the structural materials used. This resulted

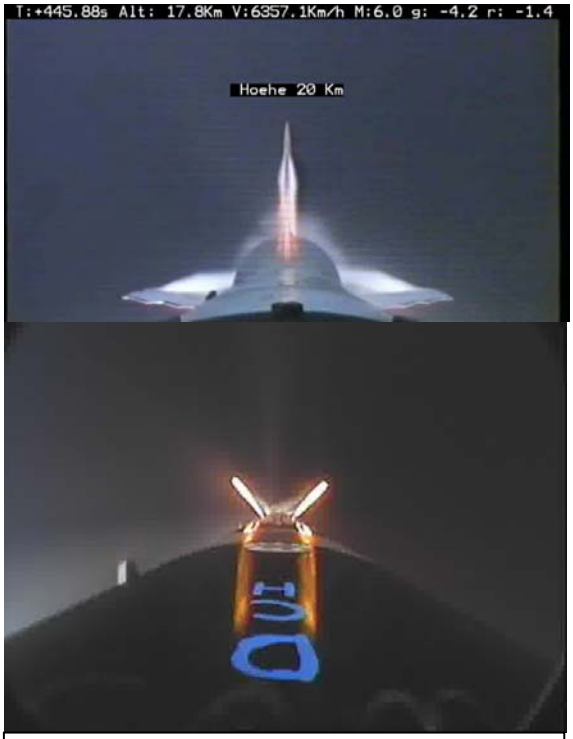

Figure 9: Fin leading edges of SHEFEX I (top, tainless steel) and HiFIRE 3 (Glass/Phenol) during entry at approx.. Ma 6-7 at 20 km.

in uncontrolled spin effects during flight. Thus, the leading edges of the first stage of SHEFEX II were made from a CFRP material with well adapted fiber orientation to balance the Aluminium expansion. That results in a spin rate which was very close to the predicted value. The Stabilizers of the re-entry vehicle were completely made from CFRP with special resin to act as an structural ablator at the leading edge. Not used within SHEFEX II, but important for the VS-30/ improved Orion system which was used within SHEFEX I the second stage stainless steel stabilizers were replaced by an glass fiber reinforced phenol. This reduced thermal deformation dramatically and was applicated during the HIFIRE 3 and 5 flight. Especially during HIFIRE 3 these stabilizers worked reliable during the whole mission down to 20 km altitude.

The fairing structures for SHEFEX II were designed as a CFRP sandwich structure with a 2 mm thermal ablative protection cover. This cover worked as estimated and shields the load carrying sandwich till fairing release. The weight reduction in comparison to a conventional aluminium structure reached 50 %.

Outlook

After successful flight of SHEFEX II the next step, SHEFEX III is under development. In the opposite of recent SHEFEX Flights, SHEFEX III will be a free flying vehicle with continuous deceleration during entry at full aerodynamic control. The interface velocity is aimed above Ma 20 at 100 km. Tha vehicle mass is estimated with 500 kg.Thus, the recent SHEFEX launch systems are to small. In coopartion with brasil a suitable launcher called VLM is underdevelopment, which could reach the required performance. However, the SHEFEX II launcher configuration keeps alive and will be used for the Australian/US Hifire 8 and the European/International HEXAFLY Hypersonic experiment missions.

Acknowledgements

I have to thank the whole DLR SHEFEX Team, especially the MORABA People and our partners at EADS-ASTRIUM, MT-Aerospace, IRS, DSTO and AFRL. Special Thanks to DCTA in Brasil, which are the key partners to keep the SHEFEX Program alive.

The following DLR Institutes and Facilities participate within the SHEFEX II Project:

Institute of Aerodynamics and Flow Technology, Braunschweig / Göttingen and Wind Tunnels Section, Cologne, Institute of Structures and Design, Stuttgart, Institute of Flight Systems, Braunschweig; Institute of Materials Research, Cologne, Institute of Aerospace Systems, Bremen, Mobile Rocket Base MORABA, Space Operation and Astronaut Training, Oberpfaffenhofen

References

[1] Barth, T., Aero- and Thermodynamic Analysis of SHEFEX I, Engineering Applications of Computational Fluid Mechanics Vol. 2, No.1, pp. 76–84, 2008

[2] Eggers, Th., Gräßlin, M., Layout of Hypersonic Vehicles by Coupling of Aerodynamics and Flight mechanics, 2nd International ARA Days, Arcachon, October 2008.

[3] Korfanty, M., CFD based Dynamic Analysis of

Atmospheric Re-Entry Vehicles, 2nd International ARA Days, Arcachon, October 2008.

[4] Weihs, H., Longo, J., Gülhan, A.: The sharp edge flight experiment SHEFEX. 4th European Workshop on Hot Structures and TPS for Space Vehicles, Palermo, Italien, 26-29 November 2002, ESA/ASI/DLR/CNES, (2002)

[5] Boscov J. and Macera S.R., *Programme Spatial Brésilien: La Fusée VS-40,* Proceedings of the 11th ESA Symposium on European Rocket and Balloon Programmes and Related Research, Montreux, Switzerland, 24 – 28 May, (ESA SP-355, March 1994).

[6] Eggers Th., "Aerodynamic and Aerothermodynamic Layout of the Hypersonic Flight Experiment SHEFEX" *5th European Symposium on Aerothermodynamics for Space Vehicles, ESA Nov. 2004*.

[7] Eggers Th., Longo J., Hörschgen M., Stamminger A., "The Hypersonic Flight Experiment SHEFEX" *AIAA 13th Space Planes and Hypersonic Systems and Technologies Conference, AIAA May 2005*.

[8] Eggers Th., Stamminger A., Hörschgen M., Jung, W., Turner J., "The Hypersonic Experiment SHEFEX – Aerothermodynamic Layout, Vehicle Development and First Flight Results" *ESA 6th International Symposium on Launcher Technologies, ESA Nov. 2005*.

[9] Longo J., Püttmann, N., "The DLR Sharp Edge Flight Experiment SHEFEX" *Proceedings of the DGLR Jahrestagung, DGLR 2004-072, September 2004.*

[10] Stamminger A., Turner J., Hörschgen M., Jung W., "Sounding Rockets as a Real Flight Platform for Aerothermodynamic CFD Validation of Hypersonic Flight Experiments", *5th European Symposium on Aerothermodynamics for Space Vehicles, ESA Nov. 2004*.

[11] Turner J., Hörschgen M., Turner, P., Ettl, J., Jung W., Stamminger A., "SHEFEX – The Vehicle and Sub-Systems for a Hypersonic Re-Entry Flight Experiment", 17th *ESA Symposium on European Rockets and Balloon Programmes and Related Research, ESA 2005*.

[12] Weihs H., Turner J., Hörschgen M.., "SHEFEX II – The Next Step within Flight Testing of Re-Entry Technology", 57th International Astronautical Congress, Valencia, Oct. 2006.

REDEMPTION:
AN EXPERIMENT ON SOUNDING ROCKET TO TEST A SYSTEM FOR ACTIVAL DEBRIS REMOVAL – REXUS12

Valdatta Marcello[1] mailto:marcello.valdatta@gmail.com, Romei Fedrico[1] fede.pulsar@gmail.com,
Spadanuda Antonio[1] Antonio.spadanuda@gmail.com, Toschi Stefania[1] ste910@gmail.com,
Piattoni Jacopo[1] piattoni.jacopo@gamil.com, Candini Gian Paolo[3] gpaolo@iaa.es ,
Santoni Fabio[2] fabio.santoni@uniroma1.it , Piergentili Fabrizio fabrizio.piergentili@uniroma1.it [2]

[1] *University of Bologna (Italy)*
[2] *University of Rome "La Sapienza" (Italy)*
[3] *Instituto de Astrofisica de Andalucía - CSIC (Spain)*

ABSTRACT

REDEMPTION (REmoval of DEbris using Material with Phase Transition: IONospherical tests) is a student experiment aiming to propose a feasible solution for Active Debris Removal. Completely conceived, designed and realised within the Space Robotic Laboratory (SRL) of the second Faculty of Engineering of Bologna University "ALMA MATER STUDIORUM", REDEMPTION was selected to participate in REXUS/BEXUS 2012 Programme. This programme was realised under a bilateral Agency Agreement between the German Aerospace Center (DLR) and the Swedish National Space Board (SNSB). The Swedish share of the payload was made available to students from other European countries through collaboration with the European Space Agency (ESA). REDEMPTION experiment base-concept is definitely up-to-date, as at the moment space debris problem is one of the most challenging space research fields: currently the situation of debris population is quite critical, because every new collision produces at its time other satellite fragments, raising the total number of debris and making the probability of a new impact more likely (the Kessler- Syndrome). Due to the complexity of the task, no feasible solution has been found so far. One of the most critical aspects to be solved in debris removal framework is how to connect the debris to be removed to the cleaner satellite. On this matter, through REDEMPTION experiment, students aim to evaluate the feasibility of an ADR system based on a polyurethane foam. The foam under evaluation is generated starting from two liquid reagents, which need to be mixed to produce a polymeric structure that after a short time becomes solid and rigid. The opportunity to launch the experiment onboard REXUS rocket allowed verifying the behaviour of the foam in near space conditions, that is, milli-gravity and vacuum conditions. REDEMPTION flew in the space on board of REXUS12 Rocket on the 19th March 2012. In this paper the educational aspects of the project and the technical details regarding the three sub-experiments which constitute REDEMPTION module are depicted. As well, the results of the launch campaign are discussed, drawing the conclusions of the project.

INTRODUCTION

Space debris is an increasing problem[1]. The exponential increase of satellite launches in the last 50 years has determined the problem of space debris, especially in LEO. The remains of past missions are dangerous for both operative satellites and human activity in space. But not only: it has been shown that uncontrolled impacts between space objects can lead to a potentially dangerous situation . It is possible to reach a situation of instability where the big amount of debris could cause a cascade of collisions, the so called Kessler syndrome, resulting in the infeasibility of new space missions for many generations. Currently 19000 debris larger than 5 cm are tracked, while 500000 are smaller than 1cm. Leo polar orbit represents the most critical and risky area. In spite of that, the gravity of the situation and of the numbers listed above is offset by the apparent easy solution to the problem: recent studies indicates that to stop the population growth, it could be enough to remove only 5 big debris a year. Even if it could appear relatively a little effort with respect to the big amount of debris, recent technology did not enable active debris removal.
The project faces the problem of how to deorbit an existing debris, applying the studies about the use of polyurethane foam developed by Space Robotic Group of University of Bologna. The research is started with the Redemption experiment, part of last ESA Rexus program. The foam is composed by two liquid components that, once properly mixed, trig an expansive reaction leading to an increase of volume whose entity depends on the chemical composition of the two starting components. The idea is to create a link between the satellite and the object. [8]

Proc. '21st ESA Symposium European Rocket & Balloon Programmes and Related Research',
9–13 June 2013, Thun, Switzerland (ESA SP-721, October 2013)

MISSIONS CONCEPT

This ADR system is suitable to be integrated on satellites of different classes (from nanosats to big satellites). With the foam it is possible to plan 2 different missions of debris removal: controlled and not controlled removal mission. [6] [7]

Not Controlled Removal

The target of the "not controlled" removal consists in altering its passive deorbiting time: after the rendezvous maneuver, the debris is shooted with the ADR in order to attach to it a certain volume of expanded foam, as to increase its aspect - mass ratio (Fig.1).

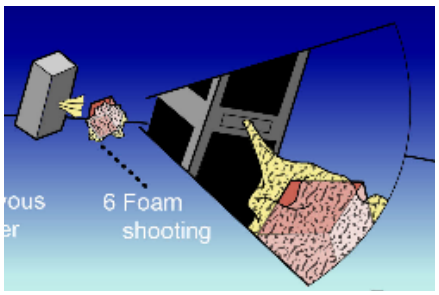

Fig.1 Example of debris capture

Thanks to the foam's property, in fact, it is possible to greatly increase the wetted surface area in relation to a minimal increase in mass. For this kind of mission it is necessary to define specific foam properties to maximize the expansion ratio reducing in that way the mechanical properties that are not relevant for the purpose. The reduction in terms of orbital decay time (t_f-t_0) is expressed by the following formulas (Eq.1 & Eq.2) in which it's possible to underline that it depends from the ballistic parameter B; r_0 is the starting orbit radius, H is the scale height of the atmospheric model, A is the wet surface, m is the mass, C_d is the drag coefficient and μ is the Earth gravity constant

$$(t_f - t_0) = \frac{H}{B\sqrt{\mu r}} \frac{1}{\rho(r_0)}$$

Eq.1 Orbit lifetime[2]

$$B = c_d \frac{A}{m}$$

Eq.2 Ballistic Parameter[2]

Controlled Removal

This kind of mission consists in creating a rigid link between the cleaner satellite and the debris. In that way it is possible to use the deorbiting devices of the cleaner satellite or, better , a dedicated propulsion system to accomplish the removal. In this case the foam is used to strongly connect the two objects after the rendezvous maneuver. It is obvious that the success of the link depends on the mechanical properties of the foam instead of the expansion ratio.

The great potential of this solution is due to the possibility to grab a moving object that cannot be controlled. Most of the problems of active debris removal solutions (above all robotic arms) are connected to the trouble in catching a spinning object: the foam technology allows to resolve these problems allowing to incorporate the object, whose spin can even promote adhesion of the foam.

THE FOAM

The system is based on a particular polyurethanic foam, developed especially for the purpose. The foam is generated by a chemical reaction of 2 liquid components. The product of reaction is CO2, that allows to inflate the compounds, which expands. After the expansion, the solidification starts. The process of foam generation and formation is really rapid, and is completed in some seconds.
In order to test the capability of the foam to work in vacuum, a test was performed (Fig 2). The test consisted in realizing the reaction in a vacuum chamber and observing the result. The test gave two main results. First of all, it was confirmed the possibility to use the foam in space environment; then, the second finding, was that there is the possibility to modify the reaction to have different level of hardness of the foam, by the regulation of the quantity of gas produced by the reaction (Fig 3). [2] [3] [4]
The foam is produced by the reaction of two liquids mixed together. The speed of reaction and quality of the foam are influenced by the starting temperature of the reagents: this is why after several tests it has been decided to require 50°C at the moment of the fluid injection. The chemical formulation of the foam has been developed and calibrated by the producer, *Duna Corradini Group.*

The foam has never been space qualified, so it has been decided to test it on a sounding rocket programme. Rexus programme was very suitable for this purpose.

Fig. 2 Vacuum Test of the foam

Fig 3 *Chemical modification of the foam*

To evaluate the possibility to use the polyurethanic foam for grabbing the debris, an adhesion test was performed. This test has been performed on aluminium, the most common material space debris are made of. Two aluminium beams have been cross-linked together by casting on them the foam (without incorporating the beams, but just to verify the adhesion, see figure 4). The link was characterized by an interface surface of about 2000 mm^2. It has undergone subsequent load test, by increasing the suspended mass step by step. As a result, the maximum load supported by the link is about 6,3 kg.

Fig.4 Adhesion test in normal condition

In order to test the foam on a sounding rocket also a thermal test was performed, in order to ensure that the liquids would have survived to the climatic condition. The two reagents survived without problems the cold/hot cycle, passing fom -19°C to 70°. The cycle was repeated 3 times on the same samples. After the cycle, the reaction was started. resulting in a nominal reaction (Fig 5). [3]

Fig 5 Thermal test of the material

One of the liquids of the foam is very sensible to the humidity and the water. This was discovered during test campaign, in particular during the bench tests of the experiment. As mitigation to this possible problem, the experiment was assembled before the flight in a controlled humidity room.

FOAM RELASING SYSTEM

To test the foam in space, the foam was boarded on the Rexus sounding rocket, in frame of ESA Rexus/Bexus educational programme. [2] [3] [4] [5]
To test the material, a system for the automatic release of the foam was developed. The system called “test cell” (fig 7 and fig 8). Each test cell has its own not pressurized tanks, which are made from metallic material, separated from the other ones, and a double syringe. The syringe contains two reagents in separated containers and has a plunger that simultaneously pushes them out in a static mixer (provided my Maxver). The valves between the tanks and the mixers are important in order to avoid that reagents come in contact before the right time.

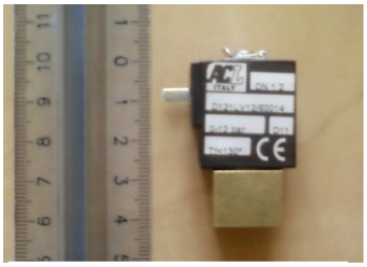

Fig.6 Electrovalves provided by ACL

A dedicated connector between the valves and the mixer was designed; it allows sending the two liquids from the syringes to the inlet of the mixer. The reagents are pushed out of the tanks using springs which are opened by thermal cut system. There is a safety dynema wire to keep the spring in position without applying force on the pistons. This is a redundancy system because the electrovalves (Fig. 6) are enough strong to support the pressure of the spring.

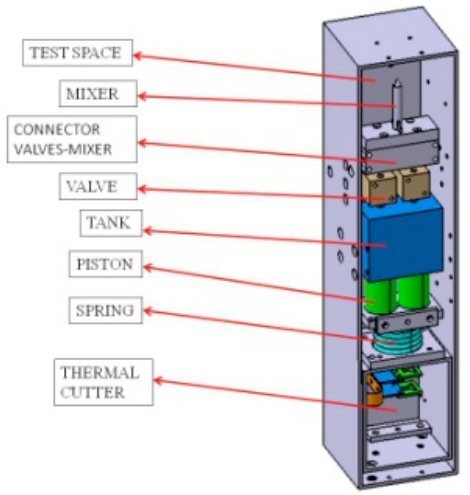

Fig 7 *Redemption foam Release system*

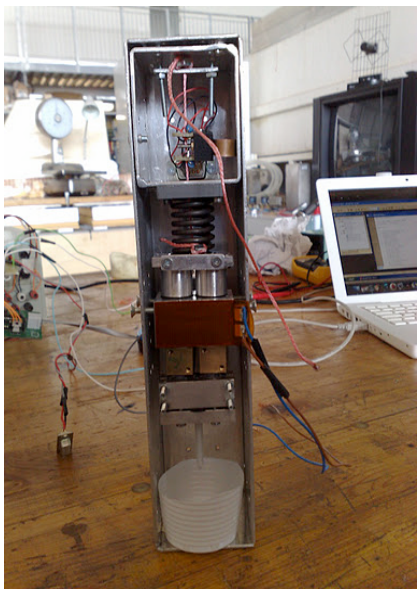

Fig 8 Prototype of test cell

Thermal cut is powered by battery pack. The liquids need to be heated to reach 50°C using a heating system powered by the external umbilical, for this the test cell were provided with kapton heaters film (provided by FrancoCorradi srl). These heaters are structured as a tape that had to be applied directly on the surface to heat. The power of the heaters was chosen to meet the operational conditions of the launch site; ESRANGE in Kiruna, where external temperature was expected to be between -10 and -20°C. For this reason, the heating system was tested inside a freezer. The heaters (Fig 9) had to rise the temperature of the liquids from -18 to 60°C. After the test, 60 Ohm heaters were chosen (15W for each one). Each test cell is aimed to test a different kind of foam with a different chemical formulation.

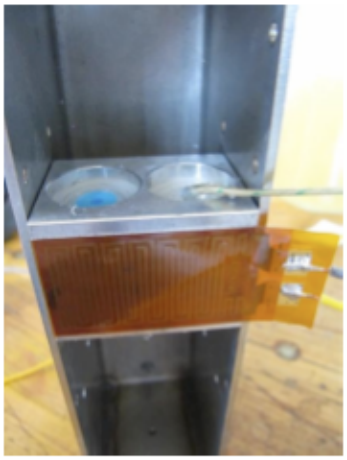

Fig. 9 Thermal control system based on kapton film

REDEMPTION MODULE

The REDEMPTION experiment module is composed by five Test Cell, with three different experiments. Inside the module there are four cameras to record the deploy and the evolution of the foam and thermal sensor to register the temperature of the foam. Three cameras are connected to an internal digital recorder and one camera to the tv channel of the rocket (fig 10).

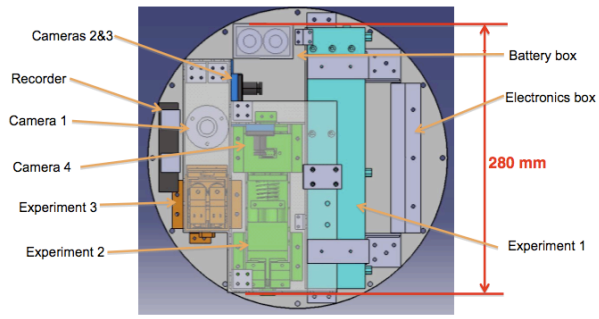

Fig 10 Overview of Redemption module from above

Three test cells are filled with three different kind foam with different proprieties. The aim of experiment is to evaluate the best expansion ratio and the speed of hardening of the foam. The expansion ratio is checked through the cameras and the hardening through the thermo sensor. The rigidity and the mechanical

properties of the foam depend on the temperature of the foam. Having data on temperature evolution means to have data on mechanical proprieties of the foam.
The second experiment consists in a free spray experiment where foam is sprayed in a free space to check the disposition of the foam. Basically the liquids, when are in space condition, without gravity, are disposed in bubbles. The foam starts its reaction and solidification in the same moment of contact between the liquids. It means that the foam just outside of the mixer, it is already under solidification. It is expected that, through this reaction, the foam will not assume a shape of a bubble just outside the mixer but that it will be possible to spray on the Plexiglas surface located at 5 cm from mixer. The importance of this instrument is that it will give data on the feasibility of an ADR mission with this system.
The last experiment consists in inflating a structure with the foam [5]. This structure is a kind of sock that allow the gases of the reaction to go out form the fabric, to guarantee that the inflation is provided only by the foam. In future, it may be possible to use foam to inflate larger structure.

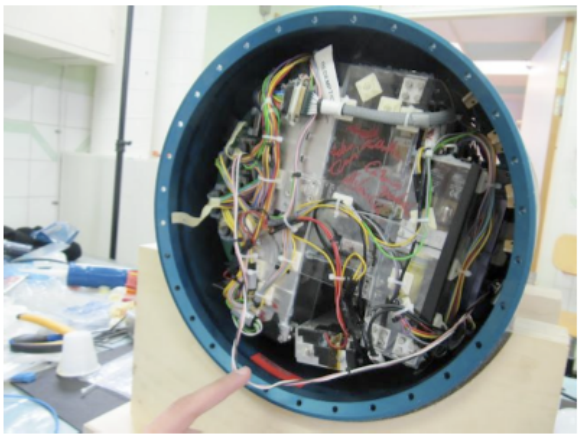

Fig 11 Redemption module fully integrated in the skin

The Redemption module (Fig 11) was also provided with a safety plug for the tests. Redemption is a "one shot" experiment. After the production of the foam, it has to be completely opened, cleaned and reassembled. The safety plug was used to avoid accidentally deploy of the foam during the tests (Fig 12).
The module was provided by an anti leak system. It was covered by polycarbonate around the test cell to avoid foam and liquid leakages. The polycarbonate (provided by Mareco plastic) was sealed. There was also a sponge on the bottom with the capability to absorb the entire amount of liquids present in the module. [2]

1 Fig 12 safety plug of Redemption

TESTS ON THE MODULE

Redemption experiment had to pass different tests to be integrated on Rexus12 sounding rocket.
The first test was the vibration test. Redemption module performed vibration test at ZARM Laboratory of DLR in Bremen. During this test the tanks of the foam were filled with water. Using water is a conservative way to make this kind of test, because water is less viscous and dense than the foam liquids: if water leakages were not registered, the experiments can be considered safe also for the foam. The vibration test went as expected,with no leakages detected; the experiment was ON during the vibrations, to simulate the launch conditions. During the vibration test, from the internal cameras of the experiment, also some videos of the vibrations of the test cells were recorded. The initial and last resonance vibrations were very similar. Only one screw from the video recorder (a commercial component of the experiment) was affected by vibrations. As a solution to this problem, all the screws from commercial components were glued and the test was considered as passed (Fig 13).
The integrations test was performed just after the vibration test. All the experiment of the rocket were integrated, and it was performed a cold countdown. Again all the part of the experiment were working nominally and there no conflict with others experiments or Rexus modules was detected.

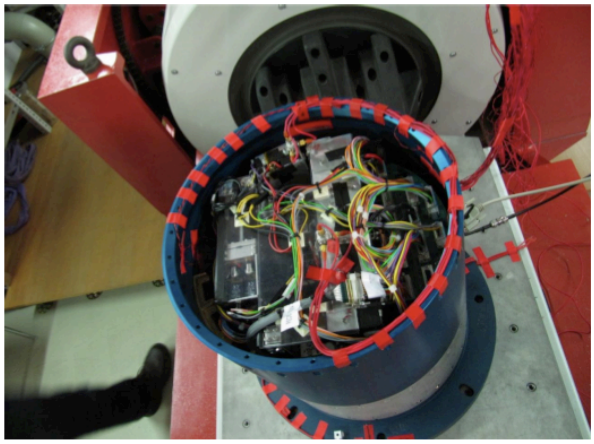

Fig 13 Redemption module at vibration test in ZARM

The bench tests were performed after a couple of week. This test gives a lot of important information about the liquids. The tests consisted in the integration of the payload with the service module and the recovery system, two cold countdowns and one "hot" countdown where all the experiments had to run. The test was in part failed because the liquids did not pass trough the electro valves. After an investigation it was discovered that the problems were caused by some water trapped inside the valves. The valves used during the bench tests were the same used during the vibration test, where water was used. The valves, after the vibration test, were dried but were not open. The little amount of water inside the internal pipes of the valves was enough to make a reaction with one of the two liquids and to stuck the fluids (Fig 14). During the bench test al systems worked nominally and the problem was just the reaction of the liquids with water, so there was no need to change the experiment design. For mitigate the humidity problem, it was decided to avoid any contact with water or humidity of the liquids and of all parts that had to be in contact with reagents. [2]

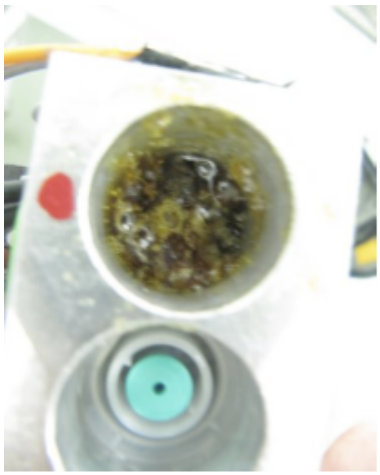

Fig 14 Effect of the humidity on one of the liquids

LAUNCH CAMPAIGN

REDEMPTION flown on board of Rexus12 on 19 march 2012. To avoid the humidity problems all the components that during the experiment had to be in contact with liquids was replaced with new components in a special room provided by SSC (Space Swedish Corporation). Redemption was totally dissembled and reassembled. In this room the humidity never exceeded the 15%. During the filling operation of the syringes only one person was present, to avoid the rise of the humidity level due to the number of people in the room (fig 15). [4]

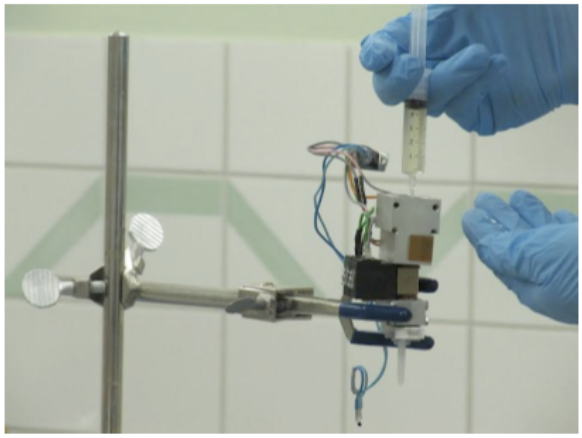

Fig 15 Selfshoot in dry room during the filling operations

Then, Redemption (Fig 16 and Fig 17) was integrated with the payload and sub systems of the rocket. It was performed a ground test before the integration of the engine and all was nominally. The launch window was scheduled three days after from the integration. During the Test Countdown Redemption lost the TV channel camera, which was working during the bench test. After a discussion it was decided anyway for the GO.

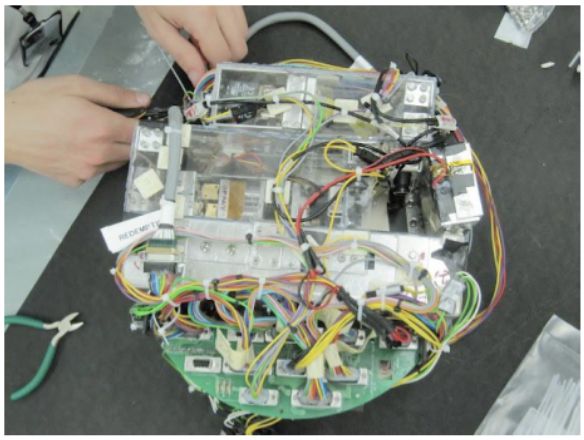

Fig 16 Redemption reassembly operations

During the pre launch the condition of the experiment were nominally. The temperature of the liquids were 60°C, thanks also to the hot air blower on Redemption module provided by SSC. During the countdown the signal to switch off the Redemption heater (powered by the umbilical) was delayed after the switching to internal battery of the rocket. It means that the internal rocket battery powered heaters of Redemption. This situation was meant to be avoided to not discharge the battery of the service module; during the preparation of the launch campaign it was indeed a requirement of the launcher. At the moment of LiftOff Redemption lost its telemetry that never came back during all the flight. Moreover Rexus12 (Fig 19) also showed problems. The recovery system did not work and the payload crashed instead of soft landing. From the analysis of the telemetry of the rocket it was clear that the problem on Redemption experiment was not due to a communication problem but to a failure on the Redemption power line.
After the recovery of the module it was possible to start an investigation. The structure of the experiment (produced by MCM spa) and the testcells survived to the crash. There were no leakages from the system. Test cells were still intact. To be sure that there were no problems of humidity some test cell were fired with success. The main board broke at the crash, but giving powering it directly from the cable of the module it was possible to detect a power consumption, so a problem in harness was excluded (Fig 18).

Fig 17 Payload of Rexus12 fully integrated

Moreover the camera that was not working during the test countdown was working after the crash.
The investigation did not show a reasonable cause of the power failure from the part of Redemption module. One of the possibility could be that the microcontroller did not survive to the G loads. Anyway the micro controller survived without problem to the vibration test and it was successfully used in previous REXUS missions.
On the digital recorder, the registration was interrupted just in the moment of the liftoff and it is not possible to see any vibration. Unluckily the micro controller was physically damaged by the crash and it was not possible to check it to rule out a failure at lift off.

Fig 18 Investigation after the crash: PCB damaged

CONCLUSION

Redemption experiment flown on board of Rexus12 rocket the 18th march 2012. Unluckily, the experiment lose the power at lift off. The analysis indicates that the rocket may had some malfunction, but it was not possible to find an exact cause of the issue.
In any case, the foam releasing system passed without problems all the test campaign before being accepted and integrated on the rocket.
The structure survived the launch and the crash, and after the recovery the mechanical system was still in working condition. The heating system also was maintained the temperature or the reagents before the launch as expected.The liquids did not create any problem to the rocket even after the crash, and the anti leak measures worked as expected.
Even if all the ground test show that the experiment can work, a test on milli gravity condition is still required to prove the feasibility of the ADR system based on polyurethanic foam. For these reason the team is still looking for a flight opportunity.

Fig 19 Rexus 12 Rocket

REFERENCE

[1]“Controlling the growth of future LEO debris populations with active debris removal” J-C. Liou, N.L.Johnson, N.M.Hill

[2] Toschi S., Valdatta M., Spadanuda A., Romei F., Piattoni J. Candini G.P. REDEMPTION SED (Student Experiment Document)

[3]F. Piergentili, M.L. Battagliere, G.P. Candini, J. Piattoni, F. Romei, A. Spadanuda, S. Toschi, M. Valdatta, F. Santoni, “REDEMPTION: a microgravity experiment to test foam for space debris removal” IAC-11- A6,5,7,x11777, 62nd International Astronautical Congress, 3 – 7 october 2011, Cape Town, SA.

[4] Toschi, Valdatta, Spadanuda, Romei, Piattoni, Candini Santoni, Piergentili "Redemption: a student experiment proposing a solution to Active Debris Removal", IAC-12,E1,9,9,x14722, 63rd International Astronautical Congress, Naples 2012

[5] Valdatta, Romei, Spadanuda, Toschi, Candini, Piattoni, Piergentili, Sanotni "Inflatable system based on polyurethanic foam", IAC-12,D1,1,12.p1,x15216, 63rd International Astronautical Congress, Naples2012

[6] Valdatta M., Bellini N., Rastelli D., “Adr mission with small Satellite”, UNISEC Mission Idea Contest 2 finalist paper, 4th Un/Japan Nanosatellite Symposium, Nagoya October 2012

[7] Valdatta M., Bellini N., Rastelli D., Pirgentili F., Santoni F., “Demonstration of feasibility of ADR mission using cubesat”, “IAA-B9-1407P – 9th IAA Symposium on Small Satellites for Earth Observation. April 08 - 12, 2013 Berlin, Germany

[8] Rizzitelli, Bellini, Candini, Rastelli, Romei, Locarini, Spadanuda, Valdatta, Bagassi "Active Debris System based on polyurethane foam". 6th European conference on Space Debris ESA/ESOC 22/ 25 April 2013 Darmstadt , Germany 6a.P5ID:2818781

SOUNDING ROCKET SYSTEM OF CHINA "MERIDIAN SPACEWEATHER MONITORING PROJECT"

QinSu Peng[(1)] QuanBin Ren[(1)] YangJun[(2)]

(The 41st Institute of The Academy of China Aerospace Science And Technology Corporation, National Key Laboratory of Combustion Flow and Thermo-structure. 710025)

[(1)]NO.112 section office, 169# mail box, Xi'an, China. Email: chbert@aliyun.com
[(2)]169# mail box, Xi'an, China. Email: chbert@aliyun.com

ABSTRACT: Sounding Rocket System of China "Meridian Space Weather Monitoring Project" (MSWMP) refers to TY-4A meteorological rocket and TY-3C sounding rocket which developed by the 4th Academy of China Aerospace Science And Technology Corporation. The two rockets had completed flight missions in 2010 and 2011. During the flight process, the rocket accomplished body separate, nose separate, payload release and the like action, which provide a favorable environment for sensors carried on them. TY-4A is a reformative type of the TY-4 rocket, which had completed flight mission for 40 times, and also it is the first prototype in China. The carrying capacity and the flight height of TY-3C Rocket are the most excellent in China at present. The synthetical technology level of the rocket is also on domestic top level as well as the same level on overseas.

KEY WORDS: Meridian Space Weather Monitoring Project, Sounding Rocket, Flight test.

Project background: Magnitude basic establishment technology project of China "Meridian Space Weather Monitoring Project".

1 Introduction

"Meridian Space Weather Monitoring Project" is the first magnitude basic establishment technology project of China. It aims to build a large integrated space environment monitoring system which can continuous operate cross-region. By using detecting means such as geomagnetism, wireless, optics and sounding rocket, the project will keep monitoring the atmosphere, ionosphere and magnetic field between 20km and hundreds kilometers up the earth, and also monitoring the environmental parameters of interplanetary space [1].

The Sounding Rocket System is an important part of "Meridian Space Weather Monitoring Project System". The Rocket System can send scientific equipment to as high as 60 to 200 kilometers height using series of sounding rockets, and the equipment can detect the electric field as well as plasma of interspaces between 60 to 200km height, which offers data to study the territorial characteristic in low latitude area of the country [2].

2 Sounding Rocket System

Sounding Rocket System of China "Meridian Space Weather Monitoring Project" refers to TY-4A meteorological rocket and TY-3C sounding rocket which developed by the 4th Academy of China Aerospace Science And Technology Corporation (ACASTC). The major properties of the rocket system present in Tab. 1 and Tab. 2.

Table 1 TY-4A rocket system properties

Item	Value
Rocket length	3380mm
Payload Capsule Diameter	ϕ204mm
Tail wing span	704mm
Take-off weight	150kg
Payload mass	3kg
Instrument cabinet Temperature	≤70℃
Flight axial overload	≤25g
Max velocity	1300m/s
Apogee	≥70km
Detector fall speed	≤150m/s
Payload working height	15km～60km

Table 2　TY-3C rocket system properties

Item	Value
Rocket length	6800mm
Payload Capsule Diameter	ϕ400mm
Tail wing span	1460mm
Take-off weight	1100kg
Payload mass	50kg
Instrument cabinet Temperature	≤70℃
Flight axial overload	≤25g
Flight lateral overload	≤10g
Max velocity	2000m/s
Apogee	200km
Payload working height	15km～200km

2.1　TY-4A meteorological rocket

TY-4A meteorological rocket is a reformative type of the TY-4 rocket. It is a single stage uncontrolled rocket. It is composed of nose and body two parts. While head part contained fairing, crew module, ejection separating unit and scheduling control electrocircuit unit. Space detector fixes in fairing, the bottom of it is connect with a special instrument locate on the bottom of fairing. The body part of the rocket is composed of motor, tail capsule and four tail wings.

Figure 1　The theoretical configuration and ensemble composition of TY-4A rocket

The space detector on the rocket is “HaiYan-A”, which applied to detect the vertical distributing plane of atmosphere meteorologic factors among 60km height, such as temperature, air pressure, wind speed and wind direction, etc.

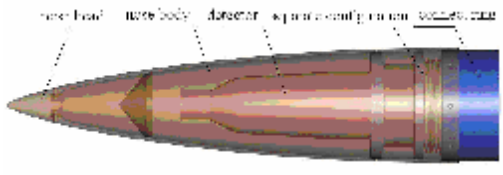

Figure 1　TY-4A nose configuration

Working programme: When rocket fires and takes off, scheduling controller starts to time, when goes to the scheduling time point, controller gives out firing orders to complete nose separate and body separate, parachute with detector together is shot off, fairing separate configuration acts at the same time to pop fairing. Parachute puffs when descending to 70km height. Under the effect of the parachute, detector falls slowly and detects atmosphere parameters.

Flight test results: at June 3rd, 2010, the magnitude basic establishment technology project-“Meridian Space Weather Monitoring Project” and the synthetical test project of the eastern hemisphere space environment, TY-4A rocket with GPS detector on it successfully completed the flight test, which obtained the high precision data about atmosphere temperature, pressure and wind spread between the height of 20km and 60km in the low latitude area of China.

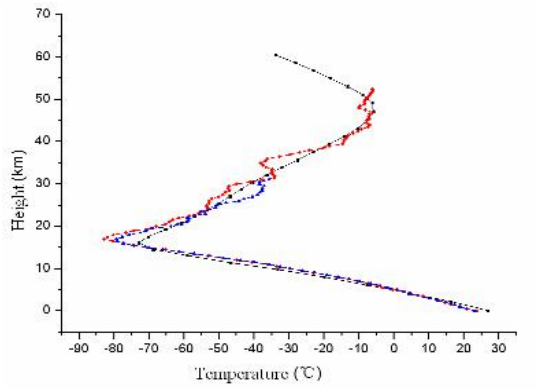

Figure 3　Height-Temperature

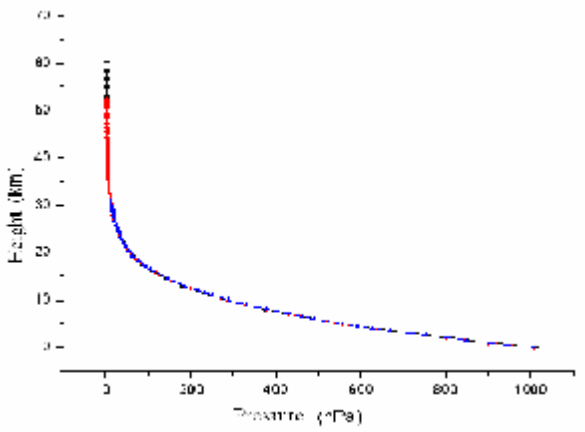

Figure 4　Height-Pressure

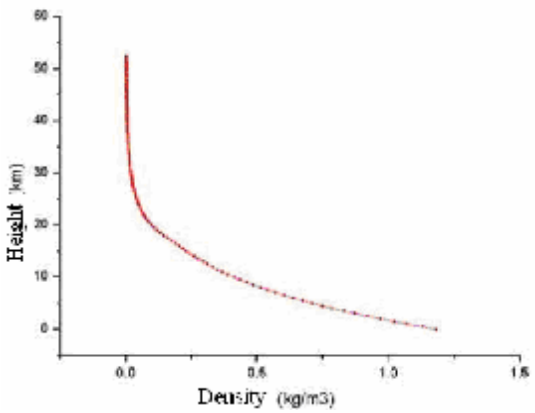

Figure 5 Height-Density

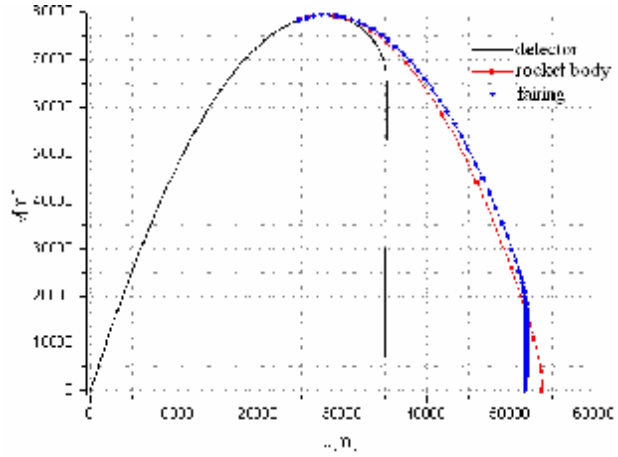

Figure 6 Trajectory

2.2 TY-3C Sounding rocket

TY-3C sounding rocket is a single stage and empennage stabilization rocket without attitude control system. It is composed of four subsystem when partition on function, they are body structure, solid propulsion rocket motor, scheduling control system and payload.

Body structure is the main body of the rocket, go through the whole flight process. It need to complete actions such as body separate, nose separate and payload release, which can offer reliable environment for payload. Body structure includes nose sect and body sect, while nose sect include fairing, instrument cabinet, payload module and crew capsule. Body sect includes motor and tail combination (tail fin and stern compartment). The fairing composed with helmet and cone. The joint surface between helmet and cone is the fairing separate surface. The joint surface between payload module and crew capsule is the separate surface of nose-body. Body structure shows in Fig 7.

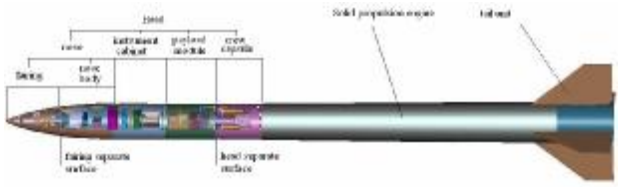

Figure 7 The theoretical configuration and ensemble composition of TY-3C rocket

Control system composed with scheduling control computer, distributor, cable and batteries. The function of the control system include: Accomplish schedule setup and detect cooperated with ground system before take off, give out scheduling orders during the flight process which control the action of rocket system such as nose separate, head-body separate, electronic sensor spread

Rocket motor is composed of igniter, combustion chamber and nozzle. Igniter uses dual insensitive combustion tube, which has the characteristic of electrostatic prevention, RF prevention, high security and reliability. Combustion chamber connects with crew capsule and stern compartment. The fuel of the motor is HTPB composite solid propellant. There is a layer of thermal protecting coating outside the shell of the motor, which can protect outside shell of the motor to resist aerodynamic heating during the flight process.

The payload on the rocket is “KunPeng NO.1” sonde system which developed by Space Science Center of Chinese Academy of Sciences. It includes three detecting instrument, they are electric field instrument, atmospheric element detector and Langmuir probe. There are some rocket instrument also in the payload module, such as rocket communal equipment, rocket launch system, attitude measurement instrument and GPS, etc.

Working programme: Sounding rocket is controlled by scheduling control system, when rocket fires and takes off, attitude measurement instrument, GPS and control system are working. Between the ascend height of 15 to 75 kilometers, atmospheric element detector working. On point of 43s, the explosive bolt which connectted payload module and crew capsule unlocked, the head of the rocket then separate from body, while electric field sensor working. On point of 46s, the explosive bolt which connected fairing and cone

unlocked, fairing then separated. On point of 47s, pin puller unlocked, electron detector working, while the flight height of the rocket achieved 70km on this point, satisfying the exploration environment of Langmuir probe and electric field instrument.

Flight test results: The rocket system had finished it's first flight test on may 7th, 2011. The rocket flied well, system on rocket worked well, telemetering system tracked well. This is the first time in China that had accomplished the exploration of space electric field between 60km to 200km, also the first time for detecting the space ionosphere between 60km to 200km by using Langmuir probe. During the flight process, the attitude parameters was got from attitude measurement device, the trajectory was got by GPS. Data indicate that the apogee of the rocket flight path reached 194km, that 's the highest among the sounding rocket in China, the flight test is succeed totally.

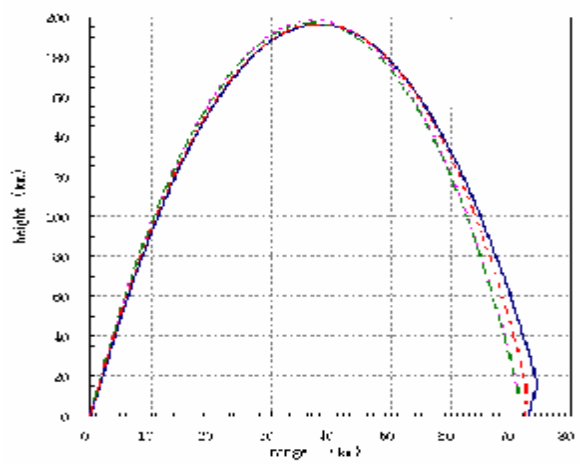

Figure 8 Range-Height curve

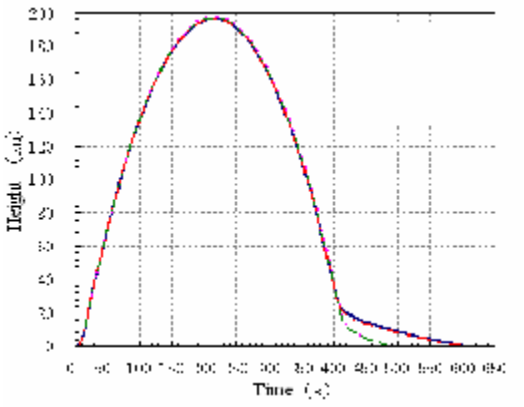

Figure 9 Time-Height curve

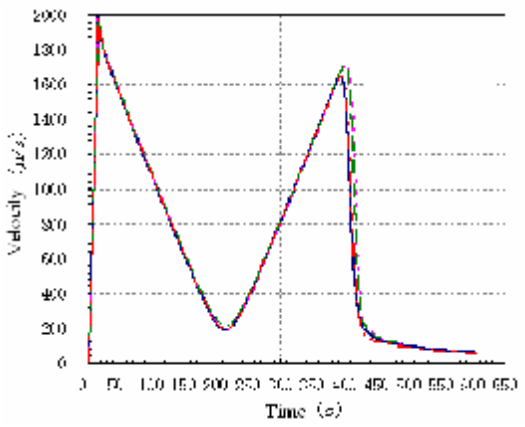

Figure 10 Time-Velocity curve

3 Ground equipment

Ground equipment include test-launch control system, launch equipment and telemetering ground equipment. Test-launch control system complete the synthetical test of rocket electrical system and launch control of the rocket. It adopts distributed arrangement for fore-end and back-end. Fore-end includes conditioning controlled computer, electrical source module, instrument module, cables and UPS power. The system accomplishes test and control of rocket equipment besides sending the test data to back-end. back-end includes test computer, launch control platform, GPS time unification equipment. It accomplishes inspecting rocket state, saving data and firing. There are two cables connect the fore-end and back-end——a straight cable and a serve optical cable.

The rocket launcher is also made by ACASTC. It applied fluid drive system to finish the angle adjusting and locking, combined a mechanism lock. When the attitude angle was locked, ground bolts used to fix launcher on the ground. By this method, the whole equipment seems to hold well stability. The Launch elevation can be tuned between 0 and 90 degree. The longest time for tuning is about 8 minutes. A optical measuring instrument was used to measure the elevation angle with a precision about 1 cent. The azimuth angle is fixed by the position of ground bolts which connected to the pedestal of the launcher.

Figure 10 The configuration of launcher

Telemetering ground equipment composed with telemetering receiver. It was developed by National Space Science Center. It accomplishes the task of trajectory tracking and exploration data real time receiving.

4 Tag

Sounding Rocket System of China “Meridian Space Weather Monitoring Project” is the first time to use minitype rocket to accomplish space exploration between 15km and 200km height. It padded the vacancy of upper air space detection in China. The synthetical technology level of the rocket is also on domestic top level as well as the same level on overseas. As a low cost, high reliability, quick launch, high detect scope platform, the rocket can carry all sorts of payload on user’s demand, such as atmosphere physics exploration, micro-gravity test, missile technology test, communication relay, electric disturbance, reconnaissance and so on, which makes a good currency and well foreground of the rocket system.

References

1. Jiang.XiuJie. The develop status and trend of Sounding rockets. [J]. Science Technology Review, 2009, 27 (23)
2. Construction project management team of MSWMP. Introduction of the mission about MSWMP sounding rocket system.[M]. 2011

MASER-12 SOUNDING ROCKET; A HOT MISSION IN COLD ENVIRONMENT

G. Florin[1], M. Abrahamson[1], P. Holm[1], Y. Houltz[1], C. Lockowandt[1], M. Lundin[1], J. Thorstenson[1]

[(1)] Swedish Space Corporation, Science Services Division, P.O. Box 4207, SE-171 04 Solna, Sweden
E-mail: gunnar.florin@sscspace.com

ABSTRACT

MASER 12 sounding rocket with five experiments was launched from Esrange Space Center in northern Sweden on 13 February 2012. The payload, which accommodated 272 kg of scientific experiments involving science teams of universities and institutes from six European countries, experienced 6½ minute of high quality micro gravity conditions below 10^{-4} g. The payload, including human blood cell samples, was safely retrieved to the launch area 2½ hours after lift-off, and the mission was declared 100 % successful.

MASER 13, scheduled for launch in spring 2015, will provide more than six minutes of micro gravity to 5 experiments; CDIC-3, XRMON-SOL, ARLES, GRAMAT and SPARC, where the latter two are plant experiments re-using the BIM experiment module flown on MASER 12 while ARLES is a new droplet evaporation experiment. CDIC-3 and XRMON-SOL experiment modules are re-flights of previously flown modules but adapted to the science requirements of the new experiments.

1. MISSION DESCRIPTION

MASER 12 was launched on 13 February 2012 at 07:32 LT from Esrange Space Center in northern Sweden. The mission was accomplished by SSC and its sub-contractors for the European Space Agency (ESA).

Figure 1. MASER 12 Launch from Esrange Space Center

SSC's sounding rocket programme MASER provides a payload, consisting of 4 to 7 experiment modules (17" diameter), with about 6-8 minutes of high quality microgravity, normally less than $1x10^{-5}$ g in all axes. During the flight, it is typical to interact with the experiments in real-time using high speed telemetry and telecommand as well as real-time high resolution digital video received on ground.

For MASER 12, the since 2-stage VSB-30 solid fuel rocket motor was used, the new work horse which has replaced the formerly used Sky Lark 7 rocket motor. The payload accommodated five experiments in four experiment modules and had a total mass of 389 kg and a length of 4.92 metres.

The duration of the microgravity phase was 6 minutes and 30 seconds, during which the five experiments were carried out, see Tab. 1.

Table 1. Scientific experiments flown on MASER 12

Acronym	Investigators	Exp. title
STIM	Dr. A Cogoli, Zero-g LifeTec GmbH, Zurich Pr. O Ullrich, University of Zurich Pr. P Pippia, University of Sassari	Signal Transduction in human T-cells in microgravity:
MICIMMUN	Pr. Maikel Pepplenbosch, Erasmus Medical Centre, Rotterdam	Microgravity in adaptive Immunity
BIOMICS-2	Dr. T Podgorsky Université J. Fourier Grenoble	Dynamics of cells and Biomimetic Systems
SOURCE-2	Dr C Colin, IMFT Toulouse Dr P Behruzi, Astrium Bremen Dr J Lacapere, AirLiquide Sassenage Dr M Dreyer, ZARM Bremen	Convection boiling and condensation: local analysis and modelling of dynamics
XRMON-GF	Dr. Henri Nguyen-Thi, L2MP, Univ. Paul Cézanne Aix-Marseille III	In-situ X-ray monitoring of advanced metallurgical processes under microgravity and terrestrial conditions

Proc. '21st ESA Symposium European Rocket & Balloon Programmes and Related Research', 9–13 June 2013, Thun, Switzerland (ESA SP-721, October 2013)

1.1. Summary of the mission preparations and flight

The STIM and MICIMMUN experiments required careful planning, thorough preparations and co-ordinations, making good use of the laboratories in the launching area before and after flight. XRMON Gradient Furnace had requirements on pre-heating prior to lift-off. As during its previous flight, BIOMICS-2 utilized one of the advantages with sounding rockets; installation of the experiment cells into the payload shortly before launch during the countdown sequence. Source-2 experiment contained 4 consecutive experiment phases, and in order to execute the full experiment sequence during the flight, extensive trimming, training and rehearsal of the flight sequence and operators had foregone the flight.

All experiments but the biological STIM and MICIMMUN experiments used systems for optical monitoring. The X-ray diagnostics system of XRMON-GF used on-board storage of the scintillator CCD images. BIOMICS-2 and SOURCE-2 modules used digital video cameras, and during the flight the images from the in total 4 cameras were stored and also transmitted to ground in compressed format by the Digital Video System (DVS) and the MASER Service Module, occupying 10 Mbps dedicated bandwidth, of which SOURCE-2 with its single high-speed camera occupied one full link on its own. In addition to the experiment cameras, there were one analogue camera recording the deployments of the recovery parachutes and two on-board flight observation cameras, one of which being HD-camera, filming the complete flight and recovery operations.

100 % scientific success rate is attributed to the Maser 12 flight, and in the case of SOURCE-2, there was quite unexpected behaviour of the experiment. Two of the experiments modules are planned for re-flight on the next MASER 13 mission, but with different scientific objectives and requirements.

1.2. Mass saving technologies

As a means to improve the capabilities of sounding rockets, mass-saving technologies were applied for the MASER 12 mission such as use of batteries with higher energy density and use of outer structure materials of less mass than the commonly used aluminium alloy.

Following the recommendations of the outcome of the preliminary design, Li-ion batteries with higher energy density were implemented in BIM-2 and SOURCE-2 modules.

Regarding structure materials, after considering several alternatives such as a more optimised Al alloy design or using Mg alloys, the choice fell on the introduction of CFRP (Carbon Fibre Re-inforced Plastics) as outer structure material for appropriate modules, which theoretically could provide a 40 % mass saving. The module that was found most suitable for application of CFRP outer structure was the SOURCE-2 module (see Figure 2), with its 70 cm length resulting in a considerable mass saving of 6 kg. For heat protection against the thermal environment during the descent phase, the CFRP was covered by an outer layer of Zirconium dioxide.

Figure 2. Outer structure of the SOURCE-2 module made of CFRP with glued inserts and fitting port-lets

Moreover, light-weight material in carbon-fibre reinforced plastic material (CFRP) was adopted for the outer structure of SOURCE-2 module, gaining approximately 7 kg of payload mass. There were 24 layers of CFRP covered by a layer of ZrO2 acting as heat insulator.

1.3. Payload configuration

When configuring the payload, due attention was to be given to placing XRMON-GF and SOURCE-2 as close as possible to the centre of gravity CoG, so that they would be least affected by residual accelerations during the microgravity phase. BIOMICS-2, which housed the GPS and flight observation cameras as a heritage from Maser 11 flight, had hence already its predetermined position in the forward end, as was the case on MASER 11. BIM-2 was therefore positioned in the aft end. With this configuration, CoG was positioned in the lower third of XRMON-GF module, complying with the needs of SOURCE-2 and XRMON-GF.

The mass of the scientific modules, 272 kg, constituted 70 % of the total payload, which was 4.92 m long and had a lift-off mass of 389 kg.

1.4. Campaign and flight preparations

Initially, MASER 12 was to be launched in November 2011. As a consequence of the fairly mild autumn in the impact area, lakes and rivers were judged not sufficiently frozen to allow for safe recovery of the payload of the preceding TEXUS mission, scheduled for launch in early November 2011. With postponement of Texus launch campaign by three weeks into the colder part of November, MASER campaign was shifted to February 2012, as the short days in December would not provide enough hours of day-light conditions to allow

for safe recovery of the biological samples within four hours after launch.

The over eighty launch campaign participants were then welcomed in February by an arctic climate at its peak, with temperatures not exceeding -30°C during a week, and mostly ranging from -40°C up to -35°C. Not only was this extraordinary for scientists coming as far away as from southern Italy, but also for the maintainers of the Esrange ground facilities, who day and night had a person in place to survey the temperature in the launch tower, safeguarding that minimum temperatures for the rocket motor were not exceeded. When the high pressure positioned over northern Scandinavia with pressure readings up to 1058 mbar finally weakened, the payload installation in the launch tower could finally take place after two days hold.

All four laboratories of Esrange Space Center were used by experiment teams during the campaign. The biological experiments STIM and MICIMMUN required three laboratories all together for preparation and post-flight handling of the samples. With weather being bitterly cold during preparations, the humidity levels were, as a consequence, below 5 % Rh, which required installation of humidifiers in the laboratory to safeguard the survival of the bio samples.

The count-down procedure had to be carefully co-ordinated with accessibility at Kiruna Hospital blood centre, where blood samples were collected from local blood donors every day 24 hours before each launch attempt. As a matter of fact, the constraints on early launch preparations reduced the launch window to some few hours, as preparations for next launch attempt had to commence around noon the day before the attempt. In order to mitigate the risks for unwanted and unplanned holds in the narrow count-down window, a full dress rehearsal involving ground stations as well as scientific preparations was carried out, following the same time scheme as foreseen for hot preparations and count-down. The outputs from the dress rehearsal were valuable and our experience was that all planned interventions, actions and operations shall be part of a dress rehearsal.

Although the block-house in launching area – from where the payload preparations and flight operations were co-ordinated and from where interaction on experiments were carried out – gave an impression of being more than filled with scientists and payload engineers, the Science Centre in Esrange main building was extensively used by scientists and ESA staff following the experiments' behaviours during flight, in communication with the colleagues in the block house.

1.5. Flight and recovery

The mission was 100 % successful. The flight was flawless. During microgravity phase, no rate control correction pulses were needed. The payload reached the expected apogee of 260 km and the microgravity phase was 390 seconds (6½ minute) long. The deceleration forces at re-entry were however quite high, 46 g. The payload was retrieved back to the science teams waiting at the launch area within 2½ hours after launch.

As an eyebrow raiser, the two first layers of SOURCE-2 CFRP structure had been delaminated together with the ZrO_2 layer, making the module look worn and haggard, although the experiment and payload never was put at risk. CFRP structures experience significantly higher temperatures than aluminium structures, due to local heating, at least 370°C, possibly up to 450°C or more, and when using CFRP in future flights a CFRP resin with higher temperature resistance value will be used.

Figure 3. Post-flight photo of CFRP Structure

1.6. Video System performance

The digital video system performed for XRMON-GF, SOURCE-2 and BIOMICS-2 experiments loss-less on-board storage of over 53,000 frames of which 99.84% were good; only 84 frames were corrupt or missing. The real-time downlink of images was equally successful; only 0.2 % of the frames transmitted over the total 10 Mbps links were corrupt.

2. MISSION OBJECTIVES

In the initial phase, eight experiment candidates were part of the evaluated possible payload configurations. With due consideration of the scientific priorities, rocket boundary conditions such as mass and length limitations, and in order to limit the potential development risks, the final payload complement selected for MASER-12 consisted of the modules BIOMICS-2, SOURCE-2, XRMON-GF, and BIM-2 (with STIM and MICIMMUN experiments) (see Fig.1) while the non-selected experiments now have been selected for the next-coming MASER flight number 13.

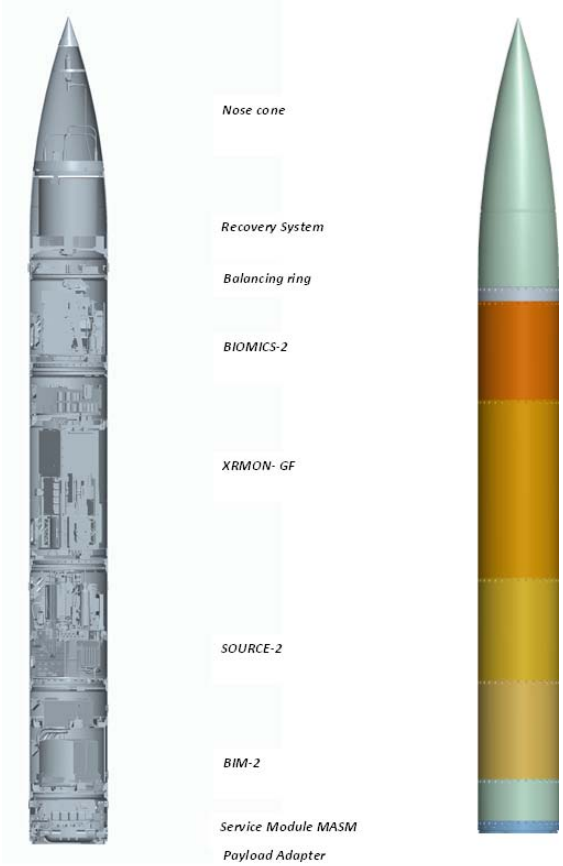

Figure 4. MASER 12 payload configuration

2.1. BIM-2 experiment module

The BIM-2 (Biology In Microgravity) experiment module contains two cell biology experiments, STIM (Signal transduction in human T-cells in microgravity), and MICIMMUN (Influence of Microgravity on the Activation of NF-κB/Microgravity in adaptive immunity).

The main objective of the first experiment, STIM, is to investigate in T-cells the early events involved in signal transduction through membrane-proximal pathways and to link the initial signals to nuclear transcription, factor activation, and nuclear response.

In the second experiment, MICIMMUN, the influence of microgravity was studied on the mechanism that activates the NF-κB enzyme, one of the principal regulators in monocytes and lymphocytes, as a transcription factor, of inflammation and immunity.

BIM-2 design is to a large degree similar to the BIM module flown on MASER 10 in 2005, however the module overall design has been adapted to host biological late access systems for different biological disciplines, and will be reused in next mission for performing plant experiments.

2.1.1. BIM-2 Experiment System

The BIM-2 experiments are performed in 48 experiment units of two different types, one where the culture medium is mixed with other liquids and one where the culture medium is flushed and replaced during the microgravity period of six minutes. Cultures in microgravity conditions, and on a 1 g reference centrifuge on board the module, are activated simultaneously with a reference on-ground culture.

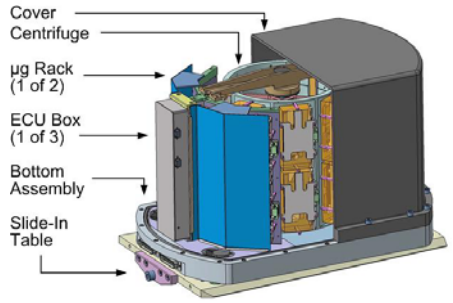

Figure 5. BIM-2 Experiment System

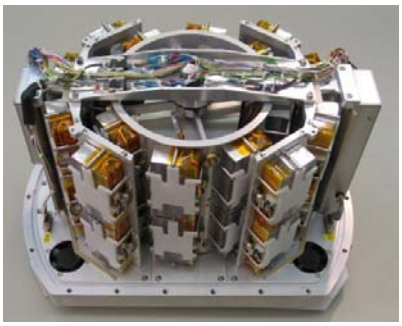

Figure 6. BIM-2 Experiment central centrifuge

The experiments are performed in 48 experiment units of two different types; a flushing cassette type and a mixing cassette type. In the flushing cassette, the scientific samples adhere on a sample glass and are exposed to the activation and fixation liquids by means of flushing the sample glass. In the mixing unit, which was new development for BIM-2, the activation and fixation liquids are mixed in a larger container with the scientific samples solution.

Cultures in microgravity conditions, and on a 1 g reference centrifuge on board the module, are activated simultaneously with a reference on-ground culture.

The experiment units are prepared few hours before launch, then integrated in the late access unit systems which are, because of the limited lifetime of the samples, designed to be retrieved from the module already at the landing site.

Compared to BIM flown in 2005, the BIM-2 module has improved thermal system with new heat exchanger design in the late access unit, new location of electronic deck and larger hatch for alternative experiments.

Figure 7. BIM-2 module with Experiment System.

2.1.2. BIM-2 flight preparations

Both experiments required carefully planned and detailed schemes, with blood sample collecting at specific times from local blood donors carried out at the Kiruna hospital almost 24 hours before anticipated lift-off. BIM-2 definitively set the pace for the ground preparations of the flight! Once the blood cell samples were installed in the late access unit incubator, the control system maintained the temperatures within specified 36.5 ±0.5°C range for the quality and life of the samples, with a maximum gradient between all experiment cells of ±0.2°C.

The extremely cold weather conditions during launch preparations forced the experiment team to install humidifying equipment in the laboratory; else the low relative humidity of 5 % would harm the samples during preparations.

2.1.3. BIM-2 flight result

The experiment system performed excellently during ground operations as well as during the whole sequence in microgravity, with the centrifuge spin-up and the activations of each experiment cassette were carried out as pre-programmed.

During the experiment phase in micro-gravity the sample temperatures, which were one set of the challenging critical parameters to design for, were well within the required limits, with less than 0.4°C temperature difference among the cell culture chambers.

In parallel with the experiment activations during flight, the 1g Ground Reference Unit placed in an incubator at Esrange, was operated and – for equal g-force direction as the on-board centrifuge samples – physically turned when the flying centrifuge started, and was turned back when it stopped.

As often is the case with flight of biological material experiments, the specimens were brought back by a dedicated retrieval helicopter from the payload impact site (see Figure 8). Two and a half hour after launch the experiment system was back to the launch area, where the flown microgravity and 1-g reference samples were handed over to the science teams, together with the ground reference samples. Visual inspection of the BIM-2 module after flight showed no visible mechanical damages.

Figure 8. Recovery operation of STIM and MICIMMUN experiment samples at landing site.

The main module will be refurbished and reused in the Maser 13 mission, this time with a different type of biological experiment.

2.2. SOURCE-2 experiment module

Inheriting from the successful MASER 11 mission, the SOURCE module, which was dedicated to research of fluid behaviour in propellant tanks as part of the ESA MAP project AO-2004-111 and of the COMPERE program, was selected to re-fly with thoroughly modified experiment H/W, in order to study convective boiling and condensation in a single component fluid, namely hydrofluoroether (HFE) a complex organic solvent, in co-existence with its vapour. The scientific responsibility of the SOURCE-2 experiment again included the four participant teams of SOURCE-1: ZARM, IMFT, Astrium and Air Liquide.

SOURCE-2 experiment type was a benchmark on fluid behaviour in tanks to test hypotheses and numerical predictions

The multiple objectives of the experiment were to

- follow the liquid and the vapour stratification and the pressure evolution during all flight phases correlated to the free surface position
- follow the effect of wall heat flux on the contact line and the free surface during the ballistic phase, together with boiling at the heated lateral wall

– follow the boiling bubble behaviour (growth, detachment, motion and recondensation) on a local heater during the ballistic phase and obtain transferred heat flux to the bubble formation.

– follow the effect of depressurisation and repressurisation at the end of the ballistic phase.

– follow the effect of pressure evolution in the tank due to active mixing of the bulk liquid by recirculation.

2.2.1. SOURCE-2 Overall design

The 693 mm high and 58 kg module contains a pressurised experiment cell with transparent wall, in which the experiment liquid during the flight is exposed to pressures varying from 4 to 0.5 bar and 25-100° C temperatures. To achieve local boiling, a local heater in contact with the experiment liquid is used.

The optical system with digital Dalsa 4M60 camera (2352x1728 pixels) provided a resolution of 20 px/mm for a view of 120x70 mm. Images at a speed of 32 MBps were stored in a solid state flash memory, and downlinked to ground in compressed form at 5 frames per second for real-time analysis and interaction during the experiment.

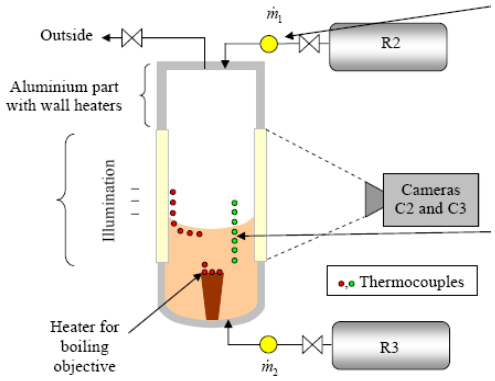

Figure 9. SOURCE-2 experiment system (ESA picture)

Many hours before launch, the R2 and R3 reservoirs are filled with HFE liquid and gaseous HFE. The experiment tank is evacuated, thereafter – starting as early as possible after de-spin – filled to a certain height, bringing free surface into the cylindrical part of tank R2.

The top aluminium part of the cylindrical section is heated to impose a linear temperature gradient from the top to the bottom, and during the filling, cold liquid comes into contact with the hot wall and nucleate boiling occur. Thereafter vapour pressurisation of tank R2 is performed in order to create a hot liquid layer at the free surface. After temperature and pressure stabilisation, boiling is observed. Finally, a rapid depressurisation of the tank is performed before the end of the microgravity phase, and the behaviour of the gas bubbles and the free surface are observed. At the end of the experiment the tank is repressurised in order to observe the recondensation of the bubbles.

2.2.2. SOURCE-2 Flight Result

The pre-programmed experiment sequence worked perfectly during flight and followed the sequence decided from the pre-flight test results. The behaviour of the experiment liquid in flight presented quite some surprise, being nothing like during the tests on ground.

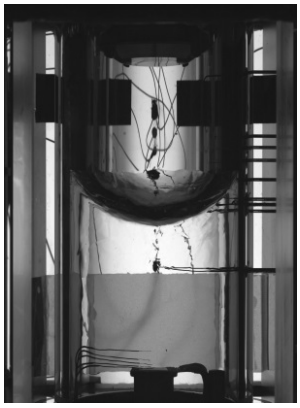

Figure 10. HFE in Experiment tank

2.3. XRMON-GF

The main objective of the ESA - MAP research project entitled XRMON is to conceive and perform *in situ* X-ray radiography experiments on metallurgical processes in microgravity environment. XRMON-GF (Gradient Furnace) was selected for flight on Maser 12 which was the third sounding rocket flight within the XRMON programme

2.3.1 XRMON-GF Scientific objectives

The XRMON-GF module was the first experiment on directional solidification of metallic alloys with in-situ X-ray monitoring in microgravity conditions, focussing upon the study of columnar and equiaxed dendritic growth.

2.3.2 XRMON-GF Overall design

XRMON-GF is a 115 cm tall module of 112 kg mass.

The module accommodates an advanced X-ray diagnostics, a Bridgman type solidification furnace. A micro focus transmission type X-ray tube with ≤ 5 µm focal spot was used in order to meet the resolution requirement. The X-ray tube used in XRMON -GF was a compact oil-free version of an X-ray tube of European made, also intended for use on ISS. For human safety, 25 kg of led sheets are used to create a radiation protecting box around the experiment compartment for shielding from the X-rays. As the radiation source is sensitive to the launch vibrations, the system is suspended on a tuned damper system.

Since the furnace-mounted sample should be pre-heated to 300°C 30 minutes before launch and even to over 500°C ten minutes before launch, an efficient cooling system is used for keeping the module at ambient temperature until lift-off and for maintaining module temperatures sufficiently stable during flight.

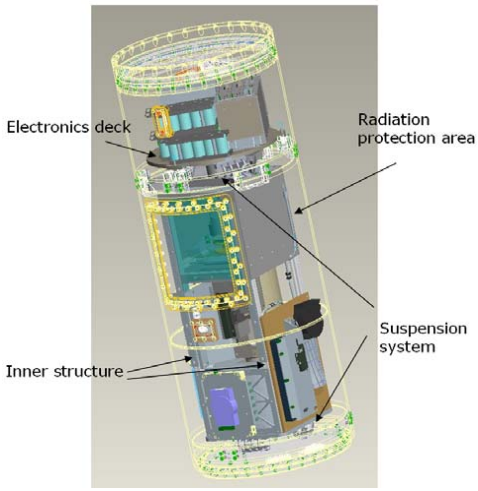

Figure 11. XRMON-GF Module assembly

Uncompressed images were stored on-board by the Digital Video System with a frame rate up to 6 frames per second. During flight, compressed images were down-linked in real time at a speed of two frames every three seconds.

The camera system is made of a digital camera with a 24x36 mm CCD-sensor adapted for X-ray usage by the integration of a 5 cm thick fibre optical plate that protects the sensor from radiation. A scintillator plate placed in front of the optical fibre converts X-ray radiation to visible spectrum light.

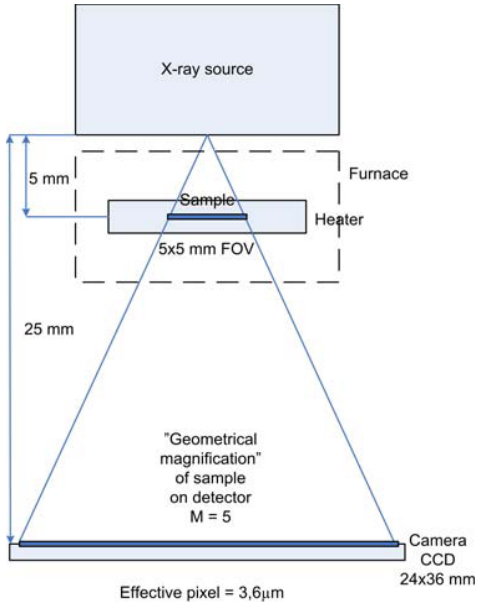

Figure 12. XRMON -GF optical path

2.3.3 XRMON-GF Flight results

The performance during flight was flawless.

Furnace temperature reached the planned 700°C followed by a correct subsequent cooling-down phase.

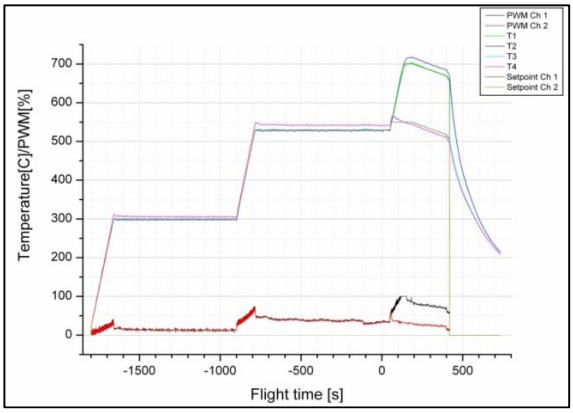

Figure 13. Furnace profile before and during flight

The development of the solidification front could be monitored throughout the whole microgravity phase, ending with a quick solidification of the sample just before end of microgravity, providing the sample in condition for post-mortem analysis, (see Figure 14).

Figure 14. X-ray image of a growing columnar structure of Al-Cu alloy

2.4. BIOMICS-2 experiment module

The purpose of the BIOMICS (BIOMImetic and Cellular Systems) experiment is to study the flow of cells in the blood vessels, specifically the dynamics of blood platelets. Vesicles can mimic a few but fundamental cell flow behaviours. The main goal of the experiment is to study the 3 dimensional movements of the vesicles, produced from lipids by the scientific group, in the liquid under shear flow.

The re-flight of BIOMICS had the objective to extend the excellent fluid dynamics results obtained during the MASER 11 mission and to provide the scientists with the benchmark data required to support the validation of current models. With BIOMICS-2, new composition of

samples and new experiment parameters are introduced as well as some small modifications to improve the performance of the system and the reliability.

2.4.1. BIOMICS-2 Overall design

The 58 kg 640 mm module is pressurised and temperature controlled with an external heater/cooler.

In addition to generic subsystems, it contains an advanced optical system with digital holographic microscope, overview system to visualize if bubbles are inserted during shear flow chamber filling, shear flow chamber, liquid systems, laser light sources and digital video system.

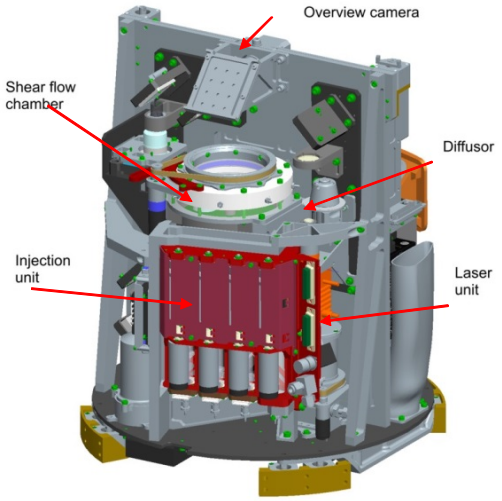

Figure 15. BIOMICS-2 Experiment module

The shear flow chamber is the heart of the experiment. The experiment is performed in this chamber. The chamber comprises one fixed bottom disc and a rotating top disc. The discs are separated with a small distance and the samples will fill this volume between the discs. The top disc can rotate with different speeds. The observation of the sample is performed trough the discs that are transparent.

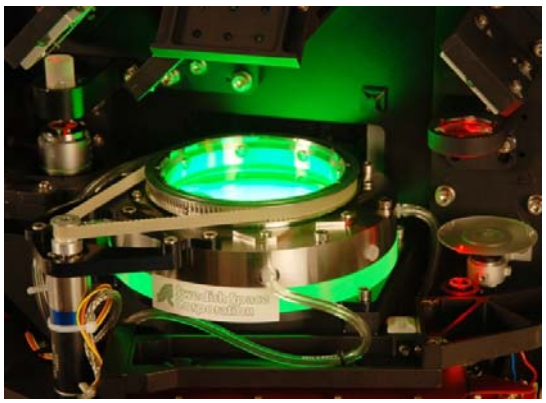

Figure 16. Shear flow chamber.

2.4.2 BIOMICS-2 Experiment process

Six samples were processed during flight. There were only three syringes for different samples, and the six samples were achieved by mixing samples from the syringes. To avoid sedimentation of vesicles in the injection unit, it was turned manually in the lab before installing in the module through the late access hatch. After the unit was mounted in the module the samples were stirred with a magnetic stirrer in the module each ten minutes for 5 to10 seconds.

To avoid bubbles in the chamber during filling a high flow rate was necessary, but the high flow rate could damage the vesicles. Therefore the rinse liquid was used for filling the chamber. Directly after the chamber was filled with liquid, the sample was injected in the chamber. Before the next sample was injected, the chamber was rinsed with the rinse liquid.

2.4.3 BIOMICS-2 Flight results

The movements of the vesicles in the liquid were monitored with the holographic microscope. The images were processed after flight and revealed the 3D pictures of the vesicles. The pictures were used for analyses of the 3D motion and distribution for the vesicles in the shear flow chamber.

The deformation of the shapes of the vesicles was studied with the holographic images, which also were transmitted with a lower frame rate to ground during the flight, enabling for the operator to follow the experiment.

3. UPCOMING MASER MISSION

MASER 13 is scheduled for launch in spring 2015. Five experiments were selected for the mission, accommodated in four modules.

CDIC-3 is a follow-on of CDIC-2 flown on MASER 11 in 2008, but with completely different experiment cell; here an investigation of chemical front propagation will be performed. The front is generated within an iodate / arsenious acid reaction, generated by the oxidation of the arsenious acid by electrodes.

XRMON-SOL is a new MAP experiment using X-ray diagnostic system for study of solidification in an isothermal furnace.

ARLES is an experiment studying droplet evaporation, accommodated in a new experiment module.

GRAMAT and SPARC are two biological plant (*Arabidopsis thaliana;* Wall Cress) experiments accommodated in BIM-3 experiment module, which is re-flight of BIM-2 but with experiment unit being rebuild to be adapted to the requirements of the plant experiments.

SWEDISH SOUNDING ROCKET PROJECTS

Christian Lockowandt[1], Krister Sjölander[1], Stig Kemi[1], Kenneth Löth[1]

[1)] Swedish Space Corporation, Science Services Division P.O.Box4207, SE-17104Solna, Sweden
Tel: +46-86276200, Fax: +46-8987069, E-mail: christian.lockowandt@sscspace.com

1. ABSTRACT

SSC has a long tradition of developing and launching scientific sounding rockets from Esrange Space Center with the aim to study the different layers of the atmosphere and near space. The latest, PHOCUS, was launched in 2011 with very successful results. Now a new era has started with an initiative from the Swedish National Space Board, SNSB, the sounding rocket and atmospheric balloon activities will be vitalized with a national program offering the scientific community approximately yearly rocket launches and balloon flights. The two upcoming sounding rocket missions that have recently started are O-STATES and SPIDER

2. PHOCUS

The PHOCUS rocket was successfully launched from Esrange on 21 July, 2011, 07:00:56 UTC
The Nike boosted Improved Orion motor system preformed nominally and the rocket reached an apogee of 107.8km.
All instruments were active and delivered data during the flight. The MAGIC instrument performed its collecting sequence and was consequently closed and sealed, as nominal, for later analysis. The data from the instruments was collected and transmitted to ground through the newly developed SSC service module.
The newly developed service module, SM14, performed nominally over the entire flight delivering housekeeping and scientific data to ground. It also saved a subset of housekeeping data on-board as backup to the ground system.
The Roll gimballed Inertial Navigation System D-MARS provided good uninterrupted attitude data during the scientific measurements.
The new NOVATEL GPS system, included in the SM14 setup, performed nominally during the flight. The GPS system experienced no drops of data until the first stages of re-entry flat spin, as can be expected.
The ground system provided uninterruptedly data to the operators and scientists for the entire flight. It also provided multiple redundant instances of data saving.
Nosecone- and payload- separation events occurred at the correct time and with nominal performance.
The recovery system and beacon performed nominally and the payload had a vertical landing velocity of approximately 7m/s. The landing was soft slightly to the side of the payload, as designed. As expected the CONE instrument sensor was damaged due to its position.
The payload was transported back to Esrange by helicopter within a few of hours after lift-off.

1.1. PHOCUS Scientific description and objectives

PHOCUS - Particles, Hydrogen and Oxygen Chemistry in the Upper Summer mesosphere
Particle layers in the mesosphere are a central topic of current atmospheric research. The relationships between various particle phenomena and their mesospheric and ionospheric environment provide particularly challenging questions. Important topics concern the nucleation and evolution of ice particles, the properties of meteoric smoke, and the possible influence of these particle populations on mesospheric chemistry. With the PHOCUS project these different lines of scientific research are brought together.
From MISU's side, the scientific approach was based on their capabilities in the optical probing of mesospheric chemistry (O-probe, H-probe, IR channels), their capabilities in the optical characterization of Noctilucent Cloud Particles (NLC photometers), and the capability to study mesospheric smoke particles (MAGIC). An exciting new development was the microwave experiment for measurements of water vapour by Chalmers. The background state of the neutral mesosphere was characterised in terms of density, temperature and small scale fluctuations by the CONE instrument of the Leibniz Institute of Atmospheric Physics (IAP), Germany. The background ionosphere was probed by standard rocket instrumentation (radio wave propagation, ion probe) of the Technical University of Graz (TUG). Complementary measurements of charged particles were provided by the University of Colorado, the University of Tromsø (UiT), and Leibniz Institute of Atmospheric Physics IAP.

Proc. '21st ESA Symposium European Rocket & Balloon Programmes and Related Research',
9–13 June 2013, Thun, Switzerland (ESA SP-721, October 2013)

The rocket-borne measurements were complemented by ground-based studies. Most important for the continuous observations of ice particle phenomena were the Esrange lidar and the Esrange radar. Laboratory and model studies related to the PHOCUS project will be carried out at a number of research groups in Europe and the U.S.

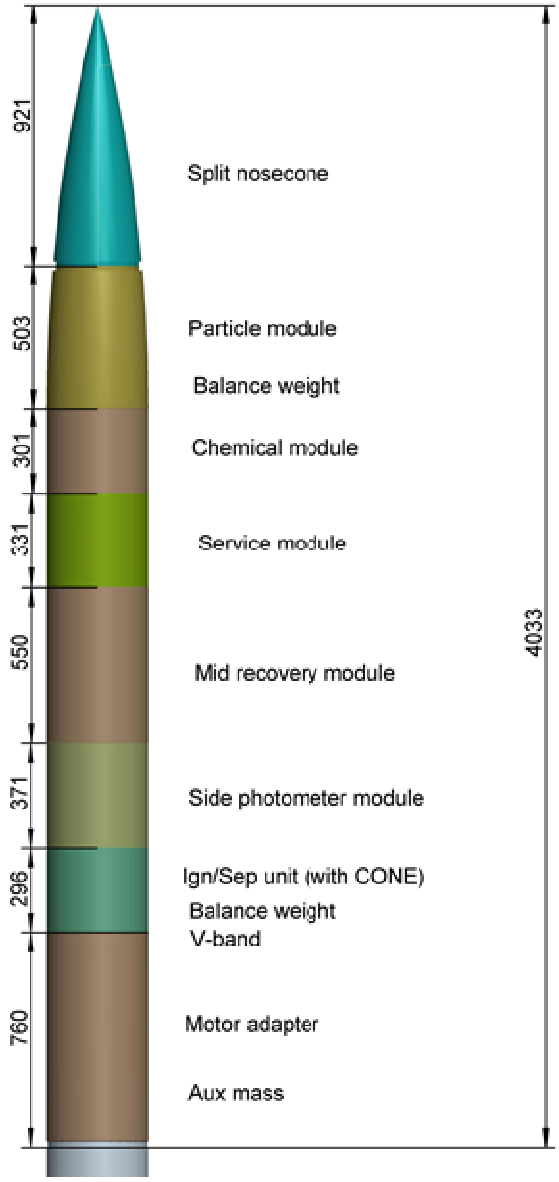

Figure 1. PHOCUS payload

3. NEW SWEDISH NATIONAL SOUNDING ROCKET PROGRAM

The Swedish National Space Board has started a new sounding rocket and balloon program in 2012. The launches will be performed at the Esrange Space Centre in northern part of Sweden. The idea is to offer regular flight opertunities with sounding rockets and stratospheric balloons. International cooperation is welcome in the program. The program is also open for international cooperation. Two first Sounding rocket missions; O-STATES and SPIDER in the program are described below.

4. O-STATES

O-STATES (Oxygen transformation in the thermosphere) is scientific mission with Prof. Jörg Gumbel at vid Meterologiska Institutionen Stockholms Universitet, as responsible scientist. The mission will study the oxygen transformation in the thermosphere.

The campaign (3 weeks) includes a double launch of the payload, the same payload will be launched twice during the same campaign with a short refurbishment of the payload during the campaign. The purpose of this is to achieve two measurements during different conditions but only manufacture one payload. This will result in a high scientific output to a relative low cost but of course with a higher risk.

The payload will be launched to an apogee of 250 km. The newly developed service module SM14 that was developed for the PHOCUS mission will be used in O-STATES for communication, position and attitude measurements.

The launch is planned in August 2015 from Esrange Space Center.

Instrument	University
Spectrometer TOM 755-780 nm	MISU, Sweden
Photometer 1, 630 nm	MISU, Sweden
Photometer 2, 391,4 nm	MISU, Sweden
2 Faraday antennas	TUG, Austria
Ione probe	TUG, Austria
Electron probe	TUG, Austria
FIPEX	MISU, Sweden
2 Oxygen probes	MISU, Sweden

Table 1. Instruments planned to fly on O-STATES

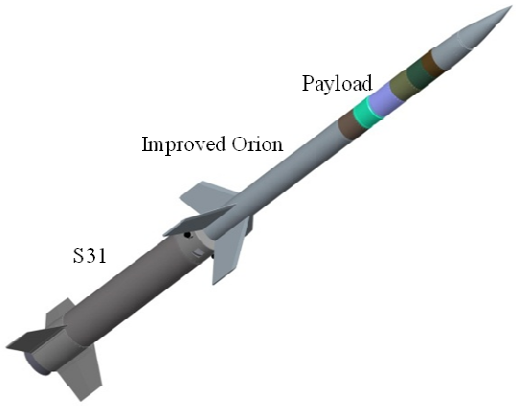

Figure 2. O-STATES vehicle

5. SPIDER

The SPIDER (Small Payloads for Investigation of Disturbances in Electrojet by Rockets) mission will perform measurements of the structure of the electrostatic turbulent in the ionosphere. The responsible scientist is Dr Nickolay Ivchenko at Space and Plasma Physics, Royal Institute of Technology, Stockholm, Sweden.
The mission will perform simultaneous multi point measurements during the flight. This will be achieved by ejecting 10 small daughter payloads from the main payload at 60 km altitude. The daughter payloads will be ejected in different directions and with different speeds to achieve a large distribution of the daughter payloads. Each daughter payload has 8 wire booms that will be deployed. Each daughter payload is fully autonomous performing the measurements and storing the data on-board. The daughter payloads has recovery systems and will be recovered in the impact area at Esrange Space Center. Daughter payload preliminary dimensions: 2,5 kg, diameter 220 mm, height 80 mm

The launch with an apogee of 140 km is planned for January 2015 at Esrange Space Center
Ejection at 60 km altitude

6. ACKNOWLEDMENTS

This project is financed by Swedish National Space Board.

MATERIAL PHYSICS ROCKETS MAPHEUS-3/4: FLIGHTS AND DEVELOPMENTS

Martin Siegl[(1)], Florian Kargl[(2)], Frank Scheuerpflug[(3)], Jörg Drescher[(2)], Christian Neumann[(2)], Michael Balter[(2)], Matthias Kolbe[(2)], Matthias Sperl[(2)], Peidong Yu[(2)] and Andreas Meyer[(2)]

[(1)]Institut für Raumfahrtsysteme, Deutsches Zentrum für Luft- und Raumfahrt (DLR), Robert-Hooke-Straße 7, 28359 Bremen (Germany), Email: martin.siegl@dlr.de
[(2)]Institut für Materialphysik im Weltraum, Deutsches Zentrum für Luft- und Raumfahrt (DLR), 51170 Köln, Germany Email: florian.kargl@dlr.de, joerg.drescher@dlr.de, christian.neumann@dlr.de, michael.balter@dlr.de, matthias.kolbe@dlr.de, matthias.sperl@dlr.de, peidong.yu@dlr.de, andreas.meyer@dlr.de
[(3)] Deutsches Zentrum für Luft- und Raumfahrt (DLR), Mobile Raketenbasis, Oberpfaffenhofen, 82234 Germany, Email: frank.scheuerpflug@dlr.de

ABSTRACT

Sounding rockets can serve as a time- and cost-effective platform for a wide range of research under microgravity conditions. It is shown that MAPHEUS – *Ma*terial*Ph*ysikalische *E*xperimente *U*nter *S*chwerelosigkeit (Materials Physics Experiments under Weightlesness) – a DLR internal R&D project perfectly achieves this whilst maximizing scientific output. MAPHEUS hereby offers launch opportunities on a yearly basis and with comparatively short development cycles of about one year only. In the first three campaigns MAPHEUS provided about three minutes of microgravity time. Recent developments enable to extend this to four minutes above 100 km. Performance data of the recent MAPHEUS-3 flight together with information on the experiment modules are provided. Further an outlook is given on the experiment modules used on board of MAPHEUS-4 and the new vehicle.

1. INTRODUCTION

Sounding rockets enjoy wide adoption as a measurement platform for atmospheric physics and as a microgravity platform for experiments from different science disciplines. Several microgravity research rockets are available to the scientific community, typically run on a national basis, as European collaboration through ESA, or as an international collaboration. Prominent examples are the sounding rocket programme TEXUS run by the German Space Agency with the prime contractor ASTRIUM and the ESA led sounding rocket programme MASER with the prime contractor SSC as well as MAXUS with the prime contractor ASTRIUM. The former two sounding rocket programmes offer microgravity times of about six minutes whereas MAXUS offers up to 12 minutes. The programmes have in common that they are operated at bi- but more common only on multi-annual intervals, which means relatively long development cycles for experiments. The project management is carried out by the prime contractor and experiment modules are built by the prime contractor and industrial subcontractors. Different to the mentioned programmes the MAPHEUS sounding rocket project is an internal DLR R&D project. The scientific experiment facilities for MAPHEUS are selected, designed and built by the DLR Institute of Materials Phyics in Space. The Mobile Rocket Base (MORABA) of DLR is responsible for the provision of rocket motors and the service-, rate-control-, and recovery systems. The overall project is managed by the DLR Institute of Space Systems. The operational launch services are carried out by DLR MORABA together with SSC at ESRANGE Space Center Kiruna, Sweden.

MAPHEUS solely focuses on materials physics payloads. The setup of the project within DLR R&D allows for extremely rapid development cycles, yielding cutting-edge scientific return and short lead times. Technical limits of experiment facilities can be pushed as new developments are incorporated into MAPHEUS in a flexible manner. A particular strength of the project is to enable also systematic materials investigations, where a large number of samples and step-wise parameter variation are required. This is realized through yearly launches and re-flights of refurbished and/or upgraded experiment facilities.

The concept of a rapid-development and boundary-pushing research rocket falls in line with the relatively short microgravity time of only up to four minutes and a strong educational component within the project evidenced by bachelor, master, diploma, and doctoral thesis work both in engineering as well as physical sciences.

The following sections present the experiments, vehicle and flight of MAPHEUS-3, launched successfully on 25th November 2013 at 12.20 LT. Furthermore, the scientific and technical plans for MAPHEUS-4 are introduced.

2. MATERIAL PHYSICS ON MAPHEUS

Experiments on MAPHEUS 1-3 have covered a wide range of material physics research areas. Dedicated systems were built to investigate the gelation for forming of light-weight porous materials, the behaviour of granular gases, the diffusion in liquid metals [1], the

Proc. '21st ESA Symposium European Rocket & Balloon Programmes and Related Research', 9–13 June 2013, Thun, Switzerland (ESA SP-721, October 2013)

solidification of alloys [2], and the demixing of undercooled melts. All design is carried out with a focus on maximizing the number of investigated material samples and thereby the overall scientific return. Further, to be cost-effective the experiment module design is done such as to allow for reusability with minimal refurbishment. Performing materials research on liquid metals with the aim to elucidate their solidification, diffusion, and demixing behaviour requires high temperatures to be achieved. As a result high power is needed to be able to operate a large number of furnaces simultaneously and to prevent the materials from oxidation high vacuum-conditions have to be maintained during the flight.

3. MAPHEUS-3 EXPERIMENTS

As shown in Fig. 1 MAPHEUS-3 was launched successfully on 25 November 2012 at 12.20 LT. Propelled by a two-stage Nike/Improved-Orion motor combination, the flight offered more than three minutes of less than 10^{-4} g.

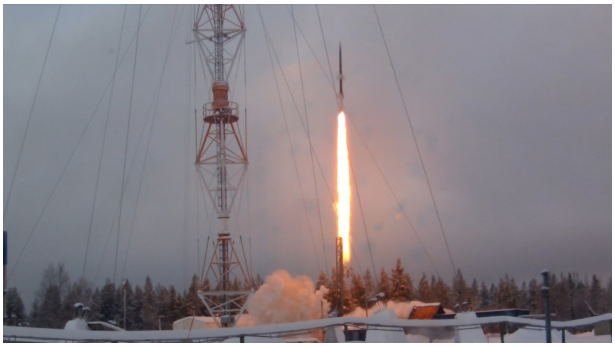

Figure 1. MAPHEUS-3 lifting off from ESRANGE

The investigated physical phenomena on MAPHEUS-3 included atomic transport processes in liquid alloys with the goal of determining diffusion coefficients (ATLAS-M); the demixing of copper-based metallic alloys during controlled cooling (DEMIX-M); and the behaviour of magnetically-excited granular matter (MEGraMa-M); a shear-cell furnace (SCID-M) serving both as a precursor experiment for the upcoming MAPHEUS-4 campaign as well as to study impurity diffusion in liquid Al base alloys. ATLAS-M, MEGraMa-M, and DEMIX-M were experiments with flight heritage, but have been upgraded, whereas SCID-M was a completely newly developed facility. For delivering power to the experiments the BATT-M module was used.

ATLAS-M (Atomic Transport in Liquid Alloys and Semiconductors, Fig. 2) is a module dedicated to the determination of diffusion coefficients. It enables to simultaneously process 32 diffusion samples in eight independently operated furnaces. The module and furnace design is in detail described in [1]. On MAPHEUS-3 self-, impurity, and chemical diffusion in liquid Al base alloys were successfully investigated. The furnaces nicely followed the set heating profiles. A net diffusion time of up to 140s was achieved depending on the samples liquidus and solidus. Preliminary data analysis of some of the samples showed excellent agreement with model predictions clearly indicating that due to the excellent thermal stability Marangoni flow did not disturb the diffusion process.

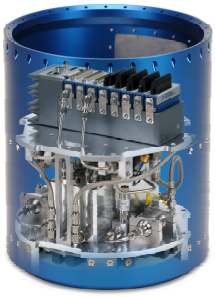

Figure 2. ATLAS-M in its experiment module

DEMIX-M (Fig. 3) is a module dedicated to the investigation of the demixing behaviour of undercooled Cu-Co melts. DEMIX allows to simultaneously operate eight furnaces arranged in two independent furnace compartments. The furnaces can be operated at temperatures of up to 1500°C. The module further enables very fast heating to maximize the microgravity time available for sample cooling. The spherical Co-Cu samples are embedded in liquid Duran glass. Heterogeneous nucleation is hereby suppressed and the liquid samples can be cooled below their liquidus. To avoid foaming of the Duran the furnaces are processed under Argon atmosphere. For fast cooling a Ar/He gas mixture is used. Preliminary data analysis showed that four of the eight samples were well homogenized during heating and showed phase separation during cooling. The MAPHEUS data complement earlier data obtained on the sounding rocket TEXUS and drop-tube experiments where the samples have been freely suspended by electromagnetic levitation and droplets have been formed through liquid injection, respectively [3].

Figure 3. DEMIX-M experiment

SCID-M is an experiment facility introducing a novel shear-cell furnace for X-ray radiography to microgravity applications. SCID-M is integrated into the other half of the DEMIX-M module. The compact shear cell furnace which is at the heart of the SCID-M facility (Fig. 4) is in detail described in [4]. The most recent update to be

used in the MAPHEUS-4 campaign is described in [5] as are *in-situ* ground-based experiments in [6].

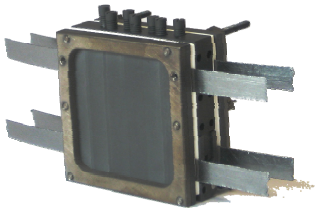

Figure 4. The shear-cell furnace of the SCID-M experiment, now employed in MIDAS-M on MAPHEUS-4

Fig. 5 shows an X-ray radiograph before shearing (left) and after shearing (right) to illustrate the working principle. In this shear-cell, the individual alloys samples are melted separately. After homogenization different samples constituting a diffusion pair are brought into contact with each other by shearing half of the furnace. Hereby the diffusion process is started at a well-defined time.

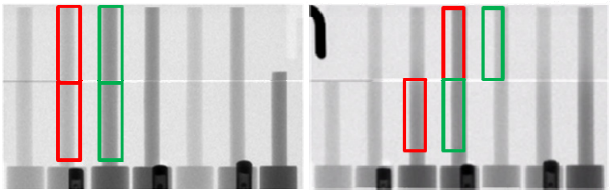

Figure 5. Working principle of the shear cell. Red and green outlines indicate different metals sheared into contact after melting.

On MAPHEUS-3 the shear-cell was cooled down to solidify the samples under microgravity. Heating and cooling as well as shearing under microgravity worked nominally. Even so the samples have been liquid already during ascent in the hyper-g phase no sample leakage from the capillary compartments was observed. Hence, diffusion time can also be maximized in future sounding rocket missions by melting the sample already in hyper-g conditions, which is due to convective flow an effective means for sample homogenization.

MEGraMa-M (Magnetically Excited Granular Matter) builds upon previous experiments in parabolic flights and drop-tower shots for observing the cooling of a magnetically excited granular gas with a high-speed camera system (Fig. 6). The system consisting of paramagnetic spherical particles is excited homogeneously and monitored by high-speed imaging at 500 fps. Particle positions and velocities can be extracted and compared to theoretical predictions both for the steady state as well as for cooling once agitation is switched off. While in the drop tower experiments already the initial stages of cooling of the gas were observed, the sounding rocket experiment enables to follow granular cooling towards much longer times. At the same time, the rocket experiment also provides access to the study of granular clustering. In addition to MAPHEUS-3 where only a single camera was used, the re-flight on MAPHEUS-4 is performed with an updated recording unit and a second camera system. In addition to enhanced reliability, with images from both cameras particle tracking in 3D becomes possible.

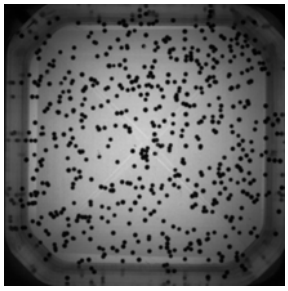

Figure 6. Excited granular gas as investigated in MEGraMa-M

4. MAPHEUS-3 VEHICLE AND FLIGHT

MAPHEUS-3 was propelled by a two-stage Nike/Improved Orion motor combination, reaching an apogee altitude of 140 km with an overall payload mass of 195 kg. This comprised a 110 kg scientific payload and 85 kg of rocket systems (recovery-, rate-control-, and service system, among others). An overview of the payload stack including dimensions is given in Fig. 7. MAPHEUS currently uses standard 356 mm (14 inch) diameter experiment modules.

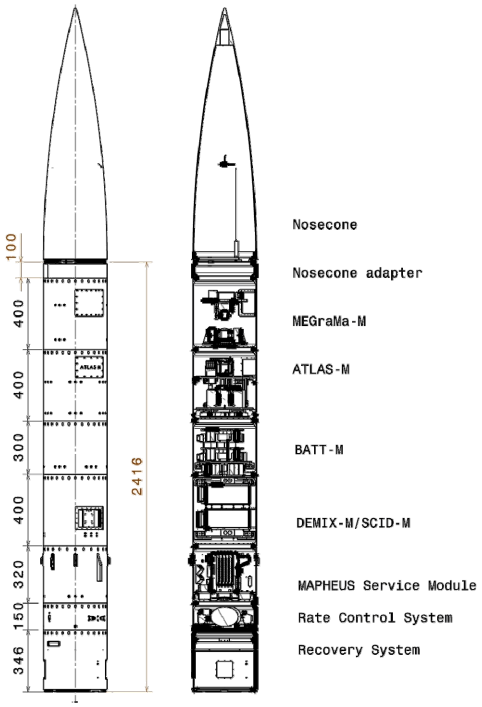

Figure 7. Overview of the MAPHEUS-3 payload stack

After a flight time of approximately 80 s, the stabilizing 4 Hz roll rate of the ballistic vehicle was compensated by a yo-yo despin system; residual rates and accelerations were suppressed by the MORABA-developed rate-control system [7]. Excellent experiment conditions in terms of accelerations (in the order of 10^{-5} g) and rotational rates were achieved (Figs. 8 and 9).

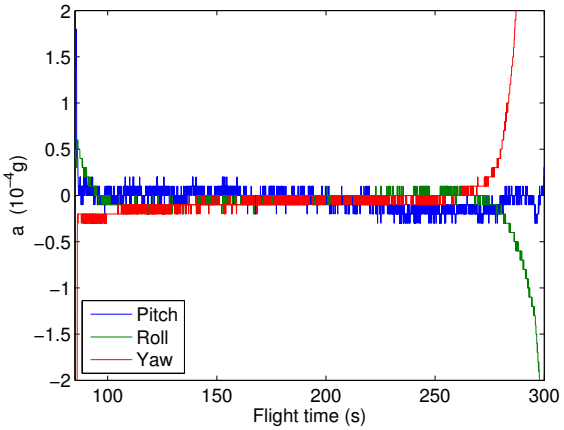

Figure 8. Accelerations in three axes after activation of the rate-control system.

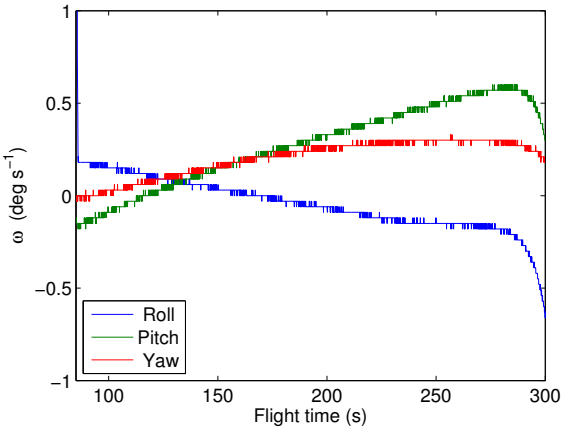

Figure 9. Residual rates after rate-control system activation.

5. MAPHEUS-4 EXPERIMENTS

MAPHEUS-4 is scheduled for launch in July 2013. Its scientific payload will combine a shear-cell furnace with *in-situ* X-ray radiography to achieve time-resolved measurements of diffusion processes (MIDAS-M experiment). The new experiment facility is complemented by a change of rocket motor to ensure up to four minutes of high-quality microgravity measurement time.

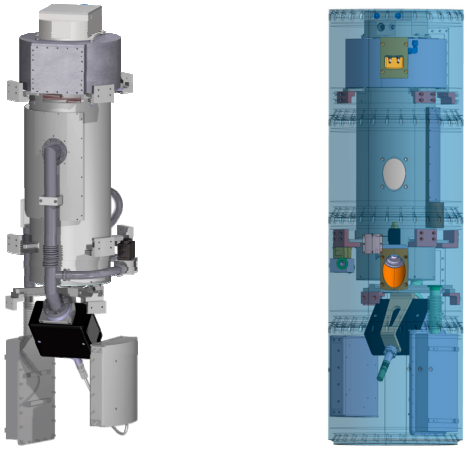

Figure 10. X-ray radiography facility MIDAS-M with sample chamber (top), X-ray tube, and ion-getter pump (bottom).

For use on research rockets, the DLR Institute of Materials Physics in Space has custom-equipped the X-ray tube with an ion-getter pump to sustain ultra-high vacuum levels from lift-off throughout the flight.
For future MAPHEUS-flights, re-flights of the same radiography facility are foreseen, potentially applied to different materials physics research areas [8]. On MAPHEUS-4, MIDAS-M will be complemented by an extended version of MEGraMa-M in the scientific payload stack.

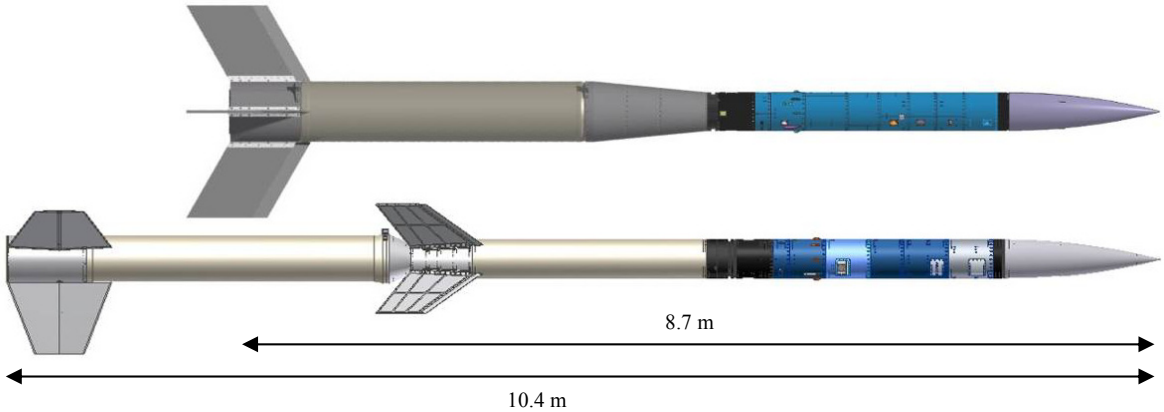

Figure 11. The MAPHEUS-4 (top) and MAPHEUS-3 (bottom) vehicles with motor(s), motor adapter and payload sections (blue).

6. MAPHEUS-4 VEHICLE

An increase in scientific payload mass with MIDAS-M is one of the reasons for employing a new motor system on MAPHEUS-4. The Nike/Improved-Orion combination of the three previous MAPHEUS flights is replaced by a S30 motor, introduced for the first time by DLR MORABA in this single-stage configuration. Its use allows maintaining close to four minutes of experiment time above 100 km. The configuration of the payload section in terms of rocket systems and module dimensions follows the standard MAPHEUS specification (Fig. 11).

7. CONCLUSION AND OUTLOOK

MAPHEUS-3 and previous flights have returned a wealth of material physics samples and allowed for a systematic investigation of diffusion coefficients and miscibility behaviour of metallic alloys. From MAPHEUS-4 onwards, X-ray radiography will open a new window by allowing direct *in-situ* observations. With a change of motor from Nike/Improved-Orion to single-stage S30, a sustainable solution offering four minutes of experiment time is provided to the project.

REFERENCES

1. Blochberger, G., Drescher, J., Neumann, C., Penkert, P., Griesche, A., Kargl, F., & Meyer, A. (2011). ATLAS-M and BATT-M: Development of flight hardware for MAPHEUS sounding rocket. *Journal of Physics: Conference Series* **327**, 012051.

2. Ratke, L., Genau, A., & Steinbach, S. (2009). Flow effects on the dendritic microstructure of AlSi-base alloys. *Transactions of The Indian Institute of Metals* **62**, 337–341.

3. Kolbe, M. (2012). Demixing of Cu–Co Alloys Showing a Metastable Miscibility Gap. In D. M. Herlach & D. M. Matson (Eds.), *Solidification of Containerless Undercooled Melts* (pp. 51–67). Weinheim: Wiley-VCH Verlag.

4. Neumann, C., Sondermann, E., Kargl, F., & Meyer, A. (2011). Compact high-temperature shear-cell furnace for in-situ diffusion measurements. *Journal of Physics: Conference Series* **327**, 012052.

5. Sondermann, E., Neumann, C., Kargl, F., & Meyer, A. (2013). Compact high-temperature shear-cell furnace for in-situ interdiffusion measurements. *High temp. High press.* **42**(1), 23–30.

6. Kargl, F., Sondermann, E., Weis, H., & Meyer, A. (2013). Impact of convective flow on long-capillary chemical diffusion studies of liquid binary alloys. *High temp. High press.* **42**(1), 3–21.

7. Pfänder, J., & Ettl, J. (2009). Rate Control System for Sounding Rockets. *Proc. 19th ESA Symposium on European Rocket and Balloon Programmes and Related Research*.

8. Kargl, F., Balter, M., Stenzel, C., Gruhl, T., Daneke, N., & Meyer, A. (2011). Versatile compact X-ray radiography module for materials science under microgravity conditions. *Journal of Physics: Conference Series* **327**, 012011.

SPACE SAILORS: EXPERIMENTAL DEPLOYMENT OF A DRAGSAIL ON A SOUNDING ROCKET

Christopher Fiebig[(1)], Wolfgang Bauer[(2)], Patrick Gerding[(3)], Kai Parow-Souchon[(4)], Anna Pongs[(5)], Matti Reiffenrath[(6)], Nino Wolff[(7)], Thomas Ziemann[(8)]

[(1)]RWTH Aachen University, Nizzaallee 9, 52072 Aachen, Germany, Email:Christopher.Fiebig@rwth-aachen.de
[(2)] FH Aachen University of Applied Sciences, Faculty of Aerospace Engineering, Hohenstaufenallee 6, 52064 Aachen, Germany, Email: bauer@fh-aachen.de
[(3)]RWTH Aachen University, Melatener Straße 148 App. 20, 52074 Aachen, Germany, Email:Patrick.Gerding@rwth-aachen.de
[(4)]RWTH Aachen University, Adalbertsteinweg 1b, 52070 Aachen, Germany, Email:Kai.Parow-Souchon@rwth-aachen.de
[(5)]RWTH Aachen University, Krefelder Straße 5, 52070 Aachen, Germany, Email:Anna.Pongs@rwth-aachen.de
[(6)]RWTH Aachen University, Nizzaallee 38, 52072 Aachen, Germany, Email:Matti.Reiffenrath@rwth-aachen.de
[(7)]RWTH Aachen University, Passstraße 78, 52070 Aachen, Germany, Email:Nino.Wolff@rwth-aachen.de
[(8)]RWTH Aachen University, Moholt Alle 4 – 2, 7050 Trondheim, Norway, Email:Thomas.Ziemann@rwth-aachen.de

ABSTRACT

A constantly increasing amount of space debris represents a tremendous problem for current and future space missions. Therefore it is necessary to develop new de-orbit technologies for disused satellites. By using a dragsail at the end of life of a satellite the aerodynamic drag of the earth's atmosphere can be increased causing an acceleration of the satellite's re-entry. With their experiment launched on the REXUS 14 sounding rocket from Kiruna in Sweden the team "Space Sailors" qualified a dragsail deployment mechanism under realistic conditions, i.e. no atmospheric disturbances and reduced gravity. The deployment of a 2 m² polyimide sail took place in an altitude of 81 km where it has been monitored by self-developed cameras, which were also to be qualified for future applications in space.

1. INTRODUCTION

The main source for space debris are disused and abandoned satellites. Space debris colliding with each other with extremely high relative velocities of a few thousands of kilometres per hour are amplifying this problem. The effect is that even if we stopped launching satellites today the amount of debris would still increase. This snowball effect is called Kessler syndrome. It is estimated that about 60000 debris larger than one centimetre currently surround the earth. At present about 5500 tons of debris are orbiting the planet in the Low Earth Orbit (LEO, <1000km), which is where 90% of all satellites are located. This amount increases annually by about 5%.

By now it is mandatory for new satellites that their resting time in orbit after their end of life shall be shorter than 25 years. The achievement of this requirement makes it necessary to develop new de-orbit technologies.

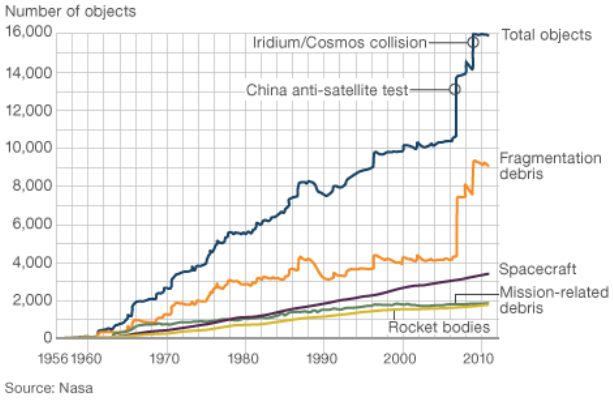

Figure 1: Growth of orbital space objects including debris

In modern rockets the burned rocket stages reaching orbit altitudes are taken back by a final deorbit boost in order to let these stages burn up in the atmosphere. For energetic reasons satellites in the geostationary orbit (GEO) are lifted to a so called graveyard orbit. In LEO the aerodynamic drag due to the earth's atmosphere is high enough to accelerate the deorbiting of a satellite. This means that no additional propellant is needed for this manoeuver. By using a dragsail at the end of life of

Proc. '21st ESA Symposium European Rocket & Balloon Programmes and Related Research', 9–13 June 2013, Thun, Switzerland (ESA SP-721, October 2013)

a satellite this aerodynamic drag can be increased. Theoretical considerations are showing that a sail with 2 m² area is sufficient to deorbit a triple CubeSat from a circular 800 km orbit within 25 years [1].

2. TECHNICAL BACKGROUND AND GOALS

Different deorbiting strategies have been investigated at the Institute of Lightweight Structures at the RWTH Aachen University (ilb) and the FH Aachen University of Applied Sciences. This led to the design and construction of a first demonstrator of a deployment mechanism for a 5 m² dragsail [1].

Figure 2: Deployment test on ground with first demonstrator [1]

As shown in Fig. 2 deployment tests on ground encountered problems due to gravity and air drag. Gravity provokes a very quick deflection of the gossamer structures, which also leads to high friction between moving parts of the mechanism and prevents a complete deployment. Air drag hinders a correct unfolding of the sail. Since then the members of the Space Sailors student team [2] are concerned with this complex of problems. The idea for their experiment arose out of that context and their main aim became to redesign the mechanism and to bring it to operability for a small satellite.

The launch at the top of an improved Orion rocket on a ballistic trajectory of around 90 km altitude promised a great opportunity to test the deployment and the mechanism for a 2 m² sail under realistic conditions – no atmospheric disturbances and reduced gravity. [3]
With regards to a future utilization in a CubeSat the guiding line was to build the deployment mechanism in accordance with the standards for CubeSats. For instance this means it has to fit into a 100 mm x 100 mm x 100 mm cube. As the test on ground had shown the time period of interest while filming a deployment is only 2 seconds long. Therefore a small camera with high frame rates had to be chosen. An assessment of different possible camera systems led the Space Sailors to the idea of developing their own camera.
In summary the Space Sailors had the following objectives:

- qualifying the deployment mechanism by recording the correct deployment of the sail with cameras.
- qualifying a self-constructed camera module. This module shall accomplish the high demands of recording a sail deployment. Furthermore the camera should be usable for similar functions during a future CubeSat mission.

3. EXPERIMENT TECHNICAL CONCEPT

An improved Orion rocket can carry different experiments in a stacked arrangement. The described experiment was mounted in the so called nosecone adapter at the top of the rocket. The locations of the different components of the experiment are depicted in Tab. 1 and Fig. 3.

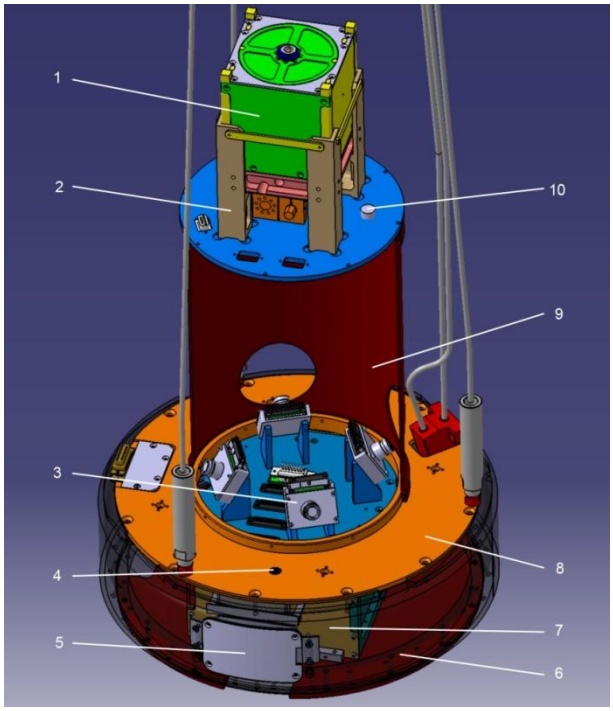

Figure 3: Overview of the experiment

The cube including the bobbin with the coiled booms and the sail is fixed on top of a central tube in order to establish a maximum distance to the nosecone adapter. This distance is required when thinking about the objective to record the deployment using cameras.

For safety reasons it was mandatory to eject the cube and the sail after its deployment and before the rockets

Table 1: Experiment components

1	Cube including dragsail coiled on the spool
2	Cube Mounting device (CMD)
3	Optical Medium-speed Cameras (OMC)
4	Optical High-speed Camera
5	Hatch
6	Bulkhead
7	E-Box
8	Heat shield with lighting LEDs
9	Central tube of the Base Unit (BU)
10	Optical Low-speed Camera (OLC)

re-entry. Otherwise the sharp-edged booms could have damaged the recovery parachute. For this reason a jettison mechanism had to be designed. This mechanism and the mechanism triggering the deployment are integrated in the so called Cube Mounting Device (CMD). The four sensors of the self-developed cameras (OMC) are located at the bottom of the central tube pointing towards the deployment plane of the sail. Protected by the rockets outer skin (nosecone adapter) the E-Box gives place to the OMC controllers and data storages as well as to the experiments power supply and controller boards. Furthermore two additional cameras are aligned to the rockets center line and served as backup. One of these (OLC) transmits the recorded data to earth via the TV-Channel of the rocket. The other camera (OHC) is a modified GoPro Hero 2 camera. Its data is stored within the experiment for a later access after the recovery of the rocket. Fig. 4. shows a ground deployment test of the fully assembled experiment.

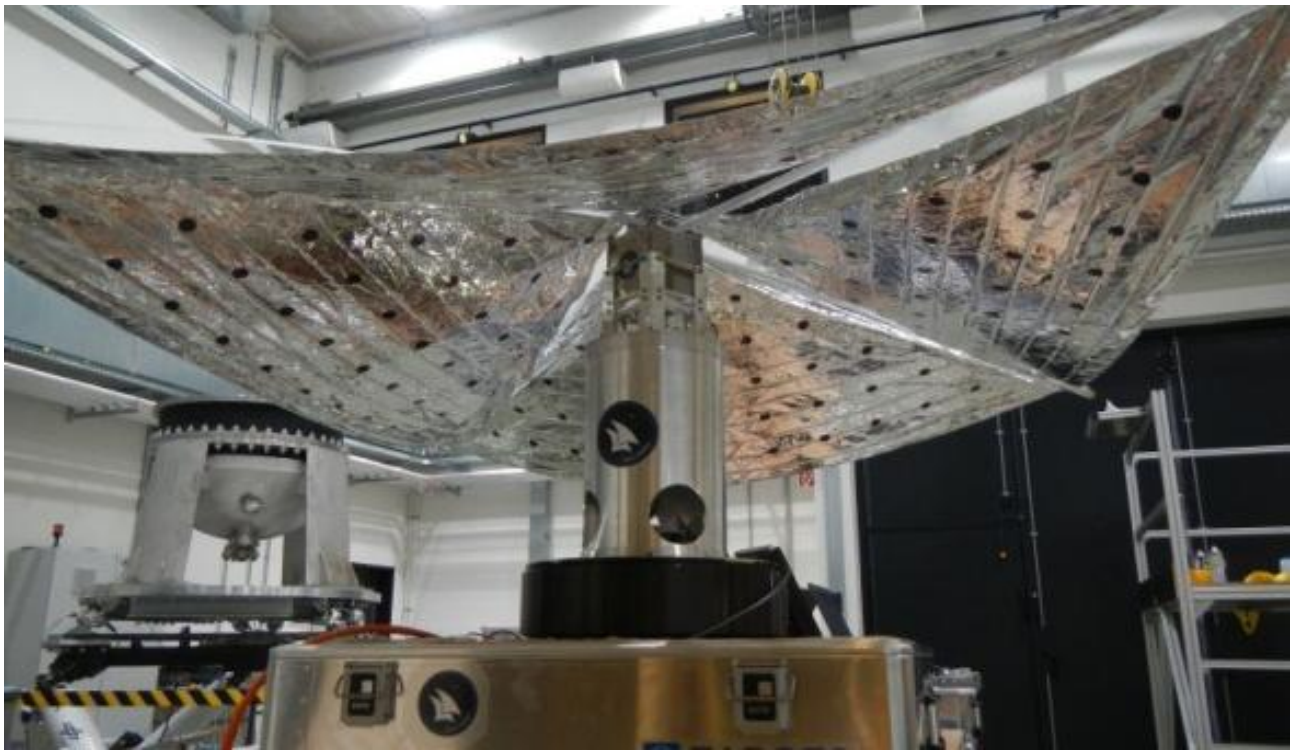

Figure 4: Experiment after a ground deployment test

3.1. Mechanical Design

This section gives an overview of the mechanical design of the experiments most important components. These are the Cube containing the complete dragsail and the Cube Mounting Device (CMD) responsible for the triggering of the deployment and jettison.

The cube represents the payload of the experiment and it is designed in accordance to the CubeSat standards. It can be handled as an individual unit separately from the other parts of the experiment setup. Most parts are milled or turned out of grade 7075 T6 aluminium. Parts with gliding surfaces are hard-coated.

Its structure gives space to two spools on which the booms and the dragsail are coiled, a boom guidance system and a conical spring which is needed to cause the sail's deployment. The energy for the whole deployment is stored in this spring and in the booms (bi-stable metal leaf springs).

As long as the spool is in the Cube its rotation is hindered by rails in the cube walls. In its initial state the spools are entirely inside the cube structure and no part of the spool is able to rotate. (Fig. 5, left side) For deployment a holding string is cut and the conical spring pushes the spools out of the cube structure. A free rotation of the Spool causing the uncoiling of the booms and deployment of the polyimide foil is then possible when the spool has left the cube structure with its rails. (Fig. 5, right side)

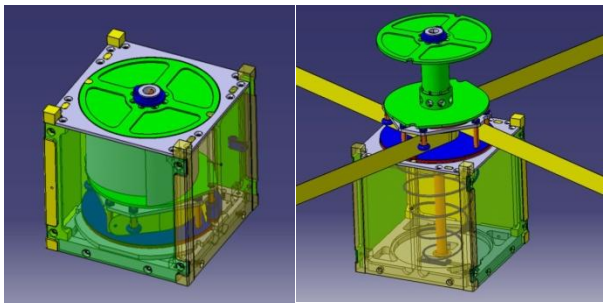

Figure 5: Cube in initial state and with deployed booms

To ensure a proper uncoiling of the booms they are guided by the guiding system with its Teflon rolls. As it should be possible to change the complete coil with the folded sail without disassembling the cube, it is held in position by an aluminium nut on the upper end of the spool. Further this nut secures the holding pin which connects the spool with the trigger mechanism. Fig. 6 gives an overview of the spool's components.

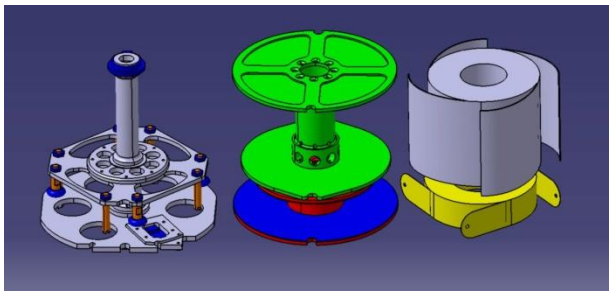

Figure 6: Central tube with boom guidance system (left), coils for dragsail and booms (centre), coiled sail and booms (right)

As the complete deployment uses the energy stored in the deployment spring and the bi-stable metal booms the friction between all moving parts has to be minimized. Concerning the movement from the spool in the cube structure this has been realized by using hard-coated aluminium on uncoated aluminium which leads to a maximal friction force of 5N. Considering the geometric boundary conditions this leads to the dimensioning of the deployment spring. The chosen spring has a force between 10N and 40N. To minimize the friction during the uncoiling of the booms the rolls of the boom guidance system are made out of Teflon and the coil which contains the booms has thin steel inlays to prevent the sharp edges of the booms from cutting in the alloy parts while uncoiling.

As mentioned before the whole energy for the uncoiling of the sail is stored in the booms making additional energy sources superfluous. Those bi-stable metal leaf springs use the difference in strain energy in their two stable states. They are made by pre-stressing metal strips in two different directions to induce inner tensions which create the mentioned bi-stable behaviour. Fig. 7 shows a bi-stable metal strip in its two stable states.

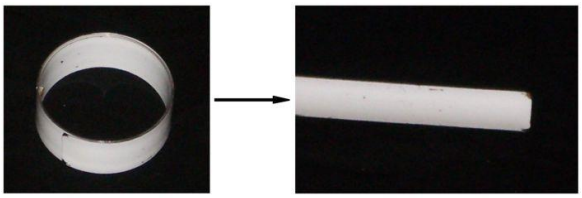

Figure 7: Bi-stable metal strip in its two stable states

Fig. 8 shows the strain energy in a bi-stable metal strip in dependence of its curvature. The energy difference of the metal strips in use is about 2.25J/m. Accordingly the available torque for deployment with four metal strips is approximated. This coincides with first measurements and was sufficient for the first deployment tests on ground. As these booms are made of steel they bend under their own weight when uncoiled under the gravitation on the ground - for this reason a test of the sail under reduced gravity conditions is necessary.

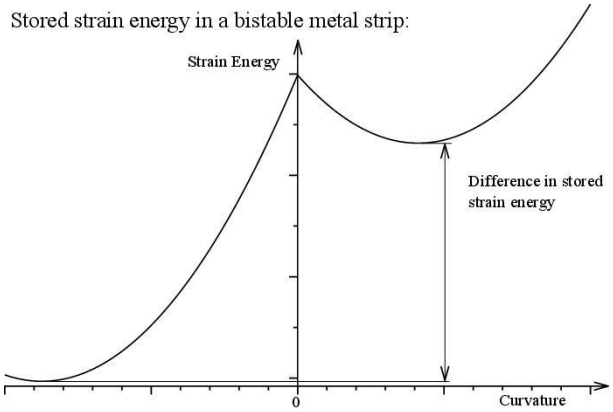

Figure 8: Strain energy in a bi-stable metal strip [4]

The sail itself consists of a 7.5 µm thick polyimide foil which is coated with aluminum. It is made of four

triangular segments witch are attached to the booms and the spool using Dyneema® strings and folded using the so called frog-leg folding method. More information about the sail and boom technology of the experiment can be found in [5]. Considering a deployment of the sail in an altitude between 80 and 90 kilometers it is desirable to build a drag sail in such a way that the drag forces are representative to those arising in orbit. Considering the influences to these forces it is visible that the flight path and the time when the deployment occurs during the flight is of great importance. Beyond the altitude and the relative velocity the attitude of the rocket is of importance for the produced drag. If the sail (vector normal to the sail) does not point into flight direction, which is likely on a ballistic flight path, the drag force is nearly zero while a maximum would arise if the sail is directed into flight direction. Between these extreme values the drag force is scaled by the sine function of the pitch angle.

The Cube Mounting Device (CMD) acts as the mechanical mounting, triggering and jettison interface of the cube. It consists of different aluminium milled parts. Fig. 9 shall facilitate their comprehension.

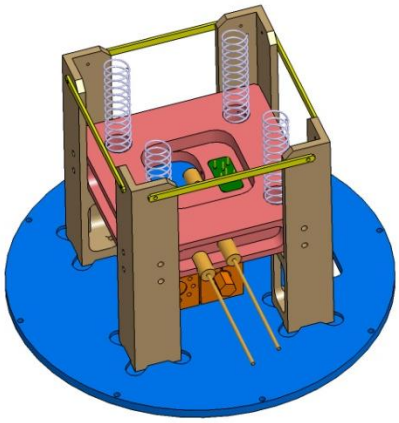

Figure 9: Cube Mounting Device (CMD) with cypress cutters and jettison springs

The CMD fixes the cube in a definite position and guides it during its jettison using four guiding rails to prevent lateral movement of the cube. In order to reduce friction between the cube and the guiding rails, the latter are hard coated. Furthermore to mitigate the safety risk of a parachute entanglement or damage the ends of the guiding rails are protected with rods.

The triggering of the deployment is initialized by a pyrotechnical cutter device which is cutting a Dyneema® holding string attached to the spool. This causes the conical spring to push the spool up and to start the uncoiling of the booms. The jettison of the cube is released by a second pyrotechnical cutter device, which separates a second Dyneema® holding string attached to the Cube Structure. Four ejection springs then accelerate the cube to a velocity of 1.5 m/s.

On the bottom side the two Dyneema® holding strings are coiled to a defined pretension. This is ensured by the so called stretching system. The position of the rod is fixed with a clamp, a set screw and a position screw. For the position screw the partition of the coil and the bearing is different and in every position of the coil there are two bores in agreement. For safety reasons each Dyneema® holding string is designed to withstand all occurring forces, i.e. the spring forces and the launch loads. Thus, there is a redundancy against an early jettison of the Cube.

3.2. Electrical Design

The general electrical architecture of the experiment is depicted in Fig. 10. The E-Box represents the mechanical housing for the Power Supply Board and the Main Board, the four OMC Controllers and a Plug Board. Here a Bus PCB provides connectors to the REXUS Service Module (RXSM) and the mentioned boards.

The Power Supply Board (PSB) transforms the 24 to 36V supplied by the RXSM to the necessary voltage levels. Further it controls the two pyrotechnical cutters for the sail deployment and cube jettison. The Main Board is the master controlling all other modules of the experiment. Its task is to interpret the information coming from the RXSM – via 2 data lines (SODS and SOE) for experiment control and a serial RS-422 telemetry interface to relay experiment status messages to the ground station. The used microcontroller is an ATxmega128A1 from Atmel. To illuminate the sail in the case of a night launch or when the sun is occluded by the sail a high performance lighting system has been conceived. In addition to the video a rotation speed sensor on the boom coil was installed in order to calculate the deployment velocity of booms by measuring the angular velocity of the spool. The Plug Board provides the connection to an electrical access hatch placed in the skin of the nosecone adapter. This hatch provides the possibility to arm the experiment using an arm plug and to access experiment data (read and delete OHC video data, download thumbnails of the OMCs, access to the live-view mode of the OMCs with

1 fps, read OMC temperatures, delete OMC video data and update the OMC firmware).

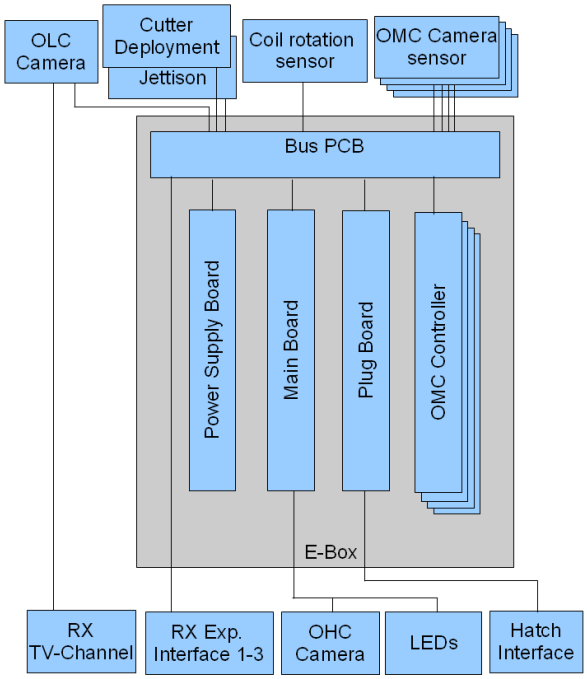

Figure 10: Block diagram of the electrical setup

The cameras on the experiment were designed to capture only a 2 second long event – the deployment of the sail as detailed as possible – both in time and image resolution. To get a high-speed video from the deployment process a self-made camera has been chosen and specifically designed for the operation in the extreme conditions given by the experiment. These conditions compose of extremely varying lighting conditions, small available space, temperature conditions and the threat of a head-first impact in the Swedish Tundra. As it is impossible to capture the whole sail with just one camera it was necessary to use multiple cameras to provide a complete image of the sail. To reduce risk at all sides the whole system with several internal developed cameras (Optical Medium-speed Cameras, OMC) is enhanced by a single professional camera (Optical High-speed Camera, OHC). Furthermore a mini-camera (Optical Low-speed Camera, OLC) has been connected to the live video-channel available from the RXSM. The main objective of this camera was to ensure that the basic experiment objectives, the monitoring of the deployment of the sail could be achieved even if every other camera system should fail.

The Optical Medium-Speed Camera (OMC) is the main camera of the experiment. With multiple cameras a high sail coverage is achieved, while a medium frame rate provides accurate information about the sail and boom deployment. Due to the special requirements for this camera the Space Sailors developed this camera on their own instead of buying a ready product. This promises to facilitate later integration of the camera on a planned CubeSat project which will test the sail in its final deorbiting purpose. The OMC modules consist of an image sensor, a high performance digital signal processor module with external data storage via the SD and ATAPI interface to capture the video stream, as depicted in the block diagram in Fig. 11.

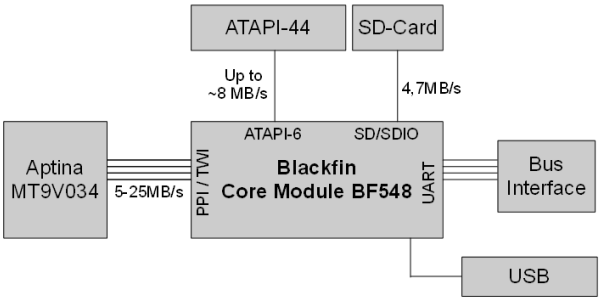

Figure 11: OMC architecture

To protect the captured data the image sensor were physically separated from the data processing and storage, so that the only exposed component is the image sensor. The Sensor module is a small PCB with the image sensor MT9V034 from Aptina. The MT9V034 sensor achieves 60fps at a WVGA (752x480) resolution, although the frame rate could be increased at a reduced resolution. For this purpose 2x2 or 4x4 binning is supported by the sensor, doubling or quadruplicating the frame rate. The 1/3” image sensor MT9V034 has been equipped with a S-Mount (also called M12x0.5) lens holder and lenses with a 120° viewing angle. The lenses require a distance of at least 200 mm distance to the booms for focusing. As signal processor an Analog Devices Digital Signal Processor (DSP) of the Blackfin family is used. The Blackfin DSP family is a high performance (up to 533MHz processor clock) controller with many useful peripherals. As shown in the OMC architecture the OMC Controller consists of the Blackfin DSP BF-548 on a core module CM-BF548 by Bluetechnix. This core module consists of the core voltage regulator, 64 MB SDRAM, 8MByte NAND Flash for booting purposes, reset circuitry and other required housekeeping functions. It greatly reduced the development efforts and risk required to get

the Blackfin running as no BGA components need to be soldered or the high-speed SDRAM Bus needs to be routed. The OMC Controller Board provided the required hardware for this experiment, consisting of two different storage-interfaces (SD-card interface and IDE-44 interface) as well as required debugging and access tools (RS232 and USB).

Figure 12: OMC controller and sensor module

3.3. Software Design

During the whole flight the Main Board collects status data and measurements from the internal voltage sensors and the coil rotation sensor. The Main Board also handles the UART communication to and from the four OMCs. All data is saved to an SD card, important messages are also passed on to the ground station via the RXSM RS-422 interface. The microcontroller processes 5 hardware UART interfaces, which immediately write all incoming data to buffers, parse it to see if there is any control information and then log it and pass it on, if it is meant for or coming from an OMC. The integrity of the data sent between the ground station and the controller is secured by an additional CRC-check. The image data from the OMCs and the OHC is saved on SSDs and not sent via the Main Board.

The software on the OMC controller has the purpose to store the image data received from the image sensor to mass storage so that it can be analyzed after the flight. The priority is to capture the deployment process at the maximum frame rate and resolution. The software interfaces with the Main Board in sending status messages (which are forwarded by the Main Board to the ground segment) and in receiving start signals for recording. It needs to be made sure that the actual deployment is being captured and saved even if the OMC receives additional false trigger signals before or after the actual deployment. The Blackfin processor runs a special Linux distribution (µCLinux) which gives the advantage of available drivers for all mass storage memory options as well as for the other interfaces of the processor. This led to a faster development process of the software. At a higher level the OMC camera software integrates in the experiment according to the flowchart in Fig.13.

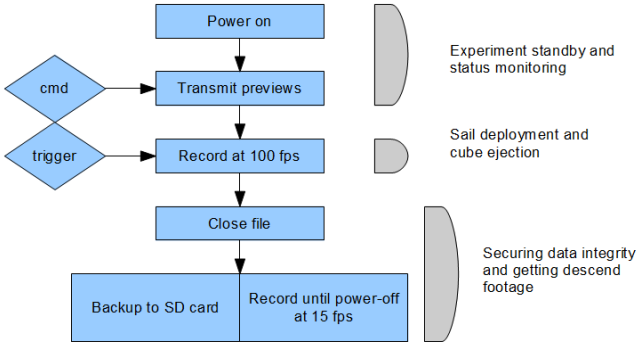

Figure 13: Flowchart OMC software

After power-on the camera regularly transmits status and temperature information to the Main Board and transmits image previews on command to verify the correct function of the camera system. During the deployment and ejection the camera records at the maximum frame rate. After jettison it makes sure the file is closed and starts to backup the video to the internal SD card. In parallel it continues to record low frame rate videos until power-off to a second file to get additional footage of the descend.

4. FLIGHT RESULTS

The deployment of the 2 m² polyimide sail took place after 142 seconds and in an altitude of 81 kilometres near the apogee of the REXUS 14 flight. All cameras monitored that the deployment was successful. The booms and the sail uncoiled completely without being visibly affected by friction. The assumed influence of friction due to gravity under ground conditions is also noticeable when comparing the 0.65 seconds it took for the deployment in flight to the 0.9 seconds for an incomplete deployment of the same system in a ground test. A sequence of four pictures depicts the different stages of the deployment and is shown in Fig. 14. Fig. 15 shows the sail in its completely deployed state maintaining its correct shape.

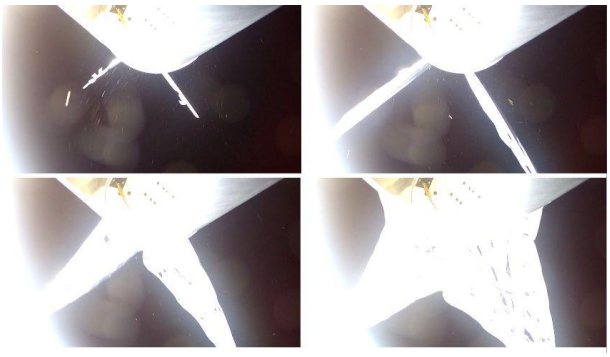

Figure 14: Different stages of the deployment

This shape is held for a few moments, before the sail collapsed like expected due to increasing aerodynamic drag and the quickly changing attitude of the unguided rocket.

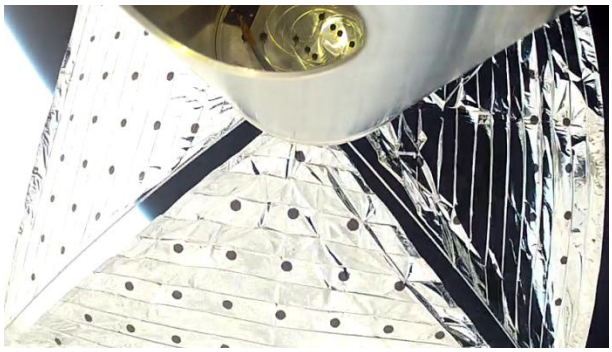

Figure 15: The completely deployed sail at the apogee of the REXUS 14 flight

The self-developed cameras (OMC) were proven to be operational even though a strong overexposure of the pictures is noticeable. Unfortunately the sunlight's effect on the system had been underestimated, involving a wrong calibration of on the automatic exposure correction. The Video of the deployment can be accessed on the Space Sailors Website. [2]

5. CONCLUSION AND PROSPECT

It has been demonstrated that the designed mechanism for a deployment of a dragsail is working as predicted in reduced gravity. The developed camera system still needs to be readjusted for a correct operation in the harsh space environment. The function of the dragsail with respect to its de-orbiting task in-orbit needs still to be verified. With regards to such a future utilization on a small satellite the guiding line was to build the deployment mechanism in accordance to the boundary conditions given by the CubeSats standards. This already led to the plan for an integration of the mechanism on a triple CubeSat which is in development at FH Aachen University of Applied Sciences in their Compass 2 project [6]. Here, besides general mass optimizations it is planned to give the sail a pyramidal shape in order to assist the attitude control system, achieving a satellite-sail-configuration similar to a shuttlecock. The integration of an improved OMC for monitoring purposes is also planned on this satellite, which is designed for a sun synchronous orbit with about 98° inclination and 350 to 400 km altitude. Depending on sun activity from that orbit on the deorbiting duration is calculated to 43 to 24 hours.

6. ACKNOWLEDGEMENTS

The space Sailors student team would like to thank the Institute of High Frequency Technology (IHF), and the Institute of Lightweight Structures (ilb), both of RWTH Aachen University, and the FH Aachen University of Applied Sciences for their support. Furthermore the Space Sailors team would like to thank all the institutes, workshops and companies who made the Space Sailors project feasible by providing and manufacturing the experiment hardware. Special thanks go to REXUS/BEXUS supervisors: Mark Fittock, Martin Siegl and Mikael Inga (SSC), as well as Maria Roth (DLR)

7. REFERENCES

1. Seefeldt, P., Reimerdes, H.-G., Dachwald, B., *"Vorentwicklung eines Widerstandssegels zur Vermeidung von Raumfahrtrückständen in niedrigen Erdorbits"*, 60. Deutscher Luft- und Raumfahrtkongress, 2011
2. Space Sailors website, http://www.spacesailors.de/ last accessed 26 June 2013
3. Eurolaunch, *REXUS User manual*, webseite, http://www.rexusbexus.net/images/stories/rexus/RX_REF_user_manual_v7-7_06Sep12.pdf, last accessed 26 June 2013
4. Kebadze, E., Guest, S. D., *"Bistable prestressed shell structures"*, International Journal of Solids and Structures, Vol. 41, 2004, pp. 2801–2820.
5. Wolff, N., Seefeldt, P., *"Alternative Application of Solar Sail Technology"*, 3rd International Symposium on Solar Sailing, Glasgow, 2013
6. Compass 2 website, http://www.raumfahrt.fh-aachen.de/, last accessed 26 June 2013

DEVELOPING TECHNOLOGICAL KNOWLEDGE IN MICROGRAVITY MISSIONS BY MATCHING PARTNERS EXPERTISE

Alessandro La Neve[(1)], Flávio de Azevedo Corrêa Junior[(2)]

[(1)] Centro Universitário da FEI – Av. Humberto de Alencar Castelo Branco, 3972 - SBC - SP - Brazil - ZIP Code: 09850-901, Department of Electrical Engineering, alaneve@fei.edu.br,
[(2)] Instituto de Aeronáutica e Espaço - Pça. Eduardo Gomes,50- S. José dos Campos - SP- Brazil – ZIP Code:12228-904, Space Project Coordination Group, flaviofacj@iae.cta.br

ABSTRACT

The article takes into account the cooperative work between *Centro Universitário da FEI* (FEI), *Agência Espacial Brasileira* (AEB), *Academia Brasileira de Ciências* (ABC), *Instituto Nacional de Pesquisas Espaciais* (INPE) and *Instituto de Aeronáutica e Espaço* (IAE) in the AEB Brazilian microgravity missions. It brings about some of the initial cares that were taken in order to better define and establish, in cooperation with the researchers, the onboard experiments for the sounding rockets (VS-30 and VSB-30) and for the International Space Station (ISS) by the establishing of researchers' reasonable requirements, by the definition of the payload/experiment interfaces and by the specification of the ground facilities needed for the experiment support. Inside this context, some mechanical, electronic and technical aspects of FEI experiments were analyzed to eventually assure a payload ready for a successful mission.

The experiments that were sent on different missions by FEI were based on two main research lines - biotechnology and materials - for the study of enzymatic reactions and carbon nanotubes .This required that special devices be developed to perform the experiment in microgravity automatically. At each new flight an upgraded version of the device was implemented, based on the previous experience The article exploits some aspects of the design, development, assembling, test from missions of different characteristics (suborbital and orbital), and comments on what was learned in the process. This would finally lead to a know-how acquisition that resulted in a steady improvement of the projects in successive missions with microgravity experiments.

1. INTRODUCTION

Brazil started to perform experiences in microgravity environment in the mid-1980, when some independent researches made some studies using the US Space Shuttle or local drop towers. In the past, Brazilian rockets were largely used to perform studies of high atmosphere and ionosphere by *Instituto Nacional de Pesquisas Espaciais* (INPE), an important partner and stakeholder of *Instituto de Aeronáutica e Espaço* (IAE).

At that time, the Brazilian space missions were concentrated mainly on this kind of research. At the end of 90´s, some simple microgravity missions were performed by IAE using a brand new rocket VS-30. In 1997 was established the Microgravity Programme from *Agência Espacial Brasileira* (AEB). The Brazilian scientific community was not so much familiarized with the microgravity environment or how to develop an equipment for perform an experiment on board a space vehicle.AEB Microgravity Programme brought a new dimension to IAE´s regular activities once it became responsible not only for the activities related to sounding rockets but also for the technical aid and verification/test of the experiments developed by the Programme stakeholders. Mission by mission, all involved institutions started to learn from their success and failures in a virtual circle spiral of increasing knowledge. *Centro Universitário da FEI* (FEI) is one of those pioneer institutions that started its microgravity activities earlier in Brazil, being also a pioneer participant of IAE's missions since the beginning, and has as an amount of knowledge created through this interface´s process. The development of an experiment, right from the conception till the point that it is accepted to be placed aboard a rocket is not an easy feature. The idea of this article is to exchange a few experiences between institutions about this dynamics.

2. SUPPORT FOR THE BRAZILIAN MICROGRAVITY ACTIVITIES

The AEB Microgravity Programme was established in 1998, when the first public announcement of opportunity (AO) for development of experiments in a weightlessness environment using a suborbital flight was also launched. Till know three AOs were launched and most of their selected experiments flew onboard on a sounding rocket (VS-30 or VSB-30) or on the International Space Station (ISS). A fourth AO for a suborbital flight has been launched in May of 2013.

Proc. '21st ESA Symposium European Rocket & Balloon Programmes and Related Research',
9–13 June 2013, Thun, Switzerland (ESA SP-721, October 2013)

In order to accomplish the microgravity missions that needed a special controlled and sea recovery payload, IAE resorted to DLR/MORABA, an old scientific international partner, whose expertise with microgravity payloads is worldwide recognized. An agreement was performed for supplying two microgravity payloads for VS-30 sounding rockets, including the technical support for customization and their flight operation.

After receiving the proposals from the AO, a first approach to select the onboard experiments should analyze the overall aspects of the proposals such as: weight, volume, power supply, fixing areas, data channels availability, on/off signals availability, environment thermal analysis, demand of a cooling environment, late access, sample life time, recharge of sample, sample pre-flight preparation time, onboard and ground logistics etc.

Based on all possible data gathered a large list of criteria should be applied in order to select clusters of compatible experiments regarding where the experiments would be placed. Safety rules are more severe for ISS then for sounding vehicles. By assuming that the experiments should not follow a regular aerospace acceptance pattern in order to not push so much the involved beginner, the acceptance tests were customized in a lighter way, without compromising safety. On the other hand, it was promoted some rough and safe interfaces between payload and experiment to avoid that a local failure would affect the whole payload. It was assumed that to work in a proto-flight concept with the experiments was an acceptable risk, in order to keep the development process simple, cheap, and fast, avoiding the development of engineering and qualification models. The proto-flight concept for aerospace developments is not usual for some aerospace institutions forcing a change of paradigms.

2.1 Technical Documentation

At that time, the researchers requirements regarding the technical specifications were made side by side with the researchers, occasion when information were exchanged and fixed, then transmitted to DLM/MORABA to perform the payload/experiment interfaces of the sounding rocket, or to ENERGIA to verify the ISS and experiment interfaces. Regarding the sounding rockets, with the evolution of experiments mission by mission, the interfaces initially simple, regarding only a microgravity start signal or/and a power supply, changed requiring data downlinks, adding new stakeholders requirements or some new pre-flight procedures from IAE team, making the experiment more complex. Comparing the project documentation generated on the 1st AO it was relatively simple, but with successive AOs the need for more and better qualified information, in a standard form, was felt. The programme documentation gained a substantial body after 2005 with the Brazilian mission to the International Space Station (ISS) when, based on the Russian mandatory documentation demanded for ISS, it was decided to apply such model to suborbital flights, in a compatible simpler version. Today documentation consists of two volumes, a pre-project proposal to be sent as a basic proposal in the AO, and the final project documentation fulfilled gradually, during the project, in a very comprehensive way.During the development of the experiments at least two revisions are made in accordance with the life cycle of the project.

3. TESTS AND VERIFICATIONS

In order to test a proto-flight isolated, at the beginning only visual check, electrical interface check, EMC/EMI test, thermo-cycling test, vibration test and the experiment activation to verify its acting performance were performed. Hardware checking was performed only at acceptance level, not to stress the prototype unnecessarily.All proto-flights were then turned to the payload electrical web were system tests are performed making exhaustive interface verifications.

4. EXPERIMENTS IN MICROGRAVITY

Experiments in microgravity have been carried out for quite a long time, at FEI, initially in the area of biotechnology, and more recently with carbon nanotubes, in the area of materials [1-7]. The experience continuously gained through the missions is undoubtedly a great learning for future projects.
In biotechnology the environment of low gravity provides a “new laboratory” to study cells and cellular systems, so as to better understand how they adapt to space, at cellular level. As for nanotubes, in material science, microgravity shows to be interesting to achieve homogeneous nanotube deposits on metal surfaces, exploring all of the properties of this carbon allotrope.

4.1. Experiments with Enzymes

The study of enzyme kinetics is a first and fundamental step to understand the mechanism of action of enzymes inside and outside cells, and for the design of enzymatic bioreactors and biosensors in space [8,9].

Research in microgravity can lead to a better understanding of basic phenomena and lead to benefits in applying this knowledge on Earth and in the development of future applications in space.

This environment has shown to be very interesting and effective to study transport phenomena and fluid behavior, that is, the phenomena that can be affected by

microgravity (or absence of weight force). In microgravity the convection, sedimentation and hydrostatic pressure tend to disappear and the spherical interface of gas-liquid appear randomly [10]. Emulsions are more stable and basic phenomena, such as sedimentation, mixing, convection and diffusion are considerably different in microgravity. Consequently, such effects induce a significant change in mass transportation which affects the nutrient supplies and cellular metabolism [10].Some works realized with plants showed that the amount of cellulose and lignin decreased in microgravity [11] but enzymatic activity of several enzymes of the cell walls of plant cells increases in space, which causes a change in metabolism and cell wall structure [12].

4.1.1. DMLM and MEK Devices

To perform experiments with invertase and lipase, specific devices were developed, to have the liquids react in microgravity. These liquids were invertase enzyme, to be mixed with sucrose substrate, and lipase enzyme, to be mixed with triolein substrate.
The first experiment with enzymes at FEI was performed in 1999, when the AEB –Brazilian Space Agency started the Microgravity Program in 1999, in cooperation with DCTA/IAE, Institute for Aerospace Studies, opened opportunities for universities to participate and send their experiments in the scientific payload, aboard sounding rockets.After this other experiments followed to investigate invertase enzyme mainly sent on board sounding rockets and also in the ISS.

The first experiments tested only one sample of enzyme and concentration substrate, but in the following experiments the samples were increased to five and finally to ten. The reason for this was to admit a broader range of different concentration and also to have multiplicity, in case of loss or failure.

The scientific and technological requirements of the experiments in microgravity changed over the time according to the facilities and characteristics that were offered aboard the carrier, sounding rockets or ISS, and the results obtained in previous missions and experiments.
These different implementations required more complex designs, especially in the mechanical conception. The evolution was a natural response that took into account the expertise that was necessary to overcome the difficulties that had aroused in the previous ones.These devices were implemented to carry the enzymes and the other liquids, necessary to perform biochemical reaction in microgravity, to fly on board VSB-30 sounding rockets in Brazilian missions [1-7], in evolution over the previous ones.

The biochemical reaction should be interrupted, in microgravity, either by heating the product of the reaction up to a specific temperature, or by introducing a third liquid, to inhibit the reaction.
The first devices were devised to work with the equivalent to a syringe of two stages, and this concept was eventually changed, as an extension, to a reaction chamber of three sections.

As mentioned before, the first approach to interrupt biochemical activity in microgravity was by heating the mixture over 90º C, which is preferably done in soil, since it avoids the use of a third liquid. This solution was used in the DMLM I and II devices, for sounding rocks applications, and even in MEK device, for ISS flights. MEK is a computerized mini-lab devised to allow for multi-variables enzymatic reactions performance. MEK consisted of mechanical parts and embedded electronics. It had 15 reaction chambers, divided in 3 sets of 5 reaction chambers, which were responsible for the mixture of two different liquids or reagents. Two sets were reserved for invertase and one for lipase: each set was filled with reagents in different concentrations.

The reaction chambers are divided in three sections, as shown in fig. 1. The liquids are loaded in sections A and B; section C is reserved for volume expansion, as it can be seen in this figure. At the opposite side of the embolus there are the thermal sensor and control terminal. The two different liquids, loaded in compartments A and B, are mixed by the action of a plunger.

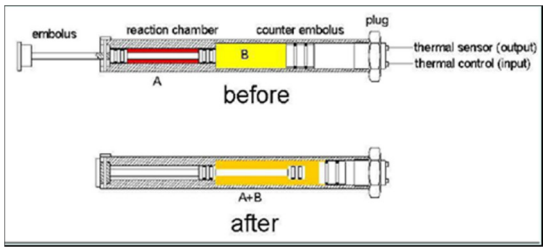

Figure 1. Reaction chamber internal details.

Then, when the embolus is pressed, the liquid in compartment A mixes with what is in compartment B. This chamber design was essentially used both for the first DMLM devices, and for MEK as well.This solution however presented some difficulties to assure proper sealing. Should an occasional leakage occur, it would affect final mass measurements, and so the bio reaction mass results.This conception, however, was abandoned in the design of next device, DMLM III, and the solution with a third inhibitor liquid to interrupt the biochemical reaction was adopted.

The new design of DMLM III device permitted that the reaction chambers could be arranged so as to admit the mixture of three or more liquids, simultaneously or in sequence, as it can be seen in Fig. 2.

Figure 2. Internal view of DMLM III device

Chambers are connected serially with a valve, which controls the flow of liquids from one chamber to another. This organization, with n chambers connected by n-1 valves, allows for a wide range of liquid mixture combinations, according to the requirements of each biochemical process.

The mixing of liquids may be performed in one single step, opening all valves in parallel, or serially, opening the valves in sequence, after the necessary time that is required at each step. In this case, two liquids are mixed at a time and the product of the reaction is then mixed with a third liquid, and so on, until the last liquid is set in the mixture.

Internal details of DMLM III device are shown in Fig. 2. It is possible to notice the two reaction chambers sets, each arranged in a slot, the pack of batteries and the electronic boards. Two sets of five reaction chambers blocks were implemented, summing up a total of ten chambers.

Each chamber block is made up of three steel chambers, as shown in Figs. 3 and 4, which contain the three liquid reagents: the sucrose substrate, the invertase enzyme and the inhibitor reagent.

Proper sealing was a main concern in DMLM III design, both to protect other experiments, inside the rocket payload, from any sort of contamination or chemical damage, and to ensure that the chemical reaction would be performed with the correct component specifications, as to volume, mass and concentration. This would be fundamental to analyze the results of the chemical reaction and compare them to those obtained in laboratory.
Reaction chambers, serially connected and separated by a valve each, proved to be convenient and effective in the mixture automation of liquid reagents in an established sequence. The organization used for the reaction chambers was very adequate to load liquids, and minimized the number of leakage points, maintenance and processing time. The device was successfully submitted to all the required tests for flight validation.

4.1.2. The Device Mechanism

All valves of each set in the block are interconnected with a transmission shaft, as it can be seen in Fig. 3, so that they can be opened all at the same time, ensuring that the liquids in all chamber sets have the same reaction time.

There are two valves per block of chambers, in a total of ten, with two transmission shafts, each one controlling five of them: the first one puts the enzyme and sucrose in contact for reaction, and the second injects the inhibitor to stop the biochemical reaction. Step motors drive the shafts of each block set, to ensure simultaneity of events in all chambers, as in fig. 3.

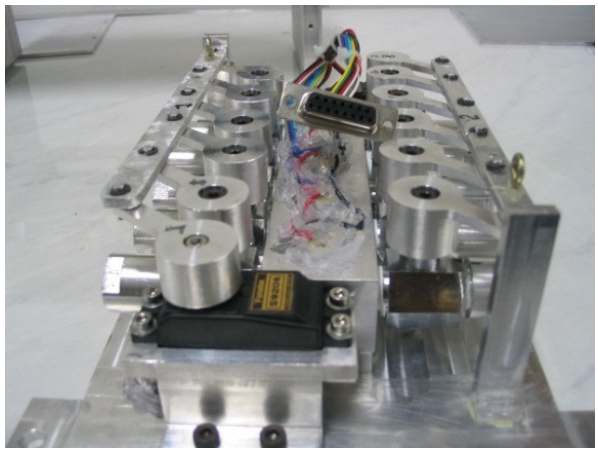

Figure 3.Two 5-chamber sets.

Steel chambers, as seen in Fig. 3, were used to avoid any possible chemical reaction of the container material with the liquids of the experiment, which would adulterate the biochemical reaction.

The three liquids are loaded, in each chamber, before starting the experiment. When the microgravity signal is triggered, the first valve of each set is driven by a step motor system, which powers the entire valve assembly through a transmission lever. After this, the enzymes and the substrate, at different concentrations, are put in contact and the biochemical reaction starts. After 5

minutes, the second set of valves is driven by another step motor, which puts them in contact with the inhibitor to stop the biochemical reaction. During the experiment, the internal temperature is monitored. Data are periodically stored in the processor memory and also sent by telemetry.

The reaction time is such that the process may happen only in microgravity, to avoid any external interference. Four step motors are used, two for each set of block chambers, as it can be seen in Figs. 1 and 3, powered with 12 Volts, by a set of 10 batteries (1.2V each one).

Chamber loading represented a main problem to deal with, since this process had to be done very carefully and in a very limited time, before launching.Chambers should be filled with the exact dose of reagents, avoiding any leakage, to ensure that they have the exact mass of reagents. Invertase and sucrose samples, if not used, should be replaced every 24 hours, not to lose their properties after this period of time, when they are not kept in proper cooling conditions.

Loading was performed with a syringe for each liquid, starting with the inhibitor, and then proceeding ahead with the others. After filling in a chamber, the corresponding valve is closed, sealing the liquid off that chamber and isolating it from the other ones, to avoid any possible contamination in the process. The process continues up to the last chamber in the row, which is sealed off with a screw.

4.1.3. Electronics

On board electronics required a CPU especially designed for this purpose, using an ADuC814 microcontroller [13] with the necessary peripheral circuits. The CPU was responsible for control, variable monitoring, data acquisition, and serial communication for the rocket telemetry system.

The ADuC814 microcontroller was chosen for its compactness, low power consumption, simplicity of use and multifunctional features, which reduced peripheral hardware. It is an 8-bit microcontroller and it works with a low frequency external clock of 32 kHz, and higher internal clock of 16.78 MHz [13]. The PLL circuit allows working with low frequencies, off the chip, avoiding electromagnetic interference, due conduction and /or radiation emission, with other electronic equipment. This was verified with the Electromagnetic Compatibility Tests realized at INPE-Instituto Nacional de Pesquisas Espaciais, at São José dos Campos, SP, Brazil, as one of the procedures to go through, for flight validations and acceptance tests, for the device to be qualified to fly aboard aerospace vehicles.

A 12-bit A/D (analog-digital) built in converter was most convenient and satisfactory for this application, to read analog variables and store them after conversion. The use of flash memory was also an important feature and an easy way for data recovery.

This microcontroller series was also used in other microgravity projects, and proved to be efficient and reliable [7-10]. Fig. 4 shows some details of a DMLM III CPU used in the embedded electronics.

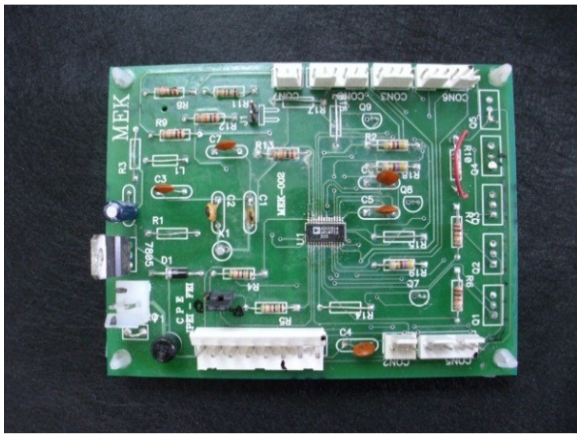

Figure 4 . DMLM III CPU electronic board.

Temperature data acquisition is performed through the microcontroller A/D inputs, which reads voltage levels of a temperature sensor transistor, and converts them into a 12-bit word. Fig. 5 shows the temperature behavior, inside DMLM III, during runtime in microgravity.The temperature inside DMLM III, in microgravity, varied from 27.5°C to 32°C along the flight.

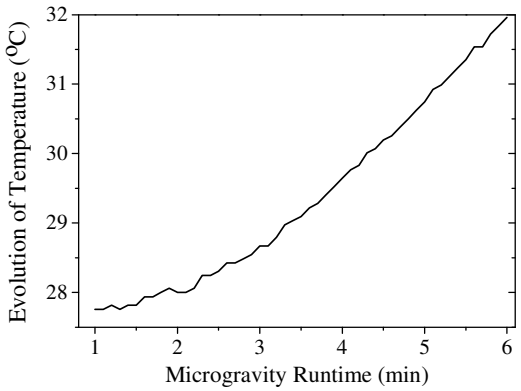

Figure 5: Evolution of the temperature measured inside DMLM III device in microgravity.

As a means to overcome possible failures, redundancy was implemented whenever possible, to reaction chambers, for instance, and to the sounding rocket telemetry system, as a support to back up data. This would ensure that some important parameters, be

reproduced in lab tests, on Earth, to simulate the flight environment.

4.1.4. Biochemical Results

Results obtained in microgravity were compared with the same experiment performed on ground, called Control 1g DMLM III, and with two other standard tests performed in laboratory as usual, modules 1 and 2. Comparison of results between module 1 and module 2 showed an unexpected lack of reproducibility of reaction rate in some chambers. This suggests that there was probably not proper fluid contact, when the valves were opened, between the substrate and the enzyme. Since there was no forced agitation, the only mechanism of fluid mixing was due to diffusion, which is very dependent on liquids phase contact, and it may have not occurred if bubbles were present in the interface. Those chambers that had an efficient contact resulted in values of reaction rate ranging from 2 to 4.5 times higher than those obtained in ground control. Further experiments are needed to clarify the gravitational effect on this enzymatic reaction.

4.2. Experiments with Carbon Nanotubes

More recently, another experiment was carried out in microgravity, this time with carbon nanotubes, in the area of material science, and it benefitted from the expertise acquired with enzymes experiments

Carbon nanotubes (CNT) have been intensively studied because of the unique electrical and mechanical properties of this carbon allotrope, such as high specific surface area and electrical conductivity in the direction of the nanotubes axis [14-18]. This makes them potential components for applications in catalysis and microelectronics. One of the ways in which the CNT can be used is through the formation of a thin film on metal surfaces, which can provide metal structures with part of their properties. The formation of thin films may be obtained through electrophoretic deposition (EPD), by which electrically charged CNT in suspension are moved under an electric field towards a conductive substrate, where they are homogeneously deposited [19-21].Though this is a relatively simple process, some characteristics of the CNT suspension may affect the film homogeneity. The effect of gravity during the EPD process have been described in the literature as an influencing factor, because of sedimentation force, causing a concentration gradient of CNT in suspension. This behavior could result in heterogeneous CNT deposits on the surfaces and extensive disruption of nanotubes films [22, 23].

The microgravity environment would appear, therefore, as an ideal condition to achieve homogeneous nanotube deposits on metal surfaces, exploring all of the properties of this carbon allotrope, which has its own characteristics strongly dependent on its alignment.

4.2.1. 2.2 CADEN Device

In order to carry out this investigation, it was necessary to develop and implement CADEN device. CADEN device comprises a set of 12 deposition chambers to work simultaneously, under specific conditions each, like CNT concentration, electric potential and deposition time. The effects of these variables would be investigated both in microgravity and in the laboratory, to verify gravity effect on the CNT film homogeneity and electric conductivity of the system.

CADEN device consists of 3 sets of 4 metallic reaction chambers each, embedded electronics, for the control of the system and for monitoring the electric current that flows through each chamber, when the device is operating in microgravity.

The chambers contain CNT suspensions with two different concentrations (0.1 mg/ml and 0.5 mg/ml), flowing an electric current, according to the voltage applied to the plates, anode and cathode, respectively. Each set of chambers is biased by a different dc voltage (5V, 12V and 18V) and contains different CNT concentrations in each pair of chambers.

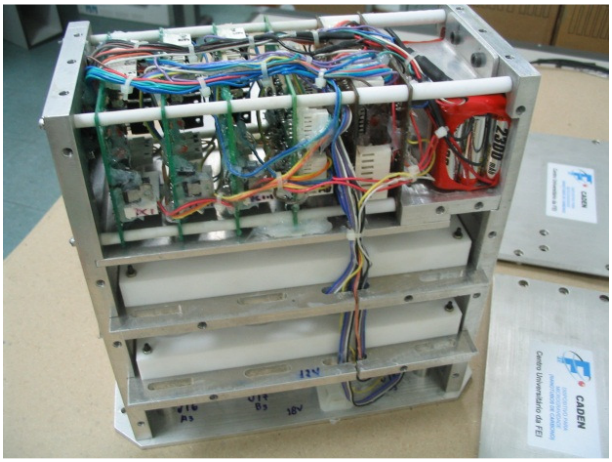

Figure 6. Internal view of CADEN device.

Fig. 6 shows internal details of CADEN device. It is possible to notice the three chambers set, arranged one over the other, the batteries pack and the electronic boards. Upon detecting microgravity, the control system applies a different bias to each of the three sets, which are powered by their own battery. From this moment on, each pair of chambers, in each of these sets, is active only for the first two minutes, that is half the microgravity scheduled time, and the other is powered for four minutes.

The currents that flow through all chambers are measured periodically throughout the experiment. Data are stored in the internal processor memory and are also sent by telemetry, to ensure redundancy for data recovery.

The electric current should therefore be monitored, for further analysis, and data should be saved along the electric activity, while they are in microgravity.The morphology of CNT deposition layer on aluminum plates would later be analyzed on MEV microscopy.

4.2.2. CADEN Chambers

CADEN equipment is composed, as mentioned above, of three sets of four chambers each that contain CNT suspensions at different concentrations. The main body of theses chambers is made of Teflon, whose dimensions are 276mm (L) x 126mm (W) x 272mm (H). The chambers are cylindrical, with internal diameter of 10 mm, and height of 20 mm.

4.2.3. Electric Current in CNT Chambers

The suspension is prepared with CNT, properly functionalized in a solution of nitric acid (HNO3) and then washed up [18, 19].Once the aluminum plates are connected to the battery a current will be established in the chamber, loaded with CNT suspension. This current flows through a "voltage sensor resistor", which is connected in series with the power supply and causes a potential difference on it. This voltage is applied to the input of an operational amplifier, which amplifies it at the output, making it appropriate for reading and analog/digital (A/D) conversion. The op-amp, biased in the linear range, ensures a suitable voltage to be read by an A/D converter. In this way it was possible to transform the current flowing in CNT chambers in a linearly corresponding voltage.

Since the three sections of chambers work with three different power supplies, different currents will flow through them, and their corresponding op-amps were dimensioned accordingly.

4.2.4. Electronics

CADEN device is controlled by embedded electronics, which consist of three CPU - Central Processing Unit built around a microcontroller ADuC814 [13], to perform monitoring and data acquisition of variables for control, including bias chambers, measurement of the electrical current in each chamber, data storage in flash memory and serial communication for the sounding rocket telemetry data system.The CPU was built around the ADuC814 microcontroller, because it had already been used in previous microgravity experiments with enzyme devices, and had proved to be very efficient, practical and reliable [1-3].

Parallel architecture also ensured, to some extent, fault tolerant computing, though this concept was not set as a design goal at this stage. One of the CPUs was set as master, in relation to the other two, which would act as "slaves". This architecture was necessary to ensure synchronism with all CPU's, so as to decide when CNT chambers would activated and data acquisition would start. Each CPU was also prepared to transmit its own data to the sounding rocket telemetry system, under supervision of the master CPU. However, since only one serial channel was made available for each experiment, this architecture had to be changed.A serial communication bus was adopted, where each CPU loads and sends its own data, under supervision and control of the master CPU.

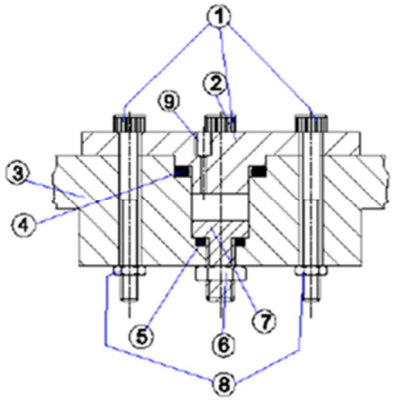

Figure 7. Construction details of an electrophoretic deposition chamber:(1) bolts; (2) top plate; (3) chamber body; (4) and (5) O-rings;(6)nut; (7) bottom electrode; (8) nut.

A major concern, in the design of this mini-lab, was to ensure an easy way to load CNT chambers with CNT suspensions, since they should be changed every 24 hours, to maintain their physical-chemical properties, when kept at a controlled temperature.

Loading and re-loading of CNT suspensions would be performed with a syringe and a removable electrode, which works also as bottom base of the cylindrical chamber, as seen in fig. 7.

4.2.5. Carbon Nanotubes Results

The experiment results obtained from CADEN in microgravity are under evaluation. The first analyses show that there was an increase in the electric current in microgravity. Besides electrical characterization of all 12 electrodes, which is necessary to evaluate its electrical resistivity, further investigations will be carried out about CNTs deposition, on the aluminum

surface, performed with SEM images, before it may be possible to draw some consistent conclusion.

5. CONCLUSIONS

The experiments sent on different missions by FEI were based on two main research lines - biotechnology and materials - for the study of enzymatic reactions and carbon nanotubes .This required that special devices be developed to perform the experiment in microgravity automatically. At each new flight an upgraded version of the device was implemented, based on the previous experience.

The results derived from biochemical analyses for the enzyme experiment show an increase in enzyme activity in microgravity environment in some samples, but not in all. As for the nanotubes experiment, the first analyses show that there was an increase in the electric current in microgravity environment, when compared to similar experiments carried out on earth.

The article exploited some of the design, development, and mission aspects. This finally led to a know-how acquisition that resulted in a steady improvement of the projects in successive missions with microgravity experiments.

6. ACKNOWLEDGEMENTS

We want to express our acknowledgements to the entities that made possible this accomplishment, namely *Centro Universitário da FEI* and AEB (Brazilian Space Agency) for the engagement and financial support to the missions, DCTA/IAE, INPE (National Institute of Space Researches, Brazil) and DLR/MORABA (*Deutsches Zentrum für Luft und Raumfahrt e. V.*) for the mission technical support, and CLA (*Alcântara* Launching Centre, Brazil) for the ground and test facilities offered for launching.

Finally, the authors would like to express their special gratitude to **FUNCATE** (Space Science, Applications and Technology Foundation, Brazil) for the financial support that enabled the participation in the 21st ESA Symposium on European Rocket and Balloon Programmes and Related Research in Thun, Switzerland.

7. REFERENCES

1. Neve,A.L.,et al.” Invertase Enzyme Biochemical Reaction Experiment In Microgravity” ,Proceedings of 62nd International Astronautical Congress, IAC 2011, A2.3.13,Cape Town, South Africa , 2011.
2. Neve,A.L.et al., “CIM device for enzyme kinetics experiment aboard the International Space Station” IAC 2011, A2.6.9,Proceedings 62nd International Astronautical Congress, Cape Town,South Africa, 2011.
3. Neve.A.L.,et al.,"MEK-multivariables device development for enzymes kinetics experiment in microgravity“, IAC 2012,A1.7.8,Proceedings of 63nd International Astronautical Congress, Naples, Italy , 2012.
4. La Neve, A., Lucarini A.C., International Conference on Engineering and Computer Education ICECE 2000, CD ROM, 2000.
5. La Neve, A. et al.., International Congress on Engineering Education ICEE 2000,Cd ROM, 2000.
6. La Neve, A. et al.., AEB Technical Report, 2003.
7. “Missão Centenário”, Seminário Sobre Os Resultados, Organizado Pela AEB- Agencia Espacial Brasileira, INPE, São José Dos Campos, SP, November, 2006.
8. Lewis, M.L., *Earth Space Review*, Vol.03, n.1, 22-28, 1994.
9. Clément, G., Slenzka, K., *Fundamentals of Space Biology*, Cap. 8, 337-362, 2006.
10. Hu, W. R., *et al*., *Chinese Science Bulletin*, Vol.54,n.22, 4035-4048, 2009.
11. Perbal, G., *Fundamentals of Space Biology*, Cap. 6, 227-290, 2006.
12. Gaubin, Y., *et al., Advances in Space Research*, Vol.18, n.12, 221-227, 1996.
13. http://www.analog.com/static/imported-files/ data_sheets/ADUC814.pdf, accessed in 05.12.2011.
14. Andrews, R., *et al., Accounts of Chemical Research*, Vol. 35(12), 1008-1017, 2002.
15. Iijima, S., *Physica B: Condensed Matter* (Amsterdam, Netherlands), Vol. 323, 1-5, 2002.
16. Kaneto, K., *et al., Synthetic Metals*, Vol.103, 2543-2546, 1999.
17. Berber, S., *et al., Physical Review Letters*, Vol. 84,4613-4616, 2000.
18. Krishnan, A. *et al., Physical Review B*, Vol. 58,14013-14019, 1998.
19. Boccaccini, A.R., *et al., Carbon,* Vol.44, 3149-3160,2006.
20. Shaffer, M.S. *et al., Carbon*, Vol. 36, 1603-1612,1998.
21. Esumi, K., *et al., Carbon*, Vol. 34, 279-281, 1996.
22. Kutner, W., Pieta, P., Nowakowski, R., Sobczak, J.W., Kaszkur, Z., McCarty, A.L., D'Souza, F. Composition, structure, surface topography, and electrochemical properties of electrophoretically deposited nanostructured fullerene films (2005) Chemistry of Materials, 17 (23), pp. 5635-5645.
23. Dokou, E., Barteau, M.A., Wagner, N.J., Lenhoff, A.M. Effect of gravity on colloidal deposition studied by atomic force microscopy. (2001) Journal of Colloid and Interface Science, 240 (1), pp. 9-16.

DATA LOGGING A WATER ROCKET WITH ARDUINO

Tim Joris [(1)], Jo-Hendrik Thysen [(1)], Michel De Roeve [(1)], Dirk Geeroms [(1)], Sabine Bertho [(1)]

[(1)] Hasselt University - Campus Diepenbeek, Agoralaan – Building D, 3590 Diepenbeek, Belgium
Email: michel.deroeve@uhasselt.be

ABSTRACT

Water rockets can achieve great acceleration and height. The takeoff of these rockets, i.e. the period during which the rocket is accelerated upwards, typically lasts 200 ms. To accurately visualize e.g. the acceleration during takeoff, a measuring frequency of 1000 Hz is desired. In this project, we show that this is possible using a fairly simple, student friendly micro-controller, namely the Arduino nano 3.0.

1. INTRODUCTION

When making a water rocket, a lot of effort is put in the design in order to reach a great height. The world record height is 609 m and during this flight a speed of 200 km/h was achieved [1]. When launched, the acceleration of a water rocket can exceed 100 *g*. The aim of this project is not reaching the greatest height with a water rocket but rather to adequately record the height and acceleration of the water rocket during its flight.

2. EXPERIMENTAL SETUP

The starting point for assembling the water rocket with a measuring unit is Arduino [2], an open-source electronics prototyping platform based on flexible, easy-to-use hardware and software. An Arduino board can be combined with several components that are capable of measuring the desired quantities.

2.1. Components

For the measurement of the acceleration, the ADXL001-70 (Analog Devices) was chosen. This accelerometer has a range of -70 *g* to +70 *g* and has an accuracy of 1 *g*. It is a capacitive acceleration sensor. Its working principle is depicted in Fig. 1. A movable frame is attached with 2 springs. When accelerated, the frame will move a distance *x* with respect to the capacitors according to Hooke's law:

$$F = k \cdot x \qquad (1)$$

where *k* is the spring constant and *F* if the spring force. The 2 capacitors in the accelerometer (Fig. 1) measure the distance *x* that the frame has moved by the change in their capacitance. The acceleration *a* is then deduced from Newton's second law:

$$a = k \cdot x / m \qquad (2)$$

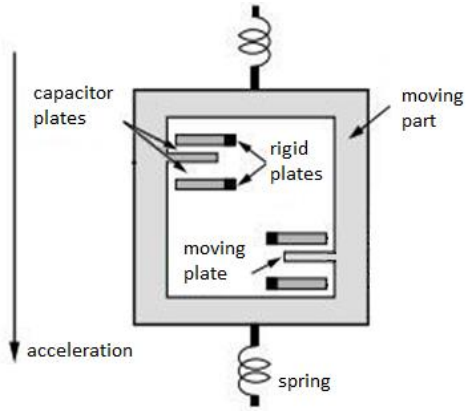

Figure 1. A capacitive accelerometer.

For the measurement of the altitude, the altimeter module MS5607 from Parallax was used. This device uses measurement of the air pressure *P* and temperature *T* to determine the altitude *h* with an accuracy of 20 cm:

$$h = \frac{T_0}{L} \cdot \left(\frac{P}{P_0}\right)^{\frac{-L \cdot R}{M \cdot g}} - \frac{T_0}{L} + h_0 \qquad (3)$$

where T_0 is the temperature at sea level, L is the change in temperature per length unit in the troposphere, P_0 is the pressure at sea level, R is the universal gas constant, M is the molar mass of air, g is the gravitational constant and h_0 is the altitude at sea level.

To make sure that the rocket and the accompanying measuring equipment land safely, a parachute mechanism was designed. This mechanism consisted of a compass module, a cap containing a parachute and a servo motor to release the cap. The compass module CMPS10 from Robot Electronics is capable of measuring the orientation of the rocket using the magnetic field of the Earth. The microcontroller was programmed to trigger the servo motor when the rocket tilts more than 45°. This is shown in Fig. 2.

The Tower Pro Micro 9 gram SG90 servo motor can rotate over a maximum of 180°. When switched on, it will release a parachute by opening a cap. Inside the

Proc. '21st ESA Symposium European Rocket & Balloon Programmes and Related Research',
9–13 June 2013, Thun, Switzerland (ESA SP-721, October 2013)

cap, a small parachute is attached to a large parachute. The small parachute will first leave the cap and pull the large parachute out of the cap.

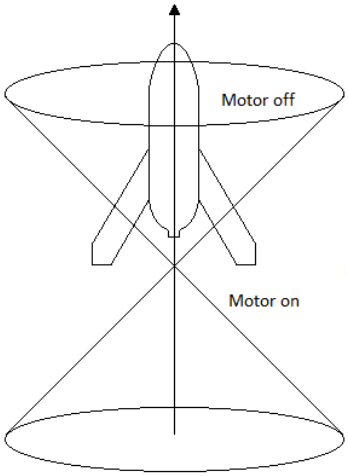

Figure 2. Once the rocket points out of the cone, the servomotor is switched on and the parachute is released.

2.2. Assembly of the measuring unit

The above-mentioned components were connected to 2 Arduino Nano 3.0 boards. One board was connected to the accelerometer, the altimeter and an microSD board (Fig. 3). A 16 GB microSD-card was inserted in the microSD board for the data storage. The second Arduino Nano 3.0 was connected to the compass and the servo motor as shown in Fig. 4.

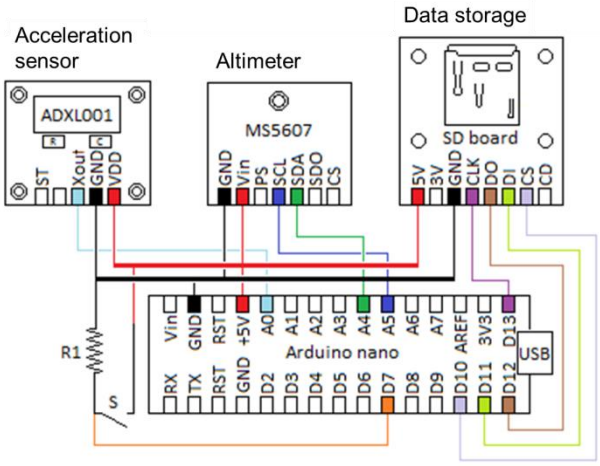

Figure 3. An Arduino Nano 3.0 connected to the accelerometer, the altimeter and an microSD-board. R1 is a resistance of 10 kΩ and S is a switch.

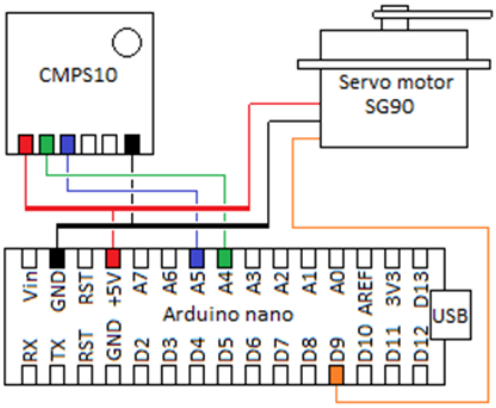

Figure 4. An Arduino Nano 3.0 connected to the compass and the servo motor.

The whole measuring unit was united in a circular cap that was mounted on top of a water rocket. The measuring components were distributed across 3 PCBs (printed circuit boards). The bottom PCB (Fig. 5) contained two 9 V batteries (each with its own switch) for powering the Arduino Nano 3.0 boards. The middle PCB (Fig. 6) contained a switch for starting the measurement, an Arduino Nano, the microSD board and the altimeter. The top PCB (Fig. 7) contained the second Arduino Nano, the compass, the accelerometer and the servo motor.

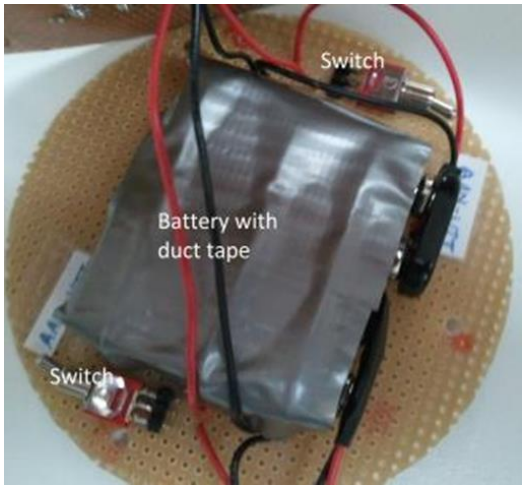

Figure 5. The bottom PCB contained two 9V battery, each with its own switch.

When mounted on top of each other, the complete measuring setup looked like Fig. 8. This measuring unit was attached on top of the water rocket as in Fig. 9. A cap that could be opened by the servo motor contained the parachute. A smaller parachute was intended to pull out the larger parachute.

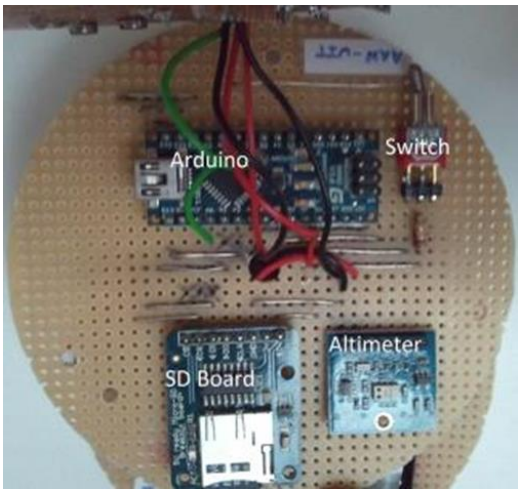

Figure 6. The middle PCB contained a switch, an Arduino Nano, the microSD board and the altimeter.

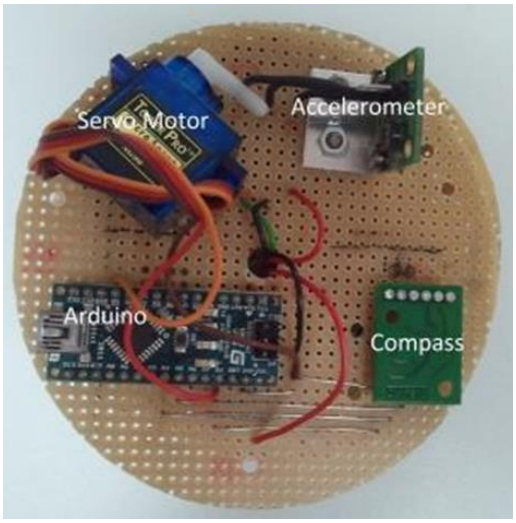

Figure 7. The top PCB contained an Arduino Nano, the compass, the accelerometer and the servo motor.

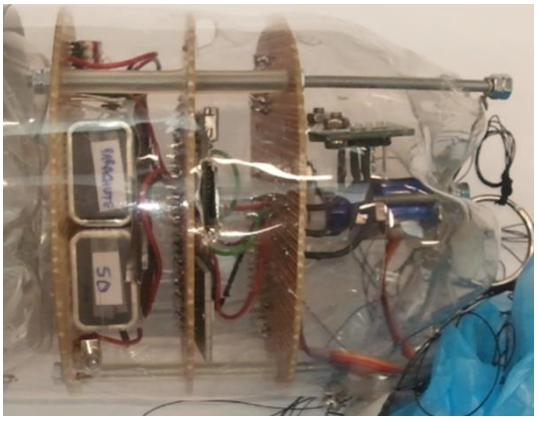

Figure 8. The whole measuring unit put together in a circular cap.

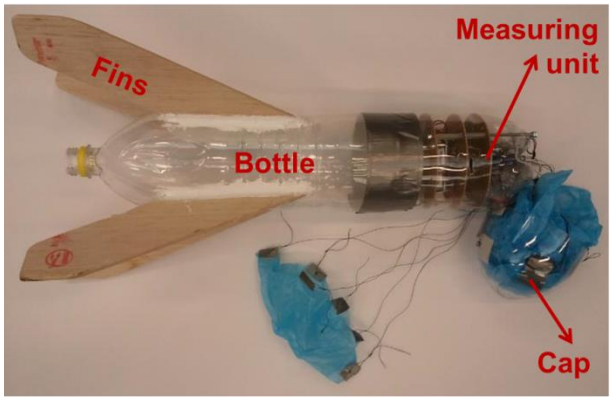

Figure 9. The water rocket with the measuring unit attached on top. The parachute was inserted in a cap that could be opened by the servo motor.

2.3. Software

The open-source Arduino software was used to program the measuring setup. The C-based Programming Language is called Processing. The code had 2 main parts. It started with a *void setup* for initializing all variables. The actual measurements were programmed in the *void loop*. The code could be uploaded to the Arduino via USB communication.

An important requirement for the software was the high measuring frequency. The water driven phase of a water rocket typically lasts only 200 ms, making a measuring frequency of about 1000 Hz desirable for accurately monitoring the acceleration during this phase. The altimeter performed quite complex calculations (Eq. 3), therefore each measurement of the altimeter lasted 89 ms and with this it was not possible to achieve the desired measuring frequency of 1000 Hz. Therefore, the altimeter was programmed to start measuring after the initial launch phase. In this way it was possible to measure the acceleration during takeoff with a high measuring frequency. Once the propulsion due to the ejecting water had ended, the rocket only accelerated due to gravity and the fast measurement of the acceleration was no longer necessary.

Another crucial point that took time during the measurement was the writing command from the Arduino to the SD card. In a standard code, each measurement point was written to the memory card separately. A lot of time could be saved by storing data in the Arduino board until its memory was full and then flushing this memory as a large data block to the memory card. With this adjustment in the code, it was

possible to record one measurement every 0,8 ms. This means that a measuring frequency of 1250 Hz was achieved which was high enough to monitor the acceleration of the water rocket during take-off.

3. RESULTS

3.1. Height measurement

The height sensor was tested with a very simple experiment. The height of a room was measured either with a tape-measure or by holding the height sensor at the floor and the ceiling of the room. The tape-measure indicated that the room had a height of (2.41 ± 0.05) m and the height sensor gave a result of (2.5 ± 0.4) m. Both results corresponded so the height sensor was properly installed and correct results could be expected.

3.2 Acceleration measurement

The acceleration sensor was tested by dropping the rocket from the third floor of a building. The results are shown in Fig. 10. As can be seen in the graph, there were a lot of fluctuations on the acceleration but the average values of the acceleration (full lines in the graph) correspond to plausible values of the acceleration.

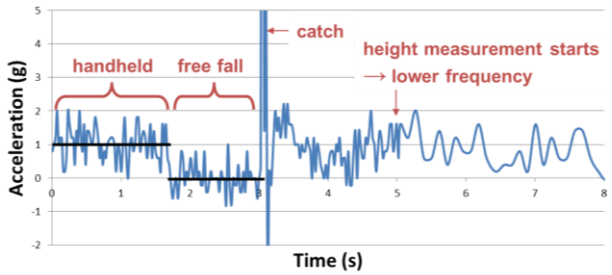

Figure 10. Free fall of the acceleration sensor from the third floor.

At first sight this did not seem to be the case. When the rocket was handheld an acceleration of 0 *g* was expected but an acceleration of about 1 *g* was measured. When the rocket was in free fall the acceleration sensors measured 0 *g* while 1 *g* was expected. The layout of the acceleration sensor (Fig. 1) gave the explanation for this phenomenon. The displacement of a movable frame with respect to a fixed frame is a measure for the acceleration. When the sensor was handheld, the movable frame moved a little out of its equilibrium position until the spring force balanced gravity. This small deviation thus corresponded to an acceleration of 1 *g*. When the rocket was in free fall, both the movable and the fixed frame experience the same acceleration due to gravity and the movable frame stayed in its equilibrium position with respect to the fixed frame. The acceleration sensor thus registered an acceleration of 0 *g*.

Furthermore, Fig. 10 shows a sharp acceleration peak around 3 s. At this point the rocket was caught, which corresponded to a very high acceleration: a value of 47.4 *g* was registered (not shown in the graph).

In paragraph 2.3. it was said that the measurement of height started after a certain time delay to increase the measuring frequency during takeoff of the rocket. This is visible in Fig. 10 where 2 seconds after the acceleration peak, which acted as a trigger point for the height measurement, the measuring frequency clearly slowed down.

3.2. Rocket launch

The water rocket was launched with a homebuilt system. The rocket was mounted on a launch tube where it was attached firmly to prevent it from launching too early. With a simple air pump, the pressure inside the water rocket was increased. For the launch of the rocket, an inside pressure of 8 bar was chosen before the rocket was allowed to take off. During the first actual flight of the water rocket, the parachute mechanism opened at the right moment but unfortunately, the parachute itself got stuck behind a screw inside the parachute cap. This resulted in a fatal crash of the water rocket and the measuring equipment. However, the microSD card could still be retrieved from the measuring unit.

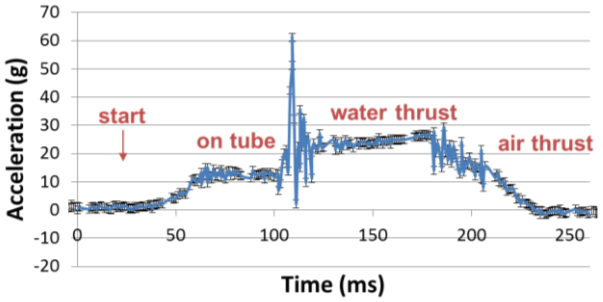

Figure 11. The measured acceleration during takeoff of the water rocket. Three phases can clearly be distinguished.

The acceleration during takeoff (Fig. 11) was correctly stored on the memory card but no data concerning the height could be retrieved. A possible explanation for this error could be the data transmitting process where data was not flushed to the memory card until a data block was full. If the data block for the height measurement was not full yet at the moment of the crash, it would not have been transmitted to the memory card.

Because of the high measuring frequency of the software, it was possible to very accurately record the acceleration during takeoff. In Fig. 11 three phases can clearly be distinguished. During the first phase the water rocket moved along the launch tube. The tube limited water flow, which kept the acceleration on average at (11.4 ± 0.4) *g*. When the rocket left the tube, the acceleration peaked at (60 ± 1) *g*. During the second phase the rocket lost all of its water. On average the acceleration was (23.0 ± 0.3) *g*. Due the decreasing mass of the rocket, the acceleration increased slightly. In the third phase, high pressured air left the rocket and caused thrust. As the pressure decreased, so did the acceleration. The three phases combined took about 190 ms.

4. CONCLUSION

This manuscript described a project carried out by 2 students during a time period of 15 days spread across 10 weeks. It shows that in this short time period it was possible to achieve nice results concerning the launch of a water rocket. The open-source platform Arduino was the base of this project and proved to be very student friendly. It was possible to build a measuring setup that can record the height and acceleration of a water rocket during its flight. Unfortunately, the parachute got stuck during the first launch (though the parachute mechanism had worked correctly) but still nice results concerning the acceleration during takeoff could be recorded. Due to a well written program with a high measuring frequency of 1250 Hz, it was possible to clearly visualize the three phases of the rocket launch.

5. REFERENCES

1. Official water rocket world record standings, URL: http://www.wra2.org/WRA2_Standings.php

2. Arduino Blog - The Arduino Documentary, URL: http://arduino.cc/blog/2012/02/20/the-arduino-documentary-2/

MULTI-DISCIPLINARY CONCEPTION APPROACH FOR A REENTRY PLATFORM

Tiago Henrique Matos de Carvalho [(1)], Dr. Luis Eduardo Vergueiro Loures da Costa [(2)], Dr. Maria Luisa Gregori [(3)]

Institute of Aeronautics and Space (IAE), Praça Marechal Eduardo Gomes, 50, Vila das Acácias, 12228-904 – São José dos Campos – SP – Brazil, Tel.: +55 12 3947 4628
Email: [(1)] tiagomatoscarvalho@gmail.com, [(2)] loureslevlc@iae.cta.br, [(3)] marialuisamlg@iae.cta.br

ABSTRACT

This work presents the conception process of the Brazilian Reentry Suborbital Platform, SARA-2, by means of a multi-disciplinary approach, in order to achieve a reasonable platform concept in a fast way. At the present development phase, this new platform incorporates the progress of the previous suborbital platform (SARA-1) and aggregates changes and new functionalities. These two vehicles are the initial part of a project that aims to the general development of an orbital platform for experimentation under microgravity and reentry environment. Two different approaches are applied in this conception development, one considering a physical and the other a systemic point of view, leading to results that interact with each other to present an acceptable platform concept or a new iteration necessity. Guided mainly by aerodynamic and mechanical models, the "physical" concept development defines the system and its architecture using structural and dynamical aspects applying compatible tools in the conception phase. On the other hand, the statement of the high level systems and mission requirements guides this conception through a systemic point of view. The physical conception employs specific tools that generate results like general dimensions, mass, aerodynamic coefficients and stability margin. Considering the systemic conception, the main constraints of the system are presented by means of system specification and requirements as well as mission requirements. With the interaction of these results and re-feed of the conception approaches, a general concept of the platform can be defined. Together, both approaches and their results lead to a system conception allowing an assessment of future issues and guiding specific and detailed studies about critical points of the system and its architecture. This concept development makes possible the rapid iteration through the possible configurations of the platform with relatively low computational effort compared to the application of conventional tools and methods, usually applied for advanced studies.

1. INTRODUCTION

During a project conception phase there is the need for interaction between the many parts that compose it, in order to reach a configuration that can be considered as "baseline" for future accurate studies and definitions for the next project phases. The search for a specific configuration – mostly optimal configuration – can be performed through multi-disciplinary approaches, depending on the needs. Looking to the project by a systemic point of view, the definition of the main requirements of the vehicle – high level at this point – and the definition of the main functions related to its mission can establish the general system architecture. At this phase, architecture changes are expected and have relatively low impact in the whole project. This step helps not only for the architecture definition, but also in the definition of lower level requirements and specific function for the future phases. From another point of view, the architecture definition through physical aspects can provide vehicle characteristics (dimension, mass…) as well as the checking of the requirements fulfillments. The iterations between these two points can generate fast results for general or specific tunings of the approaches and inputs adopted.

This work presents the conception process of the Brazilian Reentry Suborbital Platform (SARA-2), based on a multi-disciplinary approach, guided mainly by systemic and physical points of view. Actually, this new platform incorporates the progress of the previous suborbital platform (SARA-1) [1] and aggregates changes and new functionalities. These two vehicles are the initial part of a project that aims to the general development of an orbital platform for experimentation under microgravity and reentry environment. In general aspects the whole project development, from the suborbital to the orbital vehicle, is based on evolutionary characteristics that can (and shall) provide useful information from early ones to the new ones [2, 3]. Herein, with focus on the conception phase, information from the previous vehicle, in addition with the mission requirements, constraints and statements of the new vehicle, present a first systemic view of the system. Translating the systemic level, the physical concept development defines the system and its architecture using structural and dynamical aspects, guided mainly by aerodynamic and mechanical models, applying compatible tools in the conception phase. Due to the evolutionary characteristics and assumptions for the new vehicle, the field of search for a specific (optimal) configuration is already well defined and from the possible configurations inside this field, a concept can be chosen based on the criteria/objectives defined.

Proc. '21st ESA Symposium European Rocket & Balloon Programmes and Related Research', 9–13 June 2013, Thun, Switzerland (ESA SP-721, October 2013)

By application of these approaches and based on the results, the system conception allows an assessment of future issues and guides specific and detailed studies about critical points of the system and its architecture. This concept development makes possible the rapid iteration through the possible configurations of the platform with relatively low computational effort compared to the use of conventional tools and methods, usually applied for advanced studies.

2. METHODOLOGY

Starting with the main definitions of systems engineering, a systemic view is presented for the vehicle mission and architecture. The physical view applies the main metrics from the systemic view into specific tools and prediction codes, creating the conception physical architecture.

Figure 1 illustrates the multidisciplinary characteristic (broad view), presenting the systemic and physical views, with the respective main aspects.

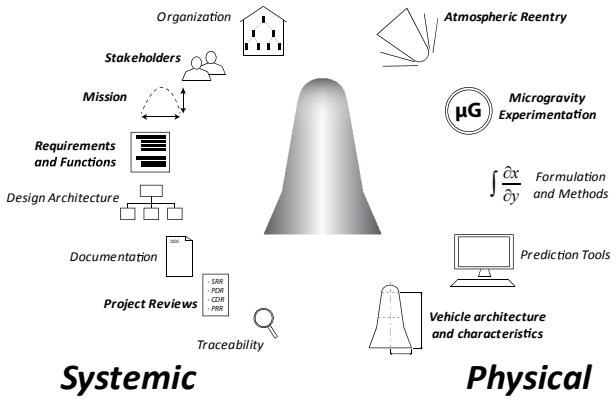

Figure 1. Multidisciplinary characteristic – Points of view

Through the inputs combinations and iteration with the systemic view, a large number of concept configurations are tested and evaluated.

2.1. Systemic View

Initially the requirements are defined in order to fulfill the mission and system specification, following the conventional Systems Engineering procedures [4, 5].

Beyond microgravity experimentation and characterization of the atmospheric reentry phase, the mission for this vehicle incorporates the new technologies qualification for the next phase of the project (materials and reentry induction system). The mission general architecture is illustrated in Fig. 2.

Figure 2. Mission General Architecture

The systemic point of view is defined based on information from previous vehicle (SARA-1) and on actual vehicle stakeholders, mission and system requirements. In Fig. 3 is presented the general systemic view of the project.

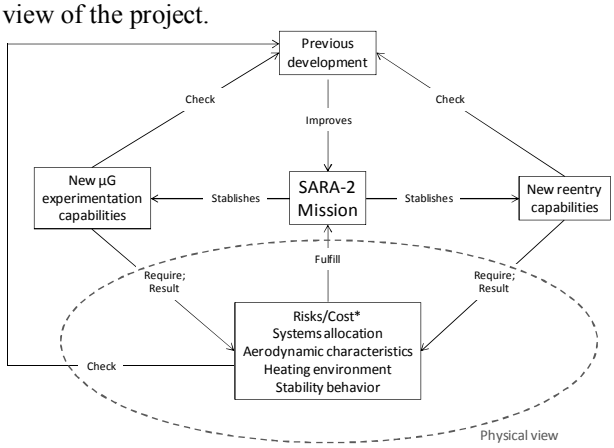

Figure 3. Systemic View

Figure 4 presents the high level iteration between the vehicle mission and architecture.

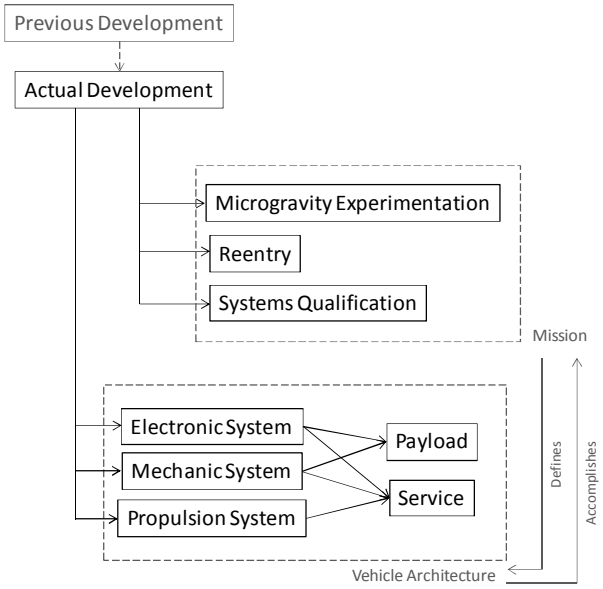

Figure 4. Iteration – Vehicle Architecture and Mission

From these approaches and by the main high level requirements, it is possible to set the following inputs/metrics and respective rationales:

- Mission duration: higher apogee and longer experimentation time, leading to a new environment;
- Vehicle layout (bi-conic): heating and stability;
- Launch vehicle interface: stakeholders and available launching platforms;
- Payload masses: experimentation stakeholders;
- Vehicle modules layout: heating, mechanical properties;
- Recovery system position: evolutionary characteristic.

Relating these inputs with the main requirements is possible to track them directly (Table 1).

Table 1. Requirements and Inputs relation

	Stakeholders Requirements	Mission Requirements	System Requirements
Mission duration			
Vehicle layout (bi-conic)			
Launch vehicle interface			
Payload masses			
Vehicle modules layout			
Recovery system position			

Through the application of a physical view, that translates the main metrics to a vehicle concept, the iteration is performed by checking and re-feeding requirements and even some aspects of the systemic view, if necessary. Figure 5 presents a simple view of the iteration between the two approaches.

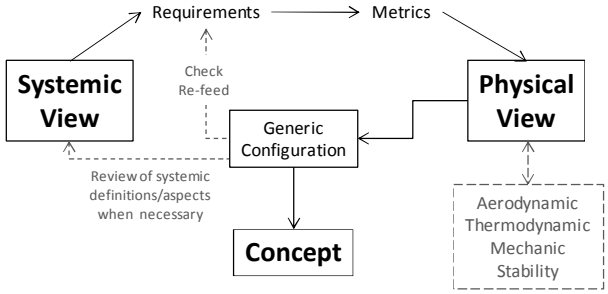

Figure 5. Systemic and Physical iteration

**Risks and cost can be indirectly variants regarding many aspects of systemic and physical view and due that, demand one specific analysis and a dedicated core to deal with them.*

2.2. Physical View

Although the systemic view deal with the vehicle regarding the general aspect of the mission, the physical view considers the reentry phase of the mission. As a flight critical phase, the conditions applied here aim to a "conservative" vehicle characterization.

Once the systemic aspects being defined (Fig. 3), it is possible to choose a compatible strategy of inputs (physical characteristics) regarding the available tools. Through the Missile DATCOM a relatively amount of information can be obtained regarding the aerodynamic characteristics of a vehicle. Missile DATCOM is a semi-empirical aerodynamic prediction code developed by USAF [6]. Due to its characteristics, compared to the conventional CFD codes available, Missile DATCOM can be efficiently applied depending on the desired vehicle characteristics, in order to achieve a first idea of aerodynamic properties. Reference [7] presents the application and verification of Missile DATCOM and other semi-empirical methods compared to the real results. From the results presented, checking particularly for a specific range of velocities, the Missile DATCOM presents an acceptable correspondence with the wind tunnel values mainly regarding to the center of pressure position.

For validation considering conventional blunted body, the configuration (Fig. 6) presented and tested [8] is compared with DATCOM results and analytical method presented [9]. The results from experimental analysis, analytical analysis and DATCOM analysis are plotted for comparison.

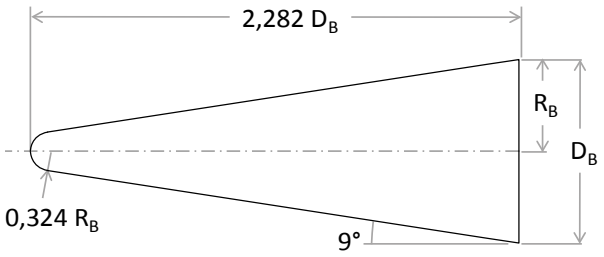

Figure 6. Blunted body configuration (Adapted from [9])

Figure 7 to 9 show results for axial coefficient, normal coefficient and aerodynamic efficiency respectively.

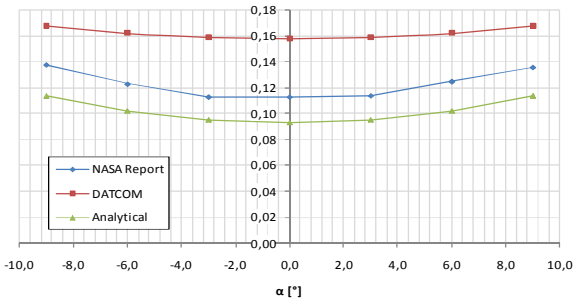

Figure 7. (CA) Axial coefficient comparisons

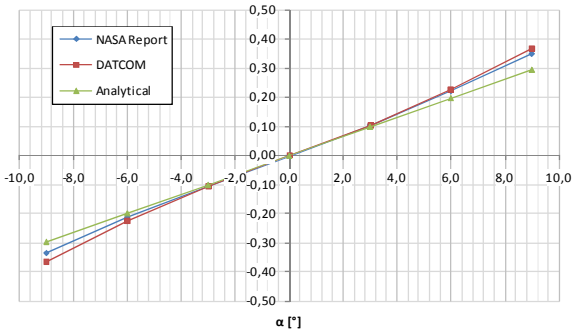

Figure 8. (CN) Normal coefficient comparisons

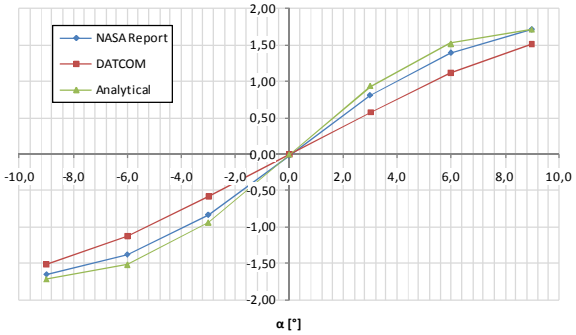

Figure 9. (L/D) Aerodynamic efficiency comparisons

Although the good correspondence of analytical and experimental results, the analytical method is limited with respect to flight regimes, vehicle geometry and can present inadequate results for the center of pressure location and thus, is not sufficient for the method applied in the work. Compared to the analytical method, the DATCOM can represent better the vehicle conditions, mainly for the center of pressure position.

The mechanical aspects of the vehicle are obtained in a simple way based on the geometrical information and the equipments/masses distribution. A simple heating flux estimative at the stagnation point is obtained by the relation of the flight regime and the nose radius.

The primary inputs chosen for the physical vehicle definitions are:

- *RB* – Base radius**
- *LMS* – Service Module Length
- *LME* – Experimentation Module Length
- θ_c – Forward Conic Angle
- θ'_c – Afterward Conic Angle
- $D\theta'_c$ – Afterward Conic Length

The primary inputs are presented in Fig. 10.

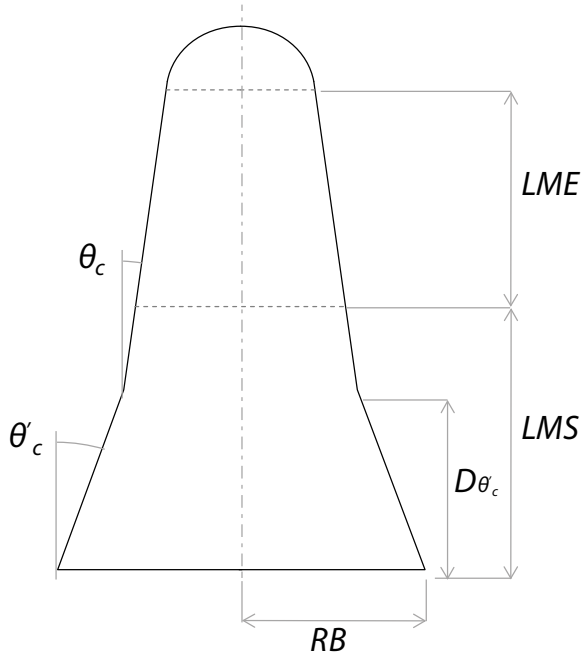

Figure 10. Primary inputs

Through the primary inputs, other important physical characteristics are defined like total length (L_{total}), nose radius (*RN*) and stagnation point heat flux (q).

From a configuration defined by the primary inputs and with the main flight conditions (altitude, mach, angle of attack), the DATCOM provides the vehicle aerodynamic characteristics (aerodynamic coefficients and center of pressure location). Through the center of pressure location and the vehicle mass characteristic (*CG*) a general stability margin is obtained, and with addition of the heating characteristics the configuration effectiveness is checked regarding the main aspects defined by the requirements.

2.3. Combination and iteration

Aiming a search through a large number of possible configurations, intervals are defined for each input of the physical definition and the combinations of them are performed.

The combination process must check if each one of the created configurations do not conflicts with the general metrics defined by the requirements.

***The base radius is a primary input, however it is directly linked with requirements presented by systemic view, therefore the combination process deals with all other inputs presented, except with the base radius (RB)*

The combination of the primary inputs, each one with a specific interval, is made through an auxiliary tool developed on Microsoft Excel and VBA. The intervals definitions are made based on a first layout and steps can be defined to refine the combination. During the combination process, the tool checks if each configuration created is in accordance with the metrics and design constrains defined, mainly, by requirements. It results in a list of possible configurations inside the defined intervals. The main combination described and the iteration between the two points of view are presented on the Fig 11.

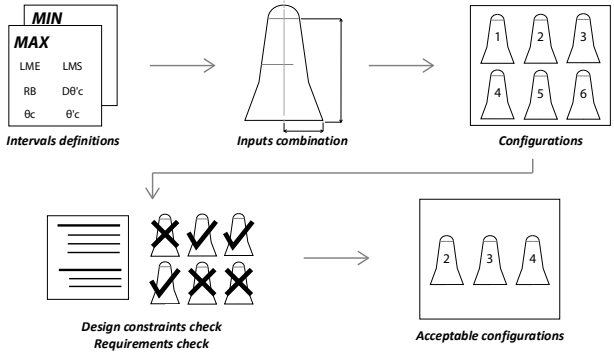

Figure 11. – Combination process and iteration

3. RESULTS

A large number of results are generated from the possible combinations inside the specified interval for each input, but aiming for the method presentation, not all configurations are presented.

Table 2 presents the primary inputs of the three different configurations evaluated. The inputs presented are normalized by the vehicle base dimensions (*RB* and *DB*) where:

- *RB* – Radius of the Base
- *DB* – Diameter of the Base

Table 2 also presents DATCOM results, the correspondent static margin and an estimative heating flux at stagnation point.

The results presented intend to illustrate the method application and the multidisciplinary approach. As a large number of configurations can be created, the main focus is to check these configurations with the definition aspects for each point of view. From these checks and through specific methodologies, an optimal configuration can be defined, but this is not the actual purpose of this work.

Figure 12 presents the three selected configurations.

Table 2. Primary inputs and results

	Primary Inputs							***Results***			
ID	*Ltotal / DB*	*LMS / DB*	*LME / DB*	*Dθ'c / DB*	*θc* [°]	*θ'c* [°]	*RN / RB*	*X CP / DB*	*X CG / DB*	Static Margin	*q* [W/m²]
Config 1	**1.579**	0.750	0.699	0.488	7.007	25.740	0.296	1.268	0.940	0.328	**1.743E+06**
Config 2	**1.710**	0.723	0.591	0.296	1.887	11.000	0.818	0.888	1.109	**-0.221**	1.047E+06
Config 3	1.488	0.723	0.591	0.517	5.500	24.167	0.384	1.174	0.892	0.282	1.529E+06

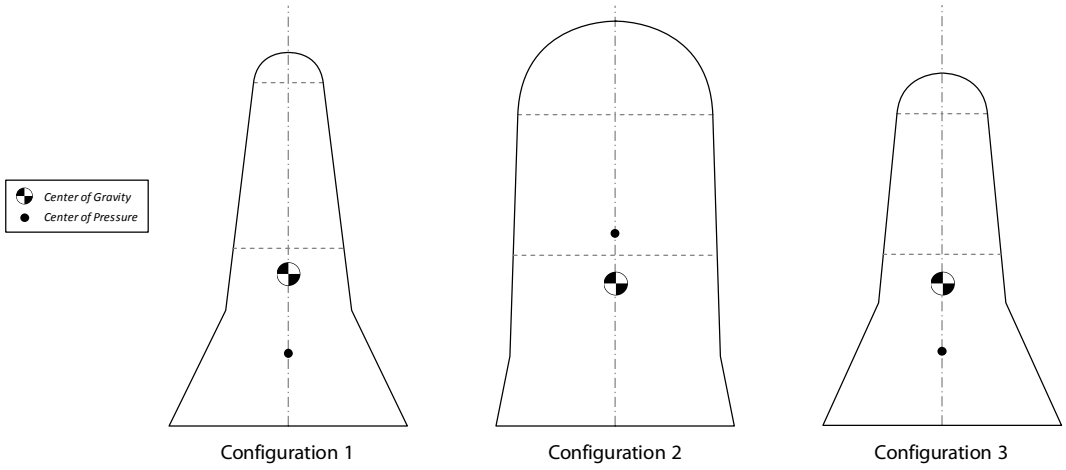

Figure 12. Vehicle configurations

From Tab.2 is possible to identify the configurations directly conflicting with the requirements defined (stability and heating), and design constraints. Checking the system requirements and design constraints is possible to comment:

Configuration 1 presents high value of heat flux at stagnation point, affecting directly the main equipments and systems. Although this configuration presents the best static margin, the high heat flux can demand the study of systems reallocation and search for compatible materials. As a result of systems reallocation, the static margin will change.

Configuration 2 presents negative static margin, which automatically excludes this vehicle regarding its requirements. As a design constraint, the longer total length affects the vehicle structural properties, manufacture process and consequently, the stakeholder requirements. The available volume for systems and experimentation sets a positive point regarding stakeholder requirements, but cannot "overpass" the main restrictions presented.

Configuration 3 is closely similar to the Configuration 1, but with lower values of heat flux and total length. Compared with Configuration 2, the lower volume available mainly for experiments (still better than in Configuration 1) shows a possible improvement point. Considering the Configuration 3, Fig.13 presents the variation of center of pressure and center of gravity positions with a specific range for Mach number. In the general aspect, this configuration fulfills the presented requirements and constraints.

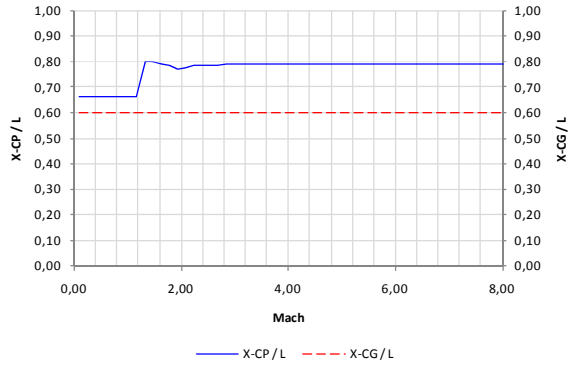

Figure 13. X-CP and X-CG – Configuration 3

Figure 14 illustrates another view of the vehicle from Configuration 3.

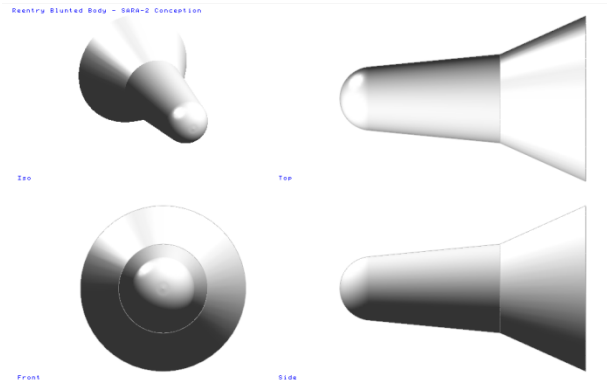

Figure 14. General view – Configuration 3

4. CONCLUSIONS

In this work is presented a multi-disciplinary approach for a reentry vehicle conception. Starting from the previous vehicle configuration, through the application of two defined points of view and respective methods, tools and prediction codes, some particular results are presented and discussed regarding the fulfillment of the main aspects of the general requirements.

Despite the well dominated methodology provided by traditional tools for these kind of problems, the characterization of the problem and its solution, mainly for a reentry condition, can be unacceptable for a conception phase by many aspects, like computational efforts leading to time for solution and costs. The application of a multi-disciplinary approach, based on reasonable tools and codes available provides a good conception generation.

The amount of possibilities checked and the results generated are important, not only from the physical but from the systemic point of view, which can be a base for discussions, meetings and decisions for the lower levels and next phases definitions. Considering only three samples from a large list, the results presented herein illustrate the broad vehicle variation which permits the application of a search strategy of these results in order to look for vehicles with some desirable characteristics.

The capacity of metrics establishments can help directly in the interface between the systemic and physical views, defining constraints and search intervals, filtering and ranking results.

Auxiliary tools can be incorporated in both approaches, improving the concept creation. As an example, tools from Model Based Systems Engineering (*MBSE*) [10] can help in the tracking and definition of requirements and functions from the systemic view and link its aspects with the physical view. However, the incorporation and application of these additional tools

must maintain compatibility with the conception phase, avoiding the increase of complexity, time and costs, which can lock down a conception process.

5. REFERENCES

1. Vidal, C.D., Loureiro. G, Costa, L.E.V.L (2007). SARA Suborbital Mission Specification, Internal Technical Report.

2. Farr, R.A., Christensen, D.L., Keith, E.L. (2005). The Business Case for Spiral Development in Heavy-Lift Launch Vehicle Systems, National Aeronautics and Space Administration, Huntsville, AL. George C. Marshall Space Flight Center.

3. Sabathier, V., Faith, G.R. (2007). Spiral Development, Real Options, and Other Development Methodologies, Center for Strategic and International Studies, Washington, DC.

4. NASA Systems Engineering Handbook, NASA/SP-2007–6105 Rev. 1, NASA Headquarters, Washington, DC, December.

5. Wertz, J.R., Everett, D.F., Puschell, J.J. (2011). Space Mission Engineering: The New SMAD, Space Technology Library, Microcosm Press, Hawthorne, CA.

6. Blake, W.B. (1998). Missile DATCOM: User's Manual – 1997 Fortran 90, U.S. Air Force Research Lab./Air Vehicles Directorate, Wright-Patterson AFB, OH, February.

7. Sooy, T.J., Schmidt, R.Z. (2005). Aerodynamic Predictions, Comparisons, and Validations Using Missile DATCOM (97) and Aeroprediction 98 (AP98). *Journal of Spacecraft and Rockets*, Vol. 42, No. 2, 2005, pp. 257-265

8. Neal, J. (1963). NASA Technical Note D-1606 - Aerodynamic Characteristics At A Mach Number Of 6.77 Of A 9° Cone Configuration, With And Without Spherical Afterbodies, At Angles Of Attack Up To 180° With Various Degrees Of Nose Blunting. Langley Research Center, Langley Station, Hampton, VA.

9. Bertin, J.J. (1994). Hypersonic Aerothermodynamics, AIAA Education Series, American Institute of Aeronautics and Astronautics, Washington, DC.

10. Foster, M.A. (2011), Developing a Heavy Lift Launch Vehicle Systems Architecture using a Model Based Systems Engineering Approach. *Orbital Sciences Corporation – AIAA SPACE 2011 Conference & Exposition*, Long Beach, CA.

Projects & Missions for Balloons

Chairs: P. Cocquerez & C. Lockowandt

REQUIREMENTS VERSUS CONSTRAINTS IN DESIGNING STRATOSPHERIC PLATFORMS FOR HEAVY MULTI-USER PAYLOADS: THE LARGE-SCALE POLARIZATION EXPLORER (LSPE) EXPERIMENT

L. Fiorineschi[2], A. Boscaleri [1] P. Rissone [2], M. Baldi[1]

[1]Andrea Boscaleri –M.Baldi-IFAC-CNR, via Madonna del Piano, 10 – 50019 S. Fiorentino, Florence, Italy E.Mail: a.boscaleri@ifac.cnr.it and m.baldi@ifac.cnr.it

[2] Lorenzo Fiorineschi-Paolo Rissone -DIEF – Università degli Studi di Firenze-Via Santa Marta, 3 – 50139, Florence, Italy- E.Mail:name.surname@unifi.it

ABSTRACT

In considering the design activities of a stratospheric gondola for a multiuser experiment, the exchange of information between the structural designer and the various teams involved may be a critical issue. In fact, only part of the information is available at the beginning of the project, thus necessitating the use of a trial-and-error approach that leads to results which involve considerable expenditure.

For small-and medium-size experiments, the problem of the exchange of information from the mechanical designer's point of view can easily be solved by using a pre-built gondola supplied by a hypothetical launch consortium. This is what we proposed as the "Strato-Bus" approach at the ESA Symposium 2009. Furthermore, in 2011 we also introduced a possible solution of a multi-user gondola design: a shared design for many combinations of experiments, the total weight of which is just below the maximum lift capacity of the balloon produced by several dedicated manufactories.

But when the characteristics of the instrumentation make the use of a pre-built platform impossible, the problem of exchanging information arises once again, and this is what we have experienced in the case of the Large-Scale Polarization Explorer (LSPE) experiment. The design activities of the LSPE gondola are used here in order to introduce a "systematic approach" that is capable of saving both time and money for each team involved in the overall project.

1. INTRODUCTION

An engineering design process is based on a structured approach which transforms a set of requirements and constraints into the final product by following a number of iterative steps. But the number of these iterations closely depends, in turn, on the quantity and the quality of the information available to the designer, i.e. the requirements to be met and the constraints to be observed.

In the case of design activities involving a stratospheric gondola for a multiuser experiment, the exchange of information between the designer of the structure and the developers of the instrumentation can be a critical issue. In fact, while much information is needed by each team, only a part of it is available at the beginning of the project, thus necessitating the use of a trial-and-error approach that leads to results which involve considerable expenditure. This depends substantially on the compatibility of each instrument with the other experiments and on the flight constraints imposed by the launch base.

When considering small-and medium-size experiments, the problem of the exchange of information from the mechanical designer's point of view can easily be solved by using a pre-built gondola supplied by a hypothetical launch consortium. In fact, in this case, it is the master flight organization which, by being acquainted with the features of its mechanical structures, can evaluate which experiments can be hosted on the same flight during a given campaign. This is what we proposed in 2011 as the "Strato-Bus" approach [1], and we also introduced a possible solution for its gondola [2].

But when the characteristics of the instrumentation make the use of a pre-built platform impossible, the problem of exchanging information arises once again. This is what happened in the case of the Large-Scale Polarization Explorer (LSPE) experiment [3] in which the coexistence of two heavy telescopes was imposed in order to cover a larger bandwidth in the Cosmic Microwave Background (CMB) measurements. Moreover, it should be noted that the LSPE can be considered a multiuser experiment, since different teams and locations were involved in the development of specific instruments. The design activities of the LSPE gondola can be considered here as an example in order to introduce a "systematic approach" capable of reducing the number of iterative steps needed to reach its final form, with a savings in time and money for each team involved in the overall project. The proposed approach takes into consideration an accurate definition of the "engineering design process", as well as the well-known advantages provided by the principles of modularity.

In the following section, a brief introduction on systematic design processes is provided. In Section 3, the benefits of modularity and a short explanation of basic definition are presented. Section 4 is dedicated to a description of the LSPE case study, from the

Proc. '21st ESA Symposium European Rocket & Balloon Programmes and Related Research', 9–13 June 2013, Thun, Switzerland (ESA SP-721, October 2013)

perspective of the design process. In Section 5, future developments regarding the multi-user issue are introduced. Lastly, Section 6 reports our conclusions.

2. SYSTEMATIC DESIGN PROCESSES

In the field of engineering design, the first step to be carried out when approaching the development of a new product is normally to define the requirements and constraints. The meanings of these terms are as follows:

- **Requirements**: represent what the system should do (Functional requirement) and, when possible, can be used as a criterion to evaluate the validity of a solution (non-functional requirement). A requirement can be considered to be one of the objectives of the design process.

- **Constraints**: something imposed which limits the "space" of the possible solutions. They may refer to physical limitations, e.g. mass or weight, to process limitations, e.g. limited budget, or to normative limitations.

This set of data usually concerns the entire life-cycle of products or systems, and can be considered to be formed by four main phases, namely:

- **Design phase**: during which calculations, simulations, drawings and virtual prototypes of the system are produced.

- **Production phase**: during which, starting from the information provided by the previous phase, each part of the system is realized or supplied and then assembled in its final form.

- **Use or Operational phase**: during which the system performs the functions for which it has been created.

- **Withdrawal phase**: during which the product or system is withdrawn from the market or abandoned. During this phase, problems related to disposal and possible reuse are confronted.

At first sight, all of the above-mentioned phases can be considered simply as consecutive steps to be followed in order to reach the end life of a product. Obviously, each phase needs information associated with the results belonging to the previous phase; but by considering the first phase of the cycle, i.e. the design phase, information can also be obtained from other subsequent phases. This happens when new product requirements or constraints that have never been considered previously are discovered, e.g. when problems that cannot be evaluated during the product-planning activities are dealt with only when producing, using or withdrawing the product. The requirement list and the constraint list can then be updated in order to start a new design process that will make it possible to bring about modifications in specific phases of the life-cycle (Figure 1). This is, in fact, an iteration of the process, and involves more or less consistent costs, depending on how far away the new information originated. In fact, it can simply be assumed that a feedback coming from the design phase will cause only an extension of the time initially foreseen for that particular task, while a feedback from the "use" may (for example) necessitate a re-design, together with an update of the production process. At this point, it becomes obvious that performing an accurate definition of the initial set of requirements and constraints is the most important activity to be carried out in order to avoid as many iterations as possible.

The problem resides in the fact that some types of information are strictly related to the type of solution adopted; therefore, by definition, certain iterations are needed. Then, in order to save on costs, the strategy to adopt is to obtain the greatest amount of feedback from the first phase of the life-cycle, i.e. the Design phase.

By observing that phase with a virtual magnifying lens, it is possible to identify three sub-phases, namely the "concept design", the "embodiment" design, and the "detailed" design [4] (Figure 2). Each of these sub-phases could be further subdivided [4]; however, a description of this kind is beyond the scope of the present paper. The important things to know are which activities are performed in each sub-phases and what partial results can be obtained from them.

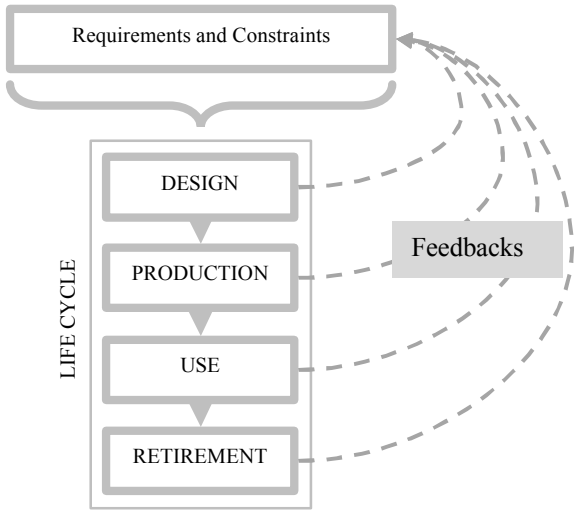

Figure 1. Schematic representation of possible iterations in the development process of a product.

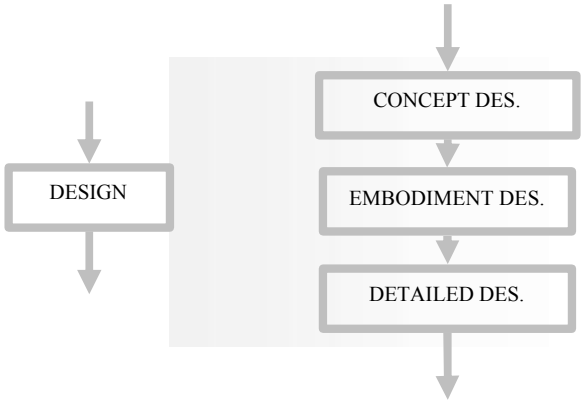

Figure 2. Composition of the design phase.

- **Concept design**: during this sub-phase, the functionalities of the systems are modelled, the physical principles to adopt are chosen, and preliminary sketches of the overall solution are executed. Thus, the first pieces of information concerning the basic functioning of the system and the production process are available at the end of this step.

- **Embodiment design**: here, the sketches produced during the previous steps are developed in order to form a first layout of the system from which to extract more detailed information about the physical characteristics, performance, and production costs. In this step, the use of Computer Aided Engineering (CAE) tools is very important, because they make it possible not only to visualize the actual geometry of the solution, but also to acquire important data concerning its performance without the need for an actual prototype.

- **Detailed design**: this is the final design step, during which the system is entirely developed at all levels of detail. The output of this phase consists of the production of documents and Computer Aided Design (CAD) models ready to be processed by means of Computer Aided Manufacturing (CAM) software.

Thus, keeping the iterations as much as possible within the design process corresponds to performing iterations among the three above-mentioned sub-phases[fig .2]. In other words the time-saver logic must be repeated massively inside the Design phase: i.e. it is necessary to extract as much information as possible from the concept design results in order to avoid useless sub-iterations.

3. BENEFITS OF MODULARITY

Modularity and Integrality are the two possible types of Product Architecture. The definition of Product Architecture is based on the distinction, made by Ulrich and Eppinger [5], between functional elements and physical elements:

- **Functional elements** are individual operations and transformations that contribute to the overall performance of the product.

- **Physical elements** of a product are parts, components, or sub-assemblies that implement the product's functions.

Pahl and Beitz [4] define Product Architecture as a scheme that shows the relationship between the functional structure of a product and its physical configuration.
Another widely-acknowledged and almost equivalent definition has been provided by Ulrich and Eppinger [5], who define Product Architecture as a scheme by which each function of a product is allocated to physical components. Modular and integral architectures can, in short, then be distinguished substantially by the type of mapping existing between the physical components and the functional components. In fact, a modular product is characterized by a "one-to-one" inter-mapping, while an integral product is characterized by one-to-many or many-to-one mapping.
While integrality is considered a good way to attain the best global performances of products, modularity is assumed to be capable of giving rise to benefits that involve many other parameters. A list of these parameters is given in table 1.
Basically, most of the currently coined definitions regarding modularity types can be grouped as follows:

- Interface types of the system: describe the connectivity between elements of the system.

- Interaction within the system: describes how the elements of the systems interact in order to form the architecture.

- Physical configuration of elements: describes how the building blocks of the systems are provided.

Component interfaces play an important role in Ulrich's definition of modular architectures [5] since, in addition to a one-to-one mapping between functions and components, it states that a modular product includes decoupled component interfaces. A decoupled interface is understood to be capable of permitting modifications to a component without any need for modifying the adjacent ones.

In observing the list of parameters associated with modularity benefits shown in table 1, it can be noted that some of these refer to characteristics relative to a customizable multi-user gondola development project:

- Design team management: in fact, in a multi -user project a complex design team, consisting of a sub-team for each part involved in the flight, can be delineated.

- Parallel development: in a multi -user experiment, each instrumentation "module" has to be developed independently of the others.

- Ease of assembly: each part of the experiment must be easily assembled without having an effect on] the equipment of the other teams.

Table 1. Parameters influenced by modularity.

BENEFITS	REFERENCES
Upgrades/Part changes	[6], [7]
Customization	[7], [8]
Design Re-use	[9], [10]
Design Team management	[11], [12]
Disassembly time	[8] , [9]
Ease of Assembly	[8] , [9]
Ease of maintenance/repair operations	[8], [13], [14]
Economy of scale	[6], [8], [13]
Late point differentiation/customization or postponement	[11], [13]
Logistical optimization for production/assembly	[8]
Material Recycling facilitation	[8], [14]
Parallel development	[8], [6], [9], [12]
Part/component re-use	[8] , [12]
Reconfiguration	[8], [9], [13]
Variety	[6],[8], [9]

At this point, the question is: Can modularity be used in order to improve the development of a multi -user customized gondola? The application of modularity principles to the LSPE Gondola design management is shown here as follows.

4. THE LSPE GONDOLA

As shown in section 2, a systematic design approach starts from a definition of the requirements (or design objectives) and constraints. Thanks to interviews in which the developers of each team were involved, the following requirements for the gondola were obtained:

- Transportability: the gondola must be easily transported to the launch site. It must also be dismountable in order to be carried on the chosen means of transport.

- Ease of assembly: the gondola with the entire set of equipment must be easily assembled almost anywhere, and dependencies between different sets of instrumentation must be avoided.

The list of constraints is the following:

- Structural constraints: the gondola frame must be designed by observing a list of reference values that mainly concern flight safety .

- Launch site constraints: spatial constr aints are defined in order to perform the launch with a given tonnage of the crane.

- Budget constraints: only a limited budget is available, and thus the technological choices are influenced.

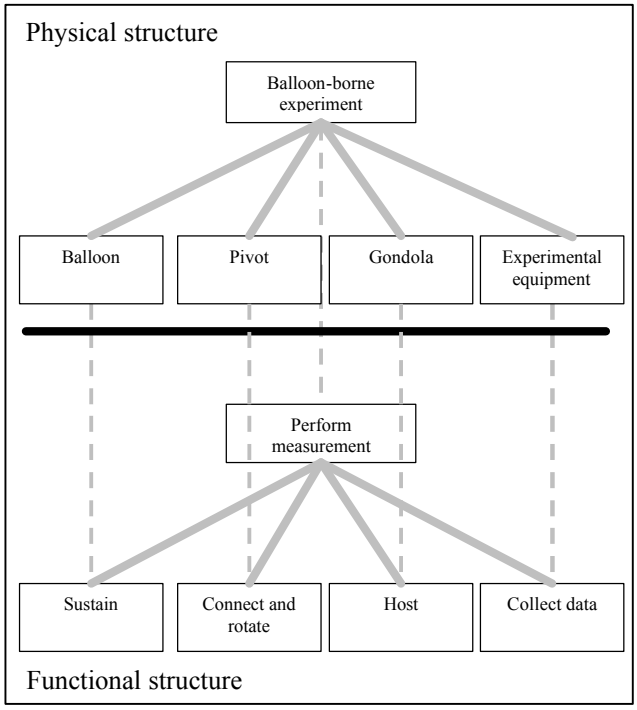

Figure 3. Schematic representation of the most relevant components of the flight-chain system and their functionalities. It represents the architecture of the system at a first level of detail.

Once the above-mentioned design parameters have been defined, the conceptual design can begin.
As shown below, the modularity has been considered starting from the early-concept design sketches . This has been possible , thanks to the observation of the "gondola" system which, in performing only one function, i.e. "host ing", can be considered to be a module.
Moreover, as shown in Figure 3, the entire flight-chain system except for the pivot, which implements two functions, can be considered as modular, at least when observing it at a first level of detail.
Then, the decoupled-type interfaces have been checked by considering the gondola and the other equipment systems as different modules in order to allow parallel development. In this way , each module of the whole "flight-chain" system can be developed in a parallel way, unless some crucial exchange s of information are needed.
The outcomes of the concept design phase are the first sketches of the system, and in these it is possible to observe solution principles and a preliminary configuration of the structural layout (Figure 4).

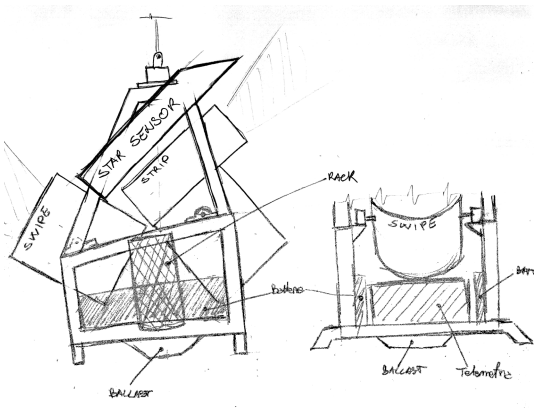

Figure 4. Outcomes of the concept design. First free-hand sketches of the gondola.

Concept sketches are very important in the development of the project , because they make it possible to communicate ideas rapidly to the other teams, so that a first check can be made of the feasibility of the proposed solution.
The successive step is that of the embodiment design, in which more detailed information about size and shape of the system can be evaluated. Here, CAD models representing the layout of the equipment have been used in order to find the ir best spatial configuration (Figure 5). In this step , important information regarding the shape and the size of the gondola has been acquired, and first embodiment solutions of it can then be modeled.

With these models it was possible to perform structural analyses from which to extract critical information for the other teams concerning the feasibility of their proposed solutions. Th is information consists of a respect of the structural constraints (Figure 6) and of the spatial constraints imposed by the launch site (Figure 7).

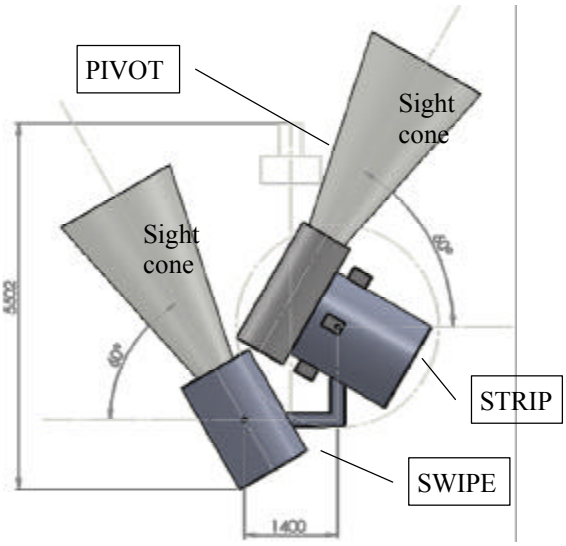

Figure 5. Layout configuration of the most important parts of the flight-chain system.

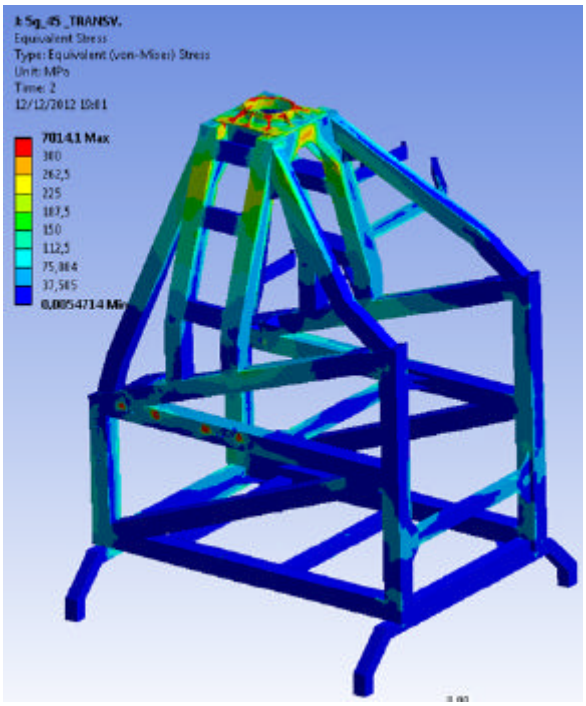

Figure 6. Structural analysis performed on a model of the embodiment phase.

Eventual iteration loops must be limited as much as possible to these two design steps, i.e. the concept and

the embodiment ones. In this way, only limited efforts are possibly wasted; furthermore, easy-to-manage CAD and FEM models enable them to be rapidly re-adapted to subsequent solutions.
Then, and only once the final solutions have been approved, the detailed design phase can be performed by defining in detail the joining or support systems and other low-level detail parts.
If pursued by all the development teams, this design logic leads to an efficient project management, thus making possible an agile exchange of crucial information without having to follow the costly and outmoded trial-and-error approach. This has been proved with the LSPE experiment, the design activity of which is currently active and the advanced embodiment solution of which is shown in Figure 8.

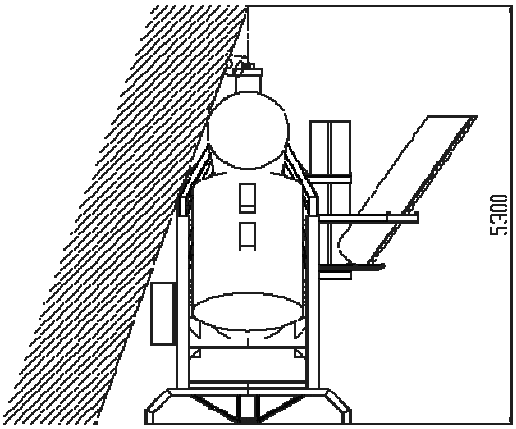

Figure 7. Spatial constraint verification.

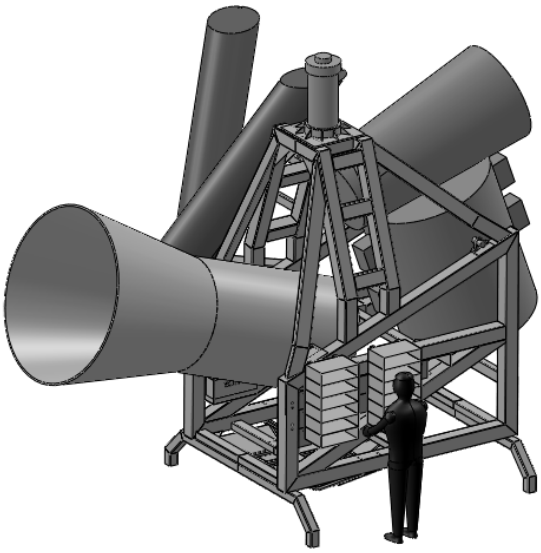

Figure 8. The LSPE experiment layout.

5. FUTURE STRATOBUS DEVELOPMENTS

It is widely recognised that even if a multiuser platform has to host an indeterminate set of instruments, some electronic and mechanical parts are shared by different flights, since they belong to the same gondola system. However, due to the extreme variability of the types of experiments which could be carried out, the likelihood of adaptations and a technological upgrading of the above-mentioned parts have to be considered. The pivot for example, could be modified in order to fit a set of different payload needs. A drawing of the current pivot assembly used in previous flights is shown in Figure 9 [1]. In fact, different motor types (brush or brushless), sizes (different torque sensitivity), and a gear-box module capable of reducing the power supply consumption may be needed. Moreover, heat transfer may play an important role. In fact, depending on the type of motor and the type of experiment, different thermal insulation can be considered in order to keep the devices within their appropriate temperature range (in the case of the LSPE, the range spans from -40°C to -85°C).

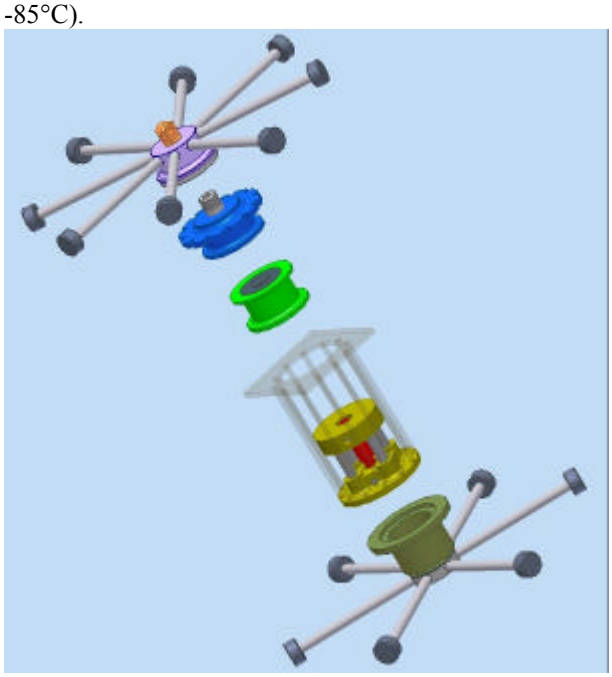

Figure 9. Current Pivot structure.

Also the control electronics, hosted in the structure of the pivot, may be different, according to the type of motor commutation. For the LSPE experiment, the motor drive electronics was re-designed by means of a "mother" board (an array of half bridges of MOSFET power can host piggy-back cards that realize different commutation sequences depending on the different motor winding assembly, i.e. a DC motor or BLDC motors with Hall Sensors. In both cases, the mother and piggy-back cards feature an effective commutation method that is based on a four-Quadrant Non-Simultaneous Complementary PWM technique [15]. All

the electronic cards have been embedded inside the bottom part of the pivot's structure, thus offering them adequate protection from mechanical stress and thermal dissipation if necessary.
In order to manage this kind of variability among the different flight configurations of a multi-user gondola, modularity principles can provide potential solutions also for the pivot. For this reason, a new concept of a Modular Pivot is under investigation, with the aim of reducing costs by avoiding the need to redesign the entire assembly for different applications. In this case, and in consideration of what is reported in Table 1, the main modularity benefits involved are:

- Upgrades: by using a smart modularization, some modules can be upgraded without involving any changes in the other ones.
- Customization: if needed, some standardized modules may be replaced with customized parts.
- Component re-use: if damage occurs, the pivot can be re-used by repairing only the modules involved, without a complete reconstruction.

The new pivot conceptual design activity is thus focused on an identification of the most appropriate module configuration, with the aim of covering wider weight/inertia-moment combinations of possible payloads by means of a limited set of reusable and/or customized components.

6. CONCLUSIONS

This paper describes an application of the systematic methodologies used in the field of engineering in carrying out the design process of a custom-made multiuser gondola. It is worth noting that, whenever possible, a modular and adaptable platform should be preferred. However, when the dimensions, the weights and, in general, the requirements of the parts are in contrast with the given set of constraints, the choice of a custom-made platform seems to be inevitable. This is the case of the Large Scale Polarization Explorer (LSPE) experiment, in which the coexistence of two heavy telescopes and a lot of other experimental equipment has to be guaranteed. The aim of this work is to show how systematic design methods can be used to advantage by an hypothetical launch consortium, in order to avoid the costly trial-and-error approach. In fact, management of the requirements belonging to the various teams that, with their experiments, constitute the flight payload, may be a critical issue. In addition, a short introduction to the modularity principles, involved in the design process, has been presented. Furthermore, future developments concerning the modularization of the pivot have been introduced. We can thus assert that what is presented in this paper is a further development of our past investigations concerning the multi-user issue performed by the authors. In any case, other studies will be needed in order to obtain further details concerning the variability of each flight component, thus enabling a more accurate definition of the list of requirements to upgrade the multi-user proposal.

7. REFERENCES

1. Boscaleri A., Castagnoli F., Rissone P., Corti M., *Stratobus: a Multiuser Platform System for Making access to LDB Flight Easier and Cheaper*, European Space Agency, (Special Publication) ESA SP, 671 SP, pp. 209-213, 2009.
2. Boscaleri A., Fiorineschi L., Rissone P., Baldi M., Zannoni M, *A new approach in designing of stratospheric platforms aimed at multi-user LDB flights,* European Space Agency, (Special Publication) ESA SP, 700 SP, pp. 593-598., 2011.
3. Aiola, S. et al., *The Large-Scale Polarization Explorer (LSPE)*, Proceedings of SPIE - The International Society for Optical Engineering, 8446, art. no. 84467A, 2012.
4. Pahl G., Beitz W., *Engineering Design. 2nd ed.*, Springer-Verlag, London Ltd. 1999. ISBN 3-540-19917-9.
5. Ulrich K. T., Eppinger, S. D., *Product Design and Development*. McGraw-Hill. 5th edition. 2003. ISBN 0-072-47146-8.
6. Huang, C.C. (2000) 'Overview of Modular Product Development'. Proc. of the Natl. Sci. Counc. Republic of China 2000, vol. 24, no. 3, pp. 149-165
7. Kamrani, A.K., Salhieh, S.M. (2002). *Product Design for Modularity*, 2nd edn. Kluwer Academic Publishers
8. Gu P. and Sosale S., *Product modularization for life cycle engineering*, Robotics and Computer Integrated Manufacturing, vol. 15, 1999.
9. Gershenson J. K., Prasad G. J., and Zhang Y., *Product modularity: Definitions and benefits*, Journal of Engineering Design, vol. 14, no. 3, pp. 295–313, Sep. 2003.
10. Hölttä-Otto, K. (2005) *Modular Product Platform Design*. Doctoral Dissertation, Helsinki University of Technology.
11. Fixson S. K., *Product architecture assessment: a tool to link product, process, and supply chain design decisions*, Journal of Operations Management, vol. 23, no. 3–4, pp. 345–369, Apr. 2005.

12. D. Krause and S. Eilmus, *A Methodical Approach for Developing Modular Product Families*, Components, no. August, 2011.

13. Ulrich K., *The role of product architecture in the manufacturing firm,* Research Policy, vol. 24, no. 3, pp. 419–440, May 1995.

14. Newcomb, P.J., Bras, B., Rosen, D.W. (1996) *'Implications Of Modularity On Product Design For The Life Cycle',* in The 1996 ASME Design Engineering Technical Conferences and Computers in Engineering Conference, August 18 -22, 1996, Irvine, California, 1996, pp. 1–12.

15. Dal Y. Ohm, Richard J. Oleksuk , *Influence of PWM Schemes and Commutation Methods for DC and Brushless Motors and Drives. Drivetech INC and Nortrop Grumman Poly-Scientific, Blacksburg, Virginia*

VEXREDUS: A STUDENT HIGH ALTITUDE GLIDER PROJECT TO DEMONSTRATE THE CAPABILITIES OF A BLENDED WING BODY CONCEPT

David Steenari[(1)], Tobias Kuhn[(2)], Sven Wlach[(3)]

[(1)]Lulea University of Technology, Fyrmästarevägen 5, 44150, Sweden, david@steenari.se
[(2)]University of Stuttgart, Am Strohberg 30, 70180 Stuttgart, Germany, tobias.too.kuhn@gmail.com
[(3)]University of Stuttgart, Schloßstraße 85, 70176 Stuttgart, Germany, sven.wlach@gmail.com, [(3)]+49173/3941113,
www.vexredus.de

ABSTRACT

The goal of the project was to investigate the flight behavior of a futuristic blended wing body concept in high altitudes. The shape to be tested was based on cooperation with its Swiss inventor Koni Schafroth from Team Smartfish [1]. The overall motivation for the project is the search for new reentry technologies. VEXREDUS stands for „Vehicle with EXtended REentry Duration – University of Stuttgart“, referring to reentry vehicles with a high Lift to Drag ratio.

The project work involved the following tasks:

- CNC/CAM based mold construction
- Building of airframe in CFRP/GFRP sandwich technology
- Development of own autopilot software on existing open source hardware
- Implementation of own telemetry protocol
- Development of a ground station
- Development of a Redundant power supply
- Development of a parachute system
- Thermal and vacuum testing

As a BEXUS team we were part of two launch campaigns at the ESRANGE facility in Northern Sweden. Though we had our share of setbacks, we were able to demonstrate the airframe's excellent flying characteristics and suitability for high altitude missions. The paper shall take a look at the technical challenges we've been facing and the investigations we made to learn more about the things that didn't work as expected, as well as the results drawn from the whole experiment.

1. INTRODUCTION

The scientific and technical background is the search for new reentry methods, with the goal to make this very critical phase of every returning space mission less dangerous and therefore more convenient.

One Way of solving this problem might lie in the construction of reentry vehicles with a high lift-to-drag-ratio, making a separation and overall reduction of mechanical and thermal loads possible.

2. EXPERIMENT AND SCIENTIFIC GOALS

The first step towards this goal is to achieve controlled flight at a high altitude relative to the size of the plane. The experiment consists of a glider that shall partly test the reentry behavior of an unconventional shaped blended wing body concept. The glider is placed beneath a balloon and dropped when reaching a desired height. The whole flight is controlled by an autopilot system that can be monitored and commanded by a ground station via telemetry link. Having a system that has the potential to travel quite far on its own, made numerous safety features mandatory.

3. DESIGN AND CONSTRUCTION

Since the length of the paper is limited, one aspect of the project design and construction process shall be looked upon a bit closer, in this case the construction of the airframe. After that, only brief statements towards the other aspects shall be given.

3.1. Structure

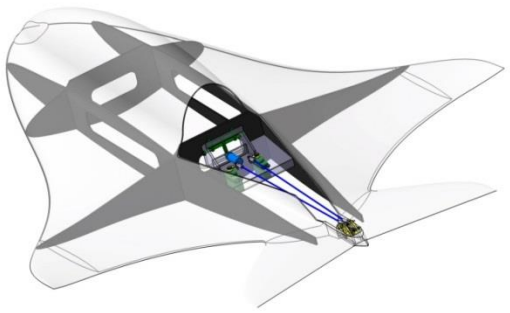

Figure 1. Shell and inner structure

Proc. '21st ESA Symposium European Rocket & Balloon Programmes and Related Research',
9–13 June 2013, Thun, Switzerland (ESA SP-721, October 2013)

The structure of the Glider consists of the outer shell and the inner structure. For the production of the outer shell we milled molds out of a material, specially designed for this purpose, called Ureol. The outer shell is directly hand laminated into the molds and can be described as a sandwich of layers.

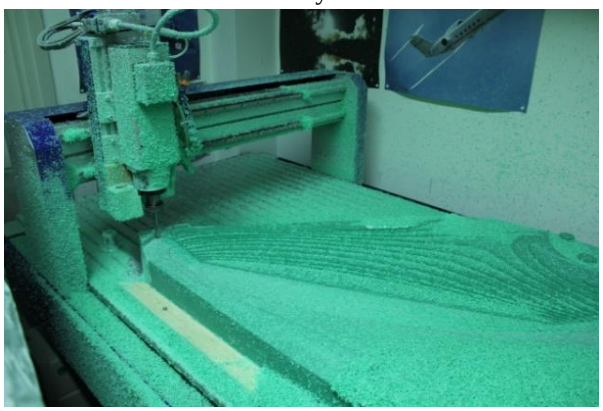

Figure 2. Milling the molds in our Workshop (Akamodell Stuttgart e.V.)

Figure 3. Finished bottom mold

Figure 4. Gel coat as "skin"

After the milling the molds had to be sanded, polished and waxed in order to achieve a smooth surface of the glider.

The first step of the glider construction is to spray a gel coat into the molds. This gel coat is a special polyester based paint commonly used in aircraft and model plane construction. It acts as the outer skin of the aircraft, giving it a slick surface and protecting the underlying resin/fiber matrix against the UV-Radiation of the sunlight. After the hardening time the lamination process can be started.

The shell laminate is composed of a total of 4 layers (outer to inner layer): 27g/m^2 glass fiber, 80g/m^2 carbon fiber (Textrem), Foam (Airex), 80g/m^2 glass fiber. The 27g/m^2 glass fiber is a really thin fabric which keeps the rather rough but stiff Textrem from pushing through the gel coat and thereby the outer surface smooth. In the nose section of the model the carbon fiber is replaced by 160g/m^2 glass fiber for here the telemetry antenna is placed and carbon fiber shields radio signals. The Airex is a lightweight foam to increase the thickness of the laminate and by that increasing the buckling stiffness. In the stabilizers a double layer Textrem is placed to increase the overall stiffness in order to prevent rudder oscillation at high velocities.

Each layer of fabric gets soaked with resin before it is placed within the molds. When the laminate is set up, it gets covered by a punctured plastic foil followed by tissues and another, but this time airtight foil, which is sealed with silicon around the molds. Then vacuum is applied to make sure that the layers are pressed into the mold and follow its shape, simultaneously extracting air bubbles and excessive resin. This way all layers are bonding well and unnecessary weight is removed.

Figure 5. Vacuum applied

This procedure is applied to each mold separately. After 24h the laminate is hardened and can be unpacked. Now the edges can be cut and the inner

structure placed and fitted. To make sure there is a perfect fit, imprints with modeling clay are made.

Figure 6. Closing the molds

3.2. Overview of design and construction details

Structure

CAD mold design:

The molds are modeled in CATIA V5, using the NC-machining workbench to create 3D milling paths.

CAM/CNC Mill mold construction:

At our local academic model club, the "AKAMODELL STUTTGART e.V." [2] we have the luxury of owning a CNC-mill that makes many interesting project possible.

Carbon and glass fiber airframe:

Knowledge about this building technique has been accumulated over the years among the members of the club and is passed on over generations of students. Two airframes where build.

Thermal design

As insulation common styrofoam is used that creates different zones of insulation. There is a bigger room, in which the heat producers are located, namely batteries, the power supply or the Xbee-data-modem. Within this room, a smaller foam box is placed which houses the autopilot with its temperature change sensitive IMU (Inertial Measurement Unit). This two stage insulation worked very well for us.

Parachute release mechanism:

The aft top part of the fuselage is kept attached by an electro magnet, which holds up to 16kg while being very power efficient. So, even if there is a complete loss of power, the parachute packet gets deployed.

Electronics

Open-source autopilot hardware:

We use the Ardupilot Mega 1.0 [3] which is equipped with an Atmel Atmega 2560 microprocessor and is compatible to the Arduino Environment.

Telemetry modules:

Here we use the Digi Xbee Pro modules operating at a frequency of 868Mhz.

Antenna:

On the plane a simple omnidirectional antenna is installed, whereas on the ground end a directional Yagi-Uda antenna is utilized. During the first campaign 2011 we tracked the plane using GPS coordinate differences and a pan/tilt mechanism. This combination gave us a telemetry link over a distance of 185km, which is a lot with this kind of transmitters.

Redundant power supply:

Two batteries, with two voltage converters linked together to provide a secure power supply.

Parachute control:

This is realized as a separate parachute control board. The microcontroller listens to a heartbeat sent by the autopilot. If the heartbeat stops, for example in the case of crashed autopilot software, one chance to reboot is given before the parachute is released. Also a direct release command sequence is implemented.

Software

Selfwritten autopilot logic:

Only basic libraries for hardware and attitude estimation are used. Some of the problems to cope with where performance on microcontrollers, our main loop runs at 200Hz, as well as machine accuracy on an 8-bit processor.

Groundstation:

An in/outgoing datahandler sends and receives data over the Xbee data modem, shares it with the control software and logs the raw transmission data. The control software displays interpreted data and allows instructions, like a change in control parameters, to be uploaded to the plane. The programs are multithreaded and communicate over UDP. The position is plotted in a map using web based technology and can therefore be viewed in a common browser on multiple clients (all our laptops).

Own telemetry protocol:

Since the 868Mhz modems are bound to a 10% duty cycle (only 10% of the possible maximum transfer data rate is allowed to be used continuously) we wrote a simple, compact and checksum verified protocol to have control over the sent data.

Logfile Simulator:

This is a program that replaces the datahandler and plays back logfiles of flown missions.
Hardware in the loop simulation:
This is a current work in progress. We developed an interface to the X-PLANE flight simulator and are hoping to fly our autopilot virtually.

Prototyping and Testing
We built two scaled down versions of the glider in styrofoam for flight and parachute testing as well as we used two commercially available delta wing models for autopilot development.
The thermal concept was verified in the vacuum/thermal chamber.
Since the parachute was also an own development it was tested by car runs and drop tests.

4. THE FLIGHT

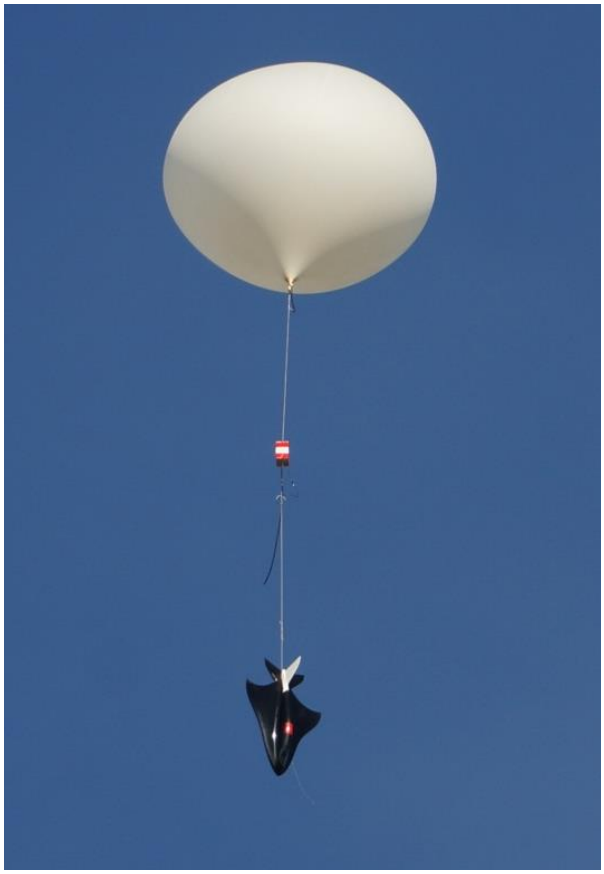

Figure 7: Glider, backup cutter system and balloon

The balloon was launched on 26 September 2012 at 11:27am from ESRANGE. The decision was made due to a changing weather situation making a launch on one of the remaining days of the launch campaign very unlikely. Despite relatively high ground winds with a speed of 10m/s and more the overall conditions were good with excellent visibility and small cloud coverage.

The glider was given the telemetry command to release at 11:52am after an ascent time of 25min and an altitude of 9525m. The following descent took 8min and 15s. The drop recognition worked as planned and switched into return to launch mode after a free fall of 100m. The readings in the ground station led us to think that the glider might be in a stall. The actions we took were towards fighting that spin, though, as revealed later, there was no stall to fight.

The counter measures involved leveling the control surfaces and changing control parameters for speed scaling the control loop output. Also different fixed descent and fixed course angles were tried.

When it became obvious that the base wouldn't be reached it was decided to land on parachute. Upon telecommand for releasing the parachute, the system confirmed the execution right away. The last radio contact happened at 300m above ground, showing vastly decreased groundspeed.

We gathered our ground station equipment right away and drove to the point closest to the touch down site but still reachable by streets. We were hoping for a radio contact giving us the final coordinates, but we didn't get a signal.

The next day we geared up and moved out to retrieve the glider. Though the line-of-sight distance was only 5km from the parking position of our car to the glider's last known position, the difficult terrain with flooded meadows and several hard crossable streams allowed us only to cover half of the distance. We returned for not getting caught by the soon to come nightfall. The next day we started a new attempt. Now being already more used to the terrain we made good progress so that we reached the last known position within two to three hours. Having calculated a rough estimate on were to expect the glider based on the wind situation of the flight day we started searching in a grid pattern. After only 45min we stumbled upon the glider. It had hit the trunk of a fallen tree, inflicting major damage to the structure and causing all batteries to be disconnected from the system, which was therefore not being able to transmit anymore. Having returned to base we were

glad to see that the captured HD-video footage was intact and usable.

5. Results and Discussion

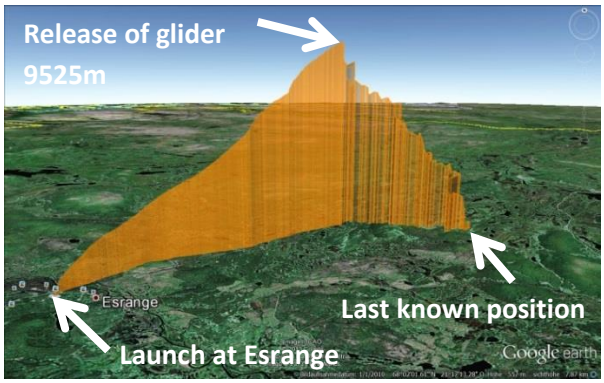

Figure 8. Mission path drawn in Google Earth

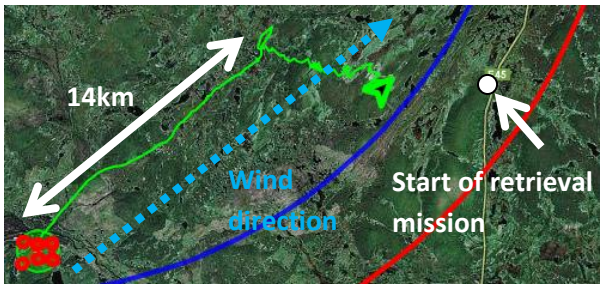

Figure 9: Ground track of ascent and descent

"*Fig. 8*" and "*Fig. 9"* show a plot of the received positional data from the glider. When the glider was commanded to release at an altitude of 9525m it was currently about 14km away from base. Already short after the flight, without having recovered the video footage, we came to the conclusion that something else had to been going on than a flat spin or some other stall related aerodynamic phenomena. By looking at the flight path we saw a drastic difference between the wind direction, in which it would have been drifting during a flatspin and the actual flown overall direction.

Also note the marked parking position of our car from where we started our recovery hike, as well as the boundary boxes for our experiment. The partial red circle marks the outline of the permitted flying zone, the blue one indicates the boundary where the glider would have released itself automatically in case of trespassing it. As one can see we haven't left the permitted airspace at any given time.

Looking at the retrieved video footage we quickly noticed two things:

1. There was no stall problem, the airframe shape was behaving aerodynamic wise excellent
2. The spinning motion actually was a long, slow turning spiral and seemed to be autopilot induced

Let's first get some material to support the claim of the aerodynamic shape performing well.
Take a look at "*Fig. 10".* This shows a sequence of shots taken from the onboard video. The sequence covers the time from right before release, with the glider still hanging on the rope, till the time where the control kicks in. During the complete time the control surfaces stay still in level position. As observable in the sequence and far better even in the actual video the glider reacts to the sudden loss of supporting force by the rope with a pitch up, followed by a nose down momentum and dampening out any residual angular movement resulting in a stable nose down and accelerating trajectory. This maneuver for itself might have already led to a stall. This has happened at other BEXUS UAV projects namely ICARUS and MARVEL at a lot lower altitudes, as well as in many other amateur projects worldwide.

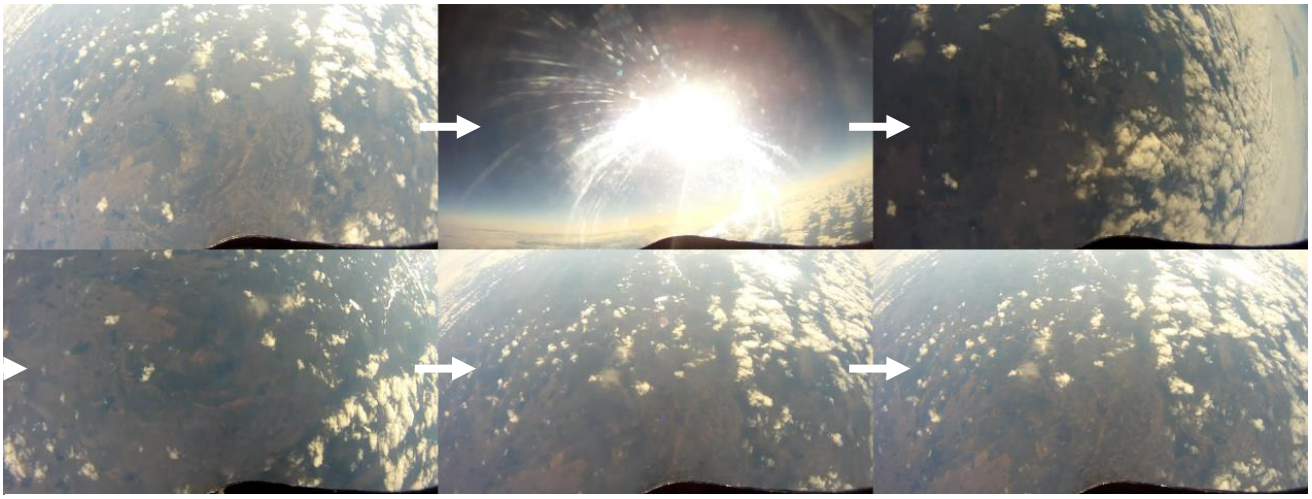

Figure 10. Pitch up after release, aerodynamic stabilisation within seconds

A second occasion where the shape performed exceptionally well was during the commanded control-surface-neutral action to fight the, so believed, but non existing stall. The static stability combined with the massive over speed made the glider fly a looping at an altitude of 8,5km with a calculated diameter of over 200m. In the top part, the speed dropped very low, but it continued the loop without break out tendencies ("*Fig. 11*").

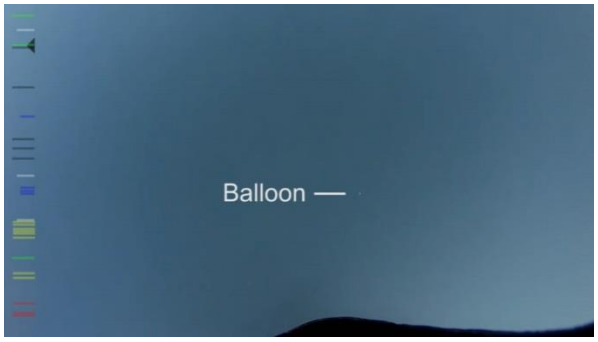

Figure 11

Also the shape demonstrated smooth behavior at very high speeds. 30s into the flight, the glider pulled into a horizontal trajectory, so that the ground speed given by the GPS matches closely the actual airspeed. The telemetry shows 176m/s, so to say more than 633km/h!

Several times the autopilot commanded a radical change in rudder positions. The reaction of the airframe was always very direct and precise.

So the problem, why the glider wasn't flying the direction we wanted it to, was not an aerodynamic problem.

Figure 12. Slow roll, commanded by autopilot

The video footage reveals a slow but continuous rolling motion ("*Fig. 12*"). Our first guess was that this might be an IMU problem. We thought, that though tested, the IMU might have had begun drifting during the balloon ascent. But there is a part in the video that rules out many possibilities. 5min and 30s into the flight the glider turns towards Esrange and stays on that course for a full minute, just to suddenly start with the rolling motion again.

For further investigation we needed to bring all existing data together. First of all we had logged every upload sent to glider with a time stamp. Those were put into the flight video as an overlay. This can be seen in "*Fig. 11*". On the left hand side are color-coded bars that indicate different actions. A marker, the triangle, moves from top to bottom during playback of the video, making it easy to navigate between different points of interests. But a logged upload command itself doesn't guarantee that the glider actually got it. That's why this needs to be cross referenced with the received telemetry from the glider.

To do just that, we first wrote a program that is able to prepare the logfile with timestamps in front of every message. These timestamps are generated by the onboard processor time sent every several packets and the knowledge of the working scheme of the telemetry packet scheduler.

This so prepared logfile is then read by a program that replaces the normal connection data handler program. It sends message packets according to the timestamps to the actual groundstation software. The groundstation software thereby never gets to know that it's not actually flying and displays everything just like it did during the flight ("*Fig. 13*" and "*Fig. 14*").

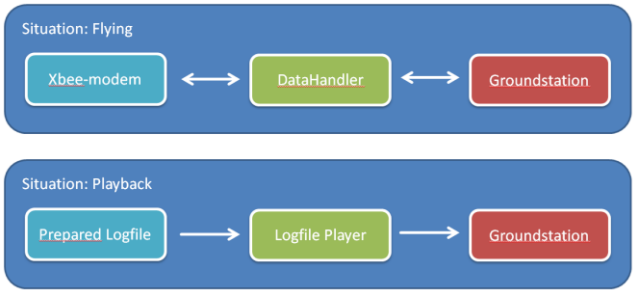

Figure 13. Simulated data link

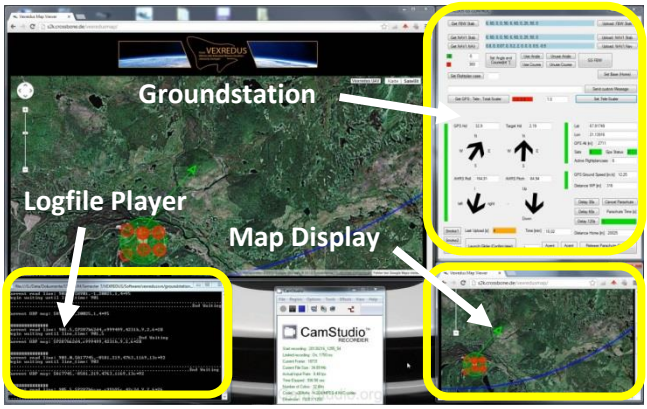

Figure 14. Playback setup

The setup as seen in "*Fig. 14*" was recorded with CamStudio while it was playing the log file. This was then brought together with the already combined upload commands and onboard footage video.

The result looks like this:

1: Color coded event markers

2: Moving triangle marker for current position on timeline

3: Current sent/active upload command

4: Onboard HD video footage

5: Logfile player

6: Groundstation: Control interface

7: Groundstation: Map display

So by simply scrolling through the video, all the information is in one place.

It was already mentioned that at some point the glider seemed to fly towards Esrange in a straight way for a full minute. A look at the just mentioned video revealed that we just had instructed the glider to fly a fixed course heading. The video also shows that we never got confirmation by telemetry for it using this fixed course. This is also noticeable by us, trying several times to activate the function with the corresponding upload command. Nevertheless the onboard video shows a direct reaction to the first

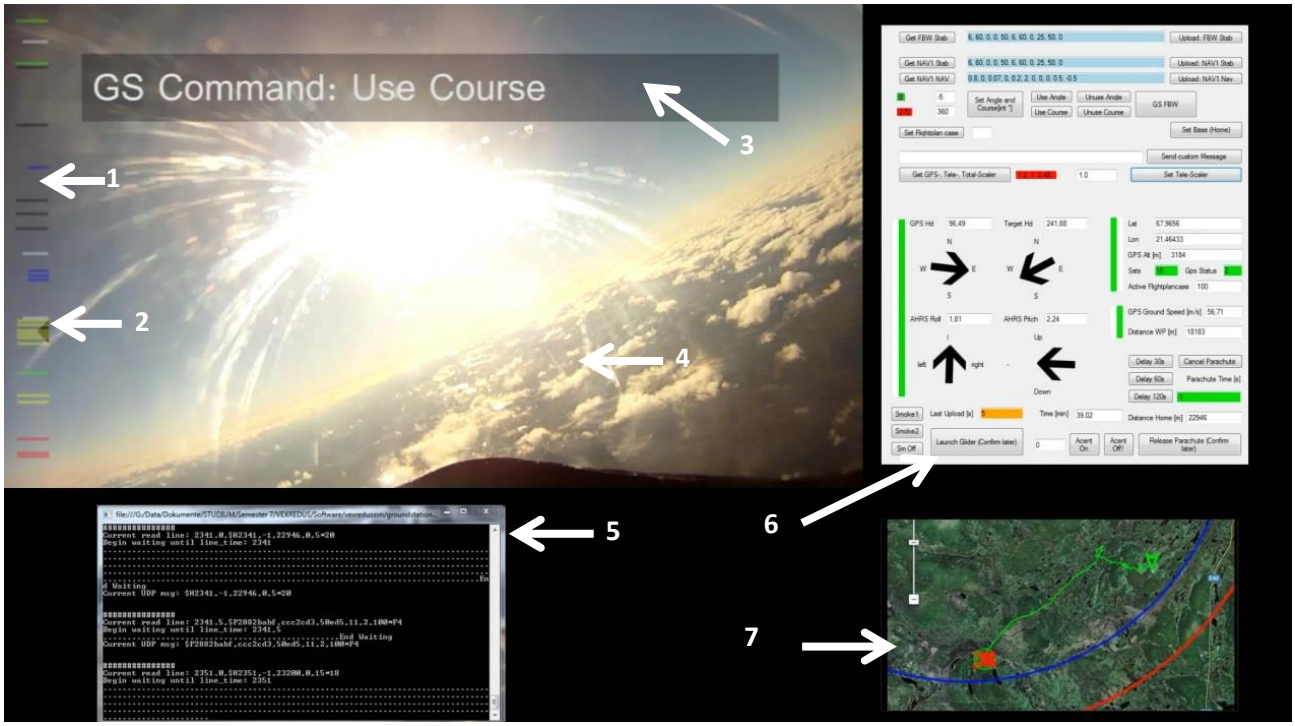

Figure 15. All data combined in a video file

command, while at the same time the telemetry link got bad, so we only received packets sporadically from the glider. Within these packets the glider told us the time since it last had received an uploaded packet by the groundstation, which does this routinously once a second. The data indicates that for over 73s the glider wasn't receiving upload commands.

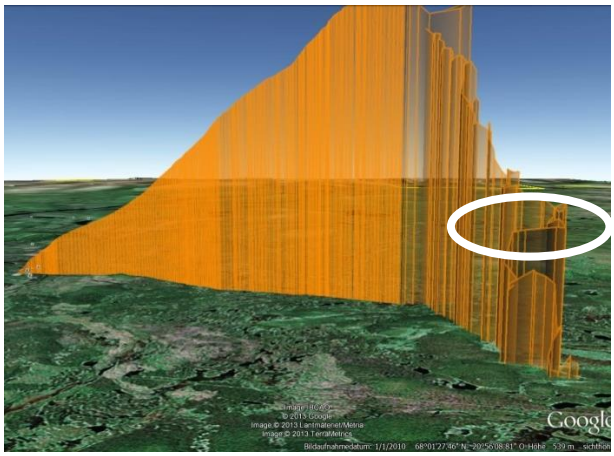

Figure 16: Correct autopilot behavior. Ended after 1min due to safety time limit in the active function

The function for flying by a fixed course, which we think was active, though we never got a confirmation due to a bad link at this time, was limited to a 60s timespan, as a precaution for not having the plane fly away with fixed course in case of a lost telemetry link. It kept on flying in the desired direction until it hit the time limit, due to no upload command coming through to reset the timer, and then continued with the course calculation on its own. This leads to following statements:

- The routine to calculate the desired course seems not to have worked as desired, generating weird desired bank angles sending the glider in a continuous rolling motion
- The inner control loop, as well as the function to calculate the desired bank angle as a function from current heading to desired heading worked, as demonstrated by the 1min part of the flight
- The fixed route routine was cancelled as expected due to no upload link reception

As an interesting side note: The path during the controlled flight part (highlighted in "*Fig. 16*") had such a low descent rate that the remaining altitude very likely would have been enough to reach Esrange.

6. CONCLUSION

The experiment was successful because the goal to verify the shape's high altitude air worthiness was achieved. The aerodynamic behavior can be described as excellent, with very good stall tolerance and direct following of control surface inputs.

The autopilot was at least part time capable of achieving controlled flight.

ACKNOWLEDGEMENT

First of all, our two old team members, Thorn Schleudtker and Tim Teutsch, shall be mentioned for contributing a lot during the first year of Vexredus.

Also the members of the AKAMODELL Stuttgart e.V. shall be thanked; especially Ruben Bühler and Jonas Illg for being always supportive in the field of glass and carbon fiber reinforced plastic building techniques.

A huge thank you goes out to the REXUS/BEXUS supervisors, especially Martin Siegl, Olle Persson and Mark Uitendaal.

VEXREDUS was supported by the DLR, Institute of Space Systems – University of Stuttgart, Rampf, SAFT and the "Jump and Fun Factory"

7. REFERENCES

[1] **www.smartfish.ch**

[2] **www.uni-stuttgart.de/akamodell**

[3] **www.diydrones.com**

SMALL WHISKBROOM IMAGER FOR ATMOSPHERIC COMPOSITION MONITORING (SWING) FROM AN UNMANNED AERIAL VEHICLE (UAV)

A. Merlaud[1], D.-E. Constantin[2], F. Mingireanu[3], I. Mocanu[4], C. Fayt[1], J. Maes[1], G. Murariu[2], M. Voiculescu[2], L. Georgescu[2], and M. Van Roozendael[1]

[1]*Belgian Institute for Space Aeronomy (BIRA-IASB), Avenue Circulaire 3, 1180 Brussels, Belgium (alexism@oma.be)*
[2]*University of Galati, 111 Str. Domneasca, 800008, Galati, Romania*
[3]*Romanian Space Agency (ROSA), 21-25 Str. Mendeleev, 010362, Bucharest, Romania*
[4]*Reev River Aerospace, 21 Str. Stiintei, 800146, Galati, Romania*

ABSTRACT

We describe a new instrument, the Small Whiskbroom Imager for atmospheric compositioN monitorinG (SWING), and its first test flight on a dedicated Unmanned Aerial Vehicle (UAV). One important objective is the mapping of NO_2 columns at high spatial resolution allowing to subsample satellite measurements within the extent of a typical ground pixel. Simulations show that tropospheric NO_2 columns can possibly be monitored at a ground resolution of 200x200 m^2 in polluted zones. The instrument is based on a compact ultra-violet visible spectrometer and a scanner to achieve whiskbroom imaging of the trace gases fields. Including the housing and the electronics, the weight, size, and power consumption of the SWING payload are respectively 920 g, 27x12x12 cm^3, and 6 W. The custom-built UAV wingspan is 2.5 m and can reach an altitude of 3 km during 2 hours, flying at 100 km/h in preprogrammed tracks. Considering the 120° swath of the instrument, it is able to cover an area of 20x20 km^2 in less than one hour. The spectra are analyzed using Differential Optical Absorption Spectroscopy (DOAS). Several atmospheric species are detectable in the spectral range covered by the spectrometer (250-750 nm). Water vapor, ozone, and O_4 have been identified in the spectra recorded during the test flight, which took place on 11 May 2013 near Galati, Romania. From this experiment, the detection limit of the SWING-UAV observation system for NO_2 is estimated to lie around 2 ppb, as expected from the simulations. Beside the validation of air quality satellite or local chemistry and transport models, other potential applications include monitoring NO_2 and/or SO_2 emissions from power plants, industries, ships, or volcanoes.

Key words: DOAS; Imaging; UAV; air quality.

1. SCIENTIFIC RATIONALE

Several instruments have already been described which achieve trace gases mapping from traditional aircraft in the UV-visible range [6, 16, 14]. These measurements are based on the Differential Optical Absorption Spectroscopy (DOAS) technique [13]. They are valuable compared to ground-based mobile DOAS experiments, which only measure horizontal gradients along roads (e.g. [2]). Airborne measurements also offer a much finer spatial resolution when compared to spaceborne sensors. For instance, [14] derived maps of tropospheric NO_2 over Zurich at a resolution 50x120 m^2 using the Airborne Prism Experiment (APEX), while the best satellite instrument in this respect is currently the Ozone Monitoring Instrument (OMI, [8]), whose pixels are 13x24 km^2 (13x12 km^2 in zoom mode). For short-lived species like NO_2, the coarse resolution of satellite data actually yields representativity problems in validation exercises with ground-based measurements. This problem can be reduced using an aircraft covering a pixel extent in a relatively short time. Beside satellite validation, airborne instruments are valuable to study the accuracy of local chemistry and transport models (see Fig. 1 for such a model above the Antwerp urban area) and monitor NO_2 and SO_2 emissions from point sources such as power plants and industries [6] or ships [1].

We have developed such a payload for trace gases imaging, but from an Unmanned Aerial Vehicle (UAV). The latter has been built in parallel and we are currently investigating the capabilities of this new observation system for atmospheric research. The instrument, namely the Small Whiskbroom Imager for atmospheric compositioN monitorinG (SWING) has already been tested from an ultralight aircraft in 2012 and from the UAV in May 2013. The Belgian Institute for Space Aeronomy (BIRA-IASB) has been interested on atmospheric measurements from UAV for some years [5] and has recently performed airborne DOAS experiments from traditional aircraft [11, 12]. SWING-UAV originates from the experience gained with these airborne DOAS systems and from the opportunity of using a dedicated UAV platform,

Proc. '21st ESA Symposium European Rocket & Balloon Programmes and Related Research', 9–13 June 2013, Thun, Switzerland (ESA SP-721, October 2013)

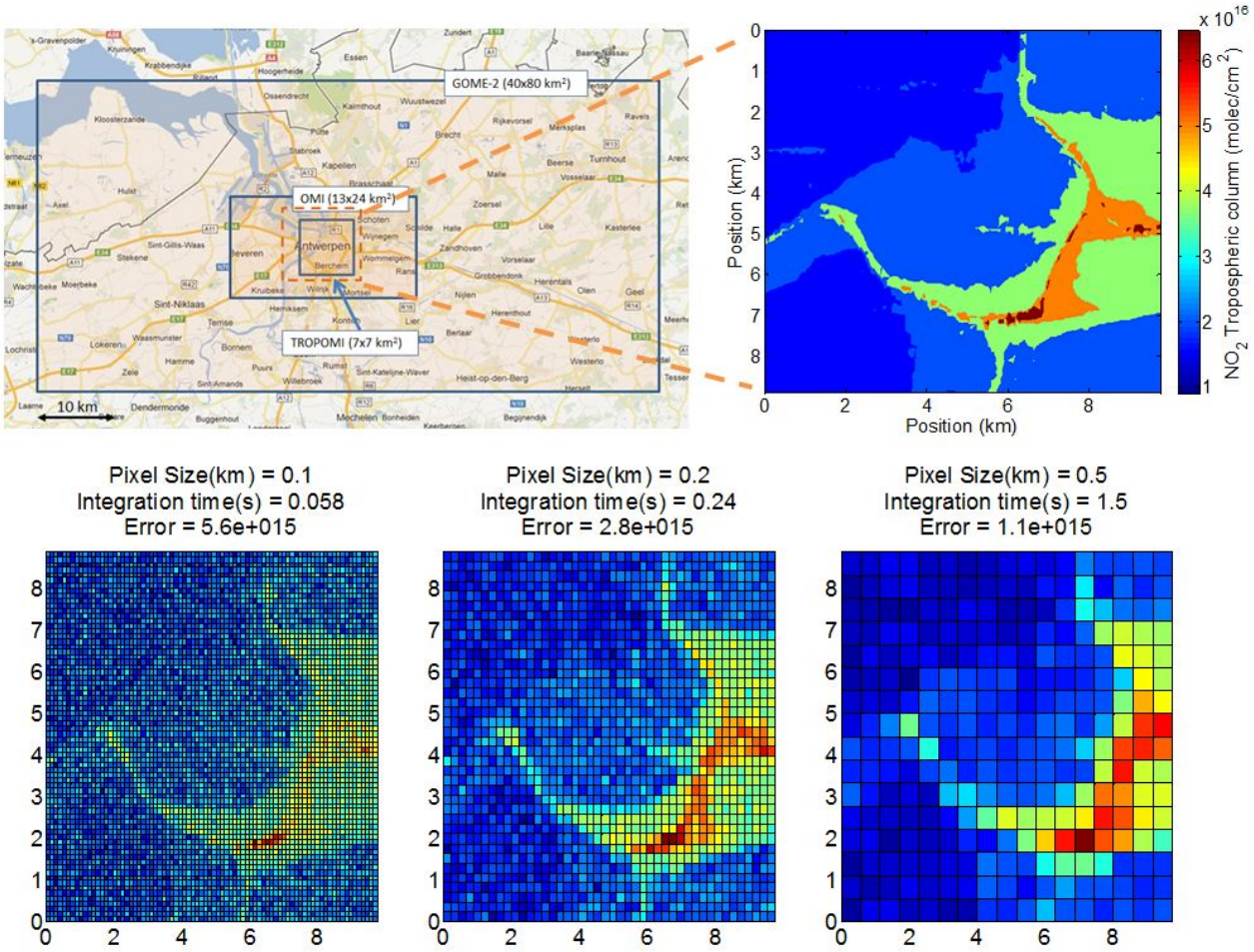

Figure 1. Simulations of NO_2 observations from an UAV flying at 3 km at different pixel size. The figure illustrates the trade-off between the ground resolution and the signal-to-noise ratio. Also shown are the pixel extents from current (GOME-2, OMI) and near-future (TROPOMI) satellite instruments, and the model field used as an input in the simulations.

which was made possible through the collaboration with the University of Galati. An advantage of operating from a UAV compared to a manned aircraft is the cost efficiency. The platform can also fly at lower altitudes and in hazardous environment such as inside a volcanic plume. Another whiskbroom instrument has recently been operated from a UAV for DOAS measurements, the Airborne Compact Atmospheric Mapper (ACAM, [7]). It has already measured NO_2, formaldehyde, and even tropospheric ozone above Houston. However, the platform used (the NASA Global Hawk, 40 m wingspan) is much larger than our flying wing (2.5 m wingspan) and the ACAM payload itself is over 20 kg, compared to the 900 g of SWING.

The next section presents initial simulations on the possible ground resolution of a whiskbroom imager operated from a UAV. Sect. 3 describes the hardware of the SWING instrument and the UAV platform. Sect. 4 presents the results of our first UAV test flight. Finally, Sect. 5 sums up lessons learned and states the near-future developments and perspectives for the SWING-UAV observation system.

2. INVESTIGATIONS ON THE ACHIEVABLE GROUND RESOLUTION

We performed simulations of NO_2 measurements above a polluted zone, namely the Antwerp agglomeration in Belgium, to estimate a realistic ground resolution of a whiskbroom system from a UAV at 3 km. High resolution NO_2 field forecasted around this area were taken from the PROMOTE air quality forecast service[1], which is based on the Immission Frequency Distribution Model (IFDM,[3]). Only surface concentrations were available so the columns were roughly built assuming an homogeneous boundary layer of 500 m.

The relationship between the pixel size (P_s) and the integration time (τ_D) used in these simulations is as follow:

$$\tau_D = \frac{P_s^2}{vS} \quad (1)$$

where v is the speed of the aircraft and S is the swath. They were set in these simulations to 60 km/h and 120°, respectively. This does not take into account the panoramic distortion for instance, which leads to larger pixels at the end of the swath. The objective of the simulations is to estimate the level of horizontal details due to the trade-off between spatial resolution and signal-to-noise ratio.

The baseline for the measurement noise was derived from a previous airborne experiment with the compact spectrometer used in SWING [12]. The typical error on the fitted NO_2 DSCD was scaled for the shorter integration times and for the different geometry assuming photon-noise limited conditions and using relative intensities calculated with the UV-Spec/DISORT radiative transfer model [9].

[1] http://promote.vito.be/webtool/

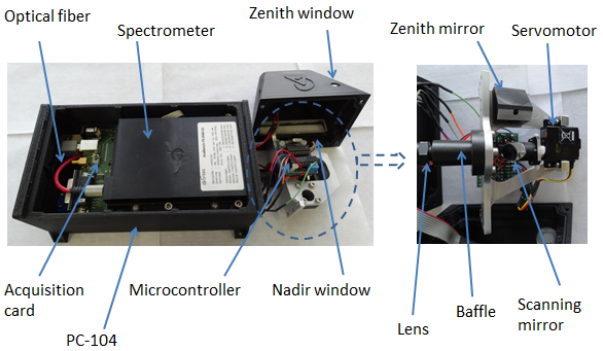

Figure 2. The SWING instrument. The size is 27x12x12 cm^3 for 920 g, the power consumption is 6 W at 5 V. The right panel shows the scanning system in more details.

Fig. 1 presents the NO_2 model field used as an input and corresponding simulated observations for three different ground resolutions: 100 m, 200 m, and 500 m. The figure also shows, for a comparison, the pixel size of the current and near-future satellites GOME-2 ($80 \times 40\,\mathrm{km}^2$), OMI ($80\times40\,\mathrm{km}^2$), and TROPOMI ($7\times7\,\mathrm{km}^2$). An interesting pattern for its horizontal gradients is the South West part of the Antwerp ring-road. It appears in the model field highly polluted and it is surrounded by cleaner areas. According to the simulations, the noise level for a 100 m pixel still enables to distinguish the road from the background. In comparison, for a 500 m pixel, the image is much less noisy but the small scale of the road is almost completely diluted in the broader pixels. In real conditions, flying directly above such a perfect NO_2 source may be difficult in the near-future due to clearances reasons. The intermediate value of 200 m for the ground resolution below the aircraft represents thus, from these simulations, a good compromise.

3. INSTRUMENT AND PLATFORM DESCRIPTION

3.1. The SWING payload

Fig. 2 shows the SWING instrument with its open housing. It is based on an Avantes AvaSpec-2048 spectrometer, with a 50 μm entrance slit and a 600 l/mm grating. It covers the spectral range from 250-750 nm at a resolution of approximately 1.2 nm Full Width at Half Maximum (FWHM). Light is collected by a 400 μm diameter optical fiber and a lens facing a mirror installed on a servomotor shaft. The mirror scans at $\pm$ 60°in the nadir direction. The instantaneous and angular field of view (FOV) are 2.5°and 120°, respectively. It is also possible to record

Table 1. Main characteristics of the SWING-UAV observation system.

SWING	Size	27x12x12 cm^3
	Weight	920 g
	Power consumption	6 W
	Angular FOV	120°
	Instantaneous FOV	2.5°
UAV	Ceiling	3 km
	Wingspan	2.5 m
	Speed	60-130 km/h
	Autonomy	2 h
SWING-UAV	Pixel size	200 m
	Detection limit (NO_2)	2 ppb

Figure 3. The Unmanned Aerial Vehicle built by Reev River Aerospace and dedicated to the SWING payload.

spectra in the zenith direction by rotating the scanning mirror at 90°relatively to nadir, pointing to a zenith mirror. This possibility is useful to estimate the contribution of the total column of NO_2 which lies above the platform. A PC–104 controls the spectrometer and the motor, the latter via a driving circuit based on a microcontroller. A GPS antenna is also connected to the PC. The whole system is powered by 5V, which is supplied by a compact battery. Considering the application, the optical windows are not in BK7 or fused silica glass but in a plastic material suitable for optical applications (Zeonex). Except the scanner support which is aluminium made, the structural parts and the housing are in plastic material (ABS). They were manufactured by 3d printing to optimize their weight and shape. More technical details about the electronics circuits and other miniaturization effort are given in [10].

Everything included, the weight, size and power consumption of SWING are respectively 920g, 27x12x12 cm^3, and 6W.

3.2. The custom-built UAV

Fig. 3 shows the UAV dedicated to the SWING payload. The latter is fixed on the back of the aircraft, in measurement position. This UAV was customly-built for the

Figure 4. Flight tracks of the UAV test flight in Romania.

experiment by Reev River Aerospace. It is an electrically powered flying wing, with a wingspan of 2.5 m and it can reach an altitude of 3 km during 2 hours. The aircraft equipment includes attitude sensors, whose accuracy is around 0.1°, a GPS, and a steerable camera. All of these instruments are accessible through the radio during the flight, and logged four times a second. SWING being powered by its own battery, the platform and the payload are currently completely independent. Take off is achieved with a catapult and the whole flight can be preprogrammed and controlled with an autopilot. The ground segment is mainly composed of a radio antenna and a computer, and the whole set-up is easily transportable in a normal car.

4. RESULTS FROM THE UAV TEST FLIGHT

The first flight with the SWING instrument on the UAV took place on 11 May 2013, 15 km NW of Galati, Romania (45.53°N, 27.9°E, 95 m.a.s.l.). The aircraft took off at 7h30 UT and landed at 9h10 UT, in clear sky conditions. Fig.4 shows the flight pattern, which consisted of loops at 420 to 450 m.a.s.l, around predefined waypoints. The attitude variation during the flight are visible on Fig.6. The instrument did not stop neither at take off nor at landing. The wind was blowing from the NE direction.

Fig. 5 presents some DOAS fits of the spectra collected during the flight, performed with the QDOAS software [4]. The DOAS analysis settings used for the retrievals are similar to a previous airborne experiment with the same spectrometer [12]. Spectral signatures of four different absorbers, namely NO_2, water vapor, O_3 and O_4 are clearly identified. However, the reference spectrum was recorded in Brussels and therefore the negative NO_2 differential slant column density (DSCD) corresponds to

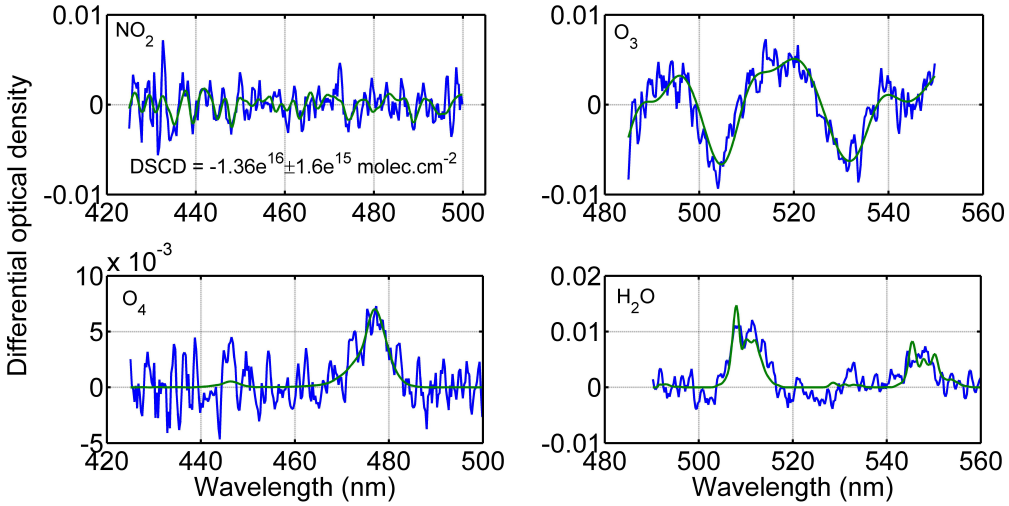

Figure 5. Examples of DOAS fits of NO_2, ozone, O_4, and water vapor, from the spectra recorded during the UAV test flight.

a larger absorption of NO_2 in the reference spectrum than in the spectrum from the flight.

From the NO_2 DOAS fit, it is possible to estimate a detection limit for the NO_2 vertical column and volume mixing ratio (vmr). The uncertainty on the DSCDs retrieved from the spectra is estimated from the DOAS analysis to lie around 2e15 molec.cm^{-2} (1σ). The air mass factor in nadir geometry is around 2 (see lowest panel in Fig. 6). The minimum vertical column that can be detected with the SWING-UAV is thus 1e15 molec.cm^{-2}. Assuming a 500 m well-mixed boundary layer, this column corresponds to a vmr of 0.8 ppbv. The 2σ detection limit in vmr can thus be conservatively estimated to 2 ppbv. This value could be further reduced when flying at a higher altitude, but the actual detection limit depends also on the weather conditions and solar zenith angles.

Besides checking the quality of the spectra, the test flight enabled us to study the attitude stability during the flight. Fig. 6 presents an excerpt of the time series focusing on the measurement geometry. Starting from the top, the first panel shows the angle of the scanner relative to nadir. The second presents the pitch and roll angles of the aircraft. The elevation of the scanner compared to the ground (third panel, 0°corresponds to nadir) is calculated combining these two angles with the heading direction, following [15]. The largest elevation angles with respect to the nadir direction corresponds to the time periods when the UAV is changing heading direction, which are in fact more visible in the roll angle time series. Focusing on the period when flight is straight, the pitch and roll stay within $\pm 10°$.

The lowest panel of Fig. 6 presents air mass factor (AMF) calculations based on the measured attitudes and heading direction of the panels above, but for observations at 3 km. The AMFs corresponding to two different ground albedos are presented. We used the radiative transfer code UV-Spec/DISORT [9], with the same well-mixed boundary layer assumption. The solar azimuth angle was set to 45°. Interestingly, the AMF appears quite stable with the scan angle, at least when the scan elevation is below a threshold at around 65°. Under this value, the AMF varies weakly (¡10%) with the scan elevation. Large variations of the AMF (50%) are only observed when the scan elevation is above 65°, i.e. when the UAV is changing direction. This finding reduces the importance of the pointing error for the AMF calculation. By contrast, the figure points out the importance of using a correct albedo for the AMF estimation since the effect of this parameter appears important for the absolute value of the AMF.

5. CONCLUSIONS AND PERSPECTIVES

A miniaturized instrument for trace gases mapping from a UAV was developed. Everything included, the weight, size and power consumption of SWING are respectively 920g, 27x12x12 cm^3, and 6W. The first test flight on the custom-built UAV took place in Romania on 11 May 2013. Water vapor, ozone, and O_4 were identified in the spectra, whereas NO_2 detection limit could be estimated at 2 ppb. We also started to investigate the AMF calculations for the considered geometry. This step will be necessary to convert the DSCDs retrieved with the DOAS analysis to more geophysically relevant vertical columns. Our findings indicate that the pointing error appears negligible compared to the albedo effect.

Some work is ongoing to improve the capabilities of the SWING-UAV observation system. First, the scanning loop will be optimized, to increase the number of points per scan (upper panel, Fig. 6). This is important to increase the ground cover of the measurements. The angular offsets between the attitude sensor and the scanner will be characterized accurately. Indeed, if the pointing error is not important for the AMF calculation, it plays a great role for the georeferencing issues. Other charac-

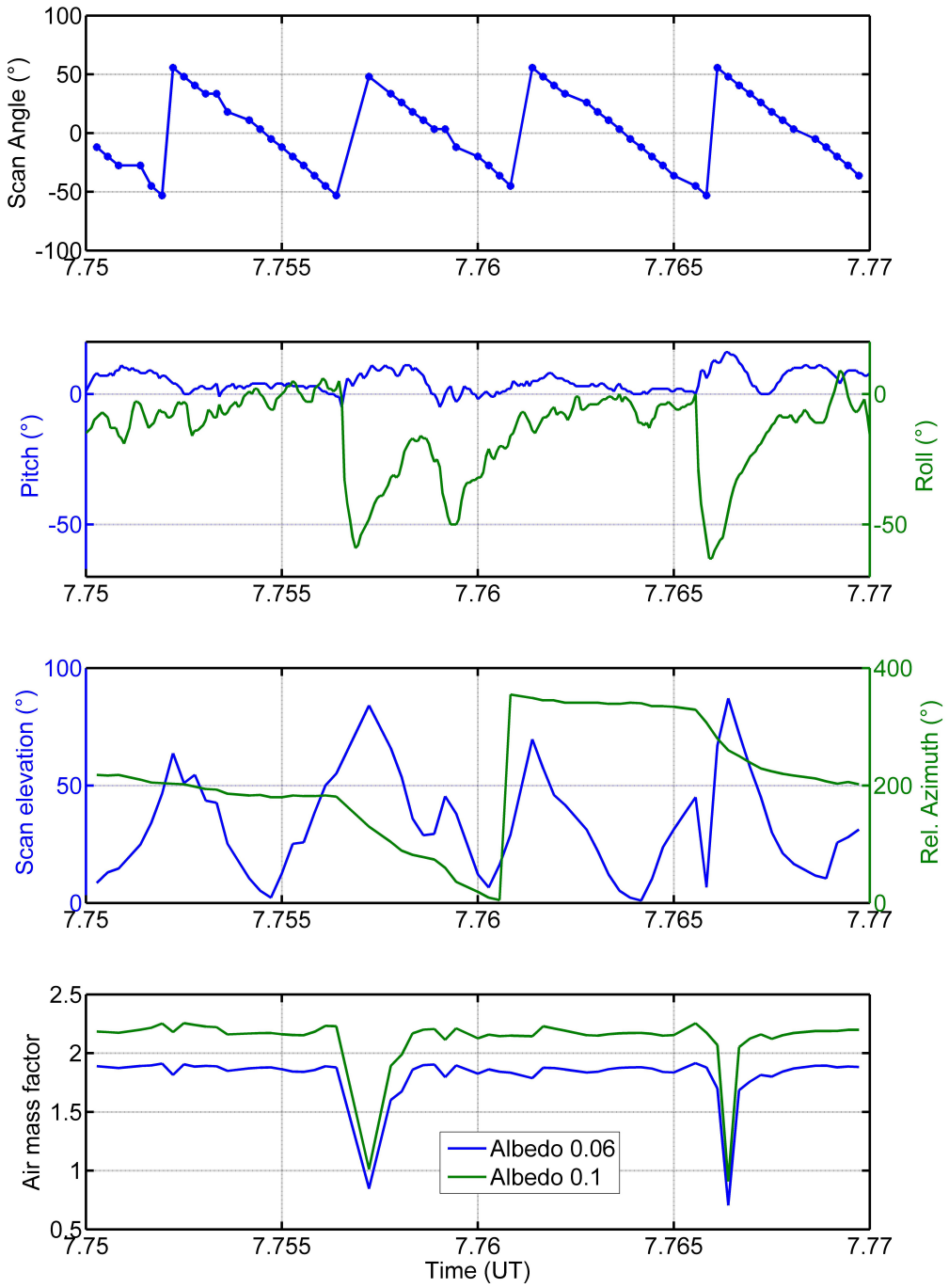

Figure 6. Geometry of the measurements during the test flight (three upper panel) and their simulated effect on the air mass factors for two different ground albedo (lowest panel).

terizations include the optical properties. The polarization response of the spectrometer will be characterized accurately since it is a well-known issues in atmospheric optics based on grating spectrometers. The absolute radiometric calibration of the spectrometer will help us to retrieve the ground albedo from the spectra. A major improvement would consist in using a spectrometer able to measure both NO_2 and SO_2 at the same time. The spectral range of the current SWING system does not permit to study SO_2 absorptions. We are currently looking for an optimal spectrometer, possibly also using a more sensitive detector.

In the near future, the SWING-UAV observation system will perform further test flights above NO_2 sources, such as power plants or chemical factories in Romania. We have also initiated a project to measure NO_2 and SO_2 from ships. Flying above a city to monitor air quality appears a middle-term project due to legislative issues, but it appears technically feasible and it fits the increasing number of civilian UAV applications.

ACKNOWLEDGMENTS

This project is supported by the Belgian Science Policy (BELSPO). D.E. Constantins work for this study was supported by the Grant SOP HRD/107/1.5/S/76822 TOP ACADEMIC co-financed from ESF of EC, Romanian Government and Dunarea de Jos University of Galati, Romania. We thank Dirk Schuttemeyer for useful discussions.

REFERENCES

[1] Berg, N., Mellqvist, J., Jalkanen, J.-P., & Balzani, J. 2012, Atmos. Meas. Tech., 5, 1085

[2] Constantin, D., Merlaud, A., Van Roozendael, M., et al. 2013, Sensors, 13, 3922

[3] Cosemans, G. & Mensink, C. 2005, in Proceedings of the 10th Conference on Harmonisation within Atmospheric Dispersion Modelling for Regulatory Purposes, Heraklion, Crete, Greece, 206–210

[4] Danckaert, T., Fayt, C., De Smedt, I., et al. 2012, QDOAS, Software User Manual, Belgian Insitute for Space Aeronomy, Brussels, Belgium

[5] De Mazière, M., Van Roozendael, M., & Merlaud, A. 2006, in ISPRS Archives. Vol. XXXVI-1/W44, Second International Workshop: The Future of Remote Sensing

[6] Heue, K.-P., Wagner, T., Broccardo, S. P., et al. 2008, Atmos. Chem. Phys., 8, 6707

[7] Kowalewski, M. G. & Janz, S. J. 2009, in Proc. SPIE 7452, Earth Observing Systems XIV No. 74520Q

[8] Levelt, P., van den Oord, G., Dobber, M., et al. 2006, IEEE T. Geosci. Remote., 44

[9] Mayer, B. & Kylling, A. 2005, Atmos. Chem. Phys., 5, 1855

[10] Merlaud, A. 2013, Development and use of compact instruments for tropospheric investigations based on optical spectroscopy from mobile platforms (Presses univ. de Louvain)

[11] Merlaud, A., Van Roozendael, M., Theys, N., et al. 2011, Atmos. Chem. Phys., 11, 9219

[12] Merlaud, A., Van Roozendael, M., van Gent, J., et al. 2012, Atmos. Meas. Tech., 5

[13] Platt, U. & Stutz, J. 2008, Differential Optical Absorption Spectroscopy: Principles and Applications, Physics of Earth and Space Environments (Berlin: Springer)

[14] Popp, C., Brunner, D., Damm, A., et al. 2012, Atmos. Meas. Techn., 5

[15] Roy, D. P., Devereux, B., Grainger, B., & White, S. J. 1997, International Journal of Remote Sensing, 18, 1865

[16] Schönhardt, A., Richter, A., Krautwurst, S., et al. 2011, in 5th International DOAS Workshop

STATION-KEEPING CONTROL STRATEGIES ANALYSIS FOR STRATOSPHERIC AIRSHIP

Zhang Lixue, Wang Zhongwei, Zhao Kun, Yang Xixiang

Staff Room of Aerocraft Integrated Design , College of Aerospace Science and Engineering, National University of Defense Technology, No. 47 Yanwachi Street, Kaifu District, Changsha, 410073, China ,Email: zhanglixue1014@163.com, wangzhwei2001@163.com, zk198907@qq.com, nkyangxixiang@163.com.

ABSTRACT

The purpose of this paper is to develop a station-keeping performance analysis model for stratospheric airship with thermal and wind effects during its conceptual design and help provide insight into the control strategies analysis of stratospheric airship. Firstly, an extreme differential pressure estimation model for stratospheric airship was introduced. Secondly, a thermal analysis model to describe the heat transfer behavior of stratospheric airships was developed. The temperature and pressure variations about the upper envelop, lower envelop and internal helium during its station-keeping are obtained. Finally, the ways for airship pressure adjustment was analyzed and the corresponding control strategy to different scenario was discussed.

1. INTRODUCTION

The capability that wide-area surveillance for months at a time is urgent needed, but it can't be provided by neither satellites nor aircrafts. Among various conceptual designs, stratospheric airships, unlike aircrafts, generate lift by filling airship envelope with lighter-than-air gas and get power for flight by using thin-film solar cells have attracted substantial interest in both commercial and military arena[1,2].

However, the design of stratospheric airship offers unique design challenges compared to conventional aerospace vehicles. One such challenge is the pressure difference between the inner gas and the surrounding air estimation and control, because it was easily influenced by the flight environment such as solar radiation and winds. So in this paper, we want to develop a station-keeping performance analysis model for stratospheric airship with thermal and wind effects during its conceptual design and make control strategies analysis according to different flight scenario.

2. EXTREME DIFFERENTIAL PRESSURE

Envelop is the main load bearing parts for non-rigid airship[3,4]. And its function mainly reflects in two aspects, On one hand, it keeps airship contour through the pressure difference between the inner gas and the surrounding air. On the other hand, supports suspension system such as warehouse through cable and cord fabric. In addition, the wind and thermal environment around stratospheric airship will carry force and moment of force to it also.

2.1. Maximum design bending moment

During the process of flight, in order to keep balance, stratospheric airship has to resist the force moment carried by the winds[5]. We can use integration method to calculate the total bending moment along airship envelop. The maximum design bending moment expressions given by Goodyear company in 1975 is shown in Eq. 1.

$$M_{\max} = (0.11 + \frac{3\lambda}{80})\frac{u}{v} qV \qquad (1)$$

Where λ is the length diameter ratio, u is wind speed, v is the airship flight speed, q represents the dynamic pressure and its expression is $q = 0.5\rho v^2$, V means the total volume of airship. From the expression Eq. 1, we can see that when the size of airship is determined, the maximum bending moment of stratospheric airship is closely related with its operation condition and working environment.

2.2. Hanging load impact analysis

The suspension system's main function is that passing the gravity of gondola to the top skin of airship by tension cable and curtain which is used to decentralize the stress to avoid the distortion of airship envelop. And the stress put on the airship skin by suspension system can be divided into two categories, longitudinal and circular stress. After assuming skin tiny deformation, the longitudinal stress leaded by suspension can be calculated as Eq. 2.

$$F_1 = F_2 = \frac{G}{2nL\sin\theta} \qquad (2)$$

In Eq.2., G is the weight of load, L is the length of tension cable, n is the number of tension cable and θ is the angle of longitudinal tension to horizontal.

Fig.1 illustrates the geometric relationship of airship's cross section after skin tiny deformation and the force synthesis of point A.

From them, we can calculate out the stretching force of

Proc. '21st ESA Symposium European Rocket & Balloon Programmes and Related Research', 9–13 June 2013, Thun, Switzerland (ESA SP-721, October 2013)

point A. And the circumferential force of top envelop can be expressed using Eq.3.

$$T_1 = p_A R_1 = T_n \frac{\cos(\alpha - \theta_A)}{\sin(\varphi - \theta_A)} \qquad (3)$$

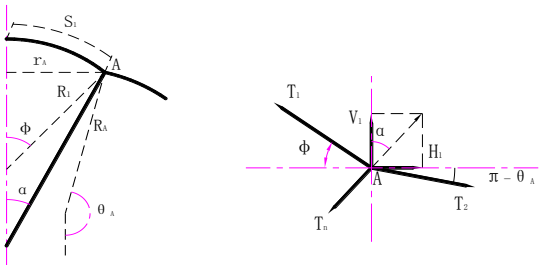

Figure 1. The geometric relationship of airship's cross section after skin tiny deformation and the force synthesis of point A.

For a fixed concept design, the variables(α θ_A φ) in Eq.3 are determined, so we can obtain the unique solve.

2.3. Extreme differential pressure estimation model

The differential pressure of non-rigid airship should be between minimum overpressure and maximum overpressure. And in this paper, we take the influence of initial differential pressure, wind environment and weight of gondola into account. Fig.2 shows the stress distribution of airship skin under the effect of different pressure and wind environment.

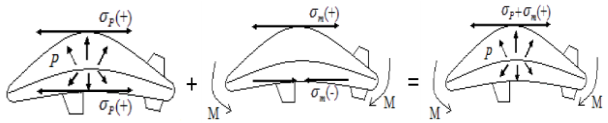

Figure 2.Stress distribution of airship skin.

Among them, the function of minimum overpressure is that prevent stratospheric airship envelop appearing fold. So it must satisfy Eq.4.

$$\sigma_\alpha = f_2 t = \frac{1}{2}\Delta P_{\min} r \geq \sigma_{\alpha 1} + \sigma_{\alpha 2} \qquad (4)$$

And from it, we can deduce the estimation expression (Eq.5) for minimum overpressure

$$\Delta P_{\min} \geq \frac{2M_{\max}}{\pi r^3} + \frac{G}{nrL\sin\theta} \qquad (5)$$

For the limit of envelop material strength, the maximum overpressure of airship should be limited to avoid skin avulsion. And it should satisfy Eq.6 and Eq.7.

$$[\sigma_\alpha] = \frac{\sigma_\alpha^0}{k} \geq \sigma_{\alpha 1} \qquad (6)$$

$$[\sigma_r] = \frac{\sigma_r^0}{k} \geq \sigma_{r1} \qquad (7)$$

Among them, k is the safety coefficient of envelop material (generally take to 4), and $\sigma_\alpha^0, \sigma_r^0$ is the upper limit of the envelop material in longitudinal and circumferential. By integrate the force calculation expression and stress relationship between them(Eq.6 and Eq.7), we can deduce the estimation expression (Eq.8) for maximum overpressure.

$$\begin{aligned} \Delta P_{\max 1} &\leq \frac{2[\sigma_\alpha]}{r} - \frac{2M_{\max}}{\pi r^3} \\ \Delta P_{\max 2} &\leq \frac{[\sigma_r]}{r} - T_n \frac{\cos(\alpha - \theta_A)}{r\sin(\varphi - \theta_A)} \\ \Delta P_{\max} &= \min[\Delta P_{\max 1}, \Delta P_{\max 2}] \end{aligned} \qquad (8)$$

Here we take a common stratospheric airship that the length of it is 200m as an example, and calculate the extreme differential pressure of it with the differential pressure model developed above. The lower limit of stratospheric airship differential pressure is 196 pa and the maximum differential pressure of it is 1128 pa. From the data, we can see that the range of differential pressure variation of airship pressure is relatively narrow. When we consider some other factors such as the capacity of carrying, the differential pressure range will become smaller. So the research of stratospheric airship pressure control strategies is an important premise for stratospheric airship subsequent design.

3. HEAT EXCHANGE

As shown in Fig.3, the inside hull of stratospheric airship consists of helium bag and air ballonets. In helium bag, they are filled with lighter-than-air gas and have no mass transfer with external environment. While air ballonets are filled with air and they transfer mass with external atmosphere to modify the weight of airship. When releasing air from ballonets, the mass of the airship reduces, the net buoyancy becomes positive. Oppositely, when pumping air into ballonets, the airship mass increases, the net buoyancy decreases and becomes minus. So stratospheric airships, unlike aircraft, can generate lift from net buoyancy instead of completely dependent on aerodynamics. Consequently, airships do not need to stay in motion to remain aloft. And they can loiter over a specific location as well as move to a new location.

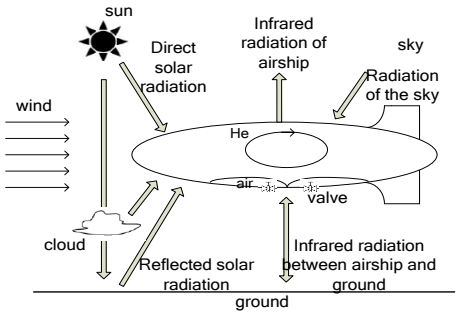

Figure 3. Sketch of thermal environment and heat transfer of airship.

3.1. Thermal balance equation

For the purpose of simplify the analysis process, lumped method is used for developing stratospheric airship thermal balance model. When stratospheric airship is on the state of station-keeping, the air remained in the ballonets is little and the quality exchange with outside atmosphere is little also. So its influence can be neglected. In addition, in order to get enough energy, stratospheric airship would keep a flight pose with its backside upwards during the flight process. So the quantity difference of radiation that put up on airship's top and down surface is larger. And we should calculate the heat exchange process of them with different models. In this paper, the structure of stratospheric airship is divided into three parts, including upper part airship envelope, lower part airship envelope and helium bag. For each part, it is assumed that the temperature of them is spatially averaged values. And the energy equations for them are

$$C_{pfs} m_{fs} \frac{dT_{fs}}{dt} = Q_{fs} \tag{9}$$

$$C_{pfx} m_{fx} \frac{dT_{fx}}{dt} = Q_{fx} \tag{10}$$

$$C_{phe} m_{he} \frac{dT_{he}}{dt} = Q_{he} \tag{11}$$

3.2. Heat transmission model

With the change of working places, stratospheric airships are exposure to complicated and different thermal environment[6,7]. By considering all possible heat transfer types, thermal environment of stratospheric airship is diagrammed in Fig.3. It includes two types, namely heat convection and heat radiation. Among them, heat convection occurs between the airship envelop and surrounding air, airship envelop and inner helium. While the radiation behaviors on airship include: direct solar radiation, solar radiation reflected by ground or clouds, infrared radiation from earth and atmospheric, infrared radiation emitted by airship envelope and inner gas and so on.

When upper part airship envelope, lower part airship envelope and helium bag are considered as nodes, the heat transfer equation for them can be expressed as

$$\begin{aligned} Q_{fs} &= I\alpha_{fs}A_{fs} + \varepsilon_{hf}\sigma(T_{he}^4 - T_{fs}^4)A_{fs} \\ &+ h_{hf}(T_{he} - T_{fs})A_{fs} + h_{aof}(T_{ao} - T_{fs})A_{fs} \\ &+ \varepsilon_{fs}\sigma(T_{bb}^4 - T_{fs}^4)A_{fs} \end{aligned} \tag{12}$$

$$\begin{aligned} Q_{fx} &= \tau I\alpha_{fx}A_{fx} + \varepsilon_{hf}\sigma(T_{he}^4 - T_{fx}^4)A_{fx} \\ &+ h_{hf}(T_{he} - T_{fx})A_{fx} + h_{aofx}(T_{ao} - T_{fx})A_{fx} \\ &+ \varepsilon_{fx}\sigma(T_{bb}^4 - T_{fx}^4)A_{fx} \end{aligned} \tag{13}$$

$$\begin{aligned} Q_{he} &= I\tau_s\alpha_{he}A_{he} + \varepsilon_{hfs}\sigma(T_{fs}^4 - T_{he}^4)S_{hfs} \\ &+ \varepsilon_{hfx}\sigma(T_{fx}^4 - T_{he}^4)S_{hfx} + h_{hf}(T_{fs} - T_{he})S_{hfs} \\ &+ h_{hf}(T_{fx} - T_{he})S_{hfx} + \varepsilon_{he}\tau_R\sigma(T_{bb}^4 - T_{he}^4)A_{he} \end{aligned} \tag{14}$$

3.3. Simulation results and analysis

From launch on at sea level to station-keeping at residence altitude, stratospheric airship will fly through a wide range of wind conditions. From the sea level to the altitude about 13km, the wind velocity increases with the altitude. Above this point, the wind velocity becomes more and more slowly. And at the height of 19-22km, the average wind velocity is just about 5m/s, where is a suitable resident area for stratospheric airship. But there is some fluctuation still. In order to make the results suit for a wide range of environmental conditions, we simulate it under wind velocity 0.1m/s,5m/s,10m/s and 15m/s. And the model was solved with fourth-order Runge-Kutta method. Fig.4 to Fig.7 is the results.

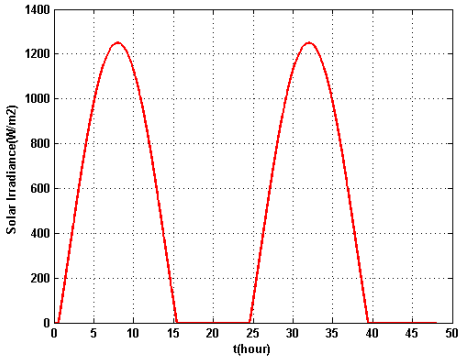

Figure 4. Variations of solar irradiance with time.

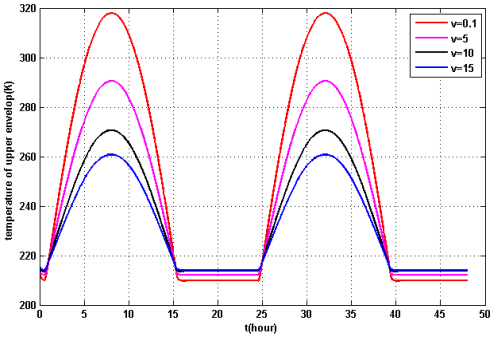

Figure 5. Variations of upper envelop temperature with time.

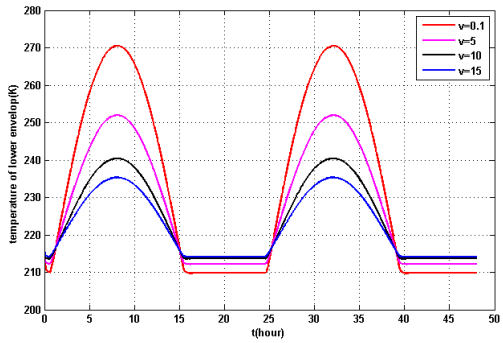

Figure 6. Variations of lower envelop temperature with time.

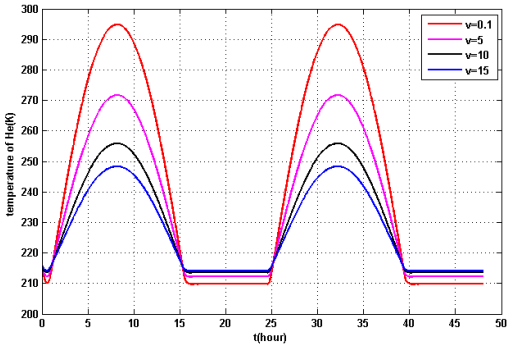

Figure 7. Variations of helium temperature with time.

Among them, Fig.4 is the variations of solar irradiance with time. Fig.5, Fig.6 and Fig.7 are the sketch map of temperature variations of upper envelop, lower envelop and inner helium with time. From the simulation results above, we can make some conclusion as follows:

1) The temperature variations trend of upper envelop, lower envelop and inner helium with time keeps consistent with the variations trend of solar irradiation. They all changes circularly, and the circular period is one day. This indicates that during the station-keeping process, when the change of wind speed isn't considered, the change of all parts' temperature is mainly affected by the variations of solar radiation.

2) Among the upper part of envelop, lower part of envelop and inner helium, the temperature variations of upper part of envelop is most intense. The temperature variations of inner helium is smaller, while the variations of lower part of envelop is smelliest.

3) The speed of external wind has a great influence on the temperature change. When the wind speed is small, the amplitude of airship temperature changes is great. And with the increase of wind speed, the amplitude of airship's temperature variation is smaller. This is mainly due to the change of wind speed affects the airship's convection coefficient which plays an important role in airship's heat exchange with the outside world.

4) During the station-keeping process, the maximum superheat temperature of inner helium is 85℃. And the relative wind speed at this scenario is 0.1m/s. When the initial helium-filled ratio is 0.077, the pressure of inner helium will increase 2380 pa which is over the range of extreme differential pressure. However, the superheat phenomena will be mitigated with the increase of wind speed. And it will disappear during night, the temperature of helium is always keeping at 210K which is near to the temperature outside.

4. CONTROL STRATEGIES ANALYSIS

When the internal pressure of airship gasbag is too high, the structure of airship gasbag is facing the danger of being destroyed, and when the internal pressure of it is too low, the structure of airship gasbag is facing the danger of producing fold. So we must take the pressure control into account during stratospheric airship's concept design.

4.1 All kinds of pressure control measures

There are a lot of pressure control measures can be used for airship pressure control at present with the development of science and technology, especially with the progress of low altitude airships. Here we make a classification of them from the realize principle. And it mainly includes the following several kinds:

1) Control the variations of helium temperature by conventional heating or cooling equipment. Such as adopt air condition to accommodate the temperature of it. It seems to be an easy and direct way, but we must pay the cost of too much energy consumed. In addition, it is unable to achieve rapid, effective and reliable to reduce inner helium overpressure.

2) The second tool to control the variations of helium pressure is normal pressurizing equipments, including booster fan, pressure increasing valve, relief valve unit, dry ice increase pressure and wind increase pressure, etc. Currently, booster fan and relief valve unit are the most common equipments used on low altitude airship, but for a stratospheric airship, due to its lager volume, the flow variation in discharge is lager also, so we should choose the multistage fan.

3) Adoption of active or passive thermal protection measures is a new way to control pressure variations. It mitigates internal gas temperature change by controlling the heat transfer process, Such as using variable emissivity materials covering the surface of airship. But these method dependents heavily on the development of new materials.

4) Using new design scheme is another way to control the inner pressure fluctuation. For example, we can adjust the pressure of airship envelop by compressing,

storing and releasing the inner helium with light weight compressor and fuel tank.

4.2 Overpressure control strategies analysis

1) Among the ascent process of stratospheric airship, there is a lot of air needed to be vented out from the ballonets. So we mainly adopts relief valve unit which can release a great deal of air by increasing its amount.

2) During the descending process of stratospheric airship, there is a lot of air needed to be breathed into the ballonets. Here we mainly adopts multilevel booster fan which can pump a great deal of air in a short time.

3) When stratospheric airship is on the state of loitering over a specific location, the pressure control strategy should change with flight scenario respectively. When the relative velocity between airship and wind is small(less than 10m/s), the change of internal helium temperature is larger. But due to the special requirements of station-keeping, we can't use the conventional methods to control its pressure by suction or exclude air from ballonets, because it will change the total weight of the airship and then change its position. So we can adopt the fourth measure discussed above. When the airship is on the state of superheat, the helium inside is compressed and storied. And when the dangerous situation becomes mitigated, the helium should be released to compensate the pressure. The other scenario is that the relative velocity between airship and wind is large(greater than 10m/s), the internal gas temperature change is not acute. At this time, we can ignore the pressure variations of inner helium or control it with the same strategy with the first scenario.

5. CONCLUSIONS

1) Limited by the airship's construction and envelop material strength, the inner pressure can change in a small range. And the minimum extreme differential pressure of a stratospheric airship is about 200Pa, while the maximum extreme differential pressure is about 1100Pa.

2) During the process of station-keeping, stratospheric airship will face rigorous overpressure environment during the daytime, especially when the speed of wind is small. The maximum change of pressure can reach to 2380Pa, which is far from the permissible limit.

3) Although there are a lot of pressure control measures, when it comes to the scenario of station-keeping, little measures can satisfy the requirements that adjusting the inner pressure without change the total weight of airship. Adopting new material or new design concept is the way to solve this problem.

6. ACKNOWLEDGEMENTS

The work is also supported by National Natural Science Foundation under Grant 11102229.

7. REFERENCES

1. Colozza, A. High-altitude, Long-endurance airships for coastal surveillance. Technical Report No. NASA/TM-2005-213427, Analex Corporation, Brook Park, Ohio, 2005.

2. Khoury,GH, Gillett,JD. Airship technology, Cambridge, Cambridge Univ Press, England,U.K,1999.

3. Burgess, CP. The required strength of airships. Memo # 263, Bureau of Aeronautics, May 1937.

4. Burgess, CP. The longitudinal strength of rigid airships. Memo # 361, Bureau of Aeronautics, July 1944.

5. Azinheira, JR, Paiva, EC, Bueno, SS. Influence of Wind Speed on Airship Dynamics. J.of Guidance, Contr.and Dynamics, 25(6), 1116–1124, 2002.

6. Xia, XL, Li, DF, Sun, CH, Ruan, LM. Transient thermal behavior of stratospheric balloons at float conditions. Advances in Space Research, 46, 1184-1190, 2010.

7. Wang, YW, Yang, CX. A comprehensive numerical model examining the thermal performance of airships. Advances in Space Research, 48,1515-1522,2011.

SUPERHEAT SIMULATION OF THE HIGH ATTITUDE SCIENTIFIC BALLOON DURING FLOATING FLIGHT

Kun Zhao, Xixiang Yang, Zhongxi Hou, Lixue Zhang, Weihua Zhang

College of Aerospace Science and Engineering, National University of Defense Technology, Changsha, Hunan, P. R. China, 410073, Email: zk198907@qq.com

Abstract

Superheat during the floating flight is one of the key thermal issues that have strong effects on the performance of the high attitude scientific balloon. In this paper, a three-dimensional numerical model based on the control volume method was developed to analyse the balloon`s steady thermal performance, taking solar radiation, infrared radiation, convection, etc. into consideration. SIMPLER algorithm was adopted to solve the control equations. This approach was able to give detailed insight into the diurnal temperature variations of the skin and the lifting gas under floating conditions. The proposed models were validated in comparison with the experiment on the temperature measurement made by Japan. A simulation example of high altitude scientific balloon during floating was given. The results clearly depicted temperature distribution of the skin, the lifting gas and the internal flow field.

1. INTRODUCTION

The high altitude scientific balloon, an important platform for scientific research, can carry out various experiments in the near space environment when taking special payload. Consequently, its wide applications have attracted increasingly more interest in recent years. As one category of aerostat, whose lift originates from buoyancy depending on lifting gas properties, the high attitude scientific balloon is strongly affected by its thermal performance. Among the thermal problems that need investigating, superheat has heavy effects on the floating flight.

Superheat usually arises during its float. On account of the intense solar radiation and the low convective heat transfer coefficient [1], the temperature of the lifting gas as well as the skin's will increase dramatically, which may cause the temperature distribution with a large gradient. For the high attitude balloon, superheat is one of the most serious problems, which deteriorates the balloon's capability. More precisely, superheat results in the expansion of the inner gas and change the buoyancy so that the float altitude and the attitude will vary with time. What is worse, it can cause the flexible structure to deform, and may even cause the burst of the skin [2]. Therefore, it is of significance to explore this phenomenon by the numerical method.

In the past decades, a number of investigations have been conducted in the thermal performance of high attitude balloons, including superheat. Stefan [3] researched on the heat transfer of hot air balloons. Lew and Grant [4] discussed an approach for controlling the lifting gas temperature of a transparent balloon in order to extend the flight duration. The "black ball" model was adopted to calculate the IR flux of CO_2 and H_2O in the ambient air. Farley [5] developed a software to predict the trajectory of high altitude balloons by considering the thermal behaviour. Cathey Jr. [6-8]reported the evolution of the NASA Ultra Long Duration Balloon (ULDB) and a series of experiment results, which include its temperature change. Xia et al. [9] numerically studied the transient thermal behaviour of stratospheric balloons under floating conditions and gave the temperature distribution.

The foregoing research mainly focused on the modelling of general thermal performance. However, less has been given to specialty of superheat and its effects on the inner flow field of the balloon. In this paper, a three-dimensional numerical model based on the control volume method was developed to analyse the balloon`s steady thermal performance, taking solar radiation, infrared radiation, convection, etc. into consideration. This model can clearly depicts the temperature distribution of the balloon skin as well as the lifting gas (helium). Further, the effects on internal flow field of the balloon were discussed as well.

2. THERMAL AND FLUID GOVERNING EQUATIONS

2.1. Atmosphere models

The conditions of atmosphere, i.e. its density, temperature, pressure, etc., have significant effects on the performance of high attitude balloons. Therefore it is of great importance to adopt appropriate atmosphere models. In this article the US standard atmosphere [10] was used, whose parameters simply depend on the altitude.

2.2. Thermal governing equations

Scientific balloons working at the high attitude are exposed to a relatively complicated thermal environment. In this research it is assumed to be a sunny day with no clouds, the balloon is a zero-pressure one with spherical shape (maximum radius is equal to 15 metres [11]) and the inner lifting gas is helium, the thermal environment of a high attitude balloon is illustrated in Fig. 1. The external factors, which interact

Proc. '21st ESA Symposium European Rocket & Balloon Programmes and Related Research', 9–13 June 2013, Thun, Switzerland (ESA SP-721, October 2013)

on the skin and the exterior environment, consist of solar radiation (direct, diffuse and albedo), infrared radiation (from the earth, atmosphere, and between the skin and itself) and convection (both the forced and the natural convection). The internal thermal factor, which interacts on the lifting gas and the inner surface of skin, is convection (only the natural).

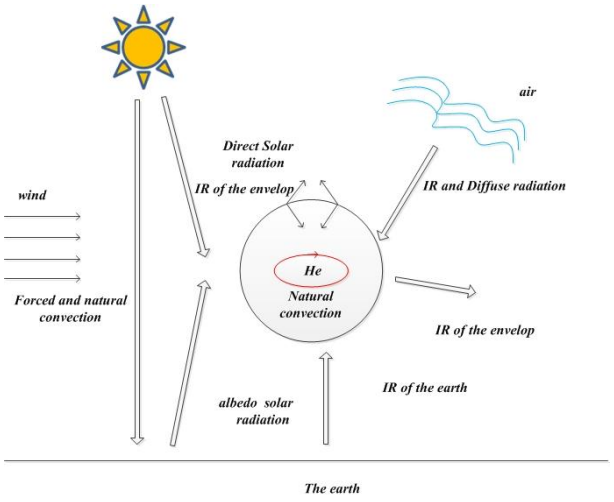

Figure 1. Thermal environment of a high attitude balloon.

Because the supposed thermal environment varies slowly with the time, accordingly each state can be approximately treated to be thermally balanced. In other words, steady calculation can be used to do analysis. Though transient analysis is thought to be more reasonable, it is considerably difficult to find accurate initial values of the balloon such as the temperature, the flow velocity, etc., which will affect the calculation result. As a consequence, it is more advantageous to use steady calculation for a fixed time because steady analysis theoretically has nothing to do with initialised values if it is convergent.

The skin of the balloon can be divided into N rectangular elements as small planes. With these assumptions, the thermal balance equation on one small element can be obtained based on the conservation of energy, i.e.

$$Q_{s,i} + Q_{IR,i} + Q_{c,i} + Q_{con,i} = 0 \qquad (1)$$

where $Q_{s,i}$, $Q_{IR,i}$, $Q_{c,i}$ and $Q_{con,i}$ are the heat that element i absorbs from solar radiation, infrared radiation, conduction with the adjacent elements and convection.

2.3. Fluid governing equations

As the natural convection exists in both the internal and the external flow field of the balloon, the slight alteration of the density cannot be ignored despite that they are low speed flow. Since the temperature changes may be not small (tens of degrees Kelvin), the Boussinesq model [12], which is widely used in the natural convection approximation, is not reliable in the simulation of internal flow. Hereinafter, the lifting gas, helium, was treated as the ideal gas, which linked parameters of the pressure, density and temperature as:

$$p_{he} = \rho_{he} R_{he} T_{he} \qquad (2)$$

R_{he} is the helium gas constant, which is equal to $2077 J/(kg \cdot K)$. Then, the governing equations for the mass, momentum and energy can be simplified as follows:

Mass: $$\nabla \rho_{he} \boldsymbol{u}_{he} = 0 \qquad (3)$$

Momentum: $$\boldsymbol{u}_{he} \cdot \nabla \boldsymbol{u}_{he} = -\frac{1}{\rho_{he}} p_{he} \qquad (4)$$

Energy:

$$\boldsymbol{u}_{he} \cdot \nabla (C_v T_{he} + \frac{u_{he}^2}{2}) = -\frac{1}{\rho_{he}} \nabla \cdot (p_{he} \boldsymbol{u}_{he}) + q_{he} \qquad (5)$$

$\boldsymbol{u}$ represents the velocity of helium; C_v is the specific heat at constant volume, i.e. $3115 J/(kg \cdot K)$; q_{he} depicts the source energy, which originates from the natural convection with the skin.

3. THERMAL MODELS

3.1. Solar radiation models

Solar radiation, a sort of important heat flux that the balloon absorbs, can be classified into 3 parts: the direct radiation, the diffuse radiation and the albedo radiation. A good methodology can be used to calculate their values [13-15].

The solar direct radiation flux I_d that is normal to the plane can be expressed as

$$I_{direct} = I_0 d_m^2 \tau_{atm}^n \qquad (6)$$

where $I_0 = 1353 W/m^2$ [14].In Eq. (6), the Sun-Earth distance correction, along with the extinction of the solar radiation through the atmosphere is considered. τ_a, the atmospheric transmittance, generally is defined as 0.6 to 0.7. d_m and n can be calculated by

$$d_m = 1.000110 + 0.03422\cos(\gamma) + 0.001280\sin(\gamma) + 0.000719\cos(2\gamma) + 0.000077\sin(2\gamma) \quad (7)$$

$$n = \frac{1}{\cos(\beta) + 0.1500(93.885 - \beta)^{-1.253}} \frac{P_{atm}}{101325} \quad (8)$$

where γ and β are the solar day angle and the zenith angle. φ is the local latitude and ξ is the solar declination angle. As the solar hour angle, ω can be expressed as

$$\omega = \frac{\pi}{12}(t - 12) \quad (9)$$

The diffuse radiation flux can be evaluated with

$$I_{diffuse} = \frac{I_0 {\tau_{atm}}^n (1 - {\tau_{atm}}^n)}{2(1 - 1.4\ln \tau_{atm})} \quad (10)$$

The albedo radiation flux is given by

$$I_{albedo} = \chi I_{direct} \quad (11)$$

where χ can be approximately adopted as 0.18 for clear sky and 0.57 for overcast sky [15].

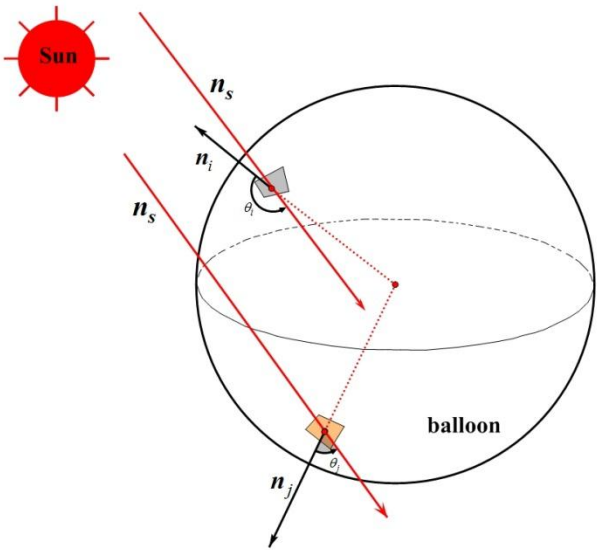

Figure 2. Included angle between the solar radiation direction and unit normal vector of the element

Because the heat absorbed from the sun in an element is corresponding to the angle between the normal vector and the sunlight direction, the solar heat need calculating in a special way. The element that stays in the shadow of other elements will not absorb the sunshine directly, which should be considered. As is depicted in Fig. 2, the direction of the solar radiation ($\boldsymbol{n_s}$, $|\boldsymbol{n_s}|$=1) has an included angle (θ_i) with the unit normal vector of the i th element ($\boldsymbol{n_i}$, $|\boldsymbol{n_i}|$=1), which can be the criteria for judging whether the element is covered. When $0 \le \theta_i \le \frac{\pi}{2}$, the element i is in the shadow of others, those elements whose $\frac{\pi}{2} < \theta_i \le \pi$ can see the sunshine. Therefore, a function λ is defined as

$$\lambda(\boldsymbol{n_s}, \boldsymbol{n_i}) = \frac{|\boldsymbol{n_s} \cdot \boldsymbol{n_i}| - \boldsymbol{n_s} \cdot \boldsymbol{n_i}}{2|\boldsymbol{n_s} \cdot \boldsymbol{n_i}|} \quad (12)$$

$\boldsymbol{n_s}$ can be obtained by [16]

$$\boldsymbol{n_s} = -\cos\beta \cdot \cos\psi \cdot \boldsymbol{i} - \cos\beta \cdot \sin\psi \cdot \boldsymbol{j} - \sin\beta \cdot \boldsymbol{k} \quad (13)$$

ψ, the solar azimuth angle, is defined as

$$\psi = \arccos \frac{\sin\beta \cdot \sin\phi - \sin\delta}{\cos\beta \cdot \cos\varphi} \quad (14)$$

Therefore, when $0 \le \theta_i \le \frac{\pi}{2}$, λ is equal to 0; $\frac{\pi}{2} < \theta_i \le \pi$, $\lambda(\boldsymbol{n_s}, \boldsymbol{n_i})$ is 1. Then the heat from direct solar radiation that element i absorbed can be expressed by

$$Q_{direct,i} = \lambda(\boldsymbol{n_s}, \boldsymbol{n_i})|\boldsymbol{n_s} \cdot \boldsymbol{n_i}| \alpha_s A_i I_{direct} \quad (15)$$

where α_s is the solar absorptivity of the skin material, A_i is the area of the element i.

Likewise, the heat from albedo can be obtained by

$$Q_{albedo,i} = \lambda(\boldsymbol{n_g}, \boldsymbol{n_i})|\boldsymbol{n_g} \cdot \boldsymbol{n_i}| \alpha_s A_i I_{albedo} \quad (16)$$

$\boldsymbol{n_g}$ is the direction vector of the ground radiation, including the albedo solar radiation and infrared radiation. If the ground is assumed to be an infinite plain, its radiation direction is vertical to the plain, pointing upward. The diffuse solar radiation comes from the atmosphere that the balloon was immersed in, so every element can see the radiation. Accordingly, it can be given by

$$Q_{diffuse,i} = \alpha_s A_i I_{diffuse} \quad (17)$$

Hence, the total solar radiation element absorbed is

$$Q_{s,i} = Q_{direct,i} + Q_{albedo,i} + Q_{diffuse,i} \quad (18)$$

3.2. Infrared radiation models

As is discussed hereinbefore, the infrared radiation of the skin element consist of four parts, i.e. $Q_{IRground,i}$, $Q_{IRair,i}$, $Q_{IRskin,i}$ and $Q_{IRout,i}$.

$Q_{IRground,i}$ is the heat from the infrared radiation of the ground. Similar with solar radiation, the amount of the

infrared radiation absorbed by the element i partially depends on the included angle between the normal vector of element i and the infrared radiation direction, Which has been discussed above. Consequently, $Q_{IRground,i}$ can be calculated by [5].

$$Q_{IRground,i} = \lambda(\mathbf{n}_g, \mathbf{n_i}) \left| \mathbf{n}_g \cdot \mathbf{n_i} \right| \alpha_{ir} A_i I_{earth} \tag{19}$$

As for the radiation flux from the ground ($I_{IRground}$), it is obtained by

$$I_{IRground} = \tau_{ir,atm} \varepsilon_{ground} \sigma T_{ground}^{\ 4} \tag{20}$$

As the standard atmosphere model is adopted, T_{ground} is equals to 288.15K. ε_{ground} is the ground emissivity. For average ground, it is equal to 0.95 [5]. $\tau_{ir,atm}$ is the infrared radiation transmissivity of air, which can be expressed by

$$\tau_{ir,atm} = 1.716 - 0.5 \cdot (e^{-0.65\frac{P_{air}}{P_0}} + e^{-0.95\frac{P_{air}}{P_0}}) \tag{21}$$

P_{air} and P_0 are the pressure of the corresponding altitude and that of the ground surface.

$Q_{ir,air}$ is the infrared radiation heat from the ambient air. Here the "blackball" model can be used to define its value [15, 17]. Specifically, the sky is assumed to be a black ball with a certain temperature at a certain altitude. Therefore,

$$Q_{IRair} = \varepsilon_{skin} A_i \sigma T_{bb}^{\ 4} \tag{22}$$

where T_{bb} is the temperature of the blackball, which is calculated by

$$T_{bb} = 0.052 T_{atm}^{\ 1.5} \tag{23}$$

$Q_{IRskin,i}$ and $Q_{IRout,i}$ are tow corresponding parts. More precisely, Q_{IRskin} is the infrared radiation absorbed by the skin and originating from Q_{IRout} that the skin itself generates. The skin element can be assumed to be a grey body and both the inner and the outer surfaces will emit infrared rays, which can be expressed as

$$Q_{IRout,i} = 2\sigma\varepsilon_{skin} A_i T_i^4 \tag{24}$$

$Q_{IRskin,i}$ is proportional to the infrared radiation of the inner surface, i.e. $\frac{1}{2}\zeta Q_{IRskin,i}$. ζ is the proportion coefficient, which is subject to the sunlight reflectivity, transmissivity, etc. of the skin. Therefore, its accurate value will be difficult to obtain. However, as the skin transmissivity has been assumed to be zero, the coefficient can be simply written as $\sum r^n, n \to \infty$ [5], where r is equal to $1-\alpha_{sun}$. The sum of the item number goes to infinity, and it is unable to be calculated. Nonetheless, because the absolute value of r is less than 1, according to Taylor series theory, which is

$$\sum_{n=0}^{\infty} x^n = \frac{1}{1-x},\ if\ |x|<1 \tag{25}$$

ζ is equal to $\frac{1}{1-r}$. Thus, $Q_{IR,skin}$ can be expressed as

$$Q_{IRskin,i} = \frac{1}{2(1-r)} Q_{IRout,i} \tag{26}$$

So the infrared radiation that the balloon skin element i absorbed is

$$Q_{IR,i} = Q_{IRground,i} + Q_{IRair,i} - Q_{IRout,i} + Q_{IRskin,i} \tag{27}$$

3.3. Conduction

Heat conduction between the adjacent elements is crucial to the skin as it is an important way to balance the temperature difference. For the control volume method and the grid system, the information on temperature is stored in the centre of the grid volume. Therefore, the conduction heat of element i from the adjacent elements can be expressed as

$$Q_{con,i} = \sum_{j=1}^{n} k\delta l_j \frac{t_i - t_j}{d_j} \tag{28}$$

where δ represents the thickness of element i; l_j is the length of the edge shared with other element; d_j is the distance between two centres.

3.4. Convection

The heat of the balloon from convection involves transfers between the ambient air and the exterior skin, along with the lifting gas with the interior skin. Further, the external convection incudes two parts: free convection and forced convection, which can be written by

$$\begin{cases} Q_{EXfree,i} = H_{free,i} A_i (T_a - T_i) \\ Q_{EXforced,i} = H_{forced,i} A_i (T_a - T_i) \end{cases} \tag{29}$$

where $H_{free,i}$ and $H_{forced,i}$ can be calculated[5] by

$$\begin{cases} H_{free,i} = \frac{k_{air}}{2R}(2 + 0.41 \cdot Re^{0.55}) \\ H_{forced,i} = \frac{Nu \cdot k_{air}}{2R} \end{cases} \tag{30}$$

The convection between the lifting gas and the interior skin is natural convection. The heat amount can be obtained by

$$Q_{INfree,i} = H_{INfree,i} A_i (T_{He} - T_i) \tag{31}$$

T_{He} is the temperature of the helium that adjacent to the skin of the balloon. To get the free convection heat transfer coefficient $H_{INfree,i}$, k_{He} (thermal conductivity), μ_{He} and(dynamic viscosity) Pr_{He} (Prandtl number) of Helium gas needs to be calculated by [5]

$$\begin{cases} k_{He} = 0.144 * \left(\dfrac{T_{He}}{273.15} \right)^{0.7} \\ \mathrm{Pr}_{He} = 0.729 - 1.6 * 10^{-4} * T_{He} \\ \mu_{He} = 1.895 * 10^{-5} * \left(\dfrac{T_{He}}{273.15} \right)^{0.647} \end{cases} \tag{32}$$

Then the coefficient is[18]

$$H_{INfree,i} = 0.13 * k_{He} * \left(\frac{\rho_{He}^2 * g * |T_i - T_{He}| * \mathrm{Pr}_{He}}{T_{He} * \mu_{He}^2} \right)^{\frac{1}{3}} \tag{33}$$

$Q_{con,i}$ can be obtained by:

$$Q_{con,i} = Q_{EXfree,i} + Q_{EXforced,i} + Q_{INfree,i} \tag{34}$$

4. Validation

To evaluate the accuracy of the present models, a ground experiment data of a 35m long airship, made by National Aerospace Laboratory of Japan [1], was used. In this study the effects of photovoltaic arrays was ignored. The solar absurdity is 0.33 and the IR emissivity is 0.88 [19]. The experiment data and simulation result is shown in Fig. 3.

It can be seen from Fig. 3 that though discrepancy exists between experimental data and the simulation results, the trend is in good agreement with the experiment. Considering the influence of materials, environment, etc., these models are acceptable and can be used to do the analysis.

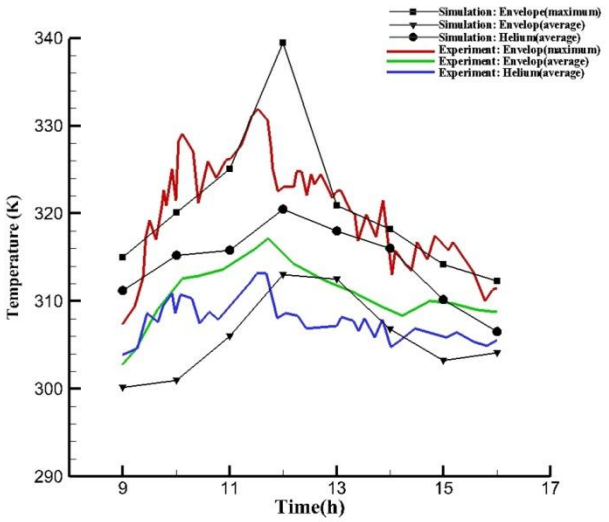

Figure 3 Comparison of models with experiment data

5. RESULTS AND DISCUSSIONS

5.1. Initial conditions

In order to simulate the temperature distribution of the balloon, a three dimension model needs to be established. A case had been performed (*Figure 4*) with 241,839 grids.

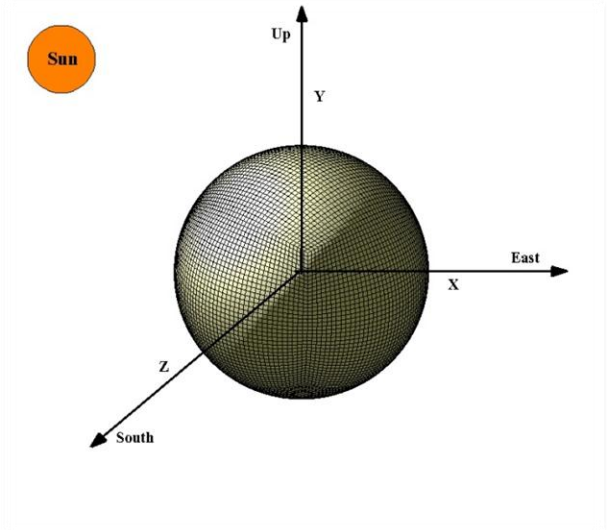

Figure 4 Hexahedral Mesh and the coordinate of 15m radius balloon

For calculation, it is extremely important to select the material radiation properties, which will significantly affect the thermal performance as well as others of the balloon. In this study the PVF membrane was adopted due to the excellent physical and chemical properties. The radiation index is showed in Tab. 1 [20, 21].

Table 1 Radiation properties of PVF

Solar absorptivity	IR emissivity	Thermal conductivity
0.3~0.35	0.8~0.88	0.18~0.45 W/(m·K)

In this article, α_{sun}, ε_{en} were assumed to be 0.3 and 0.86 respectively. Thermal conductivity and specific heat were $0.2\,W/(m\cdot K)$ and $1506\,J/(Kg\cdot K)$ [22]. According to the Kirchhoff's law of radiation heat transfer, the IR absorptivity was assumed to be equal to IR emissivity, i.e. $\alpha_{ir}=\varepsilon_{en}=0.86$. In addition, the density of the skin material was needed as well, which was $1580\,kg/m^3$ [22]. The lifting gas is helium, the test time and date were assumed to be June 21, 2012. The location (longitude and latitude) was in some area of Beijing ($N40^0$ $E116^0$). This balloon`s floating altitude was 20 km and the wind speed was assumed to be $25m/s$ [23]. As for the sphere, the maximum radius was 15 m and the thickness of the skin was 0.2mm. So the mass of the skin could be calculated by $4\pi R\delta\rho_{en}$, i.e. 893.5 kg. Meanwhile the mass of the helium was 136.84 kg. According to Archimedes' Law, it could be obtained that the payload was equal to 226.6 kg. However, the thermal effects from the payload were not discussed here. For the turbulent model of helium, realizable $k-\varepsilon$ model was used and the full buoyancy effects were taken into consideration. The Semi-Implicit Method aiming at the Pressure-Linked Equations (SIMPLER) algorithm was adopted to solve the control equations. ANSYS FLUENT was used as the sover.

5.2. Temperature alterations

Fig. 5 and Fig. 6 illustrate the temperature variation of the skin and helium, including the maximum, minimum and average. It is manifest that the temperature, both the skin's and the helium's, peaked at noon and has big difference between day and night. This is mainly because the solar radiation varies within a day and has great effects on the temperature of the balloon, especially on the temperature distribution, which will be discussed later. Considering the temperature of the external environment is only 216.65 K, the peak temperature difference could be approximately 100K, which arose on the skin. This picture can illustrate the superheat.

The maximum of the helium`s is smaller than that of the helium because the heat that the skin absorbed was from the convection between the skin and helium and therefore its peak temperature cannot be higher than the skin's. While the bottom temperature of the skin is lower than the helium`s. Meanwhile, temperature difference of the skin is much smaller than helium`s because there is natural convection in helium besides conduction, which contributes to the balance the temperature. As is shown in Fig. 6, the average temperature of the skin is inferior to the helium`s. This can be attributed to the difference of fluid and solid as well, namely the existence of convection.

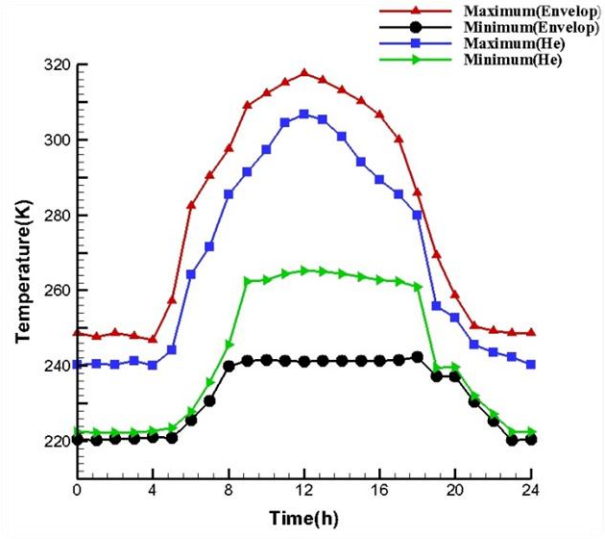

Figure 5 Maximum and minimum temperature of the skin and helium

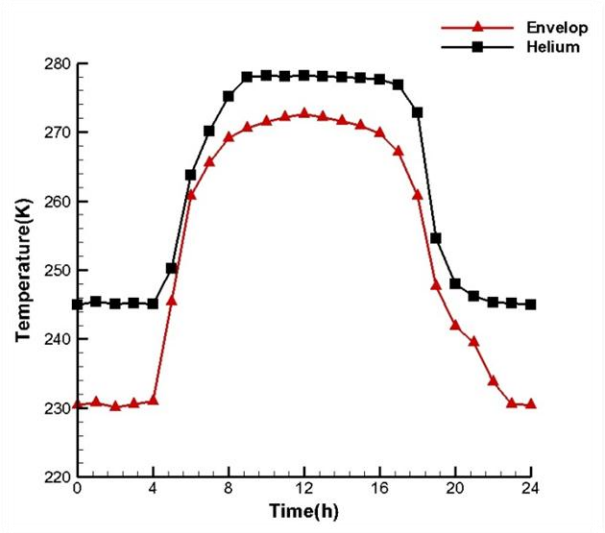

Figure 6 Average temperature of the skin and helium

5.3. Temperature distribution

Fig. 7 gives the temperature distribution of the balloon skin at different time: (a) 09:00, (b) 12:00 and (c) 01:00. The high temperature region moved with the time. At 09:00 and 12:00, those parts that faced the sun had high temperature. In the morning, the sun rose from the southeast. Therefore, the temperature of this corresponding part would notably increase. Likewise, as

the sun moved slowly, the high temperature region moved with the sun. At midnight, because there was no solar radiation, the top of the balloon skin lost its high temperature and the bottom became the high temperature region for the infrared radiation from the earth, which therefore became the prior factor that affected the temperature during night. Apparently, the temperature distribution had great difference among different times, especially between day and night.

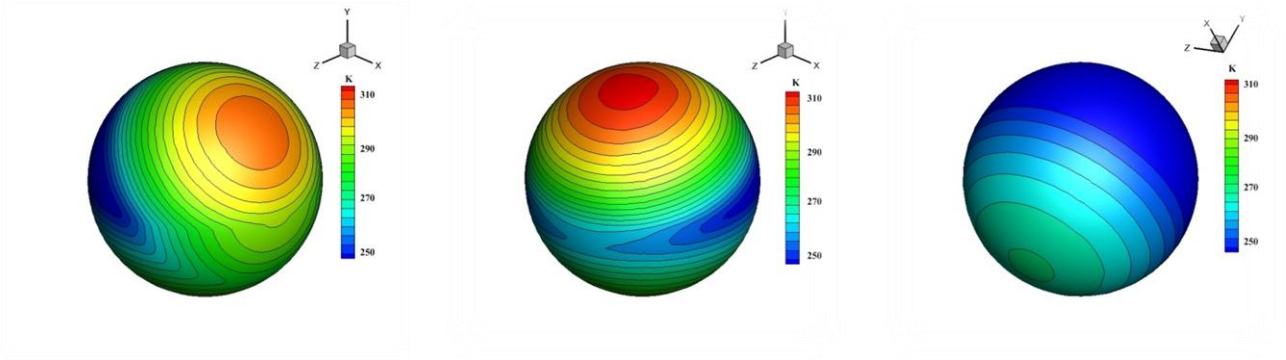

(a) 09:00 (b) 12:00 (c) 01:00

Figure 7 Temperature distribution of the balloon skin

5.4. Inside natural convection

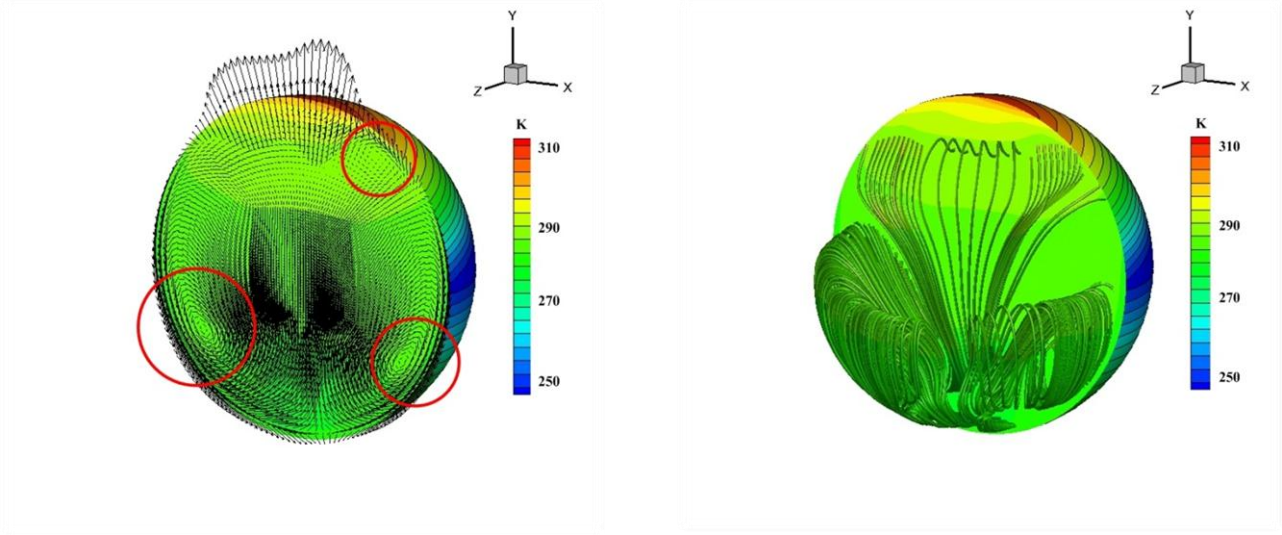

(a) *(b)*

Figure 8 Internal field of the balloon

Fig. 8 shows the internal field of the balloon at 12:00, in which there exists obvious natural convection. When the temperature of the balloon skin increased, the heat would be transferred to helium. Therefore, the density of this part would decline. Because of the gravity, this light part would ascend. At 12:00, the top of the balloon got more solar radiation, so the helium close to this skin part would ascend, which is clearly depicted in Fig. 8(a) by velocity vectors. When this helium hit the skin, its velocity would change the direction and finally, the natural convection arose.

There are many vortex structures in the inner gas. In Fig. 8(a), the velocity vectors in the regions with red circles have apparent vortex structures. The streamtraces with volume rod in Fig. 8(b) showed these vortex structures as well. Some small structures could not be clearly showed from the vector photo. But the clues of their existence can be found from the velocity direction showed by the vectors. The natural convection, especially these vortex structures, can contribute to balance the temperature difference of the balloon in the skin as well as the inner gas, which hence, should be strengthened. However, the complex internal flow field may cause the instability of the balloon`s attitude and a

few other problems, which will be investigated in the future research.

6. Conclusion

In this study, a numerical steady model was developed to investigate the thermal and fluid characteristics on the skin and internal lifting gas. This model took all thermal factors into account that would affect the high attitude scientific balloon and was validated by the experiment data from Japan. To research on the superheat phenomena of the balloon, a detailed simulation was carried out at different time during an entire day. Several conclusions were drawn here:

(1) The peak temperature difference between the ambient atmosphere and the balloon happened during daytime, which could be as high as around $100\,K$. So superheat mostly happened in daytime. Meanwhile, the average temperature of helium was higher than that of the skin`s.

(2) There existed a large gradient in the temperature distribution of the skin. The region with high temperature directly faced the sun and moved slowly with the time because of the solar position change. At midnight, the balloon`s high temperature region arose at the bottom of the balloon because the main factor that affected the balloon became the infrared radiation from the earth.

(3) Due to the existence of the density gradient and gravity, natural convection was inside the balloon. The natural convection would cause vortex structures with different scales. These vortex structures could help to balance the temperature difference of the balloon, but might cause other problems like attitude control.

Our future research would focus on the effects of the internal fluid field, especially about its effects on the altitude and attitude of the balloon.

Acknowledgements

This work is supported by the Science Research Foundation of NUDT under the Grant No. JC12-01-05.

References

1.Kenya H, Kunihisa E, Masaaki S, Shuichi S: Experimental Study of Thermal Modeling for Stratospheric Platform Airship. In: *AIAA*. Denver, Colorado; 2003.
2.Li X, Fang X, Dai Q, Zhou Z: Modeling and analysis of floating performances of stratospheric semi-rigid airships. *Adv Space Res* 2012, 50(7):881-890.
3.Stefan K: Performance Theory for Hot Air Balloons. In. Edited by *AIAA*, vol. 77-1183; 1977.
4.Lew T, Grant D: Gas Temperature Control for Long Duration Balloons. In: *AIAA*. vol. 1994-0745; 1994.
5.Farley RE: BalloonAscent: 3-D simulation tool for the ascent and float of high-altitude balloons. In: *AIAA*. vol. 2005-7412; 2005.
6.Cathey Jr HM: Evolution of the NASA Ultra Long Duration Balloon. In: *AIAA*. vol. 2007-2615; 2007.
7.Cathey Jr HM: Development overview of the revised NASA ULDB. *Adv Space Res* 2008, 42:1624-1632.
8.Cathey Jr HM: The NASA super pressure balloon – A path to flight. *Adv Space Res* 2009, 44:23-38.
9.Xia XL, Li DF, Sun C, Ruan LM: Transient thermal behavior of stratospheric balloons at float conditions. *Adv Space Res* 2010, 46:1184-1190.
10.U.S. Standard Atmosphere. In. Washington, DC: U.S. Government Printing Office; 1976.
11.Cathey Jr HM, Pierce DL: Duration Flight of the NASA Super Pressure Balloon. In: *AIAA*. vol. 2009-2808. Seattle, Washington; 2009.
12.Yang S, Tao W: Heat Transfer, 4 edn. Bejing: *Higher Education Press*; 2006.
13.Colozza A: Initial Feasibility Assessment of a High Altitude Long Endurance Airship: *NASA CR-21272*; 2003.
14.Ran H, Thomas R, Mavris D: Comprehensive Global Model of Broadband Direct Solar Radiation for Solar Cell Simulation. In: *AIAA*. vol. 2007-33; 2007.
15.Shi H, Song B, Yao Q, Cao X: Thermal Performance of Stratospheric Airships During Ascent and Descent. *J Thermophys Heat Tr* 2009, 23(4):816-821.
16.American Society of Heating RaA-CE: *ASHRAE Handbook: 2001 Fundamentals*. Atlanta; 2001.
17.Carlson LA, Horn WH: A new thermal and trajectory model for high altitude balloons. In: *AIAA*. vol. 81-1926; 1981.
18.Morris AL: Scientific Ballooning Handbook: *NCAR, Boulder*; 1975.
19.Stefan K: Thermal effects on a high altitude airship. In: *AIAA*. vol. 83-1984; 1983.
20.Terao T, Bando Y, Mitome M, Zhi C, Tang C, Golberg D: Thermal conductivity improvement of polymer films by catechin-modified boron nitride nanotubes. *Journal of Physical Chemistry C* 2009, 113(31):13605-13609.
21.Liu DX, Yang YX, Lv MY, W Z: Effect of envelop thermal radiative properties on the stratospheric super-pressure LTA vehicle helium temperature. *Journal of Beijing University of Aeronautics and Astronautics* 2010, 36(7):836-840.
22.Li XJ, Fang XD, Dai QM: Research on Thermal Characteristics of Photovoltaic Array of Stratospheric Airship. *J Aircraft* 2011, 48(4):1380-1386.
23.Selby CR: High attitude airship station keeping and launch model development using output from numerical weather prediction models. *West Lafayette*, : Purdue University; 2008.

NOSYCA: A NEW STANDARD FOR BALLOON OPERATIONS, FLIGHT PROVEN 2013

Tony MOULE[(1)], Jacques MONGIS[(2)], Patrice DEZEN[(3)], Christophe CHATAIN[(4)]

[(1)] Balloon Product Manager at ELTA, 26 rue des Cosmonautes, 31400 Toulouse FRANCE, Email: anthony.moule@areva.com Phone: +33 (0)5 67 04 85 22

[(2)] CNES NOSYCA System Project Manager, Centre Spatial de Toulouse 18 Av. Ed. BELIN 31401 Toulouse cedex 9 FRANCE, Email: jacques.mongis@cnes.fr

[(3)] Balloon Systems and Terminals Product Line Manager at ELTA, 26 rue des Cosmonautes, 31400 Toulouse FRANCE, Email: patrice.dezen@areva.com

[(4)] Space Sales Engineer at ELTA, 26 rue des Cosmonautes, 31400 Toulouse FRANCE, Email: christophe.chatain@areva.com

ABSTRACT

The year 2013 marks the end of the NOSYCA system's rigorous validation and qualification phases and its first qualifying flights.
This paper recapitulates the objectives and the features of the NOSYCA system.
NOSYCA (New Operational SYstem for the Control of Aerostats) is the project started by the French Space Agency (CNES) in 2007 to provide scientists with a reliable and fail safe reusable stratospheric balloon platform.
The NOSYCA system is designed from start to end according to fail safe principles - from the ground operator to the on-board actuators. The safety requirements of the French Space Agency will be discussed and we will explain how they have been met.
The fail safe design approach will be described as well as the qualification campaigns that validated both the ground and the flight hardware and software. We will summarize the software design to ECSS-B levels with test coverage of 100% and V&V (Verification and validation) cycle applied to the project.
The NOSYCA flight equipment and Ground Control Centre provide all operational command control requirements for flying stratospheric balloons from winter polar to equatorial summer conditions for flight durations of up to 72 hours. We will describe the architecture of the NOSYCA system that achieves this.
The system incorporates both operational and scientist communications requirements (2Mbps downlink, 100kbps uplink on S Band) as well as back up communications links (Iridium). The scientist on board and ground equipment provides diverse interfaces that cover all scientists' needs (Internet Protocol synchronous, asynchronous) which we will detail here.
Maintenance is an integral part of the NOSYCA system and we shall be presenting the dedicated Test Bench and preventative maintenance philosophy that ensures continued fail safe operation as well as enabling quick turn around between flights whilst minimizing preparation and maintenance costs.
The modularity of the scientist interfaces and the operational equipment will be discussed to demonstrate NOSYCA's adaptability to various scientific, operational and safety requirements.
We will outline the future developments of NOSYCA, such as ELTA studying the application of the architecture to long duration pressurized balloons with solar energy management and the addition of alternative communications links.

1. INTRODUCTION

During the noughties the CNES was led to specify a new command control system for their stratospheric balloons with the following requirements:

- Fail safe operation of flight critical functions.
- 72 hours flight from polar winter to equatorial summer.

In 2008 the CNES put out a tender for various parts of the NOSYCA system, parts of which were awarded to ELTA.
Now, in 2013, the NOSYCA system is being installed in Timmins, Ontario, for flight testing.

2. GENERAL DESCRIPTION OF THE NOSYCA SYSTEM

The NOSYCA system is composed of the following elements:

- Ground Control Centre.
- NOSYCA flight equipment.
- SCILA S Band Ground Station.
- SIREN Board and Ground scientist interfaces.
- Flight test & Maintenance equipment.

See also [1] and [2].

2.1. Communications architecture

The NOSYCA communications architecture is schematised in Figure 1.
The ground control centre is composed of two independent parts: One part is for backup and low bit

Proc. '21st ESA Symposium European Rocket & Balloon Programmes and Related Research', 9–13 June 2013, Thun, Switzerland (ESA SP-721, October 2013)

rate communications with the operational gondola via the Iridium constellation. The other part is for nominal and high bit rate communications via a line of sight RF link in the S band. The ground control centres are provided by the CNES and its subcontractors (CAP Gemini France, BT Services France …). The SCILA RF ground station (*Station de Contrôle sous Internet pour les Lancements d'Aérostats*) is provided by ELTA.

The SCILA ground station and CNES control centres are installed in standard shipping containers. This allows transporting the ground segment for a stratospheric balloon launch campaign just about anywhere in the world.
Via Internet it is possible to connect multiple SCILA ground stations to the control centre to increase the operating range of the high bit rate link. Currently, safety requirements demand that the balloon has at least two communications links with the control centre at all times. However, in the current flight models the RF compatibility issues between Inmarsat and Iridium have not been satisfactorily resolved and so the current principle is that balloon flight must be terminated before the balloon falls below the S band radio electric horizon. Integration of Inmarsat or other communications links will be part of future NOSYCA developments and this will enable balloon flights beyond the S band horizon.

The ground and board S band links respect CCITT and CCIR regulations. The board antenna was the subject of a specific development and is designed to conform to the very harsh radiation patterns imposed to keep radiation levels within the imposed limits.

The NOSYCA philosophy is to provide both operational data flows and scientist data flows over the same communications links, thus avoiding potential RF compatibility problems. The separation between operational and scientist flows is highly secured. The control centres use CNES OCTAVE software for the management of CCSDS encapsulated TMTC flows.

The scientist receives a data flow in the scientist mission centre via the SIREN (*Système d'Interface du REseau NOSYCA* or Network interface system) board and ground units. These units allow the scientist direct Internet connectivity with the payload.
In principle the scientist mission centre can be located anywhere where the NOSYCA secure network can reach.

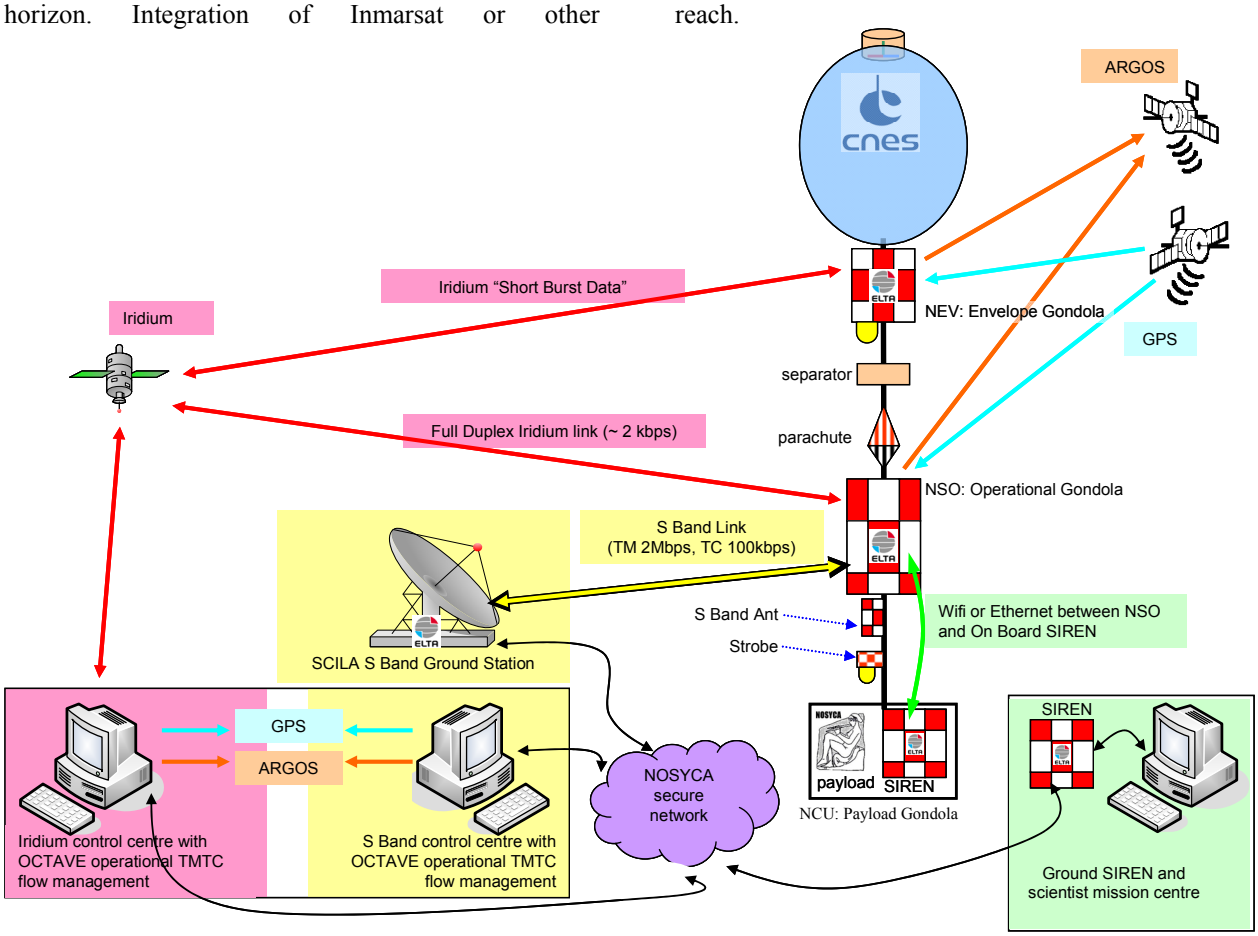

Figure 1. NOSYCA system overview

2.2. Operational gondola

The NSO, (*nacelle de servitudes opérationnelles* or "operations gondola") is comprised of two command/control modules (ITAC, ULIS) and a ballast reservoir (BAL) module. Its position in the flight train is schematised in figure 2.

The ITAC (*Interface de Télé Acquisition de Commande*) module is used for nominal operation. The ULIS (*Unité légère d'Interface Satellitaire*) module is used in case of failure on ITAC, for backup operation.
The ITAC and ULIS OBCs (on-board computers) are identical in design with identical flight software. However, their tasks differ slightly and configuration between ITAC and ULIS operation is stored in non volatile memory in each OBC. In addition, the ITAC OBC has an extra force sensor function which is not present on the ULIS OBC.

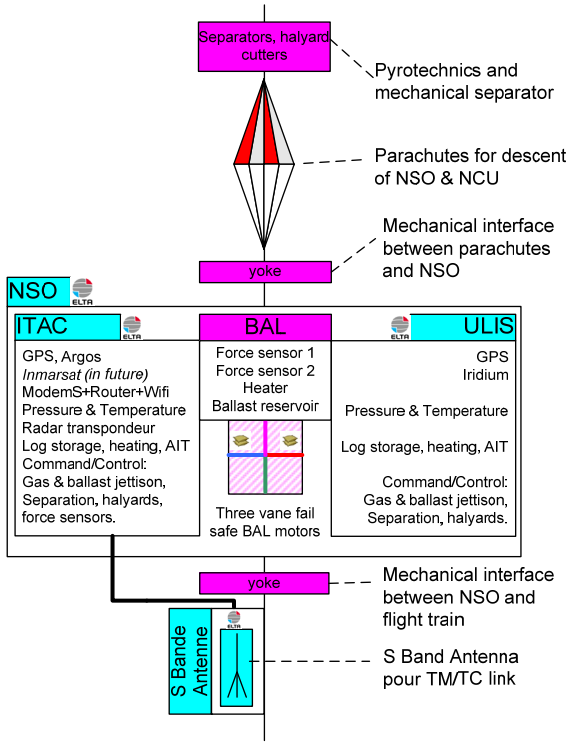

Figure 2. NOSYCA NSO: Operations gondola

The common features of the ITAC and ULIS modules are as follows:

- Telecommand (TC) and telemetry (TM) management with the physical link using CCSDS streams.
- Various voltage, current, temperature and pressure measurements which are sent by telemetry to the control centre.
- Programmable heating and fixed safety heating.
- Power distribution from main and pyro battery packs.
- Storage memory for flight logs.
- Links to Assembly, Integration and Test (AIT) benches.

The following critical functions are also common to ITAC and ULIS:

- Balloon piloting: Gas and ballast jettison with a capacity for driving fail safe (three vane) motors.
- Balloon localisation. Information from an on-board GPS receiver is sent of telemetry to the ground control centre. For diversity, it was decided use different GPS receivers between the ITAC and ULIS modules.
- Balloon separation and halyard cut-down via telecommands from the control centre.

Unique to the ITAC module are the following functions:

- Communication with the ground control centre via an RF link in the S band.
- Routing of a part of the available communications bandwidth to the scientist payload, either by Ethernet or by WiFi.
- Balloon navigation: Radar transponder. The radar transponder is activated either automatically by a pressure switch or directly by telecommand. Note: a backup radar transponder is not necessary on the ULIS module, according to system safety requirements because there is also a radar transponder on the envelope gondola.
- Force sensors, located in the BAL. The force information gives the current weight of the NSO and is relayed to the control centre via TM.
- Argos beacon. The ELTA constructed Argos Beacon (VHAL2) integrates a GPS receiver. After NSO and payload landing the Argos transmissions can be captured in real time by a portable receiver used by the recovery team.

Note: The force sensors also allow a relaxation function, whereby the ITAC OBC activates the pyrotechnics for separation in case a sudden loss of weight. The sudden loss of weight is usually attributed to a rapid descent caused by a rip in the balloon envelope.
The current flight models are equipped with this function but the CNES decided to inhibit it for the first technological flights

The ULIS module contains an Iridium modem instead of an S band modem. It has neither force sensors, nor Argos beacon nor radar transponder.

2.3. OBC flight computer

The NOSYCA flight computer, common to ITAC and ULIS, contains multiple microcontrollers for separation of critical functions. TMTC flow is managed by the MAF (*mise à feu*, Fire) microcontroller which also activates the final stages of critical functions (see fail safe chapter below). The ARM (*armement*, Arm)

microcontroller manages only TMTC involved in the pre-activation of critical functions. The BD (battery distribution board) microcontroller is responsible for segregation of power supplies and for measurements of current, voltage and temperature.
The ITAC OBC contains two additional microcontrollers, RLX-MAF and RLX-ARM for the force sensor and relaxation functions.

2.4. Envelope gondola

The NEV (Nacelle Envelope or envelope gondola), also called SIRSE (*Système Iridium de Suivi d'Enveloppe*), remains with the balloon envelope at all times, including after separation.
Its purposes are:

- To signal its presence with the radar transponder and strobe light as the balloon envelope traverses the flight corridors.
- And to follow the balloon envelope during descent to allow safe and timely recovery

Its position in the flight train is schematised in figure 3.

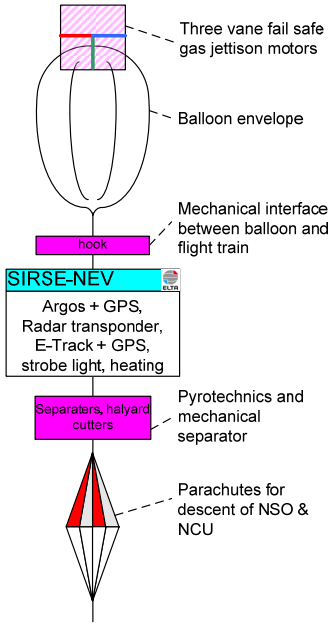

Figure 3. NOSYCA NEV: Envelope gondola

For tracking of the NEV there are two pieces of equipment on-board:

- E-Track Short burst data (SBD) Iridium modem with GPS position data in the SBD messages.
- Argos VHAL2 beacon, also with GPS position in the Argos messages.

The SBD is visible over an Internet server typically a few minutes after the board transmission. The board transmission rate is configurable and will be at a rate of between 30 seconds and 5 minutes for most NOSYCA flights. The transmission rate can be configured to automatically go from slow to fast after separation.
The Argos data is available on the Argos Internet server but two hours or more after transmission. However, portable Argos receivers can receive the signal from this beacon during the recovery of the balloon.
The strobe light and radar transponder function automatically when in flight corridors (FL660 = Flight Level 66000 feet).

2.5. Scientist connectivity

The SIREN system (*Système d'Interface du REseau NOSYCA* or Network interface system) consists of flight and ground equipment.
The SIREN flight module is located in the scientific payload (NCU, *Nacelle charge utile*). It connects to the NOSYCA network via a link to the NSO and then through the S Band link to the SCILA RF ground station.
The SIREN ground equipment is located in the scientific mission centre and is connected directly to the NOSYCA network by Ethernet.
It is schematised in figure 4 and described in more detail in chapter 6.

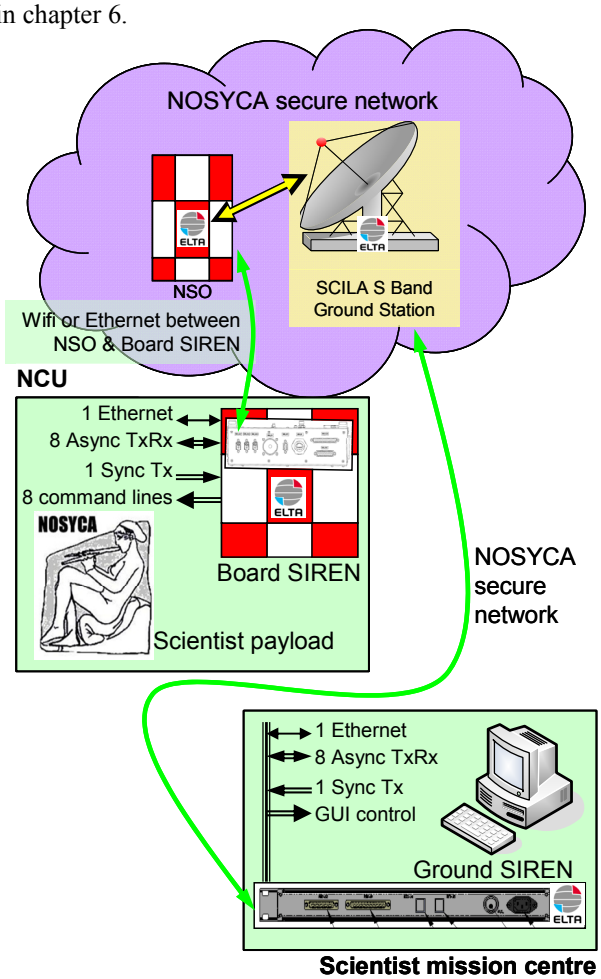

Figure 4. NOSYCA SIREN

3. FAIL SAFE PHILOSOPHY

The fail safe requirements of the CNES concern the safety of goods, persons and the environment.

The CNES identified the following functions as being critical to flight safety:

- Balloon piloting (ballast jettison and gas jettison)
- Balloon separation (pyrotechnical cut-down)
- Aeronautical navigation (Radar transponder and strobe light when in air corridors).
- Balloon localisation (latitude, longitude, altitude and speed).

The continued operation of these functions must be assured even in case of a single point failure.

Each safety critical function is allocated an allowed failure rate for each of the flight phases.

In case of the failure of one element then a redundant element must assure the continued operation of the function until safe balloon landing.

In the NOSYCA system, safety critical analysis defined two "Feared Events" to be:

- The non-execution of wanted commands (example: non executed separation)
- The execution of unwanted commands (example: unwanted separation)

In addition, safety critical design of the NOSYCA system requires that

- No single point failure should lead to a feared event.
- A single point failure should not inhibit the functioning of a safety critical function.

This last point implies a design that satisfies no failure propagation and which also incorporates redundancy.

System analysis was done by ELTA and also by CNES to ensure compliancy of the final design with system requirements. This was carried out both in the early design stages of the project and again before production of the flight models.

Early fail safe analysis identified that the safety critical functions must be made completely redundant, from ground operator to on-board actuator. An example, the balloon separation function, is schematised in figure 5: There are two completely independent paths to the mechanical separator used to terminate the balloon flight.

The first path is through an operator at the ground control centre who sends the separation orders from the main ground control centre over the S band link to the ITAC module. The ITAC module interprets the received orders and actuates the pyrotechnical bolt cutters.

The second path is through a second operator at the ground control centre who sends the separation orders from the backup ground control centre over the Iridium link to the ULIS module. The ULIS module interprets the received orders and actuates a second set of pyrotechnical bolt cutters. Note: for the first NOSYCA flights the two control centres are combined in a single container and there is a single operator.

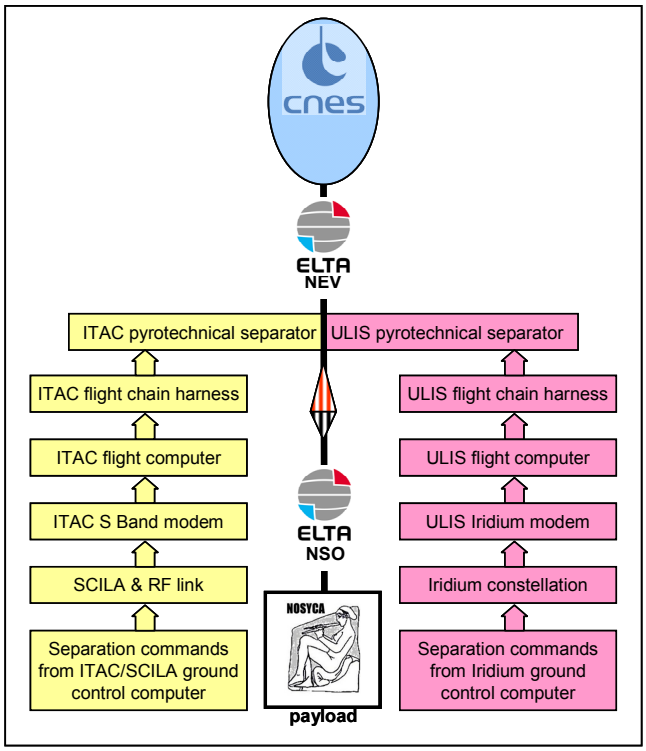

Figure5. Example of redundancy

Whilst the above redundancy scheme guards against one type of feared event, "the non-execution of wanted commands", it does not protect against the second type of feared event, "the execution of unwanted commands". To protect against the second type of feared event it is necessary to add protection barriers in each path. The example in figure 6 shows the general method used in the flight electronics:

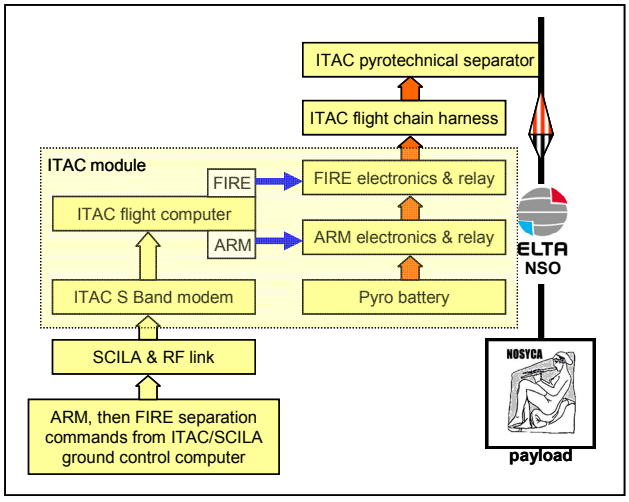

Figure 6. Example of protection barrier

A single point failure that causes the unwanted closing of

the ARM relay will not cause an unwanted firing of the pyros because the FIRE relay has not been activated. The state of the ARM and FIRE relays are sent to the control centre in a telemetry stream updated once per second. If the control centre sees that a FIRE relay or an ARM relay has been activated due to a failure, then the module (ITAC in this example) will be pacified by sending the DISARM command and the flight will be terminated at the next safe landing zone using the other module (ULIS in this example).

This kind of protection barrier is applied to the separation function, to the halyard cutting system and to the ballast and gas jettison functions.
It was deemed unnecessary to apply such protection barriers to the navigation and localisation functions for the following reasons: The localisation function is on during all phases of balloon flight; And a radar transponder that is functional above flight corridors is not catastrophic and will lead simply to more on board power consumption which will be detected at the control centre.

3.1. Ballast and gas jettison require three valves

During the early part of the design cycle it was found that a simple valve connected to ITAC and a backup valve connected ULIS would not fulfil fail safe requirements for the jettison functions. If for example, the two valves were connected in series; then a blocking "closed" on one valve would also block jettison when the other valve was opened. On the other hand, If the two valves were connected in parallel, then an unwanted opening of one or the other valves would cause unwanted jettison. Both parallel and series configurations were lacking in addressing the two feared events. The solution for NOSYCA is to use three valves, as shown in a simplified schematic in figure 7.

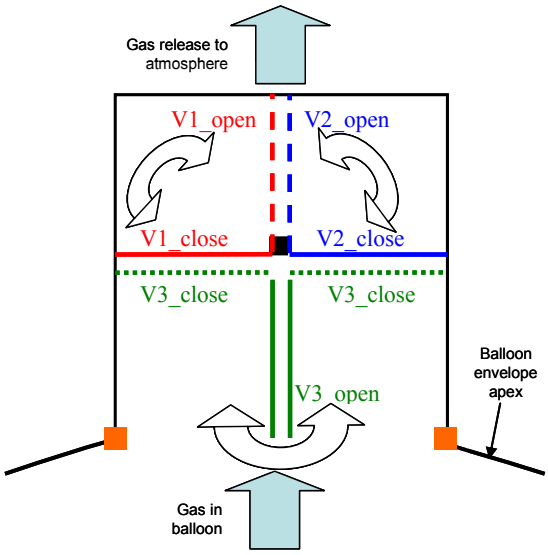

Figure 7. Three valves for gas jettison

This failsafe actuator is composed of three vanes.

- Vane V1 is opened and closed by ITAC.
- Vane V2 is opened and closed by ULIS.
- Vane V3 is opened and closed by ULIS and ITAC.

In case V1 is blocked open, then an unwanted gas flow can be stopped by actuating V3 to the closed position, either from ITAC or from ULIS.
In case V1 is blocked closed then the gas valve can be opened via V2 by ULIS.
V3 is left nominally open and is only used in case of a failure on V1 or V2. NOSYCA requires only a single failure to be taken into account. So, in case of a failure on V1 or V2 we do not need to take into consideration a failure on V3 blocking closed because we designed for single failure and no failure propagation.

The same principals apply to the ballast jettison valves.

3.2. Fail safe implementation of flight electronics

To avoid execution of unwanted commands, each actuator (Separation, Gas Valve, Ballast) of a given function has a protection barrier. This protection barrier consists of pre-activation (or arming) and activation (firing) electronics.

Before an actuator can be actuated the ground control centre must first send a pre-activation TC This is interpreted and executed by the ARM microcontroller and associated electronics.
Then the ground control centre must send an activation TC. This is interpreted and executed by the MAF microcontroller and associated electronics.

The software for the microcontrollers is to ECSS-B level.
The two microcontrollers have limited connectivity with electrical protection barriers to prevent failure propagation between these microcontrollers.
Each microcontroller chain has independent supplies.
In case of a single point failure leading to an unwanted pre-activation or an unwanted activation without prior pre-activation then this will be detected by current, voltage and relay status measurements of the OBC. This information is communicated to the control centre once per second in operational TM. If the control centre detects such anomalies then the decision can be made to pacify the module (ITAC or ULIS), switch to the other module and terminate the flight at the next safe landing zone.

CNES has performed analysis of the final design to ensure compliance.

4. RIGOROUS VERIFICATION, VALIDATION AND QUALIFICATION

To ensure that the flight models are fail safe by design, a development model was adopted. The NOSYCA flight electronics, both software and hardware, was developed according to the V Model, shown in figure 8.

- Specifications and requirements are formalised and entered into a requirements management tool. ELTA uses Telelogic DOORS.
- Design documents are entered into the same requirements management tool. Links are drawn between requirements from the specification documents and satisfactions from the design documents.
- Test plans and procedures are generated using the same requirements management tool.
- Test results are input to the requirements management tool.
- Traceability matrices are generated at milestone reviews to ensure that all requirements are satisfied.

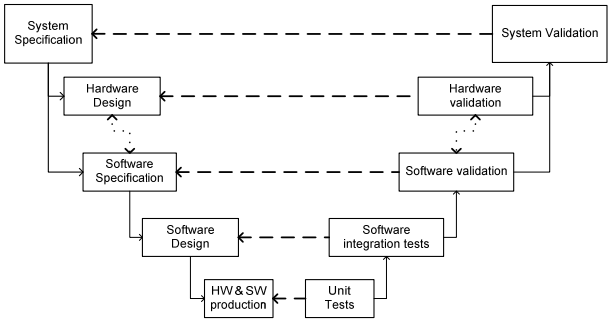

Figure 8. V Model development

The SCILA RF ground station was also developed using this model.

4.1. Software validation and qualification

Flight software in the OBC has been developed to ECSS-B (~DAL-B/C) quality level.

The development and validation of software for the MAF microcontroller was subcontracted to CS-SI according to specifications written by CNES and ELTA. The software for the remaining processors was written in-house at ELTA.

The flight software was tested and validated in flight hardware adapted for use in the software laboratory.

The flight software was then tested in a mock-up of the complete ground/board system using adapted flight hardware and ground components.

Test coverage of 100% of decisions, no dead code and analysis of scheduling were part of the software validation process [2].

4.2. COTS validation and qualification

As well as specifically developed hardware, NOSYCA flight hardware also incorporates several "custom off the shelf" (COTS) units. Examples include the radar transponder, the VHAL2 Argos Beacon, Iridium modem and the WiFi modules.

A decision was made in the early stages of the project that all COTS equipment should be environmentally tested and flight qualified before integration into flight hardware. The main reason for this is because the manufacturers' specifications of the COTS units are mostly lacking in information for low pressure and shock vibration / performance.

The CNES and ELTA, with their mechanical and thermal experts, defined the limits to which each type of unit should be subjected. The following tests are carried out on all units destined to be integrated into flight hardware:

- Random vibration in 3 axes. The vibration levels chosen are to reproduce the expected vibration that the flight hardware will undergo during gondola recovery and transport.
- Shocks to 3 axes. The shock levels chosen are to reproduce the expected shocks that the flight hardware will undergo at separation and at landing.
- Thermal and pressure cycling. The thermal profiles chosen are in respect of the COTS' datasheet because the thermal design of the gondolas takes into account the manufacturers thermal limits. However, for most of the COTS, low pressure operation does not figure in the manufacturers specifications and we do not use pressurised gondolas. So the remaining choice is to cycle the COTS at the actual pressures that it will experience during flight.

Functional tests are carried out before and after the shock and vibration tests and during the thermal and pressure cycling.

Before testing, a formal review is held between ELTA and CNES to verify the test setup and test conditions. A second formal review is held between ELTA and CNES when the test reports have been written up and results are presented.

4.3. OBC validation and qualification

Flight hardware specifically designed and manufactured by ELTA underwent similar qualification cycles to the COTS equipment.

The flight hardware concerned includes the OBC, the on board router and s band modem.

Climatic testing is carried out on ELTA's premises using standard climatic chambers and a portable vacuum chamber. Shock and vibration testing is subcontracted.

Functional tests are carried out during climatic testing and after shock and vibration testing.

The ATTENA test bench (see below) is used for the functional testing of the flight hardware and semi automatically produces test reports for each unit.

Only after such testing can the units be integrated in the flight gondolas.

4.4. SIMEON environmental test chamber

The CNES has invested in a new facility, supplied by *Intespace*, for the thermal and near vacuum qualification of stratospheric balloon hardware. The SIMEON (*Simulateur Environnement Opérationnel Nacelles*) facility is shown in figure 9. It is voluminous enough to accept a complete NSO, including its thermo-mechanical protection, or two NEV modules. It can generate temperatures as low as -110°C and pressures from ambient to lower than 1hPa.

All flight modules are thermally and pressure cycled using this facility. The temperature and pressure profiles are chosen to take the flight hardware to the extremes of temperature and pressure that it has been predicted to encounter during all phases of flight and for all types of flight for which the hardware is designed.
Thermal and pressure cycling of an NSO or a NEV module typically takes up to a week. During cycling the flight hardware is exercised and monitored at various stages using the NOSYCA test benches (ATTENA, see below). The work is typically undertaken with shift teams that keep the tests going 24 hours per day.
The verification of the thermal modelling was also carried out on NEV, NSO and SIREN modules.

Figure 9. SIMEON at CNES, Toulouse

4.5. Flight module thermal qualification

After COTS and flight hardware qualification the equipment is assembled to form complete modules (NEV, ITAC, ULIS, NSO, Board SIREN). These must in turn be flight qualified with similar qualification cycles:

- Random vibration in 3 axes.
- Shocks to 3 axes.
- Thermal and pressure cycling.

Functional testing is carried out before, during and after test phases. The ATTENA test bench is used extensively to exercise the modules under test.

Similar to the COTS qualifications, formal reviews are held before and after qualifications.
The above qualification was carried out for all modules that will fly and will be carried out for any future models that fly.

Additional testing was carried out on qualification models to validate the NOSYCA design. This included:

- Electromagnetic compatibility (with NSO connected to a dummy flight train)
- RF compatibility between all radio transmitting and receiving parts of the flight train.
- Integration tests at Aire sur l'Adour (France), including two NSO flights under a helicopter
- Thermal model verification in SIMEON.
- GPS simulator verification of the board GPS receivers.

In the spring of 2013, NOSYCA flight and ground equipment was shipped to Timmins, Ontario. The first tethered balloon flight is scheduled for June 2013.

5. MAINTENANCE AND THE ATTENA TEST BENCH – AN INTEGRAL PART OF THE FAIL SAFE DESIGN

A typical problem with systems incorporating redundancy is that the redundant parts are not always tested. The redundant part could already present a failure mode when solicited leading to possible catastrophic failure.
The NOSYCA fail safe design philosophy and the ATTENA (*ATelier pour TEsts NAcelles* ~ Gondola test workshop) test bench address this potential problem. All parts of the NOSYCA flight hardware, including redundant equipment, are tested pre-flight and post-flight. This pre-flight validation effectively "resets" the "fail-rate counters" to zero [1].
There are a few exceptions to this rule: Certain components (thermo safety switches, fuses, power diodes, baro-switches) require the disassembly of the flight hardware or require thermal and pressure testing. These exceptions have been examined in detail for reliability and the programmed maintenance interval is decided as a function of their mean time before failure (MTBF).

The ATTENA test bench connects as follows (see figure 10):

- Connection via an electrical harness that replaces the flight train to NSO (ITAC and ULIS) and to NEV.
- Provision of DC power to NSO and NEV to avoid prolonged battery discharge. It is also possible to solicit the flight batteries when connected to ATTENA.
- Connection to NSO & NEV flight train connectors providing dummy loads for pyrotechnics, gas and ballast jettison actuators, external temperature

measurements and force sensors, heating as well as return acknowledgement signals from the various captors and sensors of the flight train.

- Dedicated AIT serial link to the ULIS OBC which bypasses the Iridium link in order to avoid excessive call charges. The Iridium link is also available and tested at certain phases.

The dummy loads are configurable and programmable which enables the simulation of fault conditions as well as the testing of nominal operation of the flight hardware.
Voltage and current are made by the test bench.
Pulse measurements, current and duration, are made on the flight hardware's pyro outputs.
ATTENA contains RF equipment for an S Band connection with ITAC. RF measurements of the flight hardware are made.
The ITAC and ULIS modules' TMTC flows are linked to ATTENA via an integrated OCTAVE PC which partially reproduces the ground control centre functions.

Software and scripts running on the main ATTENA PC can intercept the operational TMTC flows from the OCTAVE PC. Scripts can control the ATTENA hardware. Scripts have been developed for the semiautomatic testing of the flight equipment. These scripts execute operational TCs, intercept the TM flow, control the ATTENA hardware and produce test reports.
The ATTENA test bench, whilst connected to the flight equipment, can hand over operational TC control to the real Ground Control Centre during pre-flight testing and checkout. Operational TM is piped both to ATTENA and optionally to the Ground Control Centre.
For production, maintenance and service ATTENA can connect to and can test in standalone mode the OBC flight computer.
ATTENA was and is used during all production and qualification phases of the current NOSYCA flight hardware.

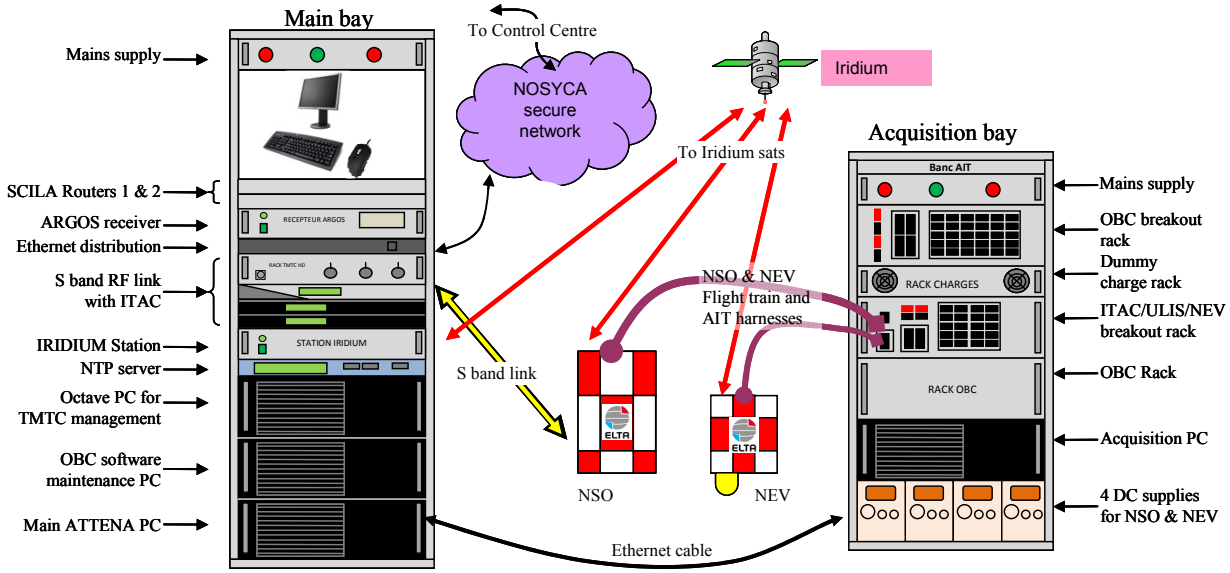

Figure 10. ATTENA connected to NSO & NEV

6. SCIENTIST GROUND AND BOARD INTERFACES

The NOSYCA SIREN system is schematised in figure 4 of chapter 2.5 above.
The SIREN board unit is modular. It can be integrated on the payload gondola as an autonomous unit, providing its own thermal protection, heating and power. The number of battery packs can be varied according to flight requirements.
Alternatively, SIREN board equipment can be integrated directly in the scientist's payload if the latter already provides thermal protection and power, thus saving weight & volume.

The SIREN system consists of the SIREN board module and a ground module contained in a 19" rack. The SIREN pair can be delivered to the scientist's laboratory for integration testing of the scientist's payload and mission centre. The SIREN pair can operated back to back with an Ethernet cable or over the NOSYCA secure network (via NSO & SCILA).
The SIREN system provides the following interfaces:

- Ethernet board and ground link to scientist's board and ground equipment.
- Eight duplex RS232 asynchronous board and ground links at programmable Baud rates.
- One RS422 synchronous TM link, up to 1Mbits per

second.
- Eight on-board command lines for switching relays on the scientist's payload. These are commanded from the scientist mission centre.
- A board GPS receiver with NMEA dialogue and 1 pulse per second output.

At the mission centre the SIREN ground unit is connected to the scientist network on one side and the NOSYCA secure network on the other side.
By connecting a web browser to the network a graphical user interface is made available for monitoring and controlling the SIREN system.

Total bandwidth available between SIREN board and SIREN ground is 1700kbps for TM and 80kbps TC

7. MODULARITY OF NOSYCA

The current NOSYCA design is modular and can be adapted to differing needs.
- Flight duration: Between one and four battery packs can be used in the ITAC and ULIS modules.
- Safety: The OBC has the capacity to accept an additional communications vector
- SIREN: The modularity of SIREN was also discussed in chapter 6.
- Scientist payloads can be on a pivot if WiFi is used for the scientist links. Otherwise Ethernet can be descended from the NSO to the NCU.

8. FUTURE DEVELOPMENTS

Possible future developments are manifold and will of course also depend on the first flight results as well as CNES and ELTA budgets.
There are already improvements and evolutions in the pipeline which CNES consider essential for the continuation of the NOSYCA project and zero pressure balloon (*BSO*, ZBP) flights especially for longer duration ZPB flights.
For over-the-horizon ZBP flights, the most important of these is the third communication link. Inmarsat is a definite possibility and our studies have proven that Inmarsat can cohabit with Iridium as long as sufficient distance is given between the antennas. In view of our tight schedule it was deemed that the flight train constraints were too difficult to apply in a timely fashion for the first NOSYCA flights. The OBC is already designed to accept an Inmarsat modem in the ITAC module.
Weight reduction is also an important issue. During production certain elements were found be heavier than their original specifications. The reasons are known (for example, difficult process control in the production the NSO and NEV thermal shells, leading to too much resin being applied). Weight reduction measures are actively being studied and will be applied shortly after the first flight results.

The translation from the heavy weight ZPBs to light weight and long duration pressurised stratospheric balloons (*BPS*, PSB) is a CNES objective. It is under consideration at ELTA. We are looking into developing a light weight fail safe product based on the NOSYCA architecture incorporating solar energy management. This will, of course, be based on our experience with the NOSYCA project as well as our existing solar energy products used in Concordiasi flights.

Other ideas for improvement which we intend to study in the near future are:
- Argos 3 type bidirectional communications with the aerostat using ground based transceiver stations as well as satellite links.
- UHF or HF communications [3].
- Use of new vectors that will be available with the GALILEO system.
- Use of the Iridium Next constellation.
- More weight reduction – for example, use less wire to reach the apex gas valves from the NSO.

9. CONCLUSION

After five years of intensive activity the NOSYCA team, CNES, ELTA and others, is waiting to see the fruits of all our hard work. This will be after the first flights in 2013.
ELTA and CNES regard the NOSYCA project as the way forward in fail safe stratospheric balloon flights and that NOSYCA is the first and only product for fail safe flights and for optimizing Scientific missions success.

10. REFERENCES

1. Mongis J., Denis I., Chatain C., Gagne, JM. (2011). NOSYCA: A New System For Balloon Operations. In Proc; *20th ESA Symposium on European Rocket and Balloon Programmes and Related Research*, Hyère, France.

2. Zenone, I., Valero C., Donadieu J. (2011). Ground And Board Interface Of The NOSYCA Command Control Gondola: An Adaptable Interface. In Proc; *20th ESA Symposium on European Rocket and Balloon Programmes and Related Research*, Hyère, France.

3. Lefèvre, J-P., Verdier N. Flight Telecommunication Systems Under Balloons. In Proc; *20th ESA Symposium on European Rocket and Balloon Programmes and Related Research*, Hyère, France.

BALLOONING IN SPAIN: ZERO2INFINITY DEVELOPS NEW LAUNCH CAPABILITY FOR MEDIUM TO HEAVY PAYLOADS ON STRATOSPHERIC BALLOONS

José Mariano López Urdiales, Annelie Schoenmaker

zero2infinity
Masia Nova, Ronda Can Fatjó s/n, 08290 Cerdanyola del Vallès, Spain
Emails: jmlu@inbloon.com, as@inbloon.com Tel: +34.93.582.44.22

ABSTRACT

On November 12, 2012, zero2infinity launched a life-supporting capsule to 32 km from León, Spain, using a 43,000 m^3 balloon and its own launch vehicle and ground equipment thereby officially entering the small club of heavy balloon launch providers.

As demonstrated by the successful test flights to develop internal technologies, zero2infinity is already able to provide flights opportunities to researchers, institutes and space agencies at an affordable price. This paper will describe the launch capabilities that zero2infinity is currently developing for conducting experiments and tests ranging from tens of kilograms to a ton. Internal (controlled environment) and external (direct exposure) mounting capabilities are available in zero2infinity's pods on both dedicated and shared flights. Small and medium payloads can benefit from the availability of shared flights to cost-effectively reach Near-Space. As a privately held company based in Spain, launches will eventually be available from several locations both in Europe and internationally, and will be available to all types of customers, governmental and non-governmental, on a first-come first-served basis.

zero2infinity has successfully flown several prototypes and other technology demonstrations payloads, and has conducted two large balloon campaigns culminating with a successful flight in November 2012. zero2infinity has partnered with the ISTAR group for the development of this capability and is now ready to accommodate scientific payloads with very diverse needs. In a 3-year horizon, when zero2infinity starts operating its crewed pods, scientists will be able to fly with their payloads and interact with them during the whole 5-hour flight.

1. COST-EFFECTIVE ACCESS TO NEAR-SPACE

1.1. The bloon family

zero2infinity has been working on developing a fully operational and sustainable high-altitude balloon family of vehicles since 2009. Several short-duration missions have already been conducted with various balloon sizes up to 43,000 m^3 Located in Spain and an entirely private company, zero2infinty relies on a small and effective structure, and works with renowned ballooning experts. This allows for a lot of flexibility in terms of operations, management and scheduling of launches.

A usual zero2infinity flight campaign includes a launch from Spain, with a helium polyethylene balloon. Payloads can be mounted internally in a pressurized environment or externally exposed to the outside environment. All specific requirements from customers can be discussed, from altitude to launch location.

zero2infinity's family of vehicles is called bloon, with microbloon, minibloon and bloon as its members. As its name suggests, microbloon is the smallest pod. It is an unmanned vehicle capable of hosting up to 500 kg of payload. It is equipped with 4 windows of 0.14 m^2 offering the possibility to carry out observations in a controlled environment.

Figure 1. microbloon during flight preparation

minibloon is the first human-rated pod and is currently under construction. The original pod was designed and manufactured by the Rutan brothers and is expected to start flying in 2014. It provides room for 2 pilots or 1 pilot and 1 scientist who would be capable of manipulating the experiments during flight as well as carry out direct space observation through the windows. Nominal flight altitude will be 36 km with possibilities of flying higher or lower according to the payloads' needs, in case of a dedicated flight. The total weight of

Proc. '21st ESA Symposium European Rocket & Balloon Programmes and Related Research',
9–13 June 2013, Thun, Switzerland (ESA SP-721, October 2013)

the pod will be approximately 1,000 kg, with the possibility to add up to 1,000 kg of payload distributed between the controlled and the external environment.

Figure 2. minibloon in the workshop

bloon will be the largest pod and the head of the family. Its capacity will be to transport up to 6 passengers, including 2 crewmembers. This configuration can be tailored in order to, for example, increase the available volume for payload or include seats for researchers. This creates the possibility to get full-time total access to payloads inside the cabin during dedicated scientific flights. The internal field of view is one of bloon's strong points. bloon offers a total window surface of 15 square meters divided in 5 windows.

Figure 3. bloon model

1.2. Flight and payload mounting specifications

The nominal short-duration mission flight profile consists of three stages. The first one is the ascent of the lighter-than-air vehicle using a stratospheric helium balloon attached to the pod. The second stage involves a cruise at altitude using the same balloon. The final phase is the descent of the vehicle using textile-based decelerators (mainly parachutes and/or parafoils) and an inflatable impact absorbing system to safely decelerate the pod and its payload on the ground.

• Ascent phase: From the ground to the cruise altitude (up to 44 km ASL). The estimated duration is between 2 to 3 hours.

• Cruise phase: Typically 2 to 3 hours phase at constant altitude (up to 44 km ASL).

• Descent phase: In the case of bloon, a guided descent to one of the pre-defined landing spots. In unmanned flights, descent is non-guided under parachute. The estimated duration is about 1 hour.

Internal mounting of experiments provides a controlled environment. This environment is adapted to the needs of passengers during standard campaigns, but can be adapted to the mission needs in dedicated flights. No space-adapted designs are necessary in these placements, if it works in the lab, it will work in the pod. Experiments designed to operate at standard sea level conditions will work in our internal racks during the flights. Experiments that are designed for the outside environment can also benefit from the controlled environment to keep the support systems like batteries, electrical circuits, etc. Inside the pod, the environment is regulated to support human life conditions. The pod's cabin pressure is maintained at approximately 80 kPa. Normally, cabin temperature varies from 18 to 25 degrees Celsius and its humidity is maintained at about 60%. All internal environment conditions are customizable on dedicated flights. bloon's windows offer a terrific field of view. The windows are manufactured from polycarbonate, which has a light transmission coefficient of 87% and a reflection coefficient of 1.6. Different coatings are added to protect experiments and passengers from UV-radiation, freezing and steaming while ensuring optimal viewing conditions. Special windows with customized optical properties can be adapted to our vehicles.

External experiment mounting provides a direct access to the Near-Space environment with real-time control and data analysis from the ground. On externally mounted experiments, ambient conditions offer atmospheric pressure of ~0.2 kPa, temperature of ~60ºC and humidity near 0%. External mounting has very low

constraints because the flight profile does not involve extreme accelerations or decelerations. Different positions and facing- directions are possible. The only constraints are meant to ensure safe operations by avoiding interference with the landing subsystem, the textile-decelerators subsystem or the balloon itself.

Our pods are equipped with standard 19'' racks and 1U (10 cm cube), 3U and 6U containerized payloads' supports (both internally and externally). Payloads of different sizes can also be hosted after discussion.

Microgravity can be provided in different ways. When the pod separates from the sail at high altitude up to 25s of microgravity can be obtained from the free fall. The expected noise level during microgravity is ~10^-2 g rms, similar to that of a parabolic flight. The versatile pods can accommodate a small drop tower that would allow experiments to be dropped at cruising altitude on a tether and reeled back to the pod for another drop. This would allow for hundreds of bursts of microgravity. In the case of manned flights, it is possible for a scientist crewmember to inspect experiments between drops. This system, like most on the pod, can be customized to mission requirements on dedicated flights. A rocket-shape vehicle is released from high altitude equipped with small thrusters to compensate air disturbances. Up to 1 minute of microgravity can be obtained from such a drop test. The payload can be recovered after a parachute landing.

A full release drop test can also be conducted from stratospheric balloons, making it a quick and affordable platform for testing supersonic effects. Velocities greater than Mach 2 are easily achievable when dropped from 36 km. zero2infinity also offers design, integration and operation support for ballistic recovery systems.

1.3. Pricing

Two options are available to fly experiments and technical payloads to Near-Space: dedicated or shared flights. The following tables give an idea of the prices offered by zero2infinity in a number of pre-defined cases. These are rough estimates of prices. Specific cases can be discussed and studied accordingly.

For educational payloads, pricing is a bit different and will be charged for now at 460 €/kg as secondary payload. An educational project is under construction to be able to offer free flights for educational experiments as well as free flights for the students and the teachers themselves when bloon will be ready (see section 4.2. for more detail).

Weight (kg) / Altitude (km)	Price (€)
10 / 31	132,000
45 / 40	175,000
300 / 32	260,000
700 / 25	600,000
1,000 / 36	1,000,000

Figure 4. Estimated price table for dedicated flights

Weight (kg)	Price (€)
1	900
5	4,100
10	8,000
20	15,800
50	38,400

Figure 5. Estimated price table for secondary payloads

2. A RELIABLE SERVICE TO NEAR-SPACE

2.1. Services provided

The services included in the prices mentioned above are the following:

- Payload and balloon integration, balloon launch, balloon operation and payload recovery
- Any facility, equipment, hardware, documentation, personnel, labor, analysis, service and know-how necessary to carry out the mission
- Solutions for the design of support equipment for optimal integration of payload
- Safety verification process
- Any data and/or power connection onboard
- Downlink and uplink communications
- Mission simulation, rehearsal and test to ensure operational readiness, both for the vehicle and for ground systems
- Post-flight analysis support: a report documenting flight data, mission profile accomplishment, environment requirements and any topic agreed as a key success factor of the mission
- Management of relations with Authorities and generation of any permit necessary to carry out the flight
- State of the art sensors, including spherical video in several locations of the flight train to enhance awareness of the whole process
- Pods with ECLSS

In case of a mishap during the flight where zero2infinity is at fault and which results in the experiment not completing its intended mission, zero2infinity can either offer the option of purchasing insurance (recommended for large payloads with high monetary and know-how

value), or another priority flight opportunity in a subsequent flight. In the case of a dedicated flight, redundancy of systems like balloons and helium are always foreseen to allow for quick turn-around and another launch could be scheduled during the same campaign.

2.2. Launch experience

zero2infinity has already launched numerous payloads of various sizes at over 30 km in altitude, from telemetry sub-systems to the large pressurized microbloon pod with a 43,000 m^3 balloon. Many more test flights are coming in late 2013 and 2014 to prepare the human flights. On these internal flights, secondary payload space will be available. Apart from that, dedicated flights can also be scheduled, with a possibility of lowering the cost of the flight by scheduling it together with other flights in a same campaign.

The latest flight to Near-Space happened on 12 November 2012 from León, Spain. The pressurized microbloon pod flew to 32 km, with all systems and equipment working. The temperature and pressure remained stable inside the pod, the launch and recovery went smoothly.

Figure 6. microbloon as seen from the spherical camera

All our flights embark many cameras, for both photo and video full coverage. We have been testing spherical cameras with GoPros which allow for a 360º view of the whole flight. Specific cameras and telemetry systems may be required for some payloads, and we have the relevant experience and partners to provide the customers with the best solution. We are also currently working on live-coverage of flights.

The previous test flights were conducted from Zaragoza and León, Spain. Due to better wind projections and trajectories, the launch base has been moved to Cordoba, in the South of Spain.

Thanks to many successful flights conducted in Spain with no bad experiences, zero2infinity has built a relationship based on trust with the national aviation authorities. Permits to fly are therefore a necessary but easy-to-obtain formality. Moreover, a yearly $10 million third-party liability insurance has been secured to cover all of zero2infinity's experimental launches.

2.3. Partners

Key elements of a successful launch are the team and the partners. The company has a small full-time team of engineers that combines the relevant expertise and the necessary dedication. Other key affiliates for launch campaigns include a world-renowned flight director and campaign manager (Steven Peterzen from the ISTAR Group, awarded the NASA Public Service Medal in 2002 for his work as campaign manager of the Antarctica Long-Duration Balloon Program) and a very experienced meteorologist who used to work for the French Defense and the French Space Agency CNES (Pierre Dedieu).

Figure 7. The crew in León, May 2012

zero2infinity relies on tried and tested equipment, both Space and non-Space components, but always non-ITAR restricted. Some equipment is designed in-house to cater to specific needs, such as the spools or the telemetry system. As the company and its operations are completely private, payloads' and customers' confidentiality can be protected if needed. This provides for high flexibility as well as efficiency and allows us to adapt to the reality of the customers.

Balloons themselves are one of the most critical elements of the launch and we have created secure relationships both with Z Marine (former Zodiac, France) and Tata Institute of Fundamental Research (TIFR, India) as our main providers for timely delivery and state-of-the-art reliable stratospheric balloons.

Figure 8. The TIFR balloon inflation, 12 Nov. 2012

This combination of partners and lean operations make the timeframe for launches very efficient and reliable. For a large dedicated launch, 5 months are enough from the date of signature of the contract until launch, to buy the balloons, prepare the pod or the specific structure for the payload, get the permits, prepare the launch, and conduct the launch campaign. For smaller payloads, 3 months lead-time may be enough. For secondary payloads, schedules are less flexible as they depend on another flight to be ready.

3. WHY FLY FROM SPAIN?

When thinking high-altitude ballooning, harsh environments come to mind, such as frozen places in the north of Sweden or Antarctica or scorching deserts in the USA or Australia. But it doesn't have to be this way. Spain also has a heritage in stratospheric flights, and even in human high-altitude ballooning.

In the 1990s, the Spanish National Institute for Aerospace Technology (INTA) in collaboration with the French Space Agency (CNES) conducted many scientific high-altitude balloon launches from the military airfield of Virgen del Camino in León, North of Spain. The experience gathered there allowed zero2infinity to also use the León airfield for its test flights until 2012. The good relations created there were critical for the company to be able to gain experience and to build trust with the Spanish authorities. However, apart from the political and historical advantages of launching from León, it was found that the meteorological conditions were less than optimal, the North-West of Spain being subject to some of the least favorable weather conditions of the country. This caused many delays in test flight launches with the crew forced to be idle for weeks at a time waiting for the winds to quiet down.

A launch base should be selected according to several criteria. The main concern is weather conditions, especially wind intensity and direction, both on ground and in altitude. Other criteria to consider are the local infrastructure available (hangars + launch pad), the surrounding population density, other surface risks (power lines, wind farms, train tracks, roads...), the surrounding geography (abrupt terrain, proximity to open sea or to other countries), the surrounding air traffic density, the technical/scientific interest of the flight and other political issues.

There are many advantages for flying from Spain. First of all, thanks to fiscal incentives for wind power plants, there is a lot of wind data available. It's enough to look at the map of Spain's wind farms to deduct where there is no wind. For our current operations, we have selected Córdoba, in Andalucía, South of Madrid, as our launch base. This area has a very low population density; except the city of Sevilla (located at 100 km south-west) as the high population density appears close to the coast. The terrain is roughly flat, covered with crop fields easing the recovery of the payload.

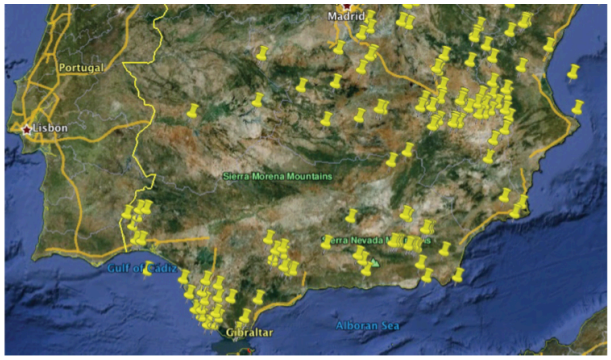

Figure 9. Wind farms of the South of Spain

The airfield is located 6 km southwest from the city of Córdoba (N37º50'36'', W4º40'31'') at an altitude of 90m (ASL). It is an airfield managed by AENA (Aeropuertos Españoles y Navegación Aérea), the Spanish Airports and Navigation Authority. It offers a 2.3 km x 60 m paved runway, two separated platforms, offices and hangars. No control tower is available, so VFR is applied. It had 6,400 operations in 2012 (general aviation).

The main concern during launch operations is ground wind. Ground winds shall be below 3-4 m/s both during inflation and launch to avoid any damage on the balloon or the payload. Córdoba is located in an area that offers average ground winds below 3 m/s. In the early morning hours of the summer months, the average ground winds below 1.5 m/s. There are other areas with even better wind conditions, but their geographic location is not as optimal as the one of Córdoba.

Figure 10. General view of Córdoba airfield

Córdoba is an ideal launch base for mid-latitudes and short missions, and also has the advantage of being located in a pleasant climate, easily accessible from anywhere in the world, thanks to good connections by plane through Madrid or Sevilla and high-speed trains. For commercial flights, Andalucía is also an ideal place as it is a destination in itself, and a launch can be combined with other travels and experiences.

4. FUTURE PLANS

4.1. Human flights

Human high-altitude balloon flights are not reserved to daredevils like Felix Baumgartner who completed the highest space dive from a high-altitude balloon capsule for the Red Bull Stratos Project on October 14th, 2012. He was indeed the first human to fly with a balloon to these altitudes in 40 years, but in the 1960s before the rocketry race begun, many manned high-altitude flights took place.

Balloonists were actually the first "astronauts" in the 1930s, if by astronauts we mean people that have seen the Earth from outside the boundary of our atmosphere. No need indeed to go up to 100km or more to be outside most of the mass of our atmosphere, or to see the view from Space as we imagine it: the black sky, the white sun, the blue line of the atmosphere and the curvature of the Earth clearly visible.

Spain also has a heritage in human high-altitude ballooning. In 1935, Emilio Herrera, a Granada-born scientist and aviator, designed the first ever spaceflight suit, which he intended to use to fly to an altitude of 30km with a balloon. He tested his suit in an airless chamber, and conducted many other experiments, until he was ready for flight with the balloon and the basket constructed. The start of the civil war in Spain abruptly halted the project, he went into exile and could never fly. The Apollo mission space suits design was based on that of Emilio Herrera. It may be symbolic but zero2infinity's founder comes from the same city and graduated from the same University as this Spanish Space pioneer.

New Stratosphere Flying Suit Tested In Airless Chamber

LOOKING like a man from Mars, Lt. Col. Emilio Herrera demonstrated the feasibility of his stratosphere flying suit in an impressive test of man and equipment. Simulating conditions he expects to find on his proposed stratosphere flight, he remained in an airless chamber at a temperature of 70 degrees below zero for a period of more than two and a half hours.

His specially designed flying suit is fitted with a device for maintaining proper atmospheric pressure. It also features an oxygen generator and a heating system for maintaining a comfortable body heat.

Lt. Col. Herrera is the Director of the Superior Aerotechnical School of Spain. He hopes to be the first man from his native land to make a successful stratospheric trip. No date has been actually set for the flight, but he expects to start as soon as his present experiments, which are being conducted in Mexico, have been completed.

Figure 11. Article about Emilio Herrera in 1936, USA

But why fly with humans? For the view, but not only. Several significant scientific discoveries were made by man-made observations from high-altitude platforms back in the beginning of the previous century, including cosmic rays, the effect of solar flares on humans in Space, water ice on the Martian poles, water vapor on Venus, etc, especially during Projects Strato-Lab and FATSO (First Astronomical Telescopic and Spectrographic Observatory) with Audoin Dollfus in the 1950s-60s. [1]

zero2infinity is not inventing anything fundamentally new but revisiting these historical capabilities in a 21st century fashion. Scientists on our flights will not need to be test pilots, they will not need any particularly strenuous training. They will be able to focus on their research in a pressurized, shirt-sleeved environment, not on the technicalities of the flight.

Flying scientific experiments inside a human-rated pressurized pod allows direct manipulation of experiments by expert hands upon previous request. Lights will also be installed in the pod cabin; these provide sufficient light to support manual work or the photography of most open test equipment.

4.2. Educational projects

Education and hands-on experiments for students and teachers is a key component of the aerospace industry. The Teachers in Space Program of NASA was one of the most popular programs since the Apollo missions, although it ended dramatically, killing one teacher in the Challenger accident. zero2infinity is very conscious of the importance of providing educational experiences and of the lack of current concrete possibilities. The high-altitude educational project we are working on is called SATINS – Students and Teachers in Near-Space. This project would allow in a first step, high school and university students to fly their experiments to Near-Space, involve them in hands-on activities, invite them

to launches and stimulate their interest in STEM. This stage of the project is feasible today.

Once human flights are available, the plan is to send teachers with their students themselves to Near-Space for them to enjoy a real hands-on experience, and finally make Space accessible.

We aim for these flights to be at no or very little cost to the schools. We are actively looking at partners for this operation and are looking into crowd-funding options. Regular sponsorship is also available, with the sponsor then able to fund specific experiments, specific schools, propose their own experiment of support the educational objectives generally.

5. CONCLUSION

The last four years of the company saw the development of a full-fledged capacity for launching stratospheric balloons for unmanned payloads up to 1,000 kg. The next four years will see the scaling of this capacity to a fully operational crewed and uncrewed line of vehicles to regularly fly to Near-Space. We hope we will contribute to the blossoming of the true potential of high-altitude ballooning for science. This will be enable us to provide solutions to meet many of the scientific objectives of space agencies, such as NASA's Decadal Survey or ESA's Cosmic Vision.

6. REFERENCES

1. Ryan C. (2003). The Pre-Astronauts, Manned Ballooning on the Threshold of Space. *Bluejacket Books,* Naval Institute Press, Annapolis, Maryland, pp225-251.

Life & Physical Science

Chairs: B. Zappoli, Y. Houltz, M. Egli & M. Cogoli

THE XRMON-GF MICROGRAVITY EXPERIMENT MODULE ON MASER 12 AND ITS CONTINUATION

Y. Houltz[1], J. Li[1], H. Nguyen-Thi[2], G. Reinhart[2], G. Salloum Abou Jaoude[2], R. Mathiesen[3], D.J. Browne[4], A.G. Murphy[4], G. Zimmerman[5]

[1)] Swedish Space Corporation, Science Services Division P.O.Box4207, SE-17104Solna, Sweden
Tel: +46-86276200, Fax: +46-8987069, E-mail: ylva.houltz@ssc.se
[2)] Aix-Marseille University and CNRS, IM2NP UMR 7334 Campus Saint-Jérôme, Case 142, 13397 Marseille Cedex 20, France
Tel : +33-491282893, Fax : +33-491288775, E-mail : henri.nguyen-thi@im2np.fr
[3)] Department of Physics, Norwegian University of Science and Technology, N-7491 Trondheim, Norway
[4)] School of Mechanical & Materials Engineering, University College Dublin, Belfield, Dublin 4, Ireland
5) ACCESS, e.V. Intzestrasse 5, 52072, Aachen, Germany

1. ABSTRACT

The XRMON (X-Ray MONitoring of advanced metallurgical processes under microgravity and terrestrial conditions) MAP programme contains a series of microgravity topics on materials science using X-ray radiography as advanced characterization technique for in situ and real-time monitoring. The XRMON-GF module was the third sounding rocket flight within the XRMON programme. It was launched on Maser 12 from Esrange Space Center in February 2012. Three Parabolic Flight Campaigns with in-situ X-ray monitoring have also been performed within the programme.

The XRMON-GF module was the first ever sounding rocket experiment with in-situ X-ray monitoring during flight. The module was designed with the aim of being possible to re-use for future experiments on directional solidification of alloys within the XRMON MAP programme and is planned to be re-flown as the XRMON-SOL experiment on MASER 13 in 2015.
The same technology as developed in XRMON-GF has been used when designing the XRMON Parabolic Flight Facility, a reusable flight rack that had its first flight on the ESA 58 Parabolic Flight Campaign in May 2013.

2. XRMON PROJECT

Structural material properties are related to their solidification microstructures which can be columnar (oriented properties) or equiaxed (isotropic properties). The control of the columnar-to-equiaxed transition is thus crucial in engineering and is still a debated subject [1]. On Earth, natural convection in the melt is the major source of various disturbing effects [2,3]. Solidification under microgravity is an efficient way to eliminate buoyancy and convection to provide benchmark data for the validation of models and numerical simulations [4,5].

In situ and real-time imaging of the metallic alloy solidification can be achieved by applying synchrotron X-ray techniques, in particular X-ray radiography [6,7]. In this technique, the contrast in the recorded image is due to local changes in the amplitude and/or phase of the X-ray beam transmitted through the sample. A (monochromatic) X-ray beam illuminates the sample and a 2D-detector (photographic film or CCD camera) is placed close to the sample to record the transmitted beam. In alloy systems, contrast mainly results from segregation of the chemical species and is generally weak and therefore difficult to reveal with conventional X-ray sources.

The main objective of the ESA - MAP research programme entitled XRMON is to conceive and perform *in situ* X-ray radiography experiments on metallurgical processes in microgravity environment.
Previous projects in this program were XRMON-foam on forming of metal foams and XRMON-diffusion on diffusion in melts, which both used different experiment set-ups and imaging technology. Full-frame X-ray *in-situ* observation has not been implemented on sounding rockets until this project.

The XRMON-GF experiment on directional solidification of AlCu alloys was flown on the MASER 12 sounding rocket mission, in February 2012. This paper reports on the technical description of the dedicated novel experimental set-up developed by SSC (Swedish Space Corporation), the outcome of the MASER 12 flight and the continuation of this project on both sounding rocket and in parabolic flight.

Proc. '21st ESA Symposium European Rocket & Balloon Programmes and Related Research', 9–13 June 2013, Thun, Switzerland (ESA SP-721, October 2013)

3. XRMON-GF MODULE

The XRMON-GF sounding rocket module contained an fine-focus X-ray imaging system and a Bridgman type solidification furnace. The module infrastructure provided interfaces for automated control and operator interaction during flight. Live image and data was down-linked during flight and high resolution image and data stored on-board.

Figure 1. XRMON-GF module

3.1 Gradient furnace

The gradient furnace was of Bridgman type and has two identical heaters for the "hot" and "cold" zones (Fig.2). In order to provide the same thermal behaviour in microgravity environment as on 1g these were designed so that the sample is enclosed inside the heater body. The heater wire was applied in a coil-like fashion, encompassing both sides of the heater body. Thus both sides of the sample see the same temperature.

The furnace was designed for a maximum sample size of 10x50x0.2 mm. In MASER 12 a size of 5x50x0.18 mm was used, in order to detect possible border effects in the samples.

A key issue in the furnace design was to avoid any contact between the two heaters, in order to get all maximal heat transfer through the sample. The heater assembly was designed to provide a 1 mm gap between the heater elements for insulation.

To provide optimal image an opening for the X-ray beam in the heaters was provided, leaving a 5x5 mm field of view in the sample free from any other materials than graphite which has very low X-ray attenuation. (Fig.4), but at the same time it is important to not get cooling from the sides.

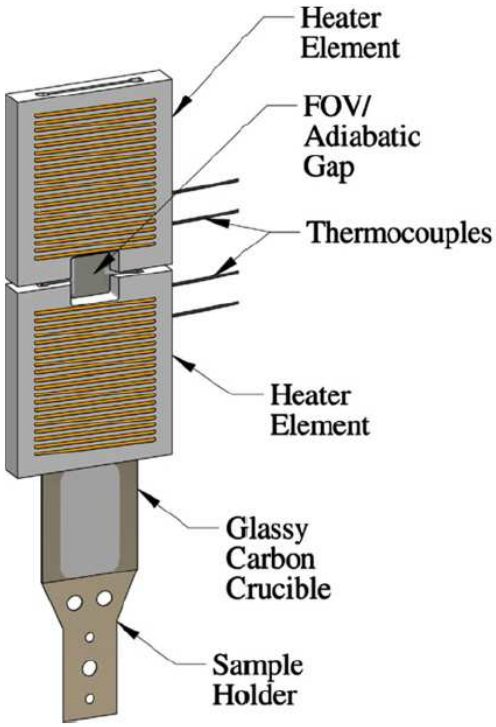

Figure 2. Heater elements and crucible

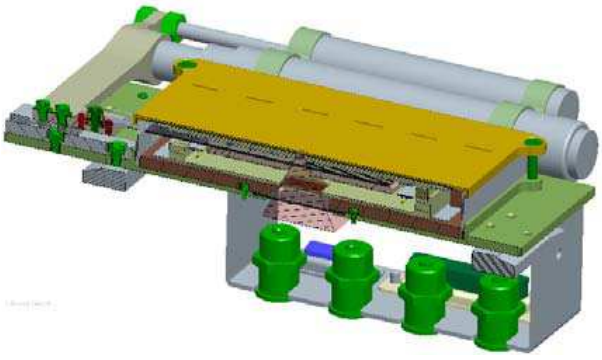

Figure 3. Cross section of furnace, X-ray beam in middle, motor on far side

The heaters were regulated independently using a PID-regulator implemented in software. Two thermocouples embedded in each heater measured the temperature close to the crucible and served as input for the temperature regulation.

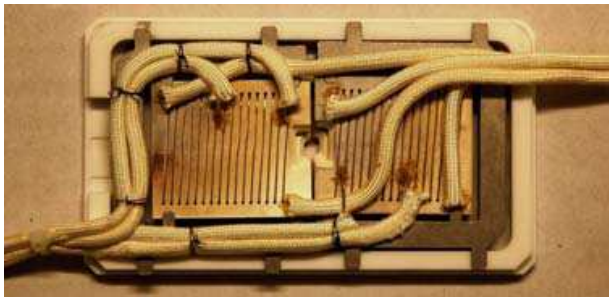

Figure 4. Heater bodies in supporting frame

In order to achieve a 5 µm resolution it is crucial to minimise the distance between the X-ray tube exit window and the sample. The distance in this furnace can be as short as 5 mm without the furnace top touching the X-ray tube, and without compromising the furnace insulation that is crucial for the thermal properties.

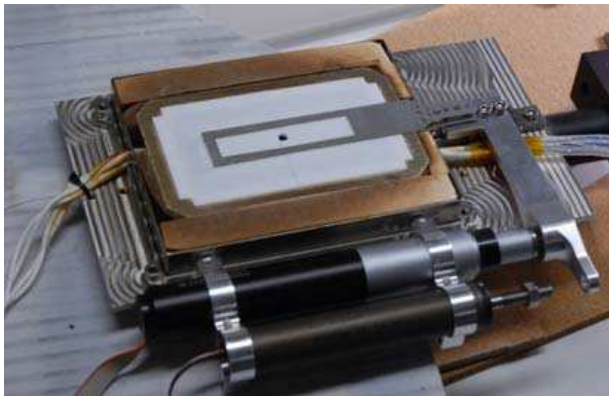

Figure 5. Assembled furnace, crucible frame placed on top to show sample placement

Solidification of the sample can either be made by regulating the temperatures of the heater elements (*power-down* method), or by pulling the sample in the furnace (*pulling* method), thus moving the solidification front along the sample. For MASER 12 flight the power-down method was used. The motorised movement can also be used to position the sample in the field of view (Fig.5).

3.1.1 Crucible and sample holder

To contain the sample and to make it possible to move the sample in the field of view/temperature field, a combined crucible and sample holder was developed. Two version of this crucible were designed: one made of quartz glass and one of vitreous carbon "glassy carbon" and stainless steel.

These two types showed different advantages:
Quartz glass is more rigid and keeps the sample in place in a better way but is harder to manufacture and sensitive to mechanical stress.
Vitreous carbon is more flexible, hard to manufacture and needs inert gas atmosphere, but once manufactured, is much more versatile and durable.

Figure 6. Crucibles/sample holders in Glassy Carbon and Quartz glass

Based on the higher reliability it was decided to use Glassy Carbon crucibles for the MASER 12 flight.

3.2 Imaging system

As AlCu alloys were studied in this project, an X-ray source having an energy range around 17 keV was specified. This radiation energy span makes it possible to take advantage of a high difference in X-ray transmission between copper and aluminium. To get optimal image quality the materials in the X-ray path was minimised and selected to have low attenuation. An image frame rate of, at least, 3 frames/s was required to follow the dynamics of the solidification microstructure formation, and the exposure time had to be minimised in order to avoid blur from dynamic processes.

Downlink of compressed image was needed in order to follow the experiment progress *in-situ,* and to be able to fine-tune the temperature gradient during flight.

The imaging system consisted of three parts: The X-ray tube, the camera and the Digital Video System.

3.3.1. X-ray tube

A micro-focus X-ray tube with 5 µm focal spot was selected in order to meet the resolution requirements. To be able to achieve the requirement of low (≤ 5 mm) focus-sample distance, a transmission type X-ray tube was needed, unlike conventional types these have the focus point close to the exit window.

A compact oil-free X-ray tube of this type was recently developed by DLR in cooperation with Viscom AG/FineTech FineFocus Technologies GmbH Germany, intended for usage on the International Space Station. The system had its first space flight on Maser 12, but is also scheduled to be used on the Mapheus 3 rocket to be launched in the summer 2013 and has recently been used in two parabolic flights.

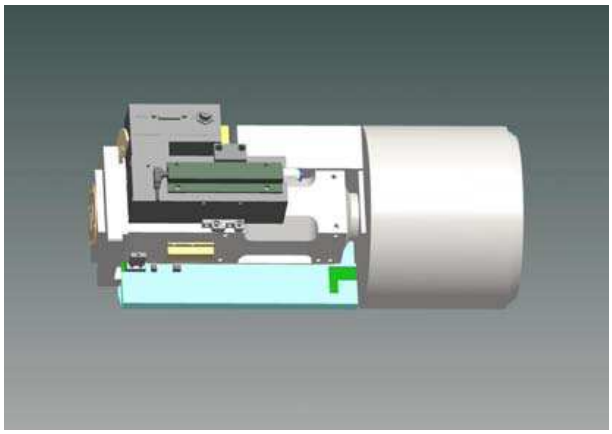

Figure 7. Compact X-ray tube assembly

3.3.2 Camera

In the scope of the ESA GSTP study "Xray Diagnostics for Space" a camera system was developed that fulfilled the high requirements on resolution (Fig.8). The camera system was made of a digital camera with a 24x36 mm CCD-sensor adapted for X-ray usage by the integration of a 50 mm thick fibre optical plate that protects the sensor from radiation. A scintillator plate placed in front of the optical fibre converts X-ray radiation to visible spectrum light. The scintillator used is a "structured scintillator", based on a new technique with channels etched in silicon and filled with scintillating material, acting as wave guides. This technology has recently been developed by Scint-X AB in cooperation with the KTH, Royal school of Engineering, Sweden. During this project further improvements on the scintillator design and integration was made that increased the homogeneity and luminescence of the camera image.

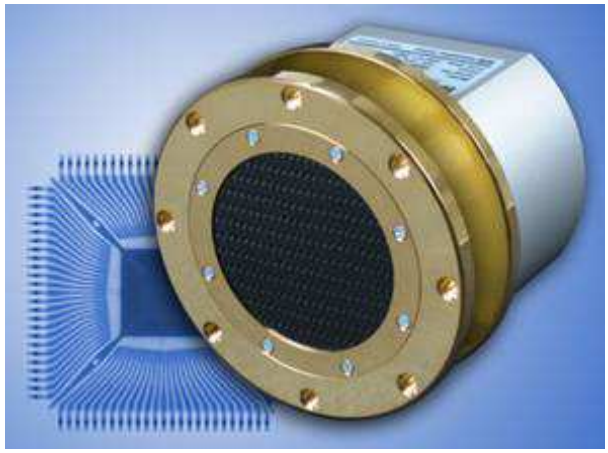

Figure 8. X-ray camera

Contrary to synchrotron radiation the radiation field from an X-ray tube has conical shape. This is possible to utilise to get a magnifying effect by adjusting the distances in the imaging system. The distances used for XRMON-GF are described in Fig.9.

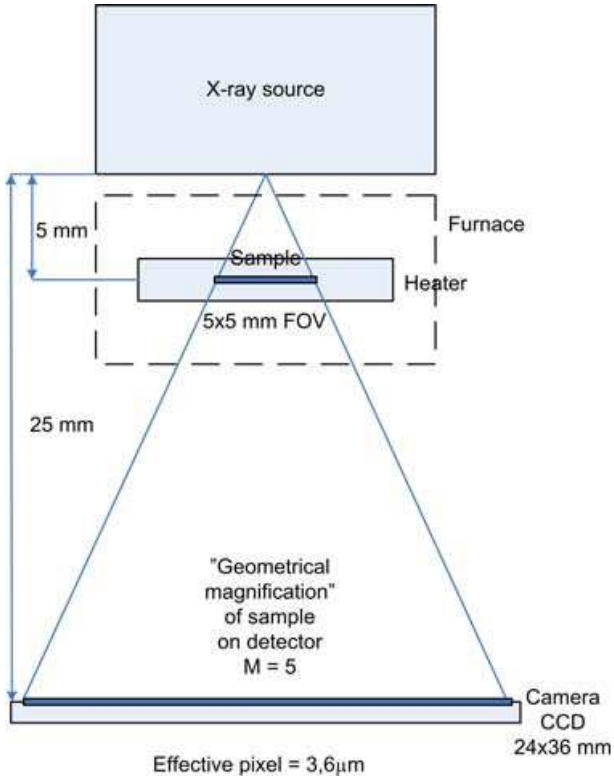

Figure 9. Distances and magnification in imaging system

3.3.3 Digital Video System

The Digital Video System interfaced the camera and provides camera control, image storage and downlink of real-time image. The system selected was a H2VMU from Techno System Developments, Italy. This unit stored uncompressed images (Fig.10) on-board with a frame rate of 3 frames/s,
Compressed images was down-linked with a frame rate of 0.5 frame/s during flight.

Real-time gain compensation implemented in the hardware, using a reference image acquired from the melted sample, further improved the detail seen in-flight. Images stored on board were not processed, but stored as raw files.

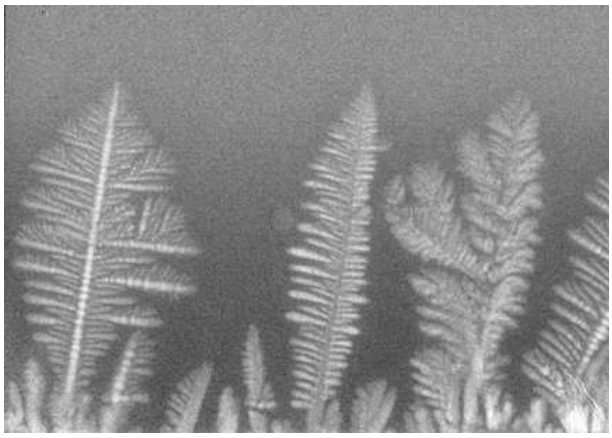

Figure 10. X-ray image of a growing columnar structure of Al - 10wt% Cu (R_H = 12K/min; R_C = 0; G ≈ 4 K/mm) Image width=4.5 mm.

3.3 Module infrastructure

XRMON-GF was a 115 cm tall and 112 kg heavy Module (Fig.11).

The main building blocks for the module were:

- Inner structure with suspension system
- Electronics deck
- Cooling system
- Outer structure with pressure-tight lids and hatches

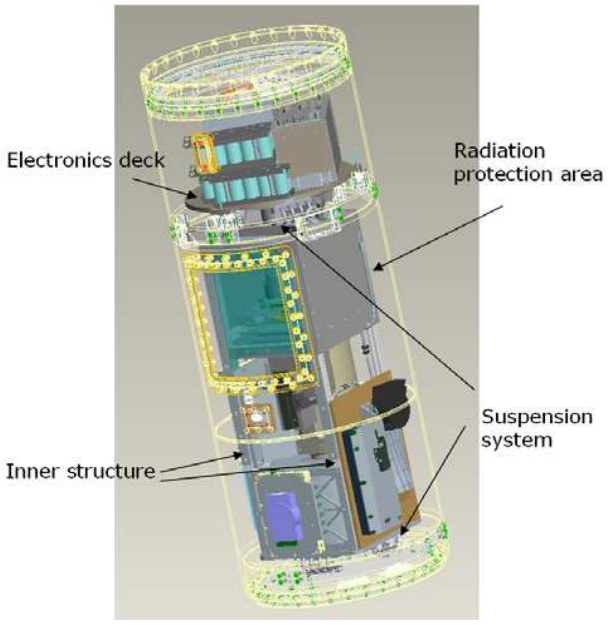

Figure 11. Module assembly, outer structure indicated

3.3.1 Inner structure

To provide a stress-free environment for the experiment system during take-off it is mounted in an inner structure suspended on a tuned damper system. The inner structure also serves as a support for mounting experiment electronics and for X-ray shielding.

3.3.1.1 X-ray protection

The furnace, camera and top of the X-ray tube were enclosed in an X-ray shielded compartment. Access to the furnace was granted via a movable hatch with safety switches that turned off radiation as soon as the hatch was opened.
In this way the integrated module could safely be operated without applying external shielding during test and integration.

A connection for external safety switch and warning light was connected to a connector in the outer structure. Radiation cannot be operated without connecting these. At a late point during the count-down procedure these safety devices were replaced by a dummy connector used during flight.

3.3.2 Electronics deck

The electronics system was mounted on the electronics deck, placed on separate dampers above the inner structure (Fig.12). On this deck the Electronics cabinet was placed. The Experiment Control Computer provided the experiment control sequence, on board data saving and in-flight communication. A separate computer board provided control for the X-ray tube.

The Housekeeping Board conditioned and monitored the module voltage and currents and other housekeeping data. The Digital Video System (H2VMU) cabinet and the battery pack were also placed on the electronics deck.

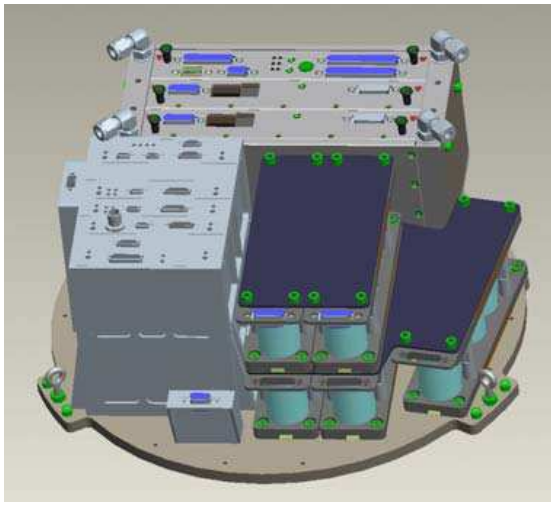

Figure 12. Electronics deck

3.3.3 Cooling system

The sample was to be kept pre-heated for at least 30 minutes during the count-down, and an efficient cooling system was needed to keep the module at ambient temperature until lift-off.
The cooling system comprised an internal heat exchanger with a fan, the X-ray tube front plate and two heat exchangers on the electronics deck. It was connected to an external thermal bath that was run during the count-down, until lift-off.

3.3.4 Outer structure

The outer structure was made of aluminium with a yellow chrome surface treatment. The module was pressurized with nitrogen to 1 atmosphere during flight. The outer structure was sealed with pressure tight lids in both ends. All hatches, umbilical blocks and access points were also pressure tightened.

3.4 Electronics and control system

3.4.1 Experiment electronics

The experiment electronics comprised a Temperature Measurement Board measuring the furnace temperatures and a Power Board that delivered the two PWM outputs for the furnace heaters and controlled the sample movement motor. These boards were microcontroller based and communicated with the Experiment control computer over CAN-bus.

3.5.2 Control system

The control system was housed in the electronics cabinet on the electronics deck.

The Experiment control Computer is an Atom-based CPU board running QNX real-time operating system. It interfaced the Experiment electronics boards and the Housekeeping board over CAN-bus and the X-ray Control Computer over serial link. Telemetry and Telecommand was performed via the Maser Service Module (MASM-2) over serial communication.

3.5.3 Battery system

The battery system consisted of a NiMh battery pack with 25 cells and a Housekeeping Board that conditioned and monitored the module voltages and currents.

3.5 Support systems

For real time monitoring and control on ground and during flight an Electronic Ground Support System (EGSE) was provided. This system consists of: Operator terminals for display of real-time down-linked data and status, and for transmission of control commands. A video down-link system is provided for reception and display of real-time downlinked images. Systems for battery charging and conditioning and for control of the X-ray tube evacuation system was also included.

4. XRMON-GF FLIGHT ON MASER 12

4.1 Preparations

Before flight environmental tests were performed: Vibration, vacuum and temperature tests.
Also the timeline intended for automated control during flight was validated and fine-tuned together with the Science Team.

4.2 Flight

The count-down and flight was nominal. Maser 12 provided 6.5 minutes of good microgravity ($10^{-4/-5}$g), which was enough to perform the experiment sequence.
Due to the rigid temperature/pressure requirements for some units a detailed count-down procedure was applied, which worked perfectly.
Two pre-heating sequences at different temperatures were performed, starting at 30 minutes before intended take-off.

The experiment was performed as planned, using only the pre-defined automated control sequence.
The only operator interaction needed was to acquire the reference image for down-link images as soon as the sample was completely melted, as planned.

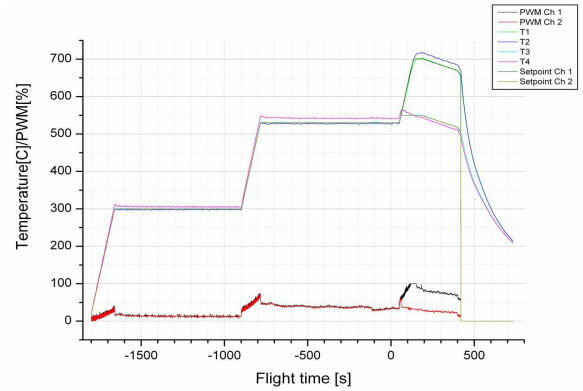

Fig 13: Flight temperature profile. Lift-off at 0 s

After the motor separation the sample was melted completely. The sample was kept at melting temperature for a short while for stabilization before starting the solidification phase.
Three different solidification speeds were used: 0.15°C/s for the main solidification period, then a cooling rate increase to 0.7 °C/s, and the natural cool-down just before the end of the microgravity period.

Dendritic growth was successfully visualized in situ, with high spatial and time resolutions. A few bubbles in the sample also provided new inputs on dendrite mechanics, shoving a different behaviour than seen on ground. Some preliminary scientific results were given in references [8] and [9]

Fig 14: Solidification of sample in µg

4.3 Reference tests

Two reference experiments running exactly with the same procedure were performed the day after flight, using a new sample from the same batch, with sample placed in horizontal and vertical position. These have been used to compare solidification properties when the g-vector varies (Fig.15 and Fig.16).

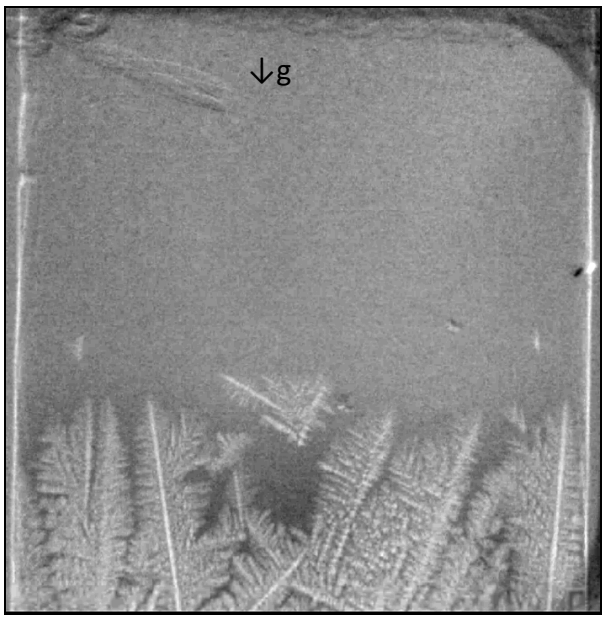

Fig 15: Solidification of vertically placed sample (g-vector along sample surface)

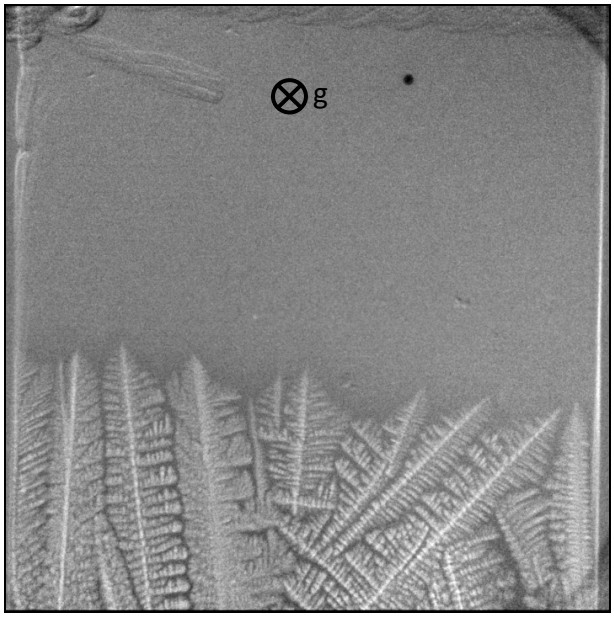

Fig 16: Solidification of horizontally placed sample (g-vector perpendicular to sample surface)

5. XRMON-SOL MODULE

Based on the knowledge from MASER 12 campaign, another solidification module entitled XRMON-SOL is beeing developed for MASER 13. The imaging system and Module Infrastructure will be re-used, but a new Isothermal Furnace will be developed. This furnace is intended for solidification experiments on AlCu samples with grain refiners. The furnace must have near-isothermal properties and the suggestion is to have a round furnace body, a round sample and use 8 heater elements arranged in two heater rings (Fig.17).

A first breadboard furnace was evaluated by the science team from University College Dublin, Ireland (UCD) in end of May. It was found to have good isothermal properties, but further work on the sample containment and sample exchange needs to be done. A second breadboard furnace is planned to be brought forward for evaluation in October.

5.1 Isothermal furnace breadboard

The first Isothermal Furnace has a round heater body with eight heater zones arranged 4+4 in two circles with 45º displacement.
The total size of the furnace with fittings and insulation is approximately the same as for the XRMON-GF furnace, making the adaptation of the module infrastructure relatively easy.

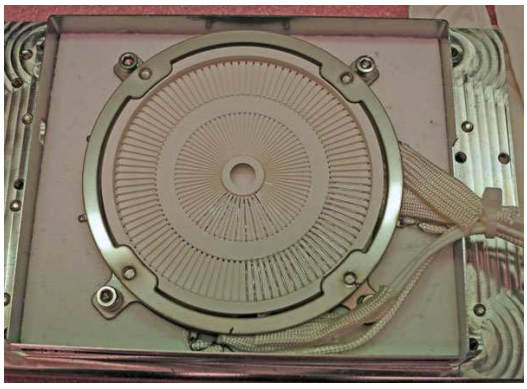

Fig 17: Top view of Isothermal Furnace heater body mounted on XRMON-GF type deck, two heater zones mounted

5.2 Sample containment

The round sample has a diameter of 25mm, and is kept in place by two sample holders in Glassy Carbon (graphite).The sample extends over the complete inner heater ring, and this can be used to fine-tune if any in-homogeneities are seen in the sample temperature (Fig.18 and Fig.19).

Fig 18: Lid with sample compartment

Fig 19: Heater body with sample and graphite sample holders

5.3 Image acquisition

Since the material used in this experiment is almost the same as used in XRMON-SOL, the same imaging parameters as used for XRMON-GF can also be applied for XRMON-SOL.

The field of view in the breadboard set-up was Ø4.5 mm during the evaluation session. The resulting magnification factor was approximately 6. Fig.20 shows the equiaxed grains distribution at a given time during the solidification phase.

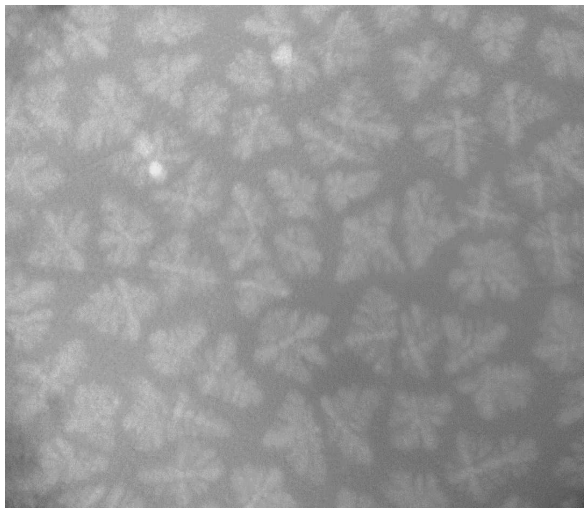

Fig 20: Test in XRMON-SOL first breadboard furnace

6. XRMON PARABOLIC FLIGHT FACILITY

On the initiative from ESA the spare parts from XRMON-GF has been utilised for building up a facility with the same characteristics as the sounding rocket module, but adapted for parabolic flights. Parabolic flight requires additional demands on structural strength and personnel safety compared to sounding rockets.

This system consists of two parts: The Experiment Rack containing the X-ray diagnostic system, a system for providing inert gas atmosphere and X-ray safety devices.
The experiment is controlled from the Operator Rack where the control system for the furnace, the solidification interface and the image system are situated.
The Experiment Rack is designed to be easily adapted to house future furnace developments.

The entire system is also designed to allow for scientists to operate it in their own home-lab, in preparation for future parabolic flight campaigns. This enables a more advanced pre-testing before future sounding rocket and possibly ISS missions.

Fig 21: Parabolic flight facility

7. ACKNOWLEDMENTS

This research work is supported by the XRMON project (AO-2004-046) of the MAP program of the European Space Agency (ESA).

8. REFERENCES

1. Spittle, J. A. Columnar to equiaxed grain transition in as solidified alloys; *International Materials Reviews* **2006**, *51*, 247.
2. Davis, S. H. Hydrodynamics Interactions in Directional Solidification; *J. Fluid Mech.* **1990**, *212*, 241.
3. Hurle, D. T. J. *Interactive Dynamics of Convection and Solidification*; Kluwer Academic: Pays-Bas, 1992.
4. Nguyen Thi, H.; Dabo, Y.; Drevet, B.; Dupouy, M. D.; Camel, D.; Billia, B.; Hunt, J. D.; Chilton, A. Directional Solidification of Al-1.5wt% Ni alloys under diffusion transport in space and fluid flow localisation on Earth; *J. of Crystal Growth* **2005**, *281*, 654.
5. Drevet, B.; Nguyen Thi, H.; Camel, D.; Billia, B.; Dupouy, M. D. Solidification of Aluminum-Lithium Alloys near the Cell/Dendrite Transition - Influence of Solutal Convection; *J. Crystal Growth* **2000**, *218*, 419.
6. Mathiesen, R. H.; Arnberg, L.; Ramsokar, K.; Weitkamp, T.; Rau, C.; Snigirev, A. Time-resolved X-Ray Imaging of Dendritic Growth in Binary Alloys; *Phys. Rev. Lett.* **1999**, *83*, 5062.
7. Schenk, T.; Nguyen Thi, H.; Gastaldi, J.; Reinhart, G.; Cristiglio, V.; Mangelinck-Noël, N.; Klein, H.; Härtwig, J.; Grushko, B.; Billia, B.; Baruchel, J. Application of synchrotron X-ray imaging to the study of directional solidification of aluminium-based alloys; *Journal of Crystal Growth* **2005**, *275*, 201.
8. H. Nguyen-Thi, G. Reinhart, G. Salloum Abou Jaoude, R. H. Mathiesen, G. Zimmermann, Y. Houltz, D. Voss, A. Verga, D. J. Browne, and A. G. Murphy, "XRMON-GF: A novel facility for solidification of metallic alloys with in situ and time-resolved X-ray radiographic characterization in microgravity conditions," J. Cryst. Growth **374** (0), 23-30 (2013).
9. A. G. Murphy, G. Reinhart, H. Nguyen-Thi, G. Salloum Abou Jaoude, and D. J. Browne, "Meso-scale modelling of directional solidification and comparison with in situ X-ray radiographic observations made during the MASER-12 XRMON microgravity experiment," Journal of Alloys and Compounds **573** (0), 170-176 (2013).

RESULTS FROM LOW-GRAVITY AND NORMAL GRAVITY EXPERIMENT "TRACE+" ON DENDRITIC GROWTH AND THE COLUMNAR-EQUIAXED TRANSITION IN THE TRANSPARENT ALLOY SYSTEM NPG-DC

Laszlo Sturz, Martin Hamacher, Gerhard Zimmermann

ACCESS e.V., Intzestrasse 5, 52072 Aachen, Germany, Email: L.Sturz@access-technology.de

ABSTRACT

In 2011 the experiment "TRACE+" (TRansparent Alloys in Columnar Equiaxed Solidification +) has been carried out onboard the sounding rocket TEXUS-49 in low-gravity environment. The experiment is a modification of the previous experiment "TRACE" on TEXUS-47.

Both experiments aimed at investigating dendritic growth and the transition from columnar to equiaxed solidification in the transparent organic alloy system Neopentylglycol (NPG)-(D)Camphor (DC). As major difference the alloy concentration was changed from 37.5 to 20.0 wt.-% DC to investigate the concentration effect on the aforementioned phenomena. Furthermore some hardware improvements were carried out to enhance the image quality, as well as to increase the fluid flow amplitude on earth. All relevant experimental parameters like thermal gradient, solidification velocity and undercooling within the bulk liquid and at the columnar dendritic tips, as well as equiaxed grain density have been determined directly from the experiments.

Here we present a summary of some of the experimental results of the TRACE+ experiment, including a comparison with reference experiments carried out under terrestrial gravity conditions. The results will serve as precise benchmark data for a comparison with different theoretical models.

1. INTRODUCTION

Liquids cooled below their freezing temperature often exhibit a complex microstructure during solidification at the interface between liquid and solid. In liquid metallic alloys these tree-like dendrites form a network with primary stems and higher-order branches. Characteristic length scales of the dendritic microstructures are within the sub-millimetre range (distance between primary dendrite stems) and the micrometer range (dendrite tip radii). The dendritic networks may form extended grains in a solidifying material. Ultimately, microstructure and grain-structure formation is, among others, of fundamental importance for the mechanical properties and casting defects of a final product. In addition dendritic microstructures are interesting from a fundamental point-of-view as examples for pattern formation in non-equilibrium systems.

Columnar and equiaxed dendritic grains are distinguished from their physics of formation and appearance in solidified materials. Columnar grains show primary dendrite stems growing continuously in a favourable crystallographic orientation towards the direction of an applied thermal gradient. The primary stems develop higher order side-arms and branches during growth. Interacting columnar grains thus have an elongated shape ("columns") in the primary stem growth direction. Equiaxed dendritic grains can form within a sufficiently undercooled isothermal melt. Usually, nucleation of equiaxed dendrites in the undercooled melt is related to heterogeneities, impurities or inoculants. Other sources without nucleation are fragmented branches from existing grains, transported by convection or buoyancy into undercooled regions, where they can grow. Equiaxed grains do also have a branched structure, but a generally more isotropic shape ("equiaxed").

Usually, for given alloy composition and properties either columnar or equiaxed grain growth is favoured in dependence of experimental parameters (i.e. thermal gradient, cooling-rate). Sometimes a mixed zone with both columnar and equiaxed grains is observed in competitive growth. As a simplified rule-of-thumb, the grain structure tends to be equiaxed, when G/v is decreased, with G being the thermal gradient in growth direction and v the solidification velocity, respectively. In technical applications like casting, experimental parameters are in general not constant, leading to transient conditions in which a transition from columnar to equiaxed grain growth ("CET") can be observed. Such a transition is not desired for a product since larger changes in mechanical properties can occur at the transition zone. Experiments with forced transitions, like the one described here are thus aimed to investigate the conditions and physical mechanisms at the CET to improve predictions for stable processing windows with either columnar or equiaxed growth.

With entropies of fusion ΔS comparable to metals ($\Delta S/R \leq 2$, $R=8.31\ \mathrm{Jmol^{-1}K^{-1}}$) some organic alloys exhibit similar dendritic structures upon solidification. These alloys are often transparent to visible light,

Proc. '21st ESA Symposium European Rocket & Balloon Programmes and Related Research', 9–13 June 2013, Thun, Switzerland (ESA SP-721, October 2013)

making them suitable to observation with light microscope optics. This allows in-situ and real-time observation of microstructure and grain formation down to the micrometer scale.
Gravity induces sedimentation or buoyancy of particles or equiaxed grains of sufficient size, depending on the density difference between them and the surrounding liquid. Gravity can also force convective motion of the melt and suspended particles in thermal or solutal instable configurations additional to transport of heat and chemical species by diffusion. In low-gravity conditions these effects can be minimized and growth is dominated by diffusive conditions. This allows for simplified experimental boundary conditions. Thus, such experiments serve as benchmarks for analytical and numerical dendrite growth and CET models under diffusive conditions. Furthermore the reference experiments on ground are aimed to characterise the additional gravity effect.
On the sounding-rocket TEXUS-49, flown in 2011, a low-gravity benchmark experiment on columnar dendritic growth and the CET was performed in the binary transparent organic model alloy NPG-20.0 wt.-%DC. This experiment, called "TRACE+" (TRansparent Alloys in Columnar Equiaxed Solidification +) was a technical and experimental modification of the experiment "TRACE" [1, 2] carried out on TEXUS-47 in 2009 using the same alloy, but decreased DC-concentration (37.5 wt.-% DC in "TRACE") and different experimental conditions. Hence, one aim of the investigations presented here is focused on the concentration dependence of dendrite growth and the CET. In addition to the low-gravity experiments, a series of three reference experiments on ground with identical experimental conditions to the low-gravity experiment were performed.
The experimental set-up, modifications and methods are explained in section 2, while results of low-gravity and reference experiments are summarized and discussed in section 3. Conclusions and an outlook are given in section 4.

2. EXPERIMENTAL PART

2.1. Alloy preparation and properties

The preparation and alloying of the organic materials have been described elsewhere [1, 2]. Fig. 1 shows the binary phase-diagram of the NPG-DC system, taken from [3]. The purified materials have been alloyed as NPG-20.0 wt.-% DC and sucked into a gas-tight glass-syringe, which is sealed afterwards for further use. The choice of the alloy composition (20.0 wt.-% DC) is a compromise between (i) the boundary condition to start solidification during the low-gravity period from a homogenized liquid state of the alloy, (ii) the available low-gravity time of about 6.5 min. on the sounding rocket TEXUS demanding a certain interval of cooling-rates to obtain CET and (iii) the maximum operational temperatures of some hardware elements of about 140°C, limiting the available axial temperature gradients within the sample.

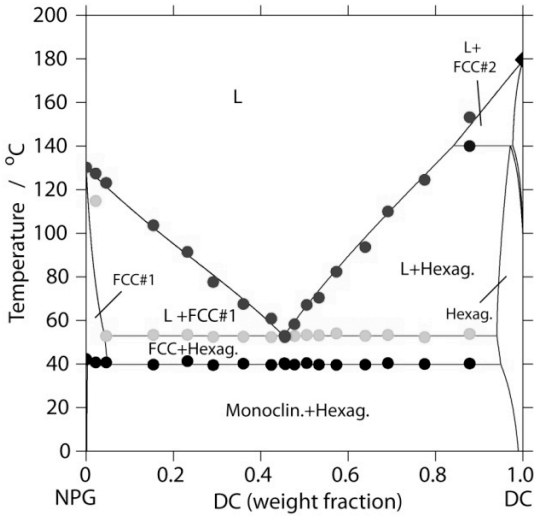

Figure 1. Phase-diagram of NPG-DC. Alloy chosen is NPG-0.20 wt.-fraction DC. L=Liquid, FCC = face-centred cubic (phases).

Tab. 1 summarizes the relevant alloy properties, adapted and updated from [2, 3] or due to new references.

Table 1. Relevant thermodynamic and thermophysical properties of the NPG-20.0wt.-%DC alloy.

Property	Value
Liquidus-temperature T_L	95.1±1°C[(a)]
Solidus-temperature T_S	52.9±0.5°C[(a)]
Transfomation temperature (FCC-monocl.)	39.9±0.5°C[(a)]
Liquidus-slope m_L	-1.59 K/wt%[(a)]
Partition-coefficient k	0.061[(a)]
Gibbs-Thomson-coefficient Γ	(7.5±0.7)*10^{-8} Km[(b)]
latent heat L (Liquid-FCC)	3.5*10^4 Jkg^{-1}[(a)]
heat of transformation (FCC-monoclinic)	9.4*10^4 Jkg^{-1}[(a)]
Thermal conductivity liquid λ_L	0.17 WK^{-1}m^{-1}[(c)]
Thermal conductivity solid λ_S	0.28 WK^{-1}m^{-1}[(c)]

(a): from thermo-dynamic CALPHAD-description [3]; (b): [4]; (c): interpolated from [5].

2.2. Experimental set-up and procedure

The current experimental set-up is based on previously used hardware developments by EADS/Astrium for sounding rockets investigating planar and cellular growth in transparent model alloys [6, 7], as well as dendritic growth and the CET in NPG-37.5 wt.-%DC [1, 2]. For the experiment "TRACE+" on TEXUS-49 the experimental volume was contained in between a

steel frame and two quartz-glass plates. The experimental volume size is 13 mm in width, about 10 mm in height and 3 mm in thickness. Compared to the previous experiment "TRACE", the height and width of the experimental volume were decreased, while the depth of the sample was increased from 1 to 3 mm. By the latter the effect of gravity driven convective flow on ground is enlarged by less viscous friction in the sheet-like cell. A bottom inlet and top outlet in the steel frame supports feeding of the pre-molten alloy and volume compensation during thermal and phase-change shrinkage and expansion to avoid bubble formation. Three thermocouples type K of 0.25 mm diameter were inserted through holes at one side of the frame to follow the temperature evolution during the experiment within the alloy at different y-positions of 1.32±0.025 mm, 4.89±0.025 mm and 8.35±0.025 mm, measured from the bottom of the experimental volume. The points of temperature measurements within the thermocouples were located at 2.25±0.10 mm distance from the edge of the cell. The acquisition rate of the thermocouples was 10 Hz. Due to the small size of the thermocouples, their lateral insertion and position we do not expect the thermocouples to influence the thermal field or the nucleation events significantly.

A schematic drawing of the set-up is given in Fig. 2. The experimental volume was illuminated from one side with monochromatic LED-light and observed with two different optical systems: A beam splitter provided a microscopic observation of solidification details within a movable field-of-view of 2.25 mm width and 1.70 mm height, while in parallel an overview image with field-of-view of 18.2 mm width and 13.7 mm height was acquired.

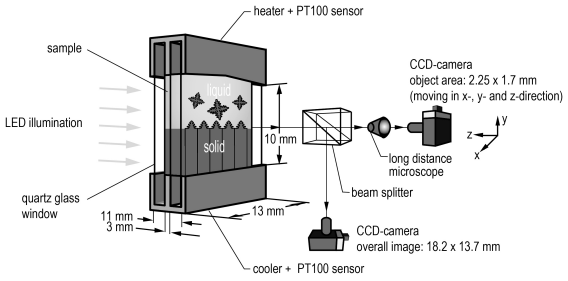

Figure 2: Schematic drawing of the main parts of the experimental set-up. Reference coordinate system for evaluations.

The experiment was controlled from the bottom with a Peltier-cooler and from the top by a resistance heater, both using PT-100 temperature sensors with locations at some distance from the edges of the experimental volume. The alloy-containing syringe was connected to the experimental cell via an inert steel tube. The cell was filled with the molten alloy material in the pre-heated syringe without bubbles and allowed for fast solidification to avoid segregation effects upon first freezing. For mixing an additional heater at one side of the cell was switched on to force convection by a lateral temperature gradient.

Tab. 2 summarizes the experimental procedure for "TRACE+". Before lift-off the cell was oriented vertically upwards in the payload and in the gravity field. The images of both of the cameras, as well as the house-keeping data and thermal data from the thermocouples were transmitted during the complete experimental run on ground and during flight, except small time-intervals after lift-off and re-entry of the rocket. Furthermore the detail images were stored digitally on-board with higher resolution than those transmitted to ground with standard video resolution. The corresponding three reference-experiments on ground were carried out after the flight experiment with the identical experimental procedure as given in Tab. 2 (except an adapted rate for the heater temperature decrease, see section 3.5) and solidification vertically upwards during the complete experiment.

The CET was intended to be provoked externally by increasing the cooling-rate at both the cooler and the heater (from -2.5 to -6.5 $Kmin^{-1}$). In addition to the CCD-images of both cameras, following scientific parameters were obtained from these or the available data as functions of experimental time: (i) gravity level, (ii) equiaxed dendrite density, (iii) equiaxed, columnar and liquid volume fractions at the growing interface, (iv) cooling-curves and thermal gradients, and (v) the solid-liquid front positions. From these data the front velocity and front undercooling can be calculated.

Table 2. Experimental procedures for the low-gravity experiment (similar for reference experiments). The times refer to lift-off of the sounding-rocket at t=0 s.

Time	Action
≅- 1h25 min.	Complete melting of the alloy from RT. T_H=105°C, T_C=85°C.
≅- 50 min.	Thermal mixing by convection. T_H ≅100°C, T_C =100°C. With side heater.
≅- 22 min.	Equilibration in liquid state, T_H =133°C, T_C =88°C.
= -90 s.	Setting of bottom and top cooling at -2.5 $Kmin^{-1}$.
0 s.	Rocket lift-off, high accelerations.
<+ 60 s.	Burn-out of rocket stages, de-spinning and stabilization of rocket.
>+ 66 s.	Gravity level < 1 mg.
≅+90 s	First crystals at the bottom, columnar growth
+ 255 s.	Initiation of CET: Cooling-rate increased from -2.5 to -6.5 $Kmin^{-1}$.
+ 450 s.	Re-entry of rocket, end of low-gravity period, gravity level > 1 mg

T_H: Heater temperature, T_C: Cooler temperature, RT=room temperature.

3. RESULTS AND DISCUSSIONS

3.1. Gravity level

The gravity level was measured within the payload of the TEXUS-49 rocket along three axes (one along the rocket axis). Following high accelerations during lift-off, the gravity level dropped below ±1 mg for all axes at about 65 s after lift-off and fell below ±0.4 mg for all axes some seconds later and kept at this level till the re-entry of the rocket into atmosphere at about 450 s. The interval 66 s to 450 s is defined as the low-gravity period of 384 s duration (<±1 mg) here.

3.2. CCD-images

Fig. 3 shows a sequence of overview and corresponding detail CCD-images obtained from the "TRACE+"-experiment at selected time-steps (Fig. 3a-c) and at one time-step for one of the reference experiments (REF#2) (Fig. 3d). In the overview images the three thermocouples are visible on the left-hand side. The conical shape of the top-part of the cell allows for gathering of bubbles filled with mainly DC-vapour, followed by dissolution in the liquid during melting of the alloy in the first stage of each experiment. The width of the experimental volume (13.0 mm) is the reference length for all position measurements. Focused microstructures are obtained in the overview images, with a resolution of about 24 µm per pixel in the image-plane. The focus depth covers the complete depth of the sample. In the detail images, shown as inlets in the overview images, several dendritic columns can be observed at different depth positions behind each other (Fig. 3c). A smaller focus depth does not allow for viewing all of them as sharp images, but the focal position can be changed during the experiments to focus on specific details. The resolution in the detail images is 1.6 µm per pixel.

The first image at t=+100 s shows nucleation of first crystals of NPG solid-solution (NPG-1.2wt.-%DC) at the bottom of the experimental cell with random orientations. In the second image at t=+250 s the columnar dendritic front can be observed close to the lowest thermocouple T3. Columnar grains having crystallographic orientations (i.e. <100> direction of the FCC crystal) close to the y-direction are favoured in the columnar front propagation, but a multi-grain structure with slightly different levels of undercooling and grains tilted up to about 30° (projected to the image plane) from the y-axis remains. After increase of the cooling-rate to nominally -6.5 $Kmin^{-1}$ at t=+255 s a relatively small amount of equiaxed crystals occurs ahead of the columnar front, shown here at t=+400 s. A slightly curved solid-liquid interface is also observed towards the lateral edges of the experimental cell, due to a heat-flux from the centre to the edges at the higher cooling-rate. A small temperature-shift (~1 K) between the temperature measured at the middle thermocouple and the identical vertical position in the lateral centre of the sample is thus present in this period of the experiment. A flat interface is observed in a centred area of width 8 mm, which is used for further analysis. The reference experiment (REF#2) shows a similar behaviour (the time-shift of 2 s in the images is negligible here), except the significantly higher average columnar front position, as can be seen in the difference between images (c) and (d). Further reference experiments are very close (REF#3) or close (REF#4) to REF#2 and are not shown explicitly here as images.

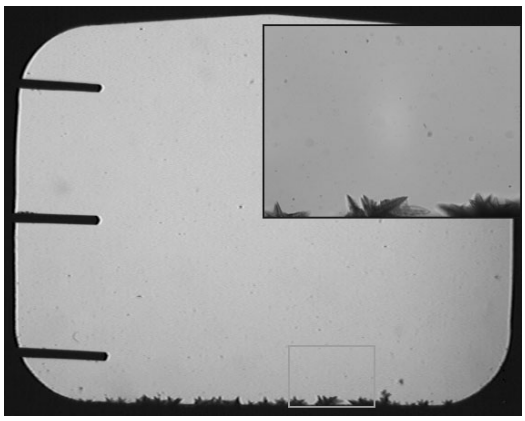

(a) t=100 s, randomly oriented crystals.

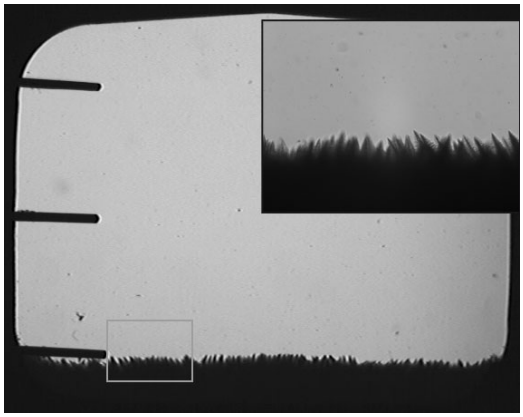

(b) t=250 s, columnar dendritic growth.

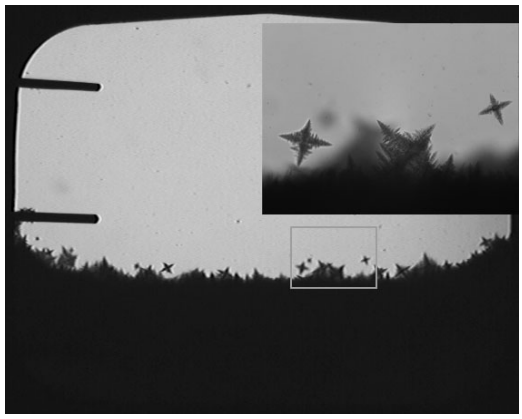

(c) t=400 s, columnar and equiaxed growth.

(d) t=402 s, columnar and equiaxed growth (REF#2).

Figure 3. Selected overview and detail CCD-images, shown as inlets. All times refer to lift-off (t=0 s).

3.3. Nucleation process and equiaxed grain density

As already observed in [1], no fragmentation of dendrite arms from the columnar front occurs. Heterogeneous nucleation on unknown substrates is the nucleation mechanism. Similarly, it was observed (for example see Fig. 3c), that the equiaxed dendrites nucleated at different axial y-positions within the temperature field. The corresponding nucleation temperatures are within a certain range, which could be attributed to substrates of either different size or type.

Here, we determined the number-density (grain density) of equiaxed dendrites in time. The volume of analysis has a centred width of 8 mm, and extends from the lowest visible liquid area in the columnar front into the liquid up to the uppermost visible equiaxed dendrite. We recall that the pixel resolution in the observation plane is about 24 µm, thus dendrites/nuclei of smaller size cannot be detected or observed in overview mode. Equiaxed dendrites engulfed into the growing columnar front with more than about 50 area% were not taken into account in the analysis. Fig. 4 shows the results for the equiaxed dendrite density for "TRACE+" and one of the reference experiments "REF#2".

No continuous increase of the equiaxed grain density is found in both experiments, as could have been expected from the increase of the external cooling-rate and a certain distribution of nucleation undercooling, as already found in [1]. While several maxima are found in "TRACE+" in low gravity environment, we observe only one obvious in "REF#2" on ground. The absolute maxima are about 0.9 grains per mm^3 and about 0.6 grains per mm^3, respectively. At the end of the microgravity period, the number of new equiaxed grains is decreased significantly in both cases. The overall smaller grain density in the reference experiment is attributed to a lower front (and thus bulk) undercooling (see sec. 3.6). In general, we face a different situation, as compared to "TRACE". In the latter we observed a continuous increase of the density in both experiments. The equiaxed grain densities obtained here are comparable with up to 0.5 grains per mm^3 in "TRACE" and 0.7 grains per mm^3 in the corresponding reference experiment, respectively at the end of the low-gravity periods.

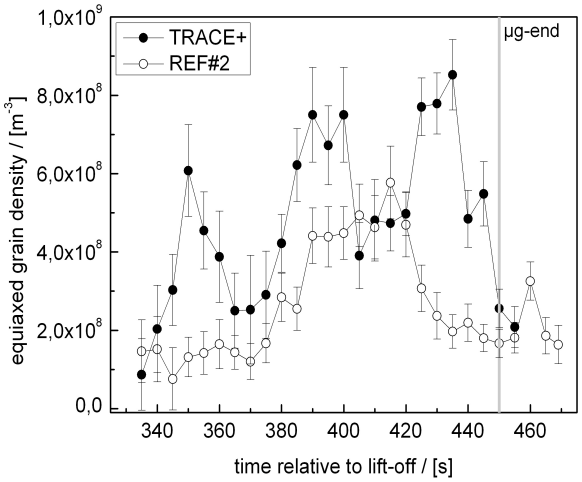

Figure. 4. Equiaxed grain densities; error bars correspond to the combined effect of counting errors of ±1 and an estimated error in the volume of analysis of 5%.

3.4. Equiaxed volume fraction

In addition to the grain density, the volume fraction of liquid, columnar and equiaxed grains at the advancing front was analysed for comparison with "TRACE" and with theoretical predictions under diffusive conditions. The method is given in detail in [1]. In Fig. 5 the volume fractions of equiaxed grains ϕ_E are given as a function of time, for two different values of h, where h is the distance from the uppermost dendrite tip position to the upper boundary of the area of analysis (width 8 mm). The higher value (h=0.5 mm) was used for "TRACE" and corresponded to about the average primary stem spacing there. Here the average primary stem spacing is λ_1=0.14 mm, measured in the columnar growth regime (i.e. Fig. 3b). Thus a comparison is carried out with a lower value of h=0.25 mm, to check the sensitivity of the result against the choice of h. In the range investigated the results do not depend much on the parameter h, as can be seen in Fig. 5.

As also observable in the equiaxed grain density (and there more pronounced for µg), the equiaxed volume fraction shows some kind of oscillatory behaviour in time. The highest volume fraction determined (ϕ_E=0.22-0.24) is comparably smaller than in "TRACE" (ϕ_E=0.36), obtained by the same method. The obtained equiaxed volume fraction is at the lower limit of model predictions for mechanical blocking as

the CET-mechanism [8]. Nevertheless, this assumption of simple mechanical blocking is questionable.

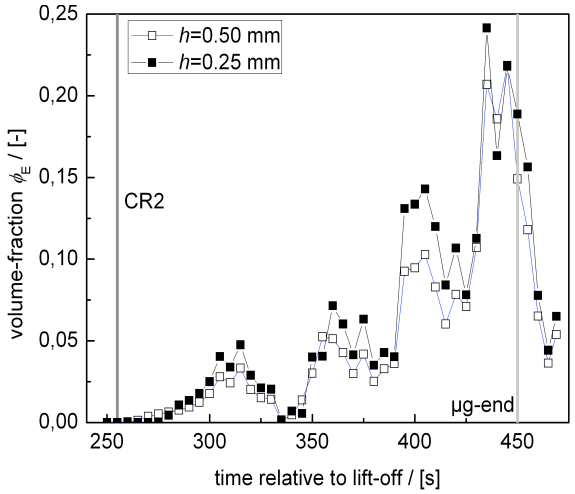

Figure 5. Equiaxed volume fractions for different heights h in the volume of analysis for TRACE+, CR2=application of -6.5 Kmin^{-1}.

3.5. Thermal data

Fig. 6 shows the temperature evolution at the control points (T_H, T_C) in the heater and the cooler for "TRACE+" and the cooling curves measured at the three thermocouples T1 to T3 for "TRACE+" and "REF#2". The temperature evolutions during the first stages of melting, mixing and equilibration are not shown explicitly here and correspond to t < -100 s. Beside the general decreasing temperature trend after application of the lower cooling rate (CR1), two important features are obvious in Fig. 6:

(i) The heater control was not able to perform the required -6.5 Kmin^{-1}, resulting in a lower constant cooling rate of -4.5 Kmin^{-1} (solid red line). The reason for this difference is the missing convective air-cooling in low-gravity, which was not taken into account sufficiently in the experimental preparation on ground. As a result the thermal axial gradient within the experimental cell increased in time after applying the high cooling-rates (CR2). The cooler temperature kept at the nominal rate. To perform the reference experiments with identical conditions, the cooling-rates at the heater were adjusted to equal -4.5 Kmin^{-1}.

(ii) Secondly, the temperatures measured at the thermocouples between lift-off (t=0 s) and beginning of the low-gravity period (t=66 s) show a significant deviation from nominal decrease. This is attributed to the controlled de-spinning of the sounding rocket at the end of the rocket boost phase and the inertia of the liquid in the cell reacting to the de-spinning and leading to a convective motion and partial thermal mixing. It was observed in the CCD-images, that the convective motion in the melt was slowing down rapidly (~20 s), while the thermal field was rebuild on a longer time-scale (about 50 s). First equiaxed crystals are observed at t=+90 s (Fig. 3a), where fluid motion was completely stopped and the thermal field almost re-established. In the low-gravity period the temperature differences between low-gravity and reference experiment REF#2 are <0.75 °C for the thermocouples T1-T3. Since the occurrence of equiaxed grains ahead of the columnar front occurs mainly between the lowest (T3) and the middle thermocouples (T2), the thermal gradients $G_{23}(t)$ between these thermocouples are calculated from the measured temperature differences and their distance of 3.57 mm (Fig. 7). $G_{23}(t)$ is similar for all four experiments within the time corresponding to the low-gravity regime. An increase is observed from 2.75 to 3.50 Kmm^{-1} after CR2, as discussed above. The differences between the reference experiments and "TRACE+" in the obtained gradients were smaller than 0.1 Kmm^{-1} in that regime.

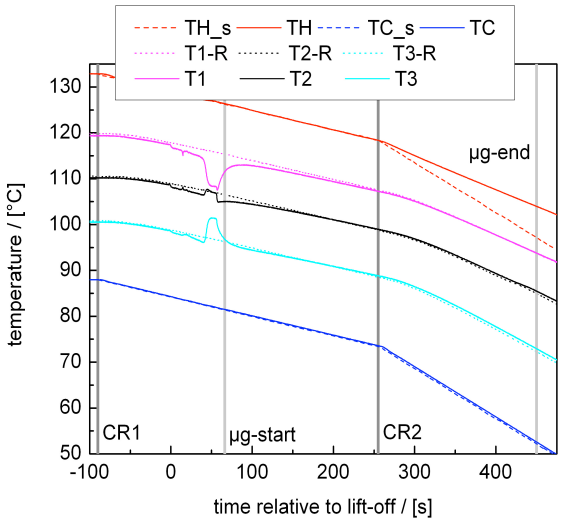

Figure 6. Temperatures in the experimental cell and at cooler and heater, CR1/2 =application of cooling-rate 1/2, dashed line=set-temp., dotted-lines: REF#2.

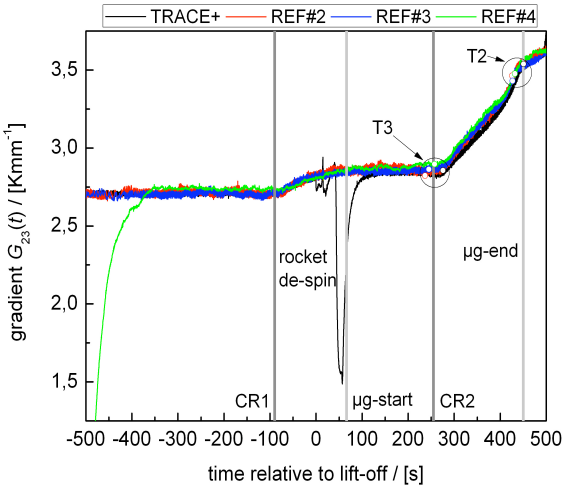

Figure 7. Temperature gradient $G_{23}(t)$ between thermocouples T2 and T3 for "TRACE+" and the reference experiments REF#2 to REF#4, CR1/2=setting of cooling rate 1/2. T2 and T3 mark the positions, when the fronts pass the position of the thermocouples 2/3.

3.6. Front position, velocity and undercooling

The position of the front is obtained by automatic image processing from the overview CCD-images in the centred 8 mm of the 13 mm wide sample. The positions are averaged and the average curves are shown in Fig. 8, standard deviations are within 0.25 mm (not shown here as error bars). The front-velocities are derived from the point-by-point derivatives of the averaged front-positions and shown in Fig. 9. The front-temperatures are derived from the front positions and linear interpolation of the measured temperatures for the two thermocouples below and above the front. The front undercooling is calculated from the difference of the front-temperature to the liquidus-temperature of T_L=95.1±1°C taken from differential scanning calorimetry measurement and is shown in Fig. 10. The extrapolation of undercooling below T3 is based on a gradient estimation, using the average gradient between T2 and T3.

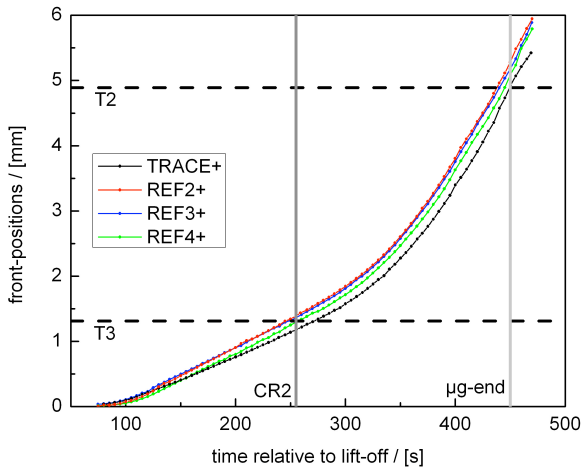

Figure 8. Front-positions for "TRACE+" and reference experiments REF#2 - REF#4. T2/3 = thermocouple positions, CR2= application of -6.5 Kmin^{-1}.

From Fig. 8-10 we observe significant differences between the low-gravity and the corresponding reference experiments. The difference in the front-position was already visible in Fig. 3c/d and is attributed to the presence of convective flow. In Fig. 9 all front velocities are shown. At t=255 s the cooling rate is increased to -6.5 Kmin^{-1}. Here, all front velocities have not approached steady-state speed, which is represented by the corresponding measured isotherm velocity V_{T3}. In Fig. 10 the undercooling of the front rises within the columnar growth regime at constant thermal gradient and cooling-rate, until the application of the higher cooling-rate (t=255 s). The solute pile-up (and hence the undercooling) is also not in equilibrium at that point, according to the slope of the $\Delta T(t)$-curves at 255 s. The undercooling increases further towards a maximum and decreases again. The latter is due to the undesired increase of the thermal gradient (Fig. 7). Without this a further increase in the undercooling would have been expected, leading to a higher number of equiaxed grains and a more pronounced transition from columnar to equiaxed dendritic growth.

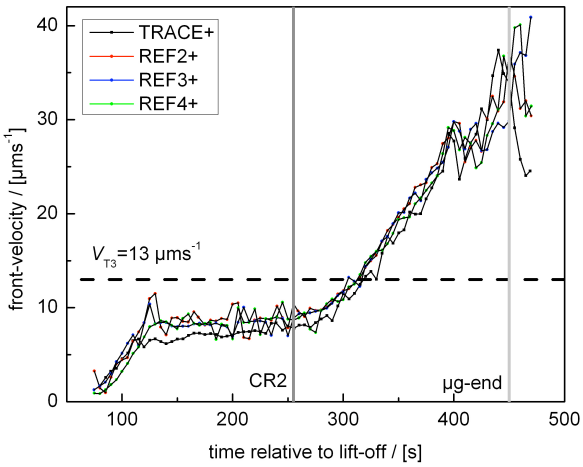

Figure 9. Front-velocities for "TRACE+" and reference experiments REF#2- REF#4. V_{T3} corresponds to the isotherm velocity at T3 at +255 s.

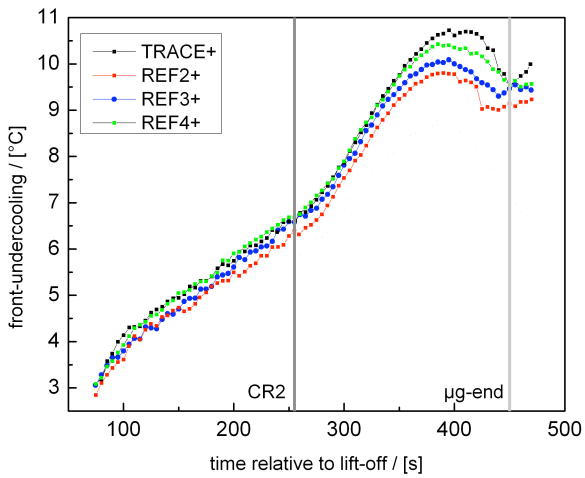

Figure 10. Front-undercooling for "TRACE+" and the reference experiments REF#2 - REF#4.

The convection observed in the reference experiments does not change the thermal field significantly (see Fig. 7), but changes the solute concentration field of DC ahead of the columnar front and at the columnar

dendrite tips. This leads to a different solutal (and front) undercooling of the columnar dendrites in the dendritic front and a different solidification velocity. This finally explains the change in the columnar front-position (Fig. 3c-d and Fig. 8).

4. CONCLUSIONS AND OUTLOOK

Dendritic growth and the transition from columnar to equiaxed growth regime were investigated within the organic alloy NPG-20.0 wt.-%DC onboard the sounding rocket TEXUS-49. Following first conclusions were drawn from the results of the experiment "TRACE+" presented here:

- A stable gravity level of less than ±0.4 mg was obtained within a period of 384 s.
- The hardware worked nominally except an undesired decrease of the heaters' cooling rate.
- A clear CET was thus not obtained, although equiaxed dendrites occurred, but with low volume fraction (~0.22-0.24).
- Data analysis and images show clear gravity-related differences between the low-gravity experiment "TRACE+" and the reference experiments, attributed to convective flow on earth.

Further analysis will include the kinetic relationship for columnar and equiaxed dendrites in detail, as well as the comparison with models and with the formerly conducted experiment "TRACE" with higher DC-concentration.

ACKNOWLEDGEMENTS

This work was financially supported by the German Space Agency DLR under grants no. 50 WM 0843 and FKZ 50 WM 1143, which is gratefully acknowledged. The authors appreciate the Team of EADS-Astrium for the hardware development and support during the preparatory and final experiments. SSC, DLR-Moraba and Kayser-Threde are acknowledged for mission support at Esrange/Sweden.

REFERENCES

1. L. Sturz, G. Zimmermann., "Comparison of results from low-gravity and normal gravity experiment "TRACE" on the columnar-equiaxed transition in the transparent alloy system neopentylglycol-camphor", Proceedings of 20th ESA Symposium on European Rocket & Balloon Programmes and related research, 22-26 May 2011, Hyeres, France, ESA SP-700, 459-466.
2. L. Sturz, G. Zimmermann: "In-situ and real-time investigation of the columnar-equiaxed transition in the transparent alloy system NPG-DC onboard the sounding rocket TEXUS-47", Journal of Physics: Conference Series 327, p. 012002, 2011.
3. Witusiewicz V.T., Sturz L., Hecht U. and Rex S., "Thermodynamic description and unidirectional solidification of eutectic organic alloys: III. Binary systems neopentylglycol-(D)camphor and amino-methyl-propanediol-(D)camphor", *Acta Mat.*, vol. 52 (19), 5519-5527, 2004.
4. Bayram, U., Aksoz, S., Marasli, N., "Solid-liquid interfacial energy of neopentylglycol solid solution in equilibrium with neopentylglycol-(D) camphor eutectic liquid", J. Cryst. Growth, vol. 338, p. 181-188, 2012.
5. Bayram, U., Aksoz, S., Marasli, N., "Dependency of thermal conductivity on the temperature and composition of D-camphor in the neopentylglycol-D-camphor alloys", Thermochim. Acta, vol. 531, p. 12-20, 2012.
6. A. Weiß, G. Zimmermann, S. Rex, „Investigation on morphological instability during directional solidification on the sounding rocket TEXUS 36", Proceedings 14th ESA Symposium on European Rocket and Balloon Programmes and Related Research, Potsdam, 31 May-3 June 1999, (ESA SP-437), pp. 523-528.
7. L. Sturz, G. Zimmermann, A. Weiß, "Transient Crystal Growth From Planar to Dendritic Interfaces Investigated during TEXUS-40", Proceedings of the 17th ESA Symposium on European Rocket and Balloon Programmes and Related Research, Sandefjord, Norway, 30 May – 2 June (ESA SP-590, August 2005).
8. V.B. Biscuola and M.A. Martorano, "Mechanical Blocking Mechanism for the Columnar to equiaxed Transition", Met. And Mat. Trans A, vol. 39A, 2285-2895, 2008.

CaRu: AN INVESTIGATION OF CAPILLARY ACTION UNDER LOW GRAVITY CONDITIONS THROUGH RUNGE INSTABILITIES

Srinivasa Rangachari Sudarsan[(1)], Christiane Rupf[(1)], Sebastian Meckel[(1)], Marcel Voss[(1)], Daniel Bock[(1)], Lakshminarasimhan Srinivasan[(2)]

(1) Institute for Space Systems and Utilization, Dresden University of Technology, Marschnerstraße 32, 01307 Dresden, Germany, Email: teamcaru@gmail.com
(2) Institute for Robotics and Telematics, Julius Maximilians University, Am Hubland, 97074 Würzburg, Germany, Email: srinivasan@informatik.uni-wuerzburg.de

ABSTRACT

The objective of the CaRu (Capillarity under low gravity shown with Runge pictures) experiment is to examine the effect of low gravity conditions on the capillary effect through investigation of "Runge instabilities". The formation of so-called "Runge" pictures under normal and low gravity conditions is studied. In the experiment, a reactant solution is applied onto chromatographic paper that has been impregnated with a different reactant solution, resulting in the first solution being absorbed into the paper and spreading through capillary action while a chemical reaction occurs, observed in the formation of circles with irregular borders on the surface of the paper. The experiment was launched as a payload on the REXUS-11 sounding rocket. In this paper, an overview of the CaRu experiment and its results are presented.

1. INTRODUCTION

Capillarity under low gravity is of interest because it can be used to transport fluids such as fuel in spacecraft. Experiments on the International Space Station (ISS) such as the "Capillary channel flow" experiment [1] are aimed at characterizing this effect for use in applications such as pumps without any moving parts. Other experiments focus on the study of the capillary effect in plants which might prove important when attempting to cultivate flora in extraterrestrial bodies. Despite this interest in capillarity, an experiment centered on the study of Runge instabilities has, under low gravity conditions, not yet been conducted. In addition, research on Runge pictures provides an interesting conjunction of science and art, as Runge pictures were referred to as "pictures that grow by themselves" [2] by their discoverer Dr. F. F. Runge.

The aim of the CaRu experiment is therefore, to provide an experimental insight into the development of Runge pictures under low gravity and thereby study the influence on Runge instabilities (see Fig. 1). The Runge instability is deeply connected to the field of capillarity as it describes the irregular borders that are observed, when a fluid A spreads through a porous structure (in CaRu: chromatographic paper) and this fluid A chemically reacts with a fluid B which the porous structure had been impregnated with before. The fluids react to form a coloured precipitate.

Figure 1 Runge picture made with prussian blue, fluid climbing vertically; created by Dr. Kuhnert

Despite the fact that Runge pictures were discovered in the 19th century by Dr. F. F. Runge, who published the book "*Der Bildungsbetrieb der Stoffe"* in 1855 as an compendium of Runge pictures created with different chemicals and under different circumstances, there exists no theoretical model for the creation of Runge pictures. Dr. Lothar Kuhnert (Berlin) and Dr. Enderlein (Department of Physics, Georg August University, Göttingen) started working on the development of a mathematical theory. Unfortunately, Dr. Kuhnert, who had the idea that research on Runge pictures under low gravity conditions could help find a model for their creation, died in August 2012, thus delaying the research. Dr. Enderlein continues to work on the theory, which has not yet reached a state where it could be presented. This paper also takes into reference, the dissertation of Dr. Nicholas Fries [3], whose

Proc. '21st ESA Symposium European Rocket & Balloon Programmes and Related Research', 9–13 June 2013, Thun, Switzerland (ESA SP-721, October 2013)

experimental work on capillary flows provided us with valuable ideas as to how our experiment could be performed.

2. EXPERIMENT DESCRIPTION

2.1 Choice of chemicals

For CaRu, two chemical combinations were under consideration: copper sulfate ($CuSO_4$) and potassium ferrocyanide ($K_4[Fe(CN)_6]$) or ferric ammonium sulfate ($NH_4Fe(SO_4)_2$) along with potassium ferrocyanide ($K_4[Fe(CN)_6]$). After several tests, it was observed that the Runge instabilities were visible more clearly in the first combination (Fig. 2).

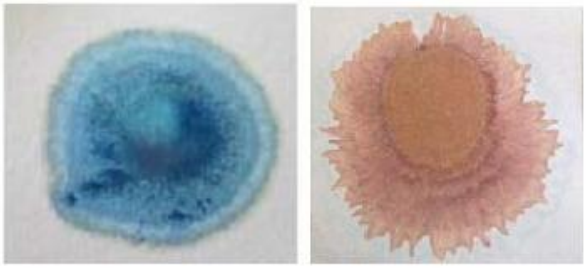

Figure 2 Left: ferric ammonium sulfate and potassium ferrocyanide, Right: copper sulfate and potassium ferrocyanide

The paper was impregnated with an aqueous solution of copper sulphate at a concentration of 1:16 (w/w). One drop of an aqueous solution of potassium ferrocyanide, at a concentration of 1:32 (w/w), was applied to the paper during the low gravity phase. The copper ions (Cu^{2+}) react with ferrocyanide ions ($[Fe(CN)_6]^{4-}$) to form dark orange copper ferrocyanide ($Cu_2[Fe(CN)_6]$), which precipitates. The chemical equation is shown in Eq. 1:

$$2Cu^{2+} + [Fe(CN)_6]^{4-} \rightarrow Cu_2[Fe(CN)_6] (\downarrow) \qquad (1)$$

The Runge instability results from combined effects of surface tension, capillarity and the reaction between both chemicals. The precipitate clogs the capillary transport channels in the microstructure of the paper until the fluid pressure is high enough to break through the clogging, allowing the fluid to spread further.

2.2 Mechanical design

The experiment chamber consists of two parts: the lower part with the bottom and the four walls of a cuboid and a lid. To ensure that the chamber is airtight, a Viton O-ring will be placed between lid and chamber. With the cuboidal shape of the chamber, two electrical vacuum feedthrough connectors are necessary, one for the REXUS interface and a BNC connector for the REXUS TV channel. The connectors are placed on the lid for easy access. This can be seen in Fig. 4.

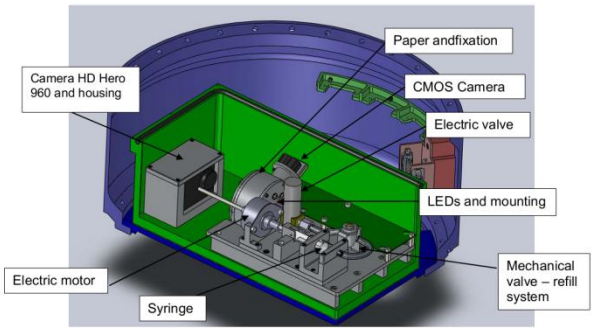

Figure 3 Mechanical CAD model (inside)

All the parts of the experiment are mounted onto a platform which is mounted onto the bottom of the experiment chamber. With this system, we can mount all the components onto the platform and afterwards simply place it in the chamber. This way, mounting is easier. A part of the platform where the experiment is mounted has to be cut out to allow cables from other experiments to pass through. A cross section of the experiment can be seen in Fig. 3.

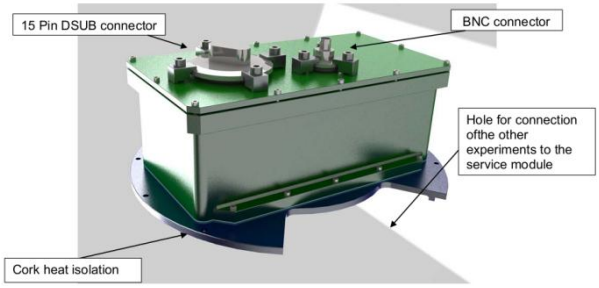

Figure 4 Mechanical CAD model (outside)

After the lid has been screwed shut with headless screws, Loctite 270, a space qualified sealant will be used to support the screws.

A "Remove before flight switch" or an arm plug is necessary to prevent the experiment from running during the testing phase, as there will be no access to the experiment for multiple test runs. This arm plug will be used to electrically separate the "Start of Experiment" (SOE) signal from the corresponding microcontroller pin. This means, irrespective of whether the REXUS service module (RXSM) activates the SOE signal, as long as the arm plug has not been attached to the experiment, the microcontroller will not trigger the events associated with the SOE signal.

A solution similar to one implemented by the team ADIOS was chosen as shown in Fig. 5. A combination of 15 and 9 pin DSUB connectors was used to achieve

SOE signal separation. To gain access to the ArmPlug from outside, it is mounted on the inside of the 150mm module. The 9 pin female DSUB with the bypass is mounted through a drilled hole in the module wall. The opening is closed with a screwed lid from the outside of the module.

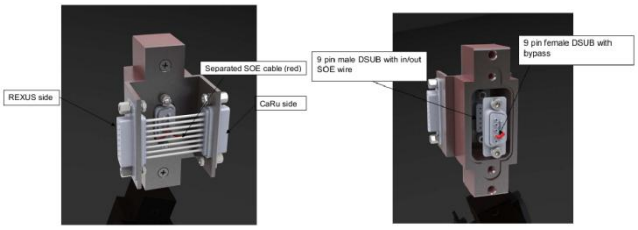

Figure 5 Arm plug design

During the time stored outside, special thermal blankets to guarantee temperatures over 10°C were required. This was to prevent freezing of the liquid inside the syringe and the tubes. To guarantee better heating of the module, a fan heater with closed air circulation around the module was also utilized. To prevent conduction of heat away from the experiment, a 2mm thick layer of cork was used to thermally isolate the experiment base from the module base.

2.3 Electrical design

A block diagram of the electronic system onboard the CaRu experiment is shown in Fig. 6. The RXSM interface provides all the power required for the experiment through the 15 pin DSUB connector. This is then converted to the required voltage levels for various parts of the circuit, such as the electromagnetic valve, linear motor etc. A set of DC/DC converters from TRACO was used, along with input filters according to manufacturer guidelines to reduce electromagnetic interference.

An easily "hackable" camera called the HD Hero from GoPro was chosen as the main video camera. This was interfaced to the microcontroller through optocouplers. A secondary analog video camera was used to prepare output for the REXUS TV channel. This entailed no control from the microcontroller, only the required voltage had to be supplied. Backlighting was provided by a string of white LEDs whose brightness could be adjusted using a pulse width modulated output from the microcontroller.

To drive the syringe, a linear motor from the company Nanotec was chosen. This worked with a 5V supply and produced 55N of thrust. To make sure disturbances from the motor run were not reflected back to the circuit, a separate step down converter was used exclusively for the motor.

Environmental sensors consisted of pressure, temperature and acceleration in 3 axes. These were interfaced to the MSP430 based microcontroller (running on a 16MHz clock) from Texas Instruments. This collected the data from the sensors, added status data about the experiment and produced a data packet to be sent to the RXSM through an RS485 interface. In addition, the microcontroller also waited for the SOE signal, after the rocket achieved the low gravity phase. Once the reception was confirmed, the microcontroller opened the valve and sent signals for the linear motor to actuate the syringe. This could be confirmed through the REXUS TV channel. It was observed later that a defect in the G sensor board prevented it from communicating with the microcontroller. Therefore, the acceleration data for analysis was taken from the GGES experiment, which was positioned below the CaRu experiment.

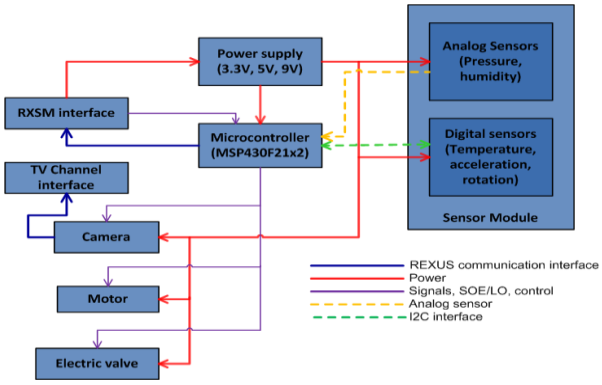

Figure 6 Electronic design

2.4 Software and ground station

A graphical user interface along with a database programmed in Java was developed at the University of Würzburg, to receive, assess and display the received telemetry. The GUI components made use of the Swing graphics library. For serial communication with the experiment, an open source java library called rxtxcomm was used. The database used was Apache Derby and the collected data was stored locally on the ground station computer. For later perusal, any free SQL client such as Emma can be used. The serial data frames are read by the program at the serial port and spurious frames are rejected. The GUI displays live data on the graphs, status data on the indicator lights and also provide buttons for control of various functions on the PCB.

3. EXPERIMENT PROCEDURE

A flowchart showing the sequence of events is shown in Fig. 7. As can be seen, as soon as power is switched on, the microcontroller becomes active, controlling the LEDs, starts collecting sensor data and

sends them to the RXSM interface. After reception of the SOE signal, it opens the valve, actuates the motor, thereby pushing the liquid onto the paper. Following this, the microcontroller sends an updated status message indicating a successful experiment run and then continues to send sensor data to the ground station.

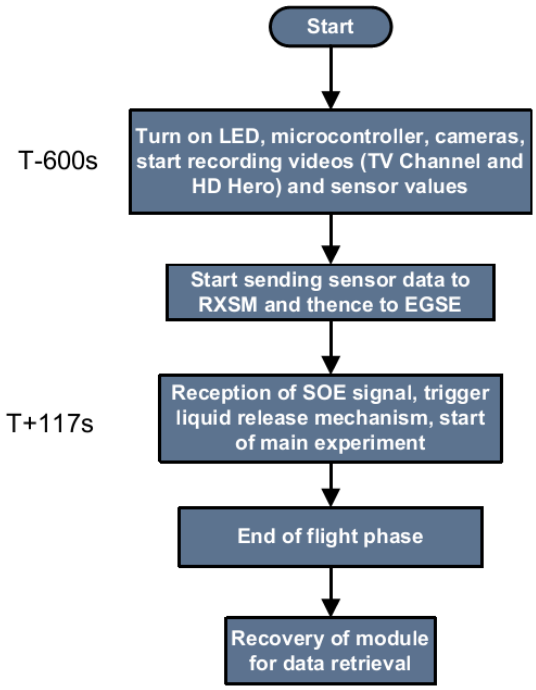

Figure 7 Experiment procedure

4. QUALIFICATION TESTS

The REXUS program mandates a series of qualification tests, consisting of a vacuum test, a thermal test and a vibration test. The first two tests were conducted at the premises of the Institute for Space Systems and Utilization (ILR), Technical University of Dresden, while the vibration test was conducted at the Centre of Applied Space Technology and Microgravity (ZARM) at Bremen University.

4.1 Vacuum test

This test was very important as the pressure chamber must never burst or break open, thus endangering the integrity of the rocket and possibly, the other experiments. Because of low pressure, if the vacuum chamber were to fail for some reason, the rocket and possibly the other experiments would be endangered. Because of the low pressure, the liquids used in the experiment would evaporate immediately, leading to contamination of the printed circuit board (PCB) or the other experiments. The conditions imposed on the experiment according to the REXUS rocket specifications [5] are that the experiment temperature and pressure must be measured continuously as the pressure drops from normal atmospheric pressure (1 bar) to (0.5 mbar) and remains at the lowest level for at least 10minutes. At the same time, the experiment must function nominally at the lowest pressure. The test was successfully completed at ILR in October 2011 and data was collected using LabView. Fig. 8 shows the experiment run as a graph.

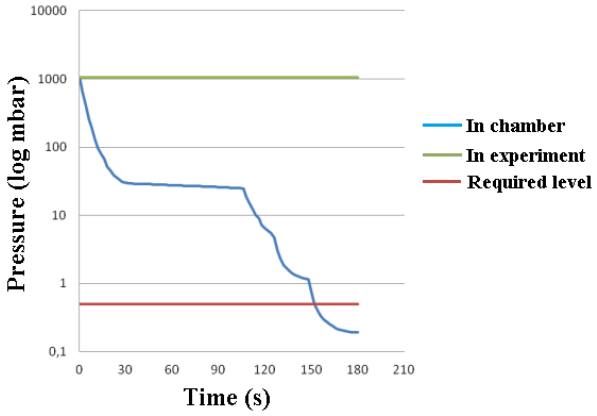

Figure 8 Vacuum test run

4.2 Thermal test

The thermal test was performed to make sure the experiment runs properly at high and low temperatures. According to the REXUS rocket requirement [5], the experiment must be functional between -10°C and +45°C. Since one of the requirements imposed on the REXUS rocket was that the CaRu experiment must always be maintained at 10°C or higher, it was necessary to perform only the high temperature test. This was done at the oven present in ILR's clean room facility. The ambient temperature was set at 60°C and the experiment was placed in the oven with 4 temperature sensors measuring ambient, wall, floor and syringe temperatures. The data was collected using LabView and analyzed later. Fig. 9 shows the thermal test run.

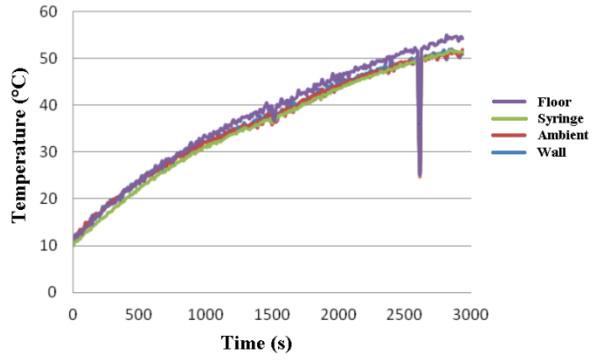

Figure 9 Thermal test results

4.3 Vibration test

During the start and reentry phases of the REXUS flight, strong vibrations are expected. To make sure the experiment functions under these conditions, a vibration test was performed at ZARM in Bremen, with the experiment placed inside the REXUS module. The characteristic frequency of the experiment on all axes was measured by applying a sine excitation of 0.25g between 20 and 2000 Hz. A random excitation was also applied subsequently on all three axes. After the test, the experiment was checked for breakage and parts that had loosened because of the vibrations. The functionality of the experiment was proven to be nominal.

5. EXPERIMENT RESULTS

After a nominal flight except for a few erroneous data packets, the mission was completed with an apogee of 79km. Fig. 10 shows the pressure and temperature data measured inside and outside the experiment. As shown, the experiment chamber was not compromised during flight.

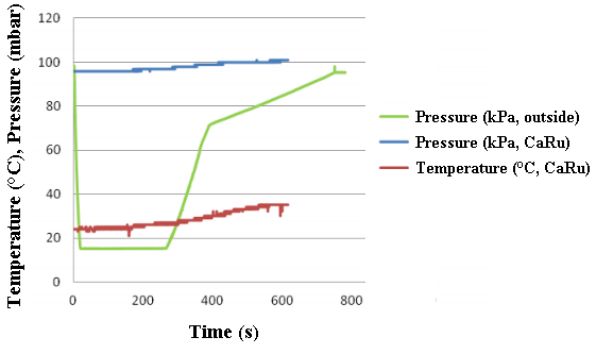

Figure 10 Flight pressure and temperature profile

After analysis of the video taken during flight, it was observed that the needle of the syringe was positioned slightly to the left side instead of the centre of the paper. This led to a slight bias in the formation of the Runge picture as can be seen in Fig. 11.

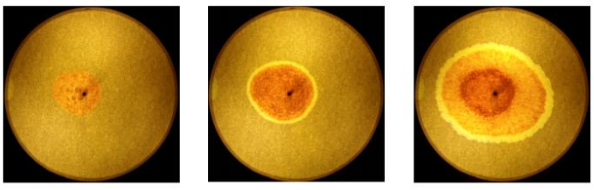

Figure 11 Runge picture: 1, 15 and 105 seconds after start

The reference video was made after the flight using the same apparatus and a similar volume of fluid. The experiment was placed such that the plane of the paper was parallel to the ground; the gravitational force would act perpendicular to the plane at all points.

The data was digitized by measuring the distance of the outer rim of the Runge picture to the center of the syringe needle. This was done for four different points of time: when the fluid drop hits the paper for the first time (defined as 0 s), and 30 s, 60 s and 90 s after the start of the experiment. One of the problems faced while making a reference video post flight was the incorrect volume of fluid being applied to the paper due to as yet unknown reasons. The exact amount of fluid used during the flight could not be replicated. In addition, as mentioned earlier, the drop of fluid at the tip of the syringe did not form symmetrically during the flight. A tiny bubble was created on the left side of the needle. This bubble caused an asymmetry of the start expansion of the fluid on the paper. To define the axes with respect to the experiment in order to analyze the acceleration data, refer to Fig. 12.

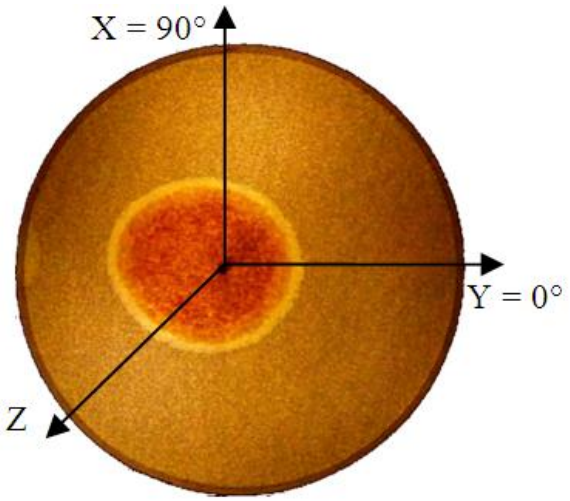

Figure 12 Acceleration axes with respect to paper

6. INTERPRETATION OF DATA

The CaRu experiment confirms the dependency of the size of Runge instabilities and the fractal dimension of the spreading velocity. As Fig. 13 shows, the spreading velocity of the fluid during the reference experiment is, at nearly all times and angles, faster than during the flight. The Runge instability can be observed far more easily in the reference video.

It is also assumed that the gravity force on earth accelerates the spreading of fluid through the paper even when it is placed horizontally to the ground, as the spreading velocity is higher in the reference video despite small acceleration of the fluid directly in spreading direction of the flight video due to the

rocket's rotation in that axis. There is yet another effect that might cause the higher spreading velocity in the reference experiment. A connection between the spreading velocity and expansion of the fluid drop on the paper at the beginning of the experiment was found. The spreading velocity at 60s and 90s after the beginning of the experiment was highest, if the expansion of the Runge picture was smaller than 32 units of length at the beginning of the experiment. This is probably caused by more clogging of capillaries channels where more copper ferrocyanide precipitated. The capillary force is then not strong enough to overcome the clogging. Furthermore, a connection between the acceleration due to low gravity and the spreading velocity of the fluid was found. The spreading velocity is higher for positive acceleration. As shown in Fig. 15, the influence of low gravity on the spreading velocity is best visible at 60s past the beginning of the experiment. At the beginning there is enough fluid to allow the capillary pressure to have a far higher influence than gravity. Later, when the influence of clogging due to the chemical reaction gains importance and slows down the expansion, resulting in better visible Runge instabilities, at 60s and the low acceleration helps to overcome the clogging.

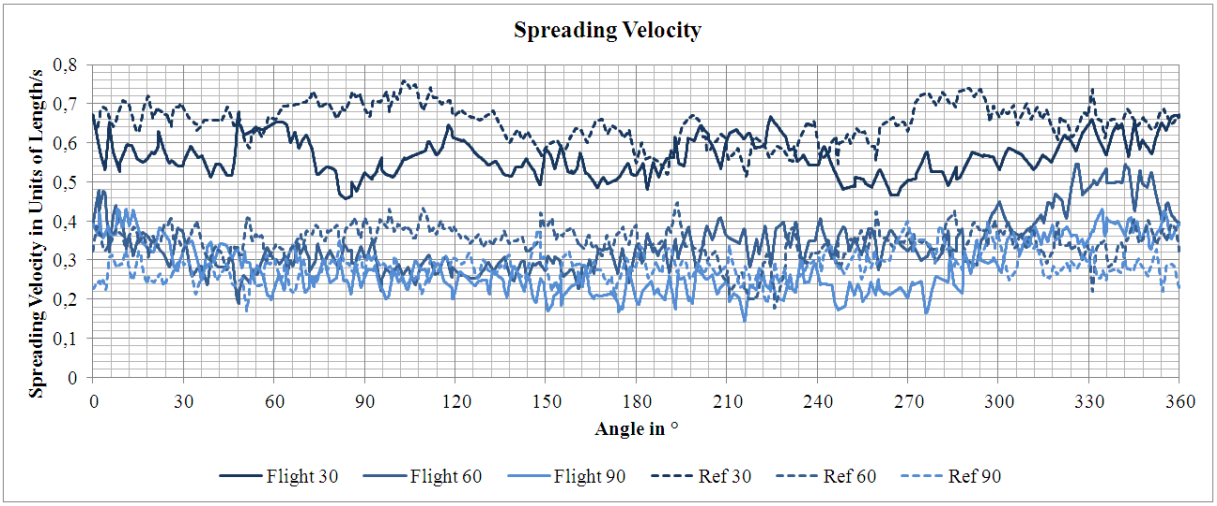

Figure 13 Spreading velocity in flight and reference video at 0/30/60/90s after start of experiment

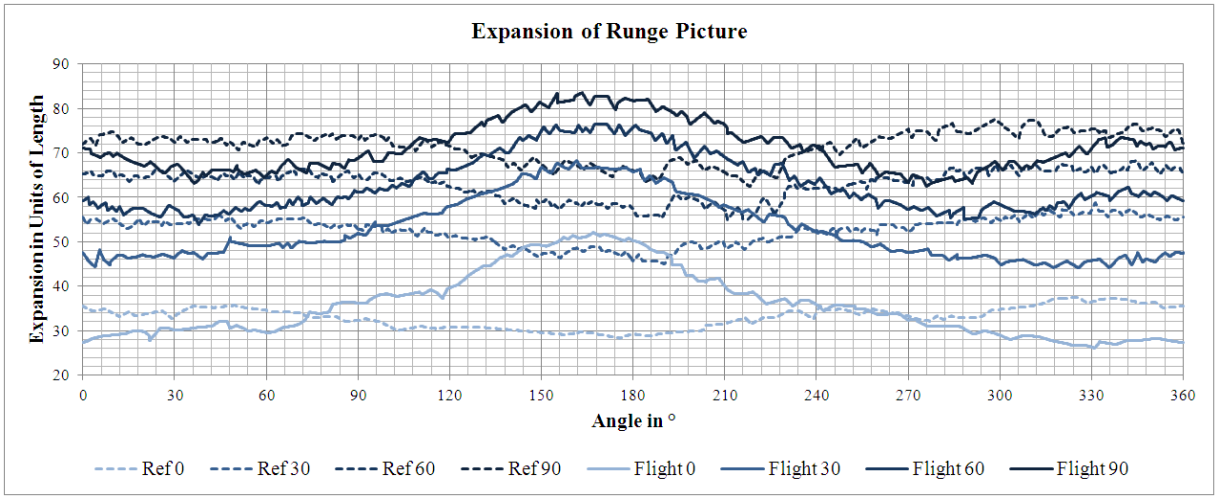

Figure 14 Expansion of Runge picture in flight and reference video at 0/30/60/90s after start of experiment

As all data presented and interpreted here is based on one flight experiment and one reference experiment which were both filmed by a camera and then measured at only four points in time in a non automatic process, it is to be assumed that uncertainties could be high. In addition, the theoretical background on Runge pictures as such is still not entirely ripe; a theoretical validation of results obtained from the CaRu experiment cannot be performed at this time.

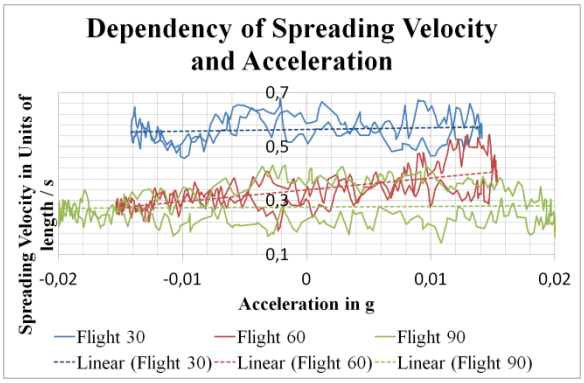

Figure 15 Dependency of spreading velocity at 30/60/90s after begin of experiment and acceleration

6. CONCLUSION

An experiment to investigate the effect of low gravity on the Runge instability was successfully flown on the REXUS 11 sounding rocket. Interesting observations such as gravity affecting the spread of the liquid on the paper in a counterintuitive manner were obtained. Further analysis is expected to provide a more detailed theoretical model to fit the experiment data. The CaRu project is the first experiment to investigate this particular aspect of capillary transport and therefore, might pave the way for future discoveries in this field. The effort put into the project provided students from the Technical University of Dresden with valuable firsthand experience in designing, manufacturing, testing and operating a complex experiment in space.

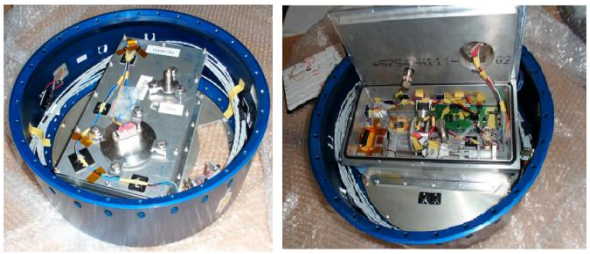

Figure 16 CaRu experiment post flight

7. ACKNOWLEDGEMENTS

We are highly grateful to Dr. Tino Schmiel and Prof. Olaf Przybilski of the ILR, TU Dresden for their support during the entirety of the CaRu mission. The CaRu team would like to acknowledge the support given by:

- DLR and SSC staff, for having supported us financially and technologically during the whole campaign
- Mark Fittock, for supporting us mentally and in myriad other ways throughout the mission and providing the best environment
- ADIOS team for letting us borrow the design of the arm plug and to the GGES team for lending us their acceleration data.
- Nanotec, for sponsoring the linear motors used in our experiment
- Dresdner Universitätsjournal, for allowing us to print articles about the mission in their magazine

8. BIBLIOGRAPHY

1. P. J. Canfield, P. M. Bronowicki, Y. Chen, L. Kiewidt, A. Grah, J. Klatte, R. Jenson, W. Blackmore, M. M. Weislogel, M. E. Dreyer. *The capillary channel flow experiments on the International Space Station: experiment set-up and first results*, 2013. Experiments in Fluids, p. 54:1519.

2. Runge, Dr. F. F. *Der Bildungsbetrieb der Stoffe: veranschaulicht in selbstständig gewachsenen Bildern.* 1855.

3. Fries, Nicholas. *Capillary transport processes in porous* . Bremen : Cuvillier Verlag , 2010. 978-3-86955-507-2 .

4. F. Bukatsch, O. Krätz, G. Probeck, R. Schwankner. *So interessant ist Chemie.* Köln : Aulis Deubner, 1997. 2. Auflage.

5. Fittock, Mark. *REXUS User Manual.* Kiruna, Sweden : EuroLaunch, 2011.

DESIGN, OPERATIONAL ASPECTS AND FLIGHT RESULTS OF A PROPELLANT MANAGEMNET DEVICE (PMD) EXPERIMENT ON A TEXUS SOUNDING ROCKET

Burkhard Schmitz, Philipp Behruzi, Andreas Schütte

Astrium GmbH, Airbus-Allee 1, 28199 Bremen, Germany
Email: Burkhard.Schmitz@astrium.eads.net

ABSTRACT

In November 2011 the first cryogenic TEXUS experiments were launched with the TEXUS 48 sounding rocket flight from the Esrange Space Center in Sweden.
In the frame of ESA's Cryogenic Upper Stage Technology (CUST) program two cryogenic experiments were developed by Astrium. The objectives of these experiments were the demonstration and validation of two Propellant Management Device (PMD) concepts usable for future launcher cryogenic upper stages. The first flight of these new technological experiments was financed by DLR on TEXUS 48 "CRYSTAL" (CRYogenic Stage Technology Advanced Laboratory).

To meet the experiment specific requirements, to cope with the cryogenic conditions of the experiment and to allow for an operational implementation of the experiment launch preparation into the TEXUS countdown sequence, it was necessary to develop specific design concepts, hardware components and operational processes for these cryogenic experiments.

From the recorded flight data and videos it could be verified that the performance of the PMD experiments and its components was always well within the specified limits. Thus an excellent quality of experiment data was obtained during the microgravity flight which could be provided to the PMD development team for further analysis.

1. INTRODUCTION

The purpose of PMD`s is to provide liquid propellant to the rocket engine not only during the thrust phase, but also during other mission phases following a thrust free coasting phase such as engine chill-down and engine restart. As such the PMD represents a retention device, containing liquid in reservoirs which are significantly smaller than the upper stage tank volume.
The correct PMD operation is a complex function of various effects and operational parameters like the propellant thermodynamic properties, its surface tension and wetting characteristics, the parasitic heat input to the propellant tank, the residual acceleration and the operational characteristics of the mission profile.
The objectives of the TEXUS 48 PMD experiments were to support the maturation of actual PMD technology developments and validation of the numerical PMD performance predictions for two specific PMD developments, the PMD for liquid oxygen (LOX-PMD) and for liquid hydrogen (LH2-PMD).
To meet these objectives a similarity analysis was performed to define the essential experiment design parameters, such as the scaling factor and the necessary experiment parameters, such as pressure level, flow rates and residual acceleration.

On the basis of this experiment requirements definition the development of the TEXUS LOX- and LH2-PMD experiments was performed. The complexity of these experiments, the specific design solutions utilized were driven by the fact, that it should be feasible to simulate a large variety of a cryogenic upper stage flight conditions and variation of performance parameter.

2. EXPERIMENT REQUIREMENTS

In the following the design driving PMD experiment requirements are listed. Some of them are unique for this type of cryogenic experiments and lead to specific design solution and operational procedures:
Experiment tank: An experiment tank with a maximum capacity of 6,5 liter shall be provided. Inside the tank a 1:10 scaled PMD shall be integrated.
Experiment fluid: liquid nitrogen (LN2) shall be used as experiment fluid for the LOX- and LH2-PMD experiment.
Experiment fluid conditioning: the experiment fluid vapour pressure shall be at a specified level at lift-off.
Tank pressure: it shall be possible to increase and decrease the tank pressure during flight.
Heating: Heating of the tank outlet and wall shall be possible. The heater power shall be selectable.

Proc. '21st ESA Symposium European Rocket & Balloon Programmes and Related Research',
9–13 June 2013, Thun, Switzerland (ESA SP-721, October 2013)

Transparent PMD design: The PMD design shall allow for the observation of the liquid motion in the PMD via transparent PMD components.
Filling level: The experiment tank shall be filled precisely to a pre-defined filling level for lift-off.
Draining: Means for draining at a fixed liquid flow rate shall be provided.
Acceleration: Radial acceleration shall be applied during the last experiment phase by a roll rotation of 15 °/sec.
Diagnostics: a visual observation, pressure, flow and temperature sensors shall be implemented.

3. DESIGN AND OPERATIONAL CONCEPT

In the following chapters the design and operational concepts are described which were adopted to meet the experimental requirements for the PMD experiments. Both experiments were developed with a high degree of commonality, therefore the description is valid for both experiments unless design features of a specific experiment module are addressed.

3.1 Overall Design Concept

The overall design concept is based on a typical TEXUS experiment layout, which basically consists of the following main elements, see also Figure 1:

The external structure, the outer skin of the experiment, which represents also the mechanical load path to the TEXUS rocket system.
The section for the avionics equipment, namely the E-Box, the battery and video system. The avionics equipment is fixed to the lower side to the so called Experiment Deck which is mounted via elastic bearings to the external structure
Finally the experiment section is located on top of the Experiment Deck.

For the PMD experiments the experiment section is divided into two separate parts, the cryo-section accommodating all those components which will be in contact with the cryogenic fluid and the pressure control and video section accommodating all components which are required for the control and observation of components in the cryo-section. In addition equipment which is sensitive to low temperatures, like pressure sensors, valves and illumination equipment, is mounted in the pressure control and video section and is interfacing via ducts, lines and optical fibers with the cryo-section.

To limit the parasitic heat flow into the cryo-section the whole cryo-section, which is chilled down to temperatures below -190 °C, is thermally insulated from the external environment by a vacuum insulated dewar housing, see Figure 1.

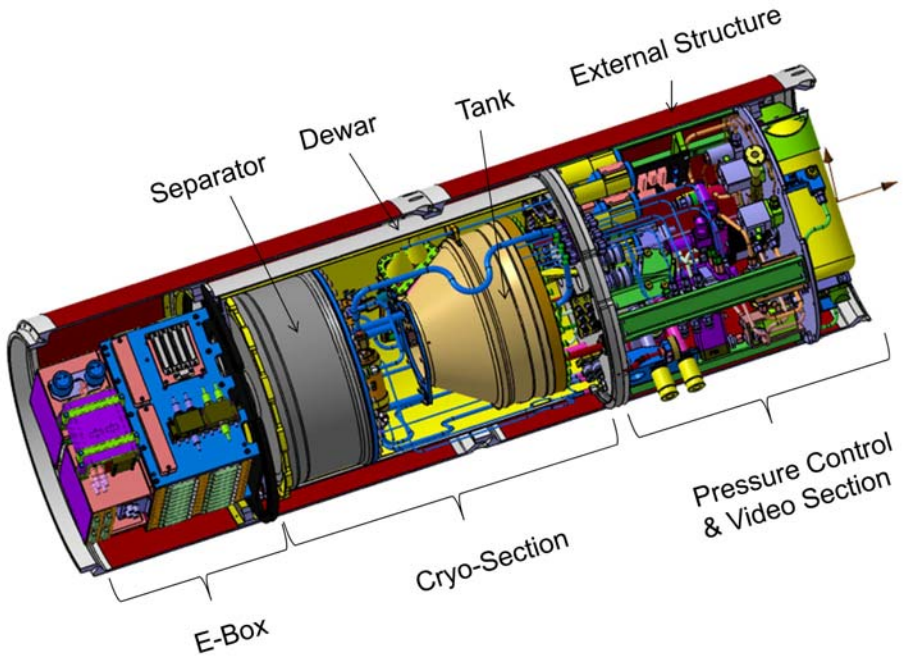

Figure 1: Overall PMD Experiment Design Concept, here LH2-PMD experiment

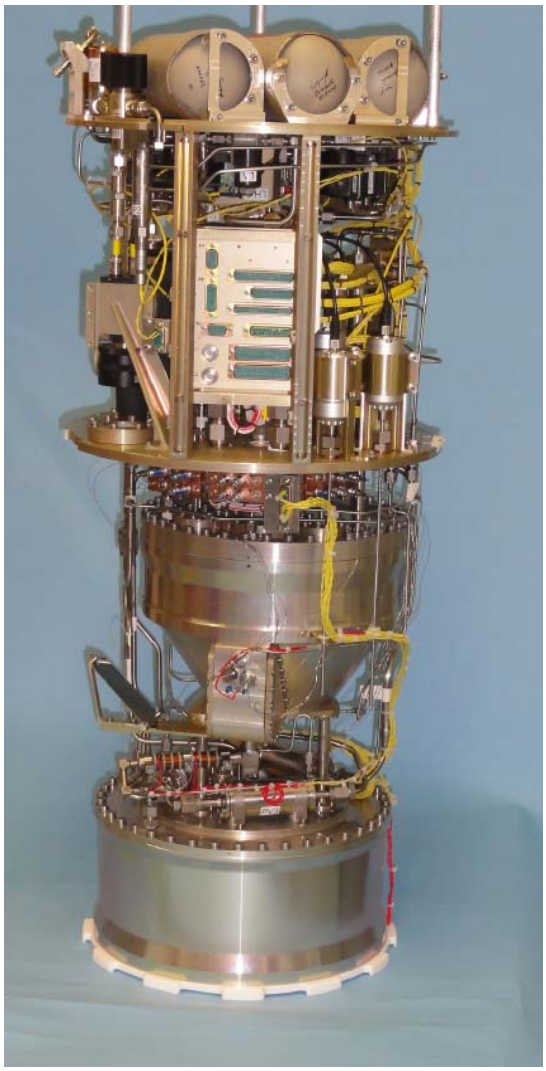

Figure 2: Photo of the LH2-PMD Experiment without Dewar, lower part: cryo-section, upper part: pressure control & video section

The main components accommodated in the cryo-section are the experiment tank, the separator, several cryo-valves and fluid lines and harness, see Figure 2.

The experiment tank was filled prior flight with LN2 and can take up to 6,5 liter of LN2. Inside the experiment tank a 1:10 representation of the PMD is located at the tank outlet.

The outlet of the experiment tank is connected to the separator which is kept at a lower pressure level compared to the experiment tank. The fluid flow between the tank and separator is controlled via an on/off valve with a fixed throttle. The operation of the valve is timeline controlled but can be also commanded via telecommand from ground.
When LN2 passes the throttle a portion of the LN2 will evaporate and the resulting two phase fluid flow will enter the separator which will separate the liquid phase from the fluid flow and maintains the liquid phase by porous media, whereas the gaseous phase can leave the separator to be vented via a ventline.

Several heaters are integrated in the experiment set-up. Some of them are simply required to maintain temperature sensitive equipment within its specified limits. Other heaters are dedicated to the specified operational performance of the experiment. These are the power controlled outlet heaters located at the PMD outlet duct and the power controlled wall heater at the inner side of the PMD wall (only applicable for the LH2-PMD). In addition a powerful booster heater is attached to the tank for the thermal conditioning of the experiment tank prior to lift-off.

3.2 Transparent PMD Design

An essential part of the experiment objectives, the maturation and validation of the PMD design concept, was the comparison of the flight results with analytical PMD performance predictions.
To allow for this comparison it is necessary to observe the movement of the test liquid inside the PMD and in the experiment tank close to the PMD.
This requirement was challenging the design in two major aspects:

- Manufacturing of transparent PMD internal components
- The second aspect was the design of transparent components and windows for cryogenic pressurized systems with a maximum proof pressure of up to 15 bar

The transparent PMD internal components were manufactured from a specific, cryo-compatible, plastic material. Due to the complexity of the PMD internal design and the further down-scaling for the PMD experiments a design of small fragile plastic components was obtained for the PMD experiments. In addition it was necessary to polish these fragile components manually in order to obtain the required optical transparency.

A specific challenge was the design of the nearly rectangular shaped observation window of the LH2-PMD, which must sustain a proof pressure of 15 bar at cryogenic temperatures, see Figure 3.

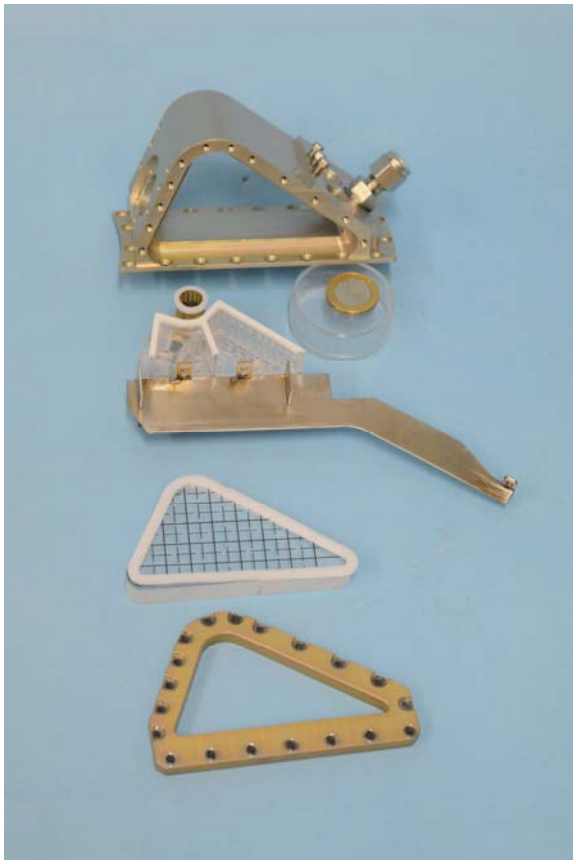

Figure 3: Delicate Design of PMD Components

For the detailed design definition of this experiment tank section it was necessary to perform a structural analysis of the complete tank with the material properties at cryogenic temperatures of the tank, the window and the sealing material.

3.3 Retraction Mechanism

The experiment timeline includes several predefined draining phases with a fixed liquid draining rate which should lead to a nearly empty experiment tank at the experiment end. This is necessary because the PMD operational conditions with the tank nearly empty are of specific interest for the PMD design validation.
To achieve these conditions at the experiment end it was important to control the LN2 filling level at lift-off with a high accuracy.

During the count-down a LN2 boil-off rate, caused by parasitic heat flowing into the experiment tank, of nearly 30 ccm/min LN2, has to be considered. Such a system is required to compensate for this boil-off rate, especially during unplanned count-down hold periods when the rocket is already armed and a manual operation in the launch tower is not allowed.
For this operation Fluid Ground Support Equipment (FGSE) was developed which allows for a remote controlled filling of the PMD experiments with LN2. The design of this FGSE includes insulated LN2 transfer lines of limited flexibility and vacuum insulated rigid Johnston couplings as interface to the rocket. To break the interface of the fluid transfer lines prior lift-off, a specific retraction mechanism was developed, see Figure 4 and 5.

Figure 4: Retraction Mechanism, connected

Figure 5: Retraction Mechanism, retracted

In the count-down sequence the retraction was planned as one of the last events prior to the lift-off, because the reinstallation of the retraction system would require manual intervention once it is driven into the retracted position.

3.4 Draining

During draining phases of the experiment a constant LN2 flow rate of 40 ccm/sec liquid shall be drained from via the PMD from the experiment tank. To achieve the specified fixed draining rate, the outlet of the experiment tank is connected via a cryogenic valve with a throttle of fixed diameter to the separator. Thus the draining rate of the LN 2 can be controlled by the pressure difference between the experiment tank and the separator.

To maintain a constant pressure in the experiment tank and in the separator, the pressure of both components is permanently measured and adjusted by either replenishment with helium or release of excessive gas into the ventline.
During the draining phases the pressure of the drained LN2 is reduced when passing the throttle and leads to a partial evaporation of the LN2. The resulting two phase nitrogen flow enters the separator and can lead to further LN2 evaporation and subsequently pressure fluctuations if the separator is warmer than the fluid entering the separator.

To avoid excessive gas generation by LN2 evaporation which cannot be released by the ventline system, it was of major importance to chill the separator temperature down to the LN2 boiling during the count-down process and observe/maintain the separator temperature until lift-off.

3.5 Radial Acceleration

Any rotation of the TEXUS payload section during the microgravity flight phase will lead to unwanted radial accelerations. Usually the Rate Control System (RCS) of the TEXUS Service System is required to keep the rates of the payload section during the microgravity phase to an absolute minimum. For the TEXUS 48 a software modification was introduced to initiate at the end of the experiment a roll rate of the required 15 °/sec.

3.6 Diagnostics

For the comparison of the experiment results with the numerical flight predictions several measurements at specific locations are required.

The most important diagnostics system is the video observation system because this will provide essential information about the location of the liquid phase, the velocity of liquid and gas bubble movement and indirect indication about the temperature distribution inside the PMD when the pressure is reduced by the observation of the onset of boiling.

To develop the optimum observation system a compromise between contradicting requirements and constraints was necessary. Such the available space for the observation path and optical elements, location of cameras and illumination components, location of windows was investigated first with computer tools but were finally verified by a bread-board test set-up.
In Figure 6 and 7 the finally selected field of view for both camera views of each experiment is illustrated. The side view is looking from the side into the PMD and the top view is focusing on the interface between PMD and bulk liquid in the tank.

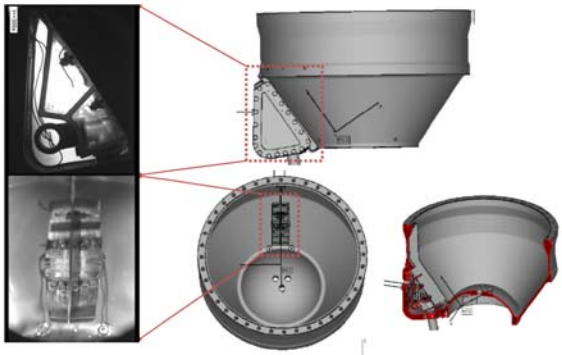

Figure 6: Field of view for the LH2-PMD experiment

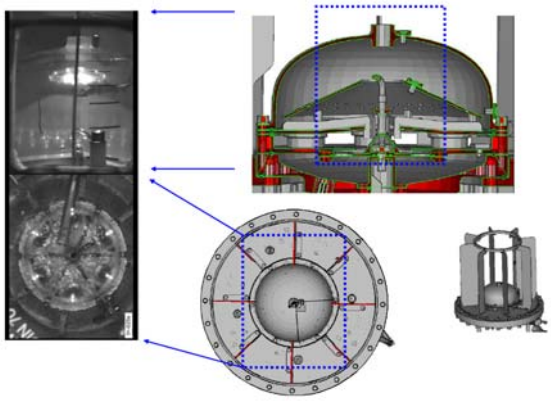

Figure 7: Field of view for the LOX-PMD experiment

For the high quality storage of the video data an on-board digital video system is integrated. For the real time control of the experiment an analog video link is implemented which provides the two video data streams of each experiment via video multiplexing to the ground station.

In addition to the video data the most important experiment data are the overall pressure level of the experiment tank and the local temperatures of the fluid in the liquid and gaseous phase. In addition the temperature distribution in the tank structure is relevant. For this purpose in total up to 30 temperature sensor channels are provided by the design.

4. FLIGHT RESULTS

Although the PMD experiments were extensively tested on ground it was obvious that several functional performance aspects which were predicted by analytical means could not be verified on ground. A typical example is the possibility to observe the motion and contour of bubbles which, due to the natural convection, will move very fast under a 1-g environment and lead to a blurry image.
In Figure 8 an example of a video image of gas bubbles inside the LH2-PMD is presented at microgravity conditions. Due to the slow movement under microgravity a clear and sharp image of the bubble and its contour is obtained.

Figure 8: LH2-PMD outlet heating phase with bubbles in the PMD

One of the experiment characteristics which could be verified already on ground was the ability of the low thermal mass inertia temperature sensors to distinguish between undercooled liquid and gas phase. The same characteristics was observed during flight and supported to localize the liquid phase and gas bubbles.

Another essential criterion for the successful experiment execution was the measurement of the pressure difference between tank and separator which is the driving force for the constant draining flow rate.
The pressure difference depends on the correct operation of several experiment functions, like the four different pressure control loops for tank and separator, the thermal preconditioning of the separator and the liquid/gas separation function of the separator. Thus the the measurements of the pressure difference was one of the most important indication of the correct operation of the PMD experiments. From the flight data it could be verified, that the pressure difference and also the individual pressure levels followed with a high accuracy the required level.
Another indication for the correct operation of the separator was, that the ventline temperature stayed always above 0°C which is an indication that no LN2 was vented via the ventline.

Finally it could be verified from the flight data that the required radial acceleration at the end of the experiment, i.e. the required roll rate was obtained with a high accuracy.

5. SUMMARY

For the development of the TEXUS 48 PMD experiments available subsystem and component design concepts were utilized wherever possible. Nevertheless the need of several new developments was identified in terms of hardware components and operational procedures. Such the design and operation of the PMD experiments includes several novelties. Due to an extensive bread-board test program, the early qualification of new components which were selected for the experiment design and finally the extensive testing phase of the flight hardware lead to the successful execution of the TEXUS 48 flight campaign.

6. ACKNOWLEDGEMENTS

The authors would like to thank the funding Agencies DLR and ESA as well as the industrial partners.

COCORAD AND TECHDOSE COSMIC RADIATION EXPERIMENTS ON BOARD BEXUS STRATOSPHERIC RESEARCH BALLOONS

Balázs Zábori[1,2], István Apáthy[1], Antal Csőke[1], Sándor Deme[1], Attila Hirn[1], Tamás Hurtony[2], József Pálfalvi[1], Tamás Pázmándi[1]

(1) MTA Centre for Energy Research, P.O. Box 49., H-1525 Budapest, HUNGARY
(2) Budapest University of Technology and Economics, Műegyetem rkp. 3., H-1111 Budapest, HUNGARY
Email: zabori.balazs@energia.mta.hu

ABSTRACT

Due to significant spatial and temporal changes in the cosmic radiation field, radiation measurements with advanced dosimetric instruments on board spacecrafts, aircrafts and balloons are very important. The main scientific goal of our experiments was to measure the effects of the cosmic radiation mainly from dosimetric point of view at lower altitudes where measurements with orbiting spacecrafts are not possible. The main technical goal was to develop a balloon technology platform for advanced cosmic radiation and dosimetric measurements.

1. INTRODUCTION

Among many other student projects ESA Education Office announces a call for proposals annually for the REXUS/BEXUS (Rocket and Ballon Experiments for University Students) flights for university students. The REXUS/BEXUS programme allows students from universities and higher education colleges across Europe to carry out scientific and technological experiments on research rockets and balloons. Each year two balloons capable of lifting their payloads to a maximum altitude of 35 km, depending on total experiment mass (40-100 kg) are launched 145 km North of the Arctic Circle from Sweden, carrying experiments designed and built by student teams [1].
The COCORAD and TECHDOSE Hungarian student experiments were selected to take part in the BEXUS-12 and BEXUS-14 projects. The experiments flew on board the BEXUS-12 and BEXUS-14 stratospheric balloons on the 27th of September 2011 and on the 24th of September 2012 from ESRANGE Space Center. The experiments used the TRITEL three dimensional silicon detector telescope and in case of the TECHDOSE experiment additional Geiger-Müller counters (GM) for active monitoring. Several thermoluminescent dosimeters (Pille system) were used in order to measure the excess absorbed dose of the flight and compare with the active results, and in case of the TECHDOSE experiment Solid State Nuclear Track Detectors (SSNTDs) to measure the contribution of the thermal neutrons. The main technological and scientifical supporter of the experiments was the MTA Centre for Energy Research (the former KFKI Atomic Energy Research Institute). The present paper addresses the main overview of the two experiments and some preliminary results are also shown.

2. THE MAIN GOALS OF THE RESEARCH STUDIES

Commercial airplanes are flying at higher and higher altitudes and the frequency of manned space flights is increasing faster nowadays than before. These facts justify the importance of cosmic radiation and dosimetric measurements with advanced instruments and techniques. Several measurements have been performed on the cosmic radiation field from the surface of the Earth up to the maximum altitudes of research airplanes (the lower limit of the stratosphere). However the cosmic radiation field is not well known between 15 km and 30 km. The incoming primary cosmic radiation interacts with the Earth's magnetosphere and the atmosphere [2] providing a complex radiation environment (see Fig.1).

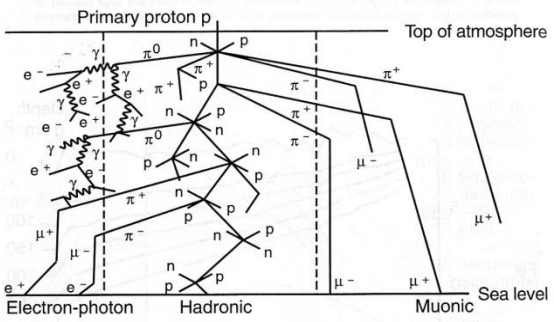

Figure 1. Schematic representation of the secondary particle production in the atmosphere [3], [4].

The main technical goal of our experiment was to develop a balloon technology platform for advanced cosmic radiation and dosimetric measurements to fulfil the scientific goals of our research studies which are the follows:

- to give an almost complete assessment of the cosmic radiation field at the altitude of the stratospheric research balloons;
- to measure the charged particles (in a wide LET range; LET – Linear Energy Transfer, means average energy locally imparted to the material by an incoming charged particle of a specified energy over a *dx* path length) and their dose contribution at the altitude of the stratospheric research balloons;

- to measure the contribution of thermal neutrons using Solid State Nuclear Track Detectors (SSNTDs) at the altitude of the stratospheric research balloons;
- to study the effects of the atmosphere, the Earth's magnetic field and the solar activity on the cosmic radiation field in the stratosphere.

3. INSTRUMENTATION

The experiments used two different types of measurement system during the flight of the BEXUS balloons. One of them was an active space dosimetry system, the TRITEL three-dimensional silicon detector telescope with additional Geiger-Müller counters and the other one was the passive monitoring system. The passive system included Pille thermoluminescent (TL) dosimeters and SSNTDs. In the following sections a short overview of these instruments is given.

3.1 TRITEL telescope

TRITEL is a three dimensional silicon detector telescope comprising six identical fully depleted, passivated implanted planar silicon (PIPS) detectors and designed to measure the energy deposit of charged particles. The detectors are connected as AND gate in coincidence in pairs forming the three orthogonal axes of the instrument (Fig. 2).

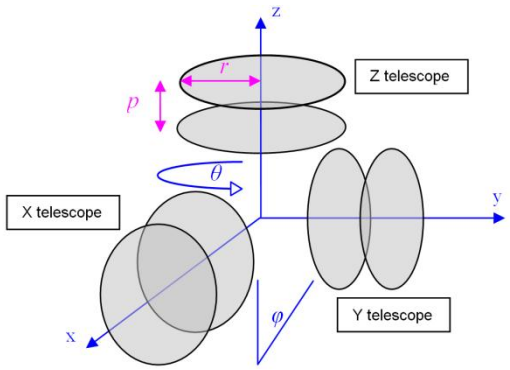

Figure 2. 3D telescope geometry (r is the radius of the detectors, p is the distance between two detectors in the telescope) [5].

By evaluating the deposited energy spectra recorded by TRITEL the absorbed dose, the energy deposition spectra in three directions, the quality factor and the dose equivalent can be determined. Since we are interested in the equivalent dose in tissue, the energy deposition spectra in silicon are converted to LET spectra in human tissue.
Although the instrument can't determine the arrival direction of the individual particles, due to the three-axis arrangement an assessment of the angular asymmetry of the radiation might be possible. Another, even more important advantage of the geometry is that TRITEL has an almost uniform sensitivity in 4π. The effective surface of each detector is 220 mm^2 with a nominal thickness of 300 μm.

3.2 Pille TL space dosimetry system

The development of the Pille thermoluminescent dosimeter system began in the KFKI AEKI in the 1970s. The aim of the development was to invent a small, compact, space qualified TL reader device suitable for on-board evaluation of TL dosimeters. The Pille TL dosimeter contains $CaSO_4$:Dy TL material produced by the Budapest University of Technology and Economics. The TL material is laminated to the surface of a resistive, electrically heated metal plate inside a vacuum bulb made of glass. The dosimeter also contains a memory chip that holds identification data and individual calibration parameters of the device such as TL sensitivity, TL glow curve integration parameters or the time of the last read-out.
The Pille TL Reader (Fig. 3) is designed for spacecraft: it is a small, light-weight device with low energy consumption. The reader is capable of heating the dosimeters, measuring the emitted light during the read-out, performing preliminary data evaluation, storing and displaying the results. The measurement results are stored on a removable flash memory card which can store up to 8000 data blocks consisting of the TL glow curve, the time of the last read-out, the results of the background and sensitivity measurement (performed in the beginning of each read-out) and all derived data such as the absorbed dose [6].
One of the main advantages of the Pille TL system is the possibility of the onsite data acquisition and evaluation, which means no transport dose in the calculations.

Figure 3. The Pille TL dosimeter system in its transporting case (reader and ten dosimeters).

3.3 SSNTDs

Taking into account that in balloon experiments it is difficult to use heavy instrumentation and devices that require bulky power supply or batteries, the Hungarian researchers elaborated a method to apply light weight and passive SSNTDs.

The SSNTD detects charged particles coming from the environment or generated inside its own material by nuclear reactions. The principle of charged particle registration seems to be quite simple: a particle entering the detector material produces radiation damage (latent track) along its path by breaking the chemical bonds. In this zone of few tens of nm, the damaged material can be easily dissolved (etched off) by appropriate chemical reagents meanwhile the bulk material removal is much less. The prolonged etching enlarges the latent track up to a measure when it becomes visible by an optical microscope. Usually, the detector material is a special plastic sheet, in our case, it is a thermoset one manufactured from Polyallyl Diglycol Carbonate (PADC), called TASTRAK, by TASL Ltd. (Bristol, UK) [7].

To detect the neutrons first they need to be converted to charged particles such as protons or alpha particles via nuclear reactions. There are few requirements to select the appropriate neutron-to-charged particle converter material: it should be easily available, chemically stable, solid material, having high reaction cross section and the generated charged particle should be well detectable. Two reactions can be considered as summarized in Tab. 1.

Table 1. Thermal neutron reactions producing charged particles detectable by SSNTD [8].

Reaction	Cross section (barn)	Isotopic abundance (%)	1st particle energy (MeV)	2nd particle energy (MeV)
$^{10}B(n,\alpha)^{7}Li$	3571	19.9	E_{α}=1.47	E_{Li}=0.84
$^{6}Li(n,\alpha)^{3}H$	941	7.5	E_{α}=2.05	E_{H}=2.73

The evident selection is the boron if an appropriate compound is available, because of the high cross section and isotopic abundance, as well as, both charged particles are possibly detectable. It means that their range in the detector material and the linear energy transfer (LET) are satisfactory to enlarge the resulting tracks by a cheap chemical reagent as shown in Tab. 2. To observe the developed tracks, the surface removal by etching needs to be less than the particle range in the detector material. From previous works [8] it is known that the surface etching velocity (bulk etch rate) of the 1 mm thick TASTRAK material is 1.34 µm/h if etched in 6 M NaOH at 70°C.

Table 2. Calculated (SRIM2008 [9]) LET and range of particles and the expected resulting particle area after etching in 6 M NaOH at 70°C for 3 and 0.75 hours, respectively.

Particle energy (MeV)	LET (keV/µm)	Range (µm)	Etching time (h)	Track area (µm^2)
E_{α}=1.47	234	6.1	3	~37.4
E_{Li}=0.84	440	3.2	0.75	~40

The area of the alpha particle tracks is predictable by a computer code, however, no such a code is available for the Li particle. After selecting the boron containing compound preliminary experiments are needed to determine the expected Li track area and prove the validity of the calculated alpha track area, in order to evaluate reliably the detectors exposed on a balloon.

Recently ^{10}B powder and natural boron coated plastic sheets are available for the converter at the Radiation Protection Department of the MTA Centre for Energy Research. Further search is needed to find commercially available boron converter or elaborate a method to manufacture it from the ^{10}B powder.

The detector assembly should contain 2 or 3 sheets of TASTRAK SSNTD in contact to the boron containing converters packed in an appropriate holder presented in Fig. 4.

The thermal neutron detection efficiency is to be studied at the neutron exposure facility of the Centre for Energy Research. In the knowledge of this the unknown thermal neutron flux can be estimated from the track detector measurements.

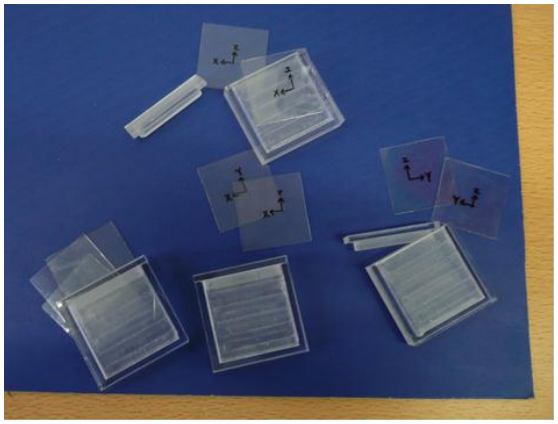

Figure 4. Holders and TASTRAK SSNTDs used in the balloon experiments.

3. EXPERIMENT OVERVIEW

The key elements of the TECHDOSE experiment setup are:

- the TRITEL 3D silicon detector telescope (function: active radiation sensor and data taking unit);
- two Geiger-Müller counters (function: active radiation sensor unit);

- Pille thermoluminescent “bare dosimeters” (function: passive radiation sensors unit);
- Solid State Nuclear Track Detectors (function: passive radiation sensors unit);
- temperature sensors (function: active thermal sensor unit);
- the Experiment Power System (function: provide energy needed for the experiment);
- the E-link interface unit (function: communication with the E-Link system);
- thermal insulation and heaters (function: thermal control).

TRITEL, the Geiger-Müller counters and the temperature sensors are supplied with power by the Experiment Power System. The temperature sensors provide temperature information in given points of the experiment. The Geiger-Müller counters provide the count rate of the incoming charged particles and photons. TRITEL provides deposited energy spectra, time spectra (primary and coincidence too) and housekeeping data. The data of the GM counters and the temperature sensors will be collected in the TRITEL data collecting unit. All the measured data, on the one hand, are stored in the TRITEL internal memory, on the other hand, transferred to the ESRANGE Airborne Data Link (E-link) system. After the experiment is over all the data are downloaded to a personal computer on ground connected to TRITEL. Data are then further processed and evaluated according to the experiment objectives.

Being passive detectors, the TL dosimeters and the Solid State Nuclear Detectors do not require power supply during measurement. The uploaded dosimeters and detectors as well as the reference dosimeters that remain on ground during the mission are read-out before and after the experiment on ground by using a portable reader. The difference of the two doses is the excess dose of the flight. In case of the TL dosimeters dividing the excess dose by the time of flight the average excess dose rate of the flight is obtained. In case of the Solid State Nuclear Track Detectors the thermal neutron contribution can be determined. The experiment setup can be seen in Fig. 7.

3.1 Mechanical design

The mechanical design had to fulfil the design requirements according to the vibration profile of the gondola and the very high accelerations present mainly during landing. The experiment box had to withstand the 8 m/s landing velocity and the design loads +/-10 g in the vertical direction and +/-5 g in the horizontal directions [1].

To fulfil these requirements a mechanical protection box is used as an external box (Experiment Unit). Inside the external box the experiment and its parts can withstand the possible accelerations during the mission. The Experiment Unit contains the electronics of the experiment, an Ethernet converter, as well as the TRITEL and the Pille dosimeters. These parts are mounted together and covered with thermal insulation. Mechanical protection inside the box is provided by spring steel sheets covered by a thin felt layer (see Fig. 5).

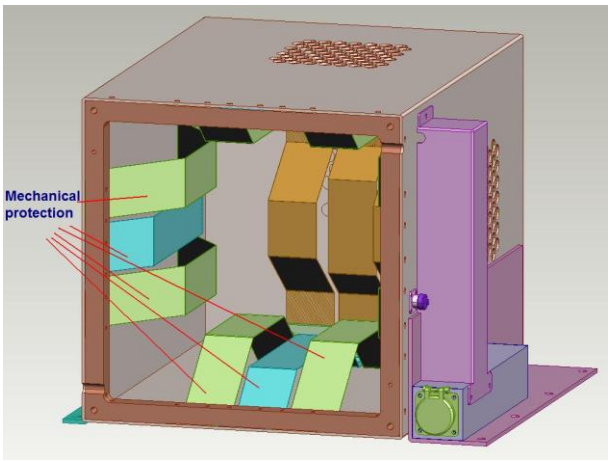

Figure 5. The mechanical protection inside the Experiment Unit.

The mechanical diagrams of the experiment hardware can be seen in Fig. 6.

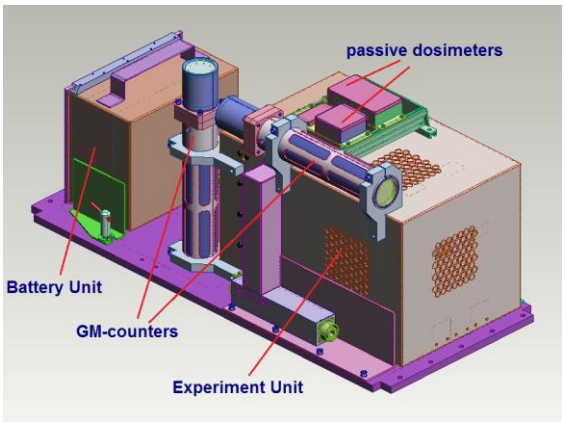

Figure 6. The mechanical design.

The batteries (Battery Unit) are separated from the experiment (Experiment Unit) itself. In this way the Battery Unit is easily removable in case of danger.

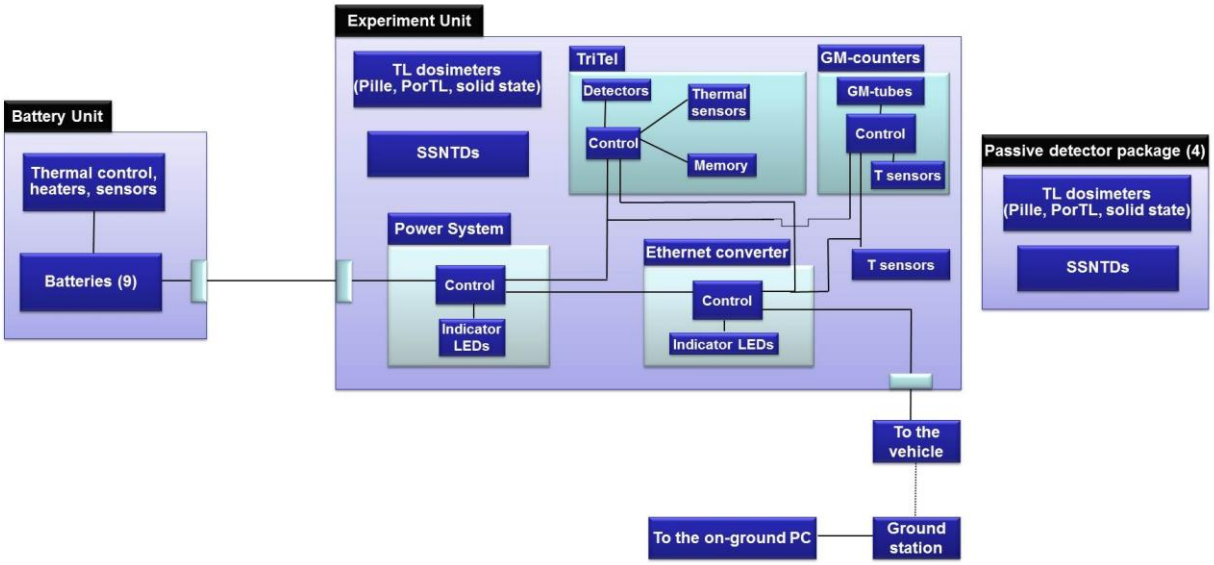

Figure 7. The experiment setup.

3.2 Thermal design

Since the stratosphere is a very harsh environment with very low temperatures it was important to use relevant thermal design to protect the experiments during the flight of the balloon.
The temperature in the stratosphere during a typical BEXUS flight can be as low as -90°C [10]. To protect the sensitive parts of the experiments we used a thermal cover and thermal heaters where it was needed. The thermal cover used in case of the Experiment Unit can be seen in Fig. 8.

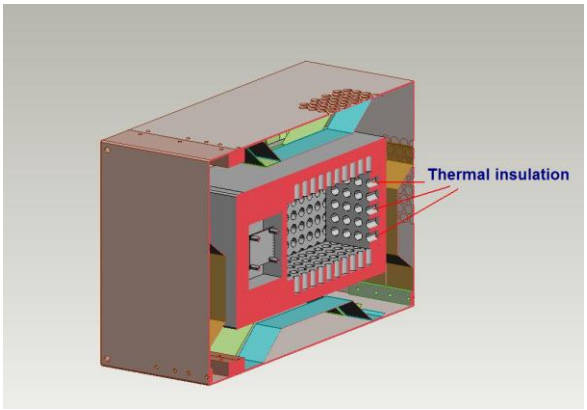

Figure 8. Thermal insulation inside the Experiment Unit.

During the BEXUS-12 mission temperature data were received every 30 seconds as part of the housekeeping data package. Before the launch the temperatures increased because of the very good thermal insulation and the dissipation of the electronics. After the launch the external temperature decreased fast and the temperatures measured inside decreased also after a peak value.
Thermal calculations were performed for the BEXUS flights [11]. The power consumption of the experiment was about 3.5 W (3 W from the TRITEL instrument and about 0.5 W from the rest of the electronics). According to the thermal model developed it results a temperature difference of 37.6 °C between the TRITEL electronics located inside and the external air temperature for the BEXUS flight. It is close to the values measured during the BEXUS flights (see Tab. 3).

3.3 Electronics design

According to the experiment setup (see Fig. 7.) the active instruments can be divided into several major parts. The basic operational concepts and principles will be presented in the follows.
The experiment is powered by its own battery unit during the mission; therefore no power interface to the gondola was needed. In order to extend the operational time of the Battery Unit, a simple analogue control circuit (Thermal Management Unit) based on a comparator with hysteresis controls the heating of the battery pack.
The Service Module (SM; consist the Power System and the Ethernet converter) has dual functionality: power distribution to and signal connection between the subsystems. In the Service Module the proper

voltage levels are provided by the power supply system for the measurement systems. Latched Current Limiters (LCLs) are used to protect the battery from overload in case of failure of any of the subsystems. Since TRITEL is sensitive to under-voltage supply its internal power supply has to be protected by using an Under-Voltage Lockout (UVLO) circuit, which turns off the LCLs when the voltage of the battery decreases to 15.5V.

4. TECHNOLOGICAL MONITORING DURING THE FLIGHTS

During the flight of the BEXUS-12 and BEXUS-14 the communication was continuous between the ground control of the experiment team and the experiment itself. Housekeeping (HK) data were received every 2 minutes, time and energy spectra every 10 minutes from TRITEL. The GM counters provided time spectra every 10 minutes.
The input voltage and the input current of the TRITEL instrument were monitored and found to be stable during the flight. The temperature of the Battery Unit was also monitored during the flight. The values measured showed that the heating of the Battery Unit was adequate.
TRITEL had nine temperature sensors inside. Seven additional temperature sensors were located in different parts of the experiment. The identification of the temperature sensors used can be found in Tab. 3.

Table 3. Temperature sensors and the temperature ranges measured.

ID of the sensor	Location of the sensor	Measured temperature range (°C)	IΔTI (°C)
EXT	Outside environment	11.5 – -54.5	66
TriTel_X	TRITEL X axis detector	17.5 – 32	14.5
TriTel_Y	TRITEL Y axis detector	17.5 – 31.5	14
TriTel_Z	TRITEL Z axis detector	18 – 32	14
TriTel_ADC_X	TRITEL X axis ADC*	17.5 – 34.5	17
TriTel_ADC_Y	TRITEL Y axis ADC	18 – 35	17
TriTel_ADC_Z	TRITEL Z axis ADC	17.5 – 35	17.5
TriTel_CPU	TRITEL CPU** Panel	18.5 – 32	13.5
TriTel_PS	TRITEL Power Supply Panel	17 – 30	13
TMP_BAT	In the Battery Unit	13 – 18	5
TMP_GM1T	On the cover of GM1	-5 – 17.5	22.5
TMP_GM1E	On the HV panel of GM1	6.5 – 28	21.5
TMP_GM2T	On the cover of the GM2	-8 – 19.5	27.5
TMP_GM2E	On the HV panel of GM2	4 – 31.5	27.5
TMP_EPS	On the EPS*** panel of the TECHDOSE experiment	19.5 – 35.5	16

* ADC: Analog-to-Digital Converter

** CPU: Central Processing Unit

*** EPS: Experiment Power System

All the parts of the experiment were in the nominal working temperature range [11] during the flight.

5. PRELIMINARY SCIENTIFIC RESULTS

The floating altitude of the BEXUS flight was 27-29 km and the balloon was floating for about 2 hours. During this time 12 primary and 12 coincidence 10-minute-long spectra were received for each telescope.
In the experiment setup the Y-axis of the TRITEL instrument pointed towards the zenith direction. The X- and Z-axes were orthogonal to the Y-axis and parallel with the side walls of the gondola. The effective thickness of the shielding in front of the detectors was ~0.5-0.6 g/cm^2 aluminium.
The dose rates measured with TRITEL X-axis and with one GM counter can be seen in Fig. 9.

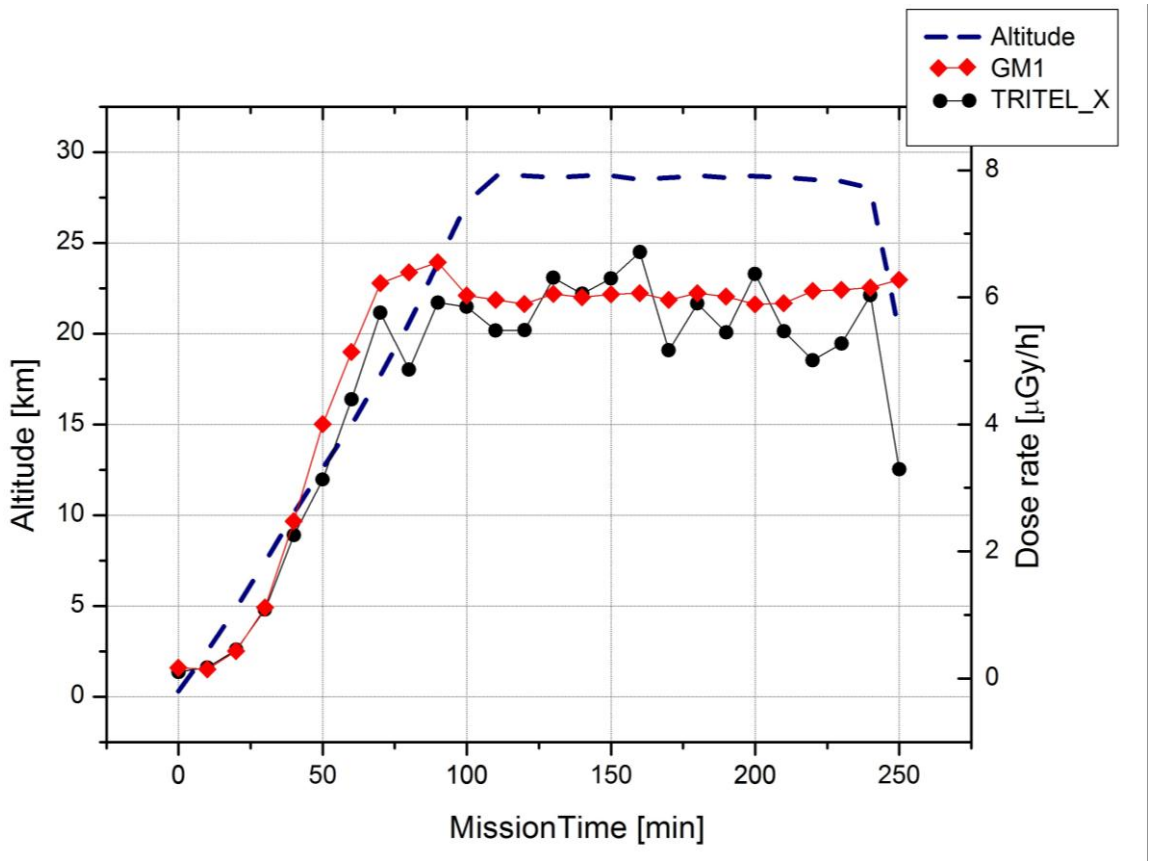

Figure 9. The dose rate profile for a BEXUS flight with a floating altitude of 28.6 km (BEXUS-14).

The energy calibration of the TRITEL telescope was performed with an ^{210}Po alpha-source (E_α = 5.3 MeV), and a ^{241}Am alpha/gamma source (E_γ = 59 keV). The GM counters were calibrated in gamma radiation field using ^{137}Cs source. During the flights the count rates were observed with the GM counters and based on the calibration estimation were given of the possible dose rates. It is only an estimation since there are in the stratospheric radiation field several other high LET particles than photons (such as muons,…).

The Fig. 9 shows the so-called Pfotzer-maximum [12] at an altitude range of about 21-22 km (see the GM1 red curve). From previous studies it is well known that this is the maximum of the secondary particle production. The altitude of the maximum varies with the geographic latitude and at the location of the ESRANGE base (67° N, where the magnetic cut-off rigidity of the Earth's magnetosphere is below 1 GV) the measured value is in good agreement with earlier measurements [13].

The measured average dose rate was about 6 µGy/h at an altitude of 28.6 km (see Fig. 9). The total absorbed dose for the whole flight (ascent, float, descent) in case of the TRITEL three axes in average was 19.9 ± 1.0 µGy and the measured average absorbed dose in case of the Pille dosimeters was 15.6 ± 1.1 µGy. The absorbed doses measured with TRITEL for the balloon flight are higher than the one measured with Pille, as it was expected due to the low sensitivity of TL detectors to particles with LET higher than 10 keV/µm.

The further scientific data evaluation is on-going and will be presented at later stages.

6. CONCLUSIONS

The Hungarian COCORAD and TECHDOSE student teams were selected to take part in the BEXUS project and designed, built and carried out a scientific experiment on board a stratospheric research balloon. The technological platform developed in the frame of the programme. This platform consist active and passive instruments to detect the cosmic radiation using stratospheric research balloons. The COCORAD experiment used first time in real mission conditions the TRITEL 3D silicon detector telescope to measure the cosmic radiation and its dose contribution during the BEXUS balloon flight. It was also the first time that an intercomparison between the results of measurements performed with the Pille TL dosimeter system and the TRITEL 3D telescope was provided. Further scientific data evaluation is in progress and will be presented at later stages.

7. ACKNOWLEDGEMENTS

The authors acknowledge the services provided by the organisers of the REXUS/BEXUS, especially the European Space Agency Educational Office, the German Aerospace Center (DLR), the Swedish Space Corporation (SSC), the Swedish National Space Board (SNSB) and the experts of the space organisations who supported the student teams throughout the project.
The BEXUS COCORAD and the BEXUS TECHDOSE experiments were co-funded in the frame of the PECS contracts No. 4000103810/11/NL/KML and No. 4000107210/12/NL/KML, respectively.
The authors wish to thank the work of the active COCORAD team members (Zsolt Váradi, Gergely Goldschmidt) and active TECHDOSE team members (Andrea Strádi, Ágnes Gyovai, Dorottya Habos, József Pálfalvi, Marianna Korsós Brigitta, Orsolya Ludmány) and the scientific and engineering support provided by the experts of the Centre for Energy Research, Hungarian Academy of Sciences. The authors wish to thank the support provided by the BL-Electronics Ltd.

8. REFERENCES

1. EuroLaunch (2010): BEXUS User Manual, REXUS User Manual
2. Schaefer, H.J. (1979). Radiation and man in space. *Adv. Space Science* 1, 267-339.
3. McAulay, I. et al. (1996). EURADOS, radiation protection 85. Exposure of air crew to cosmic radiation. *EURADOS Report 1996-01*, Luxembourg, 1–77.
4. Allkofer, O.C. and Grieder, P.K.F. (1984). Cosmic rays on Earth. *Physics Data 25-1*, ISSN 0344-8401.
5. Pázmándi, T., Deme, S., Láng, E. (2006). Space dosimetry with the application of a 3D silicon detector telescope: response function and inverse algorithm. *Radiat. Prot. Dosim.* 120, 401-404.
6. Fehér, I., Deme, S., Szabó, B., Vágvölgyi, J., Szabó, P.P., Csőke, A., Ránky, M., Akatov, Yu.A. (1981). A new thermoluminescent dosimeter system for space research, *Advances in Space Research*, 1, pp. 61-66.
7. Prediction and Measurements of Secondary Neutrons in Space (2001). *Rad. Meas.* 33, 229-387.
8. S. A. Durrani and R. K. Bull (1987). Solid State Nuclear Track Detection, Principles, Methods and Applications, Pergamon Press, ISBN 0-08-020605-0, pp.145-161.
9. Ziegler, J.F., Biersack, J.P., Ziegler, M. (2008). The Stopping and Range of Ions in Matter. ISBN 978-0-9654207-1-6.
10. Diston, D.J. (2009). Computational Modelling and Simulation of Aircraft and the Environment. John Wiley&Sons Ltd.
11. Zábori, B., Hirn, A., Pázmándi, T. (2012). The Hungarian CoCoRAD experiment in the BEXUS program of the ESA, *63rd International Astronautical Congress Paper*.
12. G. Pfotzer (1936). *Physikalische Zeitschrschift* 102, 23.
13. G.A. Bazilevskaya, I.G. Usoskin, E.O. Flückiger, R.G. Harrison, L. Desorgher,•R. Bütikofer, M.B. Krainev, V.S. Makhmutov, Y.I. Stozhkov, A.K. Svirzhevskaya, N.S. Svirzhevsky,•G.A. Kovaltsov (2008). Cosmic Ray Induced Ion Production in the Atmosphere, *Space Sci Rev* 137: 149–173.

CONTINUOUS MEASUREMENT OF THE BIOLOGICAL EFFECTS OF STRATOSPHERIC UV RADIATION – BIODOS EXPERIMENT, BEXUS-15

Veronika Grósz[1], Vilmos Gorócz[1], András Futó[1], Dávid Vatali[1], József Szabó[1], Attila Bérces[2]

[1]Budapest University of Technology and Economics, Egry János. u. 18. 1111 Budapest, Hungary; e-mail:veronika.grosz@gmail.com, gorocz@mht.bme.hu, a6futand@gmail.com, vatalid@gmail.com, szabo@mht.bme.hu
[2]Semmelweis University. Tűzoltó utca 37-47. 1094 Budapest, Hungary
berces.attila@med.semmelweis-univ.hu

ABSTRACT

Solar light and especially the ultraviolet (UV) range of the electromagnetic spectrum is an essential environmental factor for life on Earth, for its effects on living systems can be both beneficial and harmful. Studying the effect and the dynamics of solar UV radiation damage on model biomolecules and organisms can contribute to our knowledge on the evolution and survival of life in harsh environments. In order to assess the biological damage caused by stratospheric UV radiation, the experiment presented here tested a new, continuous biodosimetric measurement method on board a BEXUS balloon.

1. INTRODUCTION

The harmful effects of ultraviolet radiation on living organisms are based on the molecular changes introduced mostly in DNA. The DNA chain consists of a sugar-phosphate backbone and purin and pyrimidine organic bases. UV radiation induces the dimerisation of adjacent pyrimidine bases (Fig 1) and leads to the formation of photoproducts such as cyclobutane dimers and 6-4 bipyrimidines [1-3].

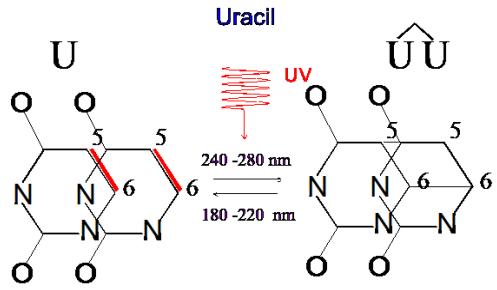

Figure 1. Pyrimidine (uracil) dimerisation due to ultraviolet radiation.

Dimers present in the DNA chain impair the replication mechanism, resulting in mutations or cell death. The ultraviolet spectrum can be divided into four wavelength ranges: UVA (315-400nm); UVB (280-315nm); UVC (200-280nm) and vacuum UV (VUV) (100-200nm). The dimerisation of pyrimidine bases can mainly be attributed to UVB radiation, while shorter wavelengths (UVC) revert this and cause monomerisation [2-3;5]. In polychromatic UV environment, the two processes run parallel and the overall effect reflects the dominant range of radiation. Several biochemical models containing pyrimidine bases are available for studying pyrimidine dimerisation, such as polycrystalline uracil thin layers, bacterial spores and the T7 bacteriophage [4]. The measurement method for the study of UV damage is based on the change in one of the optical attributes of the pyrimidine sample called optical density (OD), which is the logarithmic ratio of radiation falling on a material (I_0) to the radiation transmitted through it (I_t).

$$OD = \log\left(\frac{I_0}{I_t}\right) \qquad (1)$$

Due to the dimerisation of pyrimidine molecules caused by UV exposure, the optical density of the sample (OD) decreases. The OD decrease caused by dimerisation is most prominent in a 50nm wide range of the absorbance spectrum of a pyrimidine base (~250-300nm). The OD change on the outlying ranges cannot be precisely attributed to pyrimidine dimerisation (Fig 2).

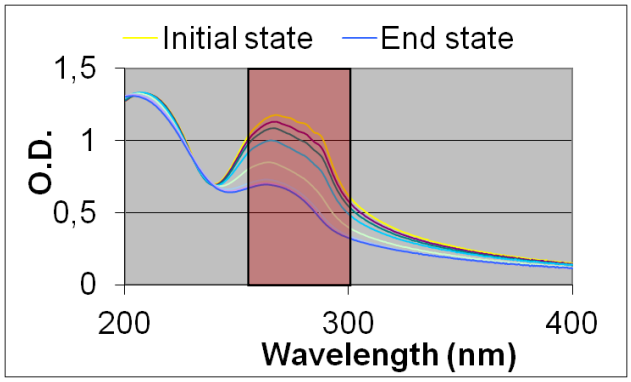

Figure 2. Decrease of optical density of uracil in the UV range. The red rectangle highlights the range of OD change associated with dimerisation

The optical density can be measured by ultraviolet-visible (UV-VIS) spectrophotometry and is usually used to register the initial and final OD of an exposed pyrimidine sample. The UV-VIS method can only produce limited data points from a measurement, and the removal of the sample from the experimental environment is always needed. As the data gained from a spectrophotometric measurement can only enable a

crude assessment on the changes in the behaviour of the irradiated samples with time, the precise analysis of the dynamics of the dimerisation processes requires a continuous measurement. This is particularly important in space applications, for example on satellite platforms where retrieving the sample material can be impossible.

2. EXPERIMENT SETUP

During the course of the BEXUS BioDos project, a continuous OD measurement method was designed and tested onboard the gondola of a stratospheric balloon. According to (1), OD can be calculated from intensity values measured before and behind a sample material. The relevant UV intensity can be monitored with UV sensitive silicon carbide photodetectors. For the calculation of OD, two sets of detectors were used in the experiment: a reference detector measured the unattenuated radiation intensity (I_0) and sample detectors were placed behind pyrimidine samples to measure the transmitted radiation (Fig 3) [6].

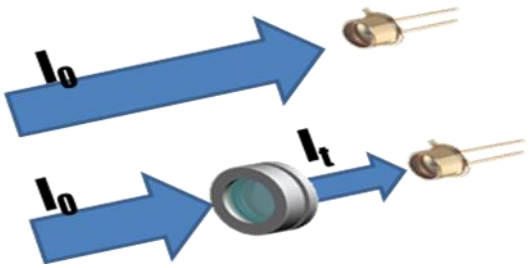

Figure 3. The scheme of OD measurement in the BioDos experiment

The voltage levels measured by the detectors correlate with the intensity (irradiance) of the UV radiation falling on them. Decreasing absorbance leads to an increase in the transmitted intensity and therefore an increase in the voltage values measured by the sample detectors. After converting the electric signals of both types of diode to irradiance values, the OD can be calculated from (1). The measurement principle was supplemented by a corresponding electrical and mechanical design which enabled the pilot flight of the experiment onboard a balloon. The experiment consisted of five separate units: four optical boxes (OB), facing towards four directions at the four sides of the gondola, and an electronics box (EB). The OBs contained the reference and sample detectors as well as the pyrimidine samples. For the purposes of the experiment, polycrystalline uracil thin layers (UD) were chosen as the model system and function as passive detectors by changing their respective absorbance values. The photodiode detectors (PD) were UV broadband sensors with their maximum sensitivity in the UVB range. Six UDs were enclosed in each Optical Box: four of them were irradiated during flight, and two served as dark samples. The latter were used to determine possible non-UV caused damage. In each OB, one of the sample holders was empty (i.e. did not contain uracil sample) and the PD placed behind it served as the reference diode.

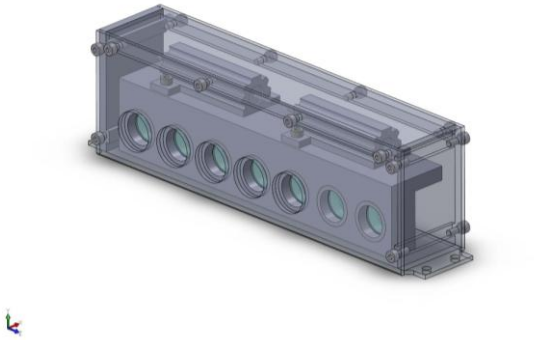

Figure 4. An Optical Box.

All Optical Boxes and sample holders were eloxated in order to minimize the noise in the intensity measurement caused by reflections on the metal surface. The OBs were designed to have thermal insulation (multi layer insulation [MLI]) and automatic heating switching on if the outside temperature dropped below -20°C.

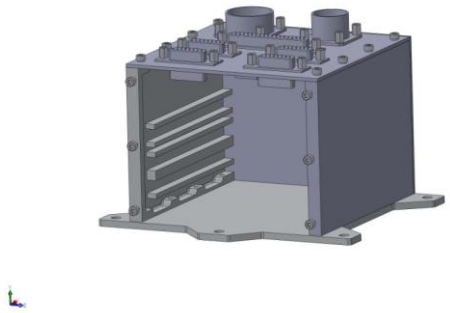

Figure 5. The Electronic Box without the printed circuit boards.

The EB (Fig 5) provided onboard data handling, telemetry, power supply, power distribution and temperature control functions. It contained four printed circuit boards (PCBs): one motherboard, an OBDH board for the digital electronics, a Power Supply (PS) board and an AUX board with the heater control and supplementary electronics. Data and control signals between the OBs and the EB were carried through 15-wire cables. The measured data was stored and transmitted to the Earth Ground Support Equipment

(EGSE) via the Esrange Airborne Data Link (E-Link) telemetry system. The EGSE continuously received the telemetry and measurement data and was used to send telecommands controlling sampling frequency and general experiment behaviour. The experiment boxes were mounted on base plates (Fig 6) and placed in the opposite corners of the gondola (Fig 7). The experiment weight was ~10 kilograms.

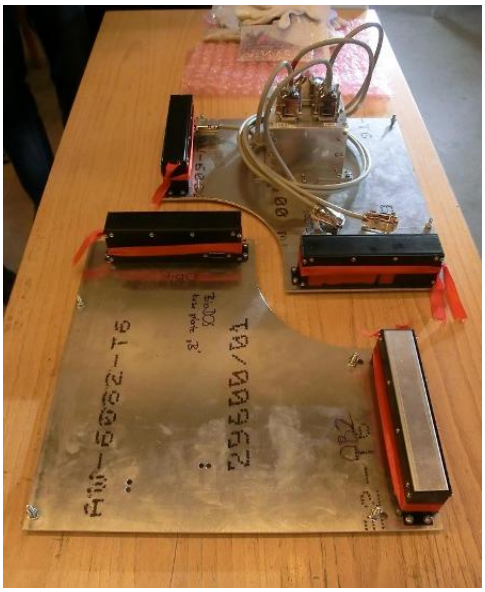

Figure 6. Experiment units: four optical boxes and the electronics box mounted on the base plates

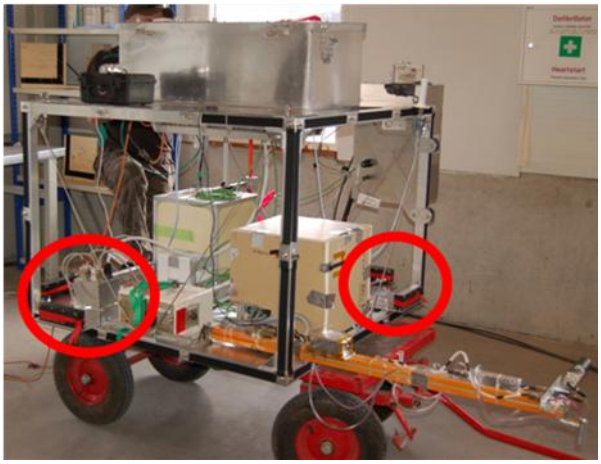

Figure 7. Experiment placement on the gondola

3. THE BEXUS PLATFORM

The BEXUS (Balloon-borne Experiments for University Students) programme offers flight opportunities to student experiments onboard a stratospheric balloon. The choice of vehicle for the BioDos experiment was based on several scientific and technical observations regarding the dimerisation process. As the main scientific objective of the experiment is the assessment of solar UV radiation, the Sun was required as the UV source. The radiation range necessary to pyrimidine dimerisation and monomerisation (UVB and UVC) is not present at ground level. This can be attributed to the stratospheric ozone layer which filters out the lower wavelengths of UV radiation. The higher wavelengths (UVA) reaching the surface cannot cause the expected photoreaction. Ground level testing of the proposed measurement method is therefore impossible. The BEXUS balloons have a minimum flight altitude of 25 kilometers. Even though the concentration of ozone at the specified height is still high, at 25-30 kilometers of altitude the UVB and UVC components of solar radiation appear in the electromagnetic spectrum, enabling the intended measurement. It should also be mentioned that a balloon flight has the necessary float time duration of at least one hour for the detectable photoreaction to take place in the sample. As the experiment is intended as a pilot project for later satellite or ISS experiments, the likeness of the stratosphere to the Low Earth Orbit (in terms of environmental factors) is beneficial for testing the overall idea.

4. LAUNCH

The experiment was assigned to the BEXUS-15 balloon which was launched on 25 September 2012 at 10:18 UTC from the Esrange Space Center, Kiruna, Sweden. During the Launch Campaign, the student team performed the necessary testing (functional and communication tests) of the experiment. Telemetry data show that the experiment operation was nominal during the flight. Voltage and current telemetries were constant. The thermal behaviour of the optical boxes is shown on Fig 8.

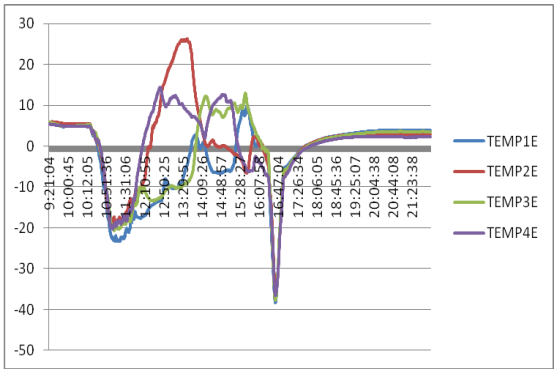

Figure 8. Thermal behaviour of the four optical boxes Temperature shown was measured outside the MLI foil.

After 6h 10 minutes of flight time the balloon was cut down and landed in Finland. The gondola and the experiment was recovered and delivered back to Esrange a few days later. The student team confirmed that the experiment sustained no damage during landing. The experiment was dismounted from the gondola and transported back to Budapest.

5. RESULTS

Data analysis and evaluation was done at the premises of the two universities cooperating in the BioDos experiment: Semmelweis University (Research Group for Biophysics) and Budapest Universiy of Technology and Economics (Space Research Group).

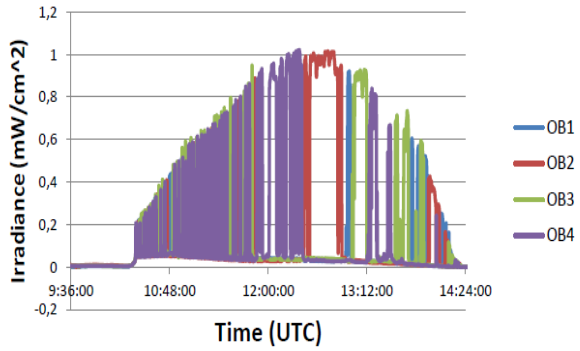

Figure 9. UV irradiance values during the flight

Fig 9 shows the UV irradiance values measured by the four reference detectors during flight. Irradiance values show sudden drops to zero – this can be attributed to the gondola turning away from the Sun, which also affected the irradiation times of the samples. From Fig 9 it can also be concluded that the gondola's rotation slowed down in time. During the ascent phase, the rotation was rapid, but by the time of the float phase (maximum altitude) it slowed down. This led to two of the optical boxes getting most of the UV-radiation during the flight (OB2 and OB4), while OB1 and OB3 were irradiated mostly during the ascent and descent phases.

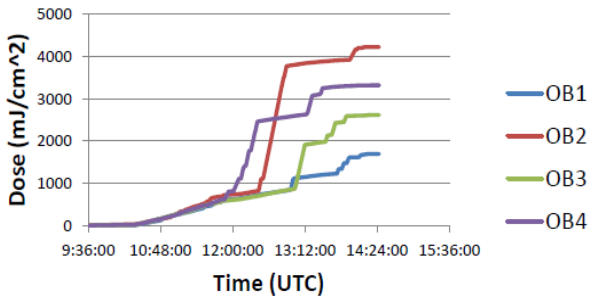

Figure 10. UV dose received by the samples

The optical densities of the samples were determined by UV-VIS spectrophotometry and by calculation from the signals of the UV diodes. Spectrophotometric measurements showed small or no decrease in OD (Fig 11).

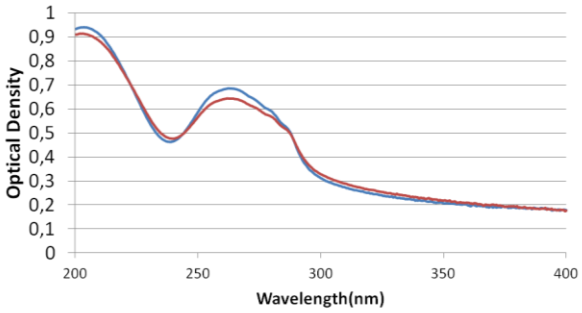

Figure 11. Example of the OD decrease of an uracil sample. Blue: before flight, red: after flight data

There were anomalous measurement data regarding the behaviour of the samples. In a significant amount of samples the OD increased instead of decreasing. The most likely explanation is a change in the crystalline structure of the sample; the exact reason is still under investigation however.

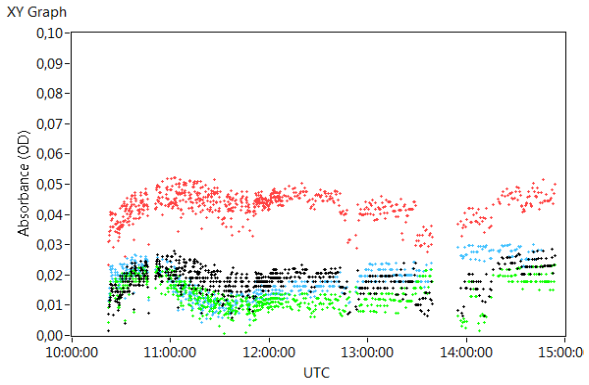

Figure 12. Result of the continuous measurement of the OD of the samples in OB1. Different colours mark the four different samples.

Fig 12 shows the calculated OD of the samples in Optical Box 1. The optical density is expectedly constant during the measurement as the broadband sensors are not specific enough to detect the small decrease in OD shown in Fig 11. There were some anomalies however in the calculated data. A significant amount of data points had negative values of OD which would mean that the unattenuated irradiance is lower than the attenuated. These kinds of readings are scientifically impossible and therefore have to be corrected during further investigations into the measurement method. The most likely explanation for the experienced anomaly is the usage of broadband sensors. Even though the sensitivity of the detectors was at the maximum in the relevant wavelength range (~280nm), the sensitivity was still high enough in the

UVA and UVC ranges to cause a very high level of "noise" in the experiment as the behaviour of the samples in these respective ranges is not as predictable and understood as in the 50nm wide range specified before. This can cause nonsensical data during evaluation.

6. CONCLUSIONS

The BioDos mission objectives were centered around the development of a continuous measurement platform for biodosimetric purposes. As it was mentioned in the introduction, an application like this counts as a pioneer in this field of study, as former experiments were carried out without complex measurement electronics. Continuous measurements require the system to collect and send the measurement data in real time to the Groud Station. This requires a custom design Data Collecting/Processing circuit. The flight results show that the Data Handler was working as intended during the mission and there were no instances of data loss. Despite the completely newly-made design, the experiment worked nominally during the flight of the balloon. Therefore, future modifications will target changes specific to the intended application rather than the experiment setup as a whole. The fulfilment of the scientific objectives depended on environmental factors rather than technological prowess. Even the anomalies described earlier can be used to improve the experiment design. As the main problem of the electrical measurement was the usage of the non-specific broadband sensors, the measurement can be improved by using UVB and UVC sensors. These detectors have a thinner sensitivity spectrum which can be beneficial twofold: first the calculation of the UV dose received by the samples can be more precise as with the usage of an UVB sensor the calculation of the useful dose would be possible. Second, the noise caused by the presence of the UVA/UVC range of radiation during the OD measurement can be eliminated this way. The possible improvements will be realized by the student team in the next cycle of the BEXUS programme. After the successful application and selection in December 2012, a follow-up experiment called Daemon will have a flight opportunity on board the BEXUS 16/17 balloon in October 2013. The data gained in the future experiment may also be used to correct the broadband data of BioDos.

7. REFERENCES

[1] G.J. Fisher, H.E. Johns, Pyrimidine photoproducts, in: S. Wang (ed.)(1976) *Photochemistry and Photobiology of Nucleic Acids*, Acad. Press, New York, 1; pp. 169-224,

[2] B.S. Rosenstein, D.L. Mitchell. (1987). Action spectra for the induction of pyrimidine (6—4) pyrimidine photoproducts and cyclobutane pyrimidine dimers in normal human skin fibroblasts. *Photochem. Photobiol*. **45**; 775-780.

[3] Setlow RB, Swenson PA, Carrier WL. (1963) Thymine dimers and inhibition of DNA synthesis by ultraviolet irradiation of cells. *Science*. **142**(3598): 1464-6.

[4] Gróf P., S. Gáspár, A. Bérces. (1993) Uracil thin layers in dosimetry of UV-radiation. *Proc. Internat. Symp. on Biomedical Optics*, Budapest, SPIE 2086 420-424.

[5] Kovács G, Fekete A, Bérces A, Rontó G (2007). The effect of short wavelength ultraviolet radiation. An extension of biological dosimetry to the UV-C range. *J Photochem Photobiol* B: Biol. 88:77-88.

[6] G. Goldschmidt, É. Kovaliczky, J. Szabó, G. Rontó, A. Bérces. (2012) In Situ Biodosimetric Experiment for Space Applications. *Origins of Life and Evolution of Biospheres*,. doi: 10.1007/s11084-012-9286-1.

CYTOSOLIC CALCIUM, HYDROGEN PEROXIDE, AND RELATED GENE EXPRESSION AND PROTEIN MODULATION IN *ARABIDOPSIS THALIANA* CELL CULTURES RESPOND IMMEDIATELY TO ALTERED GRAVITATION: A HOLISTIC VIEW

[1)]Maren Neef,[1)]Svenja Fengler,[1)]Niklas Hausmann, [1)]Margret Ecke, [1)]Anne Hennig, [2)]Mirita Franz-Wachtel, [1)]Rüdiger Hampp

[1)]University of Tübingen, Physiological Ecology of Plants, Auf der Morgenstelle 1, 72116 Tübingen (Germany); *ruediger.hampp@uni-tuebingen.de*

[2)]Proteome Center Tübingen, Auf der Morgenstelle 15, D-72076 Tübingen (Germany)

ABSTRACT

To decipher the signal transduction chain in *Arabidopsis thaliana* (A.t.) cells upon different gravitational fields, callus cultures were exposed to parabolic flights. Wild type (WT) A.t. cells were used to detect both changes gene expression and protein phosphorylation. For this purpose, the cells were metabolically quenched by manual injection of RNAlater at distinct stages of a parabola (start of the parabola (1g), end of the first hypergravity-phase (1,8g), end of microgravity (µg) and finally at the end of the parabola (1,8g)). In addition, transgenic A.t. cells, expressing either a calcium (YC3.6) or an hydrogen-peroxide (HyPer) sensor, were analyzed fluometrically *in vivo* during the entire flight. In summary, we observed (i) significant gene expression changes, (ii) multiple phosphorylation / dephosphorylation processes, (iii) cytosolic calcium (Ca^{2+}) fluxes, and (iv) alterations in the cytosolic hydrogen peroxide (H_2O_2) level as specific gravity dependent response in A.t. cells, which took place within seconds.

1. INTRODUCTION

An important factor controlling plant development and growth is gravity. Perception of the gravitational factor can be via specific tissues such as root caps with their statocytes, but also by single cells like in rhizoids of algae. In principle, however, any plant cell can perceive gravitational forces and respond to changes with physiological answers. Model systems which are primarily investigated are Arabidopsis and rice. For Arabidopsis with its small genome, large data banks exist in meanwhile which support expression studies for both, genes and proteins.

First reports about the long-term effect of microgravity (µg) on whole plants have just been reported from material exposed on the International Space Station (ISS) [1, 2]. A considerable number of gene transcripts were altered in amount, including those involved in the jasmonic acid pathway. Down-regulated genes included one coding for a peroxidase. Other ISS-related studies with dwarf wheat were not able to detect alterations in gene expression in 24-day-old leaves [3].

Changes in gene expression due to freefall can be very fast. Callus cultures of Arabidopsis thaliana responded within min of microgravity as obtained by sounding rockets [4, 5]. The impact of microgravity on gene expression results from perceived and transmitted signals. For gravity sensing a range of theories exist [6, 7, 8]. Independent of the external signal and its perception, environmental changes are transmitted by a transient increase of the intracellular Ca^{2+} concentration. This has also been shown for changes in the gravity vector [9].

Another trigger is the production of reactive oxygen species (ROS). They are no longer considered only as protectants against invading pathogens. ROS such as hydrogen peroxide have been shown to be also important in cellular signalling, and a ´ROS gene network' has been suggested [10, 11, 12]. There are also reports about a close interrelationship between the hydrogen peroxide producing NADPH oxidase, hydrogen peroxide, and Ca^{2+} [13, 14].

In this study we used callus cultures of A. thaliana to investigate short time alterations in the pools of these secondary messengers, as well as related gene expression and protein modification. We show that 20 sec of microgravity, obtained by parabolic flights, are sufficient to result in an immediate rise of hydrogen peroxide and cytosolic Ca^{2+}, altered gene expression, and altered protein phosphorylation. The data are used to develop a model for early responses to missing perception of gravitation.

Proc. '21st ESA Symposium European Rocket & Balloon Programmes and Related Research', 9–13 June 2013, Thun, Switzerland (ESA SP-721, October 2013)

2. MATERIALS & METHODS

2.1. A.t. cell cultures

For details regarding the establishment of cell culture see [4, 5, 15]. A.t. seeds expressing the calcium sensor YC3.6 were kindly provided by K. Schumacher (University of Heidelberg, Germany) [16]. HyPer cell cultures originate from the laboratory of A. Costa (University of Padua) [17].

2.2. Total RNA and protein fixation

Approximately 5 g WT A.t. cell cultures were used for both gene expression and protein analyses. Samples were taken at four distinct phases of a parabola (fig. 1, numbers 1 -4), by manual injection of RNAlater (Ambion, Darmstadt, Germany).

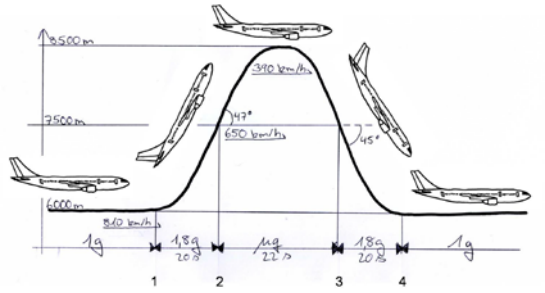

Figure 1: Sketch of the different phases of a parabolic flight. The numbers identify the sampling events at the end of 1 g, before the first parabola (1), at the end of the first hypergravity phase (2), at the end of the microgravity phase (3), and at the end of the second hypergravity phase (4).

2.3. Gene expression and phoshoprotein analysis

All methods regarding gene expression and phosphoprotein analysis are described precisely in [5, 15, 23].

2.4. Fluorimetric detection of cellular fluctuations of Ca^{2+} and H_2O_2 concentrations

Sample fluorescence was recorded by a microplate reader (POLARstar Optima; BMG, Germany) which, together with the control unit (note book) was fixed within a rack. The latter was firmly attached to the floor of the plane. Wells of a 96-well-microplate (Nunc, Germany) were filled with 200 µl MS medium (SigmaAldrich) containing 1.6% Agar (SigmaAldrich). Cameleon-expressing, HyPer-expressing, or wild type cells (100 mg each) were transferred into the wells. The microplate was then sealed with a foil (Axygen) in order to prevent spilling or evaporation. Fluorescence ratios (cameleon-dependent YFP-CFP: 535 nm / 480 nm) were determined in real-time. For HyPer cells, emission (at 530 nm) was calculated as a ratio upon excitation at 480 and 420 nm. With increasing hydrogen peroxide, excitation at 480 nm yields increased emission at 530 nm, while that at 420 nm results in a decreased emission. For each parabola, samples of one distinct well were recorded. The data were analyzed using the software MARS (BMG, Germany).

2.5 Determination of pyridine nucleotides (NADP, NADPH)

Quantitation of triphosphopyridine nucleotides was by a cycling technique (BioVision, BioCat, Heidelberg, Germany). As this works for both, oxidized and reduced forms, we subjected the samples to acid (0.1 N HCl) and base (0.1 N KOH) extraction, followed by 5 min of heating (Lowry and Passonneau 1972). This treatment selectively destroys reduced or oxidized pyridine nucleotides. The neutralized samples (50 µl) were mixed with 100 µl cycling mix and handled according to the manufacturers instructions. Background readings (no pyridine nucleotides) were obtained from acid treated extracts (no NADPH) mixed with the NADP/NADPH extraction buffer, contained in the kit. This sample was kept at 60°C for 30 min, which destroys NADP. Extinction at 450 nm was determined in a microplate reader (TECAN, Salzburg, Austria) in 15 min intervals. Total assay volume was 160 µl (Costar 96 well plates). Usually, readings obtained after 30 min were used. Amounts were quantified by using internal standards (10 to 100 pmol).

3. RESULTS

3.1. Gene expression changes and protein modulation

By combining both microarray screening and 2D gel electrophoresis, we obtained an entire view of all changes in the gene expression and protein modification level in A.t. as a response to the different gravitational forces during the first parabola of one flight. The gene expression analysis revealed thousands of significantly altered transcripts due to both hyper and microgravity treatment (table 1). Although most of the transcripts are changed in amount due to any phase of a parabola, we were also able to detect hundreds of genes that are particularly expressed during µg (for details see [15]). Regarding protein modifications relatively few proteins were identified. However,

here we do not have an overlap between the different g-forces, indicating a high specificity of the modified proteins.

Table 1: Gene expression changes and protein modulation (phosphorylation ≥ 2fold; dephosphorylation ≤ 0,5fold) upon the different phases of a typical parabola compared to the in flight 1g control (1). Numbers identify altered transcripts or phosphorylated peptides, those in parantheses the sampling events (see fig. 1).

	1st 1,8g (2)	
	gene expression	protein modulation
≥ 2fold	2111	2
≤ 0,5fold	2815	6
	µg (3)	
	gene expression	protein modulation
≥ 2fold	2487	6
≤ 0,5fold	2947	6
	2nd 1,8g (4)	
	gene expression	protein modulation
≥ 2fold	2330	4
≤ 0,5fold	2871	5

Our data prove that plant cells respond extremely rapidly, i.e. within seconds, to environmental changes.

3.2. Pool sizes of Ca^{2+}, and H_2O_2, and the triphospho pyridine nucleotide redox charge

A typical parabola is illustrated in fig. 1. The flights (Airbus A300, Novespace, France) take place between 6000 a nd 8500 m a.s.l. They consist of several phases: initial acceleration with climbing in an angle of about 47°. This results in 1.8 g. Then the thrust is decreased and the plane moves around the top of the parabola by its residual speed, with some acceleration to overcome the air resistance, yielding 20 to 24 s of reduced gravitation (see Fig. 2). Finally, the plane comes back to the horizontal orientation which is connected with a second 1.8 g period. Numbers 1-4 (fig. 1) indicate the critical time points where samples were taken (e.g. for extraction of RNA, proteins or metabolites), if no continuous measurements were taken (e.g. fluorescence).

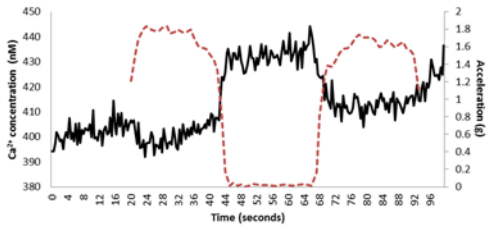

Figure 2. Intracellular Ca^{2+} concentration as calculated from the emission ratio of 535/480 nm [18] (left vertical axis). The graph shows a typical behaviour of a responsive callus. The dotted line represents the respective kinetics of the acceleration, ranging from <0,01g to about 1.8g (right vertical axis; data from Novespace, Bordeaux, France).

Fig. 2 shows changes for Ca^{2+} and hydrogen peroxide during an individual parabola. Fig. 2 also gives the kinetics of changes in acceleration. The period of reduced gravitational acceleration (< 0.01g) lasted for about 20 sec. Typically, we found an increase upon onset of µg, and a decrease thereafter, but no response to the initial hypergravity phase of a parabola.

For the determination of hydrogen peroxide we employed cell cultures expressing the yellow fluorescent protein based sensor HyPer [17]. This sensor is specific to this component of reactive oxygen species. Here, we also found an increase (not shown) similar to that of Ca^{2+} (fig. 2). Altogether, we evaluated up to 60 parabolas during independent flights (in 2011 and 2012). The responses of the cell cultures were quite consistent with regard to Ca^{2+}, but more variable for hydrogen peroxide.

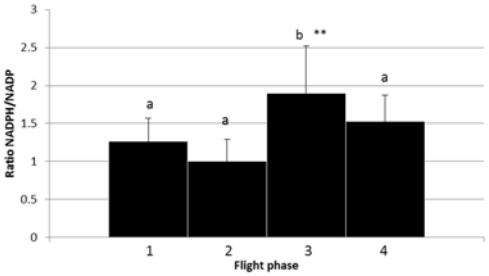

Figure 3. Redox state of the triphospho pyridine nucleotide system; numbers 1 to 4 correspond to the different flight phases shown in fig. 1. Bar: standard deviation (n = 7). The differences between 1.8g and µg are highly significant according to ANOVA (p = 0.005).

Hydrogen peroxide can be produced by NADPH oxidase, located in the plasma membrane. This enzyme is activated by Ca^{2+}, and releases hydrogen peroxide to the apoplast [13]. Electron supply is by intracellular NADPH, which probably is generated by glucose 6P dehydrogenase (oxidative pentose phosphate cycle). If indeed significant amounts of hydrogen peroxide are formed during onset of microgravity, pool sizes of NADPH should respond. We thus assayed the amounts of NADPH and NADP. In this case samples were taken at the points indicated in fig. 1, and metabolically quenched in either acid (NADP) or base (NADPH). The calculated ratios are given in fig. 3. At 1g (before acceleration) the ratio was around 1.2. At the onset of µg, the ratio dropped (0.9), but rose during the µg phase, reaching nearly 1.7 at the end. After the second 1.8g phase, the ratio decreased again. Especially the behaviour during microgravity, which is opposite to that of hydrogen peroxide, indicates some interdependence: the onset of hydrogen peroxide production consumes NADPH, the later decline relieves the pressure on the redox charge.

4. DISCUSSION

Arabidopsis thaliana cell cultures sense a lack of gravitation immediately. Within seconds there is an increase of cytosolic Ca^{2+} which is continued over 20 s. In parallel, the amount of hydrogen peroxide rises, with some decline later on. The NADPH/NADP redox status is also affected; it decreases at the beginning of the microgravity phase and then increases again, when hydrogen peroxide possibly declines. According to this scenario, we suggest the following interrelationship: Lack of gravity is sensed at the plasma membrane [19] and causes an influx of Ca^{2+}. Ca^{2+} then activates the NADPH oxidase within the plasma membrane which produces hydrogen peroxide under consumption of NADPH. This activity would explain both the rise of hydrogen peroxide and the decrease of the NADPH/NADP ratio. The later rise of the redox state together with the amount of Ca^{2+} and the decline of hydrogen peroxide during the µg phase could be explained by a scheme for NADPH oxidase regulation as suggested by [13] for plant defence responses. They postulate that Ca^{2+} influx activates a Ca^{2+}-dependent protein kinase (CDPK). This enzyme phosphorylates the N-terminal region of the NADPH oxidase. The resulting change in conformation allows for the phosphorylation/activation of the oxidase by Rac GTPase, and thus the synthesis of hydrogen peroxide. The later decline of hydrogen peroxide together with the rise of the redox charge can also be explained by this scheme: Increased hydrogen peroxide production supports further Ca^{2+} influx (still rising towards the end of the µg period), which in due course will inhibit the activation of the oxidase. In consequence, hydrogen peroxide production will decline and the redox charge increases.

A fast way to modify cellular metabolism is by altering protein phosphorylation. Such a response has been implicated in the transduction of many environmental signals in plants (for a review see [20]). Addition or removal of phosphate can lead to changes in the activation status, catalytic activity, or cellular localization of effector proteins [21].

The results of our screening for changes in protein phosphorylation resulted in about 29 protein spots with altered degree of phosphorylation [15].

The rapid changes in the degree of phosphorylation of enzymes involved in primary metabolism indicates a rapid but distinguished metabolic response to both hypergravity and reduced gravity. It has, however, to be kept in mind that the effects on the respective protein function are in many cases still not known.

Under hypergravity, phosphorylation is increased for enzymes involved in the detoxification of reactive oxygen species (ROS) such as superoxide dismutase and ascorbate peroxidise [15]. Increased production of ROS is connected to most stress reactions of cells [22], and own as well as data of others show that this response holds also for gravitational forces. However, for the short time exposures to hypergravity reported here, we did not find corresponding changes in the hydrogen peroxide pool, which only occurred under microgravity. Another identified protein, glycerol kinase can be related to lipid metabolism, and changes in membrane properties are well connected to gravity effects. The same holds true for a microtubule associated protein which indicates responses involving the cytoskeleton. Annexin, also altered, is a Ca^{2+}-dependent protein and participates in vesicle transport and calcium ion channel formation. Under long-term hypergravity exposure the amount of annexin is also increased, not only the degree of phosphorylation [23]. Related to the pyridine nucleotide pool is an ATP-dependent

NAD(P)H hydrate hydratase. This enzyme is involved in the formation of NAD(P)H out of (6S)-6beta-hydroxy-1,4,5,6-tetrahydronicotinamide-adenine dinucleotide (P), and could be related to NADP(H) changes due to the activity of the NADPH oxidase.

Changes related to the 20 sec exposure to microgravity affected to a higher degree proteins which are part of the primary metabolism. Increased phosphorylation was found for triosephosphate isomerase (glycolysis), pyruvate dehydrogenase (glycolysis), and citrate synthase (citrate cycle). If the increase in phosphorylation of these proteins also means higher rates of activity, then this finding would indicate higher rates of carbohydrate turnover in favour of amino acid synthesis and energy production. For pyruvate dehydrogenase (PDH) this assumption is possibly not right. PDH is a complex formed by three enzymatic components. This complex is inactivated by the phosphorylation of the E1 subunit [24]. This means that the activity of this complex is possibly decreased under µg, limiting the feeding of the citrate cycle. The inorganic pyrophosphatase in plants is an alternate proton pump at the tonoplast, and HSP 70-3 is involved in protein folding and repair; similar to the hypergravity effect.

For a few of these proteins, also a significant decrease in phosphorylation was found. These are partly also connected to glycolysis (fructokinase, a fructose-specific hexokinase) and the citrate cycle (isocitrate dehydrogenase, IDH).

While the phospho proteomic analysis performed in this study provided the first screen of the proteins that are differentially phosphorylated upon changes in gravity, it likely sampled only the proteins of highest abundance. We therefore plan to apply other, more sensitive quantitative approaches to study the phosphor proteome dynamics in the future.

As illustrated by table 1, 20 sec of microgravity are sufficient to alter the amounts of quite a large number of transcripts. They are mainly Ca^{2+} and ROS related, and support the respective fluorescence assays. In addition to the modulation by phosphorylation of existing proteins for rapid responses (e.g. CML14, [15]), the changes in transcript levels aim at longer lasting metabolic answers and initiate other signalling pathways such as via the expression of inositol polyphosphate 5-phosphatase which will result in a Ca^{2+}-dependent release of inositol(1,4,5)triphosphate. This compound is another second messenger (in addition to hydrogen peroxide and Ca^{2+}). Inositol triphosphate triggers the release of Ca^{2+} from intracellular stores like the endoplasmatic reticulum [25]. For the control of the cellular Ca^{2+} level, an increased expression of the glutamate receptor 2 and ligand-gated ion channel could be responsible.

Another group of genes [15] take part in ROS detoxification. Among these are a catalase (CAT1), a glutathione peroxidase (GPX3, mitochondrial; [22]), a superoxide dismutase (CSD2, plastidal; [22]), and a SOD-related transcription factor. This way the cells obviously try to control the disturbed level of reactive oxygen species (for addressed transcripts consult [15]).

5. CONCLUSIONS

In this study, the analysis of second messengers is combined with down-stream responses at the level of protein modulation and gene expression. The data show that in a sequence of changing gravitational field strengths the secondary messengers Ca^{2+} and hydrogen peroxide respond to a lack of gravity by a rapid increase (fig. 2 for Ca^{2+}). The rise of hydrogen peroxide production is most probably triggered by Ca^{2+}. Resulting changes in protein modulation indicate the initiation of signalling chains, as well as fast adaptations in primary metabolism. Concomitant changes in transcripts are connected with Ca^{2+} related steps and fine tuning of levels of reactive oxygen species. By extending the period of microgravity up to several minutes (as offered by sounding rocket experiments such as TEXUS or MAXUS) it should be possible to find out whether there is a gravitation-related signature in the Ca^{2+} response.

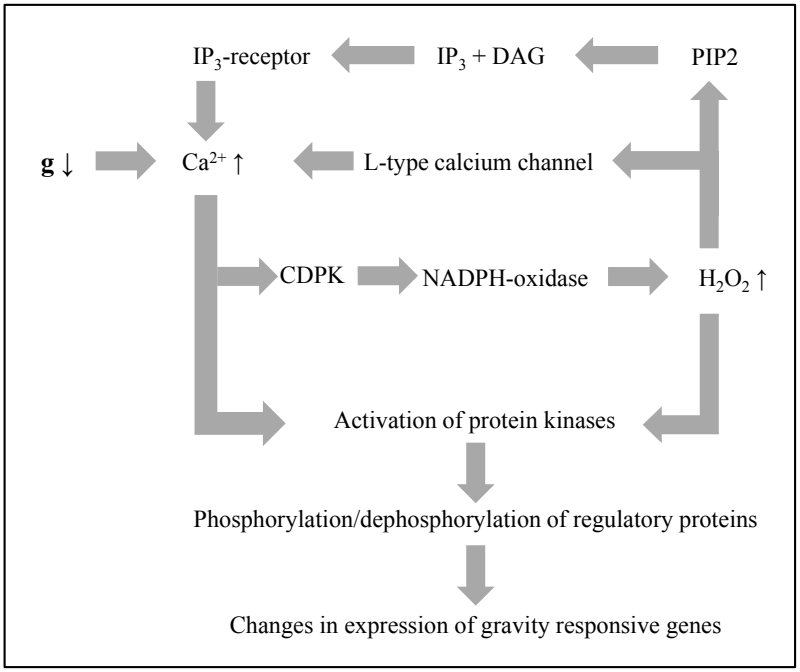

Figure 4: Schematic presentation of assumed early events upon the onset of microgravity. Loss of gravity causes Ca^{2+} influx which triggers the formation of hydrogen peroxide and initiates signaling chains. In consequence proteins are modulated and genes differentially expressed. (PIP2 = phosphatidylinositol 4,5-bisphosphate; IP3 = inositol trisphosphate; DAG = diacylglycerol)

6. ACKNOWLEDGEMENTS

This research was made possible by a grant of the DLR (Deutsches Zentrum für Luft- und Raumfahrt e.V.; grant nr. 50 WB 0723). We are indebted to the crew of Novespace for technical support, Fabian Bergwitz for help during the parabolic flights, Elke Klenk for determination of the pyridine nucleotides and particularly to Dr. Ulrike Friedrich (DLR) for perfect campaign organization.

7. LITERATURE CITED

1. Kiss J.Z., Kumar P., Millar K.D.L., Edelmann R.E., Correll M.J. (2009) Operations of a spaceflight experiment to investigate plant tropisms. Advances in Space Research, 44, 879–886.

2. Pyle T., Souret F., Correll M., Kiss J. (2011) The effects of gravity and the spaceflight environment on the gene expression profile of Arabidopsis thaliana seedlings. Ph.D. thesis, Agricultural abd Biological Engineering, University of Florida, Gainesville, FL, USA.

3. Stutte G.W., Monje O., Hatfield R.D., Paul A.-L., Ferl R.J., Simone C.G. (2006) Microgravity effects on leaf morphology, cell structure, carbon metabolism and mRNA expression of dwarf wheat. Planta, 224, 1038–1049.

4. Martzivanou M., Hampp R. (2003) Hyper-gravity effects on the Arabidopsis transcriptome. Physiologia Plantarum, 118, 221–231.

5. Martzivanou M., Babbick M., Cogoli-GreuterM., Hampp R. (2006) Microgravity-related changes in gene expression after short-term exposure of Arabidopsis thaliana cell cultures. Protoplasma, 229, 155–162.

6. Perbal G., Driss-Ecole D. (2003) Mechanotransduction in root gravity sensing cells. Physiologia Plantarum, 120, 303–311.

7. Limbach C., Hauslage J., Schäfer C., Braun M. (2005) How to activate a p lant gravireceptor. Early mechanisms of gravity sensing studied in Characean rhizoids during parabolic flights. Plant Physiology, 139, 1030–1040.

8. Braun M., Limbach C. (2006) Rhizoids and protonemata of characean algae: model cells for research on polarized growth and plant gravity sensing. Protoplasma, 229, 133–142.

9. Toyota M., Furuichi T., Tatsumi H., Sokabe M. (2008) Cytoplasmic calcium increases in response to changes in the gravity vector in hypocotyls and petioles of Arabidopsis seedlings. Plant Physiology, 146, 505–514.

10. Neill S.J., Desikan R., Clarke A., Hurst R.D., Hancock J.T. (2002) Hydrogen peroxide and nitric oxide as signalling molecules in plants. Journal of Experimental Botany, 53, 1237–1247.

11. Miller G., Shulaev V., Mittler R. (2008) Reactive oxygen signaling and abiotic stress. Physiologia Plantarum, 133, 481–489.

12. Dodd A.N., Kudla J., Sanders D. (2010) The language of calcium signaling. Annual Review of Plant Biology, 61, 593–620.

13. Wong H.L., Pinontoan R., Hayashi K., Tabata R., Yaeno T., Hasegawa K., Kojima C., Yoshioka H., Iba K., Kawasaki T., Shimamoto K. (2007) Regulation of rice NADPH oxidase by binding of rac GTPase to its N-terminal extension. The Plant Cell, 19, 4022–4034.

14. Takeda S., Gapper C., Kaya H., Bell E., Kuchitsu K., Dolan L. (2008) Local positive feedback regulation determines cell shape in root hair cells. Science, 319, 1241–1244.

15. Hausmann N., Fengler S., Hennig A., Franz-Wachtel M., Hampp R., Neef M (2013) Cytosloic calcium, hydrogen peroxide and related gene expression and protein modulation in Arabidopsis thaliana cell cultures respond immediately to altered gravitation: parabolic flight data. Plant Biology. in press

16. Krebs M., Binder A., Hashimoto K., Den Herder G., Parniske M., Kudla J., Schumacher K. (2012) FRET-based genetically encoded sensors allow high resolution live cell imaging of Ca2+ dynamics. The Plant Journal, 69, 181–192.

17. Costa A., Drago I., Behera S., Zottini M., Pizzo P., Schroeder J.L., Pozzan T., Schiavo F.L. (2010) H2O2 in plant peroxisomes: an in vivo analysis uncovers a Ca2+-dependent scavenging system. The Plant Journal, 62, 760–772.

18. Monshausen G.B., Messerli M.A., Gilroy S. (2008) Imaging of the yellow cameleon 3.6 indicator reveals that elevations in cytosolic Ca2+ follow oscillating increases in growth in root hairs of Arabidopsis. Plant Physiology, 147, 1690–1698.

19 Belyavskaya N.A. (1996) Free and membrane-bound calcium in microgravity and microgravity effects at the membrane level. Advanced Space Research, 17, 169–177.

20 Stone J.M., Walker J.C. (1995) Plant protein kinase families and signal transduction. Plant Physiology, 108, 451–457.

21. Huber J.L.A., Huber S.C. (1996) Role and regulation of sucrose-phosphate synthase in higher plants. Annual Review Plant Physiology and Plant Molecular Biology, 47, 431–444.

22. Mittler R., Vanderauwera S., Gollery M., Van Breusegem F. (2004) Reactive oxygen gene network of plants. Trends in Plant Science, 9, 490–498.

23. Barjaktarović Z., Schütz W., Madlung J., Fladerer C., Nordheim N., Hampp R. (2009) Changes in the effective gravitational field strength affect the state of phosphorylation of stress related proteins in callus cultures of *Arabidopsis thaliana*. Journal of Experimental Botany, 60, 779–789.

24. Tovar-Méndez A., Miernyk J.A., Randall D.D. (2003) Regulation of pyruvate dehydrogenase complex activity in plant cells. European Journal of Biochemistry, 270, 1043–1049.

25. Munnik T., Testerink C. (2009) Plant phospholipid signaling: “in a nutshell””. Journal of Lipid Research, 50, 260–265.

Major parts of this contribution are in press at PLANT BIOLOGY (see citation 15; Hausmann et al.)

LESSONS LEARNED FROM REXUS12'S SUAINEADH EXPERIMENT: SPINNING DEPLOYMENT OF A SPACE WEB IN MILLI GRAVITY

Thomas Sinn[(1)], Malcolm McRobb[(2)], Adam Wujek[(3)], Jerker Skogby[(4)], Fredrik Rogberg[(5)], Junyi Wang[(6)], Massimiliano Vasile[(7)], Gunnar Tibert[(8)]

[(1)] *Advanced Space Concepts Laboratory, Mechanical and Aerospace Engineering, University of Strathclyde, UK,* thomas.sinn@strath.ac.uk
[(2)] *School of Engineering, University of Glasgow, UK,* malcolm.mcrobb@glasgow.ac.uk
[(3)] *School of Information and Communication Technology, KTH Royal Institute of Technology, Sweden,* wujek@kth.se
[(4)] *School of Information and Communication Technology, KTH Royal Institute of Technology, Sweden,* jskogby@kth.se
[(5)] *School of Electrical Engineering, KTH Royal Institute of Technology, Sweden,* frogberg@kth.se
[(6)] *School of Electrical Engineering, KTH Royal Institute of Technology, Sweden,* junyiw@kth.se
[(7)] *Advanced Space Concepts Laboratory, Mechanical and Aerospace Engineering, University of Strathclyde, UK,* massimiliano.vasile@strath.ac.uk
[(8)] *School of Engineering Sciences, KTH Royal Institute of Technology, Sweden,* tibert@kth.se

ABSTRACT

On the 19th of March 2012, the Suaineadh experiment was launched onboard the sounding rocket REXUS 12 (Rocket Experiments for University Students) from the Swedish launch base ESRANGE in Kiruna. The Suaineadh experiment served as a technology demonstrator for a space web deployed by a spinning assembly. Following launch, the experiment was ejected from the ejection barrel located within the nosecone of the rocket. Centrifugal forces acting upon the space web spinning assembly were used to stabilise the experiment's platform. A specifically designed spinning reaction wheel, with an active control method, was used. Once the experiment's motion was controlled, a 2 m by 2 m space web is released. Four daughter sections situated in the corners of the square web served as masses to stabilise the web due to the centrifugal forces acting on them. The four daughter sections contained inertial measurement units (IMUs). After the launch of REXUS12, the recovery helicopter was unable to locate the ejected experiment, but 22 pictures were received over the wireless connection between the experiment and the rocket. The last received picture was taken at the commencement of web deployment. Inspection of these pictures allowed the assumption that the experiment was fully functional after ejection, but probably through tumbling of either the experiment or the rocket, the wireless connection was interrupted. A recovery mission in the middle of August was only able to find the REXUS12 motor and the payload impact location.

1 INTRODUCTION

Continuous exploration of our solar system and beyond requires ever larger structures in space. The biggest problem nowadays is the transport of these structures into space due to launch vehicle payload volume constrains. By making the space structures deployable with minimum storage properties, this constraint may be bypassed. Deployable concepts range from inflatables, foldables, electrostatic to spinning web deployment. The advantage of the web deployment is the very low storage volume and the simple deployment mechanism. The concept of a space-web, such as the Japanese 'Furoshiki' satellite [1,2,3], depicts a large net held in tension using radial thrusters or through the centrifugal forces experienced by spinning the assembly [4]. These webs can act as lightweight platforms for the construction of large structures in space without the huge expense of launching heavy structures from Earth. Utilising miniature robots that build as they crawl along the web, huge satellites to harness the Sun's energy or antennas for further exploration of the universe may become viable when implementing space webs technology. There have been several experiments conducted on the deployment of the space webs. In 2006 the deployment of a Furoshiki web by the Japanese ended in a chaotic deployment sequence due to misalignment of the radial thrusters as a result of out of plane forces. The Russian Znamya-2 [5] experiment was the first that successfully deployed and spin stabilised large space structure. More recently, in 2010, the Japanese solar sail Ikaros [6] was successfully

Proc. '21st ESA Symposium European Rocket & Balloon Programmes and Related Research', 9–13 June 2013, Thun, Switzerland (ESA SP-721, October 2013)

deployed using thrusters to introduce spinning. The Ikaros square solar sail had a 20 m diagonal and used solar pressure for acceleration, solar cells on the membrane for power generation and the attitude control using the sail.

2 EXPERIMENT DESCRIPTION

2.1 Overview

The Suaineadh experiment [7] consisted of two distinct sections, the ejected part Central Hub and Daughters (CHAD) and the Data Storage Module (DSM) which remained on the REXUS rocket. The ejected part undertook all mission operations once separation with REXUS had been achieved (Fig. 1). It consisted of the central hub, the web and four daughter sections. Ejection of the experiment from REXUS occurred at an altitude of approximately 70 km and followed a pre-determined automated deployment sequence, which allowed for a safe separation distance to be achieved. The apogee of the experiment was at 86 km altitude at approximately 140 seconds into the flight.

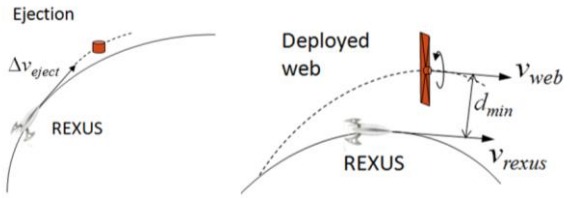

Figure 1: Schematic of Suaineadh ejection and deployment.

CHAD carried all subsystems required to achieve the mission objectives and provides stowage for the web and daughters prior to deployment. The web had the dimensions of 2 m by 2 m (Fig. 2) and was composed of ultralight and flexible braided Spectra fishing lines. Images of the deployment and stabilisation phases were accumulated by cameras located within the central hub. Data was gathered by inertial measurement units (IMUs), one IMU was located inside each of the daughter sections and another one was located inside the central hub itself. Image and data collection began two seconds before the web deployment sequence starts. The data was stored on CHAD as well as being transmitted via a wireless link to the DSM and stored there until recovery after landing. After ejection and prior to deployment, a reaction wheel was used to accelerate the central hub to a sufficient angular velocity for deployment. The daughter sections were released to initiate web deployment. Centrifugal forces acting on the released daughter sections fully deployed the web. As the deployment neared completion the reaction wheel again rotated the central hub to a sufficient velocity to reduce recoiling effects and to achieve web stabilisation. A RF-beacon was placed on CHAD to locate and recover the experiment after the mission in order to collect data.

Figure 2: Deployed Suaineadh web on ground.

2.2 Mechanical

The available volume permitted by the nosecone adapter position of Suaineadh within REXUS 12 demanded that the structural design be as simplistic and efficient as possible. The maximum footprint of the experiment was 0.33m in diameter by 0.40m in height, with a mass of approximately 12kg. For the majority of the structure Aluminium 6082 was used in an effort to reduce the mass as far as much as the mechanical loads would permit with a degree of safety factored in. The exception was the DSM top plate where sensitive flight recorded data was stored. A steel plate was used to protect this section from additional impact loads during touchdown of the recovery module. The expected mechanical and environmental loads expected to be encountered through each mission phase can be summarised as:

- 20-g maximum acceleration.
- 290 kN/m^2 maximum dynamic pressure.
- 4 Hz spin rate during launch.
- -30°C to $+200^{\circ}$C temperature range.

The modular design of CHAD (Fig. 3) allowed quick access to all the essential internal subsystems of the experiment, separable by three tubular sections; the Lower Chamber, Central Chamber, and Upper Chamber. The reaction wheel, modem and ejected section data storage facilities were housed within the Lower Chamber, with the reaction wheel mounted as closely the plane of the deployable space web as possible to position the centre of gravity as closely to this plane. Where possible, PC-104 architectures were used, and orientated vertically such that they encompassed the reaction wheel motor. This proved the most economical use of the available volume.

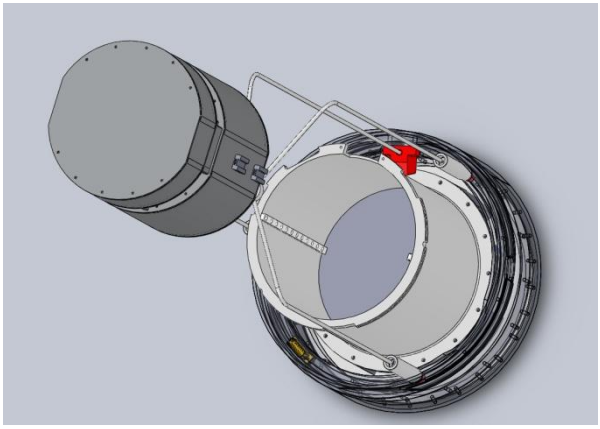

Figure 3: CAD of CHAD ejection from Magic Hat on DSM.

The Central Chamber functioned as a services pass-through between the Upper and Lower Chambers. It was also about the Central Chamber that the space web was wrapped and stowed prior to deployment. All Saft power systems were stored in the Upper Chamber, along with four cameras positioned radial to capture images of the space web deployment. The Daughter Release Spine was also mounted within the Upper Chamber, which was responsible for the simultaneous release of the corner mass Daughter Sections attached to the web. The Release Spine was actuated by stored strain contained within a compressed spring that itself was release upon command by a Cypress pyrotechnic cutter shearing a tensioned steel wire.

Transmitting antennas were appropriately positioned on the outward facing surfaces of the top and bottom plate on the Upper and Lower Chambers respectively. This provided as closely as possible full spherical coverage back to the DSM where the receiving antennas were positioned. Due to limitations imposed by REXUS 12, the antennas position on the DSM were only able to provide a half-spherical field of view, which unfortunately would result in communication breaks were the REXUS 12 rocket to begin tumbling motion.

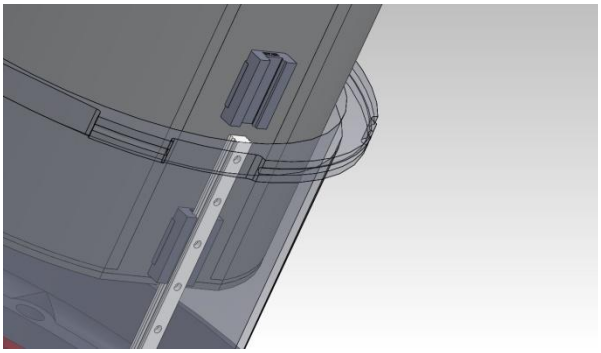

Figure 4: Guiderails inside Magic Hat and carriages on CHAD.

The ejectable CHAD module was stowed within the ejection chamber, commonly referred to as the Magic Hat, against a compressed wave spring. This allowed a Cypress pyrotechnic cutter to activate the release of CHAD once REXUS 12 reached apogee. Linear guide rails (Fig. 4) were used to prevent tumbling motion of CHAD upon release. The Magic Hat was mounted directly on top of the steel top plate of the DSM, which in turn was mounted upon radially space pillars fixed to the bulkhead plate of the Nosecone Adapter. This provided a readily accessible volume between the top plate of the DSM and the bulkhead in which the DSM subsystems were housed.

2.3 Electronics and Software

The electronics used were a mix of Commercially Off The Shelf (COTS) components and custom-made boards when COTS board were not available. This approach reduced design and production time of the electronics subsystem. The electronics and software for control and data acquisition was separated to allow for a more reliable failsafe system [8]. The main control of the experiment was undertaken by a small microprocessor (PIC (Programmable Interrupt Controller)) placed on a custom made PCB in CHAD, while the data acquisition, which required more computing power, was done by more advanced CPUs and an FPGA (Field-Programmable Gate Array).

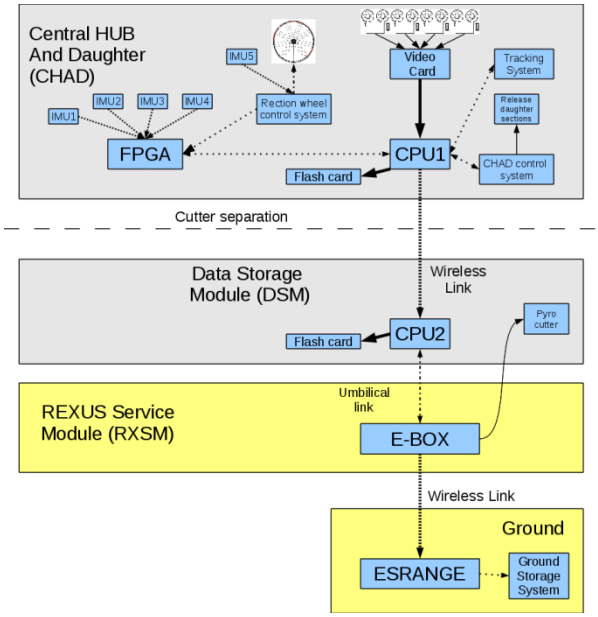

Figure 5: Schematic of electronics.

To provide data acquisition from multiple sensors, i.e. IMUs, an FPGA is used. The FPGA (Cyclone IV) was placed on the DE0-Nano board. The main purpose of the FPGA was to gather the sensor data, packet, serialize and sent it to the CHAD CPU. Data was gathered at a rate of 50 Hz from the four daughter sections as well as from the Reaction Wheel Controller (RWC). To reduce the data that was needed to be sent

over the wireless link, the unnecessary information sent from the IMUs are filtered out in the FPGA before the data was packaged according to reference 8. The data streams from the IMUs were then combined into one stream and sent to CHAD CPU.

The RWC consisted of an FPGA, IMU and motor driver mounted on a custom-made board controlling the reaction wheel. Two VSX-104+ boards were used in the experiment. Each board contained one SoC chip with one CPU, compatible with 486SX instruction set, using a 300 MHz system clock. Both CPUs used GNU/Linux as an operating system with custom written software.

One CPU parallel with a custom made board was placed in CHAD, which was responsible for capturing images from four cameras on CHAD, storing these images on two internal flash cards and sent them through a wireless link to DSM. A second CPU was placed on the DSM which was similar to the one on CHAD without the custom made board. The second CPU stored all incoming data from the wireless link on the two flash cards.

Both CPUs included the functionality to report its route status packets received from other modules. Three different types of data were expected from the experiment. First, most important for post-flight data analysis were readings from the sensors, IMUs and RWC. As a secondary verification method, pictures from the four cameras on board CHAD were recorded. The last type of data contained status information about each component. All these types of data were stored on DSM's and CHAD's flash cards.

Communication

Four 915 MHz antennas were used for the telecommunication. CHAD had one on the top and one on the bottom. Two receiving antennas on the REXUS rocket were placed symmetrically on the outer rim of the magic hat ejection barrel. The size of the antenna was 31 mm × 31 mm. For a continuous communication between CHAD and DSM it was of great importance to account for possible tumbling of the rocket and of CHAD. Therefore, the antennas had to cover most of the sphere around CHAD.

All antennas were designed as printed rectangular spiral antennas. The reflection coefficient and the far-field polar plots of the antennas can be seen in Fig. 6. The realized gain is −6 dBi and the bandwidth is 12 MHz. When testing the communication between two Nano IPn920 platforms (separated by 100 m) using the antennas in open space, the data rate can reach 100 kB/s. Using 900 MHz frequency requires special permission from the Swedish telecom authorities, even when transmission was to be at an altitude of several km and below one minute.

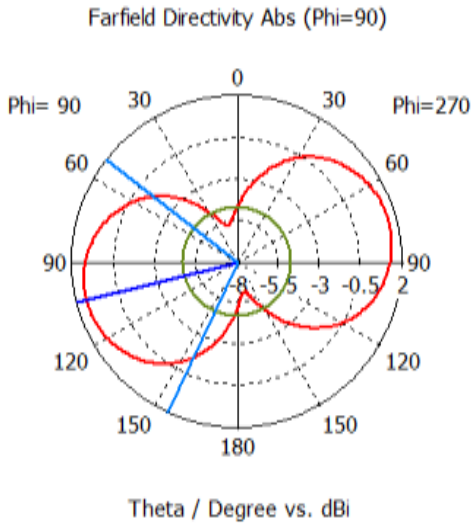

Figure 6: Polar plot of 915MHz antenna.

3 LAUNCH

3.1 Launch Campaign

The REXUS 11/12 launch campaign took place at SCC's (Swedish Space Corporation) ESRANGE close to Kiruna in Northern Sweden from the 12th until the 23rd of March 2012. During the first week the Suaineadh experiment was prepared to be integrated with the other experiments and the service module from DLR MORABA (Mobile Rocket Base). After various bench-tests and a flight simulation the Suaineadh experiment was ready for the first hot countdown on the 19th of March 2012.

3.2 Launch and Mission

On the launch day, the weather added no constrains to launch. The hot countdown of T−2 hours began at 1300 local time. The Countdown proceeded without any major delays. All experiments were powered up at T−600 s, At T−565 s Suaineadh's ground support software received the first telemetry that all systems were up and running. At T−240 s the SODS (Start Of Data Storage) signal was given and received. The switch of REXUS rocket from external power to internal batteries, which are placed in service module, was performed at T−120 s. At T−0 s REXUS 12 launched and the Suaineadh ground support successfully received notification about the LO (Lift-Off) signal. SOE (Start of Experiment) signal was given at T+26 s. Suaineadh was ejected from the nosecone position of the REXUS 12 rocket at T+80 s, the ground support software indicated successful ejection, further corroborated by post mission analysis of recovered pictures. After ejection, the amount of available memory onboard the rocket should decrease with data rate of wireless link (up to 100 kB/s), which would indicate that a wireless connection between CHAD and

the DSM was established. Only minor changes of free space were observed. 420 s into the flight, the Suaineadh ground support software and all the other ground stations ceased to receive further telemetry from REXUS 12. Approximately 30 minutes after lift-off, the recovery helicopter team began its search for the REXUS 12 payload and Suaineadh's CHAD. After a two hour search, only the REXUS 12 payload could be recovered. Investigations into the lost signal showed that the parachute of the REXUS 12 payload had malfunctioned and therefore the radio beacon was unable to function. The non-parachuted REXUS 12 payload hit the ground at terminal velocity.

3.3 Post Flight

After the recovery of the REXUS 12 payload, the Suaineadh team disassembled the DSM. Unfortunately, the helicopter team was unable to detect the radio beacon from CHAD and therefore did not recover the ejected section. Due to the REXUS 12 parachute malfunction, the REXUS 11 launch was postponed and successfully launched in November 2012.

4 RECOVERY MISSION

4.1 Overview

The Suaineadh team embarked on a recovery mission from the 17th until 26th of August 2012 in order to search for the missing CHAD section. Shortly after the launch campaign, the experts from all organisations involved in REXUS/BEXUS provided the Suaineadh team with the GPS ground track of the REXUS 12 rocket, the GPS coordinates of the impact zone from the helicopter team that recovered the payload, rocket motor and nose cone. The Suaineadh team was also provided with the acceleration profile of the REXUS 12 rocket during the mission and the recovery video from the payload prior to impact.

With this data it was possible to estimate the approximate impact location of CHAD. The recovery expedition consisted of Suaineadh launch campaign team members and new partners from across Europe. The search began at the impact location of the REXUS payload employing a spiral search pattern. Due to the fact that the parachute of the REXUS 12 payload did not deploy, it could be assumed that CHAD may be located within close proximity to the impact site of REXUS 12. Fig. 7 shows the location of the rocket motor (68.341017N, 20.979600E), the REXUS12 payload (68.336983N, 20.990333E) and the nosecone (68.320267N, 20.986750E).

The ground track of REXUS12 runs along 51 km from Esrange to the impact zone (red line in Fig. 7). The selection of the separation spring and bench tests on the ground indicated a velocity differential between Suaineadh and the rocket of approximately 1 m/s at Suaineadh separation. Due to the fact that the parachute of the REXUS rocket malfunctioned, the Suaineadh experiment and the REXUS payload should have followed a similar ground plane trajectory up until impact. The nose cone and the rocket motor where ejected in opposite directions. It cannot be predicted if the impact location of the Suaineadh experiment lies between the REXUS payload and the nose cone or the payload and the motor. It was decided to establish a base camp at the impact location of the REXUS 12 payload.

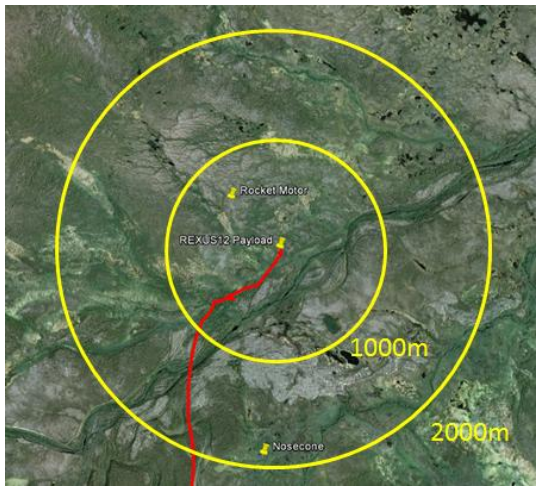

Figure 7: Landing position of REXUS12 payload, nosecone and rocket motor (source Google Earth).

Fig. 7 shows that the payload impact position in between the nose cone and the rocket motor location. The rocket motor impacted in a north-ward distance of 631 m with respect to the REXUS 12 payload and the nose cone impact position is within a south-ward distance of 1880 m. The base camp was used as an origin point for daily missions to various location of interest.

4.2 Mission

The recovery crew parked at Järämä, the Sami settlement north of the suspected impact zone. The 5 km walk to the base camp already showed the high density of swamp land. On the way to the base camp the REXUS 12 rocket motor was found. The base camp was set up around 400 m north of the original set up place because of swamp around the payload impact zone. In the following six days the recovery team tried to cover as much area as possible through swamps, forests, bushes and rivers. At the end of the week the only piece of Suaineadh that was found was a bracket which was mounted to the magic hat onboard the rocket (Fig. 8).

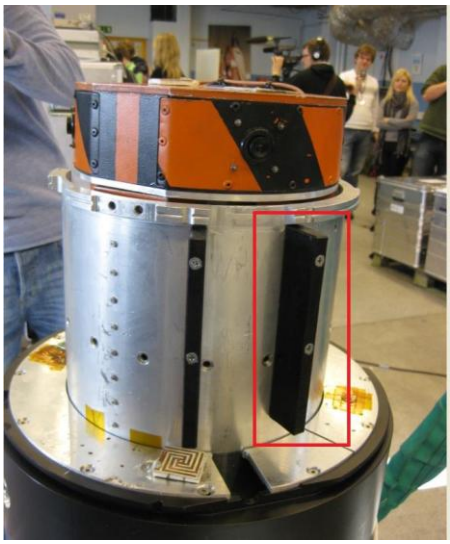

Figure 8: Only Suaineadh part found during recovery mission: bracket from magic hat.

5 RESULTS

After the recovery of the rocket on the 19th of March, 22 pictures were recovered from the internal storage module on the DSM. These 22 received pictures were recorded by the four cameras on the ejected section CHAD. These four cameras were separated by 90 degrees and therefore observed in full 360 degrees.

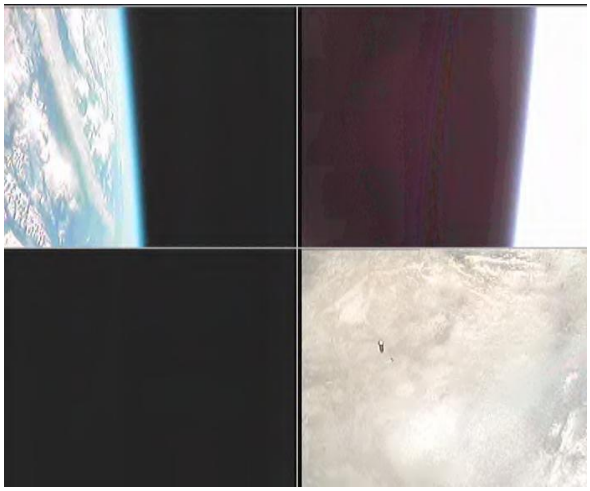

Figure 9: Picture recorded from ejected section shortly after ejection (cameras 90° apart).

Fig. 9 shows one of the first pictures received after separation. The curvature of the Earth can be seen in two frames and the Earth and the blackness of space in the other two. The recording of the images started in between 15 to 20 s after the ejection from the rocket, depending on how long the reaction wheel took to spin up CHAD to the required spin rate. By sequencing the received images, it was possible to conclude that CHAD was indeed spinning and therefore it is concluded that the reaction wheel was operational.

In the last two frames of the received images the successful release of the daughter sections can also be seen, but that it is at this point that the images cease. The reason of the data loss was likely a result tumbling of either the ejected experiment or the REXUS12 rocket after separation. Based on the information received over the wireless link it can be said that all the systems worked nominally at least up to the point of transmission loss and that it is suspected that a more complete data set could be stored on the CHAD data storage.

6 LESSONS LEARNED

The following subchapters will give an overview on the main lessons learned during the two year project. These lessons learned should help future teams to design, build and fly their experiments. A more detailed list can be found in reference [9].

6.1 Experiment Design & Requirements

- It is important to establish and document a comprehensive list of requirements during the initiation of the project, and that these should be continuously updated where necessary
- Requirements should always be achievable within the scope of the project. If they are not, then this can lead to unnecessary diversions of resources which in turn may compromise progress.
- A regimented system for logging requirements should be established from the beginning of the project and properly managed throughout. A numbering system is advantageous here, provided that team members are careful not to renumber requirements without consent.
- If using a wireless communication between ejectable experimental hardware and the REXUS rocket, then full spherical fields of view are essential so that communication is not lost during tumbling motion of either body. The REXUS rockets have since been shown to begin tumbling prior to experiment ejection, and is the likely cause of lost in data transmission between CHAD and the DSM in the Suaineadh experiment.
- Recovery measures should be applied to any ejectable experiments where data recovery is required. This should include a parachute system and tracking facilities so that the recovery crew can locate the experiment in quick time.

- Proposed projects must be realisable within the campaign duration provided by REXUS. Proper scheduling, including key milestones, should be used to track progress and that any deviations are highlighted as early as possible. It should be the responsibility of participating universities to observe this and to supply additional resources if necessary.

6.2 Mechanical (Design & Fabrication)

- It must be realised from the beginning of the project that when designing systems with extremely limited volumetric envelopes, with no scope for increasing, then the mechanical and electronic system will intrinsically influence the design of each other. This means that every effort should be made to freeze the conceptual design of these components as early as possible, so that the impact of any future modifications is minimised as far as possible.
- Any necessary changes to design features must be identified and logged with all team members as early as possible, with actions only taken once the required modifications have been discussed and agreed with those team members that will be affected. Ultimately, severe changes must be approved by the project manager.
- Where possible, a particular screw standard should be adopted and documented. A useful approach is to compile a list of screws, and indeed all fastener types, with their location in the experiment and number required noted. This method makes it simpler to track supplies and to ensure all necessary tools are available at all times.
- Where possible, established standards should be adopted, such as PC-104 architectures, which will allow for multiple components to be stacked and subsequently mounted together. The advantage to this is that should access to these components be required, then the entire assembly may be removed together more easily.
- Manufacturing standards should be considered and applied at all points during the design process. Careful consideration must be given to this when designing with CAD software and that manufacturing tolerances are given in all technical drawings given to manufacturers.
- In a scenario where mass and volume are paramount, effort should be given to verifying the mechanical design to ensure that over-engineering is minimized. FEA (Finite Element Analysis) is a useful resource in this respect, but in the least manual calculations of simplified structures should be made.
- Prototyping can be a useful resource for verification. Rapid prototyping is recommend for form and fit testing, whereas simplified engineering models can be used to verify mechanically loaded features.
- Where possible, design should attempt to include COTS so reduce lead times in manufacturing. It can also be prudent to simplify designs such that the student s themselves can fabricate many of the parts. This will reduce mechanical workshop costs and lead-times.
- Account for significant manufacturing delays of the university workshop and make sure to order parts from workshops outside university before summer to be able to have the parts in the early autumn. University workshop lead-times can often fluctuate throughout the academic year, and that every effort should be given to track this and account for it during project scheduling.
- If possible, it is recommended that particular technicians be assigned to the project so that liaising becomes more transparent.
- A thorough understanding of the mechanical and environmental loading conditions should be obtained, and that all material and parts selections are considerate of these.
- Attempt to where possible to follow ESA ECSS-Q-ST-60C guidelines for parts selection. This will improve the knowledge and understanding of the student teams, but do take care to consider the project budget when following this advice as these components will typically be more expensive.

6.3 Electrical

- Specify rough PCB dimensions and numbers early in the project for the mechanical team for the structural design.
- Try to use designs that have been flown before and thus proved themselves.

- Use components that are easily available almost everywhere. Use COTS components when possible to save time.
- If radio beacon is used to find the ejectables: design receiver to properly receive sent data. At the launch campaign everyone is rather busy and especially if problems occur it is difficult to get a hold of the person responsible for the receiver.
- Make sure that there is a connector outside the experiment to directly reprogram the microcontroller inside the experiment.
- Use LEDs visible from the outside to show that critical functions are working (e.g. LO given, microcontroller powered up, radio beacon transmitting, camera recording, etc.)
- Separate experiment's control functionality (LO, SOE, SODS and activation of actuators) from data management. In the best case implement experiment's control in simple microcontroller.
- When removing isolation from cables it is very easy to damage the wires. Consider buying rotary wire stripper.
- Buy crimping tools for Dsub connectors, it is much faster and more secure than soldering.
- Use PTFE cables which are resistant to soldering temperatures.
- Use separate fuses for each component (camera, CPU and sensors) on power distribution boards.
- Order professional PCB's for custom boards for final version.
- When buying anything advert yourself as a university representative, many times companies donate or give discounts for their products (experience shown that it easier to get such a discounts from smaller retailers/companies).
- Design and order/create prototype hardware (PCBs and components) early.
- Design the prototype with as much functionality as possible, even things that might not be needed later on (it is easier to remove components than add).
- While waiting for PCB orders, test components on breadboards or similar (if possible), read their data sheets thoroughly.
- Stick with components where information on the usage can be found on online, it makes designing/debugging of electronics much easier.
- Be realistic and do not overdo the component choice, e.g., do not put in the fastest, most complex CPU if a small 8-bit will do the job just as good.

6.4 Software (Design, Implementation, Testing)

- When using an online compiler, be aware that you will not have access to the Internet all the time, especially during tests or even reviews.
- Use an explanation for each function so that other team members can help while fixing bugs.
- Keep software simple, use modular design, for more powerful CPUs use Linux, there is lot of ready to use software for it.
- Implement ground support software early and make it solid, it will benefit later.
- Implement remote clearing flash memories of experiment.

6.5 Testing & Validation

- A useful alternative to testing the mission timeline which includes pyrotechnic cutting to use an LED in place of the pyrotechnic cutters for repeated tests. However, care must be given to ensure that no power spikes are observed when integrating actual pyrotechnic cutters as this can lead to premature deployment. It is recommended that at least three deployment tests include actual pyrotechnic cutters to ensure safe operation.
- Any changes to system designs post testing and validation must be followed by repeated tests to ensure that modifications have not compromised the operation of the experiment.
- Where possible, identify, assign and commence component testing as early as possible to allow time for required modifications.
- If tests can be performed prior to the CDR, this will allow for additional support from the REXUS team should complications be encountered.
- Produce simple flight simulator (electronics in parallel with all other design).
- Produce a "fuse box" which is useful during first connection of experiment to simulator or REXUS control module.

6.6 Workshops & Launch Campaign

- The REXUS reviews (PDR (Preliminary Design Review), CDR (Critical Design Review), etc.) sometimes collide with exam periods so careful planning of the students' studies is vital to avoid that the REXUS project

work is affecting the other courses or vice versa.

- When travelling to the launch campaign, it is a good idea if not everyone arrives at the same time, so team members that come later can bring missing components or tools.
- Make sure that there are always at least two team members that know the electronics/software at each review and official test (integration and bench test).
- Bring red tape for RBF (Remove Before Flight) items.
- When getting closer to delivery time, set a time when experiment should be good enough to fly, after that only perform timeline tests and fix bugs. The last tested timeline before a big test should always be without any problems.
- If the team is a multi-location team similar to Suaineadh, it is recommended to make the most use of the time at the workshops, possibly stay a few days longer to work as a team.
- When possible, bring hardware to the workshops, experts can give advice directly.
- The soldering course offered by ESA is a valuable workshop to learn how to manufacture space certified electronics.
- Find dedicated transport boxes for experiment early.

6.7 Project Management

- Try to work only with students that geographically are studying in the same campus. Communication and resolving of problems will be much easier if students from the same campus are involved in the experiment. Having meetings with all members present in the same room can't be replaced. Video- and teleconferencing are not very effective when it comes to resolving problems.
- Be aware of different time zones and clock chances, always schedule meetings in UTC but also write in brackets the time of each participating country to reduce confusion.
- Find a good project management tool and let all the communication go through this tool to keep track of the discussion on particular topics. (Skype is recommended to use for telecons, Dropbox and Google docs are useful to share documents, Doodle.com is a great tool to schedule meetings, facebook groups is a good tool for online communication/discussion and file sharing but everyone needs to be signed up on facebook. Basecamp has been used by the KTH REXUS projects SQUID, RAIN and MUSCAT.)
- When working on a big document together, it is recommended to inform the other team members of the document usage time and renaming the document with date and initials (check out a document).
- A good GANTT chart enables the project to meet all necessary deadlines. The more detailed an estimate can be made for each task, the more precise and reliable GANTT chart can be created.
- Weekly meetings are obligatory to keep status updated within team.
- If students work on experiment as part of their coursework, make sure that student is also available during summer.
- Have a dedicated room where experiment can be assembled and kept without disturbance.
- Most students have not worked in such large teams and together with students from other disciplines before, so an introduction to group dynamics would be advisable to avoid future problems related to, e.g. different expectations, priorities and levels of commitment within the team.
- Many students are getting course credits for their work, but it is important that both the requirements for the course and the requirements from the REXUS team are met. The team members and their supervisors need to understand that the deliverables for the project and the deliverables for the course can be two separate things. Technical reports are of courses necessary for the documentation, but more important is to build and test as quickly as possible. The report can be produced later.
- Assign a person responsible for the outreach activities. This person shall be involved with the design of the experiment, but shall not be overloaded with work. Otherwise, the outreach production and quality will suffer.
- Have dedicated supervisors that are willing to spend parts of weekends and long days to perform important tests and tasks.
- Open-minded, skilled and good team workers on both supervisor and student levels is what the REXUS/BEXUS projects need. Both supervisors and students must be prepared to work in unexpected directions not thought of from the beginning when they joined the project and be willing to quickly gain new knowledge in fields that are further away from the main studies and knowledge.

7 ACKNOWLEDGEMENTS

The authors would like to thank the German Aerospace Centre (DLR), the Swedish National Space Board

(SNSB), the European Space Agency (ESA) and everyone involved in REXUS/BEXUS for giving us amazing support and the opportunity to launch our experiment into space. We would like to thank Leopold Summerer of ESA's Advanced Research Team for his continuous support over the entire length of the Suaineadh project. A very big thank you goes to the recovery team members Michael Sinn and Jeremy Molina from Stuttgart, Germany for spending their free time with us searching for Suaineadh from the 17th till 26th of August 2012. Furthermore we would like to thank Matthew Cartmell for his continued support and guidance throughout the REXUS campaign, and for his contributions to the development of the reaction wheel technology. Also Andrew Feeney, John Russell and Neil Smith from the University of Glasgow, Johannes Weppler former student of the University of Strathclyde and Carl Brengesjö, Niklas Hansen, Ali Dabiri, Mengqi Zhang and Martine Selin from KTH for their work during the Suaineadh project. The authors would like to acknowledge Johnny Öberg for his participation in the project. We would also like to thank our sponsors and supporters; M-Comp, Evonik, Radiometrix, Altera, ACKSYS, BAUMANN springs and ClydeSpace. Thank you also to the Open Source community for GNU/Linux whose software was used on the CPUs and our ground support software.

8 CONCLUSIONS

On the 19th of March 2012 the Suaineadh experiment was launched into space onboard REXUS 12. The Suaineadh experiment had the purpose of deploying a web in space. The team was comprised of students from the University of Strathclyde (Glasgow, UK), the University of Glasgow (Glasgow, UK) and the Royal Institute of Technology (Stockholm, Sweden), designing, manufacturing and testing of the experiment.

Unfortunately, the ejected section could not been recovered by the recovery helicopter team. 22 pictures were received over the wireless link between the experiment and the REXUS rocket confirming that the experiment was fully functional with initiated spinning up after ejection. In the last two frames that were received, it could be seen that the daughters were successfully released. The wireless connection was interrupted before web deployment, likely caused by tumbling of the experiment or the rocket.

A recovery mission in mid August 2012 at the landing site was not able to recover the ejected section on which it is hoped that more data should still be stored. There remains one last hope of recovering Suaineadh during to the start of the hunting season within the impact area.

9 REFERENCES

1. Nakasuka, S., Aoki, T., Ikeda, I., Tsuda, Y. & Kawakatsu, Y. (2001) "Furoshiki Satellite" A large membrane structure as a novel space system. *Acta Astronautica*, 48(5-12): 461-468.
2. Nakasuka, S., Funase, R., Nakada, K., Kaya, N. & Mankins, J.C. (2006) Large membrane "Furoshiki satellite" applied to phased array antenna and its sounding rocket experiment. *Acta Astronautica*, 58: 395-400.
3. Nakasuka, S., Funane, T., Nakamura, Y., Nojira, Y., Sahara, H., Sasaki, F. & Kaya, N. (2006) Sounding rocket flight experiment for demonstrating "Furoshiki satellite" for large phased array antenna. *Acta Astronautica*, 59: 200-205.
4. Gärdsback, M., Tibert, G. & Izzo, D. (2007) Design considerations and deployment simulations of spinning space webs. *48th AIAA/ASME/ASCE/AHS/ASC Structures, Structural Dynamics, and Materials Conference*, Honolulu, HW, 23–26 April, AIAA-2007-1829.
5. Melnikov, V.M. & Kosholev, V.A. (1998) Large space structures formed by centrifugal forces. *Volume 4 of Earth Space Institute Book Series*. Gordon and Breach Science Publishers, India.
6. Sawada, H., Mori, O., Okuizumi, N., Shirasawa, Y., Miyazaki, Y., Natori, M.C., Matunaga, S., Furuya, H., & Sakamoto, H. (2011) Mission Report on the Solar Power Sail Deployment Demonstration of IKAROS, AIAA 2011-1887, presented at the 52nd *AIAA/ASME/ASCE/AHS/ASC Structures, Structural Dynamics, and Material Conference*, Denver, CO, USA, 4-7 April.
7. Sinn, T., McRobb, M., Wujek, A., Skogby, J., Zhang, M., Vasile, M., Tibert, G., Weppler, J., Feeney, A., Russell, J., Rogberg, F. & Wang, J. (2011) REXUS 12 Suaineadh Experiment; Deployment of a Web in Microgravity Conditions using Centrifugal Forces, IAC-11-A2.3.7, *62nd International Astronautical Congress*, Cape Town, South Africa, 3-7 October.
8. Wujek, A. & Skogby, J. (2012) Electronics and Software Design of the Suaineadh, REXUS Sounding Rocket Experiment, *Master Thesis, School of Information and Communication* Technology, KTH Royal Institute of Technology, Sweden.
9. Sinn, T., et al. (2013) Lessons learned from the sounding rocket and stratospheric balloon experiments Suaineadh, StrathSat-R and iSEDE, *64th International Astronautical Congress*, Beijing, China, 23-27 September.

New Techniques for Rockets

Chairs: S. Kemi, J. Ettl, P. Turner, A. Schütte, G. Florin & H. Steinau

EXPERIMENTAL IN-FLIGHT MODAL-ANALYSIS OF A SOUNDING ROCKET STRUCTURE

Andreas Gierse [1], Stefan Krämer[2], Dominique J. Daab[2], Joana Hessel[2], Fabian Baader[2], Brigitte S. Müller[2], Tobias Wagner[2], Georg Gdalewitsch[2], Engelbert Plescher[2] and Lysan Pfützenreuter[3]

[1] *ZARM Fallturm Betriebsgesellschaft mbH am Fallturm, 28359 Bremen, Germany; andreas.gierse@zarm.uni-bremen.de*
[2] *FH Aachen FB6, Hohenstaufenallee 6, 52064 Aachen, Germany; REXUS@fh-aachen.de*
[3] *DLR German Aerospace Center, Space Administration, Königswinterer Str. 522-524, 53227 Bonn, Germany*

ABSTRACT

Knowledge of the dynamic mechanical characteristics of a microgravity platform together with data of the dynamic loads while flight, enables its further development. Benefits are the possible weight reduction of the platform structure and an improved μ-g quality due to vibration control and purposeful decoupling.

Within the framework of the Adios student experiment a new type of measurement system for in-flight modal analysis was developed and tested. Aim of this setup was the in-flight validation of the system and the validation of a FEM Model of the REXUS 11 rocket.

The achieved Signal-to-Noise-Ratio was sufficient for data analysis. Beside the determined resonance frequencies of the rocket structure several events like motor separation and pyro firings of other experiments were measured. Furthermore the resolution of the measured, low frequency, mechanical stress was higher than anticipated.

Based on these results a further development of the measurement system seems worth the effort.

1. INTRODUCTION

In 2008 students of the FH Aachen, University of Applied Science, formed a team called »VibraDamp« to develop a passive mechanical decoupling system for experiments on sounding rockets in the framework of the REXUS 5 campaign. While this experiment was not finalized in time the project was redesigned to »VibraDampII« and successfully tested on REXUS 7 in 2010. »VibraDampII« contained a »free flying experiment device« (FFED) which was de- and recoupled while ascent and descent using three geared motors. The FFED was hold in the center of the rocket while μ-g phase using six steel springs and it was damped using the eddy-current effect. Two three-axis-accelerometers were used to analyse the mechanical behavior of the decoupled system and the effectiveness of the decoupling from the rocket structure. Results were presented in [1].

In 2011 based on VibraDampII a new student team »Adios« (ADvanced Isolation On Sounding rockets) formed with the objective to further develop the VibraDampII system to TRL 7 status. A big effort was spend on lightweight constructions and a highly reliable de- and relocking mechanism. Also the damping system was further developed to a two stage damping.

The object of research was enhenced to the field of vibrations and disturbances of the rocket structure. Therefore a modal analysis measurement system was developed. The development of this system and the results are presented in this paper.

2. MOTIVATION AND AIMS

While ascent and descent the rocket structure is excited by aerodynamic loads. Forces and the frequencies of this disturbances depend directly on speed, air density, spin rate and the angle of attack of the rocket and therewith vary in a wide range. Due to the fact that this effects have an influence on the flight safety, many calculations were done while a sufficient measurement system was not available.

Proc. '21st ESA Symposium European Rocket & Balloon Programmes and Related Research', 9–13 June 2013, Thun, Switzerland (ESA SP-721, October 2013)

Due to the low material damping of a typical rocket structure the energy of the aerodynamic exitations remains in the structure during μ-g phase and lowers the quality of the microgravity conditions. For the purposeful further development of the ADIOS FFED system the movements and disturbances of the rocket structure have to be well known.

Weight reduction of the rocket and payload structures is only possible if the loads are well known. This would by advantageous as it could increase the possible payloads mass at invariant apogee and μ-g time.

3. STATE OF TECHNOLOGY

3.1 Modal analysis

Modal analysis of rocket motors and payloads are nowadays commonly used to avoid dynamic interactions during flight. Numerical analysis of complex, nonlinear structures are prone of errors and hence only used for development. At acceptance- and qualification- tests, shakers are used to analyse the structures. This experimental tests are also not free of errors. The main systematic error is the connection of the analysed structure to the excited part of the shaker (mechanical impedance). The sum of the shaker mass and the mass of the tested device acts different than the device on its own or while it is fixed to the other parts of the rocket. Also all ground based tests can not consider external loads like vibrations of the rocket motor or aerodynamic loads.

An in-flight modal analysis system needs many sensors all over the rocket structure. Such a system has to consider quantitatively unknown boundary conditions. The most important conditions are the fast change of the rocket skin temperature (up to $10\frac{K}{s}$) and the electro magnetic pollution from other experiments due to the necessity of long signal cables.

3.2 Sensors

Acceleration sensors are very expensive and have a high transvers sensitivity if accelerated perpendicular to the measuring axis.

Strain gauges are cheap and small and used succesfully for modal analysis in many applications. A disadvantage of strain gauges is the high sensitivity to temperature changes. Due to the very small size a big advantage of strain gauges is the possibility to applique them to the outer structure of the rocket motor.

4. TECHNICAL REALISATION

The development process included several simulations and preliminary design circuits. Here this process is given chronologically.

4.1. Modal and aerodynamic simulations

4.1.1 Master Thesis by Lysan Pfützenreuter
»FEM CALCULATIONS ON THE REXUS 11 ROCKET« [3]

The aim of these simulations were the estimation of Eigenforms and Eigenfrequencies of the REXUS 11 rocket. Therefore several models of the rocket were designed and calculated using ANSYS. One model considered the launch configuration of the rocket another model considered the configuration during μ-g phase and so forth. The different Eigenforms were calculated to find the ideal positions for strain gauges in the payload where Eigenforms of all configurations could be verified. The main focus was on the Eigenforms while μ-g phase.

Based on this calculations, three levels in three different payload modules were defined. Each level should contain four strain gauges 90° apart of each other at the circumference of the modul.

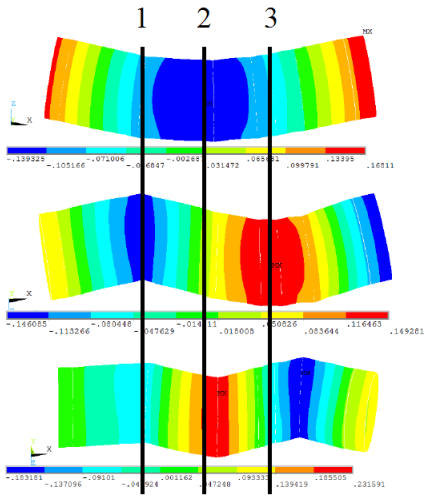

Figure 1; shows the calculated first three bending Eigenforms of the REXUS *11 payload in μ-g condition and the located ideal levels (1,2,3) for the strain gauges*

The verification of Eigenforms is based on different strain-amplitude-ratios between the levels at different Eigenforms. As can be seen in Figure 1 at the first Eigenform the strain amplitude is very similar in all levels (free free bending). At the second Eigenform the strain

amplitudes at level 1 and 3 are similar but the strain amplitude in level 2 is considerably lower. Therewith it is possible to accomplish the measured Eigenfrequencies to the calculated Eigenforms.

This thesis was finished in November 2011. All assumptions were actual at that date. The positions of the strain gauges were defined as shown and those appliqued in the modules.

After spin- and balancetest the Rexus 11 payload had to be reconfigurated with the result of new, unideal positions of the strain gauges and therewith to a loss of information in the data (see section 5. RESULTS).

4.1.2 Bachelor Thesis by Stefan Krämer
»Evaluation of Rocket Flight Load Determination Methods« [2]

NASA and DLR developed several software tools during the 1960´s to determine aerodynamic loads on rocket structures.

This evaluation compared the results of the most suitable programms on the special case of the Rexus 11 rocket.

The variation range of the results was unexpectedly huge.

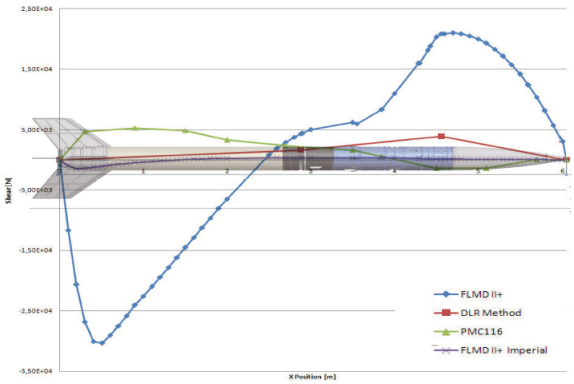

Figure 2; shows the calculated shear forces using different software tools on the REXUS 11 rocket at an angle of attack of 4°

Based on this calculations no special expectations concerning excitations or Eigenfrequencies were formulated.

However these imprecise results showed the necessity of a reliable measurement system. Therefore it was decided to collect data also while ascent and descent.

4.2 Preliminary design on shakertest

For the first tests in a Rexus modul it was decided to test strain gauges in a constant current design due to the advantages of

- small size of sensors and PCBs
- insensitivity against electromagnetic pollution and long cables
- cheap prize

The tests showed that already the warming up of the modul structure due to vibrational energy was sufficient to drift the sensors signals out of the chosen measurement range within 10 seconds. The design was extended by a DC-decoupling and temperatur sensors in all three levels and therewith tested sucessfully.

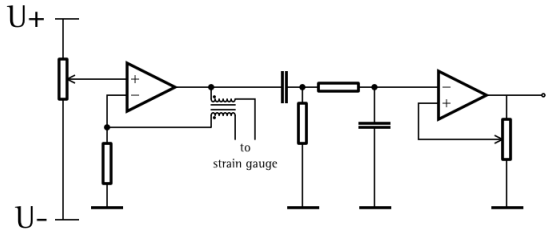

Figure 3; shows the circuits principle of a constant current source, filtering and amplification

4.3 Flight hardware

All electrical parts were manually assembled. The measurement system consisted of 20 channels on four PCBs and a NI cRIO computer system. For wiring shielded twisted pair signal cables were used which were grounded on both ends of the cable to the rocket structure.

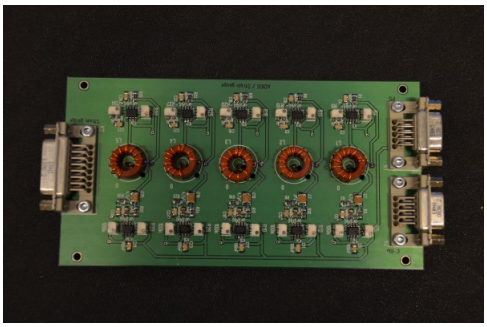

Figure 4; shows one PCB containing five measuring channels

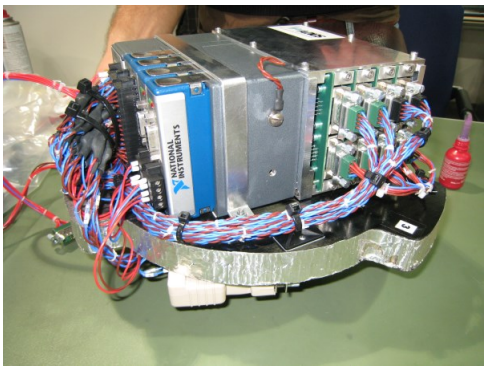

Figure 5; shows the bulkhead of the ADIOS experiment with cRIO computer and all PCBs of the modal analysis measurement system

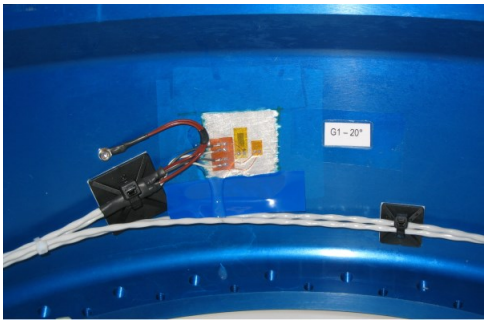

Figure 6; shows strain gauges and a temperature sensor (to the right) appliqued to a modul. Also the electrical grounding of the cable shield can be seen.

4.4 FEM recalculation of new flight configuration

After spin- and balancetest of the REXUS 11 rocket it was decided that some experiment modules of the REXUS 11 and 12 had to be switched.

This reconfiguration changed the positions of the strain gauges. Even more important was the effect on the Eigenforms. Those changed mainly due to the reconfiguration that the nosecone was not ejected. Again the bending and longitudinal Eigenforms were calculated.

bending	longitudinal
176 Hz	494 Hz
364 Hz	956 Hz
578 Hz	
791 Hz	
980 Hz	

Table 1; shows the calculated Eigenfrequencies

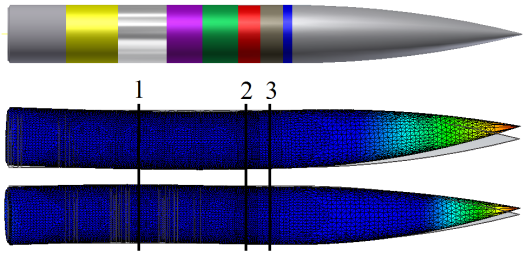

Figure 7; shows the final configuration of the REXUS 11 payload and the first two bending Eigenforms of the new configuration and the new positions of the three strain gauge levels

In the new configuration the second level is close to the third level. Therewith the strain-amplitude-ratio is at all bending Eigenforms close to 1. It was clear before flight that with this configuration the verification of the Eigenforms was going to be very difficult if possible at all.

5. RESULTS

The system worked during the hole flight and recorded about $75 \cdot 10^6$ datapoints.

Short after the end of microgravity time the cRIO system changed channels for no known reason. Still all data was relatable.

5.1 Events

Several events like motor separation and deployments of payload parts were measured qualitatively by the strain gauges.

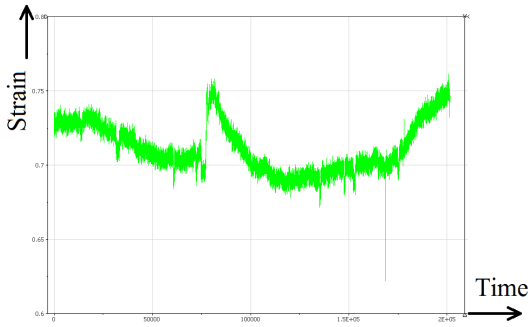

Figure 8; shows motor separation seen as strain by a strain gauge

In Figure 8 also the signal to noise ratio and low frequent shifts can be seen very well.

5.2 Excitations and Eigenfrequencies

The measured spectra are fragmented to the three phases ascent, μ-g phase and descent.

In all spectra at low frequencies the pink noise of the measurement system and the low frequent shifts due to temperature changes get visible.

5.2.1 Ascent

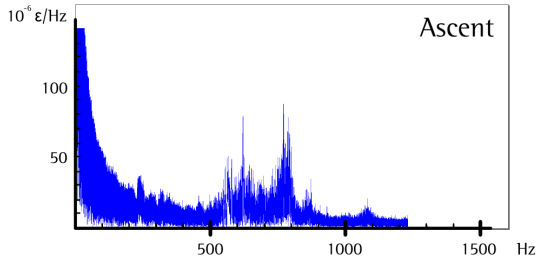

Figure 9; shows the spectrum of vibrations while ascent of REXUS 11

Compared to the spectrum at μ-g phase more energy at low frequencies is noticeable. At this time only few experiments were active. The electro magnetic pollution and therewith the noise can be considered lower than while μ-g phase. This low frequent energy seems to be related to temperature shifts while ascent.

At higher frequencies two major responses (around 600Hz and around 780Hz) can be seen. Those are similar in kind to the resonances measured during μ-g phase what leads to the assumtions of structural resonances.

Many narrow banded peaks are superposing the spectrum between 500Hz and 1000Hz. These may be strains caused by aerodynamic loads.

As the simulation results did not allow any expectations all this events can not be related to a theory.

5.2.2 μ-g phase

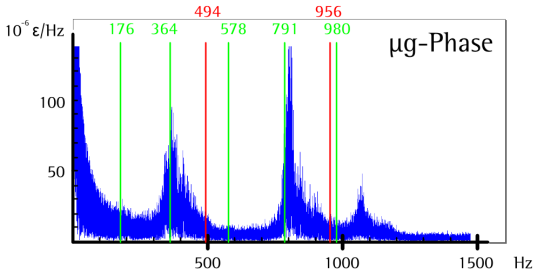

Figure 10; shows the spectrum of vibrations while μ-g phase

The vibrational energy seen in Fig. 10 is partly stored from excitations while ascent and partly caused by payloads.

The frequency ranges in which more energy is measured can be considered to be structural resonances for which are characterized by low damping and energy storing effects.

These measured frequencies are well related to the second and fourth calculated Eigenfrequencies. As assumed before, after reconfiguration the data was not sufficient to verify the different Eigenforms.

The final result therewith is that several resonances were measured which can not be definitly related to specific Eigenforms.

5.2.3 Descent

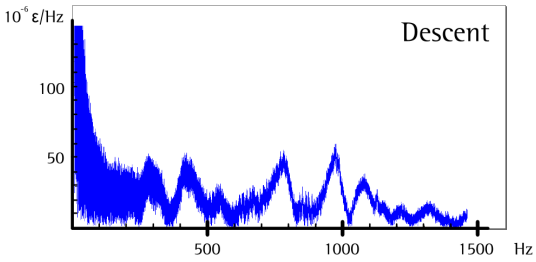

Figure 11; shows the spectrum of vibrations while descent of REXUS 11

During descent much energy in a wide frequency range was measured. Like at ascent much energy was measured at low frequencies which also should be related to temperature shifts due to aerodynamic drag.

At higher frequencies several discrete events were measured which can relate to structural resonances, tumbling movements of the whole payload and also to aerodynamic effects.

6. CONCLUSION AND OUTLOOK

- It can be summarized that the measurement principle worked out very well at all phases.
- The level of pink noise was lower than anticipated.
- Eigenforms were not identified in this case study.
- In the future the measurement range of this system could be extended down to static strain if the system was extended by Chopper Amplifiers.

7. ACKNOWLEDGEMENT

The authors would like to thank DLR, ESA and SSC who made the Rexus programm possible which was a huge enrichment for our studies.
A special thanks also to our industrial partners for their support in materials and knowledge.
Also we like to thank the FH Aachen and our professors for advice and financial support.

8. REFERENCES

1 L. Pfützenreuter, M. Lauruschkat, A. Gierse and R. Vetter. »VibraDamp«. *FH Aachen, Tech Rep., 2010*

2 S. Krämer. »Evaluation of Rocket Flight Load Determination Methods«. *Bachelor Thesis, 2012, DLR MORABA*

3 L. Pfützenreuter. »FEM Calculations on the Rexus 11 Rocket«. *Master Thesis, 2011, FH Aachen*

COMPANDERS FOR HIGH FREQUENCY AND HIGH DYNAMIC RANGE MEASUREMENTS ON SOUNDING ROCKETS AND LAUNCH VEHICLES

Heuller A. C. Procopio and Marcio Barbosa Lucks

Institute of Aeronautics and Space (IAE)
Praça Mal. Eduardo Gomes, 50 – Vila das Acácias
12228-904 – São José dos Campos – SP – Brazil
Phone: +55 (12) 3947-4949
heullerhacp@iae.cta.br and marciombl@iae.cta.br

Abstract

The use of companders to improve telemetry of sounding vehicles and satellite launchers for high dynamic range and high frequency measurements is analyzed in this paper. Companding techniques can increase the dynamic range by several orders of magnitude and eventually also improve the signal-to-quantization-noise ratio, depending on the probability distribution function of the signal. These techniques allow a non-uniform quantization of the signal using a compressor circuit in the transmitter and the reconstruction of the original signal on the receiver by an expander circuit. An analysis of the types of implementation was accomplished, showing the various possibilities of instantaneous companders implementation.

1. Introduction

During the flight of sounding rockets and satellite launch vehicles, some types of high frequency signals monitored via telemetry present a very wide dynamic range (DR), such as acoustic pressure and shock measurements [1]. In order to reduce the required bit rate on the telemetry channel and allow a sufficient number of measurements for vehicle performance analysis, the number of bits used for quantizing high frequency signals is limited to as few as possible, generally in the range of 8 to 12 bits. Unfortunately, the resolution of the acquisition system also limits the measurement dynamic range, according to the number of bits used in the A/D converter (ADC), which in general uses a uniform quantizer. In this case, the dynamic range increases at approximately 6.02 dB per additional bit [2-4]. In order to increase the dynamic range and the signal-to-quantization noise ratio (SQNR), without the need to increase the system resolution, companding techniques were developed, such as the μ-law and the A-law, which have been used for decades in telephony [4-6]. These companding techniques (a contraction of compressing and expanding) allow a non-uniform quantization of the signal by using a compressor circuit that implements a nonlinear function, followed by a uniform quantizer at the acquisition system and the reconstruction of the original signal by means of an expander at the receiver. If the signal probability distribution function is concentrated on a small range, the non-uniform quantization performed by the compander can provide a great improvement of the SQNR and dynamic range [7]. Indeed, the SQNR is improved for low level signals with a penalty on the high levels. In this paper, we analyze the various possible implementations of companders, and propose a compressor circuit based on programmable devices.

2. Companding Laws

A compander is composed by a compressor and an expander. The compressor is a hardware that implements the compression law, such as the μ-law and the A-law. In telemetry systems, the expander can be implemented by software at the post-processing phase on the ground. The μ-law compander can be defined by the following expressions:

compressor: $$f(x)=\operatorname{sgn}(x)\frac{\ln(1+\mu|x|)}{\ln(1+\mu)},$$

for $-1\le x\le 1$ (1)

expander: $$f^{-1}(y)=\operatorname{sgn}(y)\left(\frac{1}{\mu}\right)\left((1+\mu)^{|y|}-1\right),$$

for $-1\le y\le 1$ (2)

where μ is a real number, x is the input signal at the compressor and y is the expander input signal. The output of the expander is a reconstructed version of the input signal x. In Fig.2 we can see the influence of μ on the compressor function.

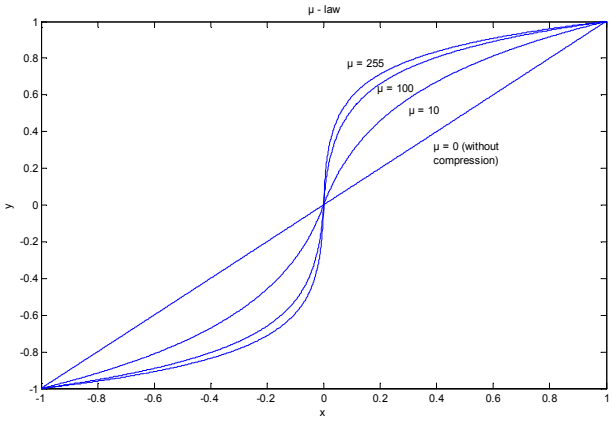

Figure 1: μ-law compression.

The A-law compression function is defined by the following pair:

$$f(x) = \operatorname{sgn}(x)\frac{A|x|}{1+\ln(A)} \quad \text{, for} \quad |x| < 1/A \qquad (3)$$

$$f(x) = \operatorname{sgn}(x)\frac{1+\ln(A|x|)}{1+\ln(A)} \quad \text{, for} \quad 1/A \le |x| \le 1 \qquad (4)$$

whereas the expansion functions is defined by the following pair:

$$f^{-1}(y) = \operatorname{sgn}(y)\frac{|y|(1+\ln(A))}{A} \quad \text{, for} \quad |y| < 1/(1+\ln(A)) \qquad (5)$$

$$f^{-1}(y) = \operatorname{sgn}(y)\frac{\exp(|y|(1+\ln(A))-1)}{A} \quad \text{, for} \quad 1/(1+\ln(A)) \le |y| < 1 \qquad (6)$$

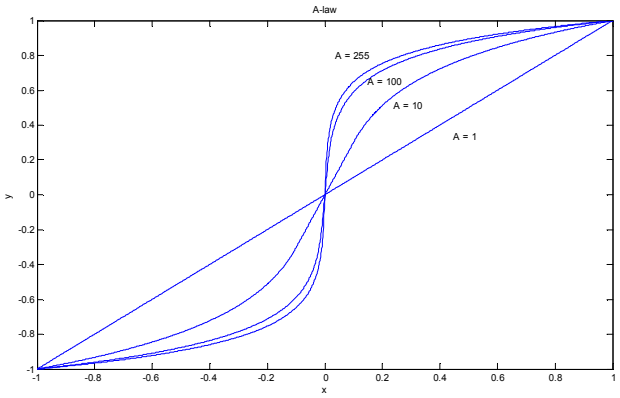

Figure 2: A-law compression for A ranging from 1 to 255.

3. Effects of Companders on DR and SQNR

As shown in [7], the DR can be greatly improved by the use of a compander. Concerning the SQRN, it can be improved for low level signals with a penalty on higher level ones, as shown in Fig. 3. The value of factor μ or A can be varied in order to adjust the dynamic range to a certain degree.

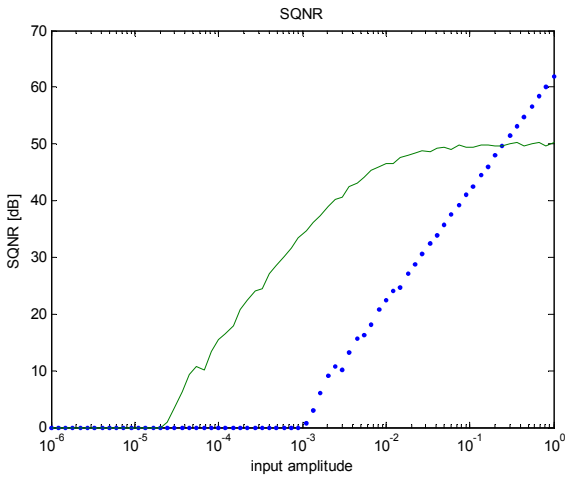

Figure 3: SQNR for μ-law compander (μ=255) and uniform quantizer (dotted).

4. Types of Companders

The companders can be divided into two broad categories: instantaneous companders and syllabic companders. In instantaneous companders, the compressing function is evaluated for each input value. However, for syllabic companders, the gain level is adjusted according to some measure of the signal level. Syllabic companders have been used for commercial applications such as wireless microphones, whereas instantaneous companders have been used in telephony for decades. For use in electronic instrumentation and measurements, the instantaneous compander seems to be more adequate.

5. Compander Implementation

Another way of categorizing companders relates to the implementation. They can be divided into analog or digital/mixed implementations. Here, only the implementation of instantaneous companders is analyzed.

5.1. Analog Companders

An analog compressor circuit is composed of an input buffer, an anti-aliasing filter with adjustable cutoff frequency, and a nonlinear circuit in the output, which implements the compression function, as shown in Fig. 4. In general, the compressor circuit can be implemented by logarithmic circuits. Advantages: Low power consumption, A/D and D/A not needed (in this case the A/D converter is supposed to be at the encoder input). Disadvantages: drift, low-precision and offsets.

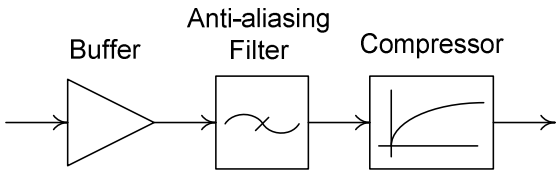

Figure 4: Analog Compressor Circuit.

5.2. Digital Companders

A digital compressor is composed of an A/D converter, a digital processing system that implements the compression function and a D/A converter for analog output and/or digital output ports, as shown in Fig.5. The digital processor can be implemented using various technologies, for example: microcontroller units, FPGA or CPLD, or DSP circuits. Advantages: precision, flexibility and programmability. Disadvantages: more power consumption. Due to their advantages, digital and mixed systems are considered more adequate to implement practical systems, but low-power solutions should be developed for the onboard circuit implementation.

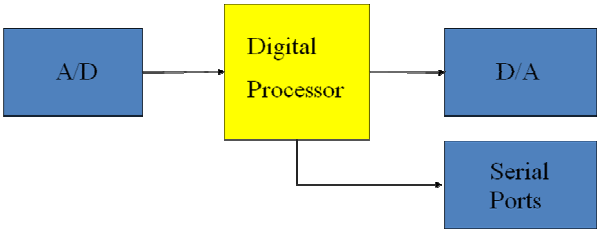

Figure 5: Digital Compressor Circuit.

6. Conclusions

Companding techniques allow an increase of the dynamic range by several decades and eventually also improve the signal-to-quantization-noise ratio, according to the probability distribution function of the signal. These techniques use a non-uniform quantization of the signal in the compressor circuit at the transmitter and the reconstruction of the original signal by an expander circuit at the receiver. An analysis of the types of implementation was performed, showing the various possibilities of instantaneous companders implementation. Digital implementations shall be explored on future works.

7. Acknowledgements

We are grateful to FUNCATE – Fundação de Ciência, Aplicações e Tecnologias Espaciais and CNPQ – National Council for Scientific and Technological Development, Process Nº 560301/2010-3 for the financial support.

References

[1] R. Pirk, W. Desmet, B. Pluymers, P. Sas, and L. C. S. Goes: Vibro-acoustic Analysis of the Brazilian Vehicle Satellite Launcher (VLS) fairing. ISMA, 2002.
[2] S. Horan: Introduction to PCM Telemetering Systems. CRC Press, 2nd edition (May 29, 2002).
[3] A. B. Carlson, P. B. Crilly and J. C. Rutledge: Communications systems. McGraw Hill, 2002, 4th edition.
[4] N. S. Jayant: Digital Coding of Speech Waveforms: PCM, DPCM, and DM Quantizers. Proceedings of the IEEE, Vol. 62, No. 5, May 1974.
[5] B. Smith: Instantaneous Companding of Quantized Signals. The Bell System Technical Journal, may, 1957.
[6] G. K. Venayagamoorthy and W. Zha: Comparison of Nonuniform Optimal Quantizer Designs for Speech Coding with Adaptive Critics and Particle Swarm. IEEE Transactions on Industry Applications, vol. 43, No. 1, January/February 2007.
[7] M. B. Lucks; H. A. C. Procópio. Analysis of Companding Techniques Applied to Onboard Telemetry Systems. Applied Mechanics and Materials, v. 232, p. 915-918, 2012.

RESEARCH ON SOUNDING ROCKET BOOM DEPLOYING TECHNOLOGY IN MERIDIAN PROJECT

Xuan Yang[(1)], Hua Yang[(1)], Xiujie Jiang[(2)], Xin Ma[(3)], Wei Zhou[(4)]

[(1)] Center for Space Science and Applied Research, Chinese Academy of Sciences, PO Box 8701, 100190, No.1 Nanertiao, Zhongguancun, Haidian District, Beijing, China,
Email: yangxuan@nssc.ac.cn

[(1)]Inner Mongolia Electronic Information Vocational Technical College, Inner Mongolia vocational park, 010011, Hohhot, China,
Email: Yanghua2062@163.com

[(2)] Center for Space Science and Applied Research, Chinese Academy of Sciences, PO Box 8701, 100190, No.1 Nanertiao, Zhongguancun, Haidian District, Beijing, China,
Email: jiangxj@nssc.ac.cn

[(3)]Center for Space Science and Applied Research, Chinese Academy of Sciences, PO Box 8701, 100190, No.1 Nanertiao, Zhongguancun, Haidian District, Beijing, China,
Email: maxin_198703140035@126.com

[(4)]Center for Space Science and Applied Research, Chinese Academy of Sciences, PO Box 8701, 100190, No.1 Nanertiao, Zhongguancun, Haidian District, Beijing, China,
Email: 123000703@qq.com

ABSTRACT

In this paper, sleeve-type tubular extension booms are developed. By overall design and analysis of electronic and electric field booms' structure, mechanical simulation analysis, single mechanical tests, rocket mechanical tests and flight tests, we find that boom deployment mechanism is both reasonable and feasible. Moreover, boom overall configuration, layout design and structural design satisfy all technical requirements. Thus, the results of this paper provide technical support for Chinese space scientific explorations by sounding rockets.

1. INTRODUCTION

Sounding rockets are mainly used to study atmospheric trace components, space electric field, ionospheric electrons, ion density, electron temperature and other parameters by detection equipments. To avoid effects of rocket body remanence and airflow, detection equipments of electrons, ions and electric filed should adopt boom deployment mechanism to extend their probes outside rocket surface by a certain distance. Since booms are often installed inside rocket fairing or pod, boom deployment mechanism should have small size, light wight and long stretch so as not to interfere with separation mechanism. Sleeve-type tubular extension booms invented by this project make significant contributions to boom deployment mechanism structure, spatial deployment mode of motion, locking and fixing structure, installation and release in the rocket and the like.

2. DESIGN REQUIREMENTS OF BOOM DEPLOYMENT MECHANISM

Electronic and electric filed booms are required by the meridian project to be installed in sounding rockets. Booms are stowed in a rocket when it is launched and deployed when a predetermined height is reached. After that, the distance between the center of an electric field probe and rocket surface should be 1.5m and the center of an electronic probe should be at least 250mm farther away from rocket surface. Since atmospheric trace components payload requires a certain rotating speed of rocket, boom deployment mechanism should not only satisfy requirements of sounding rocket layout structure, space constraints and probe mounting accuracy, but also withstand sounding rocket launching environment and adapt to centrifugal force generated by rocket rotations.

According to technical requirements of boom working performance, environmental conditions and so on, boom

Proc. '21st ESA Symposium European Rocket & Balloon Programmes and Related Research', 9–13 June 2013, Thun, Switzerland (ESA SP-721, October 2013)

structural design should meet the following requirements:

(1) Stand the test of rocket mechanical environment, satisfy requirements of the specified strength, stiffness and so on;

(2) Provide reliable installation space, fixed support and working environment for both electronic and electric filed probes and cables;

(3) Provide mechanical interfaces to connect booms with rocket;

(4) Meet technical requirements of boom design;

(5) Facilitate boom assembly and test.

3. OVERALL DESIGN AND ANALYSIS OF BOOM DEPLOYMENT MECHANISM

3.1. Overall design of boom deployment mechanism

According to the above requirements, the deployment mechanism of sleeve-type tubular extension booms is designed by taking advantage of centrifugal force generated by sounding rocket rotations. Fig. 1 and Fig. 2 display layouts of two electronic booms in stowed and deployed states, respectively. Fig. 3 depicts the flight model of electronic booms. Fig. 4 and Fig. 5 display layouts of four electric field booms in stowed and deployed states, respectively. Fig. 6 shows the flight model of electric field booms. Fig. 7 gives sounding rocket flight.

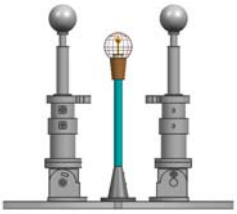

Figure 1. Two electronic booms are in a stowed state.

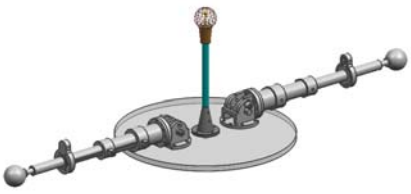

Figure 2. Two electronic booms are in a deployed state.

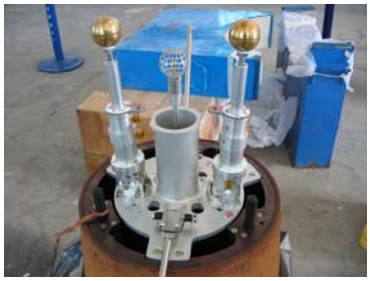

Figure 3. The flight model of electronic booms.

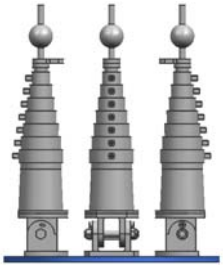

Figure 4. Four electric field booms are in a stowed state.

Figure 5. Four electric field booms are in a deployed state.

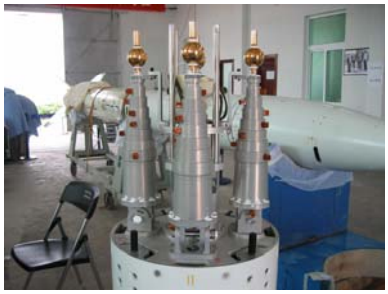

Figure 6. The flight model of electric field booms.

Figure 7. Sounding rocket flight.

Four electric field booms that are made up of nested sleeve-type tubular cylinders are systematically installed inside the rocket pod by flanges. A probe is mounted on each boom's top with its cable connecting with an electric field instrument in rocket instrument module through each boom. In the rocket launching phase, these booms are in a stowed state. There is an oblong flange atop each boom. An impacted mechanism of rocket presses these flanges by four taper pins in order to achieve the locking state of these booms. In the rocket body and arrow separation phase, these booms are unlocked which are then deployed by centrifugal force and locked so that electric field probes are thrown into their predetermined positions. The distance between the center of an electric field probe and rocket surface should be 1.5m to avoid rocket shadow and turbulence. These booms should be perpendicular to the axial of rocket in the same plane and the angle between two adjacent booms should be 90º.

Two electronic booms that are made up of nested sleeve-type tubular cylinders are systematically installed inside the rocket nose cone by flanges with probes on their tops. The electronic probe connects with a Langmuir probe instrument in the rocket by its cable through each boom. In the rocket launching phase, these booms are in a stowed state by a fixed structure. After the nose cone is thrown away, these booms are unlocked which are then deployed by centrifugal force and effects of the torsional springs in their bases and locked so that electronic probes are thrown into their predetermined positions. The center of an electronic probe should be at least 250mm farther away from rocket surface and should be perpendicular to the axial of rocket in the same plane.

3.2. Mechanical analysis of boom deployment mechanism (taking electric field boom for an example)

Boom structure modal analysis, acceleration response analysis, mechanism motion simulation analysis and impact response analysis in deployment process constitute boom structural mechanics simulation analysis. Boom structure modal analysis (Fig. 8) indicates that relatively high transverse and longitudinal fundamental frequencies of boom structure satisfies dynamic stiffness requirement of sounding rocket. Acceleration response analysis shows that maximum stress and deformation of boom structure are within allowed range of material that boom can stand the test of rocket acceleration environment. Mechanism motion simulation analysis (Fig. 9) illustrates that boom can be normally deployed at a rated speed. Impact response analysis in deployment process (Fig. 10) reports that maximum impact stress value of all nested cylinders does not exceed material yield limit. Thus, boom structural design is justified to be both valid and feasible under mechanics simulation analysis.

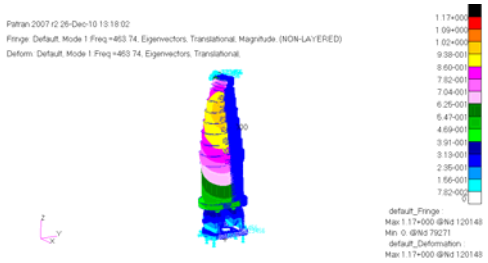

Figure 8. Electric field boom modal analysis.

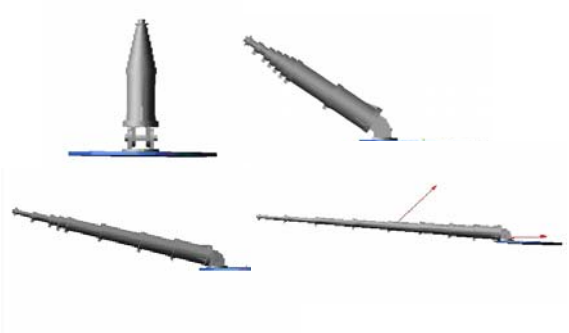

Figure 9. Mechanism motion simulation analysis.

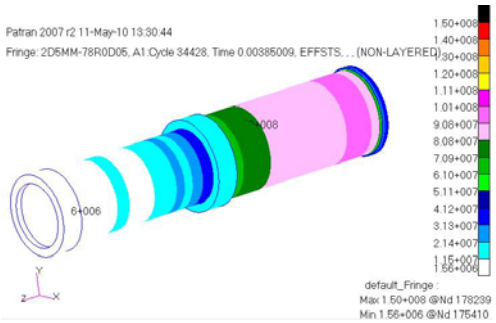

Figure 10. Impact response analysis in deployment process.

4. EXPERIMENTAL VERIFICATION OF BOOM DEPLOYMENT MECHANISM

Booms undergo single and rocket mechanical tests to verify their ability to withstand rocket launching mechanical environment and deploying capacity. Single mechanical tests include random vibration test, overload test and deploying test on the ground. Mechanical test results indicate that strength and stiffness of boom meet design requirements. Results of deploying test on the ground show that boom is properly deployed within a predetermined speed range, and has reliable structural strength and normal lock function for its sections, which satisfies sounding rocket requirements for boom deployment.

Rocket mechanical tests are constituted by electronic boom deployment test under separation of nose cone from rocket as well as electric field boom deployment test under separation of payload cabin from pod. Test results report that these booms match well with rocket interface and fixed structure, and are normally deployed under separation tests and meet dynamic stiffness requirements under mechanical tests, which justifies the reasonability and feasibility of boom deployment mechanism.

5. INNOVATIVE DESIGN OF BOOM DEPLOYMENT MECHANISM

(1) Since booms are urgently needed by a variety of space exploration missions, this project has made many important contributions under state-of-the-art process capability and m aterial development. Specifically, it makes a significant breakthrough in the development of boom deployment mechanism, and develops a 1.5m long boom and lays a solid technical foundation for future research.

(2) This project has invented a clamping and releasing mechanism for boom deployment test on the ground, which is mounted on an electric control rotating platform. Boom is stowed as this mechanism is energized. When a given rotating speed is achieved, this mechanism stops working and boom is deployed by centrifugal force and then locked in a predetermined position so that experimental verification of boom deployment process can be implemented on the ground.

(3) Since boom is deployed in a gravity free state, its ground tests should also provide a weightless environment, which is accomplished economically by giving an upward force to each section. This zero gravity devise can help prevent boom from destructive effects of downward bending moment produced by the acceleration of gravity on its structure. This devise is adopted in ground tests and provides a very good experimental environment.

(4) When boom is deployed entirely, locking mechanism locks all its sections to prevent it from axial and rotational motions, which maintains the accuracy and stability of boom deployment. A special unlocking tool is invented which makes it easy to repetitively deploy and stow booms during their development and under ground tests.

(5) Rotational friction of boom is reduced by adding PTFE material to its base since evaporation of lubricants may affect its probe's performance in deep space. The reliability of electronic boom deployment is enhanced by increasing torsional springs in its base.

The first sounding rocket of the meridian project was successfully launched on may 7th, 2011 in Hai nan province. When the rocket rose to 60km high, the rocket body and arrow were separated and electric field booms were deployed. Near the altitude of 65km, the rocket nose cone was thrown away and electronic booms were deployed. This test successfully validated the reasonability and feasibility of the sleeve-type tubular extension boom.

6. CONCLUSION

By overall design and analysis of electronic and electric field booms' structure, mechanical simulation analysis, single mechanical tests, rocket mechanical tests and flight tests can we conclude that boom deployment mechanism is both reasonable and feasible as well as its overall configuration, layout design and structural design satisfy all technical requirements.

7. REFERENCES

1. Chen Wujun and Zhang Shujie, *Deployable Space Structures And Analysis Theory*, China Astronautic Publishing House, Beijing, China, 2006.
2. Ma Xingrui, et al., *The Researching Evolvement of Spacecraft Development and Driving Mechanism*, Journal of Astronautics, Vol. 27, 1123-1131, 2006.
3. Guo Weidong, *Virtual Prototype Technology and ADAMS Application Examples Tutorial*, BeiHang University Press, Beijing, China, 2008.
4. Wan Li, Bian Wenjie, et al., *Transient Dynamics in CAE Solution-MSC.Dytran Application Examples Tutorial*, Peking University Press, Beijing, China, 2004.

THE FLIGHT CONTROL OF SHEFEX II

Frank Scheuerpflug [(1)], Alexander Kallenbach [(2)]

[(1)] *Research Associate, DLR, 82234 Wessling, Germany, Frank.Scheuerpflug@dlr.de*

[(2)] *Research Associate, DLR, 82234 Wessling, Germany, Alexander.Kallenbach@dlr.de*

1 NOMENCLATURE

ACS	Attitude Control System
DCTA	Departamento de Ciência e Tecnologia Aerospacial
DLR	German Aerospace Center
GPS	Global Positioning System
IIP	Instantaneous Impact Point
IMU	Inertial Measurement Unit
RADAR	Radio Detecting and Ranging
SHEFEX	Sharp Edge Flight Experiment

2 ABSTRACT

SHEFEX II (Sharp Edge Flight Experiment) was a two-stage sounding rocket mission to investigate advanced reentry technology. The successful launch was conducted from Andøya Rocket Range, Norway in June 2012. Comprising a suppressed trajectory, initiated by a cold-gas pointing maneuver prior to 2nd stage ignition, and spanning 800 km over the Norwegian sea, it was the most complex sounding rocket mission ever carried out by the German Aerospace Center DLR. To maximize the chances of a mission success, a mission scenario was developed that accounted for system failures and permitted to compensate for them or at least tolerate them long as no safety limits were infringed. The actual flight proved these measures very effective. A strong deviation of the unguided 1st stage from its nominal trajectory could be successfully compensated for by the flight control of the 2nd stage. This resulted in a nominal mission sequence and payload impact in immediate proximity of the nominal aiming point.

3 INTRODUCTION

3.1 Vehicle and Mission Objective

The scientific mission objective was to flight-test the behavior of a variety of advanced reentry technologies during a flat reentry at Mach 10. The rocket motors, S40 and S44, were solid propellant motors of the composite type, developed and manufactured by DCTA Brazil.

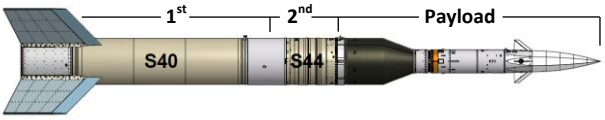

Property	Units	Value
Payload Mass	[kg]	707.9
S40 Propellant Mass	[kg]	4320.0
S44 Propellant Mass	[kg]	810.0
Total Vehicle Mass	[kg]	7057.6
Total Vehicle Length	[m]	12.76
S40 Burn Duration	[s]	54
S44 Burn Duration	[s]	63

Figure & Table 1. Characteristic Vehicle Properties.

3.2 Nominal Mission Sequence

The nominal mission sequence starts with the fin stabilized ascent of the first stage, rail-launched at a nominal elevation of 82.5 ° as a compromise between gaining as much horizontal velocity as possible for a flat reentry and keeping structural loading and aerodynamic drag losses low during the atmospheric crossing. In the interest of dispersion reduction, the fins were set at an incidence angle of 0.6 ° to impart a final spin rate of 1.5 Hz around the longitudinal axis of the vehicle. Upon reaching the upper end of the relevant atmosphere at 85 km, the burnt out 1st stage booster is jettisoned. To maximize the duration of the experiment conducted on the reentry part of the trajectory, a shallow reentry flight path is then initiated by a cold gas pointing maneuver that takes the vehicle attitude down to 38.1 ° in elevation (over local ellipsoid) prior to ignition of the 2nd stage rocket motor. The experiment itself is carried out at Mach numbers around 10, in the altitude layer ranging from 100 km down to 20 km, where the payload is split in two halves and recovered by parachute. The touch down is located 800 km down range at an azimuth bearing of 346 °.

Proc. '21st ESA Symposium European Rocket & Balloon Programmes and Related Research',
9–13 June 2013, Thun, Switzerland (ESA SP-721, October 2013)

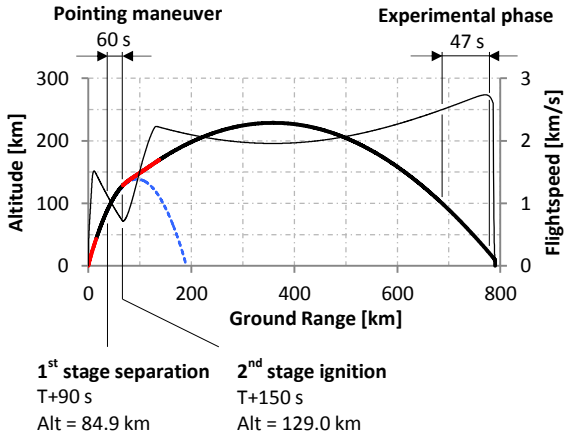

Figure 1. Nominal trajectory (thrust phases in red, S40 booster trajectory in blue)

4 KEY ELEMENTS

4.1 Failure Tolerant Mission Design

The cold gas attitude control system to conduct the pointing maneuver had specifically been developed for SHEFEX II, and is a particularly complex system, as it controls the vehicle attitude while spinning at 1.5 Hz. Novelty and complexity make the occurrence of a system failure a probable scenario. To maximize the chances of mission success, system malfunctions were accounted for and could - to a certain degree – be tolerated due to a robust mission outlined in the following.

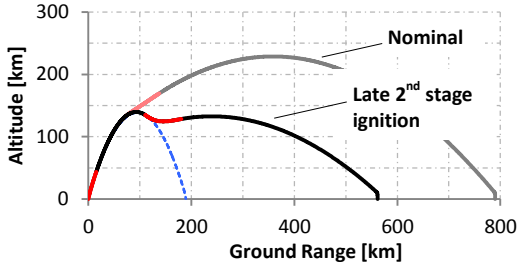

Figure 2. Nominal ascent trajectory with latest permitted 2nd stage ignition

The nominal mission sequence dedicated a 60 s timespan to the pointing of the vehicle in the coast phase after 1st stage separation. This comprised the calculation of the pointing angles after the atmospheric crossing, the tele-command operation to the vehicle and the actual pointing maneuver and is just sufficient in case the attitude control system works nominally. In case of a system failure resulting in a slower or erratic operation, the coast phase could be extended up to 140 s in order to improve the vehicle pointing. Fig. 2 depicts the trajectory shape resulting from such a "latest ignition" case while assuming all other flight parameters nominal. Any later ignition of the 2nd stage was not permitted because of the risk to re-enter the atmosphere with the 2nd stage still burning, which would inevitably result in the loss of the mission, as the 2nd stage is not aerodynamically stable.

To cover the case where the desired pointing angles cannot be reached by the system, it was foreseen to continue the mission anyways, provided that the actual pointing resulted in an impact within the conceded impact area and would not lead to the 2nd stage burning within the atmosphere. This also included the circumstance, in which the attitude control system would not work at all and the 2nd stage would be lit at the angle the vehicle left the atmosphere. In all these cases, the experiment could still have been conducted and valuable scientific data gathered. However, the resulting impact point would have been located far from nominal. Therefore the conceded impact area notified by Andøya Rocket Range was chosen as large as possible (extending 830 km in north-south and 760 km in east-west direction) while avoiding frequented ship and air traffic routes, see Fig.3.

4.2 Dispersion Reduction

The cold gas pointing maneuver accomplished prior to 2nd stage ignition was also exploited to reduce the impact point dispersion. Dispersion analysis [3] shows, that the major fraction of the impact point dispersion, roughly 90 % in area, is induced during the atmospheric ascent and 1st stage burn. A proper correction of the pointing attitude prior to 2nd stage ignition therefore permits to compensate for any deviation from the nominal trajectory, and hence reduce the 3-σ impact dispersion down to an ellipse of a half axes magnitude of 23 x 80 km, see Fig 3.

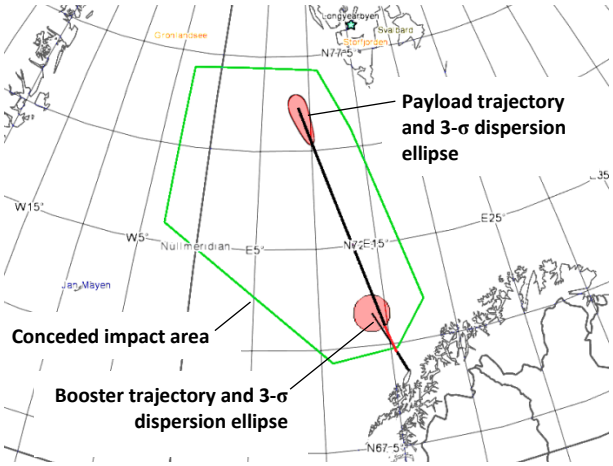

Figure 3. Map view on nominal trajectory, booster trajectory, 3-σ impact areas and conceded impact area

An algorithm was developed, that generates the corrected pointing angles for the 2nd stage and is described in detail in [3]. It was implemented in the

ground segment to provide the required computing power and also to allow for a human control of the pointing angles finally commanded to the attitude control system. The algorithm core is a linear-quadratic function of the actual deviation in position and velocity from the nominal trajectory after 1st stage burn out and atmospheric crossing. The position and velocity data required are extracted from either of the telemetry streams of the on board GPS and IMU units, therefore granting a single fault redundancy in case of a malfunction of one system.

4.3 2nd stage burn monitoring & thrust termination

Because of the involvement of an active attitude control on the 2nd stage, a possibility to terminate the 2nd stage thrust phase in case of a critical system malfunction became an essential requirement to safeguard the uninvolved public. To support a quick decision on the mission health, a software application was developed that allowed to monitor the vehicle position and instantaneous impact point (IIP) derived from all available trajectory data sources (GPS, IMU and RADAR) in close to real time. All curves and values on its single screen display are color-coded according to the data they are based on (blue = GPS, red = IMU, green = RADAR). This and the simplicity of the display ease an all-time situational awareness of the Flight Safety Officer.

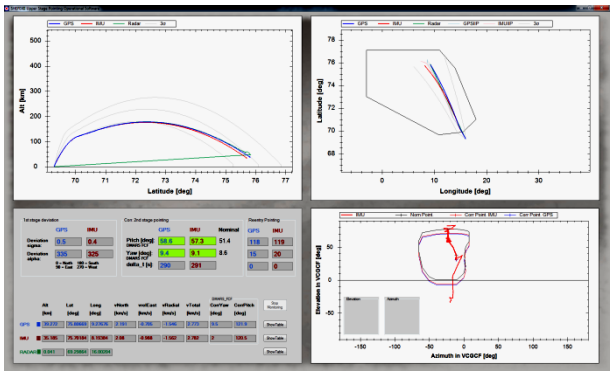

Figure 4: In-flight display of safety software

4.3.1 Flight Termination Regime

The possibility to terminate the 2nd stage burn was realized by an explosive load mounted along the motor case of the S44 rocket motor that could be activated by tele-command.

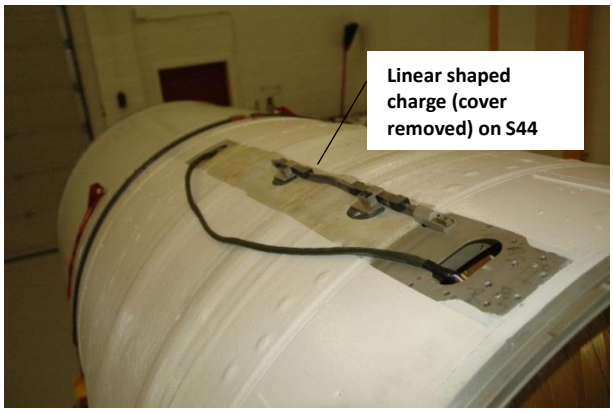

Figure 5: Linear shaped charge on 2nd stage

As destructing the hull of the thrusting motor would likely have resulted in a damage of the payload, this was considered only a last resort in the following cases:

A) Unacceptable uncertainty of the IIP

This is when no, not enough, or not trustworthy IIP or position data are available within the first 20 s of 2nd stage burn to indicate that the vehicle strides away from the mainland. 20 s was chosen as a "green time" because this is about the minimum time it takes – in the worst case that the 2nd stage points backwards - for the IIP to reach the Norwegian mainland.

B) Unacceptable IIP path

This is when the IIP infringes the conceded impact area depicted in Fig. 3.

5 FLIGHT RESULTS

GPS and IMU data were available through all critical flight phases and in good conformance until the end of 2nd stage burn.

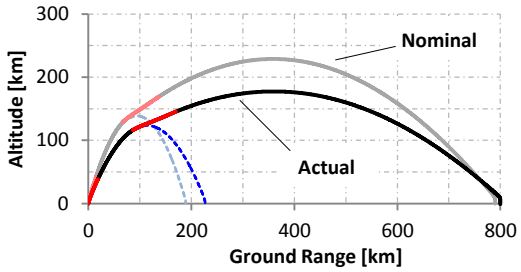

Figure 6. Actual trajectory of SHEFEX II vs. nominal trajectory. Actual from GPS data. Booster downleg and last 25 km of payload trajectory reconstructed by trajectory fitting.

The 1st stage trajectory deviated significantly from nominal, with the impact located 43.7 km downrange of the Nominal Aiming Point (= 2.5 σ) as illustrated in Fig. 6. In a post-flight analysis, this was found to be due to an overdamped aerodynamics modeling, leading to an underestimation of the influence of the launcher tip-off effect on the trajectory.

The deviation was detected by the dispersion reduction algorithm – based on GPS flight data – which proposed to lower the vehicle elevation prior to 2nd stage ignition by 7.2 ° to 30.9 °. The pointing angles were tele-commanded to the vehicle and the flawlessly working attitude control system redirected the vehicle within the nominal 60 s coast phase.

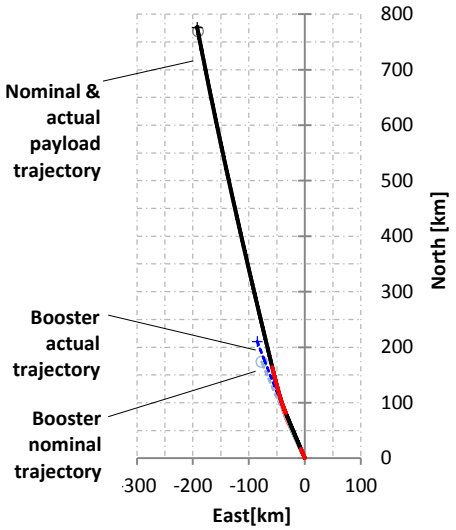

Figure 7: Actual and nominal trajectory ground tracks. Actual payload ground track in perfect conformance with nominal.

The 2nd stage was ignited at the nominal T+150 s. Impulse generated by the S44 was close to nominal and the attitude of the spin stabilized stage stable within a tolerance of ± 1 °. The reentry phase also elapsed close to nominal until loss of the telemetry link in 25 km altitude. The actual touch down of the payload occurred 8.5 km north of the nominal aiming point. Therefore, the mission was considered an outstanding success, especially in view of the complexity and novelty of its mission scenario.

6 REFERENCES

1. Cremaschi, Weikert, Wiegand, Scheuerpflug, Sounding Rocket Trajectory Simulation and Optimization with ASTOS, Proceedings of the 19th ESA Symposium on European Rocket and Balloon Programmes and Related Research, 2009
2. Scheuerpflug, Dragøy, SHEFEX II Flight Safety Rationale V1.3, Oberpfaffenhofen, June 2012
3. Scheuerpflug, Kallenbach, Cremaschi, Sounding Rocket Dispersion Reduction by Second Stage Pointing Control, Journal of Spacecraft and Rockets, Vol.49, No.6, Nov-Dec 2012
4. Weihs, Longo, Turner, The Sharp Edge Flight Experiment SHEFEX II, a Mission Overview and Status, Proceedings of the 15th AIAA International Space Planes and Hypersonic Systems and Technologies Conference, 2008
5. Turner et al., SHEFEX II Development Status of the Vehicle and Sub-Systems for a Hypersonic Re-Entry Flight Experiment

ACTIVE FALLING SPHERE FOR HIGH-RESOLUTION MEASUREMENTS OF DENSITY, TEMPERATURE, AND HORIZONTAL WINDS IN THE MIDDLE ATMOSPHERE

Qiang Li[1], Boris Strelnikov[1], Markus Rapp[1,*], Franz-Josef Lübken[1], Gerd Baumgarten[1], Sebastian Finke[2], Rolf Pohlmann[2], Jan-Berend Schumacher[3], and Hartmut Ewald[3]

[1]*Leibniz-Institute of Atmospheric Physics, Schlossstr. 6, 18225 Kühlungsborn, Germany*
[2]*Argus Electronic GmbH, Joachiam-Jungius-Str. 9, 18059 Rostock, Germany*
[3]*University of Rostock, Institute of General Electrical Engineering, Albert-Einstein-Str. 2, 18059 Rostock, Germany*
[*]*now at DLR-Institute of Atmospheric Physics, D-82230 Oberpfaffenhofen, Germany*

ABSTRACT

The well-known falling spheres (FS) technique to measure density, temperature, and wind fields in the middle atmosphere has been routinely used since 1950s. This relatively inexpensive in situ measurement technique is still of a great scientific interest since it allows to accomplish rocket soundings with sophisticated instrumented payloads. Unfortunately, the FS measurements are not available anymore and there are no another established technique to measure winds between 30 and 60 km heights. In this paper we introduce a new Active FS instrument, which is equipped with sophisticated instrumentation to measure trajectory and deceleration of the sphere and it sends the data to the ground by onboard telemetry system. Based on the data derived from CIRA-86 model, we calculate the horizontal acceleration of the FS during its movement through the atmosphere and demonstrate the feasibility of the new accelerometer regarding its sensitivity. An equation is inferred to calculate the atmospheric density and temperature from the 3-D components. For supersonic flow, the drag coefficient C_d of a sphere is derived both from the DSMC (Direct Simulation Monte Carlo) wind tunnel program and from empirical expression and the comparison shows an overall agreement, which make it possible to take the analytical values of C_d for future research. In the nutshell, we discuss in detail the principle of operation of the new instrument and its application to the atmospheric research.

Key words: Falling Sphere Technique; Wind; Temperature; Density; Middle Atmosphere.

1. INTRODUCTION

Studies of the middle atmosphere at high latitudes, extending from about 10 to 100 km altitude, are of considerable scientific interest since this is an intermediate region coupling by the dynamical processes from above and below and containing a variety of physical and chemical processes. However, this region is somewhat less accessible to observations, which stimulated development of techniques for measuring the dynamical and thermal structures of the middle atmosphere in the past decades. The remote sensing techniques are widely used as a conventional method giving a global-scale measurements of the atmosphere from satellite and continuous measurements at a few locations from ground-based radar and lidar. During summer conditions, however, optical methods are hampered by permanent daylight and radar techniques cover only the ionospheric part of the middle atmosphere. And often the direct in-situ measurements of the atmospheric properties are needed without extensive ground-based support. An alternative is to utilize an accelerometer to measure drag acceleration on a falling sphere through the atmosphere. During experiments, a 3-D accelerometer is built to measure directly the horizontal (x and y, two directions) and vertical (z) components of acceleration of the sphere from which the total aerodynamical drag was determined. In these experiments, the well-known classical equation of aerodynamic drag is used to calculate atmospheric density from the measured accelerations exerted on the falling sphere:

$$F_d = ma_d = \frac{1}{2}\rho v^2 C_d A_s \qquad (1)$$

where F_d is the drag force, m the mass of the sphere, a_d the drag acceleration, ρ the ambient density, v the sphere velocity, C_d the drag coefficient, and A the cross-sectional area of the sphere.

The uses of the passive falling sphere (FS) technique for measuring the density, temperature, and wind fields of the upper atmosphere can date back to [1]. This technique has extensively been used in the past decades [e.g., Ref. 2, 3, 4, 5] and delivered vast of geophysical results. Thus, the climatologies by [4] and [5] derived from the falling

Proc. '21st ESA Symposium European Rocket & Balloon Programmes and Related Research', 9–13 June 2013, Thun, Switzerland (ESA SP-721, October 2013)

sphere measurements are so far the only references that adequately reflect the mean temperature field of the polar mesosphere.

An alternative method to the conventional falling sphere technique is to build triaxial accelerometers inside a sphere to actively measure the acceleration of the sphere, i.e., the active falling sphere method. These systems have been considered and developed since 1970th [e.g., Ref. 6] and intensely used to measure the middle atmosphere [e.g., Ref. 7]. Unfortunately, however, the FS measurements are not available anymore due to the barrier of the accelerometer sensitivity and high costs of the rocket launch vehicles. In addition, there are no another established technique to measure winds between ∼30 and 60 km altitudes. In this paper, we introduce a new active FS instrument for high-resolution measurements of density, temperature, and horizontal winds in the middle atmosphere and carry out a preliminary calculation to demonstrate the feasibility of the new instrument for the subsequent tests and experiments.

2. NEW ACTIVE FALLING SPHERE

In 2011 Leibniz-Institute of Atmospheric Physics, argus electronic GmbH, and Institute of General Electrical Engineering at the Rostock University, initiated a new project to develop an active FS instrument for high-resolution measurements of density, temperature, and horizontal winds in the middle atmosphere. The project was funded by the Ministry of Economics and Tourism in Mecklenburg-Vorpommern, Germany. A new rigid falling sphere was designed to have diameter of 25 cm and it has currently mass of ∼3 kg (see the upper panel in Figure 1). The rigid sphere houses three 3-D accelerometers, gyroscope, GPS receivers, and a telemetry system. Meanwhile, a ground-based receiving system was also developed to receive the measured data from the sphere in a real-time mode. This ground-based equipment is much simpler and cheaper than the tracking radar system used by the conventional passive FS. Figure 1 shows the receiving antenna as well as the ground-based TM station. For more information on the new accelerometer with high sensitivities and the onboard telemetry system, the reader refer to the companion papers by [8] and [9], respectively.

The active FS technique has a potential to carry out measurements with better accuracy and height resolution exceeding those of the conventional techniques including the passive FS. Technically, it is thus necessary to improve the sensor sensitivity of the new accelerometers with a relative high mass-to-area ratio of the sphere (thus resulting in a high falling velocity). Using the model data of the atmospheric density and zonal wind from CIRA-86 [10], we calculate the horizontal acceleration of the FS as it moves through the atmosphere.

According to Newton's Laws to determine the momentum transfer rate between the atmosphere and the sphere,

Figure 1. Pictures of the new designed active falling sphere. Upper panel: Dimensions of the sphere with a diameter of 25 cm and mass of 3 kg; Middle panel: Receiving antenna with ground-TM station; Lower panel: Ground-TM station.

the horizontal acceleration a_H exerted upon a sphere of radius r, mass M and horizontal velocity v_s by an atmosphere of density ρ and wind speed v_0, is given approximately by the following formula [e.g., Ref. 11]:

$$a_H = \frac{\rho \pi r^2 (v_0 - v_s)^2}{M} \qquad (2)$$

where ρ is the density of the atmosphere, v_0 the wind speed, and r is the diameter of the sphere, M the mass of the sphere, and v_s the horizontal velocity of the sphere.

The calculated profiles of horizontal acceleration that we expect to be exposed to our sphere for 12 different months, as well as the mean profile are shown in Figure 2. From Figure 2, one can see that the horizontal acceleration that the sphere can achieve significantly decreases with hight, which makes it technically more difficult to measure the horizontal acceleration at higher altitudes. With the sensitivity exceeding 10^{-7} m/s^2 (i.e., $10^{-8} \cdot g$,

where g is the acceleration due to gravity) for our case, however, the accelerometers are sensitive enough to allow for probing the middle atmosphere (say 30–100 km).

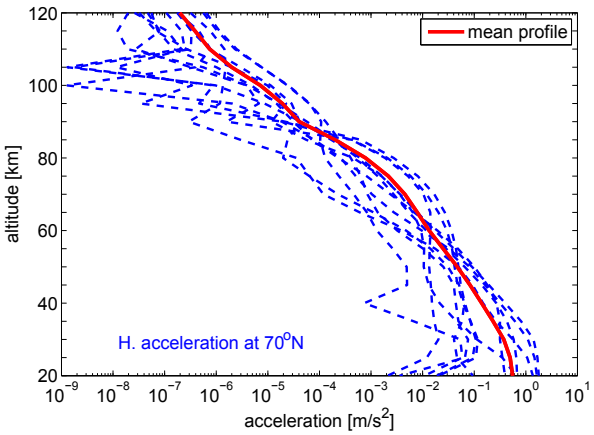

Figure 2. Profiles of the horizontal acceleration of the FS calculated using the zonal wind data from CIRA-86 [10] for individual month at 70°N indicated in blue and mean values for 12 months in red.

3. EQUATIONS FOR DATA ANALYSIS

An object moving through the earth's atmosphere is exerted to four different-type forces, i.e., gravity, drag, buoyancy, and Coriolis forces. For the FS experiments, however, the buoyancy and Coriolis forces of the sphere are more than one order of magnitude smaller than the others and therefore are neglected for further calculations. Thus, the equation to derive the density from the falling sphere measurements reads:

$$\rho = \frac{2m(a_z - g_z)}{C_d A_s |v_r|(v_z - w_z)} \tag{3}$$

where m is the sphere's mass, g_z the acceleration due to gravity, C_d the drag coefficient, a_z the vertical component of the sphere's acceleration, v_z is the vertical component of its velocity, A_s is the sphere's cross-sectional area, v_r the motion of the sphere relative to the air, and w_z is the vertical component of wind velocity. Note that the vertical winds cannot be measured from a single sphere and hence neglected. Actually, the vertical winds are much smaller compared to the vertical speed of the falling sphere. By neglecting of the vertical winds we introduce some errors especially for the lower part of the measurement range (say below 60 km). However, it will not significantly affect the results of the derived density.

We define v_x and v_y as horizontal components and v_z as vertical component of sphere velocity relative to the ambient air. And,

$$v_x = v_z \frac{a_x}{a_z} \tag{4}$$

$$v_y = v_z \frac{a_y}{a_z} \tag{5}$$

Thus,

$$\rho = \frac{2m(a_z - g_z)}{C_d A_s v_z^2 [1 + (\frac{a_x}{a_z})^2 + (\frac{a_y}{a_z})^2]} \tag{6}$$

In Equation 6, m and A_s are defined by the dimension of the sphere. The three components of the acceleration (i.e., a_x, a_y, and a_z) are directly derived from the measurements by the 3-D accelerometers. The vertical velocity of the sphere, v_z, is derived from the GPS tracking system. The derivation of the drag coefficient C_d will be discussed in detail in the next section.

From the retrieved atmospheric density profiles, the temperatures are calculated assuming hydrostatic equilibrium and utilizing the ideal gas low:

$$T_z = T_0 \frac{\rho_0}{\rho(z)} - \frac{1}{\rho(z)} \frac{M}{R} \int_z^{z_0} \rho(\acute{z}) g(\acute{z}) d\acute{z} \tag{7}$$

where T_z is the ambient temperature at z altitude, z_0 starting altitude, M the molecular weight of dry air, R the universal gas constant, g the acceleration due to gravity, and ρ the ambient atmospheric density. For the integration, an initial value of temperatures and densities at starting altitude (i.e., T_0 and ρ_0) has to be taken from independent measurements or from a model.

4. DRAG COEFFICIENT

When a sphere moves through the atmosphere, the gas molecules of the atmosphere near the sphere are disturbed and move around the sphere. Aerodynamic forces are hence generated between the gas and the sphere. In gas dynamics, the magnitude of drag force depends on the shape of the sphere, the relative velocity of the sphere, and the viscosity and compressibility of the ambient gas, etc. Hence, a dimensionless quantity drag coefficient (denoted as C_d) was introduced to quantify the drag exerted on the sphere. Note that C_d is a function of Mach number, $Ma = v_s/c$ where c is the speed of sound, and Reynolds number, $Re = (v_s \cdot L)/\nu$, where L is the diameter of the sphere and ν is kinematic viscosity of the air. Ma and Re can be related to the Knudsen number (denoted as Kn), a dimensionless quantity that is used to determine the appropriate gas dynamic regime. Based on characteristic ranges of values of an appropriate Knudsen number, gas dynamics is broadly classified into continuum flow ($Kn < 0.01$),transition flow ($0.01 < Kn < 1.0$), and free molecule flow ($Kn > 1.0$). The following equation can be used for their relationship:

$$Kn = \frac{Ma}{Re} \sqrt{\frac{\gamma\pi}{2}} \tag{8}$$

where γ is the specific heat ratio.

Based on the CIRA-86 [10], we adopted the data of temperatures and pressures to calculate the mean free path and Knudsen number Kn with the diameter of a falling sphere $L = 0.25$m for our case. The profiles of Kn are shown in Figure 3 (Upper panel). Kn in logarithmic scale shows approximately linear decrease along altitude, which can be fitted using regression analysis to obtain the altitude dependence of Kn. The relationship between Re and Kn for supersonic flows, i.e., at different values of $Ma = 2, 3, 4, 5, 6$ is shown in the lower panel of Figure 3.

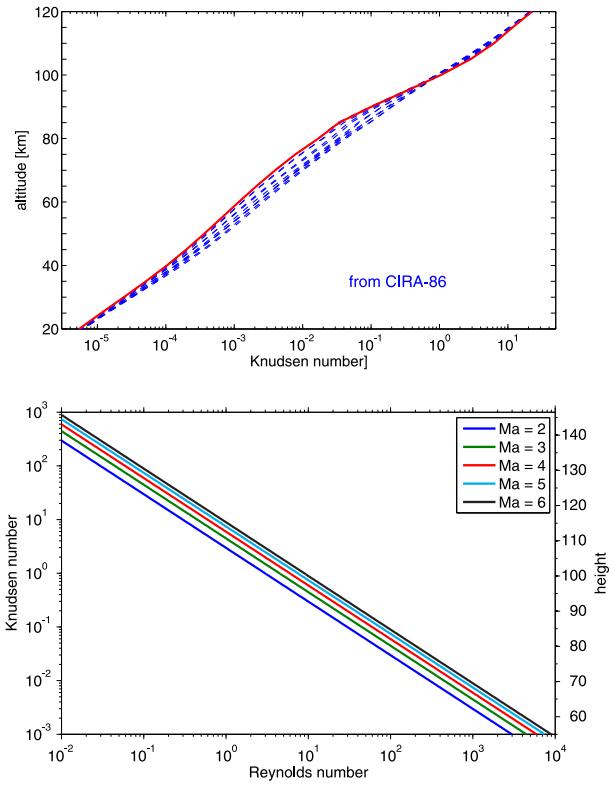

Figure 3. Upper panel: Profiles of Knudsen number calculated for 70°N based on the adoption of temperatures and pressures values from CIRA-86 [10]. The values in July are indicated in red. Lower panel: Relationship between Reynolds number and Knudsen number for different values of Mach number. The information of altitudes for 70°N is given.

According to the classification of gas dynamics, the gas below 70 km altitude, where $Kn < 0.01$, can be described by continuum flow, between 70 and 100 km – by transient flow ($0.01 < Kn < 1$), and above 100 km altitude by free molecular flow ($Kn > 1$). Besides that, above 70 km for the given Ma values, $Re < 1000$ indicates that the flow is laminar (i.e., $Re < 2300$).

The determination of drag coefficients of a sphere together with the probable errors have been empirically studied [e.g., Ref. 12, 13, 14] and many equations were suggested in the literature. According to the expressions suggested by [12], for the supersonic flows with $Ma > 1.75$, the drag coefficient is given by

$$C_d = \frac{0.9 + \frac{0.34}{Ma^2} + 1.86(\frac{Ma}{Re})^{\frac{1}{2}}[2 + \frac{2}{S^2} + \frac{1.058}{S} - \frac{1}{S^4}]}{1 + 1.86(\frac{Ma}{Re})^{\frac{1}{2}}} \quad (9)$$

where Ma is Mach number, and $S = Ma\sqrt{\gamma/2}$ is the molecular speed ratio, where γ is the specific heat ratio.

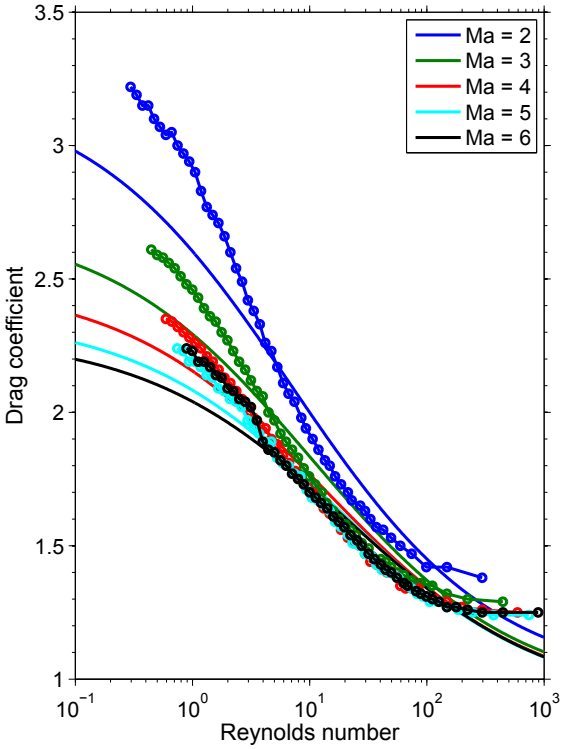

Figure 4. The analytical values of C_d calculated using the empirical equations by [12] (solid lines) and the simulated values of C_d using the DSMC wind tunnel program by [16] (dashed line with circle). The values of C_d derived from both methods show an overall agreement when the gas is in the transient regime with $Re > 3$.

For assumptions of Re within the range of [0.1–1000] and $Ma = 2, 3, 4, 5, 6$, C_d was calculated and displayed in solid lines in Figure 4. We can see that C_d decreases as Re (Ma) increases at a constant of Ma (Re). The calculated values of C_d are in an overall agreement with the prediction using the ARDC Model Atmosphere (see Fig.3 in [15]). Besides the analytical solution for C_d values, we also calculated C_d for the gas described as transient flow (i.e., $Kn > 0.01$) using the well-known DSMC (Direct Simulation Monte Carlo) wind tunnel program [16]. The derived C_d values using DSMC method are shown with dashed line with circle in Figure 4 (different colors for different values of Ma). The simulated values of C_d show a similar variation as a function of Re with the analytical C_d except that for $Re < 3$, however, the simulated C_d using DSMC method are larger than the analytical values. The reason for the difference might be due to

the fact that the gas falls in the free molecular regime for $Re < 3$ (see Figure 3 for more details). For future analysis, we can take analytical values of C_d derived from Equation 9 for calculation of the atmospheric density using Equation 6.

5. SUMMARY AND OUTLOOK

In this paper, we introduce a new active FS instrument for high-resolution measurements of density, temperature, and horizontal winds in the middle atmosphere. The rigid sphere with a diameter of 25 cm and a mass of 3 kg was built to house three 3-D accelerometers, telemetry system (TM), Gyroscope, and GPS tracking system. In addition, the ground-based receiving TM-station was also developed to receive the data sent by the onboard telemetry system. The new system has been tested using balloons and further tests with sounding rockets are scheduled for the year 2014. Preliminary calculations show that the horizontal acceleration that exerts on the FS significantly decreases along altitudes and larger than 10^{-8} m/s^2 which will get smaller than the sensitivity of the accelerometers. In the calculation of the atmospheric density and temperature, the drag coefficient C_d is more difficult to derive since the other parameters are either previously known or directly derived from the measurements. We also compared the C_d-values derived from empirical equations as well as from the simulation using DSMC method and reached an overall agreement between them. Hence, for the altitude range between 70 and 100 km we can use the analytical values of C_d for future research.

In subsequent study, we will concentrate on the experimental tests for the new system onboard sounding rocket which will be carried out during the WADIS campaign near in July 2013 as well as in January 2014. Meanwhile a joint measurements will be carried out using a Doppler Rayleigh Iodine Spectrometer (DoRIS) at the ALOMAR Observatory which is part of the ALOMAR RMR lidar [17]. The lidar has full daylight capability and allows simultaneous measurements of atmospheric temperatures, winds, and aerosols. The advantage of DoRIS will benefit a one-to-one comparison between the measurements both from the in situ instruments and from the ground. Further on, the acceleration measurements from the 3-D accelerometers on debut will be analyzed to derive atmospheric winds and temperatures. These results will be compared to the new DoRIS measurements and reported in near future.

ACKNOWLEDGMENTS

This project is funded by Wirtschaftsministerium Mecklenburg-Vorpommern in Germany.

REFERENCES

[1] Bartman F. L., L. W. Chaney, L. M. Jones, and V. C. Liu, Upper air density and temperature by the falling-sphere method, *J. Appl. Phys.*, 27, 706–712, 1956.

[2] Schmidlin, F. J., H. S. Lee, and W. Michel, The inflatable sphere: A technique for the accurate measurement of middle atmosphere temperatures, *J. Geophys. Res.*, 96, 9599–9603, 1991.

[3] Lübken F.-J., W. Hillert, G. Lehmacher, U. von Zahn, M. Bittner, D. Offermann, F. J. Schmidlin, A. Hauchecorne, M. Mourier, and P. Czechowsky, Intercomparison of density and temperature profiles obtained by lidar, ionization gauges, falling spheres, datasondes and radiosondes during DYANA campaign, *J. Atmos. Terr. Phys.*, 56, 1969–1984, 1994.

[4] Lübken F.-J., Thermal structure of the Arctic summer mesosphere, *J. Geophys. Res.*, 104(D8), 9135–9149, 1999.

[5] Lübken F.-J., and A. Müllemann, First in situ temperature measurements in the summer mesosphere at very high latitues (78°N), *J. Geophys. Res.*, 108(D8), 8448, doi: 10.1029/2002JD002414, 2003.

[6] Philbrick, C. R., A. C. Faire, and D. H. Fryklund, Measurements of atmospheric density at Kwajalein Atoll, 18 May, 1977, *Rep. AFGL TR 78-0058*, Air Force Geophys. Laboratory, 1977.

[7] Philbrick, C. R., F. J. Schmidlin, K. U. Grossman, G. Lange, D. Offermann, K. D. Baker, D. Krankowsky, and U. von Zahn, Density and temperature structure over Northern Europe, *J. Atmos. Terr. Phys.*, 47, 159–172, 1985.

[8] Schumacher, J. B., H. Ewald, S. Finke, R. Pohlmann, Q. Li, B. Strelnikov, M. Rapp, and F.-J. Lübken, High precision drag deceleration measurement system to use onboard active falling spheres, *21th ESA Symposium*, Thun, Switherland, 9–13 June, 2013.

[9] Finke, S., R. Pohlmann, Q. Li, B. Strelnikov, M. Rapp, and F.-J. Lübken, J. B. Schumacher, H. Ewald, Compact telemetry system for small satellites ejected from sounding rockets and balloons, *21th ESA Symposium*, Thun, Switherland, 9–13 June, 2013.

[10] Fleming E. L., S. Chandra, M .R. Schoeberl, and J. J. Barnett, Monthly mean global climatology of temperature, wind, geopotential height and pressure for 0–120 km, *National Aeronautics and Space Administration, Technical Memorandum 100697*, Washington D.C., 1988.

[11] Eckermann, S. D., and R. A. Vincent, Falling sphere observtions of anisotropic gravity wave motions in the upper stratosphere over Anstralia, *Pure Appl. Geophys.*, 130:2–3, 343–371, 1989.

[12] Henderson, C. B., Drag coefficient of spheres in continuum and rarefied flows, *AIAA J.*, 14(6), 707-708, 1976.

[13] Flemmer, R. L. C., C. L. Banks, On the drag coefficient of a sphere, *Powder Technol.*, 48(3), 217–221, 1986.

[14] Haider, A., and O. Levenspiel, Drag coefficients and terminal velocity of spherical and nospherical particles, *Powder Technol.*, 58, 63–70, 1989.

[15] Faucher, G. A., R. W. Procunier, and F. S. Sherman, Upper-atmosphere density obtained from measurements of drag on a falling sphere, *J. Geophys. Res.*, 68(11), 3437–3450, 1963.

[16] Bird, G. A., Molecular gas dynamics and the direct simulation of gas flows, *Clarendon Press*, Oxford, 1994.

[17] Baumgarten, G., Doppler Rayleigh/Mie/Raman lidar for wind and temperature measurements in the middle atmosphere up to 80 km, *Atmos. Meas. Tech.*, 3, 1509–1518, 2010.

UV CLEANED LANGMUIR PROBE

Christian T. Steigies[1] **and Aroh Barjatya**[2]

[1]*Institut für Experimentelle und Angewandte Physik, Christian-Albrechts-Universität zu Kiel, Olshausenstraße 40, D-24098 Kiel, Germany*

[2]*Physical Sciences Department, Embry-Riddle Aeronautical University, Daytona Beach, Florida 32114, USA*

ABSTRACT

The Langmuir probe is a standard instrument for sounding rocket campaigns, it is a simple instrument from which the plasma density and temperature can be derived. However, it is well known that the probe characteristics is distorted by surface contamination effects, which leads to erroneous measurements of plasma temperature and density. This does not only affect swept Langmuir probes, where this problem is clearly visible in the data with a properly chosen sweep function, it also modifies the spectrum of fixed-bias probes, where the contamination is not immediately seen in the data. To overcome this problem, several approaches to remove the water layer, which causes the contamination, have been undertaken. One method, that is frequently used in vacuum systems, has never been used on a sounding rocket: using UV light to desorb the water layer from the surface. The leak-rate in vacuum systems is determined by the water vapour that is deposited on the walls of the vacuum vessel. To reduce the pump-down time, the chamber walls are usually heated. However, this will only desorb the last formed water layers with weaker water-to-water bonds. UV light has sufficient energy to also desorb water layers with stronger bonds. Desorbing the water with the help of UV light leads to faster pump-down times, or, together with heating, to lower ultimate pressures. In a vacuum chamber the water has a high chance to resorb again to the surface, but in the ionosphere, the water will dissipate in the surrounding air with very low chances to resorb on the small probe surface. Thus, a UV illuminated Langmuir probe will have a reduced contamination layer, leading to improved probe measurements.

Key words: Ionosphere; Langmuir probe; Contamination.

1. INTRODUCTION

A standard instrument to measure ionospheric plasma parameters is the Langmuir probe [3]. Langmuir probes can be operated in a fixed-bias mode to deliver high-resolution relative density measurements, and in a sweep mode from which the absolute electron density, electron temperature, as well as the plasma and floating potentials can be determined. Measurements in both modes can be disturbed by surface contamination effects (see Fig. 1), which attenuate the collected current resulting in artificially lower densities [7, 10].

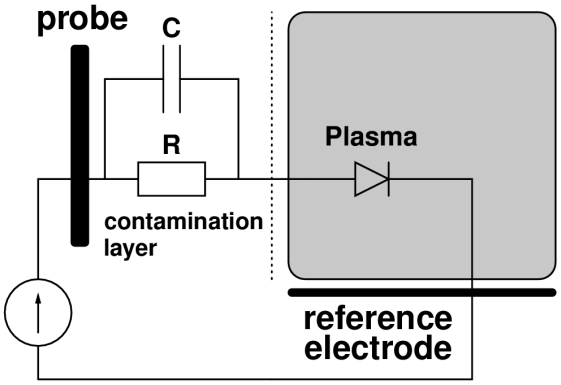

Figure 1. The Oyama contamination model showing the contamination layer between the probe surface and the plasma.

A standard Langmuir probe, that is assembled for a sounding rocket payload or a satellite, is exposed to the atmosphere and thus the water vapour in the air. The water layer on the probe surface acts as an RC-circuit between the probe and the plasma. The current, which flows from the plasma to the probe, has to pass through the resistor R and thus causes a voltage drop across the resistor, which is proportional to both R and the current I. Since a part of the voltage on the probe already falls off over the resistor, the plasma sees a smaller voltage and thus also delivers a smaller absolute current to the probe.

Proc. '21st ESA Symposium European Rocket & Balloon Programmes and Related Research', 9–13 June 2013, Thun, Switzerland (ESA SP-721, October 2013)

1.1. Contaminated sweeping Langmuir probes

In a sweeping probe, the capacitance C, which is parallel to the resistor R, can at least partially short the resistor, however the combination of R and C acts as a low-pass filter on the signal, so the measured current does not only depend on the plasma parameters, but also on the contamination constants and the speed and shape of the voltage sweep (see Fig. 2). By choosing a proper sweep function, however, the contamination constants can be determined from the measurement and the time dependent voltage drop across the contamination layer can be calculated [10]. Now, when the actual voltage that the plasma sees is known, the Langmuir probe sweep can be evaluated according to standard theory and the plasma temperature and density can be determined, provided the sweep function has been chosen properly and the contamination is not too big [6, 13].

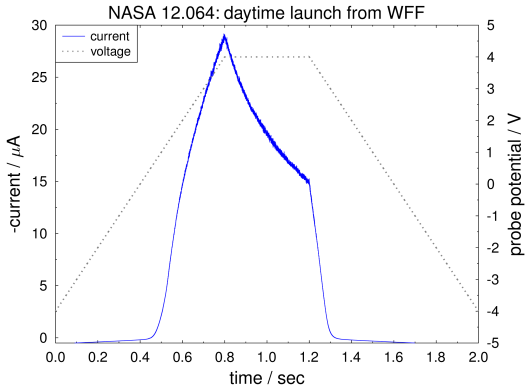

Figure 2. Langmuir probe current and applied potential versus time after the start of the sweep for one sweep during a daytime launch from Wallops Island.

1.2. Contaminated fixed bias Langmuir probes

Fixed-bias Langmuir probes are often used as a simple instrument to measure density fluctuations. The probe is calibrated with an independent measurement, like a Faraday rotation experiment, *in-situ*, and then the relative measurements by the LP are converted into absolute densities. However, these probes are usually contaminated as well, and the density fluctuations from the plasma have to pass through the contamination layer. Simulations have shown [12] that the spectrum of the fluctuations is influenced by the contamination layer which acts as a high-pass filter, see Fig. 3. Above a certain frequency, determined by the RC-constant, the signal passes nearly unchanged through the contamination layer, but below that the amplitude of the signal is reduced by an amount that depends on the resistance of the layer and the current that is delivered by the plasma, so that the reduction is larger in electron saturation mode than in ion saturation mode, and it is larger for high-density plasmas than for low-density plasmas. Since the DC current is calibrated with an absolute density measurement, the high-frequency fluctuations appear larger than they are in reality. All of this could be taken into account if the contamination constants were known, but most fixed-bias Langmuir probes are never operated in sweep mode, so the contamination and its magnitude will remain unknown and thus typically ignored in the analysis of the data.

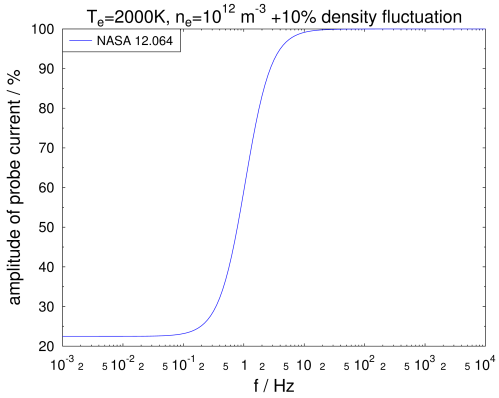

Figure 3. Simulation of the amplitude of fluctuations at different frequencies a fixed-bias Langmuir probe in electron saturation mode with the contamination parameters of NASA 12.064 would have seen.

2. CLEANING LANGMUIR PROBES

In order to derive reliable measurements from a Langmuir probe, it is highly desirable to have a contamination free Langmuir probe, and to determine the amount of contamination (by sweeping the probe at least once) to either confirm that it is contamination free or calculate the contamination parameters to allow for the correction of the contamination effects. Obviously, a clean or uncontaminated probe is preferred, and over the years there have been several different approaches to clean Langmuir probes.

2.1. Pulsed plasma probe (PPP)

Already in 1975 Szuszczewicz & Holmes [14] have developed a pulsed plasma probe which bypasses the contamination by applying short voltage pulses to the probe, thus short-circuiting the resistance through the capacitor. This method can give correct sweep measurements, but it does not remove the contamination and does not work for fixed-bias probes. Also the rapidly changing potential of the probe may be detrimental for other instruments that are on the same payload.

2.2. Glass-sealed probes

In 1976 Oyama & Hirao [8], who also developed the contamination model, built a glass-sealed Langmuir probe. The probe is baked on the ground and then sealed in vacuum. The glass seal is only broken once the payload reaches the ionosphere. While this method provides clean probes, it is technically more challenging, requires additional mechanics and pyrocutters, and prevents functional tests on the sealed probe on the ground.

2.3. Ion bombardment

Probes have been cleaned by ion bombardment by applying large negative voltages. This approach works well in a plasma chamber and for satellite missions, but since sounding rockets have a very limited flight-time, it is not very suitable on a rocket.

2.4. Heated probes

Internally heated probes have been developed for example by Amatucci et al. [1]. A small light bulb inside the Langmuir probe sphere heats the surface of the probe to accelerate the desorbtion of the water layer. While this clearly helps to reduce the contamination, it is not guaranteed that the complete contamination layer is removed, and too high temperatures, which improve the desorbtion, can modify the surface structure of the probe [2], which leads to disturbed probe characteristics and can also create other problems for the measurements.

2.5. Fast swept probes

Fast swept probes have often been used, however, just like the pulsed probes, they only circumvent the contamination and do not help for fixed-bias probes. A fast sweep with sufficient resolution also produces large amounts of data, which need to be preprocessed on-board to fit into the telemetry scheme [9].

2.6. UV cleaned Langmuir probe

A method, which has been used for many years in vacuum chambers, has probably never been tested on a sounding rocket: desorbtion of water with the help of ultraviolet radiation [4]. The largest (internal) leak in vacuum chambers is the water that is deposited on the surface of the vessel when it is exposed to the atmosphere. As the chamber is pumped down, the water is slowly desorbing from the surface. Below a pressure of 10^{-2} Pa the majority of the remaining gas is water vapour and it takes many hours to reach a final pressure of typically 10^{-4} Pa [5]. As with Langmuir probes, heating the vessel ("baking") speeds up the pump-down. Danielson [4] has shown that UV radiation can desorb the water from the surface faster than heating the walls, so that irradiating the walls with UV leads to a factor of 3 faster pump-down times. Combined with heating, the pump-down time can be reduced and a final pressure one to two orders of magnitude smaller can be achieved. In vacuum chambers both bake-out and UV light at first lead to higher pressures than a regular pump-down, since the water is desorbed from the walls and can not be pumped away as quickly as it is desorbed. Here, the water vapour also has a large chance to resorb again to the walls, since the mean free path length is on the order of the dimension of the vacuum vessel. On a sounding rocket on its way to the upper atmosphere, when the UV light is concentrated on the Langmuir probe, the water vapour should dissipate in the surrounding air, or resorb on other non-illuminated surfaces, and be removed from the vicinity of the probe by the rapidly decreasing atmospheric pressure, so that only small amounts of water vapour are able to resorb on the probe surface. Danielson [4] uses UV light at 183 and 254 nm from a conventional UV lamp. A UV lamp would be too large and fragile to fly on a sounding rocket. However, Danielson [4] mentions that any wavelength falling into the UV band may be used for irradiating.

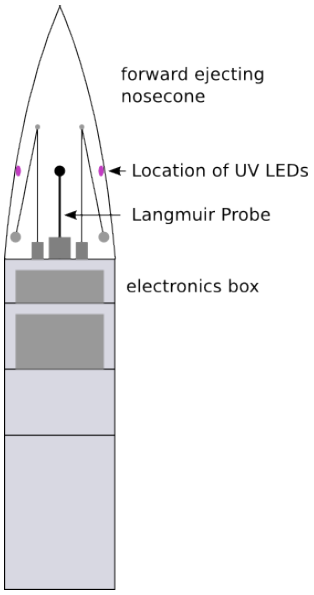

Figure 4. Placement of a UV-LED under the nosecone of a sounding rocket.

Today, UV LEDs at various wavelengths are commercially available [11] in small packages and with high optical output up to 50 mW. A small LED (TO-3 can) will fit easily at the inside of the rocket nosecone, where a Langmuir probe is typically placed on a sounding rocket. The small device has no fragile parts and will survive the rocket launch. When it is placed under the nosecone, it can illuminate the Langmuir probe until the nosecone is ejected at typically 70 km altitude. As the ascend to this altitude takes typically 50 sec, there will be at least 20 sec where the probe can be illuminated in reduced at-

mosphere, so that the desolved water vapour can be transported away in the diminishing atmosphere.

Thus we are proposing to clean the Langmuir probe with one or more UV-LEDs inside the nosecone facing the probe, see Fig. 4. The UV-LEDs would illuminate the probe after the launch until the ejection of the nose-cone, when the LEDs are turned off and removed together with the nose-cone.

3. CLEANING EFFECTIVENESS

According to [4] it takes 140 kcal to break one mole of water: 140 kcal / mol = 586 kJ / mol
The surface area of a 1 inch diameter sphere is:
$A = \pi \cdot d^2 = \pi \cdot (2.54\,\mathrm{cm})^2 \approx 20\,\mathrm{cm}^2 = 2 \cdot 10^{-3}\mathrm{m}^2$
The volume of one monolayer on the 1 in diameter sphere with 0.25 nm thickness is: $V = A{\cdot}0.25\mathrm{nm} = 5{\cdot}10^{-13}\mathrm{m}^3$
The mass of one monolayer is:
$m = V \cdot \rho = 5 \cdot 10^{-13}\mathrm{m}^3 \cdot 1000\mathrm{kg/m}^3 = 5 \cdot 10^{-10}\,\mathrm{kg}$
So the number of moles in one monolayer is:
$n = m/(18\,\mathrm{g/mol}) \approx 2.8 \cdot 10^{-8}\,\mathrm{mol}$
With this we can calculate the energy to break one monolayer: $586\,\mathrm{kJ/mol} \cdot 2.8 \cdot 10^{-8}\,\mathrm{mol} = 0.0164\,\mathrm{J} \approx 16\,\mathrm{mJ}$

According to this estimation a UV-LED with 16 mW optical output can remove one monolayer of water per second. A sounding rocket that studies the F-layer of the ionosphere will eject the nose-cone at about 70 km altitude, approximately 50 seconds after the launch. Since UV-LEDs with up to 50 mW optical output are currently available, a total of up to 150 monolayers of water could be removed from the probe, which should significantly reduce the contamination.

4. CONCLUSION

The surface of all Langmuir probes that are exposed to the atmosphere is contaminated with a water layer. This surface layer affects the accuracy of the Langmuir probe measurements. We propose a new method to remove the water contamination by illuminating the probe with UV-LEDs. A rough estimation suggests that the UV light is able to remove most if not all of the water from the probe surface on the upleg of the rocket before the release of the nose-cone. This should significantly reduce the contamination effects on the measurements and we propose to test this method *in-situ* with a rocket launched from Poker Flat, Alaska in 2015.

REFERENCES

[1] Amatucci, W. E., Schuck, P. W., Walker, D. N., et al. 2001, Rev. Sci. Instrum., 72, 2052

[2] Barjatya, A. 2007, PhD thesis, Utah State University, see http://digitalcommons.usu.edu/etd/274

[3] Barjatya, A., Swenson, C. M., Thompson, D. C., & K. H. Wright, J. 2009, Rev. Sci. Instrum., 80, 041301

[4] Danielson, P. 1987, Desorption of water molecules in a vacuum system using ultraviolet radiation, US Patent No 4,660,297

[5] Danielson, P. 2001, Desorbing Water in Vacuum System: Bakeout or UV?, http://www.vacuumlab.com/Articles/VacLab22%20.pdf

[6] Hirt, M., Steigies, C. T., & Piel, A. 2001, J. Phys. D, 34, 2650

[7] Oyama, K. & Hirao, K. 1976, Planet. Space Sci., 24, 87

[8] Oyama, K.-I. & Hirao, K. 1976, Review of Scientific Instruments, 47, 101

[9] Oyama, K.-I., Lee, C. H., Fang, H. K., & Cheng, C. Z. 2012, Rev. Sci. Instrum., 83, 055113

[10] Piel, A., Hirt, M., & Steigies, C. T. 2001, J. Phys. D, 34, 2643

[11] Sensor Electronic Technology. 2013, UVCLEAN lamps, http://s-et.com/uvclean.html

[12] Steigies, C. T. & Barjatya, A. 2012, Review of Scientific Instruments, 83, 113502

[13] Steigies, C. T., Pfaff Jr, R. F., & Rowland, D. E. 2005, in 17th ESA Symposium on European Rocket and Balloon Programmes and Related Research, Vol. SP-590, 331–336

[14] Szuszczewicz, E. P. & Holmes, J. C. 1975, J. Appl. Phys., 46, 5134

SOUNDING ROCKET GUIDANCE, NAVIGATION AND CONTROL AND ANTICIPATED NEXT GENERATION DEVELOPMENTS

Lars Ljunge

Project Manager, RUAG Space, Box 1134, SE-581 11 LINKÖPING, SWEDEN, lars.ljunge@ruag.com

ABSTRACT

This paper discusses the advantages of adding guidance to sounding rockets in order to achieve higher apogee at confined rocket ranges, more experiment time and shorter launch campaigns. It refers to two investigations in this latter area, and describes a few frequently used Guidance, Navigation and Control (GN&C) systems. Finally, future developments that could add value and efficiency to sounding rocket projects are discussed.

1. INTRODUCTION

Adding guidance and control to a sounding rocket has the following main benefits:

- Impact dispersion is most significantly reduced. The impact area is typically reduced by a factor of 25-100. This means that a much more powerful rocket can be used, with much higher apogee and thus with much longer experiment time above the atmosphere.
- The sensitivity to wind and wind variations becomes very small. In effect this means that launch is possible at almost all times, even when the wind is very strong or very variable.
- Motor thrust misalignment and offset have virtually no effect on the performance of the rocket.
- Very accurate trajectories and trajectories are achieved that can easily be tailored to scientific requirements.

2. SHORTENING THE LAUNCH CAMPAIGN

Modern rocket payloads tend to be significantly more complicated than those of a few decades ago. This means two things: The number of scientists and launch crew members nowadays is much larger, which means that each campaign day is a lot more expensive. With multiple payload modules on board, there also may be more launch criteria to fulfil before launch is given a green light. In connection to this, there is one aspect to guidance, that has not been discussed so much in the past, and that is how the launch campaign can be significantly shortened, and thus much less costly, when a guided rocket is used instead of an unguided one. This is connected to the various Range Safety related launch criteria of each rocket range. Numerous restrictions on parameters such as wind variability, launcher settings and ballistic wind limit the number of launch opportunities during a rocket launch campaign. Adding guidance to a sounding rocket greatly relaxes these restrictions, so that the rocket stays ready to launch almost every second of the launch campaign period. This means that the rocket can be launched when the scientific launch criteria are fulfilled and the payload thus is ready to launch, not when an erratic wind situation happens to be favourable.

Fig. 1 shows how a ballistic wind of 1 m/s typically affects a rocket with apogee around 270 km. If unguided, the impact point changes by 15 km, and 0.45 deg of launcher correction is required to remove this impact error. For the guided version, the change is only 0.15 km and 0.007 deg. Thus, a guided vehicle is almost insensitive to the low level wind and wind gusts, which burden every unguided launch. It also most efficiently removes all early disturbances like launcher dynamics, rail tip-off, non-symmetrical spin-up effects and thrust misalignment.

As we shall see below, this has a dramatic effect on the number of launch opportunities at all ranges with impact point restrictions. Guided high performance rockets are ready to launch under most all wind conditions, whereas unguided ones experience severe problems, even at minor low level wind variations.

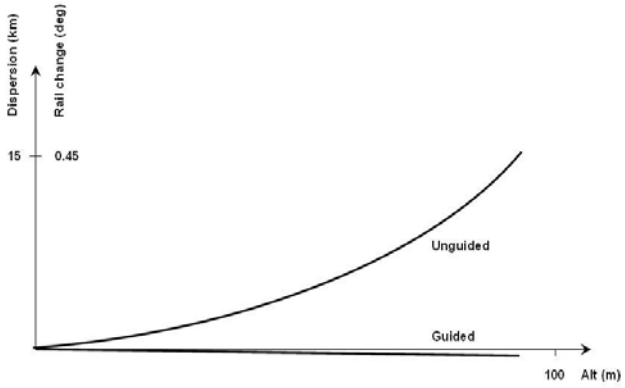

Figure 1. Guided rockets are almost insensitive to low level wind variations.

Proc. '21st ESA Symposium European Rocket & Balloon Programmes and Related Research', 9–13 June 2013, Thun, Switzerland (ESA SP-721, October 2013)

2.1. RUAG study

This relationship between lengthy or even cancelled launch campaigns and unguided rockets has been studied in detail on at least two occasions. In 1979, the author of this paper supported the launch of three guided Black Brant rockets during an auroral research campaign. In this type of campaign, it is of utmost importance that the rocket is ready to launch when the right type of auroral arc appears in the right part of the sky. During this launch campaign, I conducted a parallel study of what the launch situation would have been like, had the rockets been unguided. After the campaign, a comparison was then made between the number of launch opportunities for a hypothetically unguided and the actual guided configuration.

The nominal launcher setting was Elevation = 87.96 deg and Azimuth = 351 deg for the unguided rocket. The applicable launch restrictions during the launch campaign were as follows (see also Fig. 2):

1. Maximum angular deviation from nominal setting is 2.55 deg (upper red circle segment in Fig. 2). This is the maximum ballistic wind limit.
2. Launcher azimuth is restricted to stay within ±45 deg of the nominal azimuth (two straight red lines)
3. Maximum launcher elevation is 89 deg (lower red circle segment in Fig. 2)
4. Maximum launcher setting variation between two consecutive wind profile measurements is 0.29 deg (a highly variable wind situation is not a safe one)

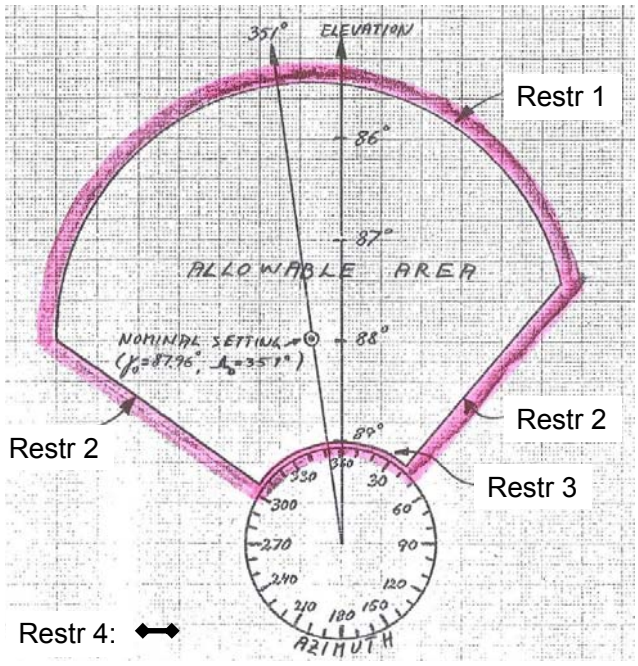

Figure 2. Launcher setting restrictions for the unguided rocket.

Thus, only launcher settings that are inside the area marked with red borderlines are permitted. However, this is not sufficient, since Restriction 4 also stipulates stable winds corresponding to less than 0.29 deg between two launcher settings for this particular rocket.

Every time a wind profile was measured, the corresponding launcher setting was calculated by wind weighting.

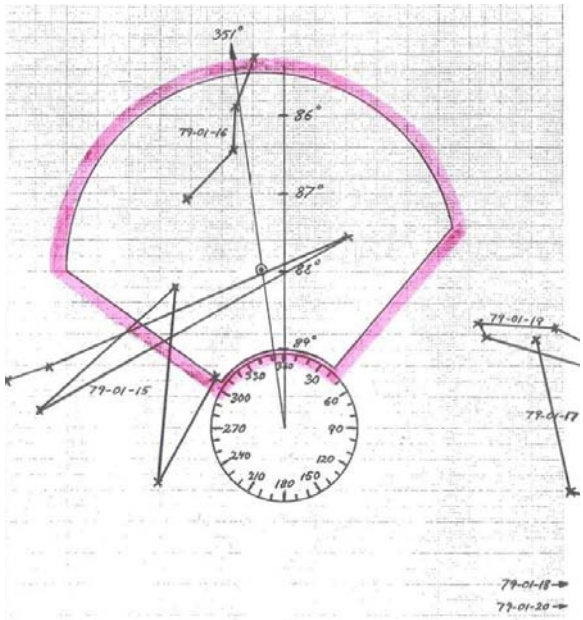

Figure 3. Launcher settings based on wind weighting for an unguided rocket during six consecutive campaign days. The launch restrictions were violated during all these days.

Fig. 3 shows what the launcher settings would have been like for an unguided rocket during the first six days of the launch campaign, which was thirteen days long. Each wind profile measurement results in a launcher setting marked with an x. Consecutive x-marks during one single day are connected by solid lines. During four of the six days (Jan 17-20), all launcher settings are completely outside the area whose red borderlines correspond to the first three restrictions above. During the remaining two days (Jan 15-16), some settings are inside the allowable area, but here the fourth restriction (related to wind variability) is violated at all times. Thus, no unguided launch would have been possible during these six days. In contrast, the guided rocket was GO for launch during all six days.

Table 1 summarizes the total results of the parallel study. The guided rockets were GO for launch at any time during 12 days out of 13 (and all three were successfully launched during the campaign), whereas no launch at all would have been possible, had the rockets been unguided. Thus, the Parallel Study clearly

demonstrates that rocket guidance was indeed needed for the launches.

Table 1. Unguided/Guided launch opportunities.

Launch condition	Unguided rocket	Guided rocket
GO	0	12
NOGO	13	1

2.2. American study

A second and much more comprehensive study was performed in 1986 by NASA, Conatec Inc and Saab Space in preparation for four time critical Halley comet sounding rocket missions to be launched from White Sands Missile Range. Together they later presented an AIAA paper [1], which addressed (quote) "the unique problems associated with launching Black Brant V, VIII and IX sounding rocket vehicles at White Sands Missile Range and the significance of the introduction of the S19 … in terms of launch flexibility" (unquote). NASA launch attempts versus cancellations of unguided sounding rockets during January through March 1976 – 1985 had been scrutinized, and out of 56 attempts, 30 were cancelled. Thus, there was just a 40 percent chance of launching at all. To make things worse, (quote) "The probability on a specific day during this period (pre-selected seventeen days in advance) can be reduced to near zero due to a combination of adverse weather patterns" (unquote).

Following the recommendations of the referenced study, S19 guidance was introduced on all four NASA's Halley comet missions, and successfully flown from White Sands Missile Range in 1986. The S19 Family of Canard Guidance Systems has been used ever since for all Black Brant class rockets at White Sands; to date close to 200 missions.

3. GUIDANCE, NAVIGATION AND CONTROL

Sounding rocket guidance is performed by pointing the rocket thrust in appropriate directions during the period of guidance. During the atmospheric part of flight, this can be performed in two ways: Through turning aerodynamic control surfaces that point the whole vehicle including its motor thrust, or by pointing the thrust vector only, using a vectorable exhaust nozzle or other devices for motor flame deflection. Both methods are widely practiced, for instance on fighter aircraft. During atmospheric flight, special attention also needs to be paid to the damping and stabilization of the bending modes of sounding rockets, which are long and slender bodies. When the rocket enters vacuum conditions, the destabilizing influence of body bending is reduced. At the same time, much smaller control forces are needed to control the attitude of the rocket in the absence of aerodynamic forces. Low thrust cold (or hot) gas actuators are sufficient for this purpose and become a third guidance alternative. Also of course, thrust vector control still remains feasible in space.

RUAG Space provides GN&C systems based on all three principles: The S19 Family of Canard Guidance Systems with its aerodynamic control, the GCS thrust vector control system and the Spinrac cold gas system.

3.1. Canard guidance systems

The S19 Family of Canard Guidance Systems has four members, all of which use canard actuators to aerodynamically control sounding rockets. The systems are completely autonomous units that may be located anywhere in the payload, though maximum performance is achieved when they are located close to the top of the rocket:

- The original S19 with its analogue autopilot and 60ies vintage MIDAS gyro platform, now retired after decades of successful operation
- The DS19 with its DMARS Inertial Navigation Platform and digital flight control software
- The S19D, using DS19 technology but with S19 guidance strategy
- The S19L which relies on the LN-200 strap-down platform and a Guidance Processing Unit
- Only the S19L and the DS19 remain in use

The S19L is the fourth generation development of the S19 sounding rocket boost guidance system that was first conceived in 1974 and successfully test flown on Jan 10, 1976 at NASA Wallops Flight Facility. Over the years since then, the four members of the S19 Family of Canard Systems have provided guidance and control to more than 225 sounding rocket flights.

Figure. 4. The S19L boost guidance system.

Wind weighting and associated launcher setting is performed on S19L-guided rockets, in order to reach the desired impact point, just like on unguided rockets, but significantly smaller launcher corrections are required.

The S19L provides constant attitude guidance for 18 s, long enough to warrant low impact dispersion, low wind sensitivity and potentially short launch campaigns. The control commands come from a Guidance Processing Unit (GPU), which receives attitude and velocity information from an LN200 strapped down inertial measurement unit. The S19L is a constant attitude system that acts to maintain the launcher attitude throughout the guided portion of flight. In effect, S19L guidance can be said to mimic a several kilometers long launch rail, with associated accuracy.

The DS19 is a true "fire and forget" system that provides rocket control throughout motor burn and navigates the vehicle along a highly precise trajectory to a pre-set impact point at very high precision. Just like with the S19L, a DS19-guided vehicle becomes extremely wind-tolerant, such that prevailing winds very seldom produce a No-Go situation. Furthermore, the atmospheric part of the trajectory can be tailored to specific needs, such as pad avoidance, curved ground tracks that do not pass sensitive areas and target-style maneuvering. Wind weighting and associated launcher setting are not required when using the DS19.

Newly built DS19 units will be based upon the same GPU+LN200 concept as in the S19L, not the second generation design shown in Fig. 5. This will decrease the total weight, increase reliability, simplify operations and lower the cost of new units, as well as the cost of post flight refurbishment.

Figure. 5. The DS19 fire-and-forget system operates throughout the atmospheric part of flight.

3.2. Thrust vector control systems

For rocket motors that are equipped with a thrust vectoring capability, the GCS provides guidance and control commands to the motor's thrust vector assembly. In its latest version, the GCS is based on the GPU+LN200 concept, thereby sharing a great deal of internal commonality with all other RUAG Space systems in terms of hardware as well as flight software.

The GCS has been successfully used in nine flights under the MAXUS project, where 800 kg payloads have been launched on GCS-guided Castor 4B motors and achieved apogees around 700 km at extremely low impact dispersion. Just like the DS19, the GCS is a true fire-and-forget system. The MAXUS is launched vertically and finds its way to its pre-set impact point without wind weighting. Trajectory tailoring to the user's needs is feasible.

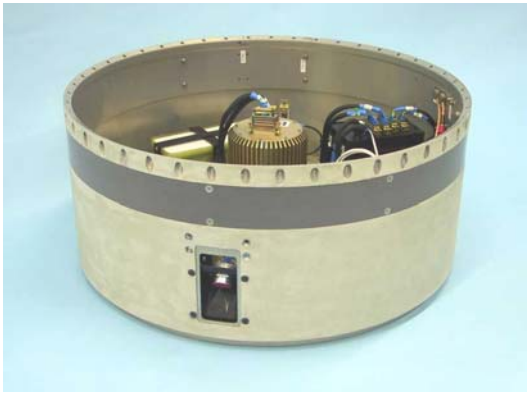

Figure. 6. A second generation version of the GCS thrust vector control system unit, used with the Castor IVB rocket (thereby its low packing density). New instrumentation to be used in its next generation means a shorter unit with lower weight.

3.3. Cold gas systems

For a rocket mission that uses an upper motor stage, which is ignited outside the atmosphere, the Spinrac spinning rocket attitude control system highly improves the accuracy of the mission. Following the laws of space physics, an unguided spinning vehicle enters into a coning motion following atmospheric exit. The magnitude of this coning is hard to predict, since it depends on interaction between the vehicle and the upper atmosphere, which fluctuates from day to day. This means that when an uncontrolled upper stage ignites, the vehicle will follow a highly imprecise trajectory and suffer from extremely high impact dispersion. If that is not acceptable, upper stage guidance can solve the problem. In a single control sequence, the Spinrac cold gas system removes the coning motion and points the rocket in a pre-selected orientation before upper stage ignition. It then holds that

orientation during motor burn, thereby acting as a virtual launcher rail in space, and impact dispersion then becomes very small, even at high apogee.

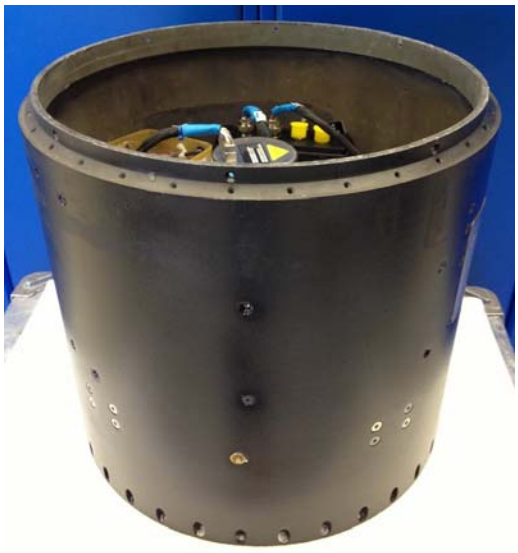

Figure. 7. The second generation Spinrac prototype. The system is designed for exo-atmospheric trajectory and impact point control. Note the yellow cold gas thruster in the lower center of the unit.

The Spinrac is available in two versions:

- As a stand-alone unit
- As a cold gas extension to any of the above S19 and GCS type systems

The original stand-alone Spinrac system was designed, built and successfully flown twenty years ago. Two years ago, its inertial navigation system was upgraded to use the same GPU+LN200 instrumentation as in the S19L. The pneumatic parts, as well as the flight control software were not modified at all. In a prototype module, it was verified through dynamic testing that the upgraded Spinrac works as specified. Thus, it is available for use in flight. It will be significantly shorter and lighter than the prototype unit depicted above.

If however a payload already has an S19 type or a GCS type system on board, it is not necessary to use a stand-alone Spinrac unit. Instead, payload weight and volume can be reduced by just adding a small cold gas unit that contains a gas supply and control valves. These valves then are controlled from the S19 or GCS, in which Spinrac flight software has been installed. Thus, the S19 or GCS first performs its part of the mission and then performs the Spinrac part too.

4. NEXT GENERATION DEVELOPMENTS

The future holds many possibilities for guidance systems, both in terms of how they will be used and in terms of new features. Several attractive features are either already waiting to be exploited or will be included in coming systems. Five such features are listed here and further commented upon below:

1. Increased data support for Range Safety and for the research payload
2. On-board automatic flight termination logic
3. Tailored trajectories, including target maneuvering
4. Added exo-atmospheric control capability
5. Inclusion of new technology

Item 1: In order to fulfill its tasks, a GN&C system generates a lot of data, such as acceleration, velocity, position, angular velocities and attitude information. The data originates from several sensors, such as inertial navigation units, GPS receivers and even sun and star sensors, and is generated throughout flight. This type of GN&C data is routinely utilized by Esrange Range Safety Officers, in order to supervise the flight path as well as the health of the GN&C system itself. The RUAG systems above also calculate the Instantaneous Impact Point and transmits it as an additional piece of flight safety information. Though these payload based sensors cannot completely replace ground based sensors, such as radar and sky screen instruments, they constitute a good complement that highly improves the Range Safety Officer's situational awareness throughout flight.

The same data of course is also available for scientific use, both during flight and afterwards, when science and GN&C data fusion may increase the scientific value of the flight. And needless to say, if unexpected events occur during flight, a well instrumented payload is in much better shape to sort out what has happened and why.

Item 2: On-board flight termination decision making is another well suited GN&C system task. Though the overall responsibility for a flight termination decision rest with Range Safety only, on-board surveillance of flight status constitutes an efficient way to ensure that Range Safety has immediate information about potential in-flight problems and thus stays on top of the situation at all times. A GN&C system expects a certain response from the rocket it is controlling, and any diversion from this behavior can be rapidly detected and reported to ground for further action. On board data fusion between the GN&C system and other vehicle parts is feasible, such that the situation is rapidly analyzed on board and distinct messages or recommendations on action can be transmitted to ground. There may even be situations

where Range Safety could assign limited rights to the GN&C system to automatically terminate the flight.

Item 3: Tailored trajectories may be generated by GN&C systems. Such trajectories make it possible to avoid flying over areas where people risk being hit by falling objects from a terminated flight, or where valuable installations could be damaged by such objects. A trajectory also could be required to follow a certain path, where ground based observation or telemetry link conditions are at their optimum.

An obvious military application of tailored trajectories is when the guided vehicle is a missile target. The flight path then could again be chosen to follow a certain route, for reasons given above. Evasive maneuvering is another feature that could enhance the value of a guided missile target. And fusion of data coming from the GN&C system, from ground sensors and from the attacking missile is helpful in post flight analysis of the missile test result

Item 4: Adding exo-atmospheric control by using thrust vector control systems like the GCS or cold gas re-pointing and stabilization systems like the Spinrac, extremely high apogee and range are possible, while maintaining small impact dispersion. This may be most important even if the rocket is launched over an extremely large impact range, since such ranges cannot be completely cleared from people or valuable property during launch. And, if payload recovery is required, this task is much easier to achieve if the impact dispersion is small.

Exo-atmospheric guidance also is a powerful tool to be used for shaping of atmospheric re-entry conditions. For example, a low performance motor could bring the vehicle just above the atmosphere, where a Spinrac system could tilt it over and an upper stage then could create a near-horizontal high-speed trajectory. Only imagination puts a limit to such possibilities.

Item 5: New technology constantly becomes available. Such technology makes it possible to do new things in guidance, such as to reduce weight and volume of guidance systems, to improve accuracy and/or reliability, to reduce the cost of an equally performing or even more potent system. The four generation members of the S19 Family of Canard Guidance Systems are good examples of how new technology has provided advantages in all these areas.

When the guidance system requires less payload volume thanks to new technology, it also becomes possible to let it share room with other payload subsystems. The next generation GCS is an example of this. Within the framework of the MAXUS project, there are plans to locate all GCS and telemetry system components in one payload module instead as in two, which has so far been the case. The weight and volume savings achieved by this can either give room for additional science experiments, or it can provide higher apogee and longer experiment time for the current experiments.

5. CONCLUSION

A guided rocket has several advantages as compared to an unguided one, such as small impact dispersion, low sensitivity to wind, to wind variations and to motor misalignments. In addition, it provides highly accurate trajectories for the benefit of Science and Range Safety.

Two studies show that guidance also means shorter and more efficient launch campaigns, since Range Safety launch criteria are much more easily fulfilled. Thus, substantial cost savings for the launch campaign becomes possible thanks to guidance,

A number of anticipated future developments also have been suggested and suggested in this paper.

REFERENCES

1) Montag, W. H., Detweiler, D. F. and Hall, L.: Application of Boost Guidance to NASA Sounding Rocket Launch Operations at the White Sands Missile Range, AIAA 86-2523-CP.

HIGH PRECISION DRAG DECELERATION MEASUREMENT SYSTEM TO USE ONBOARD ACTIVE FALLING SPHERES

Jan Berend Schumacher [(1)], Hartmut Ewald[(1)], Sebastian Finke[(2)], Rolf Pohlmann[(2)], Qiang Li[(3)], Boris Strelnikov[(3)], Markus Rapp[(3*)], and Franz-Josef Lübken[(3)]

[(1)] University of Rostock, Institute of General Electrical Engineering, Albert-Einstein-Str. 2, 18059 Rostock, Germany
Email: jan-berend.schumacher@uni-rostock.de , Email: hartmut.ewald@uni-rostock.de

[(2)] Argus Electronic GmbH, Joachim-Jungius-Str. 9, 18059 Rostock, Germany
Email: sebastian.finke@argus-electronic.de, Email: rolf.pohlmann@argus-electronic.de

[(3)] Leibniz Institute of Atmospheric Physics e.V. at University of Rostock, Schlossstr. 6, 18225 Kühlungsborn, Germany
Email: liquiang@iap-kborn.de, Email: strelnikov@iap-kborn.de, Email: luebken@iap-kborn.de

[(3)] now at DLR - Institute of Atmospheric Physics, 82230 Oberpfaffenhofen, Germany*
Email: rapp@iap-kborn.de

ABSTRACT

The conventional falling sphere (FS) technique to measure density, temperature, and horizontal winds in the middle atmosphere (i.e. between 30 and 100 km) has been the best available measurements used for decades for probing the polar mesosphere. The conventional (passive) FS-technique rely on the sphere trajectory recorded by a ground-based tracking radar. The later implies high costs and limits the altitude resolution due to the relatively large errors-bars in the derived trajectory. This paper describes a newly developed active falling spheres. The new instrument measures drag deceleration of the FS with high precision accelerometers which allows for a very high altitude resolution and is sensitive to small wind or density fluctuations.

1. INTRODUCTION

By analyzing the climate data since the begin of the weather record, a change in the temperature in the lower atmosphere can be observed. Moreover, several models predict further changes, which lead to an additional increase of the air temperature. But in contrast, while the temperature in the lower atmosphere raised, the temperature in the middle atmosphere, regarding an altitude between 50 km and 100 km, decreased by 16 °C within the last 40 years. That behaviour can only be observed by using LIDAR-systems, weather balloons, chaff, or free falling spheres.
Using a free falling sphere, a sounding rocket releases a balloon in the apogee, which inflates up to a diameter of about 1m. Because of its size and the metalized surface, the balloon can be tracked by a RADAR-system on the ground. By recording its trajectory time-related, horizontal winds, the density, and the temperature of the atmosphere can be derived. Due to the low resolution of the balloon's altitude by the RADAR-system, as well as the high costs to ship the system to the designated area, and furthermore the discontinuation of subsystems, free falling spheres are not a common tool to measure atmospheric parameters, yet. The solution could be an active free falling sphere, which uses multiple sensors to do measurements "in situ". High precision accelerometer are used, to measure the accelerations that are caused by wind fields and turbulences, just as the deceleration due to the rise of the neutral gas density as the sphere approaches the earth's surface.

2. PHYSICAL FUNDAMENTALS AND SYSTEM DESIGN

The base of the measurements, to estimate the density of the atmosphere are the second Newtonian law of motion

$$F = ma \tag{1}$$

and the drag equation

$$F = \frac{1}{2}\rho \mathrm{V}^2 \mathrm{C}_\mathrm{D} A \tag{2}$$

while "ρ" is the air density, "V" the velocity, "C_D" the drag coefficient, and "A" the cross-sectional area of the sphere. By equating both formulas, it can be seen that

$$F = ma = \frac{1}{2}\rho V^2 C_D A \tag{3}$$

and, as a result, reordered to the acceleration

$$a = \frac{\rho V^2 C_D A}{2m} \tag{4}$$

Proc. '21st ESA Symposium European Rocket & Balloon Programmes and Related Research',
9–13 June 2013, Thun, Switzerland (ESA SP-721, October 2013)

That Eq. 4 can be used, to estimate the measurement range and the resolution of the accelerometer, which are used to measure the deceleration, caused by the increase of the atmosphere's density. The value for the air density can be taken from the MSISE-00-model with $\rho = 3.2E\text{-}07\ g/cm^3$, while the maximum vertical velocity of the system depends on the altitude in which the system will be ejected, and reaches from 300 m/s to 1.000 m/s.
The drag coefficient can be estimated from theoretical studies and experimental results of the Reynolds number in a range of 20 to 10^5 and Mach numbers between 0.1 and 6. Therefore, for calculations, C_D can be chosen in a range of 0.5 to 3.5[1].
At least, the measurement system is placed in a sphere with a diameter of 25 cm, which is made out of glass fibre and epoxy resin. Combined, the mass of the sphere with the supposed mass of the measurement system, the weight of the whole system is about 3kg.

2.1. System Requirements

Hence, using Eq.4, the accelerometer must be able, to measure a deceleration between $1E\text{-}3m/s^2$ and $10m/s^2$. [1]
Additionally, the samplerate of the system should be higher than 1.000 samples per second, to gain at least one measurement value per meter at a vertical velocity of 1.000 m/s. Moreover, the resolution of the altitude of the system during flight shall be at least 10m. The system should furthermore be operable in a temperature range of -45 °C to 85 °C and withstand accelerations of 20 g and vibrations of 6 grms, which can occur during the start of the rocket. Finally, the system needs to be divided into subsystems. Therefore, single components, e.g. sensors, or modules can be changed in case of new requirements without the need to redesign the whole system. An other advantage is the possibility, that in the case of a failure, just the component that causes the malfunction needs to be replaced.

2.2. Arrangement of Subsystems

As described, the system is divided into several subcomponents, like it is additionally shown as a schematic overview in Figure 1.
The main module is the sensor system including two accelerometers with different measurement ranges. While the first of them is a high precision accelerometer with a smaller measurement range to measure the deceleration caused by the change of the density, the second accelerometer has a bigger measurement range, but a lower resolution. Therefore, the data from the high precision accelerometer can be sampled continuously to reach the best possible resolution, unless its measurement range is exceeded and the data from the second accelerometer are recorded. Next to the accelerometer, a three-axis gyroscope is integrated into the system to determine the speed of rotation. Due to that, the orientation of the system can be recorded. Additionally, through the knowledge of the rotational speed, and of the position of the accelerometer in the system, the measuring mistake caused by the centrifugal force, can be corrected.

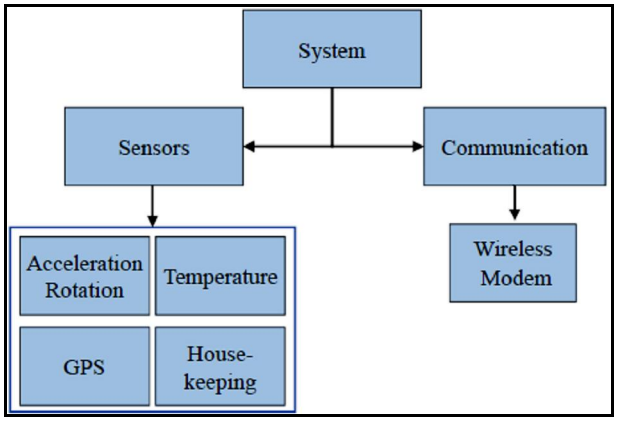

Figure 1: Schematic overview of the system design

Besides, temperature sensors measure the temperature in the system and especially near the sensors, as they do not have internal sensors. By that, a temperature correction of the measurement values can be done in a postprocesing. At least, the temperature sensors are placed on the outer structure, and used to sample housekeeping data of the system.
The housekeeping sensors are complemented by additional sensors to watch the battery voltage. Even though the batteries are installed fully charged prior flight, the sensors could initiate a charging process, if the voltage drops below a predefined limit, to ensure sufficient power during the measurement.
Finally, a high precision, two-frequency GPS module completes the sensor system. While it is used to measure the altitude of the system on one hand, to assign the data from the accelerometer to the altitude, it is additionally used to record the whole trajectory of the sphere time-related. By analyzing the raw-data of the module in combination with the data about the ionosphere after the flight, a higher accuracy of the sphere's position can be achieved.
The second main module of the measurement system is the communication module, which realizes a link to a groundstation through a wireless modem. Even though all measurement data are stored on a SD-card onboard, a recovery of the system is not possible in some cases, due to the terrain of the impact area, e.g. wood, swamp, or sea, or it is just not necessary, or too expensive to recover it. Consequently, the wireless modem is used, to transmit the measurement data to avoid its loss. At the same time, a computer at the groundstation can monitor the incoming data to prove the correct function of the

system, and in addition, use the received GPS-data to ease the recovery of the system. In case of a failure, it is also possible, to transmit a command to the measurement system, to change parameters or initiate a reset.

3. CONSIDERATIONS FOR THE SENSOR SELECTION

As described in chapter 2.2, the sensor system is a complex combination of different sensors to measure several atmospheric parameters. Due to the complexity, this paper pays particular attention to the drag deceleration measurement using accelerometers, which are the main component of the system.

3.1. General aspects of selecting the accelerometer

By selecting the accelerometer, special considerations must be taken into the characteristics of the sensor, next to its technique, e.g. Micro-Electro-Mechanical-Systems (MEMS), or Fiber-Optical-Systems (FOS), its measurement range and bandwidth. First of all, the disadvantages and advantages of analogue and digital sensors must be weighed up, regarding the requirements of the system and the sensor technique. For realizing this device, an analogue sensor was selected because of the possibility, to decide on the resolution and the signal conditioning. Furthermore, attention must be paid to the noise level of the sensor, to reach a high signal-to-noise ratio. Also, the sensitivity of the sensor and the characteristic of the output signal must be included in the selection, just as the cross sensitivity of the sensor in case of a multi-axis sensor. Moreover, the temperature dependence of the sensor, such as the power consumption, which should be as low as possible, to minimize the self-heating of the sensor and to increase the operating time of the system, shall be considered. Depending on the range of application, the resistance of the sensor against shock and vibrations play an important role, which, in this application, occurs during the start of the rocket. At least, the dimension and the weight of the sensor could be important for the development of a system, such as the operational conditions, like temperature, humidity and the capacity to work under vacuum conditions.

3.2. Sensor Selection for the measurement system

Due to the limited size of the system, such as the requirement, to choose light components, which is caused by Eq.4, the sensitivity of about 1.200 mV/g and the very low noise level of about 0.3 µgrms/√Hz, the "SF1600" by "Colibrys" was selected, to design the sensor system. As this device is a single-axis sensor, three sensors had to be mounted orthogonal, as shown in Figure 2. First measurements showed a resolution of about 250 µg, which exceeded the requirements. By analyzing the measurement data, e.g. by a Fast Fourier Transformation (FFT), two sources of error could be detected. On the one hand, the signal showed a ripple with a frequency of 50 Hz, which is caused by the radiation of the power supply system. On the other hand, the coupling between the sensor system and the measurement set up lead to errors. Due to that, vibrations e.g. caused by cars passing the building, the movement of persons, or even to talk lead to errors.
Finally, this system will be tested and characterized during the WADIS-campaign at the end of June 2013 at the Andøya Rocket Range in northern Norway, under microgravity conditions.

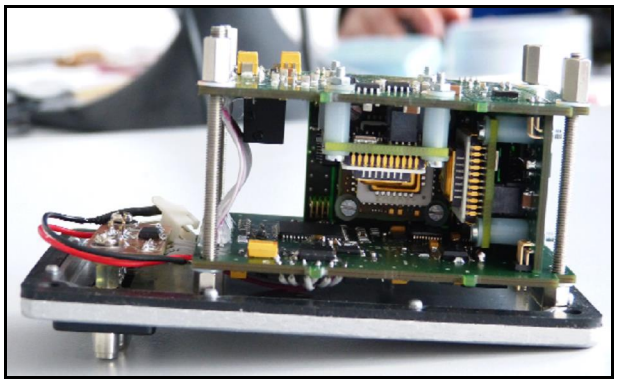

Figure 2: First Prototype with three SF1600 -sensors

Because of the sudden discontinuation of the sensor in March 2013, a new one had to be selected to measure the deceleration. The "5511LN" by the "ASC GmbH" is a three-axis accelerometer that was chosen as the new main component of the system, again, because of its dimension and weight, just like the low noise level in that class of 7 µgrms/√Hz. Furthermore, the cable of the sensor is shielded, which reduces the influence of electro magnetic radiations, which are caused by the DCDC-converter, that generates its supply voltage for example.

4. DESIGN AND LAYOUT OF THE ACCELEROMETER MODULE

Due to the different output signal of the sensor compared to the "SF1600", as well as changed dimension and pin outs of the printed circuit board (PCB), a new layout had to be done, to interface the sensor to the system.

4.1. General Layout Considerations

As described in chapter 2.1., the measurement system is divided into several subsystems, to avoid a redesign in case of changing requirements or modules. Due to that, and the selection of the "5511LN" as the new accelerometer, just that subsystem had to be redesigned.

The PCB has a size of 75 mm * 75 mm with four mounting holes, and is connected to the other components through two pinheader with a defined pinout. Because of these, it is possible, to stack all subcomponents that are needed for the measurements on each other, depending on the requirements of the system. In addition, mounting holes for other accelerometers were added, to use several types of sensors, which makes the system more flexible.
To reduce the noise of the system, different layout considerations were done. First, six layer are used for the PCB, which allows a good separation of signal lines, ground planes and the supply layer. Additionally, the layout is divided into three categories, which are: the digital part, the analog part, and the generation of the supply voltage. While the ground plane of the digital part is separated from the ground plane of the analog part and the supply voltage, it contains all digital components like the gyroscope, oscillators, and the buffer for the communication. Using a buffer for the communication, in addition with 100 Ω resistors, the radiation of the nets can be reduced, while the digital components, especially the analog to digital converter (ADC) that are used, are lightened from the load during communication, which leads to a lower noise on the measurement results of the ADCs.

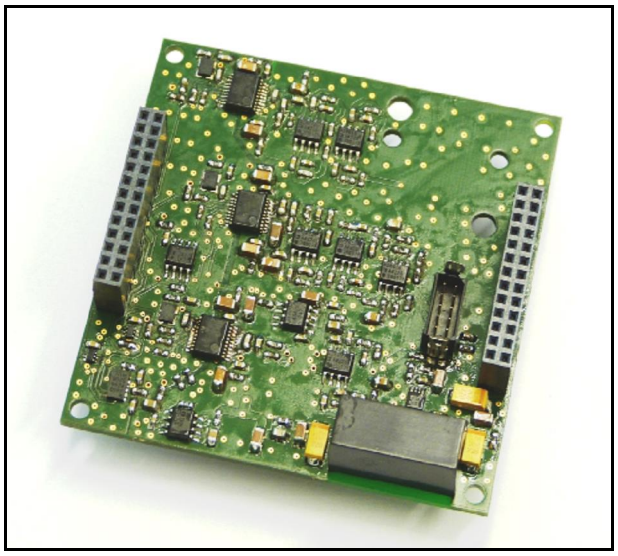

Figure 3. Subsystem with the accelerometer

To reduce the ripple on the supply planes, and to keep them as short as possible, to avoid decoupling from other subsystems, the whole supply voltages are generated onboard. By choosing low dropout regulators (LDO) with a high ripple rejection, implementing pi-filters which should have at least a corner frequency of a tenth of the working frequency of the DCDC-converter, and the use of blocking capacitors to stabilize voltages, the noise on the supply planes can be reduced.

4.2. Signal conditioning

The output signal of the accelerometer is a differential signal with a sensitivity of 800 mV/g, which leads to a full scale output of 4 V, while the input range of the ADC is up to 5 V. To increase the sensitivity of the system, a signal conditioning is necessary.

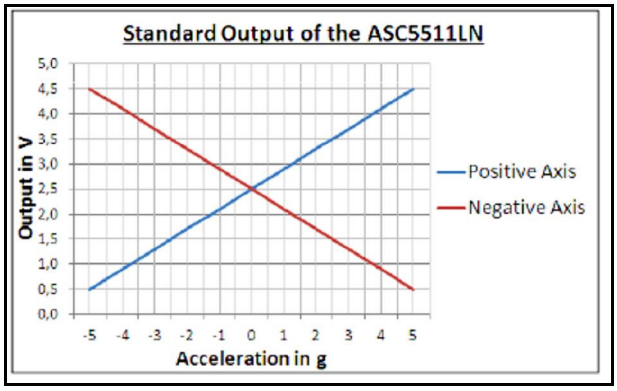

Figure 4. Standard output of the 5511LN

As shown in Figure 4. the standard output of the accelerometer reaches from 0.5 V to 4.5 V, while the output for an acceleration of 0g is 2.5 V. Due to that, it is not possible, just to amplify the output signal to increase the full scale output of the sensor. Figure 5 shows the schematic of the signal conditioning of the output signal as it is implemented.

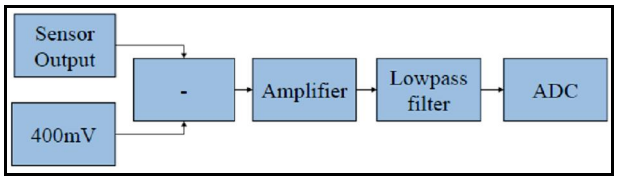

Figure 5. Schematic of the signal conditioning

Instead of just amplifying the output signal, it is necessary, to subtract 400 mV from the output first, and to amplify it afterwards by a factor of 1.2. The usage of 500 mV that are subtracted from the signal is not possible, due to a potential offset from the sensor of about ±100 mV. A low noise voltage reference is used, to generate the 400 mV, due to low temperature dependence. Through that conditioning, the output range of the sensor could be increased by 9.3%, which is even shown in Figure 6.
Additionally, an active fourth order low pass filter is implemented, to reduce the sensor's noise. Actually, the filter is a Bessel-type filter with a corner frequency of 100 Hz. Depending on the requirements and the selected sensor, the type of the filter and its corner frequency can be modified easily by changing the combination of the

resistors and capacitors, which makes the system even more flexible.
To realize the analogue circuit of the subtractor, the amplifier, and even of the low pass filter, operational amplifier with a noise level of 8 nV/√Hz are used which have rail-to-rail capability and are stable while operating with unity-gain.

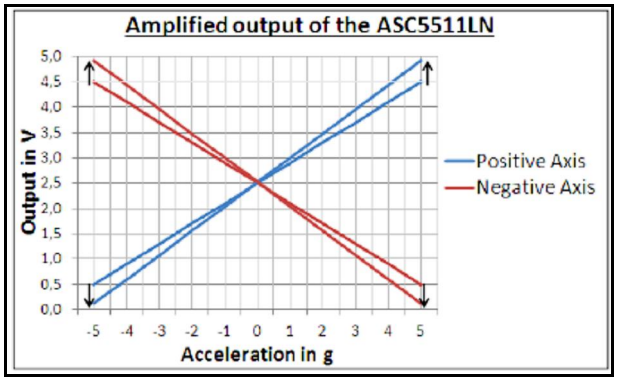

Figure 6. Amplified output of the 5511LN after the signal conditioning

Unfortunately, due to the finalisation of the new measurement system short prior the campaign, a complete characterization of the system can not be presented in this paper.

5. CONCLUSION

A new high precision drag deceleration measurement system, which measures atmospheric parameters "in situ" is necessary, to replace or complement the existing systems, that are quite expensive or do not reach the resolution, that is needed. This paper describes a system, based on free falling spheres, which allows to measure horizontal wind fields and the drag deceleration, to estimate the neutral gas density, and the atmosphere's temperature. Due to the partitioning of the system into subcomponents, it is very flexible and can be adapted to different requirements. Preliminary tests showed the functionality of the system, while first measurement data under real operating conditions will be gained during the WADIS-campaign at the end of June 2013 using sounding rockets and weather balloons. As a next step in the development, the system will be scaled down, to use it onboard of smaller sounding rockets.

6. REFERENCES

1. Qiang Li, *Dependence of drag acceleration on drag coefficient and vertical velocity*, 2012
2. Tietze et. al., *Halbleiterschaltungstechnik*, Springer, 2010
3. G. A. Faucher, et al., *Upper-atmosphere density obtained from measurements of drag on a falling sphere*, Journal of Geophysical Research, 1963
4. Analog Devices, *High Speed System Application*, 2006
5. John Ardizzioni et.al., *Analog Dialogue*, 2009

ACKNOWLEDGMENTS

This project is funded by Wirtschaftsministerium Mecklenburg-Vorpommern in Germany.

NAVIGATION AND COLD GAS CONTROL SYSTEMS FLOWN ON SHEFEX II

Josef Ettl[(1)], John Turner[(2)]
[(1)] DLR, RB-MR, Oberpfaffenhofen, Germany, josef.ettl@dlr.de
[(2)] TwIG, contracted by DLR Oberpfaffenhofen, Germany, john.turner@dlr.de

1. INTRODUCTION

The SHEFEX II rocket was launched successfully from Andenes in Norway on June 22nd , 2012 at 19:18 UTC. The rocket VS 40 consisted of the two Brazilian rocket stages, so called S-40 and S-44.
The purpose of the SHarp Edge Flight EXperiment (SHEFEX) was to investigate the aerodynamic behaviour and thermal problems of an unconventional shape for re-entry vehicles comprising multi-facetted surfaces with sharp edges. The main object of this experiment is the correlation of numerical analysis with real flight data in terms of the aerodynamic effects and structural concept for the thermal protection system. During the experiment phase between 100 km and 20 km altitude on the down leg a maximum speed of about Mach 10 was reached. There were two independent cold gas systems on-board the vehicle, which were used to perform precession manoeuvres, three axes, roll rate and rate damping control. Based on navigation data, different control sequences were performed on-board. This article describes first the different cold gas control systems and the navigation system on board consisting of an IMU (rate gyroscopes and accelerometer) and a GPS system. Furthermore, the results of the control sequences will be shown and evaluated.
During the post processing it appeared that the navigation system had experienced drifts which can be corrected by mathematical means. Further investigation is being undertaken to evaluate the causes of the drifts.

Proc. '21st ESA Symposium European Rocket & Balloon Programmes and Related Research', 9–13 June 2013, Thun, Switzerland (ESA SP-721, October 2013)

2. GENERAL FLIGHT INFORMATION

The Shefex II rocket was launched from the Norwegian rocket centre in Andenes. The coordinates of the launcher are 69.294 degrees north, 16.01884 degrees east and 46 m altitude. As there is a heavy shipping traffic between the Norwegian coastlines and the islands of Svalbard, especially during the midsummer period, the impact of the first stage and second stage were chosen far away from these routes. Before the second stage could be ignited a precession manoeuvre had to be performed in order to re-orientate the second stage to have the impact and therefore the experiment phase close to the island of Svalbard. A telemetry station on this island was contracted to receive, store and distribute the telemetry data in real time, especially during the experiment phase which was to be between an altitude of 100 km down to 20 km. During this period a Mach number of 9 to 10 was reached.

The rocket had 4 canted fins at the aft end of the first stage (S40) which produced a roll spin for stabilisation in order to reduce the dispersion of its impact. As the final spin rate was very close to the nominal spin rate of 1.5 Hz the roll rate control was not used. A calculation on ground had been initiated to define the attitude angle for the re-orientation of the second stage (S44) and payload after the separation of the first stage. On the bases of position and speed vector data, an ideal attitude was calculated which was telecommanded immediately to the payload. A precession manoeuvre was started after the reception of this command and realigned the longitudinal axis. After the ignition and burn out of the second stage, the spin was reduced to close to 0 deg/sec by a yo-yo system. Shortly after, a three axes control system was activated to move the on-board star camera away from the sun. The task of the star camera was to calculate a precise attitude on the base of known star positions. To avoid an interference with the sun, the star camera was moved into the shadow of the payload. Shortly before the payload entered the experiment phase, the angle of attack was reduced by aligning the payload vector with the velocity vector.

The actual impact was very close to the nominal impact although the trajectory of the first stage has shown a big divergence to the nominal one. At a down range of more than 800 km the distance between the nominal and actual impact was only 8 km.

3. FLIGHT DYNAMICS

The rocket reached an apogee of 178 km (GPS based) and a down range of 802 km. The maximum speed achieved was more than 2.8 km/sec. The experiment phase took about 60 sec. During this time, highly valuable data could be received which will help us to understand the aero- and thermodynamic attitudes in supersonic ranges. Furthermore the thermal protection system (flat tiles) could be tested and verified.

It is apparent that there is a small discrepancy between measured GPS and IMU (DMARS) data. Further investigation has to be undertaken in order to determine the causes of the drifts.

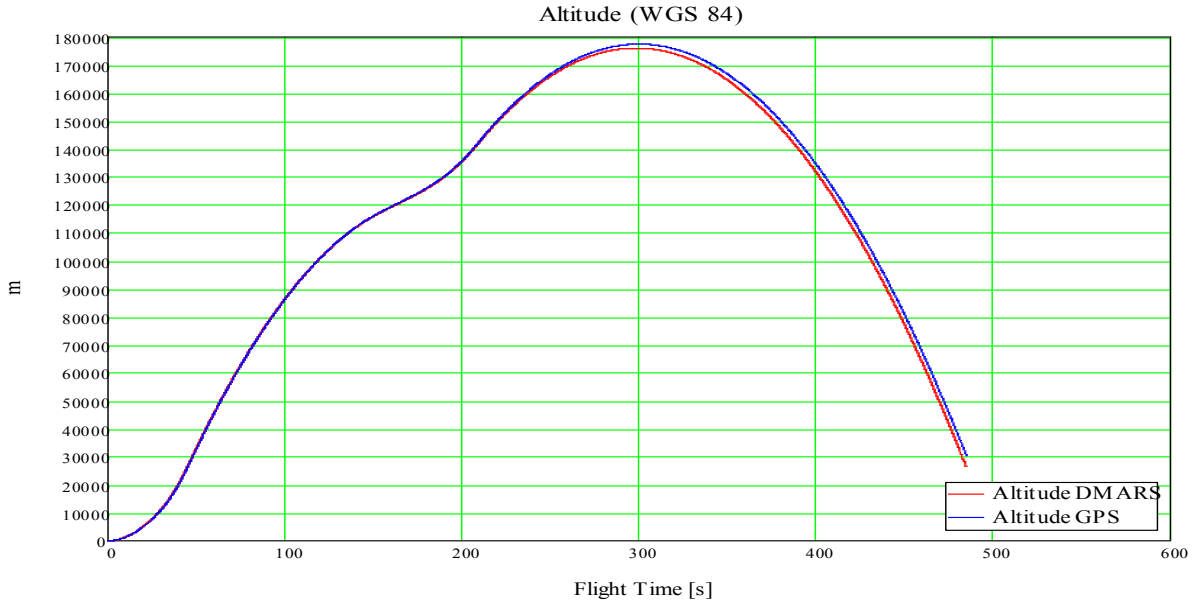

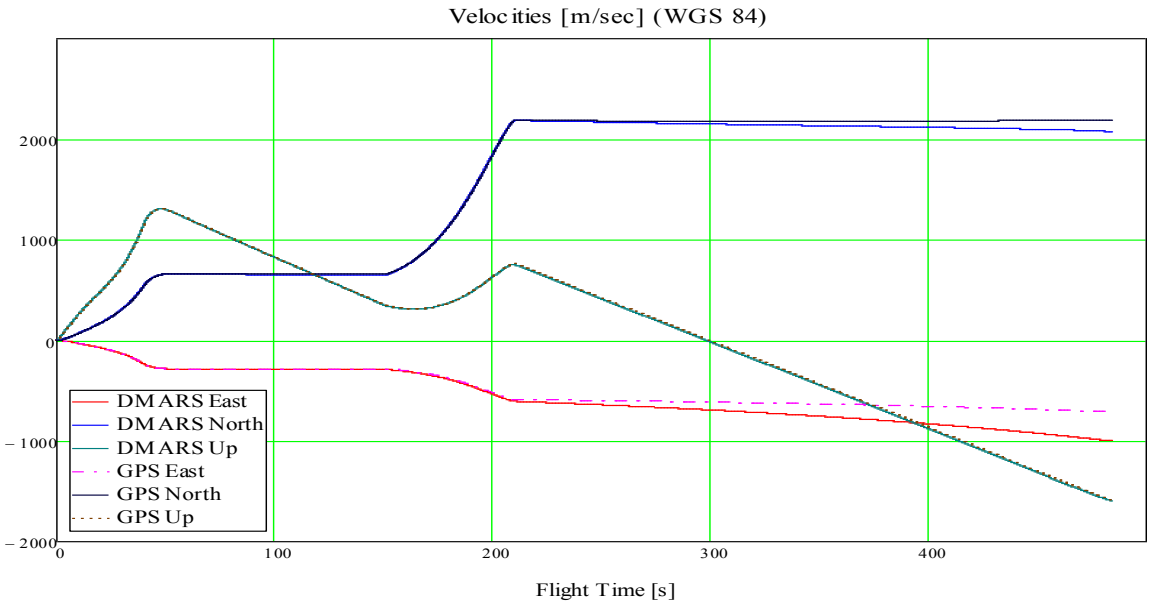

4. Navigation System

Because of the necessary attitude and precession control systems onboard there was a need to implement navigation systems. Mobile Rocket Base, a division of DLR (German Aerospace Center), has chosen an IMU (DMARS) and a GPS receiver as instrumentation means for attitude and position determination. The output of these systems were not only used for control purposes but also for the flight safety facility on ground to monitor the position, speed vector and the attitude of the second stage in order to terminate the flight in case of a dispersion from the nominal flight corridor. Radar data, generated on ground, was also used for the determination of the flight behavior.

There were 3 independent Navigation Systems onboard:

- DMARS (IMU)
- Hybrid Navigation System consisting of an IMU (INMAR) and GPS
- GPS

The first two will be described in more detail.

4.1 Inertial Measurement Unit

The DMARS platform, fabricated by Inertial Science (CA), was chosen as IMU. The DMARS (Digital Miniature Attitude Reference System) is a roll gimbled inertial navigation platform which can operate at spin-rates up to 22 rps. This platform is equipped with 3 accelerometers and a pair of 2 axes dynamically tuned rate gyros. They measure rates and the accelerations in all axes and calculate the attitude, speeds and position in the WGS 84 coordinate system with a sample rate of 100 Hz. Furthermore, it has the capability to perform gyro compassing. The following images show the components of the DMARS system.

The navigation reference system for the IMU (DMARS) is:

- WGS 84
- Local System referenced to the footprint on ground
- Pitch axis points to true north direction
- Yaw axis points to true west direction
- Roll axis points up as a normal to the ellipsoid

DMARS-R-M has the following performance:

Non-g sensitive bias	0.3 deg/hr
G- sensitive bias	0.2 deg/hr/g
Gyro scalefactor	300 ppm
G^2 sensitivity	0.3 deg/hr/g^2
Accelerometer bias	0.3 mg
Accelerometer scalefactor	500 ppm
Accelerometer scalefactor nonlinearity	7mg/g^2

4.2 The GPS Receiver

The GPS receiver has 12 channels of signal reception. It delivers position and speed vector measurements with a sample rate of 5 Hz. The measurement accuracy of the longitude and latitude position is in the range of ±10 m, while the accuracy in the vertical axis is in the range of ±50 m. The RF GPS signals were received by a wrap around antenna. Position and velocity information are calculated in the WGS 84 reference system.

5. Cold Gas Control Systems

Four different cold gas control systems were implemented on Shefex II. The first two will be described more comprehensively.

- Precession control
- Three axes attitude control
- Rate damping
- Roll rate control

The last control system was not used as the desired spin rate of 1.5 Hz was reached by means of the fins. The rate damping control system operated during the entrance into the experiment phase in order to avoid an oscillation of the payload about the flight vector. This function was switched off at an altitude of about 50 km at the descent phase. At the following lower altitudes the canard system took over the control of the payload attitude and rates.

The following figure shows a typical cold gas control system. The number of working pressure levels and the amount of valves and nozzles depends on the kind of control system. Whereas only three nozzles and valves and only one working pressure level had been used for the precession manoeuvre, 8 nozzles, 8 valves and two levels of working pressure were incorporated for the 3 axes control system.

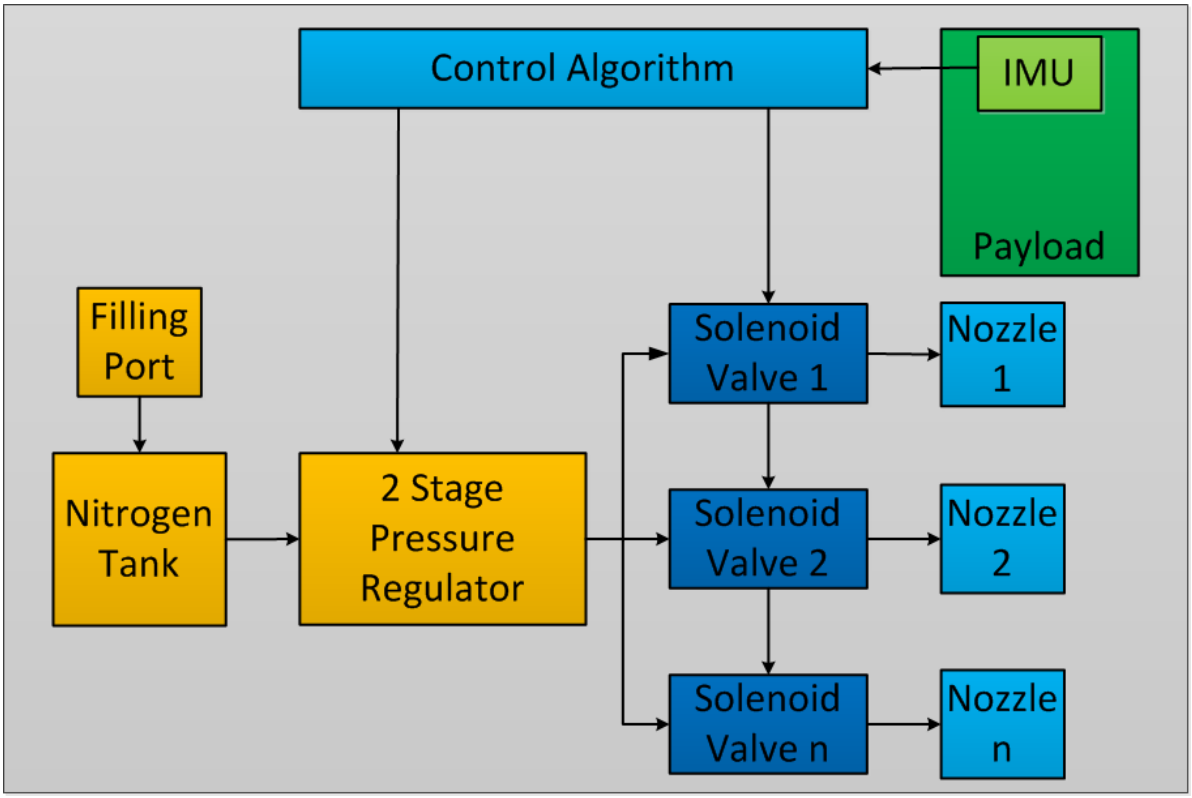

5.1 Precession control system

There are two principle ways to perform a precession manoeuvre. The first way, which is often described in the literature, proposes a movement over a half cycle of the space cone.
The impulse for movement has always to occur perpendicularly to the desired movement.

The second way of performing a precession manoeuvres is to move the longitudinal axis over very small segments of the space cone and to move the space cone towards the target. This method was more promising than the first method as a higher angular rate can be achieved.

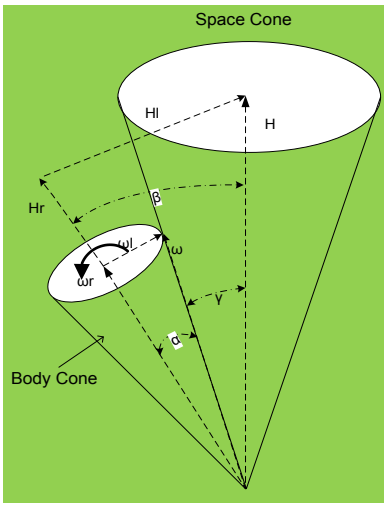

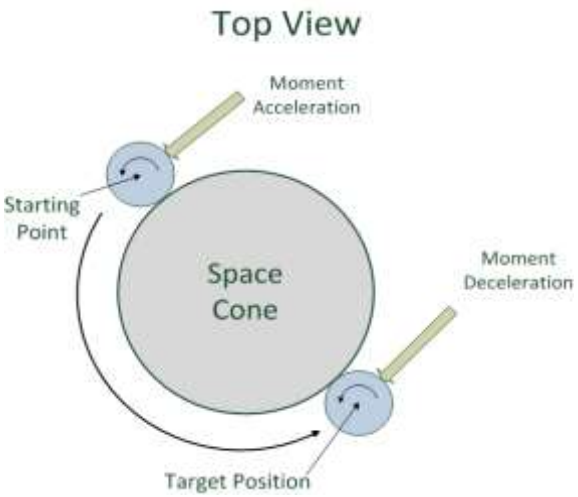

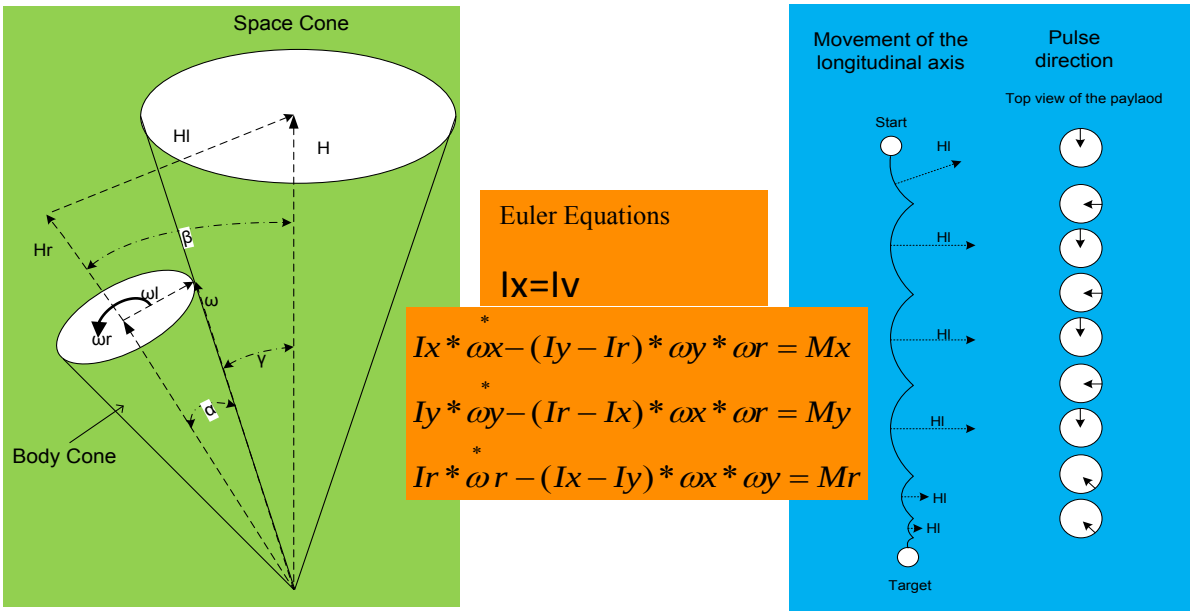

The figures above demonstrate the movement of the longitudinal axis towards the target. To perform this movement, only 3 different kinds of pulses are used.

a) Acceleration towards the target position
b) Correction pulse to keep the movement in one plane, perpendicular to the target direction
c) Braking pulse to reduce the angular rate and stop at the target position, against the moving direction

While the movement to the target position is accelerated, the sizes of the body and space cone increase. The limitation of the space cone depends on the moment which can be introduced per cycle and the moments of inertia of the roll and not of the lateral axes.

In our real case a maximum angular speed of more than 3 deg/s could have been established, but to keep the control system stable with a particular margin, a maximum angular rate of 2 deg/s was chosen. Violating the limitations, which are shown for a system with one or three nozzles at the circumference, means that the movement performed in a plane would change over to a movement over the space cone, and the control system becomes instable. The limitation also strongly depends on the spin frequency.

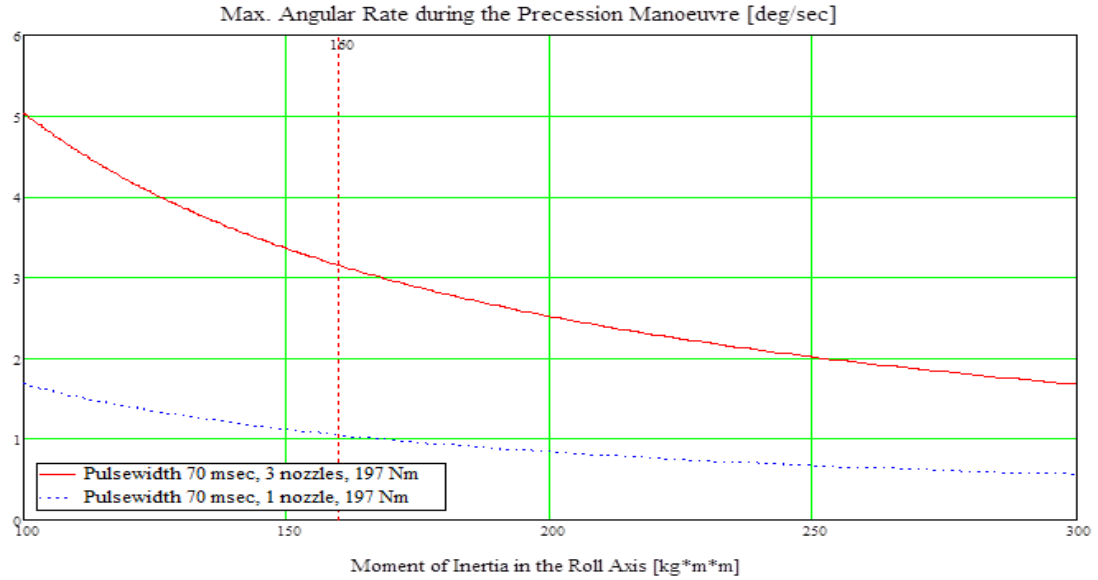

The following graphs illustrate the Pitch and Yaw Euler angles during precession manoeuvres between T+60.9s and T+184.6s. The first precession manoeuvre started at T+60.9 s and was finished at T+100 s.

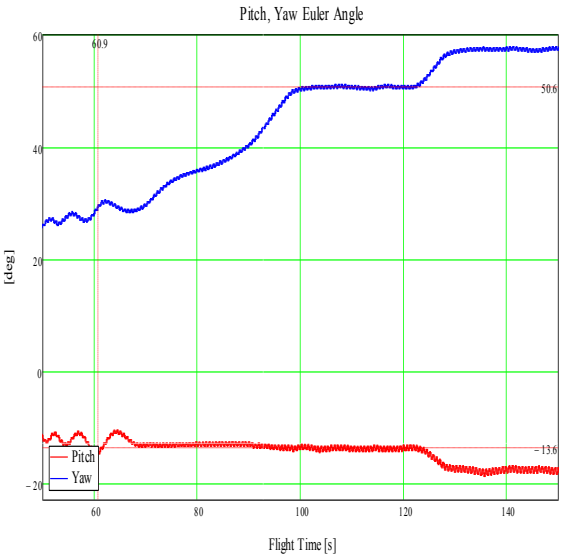

During the spinning phase, a nutation of about ± 0.38 deg occurred. This nutation can be explained by inherent imbalances and axes misalignments between the longitudinal axis of the DMARS and the vehicle.

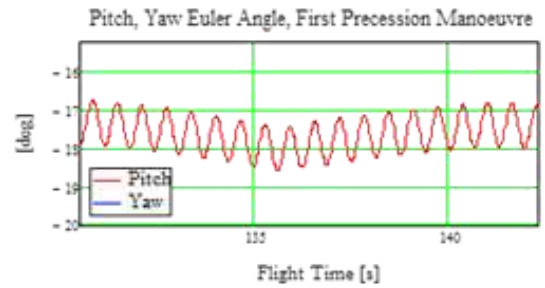

The second precession manoeuvre occurred between T+120s and 184.6s, and also controlled the longitudinal axes while the second stage was burning. At T+150s the second stage was ignited (see following graph).

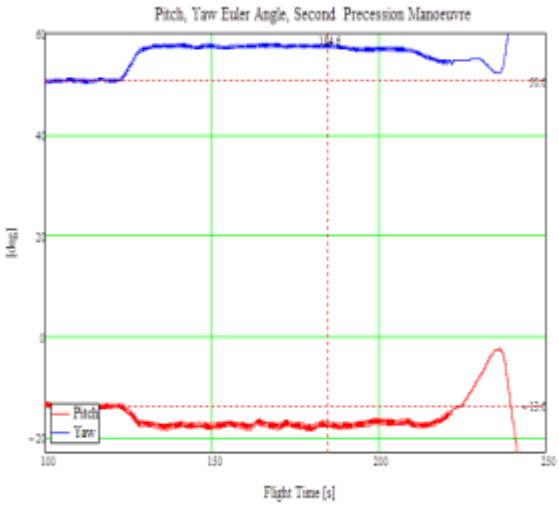

The precession control was left on during the beginning of the burn phase of the second stage. At T+184s the control was switched off. It is obvious that the precession control brought back the longitudinal axis into the desired position several times during the burn phase (see next graph).

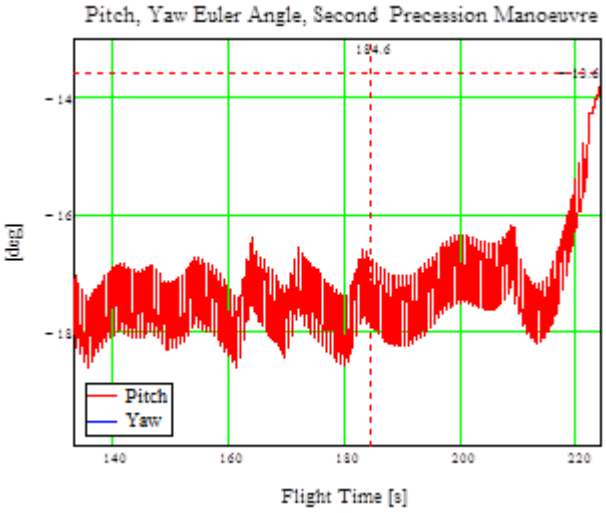

After the end of the precession control a slight drift is visible. At T+224s the YoYo system was activated, and the vehicle despun to a residual roll rate of about 10 deg/s.

The following graphs illustrate the Pitch and Yaw Euler angles during precession manoeuvres between T+60.9s and T+184.6s. The first precession manoeuvre started at T+60.9 s and was finished at T+100 s.

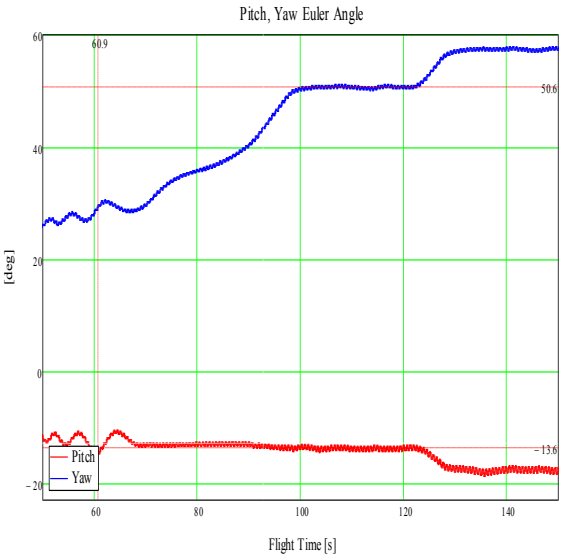

During the spinning phase, a nutation of about ± 0.38 deg occurred. This nutation can be explained by inherent imbalances and axes misalignments between the longitudinal axis of the DMARS and the vehicle.

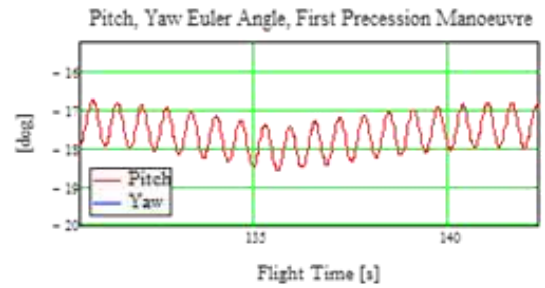

The second precession manoeuvre occurred between T+120s and 184.6s, and also controlled the longitudinal axes while the second stage was burning. At T+150s the second stage was ignited (see following graph).

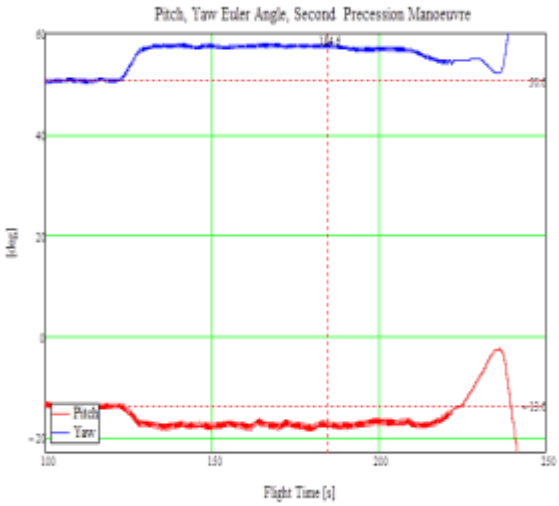

The precession control was left on during the beginning of the burn phase of the second stage. At T+184s the control was switched off. It is obvious that the precession control brought back the longitudinal axis into the desired position several times during the burn phase (see next graph).

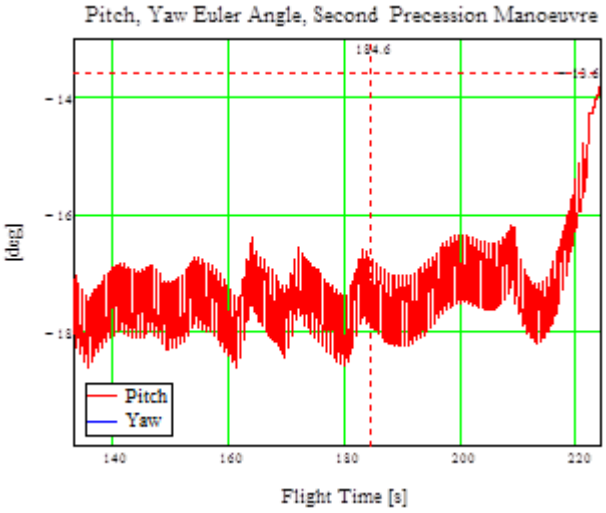

After the end of the precession control a slight drift is visible. At T+224s the YoYo system was activated, and the vehicle despun to a residual roll rate of about 10 deg/s.

5.2 Three axes attitude control system

The three axes attitude control system performed two manoeuvres after the de-spin of the payload.
First, it rotated the payload in order to bring the star camera into the shadow of the payload avoiding an interference induced by the sun light. Further it aligned the payload vector to the velocity vector, prior to the beginning of the experiment phase.
The control system consisted of two nested control loops, while the inner one controlled the speed and the outer one was responsible for the attitude. The values of the parameter K1 and K2 were chosen in order to avoid an oscillation during the approach to the desired attitude.

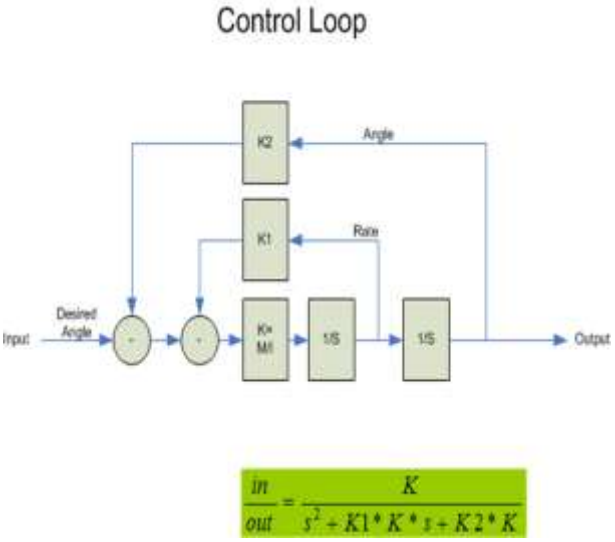

$$\frac{in}{out} = \frac{K}{s^2 + K1 * K * s + K2 * K}$$

The following graph shows the location of the three axes attitude control system.

Three axes attitude control

The following graph illustrates the first three axes control manoeuvre after the de-spin and payload separation.

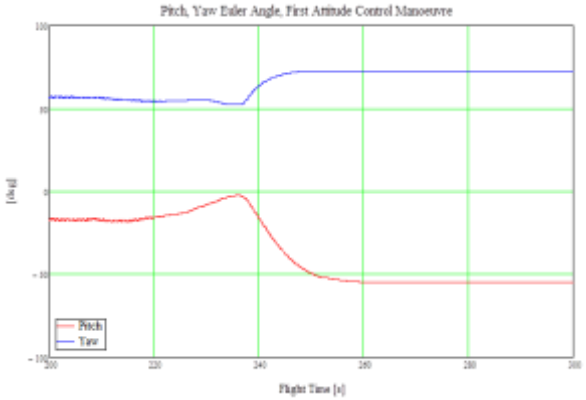

As mentioned before, this manoeuvre was introduced to bring the star camera in an angular offset to the sun of at least 90 degrees. After reaching this aim, the re-entry manoeuvre was initiated. The aim of this manoeuvre was to align the payload vector to the velocity vector.

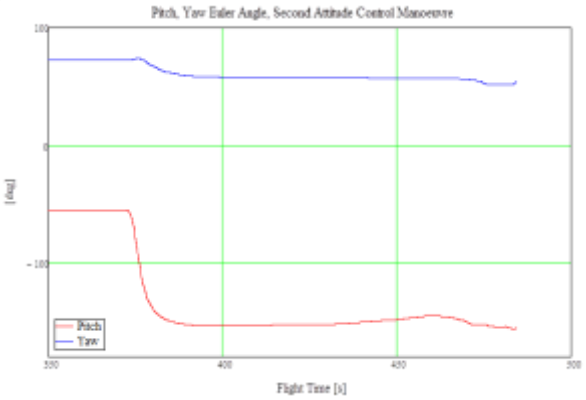

After this alignment, the rate damping mode was activated in order to avoid an oscillation about the lateral axes. This control mode was switched off at an altitude of 50 km prior the canard control system taking over the attitude control.

6. CONCLUSION

All the control loops performed well and have shown a high stability and accuracy. The navigation system, consisting of the DMARS and the DLR GPS system delivered highly reliable data during the flight. All cold gas control systems can be used for further projects, like VLM-1/SHEFEX III. The increase of the drifts in the Euler angles generated by the DMARS, after the activation of the yo-yo system, will be subject to further investigations.

7. References

SHEFEX II System Specifications, by John Turner, 16th March 2010

Precession Manoeuvre, by Josef Ettl, 3rd March 2009

SHEFEX II Post-Flight Report, Flight Safety, by Frank Scheuerpflug, 6th July 2012

MEASUREMENTS OF THE D-REGION PLASMA USING ACTIVE FALLING PLASMA PROBES

C. Baumann[1], H. Asmus[2], J. Schumacher[3], T. Staszak[4], N. Karow[4], A. Fencik[4], P. Schünemann[4], and B. Strelnikov[2]

[1]*Deutsches Zentrum für Luft- und Raumfahrt, Institut für Physk der Atmosphäre, Oberpfaffenhofen, Germany*
[2]*Leibniz-Institute for Atmospheric Physics, University of Rostock, Germany*
[3]*Chair of Technical Electronics and Sensor Techniques at the University of Rostock, Germany*
[4]*University of Rostock, Faculty of Mechanical Engineering and Marine Technology, Germany*

ABSTRACT

MEDUSA is the acronym for MEasurements of the D-region plasma USing Active falling plasma probes. The scientific scope of MEDUSA is measuring small scale fluctuations in the plasma density of the D-region. The measurements enable investigations on the physics of the atmospheric phenomenon of polar mesospheric winter echoes (PMWE), which are radar echoes in the range of 55-80 km. To observe the turbulence in that height region, we measure positive ion density and neutral density with our experiment. The MEDUSA experiment, as a part of the REXUS/BEXUS project, develops a new in-situ technique probing the lower ionosphere plasma by two free falling units (FFU). These identical FFUs contain a sensitive structure that is exposed to the atmosphere. This structure consists of a grid, which surrounds an ion collector that is connected to a electrometer. The collector has a negative potential, the measured current at the electrometer is proportional to the ion density measurements. The positively charged grid shields the collector from ambient electrons. Acceleration sensors inside each payload can be used to derive neutral gas density profiles from the FFU's equation of motion. These neutral density profiles can be used to investigate possible correlations with the plasma densities. From this density profile, assuming hydrostatic equilibrium one can integrate a temperature profile. A GPS receiver on each FFU provides in-situ horizontal information of all three physical quantities (ion, neutral density and temperature) that has not been available in this scientific field before. During the REXUS 15/16 campaign a sounding rocket will bring the two probes up to approximately 90 km, which are then ejected from the main payload. During descend, the FFU will measure the ion density. The data will be stored on the FFU directly and will also be sent to a ground station in case a recovery of the probe is not possible. The rocket launch is supported by ground based instruments and model studies at winter polar latitudes.

Key words: FFU; Rocket Payload; Mesosphere; Turbulence; D-Region; Ion Density.

1. INTRODUCTION

The Earth atmosphere is mostly influenced by solar radiation. It drives dynamical, chemical micro and macro physical processes like turbulence and ionization in the whole atmosphere. In the field of atmospheric research the polar summer mesopause region holds a prominant position since it is the coldest place in the Earth's atmosphere. Here, the phenomena noctilucent clouds (NLC) and polar mesospheric summer echoes (PMSE) are observed by ground based [e.g. 3] and in-situ measurements [e.g. 6]. The ionospheric state in this altitude region plays an important role for the PMSE phenomena and other effects which are associated with enormous interest in nowadays geophysics. Besides the resonably known NLC and PMSE the small-scale structure of the lower D-region plasma at the high latitude ionosphere is connected to the phenomena of polar mesosphere winter echoes (PMWE). PMWE are radar echoes which occur in the altitude range from 55-85 km during the polar winter. The formation process is not fully understood, but theoretical approaches explain the formation by either turbulent or non-turbulent conditions. High electron densities are likely to be essential for the echo formation process. These conditions are often fulfilled during high solar activity causing enhanced ionization in the atmosphere [e.g. 2, and references therein]. Since at least ions are connected to neutral gas dynamics [7], it is believed that breaking gravity waves and the resulting shear winds and turbulence play an important role in the formation of local high plasma densities [4].

MEDUSA (Measurements of the D-region plasma using active falling plasma probes) is an experiment which is going to be flown on the REXUS 15 rocket in March 2014.

The aim of MEDUSA is to get a better understanding of turbulent processes in the mesosphere. In case of PMWE conditions during the rocket flight we can actually gain information about the role of turbulence in PMWE physics. Ground based radar measurements will give reasonable information if these conditions are ful-

Proc. '21st ESA Symposium European Rocket & Balloon Programmes and Related Research', 9–13 June 2013, Thun, Switzerland (ESA SP-721, October 2013)

filled. The MEDUSA experiment consists of two autarc free falling units (FFU). By applying two probes it is also possible to gain information about the horizontal dimensions of turbulence and PMWE.

This paper covers the description of the MEDUSA experiment design and its components. In the following sections we present the concept of the experiment, the used sensors, the mechanical design and the electronics.

2. CONCEPT OF THE EXPERIMENT

The concept of the MEDUSA experiment is described in this section. See Fig. 1 for the conceptional overview.

The MEDUSA experiment consist of two autarc free falling units (FFU) mounted inside a REXUS module. These FFUs will be transported inside of the rocket payload up to an altitude of 80 to 90 km. Here the ejection mechanism will be activated and both FFU will leave the REXUS rocket payload. Just after ejections of the FFUs

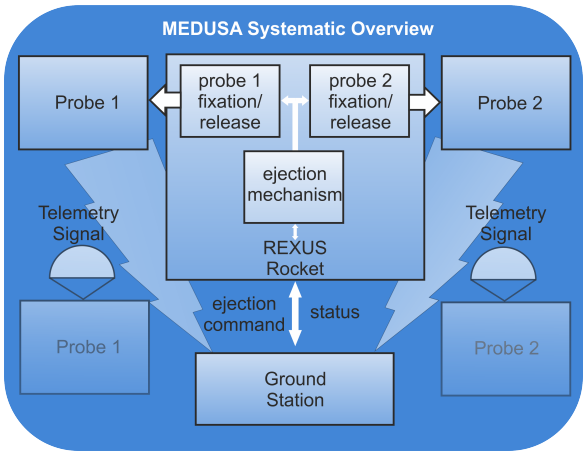

Figure 1. Concept drawing of the MEDUSA experiment

they start their measurements. Both FFUs carry identical sensors, in order to receive receive horizontally resolved measurements. Due to the fact that we can only measure during the downleg of the rocket flight, it is crucial to obtain all data from both FFUs. Since a recovery of the FFU after landing is not 100 percent secure, we use a telemetry system inside the FFU to send our data to the ground. For reasons of redundancy the data is also saved onboard.

Below 30 km the FFU will leave the region of scientific interest, since this altitude region below is also accessible by balloon systems. The FFU recovery system will release a parachute at an altitude of approximately 5 km. To reduce possible drift of the FFU due to the atmospheric wind, we will initiate the recovery system at this low altitude. The time for data transmission in this case is limited, since we expect to loose the telemetry signal at an altitude of approximately one kilometer.

In Tab. 1 a timeline of our experiment during the rocket flight is shown. The main reason to eject our FFU before the apogee is that the tumbling of the rocket is minimal in this timeframe. During ejection we need to have a very upright rocket orientation, since our sensors, situated in the front of our FFU, has to point downwards to perform reliable measurements.

Table 1. Timeline for countdown and flight

Event	**Time** (T±t)
Monitoring	-600s
Lift-off	+0.00s
Burn-out	+26.00s
Yo-Yo despin	+75.00s
Hatches open	+76.00s
Experiment Ejection	+76.50s
Start measurement	+77.00s
Activate wireless modem	+79.00s
Motor Separation	+80.00s
Apogee	+140.00s
Parachute release	+270.00s
Switch Off System	∼+730.00s
Landing	∼+800.00s

After the successful flight, we aim at a successful recovery of both FFU by a helicopter team. Since we can hand over the latest received GPS data, we expect a good chance of finding the landed FFU.

3. SENSORS

Two main sensors are used inside of each FFU. Firstly we use an electrostatic probe for the measurement of the ion density in the D-region. Secondly, we use a three axis accelerometer in each FFU to measure the atmospheric drag.

The electrostatic probe consists of a spherical grid around a solid electrode. The grid is biased on payload potential while the electrode is biased negatively, thus the grid shields the electrode from ambient electrons and negative ions. At the same time positive ions are attracted by the electrode. The current of positive ions reaching the electrode is proportional to the positive ion density [e.g. 7]. This current is measured by a highly sensitive electrometer inside the FFU.

The used accelerometer applies a capacitive method to measure the atmospheric drag. By solving the equation of motion of the FFU one can derive the atmospheric neutral density ρ.

$$\rho = -2m\frac{(a_z + g)}{C_D \cdot A \cdot v \cdot V_z} \tag{1}$$

Here, m is the mass of one FFU, a_z is the acceleration in z direction, g is the gravitational acceleration, C_D is the

FFU´s drag coefficient, A is the effective FFU crosssection, v the is the FFU´s absolute velocity and V_z the FFU velocity in vertical direction only. Under the assumption of hydrostatic equilibrium one can also integrate the temperature profile along the flight path of both FFU.

4. MECHANICS

In this section we describe the mechanical design of the MEDUSA experiment. In Fig. 2 the assembly of the MEDUSA experiment is shown. Since both FFUs are

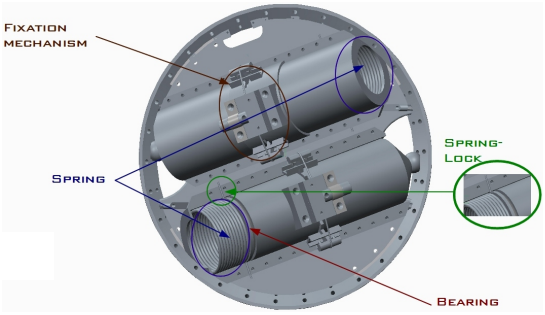

Figure 2. Experiment FFU mounted inside a rexus module

mounted inside a REXUS rocket module, an ejection mechanism is used to liberate the FFU from the rocket module. Each FFU has a cylindrical form with a diameter of 80 mm and a length of 220 mm. The FFU framework has bolts on the outside that fit into the channel of the riffled barrel that covers each FFU. For ejection we use a spring that pushes the FFU out of the module. While the spring acts, the bolts are guided along the channels of the riffled barrels. In that way the spring forces the FFU to gain translational and rotational speed at the same time. Since the spring cannot rotate, there is a bearing between the spring and FFU. The strength of the spring is designed that after ejection the FFU has a spinning frequency of 12 Hz and absolute speed of 1.8 m/s. The FFU are pointing downwards with an limb angle of 27°, because we want that the electrostatic probe to point downwards while the FFU falls to the ground. Pointing downwards reduces the turbulent influence on the positive ion density measurement.

Each FFU is fixed inside the rocket by three stamps (see Fig. 3). These stamps are locked by a wire around the complete FFU. At the point of ejection the wire is cut by a pyrocutter. Now a spring pushes the stamps out of the grooves in the FFU hull.

Since the rocket has to be sealed during takeoff, we have also designed a system that allows to open a hatch so that the FFU to leave the rocket module (see Fig. 4). The hatch opening system works as follows. There is a hatch on each side of the rocket module, one for each FFU. The hatches are locked during the start of the rocket, to avoid aerodynamical disturbances. The lock mechanism

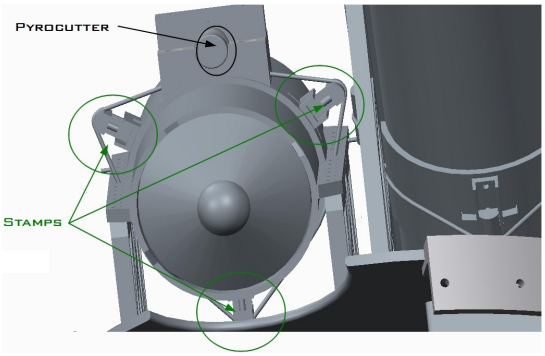

Figure 3. Fixation mechanism of the FFU inside of the rocket module

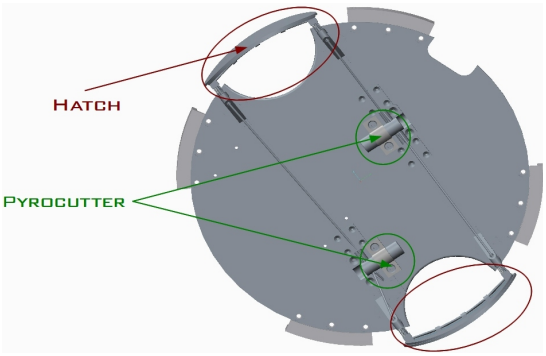

Figure 4. Ejection mechanism of the hatches, which cover the holes in the rocket module, the lock mechanism is realised by a wire locking the hatches until ejection of the FFU

is again realized by a wire that holds both hatches against the rocket module wall. This wire is cut by a pyrocutter just before the FFU are released. Then springs, which are mounted right behind the hatches, can push the hatches out of the rocket modules outer structure.

4.1. Finite element method analysis

During a rocket flight the experiments are exposed to accelerating forces that are in the order of 20 times the gravitational acceleration. This extreme force during the rocket's liftoff puts an immense stress on the FFU and the inner structure parts of our experiment. To test the stability of our experiment during a rocket flight we have applied an finite element method (FEM) analysis. FEM is a numerical technique that can be used to simulate the stress on a structure generated by a disruption, e.g. a rocket start. In Fig. 5 we show the results of a FEM analysis where the FFU is mounted on the rocket payload. The force that acts on the module and FFU has been set to 20 g, comparable to the force that act during an Improved Orion start. The derived quantity is the tension acting on the FFU and rocket module during the rocket start. The tension is colorcoded and given in units of MPa.

The tension on the wall mounted brackets holding the

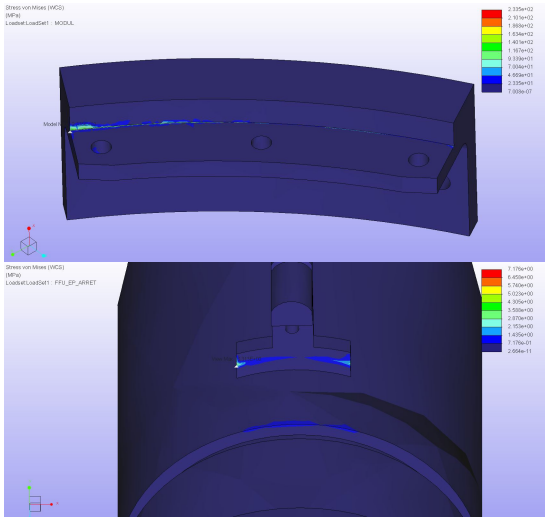

Figure 5. Finite elements method analysis of the rocket module and the FFU, applied acceleration force is 20 g, result is the tension of the structure in MPa

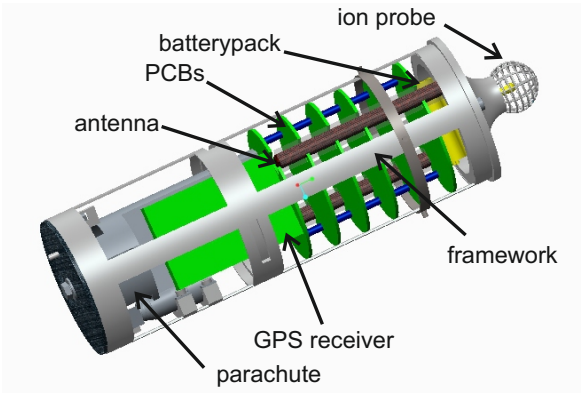

Figure 6. Inner structure of the FFU, batteries in the front, electronics on circuit boards and parachute in the rear of the FFU

experiments bulkhead is about one order of magnitude higher than the tension acting on the FFU. The tension on the brackets is apporximately 230 MPa which is a the limit what steel can withstand. Further investigations on more robust material is needed. On the contrary, the tension on the FFU stamps is only in the order of 10 MPa. This is due to the very light weight design of the FFU, resulting in a minimum of stress on the FFU structure.

5. ELECTRONICS

In this section we describe the electronical system that controls the MEDUSA experiment. At first there is a Onboard Communication Unit (OCU) mounted on the bulkhead of the rocket module. The OCU has the purpose to communicate with the REXUS service module and to check the status of the FFU. Another part of the OCU is a gyroscope which monitors the attitude of the rocket. We need the attitude of the rocket during the moment of ejection, since the knowledge about the fall direction of the FFU is crucial for the MEDUSA experiment.

Each FFU itself contains overall six sensors. The main sensors are the positive ion probe, the accelerometer and the GPS module. Onboard each FFU we have also an addtional gyroscope, temperature sensors and a pressure sensor. In Fig. 6 you can see the inner parts of the probe covered by the glas fiber. We use glas fiber as cover material since it is transparent to the electro-magnetic telemetry signal. This material is necessary since we want to send our data down to a groundstation by telemetry.

The ion density sensor is primarily a sensitive two channel current to voltage converter circuit. It amplifies currents from a couple of nano amps up to 50 micro amps. The measuring range covers the typical ion currents measured by electrostatic probes in the lower ionosphere. The two channels provide two different amplifications of the measured current. The output voltage will be converted by analog digital converter (ADC) and the digital signal will then be processed and send to the ground station by telemetry as well as stored onto a flash drive on board the FFU.

The accelerometer is assembled on a circuit board inside the FFU (green plates in Fig. 6). Details on the performance and the details of the control electronics of the sensor can be found in [5].

The GPS module will be used, to get the actual position of the probes, which is needed, to reconstruct the trajectory for the flight results. Additionally, the position will be used to track the satellite during its fall with the telemetry antenna of the ground station. This tracking achieves the best possible signal strength for the data communication. Caused by the CoCom formalities, most GPS-receiver are limited in speed, acceleration and altitude that can be measured. That is why a module must be chosen that can be unlocked by the manufacturer, to work in the desired altitude of 30 km to about 80 km and velocities of more than 500 m/s. The OEM615 by Novatel fulfils these requirements. It is a combined L1/L2 receiver with an update rate of up to 50 Hz. Due to its dimension, it has to be mounted vertically into the system. The module can stand accelerations of up to 40 g and vibrations up to 7.7 grms. Additionally it can be operated in a temperature range of -40°C to +85°C.

Temperature sensors will be used on different points within the system, e.g. near the batteries and the accelerometer. Monitoring the temperature is an important part of analyzing the housekeeping data. Using these sensors, e.g. the charging of the batteries can be interrupted if they get too warm. Additionally, by logging this value, the temperature dependance of the sensors can be corrected while analyzing their data. For that purpose the ”ADT7310” from ”Analog Devices” has been chosen. This sensor uses a SPI-Interface, which makes it easiy to be integrated into the MEDUSA system. Additionally it

guarantees an accuracy of $\pm 0.5^{\circ}$ and can interrupt the supervised part of the experiment if it exceeds a pre-defined temperature limit.

The pressure sensor will be used for the control of the parachute release. In cas of a failure of the GPS module, the measurement data of the pressure sensor will be used to open the parachute in a predefined altitude. An absolute pressure sensor will be chosen to measure the atmospheric pressure. Its data will be compared with a look-up-table that contains the air pressure in relation to the altitude and is stored in the microcontroller. "Freescale Semiconductors" offers a wide range of pressuresensors that could be used for that application. Their pressure sensors can be operated in a temperature range of -40°C to 85°C minimum and have a digital output. Their measurement range start from 200 hPa, which corresponds to approximately 10 km altitude.

6. CONCLUSION AND OUTLOOK

We present the MEDUSA experiment design for the REXUS 15/16 student sounding rocket campaign, which will be flown in March 2014. This experiment includes two autonomous FFU which will be ejected from the rocket payload at maximum altitude. These FFU will be able to measure ion and neutral density in the altitude range from 80 - 50 km. The experiment focusses on the turbulent processes in the mesosphere and D-region ionosphere. Within that scope, we want to improve the understanding of processes in the mesosphere, like PMWE, which need further investigation on dynamics and coupling between the plasma and the neutral state of the atmosphere.

Our experiment consists of a mechanism, that ejects the FFU from the rocket payload, a positive ion sensor, an acceloremter and a GPS module. By combining all three measured quantities, the positive ion density, neutral density and position information we can gain an insight into the nature of the processes of the mesosphere. To gain horizontal information about the turbulence is a major advance in this field.. Horizontal changes in the turbulent structure of neutral and charged ionosphere hasn't been analyzed in the studies of [7], [1] and others. We want to focus on these horizontal changes with our MEDUSA experiment.

ACKNOWLEDGMENTS

The authors acknowledge the opportunity given by the REXUS/BEXUS programme to fly the MEDUSA experiment on a rocket. We are also indebted to the financial support and help of the Leibniz Institute of Atmospheric Physics in Kühlungsborn, the Institute of Atmospheric Physics at the DLR in Oberpfaffenhofen and the electrical and mechanical engineering faculties of the University of Rostock.

REFERENCES

[1] TA Blix, EV Thrane, and Ø Andreassen. In situ measurements of the fine-scale structure and turbulence in the mesosphere and lower thermosphere by means of electrostatic positive ion probes. *Journal of Geophysical Research*, 95(D5):5533–5548, 1990.

[2] A. Brattli, T. A. Blix, O. Lie-Svendsen, U.-P. Hoppe, F.-J. Lübken, M. Rapp, W. Singer, R. Latteck, and M. Friedrich. Rocket measurements of positive ions during polar mesosphere winder echo conditions. *Atmos. Chem. Phys.*, 6:5515–5524, 2006.

[3] N Kaifler, G Baumgarten, J Fiedler, R Latteck, FJ Lübken, and M Rapp. Coincident measurements of PMSE and NLC above ALOMAR (69 N, 16 E) by radar and lidar from 1999–2008. *Atmos. Chem. Phys*, 11:1355–1366, 2011.

[4] F.-J Lübken, B. Strelnikov, M. Rapp, W. Singer, R. Latteck, A. Brattli, U.-P Hoppe, and M. Friedrich. The thermal and dynamical state of the atmosphere during polar mesosphere winter echoes. *Atmospheric Chemistry and Physics*, 6(1):13–24, 2006.

[5] J. Schumacher. High precision drag deceleration measurement system touse onboard active falling spheres. *Proc. '21th ESA Symposium on European Rocket and Balloon Programmes and Related Research'*, 2013.

[6] B. Smiley, M. Rapp, T.A. Blix, S. Robertson, M. Horanyi, R. Latteck, and J. Fiedler. Charge and size distribution of mesospheric aerosol particles measured inside NLC and PMSE during MIDAS MaCWAVE 2002. *Journal of Atmospheric and Solar-Terrestrial Physics*, 68:114 – 123, 2006.

[7] E. V. Thrane and B. Grandal. Observations of fine sclae structure in the mesosphere and lower thermosphere. *Journal of Atmospheric and Terrestrial Physics*, 43:179–189, 1981.

DEVELOPMENT OF THE AEROSPACE PARASHUTE SYSTEM (ASPS) OPERATING AT ALTITUDE RANGE OF 60-150 KM FOR SALVATION OF THE FIRST STAGES OF LAUNCH VEHICLES AND PROPULSION SYSTEMS

Chizhukhin V.[(1)], Mekhonochin Yu.[(1)], Zhjurov S.[(1)], Gvozdev Yu.[(2)], Yushkov V.[(2),], Lykov.A[(2),]

[(1)] *Joint Stock Company "Atmosphere" Pervomayskaya str., 3,Dolgoprudny 141700, Russia, atmvcps@yandex.ru*
[(2)] *Central Aerological Observatory " Pervomayskaya str., 3, Dolgoprudny 141700, Russia v_yushkov@mail.ru*

ABSTRACT

The purpose of the project – development of the technology for the salvation of the first steps and propulsion systems which are the most expensive part of the launch vehicle (LV). Life and reliability of control ensure their re-use in the absence of mechanical damage after use. Reuse LV stages can reduce the cost of launching rocket. This project suggests a new well-grounded concept of paracute application using high-temperature, heat-resistant silica and quartz textile materials (new in parachute building) already brought to a commercial level, which has led to the creation of a new class of aerospace parachuting systems.
The proposed concept implies that stabilization, deceleration, descending, and landing of a 3.5 -11 ton LV is performed with the same aerospace parachute system and the ASPS is initiated immediately after used rocket unit separation from booster rocket

INTRODUCTION

Despite the short time of its development, cosmic economy has made considerable progress in creating systems important in today's life. The types of manmade extraterrestrial objects already number a few hundreds, while the total number of such objects has reached several thousands. Early experiments in space communication, Earth's monitoring, space navigation, and other fields have paved the way to the deployment of multi-spacecraft systems, which, in turn, has made a revolution in these applications.

All spacecraft are carried into orbit by space cargo ships (SCSs). The energy required to launch space objects is such that the mass of spacecraft to be put into a low orbit is not more than 5.5% of booster rocket launching mass, and less than 1.5% for those carried into a geostationary orbit. This explains why the cost of launching payload is so high - from 3000 to 30,000 US dollars per kilogram.

Today, the SCS fleet mainly employs single-mission booster rockets (BRs). The criteria that determine the practicability of creating new SCSs are their economic efficiency and, recently observed, ecological safety. One of the appropriate engineering solutions, which is discussed in detail in this report, implies the recovery of the BR or its most valuable component – propulsion bay section (PBS) with fluid jet engine (FJE) - using a parachute system (PS), and their multiuse. Depending on FJE purpose and lifetime, its cost may reach 90% of BR cost. A BR can be recovered from its landing place by helicopter or other means. Then, its separate units and valves can be dismantled, checked for operability, and used in another BR .
Many schemes for engine recovery have been considered in the past. Parachute recovery of an engine module to the ocean suffers from high-impact loading and exposure to harsh ocean environments which require a complex system to fully seal off the engine. United Launch Alliance (USA) is investigating recovery of rocket engine modules. Using helicopter mid-air recovery as the engine module descends under a parafoil is a low-development-cost approach which brings back the booster engine with exposure to only benign environments.
The task of development ASPS working at heights from 60 to 150 km at hypersonic speeds requires a combination of theoretical and experimental work in the field of high temperature and dynamic loading of all elements ASPS and especially in the field of theoretical models of filling large areas of the canopy and the flow in the working (full of) state at high altitudes. Positive experience with parachute systems to save the payloads of Russian meteorological package (entering in the force of the parachute system at the height of 90 km), the modern high temperature textile materials for the parachute, gas-dynamic calculation methods for flow parachute at mesosphere conditions were the basis of the Project.

EXPERIENCE OF PARACHUTE APPLICATION FOR METEOROLOGICAL ROCKET SOUNDING

More than 10000 Russian 2-stages meteorological rocket M-100B flights (Fig. 1) were conducted in the Central Aerological Observatory for atmosphere sounding at altitudes of 30-100 km. Each payload was equipped with a parachute system of nylon materials. The surface of canopy was up to 60m^2. The primary purpose of a parachute - the stabilization and deceleration the payload with scientific instrument

Proc. '21st ESA Symposium European Rocket & Balloon Programmes and Related Research',
9–13 June 2013, Thun, Switzerland (ESA SP-721, October 2013)

weighting 80 kg.. The work phase of M-100B parachute system is shown in Fig.2

Fig.1. Russian meteorological rocket M-100B in flight

Work phase of parachute system is shown in Fig.2.The introduction of the parachute system into action at the height of 60 km at a speed of 1-2 M on the ascent lag of flight has demonstrated the reliability of this procedure.

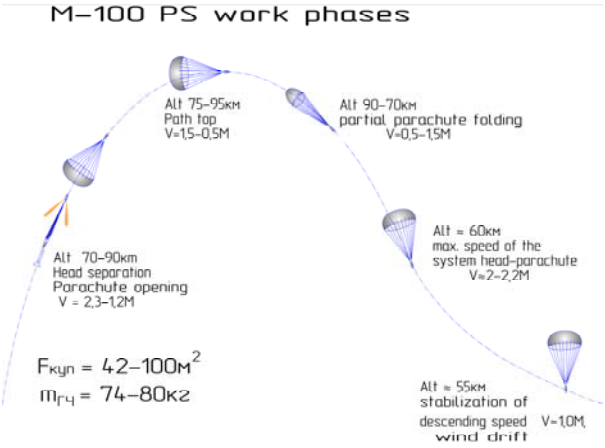

Fig. 2. Work phase of parachute system

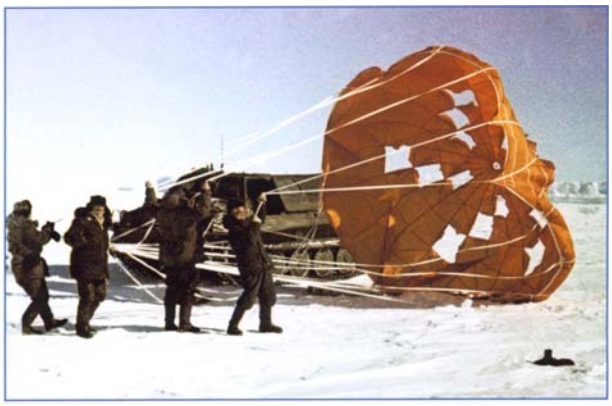

Fig. 3. Parachute recovery after payload landing from a height 90 km.

Due to the dynamic pressure the filling and opening of the parachute canopy occurs at 60-70 km on the ascent . Multiple recoveries of the landed payloads (Fig.3) showed a complete absence of thermal or mechanical damage. Parachutes after landing does not have any trace of the mechanical and thermal effects.

Parachute system input scheme with a proven reliable performance in thousands of meteorological rocket flights can be accepted as the basis for designing the separation container parachute and entry into force ASPS.

CONCEPT OF ASPS

Application of parachute system for meteorological rocket (PSMR) also shows that similar in topology canopy made of heat-resistant textile materials in principle can be operated in altitude range 60-100 km.

Of course, the specific weight load on the canopy ASPS (p = 3 - 9 kg/m2) slightly higher than that of PSMR (p = 0.5 - 2 kg/m2,) but it only gives the stability of the system during braking and lowering the propulsion system.

Due to the different operating conditions, the structural arrangement, technology of tailoring and parachute deployment the surface of basic canopy for ASPS of 500 m2 was selected. It allows to confidently predict its behavior on the base of PSMR experience at least up to a speed of 2.5 M. At the same topology of these systems of geometric similarity ratio is only 1: 2.24. ASPS input scheme is shown in Fig.4.

ASPS starts at altitudes above 60 km at hypersonic speeds ≈ 3 km / s at a trajectory angle θ ≈ 17-30 grad (Fig.4). Operational one and same parachutes which carry the stabilization and deceleration both rise to the top of the path, and the descent. The decrease rate of up to M <1, and the transition to the vertical motion is carried to an altitude of about 45 km. The landing rocket boosters occurs at a rate of 7 to 15 m / s or a helicopter pick-up is in the air.

The most important aspect of the ASPS development was that of the thermal regime of the parachute.

ESTIMATIONS OF THE TERMAL REGIME OF THE CANOPY

A numerical model of the motion rocket booster with a parachute was developed. The data flight the payload of the meteorological rocket with parachute was used for test calculations. Drag coefficient for parachute system and the structure of the flow near the canopy were determined.

For estimation the thermal regime the most heat-stressed region of the trajectory (immediately after

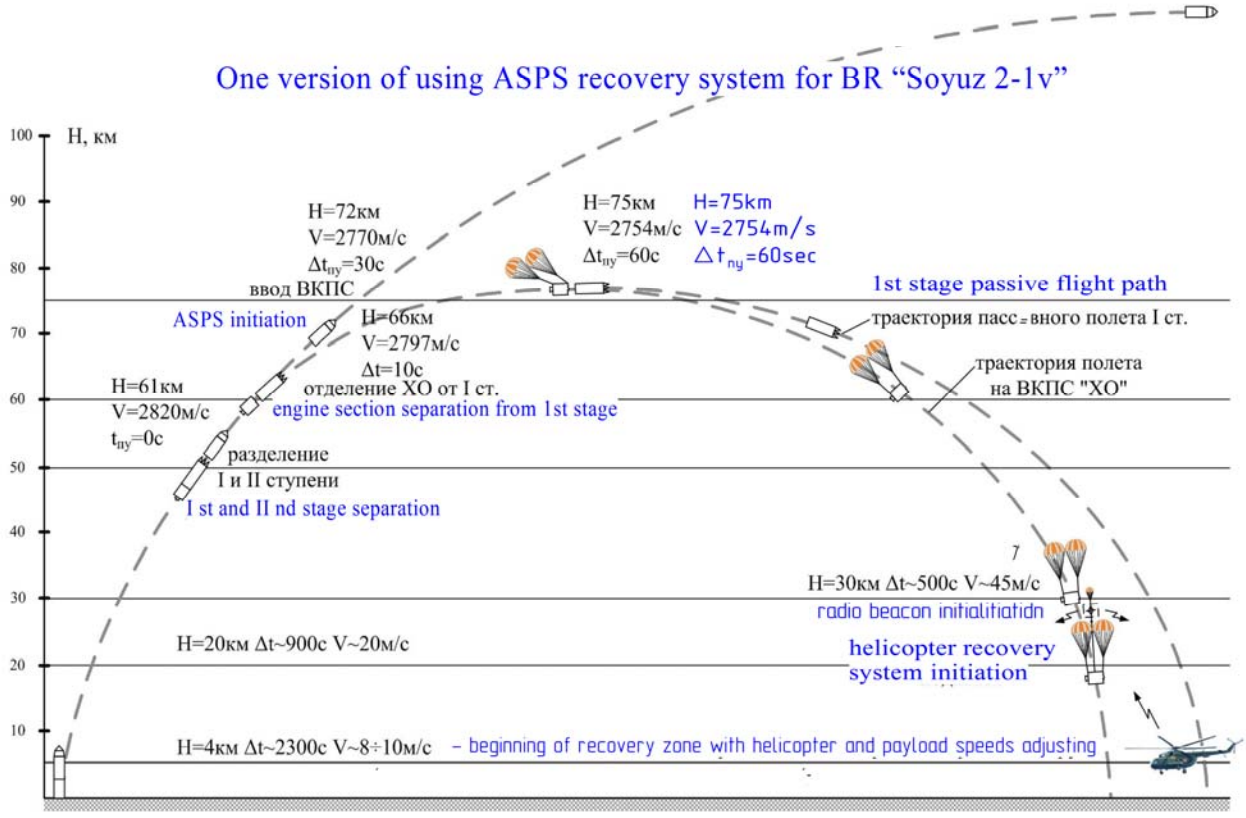

Fig.4. ASPS input scheme

opening the parachute) was considered with following parameters: altitude – 4360 m, M∞=5,62.

Continual flow regime was determined as a continual and laminar. The canopy is considered to be rigid and impenetrable.

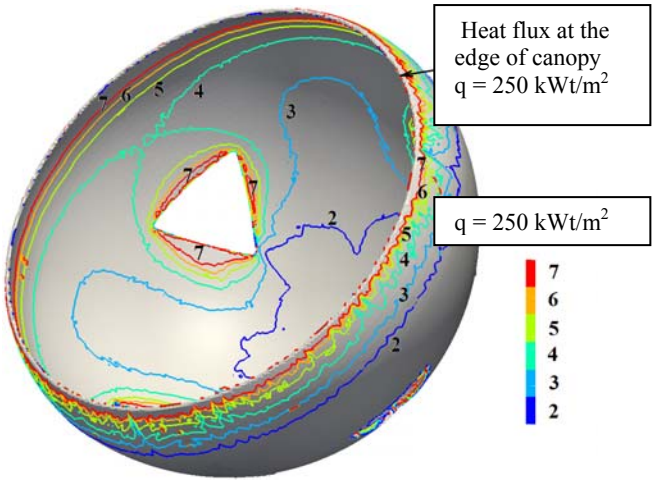

Fig.5. The distribution of heat flux on the surface of the canopy

The results of heat flux calculation is given in Fig 5. On the inner and outer surface of the canopy shows contours distribution of heat flux to the cold surface temperature Tw = 300 K.

Each contour specified number of heat flux (kW/m2) to which it corresponds. The pole part of the inner surface of the canopy is the least heat-stressed, heat flow is less than 2 kW/m^2.

Heat transfer increases significantly when approaching the edges of the triangular holes (structural permeability) and reaches values of more than 7 kW/m2.

In most of the inner surface of the canopy heat fluxes ranging from 1 to 10 kW/m^2. Estimation of the maximum heat flux at the free-edge streamlined canopy corresponds to 250 kW/m^2. On the outer surface of the canopy substantial heat flux values are observed only near the edges of the canopy, the rest of the surface heat transfer is negligible.

Fig. 6 shows the result of the calculation of radiative equilibrium temperature. For the model calculations the emissivity of the surface of the canopy was taken ε = 0,85. Radiated emissions modeled with only one side of the fabric. Estimate of the maximum radiation equilibrium temperature at the free-edge streamlined canopy corresponds to 940 ° C.

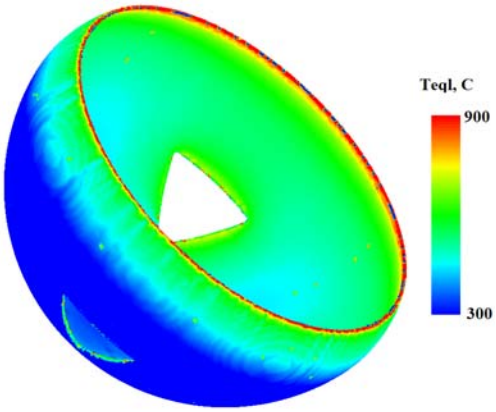

Fig.6. The result of radiative equilibrium temperature calculations for the canopy.

STUDY AND SELEC TION THE HIGH TEMPERATURE, HEAT-RESISTANCE TISSUE FOR PARACHUTE.

It is known that silica materials are excellent high temperature insulation and can continuously be used without changes in the properties at a temperature above 1000 □ C and briefly □ at higher temperatures.

It should be noted that for fiber glass fabrics and carbon fabric in technical references practically is no data on the tensile strength at temperatures above 300 C. Therefore, studies were conducted on the tensile strength of images silica and quartz fibers in the temperature range from 20 to 1300 ° C.

The laboratory bench Instron 5965 with radiative heating was used (Fig. 7), equipped with a symmetrically located alundum tube with an inner diameter of 5 mm. The test sample was placed on the axis of alundum tube for a few minutes subjected to heating to the predetermined temperature. Some results of the evaluation studies of tensile strength textile threads obtained on the bench Instron 5965 are presented in Fig. 8.

The bench Instron 5965 with radiative heating

Fig.7. Instron 5965 with radiative heating

It was shown that the tensile strength of the threads of silica and quartz fibers at 1200 □ comply with requirements imposed on them by the modes of loading ASPS when braking engine bay of the first stage of the "Soyuz-2" weighing 4.4 tones when entering at a speed of up to 3 km / s, 80 km altitude and trajectory angle 24 □ on the basis of calculating the parameters of motion of RB-ASPS and calculate the temperature at the point stagnation.

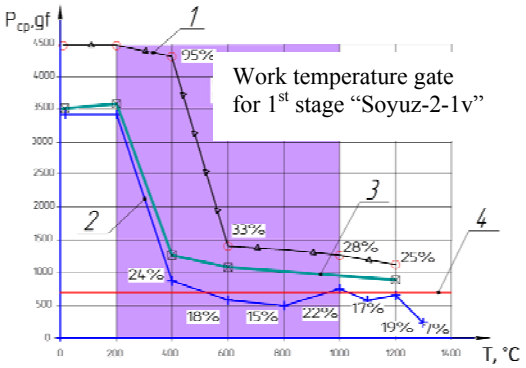

-2-

Fig.8. The results of test on thread of textile and the design criteria of strength to the threads of textile for ASPS to "Soyuz-201b". P - tensile strength in [gram].

Line 1 – for quartz thread
Lines 2,3 – for silica threads
Line 4 – design criteria

The results of laboratory research of heat-resistant silica and quartz textile materials under high temperature confirmed principle possible to create ASPS for saving the first stage or rocket engine with hardware

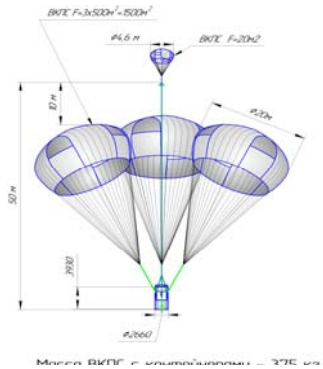

Fig.9. Thirdly canopy parachute system for saving booster rocket weighting 4350 kg providing landing speed of 7.7 m/sec.

CONCLUSIONS

It was proposed and developed a new well-grounded concept of parachute system application using high-temperature, heat-resistant silica and quartz textile materials (new in parachute building) already brought to a commercial level, which has led to the creation of a new class of aerospace parachuting systems - ASPS

This concept implies that stabilization, deceleration, descending, and landing of a 3.5 -11 ton buster rocket (BR) is performed with the same high-temperature textile parachutes, the ASPS initiated immediately after used rocket unit separation from BR.

The results of laboratory research of heat-resistant silica and quartz textile materials under high temperature confirmed principle possible to create ASPS for saving the first stage or rocket engine with hardware

At the altitude 40-45 km ASPS provides the descent velocity values less than Mach number 1 and about 30 minutes prior to landing that is comfortable for helicopter recovery

The next major steps to enable actual ASPS include: refinement and test high-temperature, heat resistant textile for application in parachute systems (1), ground and bench working off ASPS units (2), flight test the prototypes of ASPS on board of meteorological rockets (3).

DEVELOPMENT AND FLIGHT-TESTING OF A SYSTEM TO ISOLATE VIBRATIONS FOR MICROGRAVITY EXPERIMENTS ON SOUNDING ROCKETS

Stefan Krämer[1], Dominique Jonas Daab[1], Brigitte Müller[1], Tobias Wagner[1], Fabian Baader[1], Joana Hessel[1], Georg Gdalewitsch[1], Engelbert Plescher[1], Bernd Dachwald[1], Michael Wahle[1], Andreas Gierse[2], Rudolf Vetter[3], and Lysan Pfützenreuter[4]

[1]*Dept. of Aerospace Engineering, FH Aachen, University of Applied Sciences, Hohenstaufenallee 6, 52064 Aachen, Germany, Email: stefan.kraemer@alumni.fh-aachen.de, REXUS@fh-aachen.de*
[2]*ZARM Fallturm Betriebsgesellschaft mbH, am Fallturm, 28359 Bremen, Germany, Email: Andreas.Gierse@gmx.de*
[3]*EADS Astrium, Claude-Dornierstrasse, 88090 Immenstaad, Germany, Email: Rudolf.Vetter@astrium.eads.net*
[4]*DLR German Aerospace Center, Space Administration, Königswinterer Str. 522-524, 53227 Bonn, Germany*

ABSTRACT

LOW FREQUENCY VIBRATIONS are a limiting factor for many experiments in microgravity environment. Accelerations due to excited structure parts of the experiments can cause strong influences on the quality of the experiments. Especially on sounding rocket flights the time of reduced gravity is very valuable and shall be used efficiently. Constraints due to the interferences between different disturbing experiment events often force to apportion the experimenting time. By the mechanical decoupling of an experiment, the induced perturbations can be minimized in both directions. Protecting the experiment from the influences by the vehicle and shielding all other experiments from the self induced disturbances is the goal of the ADIOS platform.

Key words: Vibration Isolation, Damping, Sounding Rockets, REXUS.

1. INTRODUCTION

The ADIOS platform is a passive and contactless isolation system, based on magnetical damping, which has been designed for experiments on sounding rockets. Driven by the motivation to increase the quality of μ-gravity for experiments on sounding rockets in a easy and cost effective way, in 2008 a student team at the FH Aachen, University of Applied Science, started to develop a system in the framework of the REXUS programme (Rocket borne EXperiments for University Students) of DLR, SNSB / SSC and ESA. Already the second design study of the system, called *VibraDamp* [1], has been tested successfully on the REXUS 7 flight in March 2010. The new developed system was completely passive despite of the locking mechanism for launch and landing. This system makes it possible to decouple an experiment from the rocket structure above frequencies of about 0.5 Hz.
Basing on the results and lessons learned of *VibraDamp* a third student team formed in 2010 which set the goal to increase the performance by a redesign of the system. A much more lightweight construction saves valuable payload mass. The theoretical threshold frequency is lowered down to 0.28Hz for a decoupling above this frequency and the measurement setup has been adapted for the verification purpose.
The new *ADIOS - Advanced Isolation on Sounding Rockets* system[1] verifies the technical setup developed for *VibraDamp*. The function of the improved system was demonstrated during the REXUS 11 flight in November 2012.

In addition to the ADIOS system verification an in-flight modal analysis of the REXUS vehicle has been conducted in the context of a second experiment by the FH Aachen student team.

2. MOTIVATION

Experiments with high requirements on the quality of μ-gravity are often guests on sounding rockets. But reaching high altitudes above the aerodynamic influences of the lower atmosphere is not a surety of low disturbances. Structural vibrations can cause unexpected errors on μ-gravity experiments. The sources of the disturbances can be found e.g. in high frequency resonances of parts, induced by the random excitation of the rocket motor. Weakly damped structures can store vibrational energy like a bell. Additionally the high frequency excitations are usually superimposed with low frequency structural oscillations and vehicle

[1]Presented at the 21st ESA Symposium on Rocket and Balloon Programmes and Related Research, 9-13th of June 2013, Thun / Switzerland

Proc. '21st ESA Symposium European Rocket & Balloon Programmes and Related Research', 9–13 June 2013, Thun, Switzerland (ESA SP-721, October 2013)

movements. For most experiments the low frequency excitations are often a limiting factor. High amplitude low frequency movements even can completely disable the function of e.g. physical science experiments. For some cases interferences between the experiments must not be neglected. Due to the short experimenting time sometimes several experiments have to run in parallel. Currently, if one experiment disturbs the performance of another one, the time needs to be apportioned.
A practical solution for this problem is to decouple the sensitive or the disturbing experiment from the rocket structure. Limited power and the need of high reliability leads to a passive, lightweight and straightforward solution.

3. STATE OF TECHNOLOGY

Vibration damping for microgravity experiments can be realized with active or passive isolation systems. Active isolation systems require a high level of technology, sensors, actuators and complex software solutions. Passive systems are usually more cost effective and less complex. Both solutions have advantages which are depending on the environment and on the damping requirements.
Most systems are designed for the International Space Station (ISS). The vibrations and accelerations on the ISS are categorized into three frequency ranges. Low frequencies (below 0.001 Hz) which are caused by gravity gradients and atmospheric drag (less than 10^{-5} g). The frequencies in the range of 0.001 Hz to 1 Hz are for example caused by motion of the astronauts and attitude control maneuvers. Higher frequencies (above 1Hz) can be generated by electric motors, pumps, compressors, fans and also astronaut actions.
Currently passive vibration isolation systems are only used for the damping of high frequencies above 10 Hz and for payloads which are not sensitive to low frequencies. A practical application for even low frequencies is not far developed yet. Active damping solutions are often more convenient to low frequency attenuation and are grouped into active rack isolation and active payload isolation systems.

3.1. Active Vibration Isolation Systems

Active systems provide a vibration isolated environment by utilising actuators which are controlled by a feedback control in combination with sensors. The overall advantage is the wide application bandwidth. Even low frequencies can be isolated typically. Active systems often require much space and power.

3.1.1. Active Rack Isolation

Rack isolation systems can provide an nearly undisturbed environment for a whole experiment rack. This leads to a voluminous design on the one hand and gives the opportunity to change the experiments and further use of the isolation system on the other hand.

The *Active Rack Isolation System* (ARIS) developed by the Boeing Corporation was already tested on the ISS. "These ARIS racks are dynamically controlled by closed feedback loops around inertial sensors and voice coil rotary actuator/pushrods, which connect the rack and the space station structure"[2]. The motions of the ISS and of the rack are measured by accelerometers. That data is used for the ARIS control algorithms.

3.1.2. Active Payload Isolation

Payload isolation systems increase the μ-g level for a single experiment hence the system have fixed optimised design parameters.

- The *Suppression of Transient Accelerations By Levitation* (STABLE) developed jointly by NASA Marshall Space Flight Center (MSFC) and McDonnell Douglas Aerospace Corporation (MDAC), now the Boeing Corporation. The system consists of three actuator assemblies, nine acceleration sensors, three position sensors and the associated electronics and control boards. Control algorithms are used to operate the system.
- The *Microgravity vibration Isolation Mount* (MIM) developed by the Canadian Space Agency. The control of the isolated platform is based on six degree-of-freedom magnetic levitation utilizing eight wide gap Lorentz force actuators.
- The *Modular Wideband Active Vibration Absorber* (MWAVA) developed by NASA's Goddard Space Flight Center and University of Massachusetts Lowell. The isolation is realized via a two stage mechanical connector. One stage is connected to the other structure and the second stage which is free of vibration is connected to the device or experiment.
- The *GLovebox Integrated Microgravity Isolation Technology* (g-LIMIT) developed by NASA Marshall Space Flight Center (MSFC). The g-LIMIT system is similar to the MIM solution.

The mentioned systems were all tested and operated on the International Space Station or on Space Shuttle missions. Hence the damping of vibrations on sounding rockets is relatively new. The active *Vibration Isolation Platform* (VIP) by Controlled Dynamics Inc. has been recently presented at the Next-Generation Suborbital Researchers Conference 2013, Broomfield, Colorado. This system is designed for different applications and even usable on sounding rockets.
The realization of an active isolation system on these

rockets result in a very complex, heavy and costly solution. Especially the highly sensitive acceleration sensors and the required complex software solutions are an uneconomic factor. Also the weights of the payload and of the payload supply systems are limited. Hence a passive, lightweight and simple vibration isolation system for sounding rockets, which is also damping low frequencies, would be eligible.

3.2. Passive Vibration Isolation Systems

Passive systems often use the mass of an experiment platform as the key element for the isolation of higher frequencies. Elements made of rubber or viscous materials are often used for damping purpose. In view of a passive isolation system, the advantages are obvious, high reliability with no power consumption and usually less complexity. Nevertheless the status after Whorton [3] and Grodinsky [2] assumes a high system mass and no possibility of decoupling lower frequencies and high amplitudes without the problem of meeting the natural frequencies of the damping system. Additionally it is assumed, that the decoupling by a passive system only works in one direction: from the excited structure to the experiment. The ADIOS platform mitigates all these constraints. It works in both ways: it decouples an experiment from an excited structure and it can also save the structure and other experiments from the influences by a vibrating system.
A practical solution of a passive vibration reduction system has been developed for the *Advanced X-Ray Astrophysics Facility* (AXAF) [4]. The goal was to decrease the influence by g-jitter, induced by the reaction wheels of the space craft.

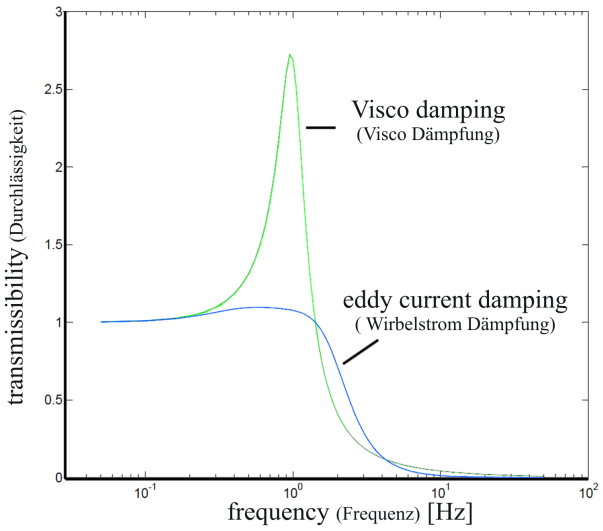

Figure 1. The magnification curve of the eddy current damping in comparison to visco damping

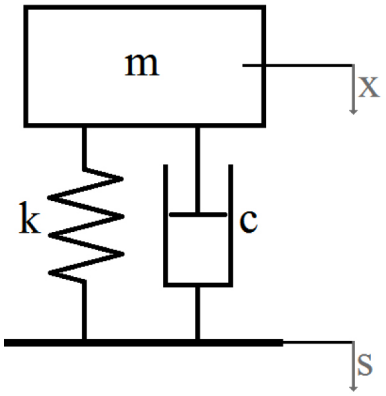

Figure 2. Single mass with spring and damper

4. TECHNICAL REALISATION

In order to achieve the goals of a high sensitive decoupling without the use of active devices which consume energy during action, the principle of the eddy current damping was first developed to damp the TITUS II Experiment on the MIR space station. The working principle has been patented by the DLR in 2002 [5].

4.1. Fundamentals of Mechanical Decoupling

A mechanical decoupling system, which is the same as a flexible machine bearing, consists naturally of springs and dampers. Both, springs and dampers, can be engineered in various designs for different applications. Here the decoupled experiment, which can be an experiment of any kind, itself is considered to be a single mass without own eigenfrequencies. The eigenfrequencies of a real experiment setup are usually of much higher frequency than the eigenfrequencies of the decoupling mechanism, which makes it possible to separate these two cases. The decoupling mechanism restrains the energy from the outer structure to affect the experiment. If the experiment itself includes sources of mechanical vibrations, these sources or at least the most sensitive parts of the experiment should be decoupled separately. Figure 2 shows a one dimensional decoupling mechanism (one DOF (degree of freedom) x) consisting of a one dimensional spring, a one dimensional damper and the experiment as a single mass. The movements of the outer structure (s) are the excitation of the spring and the damper.

Figure 1 compares the dynamic mechanical behaviour of this system using viscous dampers (green) and passive eddy current dampers (blue) with the same isolation quality at higher frequencies. A System with one degree of freedom has one eigenfrequency. This eigenfrequency is characterized by a high magnification factor. At frequencies higher than the eigenfrequency the amplitude of the experiment motion decreases and is finally much smaller than the excitation amplitude. This phenomenon is called ”decoupling”. Obviously the active eddy current damper

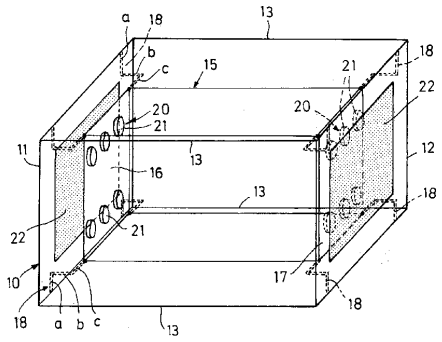

Figure 3. The magnet setup of Eddy current damping (taken from [5])

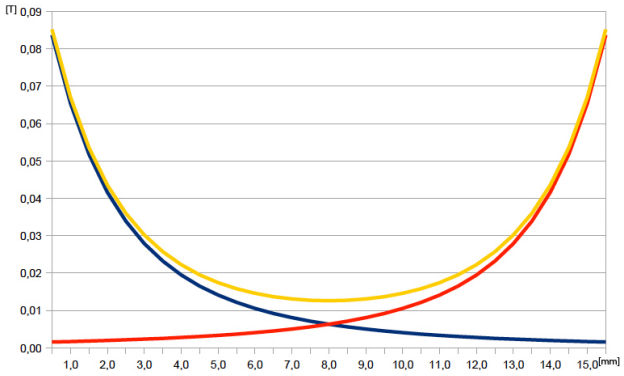

Figure 4. Magnetic field strength in dependence of the distance to the magnet

allows an increased damping close to the eigenfrequency. This results in a smaller magnification factor. Even more important is the result, that at higher frequencies a very good decoupling is achieved.

4.2. The Working Principle

In order to improve the existing μ-gravity environment, all DOF have to be mechanically decoupled. Therefore six three-dimensional springs and dampers are necessary. The dimensioning eigenfrequency should be as low as possible to achieve a decoupling even at low frequencies. Figure 3 (obtained from [5]) shows the patented decoupling mechanism of the TITUS II experiment. The three-dimensional springs are realised as bending and torsional beams, while magnets are damping the experiment using the eddy current effect. Working with eddy current dampers the damping depends on the oscillation amplitudes, frequency and the distance between the magnets and the corresponding aluminium board.

4.2.1. The Isolation Concept

The key elements for the isolation of vibrations in the mechanical decoupling due to the *free flying experiment device* (FFED). This principle is not new, but it gives the unique base for a nearly disturbance free environment. The technical design can be adapted by optimising the space for the FFED, in which it can and needs to move without contacting the outer structure. Hence the highest amplitude of motion / vibration has to be estimated in advance.

4.2.2. The Damping Principle

Figure 4 indicates the dimensions and influence of the magnetic fields due to the permanent magnets, attached to the locking mechanism. The blue and the red graphs represent the magnetic field strength of the magnets on the upper as well on the lower side of the locking mechanism in relation to the distance. Due to this certain position of the magnets above and below the FFED, the non magnetic counter plate of the FFED has its initial distance at 8 mm for the current design. The yellow graph shows the superposition of the magnetic fields. If the FFED travels towards one direction away from the initial position, the influence by the magnetic field become immediately stronger. In concern of the eddy current principle, the velocity (hence the frequency) of the movement is a driver of the resulting damping. As higher the frequency, as stronger the damping takes affect.

4.3. Design Parameter

This section deals with a brief explanation of the physical background to determine the design parameters of the presented isolation platform. The framework of this paper is not sufficient to include all considerations for the calculation. It can only give an overview of the basic approach.

4.3.1. Dimensioning of Springs

We regard in the first step the dimensioning of the springs. An effective stiffness of a spring is approximated by implicating the bending and torsion of the spring wire. A spring design shown in figure 5, gives a similar stiffness in all directions of freedom. Using the stiffness calculated as follows:

$$k = \frac{\Delta F}{\sum \Delta x} \tag{1}$$

leads to the overall spring constant.

The single Δx are calculated with the parameters I_B as moment of inertia in bending direction and I_P as moment of inertia in torsion direction. E and G represent

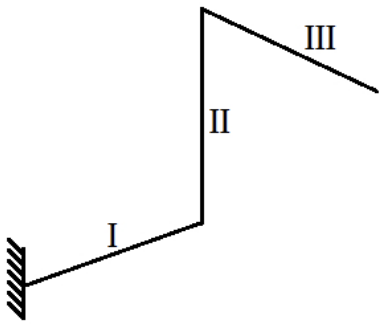

Figure 5. Three dimensional spring design

the Young´s modulus as well as the modulus of shear deformation.

$$\sum \Delta x = 2 \cdot \Delta x_{bending} + 1 \cdot \Delta x_{torsion} \tag{2}$$

$$\Delta x_{bending} = \frac{\Delta F \cdot L^3}{3 \cdot E \cdot I_B} \tag{3}$$

and for small angles:

$$\Delta x_{torsion} = \frac{\Delta F \cdot L^3}{G \cdot I_P} \tag{4}$$

Assuming a force acting in the direction of leg III, the leg II reacts as a bending beam and leg I as a torsion spring. Leg III is assumed to be rigid in force direction. If the spring length is determined this way, a practical length must be chosen. The effective spring constant k_{eff} is calculated with the set length.

$$k_{eff} = \frac{1}{\frac{2 \cdot L^3}{3 \cdot E \cdot I_B} + \frac{L^3}{G \cdot I_B}} \tag{5}$$

With the reduced mass of the FFED the natural frequency of the damping platform can be determined.

$$f_e = \frac{\omega_e}{2 \cdot \pi} = \frac{\sqrt{\frac{k_{eff}}{m}}}{2 \cdot \pi} \tag{6}$$

4.3.2. Dimensioning of magnets

First the Lehr´s damping coefficient need to be determined with:

$$\xi = \frac{1}{2 \cdot V} \tag{7}$$

using the maximal assumed magnification factor V.

To dimension the magnets the required effective damping c_{eff} has to be determined in advance. The effective field strength B_{eff} is a function of the material thickness d, the effective damping c_{eff}, the magnetic material constant of the counter material κ and k.

$$B_{eff} = \sqrt{\frac{c_{eff}}{k \cdot \kappa \cdot d}} \tag{8}$$

In order to avoid magnetic disturbances to the experiments, the field strength of the chosen permanent magnets stays below the level of the earth magnetic field already in a distance of a few millimetres.

4.4. The ADIOS Experiment Setup

The ADIOS platform uses a free-flyer, containing the sensitive experiment, which is hold in position by six tiny three dimensional beam springs shown in figure 5. This leads to a six degree of freedom mounting of the FFED. The spring wires are bent by 90° to all three axis of motion resulting in beam like displacements, which are easy to calculate. The length of the spring legs (I, II and III in figure 5) are design parameters for the natural frequency of the system. It accords to the deepest frequency which can be isolated by the ADIOS system. The springs are mounted to the rocket structure on the one hand side while they are fixated to the FFED on the other hand side in a 120° interval. After unlocking the system the springs pull the FFED out of the storage position.
The permanent magnets for the eddy current damper function are mounted in flight direction directly to the aluminium rings of the locking mechanism. The magnetic field strength decreases quadratically with the distance and a contained experiment will not feel stronger magnetic forces than the earth magnetic field strength. The optimal damping is reached by a multilevel arrangement of the magnets, which is shown in figure 6. By using different field strength in different levels, a progressive damping behaviour is realised.

In order to validate the spring and damper performance as a result of the formerly explained theoretical dimensioning, the ADIOS damping platform is equipped with measuring electronics. One three axial accelerometer is mounted to the centre of the FFED, a second one is attached to the rocket module as a reference sensor. Close to the reference accelerometer an imbalance generator is mounted to the rocket wall. During the μ-gravity phase the imbalance generator is driven in three different excitation frequencies (see table 1) to generate a valid signal in far distance to the electric noise of the measuring system. The excitation frequencies $f_{excitation}$ give the opportunity to proof the transmissibility for the higher frequencies.

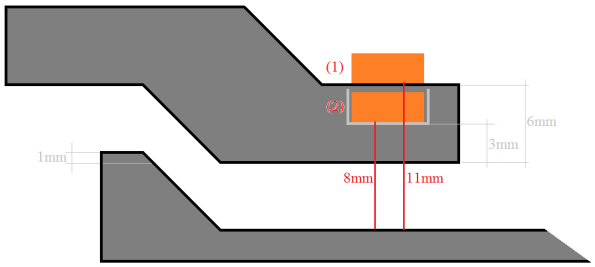

Figure 6. Multilevel magnet setup in a cross section of the locking mechanism and the counter plate of the FFED

Table 1. Excitation Frequencies of Imbalance Generator

Phase	Frequency
$f_{excitationI}$	13 Hz
$f_{excitationII}$	34 Hz
$f_{excitationIII}$	56 Hz

The ADIOS platform only works during free flight phase. Despite the time of μ-gravity the FFED need to be locked to avoid shocks to the experiment. These motors open up the space for the FFED to ensure movements of the structure relative to the locking mechanism during the μ-gravity flight phase. To cope with this a reliable locking mechanism has been developed. Two solid aluminium rings, driven by three strong geared electric motors, clamp FFED in the initial position. Before the payload enters the dens atmosphere, the FFED is locked savely again. The motors are dimensioned to re-lock the FFED after the experimenting time even when it moves out of the centre.

The ADIOS platform is currently designed to fit into a 14” standard rocket module. The structure is mounted to the wall by six aluminium brackets. The platform configuration shown in figure 7 still contains the measurement setup for the ADIOS performance evaluation. The size of the FFED can easily adapted to the given volume of a possible experiment. The current setup is fail save. If the locking mechanism does not open during the μ-g phase, the experiments container ”feels” the reduced gravity of the initial platform. Would the locking mechanism fail during re-locking, the FFED had no possibility to escape and can only move in between the few millimetres of opening space

4.5. The ADIOS Technical Level

Concerning to the classification [6] of the *Technology Readiness Levels* (TRL) for the current design of the ADIOS platform adapted to the application on sounding

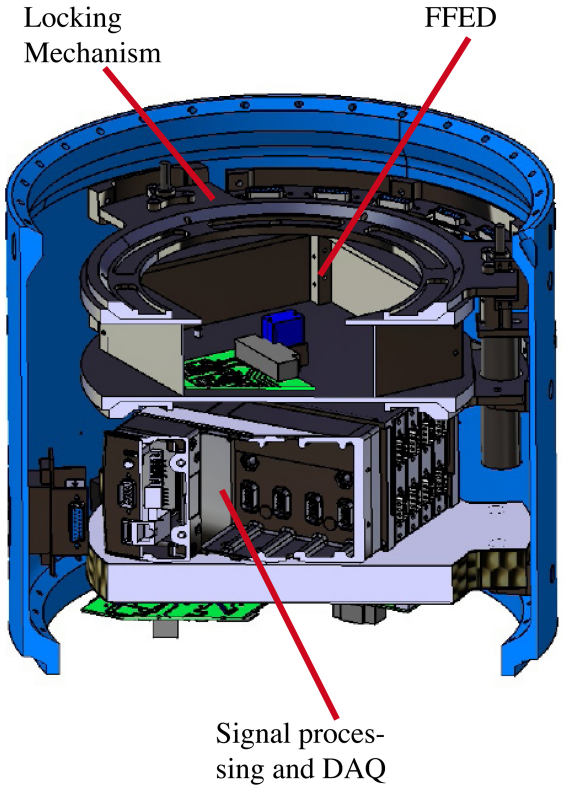

Figure 7. CAD cross section model of the ADIOS experiment setup with FFED, locking mechanism and data acquisition unit

rockets a TRL 7 is reached. This level implements the system prototype demonstration in an operational environment. For the application on other types of reduced gravity platforms like space stations and satellites, the TRL 4 (proven principle) can be assumed. Even short term experiment applications at drop tower facilities or parabolic flight aircrafts can be considered.

5. RESULTS

The in-flight test on REXUS 11 provided good processable data. Although the conditions of the REXUS 11 flight was not as good as usually, the ADIOS system could show its performance for this case. Even the very low frequent tumbling at $\frac{1}{18}$ Hz of the rocket payload was smoothed for the free flying experiment container. The presented graphs in figures 8 and 9 are the measured data of the flight axis of the vehicle. Both other directions (y and z) show very similar results and are mitigated in this discussion.
Regarding the unprocessed data of figure 8, the red graph represent the excited rocket structure, while the green graph show the accelerations inside the FFED. The first 20 seconds of experimenting time are superposed by the capacitor influence of the amplification board and are neglected here. Nevertheless, it is obvious, that the red graph reveals the slow movements ($\frac{1}{18}$ Hz) of the rocket

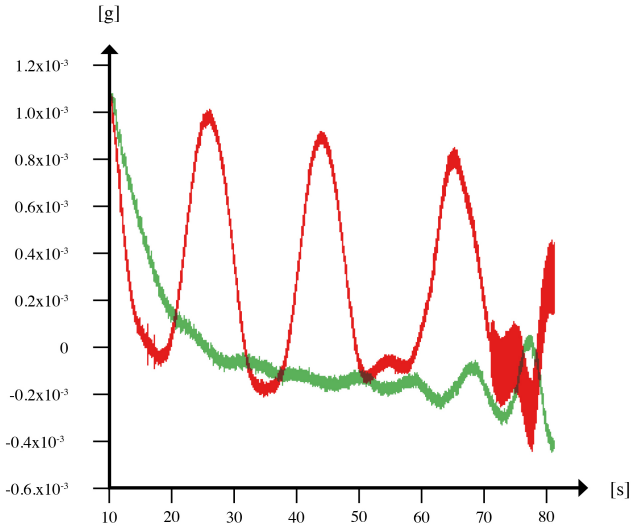

Figure 8. Unfiltered acceleration signals of the flight axis as a result of REXUS 11 test flight. RED - undamped rocket structure, GREEN - decoupled experiment containment

payload during the phase of reduced gravity. This has been triggered due to the motor separation and the absence of a rate control system. The higher amplitude of the high frequency vibration at the end of the graph indicates the run of the second stage ($f_{excitationII} = 34$ Hz) of the imbalance generator. The first and third stage are just recognisable after Fourier transformation of the data. In the time after about 60 s the movements of the rocket payload section became stronger and the FFED followed the higher amplitude of low frequent agitation. At these amplitudes a contact between the FFED and the structure of the locking mechanism could not be ruled out.
Figure 9 exhibit the processed data by Fourier transformation which point out, that the forced excitations by the imbalance generator of the ADIOS experiment setup have been almost completely isolated. While the peaks of the red graph clearly represent the three excitation frequencies of the imbalance generator, the green graph does not show any transmission of these vibrations in the outlined frequency band from 1 Hz to 100 Hz. The bandwidth between 0 Hz and 10 Hz is strongly superposed by so called ”pink noise” due to the measuring and amplification system. In this data set the natural frequency of the damping system is not recognisable. Therefore the disturbance by low frequent movements was too high.

6. CONCLUSION

The ADIOS platform offers an enhanced reduced gravity in six degrees of freedom by one order of magnitude. In view of the application on sounding rockets an effective decoupling of the experiment from the rocket structure is already reached above 0.5 Hz. The passive system comes with a reliable locking mechanism for launch and landing

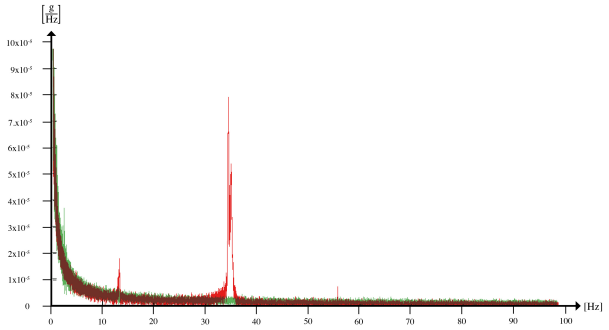

Figure 9. Fourier transformed signal of the accelerations in flight axis showing the excitation frequencies by the imbalance generator. RED - undamped rocket structure, GREEN - decoupled experiment containment

as well as for storage. Designed and demonstrated for sounding rockets the principle can be used for different type of μ-gravity platforms.
Usually very low frequency movements are covered by the rate control system of the sounding rocket system. A combination with the ADIOS platform can reach μ-g levels up to 10^{-5} g. Transient events (shocks) are damped in the range of amplitude in which the FFED does not hit the surrounding locking structure.

7. OUTLOOK

The principle has been proofed and a practical application would show the real worthiness of this system. Nevertheless the ADIOS system works well even for lower frequencies. Now technologies of combined systems are in work to further improve the quality of μ-gravity for any kind of system.

ACKNOWLEDGMENT

The authors would like to thank all responsible persons at DLR, ESA and SSC concerning the REXUS Program. A special thank goes to our industrial partners, who provided material sponsoring and skills to realise the technical experimental hardware. Also we like to thank our Professors and lecturers for mental assistance and advice and the FH Aachen for financial support.

REFERENCES

1. Lysan Pfützenreuter, Michael Lauruschkat, Andreas Gierse, and Rudolf Vetter. Vibradamp. Technical report, FH Aachen, 2010.

2. Carlos M. Grodinsky and Mark S. Whorton. A Survey of Active Vibration Isolation Systems for Micrograv-

ity Applications. Technical report, Bicron Corporation, Newbury, OH. 44065.

3. Mark S. Whorton. Microgravity vibration isolation for the international space station. Technical report, TD55/Vehicle Control Systems, NASA Marshall Space Flight Center, Huntsville, AL 35812.

4. Karl J. Pendergast and Christopher J. Schauwecker. Use of a Passive Reaction Wheel Jitter Isolation System to Meet the Advanced X-Ray Astrophysics Facility Imaging Performance Requirements. Technical report, TRW Inc., One Space Park, Redondo Beach, CA 90278, 1998.

5. Rainer Nähle, Michael Wahle, and Reinhard Röstel. Lagersystem in einem Raumfahrzeug - Patentschrift. Technical Report DE 102 27 968 B4 2006.03.02, DLR, 2002.

6. James R. Wertz, David F. Everett, and Jeffery J. Puschell, editors. *Space Mission Engineering: The New SMAD*. Microcosm Press, 1 edition, 2011.

GRAVITY GRADIENT EARTH SENSOR EXPERIMENT ON REXUS 11

Kaustav Ghose[(1)], Simon Dandavino[(1)], Hervé Meyer[(2)], Benoit Chamot[(2)], Jean-François Labrecque-Piedboeuf[(2)], Ioana Josan-Drinceanu[(2)], Yann Voumard[(2)], Muriel Richard[(2)], Herbert Shea[(1)], Jean-Noël Pittet[(2)], Deborah Mueller[(2)]

[(1)] Microsystems for Space Technologies Laboratory, EPFL, CP 526, rue Jaquet Droz 1, 2002 Neuchatel Switzerland, herbert.shea@epfl.ch

[(2)] Swiss Space Center, EPFL, Switzerland, ELD-013 Station 11, 1015 Lausanne, Switzerland, Muriel.richard@epfl.ch

ABSTRACT

This experiment is the first test of the concept for a novel attitude determination sensor in freefall, that utilizes the Earth`s gravity gradient as a reference. Current sensors require multiple optical heads with access on all faces of a satellite that might point towards the Earth [1]. Earth sensors determine the Earth vector by sensing the position of the Earth's horizon, detecting the Earth`s IR emission against the background of space [2]. The gravity-gradient based approach does not require optical access for the sensor, and one single, compact unit can be located anywhere inside the satellite, and provide complete 4π steradian field of view. The sensor principle is based on the use of a Micro Electro Mechanical System (MEMS) device that can measure the Gravity Gradient Torque (GGT) [3]. We describe the design of the experiment to test the MEMS GGT sensor on a REXUS flight and present the results obtained.

1. INTRODUCTION

The Microsystems for Space Technologies Laboratory (LMTS) of the EPFL has been developing a novel Earth Sensor that does not use any optics. The principle is based on the use of a MEMS (Micro Electro Mechanical System) device that can measure the Gravity Gradient Vector, which always points to the centre of the Earth. This is accomplished by measuring the torque, in free-fall conditions, due to the gravity gradient on an elongated proof mass. The objective is to measure the rotation of a silicon proof mass under free-fall conditions due to gravity gradient torque, and from the data, determine the accuracy of the attitude measurement for a Low Earth Orbit (LEO) satellite.

The gravity gradient torque (GGT) has been used to stabilize small satellites after launch, but never as an attitude determination scheme. Instead of the current Earth sensing methods that determine the Earth vector by sensing the Earth's IR emission, we are investigating a much lighter and more compact MEMS-based solution. Current Earth sensors use multiple telescopes and cameras. In the event that a satellite starts to tumble, existing Earth sensors that use optical sensing are severely limited in their ability to reacquire the attitude due to the limited field of view of the instruments. Also, due to this limited field of view, multiple Earth sensor units need to be placed on all faces of the satellite to ensure 4π steradian coverage. Because of the optical sensing principle of existing Earth sensors, constraints are imposed on the positioning of solar panels and antennas so that they do not block the field of view of optical sensors.

The MEMS-based approach does not require optical access, and thus one single, compact unit located anywhere inside the satellite provides full 4π steradian field of view.

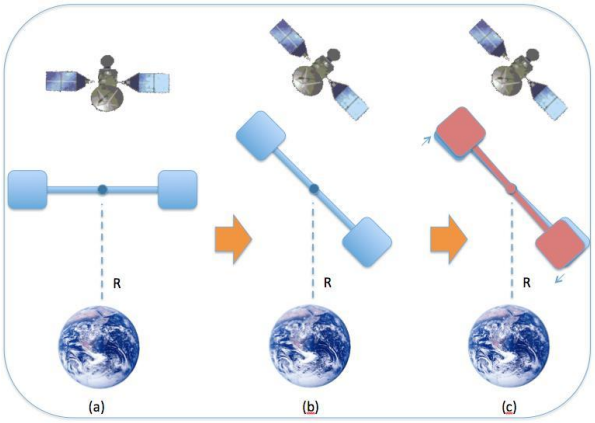

Figure 1. Diagram showing effect of the gravity gradient on an elongated proof mass. (a) the proof mass inside the satellite is perpendicular to the Earth. Both sides of the mass being the same distance from the Earth, there is no detectable effect. If the satellite rotates by a given amount (b), the mass inside also rotates. Since now one side is closer to the Earth and sees more gravity (c), the GGT will produce a displacement

Fig. 1 shows a schematic representation of a MEMS sensor. The chips have a proof mass suspended by springs from a frame. The frame is attached to the satellite body. In free fall, the proof mass is displaced in the order of a nanometer due to GGT. This displacement is dependent on the angle the proof mass

Proc. '21st ESA Symposium European Rocket & Balloon Programmes and Related Research', 9–13 June 2013, Thun, Switzerland (ESA SP-721, October 2013)

makes with the Earth. Therefore, by measuring the displacement the angle can be determined. A detailed analysis, design, fabrication of the MEMS chip is given in [3]. On Earth the GGT cannot be measured directly since the magnitude of gravity is many orders greater, and a period in free-fall is necessary to be able to test whether the sensor is able to measure GGT.

This is an inertial sensor, so any external inertial forces will produce an error in the measurement of displacement due to GGT. To estimate and eventually subtract these errors we need to measure the inertial environment that the experiment is in. For this purpose, we fly an Inertial Measurement Unit (IMU) with the MEMS, and record its output along with that of the MEMS. Redundancy is implemented in the MEMS and IMUs that forms the experiment. The data is stored on board, and we also utilize the REXUS telemetry downlink to have backup. The power supply for our experiment comes from the REXUS service module (RXSM). This experiment does not aim at proving a complete attitude determination system; just to test the MEMS Earth sensors in operating conditions that cannot be achieved in a laboratory on Earth.

2. EXPERIMENT DESCRIPTION

The main purpose of the experiment is to gather data from four MEMS chips that are sensitive to GGT. The chips have a proof mass and spring. The proof mass is displaced depending on the GGT on it, which depends on the angle the proof mass makes to the Earth's surface. This displacement is measured by means of recording a change in differential capacitance, as measured on electrodes at opposite ends of the elongated proof mass.

The experiment is divided by functions into three electronic circuit boards (Fig. 2):

- Main board for interfacing with the RXSM, and provide power supply, telecommands and telemetry for the experiment. It also processes the Start Of Experiment (SOE) and Lift Off signals from the RXSM. Two science boards are connected to the main board.

- Science board for data acquisition from the MEMS and IMU, and for onboard data storage. Two MEMS boards connected to each science board.

- MEMS board with one MEMS chip each. This provides mechanical support for the MEMS chip, contains the electronics for recording the differential capacitance and temperature values from the MEMS chip, and also has a heater to prevent moisture condensing on the MEMS at low temperatures. There are a total of four MEMS boards.

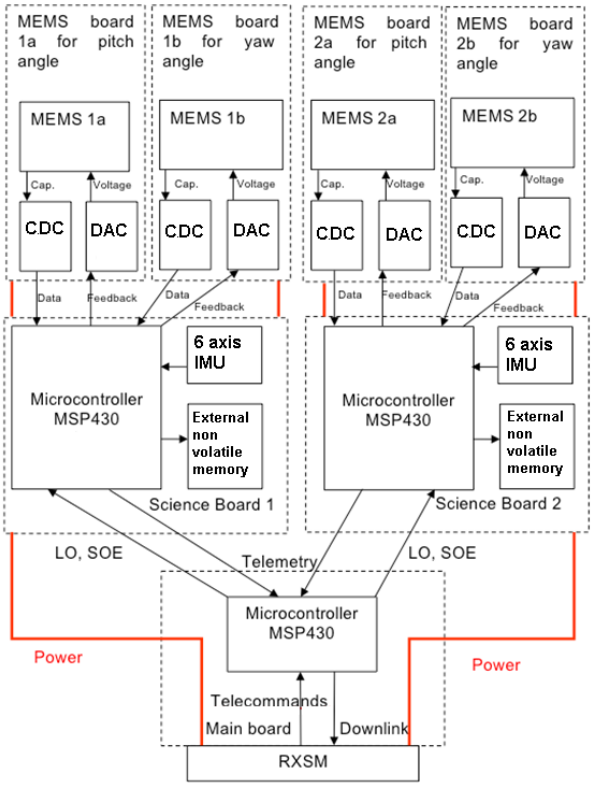

Figure 2. Diagram of GGES experiment setup

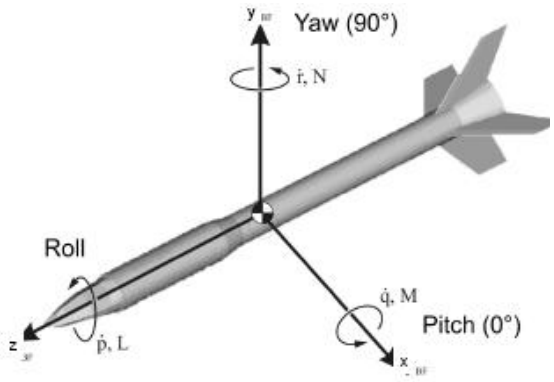

Figure 3. REXUS body frame coordinate system. [4]

With respect to the body frame coordinate system of REXUS (Fig. 3), the MEMS chips are arranged to measure the pitch and yaw angles. To ensure that there is a measurable signal irrespective of the angle at which the rocket ends up at after launch, and for some redundancy, for each angle a second MEMS chip, oriented in a plane 45 degrees is used. There are two sets of MEMS chips, one set to measure yaw, the other to measure pitch. One chip from each set is connected to a single science board for redundancy. If one science board stops working, yaw and pitch measurements should still be possible on the other science board.

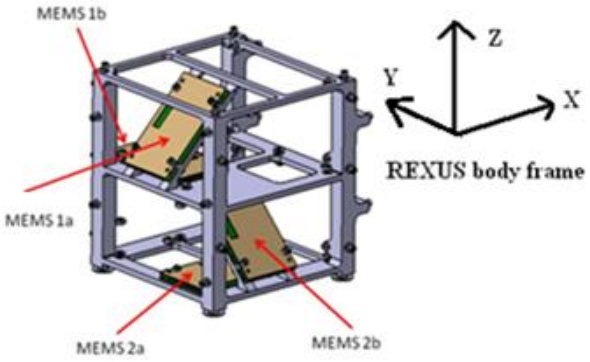

Figure 4. Mounting of the MEMS boards

To measure pitch, the Earth sensor is placed in the XY plane such that the longitudinal axis of its elongated mass is parallel to the Y axis (MEMS 2a). In such an orientation, due to GGT the proof mass will pivot around the X axis and the displacement will be proportional to the pitch angle. During the flight it is possible that the payload will not change its orientation much, even after separating from the booster. If the Z axis of the rocket stays close to the Earth's surface normal, then it is possible that the displacement due to GGT measured by the MEMS ES will be within its error limits. To obtain an Earth vector signal in this case, a second MEMS ES (MEMS 1b) is oriented at 45 degrees to MEMS 1a. The longitudinal axis of its elongated mass is in the YZ plane, but at an angle of 45 degrees to the Y axis. This will ensure that in case the payload is oriented with the Z axis almost vertical, the second MEMS sensor will have the largest possible displacement due to GGT.

Similarly, to measure yaw, the Earth sensor is placed in the XY plane such that the longitudinal axis of its elongated mass is parallel to the X axis (MEMS 2a). In such an orientation, due to GGT it will pivot around the Y axis and the displacement will be proportional to the yaw angle. A second ES (MEMS 2b) is oriented with the longitudinal axis of its elongated mass is in the XZ plane, but at an angle of 45 degrees to the X axis, to ensure a displacement due to GGT for the yaw axis.

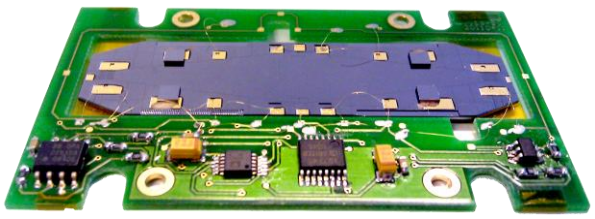

Figure 5. MEMS board showing the silicon micro-electro-mechanical sensor, and electronics to measure the displacement of the proof mass.

3. RESULTS

The GGES experiment has four MEMS sensors onboard. The sensors consist of a silicon proof mass sensitive to GGT, suspended from compliant springs. The dimensions of the spring can be modified in order to obtain springs of different compliance, resulting in different fundamental mechanical eigenfrequency.

On the GGES experiment, there are a total of four sensors, with frequencies of 3 Hz (1A), 8.5 Hz (2B), and 20 Hz (1B, 2A) as shown in Fig. 6.

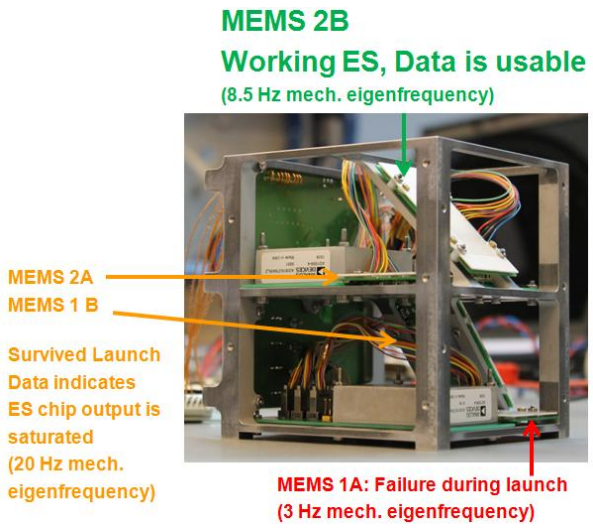

Figure 6. Performance of the various MEMS Sensors onboard the GGES experiment

- MEMS 1A - Failure at launch, the data indicates mechanical failure of the wirebonds, or the silicon springs. The wirebonds connect the silicon MEMS to the electronics.
- MEMS 1B and 2A – Data are recorded from these sensors during the entire flight. However the output is saturated, indicating that the effect of stress on the MEMS chip during launch results in the silicon proof mass getting stuck.
- MEMS 2B – Data recorded from this sensor indicate that it functioned nominally during the flight.

Fig. 7 shows the capacitance change recorded from this sensor along with IMU data for acceleration in rocket Z axis and rotation around rocket Z axis. A strong correlation is observed between the displacement of the proof mass and flight timeline events such as motor burnout, payload despin and start of re-entry as recorded by the IMU. MEMS 2B is a functioning inertial sensor.

The MEMS sensor records useful data only when the REXUS payload is in freefall. The IMU data is used to determine when the payload enters freefall.

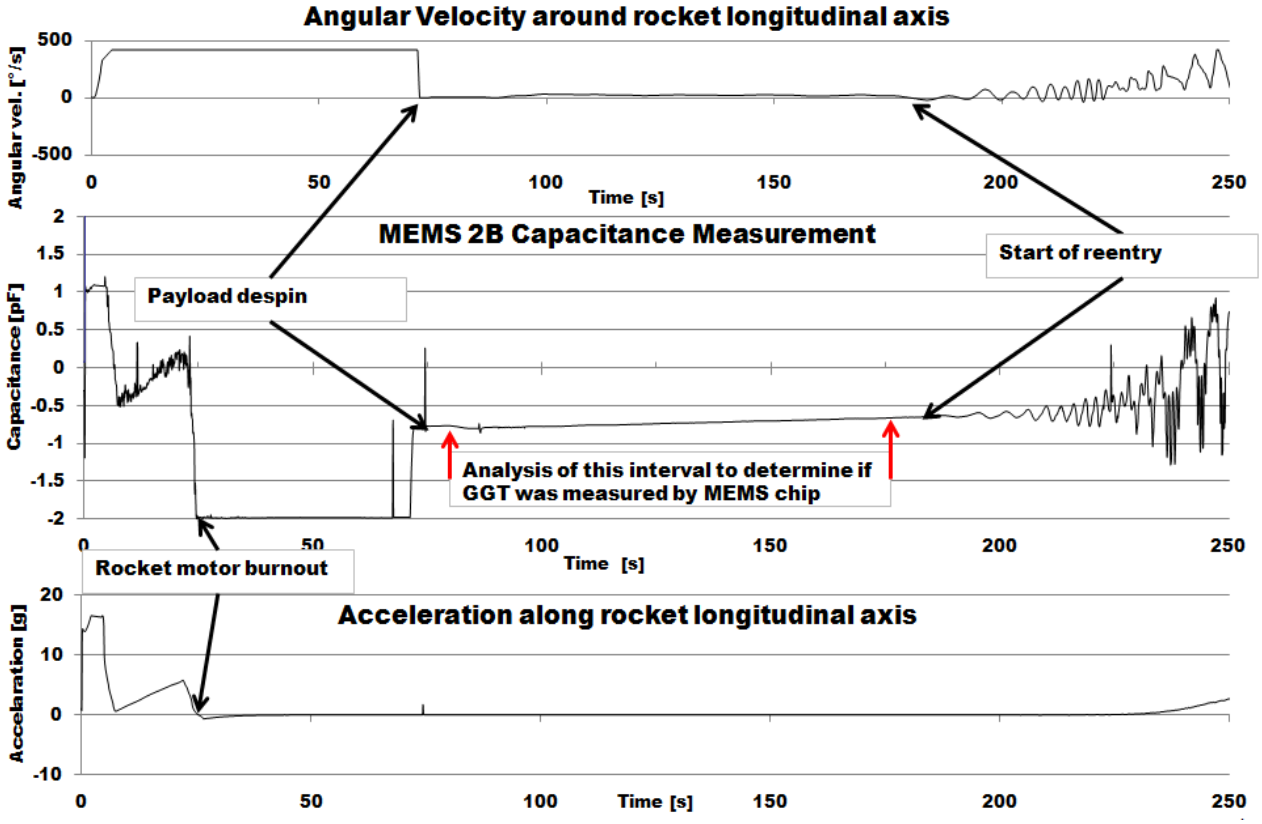

Figure 7. MEMS 2B displacement with IMU data from liftoff (LO) to LO+250 s

From Fig. 7, it is observed that motor burnout happens at ~25 seconds after LO, and the payload is despun at LO+ ~73s. During the operation of the motor and payload spin the change of capacitance of the MEMS sensor due to these external inertial forces is also indicated in Fig. 7. Events on other REXUS 11 experiments (Telescobe boom deployment, ADIOS imbalance generator) that cause an inertial perturbation on the payload are reflected in the data from the MEMS. Due to this, only data from LO+100s to LO+180s are considered. MEMS 2B is oriented such that any GGT sensed on it is due to the payload rotating about its Y (yaw) axis, as defined in the REXUS body frame reference. The IMU data for rotation about the yaw axis, measured with respect to the pitch axis (X axis of body frame) is used to determine the orientation of MEMS 2B during the freefall phase. The point at which the payload is despun is used as a reference to start computing the orientation of the payload, and therefore MEMS 2B during freefall.

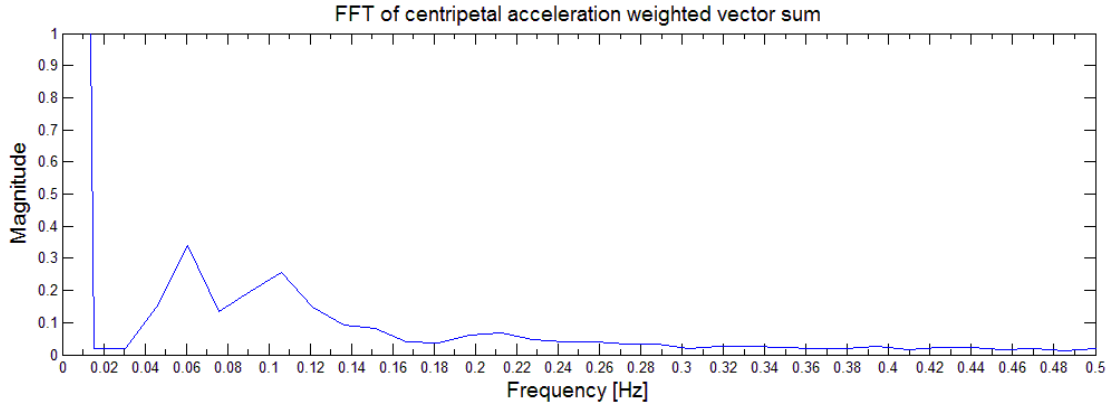

Figure 8. FFT of centripetal acceleration along REXUS roll axis during freefall; Peaks are observed at ~0.07 and ~0.11 Hz

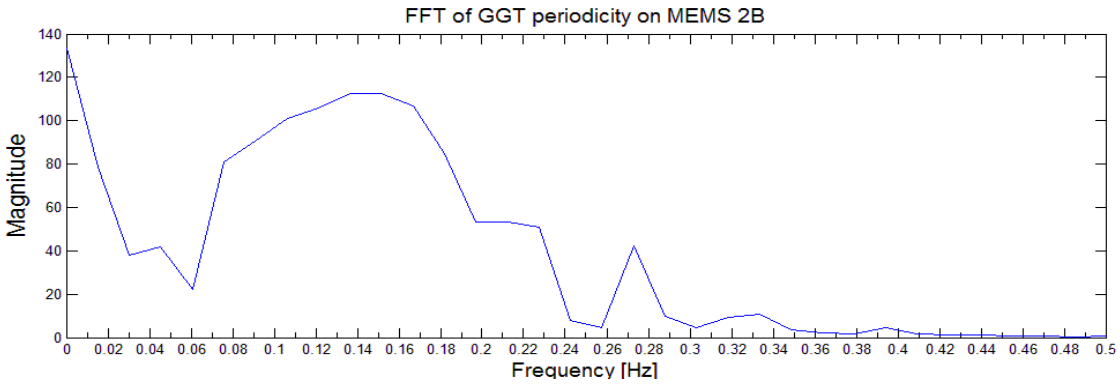

Figure 9. FFT of GGT periodicity; Peak at ~0.14 Hz

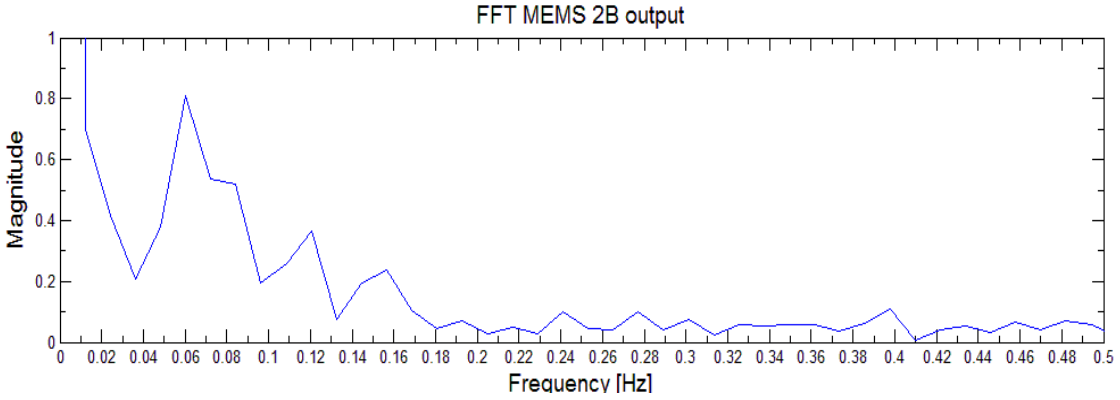

Figure 10. FFT of temperature drift compensated MEMS output from LO+100s to LO+180s; peaks at ~0.7 Hz, ~0.11 Hz and ~0.14 Hz

Fig. 8 shows the FFT of the magnitude of the centripetal acceleration as measured by the IMU from LO+100 s to LO+180 S, weighted by impact on MEMS 2B. Peaks are observed at ~0.07 and ~0.11 Hz. Fig. 9 shows the results of FFT on the GGT period of MEMS 2B as extrapolated from the angular displacement measured by the IMU on the pitch axis. Any GGT measured by the MEMS will have the same frequency distribution. The peak of the FFT is observed at ~0.14 Hz. Fig. 10 shows the FFT of the capacitance measured corresponding to displacement of the proof mass of MEMS 2B. There are peaks at ~0.7 Hz, ~0.11 Hz and ~0.14 Hz. This displacement can be due to centripetal force or GGT. The peaks observed at ~0.07 Hz and ~0.11 Hz in the MEMS 2B FFT correspond to the peaks observed for centripetal force along the roll and pitch axes.

The peak observed at ~0.14 Hz in the MEMS 2B FFT corresponds to the FFT of the GGT periodicity, and shows that GGT was measured by the MEMS chip during the REXUS ballistic phase post payload despin, and before re-entry.

4. CONCLUSION

The objectives of the GGES experiment were:
- Record the displacement of a MEMS proof mass due to GGT in free fall.

- Record the external rotational forces acting on the experiment.

- Record the external translational forces acting on the experiment.

- Post flight, from the displacement data gained, subtract errors estimated from the inertial environment information recorded during the flight and verify that the displacement of the Earth sensor corresponds to the GGT. Estimate the accuracy of the MEMS in measuring the Earth vector.

Even though only one out of four MEMS sensors functioned during flight, the first three objectives are met.

The frequency domain analysis shown in Figs.8-10 indicates that GGT was measured by the MEMS during flight. It also indicates that GGT measurement is possible using such a MEMS device even in an environment where there is significant tumble of the payload.

Due to the low signal to noise ratio of the GGT signal, a time domain analysis is not performed. Additionally an accurate reconstruction of the 6 axis motion of the MEMS based on 6 axis information provided by the IMU cannot be done accurately, due to the physical separation of the center of mass of the MEMS and the IMU reference point, and unknown distance with respect payload center of rotation. Hence it was not possible to estimate the accuracy with which the MEMS measures the yaw angle with respect to the pitch axis. For future work towards developing an Earth sensor based on measuring the gravity gradient, an improvement in the signal to noise ratio of the MEMS readout is necessary.

5. REFERENCES

[1] J.R. Wertz, W.J. Larson, Space Mission Analysis and Design, Kluwer Academic Publishers, Dordrecht, 1999

[2] Lunde B.K., "A Reliable Earth Sensor For Attitude Sensing" , IEEE Transactions on Aerospace and Navigational Electronics, Oct. 1963, Issue: 0 page(s): 3.6.4-1 - 3.6.4-6

[3] K. Ghose, "MEMS Inertial Sensor to measure the Gravity Gradient Torque in Orbit" Ph.D. dissertation, Institute of Microengineering, EPFL, Lausanne, Switzerland, 2012

[4] EuroLaunch REXUS User Manual (2010)

DEPLOYMENT AND CHARACTERISATION OF A TELESCOPIC BOOM FOR SOUNDING ROCKETS: REXUS-11

Dinesh Vather[(1)], Paul Duffy[(1)] Stephen Curran[(1)], Johnalan Keegan[(2)]

[(1)] Dublin Institute of Technology, Bolton Street, Dublin 1, Ireland, Email: spaceresearch@dit.ie
[(2)] Dublin Institute of Technology, Kevin Street, Dublin 8, Ireland, Email: spaceresearch@dit.ie

1. ABSTRACT

The upper atmosphere continues to be an area of significant interest to the scientific community. A common approach used in obtaining measurements in the upper atmosphere is the deployment of probes from sounding rockets. Payload designers continually strive towards smaller and lighter deployment mechanisms to achieve a lighter and more cost effective payload. Any reduction in the volume and mass of the payload results in a higher apogee and thus longer measurement times.

Currently a range of probes are used to take high resolution and accurate measurements of the upper atmosphere. To achieve these measurements the probes must be extended to distances in the order of metres from the sounding rocket. To meet this requirement folding boom structures are often used to extend one or more probes outside the rocket. While this technique has proven to be reliable it is not without its disadvantages. The folding nature of the boom structure adds considerably to the size, volume, design complexity and cost of the payload. Even in its folded configuration the length of the boom sections take up a considerable proportion of the payload.

The design of the Telescobe experiment yields a low cost novel method of boom deployment using telescopic carbon-fibre poles. The Telescobe experiment aims to reduce the mass, volume and cost required for such probe deployment systems whilst providing structural integrity comparable to those currently in use. This experiment was flown on-board the REXUS 11 sounding rocket in November 2012 from Esrange Space Centre in Kiruna, Northern Sweden. The boom was successfully deployed during the flight and performed nominally during the measurement phase. The success of the experiment was recorded by a camera-based measurement system which was developed to quantify harmonic deflection and determine the final boom deployment length. This approach to sounding rocket boom design showed itself capable of rapidly deploying a stable structure to a known distance with minimal harmonic deflection.

2. INTRODUCTION

Telescobe is an experiment, developed by postgraduate and undergraduate engineering students from the Dublin Institute of Technology (DIT), Ireland. The aim of the Telescobe project was to design, build and fly a telescopic boom system capable of being used to deploy E-Field and Langmuir probes for use in upper atmospheric research. A telescopic boom system potentially makes more efficient use of the available space and mass onboard a sounding rocket when compared with other boom systems.

The Telescobe experiment was first launched in February 2011 on the REXUS 9 sounding rocket. During this flight, the experiment hatch failed to open fully, resulting in the boom deploying against the inside of the hatch. A detailed discussion of this failure was presented in a previous paper [3].

The Telescobe experiment, with a modified hatch system, was subsequently granted a re-flight on the REXUS 11 sounding rocket. REXUS 11 was launched in November 2012 from Esrange space centre in Northern Sweden. During this flight the boom was successfully deployed from the experiment. The performance of the boom during this flight is the main focus of this paper.

The Telescobe experiment was developed as part of the REXUS/BEXUS programme. The REXUS/BEXUS programme is realised under a bilateral Agency Agreement between the German Aerospace Centre (DLR) and the Swedish National Space Board (SNSB). The Swedish share of the payload has been made available to students from other European countries through collaboration with the European Space Agency (ESA). Funding for the project was provided by the Dublin Institute of Technology, Enterprise Ireland, ESERO Ireland and Acra Control Ltd.

3. SCIENTIFIC BACKGROUND

Measurements of the Earth's magnetic field and the atmospheric plasma electron density are typically taken using E-Field and Langmuir probes respectively. To take accurate measurements, these probes are extended out from the spacecraft so that they are clear of any wake turbulence or electromagnetic fields created by the rocket. They can be used in single probe and multiple probe configurations. When used in a multiple probe configuration the relative positions of all the probes must be known for accurate measurements to be taken.

There are a number of different systems available to deploy these probes. Probes extended from

Proc. '21st ESA Symposium European Rocket & Balloon Programmes and Related Research', 9–13 June 2013, Thun, Switzerland (ESA SP-721, October 2013)

spacecraft by wires are compact and light weight. However the spacecraft must be spinning as centrifugal force is utilised for deployment. These probes are also prone to oscillation as they extend. Single rigid booms extended from spacecraft can support larger probes and are less prone to oscillation. However, this design does not lend itself to efficient use of the payload volume available. Folded booms are another option. However, they can also require a significant amount of storage space and the addition of hinges and motors also adds further mass and volume. A typical configuration using folded booms is shown in Fig. 1.

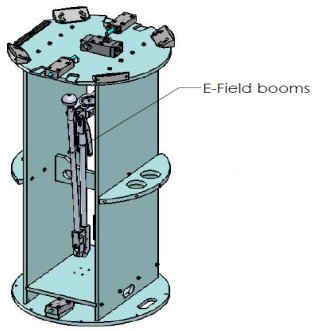

Figure 1: Typical folded boom sections for E-Field probes [2].

An effective telescopic boom system offers a more efficient use of the storage space and potentially a reduction in the overall mass. It can also take advantage of the centrifugal force generated by a spinning spacecraft to deploy, but it does not solely rely on this for deployment. By using a spring loaded configuration, the deployment time of such boom configurations is greatly reduced. This is ideal for short flight sounding rockets.

4. PROJECT AIMS

The primary objectives of the Telescobe project were:

- To design and build a telescopic boom, boom deployment and boom jettison system.
- To safely test this system on a near-space flight aboard the REXUS 11 sounding rocket [1].
- To monitor and record boom deployment length, boom vibration characteristics and boom jettison.
- To collate, analyse and disseminate experiment data via presentations and publications.
- To promote the activities of the Telescobe team, DIT and the REXUS/BEXUS program through an outreach program.

Performing electric field measurements did not fall within the scope of the experiment. Instead the probe fitted to the distal end of the boom housed an accelerometer and six LEDs. This probe was used as the datum point for measurement.

5. EXPERIMENT OVERVIEW

The Telescobe module, shown in Fig. 2, is 220 mm in height and has an internal diameter of 348 mm. An exploded view of the experiment can be seen in Fig. 3. The boom is made from tapered carbon fibre sections and, during the flight it is stored in a PEEK housing inside the module. When it is full extended, the boom is approximately 1700 mm long. A foam cap is used to prevent the boom from being damaged by excessive vibrations during lift-off. Additionally, the experiment consists two measurement cameras for measuring the deployed length of the boom and the magnitude of any boom deflections during the flight, an observation camera for providing real time video feedback of the boom when it is deployed, a hatch in the skin of the experiment module and various electronic and software systems for experiment control and data acquisition. A detailed description of the experiment design was presented in a previous paper [3].

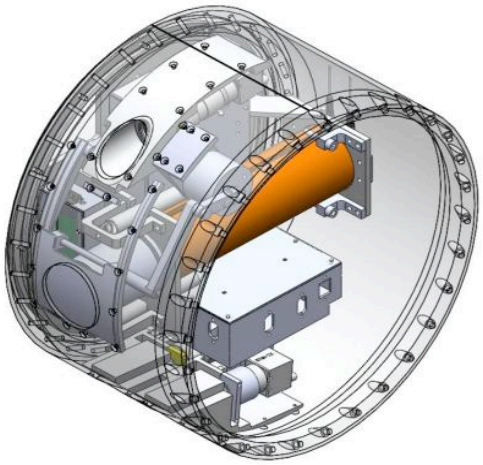

Figure 2: The complete experiment module

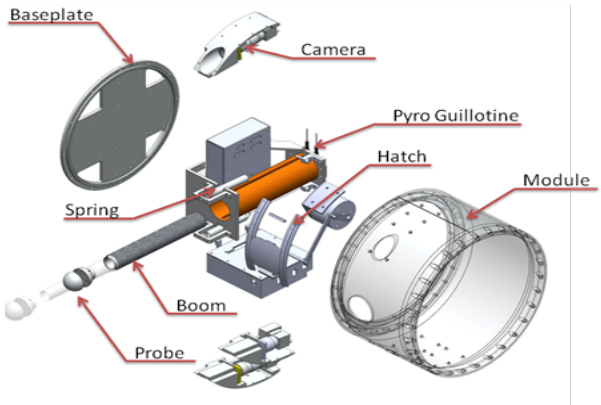

Figure 3: An exploded view of the experiment module with important components labelled.

At a designated time during the flight, the hatch in the skin of the experiment opens. Six seconds later, a pyrotechnic guillotine fires, cutting a nylon cable that retains the boom in its stored position. Two tension springs on either side of the boom housing then deploy the boom out through the hatch. The foam cap is pushed out with the boom and then falls away from it as it is in three sections.

When the boom is deployed, cameras are used to measure its length and an accelerometer is used to quantify any vibrations. After the payload has gone past the flight apogee, a second pyrotechnic guillotine fires, cutting a nylon cable that secures the base of the boom to the experiment. The remaining tension in the two springs then jettisons the boom from the experiment. The boom falls to ground and the hatch closes, preventing hot air from entering the module during re-entry. The timeline for the experiment during the flight is shown in Table 1.

#	Event	Time (s)	Altitude (km) Approx.
1	Lift-off	0	0.3
2	Motor Separation	77	~ 64
3	Hatch Opens	80	~ 67.0
4	Boom Deploys	86	~ 69.0
5	Apogee	139	82.31
6	Boom Jettisons	225	~ 61.0
7	Hatch Closes	232	~ 58.0
8	Power Switched Off	600	~ 35.0

Table 1: Experiment timeline

5.1. The Modified Hatch

The original hatch for the Telescobe experiment was actuated by a solenoid. This failed to open fully during the flight of the experiment on REXUS 9, causing the boom to deploy against the inside of the hatch door. As such, the hatch was modified for the re-flight of the experiment on REXUS 11. An exploded view of this modified hatch assembly is shown in Figure 4. The hatch design consists of a 12 Watt brushless motor and a planetary gearbox (reduction ratio of 690:1) housed inside an aluminium sleeve. The combination of the planetary gearbox and brushless motor is capable of generating approximately 250 times more torque for hatch actuation than the original solenoid. The planetary gearbox is not back-drivable and its shaft is connected to the hatch through a set of armatures, consisting of a short "S" shape armature and long armature. The short armature is above a pair of inductive sensors, which provide feedback to indicate whether the hatch is opened or closed. An additional printed circuit board (PCB) is also included in the experiment module for controlling the hatch.

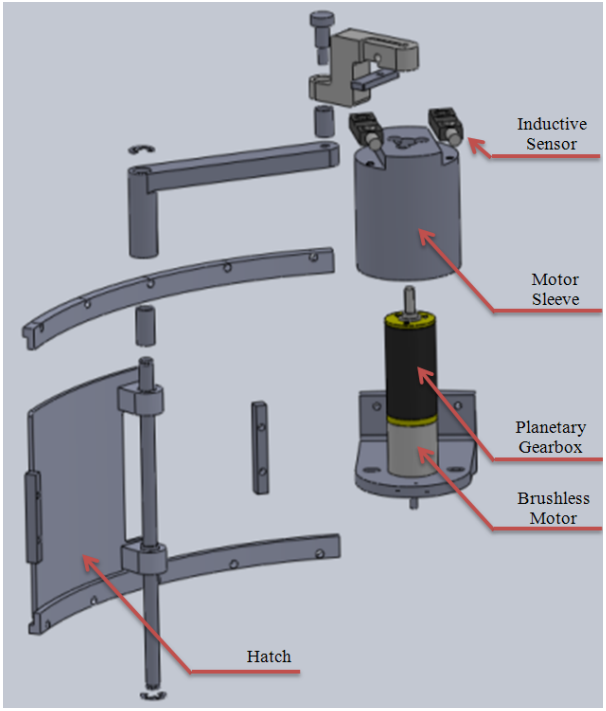

Figure 4: Exploded view of the experiment hatch assembly

6. THE FLIGHT

The Telescobe experiment was launched on the REXUS 11 sounding rocket from Esrange Space Centre in Northern Sweden in November 2012. An image of the experiment ready for final payload integration is shown in Figure 6.

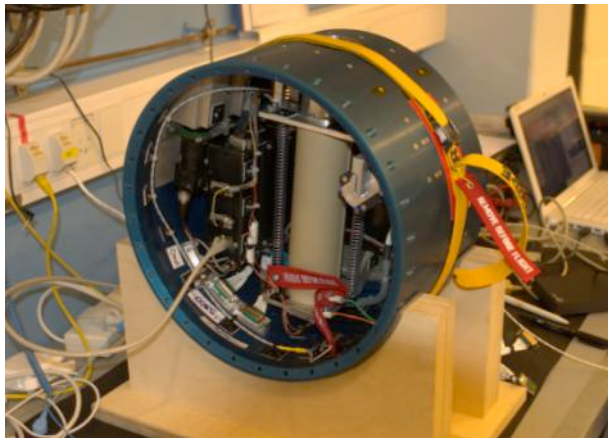

Figure 6: The Telescobe module ready for final payload integration

An issue with the experiments PC/104 flight computer during the flight meant that the telemetry stream to the

ground station and the data from the accelerometer in the distal end of the boom were lost. Otherwise, the flight was nominal.

7. RESULTS

The boom was deployed successfully from the experiment module, as shown in Figure 8 and Figure 10. The video file recorded from the measurement cameras during the flight was recovered from the experiment and analysed to determine the deployed length of the boom and the magnitude of any boom deflections. A sample frame extracted from this video file is shown in Figure 12. From analysis of this video file the boom was found to have deployed in less than 1 second to a length of 1708.3 mm during the flight and remained within the confines of the measurement resolution (±6mm) for as long as it was possible to verify (i.e. until 100s after boom deployment). This indicates that all of the boom sections locked out correctly and that the boom was rigid.

Figure 8: The boom deploying at T+86s. The image shows that the three section of the probe protector were successfully thrown clear of the boom deployment.

Figure 10: The telescopic boom deployed from the experiment module 12 seconds after boom deployment.

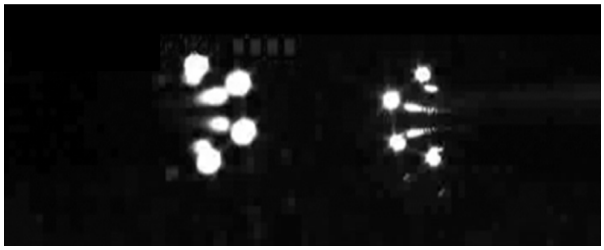

Figure 12: A frame extracted from the measurement camera video file.

Boom deflection data was also extracted from the measurement camera recordings. Figure 14 shows the deflection of the distal end of the boom in an axis parallel to a plane between the X-axis and Y-axis of the payload (i.e. left-right). Figure 16 shows the deflection of the boom in an axis parallel to the Z-axis of the payload (i.e. up-down). From both graphs it can be seen that the maximum deflection of the probe at the distal end of the boom did not exceed 5mm in any direction during the first 90s after boom deployment. In fact, for most of this period boom deflection did not exceed 2mm. There are small gaps in both graphs between 20.0s and 22.4s and between 26.1s and 27.5s. These were periods when the measurement cameras were pointing towards the sun and no clear picture was available. It was not possible to obtain deflection data for these periods.

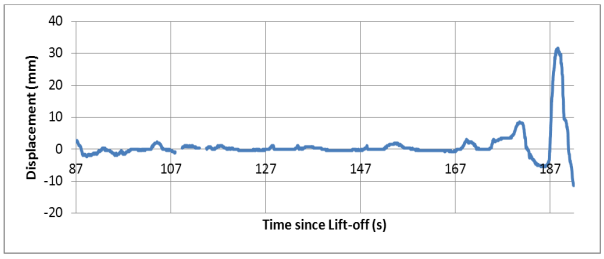

Figure 14: Displacement of the distal end of the boom in an axis parallel to a plane between the payload X-axis and Y-axis during the first 105 seconds after boom deployment.

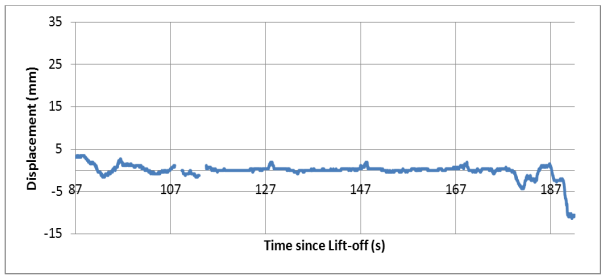

Figure 16: Displacement of the distal end of the boom in an axis parallel to the payload Z-axis during the first 105 seconds after boom deployment.

From ~T+175s onwards it can be observed from both graphs that the magnitude of boom deflection began increasing significantly. This deflection was such that the probe began to move outside the field of view of the measurement cameras after T+192s, hence making it impossible to measure boom deflection after that point. However, it is known that boom deflection eventually increased to such an amount that the boom finally fractured three seconds before it was due to be jettisoned at T+225s. Figure 18 and Figure 20 depict images taken from the observation camera feed during this time.

Figure 18: The boom deflecting at T+221s

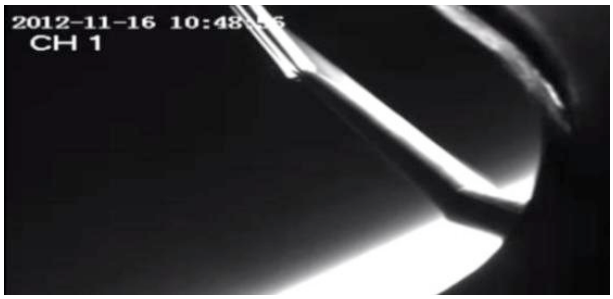

Figure 20: The boom breaking at T+222s

8. CONCLUSION

Overall the experiment can be deemed a success. The problem encountered during the launch of the original Telescobe experiment on REXUS 9 (namely the non-functional hatch) was overcome and the boom was successfully deployed from the experiment module. While some problems with the flight computer were experienced during the flight, measurement camera data was recovered successfully for post flight analysis. The carbon fibre, telescopic boom performed well during the flight. It deployed and settled quickly at T+86s and remained stable until T+177s, a period of time that took it through the apogee of the flight. The boom broke then due to the aerodynamic froces acting on it three seconds before it was due to be jettisoned at T+225s. However, had the boom been jettisoned earlier, closer to the apogee of the flight, this eventual breaking of the boom would have been avoided. Overall, this boom system has shown itself to be particularly suited for use on sounding rockets where the fast deployment time lends itself to the short payload flight time.

9. REFERENCES

[1]. Eurolaunch. "REXUS User Manual v7". December 2011. Available at: *http://www.rexusbexus.net*

[2]. Helge, L,.Hansen, G,. "*New flight qualified payload by Andoya Rocket Range*". ESA- PAC 19th Symposium, Bad Reichenhall, Germany, June 2009.

[3]. Keegan, J. et. al. "*Deployment and characterisation of a telescopic boom for sounding rockets". ESA-PAC20th Symposium, Hyères, France, June 2011.*

STRATHSAT-R: DEPLOYING INFLATABLE STRUCTURES FROM CUBESATS IN MILLI GRAVITY

Iain Dolan[(1)], Thomas Sinn[(2)], Ruaridh Clark[(3)] , Nathan Donaldson[(4)], Christopher Lowe [(5)], Daniel García Yárnoz[(6)], Roy Brown[(7)], Thomas Parry[(8)], Stanislas Bertrand[(9)]

[(1)] Electronic & Electrical Engineering Department, University of Strathclyde, Glasgow, United Kingdom, iain.dolan@strath.ac.uk
[(2)]Advanced Space Concepts Laboratory, Mechanical and Aerospace Engineering, University of Strathclyde, United Kingdom, thomas.sinn@strath.ac.uk
[(3)] Mechanical & Aerospace Department, University of Strathclyde, United Kingdom, ruaridh.clark@strath.ac.uk
[(4)]Mechanical & Aerospace Department, University of Strathclyde, Glasgow, United Kingdom, nathan.donaldson@strath.ac.uk
[(5)]Advanced Space Concepts Laboratory, Mechanical and Aerospace Engineering, University of Strathclyde, Glasgow, United Kingdom, christopher.lowe@strath.ac.uk
[(6)] Advanced Space Concepts Laboratory, Mechanical and Aerospace Engineering, University of Strathclyde, Glasgow, United Kingdom, daniel.garcia-yarnoz@strath.ac.uk
[(7)] Electronic & Electrical Engineering Department, University of Strathclyde, Glasgow, United Kingdom, roy.brown@strath.ac.uk
[(8)] Electronic & Electrical Engineering Department, University of Strathclyde, Glasgow, United Kingdom, thomas.parry@strath.ac.uk
[(9)] Electronic & Electrical Engineering Department, University of Strathclyde, Glasgow, United Kingdom, kbb12174@uni.strath.ac.uk

ABSTRACT

The StrathSat-R experiment is a student-led sounding rocket experiment to test novel inflatable structures in space conditions. This experiment is the first step in what will be the first Scottish university satellite program. A multidisciplinary team of over 25 undergraduate and graduate students was formed to design, build and test the experiment between June 2011 and the REXUS13 (Rocket-borne Experiments for University Students) launch in early May 2013. The student team is part of StrathSEDS, a subdivision of UKSEDS (UK Students for the Exploration and Development of Space) and led by a core team of six students. The experiment aims to test novel inflatable space technology in milli-gravity and micro-pressure conditions. It consists of three distinct sections, the ejection housing on the rocket and two ejectable modules that are based on a CubeSat architecture measuring 10x11x13 cm^3. Shortly before reaching apogee, the two satellites are ejected from the rocket and will deploy their individual inflating structure during free flight. After landing, the ejectable modules will be recovered by using a GPS (Global Positioning System) beacon and an RF (Radio Frequency) beacon. The two modules carry two different structures resulting in distinct mission objectives. The aim of FRODO (Foldable Reflective system for Omnialtitude De-Orbiting) is to deploy a large, conical reflective sail from a small volume (4x10x10 cm3). This is the first step in the technology development of a passive de-orbiting system for high altitude spacecraft which will in the future utilise solar radiation pressure, the J2 effect and aerodynamic drag. The objective in the REXUS experiment is to test the inflation space conditions, to validate the shuttlecock attitude dynamics and to assess the structural behaviour of the device during re-entry. The aim of SAM (Self-inflating Adaptive Membrane) is to serve as a technology demonstrator for the residual air deployment method with a bio-inspired cell design approach. The unique architecture of the membrane sub-structure opens the possibility of changing the shape of the membrane to be adapted to various space mission stages or environmental conditions. Proving this concept in micro-gravity conditions will open the door for future space structures serving multiple purposes. On the 9th of May 2013, the StrathSat-R experiment was launched onboard the sounding rocket REXUS 13 but failed to be ejected due to a procedure error.

1 INTRODUCTION

The purpose of StrathSat-R was to deploy two cubesat like structures with inflatable payloads that act as technology demonstrators for two concepts.

The first of these concepts is an SRP (Solar Radiation Pressure) augmented de-orbiting system that has developed through research undertaken by the University of Strathclyde's Advanced Space Concepts Laboratory. This was an ERC (European Research Council) funded project which investigated highly non-Keplerian orbital dynamics and applications. The de-

Proc. '21st ESA Symposium European Rocket & Balloon Programmes and Related Research', 9–13 June 2013, Thun, Switzerland (ESA SP-721, October 2013)

orbiting concept utilises solar radiation pressure and the J2 perturbation to passively increase the eccentricity of an initially circular orbit until the perigee is affected by drag and the spacecraft de-orbits. This technique is particularly effective in MEO (Medium Earth Orbit) but can be applied to even higher altitudes. After the deployment of the reflective sail the de-orbiting manoeuvre takes place completely passively. This research could open up new high altitude orbital regimes for future pico- and nano-satellite missions. A conical (or pyramidal as developed here) structure is needed to exploit the shuttlecock-effect which passively maintains the spacecraft in a sun-pointing position.

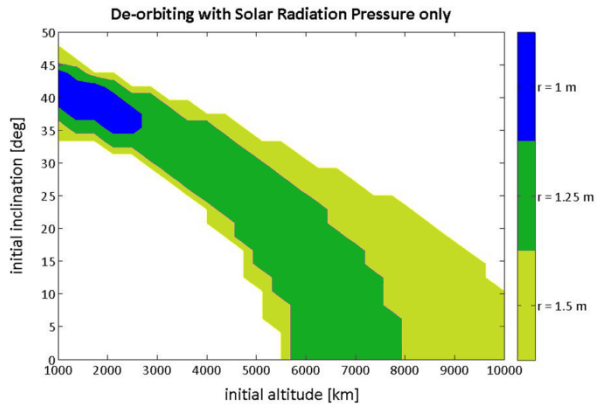

Figure 1: Regions in which a 1U CubeSat (1.3 kg) can be deorbited using solar radiation pressure only from an initially circular orbit using a reflective cone of given maximum cross-sectional radius (r)

The results of this research for orbits in the lower MEO regime [1] are shown in Fig. 1. It can be seen that a 1U CubeSat with a deployable reflective cone of around 1.2m radius can de-orbit from high altitude circular orbits with a range of different semi-major axes and inclinations. One aim of this REXUS experiment was to show that such a device could be manufactured and implemented at a low cost and by students. This will hopefully pave the way for a follow up satellite mission to demonstrate the principle in orbit.

The second concept is an inflatable membrane with the capability to change its shape in orbit. This concept is driven by the constraints that are placed on space vehicle size due to launch vehicles dimensions. These constraints make the use of deployable structures necessary with their low stowage and high in-orbit volume. For the success of future space missions involving large space structures, the development of new deployable structures and the improvement of current designs are of great importance. Applications can be easily envisioned through truss structures, masts, crew quarters, transport tunnels, large solar arrays, solar concentrators, solar sails, balloons or antennas. [2]

Various research has been undertaken in the development of ultra-lightweight deployable structures from which it has been crystallised that the use of inflatable structures is a very promising approach for the middle to long-term development of space structures. [3] Over the last 50 years, research has been conducted at various institutions all over the world in the field of inflatable structures; new membrane materials have been discovered that can withstand the space environment, advanced simulation tools were developed that capture the highly non-linear behaviour of the inflation process and rigidisation techniques have been investigated making the structure non-reliant on the inflation gas after deployment.[4]

Developed for this experiment was a cellular element structure, which has an advantage over traditional single element structures as it can exhibit both stiff and flexible properties. This effect is produced by the rigidity of the pillows combined with the flexible seam lines resulting in the ability to hold the structure in a fixed position and to reconfigure the structure. The second goal of this endeavour was to develop a structure that could be used to adapt itself to various environmental or mission conditions. For example, the structure could serve as a substructure for a solar concentrator and adjust its focal point autonomously by changing the curvature of the entire surface. By achieving an adaptable structure the number of possible applications becomes almost limitless. [5]

2 MISSION OUTLINE

The StrathSat-R experiment consists of three distinct sections; two ejectable modules and one data storage with ejector assembly that stays on the rocket and expels the experiments. The first ejectable module (FRODO) deploys an inflatable reflective sail, which represents the first step of development for a CubeSat de-orbiting device which utilises solar radiation pressure. The second ejectable module (SAM) deploys an inflatable membrane which will transfigure in flight, as a step towards a smart structure which adapts its shape to various environmental conditions. These two modules are ejected from the rocket after de-spin near to apogee, which was 83km for REXUS 13. After which the structures should have inflated passively using residual air inflation. The inflation is filmed initially by both the cameras on-board the rocket and those on the modules. During the whole flight images of the structure were to be taken and stored on SD cards in the ejectable modules. Once the modules reached an altitude of around 5 km the timeline was to trigger an event which was the release signal for the parachutes on both modules. This signal shall also activate the tracking system with GPS positions relayed through a modulated signal from a VHF (Very High Frequency) antenna, which would also act as an RF beacon for

tracking by the recovery helicopter. At this stage data should be recovered from SD cards on all three sections of the experiment, which shall be post-processed to recover the images.

2.1 Mission Objectives

Ejectable Module 1: Foldable Reflective system for Omnialtitude De-Orbiting (FRODO)

1) Test deployment of the device in milli-gravity and near-vacuum conditions. (primary objective)
2) Test the passive attitude control. (secondary objective)
3) Observe the structural integrity of the device during the re-entry when ambient pressure rises. (secondary objective)

Ejectable Module 2: Self-inflating Adaptive Membrane (SAM):

4) Observe deployment behaviour of the full size membrane from the module in a space environment (primary objective)
5) Alter shape of the membrane autonomously without the influence of perturbing gravitational forces. (secondary objective)

3 DESIGN

3.1 Mechanical

The mechanical design of StrathSat-R is based around the three main subsystems; the SHIRE (Storage Housing In Rocket for Experiment), SAM and FRODO that can be seen in Fig. 2. The SHIRE provides the structural support and necessary elements for retention during launch and jettison of SAM & FRODO in space. The structure is largely machined from Aluminium 6082-T6, with electronic components, PCBs (Printed Circuit Boards), steel machine elements, Perspex covers and Polyimide camera windows forming the rest of the assembly.

The loads experienced during launch are transferred to the experiment module skin via the D-Brackets and hatch reinforcement blocks. Upon ejection of SAM and FRODO, the experiment is exposed to the environment. Therefore Perspex snow covers are incorporated to prevent excessive ingress of debris during the landing phase.

The ejectable modules are segmented into three regions; one housing the subsystem electronics, one housing the deployable experiments and a third housing a parachute required for safe descent and landing. A loosely fitting lid panel is incorporated in order to enclose the deployable payload during launch, but is free to jettison upon ejection of the modules. It is held in place during launch by the compressive action between the hatch assembly and the spring platform.

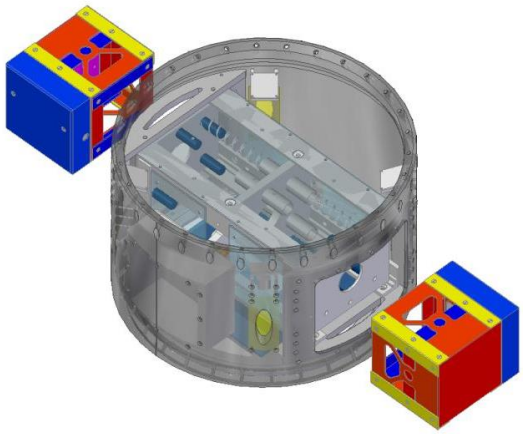

Figure 2: Isometric view of experiment after ejection (hatches not displayed)

Mounting of the electronics within the ejectable modules is achieved by strapping two SAFT batteries securely against the plate that separates the payloads from the electronics enclosure. The PCBs fill the remainder of the space in the electronics enclosure, where they are spaced using anti-vibration spacers.

3.1.1 Retention and Ejection System

As described previously, the SHIRE remains in the rocket module throughout flight and housing both experiments and provides the ejection platform. The team leaned their design on the proven REXUS11 RAIN ejection system to use a module for ejection rather than the nose cone position on the rocket. This design has the advantage that it can deploy the two cubesats simultaneously and symmetrically from the rocket. The retention mechanism employed previously for this type of ejection was to make use of a groove that was cut in the full circumference of the outer skin of the rocket, in this groove a retention cable is ran which holds the hatches in place. Pyro cutters are then used to severe the cable and the devices are ejected. During the design phase, Eurolaunch expressed concerns about the structural effect that cutting the groove in the rocket had. Based on this, the StrathSat-R team, with input from Eurolaunch, developed a new method of retaining and ejecting the cubesats from the rocket.

The route for the cable is shown in Fig. 3 the main change is the removal of the groove. Instead the single cable is entirely within the rocket and is routed through the hatch blocks and secured at both the tensioner and the rocket wall. The cable runs through two pyro cutters, the reason being that if one fails the cubes will

still be ejected. The cable has a stopper connected to it within each of the hatch blocks, the purpose of this is to ensure that all of the cable is removed from the rocket upon ejection as it is pulled out with the hatches.

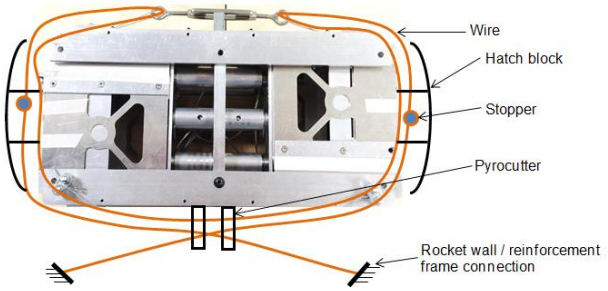

Figure 3: Retention Cable Route Highlighting Tensioner Position and Stoppers

In order to develop this system, constant feedback was required from Eurolaunch at every stage as well as thorough testing. A problem identified through vibration testing was a slip that occurred between the hatch and the hole in the rocket skin. The solution to this was to cut a lip on the inner surface of the skin where it met with the hatch. This resulted in the hatch being inset in relation to the skin of the rocket and so slip could not occur. Fig. 4 shows the slip that occurred prior to the correcting measures were taken.

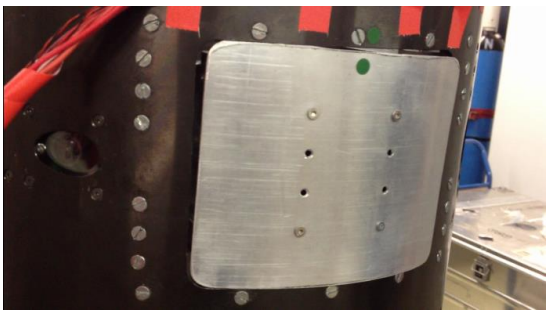

Figure 4: Hatch Slip after Vibration Testing

The retention system uses two TRW pyro cutters as they were to be operated by Eurolaunch from the RXSM (REXUS Service Module) and therefore had to adhere to the interface and component requirements set by them. The force for ejection is provided by eight springs (four for each payload) which are compressed by the retention system and are arranged to provide an even force to the base of each cubesat.

3.2 Payloads

3.2.1 FRODO

FRODO's payload consists of a self-inflating pyramidal structure that deploys from the module using residual air inflation in partial vacuum conditions once the module is ejected from the rocket (Fig. 5).

Figure 5: Manufactured FRODO Payload

Residual air inflation occurs when small pockets of air are allowed to grow in volume due to the lack of external pressure.

The inflatable structure is a square-based pyramidal sail of base length 1.772 m and height 0.512 m, see Fig. 5. A pyramid of this side length has a reflective surface area of 3.628 m^2, which is equivalent in performance to a cone of radius 1m, shown in blue in Fig. 1. This is the smallest structure which can de-orbit a 1.3 kg CubeSat effectively at altitudes just below 3000 km.

The pyramid is comprised of eight separate and independent booms along the edges of the structure, and a reflective sail on the triangular faces of the pyramid. The square-based pyramid introduces redundancy in the base booms, where one can be deflated and the structure maintains its general shape. A partial or total deflation by a leak of one of the oblique booms may introduce deformations in the shape of the structure, but it is still an improvement from having all the booms interconnected, which could result in total failure if a leak occurred.

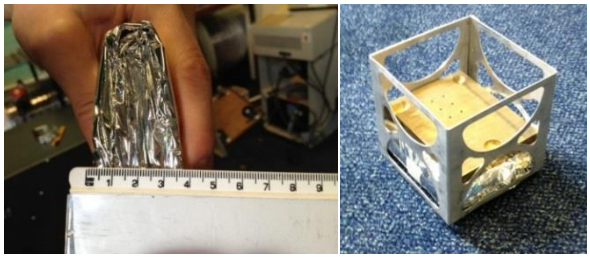

Figure 6: Packaged FRODO Payload

FRODO is a passively deployed structure, with no actuators in its design. The structure is deployed and its shape maintained by the inflated booms. The structure can therefore be packed very efficently, Fig. 6 shows the packed FRODO payload in the CubeSat prototype.

3.2.2 SAM

SAM [6] consists of an array of 18 inflatable circular cells in two rows. The diameter of the spherical

elements is chosen to be 14.5 cm to fit the storage box of 10 cm by 10 cm in the central sphere. The spheres are manufactured from 12micron thick, reflectively aluminized, Polyethylene Terephthalate (PET) which is sealed with adhesive on the cell's circumference. Fig. 7 shows a screen shot from an LS-DYNA simulation of the inflated 36 spheres of SAM.

.

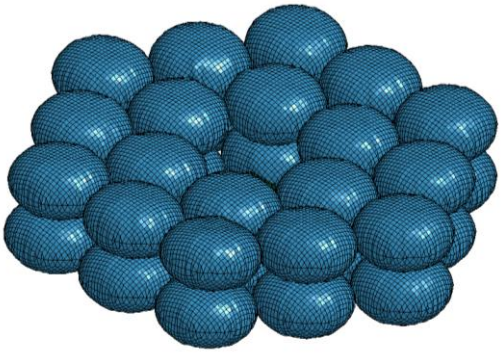

Figure 7: SAM with deployed structure (module to be placed in centre)

The experiment has two main stages, the deployment phase and the adaptive phase. After ejection from the rocket has been achieved, deployment begins as the inflatable structure is exposed to the atmosphere. The deployable structure of SAM is deployed by using the expansion of trapped air in the spheres when subjected to vacuum (space) conditions

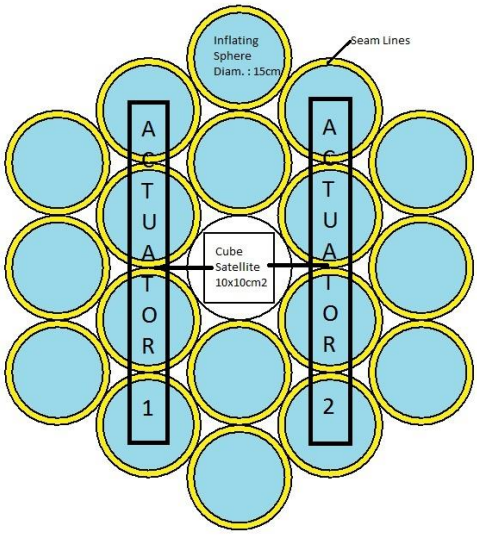

Figure 8: Top view on SAM with actuator placement

In order to make SAM change it's shape, four cells to the left and to the right of the cube are joined to form a larger actuator cell. These cells are connected to a pump in the cube via tubes. In the adaptive phase pump from the bottom array is getting pumped into the top array to deform the structure.

3.3 Electronic

The system architecture is based around three core modules which are replicated for each section in the experiment. The modules within the system are broken into; power, data handling and tracking. Each subsystem is located on its own PCB in keeping with the modular design process as well as providing EMI isolation, a necessity when using high speed digital logic and RF circuitry within the same design.

The power PCBs are identical for each of the ejectables and consist of a battery charging circuit and connectors to SHIRE and other PCBs within the module, each cable is twisted to ensure further reduction in EMI. The SHIRE module's power board consists of power filtering to meet EMC conductivity requirements and high quality switching regulators to regulate the sounding rocket's 28 V supply to appropriate power rails. The tracking PCB is identical in both the ejectable units and consists of local power conditioning, GPS, Globalstar and RF beacon circuitry. Tracking is not needed in the main unit, SHIRE, as that will remain part of the recovered rocket. The data handling PCB contains a microcontroller, FPGA and I/O support circuitry. The data handling PCB is adaptable to the variety of sensors that had originally been specified for the design but were later dropped due to reduction in scope to ensure the success of the design. During manufacture only those components needed for each module will be populated which lowers PCB design and manufacture cost.

3.4 Embedded Software

The software was developed using the MBed NXP LPC 1768 Microcontroller Unit (MCU). It utilises an ARM Cortex M3 and is a robust and flexible development unit for use in each module.

The entire development board is included on the surface of the flight computer PCB using headers. This approach was chosen to allow a modular approach to be taken to developing embedded software for subsystems, to allow flexibility, and lower design complexity.

There are not enough inputs and outputs provided on the development platform to support the intended applications alone, therefore an 8-channel I^2C multiplexer, and a 16-bit SPI multiplexer has been used. The I^2C multiplexer allows a single I^2C interface to communicate with 8 different I^2C devices. The SPI multiplexer serves to increase the number of digital I/O pins.

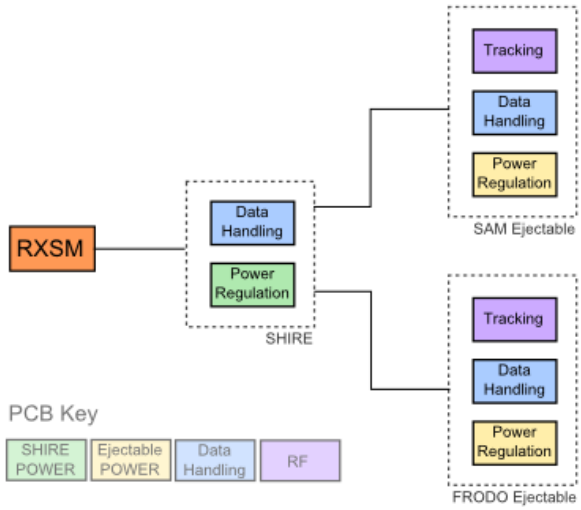

Figure 9: Electronic System Architecture

A basic block diagram of the electronics is shown in Fig. 9, this details the link between the three systems built by StrathSat-R and the interface to the RXSM. This diagram displays the modular nature of the design as it can be noted that the ejectables are identical and the data handling is replicated across all three systems.

3.5 Data Handling

The original design for StrathSat-R envisaged a system that would utilise two cameras per module and four on SHIRE. As the project developed the implementation of the cameras selected fell behind and with further pressure on ensuring a minimum level of functionality to ensure launch, the decision was taken to remove the cameras being developed and replace them with a COTS version. The selected replacement was the HackHD as it features a wide angle lens, includes all software and hardware on a single board, wrote to a micro SD card onboard and required a simple push button to activate. Also of benefit is an output line is used to activate an LED, this line was used to confirm the status of the camera as it had two modes, recording and stand by. In order to ensure successful storage of the footage to the SD card it is required that the camera is switched off and the command line and given time to save the data. If this is not allowed to happen then the data can be lost or prove difficult to recover. For this reason the cameras are switched off before impact to ground on both the SHIRE and on the two modules. The cameras on SHIRE are also cycled during descent to ensure at least the critical section of footage, the modules ejection, has been saved.

3.6 Experiment Timeline

The flight computer has to interface with the service module, of the sounding rocket, which will provide signals to notify the experiment of lift-off (LO) and start of experiment (SOE). At T-600s before launch the experiment was powered on and entered its timeline mode. The SOE signal was sent at T-115s and was used to synchronise all timelines. At T-20s prior to the LO signal the SHIRE cameras were activated. This was to take footage of the ascent of the rocket as well as the ejection of SAM and FRODO. If no LO was given after this then after 40s the system would enter a standby mode that turned the cameras off and awaited LO, this was to save memory on the SD cards. When LO is given the timeline has entered its full flight mode.Once the experiments are ejected, at T+140s, they will use their own internal timelines, with SAM aiming to perform shape changing manoeuvres for approximately one minute before switching the cameras off while FRODO's cameras are left on till after the parachute's deployment. At T+965s the microcontroller will trigger the pyro cutter to release the parachute and also switch from the data board to the RF board. The GPS data will also be modulated to a carry and transmitted via the VHF antenna that will be exposed once the parachute is unfurled.

3.7 Tracking & Recovery

The tracking and recovery stage of the mission is triggered by the timeline, which activates a pyrocutter. This severs a tensile retention wire, releasing the parachute enclosure lid. A spring and spring loaded RF beacon will then assist in removing the lid, allowing the parachute, which is fastened to the four corner screws, to unfurl. As simple method has been employed to actuate the RF beacon, this is to attach a bi-stable material (in this case a small section of measuring tape) to the beacon. When the retaining force provided by the lid is removed the beacon will experience a restoring moment due to the tape measure and then rotate into a vertical position in order to achieve an optimal gain pattern. After the parachute is deployed, the GPS receiver and RF beacon activate and continue to relay GPS coordinates to the team continuously until recovery. Fig. 10 shows the layout of the devices that have been described here.

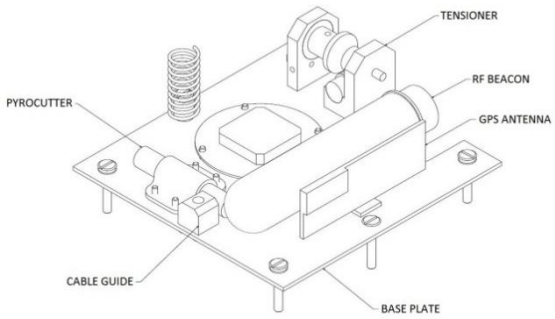

Figure 10: Drawing of the devices stored inside the parachute enclosure

4 LAUNCH CAMPAIGN

The REXUS13/14 launch campaign took place at Esrange from the 30th of April until 10th of May 2013. The first days were spent on experiment integration and systems tests. During the final integration of the experiment at the launch campaign several issues arose. The first was an unexpected issue with the pyrocutters used in the parachute deployment, due to a high amplitude transient at power on, the pyrocutter blew and had to be replaced. To correct this, capacitors were used on the line to smooth the transient and reduce the amplitude to a safe level, after testing this correction proved successful.

Electrical transients in the circuitry affected the microcontrollers and resulted in damage occurring to two of the three that were in the system, replacements were implemented and further protection built in to ensure new damage would not occur.

With these corrections in place the experiment was passed for launch and successfully completed all communication checks and timeline runs.

StrathSat-R was launched on REXUS 13 on the 9th of May and all systems worked nominally during countdown and flight. Continuous data was received on the ground station indicating a fully functional experiment at all times. However, due to a procedure error by Eurolaunch, the two cube satellites were not ejected from the rocket at apogee. The REXUS13 payload was recovered by helicopter with both cubes still tensioned inside the rocket.

5 RESULTS AND LESSONS LEARNED

Although the modules were not deployed, multiple lessons were learned from the launch campaign. The rocket launch showed that some systems can be improved to ensure more scientific return. The first improvement will be made to the deployable of FRODO. Due to an oversized deployable, the hatch did not fit perfectly which resulted in surface melting of the FRODO deployable due to entering hot gases during launch. To solve this issue a smaller deployable and a Kapton cover is suggested. This cover will be also used for the deployable of SAM. Furthermore it is suggested to implement a working Globalstar system to increase redundancy and therefore the chance of locating the ejectables after landing. The problems with the MBed microcontrollers during the launch campaign indicated that a more reliable microcontroller should be chosen. The MBed promised simple and reliable implementation but should not be used as a flight controller due to its development for prototyping applications.

Other lessons learned [7] include:

- Take as many spare components as the budget will allow. This includes all critical components and basic components.
- Ensure selection of team members on launch campaign are appropriate, they must have extensive knowledge of the entire system and be capable of taking and implementing advanced design decisions. Especially team members with knowledge in electronics and software.
- Ensure that all procedure documents are completely up to date with the design and that all members are familiar with the procedure.
- Test system completely including critical components.
- Confirm all procedures and requirements that relate to your system, even if another is in charge of them. If your system relies on something then you must confirm it. If anything is questionable, speak up.

6 CONCLUSIONS

This paper outlined the idea behind the two deployable inflatables and their implantation for a sounding rocket experiment. The design of StrathSat-R consists of a rocket module and two ejectable cubesat-like modules that contained deployable structures. Over almost two years a team of 25 students designed, build and tested the experiment to ensure full functionality in space conditions which was proved by the REXUS13 launch in May 2013. All systems worked during the whole flight but due to a procedure error, the two cubes were not ejected at apogee preventing the functional experiment to fulfil the mission objectives. The lessons learned from this campaign have also been identified and will result in a more successful iteration of StrathSat-R in the future. Currently, the team, REXUS/BEXUS and MORABA are looking into the possibility of re-launching StrathSat-R on another sounding rocket in the near furture.

7 ACKNOWLEDGMENTS

First of all we would like to thank everyone involved in the REXUS/BEXUS program, the German Aerospace Centre (DLR), the Swedish National Space Board (SNSB), the European Space Agency (ESA), the Swedish Space Corporation (SSC) and the Mobile Rocket Base (MORABA) for their continuous support and for giving us the change to launch our experiment onboard REXUS13. The authors would like to thank their supervisors Dr. Derek Bennett, Dr. Malcolm MacDonald, Professor Colin McInnes and Dr.

Massimilano Vasile for their continuous support of the project. Furthermore we would like to thank the University of Strathclyde Alumni Fund for supporting StrathSEDS. The authors also would like to thank Strathclyde undergraduate Adnan Mahmood for the manufacturing of SAM's inflatable spheres and Charlotte and Russell Bewick for their work on the project.

8 REFERENCES

1.Lücking, C., Colombo, C., and McInnes, C. R. "A Passive Satellite Deorbiting Strategy for Medium Earth Orbits Using Solar Radiation Pressure and the J2 Effect," Acta Astronautica 77, August–September 2012, pp. 197-206, ISSN 0094-5765, doi: 10.1016/j.actaastro.2012.03.026

2.Mangenot, C., Santiago-Prowald, J., van't klooster, K., Fonseca, N., Scolamiero, L., Coromina, F., Angeletti, P., Politano, M., Elia, C., Schmitt, D., Wittig, M., Heliere, F., Arcioni, M., Petrozzi, M., and Such Taboada, M. "ESA Document: Large Reflector Antenna Working Group - Final Report," Technical Note TEC-EEA/2010.595/CM. Vol. 1, 2010.

3.Freeland, R., Bilyeu, G., Veal, G., and Mikulas, M. "Inflatable deployable space structures technology summary," 1998.

4.Bernasconi, M.C. "Flexible-wall expandable structures for space applications: forty years of trying"," 1st European Workshop on Inflatable Space Structures, 21-22 May. Noordwijk, The Netherlands, 2002.

5.Crawley, E. F. "Intelligent structures for aerospace: a technology overview and assessment," AIAA journal Vol. 32, No. 8, 1994, pp. 1689-1699

6.Sinn, T., Vasile, M., Tibert, G. "Design and Development of Deployable Self-inflating Adaptive Membrane" AIAA-2012-1517, 13th AIAA Gossamer Systems Forum as part of 53rd Structures, Structural Dynamics, and Materials and Co-located Conferences, Honolulu, Hawaii, 23 - 26 April, 2012.

7.Sinn, T., et al.: Lessons learned in the sounding rocket and stratospheric balloon experiments Suaineadh, StrathSat-R and iSEDE, 64th International Astronautical Congress, Beijing, China, 23-27 September 2013

RESULTS OF THE GPS EXPERIMENT ON THE VS-30 V08 SOUNDING ROCKET

Francisco Mota[1], Fabio Spina[2], Tania Luna[3], and Fernando Miranda[4]

[1]*Univ. Fed. do Rio Grande do Norte - Natal, Brasil - Email: mota@dca.ufrn.br*
[2]*Instituto de Aeronáutica & Espaço - São Paulo, Brasil - Email:spianfds@iae.cta.br*
[3]*Univ. Fed. Rural do Semi-Arido - Caraúbas, Brasil - Email:tania.luna@ufersa.edu.br*
[4]*Univ. Fed. do Rio Grande do Norte - Natal, Brasil - Email: fcesar@ccet.ufrn.br*

ABSTRACT

A GPS receiver has been developed for high dynamics and space applications by a cooperation research between UFRN (Universidade Federal do Rio Grande do Norte - Brasil) and IAE (Brazilian Institute of Aeronautics and Space). This receiver was developed in a platform denominated "GPS Orion" proposed by Zarlink, and its software was modified in order the receiver could be able to accommodate the rocket dynamics. The main objective is to use it aboard sounding rockets produced by IAE and, in a near future, also aboard low earth orbit satellites. The purpose of this article is to present the tracking performance achieved by this GPS receiver in a flight of the Brazilian VS-30 V08 sounding rocket, produced by IAE/Brazil (Institute of Aeronauctics and Space), and launched from the Barreira do Inferno Space Center at Natal-RN, Brazil (CLBI), during the Brazil-Germany campaign held in December 2011, as well as to present the current status of the development project.

Key words: GPS Receiver; Sounding Rocket; VS-30 V08.

1. INTRODUCTION

The use of a GPS system is an alternative to the traditional rocket tracking methods, like C band radars, slant range systems and others. Advantages of using GPS for rocket tracking can be listed as low cost, global coverage, availability of service on a 24-hour basis and acceptable precision of positioning solution. In spite of commercial GPS receivers be easily accessible and cheaper today, most of then may not work properly aboard vehicles with high velocities and accelerations since they are fabricated with built-in limits. For use in a rocket then we need a special kind of receiver that is free of such operational limits and able to provide navigation solutions at an appropriate rate necessary to give a precise positioning of the vehicle during the flight. In this paper we describe the results obtained by an experimental GPS receiver, constructed using commercial off-the-shelf (COTS) items,

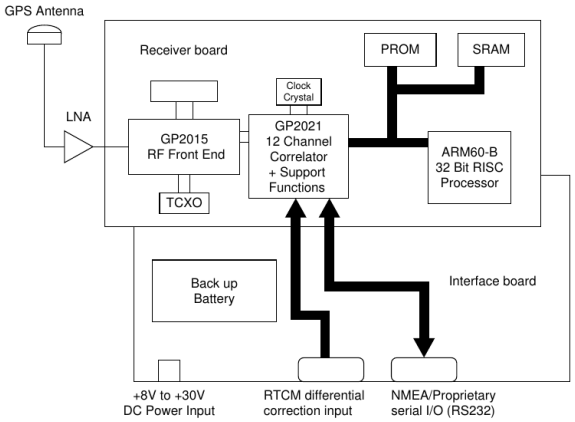

Figure 1. GPS Orion receiver block diagram

that flown aboard a sounding rocket named VS-30 V08 (developed and produced by the IAE/Brazil (Institute of Aeronauctics and Space) that was launched, during the "Brazil-Germany Campaign", from the Barreira do Inferno launching center (CLBI), located at Parnamirim city in Brazil. The mission offered an opportunity to continue the development and qualification of a Brazilian GPS receiver for use in space applications. The project for the development of the receiver was sponsored by the Brazilian Space Agency (AEB) and it is a joint cooperation between a university (Universidade Federal do Rio Grande do Norte-UFRN) and a research institute (IAE/Brazil - Institute of Aeronauctics and Space).

2. RECEIVER HARDWARE DESCRIPTION

The hardware of the receiver is based on a reference design denominated "GPS Orion" [1] proposed by Zarlink Semiconductor as an experimental platform to stimulate the use of their GP2000 Global positioning chip set. The core components of this chip set are the GP2015 and GP2021. The first one is a small format RF Front-end for Global Positioning System (GPS) receivers. The GP2021 is a 12-channel C/A code base-band correlator for use in NAVSTAR GPS satellite navigation receivers. It is com-

Proc. '21st ESA Symposium European Rocket & Balloon Programmes and Related Research', 9–13 June 2013, Thun, Switzerland (ESA SP-721, October 2013)

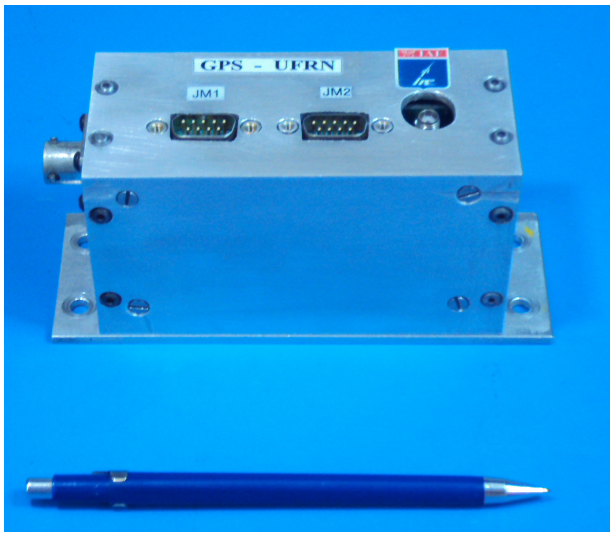

Figure 2. Photo of GPS Receiver

Weight	0.5 Kg
Dimensions	$141 \times 50 \times 63$ mm^3
Input Power Supplier	8 to 30VDC (from Payload)
Power Consumption	80mA 2.24W
Telemetry	19200 bps

Table 1. Physical Characteristics of the GPS receiver

patible with most 16-bit and 32-bit microprocessors, especially those from Motorola and Intel, with additional on-chip support for the ARM60 32-bit RISC processor. The On-Chip Dual UART of GP2021 allows two serial communication ports to the receiver. The microprocessor used in the Orion receiver is an ARM60-B, also by Zarlink. It is a high performance 32 bits RISC processor with a 32 bits data and address buses. Other important components of the receiver are the GPS band-definition SAW filter and a sub-miniature 10.000MHz Temperature Compensated Crystal Oscillator (TCXO). The general block diagram of the receiver is shown in Figure 1. A photo of the receiver is shown in Figure 2 and in Table 1 we present the main characteristics of the receiver used in Brazil-Germany Campaign.

3. SOFTWARE DEVELOPMENT

The main modifications required to adapt the original GPS Orion receiver to use it aboard rockets have to be made in its embedded basic software. For that, the company used to provide the basic software source code and a GPS development kit denominated "GPS Architect", where the software could be modified to contemplate the requirements of a rocket flight and, after that, embedded in the the receiver that will fly aboard the rocket. As far as our receiver is concerned the main software changes implemented had to do with the rocket high dynamics; big velocities and altitudes prevents the original GPS Orion

Figure 3. Brazil-Germany Operation Logotypes

receiver to navigate properly. Therefore we have to modify the original code so that the receiver could accommodate the Doppler effect produced by high velocities and accelerations of the vehicle. Other modifications were the elimination of altitude and velocity limits and inclusion of a routine to produce a clock "tic" aligned with every second of the Universal Time. The receiver is able to provide a navigation solution at every second. The first version of the customized software was done by the first author as a Post-Doctoral research at Cornell University in 1999-2000 and and flown aboard several sounding rockets in US since 2002 as "Cougar GPS Receiver" [2].

4. RESULTS

The "Operation Brazil-Germany" marked the 40 years anniversary of the cooperation between the DCTA/Brazil (Departamento de Ciência e Tecnologia Aeroespacial) and the DLR/Germany (Deutsches Zentrum für Luft- und Raumfahrt) in 2011 (Figure 3) and two rockets were launched from the Barreira do Inferno Space Center at Natal-RN, Brazil (CLBI): one Improved Orion Rocket and one VS-30 Rocket. The receiver described in this paper flown aboard the VS-30 Rocket that was launched on December, 02, 2011 (see Figure 4) and whose physical characteristics are shown in Table 2. The flight had a duration of approximately six minutes and the apogee, was approximately 138Km. In Figures 5 and 6 we show the altitude and vertical velocity (ROC), respectively, measured by the GPS during the flight. In Figure 7 we show the plot of the altitude error between the Radar and the GPS, where we had an maximum error of 290 meters. The number of allocated satellites during the flight as well as the the values of PDOP are shown in Figure 8.

5. CURRENT STATUS OF THE PROJECT

This same version of the receiver has flown aboard a VSB-30 Rocket that was launched from Alcantara-Brasil in December 2012 (Iguaiba Operation) where the vehicle reached an apogee of approximately 430Km. The GPS

Figure 4. VS-30 V08 Rocket

Total Weight	1,460 Kg
Payload Weight	260 Kg
Total Length	7.428 m
Maximum Diameter	0.557 m
Number of Stages	1
Apogee	160 Km

Table 2. Physical Characteristics of the VS-30 V08 Rocket

receiver worked as expected and the results had been published in [4].

We are currently implementing several modifications, mainly in the receiver hardware in order to replace obsolete parts as well as to maintain them as "COTS". We list bellow the main modifications under development:

- Replacement of the main processor: We are building a new receiver using the Zarlink GP4020 chip-set (GPS Receiver Base-band Processor that combines the 12-channel correlator function of the GP2021 with an ARM processor ARM7TDMI [3]);
- Redesign of the GPS Orion main board where the RF front end is separated from the digital section of the receiver. This is useful for testing new digital processing techniques.

As research topics under study we cite:

- Use of Software Defined Radio for redesigning the RF section. The idea is to get rid of analog RF filters still used in some stages of this section;
- Implementation the correlator function by software. This will make the receiver more flexible and will allow new correlation techniques to be explored.

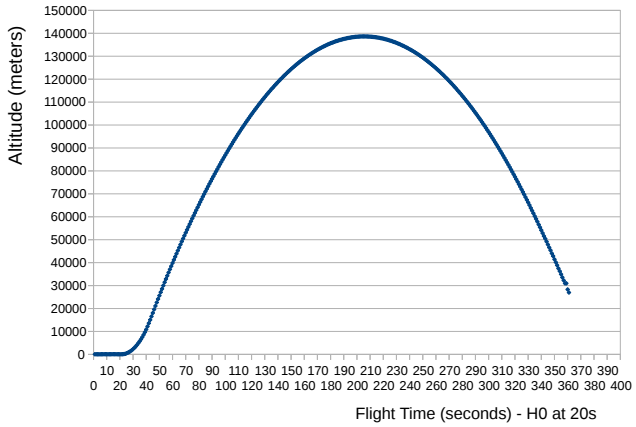

Figure 5. Rocket altitude measured by the receiver (Max.: 138636m at 22:03:03 UT)

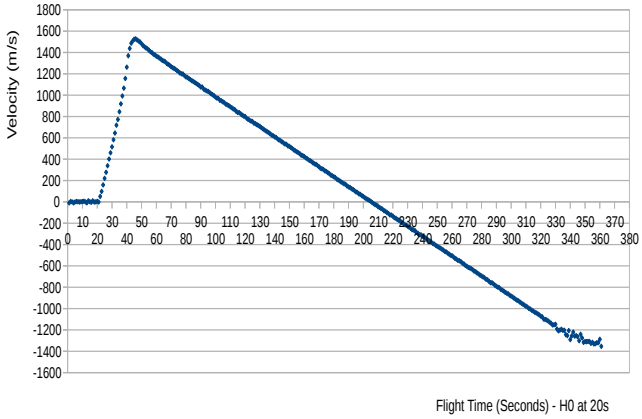

Figure 6. Rocket vertical velocity (ROC) measured by the receiver (Max.: 1527 m/s at 22:00:25 UT)

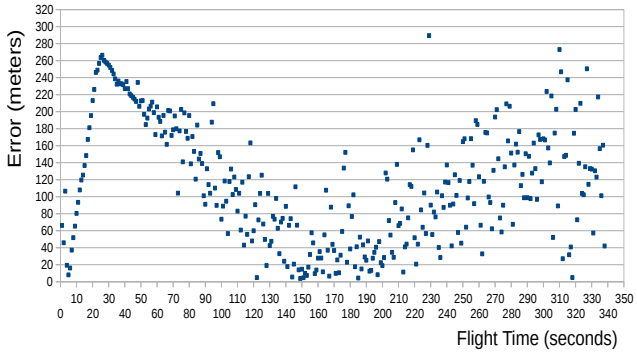

Figure 7. Radar×GPS altitude error (Max.: 290m)

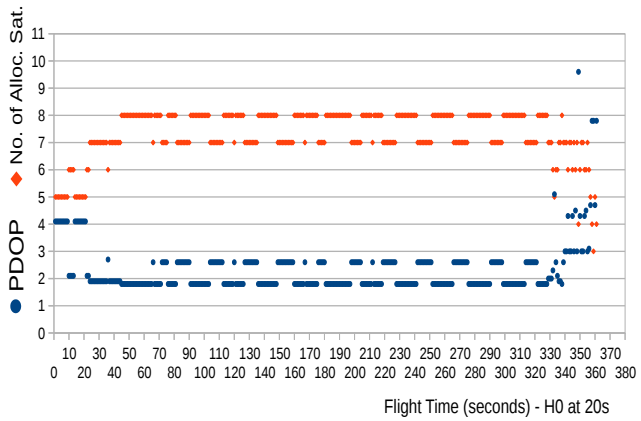

Figure 8. PDOP and Number of allocated satellites

6. CONCLUSIONS

The results obtained by the Brazil-Germany Mission and others [5] has shown that this GPS receiver is suitable for use in rockets. We are currently making some hardware and software updates in order to replace some obsolete parts as well as to improve the receiver in order it can be used in other high dynamics vehicles like small satellites.

ACKNOWLEDGMENTS

The authors are grateful to the Brazilian Space Agency (AEB) for the financial support of this project.

REFERENCES

[1] Zarlink Semiconductor, 2001, GPS Orion 12 Channel GPS Reference Design Application Note, AN4008, Issue 2.0.

[2] Paul M. Kintner, Steven Powell and Francisco Mota, 2000, Cougar GPS Receiver Manual. Cornell University.

[3] Zarlink Semiconductor, 2005, GP4020 GPS Receiver Base-band Processor Data-sheet.

[4] Francisco Mota, 2012, Iguaiba Operation - GPS technical Report (in Portuguese). Universidade Federal do Rio G. do Norte, Brasil.

[5] Francisco Mota, Glauberto Albuquerque and Tullio Raposo, 2011, A GPS Receiver for use in Sounding Rockets. Proceedings of 20th ESA Symposium on European Rockets and Balloons Programmes and Related Research, pp. 173–177.

A MATHEMATICAL MODEL TO SIMULATE ROCKET EXHAUST CLOUDS IN ALCÂNTARA LAUNCH CENTER

Davidson Moreira[(1)], Erick Nascimento[(1)], Taciana Albuquerque[(1)], Gilberto Fisch[(2)], Daniela Buske[(3)], Regis Quadros [(3)]

[(1)]Federal University of Espírito Santo, Av. Fernando Ferrari, s/n, CEP 29060-970,Vitoria, Brazil
davidson@pq.cnpq.br, erick@lcad.inf.ufes.br, taciana@model.iag.usp.br
[(2)]Institute of Aeronautics and Space, Praça Marechal Eduardo Gomes, CEP 12228-904, São José dos Campos, Brazil
Email: fisch.gilberto@gmail.com
[(3)] Federal University of Pelotas, Department of Mathematics and Statistics, CEP 96010-900, Pelotas, Brazil
daniela.buske@ufpel.edu.br, regis.quadros@ufpel.edu.br

ABSTRACT

This work presents a new model to simulate rocket exhaust clouds. The model represents the solution for the time-dependent advection-diffusion equation applying integral transform technique considering the Atmospheric Boundary Layer as a multilayer system. This solution allows a time evolution description of the concentration field emitted from a source during a release lasting time and it takes into account deposition velocity, first-order chemical reaction, gravitational settling, precipitation scavenging, and plume rise effect. A qualitative evaluation of the model to simulate rocket exhaust clouds due to a normal launching is showed. The results show that the model can be used in different conditions of atmospheric stability, making it possible to predict or simulate the concentration in accordance with emergency plans and pre and post-launchings for environmental management, in situations of rocket launches in the Alcântara Launch Center, Brazil. In particular, the model is suitable for an initial and rapid assessment of atmospheric dispersion under emergency conditions without sophisticated computing resources.

1. INTRODUCTION

The burning of rocket engines during the first few seconds prior to and immediately following vehicle launches results in the formation of a large cloud of hot, buoyant exhaust products near the ground level which subsequently rises and entrains ambient air until the temperature and density of the cloud reach an approximate equilibrium with ambient conditions. The NASA (National Aeronautics and Space Administration - USA) have computational codes that are designed to calculate peak concentration, dosage and deposition (resulting from both gravitational settling and precipitation scavenging) downwind from normal and aborted launchings for use in mission planning activities and environmental assessments, pre-launch forecasts of the environmental effects of launch operations and post-launch environmental analysis. Many these models are based on the same steady-state Gaussian dispersion model concepts used by other models.

Recently, we take a step forward regarding the Gaussian concepts in order to simulate pollutant dispersion in atmosphere. We obtained the solution, for a vertically inhomogeneous Atmospheric Boundary Layer (ABL), of the time-dependent advection-diffusion equation applying the Laplace transform, considering the ABL as a multilayer system. We call this technique of ADMM (*Advection-Diffusion Multilayer Method*) method and it is well established in the literature [1]. Therefore, the aim of this work is report the construction of a new model based on ADMM model, now called MSDEF model, to simulate rocket exhaust clouds. For a better understanding, in the sequel, we briefly discuss the idea behind this method. The main feature of the ADMM approach consists on the following steps: stepwise approximation of the eddy diffusivity and wind speed, the Laplace transform application to the advection-diffusion equation in the x and t variables, semi-analytical solution of the set of linear ordinary equation resulting for the Laplace transform application and construction of the pollutant concentration by the Laplace transform inversion using the Gaussian quadrature scheme. It is important to mention that, for the first time, the ADMM model (now MSDEF) is depending on the time release, deposition velocity, first-order chemical reaction, gravitational settling and precipitation scavenging. This solution allows a description of the time evolution of the concentration field emitted from a source during a release lasting time t_r. The model takes into account the plume rise formulation of the literature for convective conditions that is included in the computational codes of the NASA.

To reach our objective, we organize the paper as follows: in section 2, we report the physical approach. In section 3, we show the solution of the advection-diffusion equation. In section 4, we show the turbulent parameterizations. In section 5, are presented numerical results, and finally, in section 6, the conclusions.

2. PHYSICAL APPROACH

A tool for analysis of toxic dispersion in the USA and to support the release and evaluation of public risk is the

Proc. '21st ESA Symposium European Rocket & Balloon Programmes and Related Research',
9–13 June 2013, Thun, Switzerland (ESA SP-721, October 2013)

7.13 version of the REEDM (Rocket Exhaust Effluent Diffusion Model) [2] model. Thus, this program was used as reference for modeling physics and mathematics of the problem in the development of MSDEF program. The main assumption used in the model REEDM about the nature and behavior of the cloud released by the rocket is that it can be initially defined as a single cloud that grows and moves, but remains as a single cloud during the formation of the ascending phase of it. This concept is illustrated in Figure 1, and can be noticed that the model is designed for REEDM concentrations from the vertical position of the stabilized cloud.

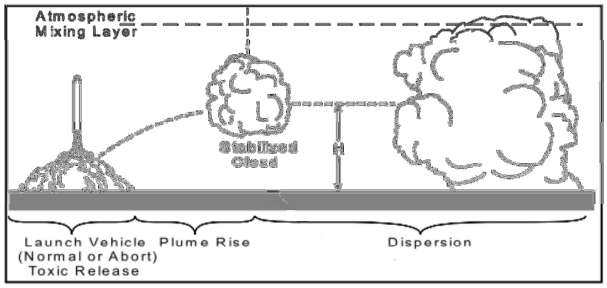

Figure 1. Conceptual illustration of cloud formation (source), "cloud-rise" and atmospheric dispersion of the cloud [3].

The aspect "multilayer" is still used in the REEDM model and relates to the partitioning of cloud stabilized in "disks" of material from the cloud represented by different meteorological levels at different altitudes. Typical levels are 20 to 50 m deep. Since the cloud is defined and has reached the condition of thermal stability with the atmosphere, the cloud is partitioned into "disks". The position of each disk with respect to the origin (launch pad) is determined based on the rise time of the cloud through a sequence of layers that are defined using meteorological measuring levels obtained from a radiosonde. Each layer can have a single meteorological speed and wind direction that moves the disk into the same cloud. The concept of partition of the stabilized cloud is illustrated in Figure 2.

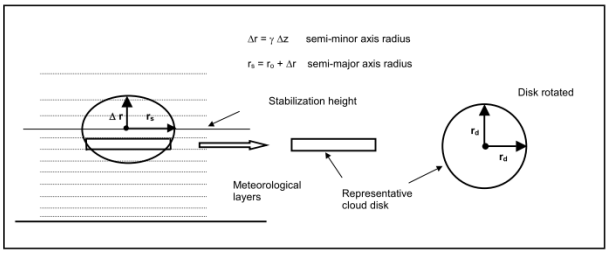

Figure 2. Partitioning of cloud stabilized "disks" [3].

3. MATHEMATICAL APPROACH

A typical problem with the advection-diffusion equation involves the solutions of problems corresponding to instantaneous and continuous sources of pollution. More precisely, considering a Cartesian coordinate system in which the *x* direction coincides with that one of the average wind, the time dependent advection-diffusion equation can be written as [4]:

$$\frac{\partial C^y}{\partial t}+u\frac{\partial C^y}{\partial x}-v_g\frac{\partial C}{\partial z}=\frac{\partial}{\partial x}\left(K_x\frac{\partial C^y}{\partial x}\right)+ \\ +\frac{\partial}{\partial z}\left(K_z\frac{\partial C^y}{\partial z}\right)-\lambda C^y-\Lambda C^y \quad (1)$$

where C^y is the crosswind integrated concentration, λ represents a chemical-physical decay coefficient and Λ is the scavenging coefficient. The decay term λ represents in situ loss associated with processes such as chemical reaction or radioactive decay.

The mathematical description of the dispersion problem represented by the Eq. (1) is well posed when it is provided by initial and boundary conditions. Indeed, it is assumed that at the beginning of the pollutant release the dispersion region is not polluted, this means [5]:

$$C^y(x,z,0)=0 \quad \text{at} \quad t=0 \quad (2)$$

and a source of constant emission rate Q is assumed:

$$C^y(0,z,t)=\frac{Q}{u}\left[\eta(t)-\eta(t-t_r)\right]\delta(z-H_s) \quad \text{at} \quad x=0 \quad (3)$$

where $\delta(z-H_s)$ is the Dirac delta function, H_s the source height, η is the Heaviside function and t_r is the duration of release. The pollutants are also subjected to the boundary conditions:

$$K_z\frac{\partial C^y}{\partial z}=0 \quad \text{at} \quad z=h \quad (4a)$$

and

$$K_z\frac{\partial C^y}{\partial z}=V_dC^y \quad \text{at} \quad z=0 \quad (4b)$$

where *h* is the height of ABL and V_d is the deposition velocity. In the following we assume that K_x, K_z as well the wind speed u depend only on the variable *z* and we assume an averaged value. The stepwise approximation is applied in problem (1) by discretization the height *h* into sub-layers in such manner that inside each sub-layer, average values for

K_x, K_z and *u* are taken. At this point, it is important to remark that this procedure transforms the domain of problem (1) into a multilayered-slab in the *z* direction. Furthermore this approach is quite general in the sense it can be applied when these parameters are an arbitrary continuous function of the *z* variable. Indeed, it is now possible to recast problem (1) as a set of advective-diffusive problems with constant parameters, which for a generic sub-layer reads like:

$$\frac{\partial C_n^y}{\partial t}+u_n\frac{\partial C_n^y}{\partial x}-v_g\frac{\partial C_n^y}{\partial z}=K_{x,n}\frac{\partial^2 C_n^y}{\partial x^2}+ \\ +K_{z,n}\frac{\partial^2 C_n^y}{\partial z^2}-\lambda C_n^y-\Lambda C_n^y \tag{5}$$

for n = 1:*NL*, where *NL* denotes the number of sub-layers and C_n^y the concentration at the nth sub-layer. Besides which, two boundary conditions are imposed at $z=0$ and h given by equation (4) together with the continuity conditions for the concentration and flux of concentration at the interfaces. Namely:

$$C_n^y = C_{n+1}^y \qquad n = 1, 2,...(N\text{-}1) \tag{6a}$$

$$K_n\frac{\partial C_n^y}{\partial z}=K_{n+1}\frac{\partial C_{n+1}^y}{\partial z} \qquad n = 1, 2,...(N\text{-}1) \tag{6b}$$

must be considered, in order to be possible to uniquely determine the 2N arbitrary constants appearing in the solution of the set of problems (5). Now, applying the Laplace transform in equation (5) in x and t variables result ($\bar{C}^y(s,z,p)=L\{C^y(x,z,t);x\to s;t\to p\}$):

$$\bar{C}_n^y(s,z,p)=A_n e^{-R_n z}+B_n e^{R_n z}+ \\ +\frac{\left(1-e^{-pt_r}\right)}{p}\frac{Q}{R_a}\left(e^{-R_n(z-H_s)}-e^{R_n(z-H_s)}\right) \tag{7}$$

Finally, applying the initial and boundary conditions one obtains a linear system for the integration constants. Then the concentration is obtained by inverting numerically the transformed concentration $\bar{C}$ by a Gaussian quadrature scheme:

For $t > t_r$:

$$C_n^y(x,z,t)=\sum_{i=1}^{k}a_i\left(\frac{p_i}{t}\right)\sum_{j=1}^{m}a_j\left(\frac{p_j}{x}\right)\Big[A_n e^{-G_n z}+B_n e^{G_n z}+ \\ +Q\frac{(1-e^{-p_i\frac{t_r}{t}})}{F_n}\left(e^{-(z-H_s)G_n}-e^{(z-H_s)G_n}\right)H(z-H_s)\Big] \tag{8a}$$

For $t_r > t$:

$$C_n^y(x,z,t)=\sum_{i=1}^{k}a_i\left(\frac{p_i}{t}\right)\sum_{j=1}^{m}a_j\left(\frac{p_j}{x}\right)\Big[A_n e^{-G_n z}+B_n e^{G_n z}+ \\ +\frac{Q}{F_n}\left(e^{-(z-H_s)G_n}-e^{(z-H_s)G_n}\right)H(z-H_s)\Big] \tag{8b}$$

where

$$G_n=-\frac{v_g}{2K_z}\pm\frac{1}{2}\sqrt{\left(\frac{v_g}{K_z}\right)^2+\frac{4}{K_z}\left[\frac{p_i}{t}+\lambda+\Lambda+\frac{p_j}{x}u_n\left(1-\frac{p_j}{P_e}\right)\right]}$$

$$F_n=2\frac{p_i}{t}\frac{\sqrt{K_z\left[\frac{p_i}{t}+\lambda+\Lambda+\frac{p_j}{x}u_n\left(1-\frac{p_j}{P_e}\right)\right]}}{\left(1-\frac{p_j}{P_e}\right)}$$

and η is the Heaviside function and $P_e=u_n x/K_x$ is the well known Peclet number, essentially representing the ratio between the advective transport to diffusive transport. In order to show time-dependent three-dimensional pollutant numerical simulations, we finalize reporting a simplified solution for this sort of problem, reliable for some physical scenarios. Indeed, we assume that the time-dependent three-dimensional solution is written in terms of the time-dependent two-dimensional solution multiplied by the steady Gaussian function in the *y*-direction. This procedure yields:

$$C(x,y,z,t)=C^y(x,z,t)\frac{e^{\left(-y^2/2\sigma_y^2\right)}}{\sqrt{2\pi}\sigma_y}\ , \tag{9}$$

where $C^y(x,z,t)$ is expressed by the previous discussed formulation. Therefore, after determining the stabilization time and the source (multiple sources due to partitioning of the cloud), the final concentration will be the contribution from all sources, ie

$$C(x,y,z,t)=\sum_{i}^{n}C_i(x,y,z,t) \text{ where } i = 1,2,3,..n. \tag{10}$$

where *n* represents the nth source due to the partitioning of the cloud of pollutants released by the rocket at the time of stabilization.

4. BOUNDARY LAYER PARAMETERIZATION

In the atmospheric diffusion problems the choice of a turbulent parameterization represents a fundamental aspect for pollutant dispersion modeling. The reliability of each model strongly depends on the way the

turbulent parameters are calculated and is related to the current understanding of the ABL. In this work we used the lateral dispersion parameter σ_y derived by [6] and the vertical eddy diffusivity K_z formulated by [7]. The micrometeorological parameters are adapted from the routine of the model AERMET / AERMOD [8], whose function is to calculate the parameters u_* (friction velocity), L (Monin-Obukhov length), w_* (convective velocity), h (ABL height) and H (heat flux) from the sounding (including the vertical wind speed) taken in Alcantara Launching Center.

5. RESULTS

We show a simulation considering a grid of 100 x 100 km in the region covered by the Alcantara Launch Center (CLA). The main points are shown in the Figure 3, which are shown the vector wind speed and dispersion of the plume. The concentration unit is *ppm*.

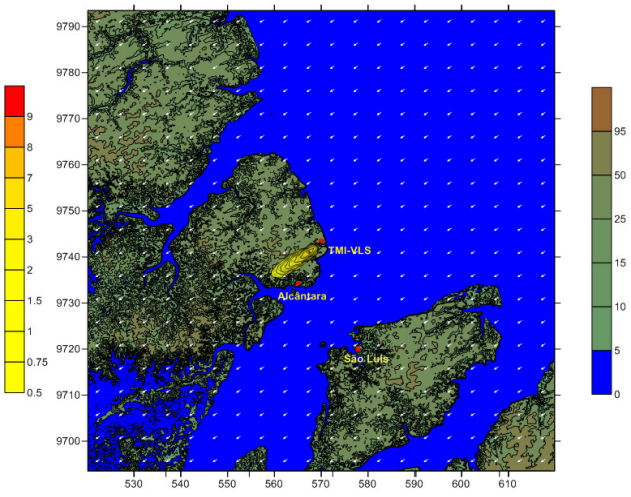

Figure 3. Topography of the region of 100 x 100 km with a resolution of 100 m, showed the vector wind speed and plume generated in the simulation. The coordinates axes are in UTM. TMI represent the Tower Mobile Integration and VLS is the Satellite Launch Vehicle.

6. CONCLUSIONS

A solution of the time-dependent advection–diffusion equation in the construction of the MSDEF model has been presented. This solution considers the duration time release, chemical-physical decay, settling velocity, scavenging coefficient From the previous results, we promptly notice the aptness this model to understand the time evolution of the concentration and its dependency on the duration of the contaminant emission. In fact, this model, allow us to simulate the continuous, short-term and instantaneous emissions. In particular, the model is suitable for an initial and rapid assessment of atmospheric dispersion under emergency conditions without sophisticated computing resources. The model can be used in different conditions of atmospheric stability, making it possible to predict or simulate the concentration in accordance with emergency plans and pre and post-launches for environmental management in situations of rocket launches in Alcantara Launching Center.

7. ACKNOWLEDGMENTS

The authors would like to thanks the financial support from the CNPq (National Council for Research).

8. REFERENCES

1. Moreira, D.M, Vilhena, M.T., Tirabassi, T., Costa, C. and Bodmann, B., 2006. Simulation of pollutant dispersion in the atmosphere by the Laplace transform: the ADMM approach. Water, Air and Soil Pollution 177, 411-439.
2. Bjorklund, J.R., Dumbauld, J.K, Cheney, C.S. and Geary, H.V., 1982. User's manual for the REEDM (Rocket Exhaust Effluent Diffusion Model) compute program. NASA contractor report 3646. NASA George C. Marshall Space Flight Center, Huntsville, AL.
3. Nyman, R.L., 2009. NASA Report: Evaluation of Taurus II Static Test Firing and Normal Launch Rocket Plume Emissions.
4. Huang, C.H., 1979. A theory of dispersion in turbulent shear flow. Atmos. Environ. 13, 453-461.
5. Moreira, D.M., Rizza, U., Vilhena, M.T. and Goulart, A.G., 2005a. Semi-analytical model for pollution dispersion in the planetary boundary layer. Atmos. Environ. 39 (14), 2689-2697.
6. Degrazia, G.A., Mangia, C. and Rizza U., 1998. A comparison between different methods to estimate the lateral dispersion parameter under convective conditions. Journal of Applied Meteorology 37, 227-231.
7. Degrazia, G.A., Campos Velho, H.F. and Carvalho, J.C., 1997. Nonlocal exchange coefficients for the convective boundary layer derived from spectral properties. Contr. Atmos. Phys., 57-64.
8. EPA-454/B-03-002, 2004. User's Guide for the AERMOD meteorological preprocessor (AERMET).

ICON, A MASS ANALYZER FOR THE ICE CONTENT OF NLC/PMSE PARTICLES

Ove Havnes, Tarjei Antonsen, Åshild Fredriksen, Sveinung Olsen, Yngve Eilertsen, Inge Strømmesen.

Institute of Physics and Technology, University of Tromsø, N-9037 Tromsø, Norway.
ove.havnes@uit.no, phone: +47 776 45132, Fax: + 47 776 45580.
tarjei.antonsen@uit.no, ashild.fredriksen@uit.no, sveinung.olsen@uit.no,
yngve.eilertsen@uit.no, inge.strommesen@uit.no

ABSTRACT

We describe the principles of a new rocket probe ICON which will, for the first time, mass analyze the evaporation products of the icy cloud particles in the mesosphere – the NLC and PMSE cloud particles. Laboratory tests show that we can, with a right choice of inlet pinhole dimension and ion pump capacity, keep the pressure in the mass analyzer chamber within its optimum range as the payload pass the NLC/PMSE clouds. The ICON capture mechanism for the ice particles should lead to a drastically enhanced relative abundance of water vapor and trace elements in the ice, compared to that expected when the water and trace elements are in the vapor phase outside the clouds.

1. INTRODUCTION

The mass influx of meteoric material is estimated to be of the order of 10 to 100 metric tons per day. Vapors from ablation are likely to condense into nanometer-sized aerosols called meteoric smoke particles (MSP). This recondensation was initially suggested by [1] and later modelled by [2]. MSPs are thought to be important in several different processes in the upper atmosphere. They provide plausible condensation sites for water vapor in the cold summer mesosphere and may be the condensation nuclei leading to noctilucent clouds (NLC) and Polar Mesospheric Summer Echoes (PMSE); see for instance [3] for a review. The ice particles in the NLC/PMSE are thought to be effective sinks for atomic metals in the mesosphere; as shown by observation of the depletion of metal layers in the presence of NLC [4]. Chemical processes responsible for the destruction of ozone in the mesosphere and stratosphere can take place on the surface of ice particles, and the MSP content on them may explain why nitric acid trihydrate, which indirectly enhances polar ozone depletion, can exist in polar stratospheric clouds [5]. Our knowledge about the chemistry of mesospheric icy particles is constrained by limited observation. Remote sensing methods are useful for monitoring transport of the particles [6], but in-situ measurements are important to discriminate between different hypotheses on ice nucleation, their subsequent growth and the influence of the ice particles on the general chemistry of the upper atmosphere. This paper presents and discuss the principles and motivation of a new rocket-borne mass analyzer ICON which will be launched in the summer of 2014. The ICON probe will collect icy NLC/PMSE particles and mass analyze their evaporation gases to map their content of trace elements besides those of water vapor.

2. THE ICON MASS ANALYZER

The idea behind the ICON (**I**dentification of the **Co**ntent of **N**LC particles) in Fig.1 is to collect the icy NLC/PMSE particles into a heated chamber

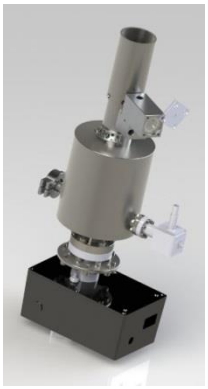

Figure 1. The ICON mass analyzer

where they will evaporate. A pin-hole into a vacuum chamber is opened some distance below the NLC/PMSE clouds and evaporation products can enter and be mass analyzed by a quadrupole RGA (Residual Gas Analyzer) . The principles of ICON are shown in Fig.2. The front end, the ice particle collecting part, is a funnel with opening angle 20°. Incoming ice particles will hit the funnel wall, there will be some fragmentation of the ice particles but a major part of the ice is expected to bounce off the funnel wall and proceed down into a collection chamber with a velocity almost parallel

Proc. '21st ESA Symposium European Rocket & Balloon Programmes and Related Research',
9–13 June 2013, Thun, Switzerland (ESA SP-721, October 2013)

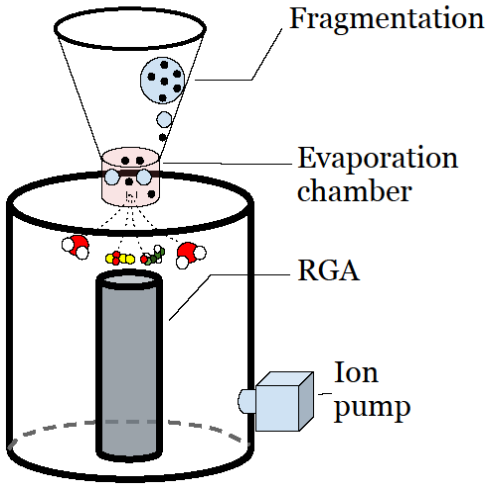

Figure 2. The principles of the ICON probe showing the collection of ice particles by the front funnel into the heated collection chamber. Evaporation molecules can enter the vacuum chamber hrough a pinhole and be mass analyzed by the quadrupole (RGA). The ion pump controls the vacuum chamber pressure.

to the funnel wall. Below the collection chamber there is a vacuum chamber into which ice evaporation gases (and the background air molecules and atoms) can enter when a valve opens a pin hole. This valve is closed on ground and in the first part of the flight but it is opened around 6 km below the NLC/PMSE region. Background gas and the evaporation gases from the ice particles in the collection chamber will enter the vacuum chamber to be mass analyzed by the RGA. The background density of the ambient gas in the collection chamber will fall as the air density drops with height. However, the density of evaporation products from the ice particles in the collection chamber will build up into a very much higher partial pressure, relative to the air, than the "normal" situation away from the payload. The reason for this is that the funnel will focus the ice particles into a small heated collection chamber and the flux of ice particles will build up a density of evaporated gas until losses, mainly by diffusion back out of the collecting chamber, balances the influx. Ice particles and their fragments will enter the collection chamber independently of the conditions in the background gas. In principle the ice particles could "fill" the collection chamber with ice if the loss is small enough. We find that the partial pressure of ice and the trace gases relative to the air can increase by a factor of more than 10^3. This rapid buildup of partial pressure is what may allow ICON to detect the trace gases in the ice, most of which we expect to originate from the ablation process of meteoric particles. Without this build up, the partial pressure of the trace gases will be very low and probably below the detection limit of the RGA. For the RGA to work efficiently it has to operate at a pressure below ~10^{-4} Torr. The lower limit for the mass analyzer for detection is for partial pressures of $5x10^{-14}$ Torr. Without any increase of the partial pressures and if we have water at ~5 ppm, corresponding to a partial pressure in air of $5x10^{-6}$, and a fraction of meteoric atoms or molecules relative to the ice in the vicinity of $4x10^{-5}$ [7], the pressure of the trace elements, when background air in the vacuum chamber is kept at 10^{-4} Torr, will become $10^{-4}x5x10^{-6}x4x10^{-5}$ Torr=$2x10^{-14}$ Torr which is below the detection limit. Our collection method should increase the partial pressure by a factor possibly above 10^3. This will bring the partial pressures up to $2x10^{-11}$ Torr which is well within the detection limits.

The input rate of water ice molecules (out of which we assume that a fraction $4x10^{-5}$ are the trace elements we look for) in particles/m^3/s is given by

$$(dn_{H2O}/dt)_{input} = \frac{\propto A_f v_R N_d m_d}{V_{coll} m_{H2O}} \qquad (1)$$

We have not yet considered any losses out of the collection chamber. In Eq.(1) α is the fraction of the ice particles which end up in the collection chamber, A_f is the upper, or entrance cross section of the funnel, v_R the rocket velocity, N_d the dust number density in the ambient gas, $m_d = \frac{4}{3}\pi\rho_d r_d^3$ the dust mass, V_{coll} the volume of the collection chamber, m_{H2O} the molecular mass of water while t is the time. Using the α=0.9 ; A_f=$3x10^{-3}$ m^2; v_R=900 m/s; N_d=$8x10^7$$m^{-3}$; ρ_d=980 kgm^{-3}; r_d=50 nm=$5x10^{-8}$m; V_{coll}=$4.4x10^{-6}$$m^{-3}$, m_{H2O}=$3x10^{-26}$ kg we get $(dn_{H2O}/dt)_{input}$=$7x10^{20}$ $m^{-3}s^{-1}$. For the meteoric trace gas the value will be $(dn_{Met}/dt)_{input}$ =$3x10^{16}$ $m^{-3}s^{-1}$. The total number density inside the collection chamber, with a compression factor of ~10 due to the ram pressure caused by the moving payload, will be n_{Tot}~$5x10^{21}$ m^{-3} at a height around 81 km. Typical cloud structures are a few cloud layers of around a km thickness each. Even with a payload flight time of 0.1 sec corresponding to 90 m, the conditions above would lead to a relative number density of water vapor in the collection chamber to build up to ~ 10^{-2} which is up by a factor 2000. There will, however, be loss mechanisms which will not allow the partial pressures of the water vapor and the trace elements to build up above a certain level. One loss mechanism is that the pressure is falling as the rocket move upwards so there will be an outflow of all gases in the collection chamber. The number density within the collection chamber will drop by a factor *1/e* over a scale height of typically 5 km, which takes the payload around 5 sec to pass. Another way of expressing this is that the column of gas within the collection chamber is to be stretched by a factor *e* in 5 sec. The height of the collection chamber will be

L_{coll} ~0.025 m so this corresponds to a very slow loss velocity of around 1 cm/sec. There will also be a small loss through the pin hole but with a pinhole diameter of around 25 µm and a chamber diameter more than 10^4 times this, a flow at around sound speed through the pinhole will be a minor loss mechanism. The dominating loss should be diffusion back out of the chamber. We assume that the gradient length in water vapor and trace gases is (Eq.2) several times the height of the collection

$$v_{diff} = -\frac{kT}{m\nu}\left(\frac{\nabla n}{n}\right) \approx -\frac{kT}{m\nu}\left(\frac{1}{L_{diff}}\right) \qquad (2)$$

chamber since the evaporation products very quickly will spread into the funnel. We neglect the increase in gas temperature from inside to outside the collection chamber, which will slow down the diffusion. In Eq.(2) we use a temperature of T=300 K, a molecular mass of 100 amu, which represent one of the molecules with metal compounds. We take L_{diff}=.1 m and a collision frequency ν = 4x10^5 s^{-1} leading to a diffusion velocity out of the collection chamber of V_{diff}~0.6 m/s. The loss rate for the meteoric trace elements , in molecules per m^3 and per second, can then be expressed by

$$(dn_{Met}/dt)_{loss} = -n_{Met}(t)A_{coll}v_{diff}/V_{coll}$$
$$= -n_{Met}(t)v_{diff}/L_{coll} = -24n_{Met}(t) \qquad (3)$$

Demanding that the sum of the two rates is equal to zero lead to an equilibrium density of the meteoric trace elements in the collection chamber to be n_{Met} = 1.3x10^{15} m^{-3}. Compared to the total compressed density n_{Tot}~ 5x10^{21} m^{-3} in the collection chamber the meteor trace elements have a relative density of 3x10^{-7}. If this holds, a vacuum chamber pressure of 10^{-4} Torr will lead to that meteor trace elements can have partial pressure of p_{Met}~ 3x10^{-11} Torr which is a factor 600 above the detection limit. This should make it possible to detect meteoric trace elements of a relative fraction, compared to ice, possibly as much as a factor ~100 below the value 4x10^{-5} that we have used, even if we lower the vacuum chamber pressure down to ~2x10^{-5} Torr to have a larger safety margin to the high pressure limit for optimum operation of the mass analyzer.

3. OPERATION AND LABORATORY TESTS OF ICON.

The ICON instrument with its quadrupole mass spectrometer, requires that the total pressure in the vacuum chamber is kept below 10^{-4} Torr for optimum performance. The lower pressure limit for detection and mass analysis is 5x10^{-14} Torr. We have chosen a solution for the pressure control where we before launch, before the nosecone is closed, evacuate the closed vacuum chamber down to a pressure of ≤10^{-6} Torr with an external pump. When the external pump is disconnected as the payload is closed the internal pressure for the closed vacuum chamber is maintained at this level with an ion pump attached to the ICON vacuum tank (see figs.1 and 2). The idea behind the operation of ICON is that the vacuum tank is kept closed until the payload is at some height below the lower height limit of the NLC/PMSE clouds at ~80 km. The height difference between opening height and the NLC/PMSE height should be large enough so that the mass spectrometer can do several sweeps over its 1-300 amu mass range. In this way ICON will map the background gas "contamination". This background can be due to outgassing within the vacuum tank, outgassing from the payload itself and a possible contribution from gas leakage from explosive wire cutters, used to release the nosecone and the pinhole cover valve. Each sweep will take 2 sec, corresponding to a height ~ 2 km. We cannot open the valve for the pinhole into the vacuum chamber before we are sure that the ion pump can keep the pressure below 10^{-4}Torr, preferably around 2x10^{-5}Torr. The pressure will go up as the pinhole is opened but we cannot have a situation where it exceeds 10^{-4} Torr. To avoid this we have made laboratory tests where the ICON is attached to a larger vacuum tank kept at a specified pressure p_{coll} which is the pressure in the collection chamber at a certain height, allowing for the increase in total pressure due to the rocket motion. We find from model calculations that the pressure in the collection chamber, compared to that of the background gas, will be up by a factor ~18 due to ram pressure and shock effects. We

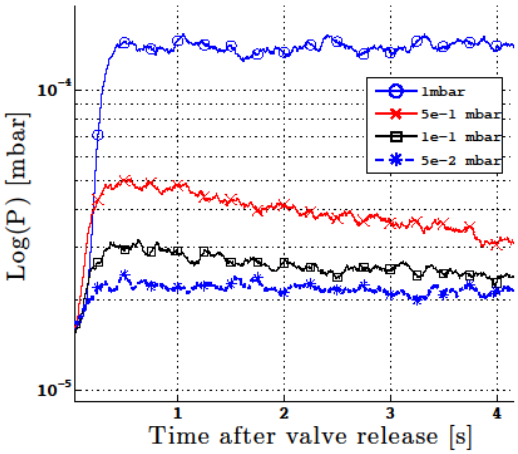

Figure 3, showing the development of the ICON vacuum tank pressure after opening of the pinhole at the 4 different heights from 75 to 88 km, the outside pressure being kept constant.The vacuum chamber pressure was initially 1.5x10^{-5} mbar for all series.

record the increase in the tank pressure when the pinhole is opened for 4 different external pressures, corresponding to payload heights from 75 km to 88

km and see how this develops with time. The results are shown in Fig.3. We find that if we open the pinhole at a height around 75 km the pressure will, within 0.4 sec, rise to a level well below 10^{-4} Torr. As the payload move upwards the vacuum chamber pressure will fall but it will remain in the optimum pressure range for trace element detection throughout the NLC/PMSE height region..

4. DISCUSSION

The ICON will attempt, for the first time, to map the chemical content of the ice in the mesospheric cloud particles. It is suspected that most of the "contamination" besides pure water ice, originates from meteor ablation products. ICON assume that most of the ice particle will bounce of the impact wall, and that it will be collected in a collection chamber from which the evaporation products will enter a vacuum chamber to be mass analyzed. One uncertain assumption is that some of the impacting ice particles may stick to the impact surface and evaporate, and not contribute to the trace gas density in the collection chamber. However, [8] finds that ice particles larger than several nm are likely to bounce off the impact surfaces and continue in a direction closely parallel to the impact surface. We therefore feel confident that our assumption that most of the ice material in the NLC/PMSE particles will end up in the collection chamber to be mass analyzed, is correct.

5.REFERENCES

1. J. Rosinski and R. H. Snow.(1961) Secondary particulate matter from meteor vapors. Journal of Meteorology, 18(6):736–745.

2. D.M. Hunten, R. P. Turco, and O. B. Toon. (1980). Smoke and dust particles of meteoricorigin in the mesosphere and stratosphere. Journal of the Atmospheric Sciences, 37(6):1342–1357.

3. M. Rapp and G. E. Thomas. (2006) Modeling the microphysics of mesospheric ice particles: Assessment of current capabilities and basic sensitivities. Journal of Atmospheric and Solar-Terrestrial Physics, 68(7):715– 744.

4. C.Y. She, B.P. Williams, P. Hoffmann, R. Latteck, G. Baumgarten, J.D. Vance, J. Fiedler, P. Acott, D.C. Fritts, and F.-J. Lubken.(2006) Simultaneous observation of sodium atoms, NLC and PMSE in the summer mesopause region above Alomar, Norway. Journal of Atmospheric and Solar-Terrestrial Physics, 68(1):93– 101.

5. C. Voigt, H. Schlager, B. P. Luo, A. Dornbrack, A. Roiger, P. Stock, J. Curtius, H. Vossing, S. Borrmann, S. Davies, P. Konopka, C. Schiller, G. Shur, and T. Peter. (2005) Nitric acid trihydrate (nat) formation at low nat supersaturation in polar stratospheric clouds (pscs). Atmospheric Chemistry and Physics, 5(5):1371–1380: 10.5194/acp-5-1371-2005

6. M. E. Hervig, L. L. Gordley, L. E. Deaver, D.E. Siskind, M. H. Stevens, J. M. Russell III, S. M. Bailey, L. Megner, and C. G. Bardeen. (2009)First satellite observations of meteoric smoke in the middle atmosphere.Geophysical Research Letters, 36. doi:10.1029/2009GL039737.

7. Plane J.M.C. Priv. communication. (2012).

8. A. Tomsic. Collisions between water clusters and surfaces. PhD thesis, Gøteborg University, 2001. p. 9-10.

ACKNOWLEDGMENTS

Tarjei Antonsen will thank ESA for sponsorship through the ESA Conference Opportunities for Sponsored Students (ECOSS) Programme.

CONSTANT FLOW UNDER FREE FALL - ENSURING CONDITIONS FOR APPLIED RESEARCH IN SPACE

Helmut Steinau, Dipl. Ing. FH

Astrium Space Transportation, Airbus-Allee 1 ,
D-28199 Bremen, Germany, E-mail: Helmut.Steinau@astrium.eads.net

1. SERVING THE SCIENCE COMMUNITY SINCE 1977

In this spring the TEXUS 50 was launched from ESRANGE Rocket Centre near Kiruna. It is the only place in Europe where we have the possibility to launch rockets and get the payload back by land recovery. There are other launch pads for rockets in Europe but with the additional risk and problematic of recovery over sea. The agencies DLR and ESA are funding the flights with experiments on board. That offers the principal investigators the chance to run an experiment under almost ideal free fall condition. The micro gravity phase is about 6 minutes with Texus or 13 minutes with Maxus. The task of industry is to build the experiment hardware as close as possible to the ground experiment setup the PI is using in his home lab. Certainly the flight experiment is more compact and miniaturised than the laboratory version but the physical environment should be the same to compare an experiment under reduced gravity with those executed under 1 g on ground.

2. ENSURING EXPERIMENT CONDITIONS

The requirements for experiments in microgravity are quite different. Material science or crystal grow experiments have other objectives than biological experiments. Temperature ranges for experiments with living cells are in the range of 37 °C and should be kept in this range permanently while investigations in material science need to change from solid to liquid phase of the material which means temperatures often very high between 1000 and 2000 °C. What is common for most of the experiments is the protection against vacuum. The surrounding pressure at apogee is about 10-6 mbar. The process chamber or experiment housing has to be tightened or must be able to release overpressure when high temperatures cause pressure increase. In some cases it is also required to execute experiments at different pressure levels.

In certain processes on board the payload as a secondary effect the temperature of some components or units is increasing drastically. To avoid damages or failure function the experiment set up has to be cooled down with separate operations.

Those operations can differ from peltier cooling for small volume units to water cooling for high efficiency systems. In any case the cooling system has to be adapted to the keep the temperature in the limits during the important flight time in microgravity.

2.1. Water cooling during flight

The Electro-Magnetic Levitator experiment is an example for application of a water cooling system to dissipate the heat in the process set up.

The central unit of this experiment set up is a combined coil system that generates the heater and also the positioning function. The total power dissipation in this coil system can reach in maximum more than 1.5 kW. The coil itself consists of a small tube with an inner diameter of 2mm. With a flow rate of 2 l/min water is streaming through this tube to avoid overheating. The flow function is combined with the safety logic. No magnetic field can be established without flow of cool water. A few seconds uncooled operation would destroy the coil.

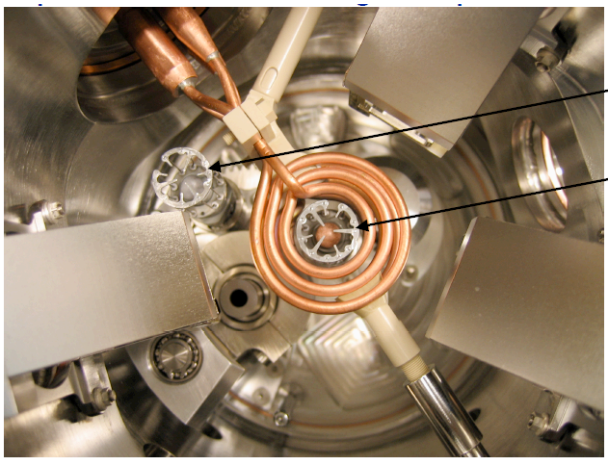

Figure 1. TEM EML water cooled heater / positioner coil system The arrows point the samples to be positioned in the coil

Proc. '21st ESA Symposium European Rocket & Balloon Programmes and Related Research',
9–13 June 2013, Thun, Switzerland (ESA SP-721, October 2013)

The flow of cooling medium is shown in figure 2 blue line (MDUK). Just after lift off during ascent the stand by flow rate of 2,25 l/min is decreasing to a value lower than 2 l/min. caused by the hydrodynamic pressure in the cooling system. The linear acceleration reaches the maximum and while the spin rate of the rocket is also increasing up to 3,6 Hz. After despin phase and the following separation of the payload from the motor at + 59 s the flow reaches the original value. At the beginning of the experiment program full heater power is applied to the coil and the temperature in the cooling fluid rises drastically.

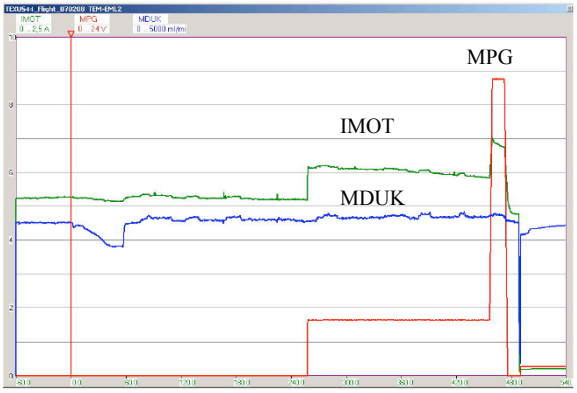

Figure 2
Housekeeping data of TEM EML 2
The blue line MDUK shows the cooler flow rate

Figure 3
HK temperature data of TEM EML 2
The red line shows the cooler fluid

Figure 3 shows the cooler temperature among the HK-temperatures. The temperature at the coil itself is quite higher. The sensor for the cooling water is located at the outlet of the cooler. Each activation of the heater results in an increase of the cooler temperature and secondary in a miner increase of the flow rate as an effect of the changed viscosity of the fluid.

For this application the constance of the flow rate is sufficient to transport the heat out of the process chamber and to protect the coil. The critical point is the early flight phase. As the safety logic is combined with the flow rate monitor the threshold has to be fitted to the flow rate decrease when the g-forces of the linear acceleration are dominant.

3. ESTABLISHMENT OF CERTAIN GAS FLOW RATES

3.1. Comparing requirements

In the some cases we have to meet the requirement of laminar gas flow condition. This is the prerequisite for combustion experiments to avoid any turbulence. In a recently flown experiment of the Fraunhofer Institute in Bremen, Nickel was to be vaporised and transported by a laminar flowing gas stream through the process chamber and collected with a sampling rod.

Picture 1 : TEM 06-34M Nano-Technology Experiment "Ni Vaporisation" Fraunhofer Institut, Bremen

In applications where gas flow is not only used for cooling purposes to drive pneumatic systems but

specified gas flow is required we need to control the gas flow.

3.2. Former found solutions

Looking back at the many Texus Experiment Modules we developed in the past we were already faced with requirements of different gas flow velocities. In the combustion experiment of Prof. Dr. S. Tarifa, Madrid we were able to apply three different gas flow rates for the combustion experiment under microgravity. Three different gas mixtures were used in this experiment to change the combustion parameter. At that time, at the end of the nineties of last century we had to design and develop our one regulator. This was realised with as a dynamic operating pneumatic regulator to keep the pressure for the flow control system constant. The different flow rate themself were realized with orifices of different sizes. Without going to much in detail the achieved results were quite remarkable.

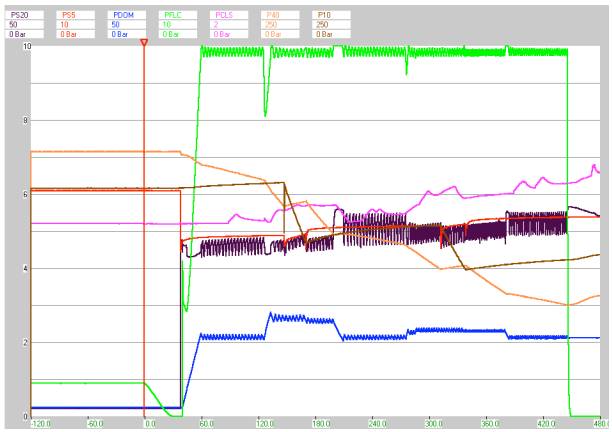

Figure 4: Pressure plot of TEM SEM Texus 38

Regarding the flow control pressure PFCL (light green line) the value was regulated to a value just below 10 bars. The disadvantage in this solution was the remaining ripple of about 2 % because of the hysteresis in the regulation loop. The laminar flow characteristic was established with a porous plate of sintered material that also equalized the continuity of flow.

Regulation processes for pressure have to be optimized especially when laminar flow conditions and low flow rates are to be established

3.3. Solutions with actual technic

For very low flow rates hysteresis effects cannot be accepted and the regulation has to operate in very narrow limits. In the meantime there are commercial units on the market which can be used and qualified for application in space.

3.4. Functionally principle of flow controller:

The measured gases were divided in two laminar flows, one through the primary tube and another through a capillary sensor tube. Both tubes are designed that laminar flow is given and accordingly the relation of their flow rates is constant. In the sensor tube a heater coil is integrated and also two temperature sensors. These are placed upstream and downstream the heater. In case of flow through the tube the heat is transferred by the gas in flow direction. The resulting temperature difference is linear proportional to the flow through the tube.

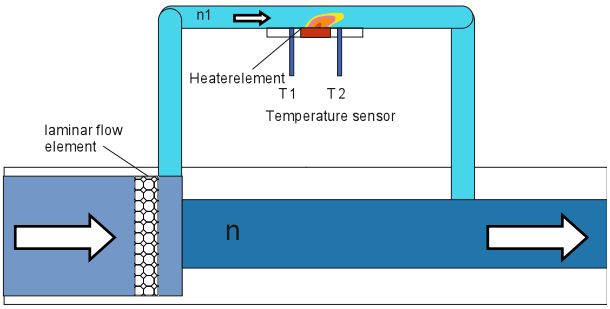

Error! AutoText entry not defined.

Figure 5: Principle function of mass flow controller

 # The flow (n1) through the by pass driven by a laminar flow element is proportional to the main flow (n).

The application of this method has to be calculated with a pressure loss because the pressure drop at the laminar flow element.

 # The flow (n1) is proportional to the temperature difference caused by the flow through the by pass.

$$T2 - T1 = a \times n1$$

Because the mass flow is detected by a sensor that works according to a thermal principle no correction of pressure or temperature is needed.

If now the amount of gas through the tube is known we can follow on to control the mass flowing through the system. With opening and closing of solenoid valves a flow rate can be kept between an upper and a lower limit. If the flow rate is high the remaining hysteresis may be acceptable, as mentioned above. That is not the case for lower flow rates.

A development in the pneumatic industry led to an analog valve or proportional valve to control low flow rates of gases or liquids. With a voltage input 0- 10 V

or current input 0-20 mA certain opening angles are activated in the valve. Those proportional valves cover a limited range and have to be selected for the designed application.

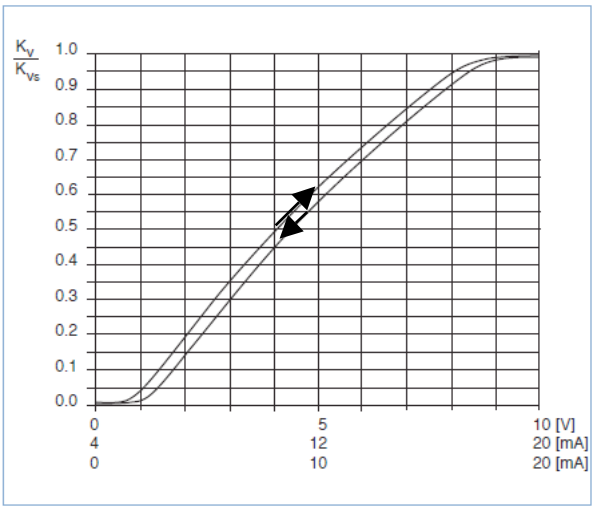

Figure 6: Characteristic of a proportional valve

The characteristic is shown in figure 6. Each line in the graph is representing one operational direction. This general function could be optimized with additional operations.
However the proportional valve requires a special activation with controller and switching unit to be controlled from total closed to total open position.

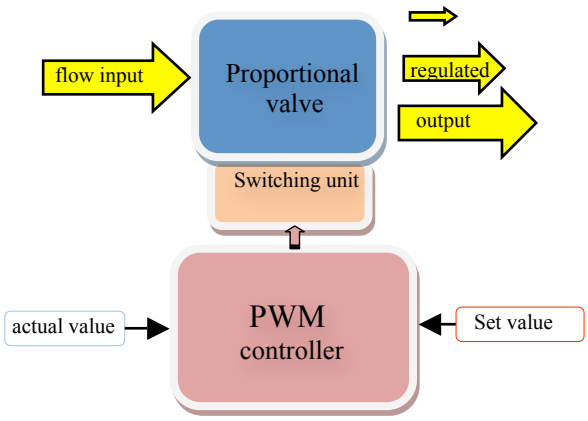

Figure 7: Control loop with proportional valve

The figure 7 shows the components to operate a proportional valve. The controller gets input of the actual flow rate and compares with the set value. According to the difference between both the controller has to increase or decrease the valve position. The controller is designed in this case as **P**ulse **W**idth **M**odulation regulator. Operational principle:

The measured deviation from set value is transformed in pulse packages of certain width.

Pulse Width Modulation visualised

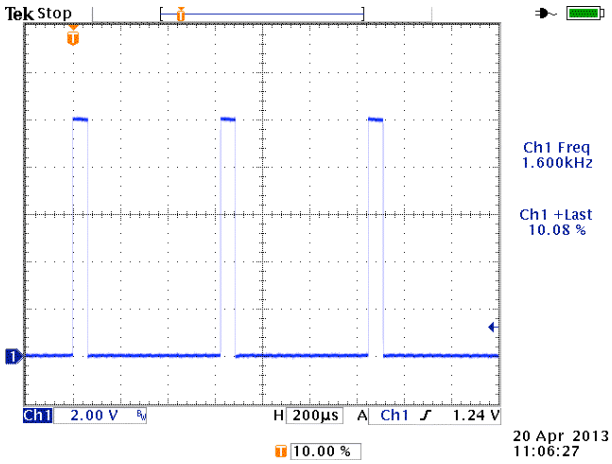

Figure 8: PWM regulator output for 10 % opening of valve

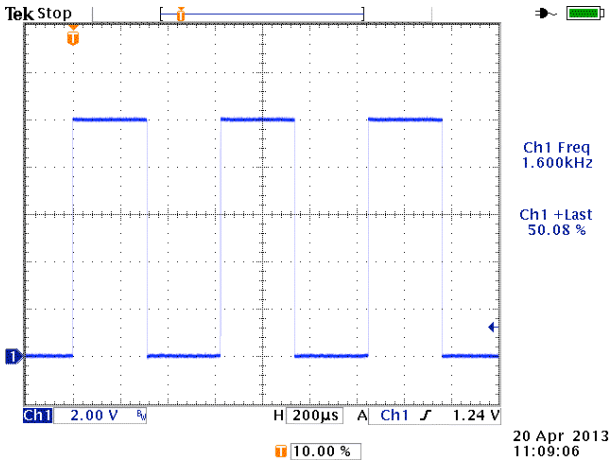

Figure 9: PWM regulator output for 50 % opening of valve

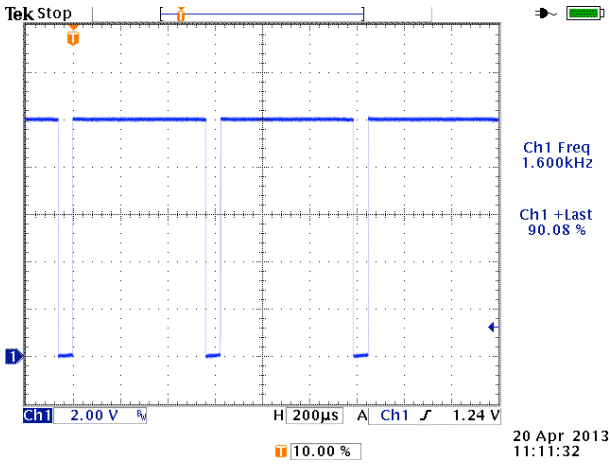

Figure 10: PWM regulator output for 90 % opening of valve

The switching unit between controller and proportional valve converts the pulse package in on / off commands for the valve. The switching frequency is 1,6 kHz. This fast switching of the valve leads to the continuity in the regulation process.
The shown principle of **PWM -**regulation is applied in the commercial mass flow regulators in different variations. For correct flow rates a calibration factor f has to be considered for different gases.

gas	factor f
N2	1,00
Air	1,00
O2	0,98
H2	1,01
Ar	1,4
He	1,42
CO2	0,77

Table 1: Calibration factors for common gases

With commercial mass flow controller high accuracy can be achieved. In order to linearize the characteristic of the proportional valve the corrected values are mapped in an internal look up table. According to the selected set point the actual value is recalled. This method of mass flow control technology is able to operate within the following limits as written in the data sheet of the supplier:

Linearity	0,1% F.S.	
Repeatability	0,1 % F.S.	
Accuracy	0,8 % F.S.	1,5% o.R.

Table 2: Detail from data sheet for mass flow controller

In our application for the above mentioned nanoparticle experiment we chose a type of mass flow regulator specified for flow rates of maximal 2 l/min. Additional we had to control the pressure in the process chamber at two different set points. For this pressure regulation we used a proportional valve and combined it with our own developed PWM regulator.

Table 3: Setting values for pressure and flow rate for the TEM 06-34 M flown on Maxus 8

set point	Pressure	Gas flow
	mbar	(l/min)
1	**300**	**1,923**
2	**300**	**0,481**
3	**300**	**0,275**
4	**300**	**0,192**
5	**100**	**0,641**
6	**100**	**0,160**
7	**100**	**0,092**
8	**100**	**0,064**

The results we achieved with this experimental set up were pretty good.

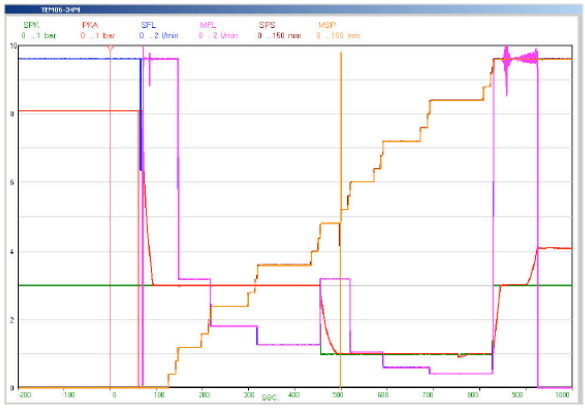

Figure 11: Flow rate (violet line) and pressure (red line) regulation of EM 06-34M on Maxus 8

After we optimised the system we reached an accuracy close to the values in the data sheet. The violet line, the measured flow rate is covering the set value, blue line. Pressure changes were realised within 20 s and also very exact; set value green line, actual value red line.

4. CONCLUSION

Scientific research in space requires special effort. Solutions could be found in detail to ensure comparable conditions for ground based experiments and in space environment. To fulfil the requirements at the time is always a question of available hardware. As in former years more solutions had to be found with own design and development in detail we can use up to date components and functional units which are available in different branches of industry. It could be an enormous reduction of weight and volume to qualify compact items from the shelf for operating in experiments under free fall. Mass flow controller and proportional valves in combination with **P**ulse **W**idth **M**odulation are details on the way to success.

5. REFERENCES

1 Figure 1: EML 2 Presentation, Astrium
2 Figure 2,3: Final report Texus 44;
ESTEC Contract No. 20500/07/NL/FC
3 Figure 4: Final report Texus 38
4 Picture 1: Astrium archive
5 Figure 6: DTS 1000083869 Bürkert
6 Table 1- 3: DTS 100095464 Bürkert
7 Figure 11: Final report Maxus 8
MX 8-RIBRE-RP-0006

NEW DEVELOPMENTS ON ROCKET PROPULSION WITH GELLED PROPELLANTS

Karl Wieland Naumann[(1)], Jürgen Ramsel[(2)] , Konrad Schmid[(3)], Helmut Niedermaier[(4)], Pedro Caldas-Pinto[(5)], Albert Thumann[(5)]

[(1)] Bayern-Chemie GmbH, PO. Box 1131, D-84544 Aschau/Inn, Germany, karl.naumann@mbda-systems.de
[(2)] Bayern-Chemie GmbH, PO. Box 1131, D-84544 Aschau/Inn, Germany, juergen.ramsel@mbda-systems.de
[(3)] Bayern-Chemie GmbH, PO. Box 1131, D-84544 Aschau/Inn, Germany, konrad.schmid@mbda-systems.de
[(4)] Bayern-Chemie GmbH, PO. Box 1131, D-84544 Aschau/Inn, Germany, helmut.niedermaier@mbda-systems.de
[(5)] Bayern-Chemie GmbH, PO. Box 1131, D-84544 Aschau/Inn, Germany, pedro.caldas-pinto@mbda-systems.de
[(6)] Bayern-Chemie GmbH, PO. Box 1131, D-84544 Aschau/Inn, Germany, albert.thumann@mbda-systems.de

ABSTRACT

Gelled propellant rocket motor (GRM) technology development started in Germany in 2000 as an activity of Bayern-Chemie (BC), the research institutes FhG-ICT and DLR-IRA and the BWB (now BAAINBw) that funded the activity on behalf of the German MoD. After two perfectly successful demonstration flights of a monopropellant GRM in December 2009 the program goes on to improve the performance and functional parameters. Based on the concept design for a kick stage / trajectory insert stage motor presented in 2011 [1], this paper describes the progress achieved within the last two years and the impact on the performance of this system and other applications like first stage motors or attitude control systems.

1. INTRODUCTION

1.1. Gelled Propellant Rocket Motor Technology

The technology of a GRM in general and the history and state of technology and science are described in [2] and the literature cited therein, and an overview on the status of GRM technology at Bayern-Chemie gives [3]. Fig. 1 shows the concept of a GRM and its key components. Like a liquid rocket motor a GRM has separated propellant tank(s) and combustion chamber(s). The gelled propellant (GP) is essentially solid in the tank. Upon injection into the combustion chamber the GP liquefies when passing the injector channels. In the combustion chamber the propellant is burnt in the same way as a liquid propellant. Summarized in very short words for the ease of understanding, the GRM in general combines the advantages of a solid rocket motor (SRM) - easy handling and long storage time – with those of a liquid rocket motor (LRM) – thrust modulation / shut-off capability and the potential for long operation times. It performs better than both SRM and LRM in terms of hazard potential, because in case of an accident or fire it creates neither an explosion nor a fireball (see for details [1]). It is inherently safe to operate, because three independent functions are necessary to put a GRM into operation:

- Pressurization of the propellant tank
- Initiation / operation of the igniter
- Opening of the GP control / opening valve

If any of these functions fails, the GRM cannot operate. Hence, a specific safety and arm unit (SAU) as for SRM is not needed. It is also easy to stop the function by either shutting the GP valve or venting, i. e de-pressurization of the GP tank, if the operation or launch process has to be stopped.

Essentially, a GP consists of a blend of preferably storable liquids and the gelling agents. Burning modifiers can be used to control the combustion behaviour and solid particles can be added to improve the density and the specific impulse of the GP without the risk of sedimentation even over long storage periods. This holds equally for monopropellant GRM representing the current state of technology at BC as for bi-propellant systems with gelled fuel and oxidator. A key element of the German approach is the use of a “green gelled propellant” that is neither toxic nor corrosive; the same holds for the reaction products.

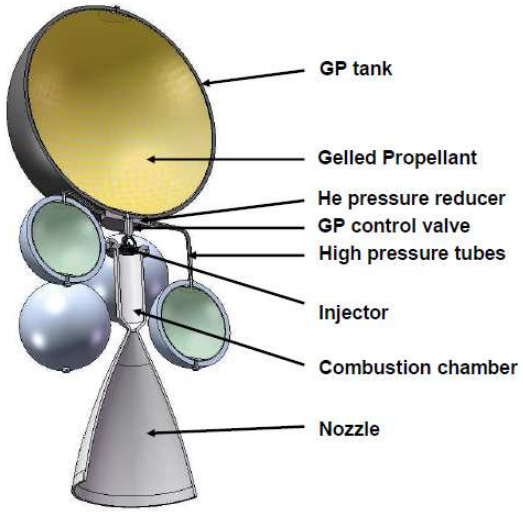

Fig. 1: Concept of a GRM with an inert gas pressurization system and a tank with a membrane [1].

Proc. ‘21st ESA Symposium European Rocket & Balloon Programmes and Related Research’, 9–13 June 2013, Thun, Switzerland (ESA SP-721, October 2013)

The GP also shows no sloshing in the tank and can be used for spinning vehicles without problems. While pressurization of the tank by a gas generator (GG) allows a compact design, the use of inert gas allows for lighter structures if the time of operation = time of tank pressurization is that long that the use of a GG that produces hot gas would require a thermal shield of the GP tank structure.

1.2. The German Gelled Propellant Rocket Motor Program

After preliminary activities in 1999 the German Gel Technology Program (GGTP) [2, 3] was initiated in 2000 as an initiative of Bayern-Chemie (BC), DLR Institute of Space Propulsion (IRA), FhG Institute of Chemical Technology (ICT), German armed forces proving grounds (WTD 91) and the German MoD. The goal was to develop a thorough understanding of the technology and to fly a missile with GRM in 2009, which was achieved by two out of two perfect ballistic flights with a monopropellant GRM with pre-programmed thrust modulation. For a detailed description of missile and test see ref. [4]. Key figures of the missile are:

- Calibre = 135 mm
- Length = 3042 mm
- Launch mass = 75 kg
- Propellant mass = 12 kg
- Nominal thrust = 5,5 kN

Fig. 2 shows the demonstrator missile at launch.

Fig. 2: The GRM demonstrator missile at launch [2, 4].

Special features of the German GRM technology, in addition to the above mentioned general ones, are:

- A monopropellant system with very stable start, combustion and throttling behaviour
- Demonstration of the predicted performance parameters, like specific impulse
- Environmental friendliness of propellant and exhaust gas
- Little primary and secondary smoke if no solid additives are used
- Good handling, transport and storage properties
- Long storage time, like solid propellant (SP)
- Lower cost for the GP, compared to (SP) or other storable propellants.

Other functions that have been demonstrated by static tests are:

- Ignition by an external gas lancet.
- A family of GRP (see Tab. 1) with different gelling agents, additives and particles that improve I_{spec} and particularly $I_{spec,vol}$, equalling the I_{spec} of aluminized composite SP (GRP 002, 004, 013). Other compositions which have a low T_c are ideal for use as GG propellants (GRP 007,008, 010). For specific applications the T_c can be adapted to the heat resistance of structural part for the intended conditions and time of operation
- Very good scalability of size; demonstrated in the range of nominal thrust levels between 300 N and 6000 N
- Wide operational temperature range from -30 °C to +70 °C
- Wide pressure range for combustion from 0,75 to 10+ MPa

Gel	I_{sp} p_e/p_o = 70:1 [Ns/kg]	Dichte [g/cm3]	Tc [K]
GRP 001	2248	1,13	2199
GRP 002	2487	1,31	2795
GRP 003	2236	1,18	2089
GRP 004	2586	1,26	2910
GRP 005	2080	NA	1883
GRP 006	2182	NA	1981
GRP 007	1900	1,11	1396
GRP 008	1878	NA	1375
GRP 009	2143	1,19	1904
GRP 010	1749	1,33	1213
GRP 013	2478	1,41	2908

Tab. 1: I_{spec}, ρ_{GRP} and combustion temperature T_c of our gelled monopropellants [3]

Our ongoing efforts aim to

- Improve further the thrust turn-down ratio, respectively the mass flow turn-down ratio
- Verify very long operation times. A first test with an uncooled C/SiC combustion chamber made by DLR-IBK showed very promising results in combining long durability with a low structural mass
- Create a GRM with re-ignition capability
- Improve further the fuel mass flow control and regulation technique

Environmentally friendly hypergolic compositions are a matter of basic research, but not yet mature enough to be tested in combustion chambers. This excludes

applications that need a high number of pulses from today´s considerations.

Taking that all, our GRM technology is ready for initial applications. Because of the very high modularity of the GRM, future improvements can be integrated into existing systems as soon as these features are mature enough for application.

2. POTENTIAL APPLICATIONS FOR SOUNDING ROCKETS AND SPACE PROPULSION

2.1. General Aspects

The GRM technology in the version flown by BC has benefits compared to SRM or LRM technology if the following requirements dominate:

- Thrust adaptation, thrust control or thrust termination ⇒ application for
  - Final stages of sounding rockets / space transport systems
  - Orbit insertion motors
  - Launch vehicle attitude control systems
- Low hazard potential, good handling, transport and storage properties, and environmentally friendliness of the propellant and combustion products ⇒ application for
  - Sounding rockets
  - Sub-orbital space tourism (etc.) vehicles
  - Launch vehicle attitude control systems
- Low cost of propellant ⇒ application for
  - Sounding rockets
  - Sub-orbital space tourism (etc.)

In the following chapters we outline some examples of potential GRM applications. We give some numbers for performance and dimensional parameters to allow comparisons with solutions based on current technologies. Please keep in mind that these are examples and that systems within a wide range of performance parameters and dimensions can be designed.

2.2. Upper Stage or Trajectory Insertion Rocket Motors with Shut-off or Thrust Adaptation Capability

For some sub-orbital or even orbital missions it is important that the payload is put on a trajectory very precisely in terms of the course of the trajectory and the speed at a given point. Solid rocket launchers, which come more and more into use, are very compact and easy to handle on the launch pad, but have no means to precisely control the burn-out velocity. Hence, a small stage using a RM with thrust modulation or shut-down capability has to be used. The purpose of this small stage is to deliver a small velocity increment that bridges the gap between the burn-out velocity of the main launcher and the required trajectory insert velocity and to add some potential energy if required. In [1] we described in detail a concept of such a motor based on the state of the technology of 2009, which is shown in Fig. 1.

The high p_c needed by this time was a severe mass driver in so far as the whole tank and tank pressurization system had to be designed for an operational pressure of p_T = 20 MPa [1]. The numbers are given in the first column “Basic concept” of Tab. 2.

In 2011 operation at low p_c using GRP 005 and 006 allowed to reduce the p_c to 2 MPa and accordingly the p_T to 5 MPa [5]. The mass savings are significant:

- The mass of the GP tank reduces about proportionally to p_T by 75 %
- The mass of the He tanks and the He gas reduces equally by about 75 %
- The mass of the tubings reduces as well, but not really proportional to p_T because of the interfaces

Even without taking into account mass savings that should come from a somewhat lighter combustion chamber, the structural mass of this concept, given in column “Low pressure” of Tab. 2, reduces from 570 kg to 198 kg, and the ratio of m_{Prop}/m_{total} increases from 0,66 to 0,85. As a matter of fact, the p_T does not differ significantly from the levels that are common for LRM that work on hydrazine as propellant and NTO or MON as oxidizer if it is a bi-propellant system. In the same way, the designs of the membrane or bladder tanks are very similar. Accordingly, the mass of tank and pressurization system is roughly equal between GRM and LRM, leaving differences in the mass balance to the rocket motor assembly and the safety devices.

Using an improved propellant with higher I_{spec} and ρ_{Prop} [5] reduces, for a system that has the same I_{tot}, the size of the GP tank and even more the structural mass to 183 kg. Because the m_{Prop} decreases from 1130 kg to 940 kg, the ratio of m_{Prop}/m_{total} is 0,84 in this case. The improvement gained by the improved propellant does not manifest in better m_{Prop}/m_{total}, but in a reduced $m_{Stage,total}$ of 1123 kg vs. 1328 kg, which means that either the reduced upper stage mass allows

- The lower stages to achieve a higher burn-out velocity, or
- A higher payload.

In order to check the validity of these parametric estimations and because we had to design a concept for another potential application, we designed the GRM concept shown in Fig. 3.

Parameter	Basic Concept, State of demonstrator (2009)	Low pressure (2011)	Low pressure, propellant potential
Nominal thrust	10 kN	10 kN	10 kN
Burning time at nominal thrust	280 s	280 s	280 s
Nominal Combustion Chamber pressure	10 MPa	2 MPa	2 MPa
GP tank pressure	20 MPa	5 MPa	5 MPa
Max GP mass	1130 kg	1130 kg	940 kg
Maximum He tank pressure	100 MPa	100 MPa	100 MPa
Maximum He mass	45 kg	11 kg	9 kg
He tank volume	6*42 l	3*21 l	3*17 l
Total mass	1700 kg	1328 kg	1123 kg
Inert GP tank mass	250 kg	63 kg	55 kg
Inert He tank mass	175 kg	44 kg	39 kg
Mass of CC, nozzle, inj. GP contr. valve	65 kg	65 kg	65 kg
Mass of tubings	35 kg	15 kg (est.)	15 kg (est.)

Tab. 2: The mass of the trajectory insertion motor concept of [1] and its evolution with progress of the technology.

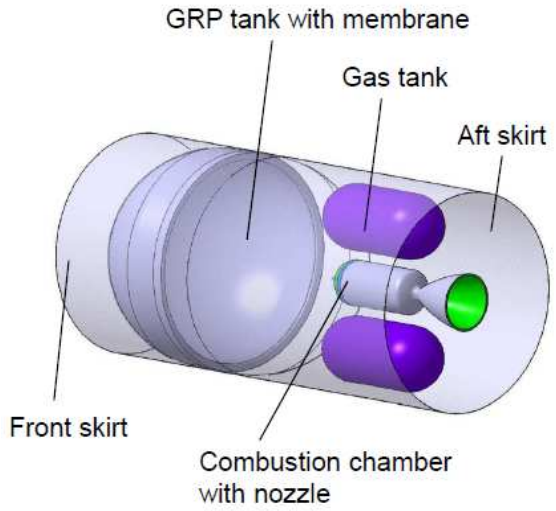

Fig. 3: Concept of a controllable trajectory insertion stage with GRM.

The basic ballistic parameters are quite similar to those of the concept shown in Fig. 1 and described in Tab. 2, and the design of Fig. 3 shows most of the features of the GRM described in [1]. Like the upgrade presented in [5], we use a p_T of 5 MPa, the $p_{c,N}$ of 2 MPa and the F_N of 10 kN. Major changes compared to the concept of Fig. 1 [1, 4] are:

- The mass of the GRP 006 is 1000 kg; its $I_{spec,vac}$ with the nozzle of A_e/A^* = 64 is 2520 m/s (or 257 s in US units)
- Given a p_T of 5 MPa, the GRM can operate in the regime 0,75 MPa ≤ p_c ≤ 3 MPa which allows a thrust level of 3,8 kN ≤ F ≤ 15 kN, i.e. a thrust turn-down ratio of 4. Hence, the thrust can be adapted to the mission requirements or to the maximum acceleration that the payload can tolerate
- The front and aft skirt of the stage are part of the design and the mass balance
- For the design of the combustion chamber the current technology using a steel structure with ceramic heat shield is taken. The full C/SIC structure should provide improvements and shows promising first results, but verification is still ongoing
- The A_e/A^* is reduced to 64 in order to arrive at a more compact design
- The diameter of the stage is reduced to 1 m which causes a GP tank with a short cylindrical section

Features that have not changed are the tank design concept, using carbon fibre reinforced resin (CFR) over a thin liner of Al-alloy, and the overall principle of operation.

Table 3 shows the ballistic and performance data and gives the essential dimensions. Table 4 shows the mass breakdown.

Since we now consider the whole stage, the mass needed for support structures that carry the elements and for the energy supply of the valve and GP mass flow control are taken into account as estimates and given in Tab. 4 as well. The front and aft skirts are able to sustain an axial load of 300 kN, allowing a maximum acceleration of 200 m/s (or 20 g) for a total mass of payload and interfaces of 335 kg.
Not included in our considerations are means for thrust vector or attitude control or specifics of interfaces to the lower stage or the payload.

For the thrust vector control the most elegant way should be to design a movable combustion chamber with nozzle like for standard LRM.

Parameter	Value	Dim.
Total Impulse	2520,0	kN*s
Maximum Thrust (pc = 3 Mpa)	15,0	kN
Nominal Thrust (pc = 2 Mpa)	10,0	kN
Minimum Thrust (pc = 0,75 Mpa)	3,8	kN
Thrust turn-down ratio with fixed nozzle	4	
GRP tank pressure	5	Mpa
Gas Tank pressure	70	MPa
Length of Stage	2688	mm
Exterior diameter of Stage	1000	mm
Exterior length of GRP Tank	1550	mm
Exterior length of gas tank	630	mm
Exterior diameter of gas tank	300	mm
External diameter of the combustion chamber	200	mm
Length of the Motor with nozzle	1038	mm
Nozzle throat diameter	60	mm
Nozzle end diameter	480	mm
Nozzle area ratio	64	

Tab. 3: Key parameters of the actual trajectory insertion / upper stage motor concept

Component	Mass
Propellant	**1000,0 kg**
Tank	45,0 kg
Tank Interfaces + Membrane	21,0 kg
Filling valve and inlet tube, estimated	1,0 kg
Tank total	**67,0 kg**
Combustion Chamber	19,0 kg
Injector	4,5 kg
Motor total	**23,5 kg**
Gas-Tanks, 2 pc.	25,5 kg
Pressure reducer, estimated	1,0 kg
Pyrovalve, estimated	1,0 kg
Gas, He	7,0 kg
Gas pressurization total	**34,5 kg**
Actuator block, estimated	4,0 kg
Tubings, estimated	4,0 kg
Support structure for gas tanks and CC, est.	9,0 kg
Electr. energy supply (Li-Ion) + control box, est.	4,0 kg
Components	**21,0 kg**
Structures total	**165,0 kg**
Stage mass total	**1165,0 kg**

Tab. 4: The mass of the actual trajectory insertion / upper stage motor concept

The attitude control can be done by small thruster blocks that combine a small GGG and a nozzle block with 3 nozzles [5]. These thruster blocks can be operated using the same GP as the main GRM if the particle load of the GP can be tolerated by the attitude control system, which is the case for GRP006. Otherwise, a separate GP tank, pressurized by the same tank pressurization system as the main tank can be used.

Another reasonable method for attitude control is to use the cold gas used for the pressurization of the GP tank. The advantage is that the mechanical parts are kept cold and hence may be much simpler than hot gas structures. Another advantage is that even after the consumption of the GP the big amount of pressurization gas is still available and can be used for control purposes. In a similar way it is possible to use the gas to assist a de-orbiting manoeuvre, but we have to keep in mind that the total impulse of the cold gas system will be limited.

The modularity of the GRM allows to combine different tank systems and GRM with different thrust regimes according to the specific mission requirements. In addition, the filling of the tank can be adapted to the specific mission requirements.

In short: one trajectory insertion GRM design can be used for a wide variety of missions, and a set of modularly usable components, especially GP tanks and He tanks of different volume and GRMs of different thrust categories allow to tailor a trajectory insertion motor from verified components according to specific mission requirements.

The modular system, for example, allows also to carry out full functional checkout flight tests of the GRM with a smaller tank and accordingly a smaller and more affordable launcher; thus leaving only the big tank to be verified with the full-size launcher assembly.

Whether the filling of the GP is done near the launch site or at the manufacturer´s facilities depend on the specifics of the program – both variants are possible.

Development activities that are ongoing and needed to realize such a stage are:
- Verify very long times of operation
- Verify the “big” GP tank and tank pressurization system
- Establish the production of GP in large quantities

Further R&T activities to improve the GRM technology for such an application are:
- Develop a method for shut-down and re-ignition of the GRM, which will allow to use such a stage as a fully capable orbital insert motor.

2.3. Insensitive and Environmentally Friendly Stages for Sounding Rockets

The stage of a sounding rocket will have basically the same components as the upper stage explained in chapter 2.2. The main changes and adaptations needed to build a stage for a sounding rocket are:
- The sounding rocket takes off in the lower atmosphere. To achieve a good efficiency of the GRM nozzle, the initial p_c has to be increased to at least 5 MPa, which means that $p_{T,max}$ has to be increased to 10 MPa as well. This doubles roughly the GP tank mass from 45 kg to 90 kg
- A first or only stage of a sounding rocket needs to have a higher L/D. The mass impact of a more slender tank depends strongly on the level of the bending moments and the associated bending stiffness required. Depending on the requirements, the wall thickness and the m_T are driven either by the higher requirement on bending stiffness or the higher requirement on p_T. If the required bending stiffness should drive the wall thickness, then the p_T and accordingly the p_c can be increased further, with an according increase of I_{spec}
- The mass of the pressurization system needs not necessarily to increase because the $p_c \approx p_T$ can be reduced as the rocket reaches higher altitudes: After 10 s of constant acceleration of 100 m/s^2, p_∞ has reduced to almost half of the MSL value which allows to reduce p_c accordingly. If the stage is very slender, then the high pressure gas tank can be integrated in line with the GP tank

- Th I_{spec} will be reduced because of the initial counter-pressure of about 0,1 MPa which means that a nozzle with smaller A_e/A^* has to be used. The optimum value will be driven by a compromise between acceptable efficiency at lift-off and good efficiency in the later phases of ascend.
- A GRM with a higher thrust for a higher acceleration. In this respect, the shortcoming of a GRM and a LRM compared to a SRM is that a higher thrust means a bigger combustion chamber (CC) and accordingly more structural mass. In contrast, a SRM benefits from the identity of tank and CC in that way that thrust level and structural mass are almost de-coupled over a wide thrust range. The trade-off to be done for a GRM (as for a LRM) is that between a higher structural mass for a bigger CC or the increased complexity of a thrust vector control system that is needed to stabilize the trajectory and compensate cross-wind effects during the early phase of a launch with low acceleration. If we use the pure pressure driven first order scaling law that for p_C = const, $m_{CC} \approx V_{CC} \approx F_N$ then, taking the m_{Motor} = 23,5 kg @ F_N = 10 kN from Tab. 4 yields a m_{Motor} = 235 kg @ F_N = 100 kN. While the initial p_C for the first stage is higher than that of the upper stage, we have to consider that the thickness of the heat shield does not scale with size or thrust level but with time of operation which is shorter for the first stage than for the upper stage. Taking as well into account that the nozzle has a smaller A_e/A^*, a reasonable estimate may be $m_{Motor} \cong$ 200 kg. This makes clear that for a GRM (and equally a LRM) the mass savings of the CC through a reduction of the thrust level with consequently reduced acceleration are higher than the additional mass of a thrust vectoring system. Only dominant budgetary constraints together with limited ballistic performance requirements promulgate a high-thrust stage that can be operated without a thrust vectoring system.
- As outlined above for the tank pressurization system, the p_c can be reduced as the rocket reaches higher altitudes. The thrust profile can be adapted to the reducing rocket mass and hence limit the acceleration load acting on the payload.

With a moderately increased F_N, a higher initial p_T and an actuation system for thrust vectoring of the GRM, the mass of the first stage with m_{Prop} = 1000 kg goes up to roughly 1250 kg. The ratio m_{Prop}/m_{total} = 0,8 is not far away from that what can be expected of a typical SRM of this size.

The advantage of the GRM is the thrust variation capability, the very low hazard potential, good handling, transport and storage properties and a high degree of environmentally friendliness.

3. SUMMARY

Gelled propellant rocket motor technology has an excellent potential to build stages with throttleable, insensitive and environmentally friendly rocket motors with good handling, transport and storage properties. A preferred applications is an upper stage or trajectory insert motor. First and second stage GRM for sounding rockets preferably use a thrust vectoring system to allow for a low motor mass, say moderate thrust and acceleration. Other potential applications worth considering are direction and attitude control systems.

Ongoing efforts aim to improve the I_{spec}, $I_{spec,vol}$ and the thrust turn-down ratio, to develop a re-ignition capability and to verify CC made of fibre reinforced ceramics.

4. ACKNOWLEDGEMENTS

We highly appreciate the continuous support of the German MoD´s Federal Office of Bundeswehr Equipment, Information Technology and In-Service Support (BAAINBw) and the exceptionally fruitful co-operation with the Fraunhofer Institute for Chemical Technology (ICT), German Aerospace Research Center´s Institute for Space Propulsion (DLR-IRA) and the Bundeswehr Technical Center for Weapons and Ammunition (WTD 91) and the DLR Institute of Structures and Design.

5. REFERENCES

1. Naumann K.W., Ciezki H.K., Stierle R., Schmid K., Ramsel J., "Rocket Propulsion with Gelled Propellants for Sounding Rockets", *20st ESA Symposium on European Rocket and Ballon Programmes and Related Research*, 22.-26.5.2011, Hyères, France

2. Ciezki H.K., Naumann K.W., Weiser V., “Status of Gel Propulsion in the Year 2010 with a Special View on German Activities”, Deutscher Luft- und Raumfahrtkongress 2010, Hamburg., Germany, August 31 to September 2, 2010

3. Schmid, K., Ramsel, J., Naumann, K.W., Stierle, R.; Weiser V., “Raketenmotore mit Gel-Treibstoffen – Stand der Technologie bei Bayern-Chemie”, Deutscher Luft- und Raumfahrtkongress 2012, Berlin., Germany, September 10-12, 2012

4. Stierle, R., Schmid K., Ramsel, J., Nauman K.W., “Free-Flight Demonstration of the Gelled Propellant Rocket Motor of MBDA Bayern-Chemie“, 4th European Conference for Aerospace Sciences, St. Petersburg, Russia, July July 4 – 8, 2011

5. Naumann, K.W., Stierle, R., Schmid, K., Ramsel, J., „Rocket Motors Burning Gelled Propellants - Potential Applications for Space Propulsion“,

6. NOMENCLATURE

6.1 Parameters

A	[m^2]	Area
F	[N]	Force, Thrust
I_{spec}, I_{sp}	[m/s]	Specific impulse
$I_{spec,vol}$	[N*s/m^3]	Volum. spec. imp.
I_{tot}	[N*s]	Total impulse
m	[kg]	Mass
p	[Pa]	Pressure
T	[K]	Temperature
V	[m^3]	Volume
ρ	[kg/m^3]	Density

6.2 Superscripts

*	Value at nozzle throat

6.3 Subscipts

CC	Combustion chamber
c	Combustion
e	Condition at nozzle exit
max	Maximum value
min	Minimum value
N	Nominal condition
Prop	Propellant
T	Tank
∞	Ambient condition

6.4 Abbreviations

CC	Combustion chamber
CFR	Carbon fibre reinforced resin
C/SiC	Carbon/Silica-Carbide
D	Diameter
GG	Gas generator
GGG	Gelled propellant gas generator
GRM	Gelled propellant rocket motor
GP	Gelled propellant
GRP	Gelled rocket propellant
L	Length
LP	Liquid propellant
LRM	Liquid propellant rocket motor
MON	Mixed oxides of nitrogen
NTO	N_2O_4
RM	Rocket motor
SGG	Solid propellant gas generator
SP	Solid propellant
SRP	Solid rocket propellant
TVC	Thrust vector control

TLM-NET: AN ETHERNET BASED TELEMETRY DATA DISTRIBUTION SYSTEM

Alison de O. Moraes, Wanderson. G. Almeida, Marcio B. Lucks and Sergio Fugivara

Instituto de Aeronáutica e Espaço, Praça Mal. Eduardo Gomes, 50
Vila das Acácias, 12228-904 – São Jose dos Campos – São Paulo – Brazil
Email: alisonaom@iae.cta.br; wandersonwmpp@gmail.com; marciombl@iae.cta.br; and fugivarasf@iae.cta.br

ABSTRACT

This paper describes improved ground station architecture namely TLM-Net. This system is capable of working with complex payloads that includes the last trend in sounding rockets instrumentations. Due to the high density of onboard instrumentation, the current systems are designed to work with several serial buses. On the ground side, the data from these serial buses must be unpacked and properly delivered to the users. The TLM-Net project is designed to work in a ground station architecture where the goal is to broadcast the payload data into a network such that several users can access and process the data independently.

1. INTRODUCTION

The current trend in avionics and sounding rockets instrumentation is the well established serial/USB communications interfaces. In the last few years onboard systems have had an increasing number of interfaces and devices working in this way, especially for data acquisition systems. This kind of architecture using high-speed serial links reduces drastically the wiring and integration issues but requires a different ground system interface. Migration on the ground telemetry system to support this architecture is leading to an Ethernet based instrumentation for sounding rockets. Figures 1 and 2 show respectively the onboard and ground architectures.

During INPE 13 and 14 payloads (VS-30 and VS-30/Orion rockets) the request of telemetry data distribution, including serial links for multiple users drove the development of the TLM-Net project. The goal of this project is to broadcast telemetry data in an Ethernet network to EGSE operation team and researchers who will receive the data in their respective positions and facilities. In particular, this system has to be able to deliver high speed serial data for multiple users simultaneously. In this work, the current development of the Ethernet based telemetry data distribution system is discussed. The paper is organized as follows: Section 2 provides a description about the hardware architecture. In Section 3 presents details about the software implementation. Finally, in Section 4 we describe our conclusions.

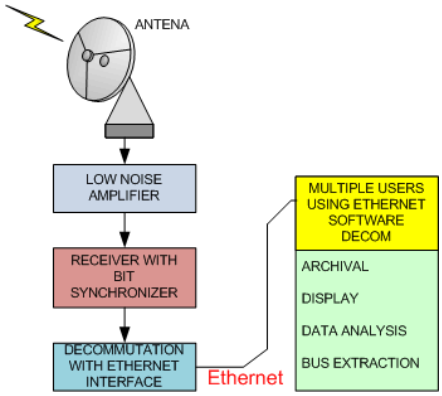

Figure 2. Ethernet Based Ground Station.

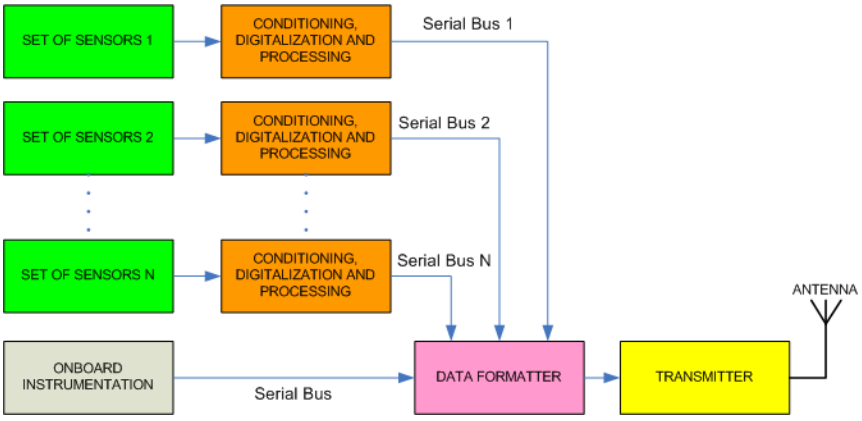

Figure 1. The current onboard telemetry topology.

Proc. '21st ESA Symposium European Rocket & Balloon Programmes and Related Research', 9–13 June 2013, Thun, Switzerland (ESA SP-721, October 2013)

2. HARDWARE

The system implementation has been made using a programmable bit synchronizer and decommutator with Ethernet adapter card, which receives the PCM data from payload and formats it to network packets working as a host. Figure 3 shows the hardware architecture of TLM-Net project.
The protocol implemented for this project is designed to provide broadcast functionality, distributing data for all users in the network.

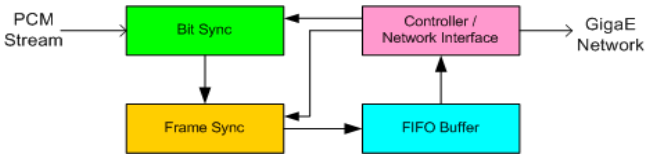

Figure 3. TLM-Net hardware architecture.

The bit synchronizer is programmable from bit rates of 10kbps up to 5Mbps. The decommutator is responsible for unpacking telemetry data and broadcast it into the Ethernet. All settings from the hardware for frame formatting and synchronization can be done also by Ethernet, accessing its specific IP address.

3. SOFTWARE

The software was developed in Java to be multi-platform and to provide for each user/client the capability of identifying and receiving onboard parameters. The TLM-Net hardware broadcasts each PCM sub frame and all users are able to select and visualize the desired parameters.

Another important capability of TLM-Net software is serial gate mode. When working in this mode, the software is able to transmit selected parameters through its own serial ports, making each client a serial gateway of the onboard serial links. Figure 4 shows the TLM-Net software interface. On the top of Figure there are the network settings, including the hardware address, on the middle it is possible to visualize the frame view where data for all PCM parameters are displayed. On the bottom, there is the serial output interface where the user can make port configurations and select the parameters to be transmitted.

4. CONCLUSION

This system receives PCM data from the payload and formats it to network packets working as a host. The telemetry broadcasted data can be used simultaneously by EGSE operation team and researchers in many positions and facilities. This system also delivers high speed serial data for multiple users. This system has been used/tested in INPE 13 and 14 payloads (VS-30 and VS-30/Orion rockets) and now improvements are in process to be used in multiple streams simultaneously.

5. ACKNOWLEDGMENTS

The authors are grateful to CNPQ – National Council for Scientific and Technological Development, through Award 560301/2010-3 for the financial support of TLM-Net development. MBL would like to thank FUNCATE – Fundação de Ciência, Aplicações e Tecnologias Espaciais, which partially supported his participation on 21st ESA Symposium.

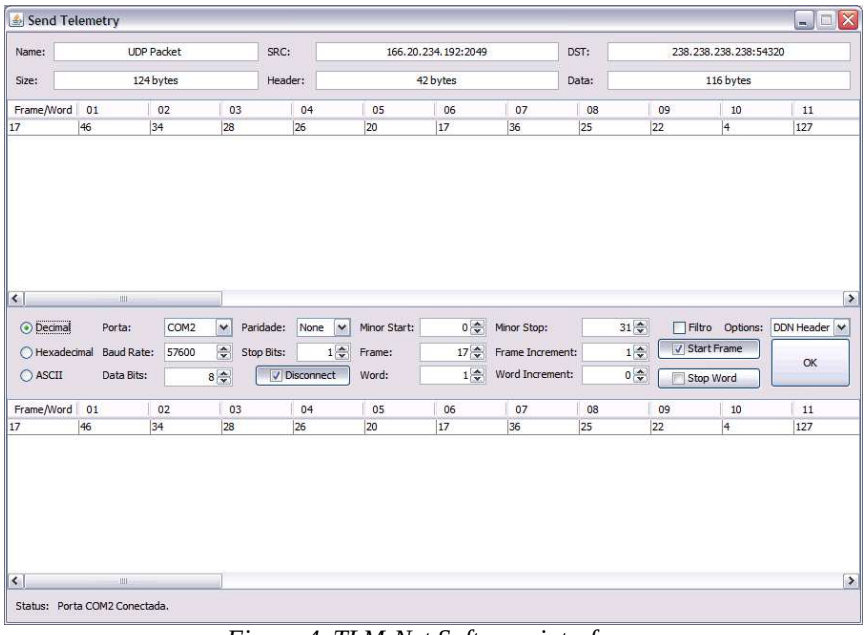

Figure 4. TLM-Net Software interface.

PROVIDING A STANDARD SUPPORT BUS FOR SOUNDING ROCKET EXPERIMENTS WITH THE CERESS EXPERIMENT

Alexander Schmitt[1], **Daniel Bugger**[2], **Christoph Friedl**[3], **and Sebastian Althapp**[4]

[1]*Technische Universität München, Boltzmannstr. 15, 85748 Garching, Germany, schmitt.alexander@mytum.de*
[2]*Technische Universität München, Boltzmannstr. 15, 85748 Garching, Germany, daniel.bugger@mytum.de*
[3]*Technische Universität München, Boltzmannstr. 15, 85748 Garching, Germany, christoph.friedl@mytum.de*
[4]*Technische Universität München, Boltzmannstr. 15, 85748 Garching, Germany, s.althapp@tum.de*

ABSTRACT

CERESS (Compatible and Extendable REXUS Experiment Support Bus) is a technical verification experiment on board a REXUS (Rocket-borne EXperiments for University Students) sounding rocket, launched in May 2013. The experiment has been realized by a team of aerospace students from the Technische Universität München (TUM). The objective is to develop and verify a standard infrastructure for future REXUS experiments, including the most demanded functionalities and meeting all necessary interfacing needs. Several sensors are part of the experiment to verify the data handling capabilities of the CERESS system.
This paper describes the experiment setup and presents results of the flight including a failure analysis. An overview on future reuse of the CERESS system is also given.

Key words: CERESS; REXUS; TUM; ViTo.

1. INTRODUCTION

An analysis of previous REXUS projects at the Institute of Astronautics at TUM has shown that for every new REXUS experiment an entire infrastructure has to be newly designed and built, despite the similarities in the requirements for the infrastructure of the experiments. These requirements include a regulated power supply, onboard data handling, command/control of the experiment, real-time communication and interfacing with the REXUS systems on the rocket as well as on the ground.
The main goal of the CERESS project is to develop a standard platform providing these most important functionalities which will enable future teams at TUM to concentrate more on their scientific objectives.
Once verified on the first flight, all used hardware (e.g. sensors) can be directly applied to future experiments. After recovery of the onboard stored data, the telemetry data from CERESS and from REXUS are merged into a unified data structure for later distribution, analysis and outreach.
In addition to acceleration, angular rate, temperature and pressure sensors, a camera documents the progression of the experiment. Monitoring and control software on the ground enables thorough surveillance of the experiment during the entire mission. Functions such as remote control of the experiment, sensor- or time-based actions are provided.
A visualization tool illustrates the rocket flight trajectory in a 3D simulation in near real-time. This meets a oft-demanded possibility for situational awareness and outreach.

2. SYSTEM OVERVIEW

The CERESS system consists of a Space Segment and a Ground Segment. The Space Segment is defined as the CERESS Rocket Module which performs the typical infrastructure tasks and the CERESS Verification Module which is used to verify the functionality of CERESS. The CERESS Ground Segment consists of the CERESS Ground Station, including the CERESS Ground Station Server and Clients which are interfacing with the ESRANGE Ground Segment and the CERESS Visualization Tool (ViTo). The interface of the CERESS Ground Segment and CERESS Space Segment is the TM/TC connection provided by the REXUS System.

3. CERESS SPACE SEGMENT SETUP

The CERESS Space Segment is built within a standard REXUS module of 120 mm in height. The main structures are the hull and the bulkhead which carries all loads and represents the basic mounting for all other parts of the module. The hull and bulkhead are both provided by DLR (German Aerospace Centre) and were modified to fulfil the needs of CERESS.

Proc. '21st ESA Symposium European Rocket & Balloon Programmes and Related Research',
9–13 June 2013, Thun, Switzerland (ESA SP-721, October 2013)

Rocket Module The CERESS Rocket Module is designed for reuse in future experiments and is the key component of the CERESS Space Segment. It retrieves data from included sensors and those of the attached CERESS Verification Module. The CERESS Rocket Module stores and processes the data on board and communicates with the CERESS Ground Module through which it can be controlled. In addition it provides regulated and monitored power to the CERESS Verification Module. It is also capable of invoking actions on the CERESS Verification Module.

Verification Module The CERESS Verification Module contains melting wires as simple actuators, which are used to verify the different control chains provided by CERESS. A variety of sensors are used to characterize the experiment's flight-environment. The sensors include temperature, pressure and a camera. The CERESS Verification Module will be replaced by the actual experiment in future REXUS missions from TUM.

3.1. Hardware

Fig. 1 shows a CAD model of the CERESS structure. The Rocket Module is enclosed in a metal box called Shielding. A frame structure exists within the Shielding to carry the loads. The Main Computational Unit is situated at the bulkhead. In the layers above, the SD-Card module and both Electric Power Supply (EPS) boards are placed on the Printed Circuit Board (PCB) mounting structure. Two accelerometers and two gyroscopes are attached to a crossbar at the centre of the rocket main rotation axis. Within the Rocket Module is also the interface board and one thermistor control board comprising three thermistors: one placed on top of the CPU, and one on each of the two DC/DC converters. For communication to the Verification Module and the other environment, multiple connectors are implemented in the Shielding. These provide a sufficient number of pins to forward all connections from the Main Computational Unit to future experiments.
Technically part of the Rocket Module but not housed inside the Shielding are six accelerometers. These are mounted on the bottom side of the bulkhead. For safety reasons they are covered by a protection plate.

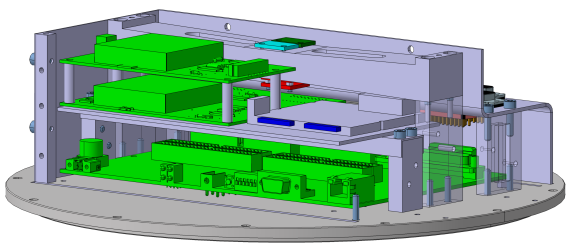

Figure 1. CERESS structure.

Thermistors are positioned in a venting hole and at the ambient pressure sensor within the Verification Module. The camera is mounted directly to the hull. A window has been installed in front of the lens for the protection of the camera and to prevent hot air flows into the module. The ambient pressure sensor is mounted directly on the bulkhead. Due to the highly sensitive filament inside, the device is wrapped into a rubber damping and held only through compression to ensure no direct connection to the bulkhead or other structures.

3.2. Electronics

The electronics subsystem's main functions can be summarized as follows:

- provide regulated power for experiment's components,
- provide communication and control infrastructure,
- condition analogue sensor data,
- enable connection to the digital sensors,
- provide data storage capability.

The CERESS experiment is supplied with power through the REXUS Service Module [1]. Since the 28V are unregulated and too high for components used in the experiment, it is converted to the desired voltage levels. The voltages used are 3.3V, 5V and 24V. 3.3V are required for the signal interpreter on the Interface Board, accelerometers and gyroscopes in the Rocket Module (RM), and for the melting wires in the Verification Module (VM). The 5V bus supplies the RS-422 converter and thermistors in the RM and the camera and thermistors in the VM. The 24V bus is the most important since it powers the Main Computational Unit as well as the ambient pressure sensor and the corresponding heater in the VM.
Incoming power is channelled through the Interface Board, where a PTC fuse is placed to protect the experiment from continuous overcurrent. It is then fed to two DC/DC converters, one providing 3.3V and 5V and the other 24V to the experiment components. Each DC/DC converter has its own PCB.

The Main Computation Unit (MCU) is represented by a NI-sbRIO 9642. It provides a powerful Field Programmable Gate Array (FPGA) with two Million Gates as well as a 400 MHz real-time CPU. Furthermore 110 digital I/Os and 32 analogue Inputs are integrated [2].
Communication with the Ground Segment is performed via the RS-422 converter on the Interface Board. It acts as an intermediate between the MCU and REXUS Service Module by converting a bit-stream to and from an inverted and a non-inverted signal according to the RS-422 standard. Three control lines are provided by the REXUS Service Module [1] and are connected to the MCU via optocouplers on the Interface Board to provide galvanic isolation.

The instrumentation of CERESS consists of scientific and maintenance sensors. The scientific part consists of eight accelerometers, two gyroscopes, a ambient pressure sensor, a camera and three thermistors. The housekeeping data includes voltage levels, current consumption of the Rocket Module and Verification Module as well as software states and temperature measurements.
Data storage capability is provided by using the NI-9802 SD-Card Module. It provides two slots and all electronics necessary for reliable storage of flight data. It is connected to one of the MCU's C-series Module connectors.

3.3. Onboard Software

The On-Board Data Handling (OBDH) main functions can be summarized as follows:

- gather measurement values from scientific sensors such as the accelerometers, gyroscopes, thermistors and ambient pressure sensors,
- gather measurement values for maintenance purposes such as temperature of the CPU, the ambient pressure sensor's heating foil, both DC/DC converters, the state of the switches attached to the melting wires as well as voltages and currents of all three power buses,
- perform actions on attached sensors and actors such as powering and activating the camera, burning the melting wires and activating the heating foil for the ambient pressure sensor,
- provide telemetry information to the Ground Station containing sensor and maintenance data,
- provide telemetry receiving and executing possibilities such as arming and triggering melting wires or restarting of the whole module,
- provide an internal Timestamper with accuracy to microseconds since power-up,
- provide an in-flight Timestamper starting at lift-off, also with microsecond accuracy,
- storing sensor data to SD-Card,
- execute actions based on the in-flight Timestamper,
- receive the three provided signals and perform defined actions,
- observe measurement values for trigger purposes .

The most important key features are explained in the following sections. The focus lies on the parts future teams are going to use.

SPI A Serial Peripheral Interface (SPI) is necessary in order to obtain data from the gyroscopes and accelerometers. The accomplished implementation allows a high flexibility to all parameters. Every sensor has its configuration stored in its depending file rendering it unnecessary to change the software in order to change parameters of the sensor. This way, different setups of the used sensors were done. The gyroscopes and accelerometers have two configurations providing a high-resolution (and small range) and a high range (and lower resolution) of measurement.
Furthermore the implementation makes it possible to run each sensor on its own sample rate which became necessary due to variations of the internal clocks of the devices and therefore drifts of measurement rates. The sensors set an interrupt line which is observed by the SPI. It is recognized and enqueued to collect the measurement data.

Storing Protocol CERESS makes use of the File Allocation Table (FAT) File System provided by the SD-Card Module. Therefore a file is obtainable. A disadvantage of this system is the time needed to open and close files - time in which data has to be buffered. Due the acquisition rates the buffer size is insufficient to perform open/close operation and therefore only one file can be used. Storing data of sensors with different acquisition rates (gyroscopes about 800 Hz, accelerometers about 1000 Hz and all analogues 1 Hz) is implemented by providing a protocol for this binary file. This enables the user to add new storing data with minimal effort.
A parsing program converts the data afterwards to readable *.txt files for each sensor with according timestamps.

Timestamper and in-flight Timestamper The FPGA enables users to implement programs that can be executed within one single tick. This means execution of complex code in about 250 ns. CERESS utilised this ability to provide two Timestampers with an accuracy of one microcsecond each.
The first Timestamper is started directly after power-on of the Rocket Module and is used for all logging and telemetry data; the in-flight Timestamper is started the moment the lift-off signal is detected. This provides the time reference for the Timeline execution.

Timeline execution Every experiment has events that have to occur during the mission (e.g. starting sensor acquistion, perform operations or shutdown systems in time). The REXUS Service Module provides some basics for this purpose represented as three signal lines.
CERESS provides more functionalities with its timeline. It runs on the real-time CPU and waits for the in-flight Timestamper (settled on the FPGA) to send an interrupt when the ordered time is reached. Such interrupts can then be handled in under 300 µs [3].

Event Logger Besides sensor storing and execution functionalities, CERESS includes an additional Logger that does not store information to the SD-Card; instead it uses the memory on the sbRIO itself and stays functional even if the SD-Card fails.
The Event Logger stores all events occuring during

the mission with a short message and an corresponding timestamp. The produced logfile provides a lot of information in addition to the downlinked data and is supposed to make failure analysis easier.
The Event Logger works in the background without blocking the normal execution.

Telemetry generation The key to providing surveillance of the experiment onboard a REXUS rocket is to transmit all relevant information. CERESS has defined 16 telemetry packages categorized to maintenance, scientific and state change data. Every package contains a header (with information about the contained data), the data itself and a trailer which provides checksum and cyclic redundancy checksum to verify the correct transmission.
Overall about 80 different parameters are downlinked during countdown and flight.

Melting wires and value observation Melting wires are the main component of a Hold Down and Release Mechanism (HDRM) already used by the FOCUS project [4]. In the case of CERESS the releasing part is removed and an additional switch is installed. There are three of these mechanisms to verify the capabilites to trigger events.
All of those mechanisms are only allowed to be activated in a specific time window which is achieved by the Timeline. Each of them is related to an individual event. One is time triggered and therefore also related to the timeline. The second is related to a Telecommand sent from ground while the third waits for microgravity measured by one of the eight accelerometers.
During the melting process, voltage, current and the state of the switch are acquired and downlinked afterwards to have feedback about the process.

4. CERESS GROUND SEGMENT

An overview of the CERESS Ground Segment's architecture (see Fig. 2) is given as well as noteworthy details of its implementation. The CERESS Ground Segment provides the following top-level functions:

- monitor and control of the CERESS Space Segment,
- validation and distribution of CERESS Telemetry and Telecommand (TM/TC) packages,
- visualization of the experiment's flight on the REXUS rocket in near real-time,
- being adaptable to future ground segment setups.

The CERESS Ground Station handles data from three different sources: *(1)* TM/TC from the CERESS Rocket Module, *(2)* POSNET from ESRANGE and *(3)* user input from the CERESS Ground Station Clients.

The Ground Station is designed around a database which handles the distribution of TM/TC packages, merges data from the different sources and provides access to the database to multiple clients running on different computers. The database is implemented as MySQL™-Server [5] and can be accessed by multiple clients on a Local Area Network (LAN) via the Open Database Connectivity (ODBC) [6] standard. Using ODBC, any kind of client can be added to the ground segment depending on the needs of future experiments.

4.1. CERESS Ground Station Server

The Ground Station Server is the interface between the CERESS Space Segment and the CERESS Ground Station Clients by which the experimenters monitor and control the experiment. TM/TC is sent and received by the Ground Station Server via a RS-232 [7] serial connection. The raw serial data stream is stored by the TM/TC Backup and forwarded to the TM/TC Transceiver by a RS-232 Port Splitter software.

TM/TC Transceiver The TM/TC Transceiver handles the low-level RS-232 serial communication functions such as byte-wise reading and writing to the serial ports buffer.

TM Decoder The TM Decoder decodes the received serial communication according to the CERESS TM/TC protocol. This includes frame validation, parsing of the report parameters, interpretation of them and writing gained data into the database.

TC Encoder The Telecommand Encoder encodes Telecommands scheduled in the database. It also handles the Telecommand verification procedure of sending a Telecommand, waiting for its corresponding Telecommand-Received-Report and eventually sending the Telecommand again.

POSNET Receiver and Filter The POSNET Receiver and Filter receives position data from the ESRANGE Tracking Stations via NMEA [8] messages. The data is filtered for invalid messages before it is written into the database.

4.2. CERESS Ground Station Clients

Multiple clients can connect to the database using ODBC via LAN depending on the mission's needs. A description of the clients implemented in the CERESS mission is given.

Scientific Displays Multiple displays show scientific data from the Space Segment (e.g. acceleration, rotational rates, ambient pressure, feedback from the Verification Modules melting wires and more).

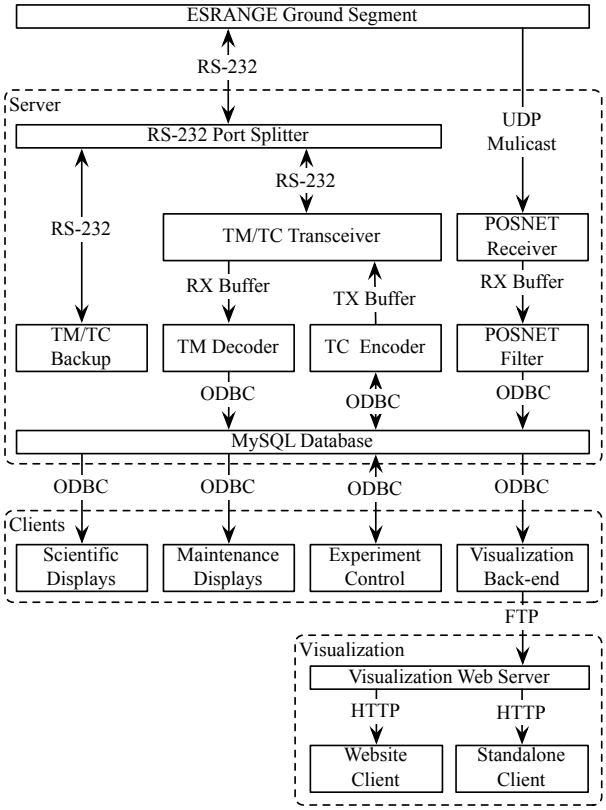

Figure 2. Subsystems and interfaces of the CERESS Ground Segment.

Maintenance Displays Separate displays for data regarding the state and health of the Rocket Module and Verification Module are implemented, featuring current- and voltage-monitoring on all three power buses and status feedback of hardware and software.

Experiment Control For controlling the Rocket Module, a user interface is implemented to schedule predefined Telecommands. The commands are cued in the database from where the TC Encoder prepares them to be send via the TM/TC Transceiver.

Mission Timeline The Mission Timeline displays the Mission Elapsed Time (MET) and corresponding flight events. It synchronizes with the real flight timeline via holds and jumps using timing information of the three signals.

4.3. CERESS Visualization Tool

CERESS's Visualization Tool (ViTO) displays the rocket's flight and flight data — GPS track, altitude, velocity, MET and load factor — in near real-time using Google Earth™.

Visualization Back-End The Visualization Back-End generates files needed for the visualization in synchronization with the MET and uploads the latest file via passive FTP to a the Visualization Web Server on the internet.

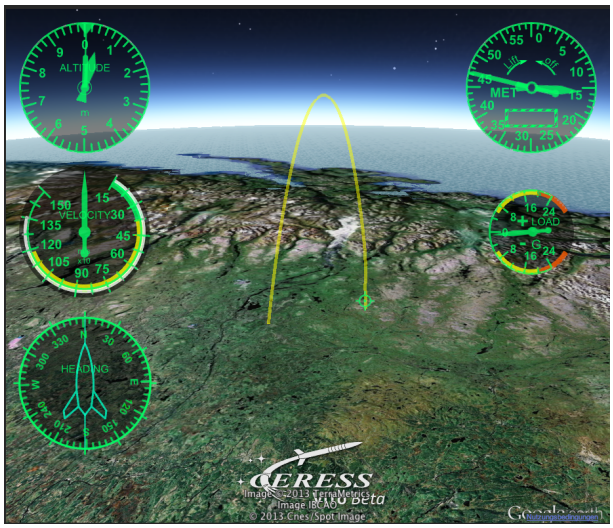

Figure 3. The Visualization Tool displaying flight data of REXUS-13.

Website Client The Visualization is accessible on the internet via a website (http://www.vito.ceress.de) running a Google Earth plugin. The website version of the ViTo is mainly intended for outreach purposes; therefore, the website also features a *Twitter™* feed as well as the REXUS public video stream.

Standalone Client The ViTo can also be used with the standalone Google Earth application, independent of the internet, to display the visualization. This version of the ViTo is intended to be used as an additional display at the experiment's control center.

5. FLIGHT RESULTS

5.1. Rocket flight data

One data set of the eight accelerometers will be shown exemplarily. Fig. 4 shows all three axis of the accelerometer. The data is smoothed via a Savitzky–Golay filter. The accelerations of the x and y axis in the beginning are results of the spin and the eccentric location. A comparison against the accelerometer data measured by the REXUS Service Module is included (z-axis only).

Fig. 5 shows details between 66 and 80 seconds after lift-off. This data set is unfiltered and the peaks of the Muscat ejection (another experiment on REXUS 13), the yoyo release for de-spin and the motor separation are easy to determine. The first two events are not covered in the measurements by the REXUS Service Module.

Fig. 6 shows the rotary speed measured by one the of

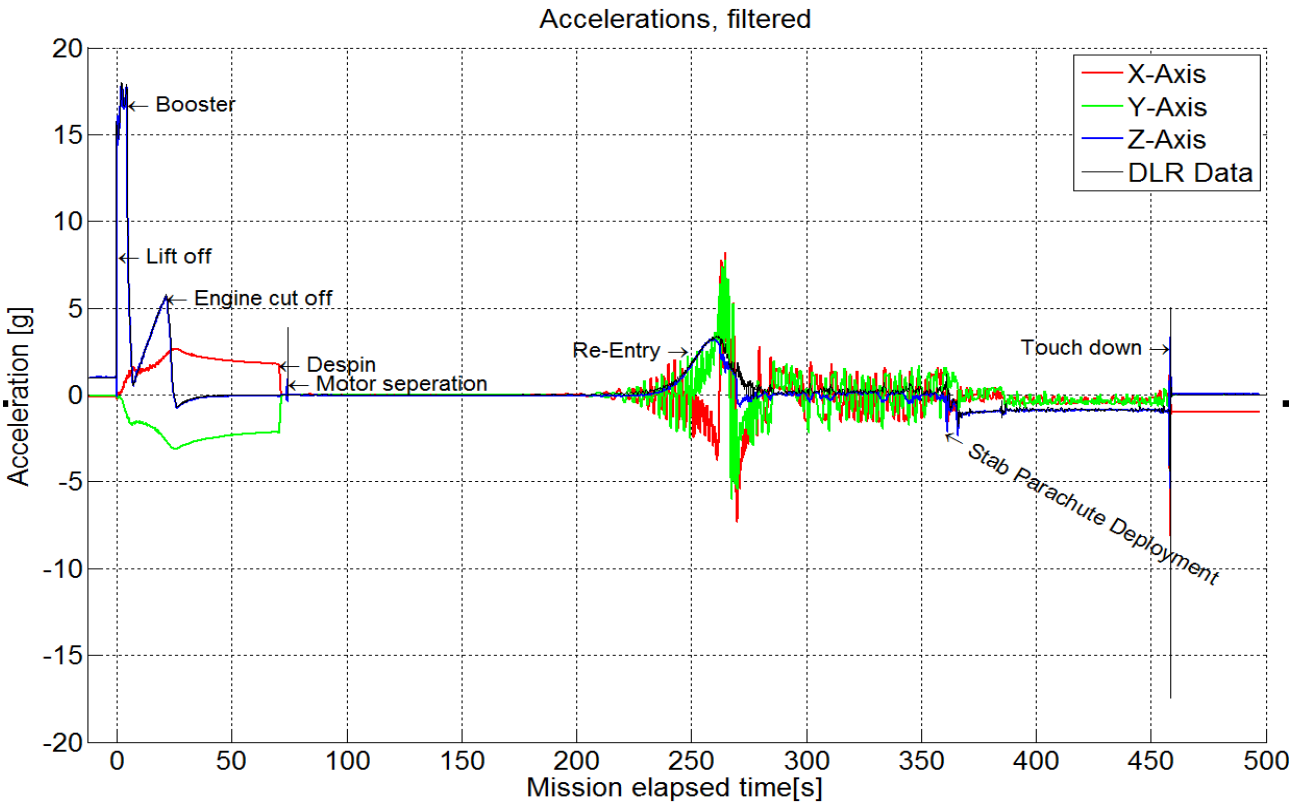

Figure 4. Accelerations measured by CERESS in comparison to the ones of REXUS Service Module.

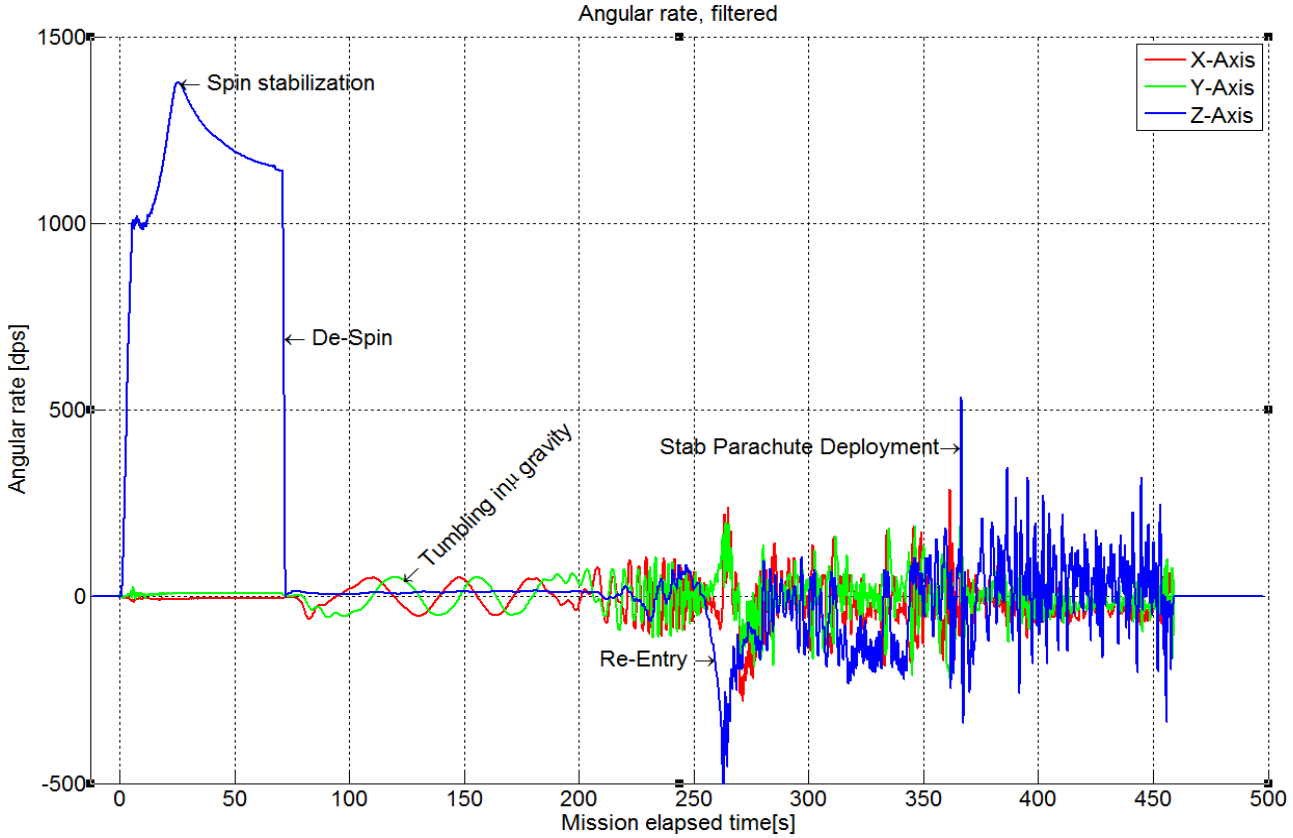

Figure 6. Rotary speed measured by CERESS.

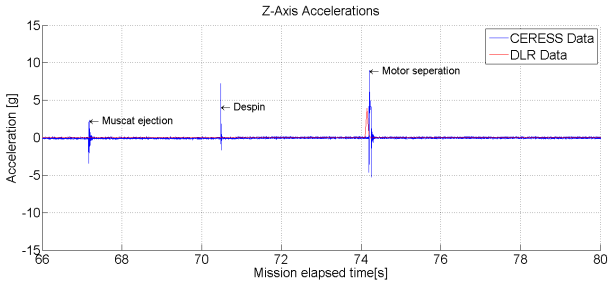

Figure 5. Detail of figure 4.

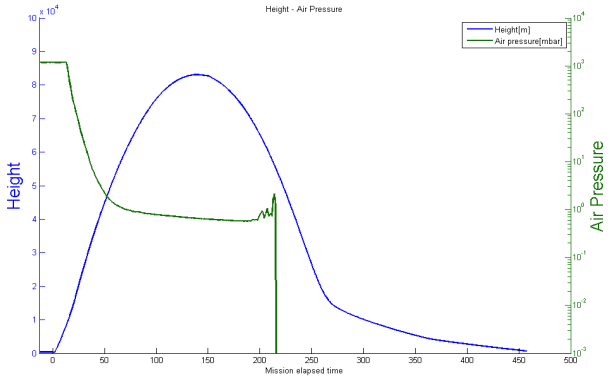

Figure 7. Pressure and height.

the gyroscopes. This data set is also smoothened with a Savitzky–Golay filter.

Fig. 7 shows the measured ambient pressure by the used Pirani sensor compared to the height above sea level (GPS data provided by the REXUS Service Module). It can be seen that the sensor got broken in an early stage of re-entry into the denser atmosphere. At this point no major acceleration or changes in rotation rate occurred, so the final reason for the failure is still to be determined.

5.2. Electronics

The electronics of the experiment worked mostly as intended. 3.3 V and 24 V were on a stable voltage level and current consumption was as expected. All components on these two buses performed very well and provided sensible data. The ambient pressure sensor did not survive re-entry; this was no electronics failure, but an internal mechanical failure that was expected due to the sensor's limitations.
The main issue is concerning the 5 V bus. Shortly after lift-off the voltage dropped to 2.5 V and stayed at this level until power-off. This resulted in a loss of scientific data, since the camera was not able to operate at this reduced voltage and the voltage references of the thermistor boards closed down the thermistor's supply lines. The RS-422 transceiver proved to be a very robust design since it still performed under reduced voltage, enabling downlinking of experiment data.

5.3. Onboard Software

During the mission nearly all parts of the onboard software were working correctly. All events were covered in according TM packages and the achieved data was sent on regular basis to the ground.
After flight all data was found in the expected manner on the SD-Card. Multiple files were created due to several checks before the launch. The main file was readable and parsed to clear physical values, which were then provided to several interested REXUS teams.
The Event Logger also performed as expected. The logfile on the internal storage was obtainable and assisted greatly in finding out what went wrong on the only malfunctioning piece of software:
The Timeline executed most of the scheduled events right after launch and some about two minutes too early.

5.4. Ground Segment

The CERESS Ground Segment worked nominally during the flight of REXUS-13. Telemetry was received and displayed as expected. Telecommands were successfully transmitted. All information were stored correctly into the database.

6. FAILURE ANALYSIS

Three major problems occurred during launch and flight of CERESS on board REXUS-13: Problem A (a power drop on the 5 V power supply down to 2.5 V) was detected right after launch; Problem B (the too quick executed of Timeline Events - most executed very close to the launch) was experienced within the first 30 seconds of flight; Problem C (the SD-Card of the camera was found in an other team's module) was discovered only after payload recovery.

Problem A The 5 V power drop: The reason for this power drop is yet to be determined. A detailed analysis of the module will be performed on return. As a consequence all thermistors and the camera were not able to work under these conditions.

Problem B The Timeline rush: A comparison of the used software deployed onto the Rocket Module and the last changes done during testing showed, that an outdated part was used during flight. Unfortunately this was not detected during benchtests and flight simulation. The addressed part was responsible for detecting signals provided by the REXUS Service Module. In the used version, there was no debouncing implemented and a jitter has started the inflight Timestamper at the moment the Service Module was switched to internal power. As the Timeline then checked the in-flight times, they were already passed and so the actions were executed immediately. Seen

from this side, the timeline worked properly and performed as expected.
The solution was already implemented and successfully tested during testing in Oberpfaffenhofen on a spinning table.

Problem C The SD-Card slot was not locked due to a wrong assumption. When pressing in the card, a gentle 'click' is audible. This does not mean that the card is locked, it means that the ejection mechanism is locked and ready to push out the card next time if it is pressed for a short length of time. Additionally, it is not known if the SD-Card slipped out during flight or during recovery and transportation with the helicopter.

7. CONCLUSION

In summary there are several points which describe the success of CERESS as a support system with enhanced situational awareness:

- Besides the malfunctions described and explained in chapters 5 and 6, CERESS can be rated as 85 % successful.
- Monitoring the data of the experiment in real-time allowed a diagnosis of off-range temperature readings. A dysfunctional power bus could be determined as the source during the ongoing mission.
- Showing the mission's timeline with major mission events helps the experimenters to keep track of their action items during the stressful operational phase, leading to a more relaxed team and less human errors.
- The ViTo turned out to effectively raise the situational awareness of the experimenters during the mission. In particular, shortly after launch teams depend on their experiment data to gain a perception of the current mission phase. If loss of telemetry occurs, like what happened during the flight of REXUS-13, teams have no information about the current situation. Going by the ViTo, working independent from the REXUS experiment's telemetry, the situation after loss of telemetry of REXUS-13 could be interpreted as a non-nominal touchdown shortly after its occurrence. Delivering more information to the team on an intuitive way, rather than by many accurate data displays, leads to a clearer view of the situation and more confident decision-making.
- Furthermore the ViTo website reached over 700 visitors, making it an effective outreach tool for future teams.

8. OUTLOOK

In future, CERESS is going be used by future teams of TUM students for their experiments onboard sounding rockets of the REXUS family. All software is kept modular and expandable to new challenges. With every team new features and utilized sensors are supposed to expand the capabilities of the current system, although smaller and more powerful NI RIO hardware could also enhance the use of all implemented software.
CERESS has established a basis from which to conduct do more scientific as opposed to standard work.

ACKNOWLEDGEMENTS

The authors would like to thank all the institutions and companies that support the CERESS project and team, in particular (in alphabetical order):

- DLR/DLR-MORABA
- ESA
- LEYBOLD OERLIKON
- NATIONAL INSTRUMENTS
- SCHOTT
- SNSB
- SSC
- TUM/LRT

REFERENCES

[1] M. Fittock and M. Inga. *REXUS User Manual*. EuroLaunch.

[2] National Instruments Corp. *NI Single-Board RIO Embedded Control and Acquisition Devices - NI-sbRIO-96XX*.

[3] National Instruments Corp. *NI LabVIEW for CompactRIO Developer's Guide*.

[4] P. Reiss, E. Breunig, P. Zimmerhakl, N. Newie, and A. Zeiner. *Investigating new space structures with the FOCUS experiment*. ESA Publications Division.

[5] Oracle Corp. *MySQL 5.6 Reference Manual*, June 2013.

[6] TimesTen Performance Software. *ODBC 2.0 - Programmer's Manual*, May 2000.

[7] National Instruments Corp. *Serial Quick Reference Guide*.

[8] K. Betke. *The NMEA 0183 Protocol*. National Marine Electronics Association (NMEA), P O Box 3435, New Bern NC 28564-3435,USA, May 2000.

POLECATS - A PLASMA INSTRUMENTATION TECHNOLOGY DEMONSTRATION FOR REXUS-14

Arrow Lee[1,*], Robert Bedington[2], Lucian Comandar[3,4], Anna Daurskikh[5], Matthew Hills[1], Daohua Hu[1], Robin Lee[6], and Tom Nordheim[1]

[1]*Mullard Space Science Laboratory, Dorking, Surrey, RH5 6NT, United Kingdom*
[2]*Japan Aerospace Exploration Agency (JAXA), Yoshinodai 3-1-1, Chuo-ku, Sagamihara, Kanagawa, 252-5210, Japan*
[3]*University College London, London, NW1 2BU, United Kingdom*
[4]*University of Cambridge, Cambridge, CB2 1TN*
[5]*International Space University, Strasbourg, 67400, France*
[6]*University of Bath, Bath, BA2 7AY, United Kingdom*
[*]*Corresponding author. Email: arrow.lee.10@ucl.ac.uk. Telephone: +44 1483 204 924*

ABSTRACT

PoleCATS - the Polar test of the Conceptual And Tiny Spectrometer - is a technology demonstration in the lower ionosphere of a new concept in space plasma instrumentation. The experiment uses CATS (the Conceptual And Tiny Spectrometer), which is a novel highly miniaturised plasma analyser head, together with an unconventional detector for low energy electrons: a CCD (charged-coupled device). CATS offers the unique ability to study simultaneously multiple energies of electrons and ions using extremely compact electrostatic optics, allowing for very rapid sampling of plasma energy distributions. Specially processed CCD detectors offer a sensor that can potentially detect both electrons and ions simultaneously and without the high voltage and high vacuum requirements of the detectors conventionally used in low energy plasma instruments. PoleCATS used these components to produce an instrument capable of analysing the fluxes and energies of electrons above 75 km altitude.

Instrumentation based on this combination of CATS and the CCD provides an attractive low-resource solution for a range of space plasma applications, and the technology developed for the PoleCATS project has the potential to drastically improve upon the current generation of space plasma instruments. The likely performance increases and the highly miniaturised design would allow them to be flown on very small-scale missions such as nano- and picosatellites.

Here, we present the results and information gained from the flight in May 2013, including the performance of the analyser, sensor, electronics and mechanical design and lessons to be learned about the design of a future instrument based on our recorded data.

Key words: REXUS; PoleCATS; detectors.

1. INTRODUCTION

The REXUS (Rocket EXperiments for University Students) programme allows teams of students from across Europe payload space on a dedicated sounding rocket. The experiments are launched on an unguided, spin-stabilised rocket powered by an Improved Orion Motor with $290\,\mathrm{kg}$ of solid propellant. It is capable of taking $40\,\mathrm{kg}$ of student experiment modules to an altitude of approximately $90\,\mathrm{km}$. The vehicle has a length of approximately $5.6\,\mathrm{m}$ and a body diameter of $35.6\,\mathrm{cm}$.

The REXUS/BEXUS programme is realised under a bilateral Agency Agreement between the German Aerospace Center (DLR) and the Swedish National Space Board (SNSB). The Swedish share of the payload has been made available to students from other European countries through a collaboration with the European Space Agency (ESA).

EuroLaunch, a cooperation between the Esrange Space Center of SSC and the Mobile Rocket Base (MORABA) of DLR, is responsible for the campaign management and operations of the launch vehicles. Experts from ESA, SSC and DLR provide technical support to the student teams throughout the project.

REXUS and BEXUS are launched from SSC, Esrange Space Center in northern Sweden.

The PoleCATS experiment was designed and built by a team of science and engineering students based at multiple institutes, mainly within the UK. The hardware was developed at the Mullard Space Science Laboratory of University College London. Since the population of energetic electrons at the altitude of REXUS 14 was highly unlikely to be sufficient, the development for the experiment was carried out as part of the development for a potential future plasma measurement mission.

Proc. '21st ESA Symposium European Rocket & Balloon Programmes and Related Research', 9–13 June 2013, Thun, Switzerland (ESA SP-721, October 2013)

2. CATS

The Conceptual And Tiny Spectrometer was developed at the Mullard Space Science Laboratory as a PhD project to develop a novel plasma analyser for small satellite applications [1]. Athough it is based on a conventional cylindrical electrostatic geometry, the instrument is only approximately $2 \times 2 \times 1$ cm in size. Narrow channels mean it is capable of selecting energetic electrons and ions in narrow energy, azimuth and elevation bins, and also that its geometric factor is low. Its small size was motivated by the need for miniaturised instrumentation for CubeSats and other small spacecraft, and the need for low-resource plasma analysers.

Currently only one prototype model of CATS has been built. It has been used for all calibration and testing pre-flight [2]. During the instrument development it was discovered that there were some manufacturing defects within this model; since calibration was only valid for this version, and because of the expense and robustness of the device, manufacturing another was not considered.

In the operation mode used in PoleCATS, a scale of voltages would be put across CATS in succession so that the full range of electron energies from $1\,\mathrm{keV}$ to $8\,\mathrm{keV}$ could be sampled in 40 energy bins.

3. THE CCD

While in a satellite instrument, the choice of detector to use with CATS would be more likely to be an MCP or similar, this would create several difficulties in a rocket environment. Far higher voltages and cleanliness would be required, and in the low-altitude, short flight-time of REXUS, the risk of arcing would be too severe. Instead a specialised position-sesitive, solid state detector was used, which has previously been used for testing and calibration of the CATS setup.

The CCD (Charge-Coupled Device) used in the PoleCATS instrument is an e2v CCD64-00 x-ray CCD sensor, a spare special-order CCD from the SXI instrument for the GOES programme [3]. The back-illuminated version was tested with CATS and has been shown to be capable of detecting electrons down to energies of $500\,\mathrm{eV}$. Although the CCD would not be capable of detecting ions at these energies, the population of ions was expected to be far lower than that of electrons, and the ion channels would be used purely for light-level calibration.

4. PREVIOUS CALIBRATION AND TESTING

CATS has been tested first using an MCP and later calibrated more accurately with a CCD, where the particle source was an electron gun.

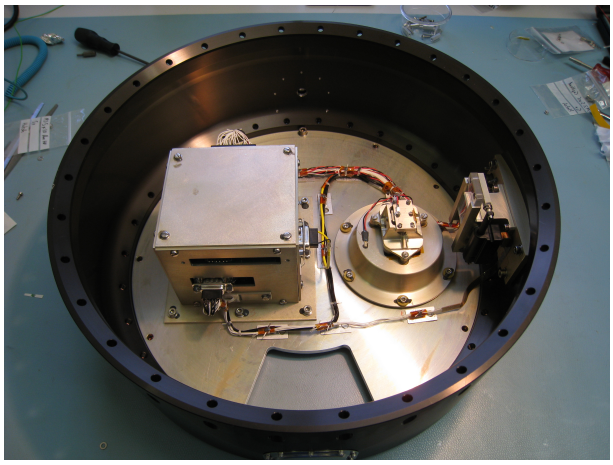

Figure 1. The experiment in the module prior to flight.

The setup used a back-illuminated CCD64, together with the engineering model readout electronics from the INTEGRAL-OMC instrument. The combination of CCD and CATS mounted together was tested in a vacuum chamber with a basic nitrogen cooling system and an electron gun producing particles of up to a few keV. The response of the CATS and CCD setup was measured for a range of azimuth and elevation for impinging particles; these results were used in designing the mechanical setup as well as data analysis in PoleCATS.

5. FLIGHT INSTRUMENT DESIGN

Since all subsystems from the laboratory-based setup were bulky and relatively high-resource, the challenge for the design was the miniaturisation and flight-readiness of each component: CCD control and readout; HV production and control; power supply; data flow and storage; interface to the service module; hatch control; and thermal control. All these systems together ready for flight are shown in Fig. 1.

The high voltage part of the experiment was only to be switched on at over $75\,\mathrm{km}$ altitude, to reduce as far as possible the risk of arcing across the CATS channels. In addition, the hatch system was designed to protect the instrument from hot air at launch and re-entry, and was only opened when the instrument was operating in 'electron detecting' mode. However, the CCD was on and recording data from the experiment switch on at T-600s until experiment switch off at re-entry.

5.1. CATS operations

The voltages across CATS were between 0 and $450\,\mathrm{V}$, with one CCD frame readout at each voltage level.

A slow readout plan for the CCD was used; similar to TDI (Time Delay and Imaging), where the CCD was read out

line-by-line over the time period of the readout. Each line was readout, placed in data storage and other tasks were performed before the next line was addressed. This allowed a linear increase in integration time over the height of the CCD, and would allow a separation of time-based and electronics-based noise sources.

Since the channels of CATS cover only a small area of the CCD, only the relevant region and a surround calibration area was read out and stored; a total area of 200×300 pixels. Although it was planned that the rate of image readout should be 1 to 10 frames per second, in the flight readout of each frame took up to $2.4\,\mathrm{s}$.

5.2. Electronics design

The format of the electronics box was similar to that of 1U of a CubeSat, using the PC104 form factor for the boards. Four boards were used, including one for low voltage supply; one for HV generation, using PWM (pulse width modulation) control; one for interfacing with with the service module and telemetry; and one for control and data handling.

A PIC24 was used as controller to run the driver for the CCD and other subsystems, and data storage was planned to use two SD cards - although only one was flown. Only housekeeping data was downlinked during flight and the rest recovered on the return of the module to Esrange.

5.3. Thermal control

The setup in the vacuum chamber used a steady nitogen supply to cool the sensor from the back of its mounting. This was both inefficient and impractical for the REXUS platform. While an optimal setup might have included a nitrogen-based cooling system for a heatsink on the launchpad, this would not have been feasible within REXUS, and a thermoelectric cooler-based sytem was designed.

Two Peltier coolers were used, for redundancy, between the bottom of the CCD mounting and a heatsink which was insulated from the bulkhead of the module. In the original plan, the heaters would be turned on when the temperature of the CCD rose above $10^{\circ}\mathrm{C}$ during flight, but the power required for this system caused the low voltage supply board to rapidly heat when the Peltier was on. Therefore, in the flight scheme, the Peltier control was set to switch them off when the supply board reading grew to above $50^{\circ}\mathrm{C}$, and the requirement for the sensor to remain below $10^{\circ}\mathrm{C}$ during the data-collecting part of the flight was relaxed.

5.4. Hatch system

Since hot gases at launch and re-entry might have damaged some parts of the instrumentation, and because uncovered openings in the rocket skin might have caused problems during the flight, it was decided to include an actuated hatch in the design of the experiment. Since it is transparent, light but not electrons would be able to penetrate and reach the sensor, allowing further calibration and image data while the experiment is not in 'electron detecting' mode.

6. FLIGHT PERFORMANCE

During the flight all subsystems behaved nominally; the hatch opened and HV cycles ran at the planned points on the timeline. However an issue with the ground station prevented some signals and downlinked data from being viewed during flight; however, since no commmands were planned to be uplinked, this caused no problem with operations. The downlinked data was successfully stored for later viewing and the data from on-board storage was recovered soon after the flight.

7. DATA ANALYSIS

The frame data recovered from the SD card in the module contained all that was expected pre-flight, but not all as planned in the as-designed experiment. The CCD data are 12-bit, but corruption occurred during data readout or storage. The three least significant bits appeared to have been replaced by a regular series of ones and zeros and were discarded from the CCD data. The one most significant bit was also missing, being always zero, and an attempt was made to estimate this bit.

In addition housekeeping data was recovered in the form of temperature data from each of the electronics boards. An attempt had been made to take four thermal readings on and around the CCD, but during integration these were found to be faulty, and this was not possible to repair before launch. However, the low voltage supply board temperatures rose and fall during the Peltier cycles, showing that the coolers worked correctly during flight.

7.1. Frame processing

The three least significant bits were discarded as being relatively unimportant, but estimating the missing most significant bit was vital for futher analysis. A simple filtering system proved to be the most successful. Each line on the CCD would be addressed in turn: each pixel on it was compared to the three closest pixels in the row below and the value of the most significant bit was decided based on which value would bring the pixel closer to its neighbours. Since the lower rows in the frame were usually correct in having a null first bit and there were not expected to be very sharp edges in the data, by propagating up the frame in this way a good estimate to the correct data could be made.

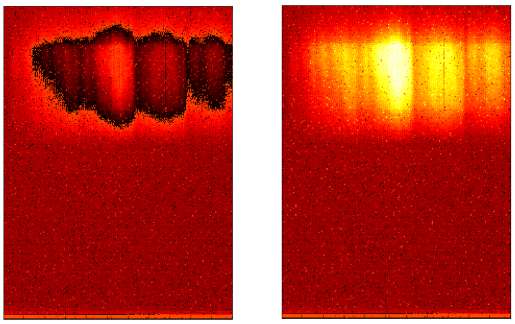

Figure 2. Example of a recovered frame, both pre- and post-processing.

By eye, this method, appeared to be very successful; only three frames did not respond well, and these were heavily saturated and could be either removed from further analysis or the beginning of the processing tweaked such that small errors at the start would not propagrate through the whole frame. An example of a frame processed this way is shown in Fig. 2.

However, it must be noted that the noise levels in many frames of the data were great enough, that some uncertainty must still remain on the best value of each pixel.

7.2. Qualitative analysis

It is clear from the obtained frames that the most significant contributors to the pixel signals are light and thermal noise. In this mission the light signal could provide information about the light reflectance through the instrument and the sensitivity of the CCD to photons, while at the times the instrument pointed away from any light source, the view was equivalent to that which would have been seen with near-perfect blacking.

Saturation of the image frame also occurred at certain points during the flight, in particular around lift off, where light conditions, and possibly fields were at their strongest. Noise levels could be seen to increase slightly around these times; it is known that the data line from the CCD would have been particularly susceptible to fields created both inside and outside the PoleCATS experiment.

7.3. Rotational behaviour

It can be seen from the changing light levels throughout the flight that the rotation of the rocket had a large effect on the light levels recorded in the images. The time between light pattern minima varies from around $14\,\mathrm{s}$ to $17\,\mathrm{s}$ during the flight, which can be compared to the rotational speed recorded by the REXUS service module of $16\,\mathrm{s/revolution}$ to $18\,\mathrm{s/revolution}$. These behaviours demonstrate the link between the flight trajectory and the experiment data.

8. LESSONS LEARNED AND CONCLUSIONS

From the recovered data, it is possible to list the major modifications that would be required to turn PoleCATS into a scientific instrument for example in a higher-altitude sounding rocket:

1. Careful choice of environment. An altitude of $50\,\mathrm{km}$ to $150\,\mathrm{km}$ higher would place the apogee in the auroral region, and the choice of a launch time with high solar activity, would allow a significant number of particles to be detected.
2. Further development is needed on surpressing light reflactions through the instrument. This would initially be attempted through a blacking process over the aluminium surface.
3. The cooling system must be redesigned to meet a harder CCD temperature requirement. The form this would take would depend heavily on the platform.
4. Analysis of CCD readout problems. The missing bits should be restored, and electronic noise should be reduced, with shorter cabling and inproved routing. A new CCD control may need to be implemented to increase the frame rate significantly.

Each of these items would fit within another development cycle of the instrument, and with a flight opportunity and interested development team, another experiment based on CATS and this, or a similar, CCD would be a feasible and worthwhile instrument for rapid, high-resolution measurements of dense, energetic space plasma.

ACKNOWLEDGMENTS

The PoleCATS team would like to thank MSSL for help with design and manufacturing support, Alan Smith for acting as mentor and our sponsors EADS Astrium, the Worshipful Company of Scientific Instrument Makers, the Science and Techonolgy Facilities Council and the Royal Astronomical Society for financial support.

REFERENCES

[1] Bedington, R., 2012, Doctoral thesis, University College London

[2] Bedington R., Kataria D., Walton D., 2012, JINST 7, C01079

[3] Stern R.A., Shing L. et al, 2004, Proc. SPIE. 77 (2004) 5171.

DEVELOPMENT OF INPE 13 AND INPE 14 PAYLOADS

E. D. Roda, M. A. B. H. Rizol, M. B. Lucks and A. O. Moraes

(1) Instituto de Aeronáutica e Espaço, Praça Mal. Eduardo Gomes, 50
Vila das Acácias, 12228-904 – São Jose dos Campos – São Paulo – Brazil
Email: doreedr@iae.cta.br; rizolmabhr@iae.cta.br, marciombl@iae.cta.br; and alisonaom@iae.cta.br

ABSTRACT

This paper describes the development of the payloads INPE 13 and 14, developed by the Institute of Aeronautics and Space (IAE), during the years of 2011 and 2012, for supporting National Institute of Space Research (INPE) in a project entitled "Studies of the Ionosphere and Upper Atmosphere with on board experiments of sounding rockets and satellites".

1. INTRODUCTION

The Microgravity Program of the Brazilian Space Agency (AEB) aims to provide access to a microgravity environment for Brazilian scientific and technological experiments. Institute of Aeronautics and Space (IAE) is the responsible for providing rockets and developing payloads for this program. In recent past IAE had an important role supporting National Institute of Space Research (INPE) in a project named "Studies of the Ionosphere and Upper Atmosphere with on board experiments of sounding rockets and satellites". As a result, two flights, without recovering, using respectively a VS-30 and a VS30/Orion sounding rockets, have been done and their payloads were called INPE13 and INPE 14. Those payloads were launched in December 2011 and 2012, the first one from CLBI rocket range in Natal and the other from CLA in Alcântara. In this work we briefly describe the development of these payloads, focusing on electronic system and its integration.

2. INPE 13

The main onboard experiment of INPE 13 and INPE 14 was a Langmuir Electronics Density and Temperature Probe (LPP) for investigating ionospheric layers E and F. INPE 13 was a less complex payload flying only with the LPP and a GPS receiver as experiments. Additionally, this payload included an onboard instrumentation with vibration and temperature transducers for a better characterization of VS-30 vehicle. A total of 23 parameters and one serial stream were transmitted via telemetry.
The main physical characteristics were: 7.1 meters (3.1 m payload) length and 1,500 kg total mass. The fairing of INPE 13 was made of composite material. This was necessary due to the LPP probe installation in the top of the fairing and due to the fact that the GPS antenna could not be installed at the modules membranes. Therefore, a specific support had to be designed for fixation of the GPS antenna inside the fairing. It is important to note that the vibration levels obtained during dynamic tests on the acceptance phase were considered the biggest challenge for this payload development. Due to its light weight, a dummy mass had to be inserted in the payload which had the effect of increasing vibration levels. To solve this problem, an extra module has been added in order to change vibration modes and achieve the desirable vibration levels. In spite of the mentioned above, this was designed, assembled and launched in approximately four months.

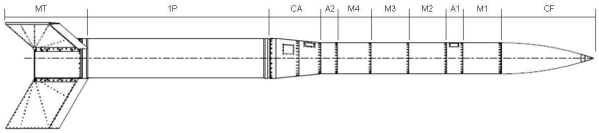

Figure 1: INPE 13 payload and VS30 vehicle.

3. INPE 14

INPE 14 was a more complex payload, with the same experiments of INPE 13 in a narrower space and the addition of a MEMS Inertial Measurement Unit – IMU to collect attitude data, in order to estimate payload dynamics; this IMU was also developed by INPE. IAE also tested in this flight two different models of accelerometer switches for pyrotechnic systems. Along with INPE experiments, in order to characterize and monitor the vehicle performance during the flight, several sensors were installed for measurement of vibration, shock, temperature, linear acceleration and magnetic field. A total of 51 parameters and two serial streams were transmitted via telemetry.
The main physical characteristics were: 8.87 meters (2.4 m payload) length and 1,700 kg total mass. The fairing of INPE 14 had also to be made of composite material due to the same reasons of INPE 13. However, it has been decided to use another fairing available. This fairing was made of two different segments. The first one is made of aluminum, and the second one of carbon fiber. Due to this it has been needed to develop an adapter to fix the fairing in the first module and change

Proc. '21st ESA Symposium European Rocket & Balloon Programmes and Related Research',
9–13 June 2013, Thun, Switzerland (ESA SP-721, October 2013)

the GPS antenna support. A payload maximum length was imposed in order to reach a specified static margin at the launching. To satisfy this and some other layout constraints, it was necessary to develop experiments modules with reduced length.
An EGSE system has been developed in LabView in order to control the ground power supplies and onboard batteries for both payloads. The ground telemetry system included visualization, archiving and serial stream data delivery. A C-band radar-transponder has been used to improve vehicle tracking. This transponder had been recovered from the VSB30 Maracati II flight.

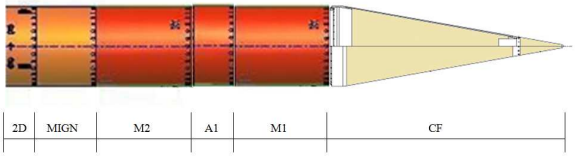

Figure 2: INPE 14 payload.

4. RESULTS AND FLIGTH PERFORMANCE

The onboard telemetry data were successfully obtained. The flight performances of the vehicles were:

INPE 13:
Apogee: 138.6 Km
Flight duration: 330 s

INPE 14:
Apogee: 428 Km
Flight duration: 652 s

5. CONCLUSION

The flights were considered normal, with the acquisition of several telemetry data for performance analysis. The payloads developed by IAE were successful on satisfying the requirements of the INPE Ionosphere and Upper Atmosphere onboard experiments.

6. ACKNOWLEDGMENTS

We are grateful to FUNCATE – Fundação de Ciência, Aplicações e Tecnologias Espaciais and CNPQ – National Council for Scientific and Technological Development, Process 560301/2010-3 for the financial support.

Figure 3: VS30-INPE 13 launch.

NEW GENERATION DVS FOR FUTURE SOUNDING ROCKET MISSIONS

Giuseppe Capuano[(1)], Daniele Titomanlio[(2)], Mariano Severi[(3)]

[(1)]TSD, Via Prov.le Pianura, 2 - Zona Ind.le S.Martino int. 23, Pozzuoli - Italy, Email:gcapuano@tsd-space.it
[(2)] TSD, Via Prov.le Pianura, 2 - Zona Ind.le S.Martino int. 23, Pozzuoli - Italy, Email:dtitomanlio@ tsd-space.it
[(3)] TSD, Via Prov.le Pianura, 2 - Zona Ind.le S.Martino int. 23, Pozzuoli - Italy, Email:mseveri@tsd-space.it

ABSTRACT

The paper is dedicated to the presentation of the new generation of the Digital Video System (DVS) that is being developed by TSD for future applications on board Sounding Rockets.
The new generation H^2VMU, that represents the core of the DVS, is characterized by the capability to offer the same functionalities and better performances of the previous generation, but with higher compactness and lower overall costs/performances, thanks to the higher integration level of its internal electronic modules, and to the adoption of new technologies, in terms of electronic devices, PCBs and thermo structural design.
A single new generation electronic module, which the H^2VMU is based on, is able to implement the functionalities of two or more electronic modules of the previous generation.
The paper provides a detailed description and the specifications of the electronics of the new generation flight unit.

1. INTRODUCTION

Techno System Developments (TSD) started the design and development of digital video systems (DVS) already in 1991 with the idea to support microgravity experiments in space overcoming the limitations of the existing video systems that could not cope with the modern digital image sensors that in a few years would have flooded the market. Most of current imaging systems devoted to space applications suffer of a lack of performances that prevent them to perform real-time image processing. This is mainly due to the adoption of centralized architectures based on general purpose microprocessors that perform image processing at software level. The approach that TSD has chosen for the realization of systems dedicated to image processing is, on the contrary, based on distributed modular architectures, where each electronic module performs a well defined task with the highest performances. Processing is always performed in parallel at hardware level by means of arrays of qualified FPGAs. Fast communication between modules is ensured by means of point-to-point high speed serial links.
The DVS has been already adopted during several space missions, thus demonstrating the capability to adapt itself to a wide range of user requirements, ranging from the support to microgravity experimentation in the field of material and fluid science (Sounding Rockets [1] and [2], Foton Capsule [3] and EML for ISS missions [6]), to earth observation and support to rendez-vous maneuvers (Prisma Formation Flying Mission [4]).

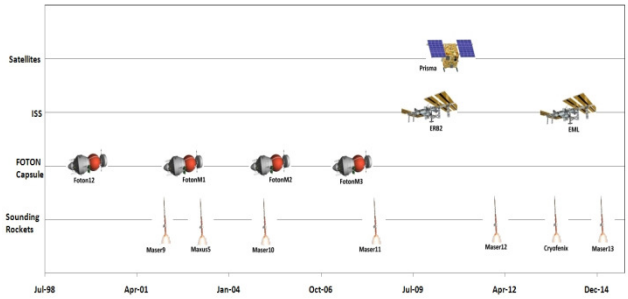

Figure 1. Space missions where TSD's DVS was employed

2. DVS OVERALL ARCHITECTURE

The DVS is a system that comprises both flight and ground equipment. Core of the DVS is the flight unit named High resolution/High frame rate Video Management Unit (H^2VMU), that, starting from 2005 (maiden fight on board MASER 10 [1]) and with continuous enhancement/customization, has been employed for a significant number of missions and on different space platforms. The H^2VMU name underlines its main characteristic that is the capability to process large amount of data at high rate in real-time.
The main tasks of the H^2VMU can be summarized in the following list:

- Camera interface & video acquisition
- Wavelet lossy and/or loss-less compression
- User definable image processing
- Video data storage on different supports (both volatile and non-volatile memories)
- CCSDS command reception and decoding for unit configuration and control
- CCSDS video data packetization and encoding
- Interface to on-board TM/TC subsystem
- Low power management

Proc. '21st ESA Symposium European Rocket & Balloon Programmes and Related Research', 9–13 June 2013, Thun, Switzerland (ESA SP-721, October 2013)

The H²VMU is complemented by the Ground Support Equipment (EGSE) that comprises a number of workstations (DVS WS) which are integrated within the Ground Network where the TM data are distributed. Task of the DVS WS is the monitoring and control of the flight equipment and the real-time reception, decoding and visualization of images. All these activities are performed at software level only, thanks to the adoption of the latest technologies like multicore CPUs and Graphic Processing Units (GPUs) that provide the necessary processing power that in the past could only be delivered by ad-hoc hardware solutions.
Fig. 2 shows a simplified diagram indicating a typical DVS arrangement: the flight equipment comprises one or more H²VMUs depending on the number of experimental modules and cameras to be served. Each H²VMU is connected to the TM/TC subsystem of the Service Module by means of a fast communication link, usually a SpaceWire connection.

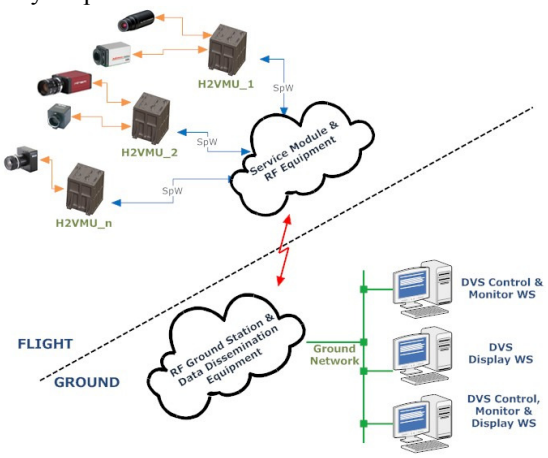

Figure 2. DVS on MASER 12

2.1. DVS ON MASER 12

As example of the Sounding Rocket DVS capabilities can be interesting to briefly describe the DVS configuration employed for the MASER12 Mission [5] and to show some flight performance data. The DVS provided support to three experiment modules (Source-2, Xrmon-GF and Biomics-2) and to the Recovery System. The flight part was composed of three H²VMUs interfacing five cameras with different characteristics in terms of video requirements, for a total processing rate of up to 3.3 Gbits/s. The ground part comprised several DVS workstations; some of them dislocated into the Esrange Block House for the real-time monitoring and control during the flight and a few others in the Esrange Scientific Center for the display of the images only. The following pictures show the H²VMUs developed for the MASER12.

Tab. 1 summarizes the characteristics of the images stored on board and the data throughput they provide.

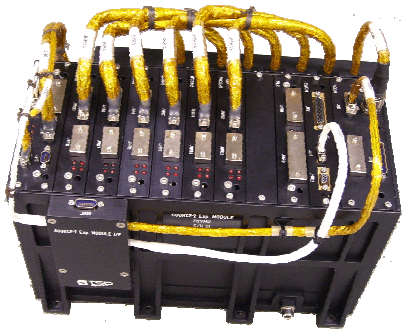

Figure 3. SOURCE-2 H²VMU

Figure 4. BIOMICS-2 H²VMU

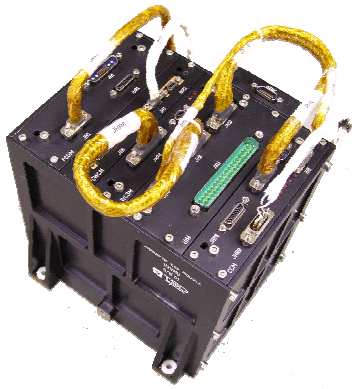

Figure 5. XRMON-GF H²VMU

Video Channel	Image Size (pixels)	Frame Rate (fps)	Throughput (Mbits/s)
Source2	2304x1728	60	2388
Xrmon-GF	2048x1344	3	99
Biomics2 (Microscope)	960x960	30	276
Biomics2 (Overview)	1280x1024	3	31
Recovery Camera	704x576	25	81

Table 1. MASER 12 DVS video input data rate

Tab. 2 shows the data reduction applied to images in order to fit the available downlink (about 9Mbits/s for all the cameras). Data reduction was accomplished by reducing the frame rate and applying wavelet compression.

Video Channel	Frame Rate (fps)	Compression Factor	Reduced bit rate (Mbits/s)
Source2	4	33.1	4.7
Xrmon-GF	1	32.0	1.0
Biomics2 (Microscope)	2.5	11.7	1.85
Biomics2 (Overview)	2.5	16.4	1.85
Recovery Camera	25	17.3	4.7

Table 2. MASER 12 DVS downlink data reduction

Next pictures show images taken during the flight and sent to ground with indication of the corresponding compression factor:

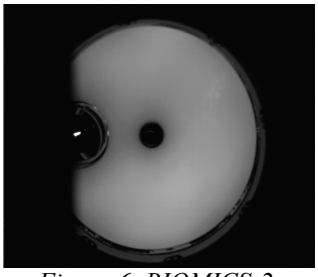

Figure 6. BIOMICS-2 Overview Camera C.F.=16.4

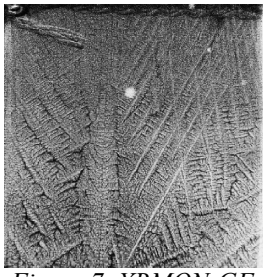

Figure 7. XRMON-GF Camera C.F.=32

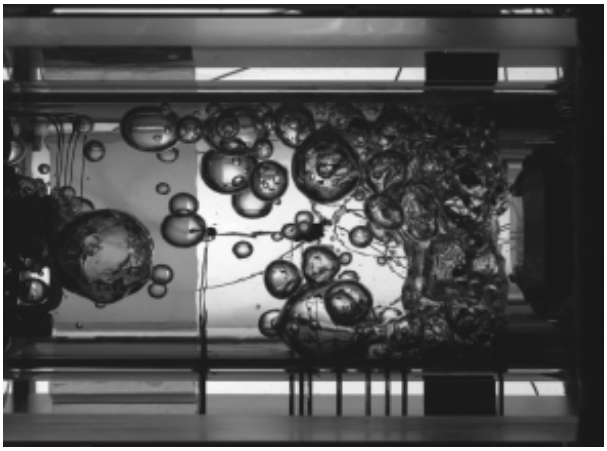

Figure 8. SOURCE-2 Camera C.F.=33.1

3. NEW GENERATION H^{2}VMU

The H^{2}VMU is based on a modular architecture comprising compact and low power modules each of them implementing a set of specific functions. Very peculiar characteristic of the H^{2}VMU is the internal communication architecture based on an application-specific back-plane that allows to provide the modules with a number of high-speed point-to-point SerDes links for the transfer of video data and a low speed serial bus only for control and configuration purposes. The specific requirements of an Experimental Module can be satisfied by putting together a proper number and type of modules.

The requirements for the video diagnostic systems, supporting the experiment execution, are increasingly demanding from the point of view of spatial and temporal resolution of the video images to be acquired, compressed, stored and transmitted to Ground

At the same time it is required to minimize the impact of the H^{2}VMU accommodation on the volume and mass of the Experiment Modules.

The new generation H^{2}VMU is characterized by the capability to offer the same functionalities and better performances of the previous generation, but with higher compactness and lower overall costs/performances, thanks to the higher integration level of its internal electronic modules, and to the adoption of new technologies, in terms of electronic devices, PCBs and thermo structural design; a single new generation module, which the H^{2}VMU is based on, is able to implement the functionalities of two or more modules of the previous generation.

The new generation H^{2}VMU will be based on the following modules:

- Camera Interface, Video Acquisition and Wavelet Compression Module (CWCM)
- Control, Communication and Storage Module (CCSM)
- Wavelet Compression & Storage Module (WCSM)
- Umbilical I/F Module
- Power Conditioning & Distribution Module (PCDM)

3.1. CWCM

The CWCM is able to implement the functionalities of both the CIVA (Camera Interface and Video Acquisition) and the WCM (Wavelet Compression Module) of the old generation.

The CWCM implements in particular the following main functions:

- image grabbing and time stamping
- frame rate reduction
- region-of-interest extraction
- camera control and configuration
- image preprocessing
- Image compression based on 5/3 IDWT and SPIHT quantizer
- Lossy compression from 4 to 100

The following figure provides a block diagram of the module.

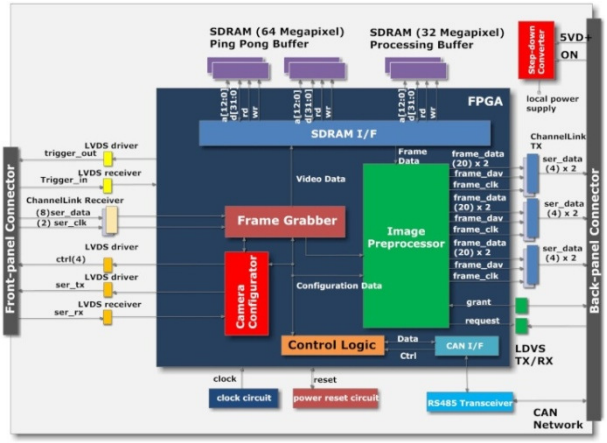

Figure 9. CWCM block diagram

The CWCM presents the following main specifications:

- Input video data : 300[Mpixels/s]
- Pixel Resolution : up to 12 [bit/pixel]
- Image Resolution: up to 32[Mpixels]
- Compatibility with CameraLink medium or CoaXPress I/F
- Two independent ChannelLink outputs (working up to 1.785Gbit/s) to download at the same time uncompressed and compressed video

The CWCM adopts video buffer based on SDRAM and high density Virtex-4 LX FPGA to improve processing capabilities.
CoaXPress is a very high data rate serial digital I/F working on a coaxial cable; the CoaXPress I/F gives the possibility to transfer on the coaxial cable not only the digital video data but also the power supply for the camera and the commands for its configuration and control. The CoaXPress I/F allows to have the H^{2}VMU remote located w.r.t. the camera and this is a very interesting feature for Experimental Modules that needs a high resolution camera but that don't have enough room to accommodate a H^{2}VMU.
The development of the CWCM working with CameraLInk I/F has been already completed and it has been successful employed on board the MASER12 Mission. Fig. 10 shows the CWCM used on board MASER12.

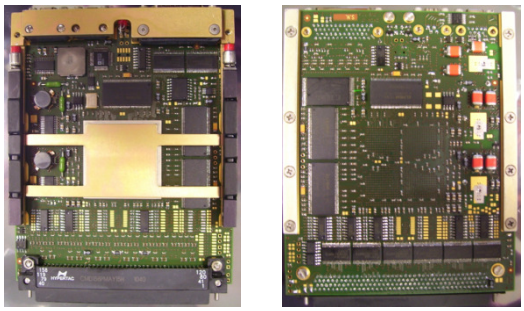

Figure 10. H2VMU's CWCM

The CWCM working with the CoaXPress I/F is under development.

3.2. CCSM

The CCSM (Control, Communication and Storage Module) will be able to implement, in addition to the control & communication functionalities, already implemented by the CCM (Control & Communication Module) used in the old generation, also the compression & storage functionalities.
The CCSM implements in particular the following main functions:

- control and configuration of all the H^{2}VMU electronic modules via CAN Bus
- multiplexing and CCSDS standard encoding of video and housekeeping data and transmission to the Rocket Service System via SpaceWire
- reception and CCSDS standard decoding of telecommands coming from the Rocket Service System via SpaceWire
- reception of video data coming from the CWCM and WCSM via Channel Link
- direct acquisition of one video data channel via Camera Link
- storage of video data on two SATA SSD
- time synchronization and time stamp management

Fig. 11 provides a block diagram of the CCSM module.

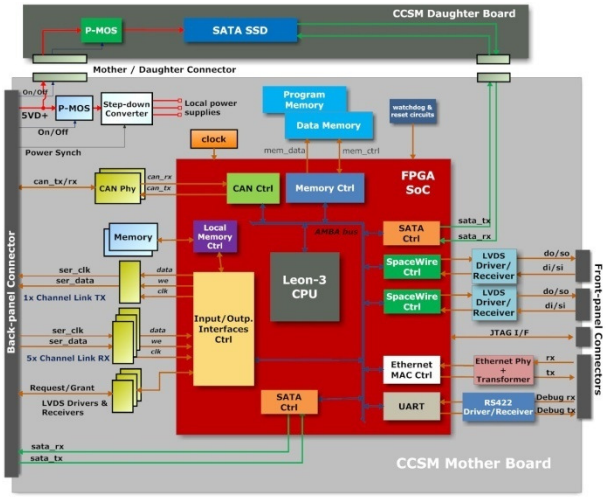

Figure 11. CCSM block diagram

COTS solid state SATA devices will be adopted for the applications requiring lower storage rates (up to about 100Mbyte/s), compatible with that technology; the CCSM shall allow the usage of up to two 1.8-inch Slim SATA SSD; the former hosted on the CCSM daughter board and the latter on the PCDM daughter board.
The TSD custom designed storage modules, named WCSM, employed in the old generation up to 244Mpixel/s, are being upgraded and they shall be still

used for very demanding storage requirements. The CCSM is also provided with one video acquisition channel that allows to implement, for low pixel rate (up to 60Mpixel/s), a H^2VMU configuration based on only two modules (CCSM and PCDM).
The module adopts a CAN BUS I/F for inter modules communication (instead of the USART RS485 present in the old configuration).
An Ethernet I/F and a RS422 UART are available for debug and test purposes; the Ethernet I/F can be also used for data retrieval on Ground.
The mother board design is based on a SoC (System on Chip) integrated into a Virtex-5 FPGA by Xilinx which implements all the processing functions and the protocols for the communication links; the core of the SoC is the LEON3 processor and the relative AMBA Bus architecture.
The CCSM presents the following main specifications:

- Five Channel links up to 1.785Gbit/s (each) for video data reception from CWCMs and WCSMs
- One camera link up to 60[Mpixel/s] for video data acquisition
- Two SpaceWire I/F up to 50Mbit/s (each) for data transmission and command reception
- Redundant CAN Bus up to 500Kbit/s
- Two SATA I/II I/Fs for continuous data storage up to 100Mbyte/s (each)
- 64Gbyte of storage capacity on one 1.8-inch Slim SATA SSD

Fig. 12 reports an isometric view of the CCSM module

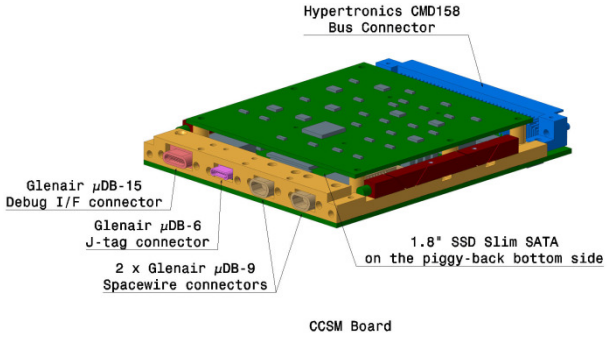

Figure 12. ISO View of the CCSM

3.3. WCSM

The WCSM (Wavelet Compression and Storage Module) is dedicated to the on-board storage on non-volatile memory (flash technology) of the video data. The new generation WCSM is based on Micron SLC flash device that is up to 4.5X faster than the Samsung k9wa device employed in the old generation. It is provided with four banks of flash devices working in parallel, and in each bank four flash devices are operated in interleaving (in the old generation the memory banks working in parallel were only two).

The WCSM performs the following tasks:

- reception of the configuration parameters from the CCSM via CAN bus
- reception of the uncompressed video data coming from the CWCM board
- loss-less or lossy compression of the video data (if required by the mission scenario)
- on-board storage on non-volatile memory of the video data
- transmission of the stored data to the CCSM (via H2VMU internal connection) or directly to the EGSE (via front-panel connector)

Fig. 13 provides a schematic diagram of the board architecture.

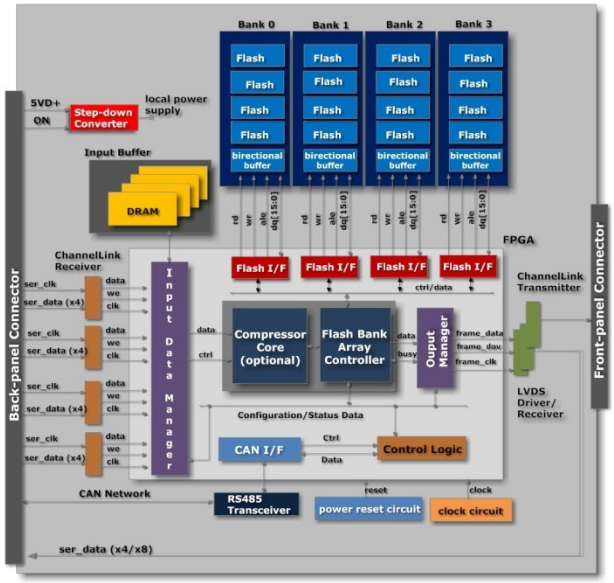

Figure 13. WCSM Architecture

The new generation WCSM offers the following performances:

- non-volatile video data storage rate: up to 200Mbyte/s sustained (instead of 64Mbyte/s of the old generation)
- data storage capacity: up to 256 Gbyte (depending on the flash memory devices mounted on-board)
- Higher rate/capacity can be reached by using more (up to six) WCSM working in parallel

The high rate data storage, the compression algorithm (if required), and all the other module functionalities are implemented on the same module thanks to the adoption of a high-density VIRTEX 5 FPGA.
Fig. 14 reports an isometric view of the WCSM module.

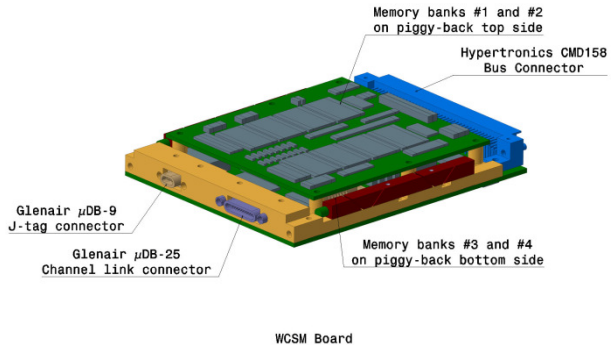

Figure 14. ISO View of the WCSM

3.4. UMBILICAL I/F MODULE

The Umbilical I/F Module (not available in the old DVS generation) is aimed at interfacing the H^{2}VMU with the EGSE via umbilical connector, during the pre-flight and post-flight phases. During the flight the Umbilical I/F Module is able to ensure an electrical isolation between the H^{2}VMU and the Umbilical connector pins, thus avoiding any damage due to possible overvoltage on the connector pins. The Module changes its configuration (active or isolated umbilical I/F) upon the reception of a command sent by CCSM by means of the CAN internal Communication Bus.

Fig. 15 provides a block diagram of the Umbilical I/F Module. The H^{2}VMU interfaces connected to the Umbilical connector are:

- Channel Link I/F
- SpaceWire I/F
- Debug I/F

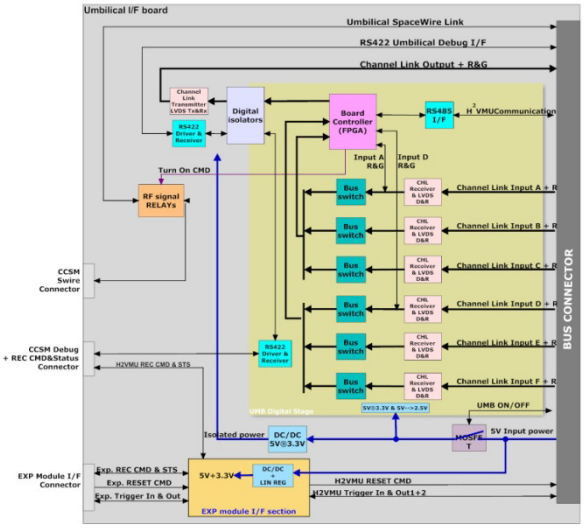

Figure 15. Block diagram of Umbilical I/F board

The Channel Link I/F allows the fast retrieval of the image data stored on-board the H^{2}VMU; the Umbilical I/F Module is provided with up to six input channel link I/Fs coming from WCSM and one output channel link transmitter for the data transmission through the Umbilical. The channel link I/F isolation is implemented with transformer coupled digital isolators, able to transfer data up to 800Mbit/s and guarantee isolation greater than 500V.

The availability of the SpaceWire I/F on the umbilical connector gives the possibility to exchange TM/TC with the H^{2}VMU after the Payload integration and without requiring the Service Module involvement. For the SpaceWire I/F isolation, high reliability mechanical relays for RF signals, able to guarantee low skew, are employed; the relays are closed during the ground activities and open during the flight.

The Umbilical I/F Module is also provided with a section dedicated to the Interfaces between the Experimental Module and the H^{2}VMU; the handled signals are:

- H^{2}VMU Reset
- Image Acquisition Trigger output
- External Image Acquisition Trigger input
- Recording Command and Status

Above listed signals are all transferred by using opto-couplers.

The development of Umbilical I/F module has been already completed and it is employed in the H^{2}VMU for the CNES Cryofenix Mission. Fig. 16 shows the Umbilical I/F module used for the Cryofenix Mission.

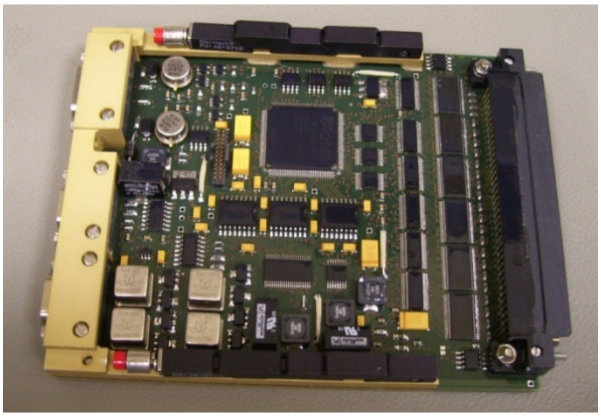

Figure 16. Umbilical I/F board used for Cryofenix

3.5. PCDM

The PCDM (Power Conditioning and Distribution Module) is dedicated to the power management and the house-keeping data collection of the H^{2}VMU electronic modules. The new generation PCDM is built around a new component: a Fusion Mixed Signal FPGA by Actel that integrates a section dedicated to the conditioning and analog-to-digital conversion of analog signals.

The Mixed Signal FPGA allows to drastically reduce the power and the component count thus allowing their accommodation on the PCDM mother board (in the PCDM old generation a daughter board was needed).

The PCDM performs the following tasks:

- power conditioning (including filtering and inrush current limiting) of the 28[V] input line
- power distribution to all the H²VMU modules with the possibility to minimize the overall power input by powering on only the needed modules
- house-keeping data collection and transmission to the CCSM board by means of redundant CAN bus

The module is also able to host and to supply an additional (w.r.t. the one installed on the CCSM) 1.8-inch Slim SATA SSD (interfaced to the CCSM) installed onto a PCDM daughter board.
Fig. 17 provides a block diagram of the PCDM.

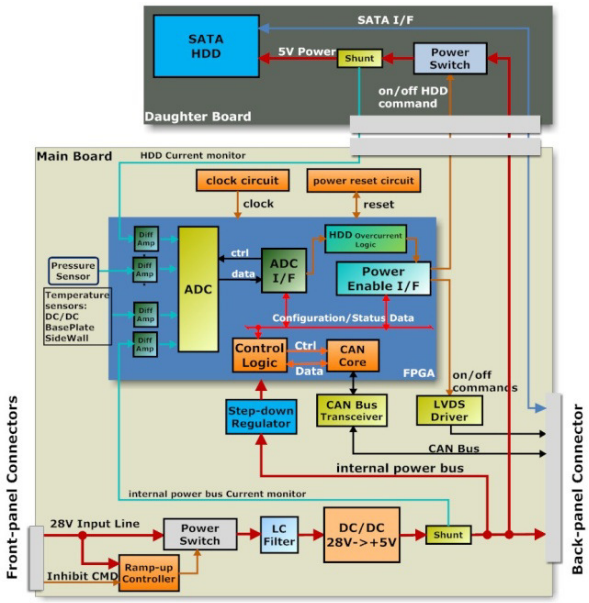

Figure 17. Block diagram of PCDM board

The DC/DC converter has in input a LC filter for EMI noise reduction and a power switch opened when the inhibit command is issued. The ramp–up Controller regulates the power switch series resistance during the turn-on time, so to limit the inrush current.
Fig. 18 reports an isometric view of the PCDM module.

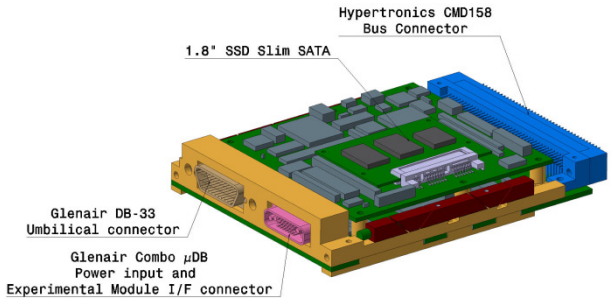

Figure 18. ISO view of PCDM board

4. MASS AND VOLUME SAVING EVALUATION

An evaluation of the mass and volume saving, that can be obtained by adopting the new generation DVS, has been carried out for some experimental modules, and in particular for a very demanding experimental module named "ARLES" that is candidate to be flown on MASER 13, and for CDIC-3 that has already flown on board MASER 10 and 11 and that will fly again on MASER 13. Table 3 reports the video requirements among which it is present a very high resolution (about 11.5Mpixel) camera that has to work at 25fps (at least) thus generating a throughput of 361Mbyte/s (as minimum data rate).

Arles Module video Channel	Image Size (pixels)	Pixel Res. (bit)	Frame Rate (fps)	Throughput (Mbyte/s)
Camera1	3400x3400	10	25	361
Camera2	2000x1000	11	25	69
Camera3	250x250	11	25	0.5

Table 3. ARLES video requirements

To fulfill the ARLES requirements by using the old generation DVS, two H²VMUs would have been necessary and they would have occupied an entire MASER plate, as shown in Fig. 19. The number of needed modules is so high that it is not feasible, for both electrical and accommodation reasons to have all the modules in one cabinet with one backplane.
Fig. 20 shows the isometric view of the single H²VMU, based on the new generation modules, that is able to fulfill the ARLES requirements; its block diagram is reported in Fig. 21.
Tab. 4 reports the very preliminary mass, volume and power budgets for both the old and new generation, highlighting, specially for mass and volume, a remarkable saving (above 50%).
The evaluation done for CDIC-3 has pointed out similar saving factors.

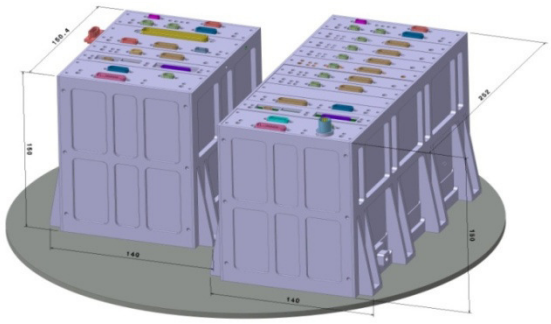

Figure 19. ISO View of old generation based solution

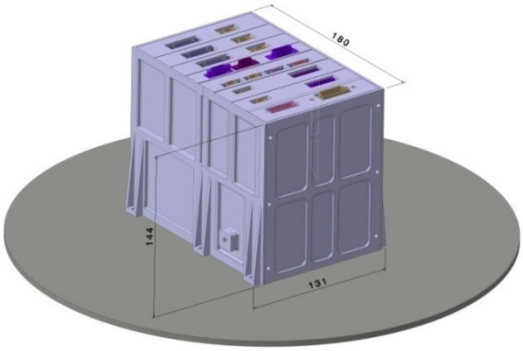

Figure 20. ISO View of new generation based solution

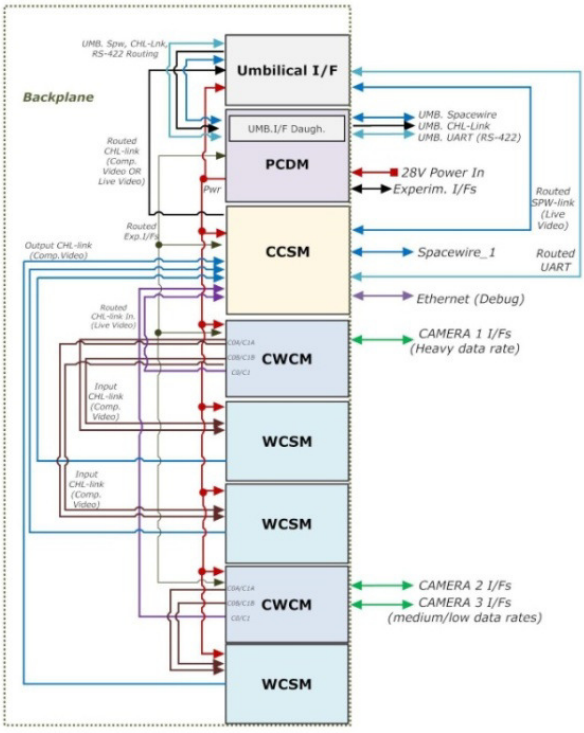

Figure 21. ARLES H²VMU Block diagram

Budgets	Old Generation	New Generation
Mass [kg]	≈ 3.0 + ≈ 5.6	≈ 3.1
Volume [l]	≈ 3.2 + ≈ 5.3	≈ 3.4
Power [W]	≈ 55@28[V]	≈ 31.5@28[V]

Table 4. Budgets comparison

5. CONCLUSIONS

Over the years the performances of the image sensors in terms of space and time resolution have grown at an impressive pace thus providing the scientific community with increasingly advanced diagnostic tools. The adoption of such high performance image sensors for a space equipment represents a technological challenge, due to the enormous amount of data they generate, that are not compatible with the handling/processing architectures typically employed for imaging space applications.

Distributed architecture, parallel processing at H/W level and very high data rate communication links represent key technologies for demanding space imaging applications, and the TSD DVS, based on the H²VMU platform, is a demonstration that, adopting those technologies, it is possible to fulfill the performance requirements and to be also compatible with the constraints in terms of mass, volume and power consumption. The performances, the reliability and the flexibility of the system have been demonstrated during several missions.

TSD is currently working on the development of the electronic modules for the new generation H²VMU that will provide higher performances and/or higher compactness. The development of some modules has been already completed, while for others is currently under completion with the goal to have the full new generation H²VMU ready to fly by 2014.

The remarkable reduction in volume and mass (above 50%) of the flight H/W will bring significant advantages on the overall mass and volume of the Experimental Modules.

6. REFERENCES

1. Capuano, G. et al (2005). Digital Video System on-board Maser10. 17th ESA Symposium on European Rockets and Balloon Related Research. ESA SP-590 Proceedings, Noordwijk, The Netherlands
2. Titomanlio, D. et al (2009). Digital Video System Performances on Maser11. 19th ESA Symposium on European Rockets and Balloon Related Research. ESA SP-671 Proceedings, Noordwijk, The Netherlands
3. Titomanlio, D. et al. (2007). Data Handling Unit for Foton-M3 Mission. DASIA 2007. ESA SP-638 Proceedings, Noordwijk, The Netherlands
4. Capuano, G., Severi M., Cacace F. et al (2008). Video System for PRISMA Formation Flying Mission. 4th Symposium on Small Satellite, Systems and Services. ESA SP-660 Proceedings, Noordwijk, The Netherlands
5. Titomanlio D. et al. (2011). MASER 12 Digital Video System. 20th ESA Symposium on European Rockets and Balloon Related Research. ESA SP-700 Proceedings, Noordwijk, The Netherlands
6. Titomanlio D. et al. (2012). Innovative Video Diagnostic Equipment for Material and Fluid Science Experiments in Space. 63rd IAC International Astronautical Congress. IAC Proceedings, IAC-12-A2.5.6, Parigi

Mesosphere

Chairs: F.-J. Lübken, M. Friedrich, J. Urban & J. Moen

IN SITU DENSITY, TEMPERATURE, AND TURBULENCE MEASUREMENTS IN THE MIDDLE ATMOSPHERE DURING PHOCUS 2011

Artur Szewczyk[1], Boris Strelnikov[1], and Markus Rapp[2]

[1]*Leibniz Institute of Atmospheric Physics, 18225 Kühlungsborn, Germany, email: szewczyk@iap-kborn.de*
[2]*German Aerospace Center DLR, Institute for Atmospheric Physics, Münchner Strae 20 82234 Weling-Oberpfaffenhofen, Germany*

.

ABSTRACT

From 28th of June to 22nd of July 2011 the PHOCUS sounding rocket campaign was conducted at Esrange (68 °N, 21 °E) in northern Sweden. One sounding rocket was launched to study mesospheric aerosols and related phenomena, i.e. the nucleation and evolution of ice particles, the properties of meteoric smoke, and the possible influence of these aerosol populations on mesospheric chemistry. The PHOCUS payload carried 18 scientific instruments including CONE (COmbined sensor for Neutrals and Electrons) to measure neutral air density with very high altitude resolution and precision. CONE measurements yield absolute neutral air densities in height range between 70 and 110 km from which high resolution temperature profile can be retrieved assuming hydrostatic equilibrium. In addition, CONE allows to investigate small-scale structures in neutral density and retrieve turbulence parameters. In this paper we present and discuss results of the CONE measurements obtained during the PHOCUS flight in the context of their geophysical environment.

Key words: CONE, neutral temperature, mesospheric inversion layer, turbulence, PMSE, NLC.

1. INTRODUCTION

The polar mesosphere in summer is host to a number of fascinating geophysical phenomena that are primarily caused by its extreme thermal structure. Owing to the gravity wave driven mean meridional circulation with upwelling and adiabatically expanding air masses above the summer pole, mean minimum temperatures of ∼130 K are reached at the mesopause at around 88 km (e.g., Lübken et al. [10]). These extremely low temperatures marginally allow ice particles to form and grow at altitudes between ∼80 and 90 km, in spite of the minute abundance of water vapor with typical volume mixing ratios of only some ppm (e.g., Seele & Hartogh [13]). Under favourable conditions the largest of these ice particles (with radii larger than ∼20 nm) can even be visually observed in the form of noctilucent clouds (NLC) which have been discovered as early as 1883 (Leslie [6], Jesse [5]). With the advent of the MST radar (MST = mesosphere-stratosphere-troposphere) 100 years later, it was then found that also the smaller subvisible ice particles lead to measurable signatures in the form of strong radar echoes. These are nowadays known as polar mesosphere summer echoes or PMSE (Ecklund & Balsley [1]; Roettger et al. [12]; Hoppe et al. [4]).

In addition, the 80-90 km altitude range is the region in the atmosphere where gravity waves propagating from below grow unstable and produce turbulence. The neutral air turbulence ultimately creates structures in the mesospheric dusty plasma that leads to the occurrence of irregularities in the radio refractive index (which is effectively determined by the electron number density at these altitudes) which, in turn, is observed on the ground as PMSE.

Making use of both in situ measurements in the mesosphere/lower thermosphere (MLT), i.e. employing sounding rockets, and remote sensing, ie. lidars and radars, it is possible to directly measure turbulence parameters during PMSE and NLC occurrence. The PHOCUS payload passed through both PMSE and NLC and was equipped with the CONE instrument [2] to measure density and temperature of neutral air with very high spatial resolution. The CONE instrument also yields turbulence parameters based on spectral analysis of measured neutral density fluctuations.

In this paper we focus on experimental results obtained by the CONE during the PHOCUS rocket flight. First, we present density and temperature measurements obtained with CONE which describes the background atmosphere. Then we discuss in situ measurements of small-scale structures in neutral air and we compare them to the temperature profile, PMSE and NLC.

Proc. '21st ESA Symposium European Rocket & Balloon Programmes and Related Research', 9–13 June 2013, Thun, Switzerland (ESA SP-721, October 2013)

2. INSTRUMENT DESCRIPTION

The data analyzed and discussed in this paper was obtained with the CONE instrument. Briefly, the CONE is a combination of an ionization gauge and a fixed biased Langmuir probe for electron density measurements [2]. CONE measurements are capable to resolve small-scale structures in neutral air density down to some centimeters. These small-scale structures are caused by neutral air turbulence. On the PHOCUS payload CONE was mounted on the rear deck and, therefore, was in a favorable (for most precise measurements) aerodynamical condition during the downleg of this spin-stabilized sounding rocket [11]. Making use of laboratory calibrations, CONE measurements yield absolute neutral air densities in height range from 70 to 110 km from which high resolution temperature profile can be retrieved assuming hydrostatic equilibrium.

2.1. Data description

The PHOCUS campaign was conducted from 28 of June to 22 July 2011. One sounding rocket was launched on 21 of July 2011 at 07:01 UTC during strong PMSE event and simultaneous NLC detected by the ESRANGE lidar. Neutral density, temperature and turbulence data were obtained by the CONE during the downleg of the rocket flight. In addition, data from Esrange radar (ESRAD) and Middle Atmosphere ALOMAR Sounding System (MAARSY) located near the Andya Rocket Range are available.

3. ANALYSIS TECHNIQUE

The current measured with the CONE instrument is proportional to local neutral density and can be converted to absolute densities applying laboratory calibration. The calibration is performed in a vacuum chamber where simultaneous measurements by both CONE and an absolute pressure standard, e.g. a baratron, are made at different pressures. The pressures are converted to number-densities using the temperature of the calibration chamber applying the ideal gas equation.

Due to the shock front that appears because of the high speed of the sounding rocket ($\sim$1000 m/s), a ram correction must be applied to the measured densities which is obtained using the Direct Simulation Monte Carlo technique (e.g., [11]).

Assuming hydrostatic equilibrium, i.e., $dp = -\rho(z)g(z)dz$, where p and ρ are the atmospheric pressure and mass density, z is height and g is the acceleration of gravity, and taking into account the ideal gas law $p(z) = \rho(z)\frac{R}{M}T(z)$, where T is temperature, R and M are the gas constant and mean molecular weight, one can obtain the equation to derive a temperature profile from measured densities:

$$T(z) = T_0\frac{\rho_0}{\rho(z)} - \frac{1}{\rho(z)}\frac{R}{M}\int_h^{h_0}\rho(z)g(z)dz \quad (1)$$

Because the density measurements by CONE are done with very high spatial resolution (down to 10 cm) and also precision ($\sim$ 0.1 %), we are able to extract tiny density fluctuations from the CONE measurements. These fluctuations are a good tracer for turbulence [8]. The CONE turbulence measurements are based on the spectral model method introduced by [8] and [9] and extended by [14]. In short, the turbulence energy dissipation rate, ε, is derived as the best fit value after fitting the theoretical model of [3] or [16] to the measured spectra of the relative density fluctuations of neutral air. From the best fit of the theoretical spectra of turbulence the inner scale, l_0, can be derived. This is the scale where inertia forces and viscous forces are in equilibrium. Then, using the formula $l_0 = 9.90\sqrt[4]{\frac{\nu^3}{\varepsilon}}$ we can obtain the turbulence energy dissipation rate ε, which is the rate at which turbulent kinetic energy is dissipated into heat at small scales.

4. MEASUREMENTS

In situ measurements performed during downleg of the PHOCUS flight provided simultaneous and high-resolution measurements of neutral air density, temperatures, and turbulence parameters.

4.1. Background atmosphere

The results of the absolute neutral density measurements at heights between 70 and 110 km are shown in the Fig. 1 as the black profile. The measured densities are comparable to the Lübken et al. [10] falling spheres measurements (red line). Above 80 km CONE density measurements are slightly lower than falling sphere measurements.

The temperature profile obtained from the CONE measurements between 70 and 110 km is shown in the Fig. 2 in black. The lowest temperatures of $\sim$ 120 K appear at the altitude of 91 km. The measured temperature profile reveals pronounced mesospheric inversion layer (MIL) at altitudes between 81 and 84 km. The amplitude of the inversion layer reaches values of about 15 K. The temperature gradient above the inversion layer is close to the adiabatic lapse rate (compare with the dashed orange line in Fig. 2), which is a typical feature of MIL and often coincides with regions of high turbulence activity. The entire temperature profile, including region with the inversion layer, reveals signatures of gravity waves.

Results from falling sphere measurements made by Lübken et al. [10] are shown in Fig. 2 as red line. Additionally, we overplot results from IAP particle detector,

which measured density of charged aerosols in-situ during upleg of the PHOCUS payload. The latter is shown as the dark blue profile in Fig. 2, and is a nett current produced by charged heavy aerosols (see accompanying paper by Asmus et.al. for more details).

At altitudes between 78 and 84 km and between 86 and 91 km the measured temperature drops below the frost point. The later is shown by two light-blue dashed lines in Fig. 2. These two profiles of the frost point temperatures were calculated using values of water vapor mixing ratios of 2 and 10 ppmv.

PMSE were observed by the ESRAD between 80 and 83 km altitude, whereas NLC were observed by NLC-photometer on board the PHOCUS payload at around 81.5 km (see Fig. 3). That is, the temperature minimum, PMSE display, and NLC were observed at the same altitude range, which is consistent with our current understanding of these phenomena.

4.2. Turbulence

Next, in Fig. 3 we present results of measurements of the turbulence energy dissipation rates, ε in the altitude range from 60 to 100 km and compare them with the temperature profile obtained with the CONE sensor. The derived ε-values are shown by dark blue crosses with error bars in orange. Whenever a continuous turbulence layer was detected, the single crosses are connected by a dark blue line. The energy dissipation rate can be converted to the heating rate as $\partial T/\partial t = \varepsilon/c_p$, where c_p is the heat capacity of air at constant pressure ($c_p \sim 1\ J/K \cdot g$). The resultant heating rates are represented by the upper axis in Fig. 3.

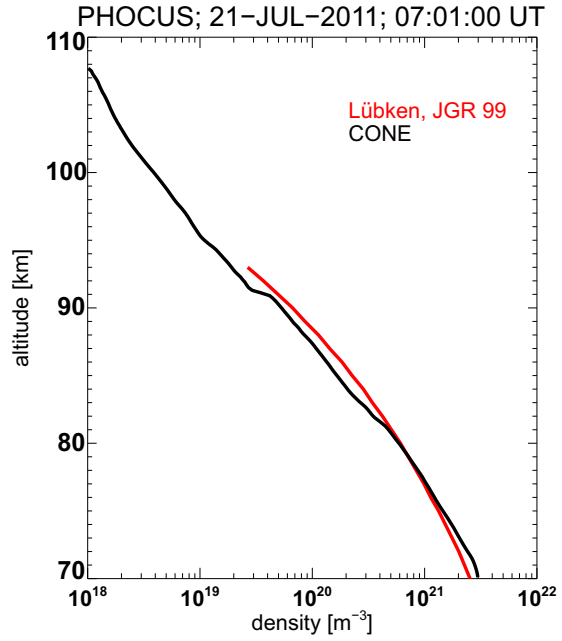

Figure 1. Neutral densities measured during PHOCUS flight (black line). Falling sphere measurements from Lübken et al. [10] are shown by the red line.

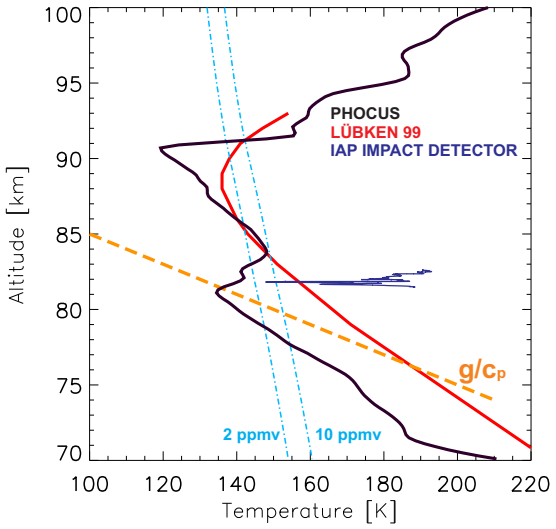

Figure 2. Neutral temperatures measured during the PHOCUS flight (black line). Falling sphere measurements from Lübken et al. [10] are shown as red line. Adiabatic lapse rate is shown as dashed orange line. Additionally, a layer of negatively charged aerosols detected by the IAP Particle Detector is shown as a dark blue line. Two dashed, light blue lines show the frost point temperatures for water vapor mixing ratio of 2 and 10 ppmv (see text for more details).

The measured dissipation rates reveal typical summer-values and are not continuous but rather confined to narrow layers, which is also typical for summer MLT. The highest dissipation rates are observed above 90 km, with the heating rates reaching 1000 K/day. Also, the measured energy dissipation rates exhibit large gradients. The ε-value often changes by an order of magnitude within one kilometer.

It is interesting to compare the measured energy dissipation rates with the temperature profile. At the altitudes from 80 to 84 km were the measured temperature profile exhibits MIL, the energy dissipation rates also reveal high values with heating rate of up to 100 K/day. This is typical for many MIL observations and was described, e.g. by Szewczyk et al. [15]. According to numerical simulations by [7], a heating rate of $\sim$10 K/day is sufficient for producing inversion layers. In our case dissipation rates is smaller and additional analysis of gravity waves and tidal activity in the region should be made to investigate the MIL creation mechanism.

Note also, that our turbulence detection technique is not sensitive to a turbulence in the regions where the temperature profile exhibits an adiabatic lapse rate and, therefore, can underestimate the actual ε-values. This implies that the turbulence dissipation above the inversion layers could be even stronger than what we observed with the CONE instrument.

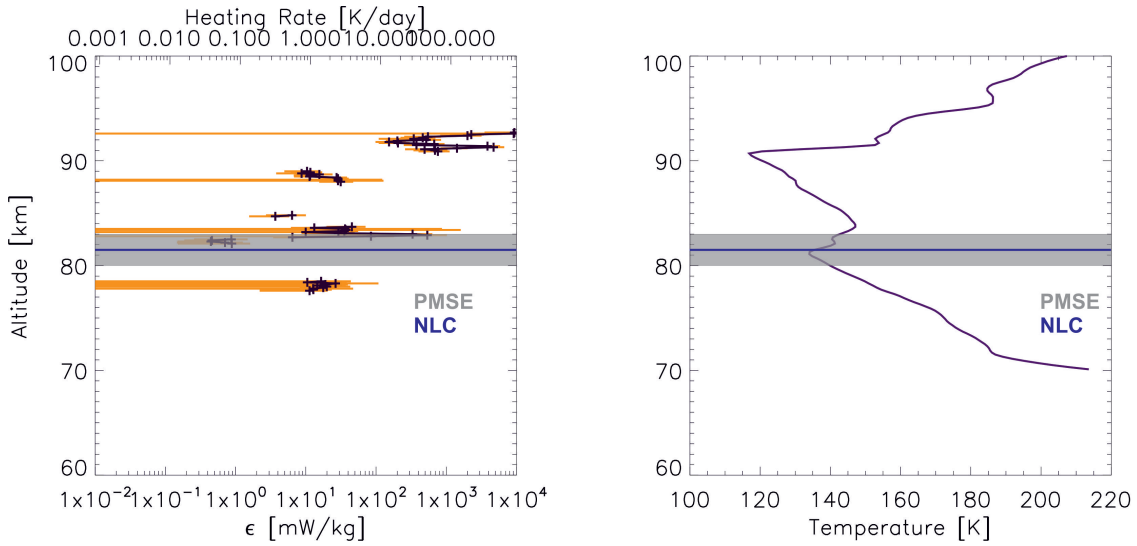

Figure 3. Left panel: Turbulence energy dissipation rate measured in situ during the PHOCUS flight shown with dark blue crosses in the left panel. The single crosses are connected whenever continuous turbulence layer was detected. The error bars for each point shown by orange line. The corresponding heating rate is shown on the upper axis. Right panel: Temperature profile obtained in the same volume (the same as in Fig. 2). Shaded grey area marks the region where PMSE was observed by ESRAD during rocket launch. The blue horizontal line marks the altitude at which the NLC were observed by the photometer on board the PHOCUS rocket.

If we now compare turbulent dissipation rate with the height of the occurrence of the PMSE (gray shaded area in Fig. 3) and NLC (blue horizontal line in the same Figure) we can see they coincide with turbulent activity. This is again consistent with the current theory.

5. SUMMARY

The PHOCUS mission provided real common volume in situ measurements of neutral densities, temperatures, and turbulence. The measured neutral densities are comparable with the falling sphere results from Lübken et al. [10]. The neutral temperature profile when compared to Lübken et al. [10] falling sphere measurements shows a relatively cold atmosphere. In the regions from 78 to 84 km and 86 to 91 km the temperature drops below the frost point. In the lower regions, from 80 to 83 km these low temperatures coincides with PMSE and around 81.5 km also with NLC. Also, IAP Particle Detector detected layer of negatively charged aerosols around these altitudes. Regions with PMSE were also connected with turbulent activity there, which agrees with the current understanding of the PMSE phenomena. The temperature profile also exhibits MIL between 81 and 84 km, which coincides with strong turbulence activity.

6. ACKNOWLEDGMENTS

We thank the Department of Meteorology at Stockholm University (MISU) for providing the opportunity to participate in the PHOCUS project.

REFERENCES

[1] Ecklund, W. L. & Balsley, B. B. 1981, 86, 7775

[2] Giebeler, J., Lübken, F.-J., & Nägele, M. 1993, ESA-SP-355, 311

[3] Heisenberg, W. 1948, 124, 628

[4] Hoppe, U.-P., Hall, C., & Rottger, J. 1988, 15, 28

[5] Jesse, O. 1885, Met. Zeit., 2, 311

[6] Leslie, R. C. 1885, 32, 245

[7] Liu, H.-L., Hagan, M. E., & Roble, R. G. 2000, 105, 12381

[8] Lübken, F.-J. 1992, 97, 20,385

[9] Lübken, F.-J. 1997, 102, 13,441

[10] Lübken, F.-J., Jarvis, M. J., & Jones, G. O. L. 1999, 26, 3581

[11] Rapp, M., Gumbel, J., & Lübken, F.-J. 2001, 19, 571

[12] Roettger, J., La Hoz, C., Kelley, M. C., Hoppe, U.-P., & Hall, C. 1988, 15, 1353

[13] Seele, C. & Hartogh, P. 1999, 26, 1517

[14] Strelnikov, B., Rapp, M., & Lübken, F.-J. 2003, 30, 2052, doi:10.1029/2003GL018271

[15] Szewczyk, A., Strelnikov, B., Rapp, M., et al. 2013, Annales Geophysicae, 31, 775

[16] Tatarskii, V. I. 1971, The effects of the turbulent atmosphere on wave propagation (Jerusalem: Israel Program for Scientific Translations)

IN SITU MEASUREMENTS OF CHARGED MESOSPHERIC ICE PARTICLES DURING THE PHOCUS 2011 CAMPAIGN AND COMPARISON OF THE RESULTS WITH A MICROPHYSICAL MODEL

Heiner Asmus[1], **Boris Strelnikov**[1] **and Markus Rapp**[2]

[1]*Leibniz Institute of Atmospheric Physics, Schlossstraße 6, 18225 Kühlungsborn, Germany, Email: asmus@iap-kborn.de, strelnikov@iap-kborn.de*
[2]*German Aerospace Center DLR, Institute for Atmospheric Physics, Münchner Straße 20 82234 Weßling-Oberpfaffenhofen, Germany, Email: markus.rapp@dlr.de*

ABSTRACT

In the summer of 2011 PHOCUS (Particles,Hydrogen and Oxygen Chemistry in the Upper Summer mesosphere) sounding rocket campaign was conducted at north Swedish ESRANGE. Among other measurements, charged aerosol particles were measured by a classical Faraday cup. These measurements showed a layer of charged aerosol particles around 81.5 km. To interpret the observation model calculations were done to derive the equilibrium temperature of spherical particles. The background temperature was measured in-situ by the CONE instrument on-board the PHOCUS payload. Model calculations show that even very big particles up to 300 nm could exist in the altitude range of the observed ice particle layer. Also, equilibrium temperature of meteor dust particles were calculated for different materials. These calculations show that dust particles with a high relative content of iron are much warmer than other materials. The model calculations also show that dust particles with a high relative iron content are inefficient condensation nuclei for mesospheric ice.

Key words: NLC; Meteor Smoke; Mesospheric Ice Particles.

1. INTRODUCTION

As a long ongoing topic in atmospheric physics polar mesospheric clouds (PMC) also known as noctilucent clouds (NLC) are still in the focus of today's mesospheric investigations. Despite the fact that these clouds are observed for two centuries [20] essential questions remain open, e.g., how condensation processes occur. Since [13] proposed microscopic meteor smoke particles (MSP) in exactly the NLC occurrence altitude range one suppose that mesospheric ice nucleate on these MSP [8, 15]. Multiple in situ measurements showed that MSP exist with particle charge density of about $10^3 \mathrm{cm}^{-3}$ [11, 10, 2, 16, 17]. These MSP originate from ablating meteoroids which deposit their material in the upper mesosphere and lower thermosphere (MLT) region. The estimates of the overall meteor mass input ranges from 10 to 100 tons per day [e.g., 13].

The PHOCUS campaign aimed to investigate chemistry and dynamics of the MLT. In particular, different instruments on-board PHOCUS payload conducted to in-situ and common volume measurements of NLC, hydrogen, oxygen, water, and plasma density including charged aerosols. We present results of in-situ measurements by IAP-particle detector (PD) which was mounted on the forward deck of the payload. We also compare the measurement results with the results derived using a microphysical model.

2. INSTRUMENTATION

Since the PHOCUS mission aimed at measuring wide range of microphysical and atmospherical parameters, the PHOCUS payload carried a huge set of instruments.

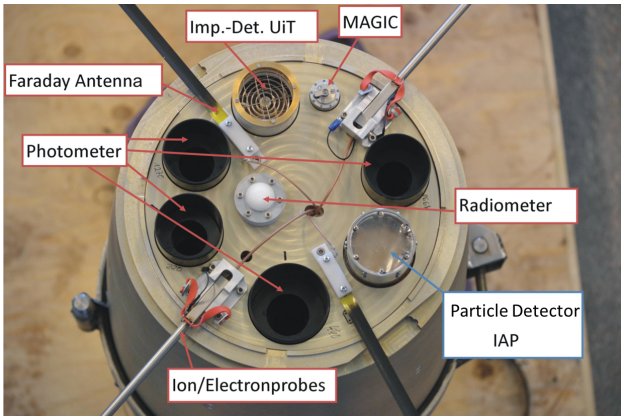

Figure 1: Picture of the front deck of the PHOCUS payload with the labeled instruments. Marked in blue is the particle detector of the IAP.

Proc. '21st ESA Symposium European Rocket & Balloon Programmes and Related Research', 9–13 June 2013, Thun, Switzerland (ESA SP-721, October 2013)

Fig. 1 shows the forward deck of the PHOCUS payload where the IAP-particle detector was mounted. Besides the IAP-PD also the impact detector from the Tromsø University was mounted on the same deck to measure charged aerosols. The IAP particle detector is based on the principle of the classical Faraday cup as first applied for sounding rockets by [11]. A schematic of the detector is shown in Fig. 2. The PD has the two grids G_1 and G_2 and the electrode. The upper grid, G_1 was biased at -3 V and the lower grid G_2 at +3 V with respect to the payload skin to shield the electrode from ions and electrons. The electrode as well as the both grids were connected to electrometers. The current measured by the electrode is therefore proportional to the number density of the heavy charged aerosols (MSP or NLC particles). Though the DSMC simulations of aerodynamics for the PHOCUS payload have not been done yet, we can assume from some of our previous calculations [14] that only particles with radii greater than 2 nm could be measured by our instrument.

3. DATA REDUCTION AND ANALYSIS

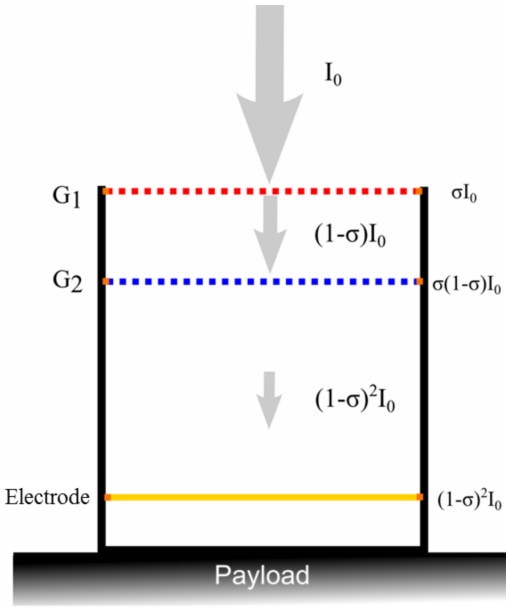

Figure 2: Schematics of the PD (i.e. Faraday cup). The two grids G_1 and G_2 are biased -3.2 V and +3.2 V, respectively. The grey arrows indicate the flow of the dust particles. The dust current into the cup is reduced by collisions with grids which depends on the grids cross section σ. $1-\sigma$ represents the grids transmissivity and I_0 is the undisturbed dust particle current.

As described in the previous section, the current measured by the electrode of the PD is proportional to the number of charges carried by the heavy aerosols. It is known that large ice particles can fragment due to collision with electrode or shielding grids and, thereby influence our measurements [11]. In this paper we neglect secondary charging effects and fragmentation for simplicity. With this simplifications we interpret the net electrode current as the true current collected by the PD by assuming that the loss current at one of the two grids is the cross section of the grid (σ = 0.2) times the incoming current. The total loss of current due to the grids is hence $(1-\sigma)^2 I_0$. The measured electrode current can be used to calculate the so called particle charge density $N_d Z_d$. Since the charge state of the impacting particles is not know, it is not possible to derive the density of the charged particles. Following [11], but neglecting the secondary charging, our measurements yield charge density as:

$$N_d Z_d = \frac{I_{DC}}{e\pi r^2 V_R (1-\sigma)^2} \quad (1)$$

with the measured net electrode current I_{DC}, the elementary charge e, the sensor radius r, the rocket velocity V_R and the grids cross-section σ.

4. MEASUREMENT RESULTS

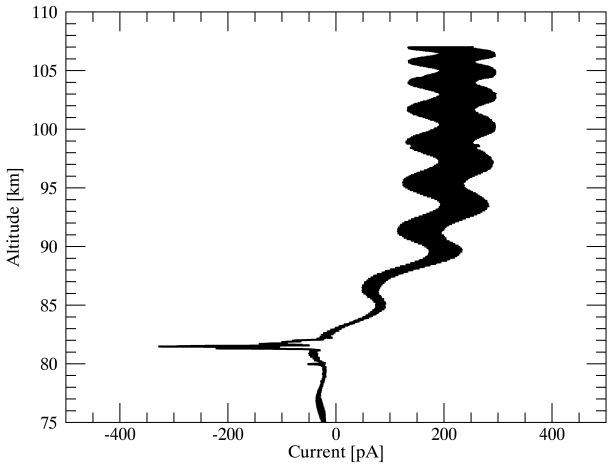

Figure 3: Current measured by PD on upleg. A clear signature of negatively charged aerosol layer appears around 81.5 km height. Modulation of the measured signal above 85 km is due to coning of the payload. Measured current above ∼83 km the is essentially positive which can probably be attributed to payload charging and hence, electrometer zero reference shifting.

Fig. 3 shows electrode current profile measured during upleg. A clear signature of negatively charged aerosol layer appears around 81.5 km height. Modulation of the measured signal above 85 km is due to coning of the payload. Also, above ∼83 km the measured current is essentially positive. This can probably be attributed to payload charging and hence, electrometer zero reference shifting. Using Eq. 1 we further derive aerosol charge density from the measured current. The result is shown in Fig. 4, where apart from spin modulation, one can see a pronounced double-layered structure. This feature is consistent with other in-situ measurements (Zoltan Sternovsky- private communication). The lowest maximum in the charge density profile appears at 81.3 km with maximum value of about 1570 cm^{-3}. The second maximum reveal somewhat higher charge density of 2300 cm^{-3} and is located

at 81.47 km. Both layers are very narrow, i.e. they have width of less than 200 m.

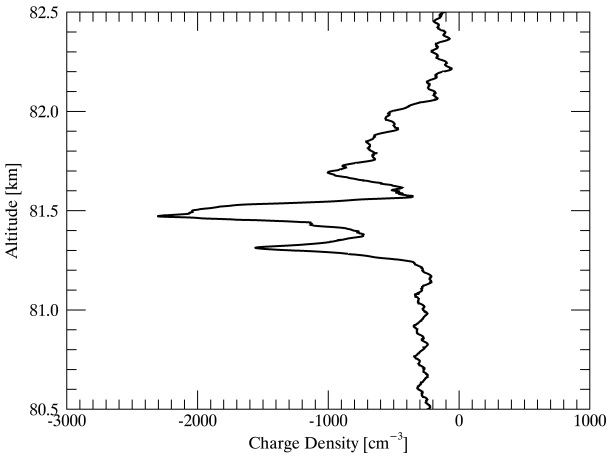

Figure 4: Upleg electrode current. Negative current means measurement of negative charges.

5. MODEL RESULTS

The in-situ measured parameters onboard PHOCUS payload allow us to estimate equilibrium temperature of spherical particles (e.g., ice) based on models by [7, 5, 6]. Our model describes equilibrium state of the aerosol particle immersed in a stationary atmospheric environment. It assumes energy balance between inputs from solar (UV and visible part only) and terrestrial infrared radiation and energy loss due to collisions and radiative cooling. The model calculates radiative energy exchange for black body and uses absorption coefficients from [19] and [1]. Fig. 5 shows results of equilibrium temperature calculations for ice particles using temperature-profile derived from in-situ measurements by the CONE instrument [18].

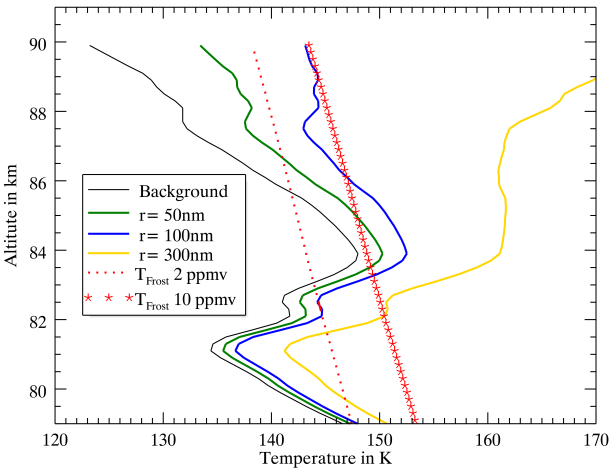

Figure 5: Equilibrium pure ice particle temperatues for PHOCUS conditions for ice particles with a radius of 50, 100 and 300 nm. Red doted line and stars indicate the frost point temperature for 2 and 10 ppmv water mixing ratio.

The black profile in Fig. 5 shows the in-situ measured temperature and the green, blue, and yellow lines show the derived equilibrium temperature of ice with radii of 50, 100 and 300 nm, respectively. The choice of particle sizes used for calculations was based on estimates by [4] and, therefore covers range of NLC particles typically observed by ground-based lidars (50 to 100 nm), as well as very large ones of 300 nm radius.

As it is seen from the Fig. 5, equilibrium temperature of ice increases with radius because of increasing cross section of radiation absorption. Also, equilibrium temperature of ice increases with altitude because of decrease of energy loss by collisions at high altitudes.

The in-situ measured temperature profile (black line) shows a local minimum of approximately 134 K at 81.2 km. This minimum is also reflected in the model calculations (color profiles) and almost coincides with the in-situ detected aerosol layer (compare with Fig. 3 or 4). Note, that the aerosol measurements were conducted during upleg, whereas temperature was measured on downleg.

In Fig. 5 we further compare the modeled temperature profiles with frost point temperatures over ice surface calculated for water vapor mixing ratios of 2 and 10 ppmv, which are show by dotted and asterisked lines, respectively. As it is seen from Fig. 5, model results show that even for very large ice particles of a 300 nm radius the equilibrium temperature is lower than the frost point temperature. This also holds for the low value of 2 ppmv and large ice with radii of 300 nm around local temperature minimum, i.e. between 80.0 and 81.5 km height.

Next, we extended the equilibrium temperature model to obtain temperatures of dirty ice, that is ice contaminated by meteoric smoke particles. We applied Maxwell-Garnett theory [9] to calculate optical properties of the dirty ice. The results of model calculations for ice contaminated by magnesio wüstite with volume fraction of 3 %, e.g., the maximum value given by [12], are presented in Fig. 6.

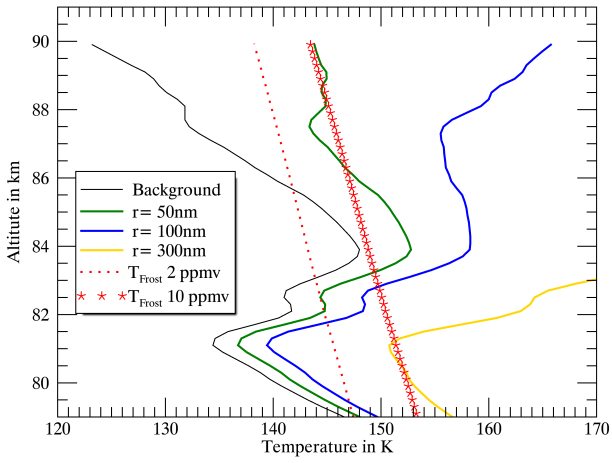

Figure 6: Equilibrium dirty ice particle temperatues for PHOCUS conditions for ice particles with a radius of 50, 100 and 300 nm. Red doted line and stars indicate the frost point temperature for 2 and 10 ppmv water mixing ratio.

It is seen, that the maximum radius for dirty ice particles is much smaller then those for pure ice by a increasing of the temperature due to higher absorption of light. Dirty ice particles with radii of 300 nm have no longer temperatures below the frost point temperatures even for high water mixing ratios. Figure 7 gives a more detailed picture of the model results for dirty ice. It shows isolines of equilibrium temperatures as function of aerosol radius and altitude. Latter accounts for the temperature change as measured in-situ onboard PHOCUS payload. Temperatures below frost point temperature for water vapor mixing ratio of 2 and 10 ppmv are marked by the gray and dark shading, respectively. Also indicated by the blue area is the altitude region of the NLC layer obtained from the PD measurements.

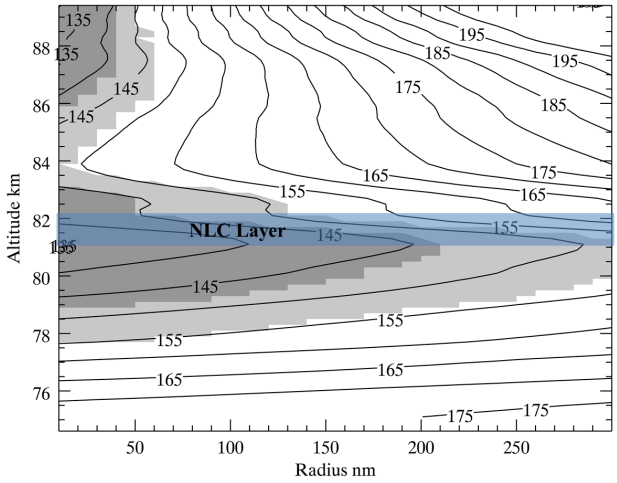

Figure 7: Calculated equilibrium temperatures of dirty ice particles (3% volume fraction of magnesio wüstite). They gray shaded areas indicating were the particle temperature is below the frost point temperature for 10 ppmv (light) and 2 ppmv (dark) water vapor mixing ratio the ice existence ranges respectively. Underlined blue is the NLC layer altitude range from the measurement of the IAP particle detector.

However, the model calculations result in favorable conditions for existence of dirty ice particles with radii of up to 150 nm at water vapor mixing ratio of 2 ppmv and for temperatures as measured around 81.5 km. We conclude that the dirty ice particles is likely constituent of the observed NLC, whereas pure ice should exceed in size all so far known assessments.

6. CONCLUSIONS

In this paper we presented results of in-situ measurements by IAP particle detector during the PHOCUS sounding rocket campaign in 2011.
A layer of negatively charged aerosols was observed around 81.5 km. The layer was fine structured, in particular, two pronounced major sub-layers are clearly seen in the measured current. Thickness of the entire layer does not exceed 900 m. The estimated charge density peaks at 81.5 km height and reaches values of 2300 cm^{-3}.

We also applied a microphysical model to assess range of aerosol sizes that would be consistent with the in-situ measured parameters. The model calculations show that ice contaminated by meteor smoke particles with radii up to 150 nm is more consistent with other accompanying observations then pure ice.

ACKNOWLEDGMENTS

We thank the Department of Meteorology at Stockholm University (MISU) for providing the opportunity to participate in the PHOCUS project.
We are grateful to Torsten Köpnick and Hans-Jürgen Heckl who construct the IAP particle detectors electronics and hardware. We would also like to thank Artur Szewczyk for support of the instrument during PHOCUS campaign for providing the CONE temperature data.

REFERENCES

[1] AIU Jena, Optical data: http://www.astro.uni-jena.de/Laboratory/OCDB/index.html, 2012.

[2] Amyx, K., Sternovsky, Z., Knappmiller, S., et al. 2008, Journal of Atmospheric and Solar-Terrestrial Physics, 70, 61

[3] Asmus, H. 2012, Master's thesis, University of Rostock, Rostock

[4] Cossart, G. v., Fiedler, J., & Zahn, U. v. 1999, Geophysical Research Letters, 26, 1513

[5] Eidhammer, T. & Havnes, O. 2001, Journal of Geophysical Research, 106, 24831

[6] Espy, P. & Jutt, H. 2002, Journal of Atmospheric and Solar-Terrestrial Physics, 64, 1823

[7] Fiocco, G., Grams, G., & Visconti, G. 1975, Journal of Atmospheric and Terrestrial Physics, 37, 1327

[8] Gadsden, M. 1981, Planetary and Space Science, 29, 1079

[9] Garnett, J. C. M. 1904, Philosophical Transactions of the Royal Society A: Mathematical, Physical and Engineering Sciences, 203(359-371), 385–420,

[10] Havnes, O., Aslaksen, T., & Brattli, A. 2001, Physica Scripta, 89, 133

[11] Havnes, O., Trøim, J., Blix, T., et al. 1996, Journal of Geophysical Research, 101, 10839

[12] Hervig, M. E., Deaver, L. E., Bardeen, C. G., et al. 2012, Journal of Atmospheric and Solar-Terrestrial Physics, 84-85, 1

[13] Hunten, D. M., Turco, R. P., & Toon, O. B. 1980, Journal of the Atmospheric Sciences, 37, 1342

[14] Rapp M., Hedin J., Strelnikova I., Friedrich M., Gumbel J. & Lübken F.-J. 2005, Geophysical Research Letters, 32, L23821

[15] Rapp, M. & Thomas, G. E. 2006, Journal of Atmospheric and Solar-Terrestrial Physics, 68, 715

[16] Rapp, M. & Strelnikova, I. 2009, Journal of Atmospheric and Solar-Terrestrial Physics, 71, 477

[17] Rapp, M., Strelnikova, I., Strelnikov, B., et al. 2011, in Aeronomy of the Earth's Atmosphere and Ionosphere, ed. M. A. Abdu & D. Pancheva (Dordrecht: Springer Netherlands), 67–74

[18] Szewczyk A., Strelnikov B. & Rapp M. 2013, ESA PAC SP721

[19] Warren S.G. 1984, Applied Optics, (23), 1206–1225

[20] Young, T. 1805, Philosophical Transactions of the Royal Society of London, 95, 65

COLLISION FRAGMENTS FROM IMPACTING NLC/PMSE PARTICLES: ARE THE FRAGMENTS MAINLY METEORIC SMOKE PARTICLES?

Ove Havnes[(1)], Jörg Gumbel[(2)], Cesar La Hoz[(1)], Jonas Hedin[(2)]

[(1)]*Institute of Physics and Technology, University of Tromsø, N-9037 Tromsø, Norway, ove.havnes@uit.no cesar.la.hoz@uit.no*

[(2)]*Department of Meteorology, Stockholm University, S-10691, Sweden, gumbel@misu.su.se jonash@misu.su.se*

ABSTRACT

The icy cloud particles in the mesosphere (NLC and PMSE clouds) must have a large number of meteoric smoke particles (MSP) embedded in them [1,2]. A considerable fraction of the MSP are released and charged when the ice particles fragments in collisions with probes or payload bodies. A new probe MUDD, to mass analyze the collision fragments and to find how much secondary electric charge which is being produced, was flown on the PHOCUS payload in 2011. Around 30% of the charged fragments had radius $r_d \leq 1.2$ nm while 50 % have $r_d \geq 1.5$ nm. Correcting for a smaller charging probability for small fragments, the total fraction of those with $r_d \leq 1.2$ nm may be 70%. We find that the filling factor of MSP in the ice particles should be between 0.1 and ~5% by volume.

1. INTRODUCTION

The meteoric smoke particles (MSP), has since long been predicted to be present as a result of a re-condensing of material released from meteors evaporating during entrance in the Earth's atmosphere [3,4]. They play an important role in the chemistry of the mesosphere and the stratosphere, they can provide condensation sites for the water ice particles of the summer mesosphere, and they act as sinks for metals in the mesosphere [5,6]. It is therefore of great interest to obtain information on their chemical composition, structure and growth, together with how they are transported from where they are created (ca 75 to 110 km height), to other regions of the atmosphere. Until very recently it was believed that MSP would have little probability of colliding with and sticking to a growing icy NLC/PMSE particle. Apart from containing possibly one MSP as a condensation site, the NLC/PMSE particles were considered to consist of mostly ice with some metal atoms and molecules based on meteoric ablation products. The transport of MSP, mainly by atmospheric circulation, was considered as a transport of mainly free MSP particles. However, recent predictions and observations have made it very probable that the NLC/PMSE ice particles have a large amount of MSP embedded in them. Ref [1] reached this conclusion from a detailed analysis of the current variation with rotation on to the grids of a dust probe DUSTY while [2], from satellite occultation observations (SOFIE), found that MSP are present in PMC with an amount from .01 to 3% by volume.

In the present paper we discuss observations with a new dust probe MUDD (Multiple Dust Detector), developed at the University of Tromsø and flown in July 2011 on the Swedish payload PHOCUS (PI: J. Gumbel). The MUDD probe is intended to obtain information on the content and structure of the icy NLC/PMSE cloud particles.

2. THE MUDD PROBE

In the MUDD probe all the incoming ice particles will collide with the inclined surfaces of grid 2 (G2) shown in Figs.1 and 2, and collision fragments will be produced. A fraction of the collision fragments will be electrically charged to –e. No incoming ice particles can reach the bottom of the probe directly. The fragments are mass analyzed by applying a variable electric field between the fragmentation grid G2 and the bottom BP of the probe. G0 at the payload potential will shield other probes from the internal fields of MUDD. Grid 1 at + 6.2 V will prevent ions from reaching the interior of MUDD. Electrons will, however, enter the probe and be registered at both G1 and G2.

Proc. '21st ESA Symposium European Rocket & Balloon Programmes and Related Research', 9–13 June 2013, Thun, Switzerland (ESA SP-721, October 2013)

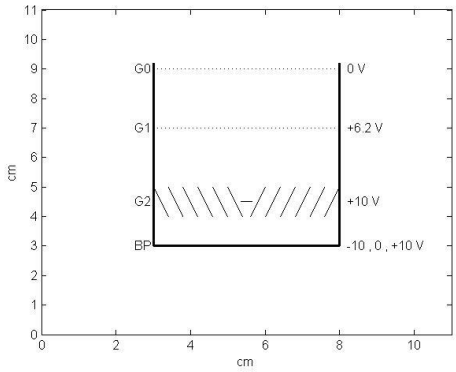

Figure 1. A sketch of the MUDD dust probe with two transparent shielding grids (G0 and G1), and one grid G2 through which no incoming ice particle can pass directly. They will first collide and fragment on G2 and the fragments will continue down to the bottom of the probe (BP). The electric field between G2 and BP is varied in steps. Currents to G1, G2 and BP are all measured but not that to G0. The opening of the probe at G0 points in the forward (ram) direction.

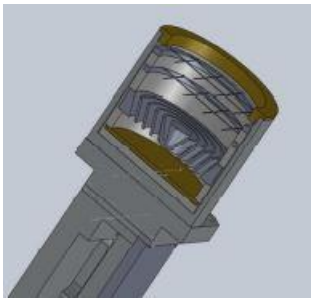

Figure 2 showing a cut-through MUDD probe with its two upper grids and G2 consisting of concentric inclined circular strips of metal which close the probe for direct entry to the bottom plate.

The potential difference U_{GB} between G2 and BP is varied in steps of 10 V through a cycle of U_{GB} = 0, 10, 20 and 10 V which is repeated. The voltage stays constant for 39 samples, corresponding to a change in height of ~ 14 m. There is a gap of ~ 5 samples (~ 2 m) without data until the voltage shifts to the next value. Already the values for the potential differences show that the fragment sizes which can be affected, if we use a fragment velocity of 450 m/s, will be in the size range below a radius r_d ~ 1.4 nm if the specific weight is ρ_d= 3000 kg m^{-3}, and below r_d ~ 2.0 nm if ρ_d= 1000 kg m^{-3}. The last case, for ice particles, will probably not be relevant for MUDD because such small ice particles tend to stick to the surface at impact and melt [7]. We therefore find that if MUDD register small nm sized particles it is very unlikely that they are ice particles but that they, with a very high probability, have to be MSP. As we will refer to later, the high probability for fragment charging that we find, makes it even more unlikely that ice fragments can be the explanation for the measurements.

3. OBSERVATIONS.

The MUDD probe was launched for the first time on the PHOCUS payload from Kiruna the 21st of July 2011 at 0701 UT. There was a persistent PMSE layer present, as measured with MST radar at Kiruna (ESRAD). The layer was descending at the time around launch, it was strong but relatively narrow with a thickness of around 1 km from ~81 to ~82 km . The payload reached an altitude of 108 km.
The electron current dominate the G1 and G2 currents, with the G2 being the largest by a factor of ~ 4 in the PMSE region (Fig.3). The reason

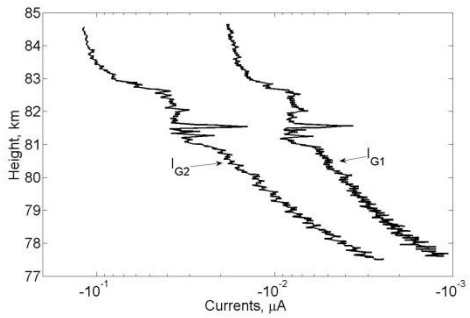

Figure 3. The currents to G1 and G2.

for this is that G1 is transparent and the majority of the electrons will penetrate it as they are attracted towards G2 by the electric field between G1 and G2. If U_{GB} is non-zero (10 or 20 V), no electrons will penetrate G2 and reach BP which in this case will register only the currents carried by the charged fragments produced by ice particles impacting on G2. However, for U_{GB} = 0, when BP has the same potential as G2 with respect to the payload, a small fraction of the electrons attracted to G2 are scattered and can penetrate G2 and reach BP where they contribute significantly to the current registered there. The current to BP in this case will therefore be caused by charged collision

fragments, and electrons penetrating G2. We remove the electron contribution by first calculating the ratio between the current to BP and G2 below and above the dust layer where charged fragments are not present. We fit the ratio as a function of height by a second degree polynomial. Assuming that the contribution by electrons follow this curve also within the dust layer we find the electron contributions in the layer by multiplying with the G2 currents there. Subtracting the electron contribution we find the current by the charged fragments also for the case where U_{GB} = 0. We have also corrected for the current contribution to G2 by the charged fragments, which will decrease the negative current to G2 by removing electrons. This correction is small, in the range of 1 to 2 % and leads to a similar percentage correction for the BP current.

In Fig. 3 we show the currents observed for the three different voltages U_{GB} . We have taken the average of the currents for each group of 39 samples at a constant U_{GB} and drawn a straight line between the average values. The curve for U_{GB} = 0 is shown as a green line while the red and blue are for U_{GB} = 10 V and the black line is for U_{GB} = 20 V. We see, especially in the upper

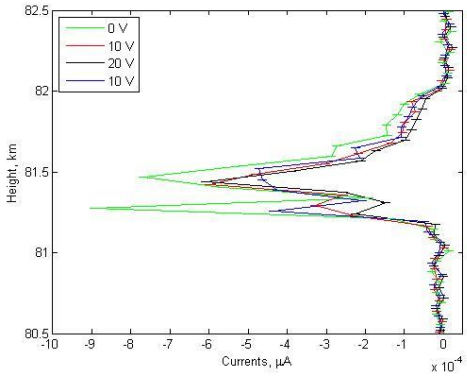

Figure 4. A sketch of the measured currents at the different electric potentials between G2 and BP. See text for details.

half of the layer that the currents go down as the retarding potential U_{GB} increases. Measuring the change in current we find that the current is reduced by ~30% when U_{GB} increase from 0 to 10 V, and by an additional ~ 20 % when U_{GB} increase to 20 V. These numbers apply especially to the upper half of the cloud which appears fairly smooth in intensity, while the scatter in the percentages for the lower half of the layer is high due to the presence of a number of narrow and strong layers. A different method where we use the full curves of the currents at each constant U_{GB} , and make what we call a "best fit" of all the various curves for each group of 39 samples, give nearly the same percentages as above also in the lower half of the layer.

We have calculated the mass and size of the particles which will be stopped by the electric potentials U_{GB}, in combination with air drag, when moving from G2 towards BP. We find that if ρ_d = 3000 kg m^{-3} particles of $r_d \leq 1.2$ nm will be stopped when U_{GB} = 10 V, and $r_d \leq 1.5$ nm if U_{GB} =20 V. If U_{GB} = 0 V all particles with $r_d \geq 0.3$ nm should reach BP. For ice with ρ_d = 1000 kg m^{-3} the corresponding values are 1.7, 2.2 and 0.6 nm. There is a relatively small effect of the air drag which lead to a higher braking effect than with the electric field alone.

In laboratory experiments, ice particles of a few nanometer and less tend to stick to the surface they hit and will eventually melt, while larger ice particles are more likely to bounce off the surface [7]. It therefore seems likely that the small fragments that we observe, are MSP which will not melt and which probably will be more likely to bounce off the impact surface than small ice particles.

30% of the charged MSP have $r_d \leq 1.2$ nm, 20% have 1.2 nm $\leq r_d \leq$ 1.5 nm, and 50% have 1.5 nm $\leq r_d$, these are the ones which are registered as a current. However, the charging probability, at least for larger dust particles, is proportional to the mass of the particles (for ice particles it is proportional to their cross section) [7]. If we correct for the difference in charging probability, the fragments with the lowest fraction being charged - the smallest MSP with $r_d \leq 1.2$ nm - may have as much as 70 % of the total number of released MSP, counting also the uncharged fragments which are not directly detected.

We now consider the secondary charging when impacting particles rub off charges from the impact surfaces. Reference [7] found that for a beam of ice particles with radius from ~7 nm and downwards, with highest intensity at r_d~3.8 nm, the probability for the particles or their fragments to be charged negatively at impact was 10^{-3} . In our case we have a maximum total current to BP of I_{BP}~ -10^{-9} A . If we have incoming ice particles of number density N_d and charge number Z_d , an effective MUDD collecting area A_{MUDD}=1.2x10^{-3} m^{-3} and a rocket velocity V_R = 708 m/s we can find the number η of unit charges e that each incoming ice particles has to produce, from

$$-e(\eta - Z_d)N_d A_{MUDD} V_R = I_{BP}$$

We have here assumed that the charge eZ_d of the initial ice particle is carried through to BP. We consider two cases for Z_d and N_d: I) Large particles with r_d = 50 nm for which we use N_d = 8x10^7 m^{-3} and Z_d = - 4. II) Smaller particles with r_d = 20 nm with N_d = 10^9 m^{-3} and Z_d = -1. We find for case I) η= 91 and for II) η=7.

Both of the cases will have charge densities comparable to that expected for the electron density at height between 81 and 82 km and should give rise to electron bite outs. We see from Fig.4 that bite outs are present. In the strongest bite out the current is reduced to ~ 35 % of the current outside the bite out.

We do not know what fraction of the MSP in the ice particles which are released in the collision and we do not know what fraction f_{chg} of the released fragments which are charged. If we use the value for small ice particles f_{chg} = 0.001, where only one out of 1000 fragments become charged, we get very unrealistic MSP volume filling factors. We get the minimum filling factor for this case if we make the, probably very unrealistic, assumption that all the MSP in the ice particles are released during the collision. Using an average size of the MSP particles of 1 nm we get a filling factor of V_f = 73% by volume for case I) and V_f =88% for case II). This cannot be the case and we must as before conclude that the charging probability for the released fragments in our case must be much larger than f_{chg}= 0.001. Assuming that all MSP are released and that all are charged, leads to V_f = .07% and .09% for the two cases. However, the kinetic energy of the incoming ice particle can only melt a fraction of the particle. If we consider that energy will be spent on deforming the ice particle and that some of the particle will continue along the impact surface down to BP, a realistic melting fraction could be around 10%. Using this value and using f_{chg} = 1 and 0.1 we find filling factors of ~0.8% and 8% . A realistic MSP volume filling factor for the cloud particles could be several percent, for which a 50 nm sized ice particle should contain several thousand MSP.

4. DISCUSSION

The observations by the MUDD probe present a strong case of support for the prediction and observation [1,2] that MSP should be embedded in large numbers within the icy NLC/PMSE particles. MUDD indicate that the majority of the embedded MSP have $r_d \leq$ 1.2 nm. The uncertainties in this radius is mainly caused by a lack of knowledge of the exact velocity with which the MSP bounce of the impact surface G2 towards BP. There may, in principle also be some ice remaining on the surface of the released MSP although we find that most of a thin ice layer should melt and evaporate as the MSP move from G2 to BP in the compressed and heated gas within MUDD.

The exact probability for charging of the released MSP particles is uncertain but it is difficult to avoid the conclusion that it must be at least two orders of magnitude higher than that for small ice particles. We find it likely that f_{chg} is of the order of 0.1 or larger. Much of the difference in f_{chg} between the MSP and small ice particles are most likely connected to the high probability that small ice particles may attach and melt and not contribute to any secondary current.

We find that in order not to run into unrealistic filling factors, we must conclude that the NLC/PMSE particles most likely have a fairly weak structure which easily crumbles and release a considerable amount of the embedded MSP.

5. REFERENCES

1. Havnes, O. & Næsheim. L.I. (2007), On the secondary charging effects and structure of mesospheric dust particles impacting on rocket probes. *Ann.Geophys*, **25**, 623-637.
2. Hervig,M.E., Deaver ,L,E.,Bardeen , C.G., Russell III, J.M.,.Bailey,S.M.& Gordley,L,L (2012), The content and composition of meteoric smoke in mesospheric ice particles from SOFIE observations. *JASTP.* **84-85**, 1-6.
3. Rosinsky, J. & Snow, R.H, (1961), Secondary particulate matter from meteor vapors,. *J. Met,* **18**, 736-745.
4. Hunten, D.M., Turco, T.P . & Toon,O.B,(1980), Smoke and dust particles of meteoric origin in the mesosphere and stratosphere, *J. Atmos. Sci,* **37**, 1342-1357.
5. Plane, J.M.C, (2004), A time-resolved model of the mesospheric Na layer: constraints on the meteor input function. *Atmos.Chem.Phys,* **4**, 627-638.
6. Plane, J.M.C, (2012), Cosmic dust in the Earth's atmosphere, *Chemical Society Review,* **41**, 19, 6507-6518.
7. Tomsic, A. (2001), Collisions between water clusters and surfaces. *Ph.D thesis.* Gothenburg University. Sweden.

MULTI-RADAR OBSERVATIONS OF POLAR MESOSPHERE SUMMER ECHOES DURING THE PHOCUS CAMPAIGN ON 21 JULY 2011

E. Belova[1], S. Kirkwood[1], M. Zecha[2], R. Latteck[2], H. Pinedo[3], J. Hedin[4], J. Gumbel[4], I. Häggström[5],

[1] *Swedish Institute of Space Physics, Box 812, 98128 Kiruna, Sweden, Email: belova@irf.se, sheila.kirkwood@irf.se*
[2] *Leibniz-Institute of Atmospheric Physics, Schlossstraße 6, 18225 Kühlungsborn, Germany, Email: latteck@iap-kborn.de*
[3] *Department of Physics and Technology, University of Tromsø, N-9037 Tromsø, Norway, Email: henry.pinedo@uit.no*
[4] *Department of Meteorology (MISU), Stockholm University, 10691 Stockholm, Sweden, Email: jonash@misu.su.se, gumbel@misu.su.se*
[5] *EISCAT Scientific Association, Box 812, 98128 Kiruna, Sweden, Email: Ingemar.Haggstrom@eiscat.se*

ABSTRACT

On the morning of July 21, 2011, the PHOCUS sounding rocket was launched from Esrange, Sweden, into noctilucent clouds (NLC) and polar mesosphere summer echoes (PMSE). We show PMSE observations during the entire day by three atmospheric radars: ESRAD located at the launching site, MORRO located at Ramfjordmoen and MAARSY at Andenes, both in Norway. We found that waves with periods of several hours are observed by all three radars in the PMSE strength. The PMSE spectral widths are in the range of 2-10 m/s and increase with increasing altitude for all radars. Strong PMSE at ESRAD at the lower heights are highly aspect sensitive and have narrow spectra which is a signature of quasi-specular scatter.

1. INTRODUCTION

At 07:01 UT on July 21, 2011, the PHOCUS sounding rocket was launched from Esrange, Sweden, into strong noctilucent clouds (NLC) and polar mesosphere summer echoes (PMSE). PMSE observations have been made during the entire day by the ESRAD MST radar located at the same site. Two other 50-MHz radars: high-power MAARSY at Andenes and medium-power MORRO at Ramfjordmoen, both in Norway, have observed PMSE from the other side of the Scandinavian mountain ridge. The radar locations are shown in Fig. 1.
We combine all these radar data to look at spatial and temporal variability of PMSE fields, waves, turbulence and aspect sensitivity.

2. EXPERIMENT DESCRIPTION

The radars belong to the same class of atmospheric radars, Mesosphere-Stratosphere-Troposphere (MST) radars. However, the parameters of the radars and radar experiments differ from each other and are shown in Table 1. More detailed description of the radars can be found in [2] for ESRAD, [3] for MORRO and [4] for MAARSY.

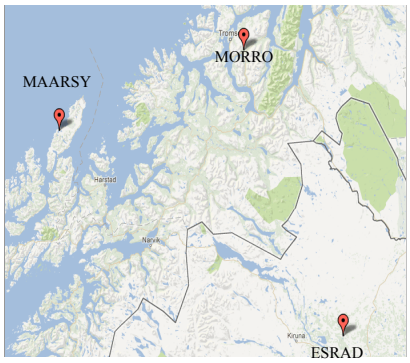

Figure 1. Map with the radar locations.

3. PMSE STRENGTH

We present here PMSE strength as signal-to-noise ratio (SNR). It is a relative measure of echo power because it depends on radar and experiment parameters, which vary from one radar to another. In Fig.2 SNR for each radar is shown for the entire day for the 75-95 km altitude range.

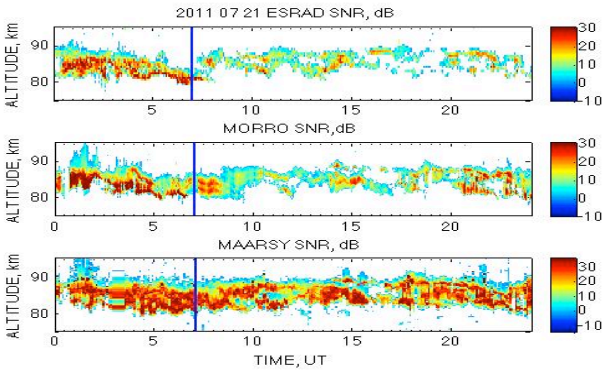

Figure 2. SNR for ESRAD (top), MORRO (middle), MAARSY (bottom). The blue vertical line indicates the time of rocket launch.

Proc. '21st ESA Symposium European Rocket & Balloon Programmes and Related Research', 9–13 June 2013, Thun, Switzerland (ESA SP-721, October 2013)

Table 1. The radar and experiment parameters.

MST radars	ESRAD	MORRO	MAARSY
Location	Esrange, Sweden	Ramfjordmoen, Norway	Andenes, Norway
Geograph. coordinates	67.9°N 21°E	69.6°N 19.2°E	69.3°N 16°E
Frequency	52 MHz	56 MHz	53.5 MHz
Beam width	4.4°	5°	3.6°
Exp/Analysis	fca_4500/FCA	vertical beam	vertical beam
Altitude resolution	600 m	300 m	300 m
Time integration	~2 min	~25 s	~6 min

Despite the difference in the strength we see similarity in the PMSE behaviour for all three radars. In order to find the altitude distribution of PMSE we averaged SNR over 24 hours. In Fig. 3 the altitude profiles of the mean and median PMSE SNR are shown for three radars. The PMSE measured by MAARSY have significantly larger SNR than other two radars because of its higher sensitivity. The SNR profiles for MORRO and ESRAD are very similar with one exception: PMSE at ESRAD have an additional maximum at about 81 km altitude. We chose 85.2 km as a reference altitude for calculation of cross-correlations of SNR (after removing mean values) for each pair of radars, which are presented in Fig. 4.

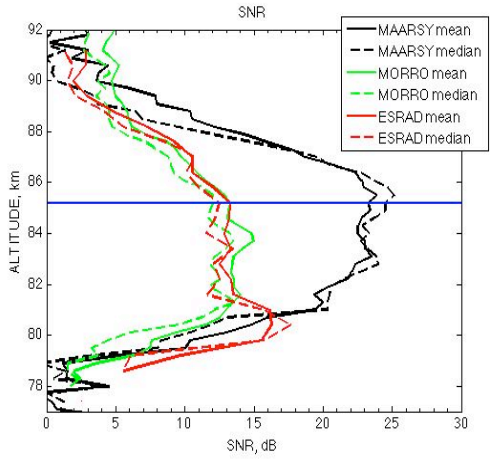

Figure 3. Altitude profiles of the PMSE SNR mean and median values calculated over 24 hours for the MAARSY, MORRO and ESRAD radars. The blue horizontal line indicates the 85.2 km altitude chosen as the reference altitude.

As seen from the figure, the correlations are moderately high with maxima at 0.2-0.5. The strongest correlation is between PMSE variations at MORRO and MAARSY, which situated closest to each other and at the same side of the Scandinavian mountain ridge. All three cross-correlation functions show several pronounced maxima for the negative lags. This is a signature of waves, which are present in the signals of all three radars.

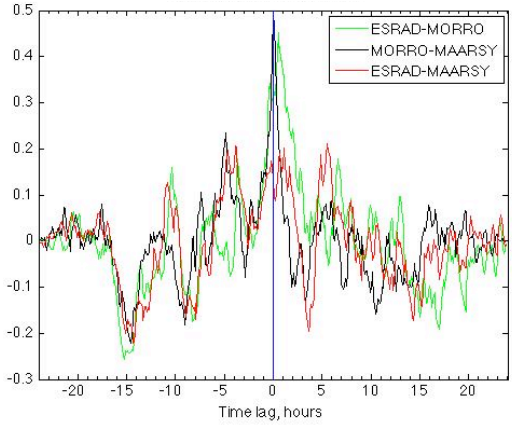

Figure 4. Cross-correlation functions for SNR measured by three radars at 85.2 km altitude.

In order to determine the periods of these waves we applied the Fourier transform to the each of the cross-correlation function. The results are shown in Fig. 5. Wave periods of about 4, 6 and 10 hours can be estimated from this figure. By taking into account the sign of the time lags corresponding to these waves and the radar locations, one can conclude that these waves propagate westward, arriving first to ESRAD and then to MORRO and finally, to MAARSY.

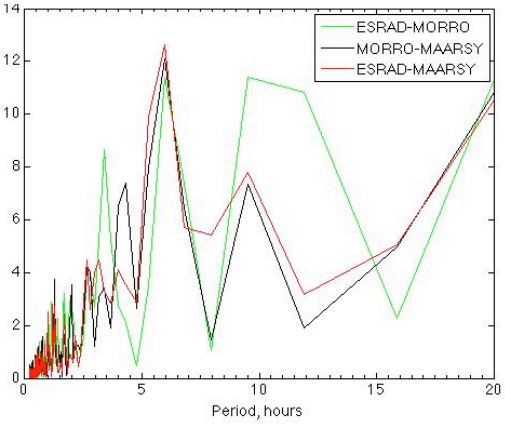

Figure 5. Spectra of the cross-correlation functions from Fig. 4.

4. PMSE SPECTRAL WIDTH

Another important characteristic of PMSE is their spectral width. It can be determine from the radar signal power spectrum, which, in turn, is calculated by applying FFT to the time-series of the radar backscattered power at sub-second time resolution. Here we define the PMSE spectral width as a half-maximum full spectral width (HMFW) and express it in velocity units (m/s), multiplying spectral width in Hz by a half radar wave length. Fig. 6 shows the time-altitude plots of PMSE spectral widths for all three radars. The MORRO and MAARSY spectral widths were corrected for beam broadening according to Eq. 46 by [5]. For the correction horizontal wind speeds from the Andenes MF radar measurements were used. The ESRAD spectral width was calculated using the full correlation analysis (FCA) based on space antenna technique and is not affected by beam broadening. As for SNR, we averaged PMSE spectral widths over 24 hours and the results are presented in Fig. 7.

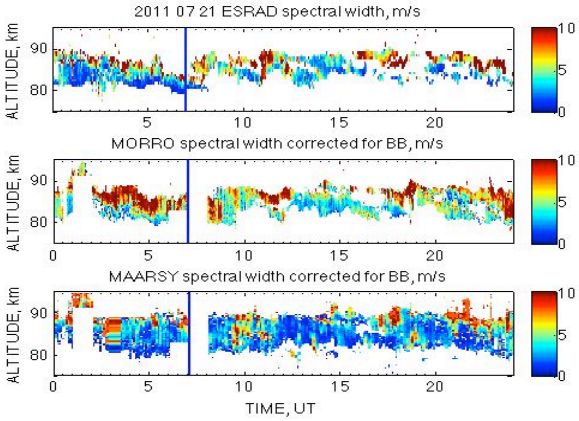

Figure 6. PMSE spectral widths for ESRAD (top), MORRO (middle), MAARSY (bottom).

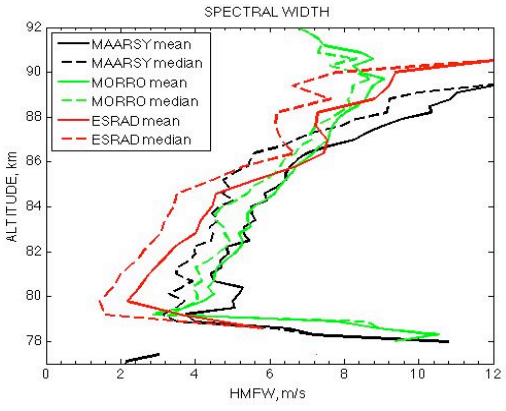

Figure 7. Altitude profiles of the mean and median values of PMSE spectral widths calculated over 24 hours for the MAARSY, MORRO and ESRAD radars.

The PMSE spectral widths at all three radars show similar behaviour for 79-90 km altitude range: they increase with increasing altitude. Below and above this range the averaged values are not reliable because of a small amount of data. Moreover, the spectral width values at MORRO and MAARSY are close to each other at 79-87 km. However, the ESRAD spectral widths at lower heights are significantly smaller than those for the two other radars.

5. PMSE ASPECT SENSITIVITY

Aspect sensitivity is a property of the scatterers and describes the variation of scattered power in respect of scattering angle. It can be characterized by so called aspect angle which is determined as the (half) width of the angular diagram of backscatter. Isotropic scatterers are non-aspect sensitive and have a large aspect angle, while anisotropic, specular scatter is highly aspect sensitive with a small aspect angle of a few degrees. On 21 July 2011 ESRAD ran an experiment applying the full correlation analysis (FCA), which allows calculation of aspect sensitivity of PMSE. By using FCA we computed an effective aspect angle, which is the aspect angle of scatterers as seen by ESRAD with certain transmit/receive beams. The effective aspect angle together with the spectral width of PMSE measured by ESRAD during 00:00-10:00 UT are presented in Fig. 8. From the figure we see that the radar backscatter is most aspect sensitive at the lower edges of the PMSE layers where spectral width is smallest.

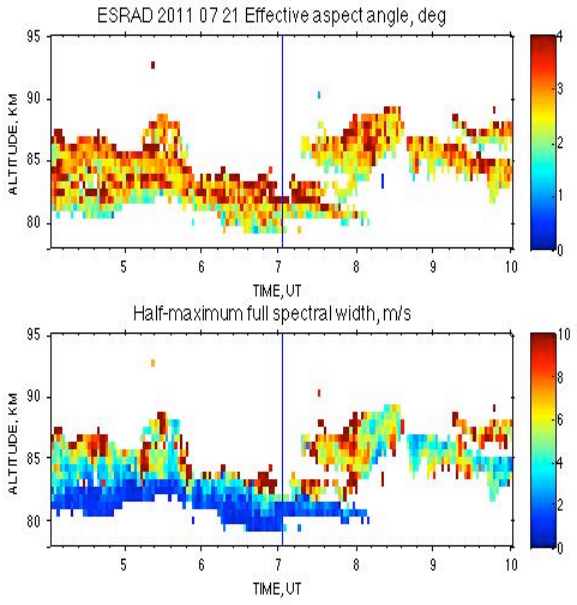

Figure 8. PMSE effective aspect angle (top) and spectral width (bottom) for ESRAD.

We averaged the PMSE aspect angle over 10 hours and results are presented in Fig. 9. The averaged aspect angles show increase with altitude, this implies that PMSE become more isotropic/less aspect sensitive with increasing height.

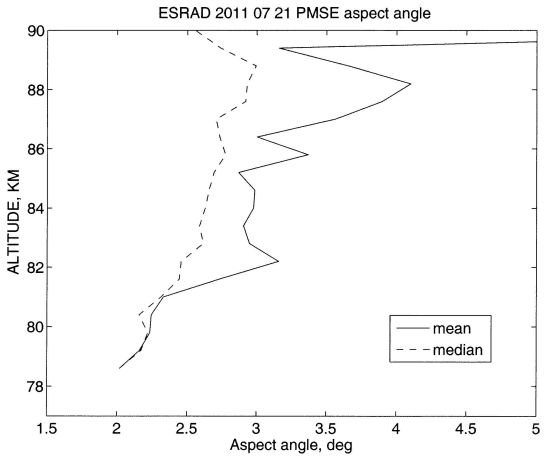

Figure 9. Altitude profiles of the mean and median of PMSE effective aspect angle averaged over interval 00:00-10:00 UT for ESRAD.

6. RESULTS AND OUTLOOK

We used PMSE observations during whole day of 21 July 2011 by three MST radars ESRAD, MORRO and MAARSY, which are located in the Northern Sweden and Norway, at a distance of 150-250 km from each other. We compared the SNR and spectral widths of the PMSE as measured by these radars.

Waves with periods of about 4 h, 6 h and 10 h in PMSE SNR were observed by all 3 radars. These gravity waves travel from Esrange in the north-west direction, arriving first to Ramfjordmoen and then to Andenes.

The PMSE spectral widths are in range of 2-10 m/s. The spectral width increases with increasing altitude for all 3 radars which is in accordance with its average behaviour over several PMSE seasons (e.g. at ESRAD or at the MARA radar in the SH). The narrow spectra at the lowest heights at ESRAD on this occasion were significantly narrower than average.

PMSE (measured by ESRAD) become more aspect-sensitive (less isotropic) with decreasing altitudes. This again in agreement with climatology of the PMSE aspect sensitivity at ESRAD over 1997-2010 [6] and at MARA [7]. The radar backscatter is most aspect sensitive at the lower edges of the PMSE layers. This correlates with strong backscatter power and narrow spectra and is a signature of quasi-specular scatter.

As a further study it would be interesting to combine the ESRAD measurements of PMSE spectral width and aspect sensitivity as a function of altitude with in-situ measurements of ice particles at different altitudes.

Additionally, during 3 hours after the rocket launch two incoherent scatter radars: EISCAT VHF (224 MHz) and UHF (933 MHz) at Ramfjordmoen, Norway ran experiments for mesospheric echo detection. Another idea for the further research is to look at the PMSE common volume measurements by the EISCAT VHF, UHF and MORRO radars: strength, spectral width at 3 different scale lengths.

REFERENCES

1. Kirkwood, S., I. Wolf, H. Nilsson, P. Dalin, D. Mikhaylova, and E. Belova, Polar mesosphere summer echoes at Wasa, Antarctica (73°S): First observations and comparison with 68°N, *Geophys. Res. Lett.*, **34**, L15803, doi:10.1029/2007GL030516, 2007.
2. http://tupac.phys.uit.no/~cesar/MORROradarSite/MORROradar.html
3. Latteck, R., W. Singer, M. Rapp, B. Vandepeer, T. Renkwitz, M. Zecha and G. Stober, MAARSY - the new MST radar on Andøya-system description and first results, *Radio Sci.*, doi:10.1029/2011RS004775, 2012.
4. Hocking, W. K.: Measurement of turbulent energy dissipation rates in the middle atmosphere by radar techniques, *Radio Sci.*, 20, 1403–1422, 1985
5. Smirnova, M., Belova, E., and Kirkwood, S., Aspect sensitivity of polar mesosphere summer echoes based on ESRAD MST radar measurements in Kiruna, Sweden in 1997–2010, *Annales Geophysicae*, **30**, 457-465, doi:10.5194/angeo-30-457-2012, 2012.
6. Kirkwood, S., Belova, E., Dalin, P., Mihalikova, M., Mikhaylova, D., Murtagh, D., Nilsson, H., Satheesan, K., Urban, J., and Wolf, I.: Response of polar mesosphere summer echoes to geomagnetic disturbances in the Southern and Northern Hemispheres: the importance of nitric oxide, *Annales Geophysicae*, **31**, 333-347, doi:10.5194/angeo-31-333-2013, 2013

SOUNDING ROCKET EXPERIMENTS WITH EJECTABLE PAYLOADS AT KTH

N. Ivchenko and G. Tibert

Royal Institute of Technology (KTH), 100 44 Stockholm, Sweden, nickolay.ivchenko@ee.kth.se

ABSTRACT

Several experiments have been carried out or are in design phase under the lead of KTH using ejectable recoverable units to achieve variable scientific and technical objectives. This paper introduces the experiments with their goals, design solutions, results and lessons learned where appropriate. The RAIN (Rocket deployed Atmospheric probes conducting Independent measurements in Northern Sweden) experiment used two radially ejected free flyers equipped with aerosol particle collection experiments. The MUSCAT (Multiple Spheres for Characterisation of Atmospheric Temperature) experiment used four free flyers ejected radially to retrieve the density, temperature and wind profiles. The ISAAC (Infrared Spectroscopy to Analyze the middle Atmosphere Composition) experiment will use two free-flyers to derive the carbon dioxide by measuring the absorption of the infrared light on the line of sight between them. The SPIDER (Small Payloads for Investigation of Disturbances in Electrojet by Rockets) experiment will use a larger number (>4) of free flyers to measure electric and magnetic field, electron concentration and temperature in order to study the electrojet turbulence.

1. INTRODUCTION

Physics of a range of critical phenomena in the coupled geospace system involves cross-scale interaction and dynamics on small scales. The small scale structure and its effects is important in the ionospheric plasma, aurora, mesosphere (e.g. noctilucent clouds), etc. Multipoint measurements are the key to resolving the coupled cross-scale dynamics. Satellite missions, e.g. Cluster, and earlier ISEE and DE, have demonstrated the strength of the approach, and more are upcoming (such as MMS, SWARM). Subauroral experiments with multiple payloads have been carried out for several decades now, and provide an important tool in e.g. studing the aurora.

To address the scales of the order of tens of meters to tens of kilometers, single launch with multiple ejectable daughter payloads provides a viable solution. Launches from Esrange have an advantage of relatively simple recovery of the payloads. Experiments of this kind have been carried out at the Royal Institute of Technology (KTH), primarily in the framework of the REXUS programme (Rocket EXperiments for University Students). Here we report on the four experiments, and discuss the technical solutions taken. Section 2 presents the objectives of four experiments: RAIN, MUSCAT, ISAAC and SPIDER, and their layout. Section 3 discussed the progression of the design solutions. The experiences are summarized in Section 4.

2. EXPERIMENTS

Two earlier REXUS experiments carried out by KTH teams, the LAPLander (Light Airbag Protected Lander) and SQUID (Spinning QUad Ionospheric deployer) included ejection of a single free flyer axially from the rocket. The objective of the LAPLander experiment [1] was the demonstration of novel inflatable landing system. The experiment was flown on REXUS- 8 launched from Esrange on March 8, 2010. The experiment was launched without the inflation agent due to pressure tank malfunction, and was lost after the ejection. The objective of the SQUID experiment [2] was to demonstrate a miniaturized wire boom deployment system. The experiment was flown successfully on REXUS-10 on February 23, 2011.

Here we concentrate on later experiments that involve ejection of multiple free flyers normal to the rocket axis. Common to the experiments (including the LAPLander and SQUID) is the use of recoverable free flyers ejected from spinning rocket, with landing and localisation systems. All the collected data are stored onboard and read out postflight, after the recovery of the payloads.

2.1. RAIN

The objective of the RAIN experiment was to collect aerosol particles in the middle atmosphere, using two identical free flyers (from here on referred to as Free Falling Units, FFUs). An extended description of the experiment is given in a separate paper [3].

The experiment was launched on November 16, 2012 on REXUS-11 from Esrange. The FFUs were ejected sideways from the rocket at 63 km before the despin. The FFUs followed a ballistic trajectory until an apogee of

Proc. '21st ESA Symposium European Rocket & Balloon Programmes and Related Research',
9–13 June 2013, Thun, Switzerland (ESA SP-721, October 2013)

85 km. On the downleg of the trajectory, a rotating table exposed multiple samples to the oncoming flow to catch aerosol particles. Postflight electron microscopy of the samples will allow to characterize the morphology and composition of the aerosol particles. Each sample is exposed over a limited altitude range, thus allowing to get altitude profiles of the aerosol distribution. Reconstruction of the exposure altitudes is achieved by postflight analysis of the collected raw GPS data.

After the aerosol collection phase, the parachute was deployed and the localisation system activated, transmitting the position of the FFUs during the parachute descent. Both payloads were recovered shortly after landing.

2.2. MUSCAT

The objective of the MUSCAT experiment is to retrieve density, temperature and wind profiles in the middle atmosphere, using four spherical FFUs. An extended description of the experiment is given in a separate paper [4].

The parameters of the atmosphere are obtained from the analysis of the trajectory of the FFUs. The aerodynamical drag force is proportional to the air density, provided that the coefficient of drag is known and the cross section area is constant. The FFUs are made in spherical shape to achieve this. This falling sphere method is well known [5], the novelty of the experiment is in using inertial sensors and raw GPS data logger onboard the spheres, rather than tracking them from the ground with a precision radar.

MUSCAT experiment was launched on May 9, 2013 on REXUS-13 from Esrange. All four FFUs were ejected from the rocket, collected the data, deployed the parachutes at the nominal altitude and were recovered shortly after landing.

2.3. ISAAC

The ISAAC experiment was selected in December 2012 for flight on REXUS-14/15 rocket, with launch in spring of 2014. The experiment has dual objectives. The technical objective is to implement a system with two ejectable FFUs, where one of them is capable of pointing an optical system in the direction of the other one. The scientific objective is to measure the concentration of the carbon dioxide in the middle atmosphere by non-dispersive infrared measurements.

Similar to the RAIN and MUSCAT experiments, the FFUs are to be ejected sideways from the spinning rocket. Thus they are spin-stabilized until after re-entry, with the spin axes in nominally parallel direction. One of the FFUs, the Tx FFU, has the light sources (infrared lamps and red LEDs for tracking), which are observed from the other, the Rx FFU. The Rx FFU is a dual-spinner configuration, with bottom part of it rotating with respect to the top, driven by a motor. A control algorithm using the data from angular rate sensors, sun sensors and a CMOS camera imaging the LEDs of the Rx FFU shall maintain the pointing of the optical system in the direction of the Tx FFU. The pointing in the elevation angle is maintained by a mirror that can be tilted with another motor.

The infrared optical system is co-aligned with the tracking camera. The IR system consists of two narrow field of view photometer channels based on the PbS photoresistive detectors.

2.4. SPIDER

The SPIDER experiment is funded by Swedish National Space Board (SNSB), with launch planned for early 2015. The objective of the experiment is to study the turbulence in the auroral electrojet.

The auroral electrojet is a horizontal current of remarkable strength and persistence flowing between about 90 and 130 km height in the auroral ionosphere. Often already before the onset of optical aurora it fills with charge density irregularities. This then affects and disturbs the propagation of radio waves, for example terrestrial TV signals, satellite communication and navigation signals. In fact, the presence of the irregularities excited by Farley-Buneman instability is the foundation of the coherent scatter radar operation [6], providing Bragg-scatter whenever the electric field is above the instability threshold. Climatology of GNSS signal scintillations [7] indicates that those tend to occur in regions of strong electric fields as well, thus suggesting a link to the phenomenon in question.

Incoherent scatter radar observations have revealed that the irregularities involve considerable heating of the ionospheric electrons, up to several thousand K [8], at altitudes where even the solar UV radiation, if present, cannot raise the electron temperature significantly above the background of 200–300 K. Thus locally exited electrojet irregularities provide the strongest known dissipation

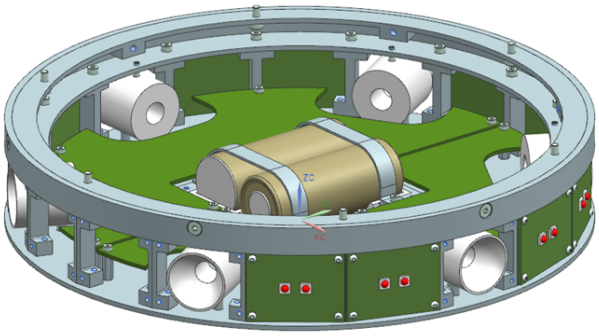

Figure 1. ISAAC TxSU.

mechanism in the upper atmosphere. Little understood is how this affects the coupling of the ionosphere and near Earth space, the electrodynamics and structure of optical aurora, and the lower thermosphere. The incoherent scatter measurements, give a height-resolved estimate of the dissipated power (subject to some assumptions), but only averaged over a volume of roughly 2–3 km across with time resolution of a few minutes. The saturation of the Farley-Buneman instability and anomalous electron heating have been a subject of theoretical debate (see e.g.[9] and references therein), but the evidence is that dissipation of non-linear current explains the heating [10, 11].

The SPIDER experiment consists of a large number (up to 10) identical FFUs, ejected pairwise from the spinning rocket. After the ejection the FFUs will deploy wire booms for measuring the electric fields, and plasma parameters by means of Langmuir probes. The FFUs will also carry a miniature fluxgate magnetometer [12]. The measurements in the region of interest (95-125 km) will be carried out both on the upleg and the downleg of the trajectory with the apogee of around 130 km.

3. SUBSYSTEM DESIGN

3.1. Free Flying Units

FFUs in the four experiments have rather different designs, as motivated by their different objectives. The dimensions and masses of the FFUs are summarized in Table 1. The RAIN FFU is cylindrical, and has three distinct chambers (see [3] for figures of the FFU): aerosol collection experiment at the bottom, the electronics and motor in the middle, and the recovery system on top. While the unit is highly integrated, keeping the modularity of the design allows to decouple (at least to some extent) the design and validation of separate subsystems. The top of the FFU is formed by a plastic hat, held down by three hooks engaging on the hat from the inside. The hooks are spring-loaded to release the hat, once a thin fishing line constraining them is melted by a thermal cutter, thus allowing the parachute deployment.

Experiment	N FFUs	D, mm	h, mm	m, kg
RAIN	2	116	93	1
MUSCAT	4	124	-	0.4
ISAAC	2	240	80	2
SPIDER	up to 10	240	90	3

Table 1. Summary of the FFUs in the four experiments

The MUSCAT FFU is spherical. The outer structure consists of two hemispherical shells made in glass fibre composite. The shells attach to a metal ring in the middle, also supporting the electronics printed circuit boards. The bottom hemisphere attaches to ring by means of a thread joint, while the top hemisphere is held down by a fishing line. Once the fishing line is melted the top hemisphere is released, and the parachute is free to deploy.

For ISAAC the modularity concept is taken further, with each FFU consisting of two independent units: a Common Unit (CU) and a Specific Unit (SU), with no electrical connection between them. The CU is identical on both FFUs, and houses the recovery and localization system, as well as the flight data acquisition system. The SUs on the other hand are quite different. The TxSU (see Fig. 1) houses two high power batteries, power conversion system and a number of light sources: six IR sources with parabolic reflectors, and 20 red LEDs, mounted along the circumference of the SU. The TxSU is statically mounted to the CU, and moves with it. The RxSU, on the other hand, attaches to the CU by means of a moving axis, actuated by a motor to achieve differential rotation of the SU and the CU about the spin axis (see Fig. 2). The RxSU houses a visible and two infrared optical systems, which are co-aligned. The systems are separated by beamsplitters in the optical path. The first mirror is tilted by a motor to allow pointing in the elevation angle.

The SPIDER experiment is still under design. The modularity concept will however be continued here, and the FFU will consist of three distinct parts. The top part of the FFU is identical to the ISAAC CU, providing the re-

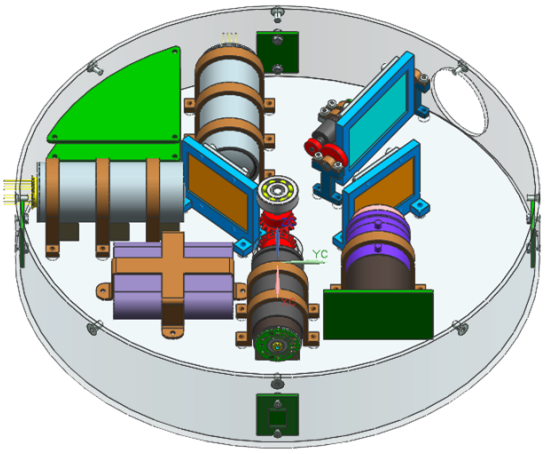

Figure 2. ISAAC RxSU.

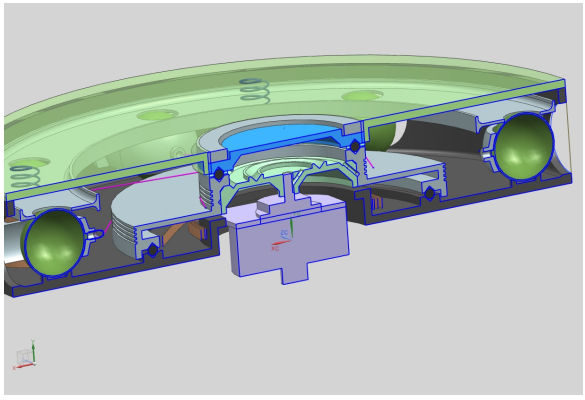

Figure 3. SPIDER boom deployment system.

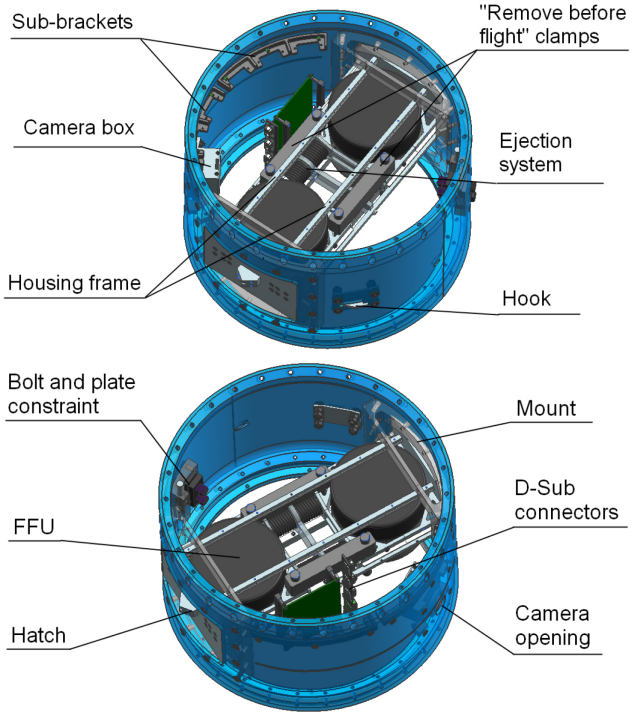

Figure 4. Ejection system for the RAIN experiment.

covery and localization system. The bottom part carries electronics of the magnetometer, the electric field instrument and the Langmuir probes. The middle part of the FFU is the wire boom deployment system, see Fig. 3, deploying two sets of four spherical probes, one set for electric field measurements (to a radial distance of over 1.5 m from the FFU axis), and the other set for the Langmuir probe instrument, to a somewhat shorter distance. All wires are initially wound on a common drum, actuated by a piezomotor.

3.2. Ejection System

The ejection of the FFUs for the RAIN and MUSCAT experiments is achieved by spring-loaded systems, Figs. 4 and 5, where each FFU is constrained between a spring-loaded pushing plate and a hatch covering the opening. The hatches are constrained by a single circumferential steel cable. One end of the cable is connected to a hook and the other end is clamped between two steel plates. For the RAIN experiment, ejection is initiated by cutting the clamped cable end by a pyrocutter while the looped end self-releases from the hook. The MUSCAT experiment used two pyrocutters, to cut both ends. Cutting the cable at a single or two positions creates a slightly asymmetric ejection of the FFUs. Other disadvantages of having an external circumferential cable are: (i) the cable is loaded transversal to its direction and is thus subjected to forces *several times higher* than the spring forces, and (ii) the cable is exposed to the same high temperatures as the rocket skin during ascent. The RAIN experiment used compression springs between the pushing plate and a plate in the middle of the ejection tunnel, while the MUSCAT experiment used tension springs connecting the pushing plates and the collars around the openings. Long tension springs do not suffer from the buckling of long unrestrained compression springs and in the case of MUSCAT, the FFUs could be places closer to the center of the cylinder by having the tension springs around the FFU.

To avoid the drawbacks of the RAIN and MUSCAT ejection systems, the ISAAC/SPIDER ejection system, Fig. 6 is designed as completely internal system aiming at creating symmetric ejection of the FFUs. The ejection tunnel is similar to that of the RAIN experiment, with each FFU radially and tangentially constrained by the pushing plate and the hatch, which both slides on rails, and axially constrained by Teflon-clad rails. The pushing plate is in contact with the the hatch on the sides of the FFUs. The hatch is constrained by self-releasing pinned hooks, one on each side of the ejection tunnel. The hook is designed with a long lever arm so that the force in the steel cables, running over the ejection tunnel through a single pyrocutter, is *several times lower* than the force in the tension spring. Hence, the force is required to load the system is much lower than for the RAIN and MUSCAT systems and it is possible to use cables of less than 1 mm in diameter which can be bent in small radii without damage. The single pyrocutter cuts all four cables simultaneously to hopefully create a symmetric ejection.

3.3. Rocket Cylinder Openings

The ejection of FFUs from the rocket cylinders requires openings of significant sizes in comparison to the cylinder diameter of 356 mm.

The rocket cylinder for the RAIN experiment had two 142 mm wide and 97 mm tall openings, Fig. 7, left, and to reinforce the 220 mm tall cylinder an equal cross-section moment of inertia approach was used, i.e. the cross-section moment of inertia of the weakest section of the cylinder with openings and suitable reinforcement was required to be equal to the cross-section moment of inertia of the unmodified cylinder with 4 mm wall thickness. This approach aimed to ensure that the rocket's aeroelastic behaviour during ascent would not change. To achieve the equal cross-section moment of inertia, massive machined collars of aluminium were screwed to the cylinder around the openings. The mass of each collar was around 0.7 kg, so the total mass of the modified cylinder and two collars was 5.7 kg; an increase in mass of 1.2 kg. The fillet radius in the corners of the openings was set to 7 mm to avoid too high concentrations of stresses.

The 220 mm tall rocket cylinder of the MUSCAT experiment had four circular openings, Fig. 7, right, each with a diameter of 134 mm. This reduced the cross-sectional area and moment of inertia by 50%. Elastic buckling analysis of the cylinder by a finite element software was

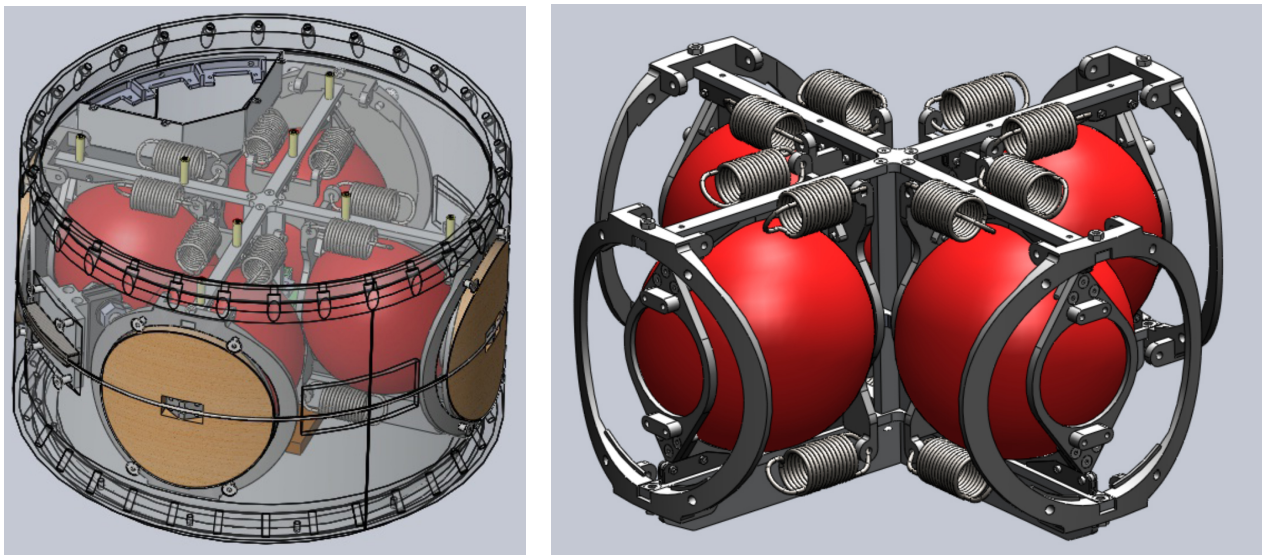

Figure 5. Ejection system for the MUSCAT experiment.

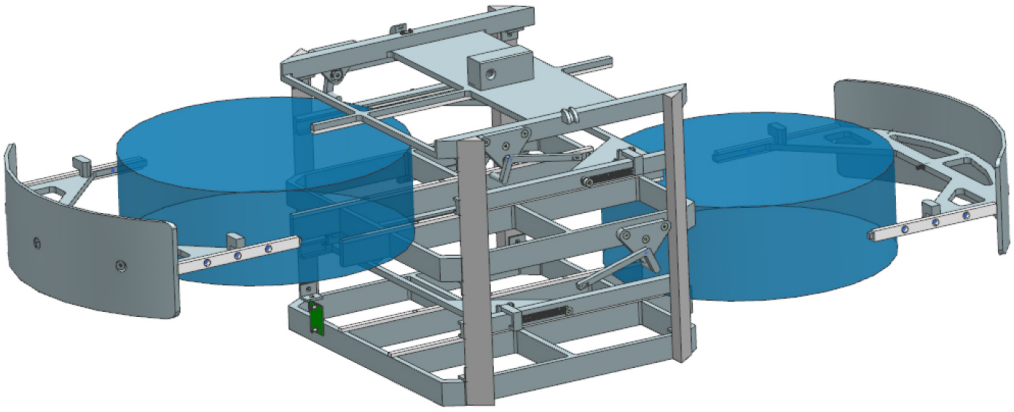

Figure 6. Ejection system for the ISAAC/SPIDER experiment.

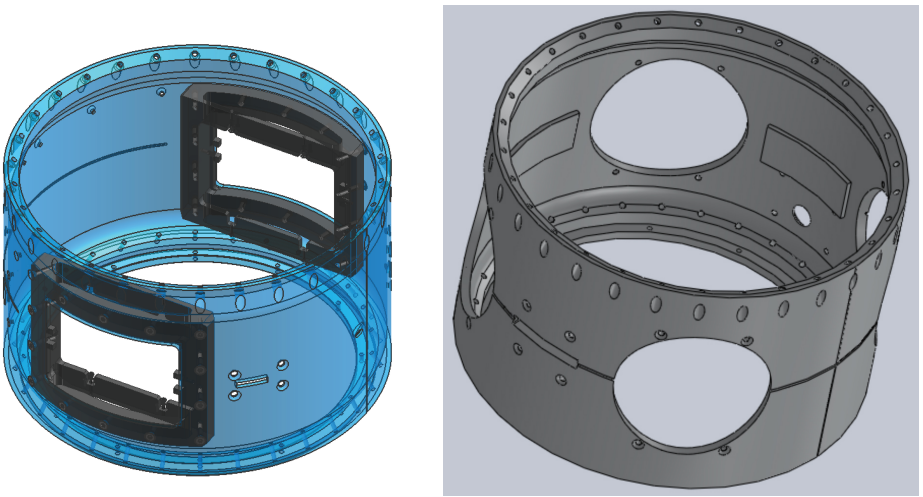

Figure 7. Left: Rocket cylinder for the RAIN experiment with openings reinforcement with collars. Right: Rocket cylinder for the MUSCAT experiment with increased wall thickness.

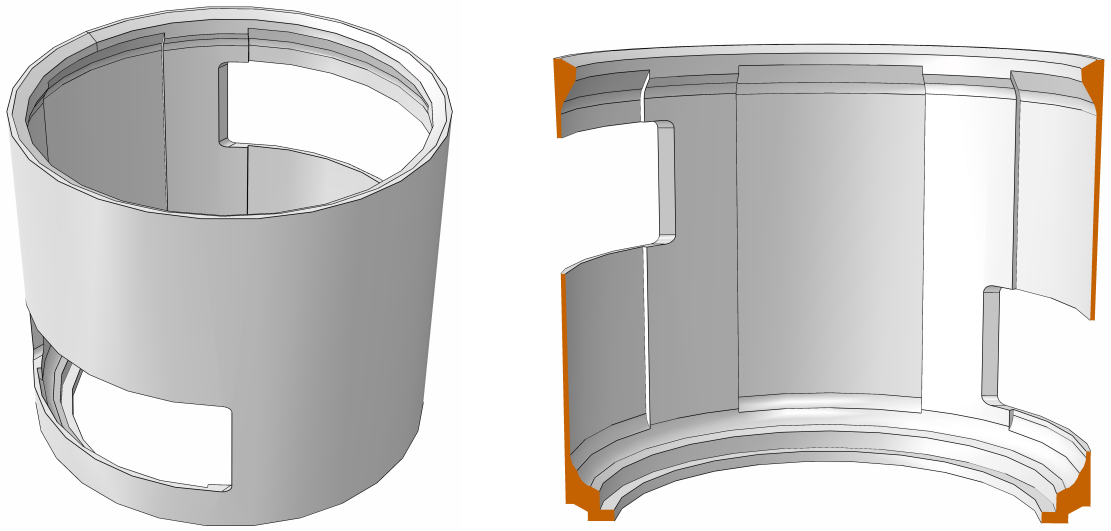

Figure 8. Rocket cylinder for ISAAC and SPIDER experiments.

performed to investigate the elastic stiffness of the modified rocket cylinder. The buckling analysis showed that very heavy collars would be required to reach the same factor of safety against elastic buckling for the modified cylinder. To lighten the cylinder, the REXUS organization was willing to manufacure a custom cylinder with larger wall thickness for MUSCAT. Further finite element elastic buckling analysis showed that a wall thickness of 8 mm would give the same safety factor against elastic buckling. The custom made cylinder had a mass of 5.4 kg, a mass increase of 0.9 kg. Thanks to the circular openings, the stress increase was very low.

The ISAAC and SPIDER experiments are planning to use a 300 mm tall rocket module and two very wide, 254 mm, rectangular openings, each with a height of 85–90 mm, on two different levels, Fig. 8. Assuming that the openings are on the same level, then the cross-sectional area and moment of inertia (in the most flexible direction) are reduced by 51% and 83%, respectively, for a rocket cylinder with 4 mm wall thickness. A quick analysis showed that the "equal cross-section moment of inertia approach" would lead to a very heavy rocket cylinder as material is removed where it is most needed for high moment of inertia. After discussions with the REXUS organization, it was decided that the rocket cylinder shall be designed for the design bending moment specified in the NASA Sounding Rocket Handbook, [14], for the Improved Orion sounding rocket. Preliminary finite element analysis showed that the highest stresses are found near the sides of the openings, so the cylinder wall only needed to be thickened to 8 mm there. This solution is very mass efficient as the mass of the ISAAC/SPIDER cylinder is 5.9 kg, a mass increase of only 0.4 kg. The finite element stress analysis of the cylinder showed that the maximum von Mises stress in the corners of the openings was 222 MPa, Fig. 9, which shall be compared with the nominal 0.2% proof stress of 280 MPa for the 7020-T6 aluminium alloy of the cylinder. The bending stiffness of the ISAAC/SPIDER rocket cylinder in the weakest direction

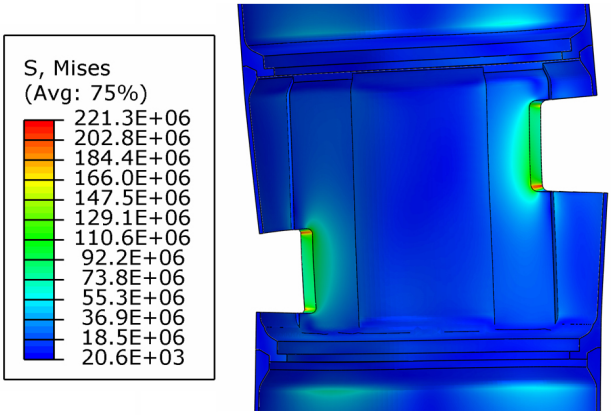

Figure 9. Elastic von Mises stresses (Pa) due to the design bending moment of the ISAAC rocket module with 254 mm × 90 mm openings and 4 and 8 mm wall thicknesses. Displacements are magnified by a factor of 20.

is significantly lower than that of the unmodified rocket cylinder with 4 mm wall thickness, which might increase the bending moment during ascent as the angle of attack for the dynamic pressure on the nose cone increases due to rocket bending. A simplified analysis, using the deflections results from the finite element analysis and typical angles of attack from literature, [13], gave that the expected increase in angle of attack due to the lower bending stiffness was less than 10%. Including the increase in bending moment, the stress factor of safety against material yielding is at an acceptable value of 1.2.

3.4. Recovery and Localisation System

Since in all the experiments the data are stored onboard, the FFU recovery is a critical element of the concept. All experiments use cross parachute for decelerating of the descent, to achieve safe landing velocities. Off the shelf amateur rocket parachutes have performed well both in a range of tests and in the RAIN and MUSCAT flights. The parachute is initially stored under the disposable plastic hat/lid of the FFU. The lid is constrained by a tensioned fishing line, which is cut by melting once the desired parachute deployment altitude is achieved (as observed by a pressure sensor inside the FFU). The parachute deployment altitude is a compromise between two conflicting requirements: achieving a landing spot within the designated zone calls for minimizing the sideway drift with the wind (and thus for minimizing the altitude of deployment), while securing a long descent time sufficient for localization calls for a high altitude deployment. The compromise altitude has been set to 6 km. On RAIN the parachute deployment was premature, as the lids have separated from the FFU in fast tumbling at altitudes above 10 km.

The localization system uses a commercial GPS module returning NMEA messages after start up, and two independent RF systems for transmitting the coordinates to the recovery team. The first system is a VHF link at frequencies in the 173.2-173.4 MHz range. The second system is the Globalstar satellite simplex modem. The VHF system requires a short whip antenna, and is demodulated by a stationary receiving system at Esrange. The antenna is made of a stripped coax cable, attached to the parachute line. The Globalstar satellite modem requires a patch antenna placed at the top of the FFU. In RAIN a dedicated Globalstar transmitting antenna and an active GPS receiving antenna were used, while in MUSCAT a custom-made wide band antenna was developed serving both RF systems.

A parsing algorithm is implemented to identify the last received valid NMEA message, and to re-pack it to the required format. While the VHF link is flexible with respect to the format (complete NMEA message was retransmitted in the RAIN experiment, while a truncated version was used in MUSCAT), the satellite message is limited to 9 byte length, so only the compressed coordinates are transmitted. The commercial GPS is not run before the parachute deployment, hence it requires some time for a cold start. During the high-altitude part of the flight, the commercial GPS module is disabled, and a simple frontend is operated instead, logging raw GPS signal for post processing.

In RAIN and MUSCAT flight both the VHF and the Globalstar link have proven functional, with messages from all FFUs received through both channels. However, the VHF signal is lost on the Esrange receiver when FFUs go below about 0.5 km. Even at moderate wind speeds, considerable drift may occur during the remaining descent to the ground. The coordinates received through the satellite link after the FFU landing provided a precise landing location. On the other hand, the visibility conditions for satellites from Esrange latitude are rather variable, and a number of messages have been lost.

4. SUMMARY

Experiments with ejectable recoverable FFUs, carried out and planned at KTH, prove the concept of using such payloads to address various scientific questions. The development of the experiments has been possible thanks to the fast turn-around time of the REXUS experiments, providing the opportunity to try out new ideas and iteratively improve the design.

The ejection systems have performed to the functional requirements in the RAIN and MUSCAT experiments. However, the interaction of the external constraining cable with the hatches and the FFUs seems to affect the FFU dynamics, and systems with constraints completely internal to the rocket module are being explored for upcoming experiments. The openings in the rocket module require reinforcement of the module walls, however careful analysis allows to minimize the mass increase of the system.

The emerged solution for the localisation and recovery system has been flight proven in slightly different configurations in SQUID, RAIN and MUSCAT experiments. The use of the redundant VHF link and satellite link has been essential for successful operation. The parachute deployment systems including a disposable dielectric lid have performed well.

Development of small and lightweight FFUs calls for highly integrated payload. Despite this, a certain degree of modularity can be achieved, allowing to reuse solutions, or even complete units, between the experiments.

ACKNOWLEDGMENTS

We thank the sponsors of the REXUS/BEXUS programme: SNSB, DLR, SSC and ESA, and external sponsors of the RAIN, MUSCAT and ISAAC experiments. The SPIDER project is funded by the SNSB. We are also grateful to all members of the student experiment teams, engineers and technicians at KTH without whom the described experiments would not be possible.

REFERENCES

[1] Sundberg, T., et al., *Small Recoverable Payload for Deployable Sounding Rocket Experiments*, ESA Special Publications 671, p. 281, 2009.

[2] Alaniz, M., et al., *The SQUID Sounding Rocket Experiment*, ESA Special Publications, 2011.

[3] Magnusson, P., et al., *Preliminary Results from the RAIN Mesospheric and Stratospheric Aerosol Particle Collection Experiment Launched on REXUS-11*, this volume.

[4] Bordogna, M. T., et al., *MUSCAT Experiment: Active Free Falling Units for in situ Measurements of Temperatures and Density in the Middle Atmosphere*, this volume.

[5] Schmidlin F. J., et al., *The Inflatable Sphere: A Technique for the Accurate Measurement of Middle AtmosphereTemperatures*, Journal of geophysical research, vol. 96, 1991.

[6] Sahr, J. and B. Fejer, *Auroral electrojet plasma irregularity theory and experiment: A critical review of present understanding and future directions*, Journal of geophysical research, vol. 101, p. 26893, 1996.

[7] Spogli, L. et al, *Climatology of GPS ionospheric scintillations over high and mid-latitude European regions*, Annales Geophysicae, vol. 27, p. 3429, 2009.

[8] Buchert, S. et al, *The Pedersen current carried by electrons: a non-linear response of the ionosphere to magnetospheric forcing*, Annales Geophysicae, vol. 26, p. 2837, 2008.

[9] Dimant, Y. S. and G. M. Milikh, *Model of anomalous electron heating in the E region: 1. Basic theory*, Journal of Geophysical Research, vol. 108, p. 1350, 2003.

[10] Buchert, S. et al, *Model of anomalous electron heating in the E region: 1. Basic theory*, Journal of Geophysical Research, vol. 1111, A02305, 2006.

[11] Dimant, Y. S. and G. M. Milikh, *Magnetosphere-ionosphere coupling through E region turbulence: 1. Energy budget*, Journal of Geophysical Research, vol. 116, A09303, 2011.

[12] Forslund, Å et al, *Miniaturized digital fluxgate magnetometer for small spacecraft applications*, Measurement Science and Technology, 19, p. 015202, 2008.

[13] Lane J. H. and C. P. Chalfant, *Development of the Aerobee 350 Sounding Rocket*, Journal of Spacecraft and Rockets, vol. 4, p. 1316, 1967.

[14] NASA, *NASA Sounding Rocket Program Handbook*, Sounding Rocket Programs Office, Suborbital & Special Orbital Projects Directorate, Goddard Space Flight Center, Wallops Flight Facility, Wallops Island, VA, USA, 810-HB-SRP, 2005.

PRELIMINARY RESULTS FROM THE RAIN MESOSPHERIC AND STRATOSPHERIC AEROSOL PARTICLE COLLECTION EXPERIMENT LAUNCHED ON REXUS-11

Patrick Magnusson[1], William Reid[1], Peggy Achtert[2], Nickolay Ivchenko[1], Erik Lindén[1], Valeriy Shepenkov[3], and Gunnar Tibert[3]

[1]*Space and Plasma Physics, School of Electrical Engineering, Royal Institute of Technology (KTH), SE-100 44 Stockholm, Sweden, Email: nickolay@kth.se*
[2]*Department of Meteorology, Stockholm University, SE-106 91 Stockholm, Sweden, Email: gunnar.tibert@mech.kth.se*
[3]*Department of Mechanics, Royal Institute of Technology (KTH), SE-100 44 Stockholm, Sweden, Email: peggy@misu.su.se*

ABSTRACT

The RAIN (Rocket deployed Atmospheric probes conducting Independent measurements in Northern Sweden) experiment demonstrates a technique for collecting aerosol particles in the middle atmosphere using multiple probes ejected from a sounding rocket. Collection samples on each probe are exposed over varying height ranges between 80 and 22 km giving an altitude distribution profile of aerosol particles. The experiment was launched on board the REXUS-11 sounding rocket on November 16, 2012 from Esrange Space Centre. The experiment operated nominally and was recovered. Initial scanning electron microscopy analysis of the collection samples indicates that aerosols were collected during the fall, however detailed analysis over all height ranges is ongoing.

1. INTRODUCTION

The influence of middle-atmospheric aerosol on climate variability is not yet fully understood. It is known that the stratospheric aerosol extends between the tropopause to about 30 km and is dominated by sub-micrometer hydrate sulphuric acid droplets which scatter incident sunlight [1]. It is also known that the upper-mesosphere aerosol is dominated by meteoric material that enters the earth's atmosphere and forms nanometer sized particles. These nanometer sized meteoric particles influence several middle-atmospheric processes, such as noctilucent clouds (NLCs), polar mesospheric summer echoes (PMSEs), metal layers and the heterogeneous chemistry that controls the budget of key species like water vapour [2; 3; 4; 5].

The size range and the concentration of stratospheric aerosols have previously been characterised by balloonborne measurements [6], lidar [7] and satellite observations [8]. The size and composition of particles in NLCs has been monitored by satellite-based instruments [9] and ground-based instruments [10], but the microphysical properties of meteoric-smoke particles are still poorly understood. This is due to the the complications involved with in situ measurements at mesospheric altitudes. These measurements have only been performed by experiments on board sounding rockets [11], and the capturing of nanometer-sized particles is constrained by the shock wave in front of the rocket [12] and by contamination from the rocket itself.

A new method for collecting middle-atmospheric aerosols that involves free falling probes that are ejected from a sounding rocket is described. The experiment is called RAIN (Rocket deployed Atmospheric probes conducting Independent measurements in Northern Sweden). Two free falling aerosol collection probes are deployed from a sounding rocket and collect aerosol particles over varying height ranges between altitudes of 80 and 22 km. By using multiple probes independent of the rocket, the risk of contamination of the collected samples from the rocket is reduced and horizontal aerosol distributions at similar altitudes can also be studied. This paper outlines the design of the experiment in Section 2, the experiment results in Section 3 and a discussion of the results and further work in Section 4.

2. EXPERIMENT DESIGN

The planned flight timeline is summarised in Fig. 1. At 63 km altitude and t+67 s, the aerosol collection probes or free falling units (FFUs) are deployed from the rocket. The FFUs rise to an apogee of 85 km at t+145 s and activate their aerosol collection experiments (ACEs). Aerosol collection continues until the FFUs fall to an altitude of 17 km at t+285 s. At 6 km, a pressure sensor on each FFU triggers deployment of a parachute. During controlled descent each FFU broadcasts its GPS coordinates via a VHF radio transmission and satellite messages. After landing, the FFUs continue to transmit their positions, at which point a helicopter recovery crew lo-

Proc. '21st ESA Symposium European Rocket & Balloon Programmes and Related Research', 9–13 June 2013, Thun, Switzerland (ESA SP-721, October 2013)

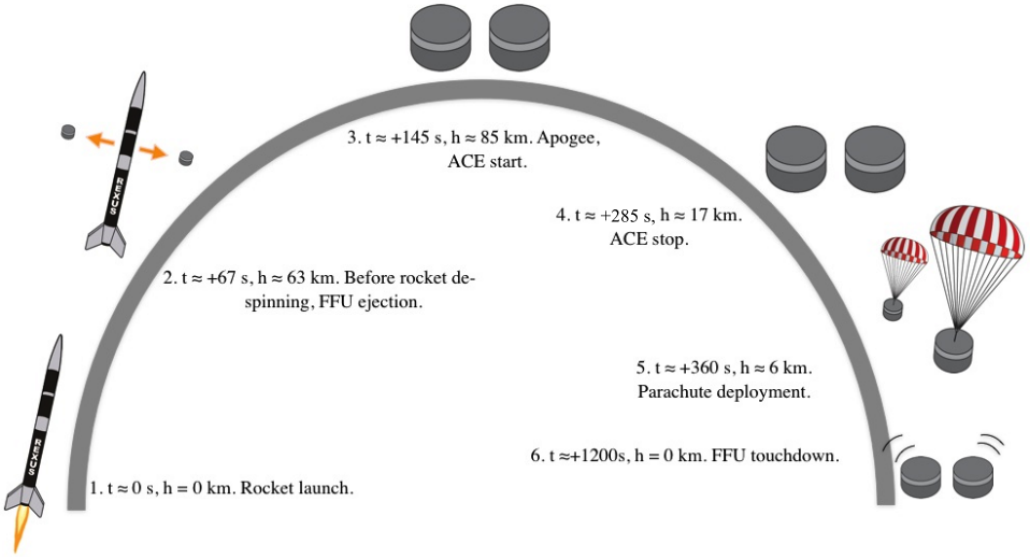

Figure 1. The flight timeline for the RAIN experiment.

cates and collects both units.

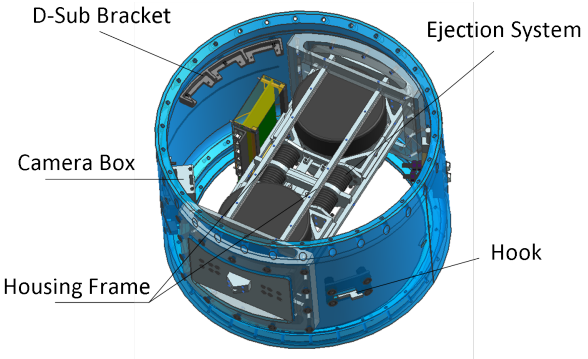

Figure 2. The Rocket Mounted Unit (RMU) that contains the two Free Falling Units up until the point of ejection. Ejection is triggered by a steel cable routed around the outside of the RMU being cut and the four 215 N compression springs pushing the FFUs out. A baffle over the hook and curved hatches was later added to protect the cable from the airflow.

The RAIN experiment consists of two parts: the rocket mounted unit (RMU) and the aerosol collecting FFUs. The RMU consists of a spring based ejection system, a camera and electronics used to charge and communicate with the FFUs. A labelled view of the RMU is shown in Fig. 2. The ejection system is a spring-based system that uses four 215 N compression springs. The FFUs are held within an ejection system housing made up of six aluminium bars. These bars are held inside two D-shaped mounts that are attached to the surface of the rocket cylinder. The mounts have been designed as reinforcements for the rocket cylinder structure so that the ejection hatches cut out of the cylinder do not detrimentally affect the rockets structural integrity. Each FFU is surrounded by a push plate. Each push plate takes the load of two compressed ejection springs while the system is in its loaded state. When the ejection springs are released the push plates slide along the ejection system housing bars, pushing the FFUs out of the rocket. On the opposite side of the FFU is a hatch assembly. The hatch interfaces with the push plates so that the force of the compressed springs is transmitted to it instead of the FFU. A 2 mm thick steel cable is routed around the circumference of the rocket cylinder and constrained at its two ends to hold the ejection springs in their compressed state. The termination of the cable has an eyelet that is placed onto the hook. The other end of the cable is held inside the rocket cylinder between two ruffled steel blocks that are bolted together. Before being placed between these steel blocks, the cable is passed through a pyrotechnic cutter that is used to cut the cable at ejection. To protect against localised heating in the airflow, the cable eyelet on the hook is shielded by a baffle.

The FFU is divided into three parts: the recovery system, the electronics system and the ACE as presented in Fig. 3. The recovery system consists of a parachute, the FFU hat and a release system for the hat. When the FFU falls past 6 km, a thermal cutter burns through a fishing line, releasing clamps that hold the FFU hat and the parachute is deployed. The electrical system's role is to control the release of the parachute at the correct altitude, operate the localisation system, collecting housekeeping and GPS data, control the ACE and allow communication with the RMU. The localisation system consists of a commercial GPS, a radio beacon and a satellite modem to send out the position of the FFU via both the beacon and the satellite modem.

The ACE is composed of a collection plate gear loaded with aerosol collection samples and the FFU's bottom plate, which has an exposure window in it. The gear is ro-

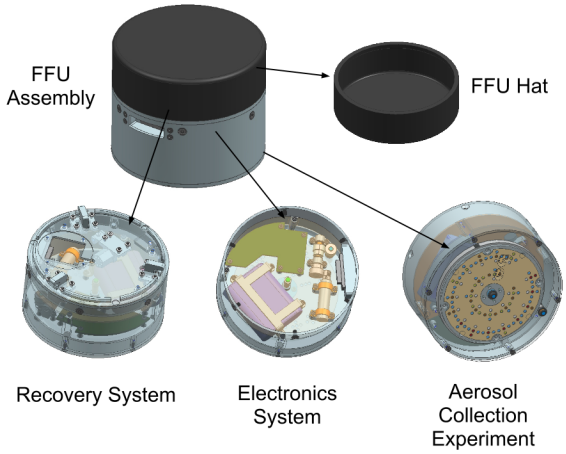

Figure 3. The FFU consists of a recovery system, electronic system and an aerosol collection experiment.

tated past the exposure window, exposing different samples at different altitudes. To prevent contamination of the samples, a seal is created between the collection plate and the FFU base plate by pressing the surfaces coated with teflon coated covered glass fibre against each other with a spring washer. The positioning of the 110 collection samples, each 3 mm in diameter, within the collection plate is presented in Fig. 4. Also shown are the positions of the different types of collection samples used. The first three are different types of standard transmission electron microscopy (TEM) grids: formvar/carbon 400 mesh, ultrathin carbon type-A 400 mesh, and ultrathin carbon film on holey carbon support film 400 mesh. The last two materials are glass fibre and silicone gel. The samples are placed in sample holders containing five samples each. The sample holders can easily be removed and directly put in to a scanning electron microscope (SEM) for analysis. The samples are arranged into six rows and 48 columns as presented in Fig. 4 where row one and six contain control samples and are not exposed to the atmosphere. A more detailed description of the experiment design is available in [13].

3. RESULTS

The RAIN experiment was launched onboard the REXUS-11 sounding rocket from Esrange Space Centre in Kiruna, Sweden at 11:45 (UTC+1) on November 16, 2012. All phases of the flight except for parachute deployment were executed according to the plan presented in Fig. 1 with minor altitude differences. The following section features a reconstruction of the RAIN flight using rocket and FFU sensor data and presents preliminary results from analysis of the ACE. The two flight units are identified as FFU C and FFU E.

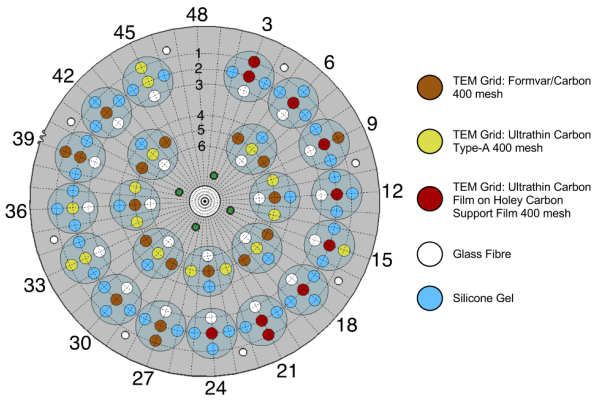

Figure 4. The ACE collection plate gear contains 110 collection samples. Rows 2,3,4 and 5 are directly exposed to the airflow while rows 1 and 6 contain control samples.

3.1. Flight Reconstruction

From the collected raw GPS data that were processed post-flight, the vertical velocity and altitude is presented in Fig. 5. The FFUs were ejected at 57 km and reached an apogee of 78.5 km. The ACEs were activated at apogee and stopped at 22 km. FFU E's parachute was prematurely deployed at 13 km, while FFU C's parachute was prematurely deployed at 10 km. At ejection, the vertical velocity of the FFUs were 630 m/s. The velocity then decreased linearly until the FFUs reached a minimum vertical velocity of -730 m/s before the FFUs underwent maximum braking due to atmospheric drag. After parachute deployment the velocity reduced to 11 m/s.

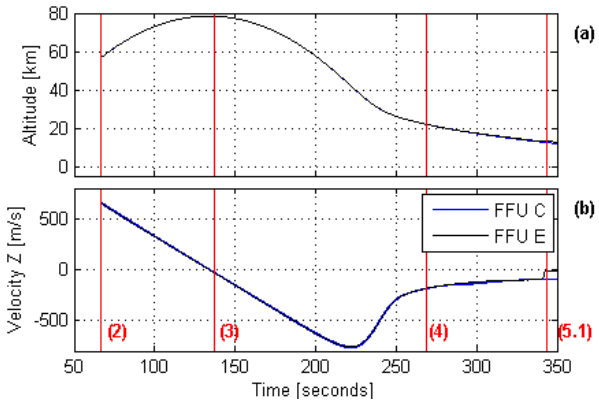

Figure 5. The altitude and velocity in the vertical direction of the two FFUs from ejection, (2), to the premature parachute deployment of FFU E, (5.1). Start of aerosol collection is at (3) and stop of aerosol collection is at (4).

The FFU ejection system operated nominally, however the ejection dynamics between each FFU had slight differences. FFU C was deployed at a speed of 5 m/s, while FFU E was deployed with a velocity magnitude of 6.5 m/s as shown in Fig. 6. In addition, the angle between the FFUs' velocity vectors is not 180° as presented in Fig. 6 and Fig. 7. It is therefore known that the FFUs were not

deployed symmetrically, and that FFU C was deployed slightly later than FFU E. All of these behaviours can be attributed to the ejection constraint cable impeding the ejection of FFU C more than FFU E. The ejection cable is cut next to FFU E's ejection hatch, while the other end of the cable is constrained next to the FFU C ejection hatch. This results in the cable taking a longer time to come free of the rocket cylinder surface on the FFU C side, thereby impeding the ejection of FFU C.

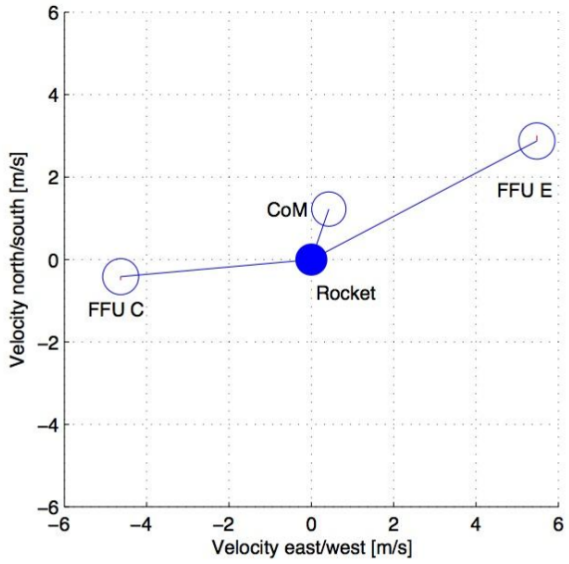

Figure 6. The velocity vectors of the FFUs 1.5 seconds after ejection from the rocket. The centre of mass of the two FFUs and its velocity vector is also shown.

Even though an asymmetric ejection was observed, the ejection system was able to fulfil its two operational requirements of ejecting the two FFUs with a velocity greater than or equal to 5 m/s, and ejecting them so that they fell with their base plates facing towards the Earth. In Fig. 8 it is shown that as the FFUs fell, they precessed for the duration of the ACE, with the FFU base plates facing into the air stream.

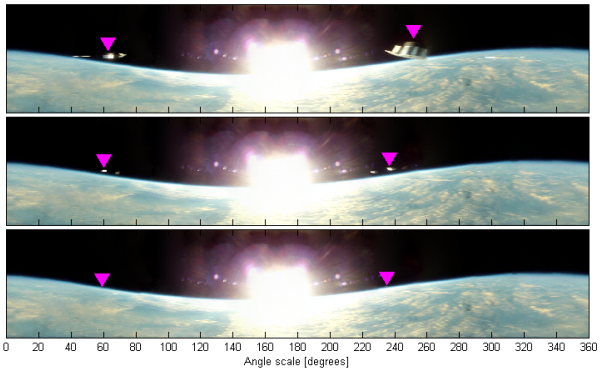

Figure 7. A panoramic view of the two FFUs leaving the rocket during the three rotations of the rocket directly after ejection.

From the vertical axis accelerometer data, presented in Fig. 8 (a), it is possible to see the acceleration increase during the peak braking which indicates that the FFU was falling with its base plate facing towards the Earth. After the aerosol collection stops, the FFU starts to autorotate, and shortly after the hats are ripped off the FFUs and the parachutes are deployed. The angular rate around the vertical axis is presented in Fig. 8 (b) and shows an interesting phenomenon at ejection where the angular rate is reduced from 3.3 Hz to 1.8 Hz for each FFU. From the angular rates of all three axes, presented in Fig. 8(b)-(d), it is observed that the angular momentum is not conserved and therefore an external torque is present during ejection. Even if the angular rate about the vertical axis decreases they are still spinning and stabilised, falling with the bottom plates facing down. The FFUs also start to precess after ejection. From Fig. 8(c)-(d) it is observed that FFU C has a larger precession than FFU E.

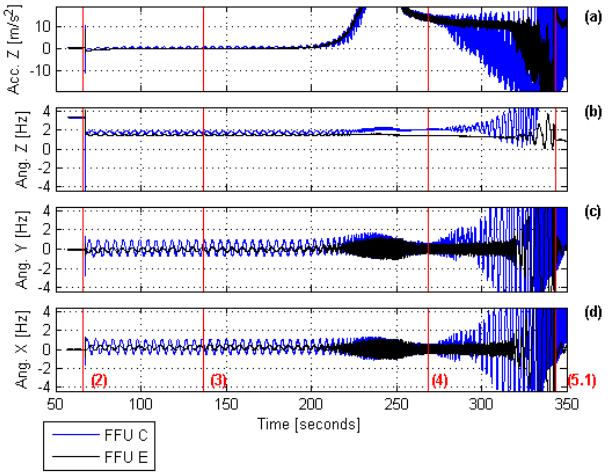

Figure 8. The acceleration in Z-direction and angular rate in all three axes for the two FFUs measured with the internal sensors. The ejection from the rocket is at 67 s marked with (2), the ACE starts at (3) and stops at (4) and the parachute deployment for FFU E occurs at (5.1).

The pressure, temperature, and battery voltage from launch to landing are presented in Fig. 9 (a)-(c). The pressure decreases below the pressure sensors' measurement range approximately 20 s after launch. The pressure then starts to increase exponentially before parachute deployment at (5.1) for the parachute deployment of FFU E. The pressure then increased almost linearly as the FFUs had lower descent speed after the parachute deployment. The temperature inside the FFUs, presented in Fig. 9(b), increases when the FFU goes into vacuum and when the FFU reaches its terminal velocity. After parachute deployment, the temperature decreases to a minimum of -13.3° for FFU C and -19.2° for FFU E. The temperature then increased and did not vary much after landing, (6.2) and (6.1). In Fig. 9 (c) the battery voltage is presented. When the FFUs are in the rocket, the RMU supplies power to the FFUs and after ejection, (2), the FFUs then start to draw power from their internal batteries, indicated by a slight voltage drop. When the the

motor starts and aerosol collection begins, it is possible to see the battery voltages decrease. At 513 s after launch the thermal cutter is activated, which was supposed to deploy the parachute. The clamps are released but the top hat had already been torn off by the turbulent fall earlier. At ∼570 s the FFUs start to send out their GPS positions through the beacons and satellite modems. The dips in the battery voltages are the satellite modems trying to send messages. A strong dependence can be seen between the battery voltage in Fig. 9(c) and the temperature in Fig. 9(b) where the battery voltage decreases when the temperature decreases. The critical voltage level for the FFU batteries is 2.2 V. Throughout the flight and recovery, the FFU batteries were in no risk of reaching this low voltage level.

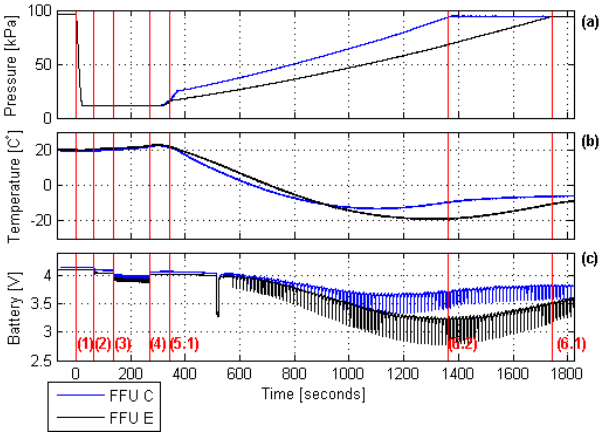

Figure 9. The measured pressure, battery voltage and temperature from launch to landing for FFU E in black and FFU C in blue. The ejection from the rocket is at 67 s at (2), the ACE starts at (3) and stops at (4), the parachute deployment for FFU E occurs at (5.1), landing for FFU E occurs at (6.1) and for FFU C the landing occurs at (6.2).

The localisation system worked and beacon messages were constantly received during the fall from 10 km to 800 m for FFU E and 7.7 km to 900 m for FFU C. Satellite modem messages were received at lower altitudes, and messages were successfully sent from the two landing sites. The FFU E drifted along a 25 km ground track and FFU C drifted along 17 km ground track from where the parachutes were deployed.

3.2. Aerosol Collection

From mapping the position of the aerosol collection plate to the altitude data it can be seen that each FFU exposed its aerosol collection samples to the airflow between 80 and 22 km. Fig. 10 shows the altitude ranges that each aerosol collection sample in FFU C were exposed to. The X axes show the collection plate column number presented in Fig. 4, while the Y axes show altitude. The four plots show exposure altitude ranges for each of the four rows exposed to the airflow. Row one and six were not exposed as they contain control samples.

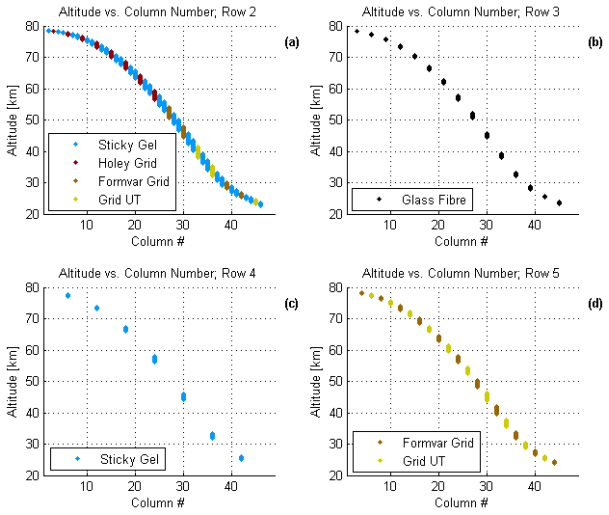

Figure 10. The altitude versus the exposed samples for row 2,3,4 and 5 for FFU C. Rows 1 and 6 are not exposed but contain control samples.

In an effort to prevent contamination the aerosol collection samples were loaded into the FFUs in a clean room. Before flight, the FFUs were cleaned using an ultrasonic bath and then wiped with isopropyl alcohol. The FFUs were stored and transported in sealed containers. After flight, FFU C was unpacked, while FFU E is still sealed and will be opened when analysis of FFU C is completed. Fig. 11 shows images of the FFU C collection plate and collection plate lid in an unpacked state post-flight. It is observed that approximately half of the aerosol collection sample holders became stuck in collection plate lid in Fig. 11 (b). It can also be seen that some of the copper grids stuck to the surface of the collection plate lid as opposed to staying in their collection sample holders. This is seen as an inconvenience when handling the samples given that more care has to be taken when removing the samples and preparing them for SEM and TEM analysis.

Preliminary SEM and X-ray material composition analysis of two silicone gel samples from FFU C is shown in Fig. 12. These two samples were selected because they were exposed at relatively low altitudes and therefore the probability of large particles being present is high. Sample C 239 was exposed over an altitude range between 30 km and 28 km, while sample C 241 was exposed between 29 km and 27 km. In image (b) a 50 μm by 30 μm feldspar particle is shown. In image (c) an unknown particle 40 μm wide and 100 μm particle is shown, however the composition for this particle is unresolved. In image (e) a 100 μm by 1000 μm quartz particle with tendrils is observed. These tendrils are assumed to be from a neighbouring glass fibre sample. Image (f) shows a 4 μm by 2 μm particle impact crater.

These preliminary results show that particles have been collected by at least two of the aerosol collection sam-

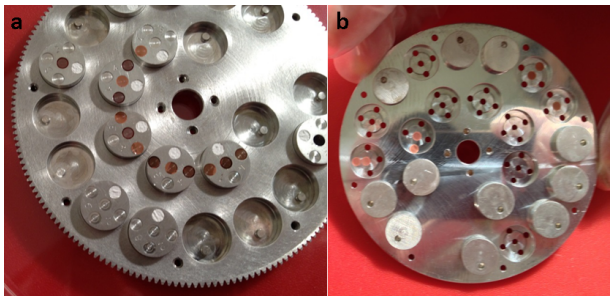

Figure 11. Images of the FFU C's collection plate (a) and collection plate lid (b) after flight. Half of the aerosol collection sample holders became stuck in the collection plate lid (b). In addition, seven TEM grids stuck to the collection plate lid in stead of staying in their collection sample holders. This will result in more complicated handling procedures for these samples.

ples. It is still necessary to determine if contaminants were introduced to the samples by analysing the control samples from rows 1 and 6. If it is shown that minimal contamination occurred then samples from different altitude ranges will be imaged to determine the specific altitude ranges over which particles were collected. Particle composition and concentration will also be investigated.

4. DISCUSSION

The RAIN experiment was successful in that it achieved all of its operational objectives. The premature deployment of the parachutes was the only unplanned event and did not detrimentally affect the performance of the experiment. The aerosol collection plates were exposed to the airflow according to plan, and the samples were exposed over an altitude range between 80 km and 22 km. During the aerosol collection the FFUs' underwent precession, however the base plates were facing the Earth's surface. Initial analysis shows that the FFUs collected aerosols but further analysis is needed to determine if the samples have been contaminated.

The ejection system for the FFUs was also proven to work, though the spin rate was reduced about the vertical axis quite substantially and the cause is yet to be determined. The cause of the asymmetric ejection angle between the FFUs is also being investigated.

The experiment demonstrated a GPS raw data collection technique. The GPS data were processed post-flight to find the ejection velocities and the positions of the FFUs which has been used to map each exposed aerosol collection sample to a height range. This proven GPS collection technique was used more recently with the KTH MUSCAT experiment and will be employed in future experiments run by the Space and Plasma Physics Department at the Royal Institute of Technology (KTH).

Possible experiment improvements include sub-system

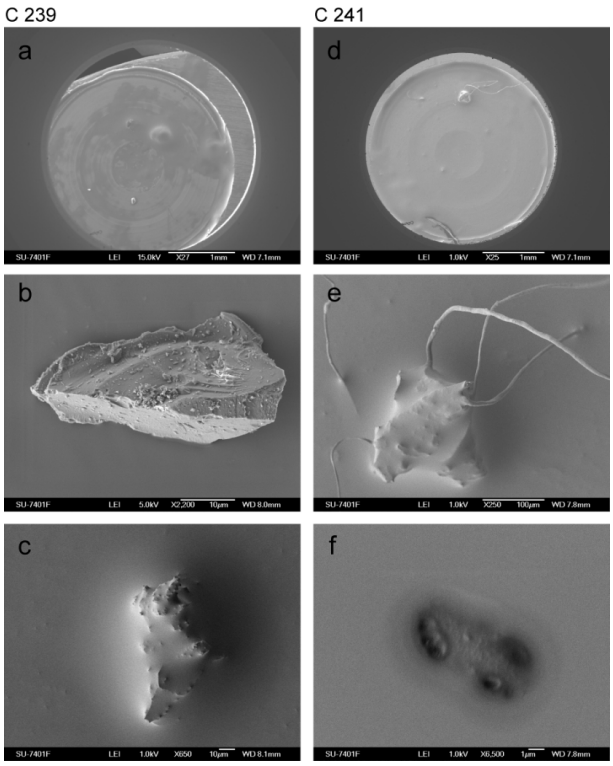

Figure 12. SEM images of two silicone gel samples from FFU C. Images (a) and (d) show overview images of the 3 mm diameter collection samples. Images (b),(c),(e) and (f) show particles or evidence of particles on the order of 10 μm in size.

re-designs within the RMU ejection system, the FFU recovery system and ACE. To perform a more symmetric ejection it is recommended that the ejection system cut the steel constraint cable at the two ends of the cable as opposed to just one. During the flight, the FFUs' recovery system top hats were ripped off while the FFUs were tumbling. To prevent this from happening again the recovery system can be modified so the lip in the interior of the top hat is wider and so the hooks can get a better grip and thus prevent strong loads from ripping off the hat. The ACE could be re-designed to prevent the aerosol collection sample holders from getting stuck in the collection plate lid. To solve this issue the tolerances for sample holder dimensions and the beds in which they sit inside the collection plate should be changed create a looser fit. Another design improvement would be making the aerosol collection sample holders usable in both scanning and transmission electron microscopes so as to prevent manipulation of individual aerosol collection samples. Currently, the design only allows for the collection sample holders to be used in scanning electron microscopy, and if it is desired to use the samples in a transmission electron microscope, then individual collection samples have to be removed from their holders and placed on another type of holder.

ACKNOWLEDGEMENTS

We would like to thank the entire RAIN team for all of the hard work and time they have contributed to this project. Team members include Tobias Kuremyr, Joakim Asplund, Axel Vidmark, Alexandra Oprea, Wenjie Jin, Baktash Samani, Sofhia Josborg, Martin Härberg, Roberto Chiarito, Daniel Brodén, Fredrik Backman, Oussama Chammam, Amer Halilovic, Kristoffer Hultgren, Adrian Ahmadi and Tobias Johansson. Thanks goes to the Swedish National Space Board and the German Aerospace Centre for making the REXUS program possible. The Swedish National Space Board also provided additional financial support to the RAIN experiment. The Swedish Space Corporation, the Mobile Rocket Base (MORABA) and the European Space Agency have been invaluable in their technical support. We would like to thank Kjell Jansson for his assistance with scanning electron microscopy analysis. We would also like to thank Space and Plasma Physics and the Department of Mechanics at KTH and the Stockholm University Meteorological Institute for all of their technical and financial support.

REFERENCES

[1] P. Hamill, E. Jensen, P. Russell, and J. Bauman, "The life cycle of stratospheric aerosol particles," *Bull. Am. Meteorol. Soc.*, vol. 78, pp. 1395–1410, 1997.

[2] R. Turco, O. Toon, R. Whitten, R. Keesee, and D. Hollenbach, "Noctilucent clouds: Simulation studies of their genesis, properties and global influences," *Planet. Space Sci.*, vol. 3, pp. 1147–1181, 1982.

[3] M. E. Summers and D. E. Siskind, "Surface recombination of O and H2 on meteoric dust as a source of mesospheric water vapor," *Geophys. Res. Lett.*, vol. 26, pp. 1837–1840, 1999.

[4] J. Plane, "The role of sodium bicarbonate in the nucleation of noctilucent clouds," *Ann. Geophys.*, vol. 18, pp. 807–814, 2000.

[5] L. Megner, D. Siskind, M. Rapp, and J. Gumbel, "Global and temporal distribution of meteoric smoke: A two-dimensional simulation study," *J. Geophys. Res.*, vol. 113, 2008.

[6] T. Deshler, M. Hervig, D. Hofmann, J. Rosen, and J. Liley, "Thirty years of in situ stratospheric aerosol size distribution measurements from Laramie, Wyoming (41°N), using balloon-borne instruments," *J. Geophys. Res.*, vol. 108(D22), 2003.

[7] H. Jager, "Long-term record of lidar observations of the stratospheric aerosol layer at Garmisch-Partenkirchen," *J. Geophys. Res.*, vol. 110, 2005.

[8] L. Thomason, L. Poole, and C. Randall, "Sticking efficiency of nanoparticles in high-velocity collisions with various target materials.," *Atmos. Chem. Phys.*, vol. 7, pp. 1423–1433, 2007.

[9] K. Pérot, A. Hauchecorne, F. Montmessin, J.-L. Bertaux, L. Blanot, F. Dalaudier, D. Fussen, and E. Kyrölä, "First climatology of polar mesospheric clouds from GOMOS/ENVISAT stellar occultation instrument," *Atmos. Chem. Phys.*, vol. 10, pp. 2723–2735, 2010.

[10] N. Kaifler, G. Baumgarten, J. Fiedler, R. Latteck, F.-J. Lübken, and M. Rapp, "Coincident measurements of PMSE and NLC above ALOMAR (69°N, 16°E) by radar and lidar from 1999–2008," *Atmos. Chem. Phys.*, vol. 11, pp. 1355–1366, 2011.

[11] J. Hedin, J. Gumbel, T. Waldemarsson, and F. Giovane, "The aerodynamics of the MAGIC meteoric smoke sampler," *Advances in Space Res.*, vol. 40, pp. 818–824, 2007.

[12] J. Hedin, J. Gumbel, and M. Rapp, "On the efficiency of rocketborne particle detection in the mesosphere," *Atmos. Chem. Phys.*, vol. 7, pp. 1183–1214, 2007.

[13] W. Reid, P. Achtert, N. Ivchenko, P. Magnusson, T. Kuremyr, V. Shepenkov, and G. Tibert, "A novel rocket-based in-situ collection technique for mesospheric and stratospheric aerosol particles," *Atmospheric Measurement Techniques Discussions*, vol. 5, p. 8161, 2012.

ROCKET-BORNE EXPERIMENT FOR THE MEASUREMENT OF THE VARIATION IN ELECTRIC CONDUCTIVITY WITH ALTITUDE (GEKKO EXPERIMENT - REXUS14)

Zsolt Váradi[(1)], Ottó Botond Lőrinczi[(2)], Gábor Balassa[(3)], Pál Bencze[(4)]

(1) Budapest University of Technology and Economics, Dep. of Broadband Infocom.
18 Egry J. street, 1111 Budapest, Hungary, E-mail: varadi@mht.bme.hu

(2) Budapest University of Technology and Economics, Dep. of Mechatronics
4-6 Bertalan L. street, 1111 Budapest, Hungary, E-mail: lorinczi@mogi.bme.hu

(3) Budapest University of Technology and Economics, Dep. of Theoretical Physics
8 Budafoki street, 1111 Budapest, Hungary, E-mail: emc2@hotmail.hu

(4) Geodetic and Geophysical Institute, RCAES, HAS
6-8 Csatkai Endre street, 9400 Sopron, Hungary, E-mail: bencze.pal@upcmail.hu

ABSTRACT

This paper deals with description of a rocket-borne experiment which is designed to carry out measurement of ion mobility by using Gerdien condensers. The development was made by a university student group at Budapest University of Technology and Economics within the REXUS/BEXUS programme. The physical background including the Gerdien condenser principle and the measurement method is described and technological aspects and feasibility of the experiment are also discussed. The paper provides a brief description of the actual capability of the experiment and a short review of the failure experienced at the flight onboard REXUS14. Further improvements regarding accuracy, reliability are also described.

1. INTRODUCTION

REXUS experiments are flown on spin stabilized sounding rockets, typical apogee of which is at about 90km (Fig.1) [1], [2]. Rockets are launched from ESRANGE Space Center, North Sweden. The REXUS platform allows carrying out measurements in the middle atmosphere. The middle atmosphere is a less known part of the atmosphere because it is hardly accessible by measurements. Thus, the launch site is located at high latitude, in the polar cap where galactic cosmic rays participate in greater degree in ionization of the atmosphere. The polar cap is a special location from the point of view of ionisation processes, taking into account the direct connection partly to the tail of the magnetosphere, partly to the interplanetary space.

The main objectives of the experiment are measurement of atmospheric ion density and composition with altitude and study of the altitude dependence of electric conductivity by recording mobility spectra of positive and negative ions. Required vertical resolution is at least one recorded mobility spectra in every 5 km in the altitude range from 22 km to 75 km.

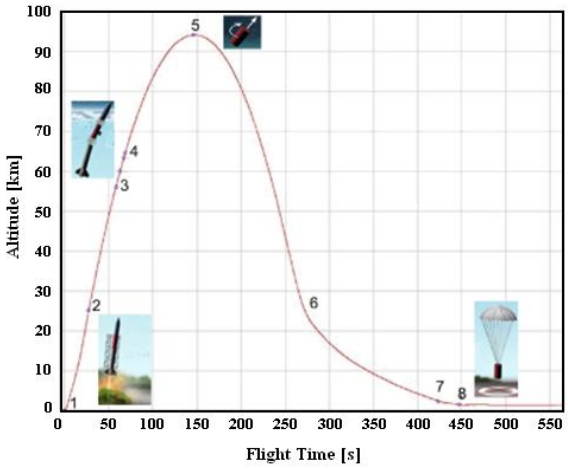

Figure 1. REXUS Flight profile[1]

2. PHYSICAL BACKGROUND

The Gerdien condenser is a cylindrical shaped condenser which has an inner and an outer electrode. A schematic of the equipment is shown in Fig.2.

The condensers are placed on the outer side of the rocket to ensure direct airflow between the two electrodes. Depending on the polarity of the applied bias voltage on the condenser, the positively or negatively charged ions will be deflected towards the inner electrode. When they hit the cathode the generated current is proportional to the ion density and also the mobility of the different ion groups [4]. In order to measure the positive and negative ions at the same time,

Proc. '21st ESA Symposium European Rocket & Balloon Programmes and Related Research',
9–13 June 2013, Thun, Switzerland (ESA SP-721, October 2013)

two Gerdien condensers were placed on the opposite sides of the rocket.

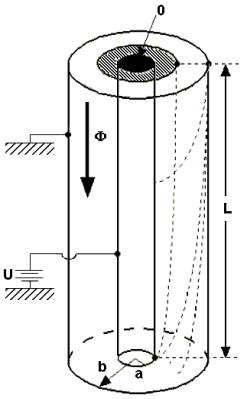

Figure 2. Gerdien condenser, working principle [3]

The requirements for the measuring device include the estimated currents and the bias voltages to be applied in different altitudes. Eq. 1 shows the expression of the measured current.

$$I = \sum_i \frac{2n_i e\pi\mu_i L}{\ln(b/a)} V \tag{1}$$

where e is the elementary charge, n_i is the ith ion density, V is the applied voltage, L is the length of the condenser, b and a are the radius of the outer and the inner electrodes, and μ_i is the mobility of the ith ion.

An ideal voltage-current characteristic for one ion group is shown in Fig. 3.

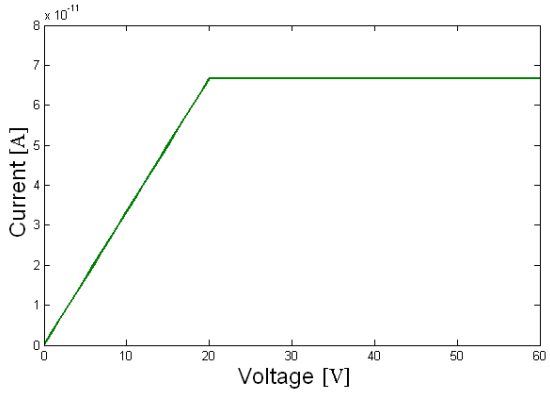

Figure 3. Ideal voltage-current characteristic

Under a critical voltage the current has a linear relationship with the applied voltage and the saturation current is measured when all of the ions from the specific ion group are captured. The slope of the curve is related to the mobility and the saturation current is related to the ion density. Section 5 contains a brief description of the data analysis.

It is known from previous studies that the main ions in the middle atmosphere are the proton hydrates, atomic oxygen, nitrogen, hydrated oxygen molecules, etc. In order to estimate the expected currents, the mobilities of these different ion groups were calculated according to Eq. 2.

$$\mu = \frac{e}{nM\nu_{in}} \tag{2}$$

where M is the molecule weight and ν_{in} is the collision frequency between the ions and the neutral molecules.

The collision frequency is estimated from Eq. 3.

$$\nu_{in} = N_A \sigma_{in} \sqrt{\frac{8k_B T}{m_{in}\pi}} \tag{3}$$

where N_A is the Avogadro number, k_B is the Boltzman constant, T is the temperatures in Kelvin and m_{in} is the effective mass of the ions and the neutral molecules.

The estimated currents are in the range of 10^{-12} to 10^{-9} [A]. In order to calculate the required bias voltages the ideal trajectory of the ions were examined taking into consideration their estimated mobilities. The critical mobility (i.e. the minimum mobility which allows for an ion to be captured at the applied voltage) is calculated from Eq. 4.

$$\mu_c = \frac{(b^2 - a^3)\ln(b/a)\Phi}{2LV} \tag{4}$$

where φ is the speed of the airflow in the condenser (note that it is not equal to the velocity of the rocket).

The required bias voltage can also be expressed from Eq. 4. Taking into consideration the average mobility of the ion groups the applied voltages shall be between 0 and 60 [V].

Another crucial requirement of the measurement is the altitude range where the measurement can be performed. If the mean free paths of the ions are greater than the distance between the inner and the outer electrode, the air cannot be considered as a continuum. Therefore, the defined altitude range of the measurement is between 20 and 85 km.

3. UNCERTAINTIES

Due to the special conditions of the measurement (e.g. supersonic rocket flight, low measured currents) the distortions that may affect the measurement had to be taken into account. These distortions were separated into environmental and measuring device uncertainties. As it is very hard or impossible to examine all of the circumstances that occur during the flight, Monte-Carlo simulations were carried out to determine the uncertainties and also the Likelihood function of the measurement.

The first examined distortion was the photoemission which is significant in the higher altitudes. The second is the ion loss due to the turbulence caused by the supersonic pipe flow [5]. This is a very crucial factor because not only the inner flow in the pipe but the shockwaves can cause such losses as well. The third is the electric field perturbation caused by the separation of the positive and the negative ions in the condenser. The generated electric field is calculated from Eq. 5 by solving the Poisson equation for two ion groups.

$$E(r) = \frac{V_0}{r\ln(b/a)} - \frac{N^+ e}{2\varepsilon_0}\left(r - b^2 - \frac{a^2}{2r\ln(b/a)}\right) \qquad (5)$$

where V_0 is the applied voltage, r is the position, b is the radius of the outer electrode, a is the radius of the inner electrode, e is the elementary charge, and N^+ is the density of the positively charged ions.

For this reason, besides the currents the voltages are measured as well, which also has an uncertainty but it is easier to handle. The distortions of the measurement device are separated into those related to the current measurement and those related to the voltage measurement. Each circuit has a bias error, a temperature drift and the current measurement is corrupted by a stochastic noise as well, following normal distribution. This can be determined by using hypothesis testing. The deterministic noises can be compensated easily after the measurement. The results of the Monte-Carlo simulations showed that the Likelihood function is the probability density function of a normal distribution.

After determining the uncertainty of the measured current it is necessary to determine the uncertainties of all expressed quantities, e.g. mobility, density.

4. DATA EVALUATION

The evaluation consists of five separated steps. The first is to find the breakpoints in the measured characteristics. The second is to express the ion density from Eq. 6.

$$n = \frac{I_{sat}}{vAe} \qquad (6)$$

where A is the aperture of the condenser, I_{sat} is the saturation current, and v is the velocity. The third step is to determine the slope of the assumed ideal characteristic from Eq. 7.

$$G_n = \left.\frac{dI}{dV}\right|_{Vn} - \left.\frac{dI}{dV}\right|_{Vn-1} \qquad (7)$$

where n means the nth breakpoint, and G_n is the slope in the nth breakpoint. From the slope, the mobility was determined from Eq.8.

$$\mu_i = \frac{G_i \ln(b/a)}{2\pi n_i e L} \qquad (8)$$

where μ_i is the ith ion mobility, and n_i is the ith ion density. The last step is to express the uncertainties. As large amount of data was expected, an evaluation algorithm was created to simplify the evaluation process by performing the evaluation steps almost automatically. To demonstrate the data analysis, a simulated measurement is shown in Fig. 4 with one sweep from 0 [V] to 60 [V] and with two ion groups whose parameters are summarized in Tab. 1.

	μ [m^2/Vs]	**n [m^{-3}]**
Ion1	$1.3*10^{-2}$	$7*10^{9}$
Ion2	$6.2*10^{-3}$	$8.8*10^{9}$

Table 1. Simulation parameters

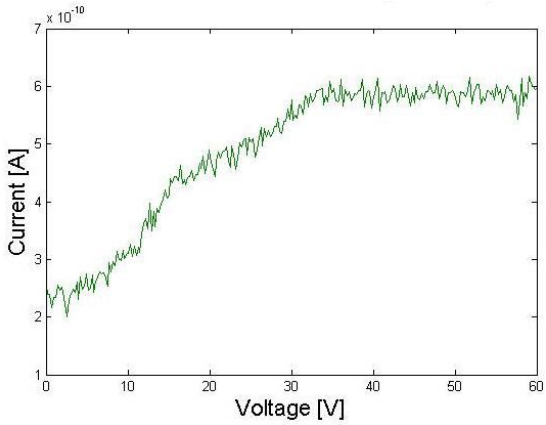

Figure 4. Simulation results, 2 ion present

A simple searching algorithm was used which calculates the first and the second derivatives after smoothing the curve. In the first derivative it searches for decreasing parts and separates them into different intervals. Between these intervals it examines the second derivatives and searches for null transitions. Each null transition means a breakpoint. The results are shown in Tab. 2.

	μ [m^2/Vs]	**Δ μ [m^2/Vs]**	**n [m^{-3}]**	**Δ n [m^{-3}]**
Ion1	$1.32*10^{-2}$	$3.94*10^{-5}$	$6.38*10^{9}$	$6.35*10^{8}$
Ion2	$6.2*10^{-3}$	$3*10^{-4}$	$8.79*10^{9}$	$6*10^{8}$

Table 2. Data evaluation algorithm results

5. SUPERSONIC PIPE FLOW PROPERTIES

It is well known that at supersonic speeds the flow in a pipe behaves very differently than at subsonic speeds. The main difference is that the flow cannot be

considered as an incompressible flow. Therefore, it was of key relevance to determine the temperature and the airflow velocity in the condenser. At supersonic flights the effects of the shockwaves shall be taken into account. This means that some parameters (e.g. temperature, density, flow speed) will have abrupt changes in their values [6]. These changes will happen in a very short length, approximately in few times the mean free path. Eq. 9 shows the rate of the temperature change.

$$\frac{T_2}{T_1} = \frac{[2\gamma M_1^2 - (\gamma - 1)][2 + (\gamma - 1)M_1^2]}{(\gamma + 1)^2 M_1^2} \qquad (9)$$

where M is the Mach number of the undisturbed flow (velocity of the rocket) and γ is the adiabatic coefficient. According to this calculation the air temperature in the condenser can reach about 600°C. Another significant consequence of the shockwaves is that the airflow in the condenser is compressible. This condition is described by the entropy law of thermodynamics.

6. DESIGN

The REXUS experiments are located in separated modules and electronic interface including power and communication lines are provided by the service module (Fig. 5.).

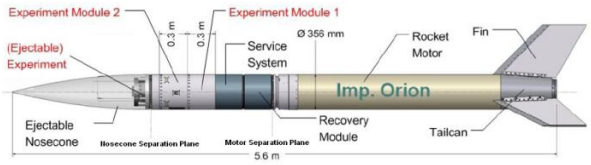

Figure 5. A standard REXUS configuration [2]

The Gekko experiment is located in a 300mm height module of the rocket under the nosecone and consists of two Gerdien condensers mounted on the surface of the rocket and an electronic box placed inside the experiment module (Fig. 6).

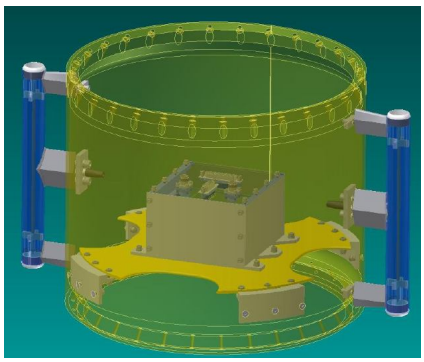

Figure 6. Gekko experiment setup

6.1. Mechanical design

From the aspect of mechanics, the critical issues have been raised by the condensers placed on the skin of the rocket. Since condensers have to withstand high mechanical loads due to vibrations and thermal load from the friction, it is an essential requirement to analyse and simulate the behavior of the condensers during flight.

Once it is proved that the condensers are able to operate safely, another main aspect was the analysis of the airflow inside the condensers. The airflow velocity in the condenser tubes has much influence on the bias voltage to apply, thus the measurement limits and precision are also affected by the airflow velocity simulation.

The only solution for the simulation of structural strength and airflow characteristics was the Finite Element Method simulation. Therefore, several simulations have been carried out to determine the natural frequencies of the condensers and after that to ensure that the strength is sufficient even if resonance is present. Obviously, it is preferable to set the natural frequencies much higher than the expected frequencies during the flight.

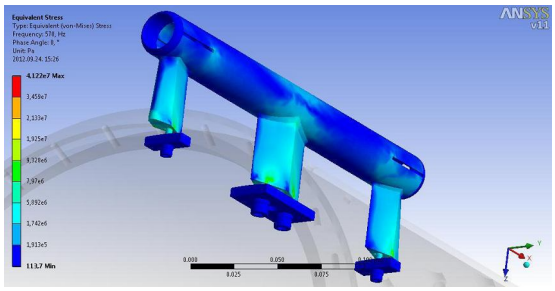

Figure 7. The results of a vibration simulation

The other main point of focus was on the aforementioned airflow analysis. When the condensers pass through the atmosphere, the air at the inlets of the condensers suffers high loads and therefore the airflow velocity drops. According to the simulation results, the velocity of the airflow inside the condensers is approximately 350 - 400 m/s which is much slower than the velocity of the rocket itself (1200 m/s). The bias voltage therefore had to be halved compared to the first plans.

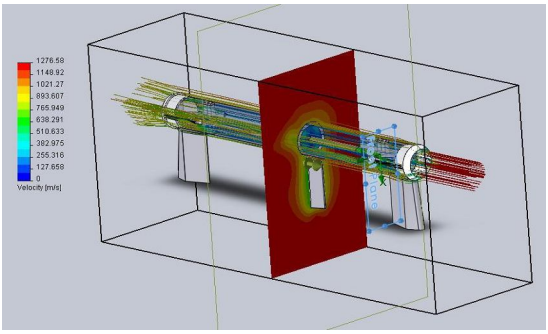

Figure 8. The trajectories of the airflow inside and around the condensers

After the production of the condensers, vibration tests had been carried out on the condensers to get more accurate results than from simulation. However, a wind tunnel test would have been desirable but there was no available supersonic wind tunnel to perform the test.

6.2. Electrical design

The main functions of the Gekko electronics are the current measurement, bias voltage adjustment, measurement control, data acquisition and communication. The electronics are built up on three PCBs: Power Supply Unit, On-Board Data Handler and Amplifier board. The PCBs are connected with a motherboard (Fig. 9).

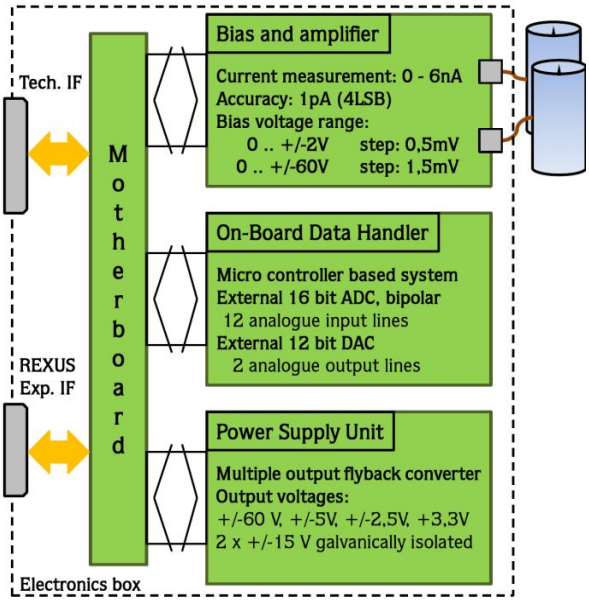

Figure 9. Gekko electronics, block scheme

The current of the central electrodes shall be measured in the range of 1pA to 6nA while the electrodes are biased in the range of 0..60V and 0..-60V. This low level current is measured by a precision amplifier applying compensating current measurement method (Fig. 10).

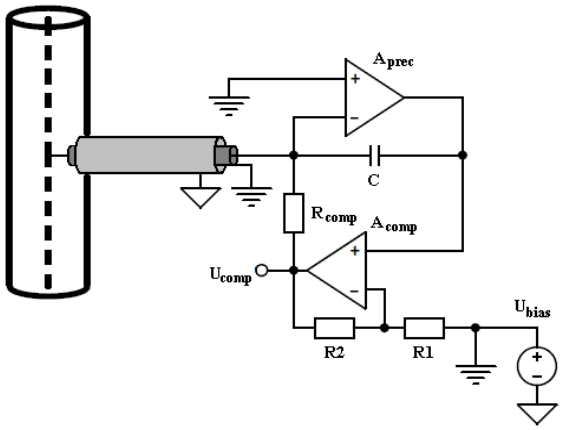

Figure 10. Current measurement method

The condenser is biased by shifting the ground level of the precision amplifier and the compensating amplifier as well. When a balanced state is reached the electrode potential is equal to the bias voltage and its current is compensated through the resistor R_{comp} by the compensating amplifier. The current of the condenser is calculated as follows: $I_{cond} = - U_{comp} / R_{comp}$.

The input bias current of the precision amplifier is compensated too, thus modifying the measurement. To reduce the measurement error the leakage current of the C capacitor and the connection of the electrode, including the PCB trace and the cabling, are also considered. The Gerdien condensers are connected by triaxial cables of which the inner shield layer is connected to the bias voltage generator thus guarding the inner conductor (Fig. 10).

The amplifier was tested with a reference current generator. The transfer characteristics of the two amplifiers are shown on Fig. 11 and 12.

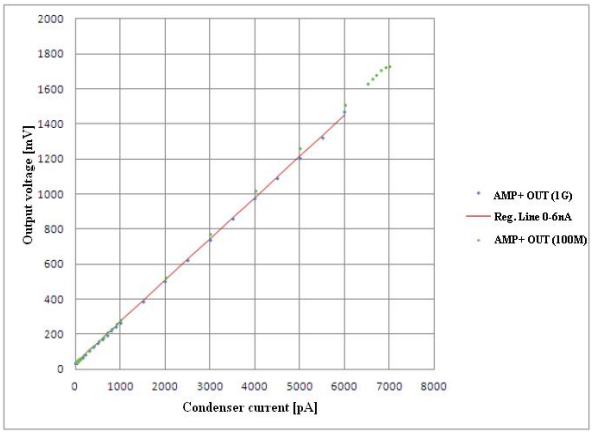

Figure 11. Positive amplifier, transfer characteristic

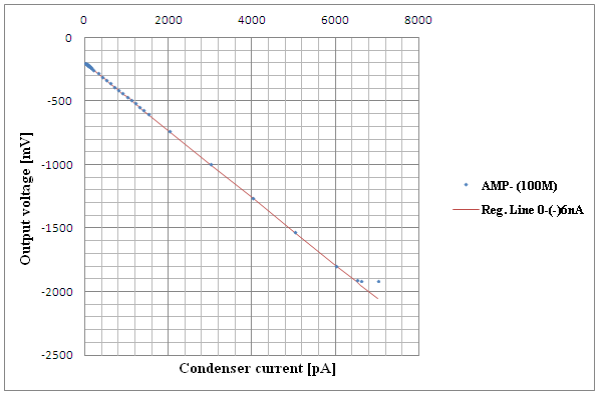

Figure 12. Negative amplifier, transfer characteristic

Fig. 11 and Fig. 12 show the regression line that was fitted to the test points. The transfer parameters of the amplifiers are presented in Tab. 3.

	slope [mV/pA]	offset [mV] (T=20°C)
positive	0,235	36
negative	-0,265	-201

Table 3. Amplifier parameters

Fig. 13 shows the complete electronics box after assembly:

Figure 13. Gekko electronics box, top cover open

7. FLIGHT RESULTS

The Gekko experiment was flown on board REXUS14 on the 7th of May 2013. The experiment was powered at T-600s (before Lift-Off) and the functional test was performed successfully at T-300s. After Lift-Off the communication with the Gekko experiment was lost.

After payload recovery several failures were identified. The ground control system reported overload on the power line of the Gekko experiment at T+1,5s. Due to a short circuit the power consumption of the experiment exceeded 20A and the power protection unit cut off the experiment.

The post flight analysis showed that the short circuit was the consequence of the static acceleration and maybe some resonance. The PSU PCB (Fig.14) bent down to an unexpected extent and some pins touched the box (Fig. 15) thus shorting the BUS 28V to the structure.

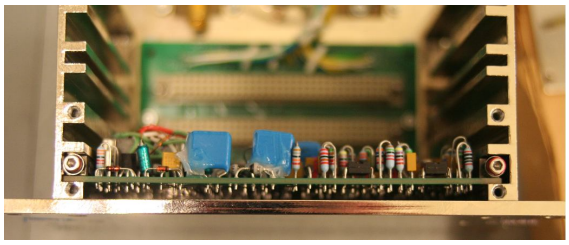

Figure 14. PSU PCB in the electronics box

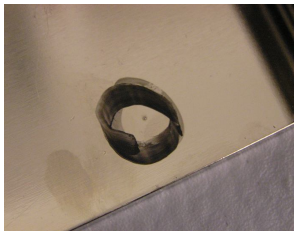

Figure 15. Blackened point in the surface

At the post flight recovery it was found out that the plastic insulation rings of the condensers were melted (Fig. 16) which was probably the consequence of the shock waves. Also the soldering thin in the cable was melted and the airflow carried the melted thin into the module (Fig. 17).

Figure 16. Melted plastic insulation ring

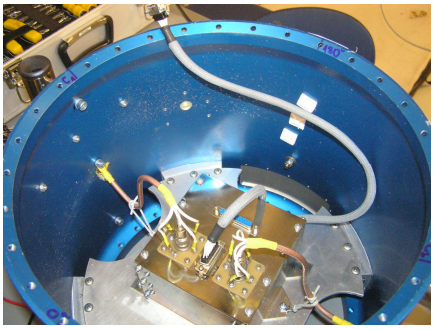

Figure 17. Melted thin on the surface of the module

8. CONCLUSION

Due to the failures presented in section 7 the scientific objectives of the Gekko experiment were not fulfilled. However, the experiment was partly successful as important experiences were gained both during the development and from the flight results. The most probable explanation for the unexpectedly high temperature that the condensers were exposed of are the shock waves. The Gekko experiment also served with important data about pipe flow properties in supersonic flights. Detailed analysis of the video recordings made by the cameras of other REXUS teams during the flight are to be carried out to extend our knowledge about the properties of the pipe flow. After detailed analysis the mechanical design will be reconsidered and the experiment is planned to be flown again to complete the scientific objectives.

9. REFERENCES

1. *REXUS Technical Overview*, www.rexusbexus.net

2. *REXUS User Manual*, Document ID: RX_REF_RX_user_manual v7-7_06Sep12

3. http://n-ion.blogspot.hu/2007/07/measurement-principles.html

4. Hashem Farrokh, Design of a Simple Gerdien Condenser for Ionospheric D-region Charged Particle Density and Mobility Measurement, Scientific report, The Pennsylvania State University, 1975

5. Ion losses in the Gerdien Condenser Intake System, Journal of Applied Meteorology, Volume 7, 456-458, 1968

6. MECH 448: Compressible Fluid Flow, Chapter Five, Normal Shock Waves, Queen's University, Lecture Notes, 2011

APPLICATION OF ROCKET RELATED LUMINOCITY SIGNATURES TO STUDY THE UPPER ATMOSPHERE

S.A. Chernouss[1], Yu.V. Platov[2] and M.V.Uspensky[3]

1. Polar Geophysical Institute of the KSC RAS, 184209, Apatity, Russia, chernouss@pgia.ru Tel. +7 8155579135, Fax +7 8155574339

2. Pushkov Institute of Terrestrial Magnetism, Ionosphere and Radiowave Propagation RAS, 142190 Troitsk, Moscow region, Russia, yplatov@izmiran.ru , Tel.+7 4958510298,Fax +7 495 8510124

3. Finnish Meteorological Institute, P.O. Box 503, FIN-00101, Helsinki, Finland, Mikhail.Uspensky@fmi.fi Tel. +358 505278649, Fax +358 295394603

ABSTRACT

Optical phenomena caused by a rocket exhaust in the upper atmosphere are presented and discussed. The most intense, large-scale and dynamic phenomena are due to special modes of rocket engines' operation. They are a separation of rocket stages and a shutdown of solid-propellant rocket engines. Optical signatures depend on both technical parameters of rocket engines and ph ysical conditions in the upper atmosphere. The archive and current ground based data collected by amateurs and/or by Northern European observatories can be used as indirect active experiments in upper atmosphere studies.

1. INTRODUCTION

Launches of powerful and/or light rockets as well as operating rocket vehicle's engines in the atmosphere are accompanied by an injection of combustion products with its complex composition. These products contain both gas and liquid/solid dispersive components, which develop as the gas-dust cloud(s) with certain geometrical and dynamic features. Such artificial clouds in the upper atmosphere create unusual optical phenomena caused by scattering of sunlight on rocket combustion products, as it was shown in the papers [1-3]. The report shows typical examples of observations and studies of these atmospheric phenomena and allows collecting information on anthropogenic pollution of the near-Earth space and an evolution of the space contamination. The sunlight illuminated space contamination can visualize dynamic processes in the upper atmosphere. A part of such observations were a sub-product of rocket launches from the Plesetsk rocket range and White/Barents sea marine range area. However, due to scanty broadcasting information the "man-made artificial aurora" appeared often unexpectedly for an observer. It has been an obstacle for special observations, although optical phenomena were always under routine low-resolution monitoring by the auroral all-sky cameras from the Northern Scandinavia and the Kola Peninsula during several decades. The optical effects of the rocket engine operating can be seen as tracks left by expanded rocket plumes moving through the sky. The most intense and spectacular bursts of luminosity are due to special modes of the rocket engine's operation, e.g. separations of the rocket stages or shutdown of solid-fuel rocket engines. A number of observations of such effects have been carried out in Northern Russia and they have been published mostly in Russian. Due to this fact, they are hardly available for international scientificfic community. In this short review we discuss the luminosity common features as appearance, visual properties, and physical mechanisms.

2. DATA AND CONDITIONS

The Plesetsk rocket range, which began its operation in 1966, has now performed several thousands rocket launches. One can find many of them in the database of space launches in Russia since 1957 [4], Now the White/Barents Sea in cludes an area, which is the marine rocket range. Optical effects of these launches observed at wide territories A lot of years routine ground-base all-sky cameras, spectrographs and, later, low-light TV and CCD all-sky cameras were used to collect data for these artificial "auroral" phenomena. A number of interesting pictures (a few shown below) have been collected by amateurs.

Proc. '21st ESA Symposium European Rocket & Balloon Programmes and Related Research', 9–13 June 2013, Thun, Switzerland (ESA SP-721, October 2013)

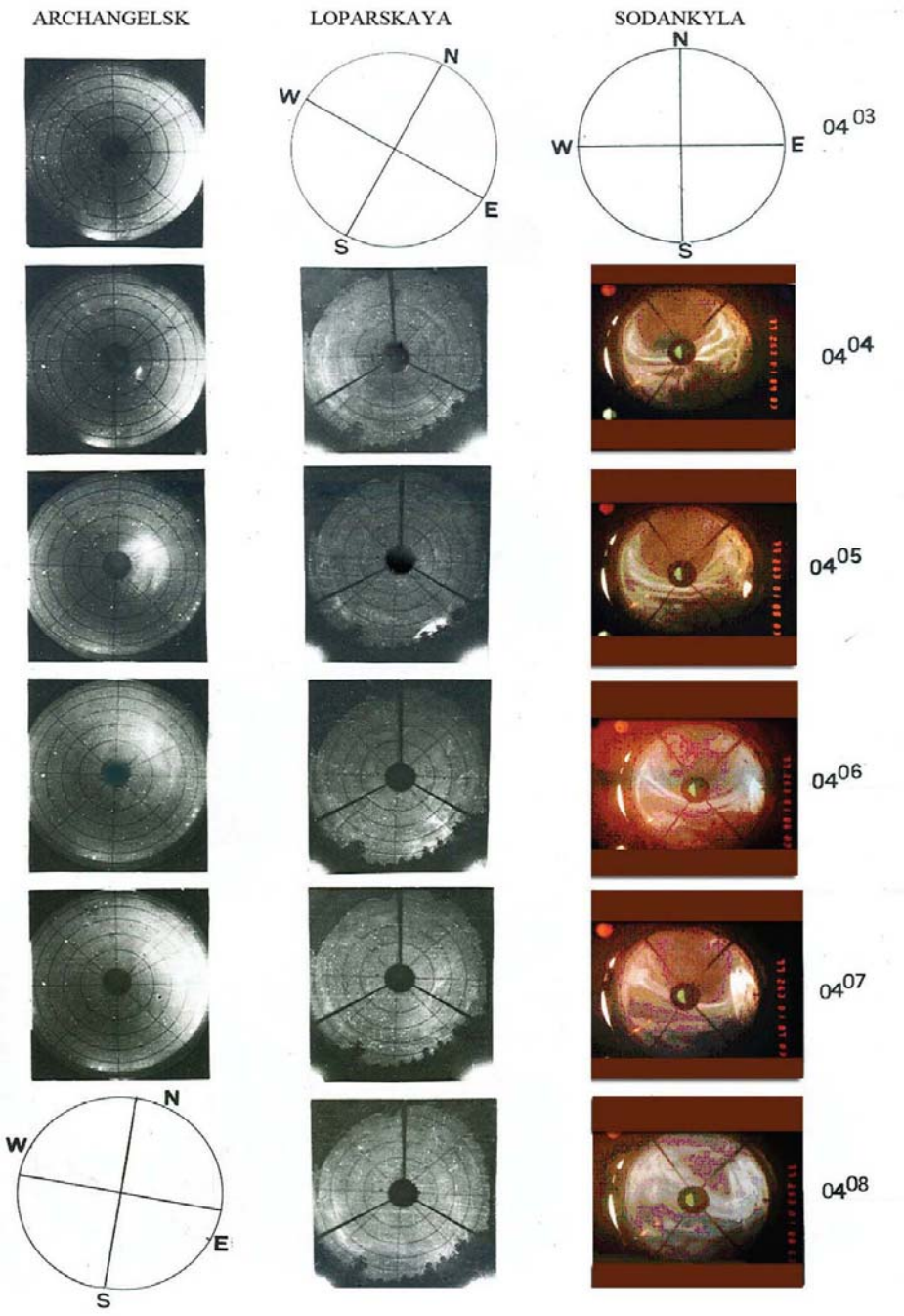

Figure 1. September 20, 1977: Photo series collected by Archangelsk, Loparskaya and Sodankylä all-sky cameras after the Cosmos 955 rocket launch from the Plesetsk rocket range.

3. TWO TYPES OF OPTICAL ROCKET ENGINE'S EFFECTS IN THE ATMOSPHERE

3.1 Liquid propellant rockets

For example so called "Petrozavodsk miracle" was seen simultaneously in the Russian Arkhangelsk region and Karelia, at the Kola Peninsula and Scandinavia. Fig, 1 shows the 1-minute sequence of all-sky photos, where time runs from top to bottom, obtained from Archangelsk (64.54 N, 40.54 E), Loparskaya (68.63 N, 33.20 E) and Sodankylä (67.75 N, 27.00 E). This about 5-min event illustrates the fast development of the artificial luminosity cloud, which in 3D configuration is rather similar to a jellyfish. The all-sky camera in the Archangelsk observatory (left hand side column in Fig. 2) captured the luminosity plume in the second frame at 0104 UT(0404 Moscow Standard Time -MSK) over Archangelsk and its fast development in the next ones. No auroral activity was seen in the Archangelsk all-sky photos. The estimated height of the luminosity cloud was slightly more than 200 km. The Loparskaya all-sky camera (the central column in Fig. 1) resolves a bright burst of glow in the southeastern part of sky at 0405 MSK (0105 UT) and the western cloud edge seen eastward from the local zenith at 0407 MSK. The best images of the luminosity cloud development were observed by the Sodankylä all-sky camera (right hand side column in Fig. 1). Background auroral activity is well seen in the first and second frames, where two auroral arcs aligned from east to west were located near the local zenith. The second frame (similarly to the second frame from Loparskaya) shows a bright spot of glow near the eastern edge of the image. The next frames show development of the event accompanied by rayed structure on outer edges of the expanded luminosity cloud (0408 MSK). Both the background aurora and the exhaust product luminosity evolved independently and were clearly seen by ground based observers, since they took place in the dawn twilight conditions. A peculiar feature of this case was the increased brightness of the dust-gas sunlight scattering, which created the glowing cloud that was visible even from Leningrad (St.-Petersburg) and Estonia at distances around 1000 km and more. The size of this luminous cloud was 100–1000 km at heights of 100–700 km, respectively,

3.2 Solid propellant rockets

As an example, Fig. 2 shows a development of the gas-dust glow at the altitude of 100-130 km [1,2]. Fig. 3 shows a similar gas-dust glow event described by [5] In latter case, the luminous clouds were formed by the gas-dust product of the "Bulava" missile launched from the White Sea marine rocket range.

Figure 2. Distorted track of the rocket flight trajectory as a result of a height-wind structure, Apatity, Russia

Any optical phenomena caused by the rocket exhaust products can be seen by a ground observer mostly in the dusk/dawn twilight. In such a case, the altitude of the Earth's shadow over the observer is not too small, e.g. 80–100 km. After a rocket moves from this shadow to the sunlight, the exhaust products become sunlit. The bright and and the so-called "Norway Spiral" case (Fig. 3) were observed in the dawn twilight conditions. They were just due to the facts that the sky was relatively dark and the exhaust products were sunlit. Even in Norway the dawn twilight was already visible (see Fig. 3 and 7). Due to later local time the eastern sky quadrant over the Kola Peninsula/White Sea was brighter and the exhaust product sunlight scattering was less contrasting and striking or even invisible.

Figure 4 illustrates the possible dynamic and morphological features of the artificial luminosity formations in the upper atmosphere. The Norway Spiral case included two spirals, which are different in scales, colours and the light scattering physics. The first one is blue-green (turquoise) with smaller transverse size. The second spiral is light-grey and larger. More details on the Norway Spiral case can be found in (*Spell,* 2010) and in our comments in the Discussion section below.

Figure 3. An amateurs' photo of the exhaust product glows after the Bulava rocket launch at 0645 UT, in December 09, 2009 (Spell, 2010), Skjervoy, Norway).

4. ACOUSTIC-GRAVITY WAVES

In addition to the optical rocket exhaust effects in the upper atmosphere (Section 3), the rocket launch and the rocket engine operation can create wave-like luminosity structures in the upper atmosphere, which could be observed sometimes by TV instruments [6]. Such wave-glow structures are likely to be a product of acoustic-gravity waves (AGW) caused by a burst-like rocket stage separation. These prolonged wave structures were observed as nightglow during a period of auroral activity, as seen in Fig. 5. The OI 557.7 nm emission takes place at ~ 100 km altitude.

Horizontal wavelength	35-40 km
Propagation (phase) speed	180-240 m/sec
Period	3-4 min
East-West scale	~1500 km
Life-time	~60 min
Wave-crests number	20

This AGW event was, supposedly, due to the Plesetsk rocket launch at 1508 UT in January 10, 1997. The pre-launch information was announced by the Information Telegraph Agency of Russia (ITAR-TASS). At the right time, Lovozero TV camera (67.9°N, 34.6°E) observed the rocket trajectory. At 15:13:20-15:13:30 UT the luminosity plume with a sharp light flash was seen at the latitude of about 60°E as a result of the rocket second stage separation (not shown).

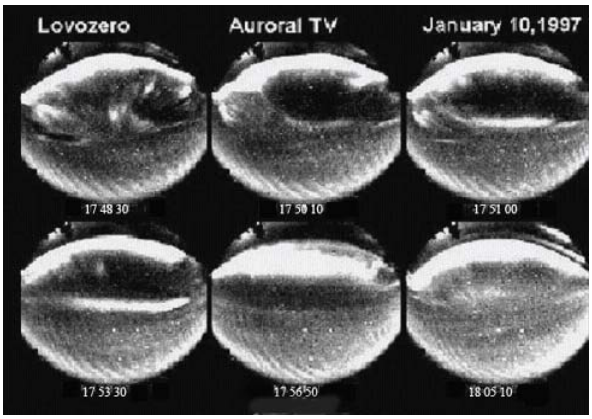

Figure.4. All-sky TV images of the AGW activity observed from Lovozero, the Kola Peninsula. The frame time is running from the left to right and from top to bottom. North is on the top and South is on the bottom of each frame.

Visible nightglow wave structures appeared above the Kola Peninsula at around 1730 UT, i.e. two hours after the mentioned stage separation. The waves persisted about 60 minutes during moderate geomagnetic activity and active auroral forms. These nightglow wave structures were easily distinguished from typical auroral structures due to their temporal stability (Fig. 5). The physical features of the observed AGW are open for future studies.

5. DISCUSSION

5.1 Public relations

We noted already above that the opportunity to see such bright luminosity clouds caused by the exhaust product sunlight scattering can cover huge territories. Their size, singularity and absence of natural analogues have frequently resulted in sensational messages in the mass media about an appearance of an Unidentified Flying Object, UFO [7,8]. For example, so called the "Petro-zavodsk Miracle" was under numerous discussions in Russian, European and US mass-media as a real UFO event. In reality it was a results of a not-quite-successful Russian "Cosmos-955" launch along westward trajectory from the Plesetsk in the early morning of September 20, 1977.

Another sample of mass media reactions on unusual luminosity was due to the "Bulava" rocket launch from the White Sea missile launch corridor in December 9, 2009. This event excited mass media with questions: "What it is: Tesla death ray, energy vortex generated by

EISCAT, heating effects of the Sura facility in Russia, an effect of the heater facility in Tromsø, or the High Frequency Active Auroral Research Program (HAARP) facility in USA or the black hole caused by the CERN collider work?"

5.2 Physical interpretation

Optical effects in the upper atmosphere that accompany the launches of liquid and solid propellant missiles are very similar. Both are physically caused by the sunlight scattering associated with a release of combustion products in the upper atmosphere. [1-3] distinguished two types of sunlight scattering by the rocket exhaust products: a) the sunlight scattering created by dispersed particles, which are mainly larger in size than the sunlight wavelengths and b) molecular sunlight scattering. For example, dispersed particles create clearly visible light-grey concentric spirals in Fig, 3, but molecular scattering forms the internal turquoise spiral cloud along the rocket trajectory. Both the light-grey and the turquoise spiral cloud are a result of a faulty rocket control, which turned out as an uncontrolled rotation of the rocket body along the longitudinal axis.

Bright or moderate luminosities are caused by the solar light scattered by dispersed combustion products, and can appear at any heights where rocket engines or chemical vehicle's boosters operate. Majority of known large-scale optical events were observed at heights above 150 km and were due to the special modes of the rocket engine operation. Enhanced luminosities accompany the shutdown of solid fuel rocket engines when they have brought a payload at a needed trajectory. The sharp dump of pressure in a combustion chamber creates an instant injection of various fuel components and combustion products into the atmosphere. The amount of matter injected by a powerful rocket may reach hundreds of kilograms. The majority of the exhaust products can be in a disperse form due to the incomplete process of combustion. Such artificial clouds may rise up to the heights of over 700 km, the speed of their expansion can be up to 2–3 km/s, and their sizes can exceed 1500 km The expansion speed mainly controls the lifetime of such formations. Such phenomena can appear repeatedly in Russia. They are also well known in USA, e.g. after the Atlantic launches [8].

The enhanced luminosities are due to the remaining fuel after the separation of the most powerful first stage of a launcher and the first stage engine shutdown. Typical features in the development of the luminous configuration are the small speeds of gas-trace expansions due to a moderate diffusion of combustion products (including spreading by the wind); the long gas-trace lifetime (hours) and an increased trace brightness. There are known events where the trace has been seen even in daytime conditions.

The second type of the luminosity cloud development is more complicated. It can happen during the rocket second stage separation when combustion products appear at higher altitudes (above 100 km). It depends on the physical conditions in the atmosphere but also on the amount of exhaust products injected. Physically the luminosity is the sunlight scatter on combustion products inside a quickly expanding cloud. The primary speed of the solid product expansion is about 1–3 km/s and the dispersed products expand nearly freely at the altitudes higher than about 120 km. The brightness of the sunlight scattering dust cloud is not so significant in comparison with the brightness of the molecular resonant sunlight scattering. In the latter process, the long-lived scatter spreads slowly as a result of diffusion processes in the upper atmosphere.

The molecular resonant sunlight scattering is usually caused by the solid propellant engines. Typically the resonant scattering appears after the final dynamic phase of the luminosity cloud development [1-3]. A weak resonant luminosity can be seen for several hours in the area of the rocket's stage shutdown. The effect of the ratio between gaseous and dispersed fuel components in the rocket exhaust is a subject for further studies. The molecular type of the sunlight scattering caused by the solid rocket propellant appears exclusively in the exhausted product interaction with the upper atmosphere. Figures 6 and 7 show events of the molecular resonant sunlight scattering, which has a distinctive turquoise colour. The aluminium monoxide molecules (AlO) in the wake of the rocket trajectory create this resonant scattering [1-3]. AGWs, seen as spatial variations of the nightglow intensity (Section 4), can be revealed also by the partial reflection method used for studying the ionospheric D region [9] found such an opportunity for the Norway Spiral case. The authors studied the interaction of the polar D-region ionosphere with disturbances created by the rocket passage through the ionosphere. They used the Polar Geophysical Institute (PGI) HF partial reflection facility located near the Tumanny, Murmansk region (69.0ºN, 35.7ºE). Figure 8 shows variations of the reflection amplitude and its wavelet spectrum after the "Bulava" rocket launch at 0645 UT, in December 9, 2009. Two minutes after the launch the partial reflection revealed a sharp increase of the partial reflected magnitude and subsequent wave pulsations.

Figure 5. A diffuse trail with a turquoise glow remains after the passage of solid-fuel rockets (Apatity, Kola Peninsula)

Figure 6. The molecular turquoise scatter along the Bulava rocket trajectory as it observed at December 9, 2009 in Norway.

A comparison of the optical and partial reflection data in Fig. 8 shows their similarity, e.g. In the wave structure and duration, but also a discrepancy, e.g. In the wave period and a delay of the wave appearance after the launch. The discrepancies can be due to observations at different altitudes.

5.3 Possibility to use the rocket launch data as indirect active experiments in the atmosphere

All direct active experiments with artificial injections of matter in the atmosphere and subsequent studies of the luminous cloud evolution, as a method, are very similar

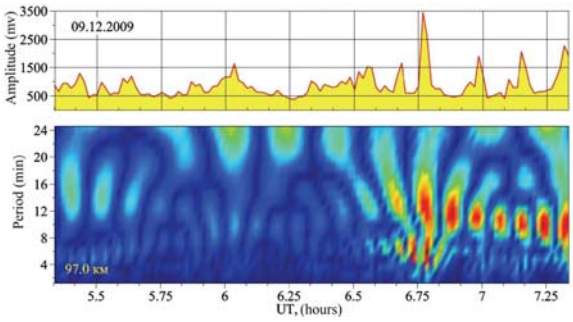

Figure 7. Variations of the amplitude of the partial reflected extraordinary wave and its wavelet spectrum during the "Bulava" rocket launch

to studies of the luminous cloud evolution created by combusted product of any rocket launch. For studies of the upper atmosphere by the exhaust product sunlight scattering it is possible to use existing optical (and other) data of rocket-related phenomena collected in Finland, Sweden and Norway during the past few decades. This topic is open for future studies.

5.3.1 Temperature measurements in the upper atmosphere

Green-blue clouds observed during rocket launches, such as the one in Fig. 5,6 and in blue-green clouds after the artificial trimethyl aluminium release [12] are both products of the aluminium mono-oxide (AlO) molecular sunlight scattering. In the latter experiment, a geophysical rocket delivered an explosive payload canister at a fixed altitude [11,12]. The atmospheric temperature derived from the observed spectrum of the luminous cloud . In case of a solid propellant rocket, the temperature estimates can be done in the form of height-time profile along rocket trajectory, where AlO is situated.

5.3.2 Chemical reactions of exhaust products with components of upper atmosphere

Launches of rockets from Russian rocket ranges and launches in numerous geophysical experiments in USA, Europe and Russia are accompanied by injections of different chemical components, such as NH4Cl04, NOClO4, Al, Mg, Be, LiH, LiClO4 and (AlH3)3 into the upper atmosphere [1,10-12]. The intensity of the spectral lines could be used to estimate of the component evaporation rate. Comparison of spectra for chemical release of known components with the spectra of rocket

exhaust products gives a possibility to estimate the rates of reactions in the atmosphere. The cross sections of the UV excited exhaust product chemistry can be used to estimate the mass of such exhausted chemical components.

5.3.3 Dynamics of luminous formations in the upper atmosphere

The velocity of the neutral wind can be estimated by following spatial dynamics of the luminous clouds. The cloud's configuration observed from several locations allows reconstruction of the spatial structure of the neutral winds. In the case of an artificial burst-like injection, the cloud structure dynamics can be seen around a fixed altitude [11]. The diffusion and sublimation estimates in the combusted product cloud are possible along the rocket trajectory. These ideas for studying the atmospheric winds at 80-110 km altitude were supported by the recent 5 rocket NASA ATREX experiment realized in March 27.2012.[13].

5.3.4 Acoustic-gravity waves (AGW)

The upper atmosphere AGW activity after rocket launches can be efficiently studied by both optical methods and by the method of partial reflection [6,9].

5.3.5 Complex study of exhaust product effects

Optical observations of the sunlight scatter by the rocket combusted products and observations of related radio-physical effects are efficient means to study physics of the upper atmosphere A lot of archived radio-physical, optical and other data are available for special analysis in a number of Northern European observatories (e.g. Loparskaya, Lovozero, Archangelsk, Heiss Island in Russia; Sodankylä, Kevo, Kilpisjärvi in Finland; Andøya, Tromsø, Longyearbuen in Norway and Kiruna in Sweden).

6. SUMMARY

Features of the artificial luminous clouds (e.g. luminosity scales, geometry, colours, dynamic processes and waves) in the upper atmosphere as a result of the sunlight scattering by rocket exhaust products have been concisely described. These features are based on numerous operations of different rockets in the upper atmosphere and observed during a few tens of years in Russia, Finland, Norway and Sweden. Dynamics of luminous clouds connected with the exhaust product interaction with components of the upper atmosphere can be efficiently used as a method of active experiments in near-Earth space. These studies are relatively cheap, since they do not include the huge expenditures related with a rocket launch.

6. REFERENCES

1. S.A. Chernouss, Yu.V. Platov, V.V. Alpatov and M.V.Uspensky. *Geophysica* (2012), 48(1–2), 65–79

2. Platov, Yu.V., S.A. Chernouss, V.V.Alpatov and A.S. Kirilov, 2011. *Óptica pura aplicada,* DIC; **44** (4), pp.713–717.

3. Chernouss, S.A. and Yu.V. Platov, 2010. Optical features of rocket launches in Arctic atmosphere. *Proceedings of the Polar Geophysical Institute*, Murmansk-Apatity, pp. 97–100 (in Russian).

4. Database on cosmic object launches since 1957 .*http://www.zabor.com/launch*/1999–2012.

5. Spell, T., 2010. Estimation of the location, trajectory, size and altitude of the "Norway Spiral" phenomenon *(http://www.spellconsulting.com/reality/Norway_Spiral.html).*

6. Chernouss, S., A. Yahnin and A. Roldugin, 2002. Optical observations of the acoustic-gravity waves (AGW) supposedly initiated by rocket launches. In *Physics of Auroral Phenomena, Proceeding. of 25th Annual seminar*, Apatity, pp. 95–98.

7. Platov, Ju.V. and V.V. Rubtsov, 1991. *UFO and Contemporary Science*. Nauka, Moscow, pp. 123–136 (in Russian).

8. Olmos, V.-Y.B. 1995, *Exedientes insolitos. El fenomeno ovni y los archivos de Defencea. Collection Espania Hoy*. 38. Madrid, 288 p. (in Spanish).

9. V.D Tereschenko, N.M. Chernyakov and V.A. Tereschenko, 2010. Wave disturbances during launches of light rockets in the low polar ionosphere. *Proceedings of the PolarGeophysical Institute*, Murmansk-Apatity, pp.125–127 (in Russian).

10. Feodosiev, V.I., 1981. *Basic foundations of the rocket flight technique)*. Nauka. Moscow, 494 p.(in Russian).

11. Andreeva, L.A., O. Klyuev, Yu Portnyagin and A.A. Hananyan, 1991. *Investigation of Processes in the upper atmosphere using artificial clouds*. Ed. Portnya gin, Monography. "Typhoon", Institute of the Experimental Meteorology. Leningrad, Gidrometeoizdat, 174 p. (in Russian).

12. *Uppsala report*. The chemistry of artificial clouds in the upper atmosphere and their response to winds and fields. **17**, part B. Stockholm, 1971.72 p.

13. http://www.nasa.gov/mission_pages/sunearth/missions/atrex.html

THE ROLE OF WAKE EFFECTS IN EXPERIMENTS BY SOUNDING ROCKETS AND OTHER SPACECRAFTS

W. J. Miloch

Department of Physics, University of Oslo, Box 1048 Blindern, N-0316 Oslo, Norway
e-mail: w.j.miloch@fys.uio.no

ABSTRACT

A relative movement of a rocket or another spacecraft and plasma can give rise to wakes in the potential and density distributions. Wake effects can modify the plasma parameters locally, and thus should be taken into account when interpreting the in-situ data. In this paper, several aspects of the wake formation are presented, such as electrostatic lensing and plasma absorption. The wake formation in various plasma environments, including multispecies plasmas, as well as wake effects on the plasma measurements are discussed. Wake effects are demonstrated with the results from Particle-In-Cell simulations of a finite-sized object in flowing plasma, with the object being charged self-consistently by plasma and other currents.

Key words: wake; plasma; rocket; spacecraft, simulations.

1. INTRODUCTION

A sheath will form around any object immersed in plasma [1, 2]. Due to high mobility of electrons, an isolated object in plasma will be usually charged negatively, and it will acquire negative potential with respect to the surrounding plasma, a so-called floating potential. At floating potential the net current to the object's surface equals zero, a part of electrons will be repelled, while positive ions will be accelerated towards the object. Thus, in the sheath, the quasineutrality of the plasma will be broken locally, and also the velocity distributions will be modified, with ions being accelerated towards the object surface to fulfill the Bohm criterion [2]. In stationary plasmas, the sheath around a spherical object will be spherically symmetric, and the characteristic shielding length at which the plasma becomes quasi-neutral again is of the order of the total Debye length λ_D, with $\lambda_D^{-1} = \sum \lambda_{D,\alpha}^{-1}$, where the sum is over all plasma species α and $\lambda_{D,\alpha} = \sqrt{\epsilon k_0 T_\alpha / n_\alpha q_\alpha^2}$.

The symmetry of the charging process will be broken when an object is moving with respect to plasma. This will be the case for ionospheric plasma experiments by sounding rockets as well as for in-situ measurements of space plasmas: the relative movement of a spacecraft and plasma leads to the formation of wake in the plasma density and potential [1, 3]. The plasma parameters in the wake can be significantly modified, which can have important implications on the results of experiments. In particular, measurements by instruments mounted on extended booms can be strongly influenced by the wake effects [4]. Thus, a good insight into the wake formation behind a spacecraft under different conditions in ionospheric and space plasmas is essential for data acquisition and interpretation.

It is challenging to study wake effects experimentally, when specific plasma conditions need to be reconstructed in the laboratory [5]. Due to complexity and nonlinearity of the problem, it is often difficult to address the problem with analytical calculations; thus such an approach is often restricted to linearized models [6, 7]. However, wake effects behind objects in flowing plasmas can be successfully studied in detail by numerical simulations. Such simulations can be carried out with for instance Particle-In-Cell (PIC) methods, in which the dynamics of a large number of simulated plasma particles are followed in self-consistent force fields [8]. The PIC method has an advantage with respect to other numerical methods that, by employing a grid for the calculation of the force fields, it can simulate a large number (millions) of plasma particles at a reasonably low computational cost. With the PIC method, the plasma particle trajectories are followed in self-consistent fields, and the smallest kinetic scales can be resolved. In the PIC simulation, at each time step, the plasma charge density is built on the grid by weighting individual particles to the nearest grid points. After solving the field equations, the fields are interpolated from the grid points to plasma particles. The particle trajectories are finally advanced in velocity-position phase space, usually with the fast, low-order *leap-frog* method [8, 9].

In this paper we discuss different aspects of wake formation and illustrate them with recent results from simulations of an object in flowing plasmas. The large-scale simulations are carried out on a super-computer with two- and three-dimensial PIC codes *DiP2D* and *DiP3D*, in which the self-consistently charged spacecraft forms internal boundary conditions for the dynamics of plasma

Proc. '21st ESA Symposium European Rocket & Balloon Programmes and Related Research', 9–13 June 2013, Thun, Switzerland (ESA SP-721, October 2013)

electrons and ions [10, 11]. We study the formation of wakes in supersonic plasma flows, and demonstrate several wake phenomena, such as plasma depletion or ion focusing, that will be important in the ionosphere. The role of magnetic fields or multispecies plasmas are also considered. The results are discussed in the context of data acquisition and interpretation. For generalization of the problem, we consider here a spherical, finite-sized object. Note that the main physical processes will be present also for other geometries.

2. WAKE EFFECTS

An object in flowing plasma will usually be charged negatively, and when only plasma currents are present, its floating potential can be often well approximated with the orbit-motion-limited (OML) approach [1, 11]. With other currents present, such as photoemission, the object can also be charged positively. In flowing plasmas, the charging currents are anisotropic, and an electric dipole moment can form on an insulating object. Since the effective screening length changes with the flow, becoming λ_{De} for supersonic flows [11], we use λ_{De} to normalize the lengths in the following.

2.1. Ion focusing

A negatively charged, finite-sized object in flowing plasmas will act as an electrostatic lens for plasma particles. While electrons are usually so mobile that they are only little affected by the wake, the electric field in the vicinity of an object can deflect ions into the wake. Electrostatic lensing of ions, also known as ion focusing, can lead to a locally enhanced potential in the wake [11]. This in turn gives rise to the wake pattern with subsequent potential maxima and minima. Note, that such a wake pattern is also observed for a point-like particle and is often described as the sound radiation pattern from a moving object [6, 7]. An example of ion focusing and the corresponding potential distribution are shown in Fig. 1.

Electrostatic lensing is more pronounced for cold ions, i.e., for large electron to ion temperature ratios [10]. It also changes with the flow speed, being more extended for faster flows. Material properties are also important: for insulating objects, most of the negative charge will be localized at the rear of the object, thus giving rise to stronger ion focusing. This effect is weaker for conducting objects, for which the charge on the object surface will be redistributed as to cancel internal electric fields.

2.2. Plasma absorption

Another important effect is the plasma absorption by a finite-sized object. Since a spacecraft usually moves supersonically, a substantial ion wake can form behind it.

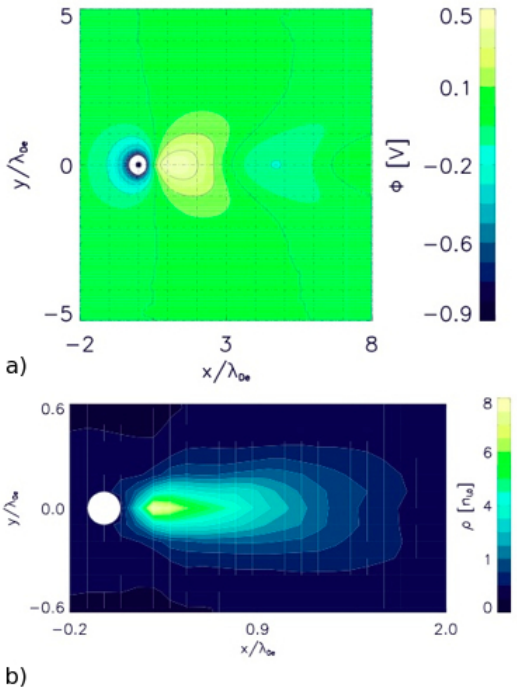

Figure 1. Example of the potential distribution in the wake (a) and the corresponding charge density with ion focusing. The electron to ion temperature ratio is $T_e/T_i = 100$, the plasma flow speed is $v_d = 1C_s$, where C_s is the speed of sound. The flow is in the positive x direction, as in all other figures. The distance is normalized to the electron Debye length λ_{De}. The results are from the DiP3D code.

Thermal velocity of electrons is often larger than the relative speed, and thus electrons can get far into the ion wake. However, ambipolar electric fields due to ion wake will arrest the electrons, forming a region, in which there is a substantial depletion in the plasma density. An example of the wake due to plasma absorption is shown in Fig. 2(a), which shows results corresponding to the object of the size of a Cubesat orbiting at 300 km altitude. Since the flow is supersonic (ca. 6.5 Mach), heavy oxygen ions give rise to a density depletion extending up to several λ_{De}. Electrons closely follow ions, and can be considered as Boltzman distributed, to a good approximation.

The results presented in Fig. 2(a) do not consider magnetic field, which through the Lorentz force can control the dynamics of plasma particles. The results of simulations with included magnetic field are given in Fig. 2(b). Here we have chosen a simple configuration where the magnetic field is parallel to the flow. Such a situation can be realized for instance for a satellite in the low-lattitude Earth ionosphere. A remarkable difference from the previous results is that, while ions remain effectively unmagnetized, electrons are strongly affected by the presence of the magnetic field. Since the electrons move faster than the object, their wake is "mirrored" upstream in the ram direction. Thus, the effects of the wake in heavy ions

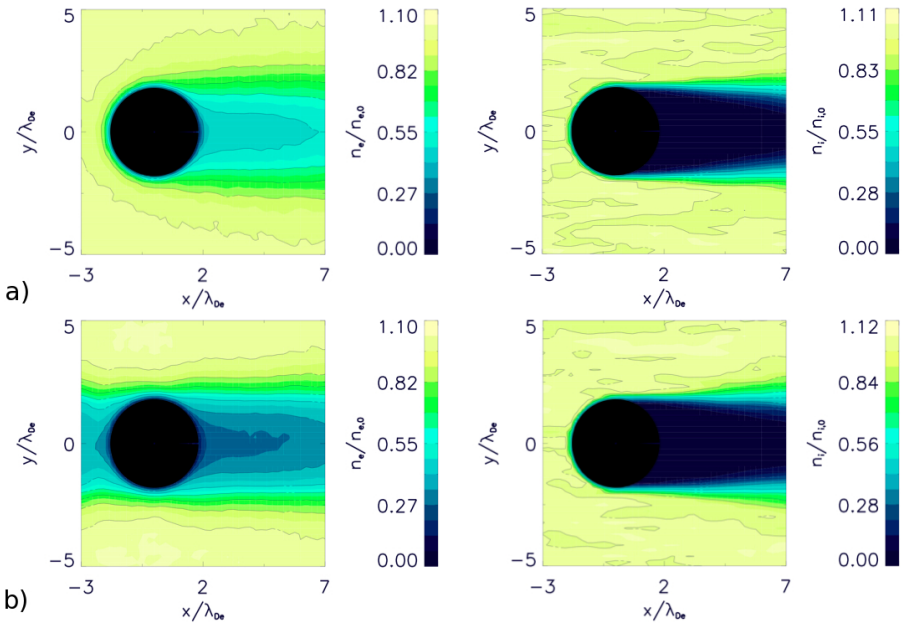

Figure 2. Normalized electron (left) and oxygen ion (right) densities for an object of a size of the Cubesat orbiting at 300 km altitude in the Earth ionosphere. Plasma parameters: $T_e = 0.13eV$, $T_e/T_i = 2$, $n = 10^{10}\mathrm{m}^{-3}$, $v_d = 6.5C_s$. (a) - results without magnetic field, (b) results with magnetic field ($B = 0.4$ Gauss) included parallel to the flow. Results are normalized to the undisturbed plasma densities. Simulations were carried out with the DiP3D code.

can be observed both downstream and upstream from the spacecraft. This can have important implications on the localization of instruments on board the spacecraft for reliable measurements. However, more studies are needed to investigate these effects in detail and asses their importance, also for different orientations of the magnetic field.

2.3. Spinning object

For stability purposes, a spacecraft, such as a sounding rocket, often spins around its axis. The spin can give rise to a modulation of the wake, while at the same time an instrument on extended booms can point into or away from the wake [4, 12].

Such a situation is demonstrated in Fig. 3, in which a potential around a spinning, insulating spacecraft moving supersonically with respect the surrounding plasma is shown at different time instances [12]. The spacecraft is being charged by plasma currents and also by photoemission current due to unidirectional photons. The potential in the vicinity of the spacecraft is modulated with the spin. Since the electric dipole moment develops on the object surface, this effect is more pronounced than it would be on a corresponding conducting object.

An important feature is that the probes measuring the potential at four different points as indicated in Fig. 3(a) will give signal modulated in time by the spin period. This effect will be most pronounced for the probe positioned in the wake. Note that often it might not be sufficient just to filter the spin frequency and its harmonics from the data, as one might also need to consider that the wake can also change with the spinning rocket.

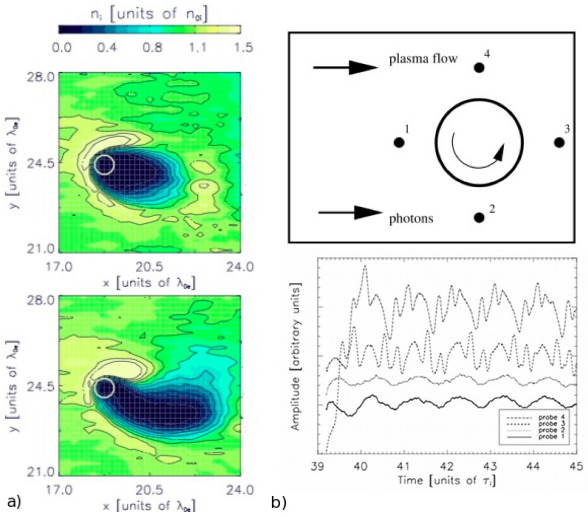

Figure 3. (a) Normalized ion density in the wake of a spinning, insulating object being charged by plasma and photoemission currents. (b) Position of the four probes, and the corresponding potential as a function of time in units of the ion plasma period τ_i. The results are from the DiP2D code [12].

2.4. Multispecies plasmas

Multispecies plasmas can be present in planetary ionospheres and magnetospheres. Such plasmas can give rise to a complex wake structure, including also separation in the plasma species in the wake. An example shown in Fig. 4 refers to the Cassini spacecraft at Saturn orbit insertion [13]. In the vicinity of the moon Enceladus, the water group ions are present, constituting the heavy ion component of the plasma. Due to the relative motion of the spacecraft and plasma, a wake forms in which there may be a clear separation of the ion species: the relatively light protons contribute to the ion focus, while heavy water-group ions give rise to the geometrical wake. Thus, two distinct wake effects can be present at the same time, which might lead to uncertainties in plasma measurements.

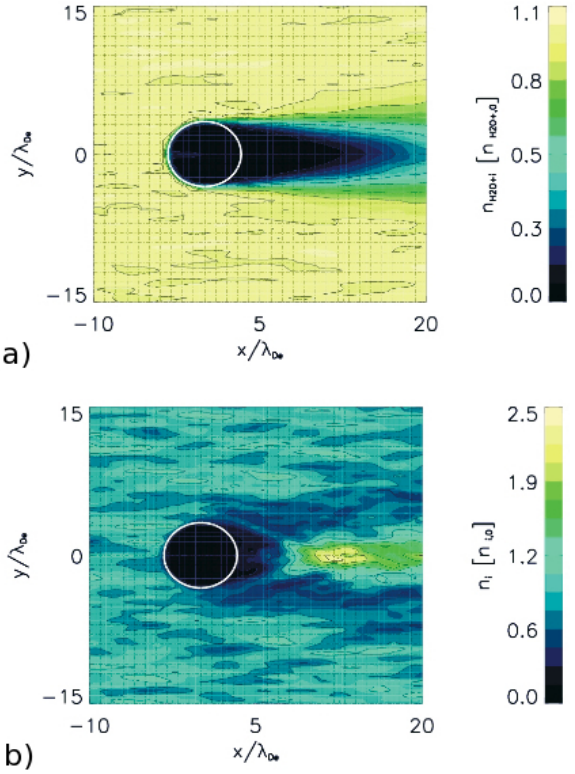

Figure 4. Wakes in the multispecies plasmas corresponding to Cassini environment [13]. (a) Wake in the water group ions demonstrating a geometrical wake due to absorption of heavy ions. (b) Wake in the proton density, showing pronounced ion focus due to electrostatic lensing. Results are from DiP3D code [13].

3. SUMMARY AND CONCLUSIONS

We have addressed a few aspects of the wake formation behind a spacecraft in flowing plasmas and illustrated them with results from numerical simulations. A spacecraft will usually be negative, but if photoemission is strong, it can also become positive, in particular in tenuous plasmas [13]. Negatively charged spacecraft will absorb incoming ions, but also electrostatically bend trajectories of ions. This can result in a non-trivial wake pattern with either plasma depletion or ion focusing downstream from the spacecraft.

Wake effects should be accounted for when interpreting the results of measurements. The plasma absorption and electrostatic lensing will be the main effects to be considered. The latter will be less pronounced for hot or mobile ions. In addition, the formation of a Mach-like cone structure in both density and potential can be observed. Spinning object can lead to pulsating wakes, while multispecies plasmas can give rise to the separation of plasma species in the wake.

The wake effects considered here relate to collisionless plasmas and quiet plasma conditions. Collisions with neutral background may significantly modify the wake pattern. On the other hand, space and ionospheric plasmas are often characterized by instabilities and turbulence, which can further complicate the problem. Thus, wakes in turbulent, magnetized, and collisional plasmas need to be investigated in detial to gain better insight into experimental conditions.

REFERENCES

[1] Whipple E.C., 1981, Rep. Prog. Phys. 44, 1197

[2] Schott L., 1968, Electrical probes Plasma Diagnostics ed W Lochte-Holtgreven, Amsterdam: North Holland

[3] Miloch W.J., 2010, Plasma Phys. Controlled Fusion 52, 124004

[4] Lai S.T., et al., 1986, J. Geophys. Res. 91, 12137

[5] Svenes K.R., Trøim J., 1994, Planet. Space Sci. 42, 81

[6] Ishihara O., 2007, J. Phys. D: Appl. Phys. 40, R12147

[7] Lampe M., et al., 2005, IEEE Trans. Plasma Sci. 33, 57

[8] Birdsall C.K., Langdon A.B., 1991, Plasma Physics via Computer Simulation, Bristol: Adam Hilger

[9] Verboncoeur, J.P., 2005, Plasma Phys. Controlled Fusion 47, A231

[10] Miloch W.J., et al., 2008, Phys. Rev. E 77, 056408

[11] Miloch W.J., Block D., 2012, Phys. Plasmas 19, 123703

[12] Miloch W.J., Vladimirov S.V., 2009, Geophys. Res. Lett 36, L18110

[13] Yaroshenko, V.V., et al., 2011, J. Geophys. Res., 116, A12218

Space-Related Education

Chairs: N. Callens, A. Stamminger & E. Zumbrunnen

BUILDING RESEARCH COMPETENCES IN SECONDARY SCHOOL STUDENTS THROUGH HANDS-ON EARTH AND SPACE SCIENCE EDUCATION PROJECTS

Erik de Schrijver

Sint-Pieterscollege Jette, L. Theodorstraat 167, 1090 Brussels, Belgium,
eds@sint-pieterscollege.be,+32 486 787063

ABSTRACT

Recent reforms of secondary education in Flanders have given schools time but also mandate to work on making youngsters (more) competent researchers, whatever their field of study. Schools are free to choose the way in which they achieve the objectives in the 'research competences' guidelines of the Ministry of Education.

In Flanders, the STEM-oriented options in general secondary education are Sciences-Mathematics, Modern Languages-Sciences, Latin-Sciences, Greek-Sciences and Economics-Sciences. All but the last option are offered at Sint-Pieterscollege Jette.

In this paper, the endeavours of students in the Sciences-Mathematics branch will be treated as a case study. As it is preferable that the students choose the field in which to carry out their scientific research project, a number of possibilities is offered to help them guide their selection process.

1. RESEARCH COMPETENCES

Succesfull action in education is achieved through a clear definition of concepts and goals, then going through the normal PDCA quality improvement cycle. For the formation of competent researchers, the different steps in a succesfull research project need to be known by the students involved. This is taught to them, not ex cathedra, but by submitting them to the entire process of setting up a full fledged science project in their 6th and final grade. Full fledged meaning the different steps of the process are covered in order by the students:

- Identify a scientific field/subject of interest
- Reconnoiter the subject
- Formulate a research question
- Define the work to be done
- Make a plan/timetable
- Execute the plan (collect data)
- Process data/draw conclusions
- Report on the project
- Evaluate the process and the product

Succesfully covering these topics implies the students acquire a number of 'competences' that can be divided into three main categories: knowledge, skills and attitudes.

1.1 Knowledge

Before being able to implement the different steps of a succesfull research project, the students must be familiar with them, so knowledge of the nine steps mentioned above is mandatory. This is not enough however, as the students must also know how to recognize a poor from a good research question. They should also know what research methods exist and what their respective strenghts and weaknesses are.

1.2 Skills

Knowing how to recognize a good research question is one thing, being able to formulate one is another. Besides this, students should also be able to choose appropriate reasearch methods, to draw realistic plans and to present results in a clear and concise manner. Evaluating ones own work in a sceptical, objective manner is the final skill that allows the student to learn from experience and hence grow towards ever greater proficiency.

1.3 Attitudes

Knowledge can be acquired through work, skills through practice. Attitudes are another matter: inborn for some, acquired only through conscient effort by others, they are nonetheless a vital hallmark of the productive researcher.

Students working on their research competences should have a hang for accuracy while bearing in mind what accuracy is required to adress the research question one is working on.

A researcher should be open to the unexpected: breakthroughs or new insights are gained quite often through unexpected and/or surprising results. These should therefore also be reported accurately.

As scientific research is most often teamwork, the researcher should be respectful of other people, their work and their methods.

Proc. '21st ESA Symposium European Rocket & Balloon Programmes and Related Research',
9–13 June 2013, Thun, Switzerland (ESA SP-721, October 2013)

2. IMPLEMENTATION

At Sint-Pieterscollege building research competences is implemented through a number of initiatives. First, all students (whatever their field of study) are working with a manual called 'My Masterplan 16+' which is to help them organize their study by teaching them how to learn (as opposed to teaching them what to learn, which is part of each teacher's job).

While working on research competences is something schools should work on in the 6th and final grade, at Sint-Pieterscollege a preparatory hands-on course is given in the 5th grade, teaching students (bio)chemistry lab techniques not covered by the normal curriculum and to teach them some basic electronics: the workings of µcontrollers, resistors, capacitors, analog and digital sensors, programming and PCB-design. All these topics are covered to help the students acquire skills and knowledge on available research techniques, so they can realistically assess the feasibility of a particular research project when in their final grade.

3. RESEARCH OPPORTUNITIES

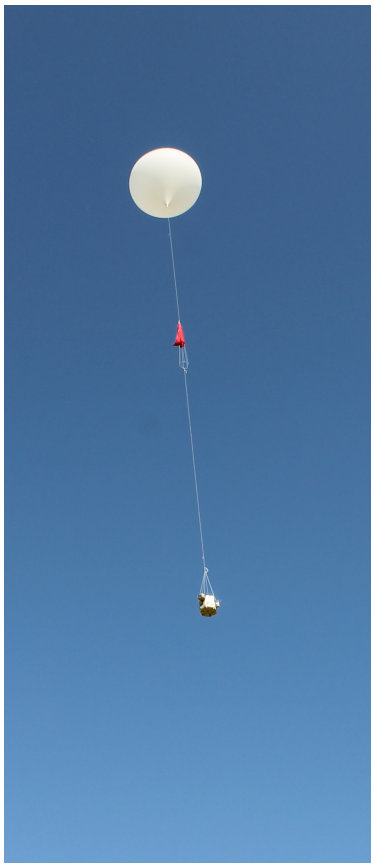

Figure 1: The Asgard balloon programme provides an annual flight opportunity for science and/or technology projects.

3.1 Asgard balloon flights

In cooperation with KMI-IRM (Belgium's Royal Meteorological Institute) and ESERO (European Space Education Resource Office), Sint-Pieterscollege Jette is flying a sounding balloon to over 30km altitude once a year, carrying science and/or technology experiments built and designed by secondary school students [1]. These so-called Asgard balloons offer access to near-space (30-35km) and stay aloft for up to 2 hours, allowing a wide range of investigations. Passive biology (exposing plant seeds or lower animal eggs to near-space conditions) requires no technical know-how and is failsafe while still providing first-class science education possibilities. Atmospheric physics and chemistry experiments range from simple dataloggers with commercially available temperature, pressure and/or gas sensors up to homebread radiation detectors and modified digital cameras. Remote sensing from high altitude allows to investigate pollution, vegetation health and urban development. Light sensors turned to the sky allow to study light absorption and scattering mechanisms. Simultaneous monitoring of different parameters can be used to confirm the Universal Gas Law. Solar cells can be flown to study how the varying altitude (and hence atmopheric absorption) affects their efficiency. The possibilities are endless.

3.2 Antarctic Science

Figure 2: Belgium's Zero -emission Antarctic Research station, with a student-built 3D solid state magnetometer.

Belgium's Zero-emission Antarctic summer station is located on the Utsteinen nunatak in Queen Maud land. Students from Sint Pieterscollege Jette have the opportunity to perform science experiments there by designing and building dataloggers that are taken there and installed by the technical support team that prepares the station a few weeks prior to the arrival of the visiting scientists (ever year at the beginning of the Antarctic summer season).

The scientific possiblilities at the station include geomagnetism, glaciology and seismology. Even UV and IR astronomy might be performed (though not at the height of summer), or solar physics, as there is very little IR absorption beacuse the Anatrctic air is so dry.

3.3 Bifrost flight research

In 2014 a pilot project called Bifrost will be initiated in cooperation with the Technical University of Delft. Bifrost stands for 'Brussels Initiative to provide Flight Research Opportunities to STudents'. The goal is to have the Bifrost project being repeated either annually or biannually from 2014 onwards.

In Bifrost a team of 4 secondary school students and a teacher are flying a scientific or technological experiment of up to 17kg aboard the Technical University of Delfts' flying laboratory, a converted Cessna Citation II (Fig 3.).

Capable of parabolic flight, the Cessna Citation II will offer students the possibiliy to work with zero-g, or reduced (Moon or Mars) gravity. As the plane is a flying laboratory, equipment can be secured on the outside of the plane too, permitting all kinds of flight research.

Figure 3: Cessna Citation II flying laboratory from the Technical University Delft (Netherlands) to be used for flight research by secondary school students from 2014 onwards.

Figure 4: The Cessna Citation from TU Delft can be used for parabolic flight (providing zero-g or reduced-g parabolas) as well as other flight research.

A typical flight could last about 90 minutes and encompass 12 zero-g parabolas of 15 seconds each. Reduced gravity parabolas last somewhat longer.

For the first edition, two teams are selected. While the students of each team only fly once, the equipment of each team stays oboard is therefore flown twice, doubling the data collecting capacity while reducing work load and costs.

3.4 The Zefyr UAV

A Sparkzone Radian RC glider could be used by students for a variety of projects including remote sensing (multispectral imaging), arial photography (as in support of archeological mapping projects), environmental monitoring (using gas sensors to produce altitude profiles of different pollutants).

Figure 5: The ZEFYR motorized glider can be used as a technology test-bed, as a low altitude imager or as an air quality monitoring device.

A precursor project ran during 2013-2014, investigating the possibility of replacing the plane's battery by wing covering solar cells [2]. A student investigated motor current draw, conversion efficiency (battery power to propellor force) and solar cell performance under various conditions. This work was preliminary and could be the basis for multiple other technology projects over the coming years.

Figure 6: The battery-powered propellor (blades folded back when not in use to reduce drag): students are investigating the replacement of the battery by wing-covering solar cells.

When considering the use of this Zefyr (Zero-Emission Flyer for Young Researchers) as an autonomous UAV, downlinking gps data and autonomous flying are required. From these, yet other projects can flow, making the Zefyr a technology testbed as wel as a research instrument.

4. POSSIBLE FUTURE PROJECTS

In order to offer research opportunities to students from other study fields then science-mathematics, some less technology driven project will be required. Biology is the science of choice here, as it offers great research opportunities for which only modest tools are required (often nothing more than a good microscope, preferably with a cross-table).

In the past, preliminary investigations [3, 4] have shown the potential of investigating life cycle parameters in invertebrates such as Daphnia Magna (water flea) and Artemia Salina (brine shrimp)(Fig. 7). Both species produce eggs that can be readily conserved for extended periods of time, allowing to investigate the brood after egg exposure to near-space conditions for example.

As both species live in the water, acidity is another factor that might influence life cycle parameters, as is food abundance, or illumination, or, for Artemia Salina, water salinity.

Figure 7: Biology experiment include determining Daphnia Magna (left) and Artemia Salina (right) life-cycle dependencies on various parameters including exposure to near-space conditions using Asgard balloons.

Plants may also be investigated, exposing seeds to near-space conditions, then monitoring growth (and comparing it to non-flown seedlings). Or plant growth could be studied under low-pressure conditions, though this may require a somewhat more elaborate setup (to prevent excessive water evaporation)(Fig 8).

Figure 8: Possible future projects include investigating plant growth under reduced air pressure or altered atmospheric compositions.

Obviously, for plant as well as lower animal research, the number of possibilities is multiplied many times over yet again if the research is not required to have some 'space related' aspect.

CONCLUSIONS

Building research competences in youngsters is a challenge for the teacher that goes way beyond mastering a certain scientific curriculum. It encompasses the acquisition of knowledge, skills and attitudes alike, which, in the authors' conviction, is best accomplished through a full fledged science research project.

As student motivation increases dramatically when the student feels personally involved, the student should have considerable impact in the choice of his/her research subject. However, making such a choice at the age of 17, and with the knowledge and maturity characteristic of that age is no small challenge. It is therefore proposed that students be offered a variety of platforms, fields of endeavour and possibilities from which to choose, or that can serve as examples to help guide the choice. Experience (while sketchy at best considering only Sint Pieterscollege for such projects) seems to confirm the validity of this approach.

REFERENCES

[1] de Schrijver E. *et al.* (2011), Proc. '20th ESA Symposium on European rocket and Balloon Programmes and Related Research' pp. 271-75, Hyères, France, 22-26 May 2011 (ESA SP-700).

[2] Lafkih A. and Van den Hove C. (2013), Proc. '21st ESA Symposium on Rocket and Balloon Programmes and Related Research', Thun, Switzerland, 9-13 June, t be published.

[3] de Schrijver E. (2005), Proc. '17th ESA Symposium on European rocket and Balloon Programmes and Related Research' pp. 77-80, Sandefjord, Norway, 30 May- 2 June 2007 (ESA SP-590).

[4] de Schrijver E. (2007), Proc. '18th ESA Symposium on European rocket and Balloon Programmes and Related Research' pp. 283-287, Visby, Sweden, 3-7 June 2007 (ESA SP-647).

CANSAT TEACHER TRAINING COURSE

Thomas Gansmoe [(1)], Jøran Grande [(2)]

[(1)] Norwegian Centre for Space-related Education, P.O. Box 54, 8483 Andenes,Norway, thomasg@rocketrange.no

[(2)] Norwegian Centre for Space-related Education, P.O. Box 54, 8483 Andenes, Norway, joran@rocketrange.no

ABSTRACT

A CanSat is the combination of the complex world of satellite design into a small and easy to understand project. CanSats are being built by high school students and university students all over the world in the last decades. In Norway, NAROM has been holding CanSat teacher training courses and national competition for high school students. Since 2008 NAROM has held several CanSat teacher training courses which over the latest years have been further developed. This paper is about the CanSat teacher training course provided by NAROM since 2008.

1. BACKGROUND

The CanSat concept was first introduced in the late 1990s by the American professor Robert Twiggs. It provides an affordable way to introduce students to the many challenges in building a satellite. Students design and build a small electronic payload that can fit inside a soda can. The CanSat is launched and ejected from a rocket or a balloon. By the use of a parachute, the CanSat slowly descends back to earth performing its mission while transmitting telemetry. In recent years, CanSat activity in Europe has been growing. These contests have proven to be an effective, practical and low-cost way to inspire students. ESA hopes to encourage many more such activities on a national and regional level. Further information about these competitions can be found by visiting www.cansat.eu.

2. TEACHER TRAINING COURSE

NAROM together with the European Space Agency hosted a four day teacher training course in November 2012 for 24 European high school teachers. The main goal for the training course was to foster more collaboration for CanSat activities in Europe. A total of 20 teachers gathered at Andøya Rocket Range to learn more about how to build a CanSat at their own school.

Figure 1. Teachers attending the European CanSat teacher training course 2012.

With the assistance of experts from NAROM and the University of Aalborg, the teachers learned all the basic steps to build a CanSat and how to accomplish the primary mission objectives. Teachers attending the workshop is shown in Fig 1. Normally the teacher training course lasts for four days were the goal is to learn all basics steps needed to run the CanSat project at high schools. The teachers also build their own CanSat and get to do a test drop from a tethered balloon. In the end the teachers learn how to analyse the retrieved data from the CanSat decent.

Proc. '21st ESA Symposium European Rocket & Balloon Programmes and Related Research',
9–13 June 2013, Thun, Switzerland (ESA SP-721, October 2013)

Figure 2. Teachers building CanSat

NAROM provided all the teachers with a free CanSat starter kit. The kit consists of components that can be found on electronics shops. In addition a shield board developed by the University of Aalborg was used as a basis as shown in Figure 3.

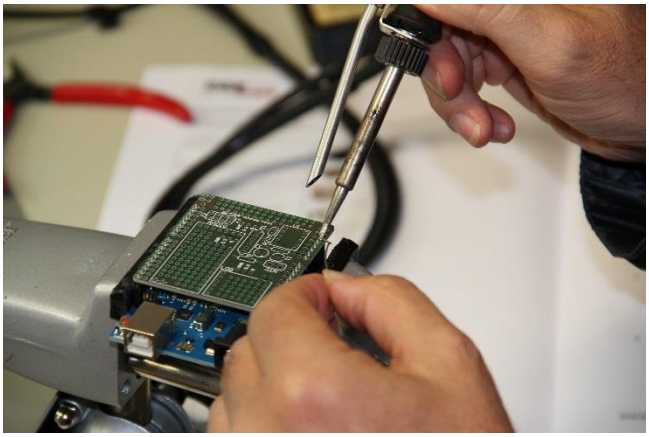

Figure 3. CanSat shield board

The CanSat kit can be ordered from the different electronic shops and a list of all the components and suggestions of where to buy this is listed in the NAROM CanSat book – 2013 edition. The main board consist of an Arduino Uno microcontroller development board were it is possible to put the CanSat shield on top. The CanSat shield board currently used by NAROM has been developed by the University of Aalborg and is meant to be an easy way to learn more about electronics and programming of the CanSat kit. The shield board consists of a communication radio (APC220), pressure sensor (mpx4115), temperature sensors (LM35DZ and NTCLE100E3103JB), a three axis accelerometer (MMA7361L) and a SD storage card (OpenLog).

3. THE NAROM CANSAT BOOK

The NAROM CanSat book has been written by personnel from NAROM together with the University of Aalborg and the Norwegian University of Science and Technology. The CanSat book is meant to be a teacher's guide to the CanSat concept. The book includes very simple step by step how to build up the CanSat kit and learn how to use it. Topics like, introduction to programming, construction and testing of the shield board, how the hardware work, setting up software, mechanical, parachute and antenna design and a list of components and were to buy them. The CanSat book can be found at www.narom.no

4. THE BALLLON DROP TEST

The drop of a CanSat from the balloon is normally used during the teacher course. A normal weather balloon is used with an in-house made drop mechanism and termination system is used. The balloon reaches an altitude of about 300 meters before the CanSat are dropped by using a remote control. Other local CanSat arrangement has been held in Norway using the same system. A picture of a release from the balloon is shown in Fig. 4.

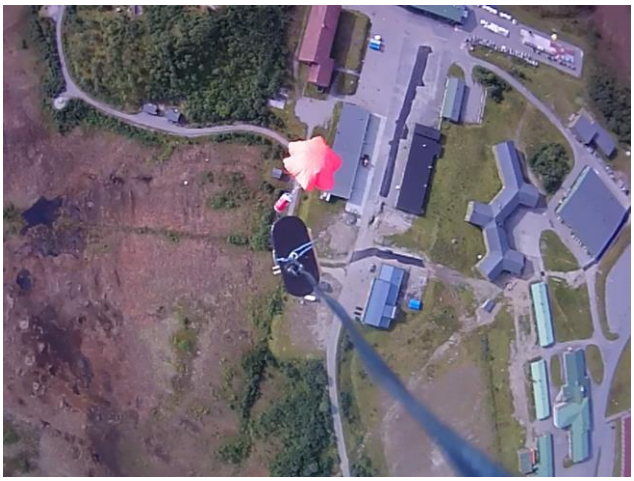

Figure 4. Balloon release system

During the CanSat competitions the CanSat are launched to an altitude of 1 km before they are deployed.

5. FUTURE CANSAT ACTIVITY

As a part of the Nordic European Space Education Resource Office NAROM has planned to run a teacher training courses during the fall of 2013. The teacher training course is open for teachers from Norway, Sweden, Denmark and Finland. In addition a Nordic CanSat competition is planned for the spring of 2014 for the same countries. Both the teacher training course and the competition is taking place at Andøya Rocket Range. More information about the Nordic ESERO activities can be found at www.esero.no.

CANSAT, SCIENCE IN A SODACAN

Mark Uitendaal,
T-Minus Engineering B.V., The Netherlands
m.uitendaal@t-minus.nl

ABSTRACT

The CanSat programme has been going on for a number of years now. The goal of this programme is to get youngsters interested into so-called STEM subjects, which stands for Science, Technology, Engineering and Math. For this reason, ESA Education department has started a competition in Europe. In 2013, the ESA European CanSat competition will be held in the Netherlands, supported by T-Minus engineering. New this year is the introduction of a standardized CanSat kit. The launch campaign of the European CanSat competition took place at the 24th of April 2013. T-Minus produces all the infrastructure necessary to launch CanSats in Europe.

1 INTRODUCTION

The CanSat phenomenon was originally conceived by professor Bob Twiggs from the Stanford University around 1998 to promote low cost "space missions". From 1998 onwards, several CanSat competitions are run in The United States, Japan and at a later stage in some European countries, including Spain, France and The Netherlands. From 2010 onwards, ESA has initiated the European CanSat competition, first (in 2011 and 2012) with a launch campaign in Andoya, Norway and in 2013 at ASK 't Harde in the Netherlands. From 2013 onwards, the European CanSat kit is introduced. This kit, provided by ESA and T-Minus Engineering B.V., is meant as a simple starting point for a CanSat project. This kit will aid the teacher and the students in their project with hardware and information.

The reason why CanSat is used as an educational project is this project can aid in hands-on experience in STEM (Science, Technology, Engineering and Math) subjects as a way to interest students for these subjects and technology in general. It can complement the curriculum of the school, or be done in extra-curricular activity in the free-time of the students and teacher. Students are stimulated to do a project in a group and to work together with different types of disciplines.

2 THE EUROPEAN CANSAT KIT

The T-Minus CanSat kit, of which a prototype can be seen in Fig. 1, consists of:

- The CanSat manual, which contains information about the contents of the kit, several building examples, technical information and project management strategies.
- The CanSat base plate, which contains an atmega2560 microprocessor.
- The sensor board, which contains the experimenting board and three different sensors which are a pressure sensor and two types of temperature sensors.
- A telemetry set, which is currently an APC-220 transceiver unit. The next versions will use a T-Minus transceiver unit, which has the same form factor as the CanSat base plate and the sensor board.
- Battery, which is a simple 9V test battery to test the system on the ground in a stand-alone modus.
- USB cable, for communication between the CanSat base plate and a computer.
- Mechanical part of the CanSat, which can be used for flights and gives the CanSat a basic structure.

An example of an assembled CanSat can be seen in Fig. 2.

The CanSat kit as delivered is completely Arduino™ compatible to allow for easy usage and the use of Arduino™ libraries. The big advantage of this board with respect to the Arduino™ is the form factor which fits exactly in a soda can and is stackable the same way as a normal cubesat.

The possibilities of missions that can be made with this system are endless. Some examples of missions using this system, as seen in CanSat campaigns include:

- Fly back ram-air parachute system: together with an GPS, the CanSat will fly

Proc. '21st ESA Symposium European Rocket & Balloon Programmes and Related Research',
9–13 June 2013, Thun, Switzerland (ESA SP-721, October 2013)

back to a pre-determined GPS coordinate and land there.

- Flyback collapsible quadcopter, which is the same system, but the CanSat transforms to a quadcopter and flies back via the same system.
- Stereoscopic camera or whiskbroom scanning camera systems which make 3D maps of the landing terrain.
- Ozone measurements, aerosol measurements, humidity measurements and other atmospheric science.

Figure 1: The CanSat kit, as used in the 2013 CanSat in Europe prototype.

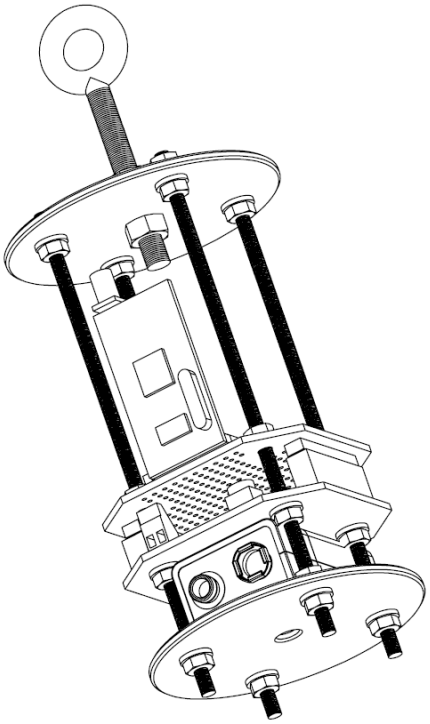

Figure 2: A render of the 2013 European CanSat kit prototype

3 CANSAT CAMPAIGNS

T-Minus Engineering B.V. has developed two types of vehicles to launch the CanSats to their ejection altitude. These vehicles are:

- The T-Minus CanSat launcher, a small type of sounding rocket to deliver CanSats at an altitude over 1 km.
- The CanSat Carrier, which is a small remotely piloted aircraft to deliver CanSats.

3.1 The CanSat launcher

The T-Minus CanSat launcher is a 3.17 meter tall vehicle, capable of launching and deploying 6 CanSats simultaneously at an altitude in excess of one kilometre. The rocket itself has a diameter of 0.2 meters. The rocket has an “ogive-shaped“ nose cone and a conical tail cone for good aerodynamic performance after motor burnout. The mass of the rocket, including 6 CanSats, parachute and rocket motor, is approximately 23 kg. The rocket is equipped with a parachute in order to safely recover the vehicle. When landing correctly, the vehicle could be re-used after a refurbishment and check-out.

The vehicle is aerodynamically stabilized and has no active stabilisation controls. The rocket motor produces 4300 Ns of impulse, and has a burn time of 4.2 seconds. The propellant formulation is chosen such that the environmental impact is as low as possible.

In order to speed up the actual launching operations, the vehicle is divided into two sections:

- A fin section, which contains the rocket motor and other pyrotechnical equipment. This section is stored away from the students.
- The CanSat bay, which houses the six CanSats, is completely non-pyrotechnical. It is the only part with which the students interact.

The bay is designed such that the loading time of the CanSats in the bay is minimized. The operations during the campaign and the design of the T-Minus CanSat Launcher are such that the time between CanSat switch-on and launch is less than 30 minutes.

The CanSats will leave the rocket in radial direction. This is done so that the ejected CanSat will not collide with the rocket itself during flight. The rocket does not use pyrotechnics to eject the CanSats, so that the deployment shock on the CanSat is reduced dramatically. The CanSats are pushed out of the rocket via a small spring, minimizing the chance of a CanSat "being trapped" in the CanSat bay itself. The hatches which secure the CanSats in the bay are disposable and will be lost after each flight. The CanSat is held in a small dispensable cardboard holder in the bay in order to secure a good and smooth deployment of the CanSat.

The rocket is powered by a simple solid rocket motor with 6.5 kg loaded mass, of which 4.2 kg is rocket propellant. The propellant is considered a green propellant and is made in such way that almost all exhaust products are biodegradable. The rocket motor and all other components which contain pyrotechnics are in a separate part of the launch-field and do not need to be in contact with the CanSat participants of the CanSat launch day. The motor is designed such that it produces smoke after motor burnout. This reduces drag and increases visibility for the CanSat participants, enabling them to track the rocket and point the antennas to the proper position in the sky.

Figure 3: The T-Minus CanSat launcher, where two CanSats are visible.

Figure 4: The CanSat launcher in the launch tower

3.2 The CanSat carrier

The T-Minus CanSat carrier, which is a remotely piloted aircraft with autonomous capabilities, capable of delivering and ejecting two CanSats to an altitude from 30 meters up to a 1000 meters. Since not every launch site is suitable for launching CanSats via rockets, the CanSat carrier can launch CanSats from lower altitude, but with a higher precision.

The launch field on where the CanSat activities are done can be smaller and the systems doesn't need any complex permits for the rocket motor. The aircraft is completely electrically powered and can drop 2 CanSats per sortie. Since the battery is easily replaceable, a high number of sorties can be performed per day. Therefore it should be possible to conduct a complete campaign with 20 teams in one day. It is also possible to drop the CanSats at a specified point in the sky, thereby lowering the dispersion of the CanSats due to wind.

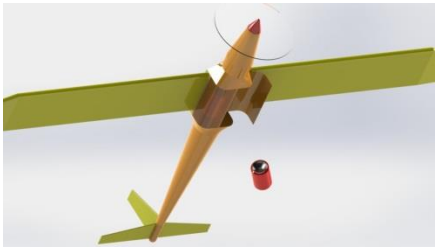

Figure 5: The CanSat carrier

4 EXPERIENCES DURING THE 2013 EUROPEAN COMPETITION

The European competition of 2013 was held at ASK ‘t Harde in The Netherlands. This is an active military artillery shooting range which T-Minus rented for the occasion. The students and participants where first allowed to do some final tinkering at Delft University of Technology, under supervision of T-Minus’ electronics experts. The CanSats were all reviewed by the CanSat jury panel members on building quality, team spirit and technical knowledge. The CanSats were also tested on descent velocity, since the launch site in the Netherlands only allows for a 90 second flight of the CanSat.

The weather of the Netherland was living up to its name by delivering a lot of rain and wind at the day of launch. The launches of the CanSats went up smooth and a total of rockets were launched before the launch window closed. 12 out of 15 CanSats were ejected properly, of which 9 were recovered by the military personnel. All participants enjoyed the experience a lot, which showed in the final evening after the launch day and the evaluation afterwards.

5 CONCLUSION

The CanSat phenomenon is spreading faster and faster through Europe. The European CanSat competitions are a big stimulator in spawning new CanSat competitions throughout the individual countries of Europe. The European competition is also used as a “price” for the winner of the national competition. It will certainly be a big driver for CanSat activities within Europe. T-Minus Engineering is working on a good infrastructure for these national and European competition in the form of CanSat kits, rules and regulations and launch vehicles.

STERN - A ROCKET PROGRAMME FOR GERMAN STUDENTS

Andreas Stamminger[(1)], Helmut Ciezki[(2)], Wolfgang Kitsche[(3)], Mario Kobald[(4)], Karsten Lappöhn[(5)], Alexander Schmidt[(6)]

[(1)] Deutsches Zentrum für Luft- und Raumfahrt (DLR), Mobile Rocket Base, Oberpfaffenhofen, 82234 Wessling, Germany, Tel.: +49-8153-28-1231, Email: andreas.stamminger@dlr.de
[(2)] Deutsches Zentrum für Luft- und Raumfahrt (DLR), Institute of Space Propulsion, Lampoldshausen , 74239 Hardthausen, Germany, Tel.: +49-6298-28-321, Email: helmut.ciezki@dlr.de
[(3)] Deutsches Zentrum für Luft- und Raumfahrt (DLR), Institute of Space Propulsion, Lampoldshausen , 74239 Hardthausen, Germany, Tel.: +49-6298-28-369, Email: wolfgang.kitsche@dlr.de
[(4)] Deutsches Zentrum für Luft- und Raumfahrt (DLR), Institute of Space Propulsion, Lampoldshausen , 74239 Hardthausen, Germany, Tel.: +49-6298-28-622, Email: mario.kobald@dlr.de
[(2)] Deutsches Zentrum für Luft- und Raumfahrt (DLR), Space Administration, Königswinterer Str. 522-524 , 53227 Bonn, Germany, Tel.: +49-228-447-520, Email: karsten.lappoehn@dlr.de
[(3)] Deutsches Zentrum für Luft- und Raumfahrt (DLR), Mobile Rocket Base, Oberpfaffenhofen, 82234 Wessling, Germany, Tel.: +49-8153-28-2704, Email: alexander.schmidt@dlr.de

ABSTRACT

In April 2012 the German Aerospace Center DLR, launched a support programme for students to develop, build and launch their own rockets. The programme goes by the acronym STERN (STudentische Experimental-RaketeN) which is also the German word for star. Supported by funds from the Federal Ministry of Economics and Technology (BMWi) and conducted by the DLR Space Administration of the German Aerospace Center DLR, the STERN programme provides aerospace engineering faculties at universities with opportunities to introduce students realistically to subjects related to space transport. During the project duration of three years the soon-to-be engineers will develop their own rockets. There are no limits regarding peak altitude or the propulsion system used (solid fuel, liquid fuel, steam or hybrid). The rockets should have a small telemetry system to transmit key trajectory and housekeeping data back to Earth during flight and provide information to the students including the rocket altitude. In order to teach students engineering and science and to put their technical knowledge to the test as early as possible in their studies, there are no altitude restrictions except the normal range restrictions.

The students will be integrated into courses which already deal with various aspects of rocket technology. In addition to the design of the engine, project activities will focus primarily on the rocket system as a whole, which, because of its complexity, demands interdisciplinary thinking and teamwork. As in a large aerospace technology project, or the development of a new launch system, future graduates will have to meet milestones that specify both timing and technical progress. It is also necessary that they have to attend various reviews to present and explain their design to an expert audience which carefully reviews their proposals and work. The students will be invited to test the engines they have built at the DLR test centre in Lampoldshausen, Germany. At the end of the project, the result should be a flight capable rocket. Some of the rockets will be launched from the Esrange Space Center at Kiruna, in Sweden, where the European altitude record of 12.6 kilometres for an amateur rocket was set. To break this record and fly even higher could be a long-term objective of the DLR programme during its planned three-year duration – offering universities a long-term prospect for training a new generation of researchers, particularly in the area of astronautics.

DLR MORABA (Mobile Rocket Base), the DLR Space Propulsion Institute, and the DLR Space Administration are a major part of the Review-Board until flight. With a large number of sounding rocket launches, DLR's MORABA has acquired total system competence when it comes to assessing the structural integrity, flight behaviour, or flight performance of a rocket and makes access to Esrange possible. The DLR Space Propulsion Institute at Lampoldshausen has decades of experience in research and testing of rocket engines, especially those belonging to the European Ariane programme that was launched in the 1970s. The centre conducts both applied and fundamental research in the field of rocket propulsion systems.

This paper will give an overview on the activities of DLR in supporting the student teams to succeed in their aim of a successful flight of their own rocket. It will give an outlook on the ideas of the already selected teams and will also explain the differences to other student projects such as REXUS/BEXUS.

Proc. '21st ESA Symposium European Rocket & Balloon Programmes and Related Research', 9–13 June 2013, Thun, Switzerland (ESA SP-721, October 2013)

1. INTRODUCTION

The last decades have shown the economical and strategic importance for Germany as well as for Europe to have the capability of launching satellites and to have the own access to space. Since the Ariane programme was established in 1979 Europe has a launcher system that is independent from other nations. It guarantees the unrestricted access to space with its launcher in the fifth generation. Also Ariane has become a brand that dominates the commercial market. To ensure Europe's autonomous and cost-effective access to space for the future an ongoing development of the Ariane 5 and its successor is necessary. The main requirements for this development are well-educated skilled employees. Responses from the economy, the universities and analysis of the DLR Space Administration have shown a considerable decrease of young scientific and technical professionals in the field of space transportation. This leads in the long-run to a lack of competence of Europe in developing new launcher systems and is a danger for the important role that Germany has in the Ariane programme.

To stop this process the DLR Space Administration has initiated the programme STERN in April 2012. The aim is to establish the subject space transportation in German universities to enthuse future generations of engineers in this research field.

The programme will run for minimum three years and will be extended, depending on the university and the scope of the project. The students will be integrated into courses which already deal with various aspects of rocket technology. In addition to the design of the engine, project activities will fo cus primarily on the rocket system as a whole, which, because of its complexity, demands interdisciplinary thinking and teamwork. As in a large ae rospace technology project, future graduates will have to meet milestones that specify both timing and technical progress. They will also be required to attend various reviews to present and explain their design to an expert audience.

2. PROGRAMMATIC AIMS

The Space Administration of the German Aerospace Center DLR in Bonn is responsible for the planning and execution of the German Space Programme for the German ministry of economics and technology (BMWi). One element of this programme is the support of the young scientific researchers and engineers. This is necessary since Germany has to compete in an international market and to en sure its com petences in key technologies.

Therefore it is the aim of the STERN programme to enthuse students on the subject space transportation by hand-on activities, to motivate universities with the help of funding and to increase the lecture activities in the field of launcher systems.

The DLR Mobile Rocket Base and the DLR Institute of Space Propulsion will take a reviewer and support role in the STERN programme. The student support programme will give the two DLR institutes in an early phase of ed ucation a good possibility to recruit its own young engineers. Gaps in recruiting of young professionals have been identified.

In the long-term view DLR has the hope that as a result of this programme the research at the universities end up in a small sounding rocket that can be used for meteorological experiments. This could be a rocket like the Viper-Dart that did eject a sm all balloon in 90 km altitude to measure atmosphere data like pressure, density, temperature and wind velocities. Even the need for this type of rocket has been identified the rocket is not produced anymore nowadays after an accident during production. The specification of this rocket is reachable for the student programme STERN.

Figure 1. STERN Logo

3. SCIENTIFIC & TECHNICAL AIMS

The programme STERN is open for all German universities that offer aerospace engineering lectures and that offer students the possibility to develop, build, test and fly own rockets in university teams.

The focus is on the development of the complete rocket system. The primary aim is to implement a telemetry payload that transmits the flight data (acceleration, velocity and position) and if possible the house keeping (pressure, temperature of tank and motor, etc.) back to Earth.

There is no limit on the flight altitude or the chosen propulsion concept. Commercially available solid propulsion motors can be used as well as own developments in liquid-, hybrid- or hot water propulsion. The student's tasks will include pressure vessels such as tanks and motor casings, the nozzle geometry and strength calculations for the rocket components.

DLR expects at beginning of the programme flight altitudes between 3 and 15 km. The actual altitude record for an amateur rocket is 12.55 km . In a later phase of the programme flight altitudes of up to 100 km are possible. Because of the expected flight altitudes and the constraints of the air space not every launch of the STERN rockets will be possible in Germany. Up to 5 km altitude it is planed to use test fields of the German Armed Forces. Some universities do cooperate already now with the German Armed Forces to use these test fields. It is planned to launch rockets that fly higher than the 5 km at Esrange near Kiruna, Sweden where the REXUS, TEXUS, MAXUS and MAPHEUS campaigns take place. The DLR Mobile Rocket Base and SSC Esrange do have a long history of cooperation.

The aim of STERN is support the competence in developing future launcher systems in Germany. This is done by a financial funding but also by the attractive possibility of a rocket launch at Esrange for the involved professors and students.

Beside the lectures the students have to do several activities until the launch of the rocket. The students have to design the rocket motor and flight hardware, perform motor tests including health monitoring which can for example be done at the DLR Institute of Space Propulsion at Lampoldshausen, do wind channel tests and compare these results with modern numerical calculation methods and analyse the performance of the complete rocket system.

The work is part of seminar papers and studies. Because of the scope of work the projects can only be conducted in team work. For this reason the team members are coordinated by a supervisor pays attention on time schedules, milestones and reviews. In this way, students gain skills in project management and the all-important social skill that are necessary in the professional life.

4. ROCKET DESIGN

The student teams follow a wide range of concepts:

- DECAN (TU Berlin): Two-staged rocket with a lift-off mass of 150 kg. 1st stage hot water propellant, 2nd stage solid propellant.
- ZEpHYR (University Bremen/ZARM): Hybrid motor using paraffin / LOX
- ERIG (TU Braunschweig): Hybrid motor using HTPB / N2O
- SMART (TU Dresden): Single stage, liquid propellant (Ethanol / LOX)
- HyEnd (University Stuttgart): Single stage rocket with a lift-off mass of 120 kg, hybrid motor using paraffin / N2O
- HyComet (FH Augsburg): single stage rocket, lift-off mass 25 kg, hybrid motor, flight altitude 3-5 km
- Aquasonic (HS Bremen): Two staged rocket, lift-off mass 60 kg, 1st stage hot water, 2nd stage hybrid motor, flight apogee 10 km
- Hyper (TU München): Single staged rocket, hybrid motor (HTPB / LOX), flight apogee 15 km

5. TECHNICAL SUPPORT BY DLR

DLR's Mobile Rocket Base (MORABA) has decades of experience in preparation and performing sounding rocket campaigns. The TEXUS, MAXUS, MASER and MAPHEUS are scientific missions which are performed with participation of DLR. The focus of the REXUS campaigns is on education. The REXUS programme offers flight opportunities to European student experiments on rockets with reduced gravitation (milligravity). These launches are conducted by Eurolaunch, a joint venture of SSC Esrange and DLR MORABA, at the Esrange Space Center in Kiruna, Sweden.

The DLR Space Propulsion Institute at Lampoldshausen has decades of experience in research and testing of rocket engines, especially those belonging to the European Ariane programme.

From the beginning of the Project till the launch of the rocket, the students have to conduct several reviews in which they will have to present their actual design of the rocket. This will increase the chance of succeeding the mission goal of the student team and decrease safety risks the launch of the rocket. With decades of experience DLR experts from MORABA and the DLR Institute of Space Propulsion have the necessary expertise required for such reviews.

The DLR Institute of Space Propulsion has built a test field at which student rocket engines can be tested. Additionally the DLR MORABA will use their campaign proven software to calculate the static and dynamic stability of the student rockets, the flight trajectory and the impact area.

The following subchapters will give an overview of work packages that will be handled by DLR. These services are primarily queried through subcontracts by individual universities to DLR

5.1. ESRANGE

The DLR MORABA is the interface to SSC that is responsible for all launches performed at Esrange at Kiruna and that runs the ground facilities. Since each university is in a different developing phase of the rocket and different durations for each project has to be assumed it is planned to launch the STERN rockets after the completion of another launch campaign. It will be also tried to bundle several STERN rocket launches in one single campaign to reduce organizational effort and costs. The support of the universities includes:

- Assistance in booking the campaigns at Esrange
- Assistance in booking flight tickets and hotel booking for the student teams
- Assistance in organization of the transport of rocket hardware to Esrange
- Assistance in writing the Flight Requirements document
- Flight Trajectory and Impact zone calculation
- Use of Esrange infrastructure

5.2. REVIEWS

The universities will have to present the rocket design to DLR Space Administration and other reviewers during the development phase and before the launch of the rocket. The DLR Institute of Space Propulsion and the DLR Mobile Rocket Base will join every obligatory review with at least two staff members. One aim of the review process is to make the student teams familiar with reviews as they are common in space related projects. The reviews will also increase the success chance of the universities in reaching the mission aim and uncover potential safety risks. It is obligatory for the university to call a review board of minimum four persons that not directly involved in the university project.

Figure 2. Review Panel at the DLR Oberpfaffenhofen

Following reviews th at cover the complete system rocket are mandatory for the universities:

- Preliminary Design Review (PDR) at the DLR in Oberpfaffenhofen
- Critical Design Review (C DR) at the DLR in Lampoldshausen
- Integration Progress Review (IPR) at the university
- Rocket Acceptance Review (RAR) at the University
- Flight Readiness Review (FRR) at the launch range

It is up to the university to call more reviews that focus on the sub-systems (rocket motor, launcher, etc.). The DLR will join these reviews only if the rocket systems complexity (e.g. l iquid propulsion systems) makes it necessary.

5.3. SPACE PROPULSION WORKSHOP

The DLR Institute of Space Propulsion organizes every year within the STERN program a workshop dedicated to propulsion relevant topics. Beside lectures the major part consists of exercises, where the students have the opportunity to strengthen their practical capabilities. The first workshop conducted in April 2013 supported the students in their preparation and conduction of rocket engine tests. Themes of exercises were e.g. conduction of experiments, use of measuring techniques and sensors, use of numerical tools for FEM structure analysis and conduction of work with as mall test facility. In order to conduct experiments safely th e students have also been trained in the conduction of risk analyses, which they also have to conduct prior to running tests.

5.4. WORKSHOP "STERNSTUNDEN"

The workshop STERNStunden will be organized every two years, conducted in Oberpfaffenhofen. The workshop will focus on the system rocket and all subsystems except the motor.

6. RESEARCH AND STUDENT TEST FIELD M11.5

At DLR site Lampoldshausen the M11.5 test field was erected and came into service in June 2013, at which beside rocket relevant research activities also the STERN student groups can come with their developed rocket combustors and engines to test them. These tests are conducted under the auspices of experienced researcher and engineers from the institute. This process of teaching, supervision and exercises shall help the students to get a deeper understanding how a development and test process runs and how to react on occurring difficulties.

The test field is equipped with an oxidizer tank for actually nitrous oxide and a separate control room from which the experiments are conducted. In order to have an effective stay at Lampoldshausen test site the students are encouraged to prepare their experiments in containers yet at their universities. After checks of flow and measurement systems these containers will be brought to Lampoldshausen. This procedure reduces start-up times so that more time is available for learning and common testing.

Two containers or experimental setups can be positioned on the concrete plate of M11.5. Hybrid engines with thrust levels up to 10 kN can be tested. Hybrid engines are favoured because of their inherent security advantages. Because of the security point of view cryogenic or poisonous propellants cannot be used.

Figure 3. Research and Student Test Field M11.5

7. SUMMARY & OUTLOOK

The STERN programme differs significant from other student programmes. Each project has a long duration at the university. A permanent supervisor at the university is very important. The programme is a great opportunity for universities and aerospace students to gain experience in building rockets and rocket engines.

8. REFERENCES

1. Alger S. / Ciezki H. / Heislbetz B. / Kitsche W. / Schlechtriem S., *First Student-Hybrid-Thruster Test Campaign at German Aerospace Center (DLR)*, 52nd Israel Annual Conference on Aerospace Science, 2012
2. Costa, G. / Kitsche, W. / Padoan, L., *Student Hybrid Thruster Testing and Research*, 5th European Conference For Aerospace Science (EUCASS), 2013
3. Kitsche W. / Schmidt A. / Stamminger A. / Ciezki H. / Lappöhn K., *Guidelines for STERN Project Documentation*, DLR, 2012-11-22

REXUS/BEXUS

ROCKET AND BALLOON EXPERIMENTS FOR UNIVERSITY STUDENTS

Natacha Callens [1], Alexander Kinnaird[2], Kristine Dannenberg [3] , Mark Fittock [4], Mikael Inga[5], Olle Persson [6], Maria Roth [7], Alexander Schmidt [8], Martin Siegl[9]

[1] European Space Agency (ESA-ESTEC), Postbus 299, NL 2200 AG Noordwijk, natacha.callens@esa.int
[2] European Space Agency (ESA-ESTEC), Postbus 299, NL 2200 AG Noordwijk, alex.kinnaird@esa.int
[3] Swedish National Space Board (SNSB), Solna strandväg 86, S-171 04 Solna, kristine.dannenberg@snsb.se
[4] German Aerospace Center (DLR), Robert-Hooke-Straße 7, D 28359 Bremen, mark.fittock@dlr.de
[5] SSC, P.O. Box 4207, SE-171 04 Solna, mikael.inga@sscspace.com
[6] SSC, P.O. Box 802, SE-981 28 Kiruna, olle.persson@sscspace.com
[7] German Aerospace Center (DLR), Koenigswinterer Straße 522-524, D 55227 Bonn, maria.roth@dlr.de
[8] German Aerospace Center (DLR), Mobile Raketenbasis, D 82234 Weßling, alexander.schmidt@dlr.de
[9] German Aerospace Center (DLR), Robert-Hooke-Straße 7, D 28359 Bremen, martin.siegl@dlr.de

ABSTRACT

Each year the REXUS/BEXUS programme allows up to 20 university student teams from across Europe to participate in a hands-on educational programme allowing them to fly their research or technology demonstrating experiment on one of two sounding rockets or two stratospheric balloons.
REXUS experiments are launched on an unguided, spin-stabilised rocket powered by an Improved Orion Motor with 290 kg of solid propellant. It is capable of taking 40 kg of student experiment modules to an altitude between 75 and 90 km. The vehicle has a length of approximately 5.6 m and a body diameter of 35.6 cm.
BEXUS experiments are lifted by a balloon with a volume of 12000 m³ to an altitude of 25-30 km, depending on total experiment mass (40-100 kg). The flight duration is 2-5 hours.
The REXUS/BEXUS programme incorporates a near space mission project life cycle, including preliminary, critical, integration and acceptance reviews, a thorough integration and testing campaign, launch and follow up activities. In the 5 years of the programme over 450 students have been involved, 10 rockets and 10 balloons have been launched with 70 experiments in total.
This paper will give an overview of this hands-on educational activity, its improvement over the years and the benefits for the university students.

1. THE REXUS/BEXUS PROGRAMME

The REXUS/BEXUS (Fig. 1) - Rocket and Balloon Experiments for University Students programme [1] is realised under a bilateral Agency Agreement between the German Aerospace Center (DLR) and the Swedish National Space Board (SNSB). The Swedish share of the payload has been made available to students from other European countries through a collaboration with the European Space Agency (ESA). EuroLaunch, a cooperation between the Esrange Space Center of the Swedish Space Corporation (SSC) and the Mobile Rocket Base (MORABA) of DLR, is responsible for the campaign management and operation of the launch vehicles. Experts from DLR, SSC and ESA provide technical support to the student teams throughout the project.

Figure 1. REXUS/BEXUS programme logo.

The programme is targeted towards science and engineering students who have good concepts for experiments to be launched on-board either sounding rockets or high altitude balloons. The students are responsible for all aspects directly associated with their experiments and must provide the manpower for the management, engineering, and scientific aspects. Technical/scientific guidance from an academic supervisor from their institute is mandatory.
In this programme, students must complete a full project lifecycle, beginning with proposal submission, development of an experiment, launch and data analysis. The students are supported in their work through contact with experts, specific training, and written materials along with planning and financial support.

Proc. '21st ESA Symposium European Rocket & Balloon Programmes and Related Research', 9–13 June 2013, Thun, Switzerland (ESA SP-721, October 2013)

2. REXUS/BEXUS SCHEDULE

A call for experiment proposals is launched each year at the beginning of September. Selected student teams participate in a balloon flight campaign 12 months later or in a rocket flight campaign 18 months later. Two sounding rockets and two stratospheric balloons are launched annually respectively in spring and autumn from SSC Esrange Space Center in Northern Sweden. Between the selection and the campaign, the student teams have the opportunity to execute a full life-cycle of a "space" project. The REXUS and BEXUS experiments must progress to pass a Preliminary Design Review (PDR) and Critical Design Review (CDR). After the acceptance of the designs, two further reviews are carried out, the Integration Progress Review (IPR) to assess progress with the experiments fabrication and assembly and the Experiment Acceptance Review (EAR) to qualify the experiments for flight before the delivery to the launch authorities. For the REXUS programme there are three additional key milestones: the Scientific Payload Integration, the Bench Test and the Spin and Balancing (Fig. 2). In return for the flight opportunity, it is mandatory for the students to execute an outreach programme, reporting their project and participation in the REXUS/BEXUS programme. This can be, for example, in the form of a dedicated website or blog, using social networks, information distributed within their university, presentations at conferences, interviews for newspapers and magazines, publications in a scientific journal, and/or presentations at schools.

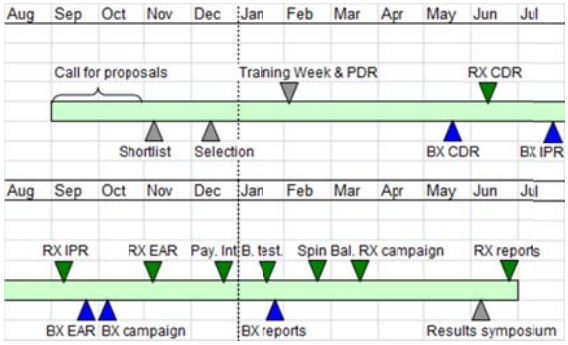

Figure 2. REXUS/BEXUS programme schedule.

2.1. Call for proposals

The call for proposal marks the beginning of the programme. The interested students have to fill in a proposal template to ensure that they provide all the necessary information for experiment assessment with respect to the scientific/technical goal, the feasibility for a rocket or a balloon flight and safety aspects as well as the composition of payloads. The due date for submission of the proposals is in the second half of October.

2.2. Selection process

The selection process is a two steps process: a pre-selection based on the review of the experiment proposals and a final selection based on the oral presentations of the projects to a panel of experts. For this purpose, at the beginning of December up to 30 pre-selected student teams are invited to selection workshops at the DLR Space Agency in Bonn (Germany) or at the European Space Technology Centre (ESTEC) in Noordwijk (The Netherlands). During these events the students also receive advice and project information as well as getting, when possible, the opportunity to visit the facilities (Fig. 3). The expert judgments from both workshops are the basis for the definition of the four vehicles' payload. The selection is announced a few days later.

Figure 3. Group picture at ESTEC during the 2012 Selection Workshop.

2.3. Applicable documentation

After selection, the selected teams are requested to use a specific template called a Student Experiment Document (SED) to report their progress in the programme cycle. Five different frozen versions have to be delivered by predefined deadlines throughout the programme. This document loosely follows the documentation related to a typical space project lifecycle but is simplified and condensed into a single comprehensive document. In order to assist the student teams with the preparation of their SED the following additional documentation is provided: SED Guidelines and REXUS/BEXUS User Manuals. The student teams also have access to the relevant ECSS standards and the ESRANGE User and Safety Manuals.

2.4. Student Training Week and Preliminary Design Review

The PDRs usually take place in February, during and in parallel with a week-long student training week which includes lectures on relevant scientific and engineering

topics, detailed explanations of the launch vehicles' systems, tours of the facilities and 'Ask an Expert' discussion sessions. They also meet their fellow students from other European countries and find out about the other experiment ideas. The venue for this event alternates between SSC Esrange (Sweden) and DLR Oberpfaffenhofen (Germany). The review panel for the PDRs is composed of experts from all partner organisations with backgrounds suited to the technical nature of the experiments being reviewed (Fig. 4). By PDR, the student teams have to demonstrate that their experiment design, including all subsystems, is feasible and reflects the experimental, interfacial, operational and safety requirements. The design should have reached a reasonable level of maturity; upon which the review panel can hopefully offer constructive advice as to how the various experiment design aspects or the general configuration could be further optimised.

Figure 4. PDR of a BEXUS team at DLR Oberpfaffenhofen in February 2013.

2.5. Critical Design Review

After the PDR, the REXUS and BEXUS projects follow different time schedules. The CDR for BEXUS takes place in ESTEC in May/June, for REXUS in June/July in DLR Oberpfaffenhofen. At that time the complete and detailed design of the experiment has to be finalised. The design documentation should be of adequate standard to allow the fabrication and integration of flight hardware to begin and component as well as system testing should have begun.
During this 2-3 days event, student teams will also have some lectures to prepare for the next steps of the programme, interface discussions (Fig. 5) for each vehicle and access to an 'Ask an Expert' session, at which any technical issues can be raised and addressed in a less formal environment. One student from each team will also get the opportunity to participate in a 2 days long Flight Soldering and Harnessing Techniques course.

2.6. Integration Progress Review

The IPR is a one-day event which is held usually in July for BEXUS and in August for REXUS at the institutes of the student teams. This review is performed by a EuroLaunch representative and its main purpose is to ensure that the teams are making adequate progress in-line with their project plan and will be able to meet their experiment delivery deadline. At this phase of the project lifecycle, the various experiment sub-systems are anticipated to have reached the following stages of development:
- The experiment design should be frozen,
- The design documentation should be of adequate standard to allow for the experiment hardware to be fabricated and integrated by a third party,
- The majority of the hardware should have been fabricated,
- The majority of the software should be functional,
- The verification and testing phase should be well underway.

Figure 5. Expert presentation during BEXUS 16 and 17 CDRs at ESTEC in May 2013.

2.7. Experiment Acceptance Review

The EAR is the final review in which the experiment is qualified for flight. The satisfactory passing of the EAR effectively signifies the hand-over of the completed and fully functional experiment from the experiment team to the launch authorities. The review is generally conducted by a EuroLaunch, representative at the institutes of the student teams or in another agreed place, around end of August for BEXUS and October for REXUS. The students should present their fully integrated experiment and perform a flight simulation test with the REXUS Service System Simulator.

2.8. REXUS Testing Phase

2.8.1. Scientific Payload Integration Week

The scientific payload integration week is held usually in December at the DLR Institute of Space Systems in Bremen (Germany). During this event, two da ys are allocated for the integration and testing of all experiments on each of the two rockets. Tasks to be completed during this time include electrical interface tests, cable harnessing, D-SUB connector bracket mounting, mechanical interference tests, vibration testing as required and flight simulation testing of the integrated payload.

2.8.2. Bench Test

The Bench test takes place at DLR Oberpfaffenhofen usually in January or February. This is the final event requiring REXUS student involvement until the launch campaign, and is also the final opportunity for any mechanical additions or modifications to be made to the experiments. After performing individual experiment checkouts, the experiment modules are assembled in flight configuration (Fig. 6), followed by the integration of the nose cone, recovery system and the REXUS Service Module. A number of test cycles and flight simulations are then performed. The flight timelines are tested and improved.

Figure 6. Assembly of the experiment modules of REXUS13 in March 2013.

2.8.3. Spin and Balancing

After completion of the Bench test, the fully integrated payloads are transported in flight configuration to Kista (Sweden) for spin and balancing, where the payload is spun to det ermine imbalances around the longitudinal access and, where needed, additional mass is added to ensure flight stability. Mass, length, moments of inertia, centre of gravity are measured and final trajectory estimations are calculated.

2.9. Launch Campaigns

The nominal launch campaigns last about ten days in autumn for BEXUS and about two weeks in spring for REXUS. The first days are dedicated to the final preparation of the experiments, the flight systems and the vehicles. Functional, interface and system tests are carried out, followed by the assembly of the payloads and vehicles for two launches. Finally, experiment sequence tests and a flight simulation test are carried out to demonstrate that the complete equipment works properly together and according to t he scheduled timeline. This also gives the students a chance to practice the communication with their experiment by telemetry as w ell as t o make a final check of th eir procedures and checklists before flight.

The best and most anticipated waited moment of the programme comes when the balloon is released (Fig 7.a) or th e rocket lifts off (Fig.7.b). But it is also a stressful event for the s tudents as th ey will discover soon if many months of ef fort has achieved a working experiment that transmits the desired data.

As soon as the scientific payload is returned, it is inspected and dissembled, the experiment data is stored and the experiments are packed for transport back to the students' institutes.

a b

Figure 7. a: BEXUS 14 launch in September 2012 b: REXUS 13 launch in May 2013.

2.10. Results Presentation

The campaign does not mark the end of the programme cycles. The students still have to analyse their data, obtain some results and draw conclusions. Around three months after the campaign, the student teams have to submit the final version of their SED document. It serves as the team's final report and must incorporating flight performance information and experiment results as well as a 'lessons learned' chapter, even if the experiment did not function nominally.

At the end of the programme cycle, students are invited to present their results at a final event, the Results

Symposium, in order to receive feedback from scientific and technical experts. Every second year the Result Symposium is organized as an integrated part of ESA *Symposium on European Rocket and Balloon Activities and related research*, where students get the opportunity to present their REXUS or BEXUS project during the various sessions of the Symposium (Fig.8).

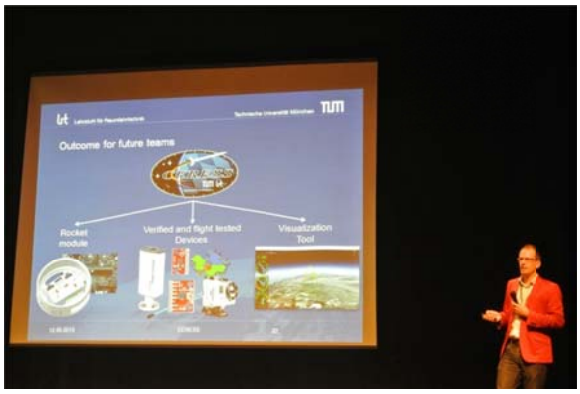

Figure 8. Student presenting a REXUS project at the PAC 2013 Symposium (Thun, Switzerland) in June 2013.

3. IMPROVEMENTS OVER THE YEARS

Over the course of the programme a number of major improvements have been made, In general these improvements have been aimed at aiding the students in having a higher chance of success with their experiment, through closer supervision, more face to face time with experts and standardisation of the design.
In terms of the programme cycles, a face to face CDR has been implemented to avoid the teams moving too far into fabrication with a potential bad design and an IPR has been added between the CDR and EAR to allow an EuroLaunch representative to check up on any design changes between the manufacturing and testing and to enable student teams to ask any questions about the testing of the their experiment. Thanks to the introduction of these two additional review, the EARs are now much smoother. For the REXUS teams, the Scientific Payload Integration Week has been added to avoid squeezing the actions into the Bench test, allow more time for trouble shooting and avoid pushing problems onto the campaign.
With regards to technical improvements significant advancement was made for student testing with the introduction of interface simulators, such as the REXUS Service System Simulator, which is available during IPRs and EARs, avoiding interface problems at Scientific Payload Integration Week or Bench test.
Within REXUS a significant modification was the full modularisation of the experiments, whereby each experiment was to be housed in its own module (rather than multiple experiments in one module or even across modules). Each experiment then has modular mechanical and electrical interfaces to the payload. This essentially makes the scientific payload a modular structure with the ability to move experiments around in the stack or remove them completely.
Standardisation was also introduced in BEXUS through, for example, the standardising of the rail characteristics on all variations of the gondola.
Finally the organisers took steps to simplify the experimenters design choices and the review process through the introduction of standardised components such as standardized electronics interfaces, MIL-connectors and pyro-cutters.

4. SURVEY: BENEFITS FOR THE STUDENTS

4.1. Introduction

It is useful for an educational programme, such as REXUS/BEXUS, to take a look back and examine the benefits of this hands-on opportunity for former participants. Contrary to what one may think, the benefits are not limited to the educational value for the students.
In 2011, after 3 cycles of the programme, a first survey was made and showed that several skills are learnt and significant knowledge is gained through involvement in a REXUS/BEXUS programme cycle that are relevant for future careers in the space community [2]. The following specific skills were investigated in this study:
- understanding of the space project life cycle,
- understanding of space project processes,
- design skills,
- practical skills (such as building/testing),
- teamwork ability,
- confidence to take on tasks in your study/workplace,
- contacts with professionals in the space sector,
- contacts with your international peers,
- opportunities for further study or employment.

This year, after 5 cycles of the programme, a second survey was made to examine the profile of former participants and the benefits of this hands-on opportunity for their studies and careers. The survey mainly focused on:
- personal details (such as gender, nationality, course),
- study at time of participation in the programme,
- involvement in the project,
- benefits of the programme,
- occupation after the participation to the programme.

The survey was conducted electronically through individual survey webpage using SurveyMonkey [3]. The organisers of REXUS/BEXUS directly sent the web link to many past-participants with the request that they try and forward it to those who were unable to be contacted. The survey was conducted confidentially with all questions being voluntary.

4.2. Survey results

163 respondents answered the survey with at least 1 student from each of the 20 survey vehicles.
The following results are detailed as percentages of those respondents who chose to answer the question (i.e. not necessarily the percentage of the full 163 respondents).

4.2.1. Gender and Age of Respondents

The vast majority (~84% of the respondents) were male. The average age of the respondents was 27 years, with the youngest respondent aged 19 and the oldest 37.

4.2.2. Vehicle

There results were skewed towards the more recent vehicles, with 58% of respondents having had experiments flown on the most recent launches in 2012/2013, 25% in 2010/2011 and only 17% in 2008/2009. One can speculate this is due to the students moving on from their universities and no longer having access to their University email accounts or the accounts they associated with their time on REXUS/BEXUS.

4.2.3. Nationality

158 respondents choose to identify their nationality, with 20 nationalities identified in total. One third of respondents identified themselves as a national of one of the top 5 counties of Germany (36), Italy (31), Sweden (17), The United Kingdom (10), Poland (10). 94% of respondents identified themselves as nationals of ESA Member or cooperating states (Fig. 9)

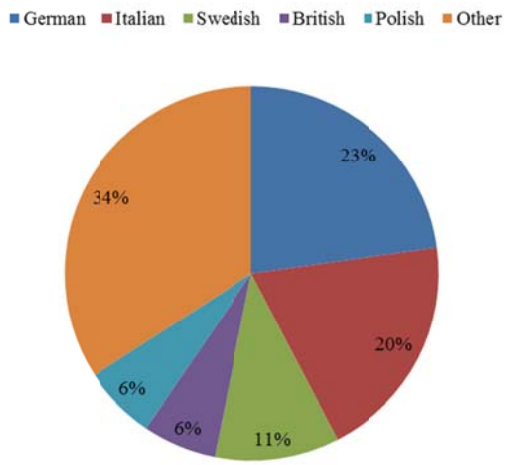

Figure 9. Identified nationality of respondents.

4.2.4. Country of Study

156 respondents identified their primary country of study. With the top 5 countries identified as Germany (39), Italy, Sweden (25), The United Kingdom (13), Hungary (9). In Fig. 10 one can see 74% of respondents studied in one of the top 5 countries, with Hungary replacing Poland in fifth position when compared to nationalities. A trend here is that some students actually studied in Sweden when they were not Swedish nationals, this is something often seen with KTH university (see University section).

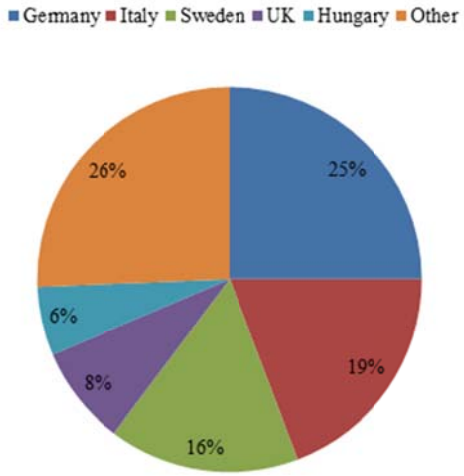

Figure 10. Primary Country of study of respondents.

4.2.5. University of Study and Department

156 respondents identified their primary University of study, numerous Universities were identified, with the most popular as University of Padua (Padova) and KTH, Stockholm, this ties well to the Country of Study of the respondents, and identifies the large groups from Sweden and Italy. In contrast the students studying in Germany come from a large selection of Universities spread throughout the country.
139 students also choose to identify the department name. By department name only, 42% of the students were in an engineering department, 10% in physics department and 13% in a science department. 26% of respondents were in an Aerospace or Space specific department.

4.2.6. University Course

Of the respondents 48.4% are still studying with 51% having completed their degree.
142 respondents identified their course level and 140 identified their specific course. The majority of the students, 63.4%, were at masters level, 19.7% at Doctorate level and 16.9% at bachelors level. Around 11% of the respondents were specifically on the German Diploma programme (labelled as masters level).
The breakdown of the course field as identified by the respondents is shown in Fig. 11. (Note respondents were able to select more than one core theme). Of these courses, 47% of the course titles contained the phrase 'Engineering', 8.6% 'Physics', 10.7% 'Science'. Overall 39.2% of the course titles contained the phrase 'Aerospace' or 'Space'. 155 respondents also identified

whether their participation in REXUS/BEXUS was part of the degree programme.

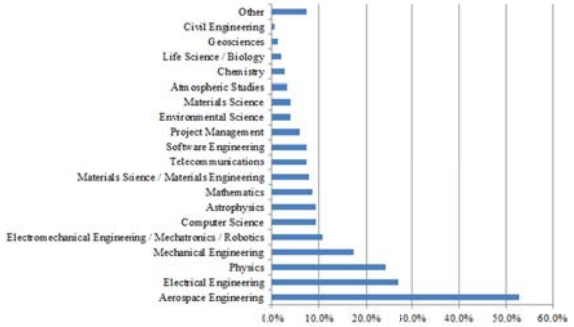

Figure 11. Percentage of respondents whose courses contained each primary theme.

Around half of the respondents stated their involvement was not part of their degree programme with a further 22% stating it was part of a course or module, 21% used it as part of a Master thesis and 9.7% as part of a bachelors thesis. Overall 34.2% stated they had gained ECTS credits from REXUS/BEXUS towards their course, with an average of 17.2 credits. 42.7% of respondents stated they delayed their course to participate in REXUS/BEXUS, the average delay was 5.4 months, with a maximum delay of 1 year.

4.2.7. Respondents roles in Experiment Teams

Of the respondents the main responsibilities identified were electronics (23.5%), mechanics (19.6%), project management (16.3%), only 3.3% of respondents' primary task was outreach and only 3.9%' testing/verification and validation.

The respondents averaged a (self-estimated) workload of 728 hours on their projects, with the highest workloads identified by team members responsible for software (1129 hours), project management (973 hours) and science (900 hours). The lowest number of hours estimated was for outreach (356 hours). The core technical areas of electronics and mechanics had average workloads of 671 and 625 hours respectively.

4.2.8. Results presentation and publication

Around 40% of respondents personally had presented their project at conferences with an average of 2 conferences each. This figure rises to 56.8% of respondents who personally contributed to conference papers. 25 respondents had also published in renowned scientific and/or technical journals (an average of 1.5 journals each), with a further 54 planning to.

4.2.9. Respondents Careers

33.5% of respondents are currently employed, or self-employed with 52.7% remaining in studies. 2.1% of respondents stated they are currently searching for employment. The vast majority of respondents (83.3%) stated that REXUS/BEXUS was relevant for their career, with 38.8% saying it was a springboard. for their career and 43.4% saying it will be at some point. 63.7% of respondents stated REXUS/BEXUS was relevant for their current employment.

Over 50% of the working respondents are in organizations with more than 1000 employees, 64.2% of the respondents are employed in 'space related; careers. 76.4% of respondents said they are now more likely to pursue a space related career

Respondents are now working across 19 countries, including 3 non ESA member of cooperating states (Fig. 12).

4.2.10. Satisfaction

92% of respondents were satisfied or highly satisfied with the result of the project. In general the respondents rated all the learning methods of the project as medium to high in terms of usefulness. Over 95% of the correspondents stated that the project had increased their understanding of space projects lifecycles and processes, their design skills, practical skills, teamwork abilities, and other soft skill sets. In the unconstrained answers the summary of the respondents can be outlined as 'learning a lot through a real hands on project', but with a large workload and occasional communications problems between the partners. In general the response in these sections was very positive with many respondents choosing to use this section to thank the organisers.

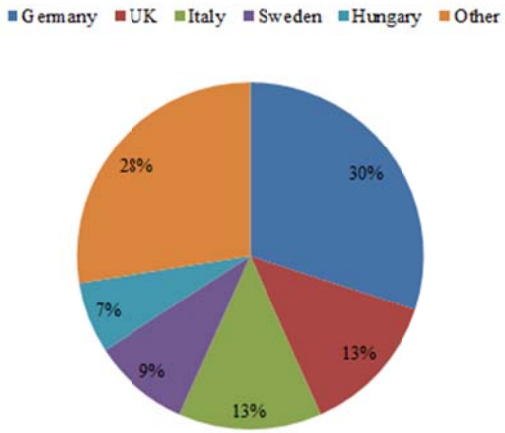

Figure 12. Countries of employment of respondents.

5. OUTLOOK

The next call for proposals for a BEXUS flight in 2014 and a REXUS flight in 2015 will be released at the beginning of September 2013. Students of Germany, Sweden and all the other ESA member and cooperating states are invited to submit a proposal.

6. REFERENCES

1. REXUS/BEXUS – Rocket and Balloon Experiments for University Students. Online at http://www.rexusbexus.net (as of 28 June 2013).

2. Fittock, M., Siegl, M., Stamminger, A., Roth, M., Page, H., Lambert , A., Uitendaal, M. & P ersson, O. (2011), REXUS/BEXUS Alumni – Looking at the long-term personal benefits of participation in a practical student programme. PAC Symposium 2011, 22-26 May 2011, Hyères, France.

3. Survey Monkey. Online at http://www.surveymonkey.net (as of 28 June 2013).
Figures 2-8 are ESA copyrights.

SOLDERING ALLOYS IN REDUCED GRAVITY

SOLAR

Anders Svedevall

Box 812, 981 28 Kiruna, Sweden,
solar.anders.svedevall@gmail.com

Co-Authors: Adrian Lindqvist, Anneli Prenta, Björn Paulström, Björn Sjödahl, Emil Vincent, Fredrik Persson, Hamoon Shahbazi, Jens Kanje Nordberg, Johan Strandgren, Johanna Åstrand, Maja Nylén, Robert Lindberg, Sara Widbom

Affiliation: Luleå University of Technology
Department of Computer Science, Electrical and Space Engineering
Kiruna, Sweden

ABSTRACT

Large funding is required each year for maintaining the International Space Station (ISS) due to need for replacement of components. The cost of this maintenance could be reduced by repairing equipment on site. However, the current method of soldering joints in reduced gravity generates defective connections of components, thus making the repairs insufficient in outer space. The main problem is to solder metals in reduced gravity without obtaining an increase of void fractions, which are inherent due to the lack of buoyant forces on flux and gases. Earlier tests done by NASA, in reduced gravity alone, show an increased amount of void fraction by up to three times as compared to solder created in normal earth gravity. The proposed solution for soldering in reduced gravity is to work in a low pressure environment which enables minimization of void fractions. In vacuum a repairing sequence can be simulated similar to the setting at the ISS but with a reduced pressure. This was tested in an experiment, which was able to melt three samples in vacuum environment and three samples in pressurized environment. To ensure accurate data the solder joints were melted and cooled while in milligravity. This was carried out as the REXUS experiment SOLAR (Soldering Alloys in reduced gravity) in cooperation with several space agencies throughout Europe. The SOLAR experiment was launched with a sounding rocket from Esrange Space Centre, Kiruna (Sweden) in May 2013. After the flight the samples have been analysed at the Kemi-Tornio University of Applied Sciences in Finland by using an Xray scanner to inspect the void fractions in two dimensions. The result of the reduced gravity soldering have been compared to the similar studies done in the SoRGE and CLEAR projects by NASA, and to the samples created in the pressurized environment of the SOLAR experiment. Suggestions on how to obtain improved soldering joints in space are given based on the final test results.

Proc. '21st ESA Symposium European Rocket & Balloon Programmes and Related Research',
9–13 June 2013, Thun, Switzerland (ESA SP-721, October 2013)

Introduction

Human space missions is a challenging task where there is a never ending demand for lower mass and volume solutions. However it's critical for the the mission that there are backup systems and backup instruments which can be used in case of failure. Currently (Jul-2013) astronauts on board the ISS rely on either replacing malfunctioning units altogether or living without them as the crews ability for in situ repairs is limited. After the unit is removed it is returned back to Earth for inspection and reparation[1]. In order to improve the efficiency of mass and volume, rather than replacing an instrument or using multiple systems for redundancy, the instrument can be repaired using backup components. The component that is the source of failure can then be removed and a new component can be soldered onto the same circuit board. In order to do so a soldering procedure suitable for space has to be set up in order to assure space qualified solder joints.

Previous NASA projects SoRGE and CLEAR were conducted on board parabolic flights and the ISS to research low gravity effect on solder joints. The result indicated an increase of voids in solder joint produced in reduced gravity [1] [2]. The voids are produced by a chemical reaction when the flux in the alloy is heated producing oxygen[1]. Other sources such as water vapour from the printed circuit board is also a possible suppliant of of voids.

Voids can also be found in most solder joints created in the standard gravitational pull at ground level on Earth. In order to diminish the voids in the solder joints, vacuum soldering has been used for decades to produce high quality joints for special high demanding applications. The vacuum provides a pressure difference between the voids within the solder and the outside environment which ultimately allows the gas bubbles in the solder to escape giving a uniform density of the alloy.

As vacuum soldering can be used for reducing the number of voids on Earth it is also an interesting aspect to investigate for reduced gravity soldering in order to improve the solder joints enough for space applications. This could resolve the issues experienced in the SoRGE and CLEAR projects.

[1]Soldering in a Reduced Gravity Environment (SoRGE) - John W. Easton, National Center for Space ExplorationResearch

[2]Component-Level Electronic-Assembly Repair (CLEAR) System Architecture - Richard C. Oeftering, Martin A. Bradish, Jeffrey R. Juergens, Michael J. Lewis, and Daniel R. Vrnak Glenn Research Center, Cleveland, Ohio

Experimental Set-up

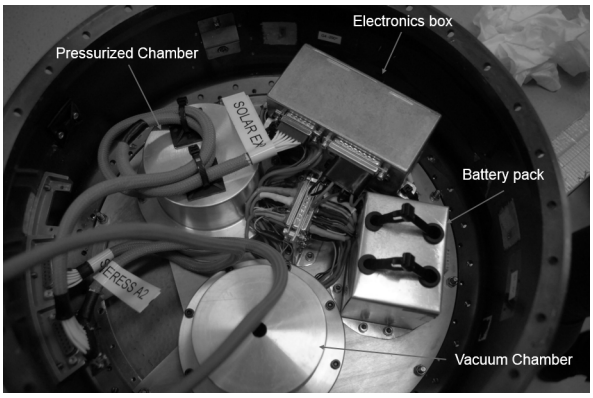

Figure 1: Experimental set-up

To investigate the effect of vacuum on solder joints produced in milligravity an experiment was set up which could be flown on a sounding rocket where the soldering procedure would take less than 30 seconds and in which the samples should be melted and hardened. In order to see whether the result is improved in comparison to specimens produced in a pressurized environment, two sets of samples were produced at the same time where the difference could then be investigated. To compare the result with the result from vacuum soldering on Earth the experiment was run under normal Earth gravity at ground level.

Table 1: Sample environment set-up of the four test scenarios

Test scenario	**Pressure** (Bar)
1G Pressurized	1
1G Vacuum	5μ
Low-gravity Pressurized	1
Low-gravity Vacuum	10μ

As the experiment had to be fully autonomous due to the lack of an uplink from the ground station, the melting process was calibrated in advance and carried out by a timer counting from lift off. This was controlled by the electronic circuits shown in Figure 1. In addition the two chambers where the samples are created can be seen. The vacuum chamber has a venting hole in it to allow for a quick transition from pressurized to vacuum environment as the rocket rapidly gains height. The pressurized chamber was sealed using an between the connection between the hat and the base of the chamber. Silicon adhesive was used to seal the feed through of the cables. All electronics and sensors were powered by the service module of the REXUS rocket. However, the resistance wires used for melting the samples were powered by an internal battery pack to accommodate for the large power consumption during the melting phase. Throughout the whole flight the system was recording the temperatures in the chambers and of the resistance wires. In addition pressure sensors were used to monitor the pressure in the vacuum and pressurized chamber. For an overview of the set-up within the experimental chambers please refer to Fig 2. The samples are prepared such that soldering wire is wrapped around a component pin carried out according to a predetermined procedure. The resistance wire is then wrapped around the component pin and soldering wire. Finally the resistance wire is connected to the battery pack through switches controlled by the on board data handling unit. The samples are numbered from one to three where three is closest to the feed through of the cables.

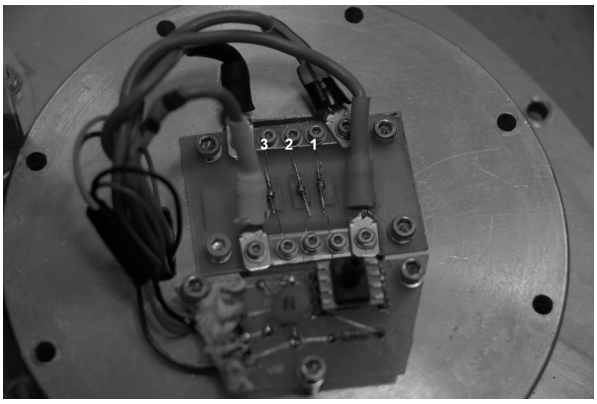

Figure 2: Close up of samples, post flight

Result

Retrieving the samples post flight, the specimens were subjected to a visual inspection which confirmed that none of the samples were damaged at impact and that all the solder had been melted in flight. They were then taken to the Kemi-Tornio University of Applied Science to be analysed with microscope and X-ray scans. Microscopic images were only taken for sample 2 in each test scenario. The resulting images can be seen in Fig 3

To investigate the voids X-ray scans were done individually for each of the twelve samples. The internal images produced could then be used to estimate the void population.

In order to calculate the void fraction in each specimen the software ImageJ was used to determine for each pixel if it belongs to a void or not. This is then compared to the total area of the void which finally yields an estimate of the void to solder ratio. The result from this can be seen in Tab 2.

Table 2: Void to solder ratio

Sample ID	**1**	**2**	**3**	Average
1G, 1 Bar	3.2%	2.4%	0.9%	2.2%
1G, 5μ Bar	3.6%	0%	0.3%	1.3%
mG, 1 Bar	0.9%	4.6%	0.2%	1.9%
mG, 10μ Bar	16.4%	4.8%	11.9%	11.0%

Discussion

As the data in Tab 2 shows, there is a significantly increased void to solder ratio when, in reduced gravity, soldering is applied in vacuum compared to the test scenario in a pressurized environment. This is the opposite of what was expected. Results of the two reference test scenarios at normal gravity were on average similar to each other and to the results from low-gravity in pressurized environment. The variations in the void to solder ratio between the different samples were quite large, so that it remains unclear if any of these three test

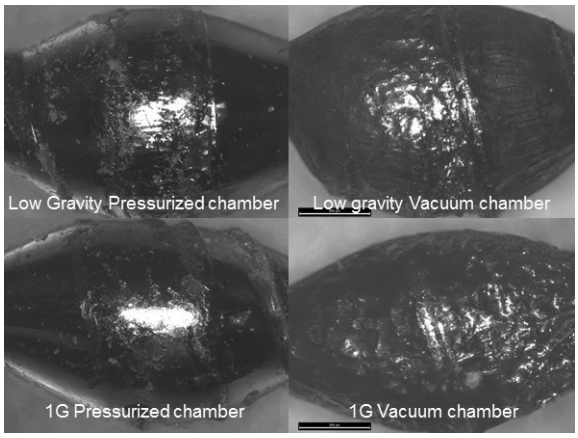

Figure 3: Microscope images of selected samples

scenarios performed better. However, the test scenario with normal gravity in vacuum seems to have produced slightly better solder joints, as expected. The cause of the unexpectedly low quality of solder joints in reduced gravity and vacuum is still not completely understood. One possible reason may be related to the lack of gas around the solder and missing interactions between the liquid lead and the gas in a pressurized environment. At ground level the external force is achieved by gravitation causing the bubbles to be pressed out by buoyancy.

Furthermore the the cooling process of the solder joint proves difficult in a vacuum environment due to lack of convection between the air and the soldering lead. This can be seen in Figure 3 where the solder joints produced in pressure have a smooth shiny surface with a nice wetting angle while the vacuum samples are rough and have a tendency of balling. To control the cooling a gas flow could be implemented into the system where the gas would not only cool the samples but also create an internal flux which could potentially reduce the number of voids.

Qualifying the solder joints for space applications with respect to the void fraction proves difficult as the ECSS documentation lack clear directions for the maximum allowed void population. However judging from the current ECSS documentation the samples produced in pressurized environment in millgravity can be considered acceptable[3].

Conclusion

The vacuum environment produces the best and worst soldering joints in terms of voids count. Combining vacuum with low gravity clearly produces the largest population of voids where normal gravity combined with vacuum causes the lowest void fraction. When the solder joints were produced in a pressurized environment the gravitation had little to no influence. Due to the low sampling statistics of three samples no conclusions could be drawn if the low-gravity environment produces better or worse solder joints.

Further Studies

As mentioned in the "Discussion" section a future project aimed at investigating the effect of a gas flow around the melted solder joints is a relevant subject which could possibly further increase the quality of solder joints in space. It would also give a chance to replicate the result of SOLAR using a soldering technique closer related to a practical and applicable soldering procedure for space use.
Furthermore new studies should be conducted looking at pressures between atmospheric and vacuum environment where a critical pressure could be determined giving the maximum quality of the solder joints.

[3]ECSS Secretariat ESA-ESTEC Requirements & Standards Division Noordwijk, The Netherlands

Acknowledgements

Thanks to Thomas Kuhn and Kjell Lundin who have been our supervisors from Luleå University of Technology and helped us to keep the project going.

Thanks to our contact persons and everyone involved in the REXUS/BEXUS program for the help and for allowing the SOLAR experiment to fly on the REXUS 13 rocket.

Thanks to the sponsors to the REXUS/BEXUS program: ESA, SNSB, SSC and DLR for making the project possible.

Thanks to the SOLAR project sponsors; LTU, LKAB, TRIBOTEC, TÄTRINGEN TEKNISKA AB and IRF for believing in the capability of the SOLAR project and giving financial support.

Thanks to the staff at IRF who's been taking time of their busy schedule to help us with design, building and testing.

Thanks to Petri Ronkainen and Jaana Kauppi at the Kemi-Tornio University of Applied Science for letting us use their lab to analyse the samples and for their expert advice.

Thanks to Jussi Putaala at the University of Oulu for the expert advice and dedication to help us.

Thanks to Esa Vuorinen at Luleå University of Technology for the expert advice and helping us to set up the foundation the project.

References

[1] - Soldering in a Reduced Gravity Environment (SoRGE) - John W. Easton, National Center for Space ExplorationResearch.

[2] - Component-Level Electronic-Assembly Repair (CLEAR) System Architecture - Richard C. Oeftering, Martin A. Bradish, Jeffrey R. Juergens, Michael J. Lewis, and Daniel R. Vrnak Glenn Research Center, Cleveland, Ohio

[3] - ECSS Secretariat ESA-ESTEC Requirements & Standards Division Noordwijk, The Netherlands

MUSCAT EXPERIMENT: ACTIVE FREE FALLING UNITS FOR IN SITU MEASUREMENTS OF TEMPERATURE AND DENSITY IN THE MIDDLE ATMOSPHERE

M. T. Bordogna, L. Fidjeland, M. Fjällid, M. Galrinho, A. Haponen, A. Hou, N. Ivchenko, D. Kristmundsson, Ó. L. Lárusdóttir, M. Lejon, M. Lindh, E. Lozano, P. Magnusson, A. Myleus, B. D. Oakes, and G. Tibert

Royal Institute of Technology (KTH), 100 44 Stockholm, Sweden, muscatexperiment@gmail.com

ABSTRACT

The main scientific objective of the MUSCAT Experiment is to develop a technique to reconstruct temperatures and density profiles in the middle atmosphere using active spherical probes. The MUSCAT experiment was launched on May 9, 2013 on the REXUS-13 sounding rocket from Esrange, in northern Sweden. The experiment ejected four probes that collected raw GPS signal. The experiment design and preliminary results are presented here.

Key words: MUSCAT; GPS; REXUS; KTH.

1. INTRODUCTION

For any study done in the middle atmosphere it is important to have the temperature profile. There are a few ways to obtain middle atmospheric temperatures through methods, each with its advantages and disadvantages. The altitude resolution of satellites and LIDAR measurements is insufficient for regional atmospheric studies. LIDARs are often limited by both clouds and daylight as well as requiring long integration times, up to many hours, to be able to find temperatures; satellites only measure at very sparse vertical locations and they also need complicated retrieval techniques to derive the temperature. There is a strong need for precise in-situ measurements to verify the temperatures derived from remote sensing techniques.

A well known technique for in-situ measurements is based on passive free falling units, usually inflatable spheres with diameter around 1 m with metallized surface to enable the radar to track their position as function of time. However to achieve the accuracy and precision required, the radar must be a high-precision tracking system [2].

The method proposed by MUSCAT is based on active free falling unites using GPS to determine position of the probes with high accuracy. MUSCAT, MUltiple Spheres for Characterization of Atmospheric Temperatures is a sounding rocket experiment developed at the Division of Space and Plasma Physics at the School of Electrical Engineering and the Department of Mechanics at the School of Engineering Sciences at The Royal Institute of Technology (KTH), together with the Department of Meteorology at Stockholm University (MISU).

The primary objectives of the experiment are:

- Proof of concept of a multi-point ejectable subpayload for the derivation of temperature and density profiles in middle atmosphere.
- Observation, using multi-point measurements, of the horizontal structure of temperature and density profiles.

The objective of this paper is to present the MUSCAT Experiment and its preliminary results. In sections 2 and 3 the scientific objectives and experiment timeline are presented. In section 4 the design of the experiment is described. Preliminary results and conclusion are discussed in sections 5 and 6.

2. SCIENTIFIC DESIGN

During the free fall the forces acting on each probe, and the direction of the total velocity vector are illustrated in Figure 1. The forces are the gravity force (mg) and the drag force (F_D) . Using the equation of motion, it is possible to write a system of equations for the forces acting in the vertical and horizontal directions respectively:

$$\begin{cases} ma_V = mg - \frac{1}{2}\rho_\infty A C_D |V_\infty| V_\infty \cos\theta \\ ma_H = \frac{1}{2}\rho_\infty A C_D |V_\infty| V_\infty \sin\theta \end{cases} \quad (1)$$

where m is the mass of the spherical probe, g is the acceleration due to gravity, ρ is the density of the atmosphere, V is the velocity, A is a reference area (maximum cross section area for a sphere) and C_D is the drag coefficient.

Proc. '21st ESA Symposium European Rocket & Balloon Programmes and Related Research', 9–13 June 2013, Thun, Switzerland (ESA SP-721, October 2013)

The subscript ∞ denotes free-stream conditions. From the vertical component the density can be obtained:

$$\rho_\infty = -\frac{2m(a_V + g)}{AC_D|V_\infty|V_\infty \cos\theta} \quad (2)$$

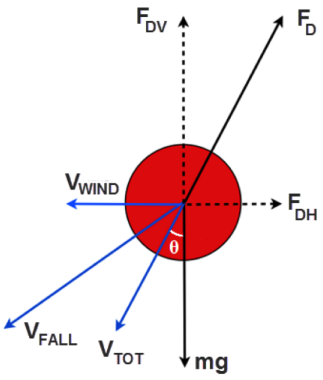

Figure 1. Forces acting on the probe during free fall.

In order to calculate ρ position, velocity and acceleration of the probe must be known. The probes carry internal sensors and an antenna which receives GPS raw signal. Using Eq. (2) one can integrate the hydrostatic equilibrium:

$$\mathrm{d}p = -\rho_\infty g \, \mathrm{d}z \quad (3)$$

where dp is a differential variation in pressure and dz is a small change in altitude. Using the equation of state for perfect gas:

$$p = \rho_\infty \frac{R}{M} T_\infty \quad (4)$$

R is the universal gas constant, M is the molar mass and T_∞ is the temperature in the free-stream, one can obtain the temperature profile:

$$T_\infty(h) = T_\infty(0)\frac{\rho_\infty(0)}{\rho_\infty(h)} + \frac{M}{\rho_\infty(h)R}\int_{z(h)}^{z(0)} \rho_\infty g \, \mathrm{d}z \quad (5)$$

where $T_\infty(0)$ and $\rho_\infty(0)$ is the temperature and density at the beginning of the fall, respectively. A detailed derivation of Eq. (5) can be found in appendix of [1].

The coefficient of drag, C_D (Figure 2), has been obtained by gathering accurate experimental data from literature [4], [5] and [6] (estimated error of maximum +/- 2%), for a suitable range of Mach and Reynolds numbers, and by the use of an accurate polynomial for the drag coefficient in creeping flow. Data on the drag coefficient were missing for a small region of low Mach numbers and high Reynolds number (above $2{\cdot}10^6$) which are expected below 10 km altitude. At these high Reynolds numbers the drag coefficient is expected to change very little and the closest value of the drag coefficient for a given Mach number is used.

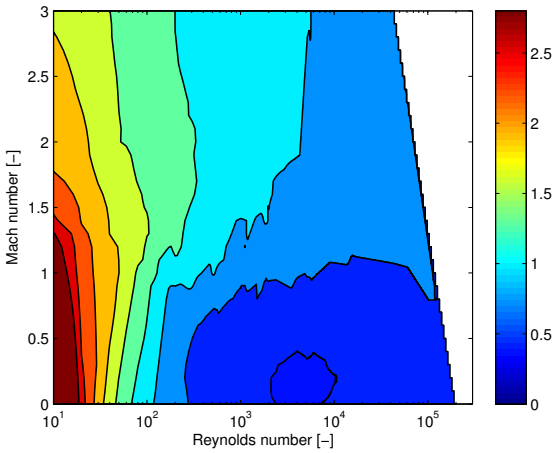

Figure 2. Drag coefficient of the sphere.

3. EXPERIMENT OUTLINE

The experiment involves ejecting four spherical probes, or Free Falling Units (FFUs), from a REXUS rocket module. The module, called Rocket Mounted Unit (RMU), carries the FFUs to an altitude of approximately 60 km where they are ejected from the rocket while it is spinning at 4 Hz. The FFUs will then continue the ascending phase until the apogee at 85 km. The FFUs record raw GPS signal and inertial sensor data as they travel through the atmosphere.

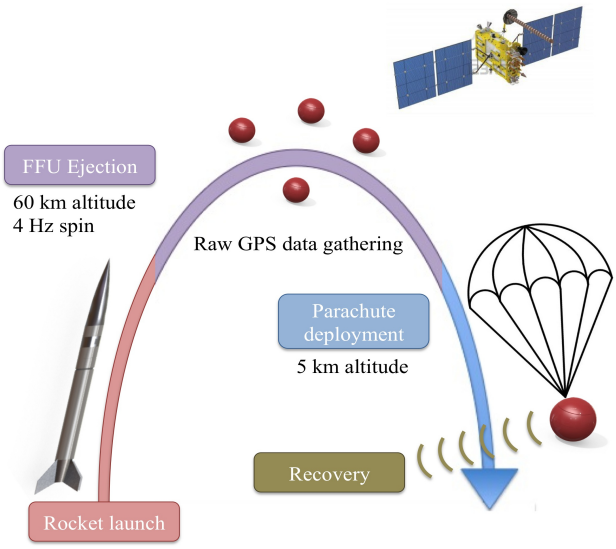

Figure 3. The flight phases of the MUSCAT Experiment.

At an altitude of 5 km the FFUs deploy parachutes and switch from raw GPS data logging to transmitting coordinates from a commercial GPS unit to the recovery team which locates and retrieves them upon landing. The GPS read-out data are then analyzed to obtain velocity and acceleration of the FFUs during the free fall. These data

are used, along with the drag coefficient of the FFUs, to derive the atmospheric density and temperature profiles. The experiment timeline is shown in Figure 3.

4. DESIGN OVERVIEW

The MUSCAT experiment occupies one rocket module in the payload stack. It consists of Rocket Mounted Unit and four Free Falling Units.

4.1. Rocket Mounted Unit (RMU)

4.1.1. Mechanics

The RMU (Figure 4) consists of a rocket cylinder, the ejection system and hatches, a pyrocutter module and rocket mounted electronics.

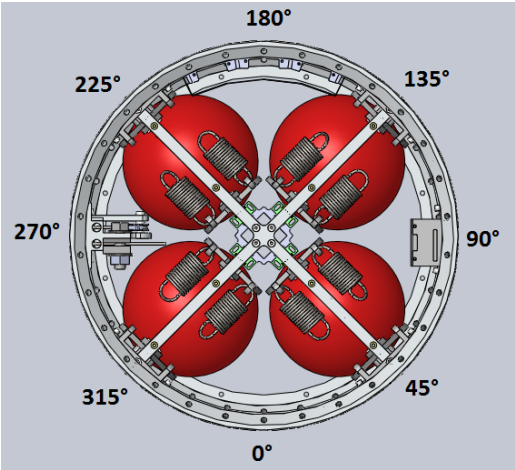

Figure 4. Rocket Mounted Unit (RMU). Openings for the ejection of the FFUs are positioned at 45°, 135°, 225° and 315°. Pycocutter module is positioned at 270° and onboard camera is at 90°.

The rocket cylinder is a REXUS rocket module with 220 mm height and 356 mm diameter, modified to accommodate four openings, a cable groove and additional components (Figure 5). A thorough structural analysis of the strength and stiffness of the rocket module with four 134 mm diameter perpendicular holes on the cylindrical surface shows that increasing the wall thickness from 4 to 8 mm (and locally to 12 mm) ensures the stiffness and strength of the module without reinforcement around the holes. The report of the FEM analysis is presented in appendix of [1].

The ejection system releases the FFUs sideways from the rocket by means of loaded springs. The system consists of a four rails, four collars, 16 extension springs and four FFU cages (Figure 6). Each of the four collars is fixed on the inside of the rocket cylinder, around the openings.

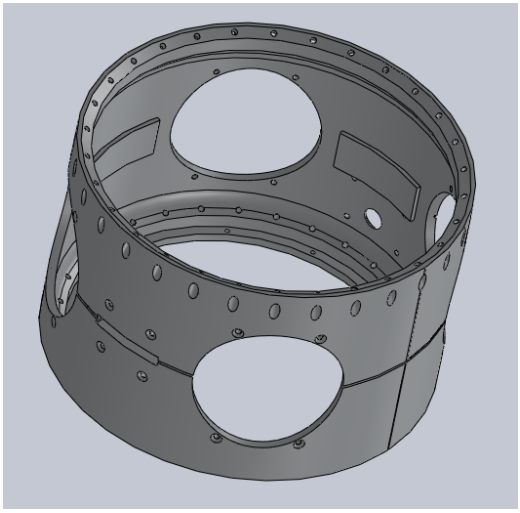

Figure 5. Modified rocket cylinder with four openings, cable groove and additional components.

The rail system consists of two aluminium crosses, with four rails each. The ends of the crosses are fixed to the collar. The FFU cages are constrained by the rails and can slide along them. Extension springs are attached between the inner part of the FFU cages and the collars and pull the FFU out of the rocket during ejection. A hatch is attached to the outer part of the FFU cage and it is ejected with the FFU. The cages are constrained by a 2.5 mm diameter steel cable strapped around the module skin, in the groove and on the hatches.

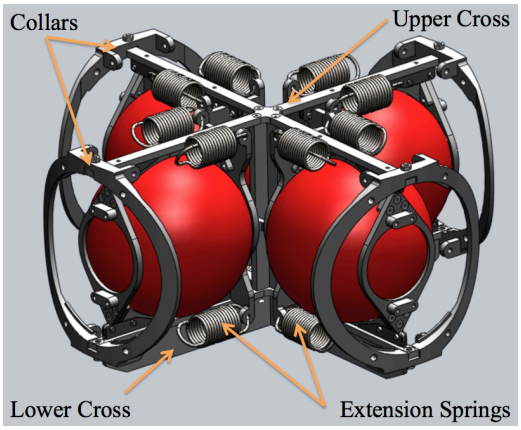

Figure 6. Ejection system with upper and lower crosses, collars and extension springs

This steel cable is cut by two pyrocutters at the ejection time to release the FFUs. To protect other experiments from hot gases and snow, when the hatches have been ejected, two aluminium plates are placed on the upper and the lower part of the rocket module.

The RMU PCB containing the electronics monitoring the FFU is located in the center of the RMU beneath the ejection system. The pin connector is attached to a platform mounted in the middle between the upper and the lower

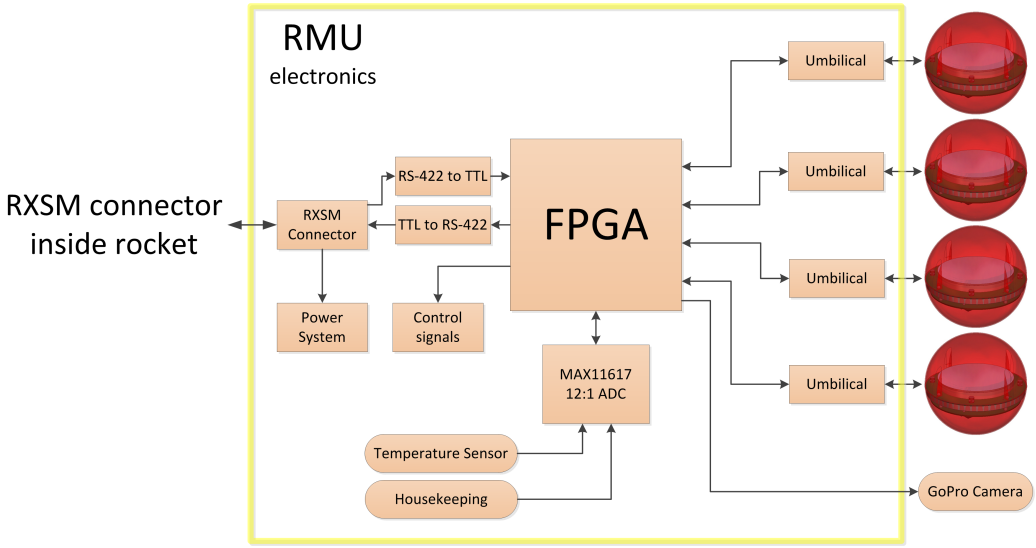

Figure 8. Conceptual diagram of the RMU electronic system.

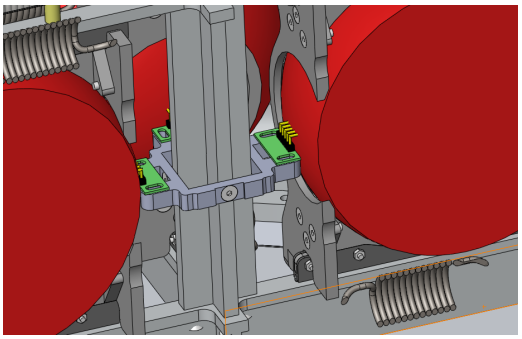

Figure 7. Position of the five pins umbilical connector.

cross of the ejection system and located behind the FFU cage (Figure 7). The receptacle connector is soldered on the top side of the top PCB of the FFU, so it is located along the FFU equator. Since the pin umbilical connectors are fixed, the sliding movement of the FFU cage breaks the connection during the ejection, when the FFUs are ejected.

4.1.2. Electronics

The RMU electronics' most important role is to serve as one part of the interface between the FFUs and ground control station up until ejection. As can be seen in Figure 8, the RMU PCB is connected to the RXSM through a RXSM interface connector and to each FFU. Inside the RMU RS-422 UART signal levels from the RXSM are converted to a standard LVTTL UART to the RMU FPGA. The RMU FPGA works as a data switch which allows commands to be sent from the ground control station and FFUs status to be received at the ground control from one FFU at a time. The FFUs can be charged as needed through the RMU.

The RMU FPGA also controls the RMU housekeeping system and the GoPro HD Hero 3 Black Edition camera that is used to observe the ejection of the FFUs. The RMU housekeeping system monitors the voltages on the RMU PCB and temperatures inside the rocket. This data is sent to the ground control via RXSM and is not saved onboard. The GoPro HD Hero camera is powered by RMU electronics and it is activated via ground control. The footage is stored to the cameras own 64 GB SD card.

4.2. Free Falling Units (FFU)

4.2.1. Mechanics

The FFU is shown in Figure 9. The FFU consists of a spherical structure, a recovery system and a PCB assembly. The FFU is 124 mm in diameter and the mass is 0.44 kg.

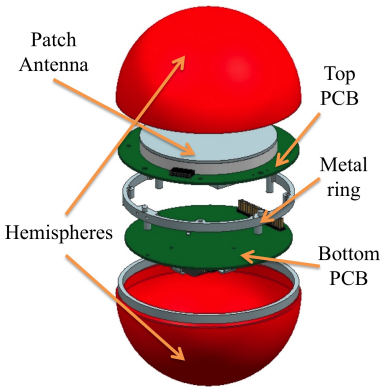

Figure 9. Free Falling Uunit explosion view with hemispheres, top PCB, bottom PCB, metal ring and patch antenna.

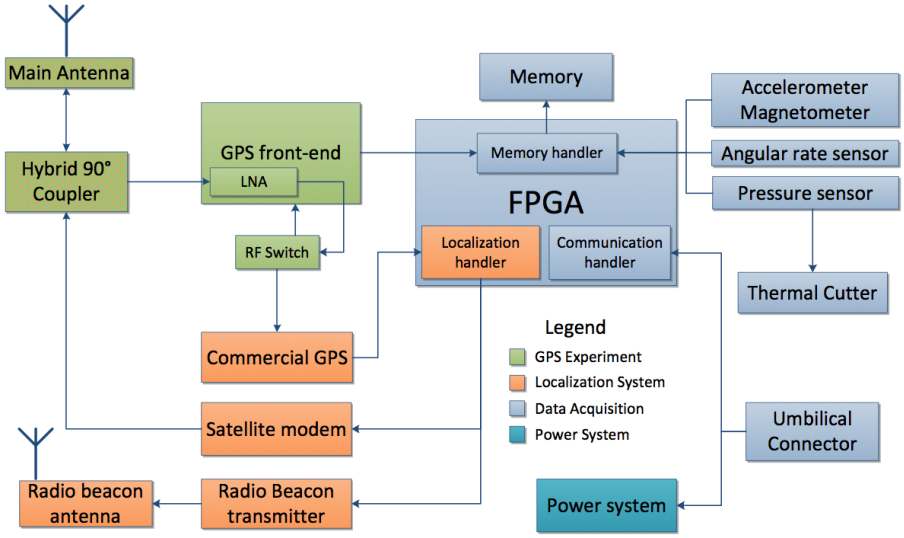

Figure 10. Schematic diagram of FFU system.

The FFU electronics is distributed between the top PCB (D=121 mm), and the bottom PCB (D=112 mm), interconnected by a vertical header/receptacle connector. The antenna is placed on the upper surface of the top PCB and the battery is mounted beneath the bottom PCB using a cage. The two PCBs are screwed onto a metal ring (Figure 11).

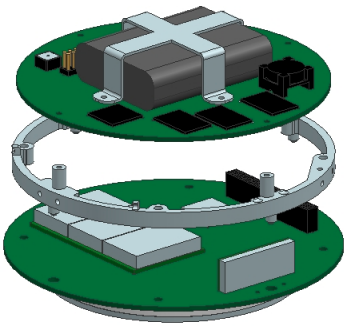

Figure 11. PCB assembly with all large electrical components, upside-down.

The two hemispherical shells that create the outer shape of the FFU are made of Glass Fiber Reinforced Polymer (GFRP). The shells are manufactured in house by Vaccum Assisted Resin Transfer Molding to achieve a controlled outer surface. Three ply symmetrical layup results in a shell thickness of 1.2 mm. High temperature resistant epoxy (Tg up to 220° C) is used.

During flight, the parachute is housed inside the upper hemisphere of the FFU. For the assembly of the upper hemisphere with the PCB assembly a fishing line (Spectra Fiber Rope) has to pass through the holes marked 1-10 as shown in Figure 12. The line is tightened using a custom made winch. On its path the fishing line goes also through a custom made thermal cutter placed under the

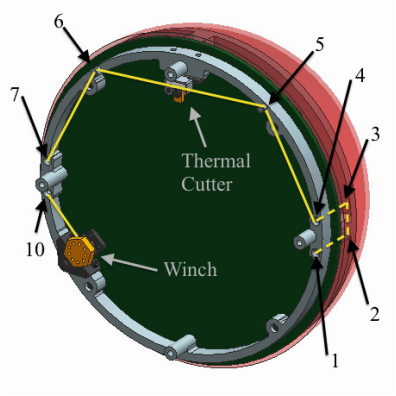

Figure 12. Nylon string securing the upper hemisphere to the PCB assembly.

top PCB. Once the FFU reaches the parachute deployment altitude the thermal cutter is activated. When the vertical constraint on the upper hemisphere is removed the parachute is deployed. A single Top Flight ThinMill 30 X-shape is used for each FFU. A cross parachute has been selected based on its low drift.

4.2.2. Electronics

All the FFUs have the same electronic system. In each FFU there is a GPS experiment, localisation, data acquisition and power system, see Figure 10. The primary objective of the electrical system is to receive and store raw GPS data. This is done with the GPS experiment system which is positioned on the top PCB and consists of a main antenna, GPS front end and a RF switch.

Figure 13. Panorama picture of the ejection of the four FFUs.

The main antenna is a custom made patch antenna with hybrid 90 degree coupler, two feeds and a substrate with ϵ_r=1 is used. These characteristics allow the antenna to transmit LHCP (left hand circular polarization) at 1615 MHz, Globalstar frequency, and receive RHCP (right hand circular polarization) at 1575.42 MHz, L1 GPS frequency. The main antenna is less directive than most patch antennas.

The raw GPS signal received at the main antenna is filtered, mixed and digitized in the GPS front end receiver MAX2769 from Maxim. First the signal is amplified in a low noise amplifier. Then it is routed out of the front-end and through a RF switch of type PE4230 from Peregrine. The switch is controlled from the FPGA and makes it possible to choose if the signal is routed back into the front-end or to a commercial GPS receiver which is used by the localisation system. When the signal is sent back to the front end it is mixed down to a desirable intermediate frequency. The outcome is then sampled and digitized and sent into the FPGA to be written to the memory.

The data acquisition system is positioned on the bottom PCB and monitors all voltages and currents and saves it to memory. Furthermore it contains angular rate sensors, accelerometer with inbuilt magnetometer and a pressure sensor. The data from these sensors are stored to memory. The pressure sensor is used to trigger the thermal cutter when the pressure has risen to a certain value. The thermal cutter is a metal wire which melts the fishing line thus releasing the parachute.

The localisation system is positioned on the top PCB and is activated after parachute deployment. The RF signal from the main antenna is then routed to the commercial GPS receiver of type ET-318 from GlobalSat. This all in one GPS receiver can after fast setup acquire the position of the FFU and send it to the FPGA. The position is then sent through an STX2 satellite modem from Axonn via the main antenna at 1615 MHz. The STX2 can send short messages of up to 9 bytes to the Globalstar service. The satellite messages containing the FFUs positions are routed to a FTP server and displayed on a webpage using Google maps. This provides an easy to follow tracking of the FFUs. For redundancy a radio beacon transmitter of type TX1 from Radiometrix also transmits the acquired position modulated into its VHF signal at 173.250MHz, 173.275MHz, 173.300MHz and 173.325MHz, one frequency for each FFU. The TX1 transmitter chip is used with a radio beacon antenna which is a one fourth the wavelength long monopole. This makes it possible to take a bearing on a FFU when using a directed receiver antenna at the same frequency. The power system makes sure the FFUs battery will last throughout the mission and sees to that all systems are kept at correct voltage levels.

5. RESULTS

5.1. Ejection of the FFUs

Ejection of the FFUs occurred at t+67s when the REXUS 13 was at 58 km altitude and the ejection mechanism performed nominally (Figure 13). All FFUs were ejected and hatches separated from the FFUs after the ejection. Upon ejection all FFUs were subjected to air drag, this can be seen in Figure 14, where in the first seconds after ejection the acceleration is negative. In Figure 14 it can also be seen that the FFUs have the antennas facing up since the acceleration is positive during reentry.

At ejection the rocket was spinning at 3.2 Hz, however the spin rate of the FFUs around the z-axis is lower, between 2.3 and 1.8 Hz, depending on FFU. During the reentry phase the spin rate decreased, this is due to the fact that the increasing air density leads to higher air drag acting on the FFUs. On the x and y axis it is possible to see a clear precession motion of the FFU. In Figure 15 it is possible to see that all FFUs have a negative value of angular rate around the y-axis at ejection. This means that the ejection system introduced a small torque during the ejection. However this did not disturb the dynamic of the free fall.

5.2. Landing and recovery

Parachute deployment performed nominally for all FFUs. Upon deployment all FFUs switched from GPS experiment to commercial GPS. The positions of the FFUs after parachute deployment can be seen in Figure 16. The total descent last between 16 and 21 minutes and the FFUs drifted between 10.2 and 26.2 km..

Signal from the beacon transmitter was lost approximatively two minutes before the actual landing of the FFUs,

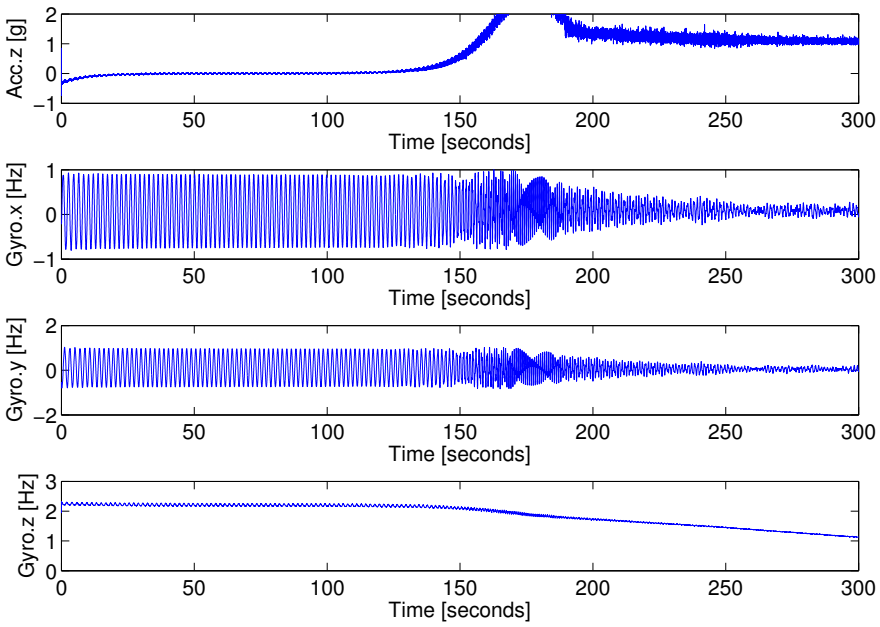

Figure 14. Inertial sensor data of a flight FFU: acceleration in z direction and x, y and z component of the angular rate.

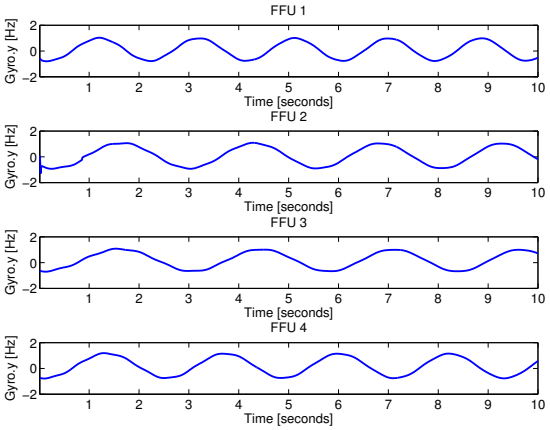

Figure 15. Angular rate around y-axis for the first 10 seconds after ejection.

however modem satellite messages were received until landing. The beacon transmitter signal was lost at low altitudes due to trees and hills between the FFUs and the antenna receiver at Esrange. In those two minute the FFUs drifted between 1 and 4 km depending on FFU.

5.3. GPS experiment

The four FFUs collected raw GPS data from 5 to 9 satellites during the free fall. The data from two of those satellites are shown in Figure 17. The post processed signal is more or less constant for these two satellites except for the high frequency oscillations. These oscillations have the same period as the precession motion of the FFU.

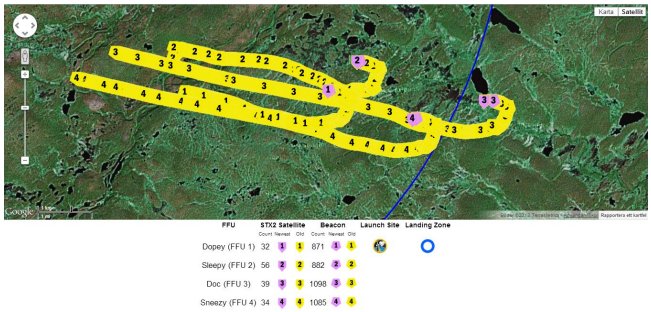

Figure 16. Positions of the four FFU from parachute deployment to landing.

For some other satellites the post-processed signal is not constant, which implies a loss of tracking. In most cases this can be solved with better post processing. In the initial analysis the position and velocity of the FFU have only be found for a limited time interval. One of these interval is shown in Figure 18. In Figure 18 is shown also the simulation of free fall obtained using the C_D introduced in section 2 and the standard atmosphere model.

The discrepancy in the altitude and velocity between the experiment and simulation is believed to mainly be caused by a difference in density between the standard atmosphere and the atmosphere above Kiruna the day of

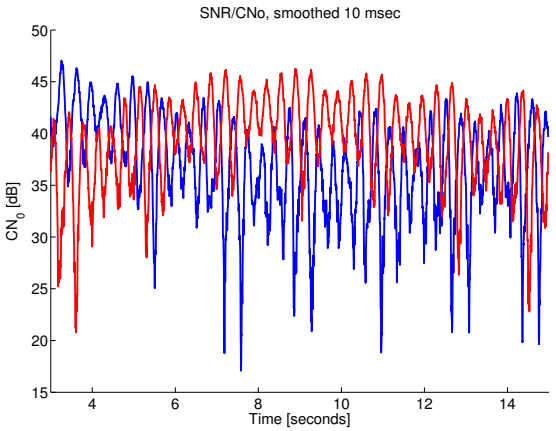

Figure 17. Post-processed signal to noise ratio for two satellites.

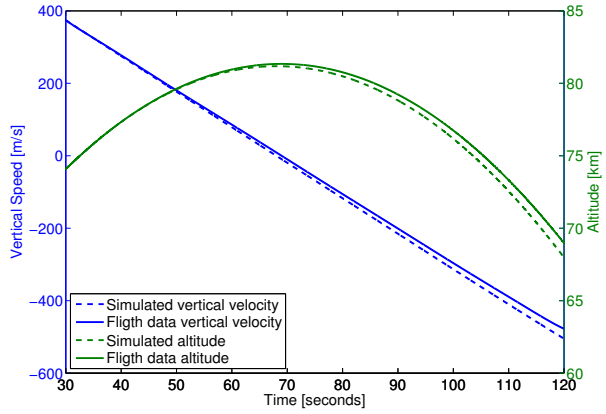

Figure 18. Altitude and vertical velocity of the FFU during free fall from flight data and simulation.

the launch. Additional sources of error can be effects due to wind, the 2% error induced by the estimated value of the drag coefficient or a small difference in the gravitational constant used in the simulation compared to the one at Kiruna. The temperature in the atmosphere may also be different than the standard atmosphere, giving a slightly different Mach number and in turn a slightly different drag coefficient. The temperature and density profiles will be obtained in future post-processing of the experimental results.

6. CONCLUSION

The experiment has proven its functionality and all systems and subsystems performed nominally. One of the four FFU malfunctioned during the flight and part of the flight data are missing. However this did not compromise the experiment data from three FFUs are sufficient to obtain the horizontal structure of temperature and density.

Raw GPS data have been saved in the Free Falling Units and preliminary results shown that the data can be used to derive position, velocity and acceleration of the falling probes. Future work includes the complete evaluation of position, velocity and acceleration for all the probes. These data will be used in the derivation of temperature and density profiles as described in section 2. Moreover GPS results will be used to capture horizontal wind data at different altitudes.

ACKNOWLEDGMENTS

The MUSCAT team has two special thanks. First we would like to thank all the personnel of the Division of Space and Plasma Physics, the Mechanics Department and the Division of Lightweight Structures for the support and the access to the laboratories. Second we would like to thank the sponsors of the REXUS/BEXUS program, SNSB, DLR, SSC and ESA, that allowed us to start this incredible adventure. Thanks also the the external sponsors that provided the MUSCAT Team with materials and components.

REFERENCES

[1] Ó.L.Lárusdóttir et al., *MUSCAT Student Experiment Description*, Royal Institute of Technology (KTH), 4.1 ed., April 2013.

[2] Schmidlin F. J., et al., 1991, *The Inflatable Sphere: A Technique for the Accurate Measurement of Middle AtmosphereTemperatures*, Journal of geophysical research, vol. 96, Dec.1991.

[3] F. L. Bartman. et. al., *Upper-Air Density and Temperature by the Falling-Sphere Method*, Journal of Applied Physics, vol. 27, no. 7, 1956.

[4] A.B. Bailey and J. Hiatt. *Free-flight measurements of sphere drag at subsonic, transonic, supersonic and hypersonic speeds for continuum, transition and near-free-molecular flow conditions*, Technical report, Von Karman Gas dynamics facility, 1971.

[5] W. R. Lawrence. *Free-flight range measurements of sphere drag at low Reynolds numbers and low Mach numbers*, Technical report, Von Karman Gas dynamics facility, 1967.

[6] K. L. Goin and W. R. Lawrence. *Subsonic drag of spheres at reynolds numbers from 200 to 10,000*, AIAA Journal, 6(5):961962, 1968.

CAESAR – CAPILLARITY-BASED EXPERIMENT FOR SPATIAL ADVANCED RESEARCH ON REXUS-14

Eric Zumbrunnen [(1)] **and David Strobino** [(1)]

[(1)] *hepia (University of Applied Sciences – Western Switzerland), 1202 Geneva, Switzerland*

ABSTRACT

CAESAR is a sounding-rocket experiment carried out by students of hepia from HES-SO within the REXUS program. The team has launched on REXUS-14 a capillarity-based experiment to reliably confirm other ground-based experiments. The objective of this flight was to place several sponges in a microgravity environment and acquire images of the fluid distribution around them.

The center element of the experiment, called a sponge, is a propellant management device (PMD) for space vehicles, often used in satellites. It is designed to work even if the vehicle undergoes small accelerations, for example during station-keeping maneuvers.

This flight was the final step to have sufficient data to publish the results of all the researches the team achieved in the past few years. If the results are validated, the team will have a reliable ground based microgravity system to test PMDs.

Key words: REXUS, CAESAR, PMD, sponge, liquid, microgravity, Switzerland, HES-SO.

1. INTRODUCTION

By this experimental campaign, the team was willing to validate theoretical, numerical and experimental data concerning the behavior of liquids in a specific type of a propellant management device (PMD) called a "sponge".

The theory and its applications are based on a publication from Don E. Jaekle Junior issued in 1993 for the 29th AIAA Joint Propulsion Conference and Exhibit [1].

Sponges, which are radial panel shaped devices, can be used at the bottom of a satellite tank to keep the propellant near the outlet.

These devices are designed to work even if the vehicle undergoes small accelerations, for example during station-keeping maneuvers. The fluid is eccentric but stays on the sponge and near the outlet. Thus the injection system of the motor is continuously supplied with the propellant. However, if the vehicle undergoes accelerations over the critical acceleration of the PMD, the fluid will leak out the sponge.

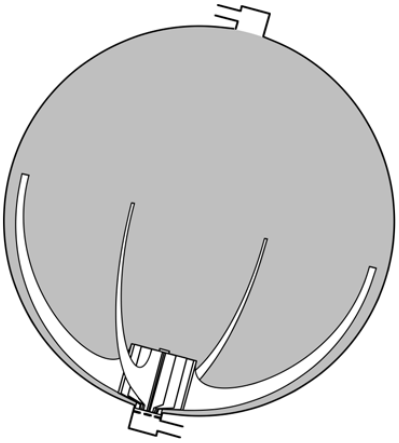

Figure 1. Sponge concept (with 4 vanes) for a satellite tank [1]

In this document, we will refer to the Bond number. The Bond number is a dimensionless measure of the importance of surface tension forces compared to body forces. A high Bond number indicates that the system is relatively unaffected by surface tension effects; a low number (typically < 1) indicates that surface tension dominates, thus the system is under a micro-gravity environment. Intermediate numbers indicate a non-trivial balance between the two effects.

$$Bo = \frac{\Delta\rho \cdot a \cdot r^2}{\sigma \cdot \cos(\alpha)} \tag{1}$$

$\Delta\rho$: difference in density of the two phases

a : acceleration

r : characteristic length (radius of the fluid between two panels)

σ : surface tension

α : angle of contact between the panels and the fluid

Proc. '21st ESA Symposium European Rocket & Balloon Programmes and Related Research', 9–13 June 2013, Thun, Switzerland (ESA SP-721, October 2013)

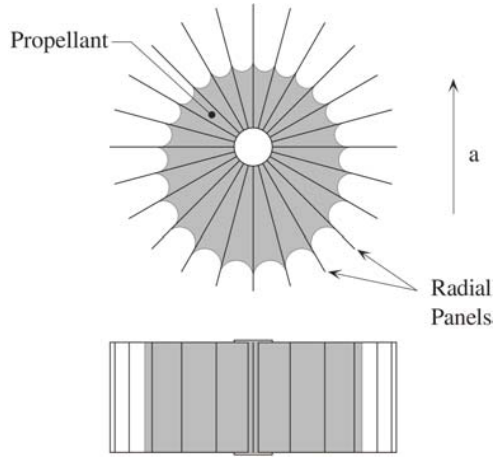

Figure 2. A conventional sponge undergoing an acceleration [1]

This number is used to determine the size of the PMD and the environment conditions. It is also possible to scale the results of all different experiments with the Bond number. By that mean, the team can compare the data of the REXUS flight with the data recorded on ground.

1.1. Experiment background

Professor Roberto Putzu, with the support of two students[1], created a ground-based test facility by buoyancy in 2011 for the observation of this particular phenomenon. In the same year, Eric Zumbrunnen designed another system by magnetic levitation to perform the same experiment. All these experiments were related to the one launched on REXUS-14.

These ground-based systems are cheaper and easier to use than a sounding rocket, a parabolic flight or a drop tower, so they will be very useful to make progress in this particular domain of science, if the results are validated by the REXUS flight.

The CAESAR team, lead by the authors, was created to reliably confirm that the results obtained on ground are valid. In order to perform this validation, they designed and built the experiment described in this document.

In particular, the team was interested in identifying experimentally the behavior of the liquid under Bond numbers approximately equals to 1, when the theory foresees two possible equilibrium states of the liquid and vapor phases arrangement. As no general public document is available and the only publications are theoretical, the team also wished to publish its results as widely as possible.

[1]Gregory Sokolowski and Alban Leandri

2. EXPERIMENT OVERVIEW

CAESAR experiment consisted basically in placing four PMD samples in a microgravity environment and in observing them with video cameras.

Four PMD samples were integrated into a so called “experiment plate”, alongside with their injection system. When the rocket was in microgravity conditions, the injection system filled all the sponges with a liquid[2] having a low contact angle with the material of the sponges (that means that a drop of the liquid will spread on the solid). Each PMD had a different fill ratio, as shown in Tab. 1. This design choice was made in order to collect as much data as possible.

Table 1. Liquid volumes

Sponge #	Volume (ml)	Fill ratio
1	1.125	11.1%
2	1.625	16.0%
3	2.125	20.9%
4	2.625	25.8%
TOTAL	7.500	

A motor integrated into the main shaft (see Fig. 3) has then caused the experiment plate to rotate, in order to impose a radial acceleration on the sponges. Four different accelerations were imposed on the experiment plate to collect more data. Thus, with four accelerations and four different fill ratios, the team recorded sixteen different experiment cases.

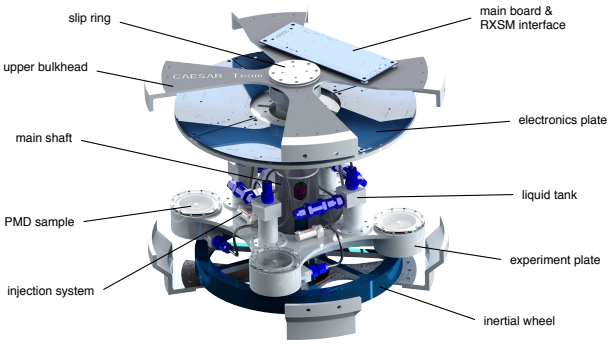

Figure 3. Assembly overview

Each PMD has been observed by a video camera mounted on the “electronics plate”. This plate was directly connected to the main shaft, so it was rotating too: the optical axis of each camera was aligned with the center of the sponge beneath it.

The absolute acceleration imposed on the sponges has been measured by four accelerometers on the electronics plate. These accelerations levels were designed in accordance with the Bond numbers defined in past experiments to ensure the principle of similarity, allowing the comparison of the different results.

[2]PDMS: Polydimethylsiloxane (a silicone oil)

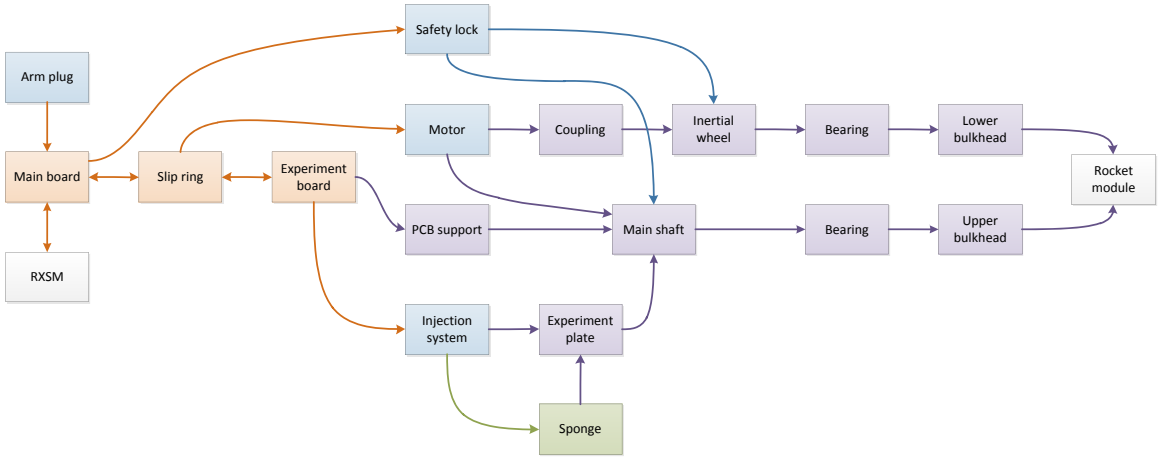

Figure 4. Experiment block diagram

The electronics stored the data on board and sent a part of it to the ground (via the REXUS Service Module interface). The signal transmission between the electronics and the rocket was established through a slip ring.

To reduce the torque transmitted to the rocket, a contra-rotative inertial wheel was integrated beneath the experiment plate. From a mechanical point of view, the whole system was connected to the rocket via a low-friction bearing on each bulkhead. The system was thus isolated from the rocket and the rotation of the experiment plate caused the inertial wheel to rotate the other way.

3. EXPERIMENT SETUP

The CAESAR module consisted of two major subsystems: the experiment and the system to control it. The "experiment plate", as described in Section 2, consisted of four sponges (green) connected to their injection system. The control system was partly mechanical (purple) and partly electronics (orange), as described in details in Fig. 4 and in the following sections. The entire module was linked to the structure of the rocket with an upper and a lower bulkhead. For the electronics, the link with the RXSM was done through a D-Sub connector attached on the main board.

3.1. Experiment

As it has been decided to have four sponges, all the controls of the experiment were also multiplied by four.

The "experiment plate" consisted mainly of the sponges, manufactured directly in a titanium plate to ensure the same state of the material for each test cell and to reduce the amount of fixations around them. Each test cell had its own independent injection system to ensure the reliability of the others in case of failure.

For the same reason, each injection system was commanded by its own experiment board. The liquid tank of this system was attached to the experiment plate, which was screwed on the main shaft. The experiment boards were screwed on the PCB[3] support plate, referred as the "electronics plate", which was also connected to the main shaft. The experiment boards carried the cameras, the lights (LED), the flash memories and the electronics to records all these data.

3.2. Controls

The experiment was driven by a motor placed in the center of the main shaft. The stator was fixed in the main shaft and the rotor was connected through a semi-elastic coupling to an inertial wheel designed to compensate the torque transmitted to the rocket from the experiment.

This inertial wheel was linked to the lower bulkhead with a bearing and the bulkhead was maintained by four brackets attached to the skin of the rocket. On the other end of the module, the main shaft was connected to the upper bulkhead with a bearing. This bulkhead was also connected to the skin with four brackets. This configuration ensured that minimal torques and forces were transmitted to the rocket, because the CAESAR module was partially independent from the rocket.

For the electronics, the experiment boards were connected altogether with a CAN[4] bus and to the main board through a slip ring fixed on the center of the main shaft. The main board was mounted directly on the top of the upper bulkhead. It was connected to the RXSM, the disarm plug and the locking system. It has ensured data and power transmission to the experiment boards, the unlocking of the module after the ascent phase and, thanks to the disarm plug, the management of the injection system during the tests.

[3] Printed Circuit Board
[4] Controller Area Network

4. THE REXUS-14 FLIGHT

The experiment has been successfully launched on REXUS-14 from Esrange in Sweden on the 7th of May 2013. During this short flight, all the systems of the experiment seemed to work as planned. Especially all the housekeeping data were received.

However, after the recovery, it has been discovered that a problem occurred in the experiment located just above CAESAR and caused its complete failure at T+1.5 seconds. The CAESAR team performed an investigation to determine the effect of this failure on the CAESAR experiment.

First of all, it has been confirmed that all the injection systems worked. So, from a technical point of view, the experiment was a success. Nevertheless, it was discovered during the investigation that some metallic particles were projected on one of the PCBs. This issue is developed in the following section.

4.1. Issue

These particles were spread from the upper module (i.e. Gekko experiment) trough the CAESAR module. After investigations, it seems that a current peak in a soldering caused its melting and the spreading of these hot metallic particles all over a quarter of the top of the CAESAR experiment. In particular, as shown in Fig. 5, over the main board and the experiment board #3.

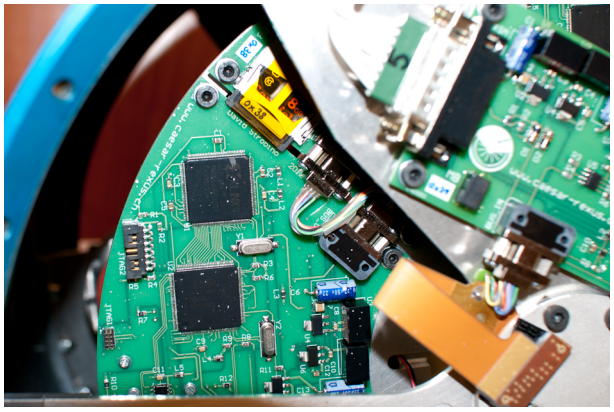

Figure 5. Metallic particles on the experiment PCB

Globally, these particles were stopped by the three layers of silicon coating protecting all the PCBs of the CAESAR experiment. Nevertheless, it has been discovered that a small particle (circled in Fig. 6) melted the coating and caused the failure of the writing process on the SD card #3. Thus, no data were recorded for this experiment board, which means the loss of a quarter of the overall expected data.

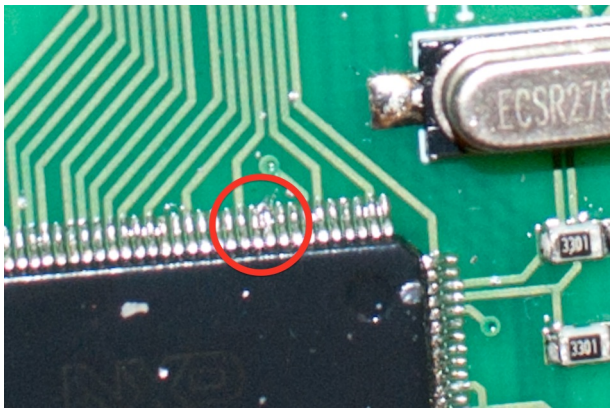

Figure 6. Zoom on the μ-controller of the 3rd experiment board

5. RESULTS

As explained, the purpose of the REXUS flight was to validate the data recorded on ground. So the team was expecting results similar to the ones observed on ground, which were already similar to the theory of the phenomenon, as shown in Fig. 2.

All the results presented below are in their preliminary form; moreover, only some samples are presented. The complete analysis and the comparison of all the different data will be the subject of a forthcoming publication.

Figure 7. Experiment #1 – During injection

Each figure includes a screen overlay, written directly during the flight, to guarantee that the data from the sensors used the same timeline as the images from the video cameras, without the need of post-processing after the flight.

5.1. Injection

The liquid was injected into the sponges right after the nosecone separation. The injection time was set to 10 seconds during the test phase of the injection system. This time was sufficient to inject all the liquid, with a margin in case of an unexpected delay.

Fig. 7 and 8 show the experiment cells a few seconds after the injection.

Figure 8. Experiment #2 – During injection

5.2. Stabilized acceleration

The main results of the experiment are the four different acceleration steps determined in Section 2. Fig. 9 shows the experiment cell #1 during one of these steps.

Figure 9. Experiment #1 – Stabilized acceleration

5.3. Maximal acceleration

Fig. 10 and 11 show the experiment cells during the last step, at the maximal acceleration. These particular results are easily observable as the liquid is clearly eccentric.

Figure 10. Experiment #1 – Maximal acceleration

Figure 11. Experiment #2 – Maximal acceleration

6. FUTURE OF THE PROJECT

In the next months, Professor Roberto Putzu will perform the analysis of all the data recorded on the experiment during the REXUS-14 flight. With these analyses, it will be possible to compare all the theoretical, numerical and experimental data collected during the past years.

If the comparison proves that the ground system by buoyancy can be used for further work, it will be possible to

do propellant management researches on ground at low cost.

The work to be done on the data of the CAESAR experiment is mainly the segmentation of the liquid interface. Some samples of the preliminary analyses are presented bellow.

Figure 12. Experiment #1 – Stabilized acceleration, with segmentation

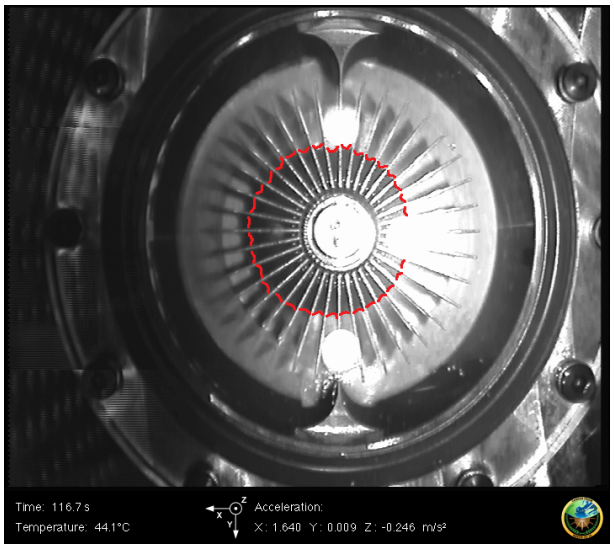

Figure 13. Experiment #1 – Maximal acceleration, with segmentation

However, due to the relatively low image contrast and the shadow of the panels, the best segmentation was achieved by hand, despite the fact that it was planned to use software image processing.

The liquid shape has been extracted, using polar coordinates from the center of the sponge, with a MATLAB script that rotated the image of 1° at a time. For each rotation angle, the end of the liquid shape was pointed along the horizontal axis. The resulting contour is shown in Fig. 12 and 13.

From a qualitative point of view, the results seem to be similar to the theory. Nevertheless, further analyses will give the quantitative aspect of this similitude.

ACKNOWLEDGMENTS

The authors would like to acknowledge the contributions of the other members of the team, Caroline Ratzenberger, for her improvements of the injector in the center of the sponges, and Ludovic Flatrès[†], for the mechanical drawings and his support on the design. They also want to thank Piero Pontelandolfo for his design of the injection system and the tests performed to validate it.

They would like to thank very much Professor Roberto Putzu and Professor Fabien Vannel for the support during all the project.

The main author would also like to give a special thanks to Professor Eric Vittecoq for the very useful talks about mechanics, which helped the team to make it possible.

ABBREVIATIONS

CAN	Controller Area Network (data bus)
PCB	Printed Circuit Board (electronic board)
PMD	Propellant Management Device
PDMS	Polydimethylsiloxane

REFERENCES

1. PMD Technology, D. E. Jaekle, Jr., *Propellant Management Device – Conceptual Design and Analysis: Sponges*, AIAA-93-1970, Andover, Massachusetts, USA, 1993

SCIENTIFIC - EDUCATIONAL MICROSATELLITE «CONDOR»

Oleg M. BREKHOV
Moscow Aviation Institute (National Research University) - MAI, sh. Volokolamskoye, nr.4, 125871 Moscow, Russia, obrekhov@ mail.ru

ABSTRACT

To encourage the development of space technology in Mexico, the Moscow Aviation Institute (MAI) is developing an educational and scientific program to train Mexican specialists in different areas of space engineering. This program is conducted within the framework of the Scientific and Technical Cooperation between the Russia and Mexico, and under the General Agreement between the National Autonomous University of Mexico (UNAM) and MAI. This program is coordinated by the MAI. During the development of the project has expanded the Russian participation with the space Company Lavochkin, and the international cooperation now has the participation of the Central University of Taiwan.The specific objectives of the project are: develop a satellite platform, with high precision pointing in space; the study of precursors of earthquakes; develop a system of remote sensing; consolidate a model of national and international cooperation for the training.

1. INTRODUCTION

MAI was founded in 1930 and is one of the oldest specialized universities in space technology in the world. Many specialists from MAI started the development of the Soviet space technology, twenty five astronauts graduated from MAI. One of the most important space areas MAI is the research and education for satellite technology. MAI is a pioneer in the construction of student satellites. First satellite was launched in 1979.

Now MAI has the status of a National Research University of Russia with four main scientific and educational priorities for the development of MAI as a national research university:

1."Aircraft Systems" (including transport aircraft, helicopters, small aircraft, unmanned air aircraft gliding, helicopter advanced aircraft unconventional layout);

2."Rockets and Space Systems" (including spacecraft for various purposes, including habitable support systems, upper stage rockets of all types and destination);

3."Power systems of aircraft, rockets and space systems" (power plants of all classes of aircraft, engines of various types of rockets, upper stages of space vehicles, engines of spacecraft power systems drives aircraft, etc.);

4."Information and communications technology aircraft, missile and space systems"(including systems, data transmission, telemetry, navigation, intelligent control, radar, optical and optoelectronic systems and their aggregation).

The UNAM is one of the most representative institutions of the Mexican nation. The university has more 300 thousands students. UNAM is a pioneer in Mexico in the development of space technology, UNAMSAT- B satellite made in UNAM, was launched from the cosmodrom of Pletsetsk in the Russian Federation by a Cosmos rocket on 5 September 1996.

2. THE SCIENTIFIC - EDUCATIONAL PROGRAM

The academic program was structured to cover the basic areas required for the design of components and subsystems that comprise the satellite, were used graduate programs and the selection of subjects required in the MAI with the cooperation of academic and research institutions, such as Moscow State University (MGU) and the Institute of Terrestrial Magnetism, Ionosphere and the radio Wave Propagation of the Russian Academy of Sciences (IZMIRAN), where carried out some academic activities.

For the implementation of the academic program is structured three stages:

Stage 1(Table 1) - Postgraduate Study (Masters, PhD) in areas critical to the design of space technology, allowing each specialist deepen their area.

Stage 2(Table 1) - Participation of all Mexican specialists in specific courses aimed at developing space engineering projects.

Stage 3 (Table 1) - Participation in the development process of the satellite technology "CONDOR UNAM-MAI" and developing its space program, including the construction, integration and operation of the satellite.

The basic conception of the scientific - educational program was the formation of a multidiscipline group of Mexican specialists in MAI that can start the development of a space school for Mexico in UNAM. The educational program is to provide an "integral space education" in order to prepare a multidiscipline group of specialists with all the basic scientific and technical knowledge to develop all the stages of a space project.

The main goals of the program are:

- To train specialists in each area involved in the development of satellite platforms.
- To consolidate a model of national and international school for the training.
- To provide the development of aerospace engineering projects for Mexico.

The structure of the education plan was designed in the following three stages:

Stage 1 Graduate Program (Tab. 1).

Each specialist according to his area of study selects Master and Ph.D. degree (2 levels of specialization);

Stage 2 Special Courses (Tab. 2).

All the group of specialists must attend a list of special courses on the main topics for developing satellite technology;

Proc. '21st ESA Symposium European Rocket & Balloon Programmes and Related Research', 9–13 June 2013, Thun, Switzerland (ESA SP-721, October 2013)

Stage 3 The practice in the framework of design and creation of the Microsatellite (Tab. 3).
Our training team has the cooperation with academic and research institutions such as the Skobeltsyn Institute of Nuclear Physics (SINP) of Moscow State University (MSU) and the Institute of Terrestrial Magnetism, the Ionosphere and Radio Wave Propagation (IZMIRAN).

Table 1. Graduate programs selected for training Mexican specialists in MAI

Graduate Programs
Methods to design spacecraft
Electromagnetic compatibility of on board systems of spacecraft
Systems of orientation and stabilization
Systems of telecommunication and telemetry
On board computer and software
On board power supply system
Construction of the satellite
Systems of thermal regulation
Satellite operation

Table 2. Special courses for all the Mexican specialists in MAI

Special Courses
Fundamentals of space systems
Methods of autonomous spacecraft design
Control systems and spacecraft stabilization
System-on board computer and software
System power supply
Electromagnetic compatibility of spacecraft on board systems
Orbital mechanics
Physics of the Sun and space environment
Study of earth station satellite remote sensing
Theory for the survey of seismic precursors
Practice of satellite telemetry

Table 3. Activities for practice defined in stage 3

Practice in the framework of design and creation of the Microsatellite
Development of the requirement specifications of the satellite
Realization of the technical project of the satellite
Integration of the satellite systems
Autonomous and complex testing of the satellite
Launch of the satellite
Flight testing
Control of the satellite
Earth complex for reception of the scientific information
Organization and realization of scientific experiments

3. RESULTS OF THE SCIENTIFIC - EDUCATIONAL PROGRAM

The most important results of the educational program are the Mexican specialists graduated in Ph.D. and Master Degrees.
The scientific results of the Mexican specialist have next 7 directions:
1. “Spacecraft construction”
2. “Strength and thermal regime of spacecraft”
3. “Stability and control of movement”
4. “Computers, complex, systems and networks”
5. “Telecommunications with mobile objects”
6. “Radio engineering”
7. “Instruments and Measuring-Calculating Complexes”

Main results of Ph.D. and Master degree works
The main results obtained through Ph.D. and Master degree works are described below:
1.Microsatellite platform for systems of research earthquakes
2.Heat and strength calculation for the satellite design.
3.The development of experimental and computational methodology for investigation of thermal materials
4.Estimation of accuracy of magnetic stabilization system
5.Design of a satellite power supply system
6.Development of algorithms for the distribution of equipment and cables tracks in according to their electromagnetic compatibility
7.Techniques of recovery computing process and

methods for estimation of their performance
8.Design of fault tolerant on board computer system.
9.Design of the equipment for the control of radio telemetry of a sensing satellite for receiving and transmitting information.
10.The interferences in digital transfer systems.

4. DEVELOPMENT OF MICROSATELLITE CONDOR UNAM MAI

For the development of the satellite CONDOR was organized international cooperation network formed by the UNAM, MAI, Russian Space Company Lavochkin, the National Central University of Taiwan (NCU), and CICESE in Mexico.
The satellite CONDOR UNAM-MAI has as technological aims to study the ionospheric seismic precursors with instruments of the NCU, the test of a solar sensor stabilization manufactured by the Institute of Geography of UNAM and the test of a camera developed by the CICESE for remote sensing of Earth images.
The Central University of Taiwan provides instruments for the study of ionosphere.
MAI develops the educational and scientific program.
MAI designs the module for the integration and operation of the payload.
MAI coordinates the interaction of all the institutions involved in the design of the satellite.
The cost of the satellite project is less than 1 million of US dollars; the duration of implementation will be 12 months and is expected more than 1 year of life time in orbit.
The Tab. 4, Tab. 5, Tab. 6 and Fig 1. show the key technical parameters of the spacecraft.
The design of the satellite has special REDUNDANCY & RECOVERY capacities. The on board computer (OBC) and the power control unit (PCU) are redundant, the Magnetorquers are redundant actuators for Reaction Wheels, the OBC have advanced Fault Tolerance & error correction features. If communication is lost, satellite can provide autonomous work for extended period. If no contact is made for 24 hours, satellite listening for the ground station and sending a short signal every 10 minutes. If the power level in the battery drops to low level, the satellite goes into low power mode, shutting down subsystems to conserve power. The OBC software can be upgraded on orbit.
The characteristics of the attitude control subsystem devices are the next: the spacecraft has as measuring devices sun sensors, Magnetometers, 3-axis gyro (MEMS), Star tracker (optional), GPS. As control devices has micro reaction wheels (3x) and magnetorquers. The modes of operation are Safe mode Sun orientation, inertial orientation, nadir orientation.
The accuracy (preliminary estimate) for Nadir and Inetrial orientation ~1.75 deg (3σ) without star tracker, 0.05 deg (3σ) or better with star tracker. Safe mode Sun orientation ~0.5 deg (3σ)
The payload will consist of a multispectral camera for take pictures with resolution of 20 to 30 m, an electronic temperature sensor and Langmuir probe for measurement of ionospheric plasma temperature, solar sensor and a magnetometer for measuring electrostatic radiation.

Table 4. Technical characteristics of satellite CONDOR UNAM-MAI.

Parameter	Value
Mass	50 kg (45-50% payload)
Life time	More 1 year
Power	50-80 Watt (20-30% payload)
Accumulator capacity	10-15 A/h
Voltage	12 - 28 V
Orientation modes	Safe, Sun, Inertial, Rotation in inertial space, Standby
Safe mode orientation requirements	Power consumption < 20 Watt, Sun orientation
Sun orientation requirements	± 5˚
Inertial orientation requirements (1σ)	± 1˚
The accuracy of the stabilization	< 0,008º/sec
Agility rate requirements	<0,5º/sec
TT&C system	S-band 512 kbit/s – 16 Kbit/s
Ranging data	No
GPS/GLONASS	GPS
Payload data transmittion	No
Orbit	SSO, 600-800
Payload	NCU, UNAM

Table 5. Mass budget of satellite CONDOR UNAM-MAI.

Component	Qnty	Mass, kg	Description
Construction	1	12	Aluminium skeleton, side panels
OBC Unit	1	1.0	OBC, GPS Receiver, UHF Receiver
PCU	1	1.0	Power Control Unit
Sun Array Panel	5	3,5	
Fine Sun Sensor	2	0.07	Digital sensor

ST-200	1	0.05	Star tracker
STIM210	1	0.06	Multi-axis Gyro Module
AMR	1	0.16	Magnetometer
Magnetorquer Rod	3	0.45	
RW90	3	2,7	Reaction Wheels
HISPICO	1	0.08	S-band transmitter
S-band Patch Antenna	1	0.05	
UHF Antenna	4	0.1	
Platform Total Mass		22.0	
SCI Payload		20	
Harness and margins		7	
Spacecraft Total Mass		49	

Table 6. Power budget of satellite CONDOR UNAM-MAI.

Component	Power Consumption, W
OBC	1.5
Sun Sensor	2
Star tracker	0.65
Gyro	1.5
Magnetometer	0.4
GPS Receiver	1
Magnetorquer Rod	3
Reaction Wheel	5.25
S-band transmitter	6
UHF Receiver	0.2
Sun Arrays Power	21 - 29.4
Platform Total Power	
Detumbling mode	6.6
Sun Pointing	8.6
Nadir Pointing, Inertial orientation	10.5
Dump momentum mode	13.5
Session mode	16.5
SCI Payload	2 - 34.5
Spacecraft Total Power	18.66 - 51

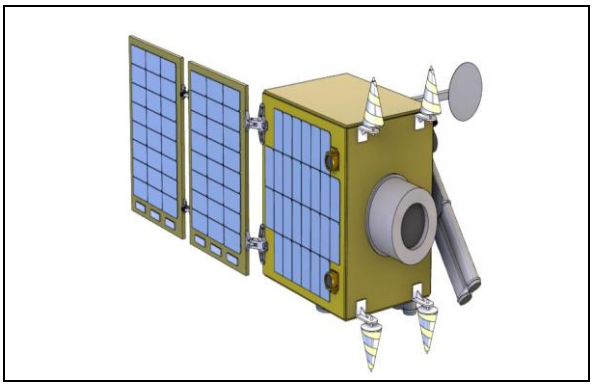

Figure 1. Preliminary 3D view of the satellite CONDOR

5. CONCLUSIONS

CONDOR UNAM-MAI is a project in cooperation that allows Mexican investigators and institutions interact with leading companies in the space area in the Russian Federation.

The project has allowed the formation of a network of international cooperation (Mexico, Russia, Taiwan), unprecedented cooperation on a satellite of this class.

Now in our cooperation Peru is included.

Participation in the project "CONDOR UNAM-MAI", so far, has provided learning and knowledge to develop space technology in Mexico, contributing to the global trend of development of small satellites to perform missions as complex as that of large satellites.

The educational space program exemplifies a model of international school for training of Specialists in space engineering.

THE NORWEGIAN STUDENT SATELLITE PROGRAM – STATUS UPDATE

Jøran Grande
Norwegian Centre for Space-related Education, Norway, joran@rocketrange.no

ABSTRACT

This paper deals with the Norwegian student satellite program (ANSAT), and focus on current status in the program. The Norwegian Centre for Space-related Education (NAROM), Andøya Rocket Range (ARR) and the Norwegian Space Center (NSC) initiated the program, which is planned to go from 2007 – 2014. This includes the development and launch of three student satellites.

1. INTRODUCTION

The ANSAT program was initiated as a successor to the completed NCUBE student satellite project. The goal of the NCUBE project was to build a student satellite from scratch, and send it into orbit it if a launch opportunity came. This is an important difference from the ANSAT program, were the satellites are guaranteed a launch opportunity when the selected university signs the agreement of building it. This will let the students focus more on the satellite, and not worrying about if it will be launched or not. About 100 students from four Universities participated at different levels in the NCUBE project during the five years that it lasted.

In 2006, The Norwegian Centre for Space-related Education (NAROM), Andøya Rocket Range (ARR) and the Norwegian Space Centre (NSC) decided to initiate a Norwegian student satellite program (ANSAT) as a subsequent program to the NCUBE projects running from 2007 - 2014. This includes the development and launch of three satellites within the CubeSat standard.

The program has three participating universities, Narvik University College, University of Oslo and the Norwegian University of Science and Technology (NTNU). Fig. 1 shows an illustrations of the three satellites in the program.

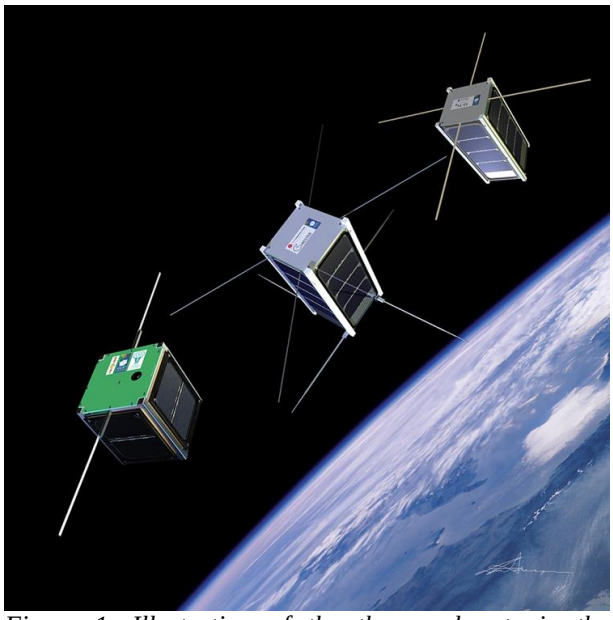

Figure 1. Illustration of the three cubesats in the program.

2. THE SATELLITES

2.1 HiNCube

The first student satellite in the program called HiNCube is a one unit CubeSat. The main goal is to build up a platform for future satellite missions at the university. The payload consists of an imaging camera and several thermal sensors. The satellite was fully integrated and tested by August 2012 and transported to the launch provider ISISpace in the Netherlands waiting for the final integration in the flight pod. The launch of HiNCube has been delayed for some time but is currently expected to be be launched with Dnepr launcher by the end of 2013 from Yasny, Russia. A total of 58 students has participated in the HiNCube project. A picture of HiNCube is shown in Fig. 2. Read more about the hincube project at hincube.cubesat.no.

Proc. '21st ESA Symposium European Rocket & Balloon Programmes and Related Research',
9–13 June 2013, Thun, Switzerland (ESA SP-721, October 2013)

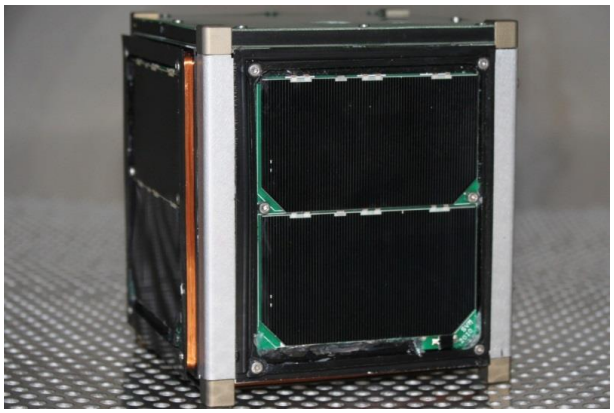

Figure 2. The HiNCube satellite.

2.2 CUBESTAR

During solar storms, turbulent electron clouds are formed in the ionosphere, causing distortion in satellite signals. The phenomenon of electron clouds is far from fully understood. Research in this area can give knowledge that later can be used to notify space weather, and to improve equipment such as GPS receivers. The CUBESTAR mission at the University of Oslo is to try to measure the structures in the electron clouds and improve the resolution 2000-fold, from today's seven kilometres down to the meter level. The payload, Langmuir probes has been in the plasma chamber at ESTEC as shown in Fig 3.

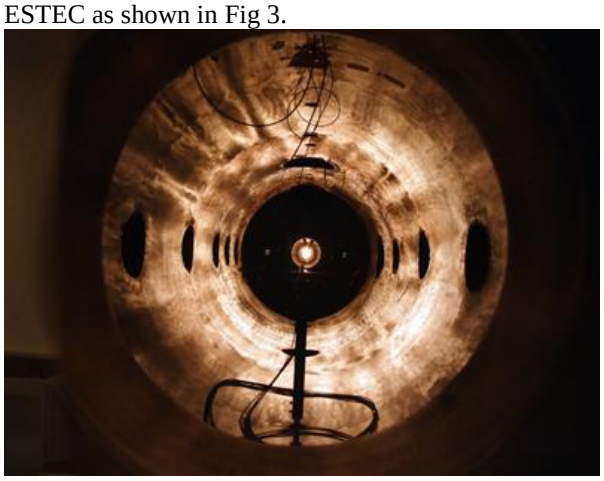

Figure 3. Testing of the CUBESTAR payload in a plasma chamber at ESTEC.

The University of Oslo (UiO) is building this two unit CubeSat called CUBESTAR. They have finalised all subsystems and are currently integrating the engineering model by the end of 2013. The satellite is to be ready for acceptance testing by June 2014 and expected to be launched by the end of 2014.

An illustration of CUBESTAR is shown in 4. A total of 18 students from the University of Oslo has participated in the program. Read more about the CUBESTAR project at cubestar.cubesat.no

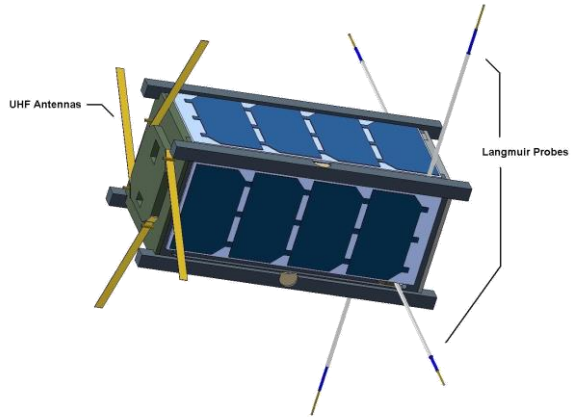

Figure 4. Illustration of CUBESTAR

2.3 NUTS

The third and last satellite in the program is built by the Norwegian university of science and technology. The satellite is called "NTNU Test Satellite" or NUTS. The main payload is an infrared camera for observing gravity waves in the upper atmosphere.

Gravity waves, created by air blowing over mountains and weather phenomena, propagate throughout the atmosphere and drive the large scale flows in the middle atmosphere. Despite this their properties are poorly understood, mainly due to a lack of observational data. At an altitude of about 90 km in the atmosphere we find a layer of OH molecules that emit short-wave infrared radiation. When gravity waves propagate through this layer wave patterns in the radiation intensity are observed. Observation of gravity waves by means of infrared camera has not yet been done from a cubesat.

Both the CUBESTAR and NUTS satellite has a chosen a different design approach than the traditional cubesat standard. This means that the main board is made as a back plane where all subsystems are slotted in as shown in Fig 5.

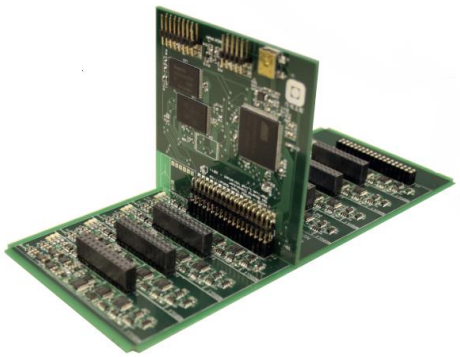

Figure 5. Backplane of NUTS satellite.

This gives an advantages in especially in the test phase where it easy to remove subsystems from the satellite. On

the negative side, they have to design all subsystems themselves and cannot buy any subsystems of the self.

Another unique future of the NUTS satellite is that the structure is made of carbon fibre which leads to a much lighter structure compared to the traditional aluminium structure. A photo of a prototype of the structure can be seen in Fig. 6. So far about 70 student from NTNU has participated in the program. The satellite is expected to be ready for launch by the end of 2014. More information about the NUTS project can be found at nuts.cubesat.no.

Figure 6. Prototype of the NUTS carbon fibre structure.

3. GROUND STATIONS

The student satellite ground station at Andøya was built in August 2008. The technical coordinator for ANSAT, as well as six students from the University of Oslo, built the station during a one week workshop. The station is a typical ground station, utilizing amateur radio frequencies for communication with student and amateur satellites. For future use, the station is aiming to be GENSO compatible. The station is located at 69° 18′ 55″N, 16° 7′ 50″E, and will be able to track 11-13 of the 14 daily passes of a polar orbiting satellite.

In addition to the ground station at Andøya, all of the institutions have built their own ground station located in Narvik, Trondheim and Oslo.

4. STUDENT ACTIVITIES

NAROM and ARR host annual workshops for the participating institutions. The aim of the workshops is to give the institutions that are working on these projects a chance to come together and discuss their ideas on design and solutions and to exchange valued experience. They learn about Norwegian space research and industry, about satellite technology, student satellite subsystems and get updated on the status and technology used in the other satellites built in the ANSAT program. Industry and professors are often invited to hold lectures in these workshops. Among the companies that have been present are, Kongsberg Defence Systems, Kongsberg Norspace and Innovative Solutions in space (ISIS).

In addition to the ANSAT workshop students can get funding to travel to other international conferences and workshops to present their ongoing work.

Thorough workshops and conferences several companies have been supportive to the program. In addition some of the satellites have received support in hardware as well. During the environmental testing of HiNCube NAROM got support from Kongsberg Defence System and NATECH.

ASGARD-II, III and III-b BALLOON FLIGHTS: GROWING A WORLDWIDE HANDS-ON SPACE EDUCATION PROJECT FOR SECONDARY SCHOOL STUDENTS

Erik de Schrijver[(1)] , Roeland Van Malderen[(2)]

[(1)]Sint-Pieterscollege Jette, L. Theodorstraat 167, 1090 Brussels, Belgium, eds@sint-pieterscollege.be, +32 486 787063
[(2)] Royal Meteorological Institute of Belgium, Ringlaan 3, 1180 Brussels, Belgium, Roeland.VanMalderen@meteo.be, +32 2 3730595

ABSTRACT

High altitude or scientific balloons provide a cheap and easy way of reaching extreme altitudes, where Earth's atmosphere gradually fades into interplanetary space. At 30km, with about 99% of the atmosphere below them, these balloons are used by scientists for research in a variety of disciplines: meteorology, atmospheric science, solar physics, cosmic ray studies, UV&IR astronomy and much more. With Asgard, the high altitude balloon becomes also a tool for hands-on space education. Formulating a good research question and figuring out how to technically tackle the problem, designing, building and testing equipment, flying it and processing the data after the flight, reporting on the project and drawing conclusions: everything the professional scientists do in their work, high school students get a chance to do with Asgard [1].

1. THE ASGARD BALLOON PROJECT

The Asgard balloon project is a cooperative effort by the Royal Meteorological Institute of Belgium (KMI-IRM), ESERO (European Space Education Resource Office) and Sint-Pieterscollege Jette. KMI-IRM is providing the balloon, lifting gas and launch logistics facilities and personnel free of charge. ESERO handles catering and transportation, and provides payload integration facilities and an auditorium for the presentations. Sint-Pieterscollege provides the gondola, the recovery team, the manual and technical support to the teams.

2. THE ASGARD PARTNERS

2.1 The Meteorological Institute

The Royal Meteorological Institute of Belgium (KMI-IRM: Koninklijk Meteorologisch Instituut - Institut Royal Météorologique) is a federal Research Institute. It is in charge of making weather forecasts but it is also a center for scientific research. Aimed at improving the forecasts, the reseach also covers other related disciplines as climate research, hydrology and geomagnetism.

2.2 The European Space Education Resource Office

The European Space Agency has been setting up ESERO offices in several of its member states. These offices are to draw upon the genuine fascination for spaceflight young people posess, to motivate them to pursue studies in the so-called STEM-fields: Science, Technology, Engineering and Mathematics. As a secondary goal, ESERO is to enhance literacy in science and technology by using space related themes and resources.

2.3 Sint-Pieterscollege Jette

Sint-Pieterscollege Jette is a secondary school for general education. Located in Brussels, it belongs to a network of schools funded and overseen by the Flemish Community. Its mission statement focusses on self-fulfillment in een open-minded relation to the world, caretaking for our planet, human compassion and the aim for excellence. Sint-Pieterscollege has been a pioneer for hands-on space education projects for high school students since 2004.

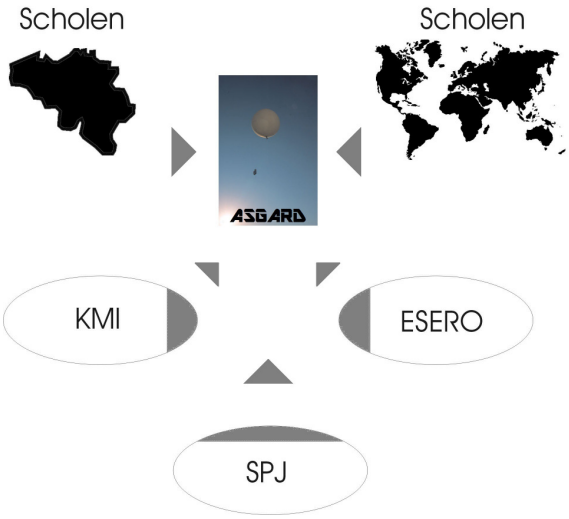

Figure 1: Three partners are running Asgard for two types of schools (Secondary schools worldwide, primary schools from Belgium)

Proc. '21st ESA Symposium European Rocket & Balloon Programmes and Related Research', 9–13 June 2013, Thun, Switzerland (ESA SP-721, October 2013)

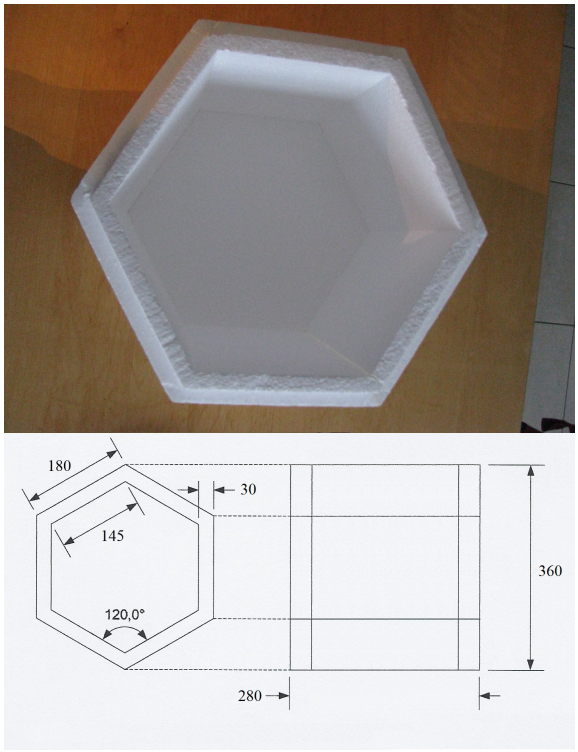

Figure 2: The manual includes technical information on the gondola, the flight parameters, atmospheric conditions to be expected during the flight, the launch location and technical 'do's and don'ts'.

3. ASGARD-II (MARCH 2012)

3.1 Launch campaign

Compared to the maiden flight in 2010, Asgard-II flew a somewhat heavier gondola and the flight was correspondingly longer, reaching a nominal burst altitude of 31417m, but landing after approximately 2,5hrs, whereas the nominal flight time is 1,5hrs. The payload consisted of 2 school experiments from two primary schools (one each) and 11 experiments from 7 secondary schools, including one from Spain and one from the UK. Furthermore, one 'professional' science experiment flew on Asgard-II, investigating DNA stability after exposure to near-space conditions. This experiment by Dr. Cora Thiel (Fig. 3.) was a late addition to the payload, but extremely lightweight, so the organizers accepted to deviate from the Asgard projects 'only student experiments' credo, as a service to Dr. Thiel.

For Asgard-II, the launch campaign calendar was expanded with presentations by the different teams to each other, to improve mutual understanding, scientific, technological and cultural cross-fertilization and a generally enhanced spirit of cooperation.

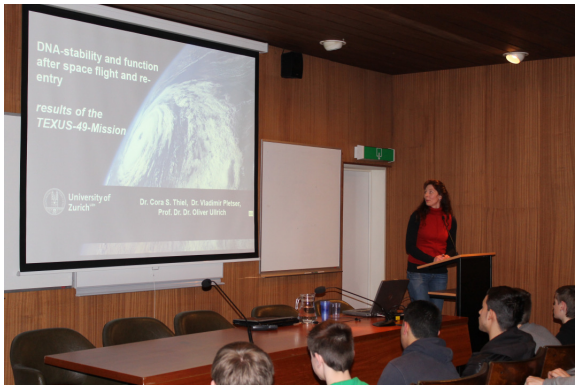

Figure 3: 'Guest-star' on Asgard-II Dr. Cora Thiel explaining her work on DNA stability during re-entry from space, and her experiments on sounding rockets and the Asgard balloon flight.

The launch campaign's overall schedule is to have the teams meet at the Brussels Planetarium (home to ESERO-Belgium) on Wednesday morning and have the teams give their presentations (Fig. 4). The afternoon is spent on payload integration and testing.

Figure 4: High school students from Sint-Niklaas College presenting their HACORD (High Altitude Cosmic Ray Detector) experiment on Asgard-II in March 2012.

On Thursday morning the teams meet at the KMI-IRM launch site in Ukkel for the launch, which takes place after the experiments are powered up and verified. Then a recovery party is sent out to chase the gondola while the balloon is still in flight, whereas the teams are offered a lecture by Viscount Dirk Frimout (Fig. 5), Belgium's first astronaut and president of the Asgard jury, and a Planetarium movie. The plan is to have the gondola recovered by late afternoon and dismantling it in the Planetarium. The teams can then recover their experiment and return to their respective hotels to read out the data stored on-board and preparing their 'first results' presentation, to be given on Friday morning. After these presentations, the launch campaign is closed with a photo session in front of the Planetarium.

3.2 Experiments

Table 1: Participating schools and experiments in Asgard-II

School (Country)(Type)	Experiment
Ecole Communale de Mons (B)(primary)	UV radiation: to know it, to measure it, to protect oneself against it
De Belhamel (B) in cooperation. with a school in Zambia (Z)(primary)	Seeds of friendship
St Paul's School (UK)(secondary)	Detecting cosmic rays in the middle and upper atmosphere
Collège St Michel (B)(secondary)	Measuring different parameters
Collège St Michel (B)(secondary)	Ionic charge distribution in the atmosphere
Colegio Retamar Madrid (E)(secondary)	The truth about the Gas law
Colegio Retamar Madrid (E)(secondary)	Ozone vs UV radiation and height
Sint-Niklaasinstituut (B)(secondary)	HACORD: High Altitude COsmic Ray Detector
Stedelijke Humaniora Dilsen (B)(secondary)	Secure-H-digital, the ideal gas law
Atheneum Willebroek (B)(secondary)	Hi Rez Hi Alt Imager
Sint-Pieterscollege Jette (B)(secondary)	Solar cell performance at high altitudes
Sint-Pieterscollege Jette (B)(secondary)	Temperature and pressure sensors
Sint-Pieterscollege Jette (B)(secondary)	Gas sensor performance at high altitudes

Figure 5: Viscount Dirk Frimout, Belgium's first astronaut (STS-45), president of the Asgard jury, giving a presentation to the teams of Asgard-II.

Figure 6: A contrast-enhanced high altitude picture from the HiRezHiAlt Imager showing the Antwerp harbour, the Dutch Delta and across the English Channel the Great Yarmouth area.

3.3 Results

A power failure occured in the sealed gondola shortly before take-off, preventing some experiments from collecting data for more than a few minutes. Some experiments were self-powered however (such as Hacord and the HiRezHiAlt Imager) and yielded good results. Also, the gas sensor experiment verified the proper functioning of the sensor at high altitudes (low temperatures and pressures). The post-flight failure analysis traced the problem back to a faulty electrical screw connector, and it was therefore decided that all future experiments should be equipped with 60cm of wiring ending in a standard 2-pin header. This should ensure easy and reliable connections to all experiments. Also, teams are reminded of the deadlines for hardware delivery as on-site last-minute changes enhance stress and thereby increase the probability for errors.

4 ASGARD-III (APRIL 2013)

4.1 Launch campaign

While the overall schedule of the launch campaign remained unaltered, compared to Asgard-II, there were some significant additions. A welcome address was given by Sint-Pieterscollege's Principal M. Paul Carlé. Two additional lectures preceded the team's presentations: one on Japanese hands-on space education projects, the other on the British team in the (then just concluded) European Cansat competition. At the launch site, a welcome address was given by M. Daniel Gellens, Director of the Royal Meteorological Institute, and guided visits to the Schmidt camera, the Solar Influences Data Analysis Center (SIDC) and the Solar Physics Department were offered while the recovery team was on its way.

4.2 Experiments

Table 2: Participating schools and experiments in Asgard-III

School (Country)(Type)	Experiment
Basisschool Sint-Jozef (B)(primary)	Space corn: to pop or not to pop
Ecole primaire Saint-Laurent (B)(primary)	The seeds of space
St Paul's School (UK)(secondary)	Examining FM Spectrum Analysis as an alternative to GPS at altitude
Collège St Michel (B)(secondary)	Stratozone: Ozone and CFC concentrations vs. UV radiation at altitude
Colegio Retamar Madrid (E)(secondary)	The truth about the Gas law
Colegio Retamar Madrid (E)(secondary)	Ozone vs UV radiation at altitude
Sint-Niklaasinstituut (B)(secondary)	HACORD-II: High Altitude COsmic Ray Detector II
Stedelijke Humaniora Dilsen (B)(secondary)	The Ideal Gas Law
Stedelijke Humaniora Dilsen (B)(secondary)	O3 vs UV radiation at altitude
Hidaka High School, Wakayama (J)(secondary)	P, T and O3 dependence on altitude in correlation with UV intensity
Sint-Pieterscollege Jette (B)(secondary)	An experimental downlink system for GPS position, T, P and gas sensor data
Sint-Pieterscollege Jette (B)(secondary)	A 3D solid state magnetometer

4.3 Results

With the exception of an experiment that was delivered before being tested, all experiments aboard performed flawlessly. The commercial tracking module failed again however (as it had on Asgard-II) but the recovery went smooth nonetheless as a helpful community worker called in to report his find. The experimental downlink system perfromed well, but an antenna malfunction caused loss of signal shortly after launch.

5. ASGARD-IIIb (MAY 2013)

A unique reflight opportunity arose as the KMI-IRM partner celebrated his 100th anniversary this year and for the occasion offered individuals the opportunity to send 'something' (however frivolous) to the edge of space. An Asgard-IIIb was proposed and accepted with some mass reduction being required to accomodate two 'civilian' payloads: a geigercounter and a CosmoSmurf.

The reflight went smooth and allowed another set of data to be collected by the Hidaka High School team from Japan. Also, the avionics downlink system was tested again. Signal loss reoccured, but the signal was reacquired in flight through a quarter wavelength wire, indicating a possible ground station antenna problem. Subsequent analysis confirmed this preliminary conclusion and precautions are taken to improve the system in preparation of the 2014 Asgard-IV flight. Recovery took somewhat longer than expected but was guided by a small smartphone operated tracking module. This did not require access to wireless internet (as the previously used commercial system did) and as it is much lighter (40grams compared to 150) it is the system of choice for future flights.

6. PROMOTING ASGARD

With 3 out of 7 secondary school teams participating in Asgard-III coming from outside Belgium, Asgard can rightfully claim to be an international hands on space education balloon project. It was noted by the organizers however, that the project is mostly unknown to science teachers in Belgium and efforts were initiated to cope with that situation. In Dutch-speaking Flanders, magazines exist that are distributed to either teachers, parents or pupils, but nothing similar exists for the French speaking part of the country.

It was therefore decided to have flyers printed, explaining what the Asgard project is (in English) and directing readers to more information that is available in either English, French or Dutch.

Figure 7: The exhibition stand at the Brussels 2013 Wetenschapsexposciences, promoting Asgard and demonstrating some student designed hardware.

Moreover, an annual science fair in Brussels called WetenschapsExpoSciences attracts several dozens of schools (most of them French speaking) and hundreds if not thousands of high school students, most of them scientifically inclined. A dedicated exhibition stand, some roll-up banners, the counter case and flyers were put to good use on both the science fair and the open days for the 100th anniversary of KMI-IRM. Interest from teachers and students alike was good, and it is hoped this will result in an increased number of project proposals for the Asgard-IV flight in 2014.

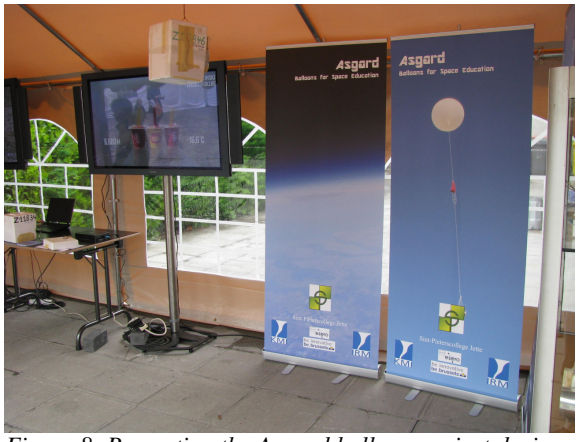

Figure 8: Promoting the Asgard balloon project during the open days at KMI-IRM for its 100th anniversary.

7. CONCLUSIONS

Having a guaranteed annual flight opportunity for an experimental setup of several hundred grams matured the hands-on space education effort at Sint-Pieterscollege considerably. The launch date of the Asgard balloon flights being fixed a full 10 or 11 months in advance, students can start thinking of challenging yet feasible projects whilst still in their 5th grade, hence allowing ideas to grow and evolve somewhat before the 6th and final grade actually starts.

As a result, the students' research projects for their 6th grade show in-depth growth and often offer potential beyond a particular student's time in school. On several occasions such projects have proven to be stepping stones for later students' even more ambitious and/or varied projects.

Furthermore, the recurrent flight opportunities offered to secondary schools in Belgium (and the world) have attracted a number of motivated teachers. While some of them had worked on hands-on projects before (e.g. ESA Cansat competition in Norway 2011, International Cansat Competition in Spain), some have just started to engage in recurrent hands-on projects of their own. This can be deduced from the list of schools that have applied for Asgard-II and Asgard-III after having participated in Asgard-I. The nature of the experiments proposed by these schools corroborates this conclusion: all are improvements on previous experimental setups, digging deeper into the subject or broadening the scope of the original research question.

As of Asgard-II, the balloon launch campaigns were lenghtened to $2^1/_2$ days, making time for preflight presentations by the teams, of their projects' scientific and/or technological goals, and to present details of their experimental setup. Technology transfer is thereby stimulated, even at this modest level. The morning after the flight, a 'first results' presentation by each team concludes the launch campaign, again stimulating students to treat their data and present conclusions the way professionals do.

ACKNOWLEDGEMENTS

The authors wish to thank Anne-Lize Kochuyt from the Royal Observatory of Belgium and Denis Cornet from ESERO-Belgium for their invaluable support of Asgard logistics.

REFERENCES

[1] de Schrijver E. *et al.* (2011). Proc. '20th ESA Symposium on European rocket and Balloon Programmes and Related Research' pp. 271-275, Hyères, France, 22-26 May 2011 (ESA SP-700).

SP. ACE 2011-2013: EXPLORING NEW APPROACHES IN HANDS-ON SPACE EDUCATION FOR SECONDARY SCHOOLS INCLUDING BALLOON, UAV AND ANTARCTIC SCIENCE PROJECTS

Anas Lafkih[(1)], Lisa Machtelinckx[(2)], Brian Segers[(3)], Chloé Vandenhove[(4)], Cedric Van Osselaer[(5)], Erik de Schrijver[(6)]

[(1,2,3,4,5,6)]Sint-Pieterscollege Jette, L. Theodorstraat 167, 1090 Brussels, Belgium,

[(1)]anas.lafkih@hotmail.fr,+32 485 640 177,
[(2)]lisa_machtelinckx@telenet.be, +32 487 385 737,
[(3)]brian-segers@live.com, +32 493 629 640,
[(4)]cvdh95@hotmail.com, +32 472 635 195,
[(5)]cedric.van.osselaer@gmail.com, +32 472 691 588,
[(6)]eds@sint-pieterscollege.be,+32 486 787 063

ABSTRACT

Secondary school students at Sint-Pieterscollege Jette have been engaged in space education projects since 2004 [1,2,3,4,5]. The developments in the 2011-2013 timeframe saw a significant growth in the range of science projects executed, though far less in the competence and know how levels required to carry out these projects. An overview is given of the opportunities that were offered to and used by the students to build their research competence and their motivation for science and technology.

1. ASGARD BALLOON FLIGHTS

Figure 1: The Antwerp harbour, Dutch Delta and in the back across the English Channel the Great Yarmouth area.(Atheneum Willebroek, Asgard-II, March 2012)

In cooperation with the Royal Meteorological Institute and ESERO (the European Space Education Resource Office), Sint-Pieterscollege Jette launches an Asgard sounding balloon to about 30km altitude once a year [6]. Providing these recurrent flight opportunities to fifth and sixth grade secondary school students allows a variety of scientific disciplines to be covered: meteorology, solar physics, cosmic ray studies, UV and IR astronomy, and more.

Lightweight and flexible solar cells were flown on Asgard-II (in March 2012) in order to investigate cell performance between sea level and 30km altitude. The performance of solar cells at a given altitude was to be determined by measuring the voltage-current relation for different resistors. It was hoped the data obtained would allow extrapolation of the results to even greater altitudes and thus permit the development of low-cost on orbit performance prediction. However a power failure during the flight caused the equipment to malfunction. A similar experiment, but with increased resolution is a possibility for a future Asgard flight.

Experimental circuits for analog gas sensors for methane, ethyl alcohol, carbon monoxide, LPG and ozone, connected to a 12 bit analog-to-digital convertor (ADC) were also flown on Asgard balloons to collect altitude profiles. The circuitry and software are being upgraded to allow the collection of enough data to draw vertical concentration profiles with a spatial resolution of about 200m. or better. The data will be used to evaluate the potential of a more extensive monitoring program of pollutants over the Brussels' metropolitan area.

Besides science, the Asgard balloons also serve as technology drivers, inciting engineering-minded students to develop useful subsystems, as a GPS-datalogger or an avionics system downlinking gondola health parameters during the flight. While datalink loss occurred on both Asgard-III and Asgard-IIIb (April and May 2013), the results were encouraging and the possible cause for the intermittent nature of the contact was identified as a ground station antenna problem. A new downlink avionics/tracking system is under development and is expected to be integrated in Asgard-IV in 2014.

Proc. '21st ESA Symposium European Rocket & Balloon Programmes and Related Research', 9–13 June 2013, Thun, Switzerland (ESA SP-721, October 2013)

2. ZERO-TO-INFINITY

Zero-to-infinity is a Spanish company hoping to fly scientific payloads (and ultimately paying customers) to the edge of space. They graciously offered to fly a student experiment free of charge. As time was limited however, it was decided not to attempt the development of a new experiment but to use existing hardware and focus on upgrading the software in order to collect new, expanded datasets. The choice fell on a sound spectrum experiment flown in 2010 out of Kiruna, Sweden [5,7]. In the original experiment 100 sound frequencies were scanned at 30 second intervals. For the upgrade, it was decided to double the data storage capabilities of the hardware by using more capable EEPROM devices. It then became possible to either double the number of frequencies scanned, or to double the sampling rate. However, as a sampling rate of once per minute seemed more than adequate, it was decided to increase the number of scanned frequencies by a factor of four, greatly improving spectral resolution.

Figure 2: The Zero-to-infinity gondola carrying an upgraded version of an earlier sounds spectrum experiment from Sint-Pieterscollege Jette.

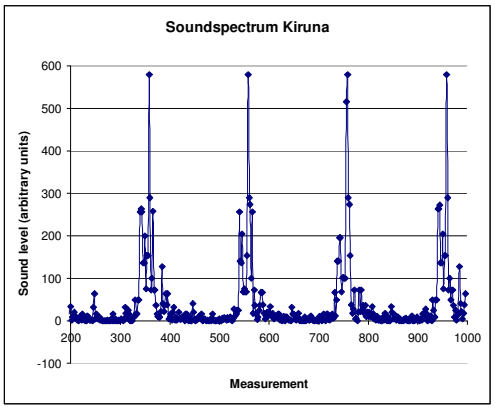

Figure3: The data from the original sound spectrum experiment, to be significantly improved upon by the upgrade.

When the original experiment was carried out over Kiruna in 2010, the results showed a very marked extinction occurring at about 25000m above sea level (Fig. 4). A reflight of the exact same hard- and software on Asgard-I over the Benelux in 2011 failed to confirm this.

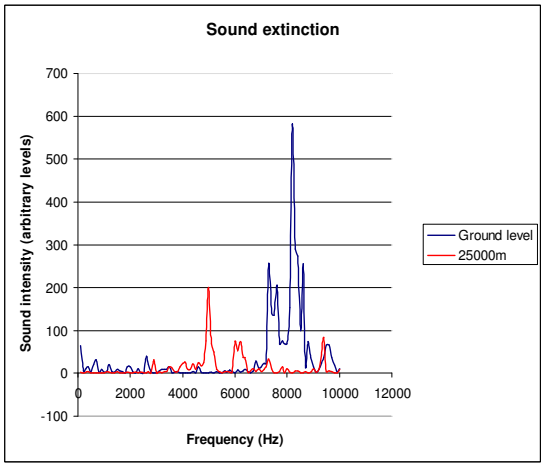

Figure 4: Significant and sudden sound extinction occurring over Kiruna in 2010, but not confirmed on a reflight over the Benelux in 2011.

The data of the Zero-to-Infinity flight are yet to be analysed, but they are hoped to shed light on the sound extinction issue.

3. THE ZEFYR UAV

An RC glider with electric propellor was purchased for remote sensing experiments and to serve as a technology testbed.

Figure 5: A Parkzone Radian RC glider is being used as a science and technology test bed for archeological and environmental monitoring studies.

3.1 The Zefyr conversion

A first technology programme for the Zefyr is also responsible for its christening: making the conversion

from a battery powered to a solar powered sailplane, at the same time improving its eco-friendliness and its maximum flight time. Zefyr therefore stands for 'Zero Emission Flyer for Young Researchers'. However, preliminary studies of propellor performance and available wing area have shown that even with the wings fully covered with solar cells, the motor could not provide enough power for take-off, and barely enough to keep the plane in flight once airborne. It was therefore decided to focus on a solar panel battery charger, pending the availability of higher performance, low weight solar cells.

3.2 Possible Zefyr applications

Contacts with researchers from the Archeology group at the University of Ghent have indicated possible interest for a low cost versatile and readily available RC flyer capable of imaging at low altitudes (tens to several hundred meters). Furthermore, using gas sensors (and possibly also fine dust detectors) may allow to set up a broader investigation into pollution caused by the presence of major traffic axes and/or industrial activities near the Belgian capital.

Cross-fertilization with the Asgard balloon programme is encouraged as the development of avionics for the Asgard balloons could permit the Zefyr to be operated as a preprogrammed aerial imaging device mapping predetermined areas. This would allow to broaden the scope of Zefyr applications from archeology and environmental projects to include agricultural monitoring.

3. ACCESS TO ANTARCTICA

Belgium's Antarctic station is a summer station: it closes up for winter (though that may change in future years as the scientific return of the station continues to increase). During the Antarctic summer season however, several weeks of data collecting time is available to students from Sint-Pieterscollege Jette provided their experiments are designed to be autonomous: once installed, they are to operate without human intervention (as far as possible). During the first year of this Antarctic project a 3D magnetometer was designed and built, equipped with a USB memory stick and additional EEPROM. While the USB-stick exhibited erratic behaviour, the EEPROMs worked fine and several days' worth of magnetic readings were collected. (See Fig 7.)

While the full interpretation of the data is still underway, a 24hr (1440 minutes) cycle is obvious. A thermal effect was ruled out because the sensor is essentially temperature independent (according to its datasheet) and the geographical configuration of the station, the Sør Rondane Mountains and the sensor cannot account for the 6hr dip in the measurements seen on Fig 7. The average value of the local magnetic field is in reasonable agreement with the general values used in geomagnetic models for the Utsteinen location of the station.

Figure 6: A student-designed and built 3D magnetometer with Belgium's Princess Elisabeth Station at Utsteinen in Antarctica in the background.

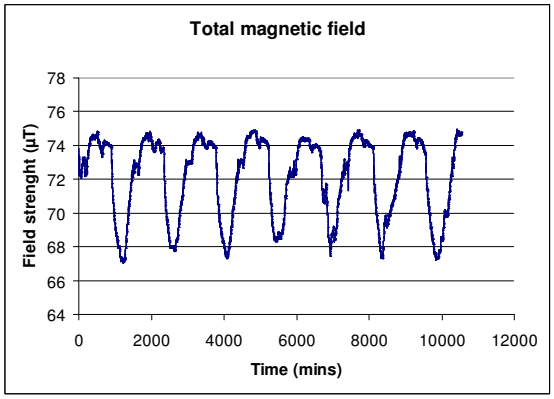

Figure 7: Magnetic field strenght as a function of time for a 1-week period in february 2013 at Utsteinen in Antarctica.

An advanced magnetometer will be shipped to Antarctica next summer providing increased on-board storage capability and a radiomodule capable of transmitting the data to a receiver within the station so data can be uploaded regularly. Accurate timing of the datapoints will also be included.

4. FUTURE PROJECTS

Future projects for Asgard include improved solar cell and gas sensor experiments, imaging of the balloon during ascent (Universal Gas Law verification), and ground imaging at different wavelengths for introductory remote sensing experiments.

Figure 8: Brussels seen from approximately 6km altitude during the Asgard-III flight in April 2013: the possibilities for remote sensing or aerial photography are obvious.

Figure 9: In archeology, the use of UAV's hold the promise of significant cost savings and a far more versatile deployment as compared to piloted aircraft.

A more advanced avionics system including gps and downlink capabilities would improve tracking and recovery, and help in the interpretation of multispectral remote sensing images.

Zefyr can be used for aerial photography in the service of archeological research projects, for environmental studies and possibly even agricultural projects. As a technology test bed, it allows more advanced work on lightweight solar power systems, avionics, radio communications, preprogrammed flying, and much more.

Annual access to the Belgian Antarctic Research Station 'Princess Elisabeth' allows more advanced projects in geomagnetism. Longer periods of data collection and shorter time intervals in between measurements can be considered. Collecting data from different geographical locations (i.e. at different latitudes) over the same period could allow some properties of the overall geomagnetic field, and of sun-earth relations to be identified and studied.

Besides geomagnetism, other geophysical disciplines could benefit: glaciology (using a GPS-datalogger to map ice sheet movements), and seismology. Even some astronomy projects can be performed (weather permitting), that are unfeasible from the ground at lower latitudes, such as IR solar physics (the air being very dry solar IR suffers significantly less atmospheric attenuation at polar latitudes).

Figure 10: A Proxxon MF70 CNC machine was purchased to support PCB milling and experiment parts' manufacturing efforts. Training for teachers and students is planned.

To facilitate the actual building of experiments, first steps into acquiring capabilities in CNC manufacturing and 3D printing techniques will be taken. A small CNC machine was already purchased, training and testing should start within a few months.

5. CONCLUSIONS

The 2011-2013 time frame has been a momentous period for hands-on space-related education at Sint-Pieterscollege Jette as a larger number of measurement locations and platforms became available. While it will certainly take a number of years for the full potential of these new opportunities to be fully explored and exploited, motivated secondary school students continue to work in challenging science projects covering an ever wider range of disciplines.

ACKNOWLEDGEMENTS

The authors wish to thank M. Roeland Van Malderen (KMI-IRM) for his contributions to the Asgard balloon programme, and M. Johan Berte (International Polar Foundation) and the entire team at Utsteinen, Antarctica for the opportunity and for their help in installing the magnetometer.

Thanks also to the people from Zero-to-infinity to fly our upgraded sound spectrum experiment.

For financial support, the authors wish to thank the Community of Jette, the Vlaamse Gemeenschaps-commissie (Flemish Community Council in Brussels) and BELSPO (the Belgian Federal Ministry for Science Policy).

REFERENCES

[1] de Schrijver E. (2005), Proc. '17th ESA Symposium on European rocket and Balloon Programmes and Related Research' pp. 77-80, Sandefjord, Norway, 30 May- 2 June 2007 (ESA SP-590).

[2] de Schrijver E. (2007), Proc. '18th ESA Symposium on European rocket and Balloon Programmes and Related Research' pp. 283-287, Visby, Sweden, 3-7 June 2007 (ESA SP-647).

[3] de Schrijver E. (2009), Proc. '19th ESA Symposium on European rocket and Balloon Programmes and Related Research' pp. 531-536, Bad Reichenhall, Germany, 7-11 June 2009 (ESA SP-671).

[4] Bettens S. et al. (2009), Proc. '19th ESA Symposium on European rocket and Balloon Programmes and Related Research' pp. 537-540 Bad Reichenhall, Germany, 7-11 June 2009 (ESA SP-671).

[5] Bettens T. *et al.* (2011), Proc. '20th ESA Symposium on European rocket and Balloon Programmes and Related Research' pp. 243-248, Hyères, France, 22-26 May 2011 (ESA SP-700).

[6] de Schrijver E. *et al.* (2011), Proc. '20th ESA Symposium on European rocket and Balloon Programmes and Related Research' pp. 271-75, Hyères, France, 22-26 May 2011 (ESA SP-700).

[7] de Schrijver E., Geeroms D., (2011), Proc. '20th ESA Symposium on European rocket and Balloon Programmes and Related Research' pp. 249-252, Hyères, France, 22-26 May 2011 (ESA SP-700).

ODYSSÉE-S2, A FRANCE-JAPAN EXPERIMENTAL ROCKET PROJECT

Hugo Charrier [(1)], Marine Martin-Lagarde [(2)]

[(1)] *Estaca Space Odyssey, 34 rue Victor Hugo, 92300 LEVALLOIS-PERRET, FRANCE*

Email: hugo.charrier@estaca.eu

[(2)] *Estaca Space Odyssey, 34 rue Victor Hugo, 92300 LEVALLOIS-PERRET, FRANCE*

Email: marine.martin-lagarde@estaca.eu

ABSTRACT

International cooperation is essential in today's Aerospace industry. As engineering students at ESTACA (Paris) we were particularly eager to bring this aspect into our training.

Within ESO, the ESTACA rocket club, we started a new experimental rocket project, Odyssée-S2, with the Japanese team TKRC.

We wanted to prove ourselves we could lead this project despite the distance, the language and cultural differences.

The French team would be responsible for the launcher, and the Japanese team for the inboard experiment. Interface and compatibility were the heart of the project.

Odyssée-S2 was launched on August 28th, 2012 at C'Space, the French national student rocketry meeting, and was awarded the CNES prize for a fruitful cooperation.

In this paper, we will introduce how we carried out this project and the key points of a cooperation project, in the hope of inspiring students to throw themselves into such an amazing experience.

1. PROJECT FRAMEWORK

1.1. ESTACA

ESTACA (École supérieure des techniques aéronautiques et de construction automobile) is a French 5-year Engineering school specialized in the design, development and production of transport systems and components.

ESTACA confers a Master's degree in four majors: Aeronautics, Automotive, Railways and Space engineering.

Founded in 1925, ESTACA is now located in Levallois-Perret (Paris) and Laval (Fig.1).

Figure 1. ESTACA is located in Paris (red pin) and Laval (blue pin).

As Space engineering major students, the authors were particularly interested in having a first experience of system engineering, joint project management and international cooperation, which are main challenges for space industries today and tomorrow.

1.2. ESO

The Odyssée-S2 rocket project was carried out within the framework of a student organization, made up of ESTACA students and supported by their school: ESO (Fig. 2).

Figure 2. ESO logo

Estaca Space Odyssey (ESO) is a non-profit student organization, created in 1992 in order to promote space-related activities at ESTACA and with the general public.

Proc. '21st ESA Symposium European Rocket & Balloon Programmes and Related Research', 9–13 June 2013, Thun, Switzerland (ESA SP-721, October 2013)

Designing, building and flying experimental rockets (Fig. 3) are our main activities. With over 20 years of experience in student experimental rocketry, ESO launches each year between 5 and 10 new projects.

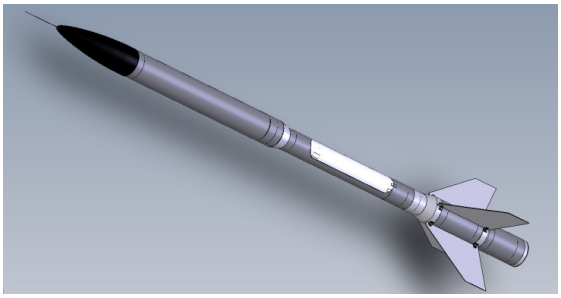

Figure 3. Marianne CAD on DS Solidworks

ESO members are also taking part in stratospheric balloon projects, microgravity experiments aboard the Novaspace Airbus A300-0G, and joining or organizing conferences (the astronaut Jean-Loup Chrétien at ESTACA, Laval, March 14th, 2013) and visits of industrial sites (Snecma, EADS Astrium, MBDA).

1.3. C'Space

C'Space is the French national launch campaign, organized annually by the French space agency, CNES (Centre national d'études spatiales) and Planète Sciences, a non-profit organization promoting sciences education.

It takes place each year during one week, at the end of August, in a French army missile test center in Biscarrosse, near Bordeaux (southwestern France).

C'Space gathers around 20 high school and engineering school rocket clubs (Fig. 4), mainly from France, but also from Russia, Austria, Australia and Japan. In 2012, 22 experimental rockets and 19 mini-rockets were launched.

Figure 4. ESO at C'Space 2011

C'Space is also hosting an annual Cansat competition and stratospheric balloon releases.

Next C'Space will take place from August 24th to August 31th 2013.

2. PROJECT CONCEPT AND ORGANISATION

2.1. First steps at C'Space 2010

In 2010, we went to C'Space with the experimental rocket Marianne (Fig. 3). The atmosphere between the teams attending C'Space is welcoming: teams usually share materials and tools. We met TKRC members (Team Kansai Rocket Club), we helped each other and finally exchanged business cards. A friendship was born!

It was for us a unique opportunity to gain experience in an international project before joining the industry.

2.2. ESO-TKRC Joint Project

One year later, Hugo was welcomed in Japan for a summer internship at Souki Systems. This startup company is supporting TKRC in Osaka. During C'Space 2012, the ESO-TKRC Joint Project (Fig. 5) officially started. The rocket name was also chosen: Odyssée (to celebrate the 20th anniversary of Estaca Space Odyssey) – S2 (the TKRC standard designation).

Figure 5. ESO-TKRC Joint Project patch

2.3. Odyssée-S2 concept

In addition to the international cooperation aspect, we wanted to work with an industrial-like approach, and to be confronted with the compatibility and interface problematic.

The main idea was to separate, as in the industry, the launcher and the payload.

ESO had to design and build the launcher itself, and to offer a “launch service” to its “customer”, TKRC. The Japanese team was making the payload, an inboard experiment made up of different PCBs (printed circuit boards).

Thanks to 20 years of ESO rocketry experience, our objective was to build a « ready-to-flight » launcher with simplicity, reliability and functionality as a guideline (Fig. 6).

The fact of assembling the rocket only few hours before launching required a functional architecture and a quick and easy access to the internal structure, holding the inboard experiment devices.

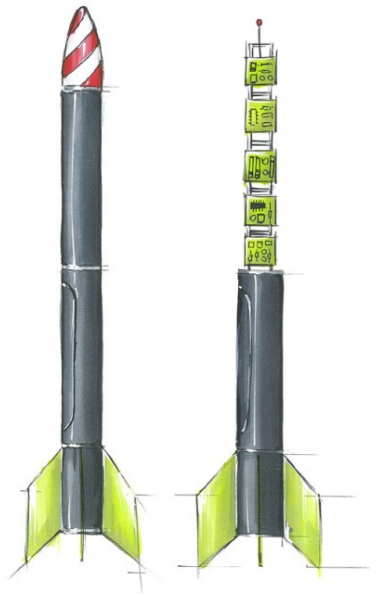

Figure 6. Preliminary sketch showing the general architecture of the rocket

2.4. Teams formation

Once the division of tasks defined, we set up the teams and started to work on the future rocket.

2.4.1. ESO

In France, the ESO team was made up of ESTACA students from the first to the fourth year, with a core group of three people, helped by occasional members at different periods of the year, giving a total of five or six members permanently.

Traditionally, ESO teams are divided in two groups (Fig. 7), the first in charge of the rocket mechanics (architecture, structure, stability) and the other dealing with the inboard electronics (recovery system and experimental devices).

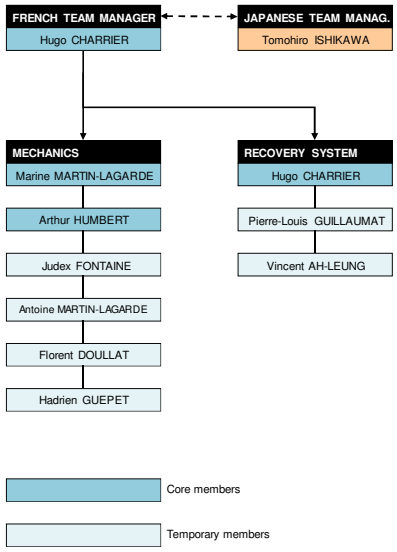

Figure 7. Odyssée-S2 French team organization chart

2.4.2. TKRC

The Team Kansai Rocket Club (TKRC) is gathering university and high-school students and young engineers and technicians from Souki Systems in Osaka.

Souki Systems is a young company, specialized in educational robotics, electronic devices for production system and 4 rotor UAV for observation. Souki Systems also build experimental rockets in cooperation with the Osaka Sangyo University (OSU), within an educational training.

TKRC already used to join C’Space for three years when we started the Joint project.

Made up of five people helped with the other TKRC members, the Japanese Odyssée-S2 team (Fig. 8) designed the inboard experiment, using in particular Souki standard microcontroller PCB.

Figure 8. Core members of the Japanese team

2.4.3. Air-ESIEA

As we will see below, a third team joined the Odyssée-S2 project during spring, 2012: the Air-ESIEA rocket club. ESIEA is another Paris school, specialized in electronics, computer and automatics engineering.

Air-ESIEA was created in 1986 and seeks to promote aerospace activities within ESIEA and to the public.

2.5. Organisation and synergy

At the beginning, it seemed important to us, to write a definition document giving the frame and the broad outlines of the Joint project. We fixed different things in order to work in the same direction and efficiently.

The definition document gathers the objectives and obligations of each team, a global schedule, a weekly skype meeting, and a list of the softwares to be used for each task: schedule, logo, electronic schematics, CAD, reports etc.

The most important aspect of this cooperation was to understand cultural differences, and respecting them even in case of disagreement (e.g. corporate hierarchy).

The more we could understand about the way the other team worked, the more we could anticipate possible issues and mistakes. It was a real improvement of our management skills and it remains as a very important part of our engineering training.

3. BUILDING THE ROCKET

3.1. French team work

The French team had two main targets: first, designing and making a functional and simple body structure; then, to design and make a reliable recovery system.

Moreover, the challenge was to put together different systems, made in France and in Japan. Interface and compatibility were the heart of our job.

3.1.1. Rocket structure

Thanks to ESO members' experience, we worked on making a « ready-to-flight » launcher with simplicity, reliability and functionality as a guideline.

The Odyssée-S2 CAD (Fig. 9) was made with DS Solidworks. This software is studied at ESTACA from the first year, and it was important since we had students from the first to the fourth year; it was also used by TKRC.

Figure 9. The rocket CAD

Careful attention was paid to the access to inboard electronics, in order to be able to solve any issue in few minutes.

The rocket we designed is 2.40 m high with an external diameter of 140 mm. It required several materials and processes. Skin and fins were made of carbon-fiber-reinforced polymer (CFRP). Rings and internal structure were made of machined aluminum, and nose cone of polymer.

ESO characteristic is our capacity to make almost every part of our rockets ourselves, in our workshop at ESTACA.

The CFRP tubes are hand-made, using a PVC pipe as a mold (Fig. 10). Aluminum parts could be machined at the ESTACA workshop, with the help of our teacher.

Figure 10. The French team manufacturing the CFRP tubes

3.1.2. Recovery system

The recovery system mainly includes:

- a timer PCB;
- a take-off detector;
- an electromagnet setting off the parachute door opening;
- a parachute.

The timer PCB (Fig. 11) includes a microcontroller processing data and making the orders.

In addition, keeping in mind the objective of our team (to offer a reliable and functional launcher), we added extra components such as a 7-segment displaying the countdown during tests; a buzzer indicating the parachute door opening, in order to warn an untimely activation; a setting mode to program the timer without connecting the computer etc.

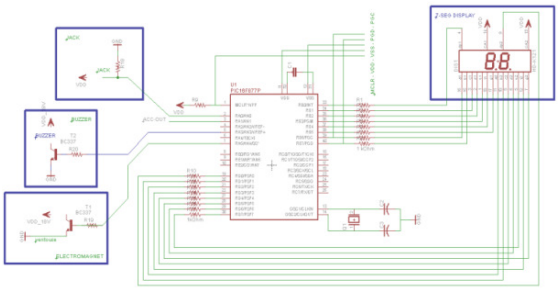

Figure 11. The timer PCB schematic on Eagle

In the context of a school project, third-year students worked on a reliability study. They studied different schematics thanks to a fault tree analysis (Blocksim7) and made recommendations.

The recovery electronics were also made at the ESO workshop, from the computer (schematics and layout on Eagle) to the PCB.

3.1.3. Interface

A large part of our work consisted in preparing the assembly and to ensure compatibility between all the components.

The interface was limited to a ladder-shaped internal structure (Fig. 12) with a standard width, fitting the Japanese PCB. We made our own PCB with the same width and, later, we checked it would also fit the Air-ESIEA devices.

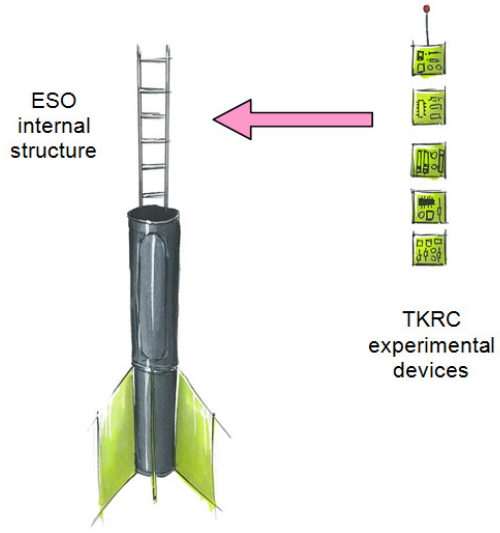

Figure 12. Integration of the inboard experiment on the internal structure

3.2. Japanese team work

TKRC worked on different experiments using Souki Systems standard PCB, including microcontrollers (Fig. 13): GPS coordinates, 3-axis acceleration measure, telemetry and data storage. Finally, the system had to be revised due to the company schedule and was composed of accelerometers, a GPS receiver and inboard storage.

They assembled the PCBs with the sensors and the GPS receiver, and programmed the microcontrollers to communicate together and store data safely.

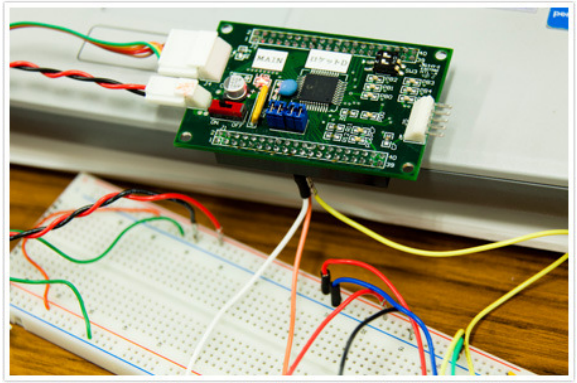

Figure 13. Standard Souki Systems PCB used for the inboard experiment

3.3. Air-ESIEA additional experiment

During spring 2012, we were confronted with a common industrial issue: due to the experiment revision, the launcher and the payload did not fit exactly.

We had to adjust the payload size (the rocket was too voluminous) and we offered Air-ESIEA, another French student organization, to join the adventure.

They proposed to set up their Cansat electronics into the rocket, in order to proceed tests and to supply the landing GPS coordinates by telemetry. We had to check compatibility between their components, the rocket structure and the Japanese systems: mechanical, radio and electrical compatibility.

4. LAUNCH CAMPAIGN

4.1. Rendezvous at C'Space 2012

The three teams, ESO, TKRC and Air-ESIEA, met finally at C'Space 2012, in order to put all the systems together and proceed tests before the launch (Fig. 14).

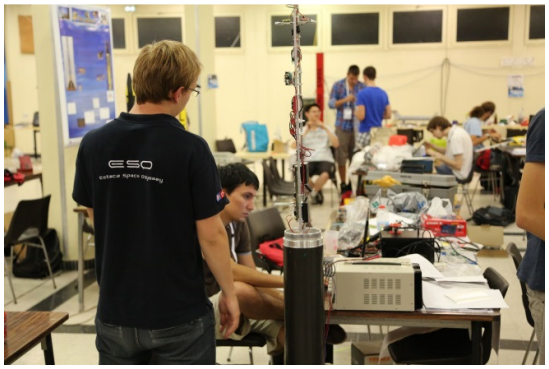

Figure 14. ESO and Air-ESIEA students finalizing details before the flight

We had three days to prepare the rocket, before the first day of experimental rocket launches.

4.2. Assembling the rocket

The fact of assembling the rocket only few hours before launching required a meticulous preparation.

Thanks to a constant communication, we shared the essential information to assemble the rocket quickly and to avoid unpleasant surprise: PCB and internal structure dimensions, wiring schematics, batteries volume, and finally an outline (schematics, chronology) of how the electronics would be integrated.

Every step was supposed to be written. However, something unexpected is always to be expected…

Before and during C'Space, several ESO members joined the team to help us. Finally, the preparation went off without major issue and Odyssée-S2 was the second rocket to pass successfully the technical controls, and to reach the launch pad.

4.3. Technical controls

Each rocket to be launched during the C'Space national launch campaign must fit to the Planète Sciences specifications, both concerning the mechanics and the electronics.

To acquaint ourselves with these specifications since the beginning of the project is essential to start in the good way.

During the pre-flight controls, our architecture and system choices were confirmed: all the tests were passed without significant problem.

4.4. Flight

Odyssée-S2 was launched on August 28th, 2012, in Biscarrosse. (Fig. 15 and 16).

Figure 15. Odyssée-S2 is placed into the launchpad

The rocket reached an altitude of 1100 m and a maximum speed of 530 km/h. The rocket was stable and the parachute opened right after the apogee (12.5 seconds after take-off). All of our « passengers », the inboard experiments, could reach the ground safely

under the rocket parachute. The rocket landed on the beach, around 2 km far from the launch pad (Fig. 20).

Figure 16. Lift-off (Julien Franc, Planète Sciences)

4.5. Flight data

TKRC and Air-ESIEA flight data could be recovered safely during flight, thanks to the telemetry system, or stored inboard and recovered after landing. We will introduce shortly their measures.

TKRC could draw the acceleration profile of the rocket during the flight (Fig. 17) and store data. A problem occurred with the GPS receiver and the signal couldn't be acquired.

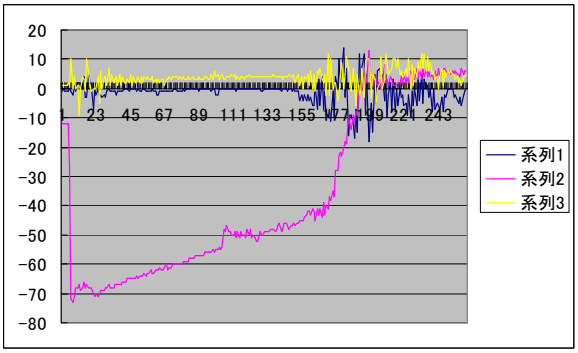

Figure 17. 3-axis acceleration raw data (TKRC)

Air-ESIEA devices transmitted a telemetry signal with the GPS coordinates and hygrometry measures (system designed initially for a Cansat competition).

Thanks to this telemetry system, we could obtain the landing coordinates (Fig. 18) in few minutes and find the rocket easily.

Figure 18. Flight under parachute, GPS coordinates (red path)

4.6. CNES Award

Each year, three prizes are awarded at C'Space: the CNES, Planète Sciences and French army (DGA) Awards.

Our team was awarded the CNES prize for a perfect flight: stability, parachute opening at the apogee, safe recovery of the rocket and data; and a fruitful international cooperation programme.

We were invited by CNES to join the 21st ESA Symposium on European Rocket and Balloon Programmes and Related Research (9-13 June 2013, Thun, Switzerland), in order to present the Odyssée-S2 rocket project and to attend the conferences.

5. PROJECT BENEFITS

The ESO-TKRC Joint Project was an important part of our engineering training, and prepared ourselves to join the Aerospace industry as system engineers.

This programme was also fruitful for ESO and ESTACA, since a total of 3 students have flown to Osaka, for summer internships at Souki Systems, in 2011, 2012 and 2013. ESO-TKRC cooperation will probably go on under different forms, in the next years.

At ESO, Odyssée-S2 was the first international rocket built.

In September, 2012, few weeks after the launch, a new team was formed within ESO, to build the experimental rocket Esther. This rocket will take on board experimental devices made by several other clubs, from France or abroad.

Taking advantage of the experience acquired making Odyssée-S2, ESO is once more designing a launcher and offering the other teams a "launch service" for their experimental devices. Esther is to be launched during C'Space 2013, from August 24th to August 31th.

CONCLUSION

Understanding cultural differences is absolutely necessary to anticipate related problems, check we understand each other and make sure the project will be carried out successfully.

Making use of our previous experiences, of synergy between teams (Fig. 19), and preparing carefully the interface between the launcher and the inboard systems, we passed the technical controls without problem and the rocket flew perfectly.

This project remains for us a rewarding experience of international cooperation, project management, and will keep a great importance in our engineer training.

At the end of our presentation at the Symposium, and of this paper, we hope we could encourage young people to throw themselves into a rocket or scientific cooperation project.

Figure 19. ESO, TKRC and Air-ESIEA with Odyssée-S2

ACKNOWLEDGEMENT

First of all, we would like to express our sincere thanks to Mr Nicolas Pillet (CNES Education) and Mr Thierry Stillace (CNES/DLA), who awarded the Odyssée-S2 teams the CNES Prize at C'Space 2012.

Thanks to Planète Sciences, CNES and DGA (French army) for giving us such opportunities to live out our passion for rocketry; to Christophe Scicluna (Planète Sciences), Mr. Faux (ESTACA) and Junpei Maruo (OSU) for their personal support and to Alix Charrier (Strate Collège) for the sketches.

And finally, this project could not have been carried out without the great help of all ESO, TKRC, Air-ESIEA and PV3e members, and the constant support of ESTACA through years.

Figure 20. Odyssée-S2 on the beach after landing

AN UNMANNED HIGH SPEED GLIDER FOR WEATHER DATA GATHERING

R. Dufour, A. Nazeeruddin**, P. Wilhelm**, M. Hoechemer†, P. Leyland**, D.Gherardi*,G. Gruener†**

*** Interdisciplinary Aerodynamics Group, Ecole Polytechnique Federale de Lausanne, GR-SCI-IAG, EPFL, Station 9, CH-1015 Lausanne*

†CSEM Alpnach, Untere Gruendlistrasse 1, CH-6055 Alpnach Dorf

** ESA ESTEC, 2201 AZ Noordwijk, NL*

ABSTRACT

An atmospheric sounding glider UAV based on an innovative design is equipped with a health monitoring system (HMS) that reacts to the vehicles aircraft performance during its whole mission from high altitude (above 35km) to ground landing . The paper describes the mission and the design of a functional engineering simulator (FES) able to support the design of the on board software verifying the HMS strategies and the design of valid flight tests. A virtual aircraft with its sensor suite are simulated to provide inputs to the prototyped flight controller and HMS softwares.

1. INTRODUCTION

The sounding the upper tropopause and the stratosphere is a challenging enterprise. This delicate zone of the atmosphere traps significant pollutants that can influence the weather; not only NOx and CO2 but also H2O and particulates for instance are critical catalysers for weather perturbation and the influence on the ozone layer. Atmospheric emissions concern directly an assessment on climate impact such as contrails and cirrus cloud formations. Contrails are function of atmospheric conditions and may give rise to formation of Cirrus clouds that can affect the balance of energy absorption and radiation through the atmosphere. This contributes to radiative forcing (RF) and hence to climate change. The transition zone to the troposphere, the tropopause is fragile, and requires precise sounding; the role of stratospheric ozone depletion by NOx and Sulphur compounds is critical, high altitude thin clouds have an impact on climate, [1, 2, 3].

Atmospheric probing is usually performed by balloons; however, these devices tend to be lost, become untraceable, or are destroyed. An attractive alternative is to monitor and collect data via unmanned air vehicles (UAV). The system devised here is a UAV capable of behaving as a lifting body in high altitude ranges, and be able to fly back to a single destination as a glider. The system described here uses an innovative design shape, with a built in health monitoring system of the aircraft capable of controlling and reacting to the aircraft's flight stages during descent. The UAV is designed to be ultra-lightweight and released from a sounding balloon at 35-40Km. The aircraft will then return to ground within a reasonable area, pre-designed by the onboard flight controller and its associated functional engineering simulator, that can account for the modifying aerodynamics of the vehicle along the flight path. The success of such missions will provide solutions for ulterior families of such concepts, that can be then equipped with emission capture data .

The paper presents the functionalities of such a system and illustrates examples of the simulations.

2. TESTBED AND MISSION DESCRIPTION

2.1. Vehicle Design

The vehicle selected to carry out the mission was based on the SmartFish technology,[4] It is a highly swept wing with a large lifting and a highly blended wing-body interface. The figure 1 shows a CAD model of the drone.

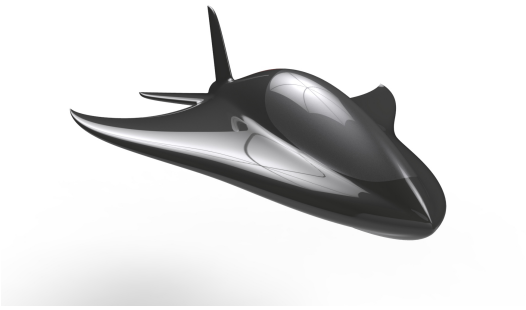

Figure 1. CAD model of the Glider SmartFish Model. (Credit : SmartFish SA)

Proc. '21st ESA Symposium European Rocket & Balloon Programmes and Related Research', 9–13 June 2013, Thun, Switzerland (ESA SP-721, October 2013)

This design presents an appreciable feature. It is capable of entering a very stable vortex lift state around an angle of attack of 30 degrees. During this state, the drone can glide safely at extremely reduced speeds. This feature allows for a so-called parachute mode: in the case of any critical system failure, the aircraft automatically enters this state. It becomes then unharmful in case of impact. Thanks to this failsafe mode, it is easier to pass an acceptance for the integration of the drone within the airspace.

The model was milled from a solid block of foam. A shell with a thickness of 15 mm remained including one or two ribs per side for reinforcement. The estimated weight of the glider version without electronics was roughly 600 g.

The wetted surface was roughly $0.8\ m^2$. The surface was relatively rough since it was made out of milled foam. No other coating or surface treatment was considered since this would only add weight, cost, and risk.

The vehicle has two control surfaces on the horizontal tail. The control surfaces act as elevons (i.e. mixed aileron and elevator). These control surfaces were also milled in foam. A foil-type hinge makes the connection to the horizontal stabilizer. The elevons are actuated using RC servos off-the-shelf. No directional control was implemented even though the use of the asymmetrical induced drag during the bank could be used under a certain limit to fit that purpose.

The on-board hardware is based on the open-source Paparazzi Lisa/M with an Aspirin IMU. Additional sensors include a GPS, a magnetometer, absolute and relative pressure sensors, and a temperature sensor. The on-board software has been special-purpose developed by CSEM to implement Guidance, Navigation and Control (GNC) as well as the HMS functionality. A GPS, a magnetometer and a pressure sensor are mounted in addition to the Inertial Measurement Unit. The HMS has the capability to detect system failures or misbehavior such as low battery level, low temperature, structural failure and change the controller policy accordingly.

This paper is in support of the paper by G. Ortega *et al.* "Use of Balloons and Sounding Rockets to Test Fly the ESAs Integrated Health Management System Demonstrator", within the same proceedings.

2.2. Mission Design

The purpose being to gather as much weather and-or high atmospheric data as possible, the vehicle remains attached to a weather balloon until the capability of the latter are reached. This corresponds to an average of an altitude of 40 kilometers. The baseline is to separate the drone from the balloon actively with a telecommand from the ground station by using the hot-wire technique. At this point the drone then begins its mission.

As the vehicle drifts along with the balloon during the climb, the dropping points are very scattered. The figure 2 shows the bursting points of a yearly campaign of weather balloon [7]. Only the clear weather days are showed as the first tests have to be done by a clear sky; Data provided by Meteolabor,[5].

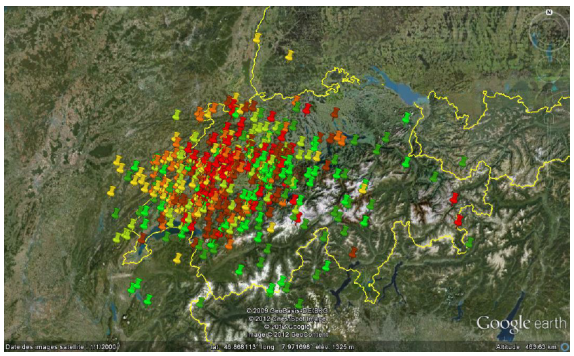

Figure 2. Drop points for valid days. Pins colors correspond to the months where balloon flew: March : Green blue / April : Green / May : Green Yellow / June : Yellow / July : Orange / August : Red / September : Brown

The large area covered by the possible points calls for a highly adaptable mission planner. The controller must adapt its policy in real time in order to go the its designated area.

The baseline mission to carry out the tests had several requirements. The drone must stay out of controlled airspace as much as possible and fly within military area when able to as these ones are easier to clear from traffic. The loading factor should remain within certain limit to avoid structural overstress. Excessively high angle of attack should be avoided as well as very fast pitching or rolling motions. The expected target performances are to have Approach and Landing phase conditions at an altitude between 20 - 100 m, with a distance to the balloon launch site less than 100 m, a flight path speed between 4 to 50 m/s, and a flight path angle between -10 and -3 degrees with a maximum dynamic pressure of 1400 Pa.

The mission are designed as follow :

- A dive phase, right after the balloon burst. A pronounced nose-down manoeuvre is engaged and high speeds can be reached.
- A level off phase where the aircraft carefully pitches up to reduce its speed.
- A backtrack phase, after a pre-selected duration, the drone flies back to selected points to get closer to the landing area.
- An energy dissipation phase where the aircraft flies either in spiral or following a polygonal shape in order to loose altitude above the landing zone.

- An approach and landing phase during which the aircraft flies a pre-selected pattern in order to reach a designated point.

The mission parameters such as waypoints, phase duration or landing spot are decided prior to flight.

The figure 3 shows a typical mission over Switzerland. The ascent correspond to real balloon flight and the descent was obtained with the further explained simulator. The green track corresponds to the balloon ascent and the data gathering. The red line to the dive followed by the level-off phase drawn in purple. The backtrack phase, in beige, is followed by the energy dissipation phase in light blue. Finally the orange line corresponds the approach and landing phase.

Figure 3. Typical mission for the drone

The figure 4 and 5 show that the angle of attack/sideslip angle as well as the g-factor remained within tolerable limits for this typical mission.

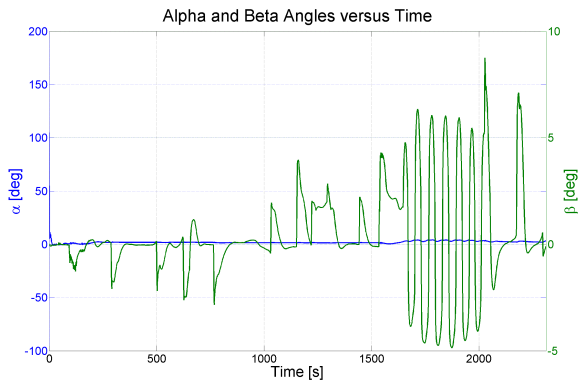

Figure 4. Typical mission angle of attack and sideslip angle

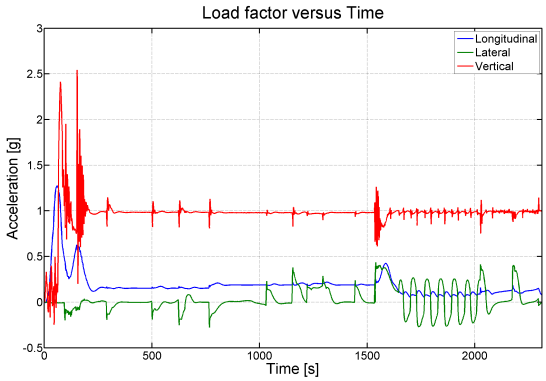

Figure 5. Typical mission load factor

3. VIRTUAL PLATFORM DEVELOPMENT

In order to design and improve the on board controller and the HMS a Simulink © Functional Engineering Simulator (FES) was developed. This provides a handy affordable solution for incrementally correcting the path planner and tuning the controller gains and to demonstrate performance capability and feasibility of the vehicle design.

3.1. Aircraft Model

Based on Wind Tunnel measurement of a propelled version of the drone an aerodynamic database has been derived using System Identification techniques described by Morrelli and Klein [8]. The latter provides a method to derive the aerodynamic model, finding the most suitable polynomial approximation, and to identify the regressors at the same time based on a least-square optimization. As the data were produced in a control environment the process noise were virtually null. Consequently a state estimator was not needed. The derived function for C_L, C_D and C_Y as well as for C_m, C_n and C_l can be found in appendix A.

The inertial parameters were derived from the CAD model of the drone.

The aerodynamic model was further enhanced by adding the dynamic effects based on Etkin's estimation methods [9]. These ones are based on both experimental knowledge and theoretical derivations cleverly gathered together into the USAF's tool DATCOM [10].

3.2. Simulation Solver

Using the forces obtained from the aerodynamic database the 6 degrees of freedom derivations of the third New-

ton's Law were solved in an ellipsoidal Planet Centered Inertial (PCI) frame (Figure 6).

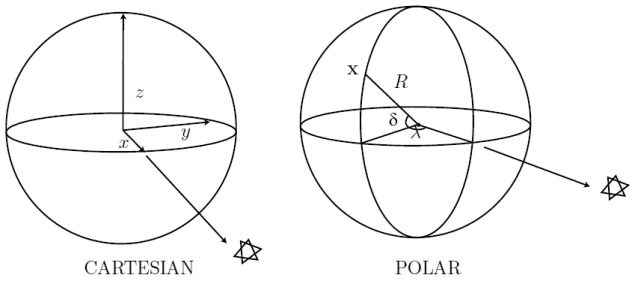

Figure 6. The celestial Frame of Reference

The use of this formulation allows for taking into account the centripetal acceleration, the Coriolis force and the gyroscopic effects in a simpler and computationally cheaper way by the successive application of frame transformations. The details of this approach are described by Stengel [11]. A brief overview of these transformations can be found in the appendix B.

As many operation, mainly matrix multiplication, are required, a quaternion formulation to describe the aircraft attitude with respect to the center of the Earth was used. It avoid the problem of the discontinuity at the Gimbal lock and reduce the number of operation. W. F. Philips [12] proposed an exhaustive formulation of the quaternion algebra applied to aircrafts.

The state vectors thus obtained contains the PCI referenced position and velocity, the quaternion of the attitude of body with respect to PCI and the rotation rates of the body. These states are integrated using the Dormand-Prince algorithm implemented in Simulink as ODE45 [13].

3.3. Environment Implementation

The environment includes the gravitational effects and the atmospheric effects. The gravity model take into account the ellipsoidal shape of the Earth. The near-field potential can be expanded into Legendre's polynomials to give a better representation of the gravity field [14]. Here the expansion was limited the J_2 degree, taking only the ellispoidity as a non-neglectable effect.

The atmospheric profiles (pressure, temperature, density, ...) were obtained by parsing the Wyoming University online atmospheric database into a FES compatible file that was interpolated at each simulation steps. The corresponding location was the military airport at Payerne LSMP. The wind, also parsed online, was defined in the NED (North-East-Down, or local geodetic) frame. It was thus transformed into the PCI frame before being applied to the PCI-velocity of the aircraft after the acceleration integration.

3.4. Aeronautical Quantity Derivation

From the PCI attitude and position, quantities relevant for the present aeronautical application such as longitude-latitude-altitude (LLA) position or the Euler Angles had to be calculated. The PCI positions were transfered into LLA positions using the WGS84 description [15]. It directly corresponds to the classical GPS positions readings.

In order to obtain the Euler Angles a algebraic characteristic of the quaternion was used. The quaternion describing the attitude of the aircraft with respect to the PCI frame was multiplied by the quaternion describing the attitude of the local geodetic frame with respect to the PCI frame :

$$q_B^G = q_{PCI}^G \bigotimes q_B^{PCI} \tag{1}$$

The obtained q_B^G describes the attitude of the aircraft body with respect to the local ground. This leads directly to the proper Euler Angles when transformed using the proper algebra [12].

3.5. Sensors Implementation

The sensors were simulated by first accounting for spurious misalignments, a rotational matrix fitted that purpose, displacements, random noise and bias. Each of these parameters were given values following a normal distribution with a standard deviation given by the manufacturers data. Finally, the sensory inputs are quantized to account for the digital representation in the on-board software with the corresponding loss of precision. The Figure 7 shows a example of a sensor implementation architecture.

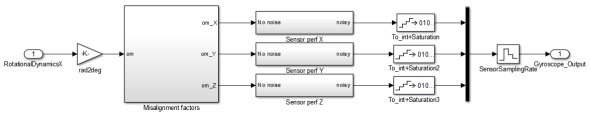

Figure 7. Simulated Gyroscope Architecture

3.6. Visual Interface

A graphical interface was made possible by the open source flight simulator FlightGear. It gave the possibility to communicate with Simulink via a network socket

based protocol. Specific S-functions were created for that purpose as well as for feeding into the FES a manual joystick input. This interface proved to be helpful for the development of the FES. Comparing the behavior of the virtual model with the physical propelled version of the aircraft allowed the tuning of the dynamic coefficients in the aero-database. A 3D model, with moving elevons and spoilers, was added for the sake of this interface credibility.

The figure 8 shows the drone virtually flying over Neuchatel's Lake.

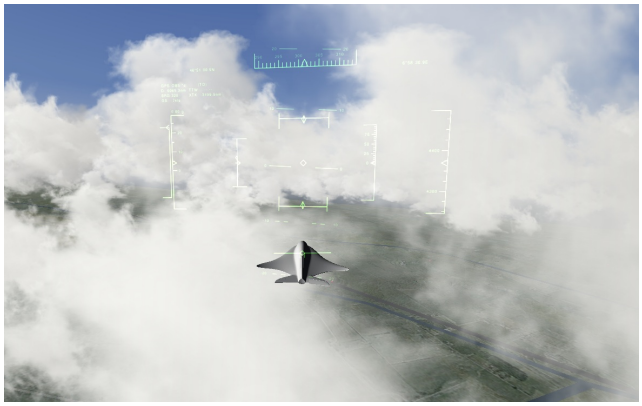

Figure 8. FES Visual Interface

3.7. Global Architecture Overview

The Functional Engineering Simulator (FES) is called EV2TSim, and is a high-fidelity 3D, 6-DOF Simulator (FES) for verifying HMS strategies and flight tests design. The main features are

- 6DOF point mass equations solved in planet centered inertial frame
- Rotating Earth effects (Coriolis force)
- WGS84 ellipsoid geodetic shape for the planet surface including rough altimeter for whole globe as well as accurate digital elevation model for Switzerland
- Gravity model associated with WGS84 using Legendre polynomial formulation of the solution for gravity potential
- Sensors models for: IMU (accelerometer and gyroscope), GPS, Magnetometer, Atmospheric (T, p), Pitot pressure, Aero models, GNC, AC, HMS with fault injection capabilities. Real-time pacer
- Joystick and keyboard control
- Live GUI output with FlightGear
- Automated post-processing including Google Earth outputs
- File-based initialisation allowing simulation campaign

The main structure is based on a Simulink model, and is interfaced also to FlightGear software package. The code contains a series of blocks: solution solver (Newton), aircraft (forces), environment (planetary science),and then the block global HMS that simulates a system which monitors the systems of the aircraft. Then follows the block sensors that simulates the different sensors of the plane: gyrometer, magnetometer, accelerometer, absolute and relative pressure sensors, temperature sensor and GPS. The flight controller block then acts as an artificial intelligent pilot. The sensors then give inputs to the actuators for GNC.

4. UNCERTAINTY DISPERSION ANALYSIS

This experiment presented intrinsically many uncertainties. The aerodynamic was based a similar yet different wind tunnel experimental model. The mass as well as the position of the center of gravity cannot be measured with infinite accuracy and the sensors are always slightly misaligned and misplaced. Above all the atmospheric conditions, in particular the wind profile, can vary substantially. The latter parameters have to be dispersed in order to assess the sensitivity of the experiment with respect to such variations.

4.1. Number of Runs

In order to assess the validity of the dispersion analysis, the number of runs required must be evaluated. The so-called margin of error describes how much the sample probability of success differs from the real probability of success. It can be written as :

$$\Delta P = n_\sigma \sigma_s \tag{2}$$

With n_σ the desired σ-confidence level and σ_s the sample standard deviation. The present probability experiment is a success-or-not-success experiment. Therefore the sample standard deviation can be written as $\sigma_s = \sqrt{\frac{P(1-P)}{N}}$ with N the number of run and P the probability of success.

Rearranging the aforementioned definition gives the required number of runs :

$$N = n_\sigma^2 \frac{P(1-P)}{\Delta P^2} \tag{3}$$

This equation corresponds to the ECSS's guidelines [16]. In the present case, the desire chances of success are $P = 95\%$. The margin of error is accepted to be $\Delta P = 4\%$ with a 2σ-confidence level, corresponding $n_\sigma = 1.96$. Using the previous formula this led to a number of runs $N = 114$.

However, because of the uncertainty introduced on the difference between the sample chances of success and the real chances of success, the simulation that be mission failures is reduced. According to the margin of error, the number of run that are a success are $N(P + \Delta P)$ in the worst case. Hence the number of runs that be mission failure is reduced to the following for a safe estimation :

$$n_{failure} = N(1 - (P + \Delta P)) = 1.14 \qquad (4)$$

Only one possible failure over 114 runs was the requirements chosen for the dispersion analysis.

4.2. Confidence Interval for the experimental variance

It can be of interest to assess the validity of the sample variance by bounding the latter one within a certain interval such that :

$$P(k_1 \leq \sigma^2 \leq k_2) = \gamma.$$

According to F. Ankersen [17] the computation of k_1 and k_2 can be obtained as follows:

$$k_1 = \frac{(n-1)\sigma_s^2}{c_1} \quad \text{and} \quad k_2 = \frac{(n-1)\sigma_s^2}{c_2}$$

For the particular case of $\gamma = 0.95$ confidence level :

$$c_1 = \frac{1}{2}(\sqrt{2n-1} - 1.96)^2, \quad c_2 = \frac{1}{2}(\sqrt{2n-1} + 1.96)^2.$$

These bounds are reported for each dispersion analysis campaigns.

4.3. Dispersed parameters

The uncertainties are applied to the following variables: mass, centre of gravity position, aerodynamic forces, atmospheric conditions and consequent drop point. These variables are organized into different sets that will form different cases. The uncertainties are activated on one set at a time to form distinct dispersion analysis.

In every cases, the variable **randn(σ)** describes a pseudo-random number following a $1 - \sigma$ normal distribution, where the σ is the standard deviation. This latter are specified as follow for every random variables. In the following a very preliminary set of parameters are chosen, and preliminary dispersion analyses run. The goal here is to show that the concept works and is the simulation chain is operational. Further dispersion analyses are at present being performed with a completed set and larger dispersion distributions.

- **MCI** This dispersion concerns the mass of the aircraft and the position of the center of gravity. The dispersion is set as follows:
  $Mass = NominalMass + randn(0.05)$
  or a 5 grams standard deviation.

  $CG_x = CG_{0,x} + randn(0.005)$
  or a 0.005 meters standard deviation.

  $CG_y = CG_{0,y} + randn(0.0025)$
  or a 0.0025 meters standard deviation.

  $CG_z = CG_{0,z} + randn(0.005)$
  or a 0.005 meters standard deviation.

- **Aero** The uncertainties on the aerodynamic forces and moments corresponds to the errors in aerodynamic model identification done previously. It helds:

  $C_X = C_{0,X} \times (1 + randn^*(0.17))$ i.e. 17%
  or from -5 % to 30 % of the nominal value in 95% of the cases. $randn^*$ is a custom skewed uncentered normal distribution

  $C_Y = C_{0,Y} \times (1 + randn(0.10))$
  or ± 10 % of the nominal value in 95% of the cases.

  $C_Z = C_{0,Z} \times (1 + randn(0.10))$
  or ± 10 % of the nominal value in 95% of the cases.

  $C_{n,m,l} = C_{0,n,m,l} \times (1 + randn(0.10))$
  or ± 10 % of the nominal value in 95% of the cases.

- **Atmo** The atmospheric conditions (wind speed, temperature, pressure and density) are taken from the real atmospheric database for a number of date equals to the number of runs. The drop point (or initial conditions) changes accordingly to these conditions.

4.4. Dispersion Campaigns Results

Thanks to the aforementioned simulator, the one hundred runs required could be ran overnight on an average workstation.

The simulations were using a baseline mission showed in figure 9 as a reference point around which the dispersions cases were all applied at the same time. The mission was

considered a success when the aircraft reached a 300 meters radius sphere around the landing spot. This distance was decided from the RC-pilot who judged it to be a safe estimate for a visual spotting and identification. The aircraft being manually landed it is sufficient to say that the mission was successful if the pilot can visually catch the drone. The latter statement might become irrelevant for later development including a fully automatic landing.

Figure 9. Baseline mission for the dispersion analysis

The figure 10 shows a Google Earth plot of the resulting trajectories. A zoom on the landing spot is showed on the figure 11.

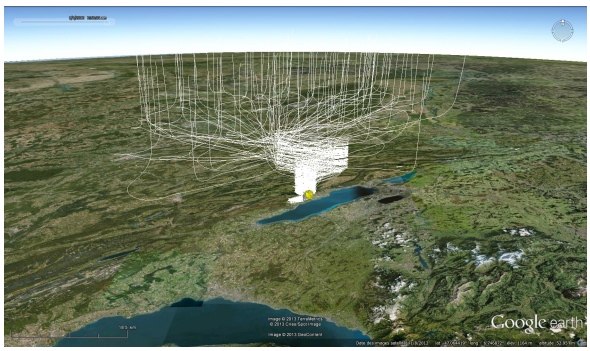

Figure 10. Dispersion analysis trajectories.

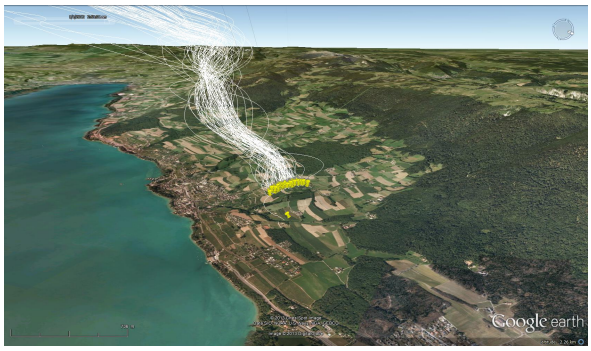

Figure 11. Dispersion analysis trajectories. Zoom on the landing location.

The figure 12 shows the latitude-longitude plot of where the aircraft entered the 300 meters sphere and the figure 13 represents the mission objectives under the form of histogrammes

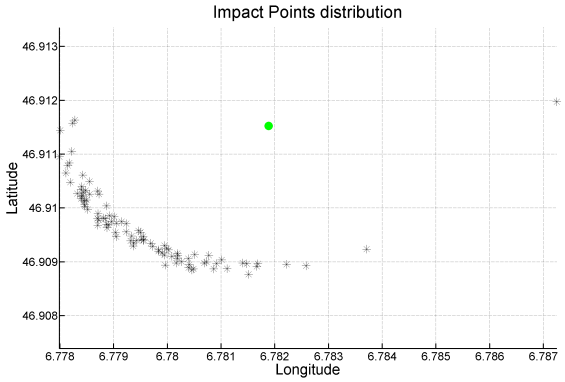

Figure 12. Dispersion analysis landing zone entry points.

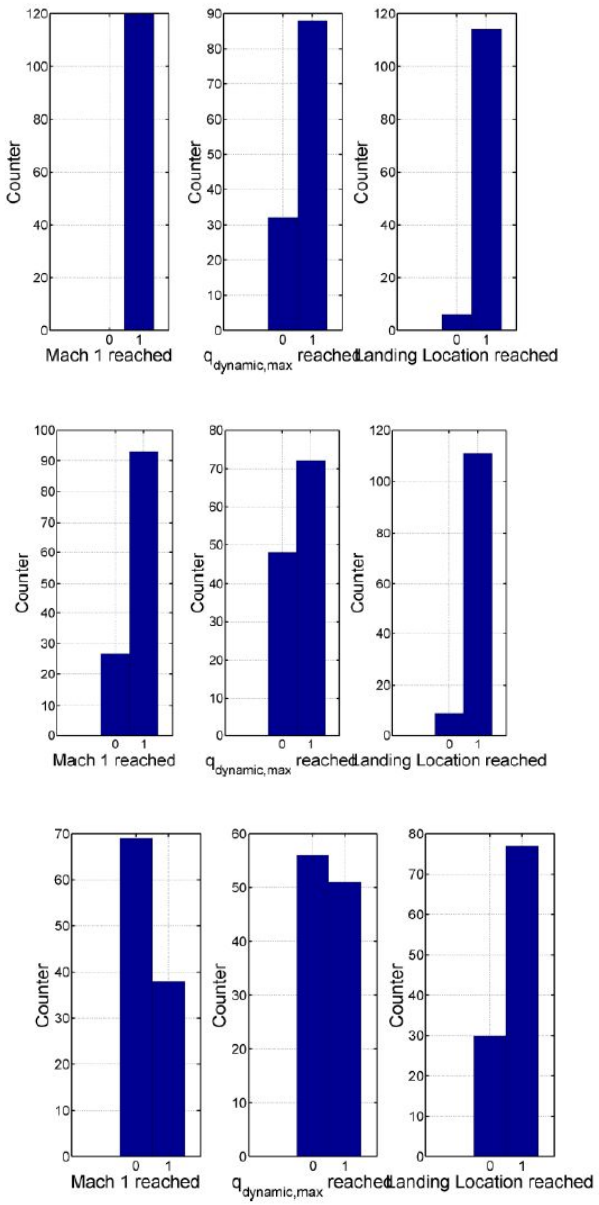

Figure 13. Dispersion analysis mission objectives: top shows dispersion on the MCI, in the middle on the Aero parameters and bottom shows taking All at Once of all parameters.. An extreme constraint of landing within 100 metres has been taken here

The results show that the aircraft is very capable of flying back home, hence flying a safe mission. However it also shows that it does not fly through Mach 1 in all cases. This is unlikely to be an issue as this is mainly for HMS testing purposes. The maximum dynamic pressure however is often reached. Although this might pose a problem, this maximum dynamic pressure was chosen to be one at which the aircraft flew the fastest at ground level. In reality, the drone can withstand much higher dynamic pressures without encountering damaging effects. This is work in progress, the results presented here are preliminary results and several improvements are being made, in particular to gain higher confidence rates; for example, refining the precision of a mission by considering a mission a success if landing in a very tight objective radius, as 100 metres for instance. the use of other random number generators. Once the simulations are approved with a high confidence limit, real flight tests will be carried out.

5. CONCLUSIONS

The project presented here offers a feasibility demonstrator for drone technology for upper atmosphere meteorology. Drone sounding of upper atmosphere climate is a very promising technology, and opens a whole era of on-board experiment technologies in these zones, with on-board data storage as the drone flies home, avoiding wireless data communication for large quantities of data. However, the experiment here is limited to the small lightweight glider, that is easier to satisfy flight path restrictions. Future projects could be oriented towards motorised versions, alternate shapes and larger sizes.

6. ACKNOWLEDGMENTS

This work was partially financed by an ESA GSTP IV project. The authors gratefully acknowledge training support received by ESA TEC-ECN.

REFERENCES

[1] V. Grewe, Potential Impact of Small Scale Supersonic Transport Airraft on the Atmosphere: Climate and Ozone Layer, Proceedings HISAC conference, AAF-EUCASS, Paris 2009.

[2] P. Leyland, V. Grewe, Emissions for high speed aircraft: a way to future trends and regulations, Proceedings HISAC Conference, AAF-EUCASS, Paris, 2009.

[3] Hamburger, T. and McMeeking, G. and Minikin, A. and Birmili, W. and Dall'Osto, M. and O'Dowd, C. and Flentje, H. and Henzing, B. and Junninen, H. and Kristensson, A. and de Leeuw, G. and Stohl, A. and Burkhart, J. F. and Coe, H. and Krejci, R. and Petzold, A. Overview of the synoptic and pollution situation over Europe during the EUCAARI-LONGREX field campaign,Atmos. Chem. Phys., 11, 1065-1082, 2011.

[4] http://www.smartfish.ch

[5] http://www.meteolabor.ch

[6] Integrated Vehicle Health Management System Demonstrator: iHMSD, *Vehicle Preliminary Design D1221*, iHMSD-SF-TN-1201.

[7] Integrated Vehicle Health Management System Demonstrator: iHMSD, *Mission Scenario Definition and Mission Analysis Document*, iHMSD-EPFL-TN-1202

[8] Klein, Vladislav, and Eugene A. Morelli. *Aircraft system identification: theory and practice*. Reston, VA, USA: American Institute of Aeronautics and Astronautics, 2006.

[9] Etkin, Bernard, and Lloyd Duff Reid. *Dynamics of flight*. John Wiley & Sons, 1959.

[10] Hoak, D., and D. Ellison. *USAF DATCOM*. Air Force Flight Dynamics Lab., Wright Patterson AFB, OH, USA (1974).

[11] Stengel Robert F., *Flight Dynamics*, Princeton University Press, 2004.

[12] Phillips, Warren F. *Mechanics of flight*. Wiley, 2009.

[13] Shampine, L. F. and M. W. Reichelt, *The MATLAB ODE Suite*, SIAM Journal on Scientific Computing, Vol. 18, 1997, pp. 122.

[14] Regan, F.J., Anandakrishnan, S.M., *Dynamics of Atmospheric Re-Entry*. AIAA Education Series, Washington, D.C. (1993)

[15] NATIONAL IMAGERY AND MAPPING AGENCY TECHNICAL REPORT 8350.2, Third Edition, Department of Defense, World Geodetic System 1984.

[16] European Cooperation for Space Standardization. *Space engineering, Control performance guidelines*. ECSS-E-HB-60-10A.

[17] Finn Ankersen, *A Mathematical Approach to Monte Carlo Simulations and their Statistical Post Processing*. ESA Work Package 2271.

DEVELOPMENT OF DROP TEST SYSTEM FOR PRETESTING OF REXUS/BEXUS EXPERIMENTS

Pawaroot Pongsuwan[1]; Mark Fittock[1]; Alexander Schmidt[2]; Jonas Andretzke[1]; Sebastian Diehl[1]

The German Aerospace Center (DLR)

Abstract

Rocket-borne/**B**alloon-borne **EX**periments for **U**niversity **S**tudents (REXUS/BEXUS Project) sometimes involves in free-fall experimental units (FFU) which subject to high risk of failure after months of preparations to the launch. This paper presents the development of a Drop Test System (DTS) to be implemented as a pretest facility for FFU by using a Helium-buoyant lifting device to drop the FFU from approximately 1500 meters above the ground. The design starts from statistical analysis of previous FFU characteristics. Practicality of the design, ease of manufacturing and low cost are critical factors for the project. The paper then concludes on the implementation of the system and expected performance from the actual experiment which is planned to be carried out during 2013.

Keywords

Drop Test System, REXUS, BEXUS, Helium aerostat, balloon, DLR

Nomenclature

A	= reference area
a	= acceleration
C	= aerodynamics coefficient
d	= diameter
F	= force
g	= Earth's gravitational acceleration
h	= altitude
L	= length
m	= mass
s	= distance
t	= time
v	= velocity
x	= distance of horizontal drift
ρ	= air density

Subscripts

D	= drag
free	= free (excess lift force)
FFU	= Free Flying Unit
He	= Helium
L	= lift
ld	= lifting device
t	= terminal
th	= tether
tot	= total
0	= on ground

Introduction

Rocket-borne/**B**alloon-borne **EX**periments for **U**niversity **S**tudents (REXUS/BEXUS Project) provides opportunities for students from European universities or higher education colleges to design and built near-space experiments to be onboard a sounding rocket or a stratospheric research balloon.

It is also possible to eject an experimental unit, called Free Flying Unit (FFU), into its own flight path involving free fall before coming back to the ground. In pursuance of a successful campaign, it can take up to 15 months to include all necessary validation and testing on functionality and reliability of both the experimental unit and the flight module; as well as compatibility of the whole integrated system. These tests allow early detection of any defects in the system while rectifications can be made effectively.

[1]Institute of Space Systems, The German Aerospace Center (DLR), Germany
[2]Mobile Rocket Base, DLR, Germany
[3]Intern students, The German Aerospace Center (DLR), Germany

Corresponding author:
Alexander Schmidt, Mobile Rocket Base, The German Aerospace Center (DLR), Münchnerstrasse 20, 82234 Wessling, Phone: +49 8153 28 2704, e-mail: alexander.schmidt@dlr.de

The Drop Test System (DTS) currently being developed will be part of this validation and testing process for future REXUS/BEXUS experiments involving FFU. It will prove validity and reliability of the FFU-related systems before the campaign flight. This simpler and smaller test bed will be used to pretest communication and control system; as well as deployment of recovery systems, including parachutes and other forms of drag enhancement, for the FFU. The test facility will compose of a tethered aerostat lofting approximately 1500 meters above the ground. The FFU is then ejected away from the aerostat by a direct manual command from the ground station; while other communication and control functions may be verified throughout the test period. From this altitude, the FFU will reach certain percentage of its terminal velocity, depending on its weight, while having sufficient time for the recovery system to deploy and the FFU to safely land on the ground. The Helium-filled aerostat is tethered to a mobile winch on the ground so that its altitude can be controlled; and most importantly, the system can be safely retrieved for future use. Figure 2 shows the overview of all subsystems of the DTS and their relationship.

Mission objective

The DTS must be able to test functionality of certain systems onboard the FFU; in particular, deployment of recovery system and effectiveness of communication and control system. The two systems are critical for success operation of the FFU in REXUS/BEXUS campaign. However, the functionality of recovery system could be well tested using this DTS; while communication and control effectiveness may be tested with other means. Thus, the design of DTS starts with setting up the minimum altitude from the ground that would be sufficient for a parachute to be fully deployed for most FFU weights, based on the statistical data of previous FFUs. Since the DTS being developed will be used as a standard system for all FFUs in the future; experiment teams will be given out the capability of DTS for them to design or select proper drag enhancement system to be onboard the FFU and capable of bringing it back to ground at a safe impact speed. Different requirements and constraints affect the design of DTS to support future experiments can be seen from Figure 3. While Table 1 shows different options considered for the design of each subsystem.

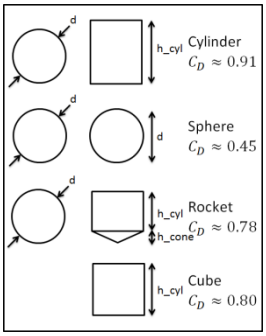

Figure 1. Drag coefficient of standard cross-sectional configurations.

An example calculation of drop height requirement, which is the fundamental requirement of the system, will now be illustrated. The assumption of constant air density and gravitational acceleration is particularly reasonable for this range of relatively low altitude and it is, anyway, conservative. The impact speed is selected to be 8 m/s. Drag coefficient of the recovery system may be estimated based on its cross-sectional shape as shown in Figure 1. The terminal velocity may be calculated from Equation (1).

$$v_t = \sqrt{\frac{g_0 \cdot m_{FFU}}{k_{FFU}}}$$

$$\text{where} \quad k_{FFU} = \frac{1}{2} \cdot C_{D,FFU} \cdot A_{FFU} \cdot \rho \qquad (1)$$

It should be noted, however, that the terminal speed is typically approached in an exponentially decaying fashion; i.e. it takes impractically long time to reach the terminal speed that 90% or 99% of the value is usually used instead and is sufficient to provide microgravity to the experiments.

The velocity and distance travelled at a particular time during the free-fall phase may be calculated using the following two equations.

$$v(t) = \sqrt{\frac{g_0 \cdot m_{FFU}}{k_{FFU}}} \cdot \tanh\left(\sqrt{\frac{g_0 \cdot k_{FFU}}{m_{FFU}}} \cdot t\right) \qquad (2)$$

$$s(t) = \frac{\sqrt{\frac{g_0 \cdot m_{FFU}}{k_{FFU}}}}{\sqrt{\frac{g_0 \cdot k_{FFU}}{m_{FFU}}}} \cdot \ln\left(cosh\left(\sqrt{\frac{g_0 \cdot k_{FFU}}{m_{FFU}}} \cdot t\right)\right) \qquad (3)$$

Once the FFU has reached 99% of its terminal velocity and has deployed the recovery system, acceleration, velocity and distance travelled by the FFU as a function of time can also be calculated as followed.

$$a(t) = g_0 - \frac{\frac{1}{2}\rho \cdot A_{RS} \cdot C_{D,RS} \cdot v^2}{m_{FFU}} \qquad (4)$$

$$v(t_n) = v(t_{n-1}) + a(t_{n-1}) \cdot (t_n - t_{n-1}) \qquad (5)$$

$$s(t_n) = \frac{v(t_{n-1}) + v(t_n)}{2} \cdot (t_n - t_{n-1}) + s(t_{n-1}) \qquad (6)$$

Engineering spreadsheet, such as Microsoft Excel®, or computer programming, such as MATLAB™, are recommended for tabulated calculation. Table 2 summarises characteristics of the previous FFUs and the calculated distance required for each FFU to reach 90% and 99% of their terminal velocity. The result is also plotted in Figure 4. From the result, it is reasonable to set up the designed altitude for DTS to be 1500 meters above the ground.

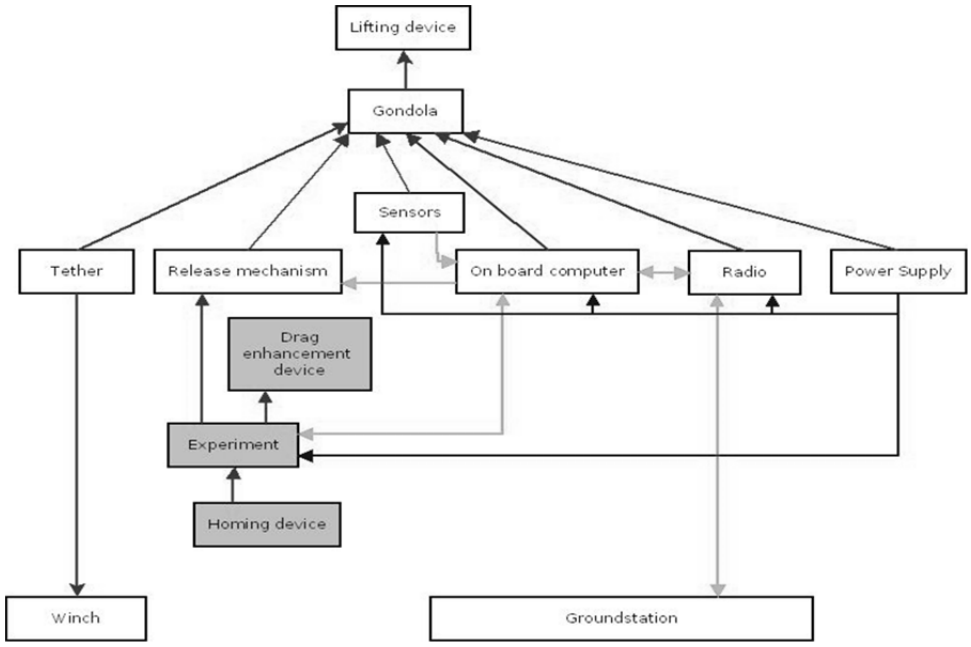

Figure 2. Overview of subsystems of the Drop Test System (DTS).

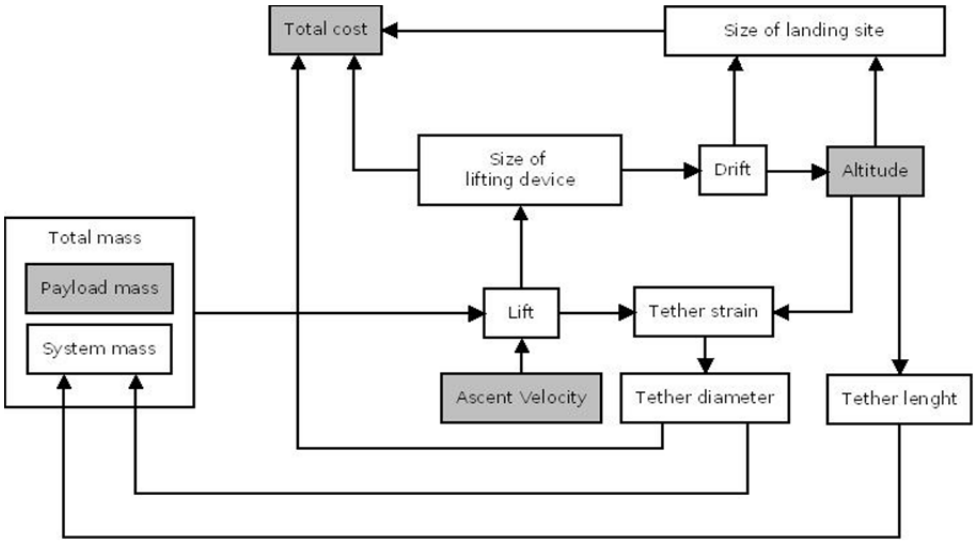

Figure 3. Relationship between different requirements of the system.

Table 1. Different options considered for the development of system.

Sub-system	Options
Tether	- Cable of different materials: Dyneema™, Spectra™, steel etc. - Multiple cables, enabling easy control of position - Cables with integrated power and/or data lines - Cables with attached power and/or data lines
Lifting device	- Balloon - Blimp - Kite - Balloon kite hybrid - Blimp kite hybrid - Rotor
Ground station	- Computer/Laptop - µC based device
Winch	- Electrical motor - Combustion engine - Hand operated - Computer operated
Gondola	- Fixed - Foldaway - Plug-in
Release mechanism	- Magnetic - Mechanical - Cable cutter
Radio	- GSM - Packet Radio - Cable
Power Supply	- Battery - Cable - Independent systems (solar cells, wind turbines etc.)
On board computer	- Different µCs - Full Computer system
Sensors	- Wind speed - Temperature - Altitude (Pressure Sensor) - Tether strain

Table 2. Characteristics of previous FFUs

Parameter	Suaineadh	Rain	LAPLander	SQUID	Reel.SMRT	StrathSat	Average
mass of FFU (kg)	3.919	1.040	2.890	3.600	1.600	1.945	2.499
reference Area FFU (m^2)	0.0360	0.0106	0.0452	0.0380	0.0201	0.0100	0.0266
drag coefficient FFU	0.91	0.91	0.91	0.91	0.78	0.80	0.87
terminal speed (m/s)	48.31	45.91	36.99	45.04	44.59	68.84	48.28
99% of terminal speed (m/s)	47.83	45.45	36.62	44.59	44.15	68.15	47.80
desired impact speed (m/s)	8.00	8.00	8.00	8.00	8.00	8.00	8.00
opening time parachute (s)	3	3	3	3	3	3	3
distance travelled when 99% of terminal speed is reached (m)	465.93	420.81	273.18	404.97	397.01	946.09	446.48
distance travelled with opened parachute (m)	23.25	23.48	22.05	23.22	23.17	25.90	23.51
distance travelled during parachute opening (m)	143.48	136.35	109.86	133.76	132.44	204.45	143.39
overall distance travelled (m)	632.66	580.64	405.09	561.95	552.61	1176.44	651.57

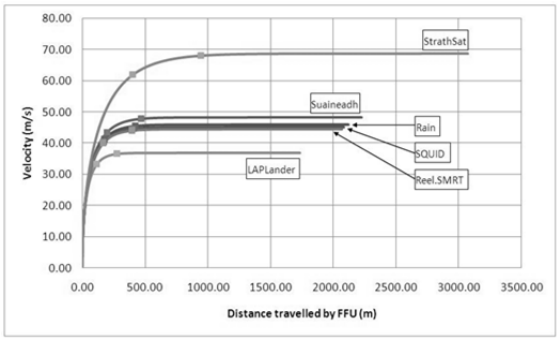

Figure 4. Calculated distance travelled and velocity of previous FFUs

In reality, when DTS is implemented for future experiments, different FFUs may reach different percentages of their terminal velocities, and face different impact speeds, depending on their weights and parachute configurations. It is also important for the team to roughly estimate the resulting impact velocity and decide whether it is within an acceptable range or further modifications to the design are necessary.

Other design considerations

The design of DTS then shifted to identifying and incorporating into the design a suitable experiment site, Commercial-Off-The-Shelf products (COTS), and ease of manufacturing and operation while keeping the cost of the project at minimum. The launch site must be a restricted airspace, to allow safe operation of the DTS without interference with other air traffic. A Bundeswehr, or Germany's military base, was deemed appropriate. However, due to unavailability and access security requirement of such areas; a small, low-traffic, local airport near DLR-Oberpfaffenhofen was chosen as an alternative.

The design was based on using as many available COTS products as possible. This would reduce development time and cost for the project. The decision implies that slight changes in design criteria may be acceptable; so far as the mission objectives remain achievable and the COTS products used offer readily available supplies and minimum development cost and effort.

A number of options for lifting device were considered, including aerostat (or blimp), kite, balloon/kite hybrid, blimp/kite hybrid and rotary-base devices. Although kite and hybrid devices tend to be more stable than others, their costs are unaffordable under the allocated budget for this project. Helium-buoyant device is preferred due to repeatability, stability and low cost. Together with the fact that DTS may be used once a year in an all-day-test, Helium cost may be more desirable than storage and maintenance of other high-tech devices. Thus, aerostat was selected as a preferred choice. Nevertheless, due to unavailability of aerostat of suitable size under reasonable cost, several weather balloons will be used together for the first phase of the design implementation. The designed FFU weight of 5 kg, estimated system weight of 5 kg and estimated tether weight of 3 kg make up a total of 13 kg for the lifting device to carry. According to specifications of quality weather balloon available from a supplier, 4 balloons with diameter of 12 ft (3.66 m) and total Helium volume of 5.48 m^3 should be sufficient for the task, although they cannot guarantee the performance of balloons for this adaptive use. It should be noted that the major variable in this test is the tether, which may add up a few kilograms to the system if flying higher or operating in stronger wind condition. Due to lack of certainty in tether specification, only rough estimation of the tether density was used and this could heavily affect the actual altitude the lifting device can achieve; and in turns, affect the impact speed an FFU must encounter. The calculations may be followed from the schematic diagram in Figure 5. And equations used in Table 3.

The tether will be connected to the lifting device and, on the other end, to a winch on the ground. This tether is suspected to carry high tension from lift force, wind gust and sustaining its own weight. In an extreme case, it is estimated that the lifting device could shift horizontally as far as vertically. That is, the lifting device, and thus the FFU before ejection, can be hovering as far as 1500 m away from the ground base where it was originally launched. This would roughly result in the total length of the tether as long as 3000 meters, excluding slight effect of catenary of the tether. The estimated tension in the tether, for the DTS operating in 5 m/s wind is about 700 N; using factor of safety as 3 in case the system encounters gust wind, the resulting designed tether strength is approximately 2000 N. High-strength low-density rope called Dyneema™ was chosen for the design due to its high strength-to-weight characteristic. However, the challenge came up as Dyneema™ rope ordered for strength test had only around 40% of the claimed strength. However, it is important to note that the failure occurred mostly near knots, in which these materials are known to have approximately 50% less in strength at locations where the fibres are bended, depending on the types of knot. At the end, a 3.2-mm-diameter Dyneema™ which was proven, by the manufacturer, to possess acceptable strength over 8000 N was chosen. Careful splicing at connecting point was taken to ensure minimum effect on strength reduction. A damping spring will also be added to a portion of the tether near the lifting device to help dampening tether snap as a result of wind gust.

On the ground side of the tether is a mobile winch which will be used to hold the lifting device and control its altitude and horizontal shift by storing in or releasing out the tether. The major requirement of the winch is mobility, and again, low cost. Another challenge of the winch is the spool capacity that must be able to store the whole 3000-m long of the tether. This results in large size of the spool, as well as stress incurred on the spool from tether weight and torque during the operation. Most commercially available winches are too large and too expensive such as those used to tow large gliders for takeoff; or too small such as those used in 4WD cars. A few custom-made winches used for recreational activities such as waterskiing, uphill-snowboarding and hang-gliding were considered as alternatives. Although these designs are normally not of industrial standard, they are practically functional. Thus, a contract was made for a custom-made winch, based on the original model which is used for waterskiing. The design configurations were also be consulted with the manufacturer who has years of experience.

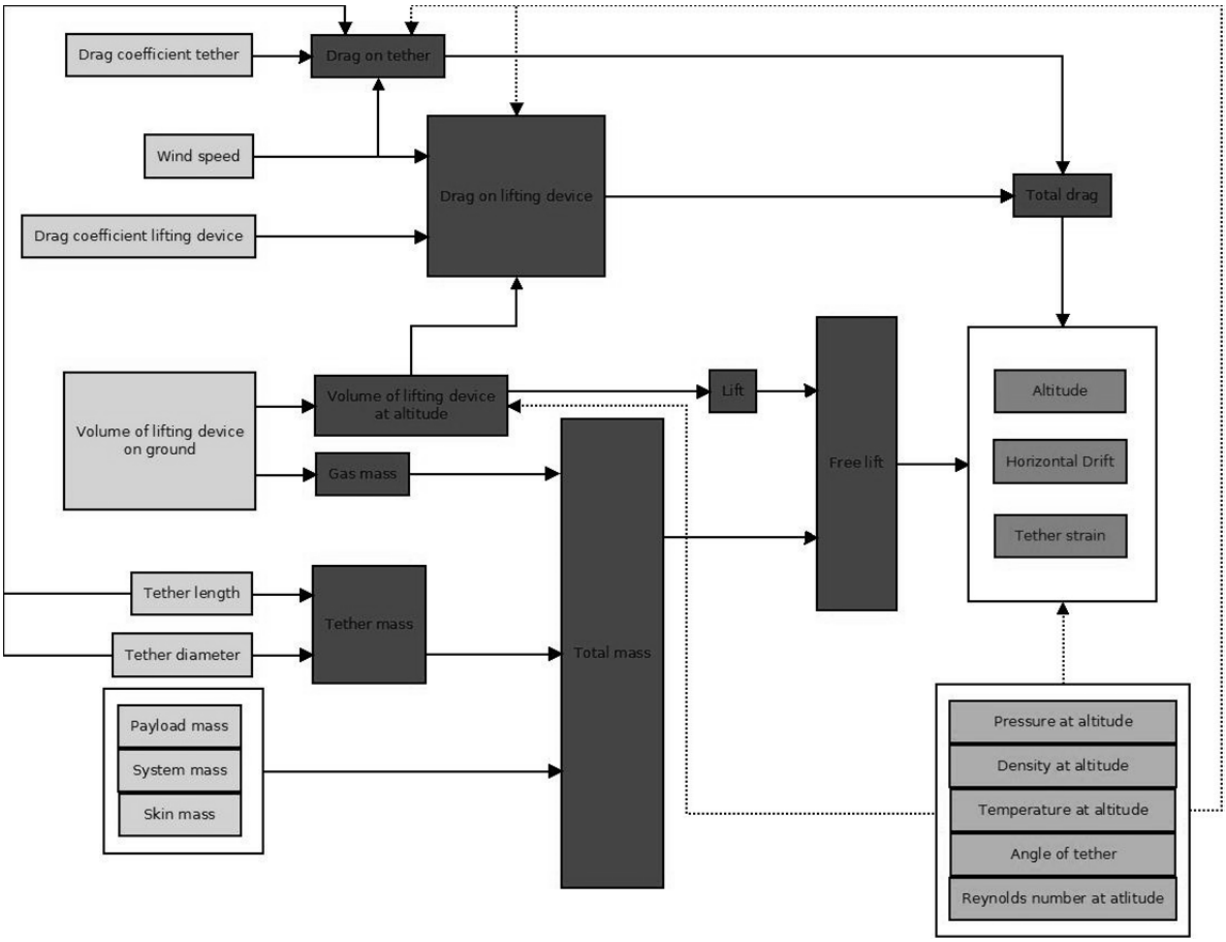

Figure 5. A schematic diagram showing calculations for the performance of DTS

Table 3. Formula used for calculation of system performance

Altitude	$h(x) = \frac{F_{D,tot}}{q}\left(cosh\left(asinh\left(\frac{F_{L,free}}{F_{D,tot}}\right)\right) - cosh\left(asinh\left(\frac{F_{L,free}}{F_{D,tot}}\right) - \frac{q}{F_{D,tot}}x_b\right)\right)$; $where\ \ q = \rho_{th}V_{th}g_0$		
Horizontal drift	$x = \frac{F_{D,tot}}{q}\left(asinh\left(\frac{F_{L,free}}{F_{D,tot}}\right) - asinh\left(\frac{F_{L,free}}{F_{D,tot}} - \frac{q}{F_{D,tot}}L_{th}\right)\right)$; $where\ \ q = \rho_{th}V_{th}g_0$		
Helium mass	$m_{He} = V_0\rho_{He}$	Tether mass	$m_{th} = \left(\frac{d_{th}}{2\times1000}\right)^2 \pi L_{th}\rho_{th}$
Tether strain	$F_{th} = \sqrt{F_{L,free}^2 + F_{D,tot}^2} + m_{th}g_0$	Lift	$F_L = \rho(h)\cdot V(h)\cdot g_0$
Drag on tether	$F_{D,th,n} = \frac{1}{2}\frac{\rho_i+\rho(h)}{2}\frac{d_{th}}{2\times1000}\pi L_{th}C_{D,th}v_{wind}^2$	Total mass	$m_{tot} = m_{th} + m_{gas} + m_{payload} + m_{system} + m_{ld}$
Drag on lifting device	$F_{D,ld} = \frac{1}{2}\rho(h)C_{D,ld}A_{ref,ld}v_{wind}^2$	Free lift	$F_{L,free} = F_L - m_{tot}\cdot g_0$
Volume of lifting device at altitude	$V(h) = V_0\frac{\rho_0}{\rho(h)}$	Total drag	$F_{D,tot} = F_{D,ld} + F_{D,th}$

The result is a winch equipped with a 9-hp motor running on fuel, with a group of high-strength steel spools of the required capacity. The winch can be trailed behind a car with its own wheel.

Finally, the release of FFU must be controlled from the ground station. The requirement of mobility and low cost still be a major consideration. Thus, a laptop installed with an in-house programming will allow operators to communicate with an onboard receiver and trigger the release. At the first phase of the design, the flying unit will be equipped with a pressure sensor and a GPS receiver; these data will be transmitted to the laptop on the ground station for decoding and determining exact location of the flying unit, especially its altitude and horizontal drift.

Figure 6. shows estimated cost breakdown of eash subsystem of the DTS. This estimation may possess small errors due to procurement of small or readily available parts which could not be accurately taken into account. However, with the set budget of €10,000, this total figure came up to be €10,512 which is 5.12% above the allocated budget. Better negotiation on winch and tether costs may result in a slight reduction of the total cost to be within the budget; however, if a long-term, sustainable lifting device such as an aerostat is used instead of weather balloons, the cost is expected to be much higher.

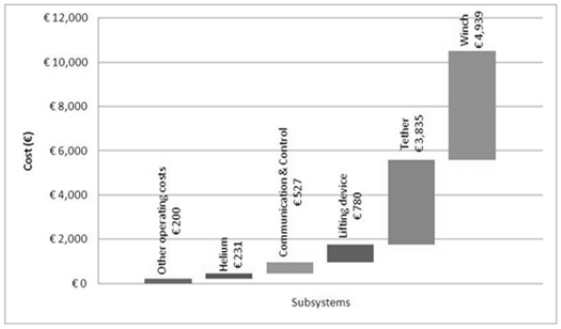

Figure 6. Estimated cost breakdown of each subsystem.

System implementation

At the time of writing this paper, the design is finished and waiting to be fully tested within this year (2013). To ensure functionality and safety of the system, the flying unit will be incrementally raised to different altitudes. For instance, it will be put up into 100-m altitude before being retrieved back to the ground. Then it will be put into 150-m altitude, pulled back and put into 200-m and so on. This will allow the operator to observe the overall capability of the system and stop the test before it exceeds the limit. In other words, it will reduce the chance of losing the whole flying unit if the wind is too strong that the tether fails or the winch motor is too weak to retrieve the unit back to the ground. Onboard the flying unit will be a dummy load of 5 kg to be dropped off for testing of communication and control, as well as the mechanical functioning of the release mechanism. The test area is depends directly on the test altitude and must be a restricted area and airspace, for safety reason. An ideal condition is a circle area with a minimum of 2250-m radius. However, if such a large area is not available, a smaller area with distance at least 1500 may be used instead; with reduced operational conditions. In other words, the system may be tested in no-wind or low-wind towards certain direction and possibly with lower test altitude.

Conclusion

The Drop Test System (DTS) is designed for pretesting of experiments onboard REXUS/BEXUS project, which involved Free Flying Unit (FFU) to be ejected from the vehicle. The system will provide functionality test of recovery system and communication and control system which are the two critical systems for a successful mission. This would allow early detection and rectification of any fault in FFU design. The DTS will be soon implemented and is expected to support participants in REXUS/BEXUS project for better design capability.

Astrophysics

Chairs: M. Wiedner & S. Kemi

RADIATION MEASUREMENT ON THE STRATOPSHERIC BALLOON BEXUS13

T. Möller[1], **B. Ehresmann**[1,2], **J. Labrenz**[1], **and L. Panitzsch**[1]

[1]*Institute of Experimental and Applied Physics, 24118 Kiel, Germany*
[2]*Southwest Research Institute, Boulder CO 80302, USA*

ABSTRACT

The Earth is permanently exposed to energetic particle radiation from cosmic rays. This energetic particle radiation yields, together with its secondary particles produced in the Earth's atmosphere, a natural radiation field inside the atmosphere. The radiation exposure is dependent on altitude and geomagnetic latitude as it is modulated by the Earth's magnetic field.
In the future, it is planned to use supersonic aircraft with operation altitudes between 20 and 25 km which is significantly higher than common aircraft altitudes. At these altitudes the radiation level is higher and reaches a maximum due to production of secondary particles. Therefore, it is important to know which kind of radiation level will be expected in these altitudes. For this investigation a particle telescope consisting of four segmented silicon semiconductor detectors was developed. Due to the arrangement of the detectors, it is possible to separate neutral and charged particles. Therefore the dose rates induced by charged and neutral particles can be determined separately. The Flight Radiation Environment Detector (FRED) conducted measurements onboard a stratospheric balloon in altitudes up to 25 km as part of the BEXUS programme. The results of the measurements will be presented.

1. INTRODUCTION

The goal of the described experiment is to measure the dose rate in dependence of the altitude in the complex radiation field of Earth's atmosphere. During the time of the above mentioned balloon launch, the sun was close to solar minimum conditions, i.e, there was a higher cosmic ray flux than at solar maximum. This can be seen in Neutron Monitor count rates [1].
The launch site of the balloon was at Esrange near Kiruna in north of Sweden. This area is well suited for this investigation as in the polar region there is the highest particle flux of galactic cosmic rays at Earth because there is a low geomagnetic cutoff [2]. Therefore, we have the highest dose rates in this region [3] and we can use the measurements as a conservative estimate for the radiation exposure in the Earth's atmosphere.
The department of Extraterrestrial Physics at the University of Kiel has a longstanding history of performing longterm measurements onboard the International Space Station (ISS) and aircraft using silicon detectors [4][5][6]. By using a balloon we can investigate the radiation field between the normal cruising altitudes of an aircraft and the ISS altitudes. The advantage of this experiment is a neutral channel so that we can investigate both the neutral and the charged component of the secondary cosmic rays with one experiment.

2. THE BEXUS PROGRAMME

BEXUS (Balloon-borne Experiments for University Students) is a German-Swedish student programme [7]. This programme offers opportunities for students to conduct scientific and technological experiments on research balloons under special atmospheric conditions. The BEXUS programme is realised under a bilateral Agency Agreement between the German Aerospace Center (DLR) and the Swedish National Space Board (SNSB). Therefore, German and Swedish students each have access to 50 percent of the balloon payload. The Swedish share of the payload has been made available to students from other European countries through a collaboration with the European Space Agency (ESA). The duration of the project is approximately 1 year. The stratospheric balloons are flying unguided and reach a maximum altitude of 30 km. The flight duration is 2-5 hours, depending on wind and weather conditions. The launching site is located near Kiruna in the north of Sweden, on the European launching site for rockets and balloons, Esrange Space Center. The BEXUS 13 launch was on the 28.09.2011.

3. THE FLIGHT RADIATION ENVIRONMENT DETECTOR (FRED)

The Flight Radiation Environment Detector (FRED) is a small and light-weight particle detector telescope. The height of the housing is 99.5 mm, with a footprint on the plate of 112 mm x 100 mm. Due to the housing being

Proc. '21st ESA Symposium European Rocket & Balloon Programmes and Related Research',
9–13 June 2013, Thun, Switzerland (ESA SP-721, October 2013)

made of magnesium the total mass is just 371 g.
Figure 1 shows a CAD drawing of FRED. The Printed

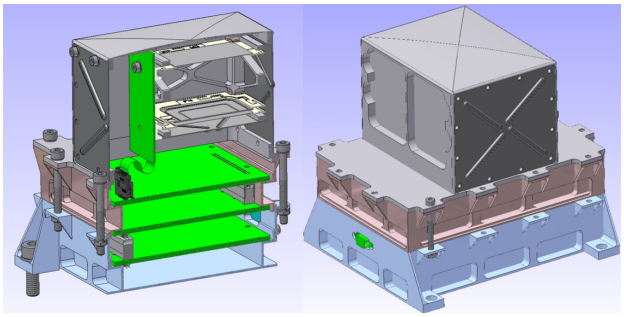

Figure 1. The mechanical design of FRED. On the left side a cross section of the experiment housing can be seen. The PCBs (green) are mounted inside the housing. On the right side one can see a CAD drawing of the whole instrument.

Circuit Boards (PCBs) are located in the lower part of the housing and the Detector Stack in the upper part. The Detector Stack is made up of 4 segmented silicon semiconductor detectors which are arranged in a telescope geometry with an opening angle of 120 degrees. The inner segments built a telescope with an opening angle of 60 degrees. Due to this geometry we can determine the Lin-

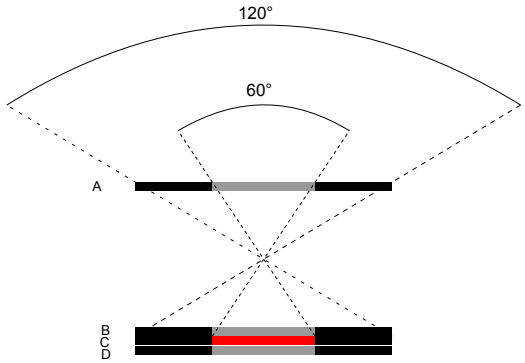

Figure 2. Schematic of the detector stack.

ear Energy Transfer (LET) by using coincident events in 2 detectors. From the LET it is possible to determine an average quality factor by using the ICRP 60 function [8]. With this average quality factor we can estimate a dose equivalent which is the unit for radiation protection as the dose equivalent includes the biological effectiveness of the radiation. Figure 2 shows a schematic drawing of the Detector Stack. The detector thickness is 300 μm - for all detectors - and the form is square with a 30 mm edge length. The inner segments of the detectors are also squared with an edge length of 22 mm. The detectors B, C, and D are glued together as close as possible (depending on needed distances for cables), to form a sandwich detector, as the detectors B and D and the outer segment of detector C are used as anticoincidence for the neutral particle channel (red area in figure 2), which builds the inner part of detector C. The detector signals circuit is connected via the filter board to the Irena which is used to handle the data processing and storage (see figure 3). It is made up of 2 PCBs, the analogue and the digital board. Figure 3 shows a schematic drawing of the instrument's

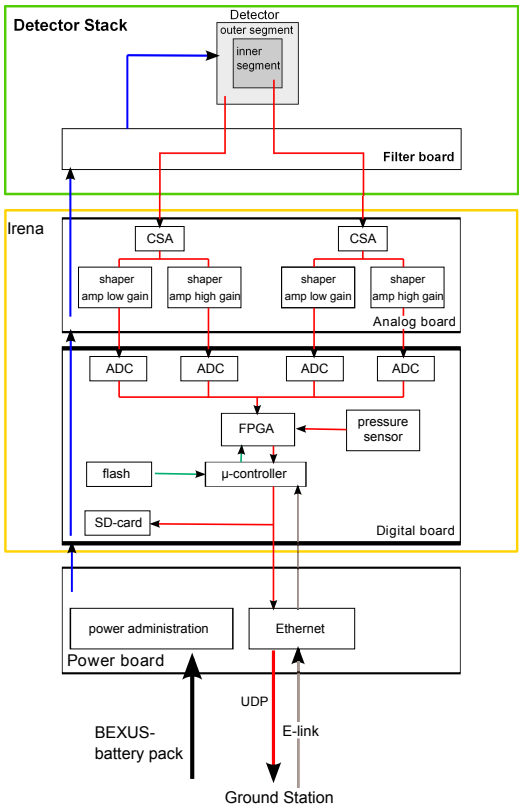

Figure 3. Schematic of the electronics.

electronics. An incoming particle interacts with the silicon in the Detector Stack. Thereby, free charge carriers are created. The Charge Sensitive Amplifier (CSA) collects these free charge carriers and converts them into a voltage pulse. The voltage pulse is shaped and amplified in two different steps (low and high gain). This voltage pulse is read out by the Analogue to Digital Converter (ADC). The Field Programmable Gate Array (FPGA) reads out the ADC signal and determines the pulse height. If the high gain amplifier output overflows the ADC output of the low gain is used. The processor stores the pulse height on a Secure Digital card (SD card). Furthermore, the data can be downlinked via User Datagram protocol (UDP). The Power board is connected to the BEXUS battery pack and is creating the -50 V detector bias voltage for the Detector Stack. Furthermore, it manages the different voltages for the components and there is also an ethernet connector located on this board.

4. RESULTS OF THE MEASUREMENT ON THE BEXUS 13 BALLOON

Figure 4 displays the count rate time profile in counts per minute from the inner segment of the A-detector (A1) during the balloon flight. Count rates for the high gain are

shown in red, for the low gain in blue. The black curve indicates the altitude profile during the balloon flight (right y-axis). From the measurement with FRED it is possible

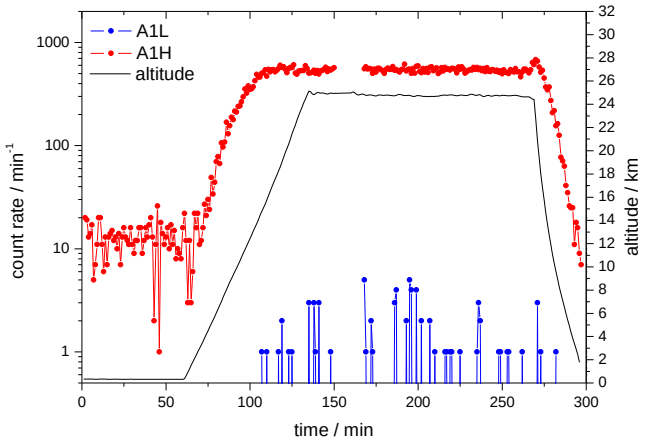

Figure 4. The count rate time profile of the balloon measurement.

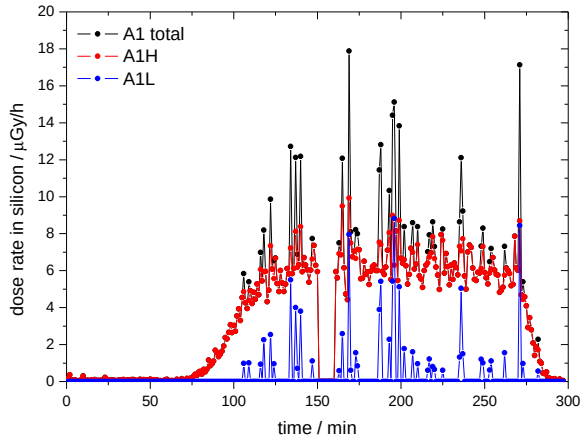

Figure 5. Dose rate time profile measured on the balloon flight.

to calculate the dose rate. The definition of the absorbed dose D is energy loss dE per mass unit dm [8]:

$$\mathrm{D} = \frac{\mathrm{dE}}{\mathrm{dm}}. \qquad (1)$$

Dose rate means dose per time. The dose rate time profile of the A-detector derived from the measurements is shown in figure 5. Shown are dose rates in silicon in the inner segment of detector A for the high (red) and low gain (blue). The black curve shows the total dose rate in silicon. A comparison of figures 4 and 5 yields that the spikes seen in the total dose stem from only a few particles measured in the low gain above 17 km altitude. Particles that can trigger the low gain must deposit at least 18 MeV in the silicon. In figure 6, one can see the determination of the Pfotzer maximum. Shown in black, are count rates in dependence of the residual atmosphere, which is a measure for atmospheric altitude. In this case, count rates are calculated by taking the mean value of all detector segments. Additionally, the poissonian error is depicted in the black error bar. To now determine the al-

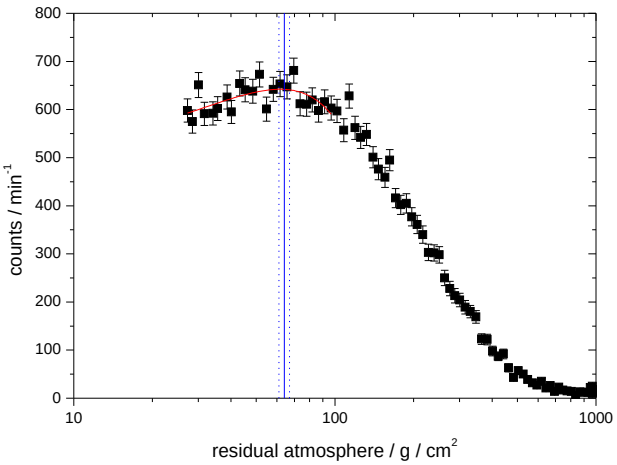

Figure 6. The determination of the Pfotzer maximum.

titude of the Pfotzer maximum, we fitted data points with a function of second order (red curve in figure 6). The resulting maximum of the fit (and, thus, the Pfotzer maximum) was found to be at $64 \pm 3 \frac{g}{cm^2}$ (blue line in figure 6). This value corresponds to a gps altitude of 19.2 ± 0.3 km on the date and time of the balloon flight which is in good agreement with other measurements [9].

Figure 7 shows the count rate in the neutral channel in

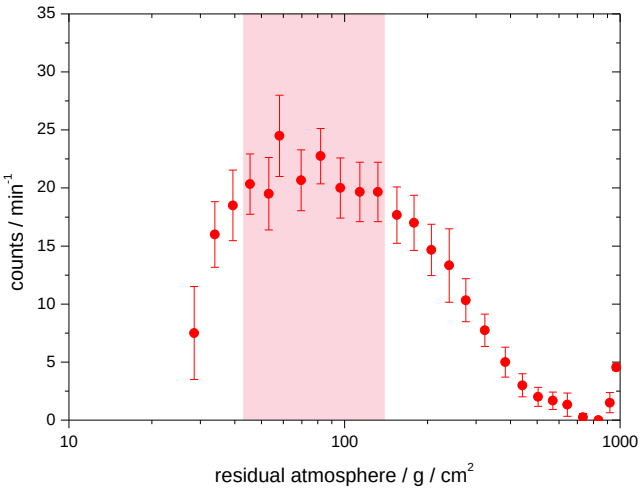

Figure 7. The altitude dependence of the neutral count rate.

dependence of the residual atmosphere. These counts are from signals only in the neutral channel and not in the anticoincidence. One can see that the count rates decrease directly after the launch due to the neutral particles which originate from the earth crust. After a few meters altitude the count rate increases up to a residual atmosphere of about $130 \frac{g}{cm^2}$. For residual atmospheres smaller than $45 \frac{g}{cm^2}$ a decreasing trend of the count rate is visible. In the range between 130 and $45 \frac{g}{cm^2}$ the count rate shows

a constant value in consideration of the poisson uncertainty of the measured count rates (red area in figure 7. Figure 8 shows a comparison of the altitude dependence of the charged particle (black curve) and neutral count rates (red curve). The grey area shows the result of the Pfotzer maximum determination. The neutral particles have a maximum between 14.5 and 22 km (red area). The comparison of the count rate shows that the neutral particle counts are smaller by a factor of approximately 30. Note that this does not considering the differing detection efficiencies for neutral and charged particles at the moment.

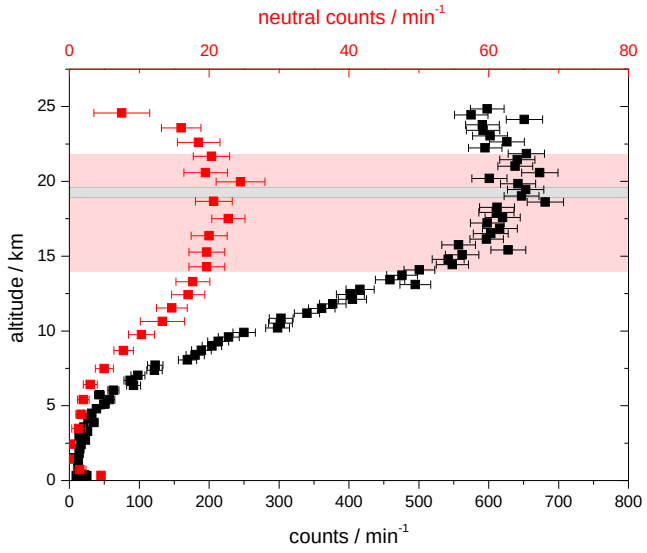

Figure 8. The altitude dependence of the count rates and the neutral count rates.

5. CONCLUSION

We have build a new instrument (FRED) based on silicon detectors. FRED flew on the stratospheric balloon BEXUS 13 and measuring successfully. The result of the calculation of the Pfotzer Maximum is $64\pm3\ \frac{g}{cm^2}$. This value of residual atmosphere is equivalent to 19.2 ± 0.3 km. Here, we also showed that it is possible to successfully distinguish between charged and neutral particles with FRED. Furthermore we showed the altitude dependence of the neutral particle count rate. It showed a maximum of the count rate between 130 and $45\frac{g}{cm^2}$ which is equivalent to 14.5 and 22 km. Further investigation considering detection efficiencies for neutral particles is still ongoing and will be published soon.

ACKNOWLEDGMENTS

This experiment was carried out as a part of the REXUS/BEXUS programme. The REXUS/BEXUS programme is realised under a bilateral Agency Agreement between the German Aerospace Center (DLR) and the Swedish National Space Board (SNSB). The Swedish share of the payload has been made available to students from other European countries through a collaboration with the European Space Agency (ESA). EuroLaunch, a cooperation between the Esrange Space Center of the Swedish Space Corporation (SSC) and the Mobile Rocket Base (MORABA) of DLR, is responsible for the campaign management and operations of the launch vehicles. Experts from DLR, SSC and ESA provide technical support to the student teams throughout the project.
The authors would further like to thank the department of Extraterrestrial Physics at the University of Kiel for their support in realising this project. In particular, the authors would like to thank Dr. Stephan Böttcher, Dipl.-Ing. Björn Schuster, and Dipl.-Ing. Lars Seimetz for their valuable technical support and Prof. Robert F. Wimmer-Schweingruber, Prof. Bernd Heber and Dr. Sönke Burmeister for the scientific support.

REFERENCES

[1] http://www.nmdb.eu/nest/search.php

[2] Smart, D.F., Shea, M.A. Fifty years of progress in geomagnetic cutoff rigidity determinations, 2009, Advances in Space Research 44, 1107-1123

[3] Wissmann F., Long-term Measurements of $\dot{H}^*(10)$ at Aviation Altitudes in the Northern Hemisphere, 2006, Radiat. Prot. Dosimetry 121,347

[4] R. Beaujean, J. Kopp and G. Reitz, Active Dosimetry on recent Space flight, 1999, Radiat. Prot. Dosimetry 85, 223-226.

[5] G. Reitz, R. Beaujean, E. Benton, S. Burmeister, Ts. Dachev, S. Deme, M. Luszik-Bhadra and P. Olko, Space Radiation Measurement On-board ISS - The DOSMAP Experiment, 2005 , Radiat. Prot. Dosimetry 116, 374-379

[6] R. Beaujean, S. Burmeister, F. Petersen and G. Reitz, Radiation Exposure Measurement Onboard Civil Aircraft, 2005, Radiat. Prot. Dosimetry 116, 312-315

[7] http://www.rexusbexus.net

[8] 1990 Recommendations of the International Commission on Radiological Protection. ICRP Publication 60. Ann. ICRP 21 (1-3).

[9] G.A. Bazilevskaja, I.G. Usokin, E.O. Flückiger, R.G. Harrison, L. Desorgher, R. Bütikofer, M.B. Krainev, V.S. Makhmutov, Y.I. Stozhkov, A.K. Svirezhevskaja, N.S. Svirzhevsky, and G.A. Kovaltsov, Cosmic ray induced ion production in the atmosphere. Space Sci Rev, 137:149-173, 2008.

AUTONOMOUS PAYLOAD FUNCTION: THE POGOLITE SOFTWARE

M. S. Jackson (for the PoGOLite collaboration)

KTH, The Royal Institute of Technology and The Oskar Klein Centre for Cosmoparticle Physics, AlbaNova University Centre, Stockholm, Sweden

ABSTRACT

I describe the software in the Payload Control System (PCS) of the Polarized Gamma-ray Observer (PoGOLite). PoGOLite is a balloon-borne Compton-based X-ray polarimeter designed to observe point sources between 25 and 100 keV. The payload is capable of pointing and acquiring polarimetric data in an autonomous manner, and this is the primary mode of operation for the multiple-day balloon flight. The philosophy and functionality of the software are described, and test results are given.

Key words: balloon borne instrumentation; control systems; polarimeters.

1. INTRODUCTION

Polarimetry at X-ray energies is an emerging topic in the field of astrophysics. By means of polarimetry, characteristics such as magnetic fields and geometry of unresolved objects can be measured, whereas this information would otherwise be largely unknown. Objects such as pulsars, X-ray binaries, and magnetized nebulae are expected to emit distinct and high levels of polarization.

PoGOLite [1] consists of a hexagonal array of fast plastic scintillators to measure Compton scattering events of incoming photons and subsequent photoabsorptions of the electrons. By determining the geometry of each Compton scattering event, the likely polarization of the incoming photon can be determined, and when many of these events are combined, the resulting modulation curve can indicate the polarization degree and angle of the radiation. Rejection of off-axis events and the rather large particle background in the upper atmosphere is provided by a thick polyethylene shield and an active anticoincidence system.

During the flight, it will be possible to issue commands to the instrument and to transfer full datasets from the instrument to the ground computers at the beginning of the flight, when line-of-sight E-Link communications [2] are possible. This will most likely last for a few hours, and an additional period of line-of-sight communication may be possible by means of a connection with the Andoya Rocket Facility in Norway. After this high-speed connection method is no longer possible, the only opportunity for communication with the instrument will be made possible with an Iridium connection [3]. This is much slower and less reliable than the E-Link connection, and does not allow large files to be transferred. Therefore, it is important that the payload be controlled by an onboard program, rather than by a user on the ground. This autonomous system is described in detail in [4].

PoGOLite was launched on its maiden flight from the Esrange facility in northern Sweden in the summer of 2011. Unfortunately, it was soon discovered that there were some problems with the balloon, and the flight was terminated. Another flight was scheduled during July 2012, but surface winds at the Esrange facility prevented an attempt during this launch window. Another launch window opens in July 2013.

During the few-hour flight in 2011, while it was not possible to obtain polarization data because of the reduced altitude, it was possible to test the pointing and tracking functionality on real stars during flight conditions. In addition, sun-tracking tests were performed on the ground in 2012. Sun tracking is not an expected pointing mode in flight; the tests were performed in this manner because Esrange is located above the arctic circle, and thus does not experience dark conditions with visible stars during summer nights. The function of the automated system has been tested independently of the tracking tests, and the results of all these tests are given in §4.

2. POGOLITE SYSTEMS AND HIERARCHY

The scientific payload of PoGOLite comprises three main systems: the polarimeter itself, the attitude control system (ACS), and the payload control system (PCS). These systems are described below, and the components contained within the gondola are shown in Figure 1.

The constituents of and interconnections between the systems are shown in Figure 2. The software on computers in the PCS provides the central control over the polarimeter and the pointing system in the ACS.

Proc. '21st ESA Symposium European Rocket & Balloon Programmes and Related Research', 9–13 June 2013, Thun, Switzerland (ESA SP-721, October 2013)

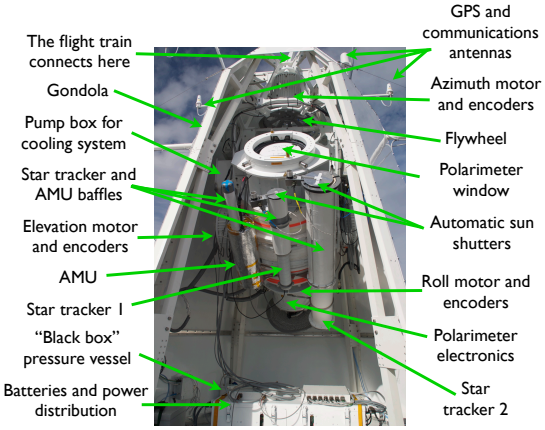

Figure 1. The polarimeter and ACS inside the gondola, with the visible components labelled.

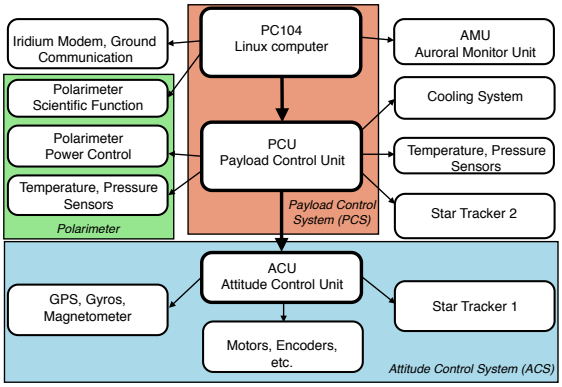

Figure 2. Control structure for the PoGOLite payload. An arrow indicates that the device at the point of the arrow is controlled or monitored by the other device through ethernet, RS422, or other connection type.

2.1. Polarimeter

The polarimeter detector system comprises a hexagonal array of phoswich detector cells (PDCs) surrounded on all but one side by anticoincidence detectors. Each PDC comprises three different scintillating elements: a hollow slow plastic scintillator for collimation near the opening, a solid fast plastic scintillator for detecting polarization events, and a bismuth germanium oxide (BGO) crystal at the bottom. The BGO anticoincidence shield continues to the sides of the detector array to the side anticoincidence system (SAS). Each SAS unit consists of three BGO crystals glued together. In addition, a neutron detector is placed behind the main array to measure the neutron background, which has been determined to be the primary source of false events. Each detector element is optically connected to a photomultiplier tube (PMT), which is in turn electronically connected to one of twelve eight-channel flash ADC (FADC) boards. These are connected through SpaceWire and two router boards to a digital in/out (DIO) board, and a SpaceWire to ethernet interface known as a SpaceCube. Additional auxiliary electronic boards combine and split the logical signals from and to the FADC boards. These boards also provide power switches and sensor interfaces.

The FADC boards distinguish events within the fast scintillators from those within the slow and BGO scintillators by means of pulse shape discrimination (PSD), exploiting the faster decay time of the fast scintillators (3 μs compared with $\sim 300\mu$s for the slow scintillators and BGO). Cosmic rays and other high energy particles are distinguished by a particularly high energy deposit in a detector, which triggers the upper discriminator (UD). When a candidate event is received by the DIO, the anticoincidence (PSD and UD) signals are checked, and if none are found, the waveforms are saved in the internal memory of the FADC boards. These are regularly transferred to the more permanent storage of a PC104 computer. Many parameters on the FADC boards, such as thresholds and PMT voltages, can be set via the SpaceCube interface. These reset to defaults with each power cycle, and must be set again when each individual FADC board is repowered.

2.2. Attitude control system

Pointing of the instrument is done by means of a sophisticated attitude control system (ACS) [5], which makes use of input from differential GPS, magnetometers, and gyroscopes to determine the current attitude, and motors and encoders to maintain and adjust the pointing direction. The ACS has motors and actuators for pointing in both elevation and azimuthal directions, and for instrument roll, which determines the orientation of the polarimeter about the pointing axis. The instrument roll is essential in the attempt to eliminate inhomogeneities in the response of the detectors in the array while measuring the polarization signal.

A real-time computer known as a Main Processing Board (MPB), called the Attitude Control Unit (ACU), is used to process the sensor input and current settings to determine the next action. Sensor input is obtained through a high-speed serial interface with multiple Industrial Utility Boards (IUBs), which convert the readings from the encoders and other sensors into signals. The ACU monitors the health of the components of the ACS, and performs appropriate action in the case that a foreseen problem is encountered, such as a motor that draws too much current or becomes too hot.

The ACS is capable of acheiving and maintaining pointing at positions defined in both Azimuth-Altitude and celestial (Right ascension-declination) coordinates. The possible modes are defined in the ACU as input signals, and comprise the following:

0. Startup – This is the default mode upon startup.
1. Initialize – After the initialization of the sensors, the motors are activated in turn to locate the reference points. This mode must be successful in order for the pointing to be possible. It is possible to choose individual systems to initialize, so if the gondola is placed on the floor and pointing is impossible, it is still possible to initialize and use the instrument roll.
2. Stow stabilized – The instrument is pointed vertically and held in place by magnets, and the azimuth is stabilized in a specified direction.
3. Stow unstabilized – The instrument is vertical as in the previous mode, but the azimuth is not controlled.
4. Exercise – This mode is designed to prevent ice formation on the motors, particularly during ascent, when the ambient temperature becomes very low at certain altitudes. The motors are gently rocked back and forth.
5. No control – The pointing motors are disengaged, but the instrument roll setting can be controlled. This mode is effectively a software-induced ”emergency stop” for the pointing.
6. Azimuth/elevation pointing – The ACS points at azimuth and elevation coordinates defined by input signals.
7. Right ascension/declination pointing – The ACS continually calculates the current azimuth and elevation from the input celestial coordinates and points as in the previous mode.
8. Power save – This mode is used to reduce the power consumption when the battery charge becomes low.

2.3. Payload control system

The payload control system consists of PC104 computers running Ubuntu Linux, an MPB similar to the one in the ACS, two IUBs (one of which is located within the polarimeter pressure vessel assembly), two network switches, DC/DC convertors, and auxiliary electronics boards providing power switches and an interface for sensors. The main processing is done with one of the PC104 computers and with the MPB, which is called the Payload Control Unit (PCU). There are three PC104 computers in total; two of these have Iridium modems connected to them, and the other is contained within a separate pressure vessel called the Black Box. The Black Box computer contains software identical to that of the two other PC104s, but is intended to be used only as redundant storage. The Iridium modem on the second PC104 provides redundancy for the first Iridium modem. Each PC104 has four 128 GB solid state disks in a RAID array, with an effective capacity of 256 GB. The data to be stored on the PC104s is intended to be identical for additional redundancy.

The PCU is connected though a high-speed RS422 connection to the ACU in a master-slave relationship, where the PCU functions as the master. This means that any input signals in the ACU which are connected to the PCU and are not manually forced through a ground connection (such forcing of signals is not foreseen during flight) are set through output signals in the PCU. Through this connection, the PCU is able to log certain ACU signals for later analysis.

3. SOFTWARE FUNCTION

This paper is intended primarily to describe the function of the software on the PC104 computers and on the PCU. Mention of other software or functions (the above ACU modes, for example) is made only for the purposes of clarity and completeness.

3.1. PCU software

The purpose of the PCU (with the two connected IUBs and the auxiliary electronic boards mentioned above) is to collect sensor data and store them as signals, and to convert input signals into specific system states, which involve power switches, electronic gates, and other settings. Some of the signals are stored as log files, and these files are routinely transferred to the PC104s.

The real-time operating system in the PCU was written in C++. The signals in the PCU are either input or output, with boolean, short, int, and float types. The PCU executes its instruction set at a rate of 200 Hz, and some of the modules are run at fractions of this speed.

The timing for the polarimeter data is done by means of a gated pulse per second (PPS) signal from the GPS receivers. The PPS signal is sent to the DIO board in the polarimeter, which in turn causes the FADC boards to

record a special type of event. Since each event is digitally timestamped by the FADCs (in units of clock cycles), and each PPS event occurs on an exact second, the times for all events can be determined by means of interpolation. The real time of each PPS signal is determined from a gating pattern programmed into the PCU. The PPS signal for the first second of every minute and for the third second of every five seconds are gated (blocked), and when this pattern is detected, the real GPS time of each event can be determined, given that the GPS time is logged at the start of each acquisition run.

3.2. PC104 software

The primary software on each PC104 consists primarily of a mutlithreaded program which connects to, monitors, and controls both the polarimeter and the PCU. In addition, it controls certain functions in the ACS through the high-speed connection described in the previous section. A script provides autonomous function by sending commands to the program after determining the next appropriate action.

The threads in the program are used to monitor temperatures of the polarimeter detectors and electronics and to control the cooling system, activate and monitor the ACS, and monitor polarimeter function, while checking regularly for new input commands from either the console or a file.

3.3. Autonomous control

The algorithm for the autonomous function is shown as a flowchart in Figure 3. The autonomous function is initiated and controlled via empty files which can easily be manipulated from the ground with even a slow connection. Two such files are used: a file called ”enable”, whose existence causes the script to perform pointing and data acquisition functions, and a file called ”shutdown”, which determines whether the polarimeter electronics will be powered down when the autonomous function is no longer enabled. The purpose of the second of these options is to allow the autonomous function to be suspended and manual control to be initiated, for observation of a transient event such as a solar flare or gamma-ray burst, for example, without the necessity to reinitialize the polarimeter electronics, which can be time-consuming and vulnerable to errors. The pointing and observation algorithm is described in § 3.4. The number of observations is determined by the remaining time during which the current target is most favourable to observe.

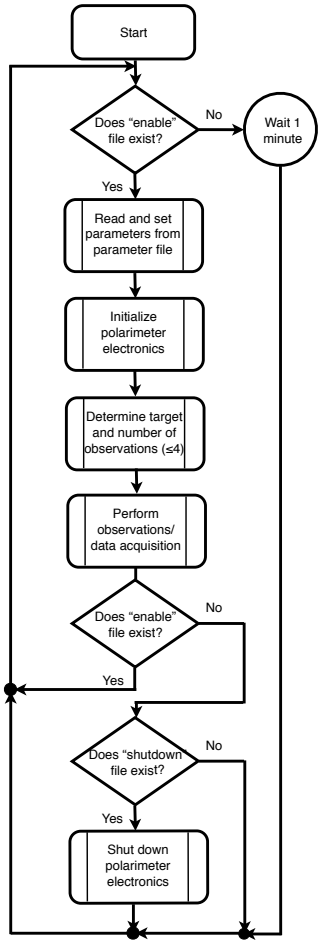

Figure 3. Flowchart showing overall autonomous function.

3.4. Pointing

A flowchart for the observation scheme is shown in Figure 4. Each cycle consists of up to four five-minute observations, the third of which is a background observa-

tion, which is pointed in a direction slightly offset from the target. Each cycle contains a test of the polarimeter electronics, which can lead to unusable data if any board enters an error state. The polarimeter electronics are set with the appropriate parameters at the beginning of each cycle.

4. TEST RESULTS AND CONCLUSIONS

The system has been tested in Linköping, Sweden in the springs of 2011 and 2012, and at the Esrange facility in the summers of 2011 and 2012 and the winter of 2013. Unfortunately, because of the long days in the arctic during June and July, and because weather and personnel issues at Esrange prevented outdoor night tests in February and March in 2013, it has not yet been possible to test the autonomous system while also evaluating the pointing quality. However, these tests have been performed separately.

The autonomous function was tested for long periods in the summer of 2012. It was determined that the system is capable of perpetual autonomous operation without any human intervention for at least a day at a time. There is no reason to believe that there would be any upper time limit to this function, and as long as no unexpected hardware problems are encountered, it could be expected that the automated system could be activated once before the Elink service is no longer available, and stopped just before the end of the time at float, and would need to be connected via Iridium only for monitoring purposes.

The pointing quality has been evaluated and has been found by various methods to be adequate for the needs of the polarimeter (e.g. [6]). This will be evaluated in more detail, with particular regard to alignment between the X-ray polarimeter and the ACS and star trackers, during the flight. This alignment cannot be definitively tested on the ground.

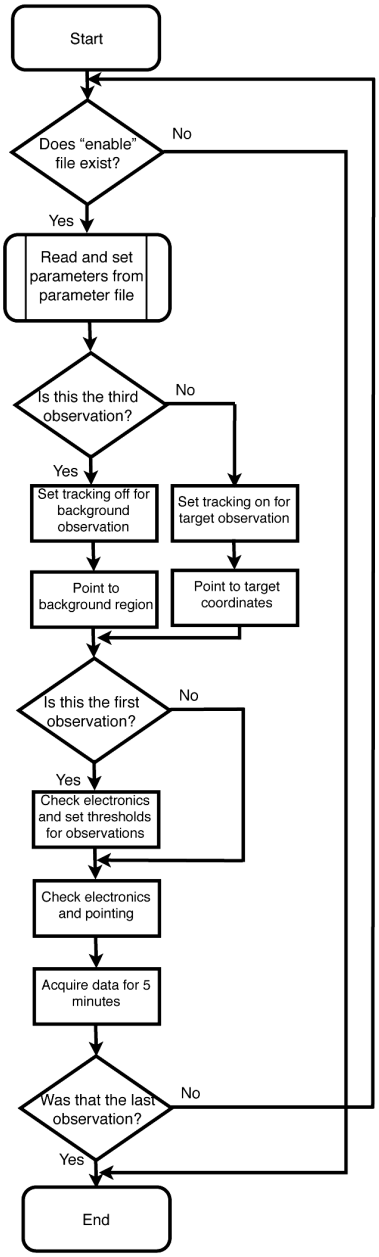

Figure 4. Flowchart for the pointing and data acquisition during the automated function.

ACKNOWLEDGMENTS

Work on the PoGOLite experiment has been made possible by a grant from the Swedish National Space Board, and work on the ACS was funded by the Swedish Research Council.

REFERENCES

[1] Kamae, T., et al., 2008, Astrop. Phys. 30, 72

[2] Jönsson, L.-O., 2009, ESA-SP-671, ESAPAC Proceedings, Bad Reichenhall, Germany 215

[3] Iridium RUDICS, `http://www.Iridium.com/products/RUDICS.aspx`

[4] Jackson, M. S., 2013, JINST 8 P04008

[5] Strömberg, J-E, 2011, ESA SP-700, ESAPAC Proceedings, Hyére, France 353

[6] Nilsson, D., 2013, Characterization of the pointing systems of the PoGOLite Pathfinder, KTH Masters thesis, Stockholm, Sweden

MEASUREMENT WITH A PHOSWICH DETECTOR ON A STRATOSPHERIC BALLOON

Enno Scharrenberg[1], **Esther M. Dönsdorf**[1], **P. Kühl**[1], **H. Lohf**[1], **J. Marquardt**[1], **and H. Winterfeld**[2]

[1] *Christian-Albrechts-Universität zu Kiel, Institut für Experimentelle und Angewandte Physik*

[2] *Christian-Albrechts-Universität zu Kiel, Technische Fakultät*

ABSTRACT

In the Earth's atmosphere primary cosmic rays interact with the present molecules and atoms. Hence, the radiation environment in the Earth's atmosphere is affected by the generation of secondary charged and neutral particles i.e. electrons, muons and protons as well as neutrons and gamma rays. At cruising altitude of commercial aircraft, neutrons yield a significant proportion to the dose equivalent rate. The student team MONSTA (Measurement Of Neutrons with Scintillators in The Atmosphere) participated in the BEXUS (Balloon Experiments for University Students) program. The team used the Phoswich Instrument for Neutrons and Gammas (PING) on the stratospheric balloon BEXUS 14 to measure the height dependent flux of the neutral component. In order to determine the contribution of neutrons to the dose, it is essential to measure their altitude-dependent energy deposition spectra. The sensor head of PING consists of two different scintillators: The inner plastic scintillator BC-412 and the surrounding inorganic scintillator CsI(Na). The scintillators are optically coupled and are read out by a common photomultiplier. Neutrons deposit more energy in the hydrogen rich BC-412 plastic scintillator while the heavy inorganic scintillator has a high cross-section for gamma rays. Because of their different decay times, the pulses of the two scintillators have a different pulse shape. An overview of the experiment and first results of the balloon flight will be presented.

Key words: BEXUS 14, phoswich detector, radiation measurement, neutrons.

1. MOTIVATION

When a primary particle of the Galactic Cosmic Rays enters the Earths atmosphere, it triggers a cascade of secondary particles. The flux of the secondary particles have a maximum at about 20 km which is the so called Pfotzer maximum. At cruising altitude of commercial aircraft, neutrons yield a significant proportion to the dose equivalent rate [1]. Hence, it is interesting to measure the altitude dependence of the neutron flux.

2. REXUS/BEXUS PROGRAMME

The REXUS/BEXUS (Rocket/Balloon Experiments for University Students) programme allows students from universities and higher education colleges across Europe to carry out scientific and technological experiments on research rockets and balloons. Each year, two rockets and two balloons are launched, carrying up to 20 experiments designed and built by student teams.

The REXUS/BEXUS programme is realised under a bilateral Agency Agreement between the German Aerospace Center (DLR) and the Swedish National Space Board (SNSB). The Swedish share of the payload has been made available to students from other European countries through a collaboration with the European Space Agency (ESA). EuroLaunch, a cooperation between the Esrange Space Center of SSC and the Mobile Rocket Base (MORABA) of DLR, is responsible for the campaign management and operations of the launch vehicles. Experts from ESA, SSC and DLR provide technical support to the student teams throughout the project.

3. THE DETECTOR PING

The Phoswich detector PING developed by Esther M. Dönsdorf consists of two different scintillators (see Fig. 1). Neutrons deposit mostly their energy in the inner hydrogen rich plastic scintillator made of BC-412 mainly due to elastic scattering. The outer scintillator made of CsI(Na) is used as an anticoincidence.

The light output of the both scintillators are read out by a common photomultiplier tube (PMT) on the top of the detector. By applying a pulse shape analysis the pulses of the two different scintillators can be separated [3].

Proc. '21st ESA Symposium European Rocket & Balloon Programmes and Related Research',
9–13 June 2013, Thun, Switzerland (ESA SP-721, October 2013)

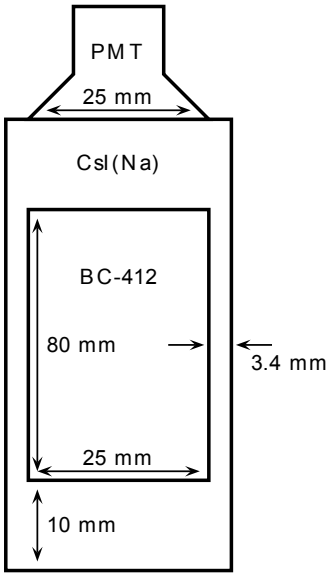

Figure 1. Schematic of the Phoswich Intrument for Neutrons and Gammas [3].

4. THE MONSTA EXPERIMENT

4.1. Electronics Design

H. Lohf designed an electronic circuit which is capable of switching on and off the PING instrument, autonomously regulating the temperature of the PING instrument, and switching off the PING instrument via watchdog.

The used microcontroller measures the temperature using NTC Thermistors and controls heat foils in order to keep the instrument in a desired temperature range (see sec 4.2). The active thermal control can be switched on and off via uplink. Due to safety instructions the microcontroller can switch on and switch off the PING instrument when a corresponding command is sent to the microcontroller. As a further security measure a watchdog is implemented. It sends signals and receives signals from the ground in a defined time interval. If the signal is lost and no answer is given over a pre-defined time interval, then the watchdog shuts down the PING instrument which includes high voltage switch off immediately to prevent any harm.

4.2. Thermal Design

The temperature range of PING is between $5°$ Celsius and $40°$ Celsius. The instrument itself does not produce much heat. Hence, an active temperature control system designed by H. Lohf was used. That means monitoring the temperature and then adjusting it with an active heating system. Additionally, several centimeters of polystyrene (1.5 cm) and EPP (expanded polypropylene) (2.5 cm) were used as an insulation. All components in the control box can operate between $-40°$ Celsius and $+85°$ Celsius so that a active heating of the control box is not necessary.

4.3. The Balloon Flight

The launch of the MONSTA experiment on the BEXUS 14 gondola was on 24. September 2012 at Esrange Space Center. The duration of flight was $4\,\mathrm{h}\,40\,\mathrm{min}$ with a maximum flight altitude of $28.7\,\mathrm{km}$, see Fig. 2. The second experiment, designed by the student team TECHDOSE, also measured the radiation caused by primary and secondary galactic cosmic rays.

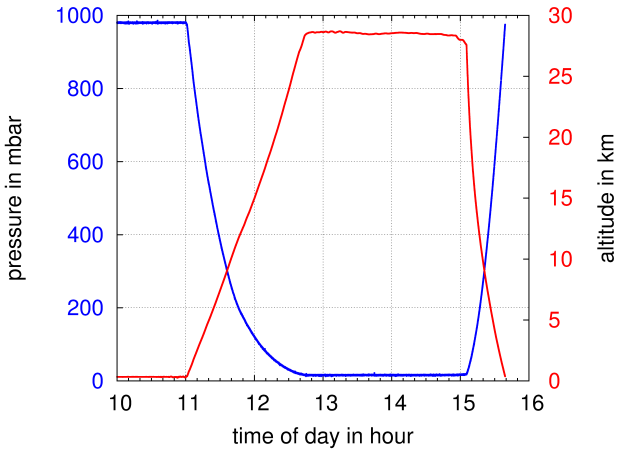

Figure 2. BEXUS 14 altitude and pressure time profile [4].

4.4. First Results of the Measurements

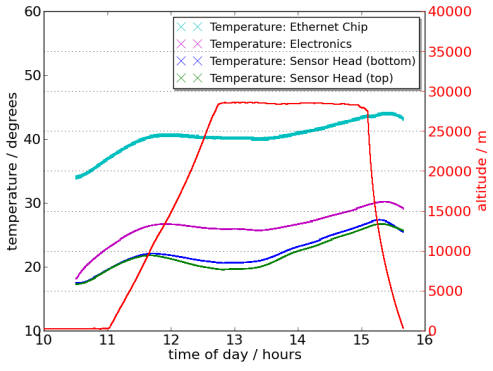

Figure 3. Thermal behaviour of the experiment during the flight.

In Fig. 3 the thermal behaviour during the flight is shown. Below a temperature of 20 degree, the active heating sys-

tem switched on the heating foils. For only one hour the top of the sensor head was heated. All other heating foils on the bottom of the sensor head and the heating resistors at the electronics were not needed for heating. The upper thermal limits of 40 degree in the readout electronics of PING and 85 degrees at the Ethernet Chip in the electronics designed by H. Lohf were not reached.

In Fig. 4 the processed data of the count rate is shown. The pressure was measured by the pressure sensor in the instrument. It gives an approximated measure of the altitude. The Pfotzer maximum (at 20 km) can be clearly seen at the ascent and descent phase.

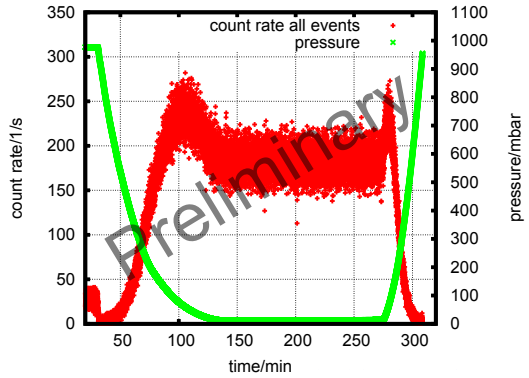

Figure 4. Count rate (in events/second) of all events in the detector versus the time in minutes [3].

In Fig. 5 the dose rate in $\mu Gy/h$ in the CsI and BC-412 scintillator versus time in minutes is shown. The dose in BC-412 is caused by neutrons with a small contribution of gamma rays. The dose rates show a similar altitude dependence as the count rates.

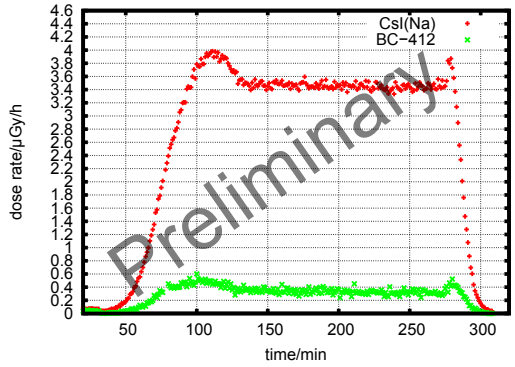

Figure 5. Dose rate in $\mu Gy/h$ in the CsI and BC-412 scintillator versus time in minutes [3].

ACKNOWLEDGMENTS

The authors would like to thank B. Heber, R. Wimmer, S. I. Böttcher, S. Burmeister, B. Ehresmann, J. Labrenz, T. Möller, L. Panitzsch, B. Schuster, L. Seimetz and all members of their department (Abteilung Extraterrestrische Physik, Institut für Experimentelle und Angewandte Physik, Christian-Albrechts-Universitt zu Kiel) for every scientific, engineering and financial support.

The authors wish to thank their tutor M. Fittock from DLR Bremen for his support during the whole project.

The authors would like to thank the German Aerospace Center (DLR), Swedish National Space Board (SNSB), EuroLaunch, ESA, SSC for every scientific, technical and financial support.

REFERENCES

1. G. Battistoni, A. Ferrari, M. Pelliccioni and R. Villari, *Monte Carlo Calculation of the angular distribution of cosmic rays at flight altitudes*, Radiation Protection Dosimetry (2004) Vol. 112, No. 3, pp. 331-343

2. www.rexusbexus.net, 2013

3. E.M. Dönsdorf, PhD thesis - not published yet

4. Data provided by Euro Launch

CIDRE –A SMALL ASTRONOMICAL BALLOON EXPERIMENT AT FAR INFRARED WAVELENGTHS (2.7 THZ)

Martina Wiedner[1], Laurent Pagani[1], Christophe Berthod[2], Fabien Defrance[1], Yan Delorme[1], Frederic Dauplay[1], Jean-Laurent Dournaux[3], Alexandre Feret[1], Paul Goldsmith[4] , Horville Horville[3], Jean-Michel Huet[3], Pascal Jeseck[5], Jonathan Kawamura[4], Jean-Michel. Krieg[1], Philippe Laporte3, Roland Léfèvre[1], Alain Maestrini[1], Imran Mehdi[4], Christian Rouille [5], Joseph Spatazza[2], Jeanne Treuttel[1]

[1]LERMA Observatoire de Paris, 61 ave. de l'Observatoire, 75014 Paris, France
Email: firsnamet.lastname@obspm.fr

[2] INSU, / Division Technique, 1, place Aristide Briand, 92195 MEUDON cedex, France
Email: christophe.berthod@dt.insu.cnrs.fr, spatazza@dt.insu.cnrs.fr

[3]GEPI Observatoire de Meudon, 5 Place Jules Janssen, 92190 Meudon, France
Email: firsnamet.lastname@obspm.fr

[4]Jet Propulsion Laboratory, M/S 180-703, 4800 Oak Grove Drive, Pasadena, CA 91109, USA
Email: paul.f.goldsmith@jpl.nasa.gov, jonathan.h.kawamura@jpl.nasa.gov, Imran.Mehdi@jpl.nasa.gov

[5] LPMAA, 4 place Jussieu,Tour 32-33 2ème et 3ème étage,75005 Paris, France
Email: firstname.lastname@upmc.fr

ABSTRACT

The CIDRE Campagne d'Identification du Deutérium par Réception hEtérodyne project is to fly an astronomical 2.7 THz/ far-IR heterodyne receiver on a stratospheric balloon. The project is to measure HD and other THz lines in our galaxy and to demonstrate the readiness of THz technology for space applications. The project is currently funded in phase A by the CNES for a detailed conceptual study and is still open for collaborations.

1. ASTRONOMY

The main goal of CIDRE is to observe HD in our Galaxy. We are also interested in observing H_2O, high-J transitions of CO and rare molecules such as HF, as well as conducting a frequency survey around 2.7 THz.

Deuterium was formed in the Big Bang and is since burned in stars (astration). The ratio of D/H is therefore a measure of the star formation that has occurred in a given place since the origin of our universe. We would expect, for example, that the D/H ratio in our galaxy is smaller in the galactic centre than at larger radii [1]. Deuterium is difficult to measure. So far it has been measured in absorption in the UV [2, 3], but these measurements are almost only possible in our neighbourhood up to ~ 500pc due to the high opacity of the lines. Varying values between 0.5 to 2.2 10^{-5} were found. In molecular clouds practically all the deuterium will combine with H into HD. HD has its first transition line at 2.7 THz or 112 microns and because of its very low electrical dipole, the line is optically thin in most cases. Because HD is confined to molecular clouds, and due to its optical thinness, the line can be observed all over the Galaxy. With CIDRE we want to measure HD in Galactic molecular clouds from the centre of the Galaxy to the outskirts (in absorption in front of strong continuum sources such as W49 and W51 or in emission inside warm regions).

Water is an important element in astrochemistry as the oxygen chemistry (including O_2, OH, and H_2O) is not well-understood. It is also thought that water is necessary for the appearance of life on other planets and a major coolant in the star-forming regions warm enough to have evaporated the H_2O ices. Obviously, it is difficult to measure water from the Earth as the Earth atmosphere contains lots of water itself. From space however it is possible to measure water in the interstellar medium (ISM) as largely done by the Herschel space observatory recently.

CO is very commonly used to trace molecular material. Usually low-J rotational transitions are used, which predominantly trace cold(er) molecular clouds (10 to 30K). Some studies have been conducted up to 1000 GHz, or J_{up} = 9, to trace warm gas. Recently, the Herschel satellite has found a surprising amount of CO in high J transitions with J up to 49 [4]. These transitions arise in hot gas (~4000 K) possibly heated in shocks.

There are other molecules which have a transition in the range 2.4-2.8 THz, such as HF (J:2-1), which we will also try to detect (the J:1-0 has been detected in many places by Herschel)[5].

Furthermore, CIDRE could extend the frequency survey of Orion conducted by several groups [6] to higher frequencies, which takes an inventory of all emission lines in this region.

Proc. '21st ESA Symposium European Rocket & Balloon Programmes and Related Research',
9–13 June 2013, Thun, Switzerland (ESA SP-721, October 2013)

2. RECEIVER

To reach the astronomical goals a receiver with high spectral resolution is required, therefore a heterodyne receiver was selected, which easily reaches spectral resolution of delta lambda / lambda of 10^7 at THz frequencies.

2.1 Heterodyne Receiver

In a heterodyne receiver the signal from the sky is mixed with an artificial monochromatic signal created by the local oscillator (LO), see Fig. 1. The beating of the two signals gives the intermediate frequency (IF) signal which contains all the information form the sky, but is at the difference of the sky and LO frequency. In the case of sub millimeter and THz receivers the local oscillator and the sky are at nearly the same frequency so that the IF signal is only at a few GHz. This signal can easily be amplified and analysed. In comparison to most existing heterodyne receivers the sky frequency of the CIDRE receiver is high at 2.7 THz, therefore the critical elements are the mixer and the LO, which both need to work at THz frequencies. Care also needs to be taken in the optics design to assure efficient coupling with little loss.

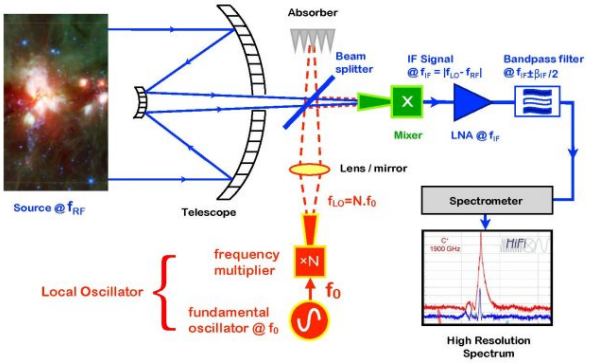

Figure 1 Schematic of a heterodyne receiver.

2.2 Mixer

The most sensitive mixers at 2.7 THz are Hot Electron Bolometer (HEB) mixers. The mixer used for CIDRE will be fabricated by LERMA and the LPN, two laboratories located in the Paris region. The HEB consists of a micro bridge made of superconducting ultra thin film. The HEB for CIDRE are made by depositing 3 to 5 nm of NbN film (purchased from the Russian company SCONTEL) on a silicon substrate. A double slot antenna is used to couple the sky and LO signal to the mixing element. Fig. 2 shows the HEB currently tested for CIDRE.

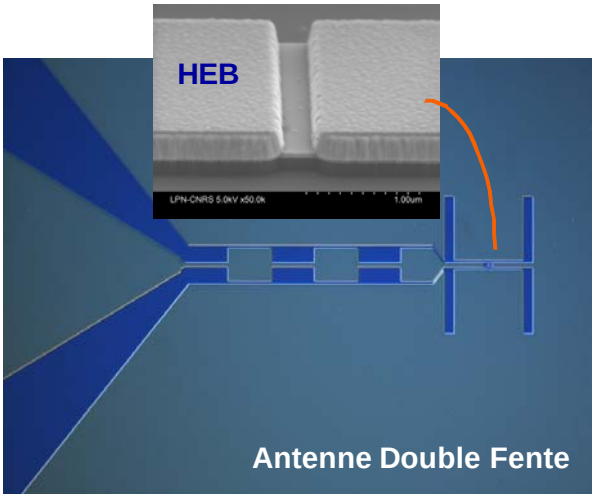

Figure 2 HEB mixer. The insert shows the micro bridge of superconducting material. The larger photo shows the double slot antenna on the right and the RF choke filter with the IF coupling circuit on the left.

To focus the light onto the double slot antenna the substrate with the antenna and the HEB is glued onto a hyper-hemispherical silicon lens, see Fig. 3.

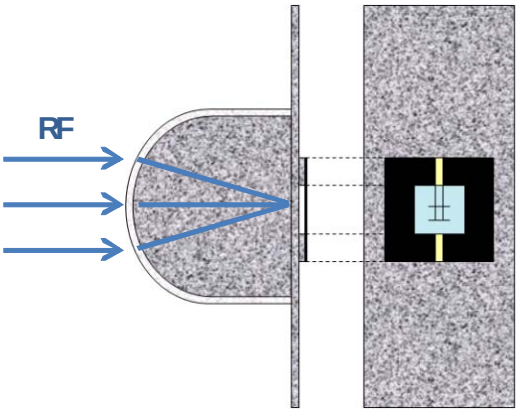

Figure 3 Schematic of the hyper-hemispherical silicon lens glued to the mixing element.

2.3 Local Oscillator

The local oscillator will probably be designed by JPL and LERMA and fabricated at JPL. CIDRE will use a multiplier amplifier chain to create a monochromatic signal between 2.4 and 2.7 THz, see Fig. 4.

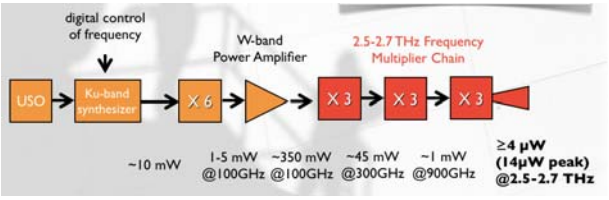

Figure 4. Schematics of the local oscillator chain.

A signal between 14.8-16.7GHz will be created by a synthesizer. This signal will be multiplied by a sixtupler to give about 100 GHz. Consequently the signal around 100GHz will be amplified and then further multiplied by three triplers to give the 2.4 to 2.7 THz signal. The signal needs to have a minimum of 4mW of power. A similar chain has been already designed, fabricated and tested at the JPL [7].

2.4 Optics

The optics needs to couple the signal of the sky to the mixer as well as that of the local oscillator. The optics consists of a ~80cm off axis parabolic primary mirror, followed by a convex secondary mirror, see Fig. 5.

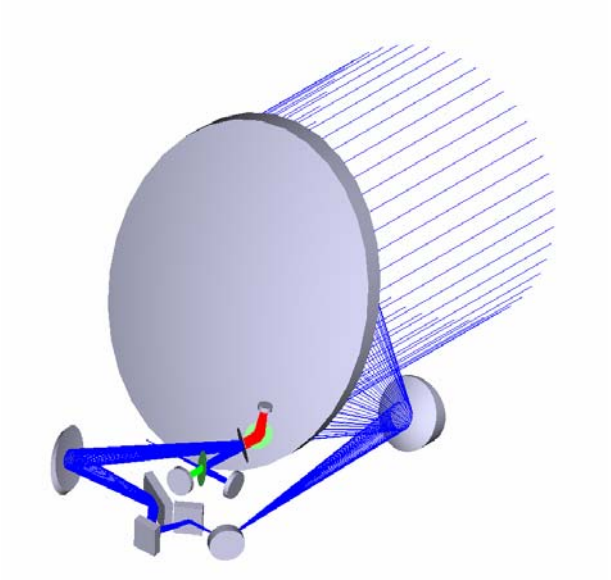

Figure 5. Schematics of the optics for CIDRE.

The optics contains a rotating mirror which directs the beam either to the source or to an off-source position about 8 arc minutes away from the source for reference measurements. The beam rotator will allow compensating for the rotation of the observed field, in case we will install a small array receiver of 4 pixels. This arrangement is followed by a refocusing mirror to be able to pass the sky signal through a Martin-Puplett Interferometer. This polarization rotating interferometer will be used to efficiently superpose the local oscillator signal onto the sky signal.

2.5 Mechanics

The optics, the cooled mixer and the local oscillator will be possibly held by a carbon fibre structure as seen in Fig. 6 and 7.

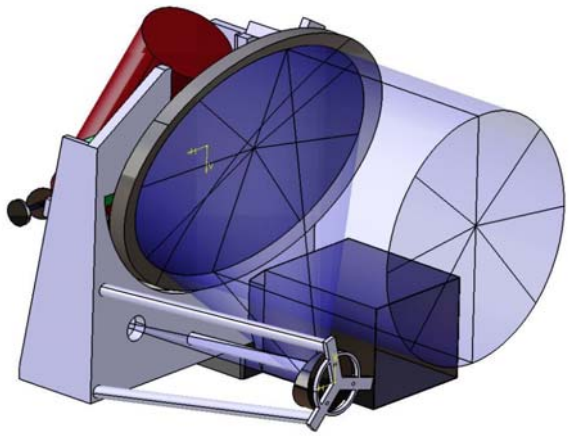

Figure 6. Front view of the CIDRE instrument with the primary mirror, the secondary mirror and the box-shaped stellar sensor.

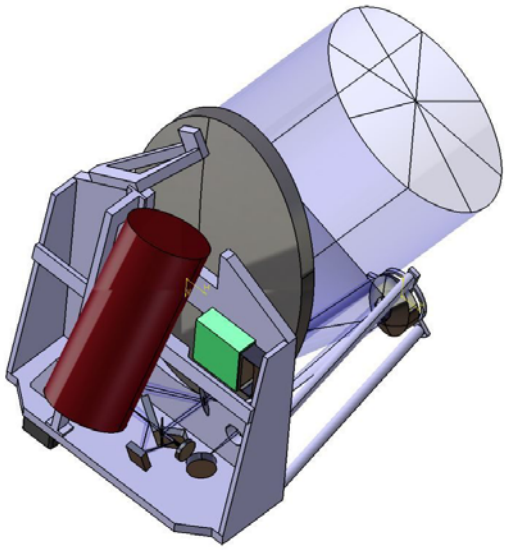

Figure 7. Back view of CIDRE with some of the mirrors. The cryostat with the mixer inside is coloured in red, the local oscillator is in the green box.

2.6 Gondula

The CIDRE instrument will be placed in the Carmen gondola built by CNES, see Fig. 8.

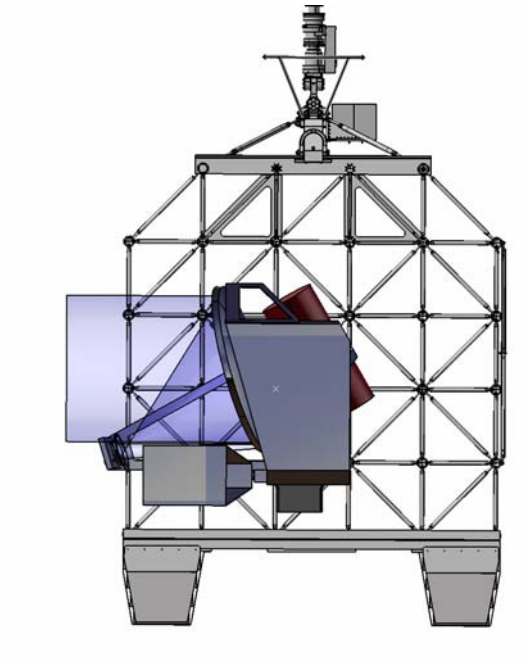

Figure 8. Side view of the Carmen gondola with the CIDRE instrument inside.

3 BALLOON FLIGHTS

The atmospheric transmission of our earth absorbs basically all of 2.7 THz / the far-infrared radiation. Therefore it is indispensable to use airborne/space platforms for far-IR telescopes. The ISO, IRAS and Herschel satellites observed in these frequency regimes, for example. Observatories carried by airplanes such as the KAO or SOFIA are other alternatives, however, they still suffer from some atmospheric absorption. We propose to use a stratospheric balloon, because the Earth atmosphere above 40 km is nearly transparent for far IR radiation.

We are applying to the CNES balloon section and are asking for two flights in the Northern and one science flight in the Southern hemisphere. Each flight will be about 24 hours long. The flights in the Northern hemisphere will most likely be conducted from Timmins in Canada, the flights in the southern hemisphere probably from Alice Springs in Australia.

4 CONCLUSION

CIDRE is an astronomical receiver to observe HD and other transition lines between 2.4 and 2.7 THz at far infrared frequencies. CIDRE will be a heterodyne receiver using a HEB mixer and an amplifier – multiplier chain as an LO. The sky signal will be collected by a ~80cm off axis mirror and the LO will be superposed by a Martin-Puplett interferometer. CIDRE is meant to have three 24h flights with the CNES balloon section, two in the northern hemisphere, and one in the southern hemisphere.

REFERENCES

1. Prantzos, N., 1996, A&A, 310, 106
2. Hébrard, G., 2006, ASPC, 348, 47
3. Linsky, J. L. et al., 2006, ApJ, 647 , 1106
4. Herczeg, G.J. et al., 2012, A&A 540, A84
5. Phillips, T.G. et al., 2010, A&A, 518, L109
6. Turner, B.E., 1991, ApJS, 76, 617
7. A. Maestrini, I. Mehdi, J.V. Siles, J.S. Ward, R. Lin, B. Thomas, C. Lee, J. Gill, G. Chattopadhyay, E. Schlecht, J. Pearson, P. Siegel (2011) Design and Characterization of a Room Temperature All-Solid-State Electronic Source Tunable From 2.48 to 2.75 THz", *IEEE Transactions*

DISCOVERY AND RESEARCH OF COSMIC RAYS ON BALLOONS

Lev Dorman [1, 2]

[1] *Israel Cosmic Ray & Space Weather Centre of Tel Aviv University, Golan Research Institute, and Israel Space Agency; Katsrin 12900, POB 2217, ISRAEL; lid@physics.technion.ac.il, lid010529@gmail.com*
[2] *Cosmic Ray Department of N.V. Pushkov IZMIRAN, Russian Academy of Sciences, Moscow, Troitsk, RUSSIA*

ABSTRACT

The first measurements of air ionization on balloons were made in 1901-1903 by the German meteorologist F. Linke, carrying an electroscope to a height of 5500 m and found an increasing of air ionization up to 4 times. This result at those times was so strong contradicted with the general accepting concepts (that the main source of air ionization is radioactivity of the soil), that F. Linke decided: obtained results are wrong and they are not published. The real discovery of cosmic rays (CR) became only later by the Austrian physicist Victor Hess during his famous flight at August 7, 1912. German physicist W. Kolhörster, achieved in 1913-1914 five flights on balloons and attained the maximal altitude 9,300 m. His results completely confirmed Hess's observation data. Many measurements of CR on balloons were made after 1920s by American scientists R. Millikan and G. Cameron, by many Soviet scientists and others. A lot of experiments for CR research were made later on long lived balloons, which are very important up to the present time.

1. THE EARLIEST MEASUREMENTS OF AIR IONIZATION ON BALLOONS (1900-1903)

Balloon experiments had been widely used for studies of atmospheric electricity for many years and it became evident that they might give an answer to the problem on the origin of the radiation, ionized the air. According to De Angelis (2010) and Carlson and De Angelis (2011), the German meteorologist Franz Linke had, in fact, made 12 balloon flights in 1900–1903 during his PhD studies at Berlin University, carrying an electroscope built by Elster and Geitel (1900) to a height of 5500 m. The PhD thesis was not published, but a published abstract concludes: “Were one to compare the presented values with those on ground, one must say that at 1000 m altitude the ionization is smaller than on the ground, between 1 and 3 km the same amount, and above it is larger with values increasing up to a factor of 4 (at 5500 m). The uncertainties in the observations only allow the conclusion that the reason for the ionization has to be found first in the Earth.” Obtained results strongly contradict with the general accepting in those times concepts, that the main source of air ionization is radioactivity of the soil. Nobody later quoted Franz Linke and although he had made the right measurements, he had reached the wrong conclusions, and the discovery of CR became only later on about 10 years.

2. MEASUREMENTS OF AIR IONIZATION BY BALLOONS IN 1909-1911

In a balloon flight Karl Bergwitz in 1909, using electroscope of Elster and Geitel (1900), found that the ionization at 1300 m altitude had decreased to about 24% of the value on the ground. However, Bergwitz’s results were questioned because his electroscope was damaged during the flight. He later investigated electroscopes on the ground and at 80 m, reporting that no significant decrease of the ionization was observed.
In 1909-1911 the Swiss meteorologist Alfred Gockel (1911) made three flights on balloons, reaching heights of 4500 m. “It is revealed, - he wrote, - the ionization reduction, however is far not in that measure as it would be possible to expect in the assumption of the radioactivity proceeding from the earth ground”. It is necessary to notice that the pressure in the device that A. Gockel used fell in the process of the sphere lifting, and consequently, speed of ionization could decrease simply at the expense of reduction of number of atoms in the volume unit, instead of at the expense of ionizing radiation easing. A. Gockel understood that “recalculation of observable ionization on initial pressure can give even increase in ionization with height”, so he does not exclude the possible presence of “Kosmische Strahlung” (or “Cosmic Radiation”). However, any definitive conclusions could not be made. The results received by A. Gockel did not bring any clarity to the question of sources of ionization of air; at best, they drew the attention of researchers to the study of absorption of γ-radiation in air.

3. DISCOVERY OF PENETRATING RADIATION FROM SPACE (1911-1912)

"In general, before Victor Hess's flights, all experimental results, - as wrote R. Millikan (1930) - could be interpreted as the proof of that all ionization of atmospheric air is caused by sources of a radioactive origin. Imperfection of used devices and impossibility at that time precisely to reproduce experimental conditions have appeared for physics of cosmic rays happy coincidence of circumstances as stimulated the further research under various conditions, especially at the big heights." Such was the situation when in 1911

Proc. ‘21st ESA Symposium European Rocket & Balloon Programmes and Related Research’, 9–13 June 2013, Thun, Switzerland (ESA SP-721, October 2013)

Victor Hess (see Fig. 1), employee of Institute of Radium in Vienna, engaged in the study of absorption of γ-rays in air.

Figure 1. Victor Franz Hess (1883-1964). Nobel Laureate in Physics on 1936 (for discovery CR).

Victor Franz Hess was born at June 24, 1883 in Austria in a family of a forester. In 1905, he graduated University in Graz and at the same place in 1910 received PhD and habilitation to teach. Since 1910, V. Hess, under the direction of Prof. Stefan Meyer, was engaged in radioactivity study. Therefore, in 1911 he undertook two flights on balloons to learn at what height γ-radiation propagates from the radioactive substances that are in the earth crust. Basing on these data, V. Hess planned to determine the absorption factor of γ-radiation in air. Knowing the works of A. Gockel (see previous Section 2), V. Hess placed the device in a hermetic vessel so that the pressure of air in it remained constant at all heights. He did it because he was surprised by results of the flight of A. Gockel, and explained the absence of falling of air ionization rate with height exclusively by lack of tightness of his device. However, having reached height of 1100 m, V. Hess in both cases, like A. Gockel, does not observe an appreciable fall of ionization rate in comparison with measurements near terrestrial surface. Therefore V. Hess (1911) made the assumption that "there should be other source of a penetrating radiation in addition to γ-radiation from radioactive substances in earth crust".

The problem with finding the absorption factor for γ-radiation in air yet remained, and V. Hess, carefully thinking over all trifles, prepared for following flights. In 1912 with the assistance of the Viennese Academy of Sciences he made seven more flights in which he used the two-wired Wulf's electrometer (see Fig. 2) with walls of thickness 3 mm that γ-rays only got through, and both electrometers had hermetic cases.

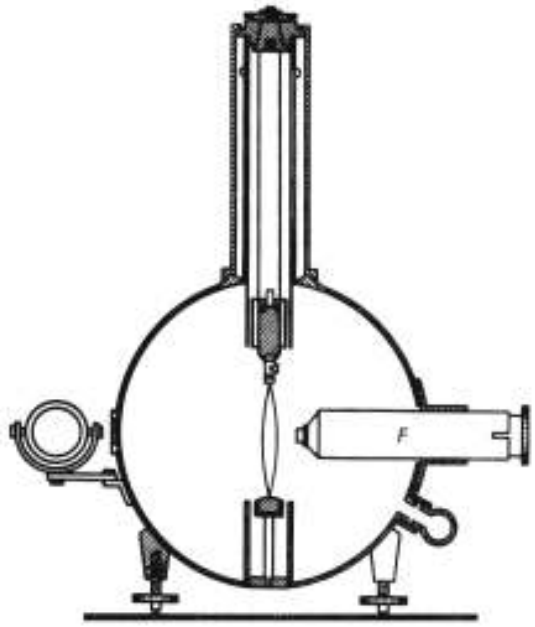

Figure 2. Electroscope of T. Wulf (1909).

The third Wulf's electrometer with walls of 0.188 mm thickness was non-hermetic and intended for simultaneous studying of behavior β-beams. Threads of electrometers were charged to voltage ≈ 200 V to provide a saturation current in the chamber; then the speed of the system discharge was observed continuously. The ionization rate I (in units ion.cm^{-3}s^{-1}) in the volume chamber W was defined under the formula

$$I = \frac{CdU}{300eWdt}, \qquad (1)$$

where C is the system electro-capacity, and e - charge of transferred one ion. For Hess's first device the voltage loss in 1 Volt/hour corresponds I = 1.56 ion.cm^{-3}s^{-1}, and for the second I = 0.74 ion.cm^{-3}s^{-1}. Some hours were spent before flight for control measurements by all three devices, which were for this purpose fixed in a balloon's basket by the same manner as during flight. The average height to which the balloon rose at different time was deduced by a graphic method from the barograph indication. It is necessary to tell that before Hess's experiments, nobody approached with such gravity to measurements during flight, and flights likely carried more adventure than scientific character. Besides, that Victor Hess himself took part in all flights and wrote down indications of devices demanded courage in those conditions. To define the position of the mysterious source of

radiation, he performed flights at various times of day, under different atmospheric conditions and in detail marked strength of wind, overcast, and temperature.

The first flight from this series was performed on April 17, 1912 during a partial solar eclipse. Any reduction of ionization rate during eclipse time was not observed, and from a height of 2000 m the ionization rate increased from what Victor Hess has drawn a conclusion has been fixed even that as the eclipse has not affected an ionizing radiation, the Sun cannot be its source. In other flights, that Victor Hess did not find a difference in measurements of ionization rate between day and night confirmed his point of view.

The seventh and Victor Hess's most well-known, famous flight began on August 7, 1912 at 6 o'clock 12 minutes in the morning about the city of Aussiga in Austria. In the balloon's gondola, there was a pilot, the meteorologist and Victor Hess. At this time the balloon was filled with hydrogen (earlier Victor Hess filled balloons with warmed-up air) and record at that time the height of 5350 m. At midday the balloon landed near the German city of Piskov, 50 km to the east of Berlin, having flown 200 km. In a unique photo (Fig. 3) we see Victor Franz Hess in a balloon gondola right after landings.

Figure 3. The seventh famous flight when cosmic rays were finally discovered: Victor Franz Hess in the balloon gondola right after landing on August 7, 1912.

This flight was described in detail in an article that appeared in a November 1912 issue of the magazine "Physikalische Zeitschrift" (Hess, 1912). As the balloon lifted to 1000 m, insignificant reduction of the ionization rate caused by absorption of γ-radiation of radioactive substances, which are in the earth's crust, was observed. After that, the air ionization rate started to increase gradually with height as though the balloon came nearer to a radiation source, instead of father away from it. In the range of heights from 4000 to 5200 m, the ionization rate became much higher than at sea level. After landing the balloon, its cover was carefully investigated to determine whether radioactive substances, which settled during flight that could cause increase of ionization rate, cover it, and V. Hess concluded that the cover of the balloon does not radiate.

Great attention was taken to weather during flight because as it was already told, V. Hess tried to find dependence of properties of unknown radiation on atmospheric conditions. The condition of weather during flight was recorded in very precise detail: reduction of barometric pressure; overcast weak to 4000 m and stronger above through which the sunlight, the strong wind quickly carrying the balloon aside poorly makes the way. To show how the ionizing radiation with height changes, V. Hess united 88 values of measurements of the ionization rate, performed at various heights during all seven flights (for each height from the several values received under various conditions, the average undertook).

From obtained data it became visible that to a height of 1000 m there was a reduction of ionization rate on the average on 0.7-1.5 ion.cm^{-3}s^{-1} (in some flights it reached 3 ion.cm^{-3}s^{-1}) that is caused by absorption of γ-radiation of the earth crust. "From here, - V. Hess wrote, - we conclude that at earth crust radiation gives ionization rate only nearby 3 ion.cm^{-3}s^{-1} in zinc electrometer". It is interesting that V. Hess as it was accepted at that time, specified, from what the electrometer is made because he knew that each device has own specific radiation. Further at increase in height from 1000 m to 2000 m ionization rate slowly increased, and in the range of heights between 4000 m and 5200 m it has appeared already on 16-18 ion.cm^{-3}s^{-1} more than ionization rate on a surface of the Earth.

What is the reason for such substantial growth of ionization rate with height, which was observed by V. Hess many times, and simultaneously by all devices? V. Hess well understood that "if to adhere to the point of view that only known radioactive substances in earth crust and in atmosphere let out the γ-radiation making ionization in the closed vessel, there are serious difficulties at an explanation of the received results". Really, V. Hess experimentally defined that at a height of 500 m the earth crust γ-radiation decreases by more than 5 times and, certainly, cannot make considerable ionization at larger heights. The congestion of radioactive emanations in the atmosphere, by V. Hess'

estimations, could cause only 1/20 of all ionization observed at heights from 1 to 2 km, and with increase in height an emanation role, naturally, should become even less. As a result, V. Hess concluded that it is possible to explain all experiments only by the existence of the radiation coming from the outside, of extraterrestrial origin. Reporting in September 1912 at Session in Munster results of the flights, V. Hess made following sensational conclusion: "Results of the presented observations are better can be explained by the assumption that radiation of the big penetrating ability is coming into our atmosphere from above and even in its bottom layers makes a part of the ionization observed in closed vessels" (Hess, 1912). V. Hess named the discovered ionizing radiation ultra-gamma radiation to underline its big penetrating ability. For that time, the assumption of existence of the radiation coming from space beyond the border of the atmosphere was extraordinarily courageous, and passed many years before it became commonly accepted. Many physicists, if not the majority, doubted that "Hess's" radiation (so named at the beginning) had an extraterrestrial origin, and attributed its more habitual then to the radioactivity phenomena.

4. KOLHÖRSTER'S BALLOON EXPERIMENTS (1913-1914)

It does not to think that scientists immediately agree with V. Hess that "Hess radiation" really exist and has an extraterrestrial origin. Opposite, even the problem on the existing of this radiation was discussed many years after experiments of V. Hess in 1912. In the first, the Hess's results should be repeated and checked by other scientists. In the second, before to be agreeing with the extraterrestrial origin of the "Hess radiation", it was necessary to try to find other, not so radical origin. For example, it was discussed hypotheses that this radiation arises in the upper atmosphere during thunderstorms when charged particles can be accelerated by big electric fields. Other scientists suggested that radioactive emanations and radioactive particles might be concentrated in the upper atmosphere what can explain an increasing of air ionization with increasing of altitude.

In the frame of these both hypotheses should be expected that on the intensity of "Hess radiation" will be a strong influence the weather and should be exist big variations with time of the day and season. On the absence of those big time-variations was underlined in the first publications of V. Hess.

The biggest criticism results of V. Hess was inflict by German physicist W. Kolhörster, who was sure that observed by V. Hess increasing of the air ionization rate with altitude is absolutely false and caused by the influence of changed air temperature during the balloon flight on data obtained by Hess's device. With the aim to 'close' the Hess's discovery W. Kolhörster achieved in 1913-1914 five flights on balloons and attained the maximal altitude 9,300 m. In Kolhörster (1913a) was described in details the device used during the flights. The device scheme and appearance are shown in Fig. 4.

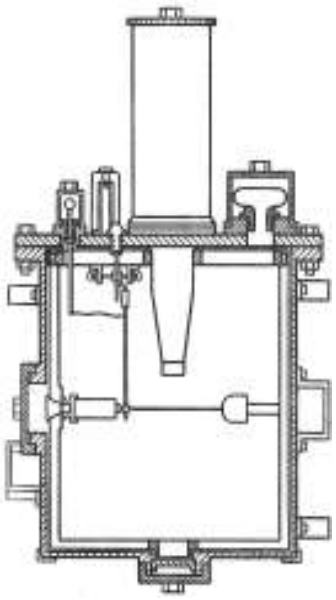

Figure 4. Scheme of apparatus for measuring air ionization rate (Kolhörster, 1913a).

The device consisted of a cylindrical chamber from steel of volume 4.5 l. In the centre of the device, on a special framework, the most thin quartz silvered threads were placed. The main results obtained by W. Kolhörster are shown in Fig. 5 (in comparison with main results of V. Hess).

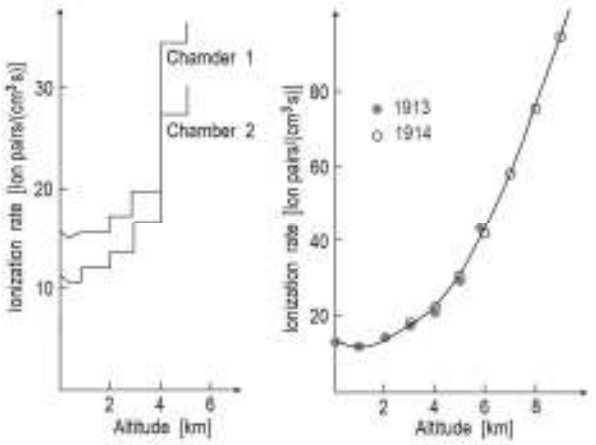

Figure 5. Variation of ionization rate with altitude. Left – data of V. Hess in 1912 of two chambers, right – data of W. Kolhörster in 1913 and 1914.

For the elimination of any influence of temperature on instrument readings, Kolhörster used as holders of threads quartz handles serving as good insulators. After charging the threads, the size of their divergence was

defined with the help of a microscope at the top cover of the device. Air that was in the chamber was preliminarily carefully dried, and besides, in the bottom of the device there was a dehumidifier. The results received by Kolhörster (1913b) during flights completely confirmed Hess's observation data, contrary to Kolhörster's desire. Upon lifting the equipment up, the speed of ionization at first decreased, then at a height of 1700 m it was the same value as on the terrestrial surface, and then it began to increase considerably. At a height of 9,000 m the difference between ionization speed observed at the given height and speed of ionization at sea level $\Delta \approx 80$ ион.см$^{-3}$.сек$^{-1}$.

Because no doubts remained that with distance away from the terrestrial surface the speed of ionization increases, W. Kolhörster assumed that the radiation causing ionization of atmospheric air is absorbed by the atmosphere under the simple exponential law:

$$I = I_0 \exp(-\mu h), \qquad (2)$$

where I_0 is the intensity of radiation in the atmospheric border, I - intensity of radiation after passage through a layer of atmosphere of thickness h (in g/cm^2), and μ - absorption coefficient (in cm^2/g).

Using this assumption, Kolhörster calculated that the coefficient of absorption of an ionizing radiation coming from above is equal to 5.7×10^{-3} cm^2/g. The received value was in 10 times less than the value of absorption coefficient for the most rigid γ-radiation from radioactive elements (for example, RaC). "Thus, - wrote W. Kolhörster, -existence of the very rigid radiation having absorption coefficient about 0.1 of absorption coefficient of known before γ-radiation is established".

Extrapolating the obtained data, Kolhörster defined that at sea level the speed of ionizing radiation coming from above is about 2 ion.cm^{-3}.s^{-1}. Let us note that in 1973-1974 absolute measurements of ionization of air by cosmic rays at sea level were executed by Kyker and Lyboff (1978); it was found that the speed of ionization at sea level by cosmic rays is equal 2.15 ± 0.05 ion.cm^{-3}.s^{-1}. Measurements were performed by means of a 900-litre chamber filled with pure air. This chamber was calibrated in a hydrochloric mine at a depth of 600 m underground; apparently, the received value is very close to value of speed of the ionization defined by Kolhörster (1913b) for sea level about 60 years earlier.). It meant that at the altitude of 9000 m the speed of ionization increases by 40 times!

The first period of investigations, on which the extent of the problem on a reality of existence of high-altitude ionizing radiation was the basic problem, came to an end with the experiments of Kolhörster. After that, to doubt that the largely detectable unknown radiation, apparently, comes from above - was not necessary any more. Kolhörster (1913b) named the radiation coming from above "Höhenstrahlung", i.e. high-altitude radiation.

5. MILLIKAN'S BALLOON EXPERIMENTS: CONTRADICTION WITH KOLHÖRSTER'S AND HESS'S RESULTS (1922-1923)

The First World War for a long time detained the further studying of high-altitude radiation. Interest to this radiation renewed again only in 1922 in the USA, and in Germany - in 1923. It is necessary to tell that R.A. Millikan from the California Institute of Technology was skeptical about the conclusion of V. Hess and W. Kolhörster about an extraterrestrial origin of high-altitude radiation, and decided to check their experimental results. Millikan and Bowen (1923) in spring 1922 adapted meteorological balloons for the raising of devices. Especially for these flights, four complete sets of devices were designed, each of which included an electroscope, a thermometer and a barometer. The dimensions of the collection device made it about 15 cm, and its weight was only 0.19 kg. Record of results was made automatically by the recording of a shadow from the electroscope's delays on a moving film. Two small balloons 47 cm in diameter, until one of the balloons was broken off under the influence of external pressure of gas expanse with pressure reduction raised the device. After that, the descent was facilitated by the remaining unbroken balloon, which played a parachute role, reducing speed of descent to one safe for preserving device integrity. Besides, the escaped balloon played a landmark role on which it was easy to find the equipment after its landing. During the most successful flight lasting 3 hours 11 minutes, a maximum altitude of 15,500 m was obtained. The equipment landed at a distance of 100 km from the start; it was been found, and the film was developed.

Results of these flights in general confirmed the existence of high-altitude radiation, but did not completely resolve the doubts of Millikan as the speed of ionization at an altitude more than 10 km obtained by means of sounding balloons appeared to be 4 times smaller than expected from extrapolation of Eq. 2.

6. THE STRUCK TO THE HYPOTHESIS ABOUT EXISTING RADIATION FROM SPACE (1923)

The reason for the big divergence between Millikan's and Kolhörster's results became clear later, in 1923, when Kolhörster (1923) defined the value of the absorption factor of high-altitude radiation more precisely. Measurements by W. Kolhörster were performed on the mountain Jungfrau-Joh glacier in Switzerland at altitudes of 2300 m and 3500 m. Placing the device in ice at a depth of 15 m, Kolhörster defined that the absorption factor μ at an altitude of 2300 m is

equal to 1.61×10^{-3} $cm^2.g^{-1}$, and at an altitude of 3500 m $\mu = 2.7\times10^{-3}$ $cm^2.g^{-1}$. Kolhörster decided to take as the true value simply the arithmetic mean of both received values. The value of the absorption factor found thus appeared almost three times less than defined earlier, and the difference between the values of the ionization rates calculated by the extrapolation given by Kolhörster's Eq. 2 taking into account the more exact factor of absorption received experimentally by Millikan and Bowen (1923) above 10 km, decreased much more. Kolhörster (1923) wrote: "Recently I more and more abandon the idea that high-altitude radiation represents the phenomenon for which origin is necessary to search in world space".

However, R. Millikan and his colleagues still were not agreeing with this conclusion. They considered that nevertheless it is possible to explain the received results by radioactive pollutions (Millikan, 1924). The scientific authority of Robert Millikan (Nobel prize winner in physics in 1923) was so huge that his skepticism towards the existence of radiation coming from space was reflected in the opinions of many physicists at that time.

7. REHABILITATION OF THE HYPOTHESES ON SPACE RADIATION (1925-1926)

It is necessary to underline thus that the truth was found out by R. Millikan and his colleagues as a result of measurements of the absorption factor of high-altitude radiation in water on high-mountainous lakes (Millikan and Cameron, 1926). To explain the received results, they assumed equal weights of a unit of the area of water and air absorb equally. Therefore, as the air layer between levels of both lakes weighs as much as 1.85 m of water, for the radiation coming from above through the atmosphere, the total weight of an absorber (air + water) is identical, when the device is shipped in lake Muir on 1.85 m more deeply, than in lake Arrowhead. The measurements performed on lakes Arrowhead and Muir, convincingly proved that the observable radiation comes from above, and is not formed in the air layer between lakes. For interpretation of the received data, Millikan and Cameron (1926) for the first time took into consideration that the investigated radiation comes also under various zenith angles θ:

$$I(x) = I_0 \int_0^{\pi/2} \exp(-\mu x/\cos\theta)\sin\theta d\theta \,. \qquad (3)$$

From this follows, that

$$I(x) = I_0\left[\exp(-\mu x) - \mu x \int_{\mu x}^{\infty} \frac{\exp(-u)}{u} du\right] = I_0\Phi(\mu x) \qquad .(4)$$

The function $\Phi(\mu x)$ in the American scientific literature received the name Gold function; it replaces the simple exponential law, fair only for vertically falling radiation. Using tables of values $\Phi(\mu x)$, Millikan and Cameron (1926) defined that the factor of absorption of high-altitude radiation is equal in water 3×10^{-3} cm^2g^{-1} that is once again evident that high-altitude radiation possesses getting ability, much bigger, than γ-rays from radioactive elements.

8. SUPPOSITION TO CALL HIGH-ALTITUDE RADIATION AS COSMIC RAYS (1926)

“These rays, - it was summarized in Millikan and Cameron (1926), - do not occur from our atmosphere and consequently can be rightfully named by 'cosmic rays', this most descriptive and most suitable name”. Thus, Robert Millikan, long denying the existence of high-altitude radiation as coming from space, entered the name, which is used all over the world to this day.

9. RECOGNIZING OF COSMIC RAYS DISCOVERY AS HIGH LEVEL IMPORTANCE

Hess's discovery of radiation from the outside caused a great interest among German physicists. If one looks to the magazine “Physikalische Zeitschrift” for those years one will not find any issue in which there is no V. Hess article or articles devoted to Hess's radiation. It is curious that in the scientific literature in England, USA, Russia, France and other countries at that time there were not any papers that noticed the new penetrating radiation. In 1919 Victor Hess received the Liben award for discovery of “ultra-radiation” and soon after that he became a Professor of experimental physics in University in Graz. In 1921 - 1923 Victor Hess worked in the USA. In 1923 he came back to the University in Graz, and in 1931 was appointed director of the newly based Institute of Radiology in Innsbruck. Near Innsbruck Victor Hess has based on a mountain Hafelekar station for continue observation and studying of CR (this station works until now). In 1932 Charl Zeis's Institute in Yen awarded Victor Hess with the memorial award and medal of Abbe; he also became a member-correspondent of the Viennese Academy of Sciences. In 1936 Victor Hess received the Nobel prize in physics "for discovery of space radiation" (see Fig. 6). Meanwhile, in the description of Nobel Prizes, it says that they should be awarded "for the latest achievements..., and for old works only when their value has not been found out until recently". Arthur Compton, in his letter nominating V. Hess for the prize, wrote, “The time has now arrived, it seems to me, when we can say that the so-called cosmic rays definitely have their origin at such remote distances from the Earth, that they may properly be called cosmic, and that the use of the rays has by now led to

results of such importance that they may be considered a discovery of the first magnitude". The award following only 24 years after the discovery of cosmic rays reflected, apparently, long existing doubts at first in the fact of existence of space radiation, and then in value of this discovery for physics.

Figure 6. At the Nobel ceremony at December 1936 in Stockholm: Victor Hess (right) and Carl Anderson (middle) are seated beside chemistry laureate Peter Debye. From Carlson and De Angelis (2010).

In the Nobel lecture Victor Hess noticed with satisfaction that the Nobel Prize was shared with Carl Anderson, who discovered in 1932 positrons in CR. In 1938, Victor Hess was compelled to leave his native land because of prosecution by the Nazis, and moved to the USA, where until 1956 he worked at Fordham University. Victor Hess died in 1964 at the age of 81 years, two years after the solemn anniversary devoted to the fiftieth anniversary of the discovery of CR.

10. REGULAR COSMIC RAY REGISTRATION ON RADIO-BALLOONS

In the period of IGY in former USSR were organized regular (usually two times per day) CR observations and latitude effects on small radio-balloons up to altitude about 35 km in Murmansk, Moscow, Simferopol, Yakutsk, Alma-Ata, Erevan, Apatity, Norilsk, and Tiksy (Belomestnikh and Shafer, 1958; Charakhchyan, 1961; Lazutin and Franzus, 1964; Dorman et al., 1967; Asatrian et al., 1995; Bazilevskaya and Svirzhevskaya, 1998). Many regular measurements on balloons in the period of IGY were made by Winckler (1960) over Minneapolis, near Guantanamo (Cuba), over Fairbanks (Alaska) and over Guam.

11. COSMIC RAY EXPERIMENTS ON LONG DURATION BALLOONS

Long duration balloon experiments can compete with satellite experiments in measuring the energy spectra and isotopic contents of CR. They have many advantages including a much smaller cost per flight and the opportunity to repeat the flight a few times. The weight of an instrument can be relatively high (up to a few tons), size can be relatively large (few m^2) and there will be no obstructions in the geometry factor, which may be expected at the satellites and space probes. These advantages may compensate for the much smaller exposure time (several weeks per single flight). Many long duration CR balloon experiments are used as prototypes for future satellite experiments. Some examples are following:

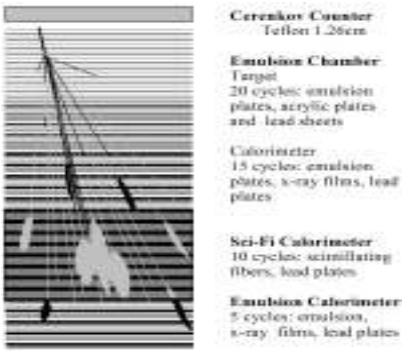

Scintillating **O**ptical **F**iber **Cal**orimeter (**SOFCAL**) was designed by Christl et al. (1999) to measure the proton and helium spectra from 0.2 to about 10 TeV (Fig. 7).

Figure 7. Con-figuration of SOFCAL.

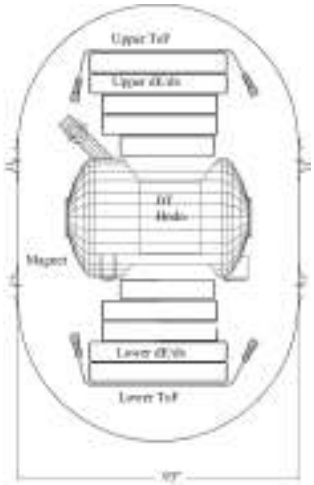

HEAT-pbar instrument (**HEAT**, Fig. 8) is designed by Bower et al. (1999) to detect the rare antiparticle species, antiprotons ($\bar{p}$) in CR.

Figure 8. Cross-section drawing of the HEAT magnet spectrometer showing the placement of drift tube hodoscopes.

Cosmic **A**nti-**P**article **R**ing **I**maging **C**heren-kov **E**xperiment, 1998 (**CAPRICE98)** is the balloon borne detector built and flown by the WiZard collaboration (Ambriola et al., 1999) for the study of antimatter in CR and the investigation of CR spectra and composition at different atmospheric depths.

Advanced **T**hin **I**onization **C**alorimeter (**ATIC**) - balloon experiment (Wefel, 2001), had the test flight from McMurdo, Antarctica at 28 December, 2000 - 13 January 2001, recording over 360 hours of data on the composition and energy spectra of CR from ~ 10 GeV to near 100 TeV (see Fig. 9).

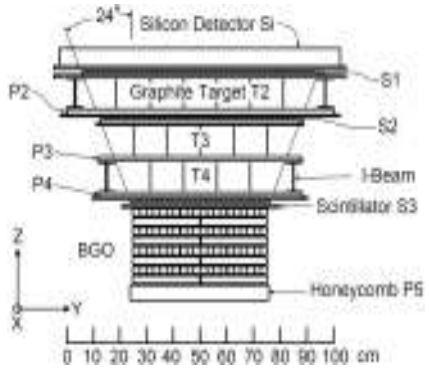

Figure 9. ATIC instrument: schematic diagram

Trans **I**ron **G**alactic **E**lement **R**ecorder (**TIGER**), developed by Link et al. (2001), is a balloon borne CR instrument designed to measure the individual elemental abundances of galactic CR from $16 \leq Z \leq 40$.
Polar BEAR. This balloon experiment is proposed by Bashindzhagyan et al. (2001) for a long duration flight around the North Pole to measure the elemental energy spectra of high-energy CR in the region up to 10^{15} eV.
Balloon borne **E**xperiment with a **S**uperconducting **S**pectrometer (**BESS**) were carried out with the aim of studying elementary particle phenomena in the early history of the Universe through precise measurements of low energy antiproton spectrum and search for antiparticle of cosmic origin (Yamamoto et al., 2001).
Cosmic **R**ay **E**nergetics **A**nd **M**ass (**CREAM**) experiment is capable of extending direct measurements of CR to the supernova energy scale of 10^{15} eV in a series of Ultra Long Duration Balloon (ULDB) flights (Seo et al., 2003).

12. CONCLUSIONS

1. Balloons were widely used for discovery and research of CR during more than 100 years. A lot of Nobel Prizes was awarded for discovery CR and discoveries based on CR research.
2. In the present time small radio-balloons are widely used for the continue registration of galactic CR variations, solar CR events, and investigations of CR geomagnetic effects.
3. In the present time are widely used big long-duration balloons for CR research in high energy region in Antarctic and Arctic.

13. REFERENCES

Ambriola M.L., et al., *Proc. 26th Intern. Cosmic Ray Conf.*, Salt Lake Sity, Vol. 5, 17-20, 1999.

Asatrian G.A., et al., *Proc. 24th Intern. Cosmic Ray Conf.*, Rome, Vol. 4, 1304-1307, 1995.

Bashindzhagyan G., et al., *Proc. 27th Intern. Cosmic Ray Conf.*, Hamburg, Vol. 6, 2147-2150, 2001.

Bazilevskaya G.A. and Svirzhevskaya A.K., *Space Sci. Rev.*, Vol. 85, 431-521, 1998.

Belomestnikh V.A. and Shafer Yu.G., *Proc. YaFAN*, Ser. Phys., No. 2, 47-56, 1958.

Bower C.R., et al., *Proc. 26th Intern. Cosmic Ray Conf.*, Salt Lake Sity, Vol. 5, 13-16, 1999.

Carlson P. and De Angelis A., *Eur. Phys. J.*, Vol. H35, 309-329, 2010.

Charakhchyan A.N., *Cosmic Rays* (Nauka, Moscow), No. 3, 134-136, 1961.

Christl M.J., et al., *Proc. 26th Intern. Cosmic Ray Conf.*, Salt Lake Sity, Vol. 5, 5-8, 1999.

De Angelis A., *Riv. Nuovo Cim.*, Vol. 33, 713, 2010.

Dorman L.I., et al., *Nuovo Cimento*, Ser. X, Vol.50, pp. 27-39, 1967.

Elster J. and Geitel H., *Phys. Ztschr.*, Vol. 2, No. 38, 560-563, 1900.

Gockel A., *Phys. Ztschr.*, Vol. 12. No. 14, 595-597, 1911.

Hess V.F., *Phys. Ztschr.*, Vol. 12, No. 22-23, 998-1001, 1911.

Hess V.F., *Phys. Ztschr.*, Vol. 13, No. 21-22, 1084-1091, 1912.

Kolhörster W., *Phys. Ztschr.*, Vol. 14, No. 21, 1066-1069, 1913a.

Kolhörster W., *Phys. Ztschr.*, Vol. 14, No. 22-23, 1153-1156, 1913b.

Kolhörster W., *Berl. Ber.*, Vol. 24, 366-377, 1923.

Kyker G.C. and Liboff A.R., *J. Geophys. Res.*, Vol. A83, No. 12, 5539-5549, 1978.

Lazutin L.L. and Franzus E.T. , *Izv. Ac. Sci. USSR*, Ser. Phys., Vol. 28, No. 12, 2085-2086, 1964.

Link J.T., et al., *Proc. 27th Intern. Cosmic Ray Conf.*, Hamburg, Vol. 6, 2143-2146, 2001.

Millikan R.A., *Nature*, Vol. 114, No. 2856, 141-143, 1924.

Millikan R.A., *Nature*, Vol. 126, No. 3166, 14-16, 29-30, 1930.

Millikan R.A. and Bowen J., *Phys. Rev.*, Ser. II, Vol. 22, No. 2, 198-198, 1923.

Millikan R.A. and Cameron G.H., *Phys. Rev.*, Ser. II, Vol. 28, No. 5, 851-868, 1926.

Seo E.S., et al., *Proc. 28th Intern. Cosmic Ray Conf.*, Tsukuba, Vol. 4, 2101-2104, 2003.

Wefel J.P. (for the ATIC collaboration), *Proc. 27th Intern. Cosmic Ray Conf.*, Hamburg, Vol. 6, 2111-2114, 2001.

Winckler J.R., *J. Geophys. Res.*, Vol. 65, No. 5, 1331-1361, 1960.

Wulf T., *Phys. Ztschr.*, Vol. 10, No. 5, 152-157, 1909.

Yamamoto A., et al., *Proc. 27th Intern. Cosmic Ray Conf.*, Hamburg, Vol. 6, 2135-2138 (2001).

A NEW PARADIGM IN SPACE BASED EXPERIMENTS USING RUBBER BALLOONS

Sandip K. Chakrabarti[(2,1)], Debashis Bhowmick[(1)], Sourav Palit[(1)], Subhankar Chakraborty[(1)], Sushanta Mondal[(1)], Arnab Bhattacharyya[(1)], Susanta Middya[(1)], Sonali Chakrabarti[(1)]

[(1)]Indian Center for Space Physics, 43 Chalantika, Garia Station Rd., Kolkata 700084, INDIA
[(2)]S.N. Bose National National Centre for Basic Sciences, JD Block, Salt Lake, Kolkata, INDIA
Email:chakraba@bose.res.in

ABSTRACT

Indian Centre for Space Physics is engaged in long duration balloon borne experiments with typical payloads less than ~ 3kg. Low cost rubber balloons are used. In a double balloon system, the booster balloon lifts the orbiter balloon to its cruising altitude where data is taken for a long time. Here we present results of muon detections and recent solar activities, including the light curves and flare spectra in the 20-100keV range. We not only show that we have successfully obtained several flares and there spectra at different altitudes, we also found that the high energy X-ray flux of strong flares at altitudes of 10-13 km (the flight altitude of commercial planes) could be more than the contribution due to cosmic rays.

1. INTRODUCTION

Indian Centre for Space Physics is interested in carrying out balloon borne experiments at a sustainable cost so that going to near space for quality data is possible on a daily basis. With miniaturization of instruments, such a goal appears to be attainable. Here we present some results of obtaining high quality data with payloads having a total mass of 2-3 kg or less. Instrumentations are fabricated in house. All payloads are returned by parachutes. In Chakrabarti et al. (2011) our early studies have been reported.

1. TYPICAL LAUNCH PROFILES

Figure 1. A double balloon being launched with a single parachute, communication box and the payload.

Figure 2. A typical trajectory of a balloon from launch site to landing site (top); The payload is returned by the parachute (bottom).

ICSP launches from Bolpur (23.67N, 87.72E). However, since we launch small balloons (Figure 1), no launch `facility' is necessary and often we choose the locations according to where we wish the parachute dropping of the payload (Figure 2). Our location on the Tropics of Cancer compensates for the Earth's tilt in summer and thus solar data is obtained without any special pointing equipment. Typically, every launch contains GPS data unit, GPS tracker, 9DOF, camera, parachute(s), communication box, sun-sensor, power supply and the Payload. We have developed Sun-tracker and it would be used in future missions when we shall observe other objects near galactic centre in relation to the sun.

Proc. '21st ESA Symposium European Rocket & Balloon Programmes and Related Research', 9–13 June 2013, Thun, Switzerland (ESA SP-721, October 2013)

Figure 3. Bicron gamma-ray detector (2 inch diameter) with a lead shielding. This instrument has been launched in nine Dignity missions.

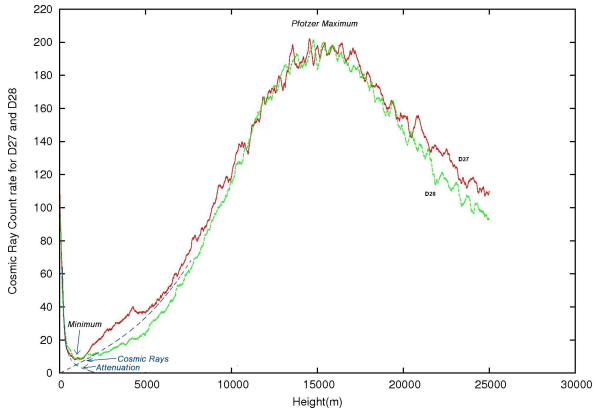

Figure 4. Examples of cosmic ray profiles (60 second average) in Dignity 27 and 28 missions by a bicron detector having a PMT and a NaI crystal. At our latitude the Pfotzer maximum is at ~15 km. The minimum caused by the competition of ground radio activity and Cosmic rays is marked.

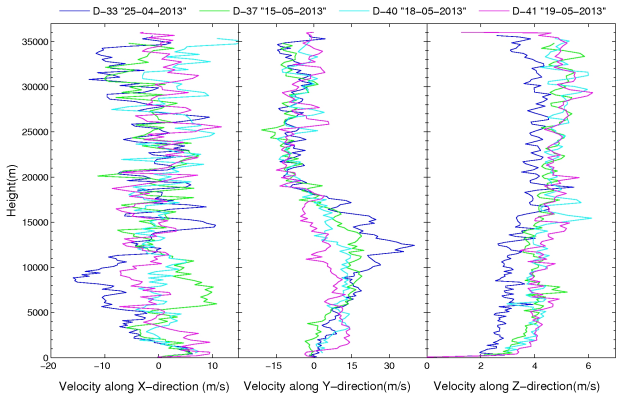

Figure 5. Velocity components at our latitude in pre-monsoon season in Dignity missions 33 (D33), 37 (D37), 40 (D40) and 41 (D41).

The same payloads are repaired, if needed, and are launched again on the next day if wind condition is favourable. The typical non-recoverable cost is about $500 per Mission if no new payload is attached.

In Figure 3 we present the photo of a payload instrument (Bicron made gamma-ray detector, 2 inch diameter), with a 0.5mm lead shielding to block hard X-rays below 100 keV. The collimator emits a line at 77keV which is used as a calibrator. All the detectors are calibrated on the ground during testing, and before and after the launching. In Figure 4, we show examples of cosmic rays we received from the bicron detector on two successive days (24/5/2012 and 25/5/2012). At our latitude we consistently have the maximum at around 15-16km. There is a distinct minimum just after launch, due to the attenuation of the ground radio-activity and the rise in cosmic rays with height. In Figure 5, we show the wind profiles measured by our GPS system. We superposed four days of data in the pre-monsoon season, which clearly indicate the switching of X- and Y- components of velocity. Typical Z-component of velocity is ~ 4 m/s.

2. LONG DURATION STUDIES WITHOUT VALVES OR BALLAST

To achieve long duration we have been using two balloons, one being the booster balloon with a larger lift while the other is an orbiter balloon with a smaller lift. The Booster bursts (Fig. 6) at its burst height (say, 37km), and the orbiter cruises at a desired altitude of 25-33km depending on initial lift and payload weight.

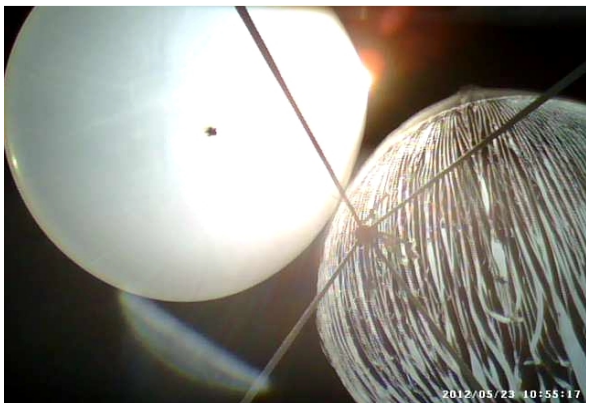

Figure 6. A double balloon with the booster bursting as seen from the payload camera. The sun is behind the orbiter balloon which is in tact.

The theory of placing a balloon at the cruising orbit is simple yet very robust (Chakrabarti et al. 2013) and will not be repeated here. It is easily shown that assuming (a) $P_i = P_o + P_w$ (i and o stand for internal and external to the balloon; w stands for balloon wall) (b) $T_i = T_o$, (c) ideal gas law $P_i Vb = nRT_i$ (d) Mooney-Rivlin model of hyperelastic material (Mooney, 1940; Rivlin, 1948). P,V,T, and R have usual meaning. The balloon characteristics is vary important to achieve this.

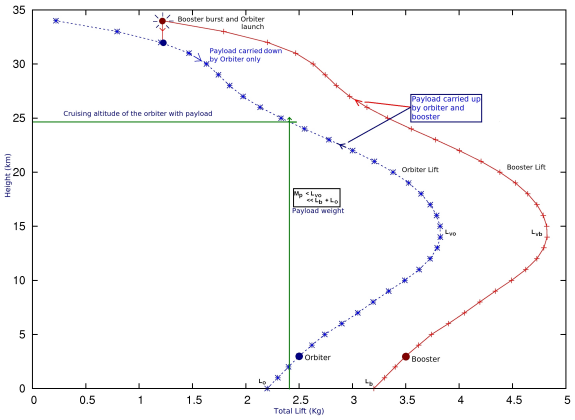

Figure 7. Analytical solution of a double balloon configuration with the Booster bursting at 40km and launching the orbiter at 25km. The region of the curve with the dHeight/dLift<0 is stable for long cruising.

In Figure 7, we demonstrate the principle of how we achieve long duration (anywhere between 5 to 20 hours) without using any valve or ballast with an example where the booster and the orbiter balloons are given lifts of 2.2kg and 3.2kg respectively while the payload is of weight 2.4kg. Initially lifts increase (we call it a *lift valve*, as it helps during ascent, but slows down the descent). The Booster bursts at its burst height due to higher lift, while the orbiter slowly descends down to its neutral buoyancy altitude and orbits there till it is ejected off the orbit or naturally drops due to cooler atmosphere at late night. In Figure 8, we show an example of the results by a long duration flight where a Hamamatsu made photo-multiplier tube with NaI crystal was chosen as the X-ray detector (Dignity 26 mission on 23/5/2012, lift off at 3:01UT from 22.37N,88.446E, Landing after 11h58m, at 23.96N,84.65E) and camera, 6DOF, parachutes are attached.

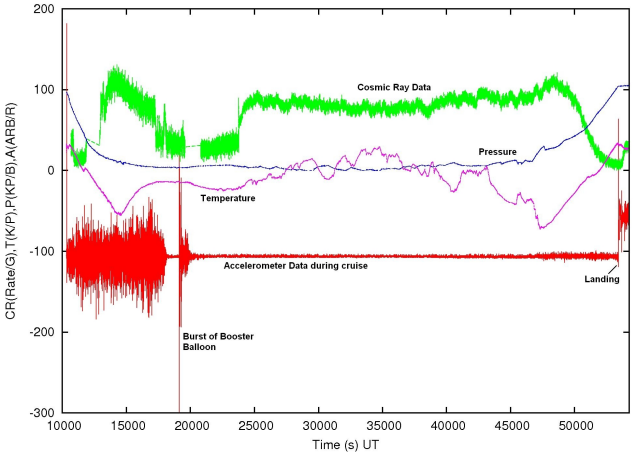

Figure 8. The cosmic rays (Green), pressure (blue), temperature (pink) and the Accelerometer (red) data for a long duration flight (Dignity 26) which lasted 12 hours. The booster burst at 37.9km and the orbiter was cruising at 25km. There were clear indications (temperature data) of some oscillations of height. Accelerometer data indicates that the flight was smooth.

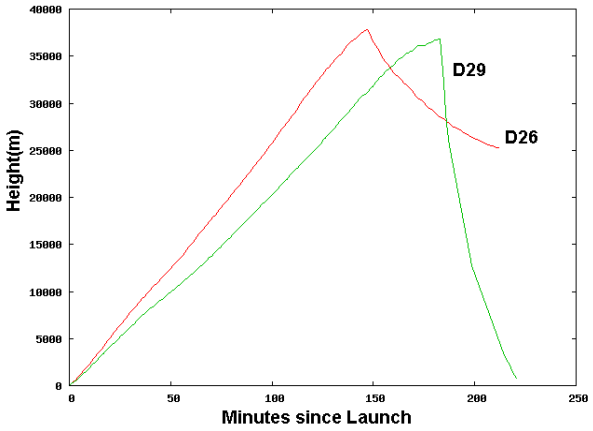

Figure 9. Time-Height profiles of two cases: Dignity-29 (D29) had no orbiter, Dignity-26 (D26) had an orbiter which settled in an orbit at ~ 25 km after initial fluctuations are settled down.

The characteristics of the descent of the orbiter after the burst of the booster is totally different. In Figure 9, we show that in Dignity-29 where there was no orbiter, the descent was normal, in about 45 minutes, by the parachute. However, the payload in Dignity-26 took long time to descend.

2. STUDIES OF SOLAR FLARES

Since 24th Solar cycle is approaching, ICSP engaged in constructing payloads with a goal to observe solar flares. In 2012, when the solar activities were lower, we failed to obtain many flares, though we obtained the spectra of the quiet sun. Our lead-shielding (of 0.5mm) could not be made thicker due to weight constraints. The collimator, also made by lead was of 40° x 40° to begin with, to study the proof of concept. To enable us to view the sun for a maximum amount of time, we adjusted the tilt of the payload with respect to the zenith so that the sun is close to the centre of the collimator when the balloon is at a high altitude. In any case, our 9 degrees of freedom (9DOF) chips enabled us to determine the RA & DEC of the axis of the payload post facto, to verify which direction we were pointing at. The on-board video camera is used to measure the balloon diameter and also the burst characteristics. The sun-sensor stamps every frame as

to whether or not the sun was inside the collimator. All these ensure us that were indeed observing the sun. In Figure 10, we present all sky location of the bright X-ray/gamma-ray sources from SWIFT/BAT catalogue. The location of Sun on 18th May, 2013 is shown. The sun is surrounded by a grey area which is covered by the axis of the collimator in five minutes before the burst (Dignity 40). The red curve indicates the coverage by a corner of the collimator. A post-facto picture of this kind, along with the on-board video camera and sun-sensor give us the time stamps of the data when our instrument was pointing to the Sun,

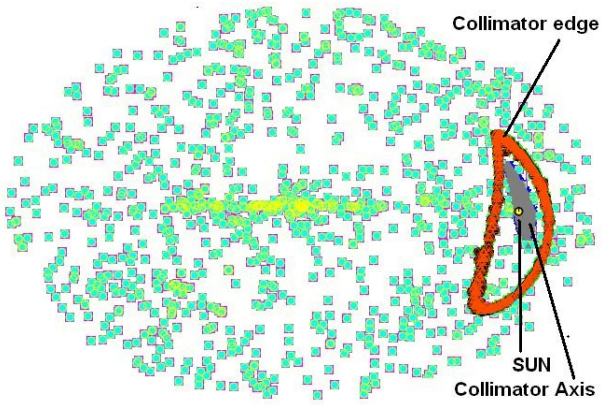

Figure 10. All sky bright X-ray/gamma-ray sources from SWIFT/BAT catalogue is super-imposed with RA/DEC information from the 9DOF sensors on board.

First, we show a weak solar flare we observed in 2012 in Dignity 28 mission (Fig. 11). All the data presented in this paper are from Bicron detector (Fig. 3). D27-D30, D33, D36-D37, D40-D41 missions carried this detector. Our light curve (time vs. Photon count rate) in D28 mission is compared with RHESSI Flux variation. Since RHESSI data included softer X-rays, its flare is wider. The inset shows the spectrum.

As the solar activities increased in 2013, we detected several solar flares. In Figure 12. we present the light curves (3s average of the raw data) of three solar flares which are observed when the balloon was at heights of 25km, 28km and 32-34km respectively. Clearly we anticipate that at lower altitude the spectrum would be harder, and as the height goes up, the spectrum would be softer and more intense. This is precisely what we see. Figure 13 shows the channel wise spectra for these flares (whole first flare data and 60s data at the rising phase of the other two flares). In Figure 14, we show the spectra of the same flares after calibration. We find that the inner most flare observed at 25km extends to

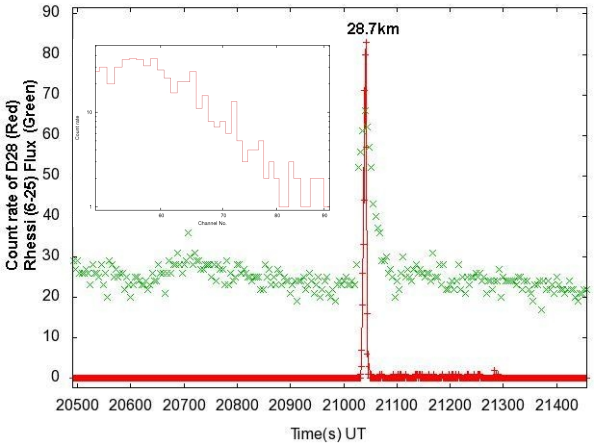

Figure 11. A short duration flare observed in D28 mission. Count rates in 50-100 channels (~ 20-25keV) is plotted. For comparison we superposed RHESSI flux data in 6-25 keV range. In the inset, we show the flare spectrum in log-log scale which is clearly a power-law spectrum. There is some absorption due to atmosphere in the lower energy.

harder X-rays and the detected energies of the flares progressively become softer and brighter. All these flares match with GOES and RHESSI data in time and shape.

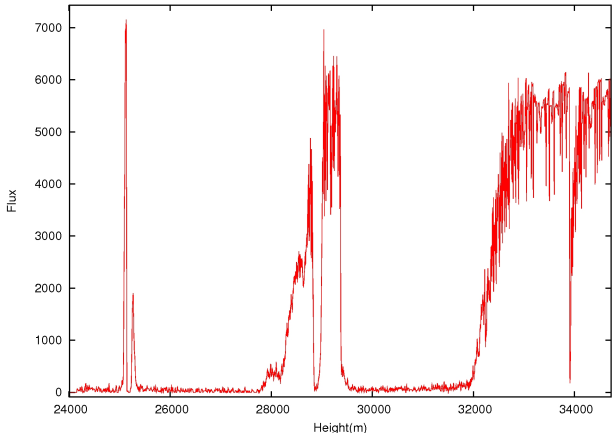

Figure 12: Raw light curves of the three flares observed in D33 mission (25 Apr, 2013).

In Figure 15, we show the dynamic spectrum (averaged over 60seconds, and binned in 1keV) of these flares. This diagram also clearly indicates the progressing increase in the detection of softer photons as the balloon climbs to higher altitude. In future these observed spectra would be reproduced through GEANT4 simulations incorporating the absorption by the atmosphere.

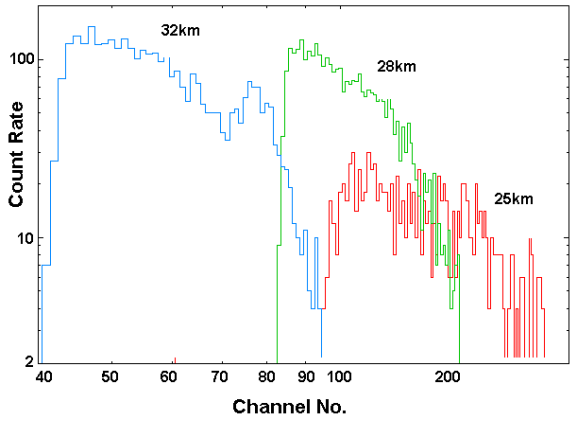

Figure 13: Spectra of the rising phase of the three flares (Channel vs. Photon count rates) for the same three flares shown in Figure 12.

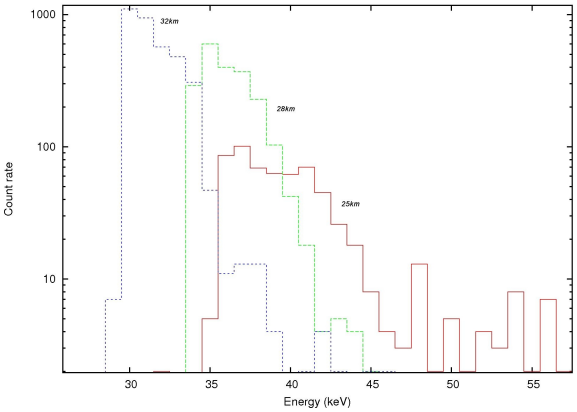

Figure 14: Energy vs. Photon count rates of the rising phase of the three spectra as in Figures 12 and 13.

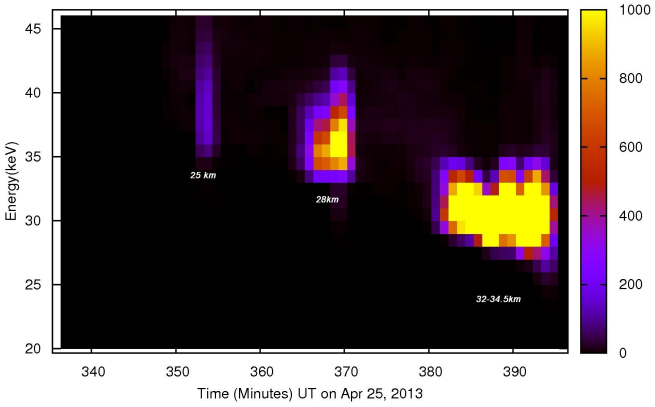

Figure 15: Dynamical spectra of the observed data, showing clearly the flares and their time-resolved spectra. Note the progressive softening of the detection limit of the spectra with time.

We now turn our attention to a strong flare which took place on 15th May, 2013. At ~ 1:30UT an X-class flare occurred and by the time we launched the balloon at 3:00UT, the flux has become M1. We detected excess X-rays right after the launch from ~ 8-9km till the end of burst of the balloon at 34.9km. In Figure 16, we show the count rates (20sq cm. Bicron detector) as a function of the height and channel number up to 17km in order to show details. We clearly see the effects of the flare in the upper branch marked as solar flare. The high counts in lower channels are from Cosmic rays. Surprisingly, the count rate at ~12-13km, the cruising altitudes of the commercial aircrafts is significant and energy wise comparable or more than that of the cosmic ray contribution. Judging from what is received at a height of 12km for a C4 flare (which is 25 times weaker than a X1flare that started at 1:30UT) when out instruments were at that altitude, we can conclude that the commercial flights are vulnerable to very high dose of radiation during strong solar flares. For instance those flying at 1:30UT were receiving at least 25 times more radiation than normal cosmic rays contribution at that altitude. Note that there is a minimum in high energy photons and very high number of low energy photons at Pfotzer maximum (~15km). The exact reason would be studied through GEANT4 simulation.

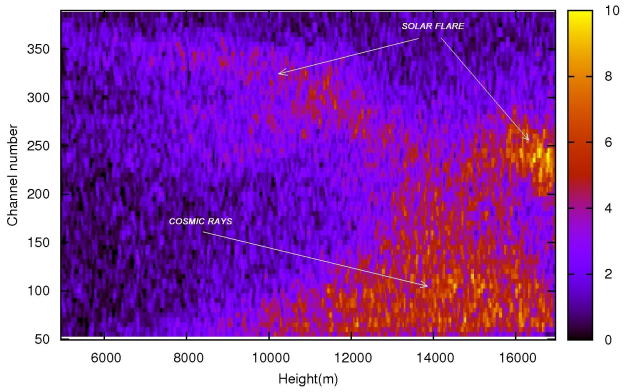

Figure 16: Alarming rate of high energy photons detected at lower altitudes due to an X1 flare occurred at 1:30 UT, 15th May, 2013. When the instruments were passing through 12km, the flare was only C4, but the radiation dose was comparable to that from cosmic rays at that height. Count rate is for 20 sq. cm Bicron.

To compare with an ordinary day, where there was no solar activity, we present in Figure 17, the dynamic spectrum obtained by our D29 mission (4 June, 2012). Clearly, we see only the cosmic ray component. It is not yet clear whether we are watching the direct Solar flare component, or the interaction of solar cosmic rays with the atmosphere. The details are being studied through GEANT4 simulations.

If we now turn to the main flare detection, we find that after the air becomes transparent enough, the entire flare could be detected. In Figure 18, we show the GOES 15 Satellite light curve (arbitrary unit) and our

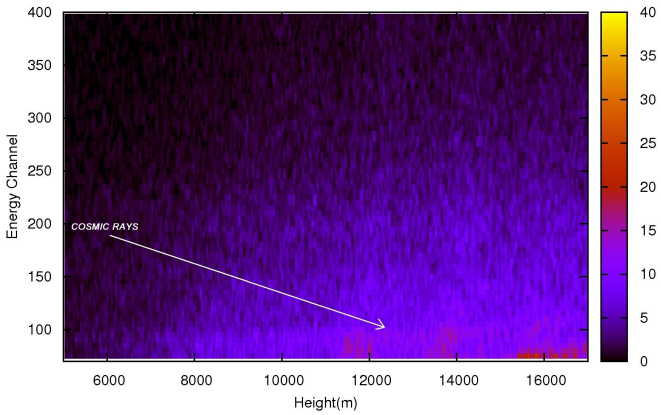

Figure 17: Only cosmic rays were detected on D29 mission on 4th June, 2012.

D37 mission flux in the 21-84keV range (Energy in each channel X count rate). After Pfotzer maximum our light curve started matching with the Satellite data and that too for high energy channels.

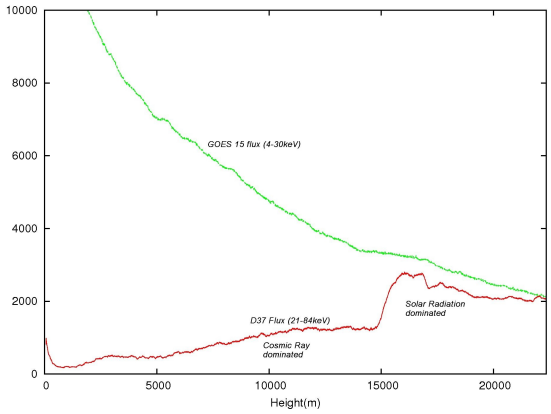

Figure 18: Light curve of 21-84keV energy flux averaged over 60s is compared with GOES 15 4-30keV energy light curve. The difference decreases as the height increases.

In order to find out how the instruments behave in a Styrofoam box in our payload, we sent a calibrator (apart from the lead shielding which was emitting at 77keV in all our missions), namely Eu152. We find that the energies drift upward (i.e., same energy appearing at a higher channel) as the instrument reaches the temperature inversion layer. After that it slowly returns back to normal. The internal temperature went down from room temperature to about 0 degree Celsius. This allowed us to calibrate the instruments dynamically. We also find that at lower temperature the energy resolution becomes excellent, only about 2keV FWHM at 39keV. In Figure 19, we show an example of the dynamically calibrated data from Bicron detector in Dignity 40 mission (18th May, 2013). We also observe a remaining of a weaker solar flare (C1), just after Pfotzer maximum.

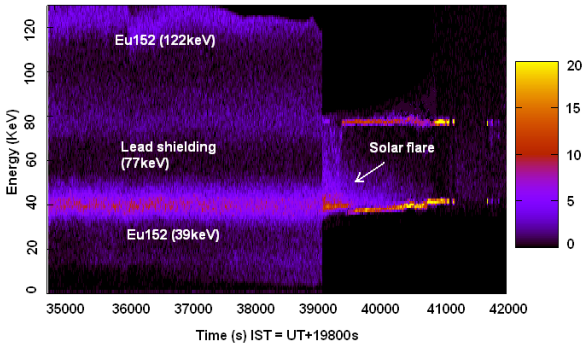

Figure 19: Calibrated dynamical spectrum showing the Eu152 lines (39keV and 122keV) and the line due to lead shielding (77keV). We see the remnant of a C1 solar flare (see, Figure 20 for details).

Since the data is fairly contaminated by the calibrators at 39keV and 77keV, we show in Figure 20 the dynamical spectrum of the solar flare between 42 and 72 keV. We find that, though the flare itself started when the instrument was at 14000m, we observe very prominently only after the resolution of the instruments became better. This was also the region after the Pfotzer maximum. Data is binned in one second in both the Figures 19 and 20.

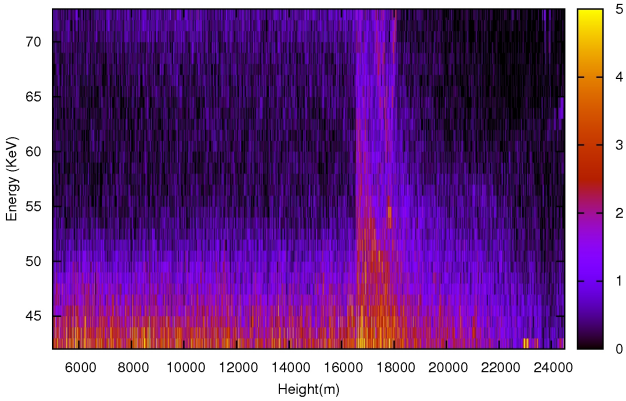

Figure 20: Dynamical spectrum of a weak solar flare as a function of height as observed by D40 mission on 18th May, 2013. The data is plotted for 42keV to 72keV to avoid contaminations from the calibrators.

In Figure 21, we show the actual spectra at three different heights, 19.5km, 20.9km and 22km which were achieved at a five minute interval. The spectra are

obtained with one minute data. The plot is shown from 40 to 80keV.

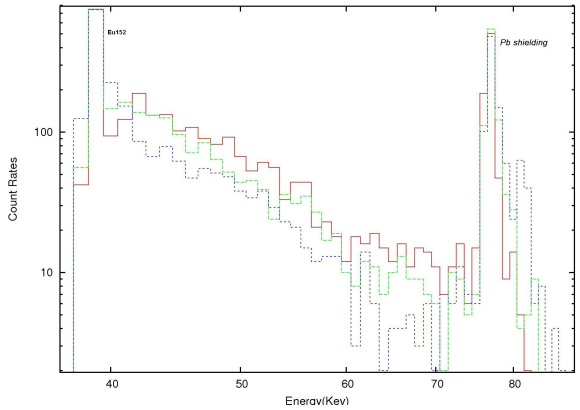

Figure 21: Spectra of the C1 flare at three different heights when the instruments were at 19.5km (red), 20.9km (green) and 22.1km (blue) respectively. The calibrator lines which are very narrow and could be modelled and eliminated, here left out for illustration. The power-law nature of the spectra is obvious.

3. OTHER STUDIES

ICSP is engaged in Muon detections, collection of micrometeorite samples and other developmental studies to have longer duration balloons. We present here a few examples.

Muon Detection: In Figure 22, we present the lead shielding (1-1.5cm thick) used for our muon detection. We used small 40.8mm long GM counters inside these lead shields.

Figure 22: Lead shielding for the muon detection.

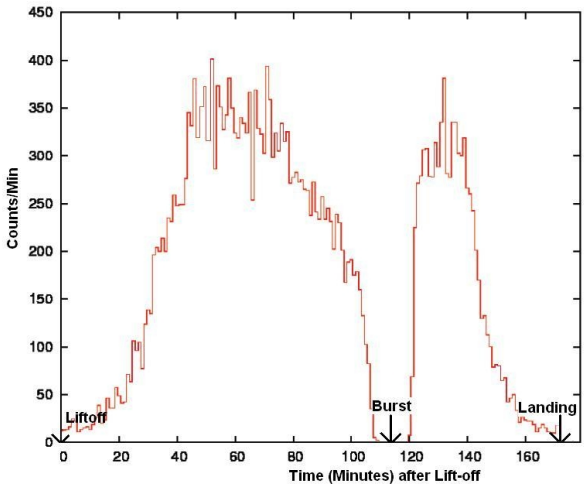

Figure 23: Muon detection as a function of time since liftoff. This is the result of Dignity 19 mission (21 Nov. 2011). The peak occurs at around 15km, same as in cosmic ray observation, though the peak is a bit broader. There were no muon after about 30km.

Figure 23 shows the muon count rate as a function of the height since liftoff. Note that close to the burst height there is no muon. Several missions had similar conclusions. In Fig. 24, we show another result (Dignity 17 on 11th November, 2011). The data obtained on the way up. Note that there is no minimum close to liftoff in both Figure 23 and Figure 24 and there is no muon emission from ground (compare Figures 4, 8 and 18 for cosmic rays).

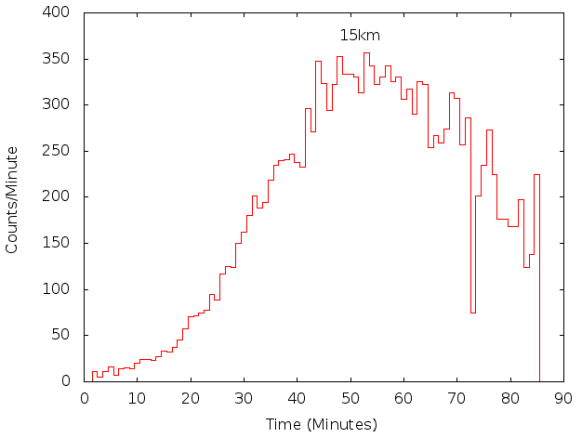

Figure 24: Muon detection in Dignity 17 mission. The counts per minute is shown as a function of time since liftoff. The peak occurs at around 15km. Unlike in Figures 4,7, and 17, there is no minimum in Figures 22 and 23 just after liftoff and just before landing.

Orballoons: In order to achieve longer duration low cost orbiter, ICSP is engaged in not only using multi-balloon concept as presented before, it is using smaller plastic balloons which could be used to more easily control the precise altitude. These non-conventional balloons have been named as Orballons as they will directly float in a given orbit without a separate booster. Figure 25 shows an example of an Orballoon with 7 micro-plastic balloons. Bursting or any one would achieve a steady orbit. The tests are in progress and the results are satisfactory.

Figure 25: Orballoon launched with seven microsized plastic balloons intended to reach a steady orbit with a single balloon burst. Tests are in progress.

Micrometeorite collection from space: ICSP is collecting micro-meteorites and had two missions to this effect. Several micro-meteorites have been collected and the analysis is going on.

All Sky Survey: ICSP has already sent a 4" Optical telescope and brought it back with a great success. This work is further improved for all sky survey in different wavelengths.

4. CONCLUDING REMARKS

With miniaturizations of instruments, carrying out quality scientific experiments using low cost rubber balloons is now a reality. ICSP has been conducting pioneering work in this direction and has demonstrated that not only high quality data can be obtained, the science return per dollar is very high. All the instruments are returned reducing the cost even further. Not only that, using innovative process of multiple balloons, ICSP has achieved very long duration flights without using any conventional valve and ballast systems. Right now a Booster and Orbiter combination is launched. However, orballoons are being tested for directly floating a payload on a desired orbit.

So far, ICSP has been carrying out high energy astrophysics related studies. However, measurements of ozone, polluting chemicals, stratospheric cloud compositions, meteorites, aerosols, biological studies, are equally possible. The biggest advantage is the flexibility of launching, frequency of launching and high returns. These are most certainly extraordinary training tools for larger space missions.

One of the exciting results we presented was the detection of high energy gamma rays coming from solar flares even at the cruising heights of commercial planes. This is particularly alarming for flights during the flares and for an extended period during solar maximum. We are in a process to use GEANT4 code to simulate these events at various heights and compare with our observations.

5. ACKNOWLEDGMENTS

We thank the entire helping team of ICSP, especially, Hiray Roy, Uttam Sardar, Ram Chandra Das, Raj Kumar Maiti who made these experiments successful. We also thank several graduate students for accompanying us during many of the flights. We thank Dr. Dipak Debnath and Dr. Ritabrata Sarkar for helpful discussions.

6. REFERENCES

Chakrabarti, S.K., Bhowmick, D., Sarkar, R., Mondal, S., Sen, A., European Rocket and Balloon Programme and related research (SP-700), 2011, p. 581

Chakrabarti, S.K., Bhowmick, D., Chakraborty, S., Palit, S, Indian Journal of Physics, 2013 (To appear).

Mooney, M., *A theory of large elastic deformation*, Journal of Applied Physics, 11(9), 1940. p. 582.

Rivlin, R. S., *Large elastic deformations of isotropic materials. IV. Further developments of the general theory*, Philosophical Transactions of the Royal Society of London. Series A, Mathematical and Physical Sciences, 241(835), 1948, p 379.

ON DIFFERENT INTERNAL EARTH´S MAGNETIC FIELD MODELS IN DEPENDENCE ON SATELLITE ALTITUDES AND THEIR GEOPHYSICAL PROPERTIES

Wigor A. Webers

Helmholtz-Zentrum Potsdam, Deutsches GeoForschungsZentrum Potsdam, Germany
E-mail: wigor@gfz-potsdam.de
Fax: +49-331/288-2321, phone: +49-331/288-2327

ABSTRACT

The global internal Earth´s magnetic field for the field sources within the Earth´s body is usually modelled by the well-known spherical harmonic analysis /series expansion (SHA).
Up to now this SHA internal magnetic field model as series expansion is calculated from multi-altitude magnetic observations (ground, balloon and satellite altitudes).

From the mathematical point of view the SHA model using a spherical coordinate system is a transcription of a convergent three-dimensional infinite Taylor power series expansion that uses a three-dimensional cartesian coordinate system with its origin in the centre of the sphere of the mean Earth´s radius.
Any power series expansion is determined for its reference point and its reference surface, respectively, from which the data for the numerical calculation of the coefficients are taken from. The reference point and the reference surface, respectively, govern the convergence area and the convergence quality of the series expansion. Consequently, the SHA field model referred to field data from the Earth´s surface as reference surface has significantly different convergent properties in comparison to a SHA model calculated on the basis of field data taken from satellite altitudes.
Therefore, it makes sense, to use the different properties of the SHA field models referred to different concentric reference surfaces for the geophysical interpretation, especially for characterizing the field sources of different depths. The different wavelength constituents of the field sources differently reach the different satellite altitudes so that separate SHA models referred to relevant satellite altitudes enable to find details of the sources.

Moreover, the mathematical properties give the understanding and the proofs for the practical procedures.

1. INTRODUCTION

The magnetic field recorded at irregularly distributed observatories and stations, contains internal and external field contributions. The internal part includes components dominated by the Earth's main or core field - the global reference field - as well as relatively smaller contributions from the Earth's mantle and lithosphere / crust.
All these magnetic field constituents are differently represented in observations taken at the Earth's surface and at satellite altitudes due to the different measurement errors and physical and mathematical properties of the field model. The external magnetic field effects, for example, tend to contaminate the lithospheric constituents of the internal magnetic field much more severely at satellite altitudes than at the Earth's surface. Consequently, field models of the two data sets will reflect fundamentally different source effects.

2. ON THE MATHEMATICAL FIELD MODEL

From potential field theory, the internal magnetic field of the Earth may be represented as the gradient of the potential V given by

$$\mathbf{B}_{\text{int}} = -\nabla V, \tag{1}$$

where the spherical harmonic expansion (SHA) of the potential is

$$V = \sum_{n=0}^{N} \sum_{m=0}^{n} a \left(\frac{a}{r}\right)^{n+1} \left(g_n^m \cos m\lambda + h_n^m \sin m\lambda\right) P_n^m(\cos\vartheta) \tag{2}$$

.
and

(3)

(r, ϑ, λ) are the spherical polar coordinates

a is the radius of the Earth's surface (nominally 6,371.2 km)

Proc. '21st ESA Symposium European Rocket & Balloon Programmes and Related Research', 9–13 June 2013, Thun, Switzerland (ESA SP-721, October 2013)

P_n^m is a Schmidt quasi-normalized associated Legendre function of degree n and order m, and

g_n^m ; h_n^m are the Gauss coefficients.

In the space external to the source region (i.e. in free space), the potential V satisfies the Laplace equation, so that

(4)

$$\Delta V = 0 \quad \text{for} \quad r \geq a$$

In practice, the series expansion (2) is usually referred to an Earth´s sphere of mean radius a = 6,371.2 km, or an ellipsoidal or other appropriate reference surface of the Earth.

The originally infinite series expansion of Eq. (2) must be approximated by the partial sum with the truncation index N.
Using the common index k instead of the indices n and m for the respective degree and order of the associated Legendre functions $P_n^m(\cos\vartheta)$ allows Eq. (2) to be expressed in terms of the orthogonal functional system $\{f_k\}$ and the coefficients $\{C_k\} = \{g_n^m ; h_n^m\}$.

(5)

$$\begin{aligned} f_1 &= a \cdot P_1^0 \\ f_2 &= a \cdot \cos\lambda P_1^1 \\ f_3 &= a \cdot \sin\lambda P_1^1 \\ f_4 &= a \cdot P_2^0 \\ f_5 &= a \cdot \cos\lambda P_2^1 \\ f_6 &= a \cdot \sin\lambda P_2^1 \\ f_7 &= a \cdot \cos 2\lambda P_2^2 \\ f_8 &= a \cdot \sin 2\lambda P_2^2 \\ &\cdot \\ &\cdot \end{aligned}$$

for all k = 1,2,..., N · (N+2).

The least squares method is applied to the derivatives of the potential V (Eq. (2)) for numerically calculating the Gauss coefficients $\{g_n^m ; h_n^m\} = \{C_k\}$ of the SHA field model.
For field components taken at the Earth´s surface the least squares determination references the functional system and Gauss coefficients to the sphere of radius $r = a$.

However, the determination for observations taken at satellite altitude h are referenced to $r = a+h$.

Eq. (6) demonstrates the different functional systems referred to the Earth´s surface and to the satellite altitude h, respectively, so that different Gauss coefficients are calculated for the different SHA field models according to the potential V (Eq. (2)).
For the first degrees and orders there are:

(6)

for r = a	**for r = a + h**
n = 1	
$f_1 = a \cdot P_1^0$	$f_1 = a\left(1+\frac{h}{a}\right)^{-2} P_1^0$
$f_2 = a \cdot \cos\lambda P_1^1$	$f_2 = a\left(1+\frac{h}{a}\right)^{-2} \cos\lambda P_1^1$
$f_3 = a \cdot \sin\lambda P_1^1$	$f_3 = a\left(1+\frac{h}{a}\right)^{-2} \sin\lambda P_1^1$
n = 2	
$f_4 = a \cdot P_2^0$	$f_4 = a\left(1+\frac{h}{a}\right)^{-3} P_2^0$
$f_5 = a \cdot \cos\lambda P_2^1$	$f_5 = a\left(1+\frac{h}{a}\right)^{-3} \cos\lambda P_2^1$
$f_6 = a \cdot \sin\lambda P_2^1$	$f_6 = a\left(1+\frac{h}{a}\right)^{-3} \sin\lambda P_2^1$
$f_7 = a \cdot \cos 2\lambda P_2^2$	$f_7 = a\left(1+\frac{h}{a}\right)^{-3} \cos 2\lambda P_2^2$
$f_8 = a \cdot \sin 2\lambda P_2^2$	$f_8 = a\left(1+\frac{h}{a}\right)^{-3} \sin 2\lambda P_2^2$
n = 3	
$f_9 = a \cdot P_3^0$	$f_9 = a\left(1+\frac{h}{a}\right)^{-4} P_3^0$
$f_{10} = a \cdot \cos\lambda P_3^1$	$f_{10} = a\left(1+\frac{h}{a}\right)^{-4} \cos\lambda P_3^2$

etc. so that different sets of Gauss coefficients C_k and C'_k, respectively, due to the relevant functional systems in dependence on its reference sphere are calculated.

To explain these differences it has to be taken into account that the SHA is a transcription of a three-dimensional Taylor power series expansion using a three-dimensional cartesian coordinate system with its

origin in the centre of the sphere of the mean Earth radius. This transcription is performed by using the interrelations between the cartesian and the spherical coordinate systems so that Eq. (2) has the three-dimensional cartesian form

(7)

3-dimensional

$$f(\mathbf{r}) = \sum_{i=0}^{\infty} \sum_{k=0}^{i} \sum_{l=0}^{k} \frac{1}{i!} \binom{i}{k} \binom{k}{l} \frac{\partial^i}{\partial x^{i-k} \partial y^{k-l} \partial z^l} f(\mathbf{r})$$

$x = y = z = 0$

being identical to

$$V = \sum_{n=1} \sum_{m=0} a \left(\frac{a}{r}\right)^{n+1} (g_n^m \cos m\lambda + h_n^m \sin m\lambda) P_n^m(\cos\vartheta)$$

for the Earth´s surface.

Some relevant details from the theory of infinite power series expansion:

There is a special Theorem from the theory of infinite power series expansions which says: if there is a convergent power series expansion for a function then this expansion is unique.
Furthermore, any power series expansion is determined for its reference point and its reference surface, respectively. This reference essentially governs the convergence area and the convergence quality. The usual SHA field model is referred to the ground in form of the sphere of the mean Earth radius. This reference governs the convergence quality of this SHA series expansion as a relative slow convergent expansion.

In practice, the Gauss coefficients of the SHA are calculated for a finite functional system referred to the Earth´s surface. An internal SHA magnetic field model for a satellite altitude and derived from these satellite data has a different convergence quality in comparison to the ground because of the other reference sphere (cp. Eq. (6)).

There is another special Theorem from the theory of infinite power series expansions that gives the analytical relations between power series expansions of two different reference points / reference surfaces for the one-dimensional case [2]. The infinite sets of coefficients of both expansions are in relation to each-other by an infinite set of linear equations between them.

For the one-dimensional case there is:

(8)

$$f(x) = \sum_{n=0}^{\infty} a_n (x - x_0)^n$$

for $|x - x_0| < r$

$$f(x) = \sum_{k=0}^{\infty} b_k (x - x_1)^k$$

for $|x - x_1| < r - |x_1 - x_0| \le r_1$

$x_1 \in |x - x_0| < r$

where

$$b_k = \sum_{n=0}^{\infty} \binom{n+k}{k} a_{n+k} (x_1 - x_0)^n$$

$\Rightarrow$

$$f(x) = \sum_{n=0}^{\infty} a_n (x - x_0)^n = \sum_{k=0}^{\infty} b_k (x - x_1)^k$$

$$f(x) \approx \sum_{n=0}^{N} a_n (x - x_0)^n \neq \sum_{k=0}^{N} b_k (x - x_1)^k$$

The interrelations between the set of coefficients can be described as

(9)

$b_k = F(a_{n+k})$
for n = 0 up till infinity and k = 0 up till infinity

i.e. b_k is a function of all the a_{n+k} for n = 0 up till infinity and k = 0 up till infinity.

The coefficients b_k do not agree to the coefficients a_n, even not for the same degree.

The one-dimensional case shows clearly that only the complete infinite series expansions correctly represent the function. The finite partial sums as approximations give a different representation, even for the case, when both the expansions use the same truncation index, but different reference points.
Moreover, for both the complete infinite expansions the coefficients of the same degree do not agree to each-other, there is an infinite system of equations between them. To use the same system of coefficients for both the expansions means to simplify the interrelations between both systems of coefficients to the lowest quality of approximation.

For the three-dimensional case:

Because of the fact that the SHA field model of Eq. (2) is a three-dimensional transcription in cartesian coordinates (cp. Eq. (7)) the properties of the three-dimensional power series expansion are adequate to the one-dimensional case as discussed before. Therefore, the usual procedure in calculating the global internal magnetic field models on the basis of the SHA formula (Eq. (2)) referred to the Earth´s surface and using its set of Gauss coefficients g_n^m ; h_n^m from multi-altitude field data gives the lowest approximation quality for the SHA model. The reason is that the interrelations between the relevant sets of coefficients of the two different SHA series expansions for two different altitudes are a more complicated infinite system of linear equations than in Eq. (9).

Now in analogy in the three-dimensional case the interrelations between both the different sets of Gauss coefficients g_n^m ; h_n^m of the different global SHA field models (referred to the different reference surfaces) is given by an infinite set of linear equations as a function of all the infinite Gauss coefficients of the other set of coefficients.
Using C_k as introduced above for the Gauss coefficients g_n^m ; h_n^m of the SHA model referred to the Earth´s surface and C_l for the (different) Gauss coefficients of the different SHA model referred to a satellite altitude h in analogy to Eq. (9) the three-dimensional case gives

(10)

$$C_k = F(C_l)$$

for all $k = 0$ up to infinity and all $l = 0$ up to infinity

i.e. the interrelations between the coefficients of SHA models referred to different (concentric) reference surfaces (satellite altitudes h) are given by functions of all the infinite coefficients of the other SHA model in the form of a set of an infinite number of equations.

Therefore, necessarily the field data from different altitudes h cannot commonly be used for deriving a common field model referred to the Earth´s surface.
SHA terms as well as their coefficients of the same order and degree cannot be related directly to each-other, wavelength constituents are differently represented in the SHA terms.
This enables a fruitful discussion which of the constituents of the field sources reach a definite altitude. Here, a new chance for a more detailed investigation of the field sources in dependence on satellite altitudes will be opened when comparable SHA field models simultaneously in time are available.

Any effort to use the interrelations between the set of Gauss coefficients has to obey the necessity to approximate that infinite set of equations in a reasonable form. But despite of this, these interrelations demonstrate the variety of the SHA field models in dependence on the altitudes where the field data are taken from. Again, this mathematics makes clear that the altitude dependence of the field and of its model has to be considered in the global field modelling as significant essentials. Moreover, there are the physical properties of the field sources with respect to field wavelengths that differently reach the altitudes. Therefore, separate SHA field models in dependence on altitudes enable essential physical interpretations with respect to the field constituents.

The form of the different functional systems f_k for a SHA field model for the Earth´s surface and the satellite altitude h , respectively, (cp.Eq. (6)) is the consequence of these mathematical properties discussed.

The complicated and infinite algorithmic forms of the interrelations between the coefficients of the series expansions of different reference points in the one-dimensional case and especially for its generalization in the three-dimensional case for the Gauss coefficients g_n^m ; h_n^m of different altitudes h (cp. Eq. (10)) make obvious that only approximations can be used in all practical calculations.
There is to pay special attention to the quality of all these approximations used in the procedures to derive the field models from the recorded data.

3. PRACTICAL CONSEQUENCES

When in the forthcoming SWARM mission simultaneously in time magnetic field data are available for the ground and for different satellite altitudes there is the challenge
- to prove the altitude dependence of the relevant separate SHA field models
- to determine altitude dependent details of the magnetic field
- to prove any approximations of field continuations, e.g. that method of the author [1].

Eqs. (8), (9) and its 3-dimensional generalization Eq. (10) demonstrate that there are essential differences for the relevant Gauss coefficients in dependence from the satellite altitude h and significant differences in the related SHA field models as the consequence.
The generalization (Eq. (10)) is a large infinite set of linear equations that is difficult to treat with. Moreover, this infinite set is to be approximated by a reasonable finite approach and by well-defined criteria. From the viewpoint of theoretical mathematics to relate SHA field models referred to reference spheres of different altitudes means to determine upward and downward

potential field continuations. These field continuations – being another form of handling an infinite number of interrelations – are therefore ill-posed inverse problems that generally cannot be solved by a unique solution [3], [4]. [5].
In order to determine a reasonable solution for most cases (upward and downward field continuation) a regularizing procedure is an available alternative where infinite relations are approximated. This mathematical characterization describes the obvious problems to receive a reasonable solution for the functional dependencies of Eq. (10).

Moreover, there is a nonlinear dependence of the internal magnetic field sources on the distances from its sources, i.e. from the geometrical distances from the Earth´s surface. Describing the nonlinear functional dependence in physical terms makes obvious that different wavelengths of the internal magnetic field reach different satellite altitudes. And there is to emphasize that the mentioned mathematical characteristics of the SHA field models correspond well with the physical model.

According to these physical as well as mathematical properties the SHA field models can be improved significantly when separate SHA models are calculated separately for the different altitudes and exclusively only from field data of that definite altitude.

In particular, in geophysics the study of the potential function V (Eq. (2)) is of special interest where the mathematical property convergence of the SHA series expansion in dependence on the satellite altitudes is used. In this way the author introduced a form of regularization to calculate an approach for a numerical downward field continuation of the relevant Gauss coefficients of the SHA model to a lower satellite altitude (Webers, 2007).

(11)

$$C_{kreg}(n, k, C_k, r_1, r_2, \gamma; c_0^{(2)}) =$$

$$sign(C_k) \cdot \left[(2n+1) \cdot 10^{(1-\cos\gamma)\, c_0^{(2)} - (k + \frac{c_2}{c_1} k^2 + \frac{c_3}{c_1} k^3 + \ldots) \cdot \sin\gamma} \cdot \left(\frac{C_k^2}{2n+1} \cdot \left(\frac{r_1}{r_2} \right)^{2(n+1)} \right)^{\cos\gamma} \cdot \frac{(4\pi r_1^2)^{\cos\gamma}}{4\pi r_1^2} \right]^{\frac{1}{2}}$$

for $r_2 < r_1$ and $\gamma = \alpha_2 - \alpha_1$,

where

r_1 is the radius of the satellite altitude reference surface

r_2 is the radius of the ground reference surface

.
The *reg* index in the downward continued Gauss coefficients C_{kreg} [Eq. (9)] indicates the fact that the downward field continuation mathematically means an ill-posed inverse problem that is solved by a regularization process. Details of the procedure and its parameters are given in the mentioned paper (Webers, 2007). Here, the regularization parameters γ, $c_0^{(2)}$, $c_j^{(1)}$ for $j = 0,1,2, \ldots$ have been derived from the inherent mathematical characteristics, i.e. the different convergence property at the ground in comparison to the satellite altitude. Therefore, no further physical explanations are necessary for the consequences of this regularization.

In this way a downward continued SHA field model can be calculated and compared with that SHA model being determined from data of its reference surface. Such comparisons enable to evaluate the different physical field properties of the different altitudes.

4. CONCLUSIONS

The mathematical SHA field model proves that there are essential different mathematical and physical properties in dependence on the satellite altitude.
Consequently,
- the SHA field models are to be calculated separately for the different altitudes.
- a common SHA field model based on the ground as reference surface and using only the geometrical coordinates of the multi-altitude data points of the field in Eq. (2) produces only a mean SHA field model because of the fact that different functional systems (cp. Eq. (6) are neglected.
- separate SHA field models referred to the relevant satellite altitude as reference surface of the SHA series expansion enable to determine the different mathematical as well as the physical properties in dependence on the satellite altitudes.
- the different physical properties of SHA field models can be determined approximately by the difference fields that are calculated for the altitudes in comparison with the downwardly continued field models using Eq. (11).

As examples Fig.1 and Fig. 2 demonstrate the amounts of such non-linear differences of the SHA fields in dependence on the altitudes. For the DGRF 1990 an approximation for a mathematical upward field continuation had bee calculated to the altitudes h = 400

km and h = 750 km, respectively. Using Eq. (11) from both altitudes downward continuations have been determined. Fig. 1 and Fig. 2 give the differences to the ground field that cannot be identical to zero.
According to the Eq. (11) the differences of the SHA fields depend on the parameters of the used regularization, i.e. the convergence properties and the finite approximations. Practically, these are the following parameters:
- truncation index N of the SHA field model
- satellite altitudes h
- approximation quality for evaluating the convergence property of the SHA
- field data quality and data distribution for the reference spheres (i.e. ground and satellite altitudes)

The Figures 1 and 2 make obvious that the forthcoming SWARM mission will give excellent chances to study the non-linear altitude dependence of the internal magnetic field when, simultaneously in time, field data from different satellite altitudes will be available. Moreover, in this way more details of the field with respect to the field sources can be studied.

5. REFERENCES

1. Webers, W. A. , *On different properties of internal magnetic field models at the Earth´s surface and at satellite altitudes*, J. Geodyn. 43, 239-247, 2007.
2. Knopp, K., *Theorie und Anwendung der unendlichen Reihen*, Springer Verlag, Berlin, 1922.
3. Huestis, S.P., Parker, R.L.. Upward and downward continuations as inverse problems, Geophys. J. R. Astr. Soc. 57, 171-188, 1979.
4 Anger, G., *Inverse problems in differential equations,* Akademie/Plenum Press, Berlin/London, 1990.
5. Webers, W. A., *Downward field continuation in combining satellite and ground-based internal magnetic field data*, J. Geodyn. 33, 101-116, 2002.

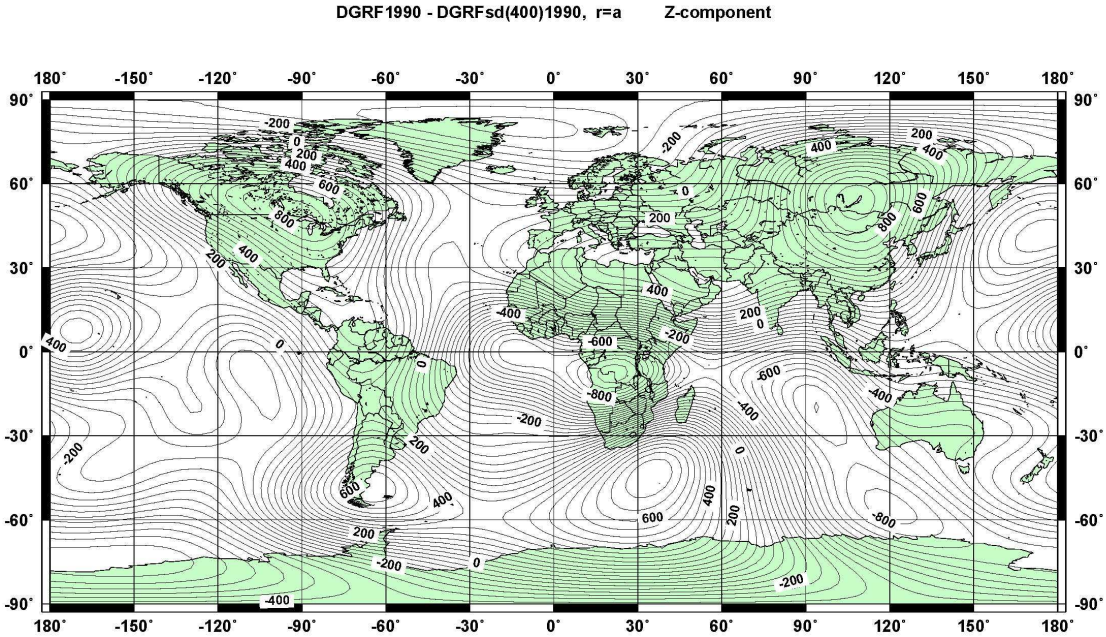

Fig. 1.
*DGRF 1990: difference chart DGRF 1990 – DGRFsd (**400**) 1990, Z-component in nT:*
*DGRF 1990 mathematically upward continued to the satellite altitude of h = **400** km as DGRFs (**400**) 1990, downward continued to the ground as DGRFsd (**400**) 1990.*

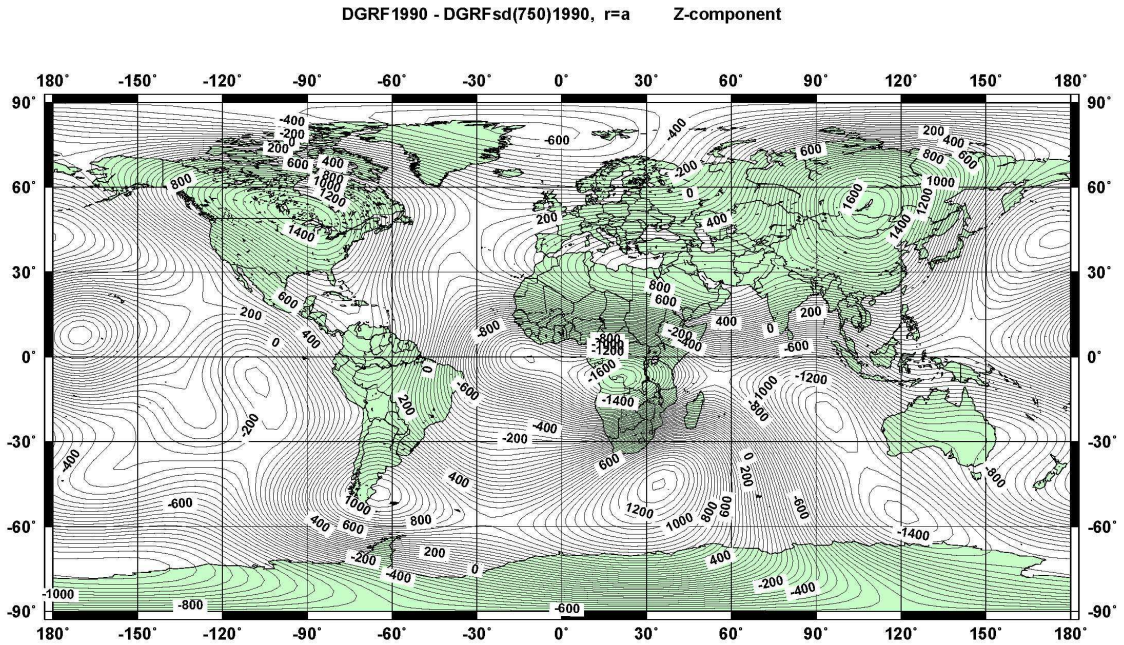

Fig. 2.
*DGRF 1990: difference chart DGRF 1990 – DGRFsd (**750**) 1990, Z-component in nT:*
*DGRF 1990 mathematically upward continued to the satellite altitude of h = **750** km as DGRFs (**750**) 1990, downward continued to the ground as DGRFsd (**750**) 1990.*

New Techniques for Balloons

Chairs: M. Zell & A. Cogoli

COMPACT TELEMETRY SYSTEM FOR SMALL SATELLITES EJECTED FROM SOUNDING ROCKETS AND BALLOONS

Sebastian Finke[(1)], R. Pohlmann[(1)], Qiang Li[(2)], B. Strelnikov[(2)], M. Rapp[(2*)], F.-J. Lübken[(2)], J. B. Schumacher[(3)] and H. Ewald[(3)]

[(1)] argus electronic GmbH, Joachim-Jungius-Str. 9, 18059 Rostock, Germany
eMail: Sebastian.Finke@argus-electronic.de
Tel: +49 (0) 3 81 / 40 59 3 24, Fax: +49 (0) 3 81 / 40 59 3 22
[(2)] Leibniz Institute of Atmospheric Physics e.V. at University of Rostock,
Schlossstr. 6, 18225 Kühlungsborn, Germany
[(3)] University of Rostock, Institute of General Electrical Engineering,
Albert-Einstein-Str. 2, 18059 Rostock, Germany
[*] now at: Deutsches Zentrum für Luft- und Raumfahrt, Institut für Physik der Atmosphäre, Oberpfaffenhofen, Germany

1. INTRODUCTION

Since several decades a very active scientific community routinely sounded the middle and lower atmosphere using MET-rockets and balloons. Different techniques applied for this research are permanently improving utilizing modern technologies. In particular, the well-known falling sphere (FS) technique used to measure density, temperature, and wind fields in the middle atmosphere, has been revised many times since early 70th. Unfortunately, those efforts did not end up as a frontend scientific instrumentation for a routine use.
In this paper we introduce a new compact and cost-effective telemetry system that was developed to run on an ”active falling sphere” instrument but can be efficiently applied for a vast of balloon sounders. The main components of the active FS instrument are the sensor system and the central data acquisition unit in combination with a compact, long range, bidirectional telemetry system to transmit the measure data from the instrument to the experimenter. The conditions under which the system has to operate limit the possibilities to do this and define the requirements.
This paper will discuss in detail the technical implementation of the new telemetry system and its application in the new “Active FS” instrument. Furthermore, other potential applications to airborne and space experiments will be addressed.

2. SYSTEM REQUIREMENTS

In the final version the carrier system of the instrument will be a small sounding rocket with dart-like payload. This means that the dimensions to store the whole measurement instrument and the telemetry system are very limited.
Due to scientific requirements, which come from aerodynamical reasons, the shape of the instrument must be an ideal sphere, which will fall at a speed of up to 3 km/s and additionally rotate and swing. After the ejection from the rocket the sphere will experience free fall and will be uncontrolled. The worst case the sphere, will rotate around all three axes.
The transmission range for telemetry is up to 140 km in direct sight line, corresponding to the planed apogee at an altitude of about 120 km, under any possible weather conditions.
Another complexity is the quantity of measurement data to generate and transmit over the radio connection. The desired local resolution of every measurement point is one meter. This means, at a velocity of 1000 m/s, a sample rate of 1 kSps is needed, at least for the main sensor system (housekeeping sensors, for example, are sampled much slower). At the end the instrument generates data at a rate of about 100 kbit/s.
In conclusion, these are very difficult conditions to establish and maintain a radio connection.
In addition, the instrument is not meant to be recovered, which clearly excludes the possibility to store data on board for the case of a radio connection interruption.
In case of unstable radio connection the data set will not be continuous which implies drastic consequences for scientific results and data interpretation. Especially in the “Active FS” application.
So the main goal of this telemetry system is 100% loss free data transmission under any possible atmospheric condition.

3. BASE SYSTEM SELECTION

Currently there are different techniques in use to transmit data from a mobile measurement system to a stationary receiver.
Recording of the data and recovering them after touchdown is already excluded by the requirements.
Another famous method is the usage of satellite based radio networks like GSM. This is an excellent possibility for transmissions over very long distances

Proc. ‘21st ESA Symposium European Rocket & Balloon Programmes and Related Research’, 9–13 June 2013, Thun, Switzerland (ESA SP-721, October 2013)

with limited data rates. Also there is no need for any telemetry equipment at the ground station. Difficult is the high outlay to reach higher data rates with these networks. In extreme cases cooperation with the network operators is essential and even if this problem is solved, there is no possibility to control the data stream. The package loss rate of such systems increases with the data rate and the network utilization is very dynamical, which is also not controllable.
This situation is clearly against our goal of a loss free data transmission.
Because of these potential difficulties, the way of choice is to establish a dedicated radio connection between the instrument and a ground station.
But there are also potential error sources with this technique, caused by the operating conditions. Especially the undefined and dynamical antenna orientation of the systems mobile part could result in package losses.
So the final decision is to develop a new telemetry system. It is based on a direct radio link, but modified to suite the special requirements of the "Active FS" instrument and to guarantee a loss free data transmission to the ground station.

4. TELEMETRY SYSTEM SPECIFICATIONS

At the time of this paper the technical situation is as follows:
The transmission range can be guaranteed to above 50 km. In field tests with weather balloons also 70 km could be reached without any problems. The experiences from these tests also implied the potential for even longer ranges. It is planned to validate this during the next flights.
The carrier frequency band can be chosen from four options:
869 MHz, 920 Mhz, 2.4 GHz and 3.4 GHz.
It is important to keep in mind that a higher frequency will result in less transmission range.
The system can be configured to a transmission power of up to 1 W, but there is also an option to get up to 2 W.
The next fact is the transmission rate. It is also configurable, in the current version up to 230 kBaud. On request it is also possible to get up to 1.38 MBaud, but this will reduce the maximum transmission range.
One of the most important points is the data reliability. As defined in the system requirements a loss free transmission is necessary.
The operating conditions of the telemetry system result in a very unstable radio connection. Accordingly the system is equipped with a memory, which works as a buffer and is big enough to hold the complete measurement data, which are generated during the whole flight time.
Another main feature of the new system is an Uplink. On the one hand it can be used to transmit control and configuration commands to the measurement system during the flight, and on the other hand, in combination with the data buffer, it ensures the 100% data reliability. For a detailed explanation of this process refer to point 5.
In contrast to the stationary receivers of other telemetry systems the ground station is very small, light weighted and accordingly mobile. It is equipped with a beam antenna and provides an integrated antenna tracking subsystem, based on GPS information. The receiver supports RS422 and USB terminals to connect an external data processing unit. In the simplest way a laptop with recording and control software could be used.
In addition to the data reliability of the radio link, the receiver logs the complete radio traffic on a SD-card. This avoids data loss in the case of a failure in the processing unit or the serial connections.
Also important for the mobility is that the whole ground station subsystem is capable of being completely supplied be batteries.
The last interesting feature is an integrated automatically ejected parachute, which is triggered on a configurable altitude level or alternatively by a radio command. This subsystem stabilizes the "Active FS" after it has left the interesting measurement zone. This way the best possible telemetry antenna orientation can be achieved for the remaining flight time. Additionally this time span is stretched by the deceleration, to increase the chance to establish the radio connection and transmit the remaining measurement data.

5. OPERATIONAL CONCEPT

The data generation inside the instrument works the same way as in other systems. The measured data from all sensors, in case of the "Active FS" these are mainly accelerometers and gyroscopes, are stored in a set of memories with enough space for a fix defined measurement period (in this system it is 100 ms). As soon as these memories are completely filled, their content is merged into a data package of a defined format and size.
In telemetry systems with a downlink only, these data would be transmitted directly in a continuous stream, in the same rate as they are generated. All data, which are not correctly received at the ground station, would be lost (except for relatively small corruptions in the data stream, which can be repaired by data restoration procedures).
In contrast to this, the new telemetry system stores the generated measure data packages in a buffer memory. It

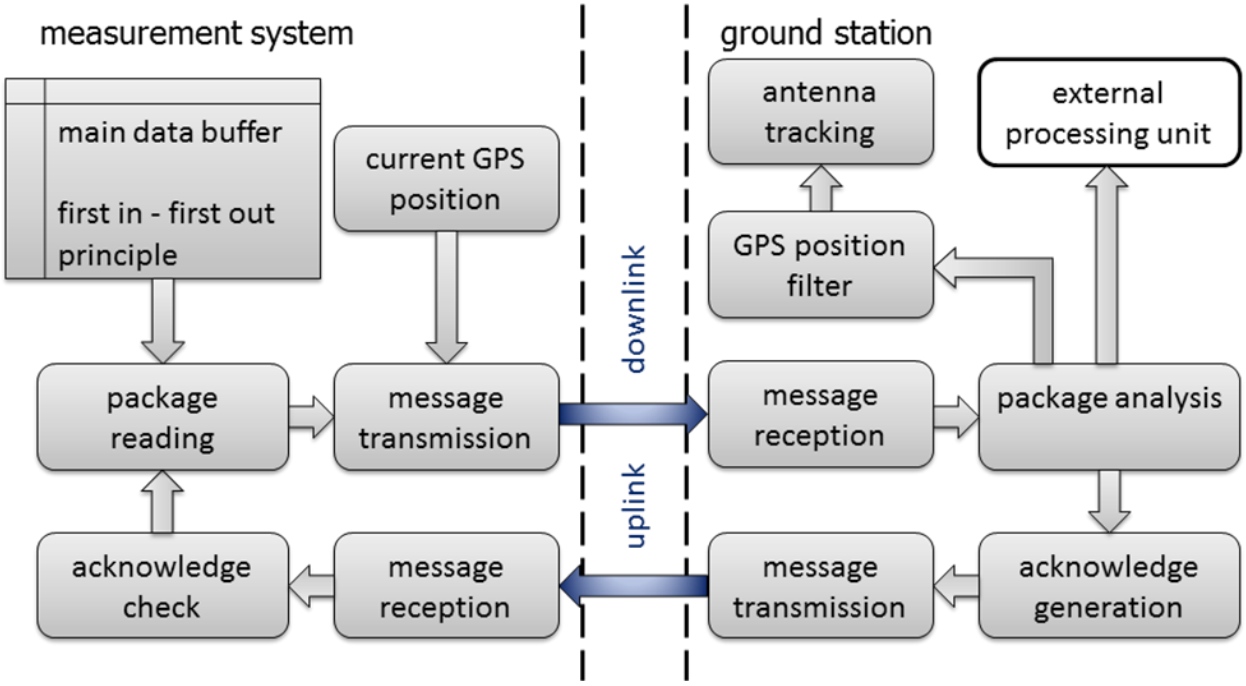

Figure 1. Schematic of the operational concept.

has enough space for the complete measured data from the whole flight and holds them in chronologically correct order.
Fig. 1 shows schematically the operational concept of the telemetry system, beginning with the main data buffer in the top left corner.
This buffer works with first in – first out principle. Accordingly the telemetry system starts reading from this memory with the oldest stored and not already transmitted data package.
In the next step a telemetry message will be created, containing the former read data package and the current GPS position of the measurement instrument. Then this message is transmitted over the downlink and eventually received at the ground station. There, the received message will be analyzed and checked for data corruption. If the content is valid, three things will be done.

- The GPS position will be read out, so the antenna tracking subsystem can be updated with this information.

- The measured data package will be transmitted over the serial terminals to a connected processing unit, like a laptop.

- An acknowledgement will be generated and transmitted over the uplink, back to the measurement system.

This last point is the essential part to ensure the indispensable data reliability of 100%.

At the instrument side, the telemetry system can assign the received acknowledgement to a former transmitted data package by its unique ID number. If it
is correct, then this package will be marked as successfully transmitted and this event finally triggers the reading and transmission of the next package from the main data buffer. This will be again the oldest not already successful transmitted one.

This is the systems normal transmission behavior as long as the radio connection is stable.
If this circle is interrupted anywhere, most likely by a radio link connection loss, this will be noticed by the absence of an assignable acknowledgement for one or more transmitted packages. In this case the telemetry system will stop reading packages from the main data buffer. Instead it will retransmit the oldest not acknowledged package periodically, until the connection is established again and the correct acknowledgement is received.
Now the system can return to its normal transmission behavior and continue with the next package from the main buffer.

To conclude, this means that every data package will be send out until the corresponding acknowledgement is received from the ground station. This way, there is no possibility for any data loss. The exception is when the whole time of a stable radio connection before the touchdown is not long enough to transmit all interesting data. But in exactly such situations the parachute is intended to help by increasing the available

transmission time span and optimizing the telemetry antenna orientation.

6. FURTHER DEVELOPMENTS

At the time of this paper the telemetry system is in a late prototype stage. The base system is functional and some of the planed additional features are also integrated.
The final result, apart from a specialized version of this system for the “Active FS” application, will be a high quality telemetry system with minimal dimensions (60x40x30 mm, except the antenna, are reachable) which can be combined with any user defined measurement system to transmit data to a small, mobile ground station.
It will be flexible to suite a wide range of requirements. This will be achieved by configurability and several optional features, which can be integrated on the need. The GPS based antenna tracking subsystem is ready and already implemented for final testing.
One of the next steps is a second high precision GPS module, without COCOM limits and modified calculation models for high altitudes. This will allow navigation at high velocities and also inside the ionosphere for example, which is essential for the “Active FS” apogee of 120km. The GPS module itself is already available, but the integration into the telemetry system is yet to be done.
Several other features are also planned, for example a boxed version with waterproof cover and terminals, chose able/redundant internal and external power supply and free configurable data terminals to feed in data, which have to be transmitted.

7. APPLICATIONS

The intended main applications for this telemetry system are sounding rockets, balloons and all experiments, which can be done from and on these platforms.
But the area of possible applications is not limited to such systems. High data reliability despite unstable connections by any reason is a critical point in other situations also.
A possible reason for an unstable radio connection is not only an unfavorable antenna orientation, but also an inhomogeneous dynamical medium or a solid barrier, which enters and interrupts the transmission path. So another application area is such difficult environments, like mountains, urban areas, forests and similar places.
And at last, also areas with a high density of other radio transmitters are such dynamic error sources.

8. SUMMARY

The prototype of the system, which is currently in operation in several field tests, already showed the functionality. The data reliability is about 99,99% under lab conditions, so there is room for improvements to reach the desired 100%. The transmission range is validated up to 70 km and will be extended in the next tests.
Different applications, apart from the “Active FS”, are in the planning phase.
The ground station subsystem is completed, including the antenna tracking and the desired mobility.
To conclude, the main requirements of the “Active FS” projects telemetry system are already achieved or on the way to be validated and the systems modification to suite similar requirements in other application areas has began.

For detailed information about the accelerometer subsystem of the “Active FS”, please refer to paper 125 by Jan Berend Schumacher et al.
HIGH PRECISION DRAG DECELERATION MEASUREMENT SYSTEM TO USE ONBOARD ACTIVE FALLING SPHERES and the scientific background of this project is explained in paper 116 by Qiang Li et al.
HIGH-RESOLUTION MEASUREMENTS OF THE MIDDLE ATMOSPHERE USING ACTIVE FALLING SPHERE: PRELIMINARY CALCULATIONS.

9. ACKNOWLEDGMENTS

This project is funded by Wirtschaftsministerium Mecklenburg-Vorpommern in Germany.

ACCURACY ESTIMATION OF THE GLOBAL ANALYTICAL MODELS OF THE MAIN MAGNETIC FIELD BY MEANS OF THE GRADIENT MAGNETIC SURVEY ON STRATOSPHERIC BALLOONS

Yu.Tsvetkov[1], O.Brekhov[2], S.Filippov[1], L.Sidorova[1], W. A. Webers[3]

[1)]*Pushkov Institute of Terrestrial Magnetism, Ionosphere and Radio Wave Propagation of Russian Academy of Sciences (IZMIRAN), Russia. E-mail: tsvetkov@izmiran.ru*
[2)] *Moscow Aviation Institute (MAI), Russia. E-mail: obrekhov@mail.ru*
[3)] *GeoForschungsZentrum Potsdsm, Germany. E-mail: wigor@gfz-potsdam.de*

Regular aeromagnetic and satellite magnetic surveys have been executed in the second half of the XXth century. The analysis of their data has shown, as the first, and the second kinds of surveys that they have series of the lacks and some influence on the results of their use in studying the crustal magnetic field of the Earth and its sources. It is necessary to have data obtained from altitudes, in numerical expression, compared with the thickness of the Earth's crust (30-40 km).

Magnetic measurements performed by stratospheric balloons at the altitudes of about 30-40 km register naturally generated magnetic signals from the whole thickness of the Earth's crust and contain the information about the processes in the lithosphere.

In the last time the conditions have created for receiving highly qualitative magnetic and other scientific data by stratospheric balloon magnetic surveys:

- Global navigating system (GPS, GLONASS);
- Stratospheric balloon gradiometer with a measuring base of 6 km length;
- Global system of data transmission from any point of the globe in FTP as server of a network of the Internet (GlobalStar, IRIDIUM);
- "Superpressure" stratospheric balloons, capable to be in nonstop flight over about100 days;
- Global analytical models of the main magnetic field of the Earth (IGRF and others) from satellite magnetic data, being a basis for the separation and the analysis of magnetic anomalies.

For studying the magnetic field in the near Earth space and for studying the deep structure of the Earth's crust in IZMIRAN and MAI a stratospheric balloon magnetic gradiometer for magnetic measuring on board a stratospheric balloon had been developed and introduced in practice. The procedure uses a measuring base of 6 km length that is oriented along a vertical line with respect to the gravity field.

The errors related to the deviation of the position of the measuring base relative to the vertical have been studied during the real balloon flight with help of GPS navigation receivers. The deviations of the measuring base in the length of 6 km within 500 m, which can sometimes reach up to 1500 m, have been obtained. This results in a decrease of the measurement accuracy of the magnetic gradient due to the errors introduced by the specification of the normal magnetic field to which the magnetic anomalies are referred. To eliminate this error, a GPS receiver was used in each magnetometer in order to observe the magnetometers during synchronous measurements and according to the applied model of the main magnetic field so that the measurements are corrected for the normal magnetic field. It has been indicated that the effect of deviations of the position of the measuring base on the results is not more than 2% of the size of the crustal magnetic field.

The errors of the stratospheric balloon experiments had bee studied with respect to the global analytical magnetic field model EMM/720 (Manoj C.Nair, Stefan Maus, Enhanced Magnetic Model. http://www.ngdc.noaa.gov/geomag/EMM) and to the magnetic field of crust and core of the Earth that had been derived from spherical harmonics up to 720. Both models had been calculated from satellite and ground data. Fig. 1 shows the differences of the measured magnetic field and the models EMM/720 at the altitude of 30 km. The resulting differences show, that in a range of the harmonics describing the crustal magnetic field, essential divergences of the measured and the modeled sizes are observed. This investigation shows that the use of ground data is practically unsuitable for a construction of the analytical model developed up to 720 spherical harmonic.

The crustal magnetic field had been extracted from measurements at the altitude of 30 km on daily average Spherical Harmonic Model (DSHM) [1]. This extraction has been made for some days with various magnetic activities. Fig. 2 gives the results of the separation of the crustal magnetic field for the following sizes of the magnetic activity:

Proc. '21st ESA Symposium European Rocket & Balloon Programmes and Related Research', 9–13 June 2013, Thun, Switzerland (ESA SP-721, October 2013)

1- ΣK_p = 460, 2 - ΣK_p = 190, 3, 4 - ΣK_p = 26. The shadowed zone ΣK_p = 4-20 (5 days).

When the DSHM had been used the analysis of the results for the extraction of the crustal magnetic field shows: (1) DSHM constructed for days with $K_p\Sigma < 20$ leads to an error of the size of that of the main field MFE, i.e. equal ±5 nT, and for a day with $K_p\Sigma \geq 20$ - to an error of 10 nT and more. These errors are non-uniformly distributed over the Earth´s surface and this non-uniformity is specific for every one day. (2) DSHM in comparison with other models proves to be expedient at $K_p\Sigma < 20$ for the extraction of the crustal magnetic field due to the small contents in a model of a field of a secular variation (~0,1 nT/day).

Ground field data and the Poisson integral enable to derive values of the crustal magnetic field at any altitude $h > 0$, but such upward recalculation of the field has not been successful up till now. To find out the reason of this failure let us compare the initial data on the crustal magnetic field represented by the map [2] (derived from low-altitude aeromagnetic survey, like all the analogous maps, which are usually used for an upward recalculation of the field) with the balloon-derived data. The results of low-altitude aeromagnetic survey demonstrate (Fig. 2) a higher sizes of the negative crustal magnetic field in comparison with the balloon-derived data. In Fig. 2 the ratio between values of positive and negative anomalies is, on average, 1.1 for the near-surface realization and 4.5 for the balloon-derived realization. This is the most important result obtained experimentally, which explains many irredundant problems appearing when studying the crustal magnetic field phenomena. Because of the fact that the anomalous magnetic field at any altitude level is a superposition of fields of some sources, being within a definite area of influence and averaging the near-surface data influences the field in almost the same way as a recalculation to an altitude does. Averaging the near-surface data gives underestimated values in comparison to the real ones. Therefore, the maps of the crustal magnetic field carry incomplete information about the sources located in the whole thickness of the Earth's crust, but mostly reflect processes in the near-surface layer of the crust, though deep processes as well, but to a lesser degree. This is the most key reason why it is impossible to recalculate the crustal magnetic field derived from small-altitude surveys into the upper half-space. A limitation of the area from which the initial data are derived has a certain influence as well, but to a lesser degree. Another result gives the averaging of balloon-derived data from the altitudes where the field is more formed in a natural way from all the crustal sources than from the near-surface sources alone.

Fig. 3 obviously shows that the Kama-Emba satellite magnetic anomaly cannot be generated from crustal magnetic anomalies presented by a map [2]. On the other hand stratospheric balloon data explain well an opportunity that satellite magnetic anomalies are formed from the crustal magnetic field.

Conclusions

1. By experimental methods is shown that the maps of the anomalous Earth's magnetic field and the other data derived from low-altitude magnetic surveys reflect processes in the near-surface layer of the Earth's crust, and the deep processes as well, but to a lesser degree; i.e., they do not contain the complete information about all the sources in the Earth's crust. This inconsistency between ground and stratospheric balloons (and satellite) follows from magnetic data.
2. When only the data derived at the altitudes are used in the numerical expression comparable with the vertical thickness of the Earth's crust enables to give a strict model of the anomalous Earth's magnetic field at these altitudes being formed in a natural way from all the sources.
3. Stratospheric balloon gradient magnetic surveys in the stratosphere in due course by virtue of its advantages will take the same worthy place in the theory and practice of geomagnetism that at present is occupied by aeromagnetic and satellite magnetic surveys.

References:

1. Golovkov,V.P, Zvereva, T.I., and Chernova T.A. Space-time modeling of the main magnetic field by combined methods of spectral harmonic analysis and natural orthogonal components. Geomagnetism and Aeronomy, 2007, Vol, 47, No 2, pp. 256-262.
2. The Map of Anomalous Magnetic Field for the USSR Territory. 1:2 500 000, Ed. by Z.A. Makarova (GUGK, Moscow, 1974) [in Russian].

The work has been executed by financial support of the Russian Foundation for Basic Research (RFBR), the grants 11-05-00182a and 13-05-10083k.

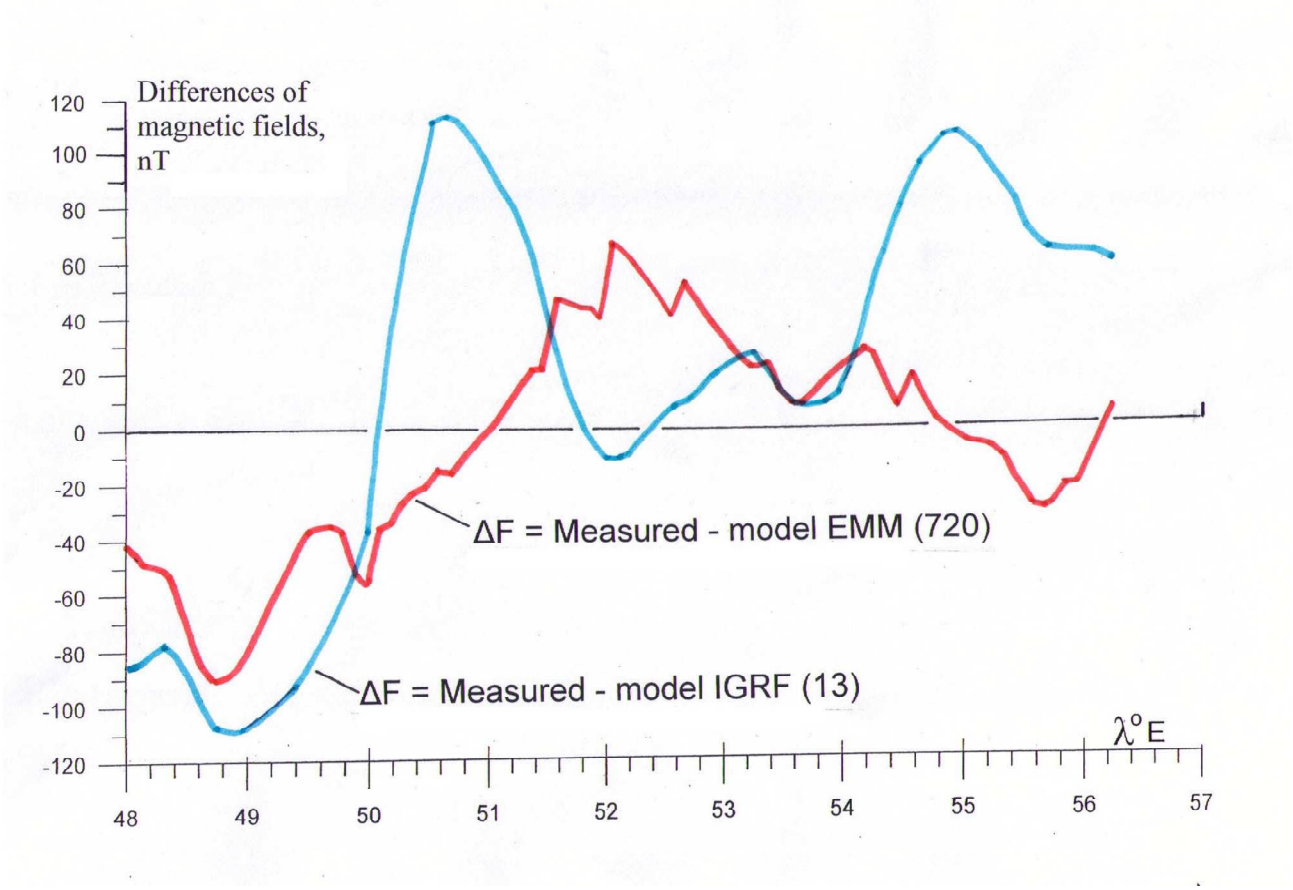

Fig.1. Differences of magnetic fields: measured and models EMM (720 spherical harmonics) and IGRF (13 spherical harmonics) at the altitude of 30 km

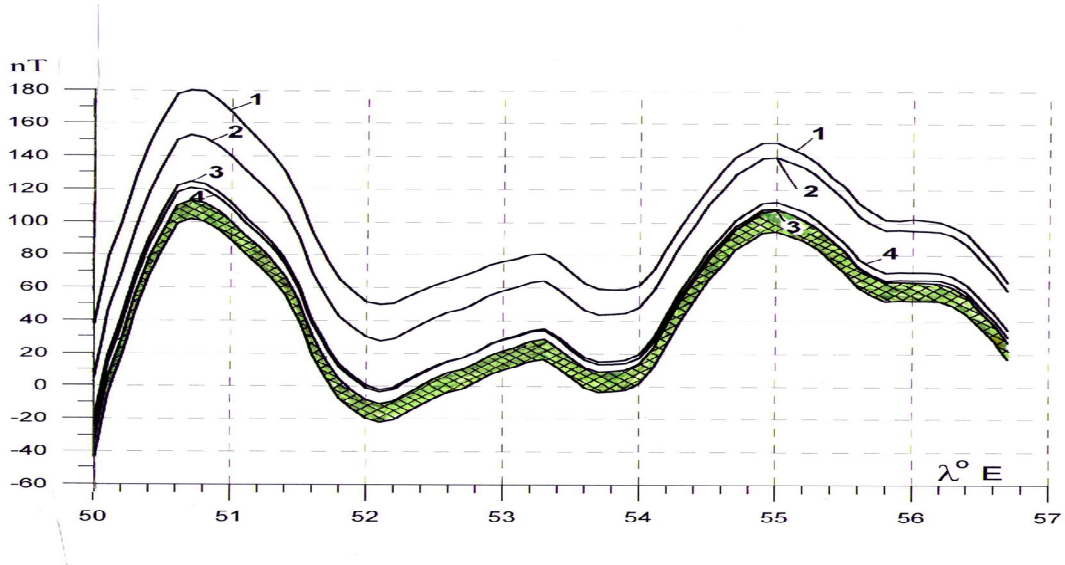

Fig. 2. Crustal magnetic field extracted from 30 km, measured at altitude 30 km on «Daily average spherical harmonic model» (DSHM) for days with different magnetic activity: 1-ΣK_p = 460, 2 - ΣK_p = 190, 3, 4 - ΣK_p = 21 - 26. The shadowed zone ΣK_p = 4 - 20 (5 days).

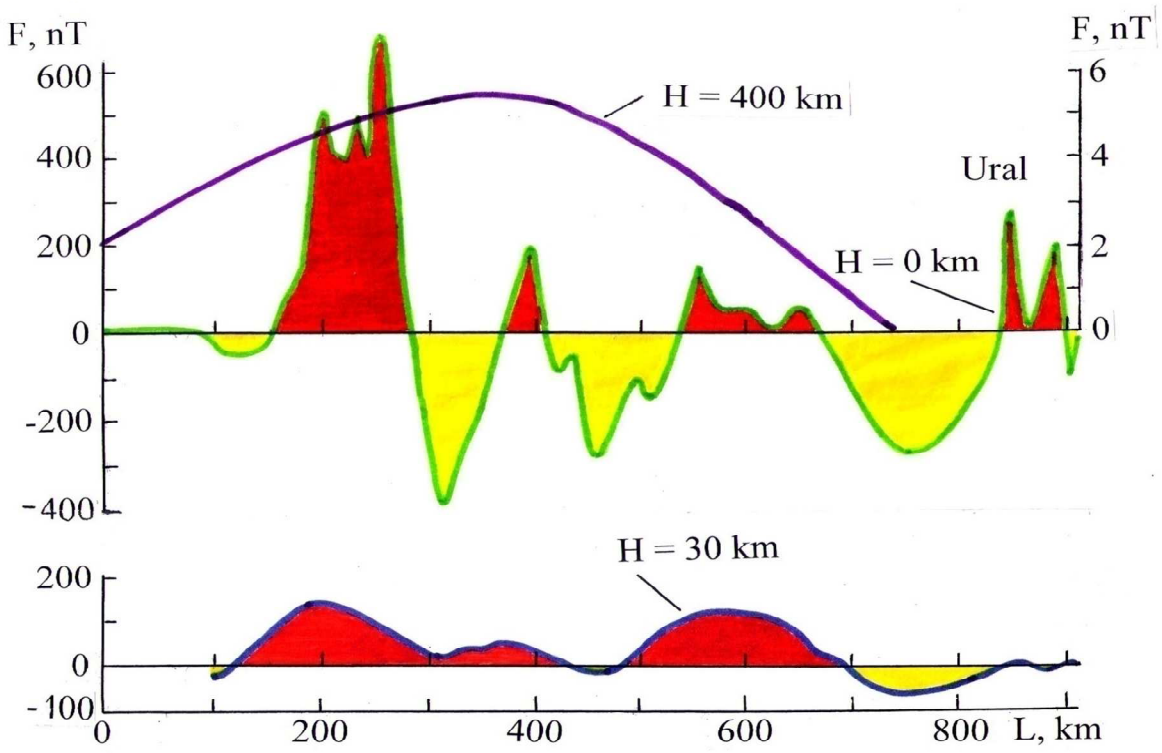

Fig.3. Form of the satellite Kama-Emba magnetic anomaly.

CALIBRATION OF THE PILOT PHOTOMETER

Ruka MISAWA[1,2], **Jean-Philippe BERNARD**[1,2], **and the PILOT team**

[1]*University of Toulouse; UPS-OMP; Toulouse, France, Email: Ruka.Misawa@irap.omp.eu;*
[2]*CNRS; Institut de Recherche en Astrophysique et Planétologie, 9, avenue du Colonel-Roche, 31028, Toulouse, France*

ABSTRACT

The Polarised Instrument for Long-wavelength Observation of the Tenuous interstellar medium (PILOT) is a balloon-borne astronomy experiment designed to study the linear polarization of the Far Infra-Red emission, 240 μm (1.2 THz) and 550 μm (545 GHz) with an angular resolution of a few minutes of arc, from dust grains present in the diffuse interstellar medium, in our Galaxy and nearby galaxies. The polarisation of light is measured using a half-wave plate (HWP). We are planning to have a first test of the instrument in August 2013 during the qualification of the new NOSYCA system developped by CNES from Timmins, Ontario Canada. The first flight of PILOT is scheduled in 2014 from Timmins. This paper describes the measurement principles of PILOT and the results of the laboratory tests of the PILOT photometer. These include stability measurements using an internal calibration source, measurements of an external polarised source, characterisation of the detector noise, polarisation measurements, measurements of interferogram and transmissions using a Fourier Transform Spectrometer at various positions of the HWP allowing, among other things, the calibration of the HWP rotation angle.

Key words: scientific balloon; photometers; polarisation.

1. INTRODUCTION

The interstellar medium (ISM), the space between the stars, consist mainly of gas (99%) and dust (1%) at very low densities. The individual dust particles are called dust grains and are extremely small, with sizes going from a few microns down to macromolecular scales. Dust grains are irregularly shaped and composed primarily of Carbon and Silicates.
Dust grains play a crucial role in the catalysis of molecule formation, the photo-electric heating of the gas, the cooling of the densest star forming regions. Their emission is also a foreground contaminant affecting the study of the Cosmic Microwave Background. In addition, grains are considered a universal tracer of the structure of the ISM, and their emission is also used to study distant high redshift galaxies.
The dust grains emit like modified black-bodies: the emission intensity is $I_\lambda = \tau_\lambda B_\lambda(T_D)$ where I_λ is the intensity, τ_λ is the optical depth, B_λ is the black body intensity and T_D is the temperature of the dust grain. The largest dust grains are in thermal equilibrium with the UV-VIS starlight and at an equilibrium temperature of T_D = 17 K in the diffuse ISM. Their emission peaks around 150 μm. The physics of their emission is currently the subject of many studies with the Herschel and the Plank satellites.
In addition, the thermal emission of dust grains is polarised, due to the grain shape asymetries and the statistical grain alignment with respect to the magnetic field present in the ISM. This produces polarization orthogonal to the magnetic field lines. For the same reason, the non-polarised star light passing through aligned dust grains also gets polarized. This produces extinction polarized in a direction parallel to the magnetic field lines. In our galaxy, the magnetic field is essentially along the plane of the galactic disk. Therefore, the stellar extinction is polarized mostly along the plane while emission is polarized orthogonal tp the plane.
Historically, measurement of polarised light in the far-infrared have been difficult because of atmospheric absorption. By far ground-based observations are limited to the bright regions in star forming regions, where they are used to probe the direction of the magnetic field, which likely plays a central role in the star formation process. In those regions, the polarization levels are low (a few %) and a systematic decrease of the polarization level with column density is observed, which origin is unclear (e.g. Matthews & Wilson [2]). For balloon borne observation, the Archeops has allowed astronomers to measure dust polarisation at 850 μm (353 GHz) over a fraction of the galactic plane (Ponthieu et al. [3]) with much higher sensitivity than grund measurements. These measurements indicated high polarization levels (up to 15%) in the diffuse ISM. Recently, the Planck satellite measured polarisation in the wavelength range from 850 μm (353 GHz) to 1.0 cm (30 GHz) with high accuracy.

2. CONCEPT AND MEASUREMENT PRINCIPLE

PILOT uses a 0.83 m diameter off-axis primary miror combined to a cold secondary in the Mizuguchi-Dragone

Proc. '21st ESA Symposium European Rocket & Balloon Programmes and Related Research',
9–13 June 2013, Thun, Switzerland (ESA SP-721, October 2013)

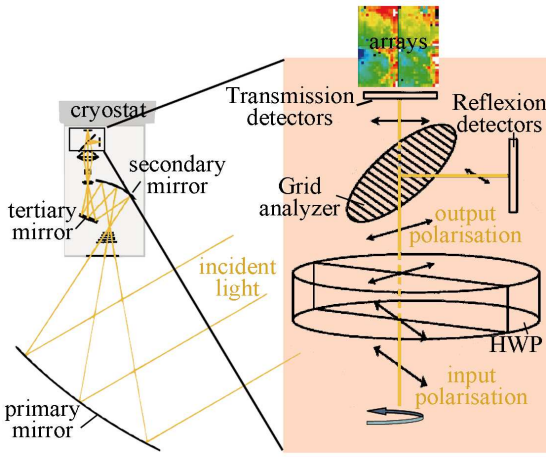

Figure 1. Left: Schematic diagram of the PILOT optics. The cold optics inside the cryostat is maintained at 4 K. The detectors operate at a temperature of 300 mK. Right: Schematic of the action of the HWP on the incident polarized signal.

Figure 2. Assembled PILOT instrument mounted in the gondola.

configuration. Appart for the primary, the rest of the optics is cooled down to 4 K, in order to reduce background emission. Detectors blocks and readout are the spare model of the PACS instruments on board the Herschel satellite. They include 2048 individual bolometers cooled at 300 mK working in two broad photometric bands centered at 240 μm (1.2 THz) and 550 μm (545 GHz). The angular resolution of the system is a few minutes of arc. The Gregorian telescope, composed of the primary and the cooled secondary is connected to a reimager, composed of two lenses and a Lyot stop, through a flat mirror, as shown in Figure 1 (see Engel et al. [1]). A modulated Internal Calibration Source (ICS) is positioned behind the flat mirror and can be used to shine calibration light on all detectors. The reimager also includes a rotating HWP and an metal grid analyzer inclided at 45°. The pointed instrument composed of the primary mirror and the photomer connected through an aluminium exapod is installed in the gondola. The gondola is made of aluminum bars and conecting spheres, as shown in figure 2. The total weight of the experiment is approximately 1 ton and the payload is to reach the altitude of 40 km.

3. PHOTOMETER TESTS

The PILOT photometer tests were carried out at the Institut d'Astrophysique Spatiale (IAS) in Orsay, France, in August and September 2012 and in March and April 2013. In figure 3, the ICS modulation current and the corresponding signal on the PILOT detectors are shown. The stability of the ICS bolometer signal was measured at a 50 min interval over a period of 13 hours. The stability was found to be better than 1 %. There is no clear correlation of the residual between detectors or between bolometer readout units. The remaining fluctuations could be caused by fluctuations of the ICS current or to temperature-induced detector gain variations. We checked the alignment of the cold optics by moving a source outside the photometer. The source image was found at the expected symmetric positions on the transmission and reflexion arrays The measured detector noise power spectrum is shown in figure 4. The noise is dominated by readout noise (1/ f noise) and the white noise level is about 3×10^{-16} W Hz$^{-1/2}$, as expected. During the tests, we observed strong variations of the signal with HWP position. This is interpreted as a partial polarization of the background, introduced by the incomplete optical configuration, due to the absence of the primary mirror during the tests. The maximum of this signal on the reflexion array (and the corresponding minimum signal on the transmission array) is observed at HWP position 5,

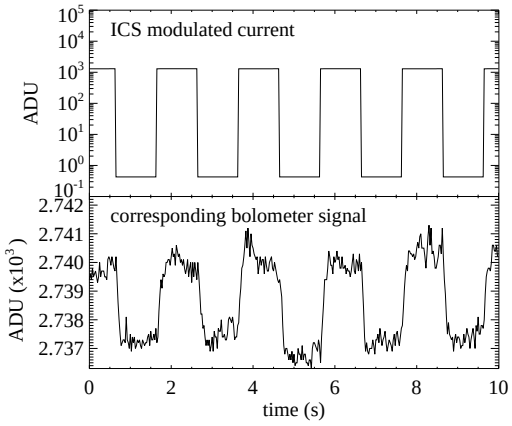

Figure 3. An example of the ICS modulated current (upper) and the corresponding bolometer signal on a single pixel (bottom) .

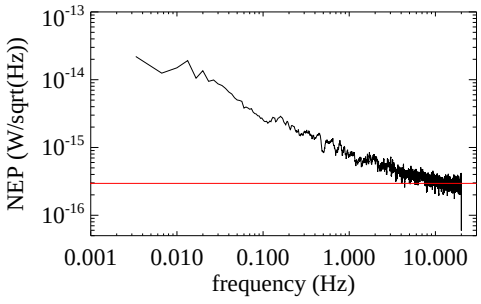

Figure 4. An example of detector noise power spectrum of a single pixel. The red solid line shows the white noise level at $3 \times 10^{-16}\ W\ Hz^{-1/2}$.

corresponding roughly to a vertical direction of fast axis of the HWP. Since the polarizer wires are also oriented

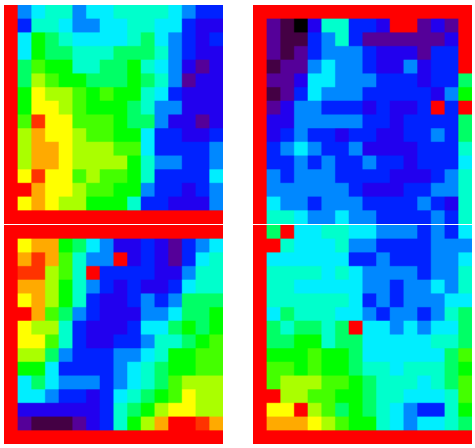

Figure 5. Example map of the background polarisation angle on the transmission arrays. The color scale shows the polarisation angle, as measured from the vertical direction and ranges from -7° to 7°.

in this direction, this indicates that the polarized background is polarized close to parallel to the symmetry axis of the instrument, as expected from the axial symmetry of the optics. The computed polarisation angle map is shown in figure 5 in bolometer coordinates. The maximum observed polarisation fraction is about 16.4 % of the background and angles are in the range from -7° to 7° from vertical. The data Determining to complement the angle of rotation from the HWP positions and response signals, obtained the result of angle between the steps as $\sim 11.3\ ^{\circ}$, we searched the Stokes parameters, I, Q and U for each pixels.

Following the above alignment and measurement tests of the PILOT photometer, we carried on spectral bandpass measurements, using a Fourier Transform Spectrometer (FTS). The scheme used is shown in figure 6. The gap between the FTS and the cryostat entrance window was filled with Helium or Nitrogen in order to avoid atmospheric absorption. In this setting, the FTS is used in the Martin-Puplet configuration so as to produce a polarized signal with polarization either vertical or horizontal. The FTS illuminates a large fraction of the PILOT focal plane, allowing us to measure the transmission of many individual pixels simultaneously. The PILOT detectors are used as the FTS detectors and therefore measure an interferogram, as the FTS mirror is displaced.

An example of the obtained interferogram is shown in figure 7. Figure 8 illustrates the spectral transmission curves

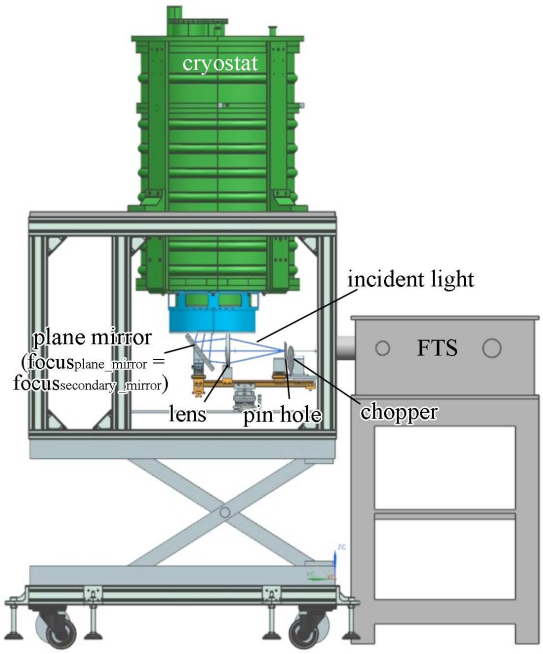

Figure 6. Side view of the instrumental setting used for the FTS PILOT photometer tests. The FTS light is injected into the PILOT cryostat through a reimaging lens, a pinhole and a chopper.

obtained by applying Fourrier transform to the interferogram. The slight differences seen between forward and backward motion of the FTS moving mirror are attributed to temporal variations of the residual atmospheric absorption.

In figure 9 we show the spectral response curves obtained at various HPW positions. While rotating the HWP from position 8 to 5, the transmission is reduced for the transmission array and increased for the reflexion array, due to the polarization of the input FTS signal. Except for time varying absorption in the water absorption lines, the transmission curves obtained during foraward and backward mirror motion are consistant. The above transmission measurements as a function of HWP position have been used to calibrate the HWP step angle at cryogenic temperature through chi-square fitting. We determined that the angular distance between consecutive referenced positions of the HWP is $\sim 10.9°$.

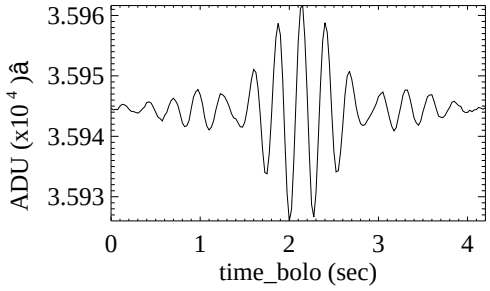

Figure 7. An example of interferogram averaged over (?) an array, obtained using the Martin-Puplet FTS interferometer.

4. CONCLUSION

We have the presented the results of the PILOT photometer calibration. The measured signal on the internal calibration source are very stable, with temporal variations lower than $\pm 1\%$. The alignement of the cold optics was found to be accurate using movable sources outside of the cryostat. The detector noise level is as expected with a white noise level at about 3×10^{-16} W Hz$^{-1/2}$. Due to the incomplete optical configuration used during the tests, the background is polarized parallel to the symmetry axis of the instrument, at a level measured to be 16.4%. We also have performed Fourrier Transform Spectrometer measurements which allowed us to succesfully measure the spectral bandpass of each bolometer and characterize the HWP transmission at cryogenic temperature.
Following these tests, the photometer is considered fully operational and ready for flight. Our next step before flight is to perform end-to-end tests of the instrument including the primary mirror, in order to characterize the focal plane geometry, measure the submm point-spread function, co-align the instrument submm optical axis with thestellar sensors and measure the polarisation of point sources at infinite distance.

REFERENCES

[1] Engel, C., Ristorcelli, I., Bernard, J.-P., et al. 2013, Experimental Astronomy, 13

[2] Matthews, B. C., & Wilson, C. D. 2000, Star Formation from the Small to the Large Scale, 445, 473

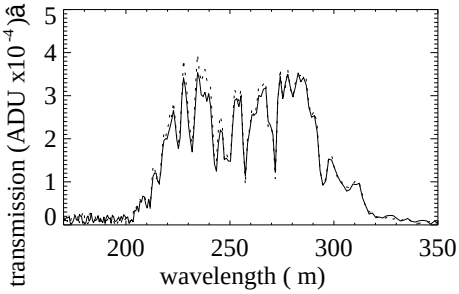

Figure 8. An example of the transmission obtained by Fourier transform of a 1 sec interferogram, centered on the intensity peak at null path difference. The transmission curve is averaged over all pixels of the array. The solid and dashed lines correspond to the two FTS mirror scan directions. The small signal differences are due to the varying atmospheric residual absorption along the path.

[3] Ponthieu, N., Macías-Pérez, J. F., Tristram, M., et al. 2005, A&A, 444, 327

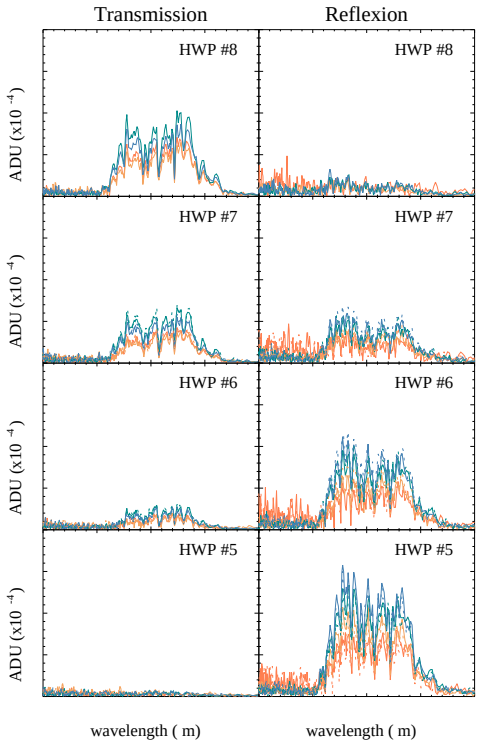

*Figure 9. Examples of transmission curves for the PILOT transmission (left column) and reflexion (right column) array obtained at four HWP positions. The transmission curves are computed for 8*8 pixel regions of the array, as coded by the different curve colors. The solid and dashed lines correspond to the two FTS mirror scan directions. The variations with HWP position are due to the input FTS signal being fully polarized in the Martin-Puplet configuration.*

ADDRESSING THE GOALS IN THE PLANETARY SCIENCE DECADAL SURVEY FROM A BALLOON-BORNE PLATFORM

Eliot F. Young[1], Tibor Kremic[2], Charles A. Hibbitts[3], John Dankanich[4], Robert Woodruff[5], Steven Osterman[6], Michael Davis[7], Kevin Dinkel[8], Zachary Dischner[9], Nicholas Truesdate[10], Jedidiah Diller[11]

[1] Southwest Research Institute, 1050 Walnut St, Boulder, CO 80302 USA, efy@boulder.swri.edu
[2] NASA Glenn Research Center, 21000 Brookpark Rd Cleveland, OH 44135 USA, tibor.kremic@nasa.gov
[3] John Hopkins University-Applied Physics Laboratory, 11100 Johns Hopkins Rd Laurel, MD 20723 USA, karl.hibbitts@jhuapl.edu
[4] NASA Marshall Space Flight Center, Alabama 35812 USA, john.dankanich@nasa.gov
[5] Lockheed Martin Corporation (retired), rawoodruff@live.com
[6] University of Colorado, Center for Astrophysics and Space Astronomy, Boulder, CO USA, Steven.N.Osterman@colorado.edu
[7] Southwest Research Institute, 6220 Culebra Rd, San Antonio, TX USA, mdavis@swri.org
[8] Southwest Research Institute, 1050 Walnut St, Boulder, CO USA, dinkelk@boulder.swri.edu
[9] Southwest Research Institute, 1050 Walnut St, Boulder, CO USA, zach.dischner@gmail.com
[10] Southwest Research Institute, 1050 Walnut St, Boulder, CO USA, truesdalen@boulder.swri.edu
[11] Southwest Research Institute, 1050 Walnut St, Boulder, CO USA, dillerj@boulder.swri.edu

ABSTRACT

Balloon-borne telescopes have several advantages over ground-based, airborne and space-based telescopes, including inexpensive access to a near-space environments, negligible image degradation, low telluric opacity longward of 300 nm and photometric stability with almost no scintillation. Two recent NASA innovations support balloon platforms for planetary science missions: 18.75 MCF super-pressure balloons that will potentially stay aloft for 100-day missions and *WASP* (the *Wallops Arc-Second Pointing System*). A community-wide workshop was held in January 2012 to identify key questions in planetary science for balloon-borne platforms. Of roughly 200 questions recommended for study in *Visions and Voyages*, the Planetary Science Decadal Survey, approximately 45 were identified as well suited to balloon-borne telescopes.

1. THE OBSERVING ENVIRONMENT IN THE STRATOSPHERE

Typical float altitudes for NASA balloons are around 35 km (around 110,000 ft for super-pressure balloons, 125,000 ft for zero-pressure balloons). The ambient pressure at 35 km is around 4 torr, a little less than 0.5% of sea-level pressure. The column of atmosphere overhead is the ratio of the local pressure over the gravitational acceleration:

$$C = \frac{P(r)}{g} \qquad (1)$$

where C is the column abundance above radius r, $P(r)$ is the pressure at r and g is the gravitational acceleration. Since P is around 4 torr at float altitudes, a balloon at 35 km floats above 99.5% of the Earth's atmosphere.

The near-space conditions at 35 km altitude enable three key observational advantages:

- Turbulence-free imaging. The thin atmosphere at 35 km does not cause measurable wavefront errors.
- Very low telluric opacity from 0.3 through 30 µm, including some bands where even airborne observatories have significant absorptions.
- Very stable photometry due to low scintillation.

1.1 Image Quality at 35 km

The 2009 Sunrise balloon mission measured the magnitude of wavefront errors due to atmospheric turbulence at an altitude of 35 km. Their 1-m telescope fed light to several instruments, including one called the CWS *(Correlating Wavefront Sensor)*, a six-element Shack-Hartmann array [1]. The main purpose of the CWS was to provide a pointing error signal to a tip-tilt mirror, but it also quantified low-order wavefront errors across the aperture (Fig 1).

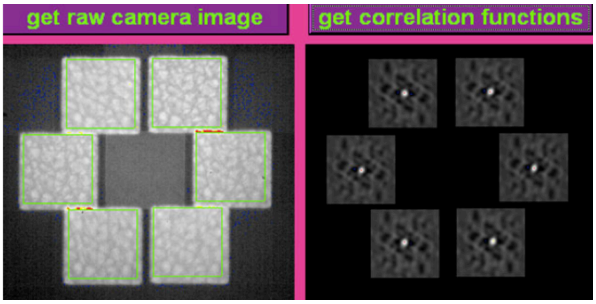

Figure 1. Shown here is Figure 15 from [1]. The original caption reads "Sub-images and correlation functions of the wave-front sensor during closed-loop

Proc. '21st ESA Symposium European Rocket & Balloon Programmes and Related Research', 9–13 June 2013, Thun, Switzerland (ESA SP-721, October 2013)

tracking." The correlation functions between every sub-aperture and the reference image are identical, as they would be in vacuum.

The CWS showed no detectable wavefront errors across the Sunrise aperture. According to the CWS results, the Sunrise telescope might as well have been in space.

1.2 Telluric Opacity & Downwelling Radiation

The infrared transmission of the Earth's atmosphere suffers from several broad opaque regions in the 2–30 µm range, including absorptions at 2.7 µm (due to H_2O), 3.3 µm (CH_4), 4.3 µm (CO_2), 5.5–7 µm (H_2O), 9.5 µm (O_3), 15 µm (CO_2), and generally poor transmission from 15–30 µm (Fig. 2). Some of these absorptions (especially CO_2 bands at 4.3 and 15 µm) are so strong that even an airborne platform like SOFIA (at 12 km) has little visibility at these wavelengths.

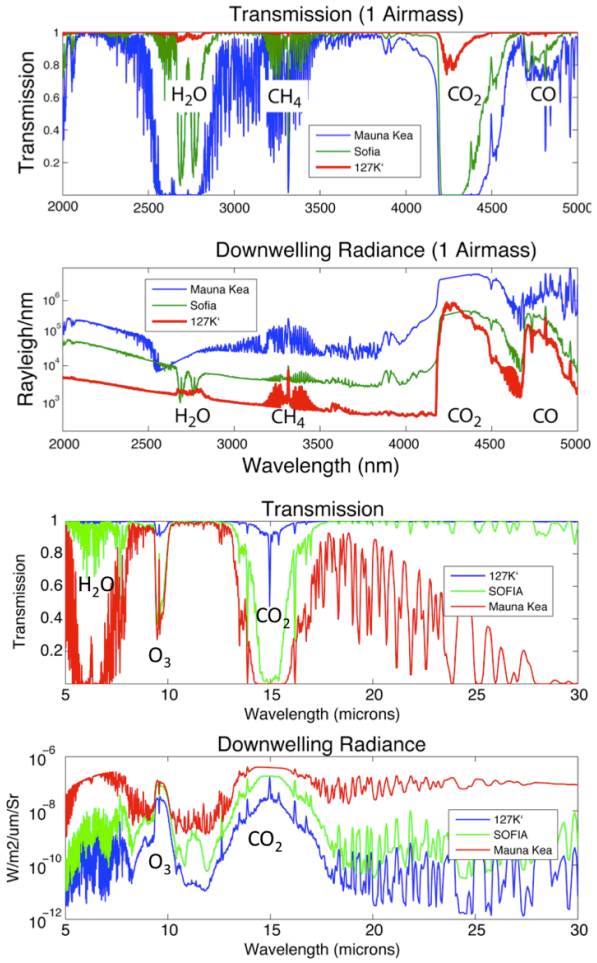

Figure 2. IR (2 - 30 µm) atmospheric transmissions and downwelling radiances for three altitudes.

A balloon platform at 35 km has excellent visibility across the 0.3- 30 µm range. Downwelling radiation is much less from 35 km than from an aircraft (12 km) or a mountaintop (4.2 km); in the 0.3–5 µm region, the downwelling radiation seen from a balloon is about ten times less than from SOFIA, which in turn is about ten times less than from Mauna Kea. The background spikes at 4.3 µm because of CO_2 emission from the Earth's thermosphere.

1.3 Photometric Stability

The lack of wavefront errors leads to very stable photometry in the stratosphere. Reference [2] developed a model of scintillation as a function of altitude and the elevation angle of the target. Figure 3 shows their model in comparison to measured intensity variations from a balloon platform at 29.2 km altitude.

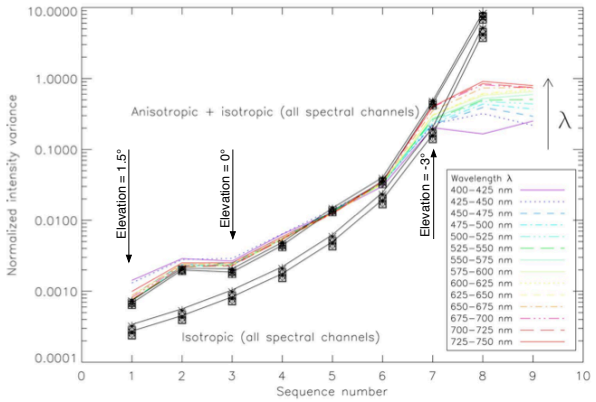

Figure 3. Shown here is an annotated figure from [2]. The top group of lines represents scintillation estimates based on anisotropic and isotropic turbulence models from an altitude of 29.2 km. A dramatic drop in scintillation is predicted as elevation angles increase to a few degrees above the horizon.

At elevations from 1.5° and greater (above the horizon), the variance in intensity is less than a thousandth of a target's normalized intensity level. For observations at these elevation angles, the intensity variations due to scintillation will be much smaller than the photon shot noise due to the background or source counts.

2. ZERO- AND SUPER-PRESSURE BALLOONS

Zero-pressure balloons have been the traditional vehicles to the stratosphere for the past six decades. They are constructed of very thin, very lightweight material. Zero-pressure balloons have open vents at the bottom of the balloon, which means that they can vent helium rather than sustain a pressure gradient with respect to the local environment. Zero-pressure balloons can lift several tons to altitudes of 35 km, but they will descend at night as their helium cools unless about 8% of their payload is jettisoned. Conversely, they will vent about 8% of their helium during the following day as their helium warms up. For this reason, zero-pressure balloons are not normally used for long-duration mis-

sions at mid-latitudes. Until recently, in fact, NASA's Balloon Program Office (BPO) did not support flights over several day-night cycles.

Super-pressure balloons are sealed and reinforced to withstand a pressure gradient. They can survive diurnal cycles with only small changes in altitude, without dropping ballast or venting helium. NASA is encouraging investigators to propose 100-day flights from mid-latitude launch sites (e.g., New Zealand).

Mid-latitude long-duration flights are enormously important for planetary science studies. Unlike Antarctic flights, super-pressure flights enable many hours of dark-sky observations under near-space conditions. To understand the significance of 100-day flights, consider that 2800 orbits are allocated in each cycle (each year) on HST (Hubble Space Telescope). While each orbit is nearly 90 minutes, acquisitions, calibrations and exclusion zones reduce the time on target to approximately 60 minutes. A single 100-day balloon flight should yield about 1000 hours of diffraction-limited dark time, equivalent to a third of the entire HST allocation across all science disciplines.

3. BALLOON-BASED PLANETARY SCIENCE

Although NASA's BPO regularly flies payloads for three of the four divisions of NASA's Science Mission Directorate (Astrophysics, Heliophysics and Earth Science), they have flown no *Planetary Science* mission in decades. Given this hiatus in planetary missions, a key activity is to assess the need and/or potential benefit of balloon-borne planetary science missions. Two specific activities were recently undertaken: a community-wide discussion to propose and discuss possible planetary balloon missions (structured around a workshop hosted at the Ohio Aerospace Institute, near NASA Glenn Research Center, on January 25-26, 2012) and a NASA-sponsored committee review of *Visions and Voyages*, the Planetary Science Decadal Survey released in 2012.

3.1 Mission Concepts from the January 2012 Community Workshop

Over 100 people participated in the 2012 NASA/Glenn workshop. At the end of the workshop, about 40–50 potential balloon mission concepts were identified, put online (http://www.lpi.usra.edu/balloon_science/) and reviewed during an online assessment period of several months. Here are some examples of mission concepts that exploit a balloon's near-space environment (good seeing, high IR transmission, photometric stability):

- *Identification of Surface Ices on Pluto, Triton and Trans-Neptunian Objects*. The 2.5–5 μm range is well-suited to balloons (where backgrounds are expected to be 100 times lower than from ground-based sites) and includes many fundamental absorptions of interesting organic molecules like CH_4, NH_3, HCN, methanol, formaldehyde, ethane, etc.
- *Synoptic Cloud-Tracking Observations on the Gas Giant Planets and Venus*. These missions combine several of the strengths of a balloon-borne platform: high spatial resolution, clear transmission around H_2O, CO, NH_3, CH_4 and CO_2 bands and continuous observations over long (100-day) baselines. The resulting data sets would allow an unprecedented mapping of waves and dynamics on Venus and the giant planets.
- *Detection of Faint Moving Objects*. A side-effect of good seeing in the stratosphere is the ability to detect faint point sources with good SNR (signal-to-noise ratios), simply because targets cover smaller areas on the sky, so less background is included in the photometry of a source.
- *Accurate Photometry of Transient Events*. In the virtual absence of scintillation, photometric noise is limited instead by the instrument read noise and the photon shot noise of the source and background counts. Transient events observations, like exoplanet transit lightcurves, will benefit from the lack of scintillation noise.

In addition to discussing potential planetary balloon missions, the workshop also came up with six mission architectures of various capabilities in which the telescope apertures varied from 50 cm to 2 m and pointing requirements varied from 0.05" to 1".

3.2 Balloons-Borne Planetary Science: Relevance to the Decadal Survey

The Planetary Science Decadal Survey, *Visions and Voyages for Planetary Science for the Decade 2013-2022*, is a roadmap for NASA's Planetary Science Division, identifying "key questions facing planetary science and outlines plans for space and ground based exploration..." The Decadal Survey combines the efforts of five subpanels, organized by topic (inner planets, giant planets, satellites, Mars, and primitive bodies) to identify about 200 "Important Questions."

Although the Decadal Survey was written to recommend specific ground-based and space-based explorations, a significant fraction of the Decadal questions could be addressed from stratospheric balloon-borne platforms. Some examples:

- *Small Bodies:* 2.5 – 5-μm spectroscopy, 10 nm resolution, 1-m aperture, responds to five "Priority Questions" under the the Objective "Determine the composition, origin, and primordial distribution of volatiles and organic materials in the Solar System".
- *Icy Satellites:* 1 – 5-μm spectroscopy, 10 nm resolution, 1-m aperture, responds to one "Priority Question" under the the Objective "Composition and distribution of volatiles " for the satellites of Uranus and Neptune.

- *Inner Planets:* high spatial resolution NUV – NIR imaging, 1-m aperture, responds to two "Priority Questions" for the goal "Determine how solar energy drives atmospheric circulation, cloud formation, chemical cycles on Venus".
- *Giant Planets:* high spatial resolution visible imaging, 2-m aperture responds to one "Priority Question," namely, "Why and how does the atmospheric temperature and cloud composition vary with depth and location on the planet?"

Table 1. Decadal Survey questions that can be addressed from a balloon-borne platform.

Category	Total # of Decadal "Important Questions"	# Answered or Significantly Addressed from a Balloon Payload
Small Bodies	23	10
Inner Planets	39	11
Major Planets	39	6
Icy Satellites	75	12
Mars	48	3
Total	**194**	**42**

4. OBSERVING COMET ISON

Comet C/2012 S1 (ISON) was discovered on September 21, 2012. Its orbit is nearly parabolic, consistent with it being an Oort cloud comet. Comet ISON is a sungrazing comet, with a perihelion distance that is expected to be only 1.1 million km above the Sun's surface. Perihelion takes place on November 28, 2013. The comet's angular separation from the Sun is greater than 40° from September 17, 2013 through November 13, 2013.

Initial observations Comet ISON led to optimistic predictions of its brightness (e.g., the "comet of the century" in the popular literature, with predictions made in October 2012 that ISON would reach magnitudes of -11.6). The brightnesses of Oort cloud comets are notoriously difficult to predict, however, and it now appears that ISON had early outbursts that led to an overestimate of its size and/or activity. HST images of ISON taken on April 10, 2013 suggest that its nucleus is smaller than 2 km in diameter (Fig. 4).

If Comet ISON survives its perihelion passage behind the Sun, it will pass over the Earth's North Pole, with its closest approach taking place on December 26, 2013, at a distance of 0.43 AU. Comet Lovejoy was a recent sungrazer that survived its perihelion passage – in a fashion. Although Comet Lovejoy's tail was seen by several spacecraft after perihelion, its nucleus "disappeared," apparently disrupted into small pieces. Comet ISON may sublimate 200 – 400 m of radius on its approach to perihelion, which may be enough to disintegrate the object. If not, Comet ISON would also have to survive tidal disruption.

Figure 4. An enhanced HST image of Comet ISON from April 10, 2013.

The initial observations of ISON led NASA to commission a study in December 2012 on the possibility of building and launching a ballon-borne telescope to look at ISON before its perihelion passage, in the September–November 2013 timeframe. It was decided that a refurbished telescope could be made ready in time, with two optical benches, one optical, one infrared. Although ISON's viewing circumstances are nominally better in December 2013, the uncertainty that ISON would survive perihelion led to the decision to launch and observe ISON during NASA's normal September-October fall campaign from Ft. Sumner, NM.

4.1 Mission Overview

The primary goals of the *BRRISON* mission (Balloon Rapid Response for ISON) are to

- *Observe ISON's CO_2 and H_2O emission in IR wavelengths.* The CO_2 emission at 4.3 μm is impossible to observe from ground-based sites or SOFIA. It is a difficult (but feasible) observation from a balloon because of the background emission from telluric CO_2. The ratio of CO_2 to H_2O emission will help constrain the ratios of those two ices, which in turn constrains the region in the early solar nebula in which ISON's constituents condensed.
- *Characterize the performance of a fine steering system.* The immediate goals of the *BRRISON* mission

are to (a) quantify the error signal (how well and how quickly can pointing errors be measured) and (b) quantify the ability to correct pointing errors (i.e., how accurately the FSM can be commanded to certain positions and at what rates). The purpose of the fine steering system is to stabilize the target on the focal plane such that disturbances are smaller than the angular resolution of the optical system. The eventual goal will be to provide diffraction-limited resolution from a balloon-borne telescope (i.e., provide stabilization at the 0.05" level to enable a 0.1" diffraction limit from a 1-m aperture at visible wavelengths).

BRRISON uses an 80-cm f/17 telescope (Fig. 5). The primary and secondary mirrors have been recoated in gold to lower emissivity in the 2.4 – 4.3 µm range. The *BRRISON* gondola uses an azimuthal flywheel to point the entire gondola and an elevation motor to point the telescope. These coarse pointing stages are expected to stabilize the image such that the rms (root mean square) pointing error is in the neighborhood of 10 arcseconds.

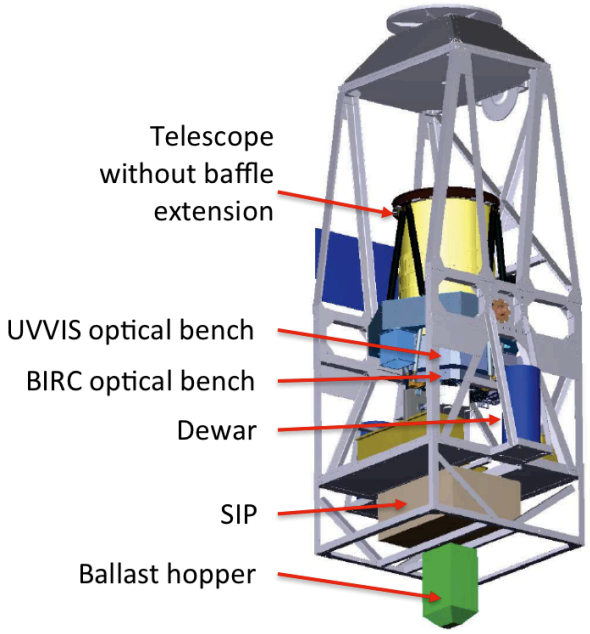

Figure 5. The BRRISON Gondola, telescope, UVVIS and BIRC optical benches, dewar, SIP (Support Instrument Package) and Ballast hopper.

BRRISON has two instrument benches, one for UV and visible observations (the UVVIS bench), the other for IR observations (the *BIRC* bench). The two instrument benches are laid out on 1-m optical breadboards, each consisting of two carbon fiber face sheets separated by 4 inches of aluminum honeycomb. This breadboard design was chosen for low CTE (coefficient of thermal expansion) and high stiffness. The two optical benches are stacked on top of each other like a layer cake with about 25 cm of separation. The UVVIS bench is closer to telescope and either passes light to the IR bench without interference or inserts a fold mirror to use the light on the UVVIS bench itself.

4.2 The Baseline Flight Plan

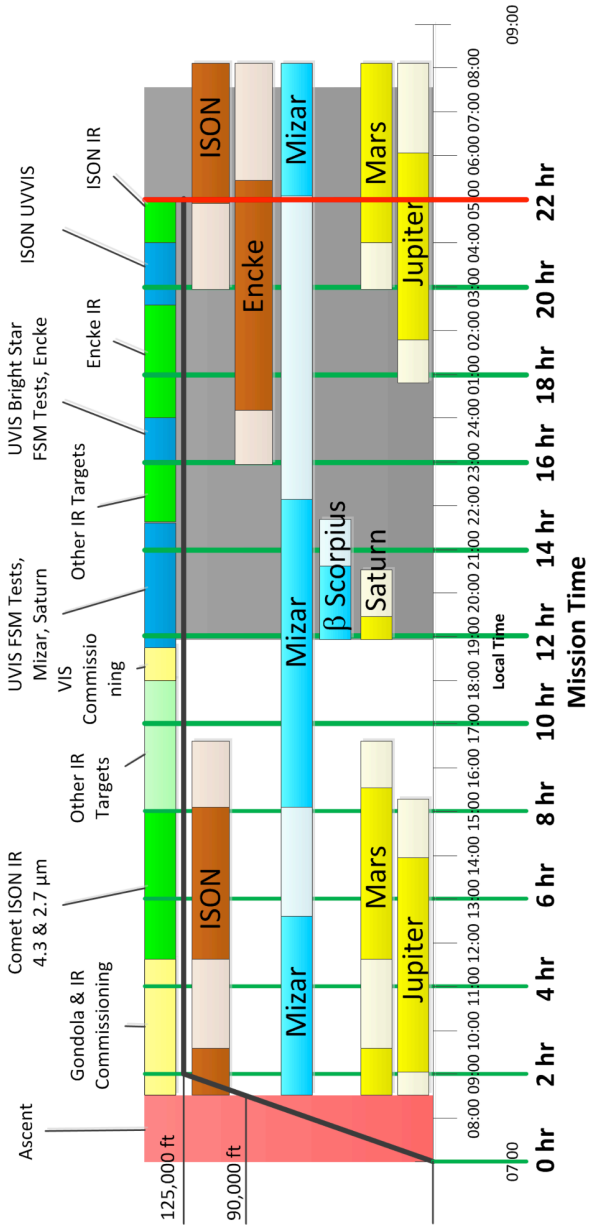

Figure 6. The baseline flight plan for the BRRISON mission. The balloon launch is expected to take place around 7:00 AM (MDT). At altitude, the first target will be a bright double star (e.g., Mizar, β-Sco or Castor) for two hours of instrument check-out, calibration and focusing with the IR bench. ISON will be observed with BIRC as a daytime target while it is at high airmass, from about 11:30 to 15:00 (MDT). Other IR tar-

gets will be observed with BIRC until about an hour before sunset. The mission then changes over to the UVVIS bench for tests of the fine steering system through evening twilight and an into night. If the mission is longer than 14 hr duration, then the UVVIS and BIRC benches will observe Comet Encke at night.

The nominal flight profile is partly constrained by safe practices, partly by ISON's visibility as a function of time of day. Because ground winds are lightest in the morning, NASA will launch *BRRISON* between 7:00 – 10:00 AM. Ascent rates are typically around 1000 ft/min, so the ascent to 125,000 ft is expected to take around 2 hours. On September 25, ISON rises at 9:15 UT (3:15 MDT), transits at 16:00 UT (10:00 MDT) and sets around 22:45 UT (16:45 MDT). Given the those times of visibility (and the desire to observe ISON above airmasses of 1.5 to reduce the telluric background at 4.3 μm), the nominal flight plan (Fig. 6) will be as follows (all times are local New Mexico (MDT) times):

- *Ascent (7:00 - 9:00)*. Assume launch at 7 AM, followed by two hours of ascent.
- *BIRC Instrument Check-out, Calibration and Focus (9:00 - 11:00)*. The instrument will be turned on and allowed to reach an equilibrium operating temperature. *BIRC* will focus on a bright standard and image standard stars to calibrate throughput in all filters.
- *IR Photometry of Comet ISON (11:30 - 15:00)*. Slew to ISON and obtain images in all IR filters. A small fraction of images will be downloaded in near-real time.
- *IR Observations of other Targets (15:00 - 17:00).*
- *Switch to UVVIS Instrument: UVVIS Check-out, Calibration and Focus (17:00 - 18:00).*
- *UVVIS Fine Steering Experiment (18:00 - 21:00).* Imaging of a bright double star (e.g., Mizar, β-Sco) to assess *BRRISON's* ability to (a) determine pointing errors and (b) control a fine steering mirror to correct pointing errors.
- *Nighttime IR Observations of other Targets (21:30 - 23:00).*
- *UVVIS Observations of Comet Encke (23:00 - 24:00).* Images of Comet Encke in five UV-Visible filters.
- *IR Observations of Comet Encke (24:00 - 3:00)*. Obtain images of Encke in all IR filters.
- *UVVIS Observations of Comet ISON (3:00 - 5:00).* Images of Comet ISON in five UV-Visible filters.

At present, the longest flight plan is 22 hr. The flight may not stay aloft for that duration, and *BRRISON* is carrying enough battery power for a 22-hr flight. If the flight is shortened to 8 or 14 hours (for example), then daytime IR observations of Comet ISON the UVVIS fine pointing experiment are the highest priorities.

4.3 The IR Bench

The *BIRC* optical design (Fig. 7) collimates the incoming f/17 beam, passes that beam through the filter wheel and refocuses the beam with a mini-Ritchey-Chretien telescope onto the IR detector. The FOV (field of view) is 3 arcminutes; the plate scale is 1.16"/pixel (with 18 μm pixels).

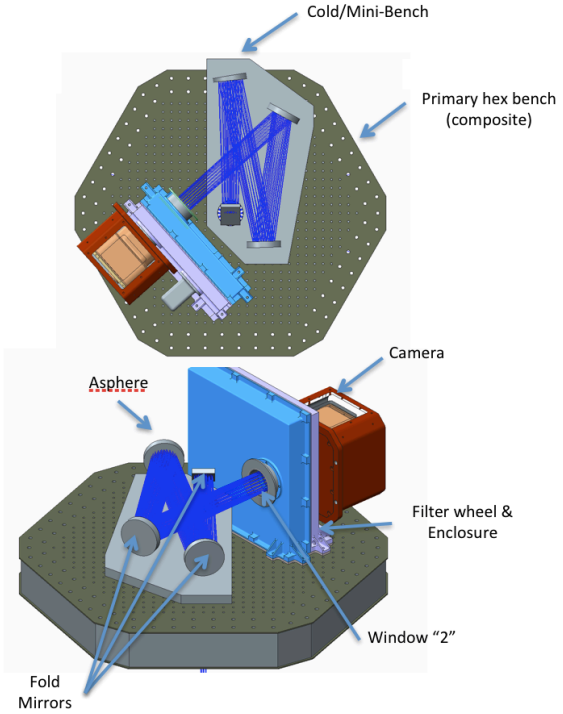

Figure 7. A schematic representation of the BIRC layout. The "cold mini-bench" is enclosed (not shown) and cooled. The only uncooled optics in teh IR path are the primary and secondary mirrors.

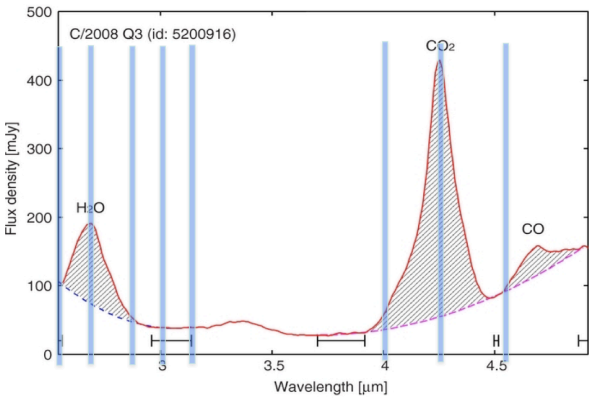

Figure 8. Location of filters in the BIRC camera. Spectrum is of C/2008Q3, Comet Garradd.

The *BIRC* instrument (*BRRISON* IR Camera) is based on a HgCdTe detector. BIRC contains 9 filters (Fig. 7):

four dedicated to H_2O bands and adjacent continua (at 2.47, 2.70, 2.85 and 3.05 µm), three dedicated to CO_2 bands and continua (3.20, 4.00 and 4.27 µm) and a long filter for CO emission at 4.60 µm. There is also an R-band filter (0.6 – 0.8 µm) to provide some redundancy over visible wavelengths.

4.4 The UVVIS Bench

The UVVIS bench contains two cameras: a fast guide camera and a UV science camera. The science camera has five filters for nighttime observations of comets: an OH filter (3.10 µm), a CN filter (3.85 µm) and continuum filters at 3.45, 4.45 and 5.26 µm. During daytime, the sky background is too bright for UV observations, but since the Rayleigh-scattered background decreases approximately as λ^{-4}, the daytime infrared background is much lower.

Both the science camera and the guide camera receive a beam from a fine steering mirror. The f/17 beam from the telescope is collimated by an off-axis parabola (OAP) and reflected off the fine steering mirror. The science and guide beams are then separated by a dichroic at 0.6 µm. Both beams are refocused by identical OAPs to an f/17 beam. The science beam passes through a filter wheel before encountering the science detector, a back-illuminated CCD. Figure 9 is a diagram of the UVVIS optical bench; Fig. 10 shows the partially populated UVVIS bench during alignment.

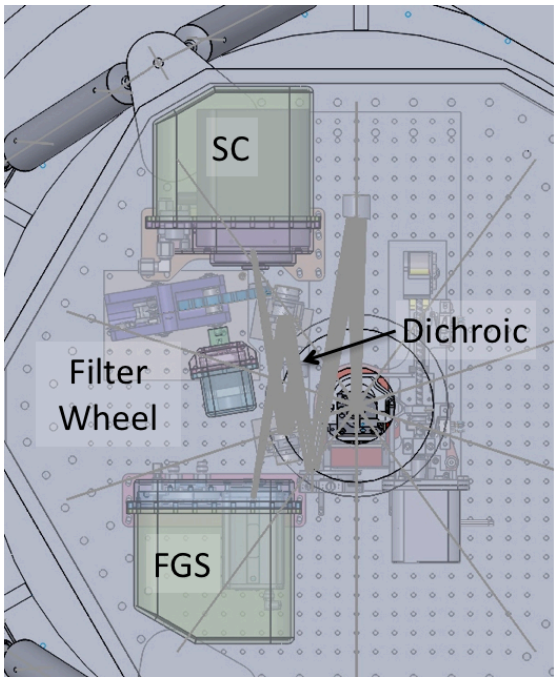

Figure 9. A diagram of the UVVIS optical bench, showing the guide camera (FGS) and the Science Camera (SC). Both cameras are housed in identical pressure vessels and cooled by circulating fluid.

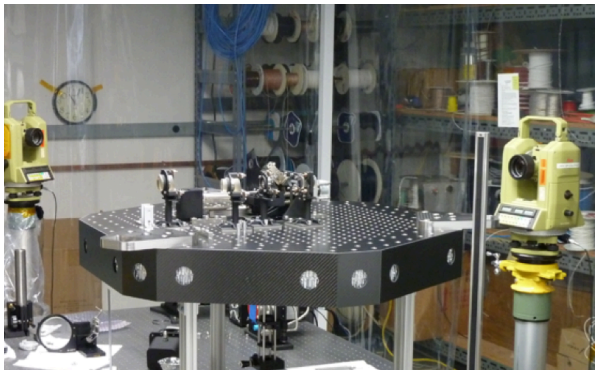

Figure 10. The partially populated UVVIS bench during alignment at the University of Colorado's Center for Astrophysics and Space Astronomy.

The guide camera is based on an sCMOS device. It combines several factors that are desirable in a guide camera: low read noise (1.3 e- per read), large format (2160 x 2560 pixels) and fast readout rates (up to 100 fps full-frame sustained rates). To take advantage of the fast frame rates, we have written software to identify guide stars and determine their sub-pixel centroids in a 9 ms period for a full frame. To determine to accuracy of the centroiding algorithm, we will image a bright double star (e.g., Mizar) where the star separations are in the 10" - 20" range. The measured time-evolution of the double stars' separation will give us an assessment of the centroiding accuracy that is independent of any incidental motion by the gondola.

The Fine Steering Mirror (FSM) is a 50-mm unit manufactured by Left Hand Design (Longmont, CO, USA). Its nominal range of motion is 5 mRad and its absolute angular positioning precision is 50 nRad. For an f/17 telescope, this precision translates to an angle on the sky of 0.0012". In the absence of other systematic errors (such as flexure between the guide camera and the science camera on the optical bench), the absolute positioning capabilities of the FSM are orders of magnitude more accurate than necessary for open-loop pointing corrections.

5. CONCLUSIONS

There have been several recent technical and programmatic advances in the arena of balloon-borne missions for planetary science. Technical advances include quantitative measurements of wavefront errors from 35 km (very low), several versions of coarse pointing systems that can stabilize a scene at the ±10" level or better, and most significantly, super-pressure balloons that will enable 100-day flights at mid-latitudes.

Programmatically, NASA studies have shown that there are significant planetary questions that are well-suited to balloon missions. The first planetary balloon project in over 40 years is expected to launch in the fall of 2013 to study Comet ISON.

1. Berkefeld, Th. *et al.* (2011), The Wave-Front Correction System for the Sunrise Balloon-Borne Solar Observatory. *Solar Physics* **268**(1), 103-123.

2. Robert, C., Conan, J.-M., Michau, V., Renard, J.-B., Robert, C. & Dalaudier, F. (2007), Retrieving parameters of the anisotropic refractive index fluctuations spectrum in the stratosphere from balloon-borne observations of stellar scintillation. *JOSA-A*, **25**(2), 379-393.

BALLOON MAGNETOMETRIC COMPLEX

Oleg M. BREKHOV [1],Yuri TSVETKOV [2]

[1] Moscow Aviation Institute (National Research University) - MAI, sh. Volokolamskoye, nr.4, 125871 Moscow, Russia, obrekhov@ mail.ru

[2]Pushkov Institute of Terrestrial Magnetism, Ionosphere and Radio Wave Propagation of Russian Academy of Sciences -IZMIRAN, 142190, Troitsk, Moscow Region, Russia
tsvetkov@ izmiran.ru

ABSTRACT

In the IZMIRAN and the MAI it is created the balloon magnetic gradiometer (BMC), the design of which and how to use the patent of the Russian Federation [1] is taken out. The BMC consists of three instrument containers, in each of which there is scalar nuclear magnetometer, GPS-global positioning system receiver, on-board computers for the collection and packaging of scientific information, satellite data modem "Globalstar" and system of automatic expansion gradiometer at the set height after balloon launch. Structure of the BMc includes also rope-magazines containing bearing cable in length of 6 km, brake parachutes, baroreles, pyrolocks and etc.

One of the containers located on the main suspension balloon, the second and third are located at the bottom at a distance from the first 3 km and 6 km, respectively.
In implementing the gradiometer solved the problem of stability.

1. INTRODUCTION

For studying of a phenomenon of magnetic anomalies and their sources maps of an abnormal magnetic field (AMF) of the Earth [1] and the data of special magnetic shootings are used usually. Maps of magnetic anomalies are adhered to level of a surface of the Earth and received mainly by aeromagnetic, hydromagnetic, foot and other kinds of magnetic shootings. Last year's maps of magnetic anomalies at heights of flights of satellites which are presented in the form of models are developed. Maps of the AMF and models of satellite magnetic anomalies, in fact, pass structure corresponding to two levels of high-rise - the earth's surface and altitude of 500 km above it. This does not allow to simulate altitude changes the AMF between these levels. Many researchers demonstrated that recreate the spatial structure of the AMF on available ground data virtually impossible. Recalculation of the upper half-space is performed using the Poisson integral, but in [2] shows that the kernel of the integral decreases very slowly. So, for sure you want to have a conversion value of the field for very large areas that practically impossible. In addition, the use of maps AMF large areas, formed from the individual maps obtained at different times and at different altitudes, leading to considerable errors converting field.
Due to the limited (up to 30-40 km) the vertical extent of the lithosphere, the manifestation of the sources of magnetic anomalies at altitudes of 30 km corresponds to the 3D-sources, and above-2D-sources. Hence the importance of magnetic survey at altitudes of 30-40 km. In this case the characteristics of magnetic anomalies for the altitude range 30-1000 km subject to a uniform pattern of variability that allows you to build a representative model of anomalies in this altitude range, with data on high levels of 30 km and 450 km.

In the atmosphere at altitudes of 20-40 km there are regular zonal air flows, which are used to fly balloons. In these air currents can circumnavigate the balloon flights along geographic parallels. The use of balloons with the appropriate size and weight characteristics (hundreds of kilograms of payload) can carry out gradient magnetic survey, with a long measuring base gradiometer.

The development of a balloon gradiometer with a base measuring several kilometers in length, oriented along a vertical line across the field of gravity, and informational support for the gradient magnetic surveys in real time, the subject of this article.

2. STRUCTURE AND DESIGN OF THE GRADIOMETER

In the IZMIRAN and the MAI it is created the balloon magnetic gradiometer (BMC), the design of which and how to use the patent of the Russian Federation [1] is taken out. The scheme of the BMG is resulted on fig. 1. The BMG consists of three instrument containers, in each of which there is scalar nuclear magnetometer, GPS-global positioning system receiver, on-board computers for the collection and packaging of scientific information, satellite data modem "Globalstar" and system of automatic expansion gradiometer at the set height after balloon launch. Structure of the BMG includes also rope-magazines containing bearing cable in length of 6 km, brake parachutes, baroreles, pyrolocks and etc.

The instrument containers, each weighing 20-30 kg, suspended in the air to the basket balloon, A balloon as at expansion they have separated from each other on distance in 3 km. Adjusting the speed of deployment is carried out using the force of aerodynamic deceleration [3].

The course of the deployment process gradiometer is shown in Fig. 1. The beginning of the first cable deployment occurs during takeoff balloon for 3 km, and the beginning of the deployment of the second rope takeoff balloon to a height of 6 km, through the contact closure barorele.

Implementing gradiometer requires solving several problems, including: ensuring the strength of suspension cable under dynamic loads associated with its deployment, provision of gradiometer in predetermined limits of deviations, information of the gradient magnetic surveys in

Proc. '21st ESA Symposium European Rocket & Balloon Programmes and Related Research',
9–13 June 2013, Thun, Switzerland (ESA SP-721, October 2013)

real time. It is also necessary to develop a methodology for implementation of high-gradient magnetic surveys at stratospheric altitudes, taking into account the instrumental and methodological errors, a method of interpretation of magnetic anomalies and their vertical gradients.

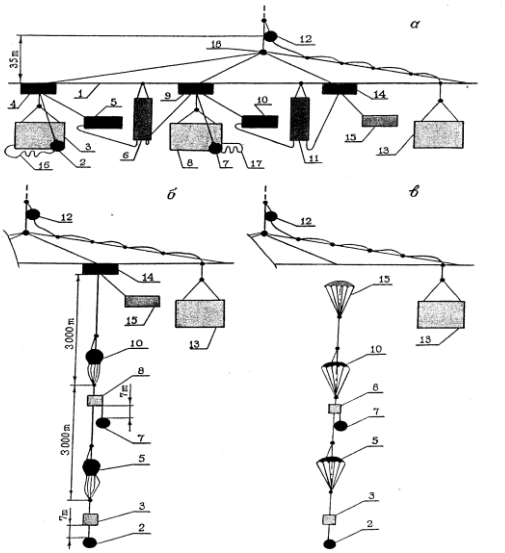

Figure1. Scheme of balloon magnetic gradiometer in stages of flight: starting (a), working (b), the finish (c)

Equipment: 1 - balloon suspension girder; 2, 7, 12 - magnetic field sensors; 3, 8, 13 – containers with magnetometers, GSP-receiver, modem and antenna "GlobalStar"; 4 – pyrolock, ensuring beginning of process of descent of container 3 and a magnetic field sensor 2; 5, 10 - parachutes; 6, 11 – rope-magazines; 9 – pyrolock, ensuring beginning of process of descent of container 8 and magnetic field sensor 7; 14 – pyrolock, ensuring division of system at landing; 15 – saving parachute; 16, 17 – convolution with cable-rope to magnetic field sensors 2 and 7; 18 – starting lock.

3. MODEL OF PROCESS DEPLOYMENT OF THE GRADIOMETER

The problem is solved in the plane formulation. Tension carrier cables determined by a system of discrete masses connected by weightless elastic elements. Initial time of deployment is shown in Fig. 2.

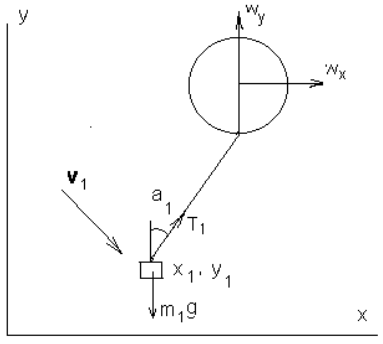

Figure2.

Here, m_1 - mass of the lower container; w_x, w_y - horizontal and vertical velocity of the balloon; T_1- the tension of the cable; α_1 - the angle of the cable with the vertical; $\mathbf{v}_1$- a vector of relative wind velocity, equal to:

$$\mathbf{v}_1 = (w_{1x} - dx_1/dt)\,\mathbf{i} - dy_1/dt\,\mathbf{j}, \quad (1)$$

where **i**, **j** - unit vectors of coordinate axes; x_1, y_1 - coordinates of the lower container; w_{1x} - wind speed at the height of the container. The origin of coordinates corresponds to the ground.

Cable tension $T_1$is equal to:

$$T_1 = C_{TP}\,(L_1 - L_0), \quad (2)$$

where L_1- the length of the deformed first element; L_0 - length of the undeformed element of the cable, which is equal to $L_0 = L_{TP}/N$; N - number of discrete masses approximating cable; C_{TP} - stiffness of the cable tension.

The system of equations of motion of the first (lower) container has the form:

$$m_1\,d^2x/dt^2 = C_{XP}\,q_X\,S_P + T_1 \sin\alpha_1$$
$$m_1\,d^2y/dt^2 = C_{YP}\,q_Y\,S_P + T_1\cos\alpha_1 - m_1 g \quad (2)$$

Here, C_{XP}, C_{YP} - coefficients of drag chute; S_P - square parachute; q_X, q_Y projection of the wind velocity pressure q, acting on a container with a parachute, with

$$q = \rho\,v_1^2/2,$$
$$q_X = 0.5\,\rho\,(w_{1X} - dx_1/dt)\,[(w_{1X} - dx_1/dt)^2 + (dy_1/dt)^2]^{0.5}$$
$$q_Y = -0.5\,\rho\,(dy_1/dt)\,[(w_{1X} - dx_1/dt)^2 + (dy_1/dt)^2]^{0.5}$$

where ρ - density of the environment at a height y_1.

To determine the equations of motion of the intermediate j-th point of the cable look at Figure 3.

The system of equations of motion for interim j-th point has the form:

$$m_j\,d^2x/dt^2 = c_N\,q_x\,d_{TR}\,L_{j-1} - T_{j-1}\sin\alpha_{j-1} + T_j\sin\alpha_j -$$
$$-c_X\,(dx_j/dt - w_j)\times abs(dx_j/dt - w_j);$$
$$m_j\,d^2y/dt^2 = c_N\,q_y\,d_{TR}\,L_{j-1} - m_j\,g - T_{j-1}\cos\alpha_{j-1} + T_j\cos\alpha_j -$$
$$-c_y\,(dy_j/dt)\times abs(dy_j/dt), \quad (3)$$

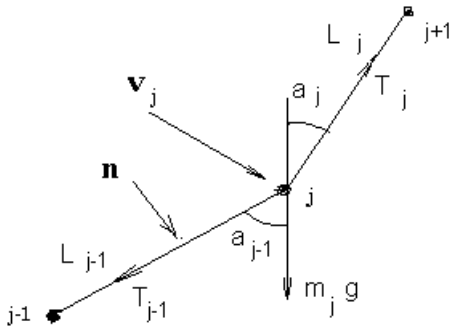

Figure3

.

where q_x and q_y projection ram q_n on the coordinate axis x and y:

$q_x = q_n \cos\alpha_{j-1}$; $q_y = -q_n \sin\alpha_{j-1}$.

$q_n = 0.5\,\rho\,v_i\,[(w_i - dx_i/dt)\cos\alpha_{i-1} + (dy_j/dt)\sin\alpha_{j-1}$.

Vector of the relative wind speed:

$\mathbf{v}_j = (w_i - dx_i/dt)\,\mathbf{i} - (dy_i/dt)\,\mathbf{j}$,

c_N is the normal coefficient of aerodynamic drag rope; c_x, c_y are damping coefficients, selected from the conditions of stability accounts; dTR is diameter of the cable. Efforts Tj-1 and Tj are determined by formulas similar to (2).

Thus, the process of deploying the system is described by

the equations of motion (2), (3). These equations are solved numerically by Euler's method for different variants of initial data: damping coefficients, stiffness rope, cable pulling efforts, the distribution of horizontal wind speed at height, vertical velocity of the balloon, the flight altitude, which begins deployment of the system integration step.

Fig. 4 - 6 shows the results of calculations for the three deployment options for the efforts of pulling rope T_0, made of polyamide fiber (Nylon), and following the rest of the source data: vertical takeoff w_Y = 7 m / s; altitude at which the deployment begins, H_0 = 3 km, the mass of the lower container, M_1 = 30 kg, the upper container, M_2 = 35 kg, the length of the lower section of the cable L_1 = 3000 m, of the top section L_2 = 3000 m, mass per unit length of cables is 0.0147 kg / m, the total number of elements that approximate the shape Rope, is 45; square parachutes S_p = 7.35 m2. Distribution of wind speed on height was described by law:

$$w_x = w_0 + w_1 \sin[\pi(H_0 - 1)/20], \quad (4)$$

where: w_0 = 7 m / s, , w_1 = 10 m / sec.

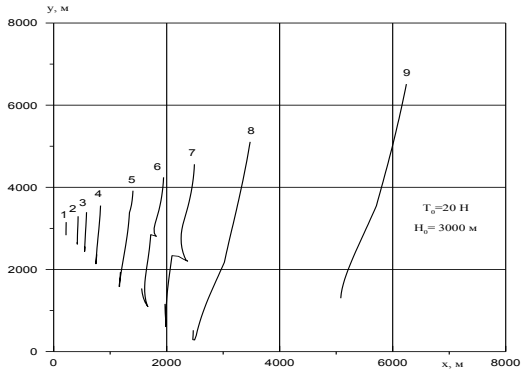

Figure 4. Changing the system configuration process

Fig.4 curves correspond to time after the start of the deployment, given in Tab. 1. The last line of Tab. 1-3 shows the total numbers of elements n of the system have emerged from two stores. Curve 7 of Tab. 1 corresponds to the end of the exit from the shop all the top rope.

TABLE 1. Numbers of elements have left two stores.

№	1	2	3	4	5	6	7	8	9
t, s	22	42	76	79	131	177	222	300	500
n	3	7	10	15	25	35	45	45	45

Tab. 2 and Tab.3 provide the relevant data for fig. 5 and fig. 6.

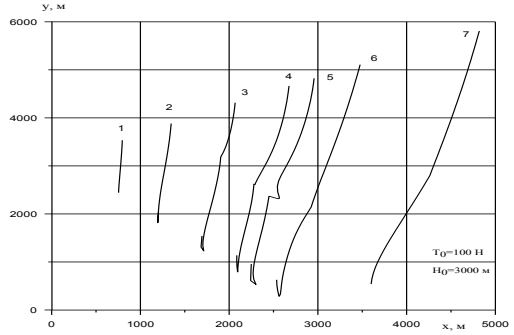

Figure.5. Changing the system configuration process

TABLE 2. Numbers of elements have left two stores.

№	1	2	3	4	5	6	7
t, s	76	126	187	237	260	300	400
n	10	20	30	40	45	45	45

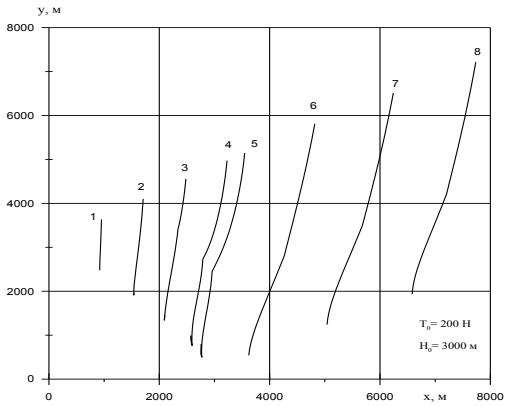

Figure 6. Changing the system configuration process

TABLE 3. Numbers of elements have left two stores.

№	1	2	3	4	5	6	7	8
t, s	90	157	221	281	306	400	500	600
n	10	20	30	40	45	45	45	45

A comparison of Fig. 4 - 6 and Tab. 1-3. show that with increasing effort pulling ropes to deploy the system becomes more "right" i.e. at T_0 = 200 H the upper cable was not ahead of the upper container, and there are only "loops" in the bottom of the container.

Were performed calculations of the deployment of the system at different values of effort pulling the upper and lower cables. The results of calculations for the zero gradient of horizontal wind speed at height are given in Tab. 4. The table shows the values of maximal effort at the lowest point of the lower rope $T_{H\,max}$ and the top point of the upper cable $T_{B\,max}$, and time values τ_1, τ_2, corresponding to these efforts (timing starts when the output of each cable from the store). The lengths of the upper and lower cables are the same, $L_1 = L_2$ = 3 km, mass per unit length of cables is 0.0132 kg / m, diameter is 5 mm, the height of the release of the second supporting cable H_0 = 5 km, Sp = 7.35m2, w_x = 0.

TABLE 4. The maximum efforts in the bottom and top points of the cable

.T_H, H	T_B, H	$T_{H\,max}$, H	$T_{B\,max}$, H	T_1, s	τ_2, s
100	100	554	1712	398.4	403.5
	150	554	1714	398.7	403.7
	200	559	1712	399	404
	500	563	1712	400.5	405.6
150	100	559	1713	405	410.1
200		555	1716	413.7	418.7
250		567	1716	427.2	432.3

An examination of Tab. 4 shows that during the descent containers maximum value of the $T_{H\,max}$, $T_{B\,max}$ practically does not depend on the efforts of T_H, T_B cables stretching from the stores. Maximum efforts in the cables occur some time after the full deployment of each of them. Table. 5 shows the maximum effort in cables and the values of the time in which they operate, for the distribution of

wind speeds for height according to the law (4) and Sp = 7.35 m^2, w_0 = 7 m / s, w_1 = 10 / sec.

TABLE 5. The maximum efforts in the bottom and top points of the cable

T_H, H	T_B, H	$T_{H\,max}$, H	$T_{B\,max}$, H	τ_1, c	τ_2, c
100	100	449	1540	394.2	399.2
	150	462	1539	394.7	398.8
	200	488	1561	398.5	397.7
	250	592	1681	391.3	396.1
	300	596	1690	392.4	397.4
	400	421	1544	396	401.1
	500	492	1551	399	398.1
50	100	491	1559	392.3	391.6
150		490	1553	403.8	407.6
200		584	1672	406.9	411.9
250		591	1688	420.6	425.7

From Tab.4 and Tab.5 it is visible that the maximum efforts in the top point of the top cable at system expansion differ not essentially: for the bottom point of the bottom cable the maximum size of an overload makes approximately 2, and for the top point of the top cable - approximately 5. From fig. 4-6 follows that the bottom cable at the expense of its spontaneous exit under the influence of weight of the left part of a cable forms of store in the bottom part a loop. At low size of speed horizontal wind components, a cable in a place of the created loop can be gushed over, form knots, therefore there is a probability of breakage of a cable on knots. For elimination of this undesirable phenomenon it is necessary to increase cohesive force of a cable with shop walls. This force should be more than 20 kg for the given type of the bottom cable (fig. 6 see) and not to exceed 60 kg (the doubled overload at weight of the container of 30 kg). The optimum size of cohesive force in this case should be an order of 20-30 kg. Precisely enough this force can be established by weak filling of a cell of store in weight of a cable (force of an exit is an order of 5-10 kg) and fastening of each loop of a cable in store by means of a thread having breaking strength about 20 kg. Also, it follows that at some points in time (for example, when n = 35-45) may happen when the upper container "comes over" on the bottom rope. Delete this can be by increasing the force pulling the top rope from a shop in the same way as suggested in the previous case.

4. CHANGE OF AZIMUTHAL POSITION OF THE BALLOON SUSPENSION GIRDER AND THE DEVIATION FROM THE VERTICAL OF MEASURING INSTRUMENTS GRADIOMETER

At measurement of vertical gradients of any physical field is necessary to know position of measuring instruments in space in the course of balloon drift. Two cases were thus studied: 1) changes of azimuthal position of the balloon suspension girder and 2) deviations of the lower containers of measuring instruments gradiometer from the vertical line passing through the upper container. In the first case azimuthally position of the balloon suspension girder was studied from the moment of start by means of three-component fluxgate magnetometers, sensors were rigidly connected with the thrust bearing beam balloon equipment. The experimental setup is shown in Fig. 7. Azimuthally position of magnetometer sensor was evaluated relative to the plane of the magnetic meridian. The experimental results are shown in Fig. 8. The experiment showed that the seed perturbations are normalized within 40 min after reaching the ceiling balloon flight. It is experimentally shown that in a long horizontal flight the balloon together with the suspension slowly rotates with a period of 1-2 turns per hour. The position of its axis relative to the vertical line located within the angular 0.2-0.5 degrees. Such minor deviations due to the rapid relaxation of the system under perturbations of air flow.

For the second case we will evaluate the magnitude of deviation of the lower container measuring gradiometer from a vertical line passing through the upper container. The balloon is affected by fluctuations of the carrier air flow, resulting in position measurement base relative to the vertical may be violated. This leads to a decrease in the accuracy of measurements of vertical gradients. On fig. 9 position of a triad of instrument containers and magnetic gauges gradiometer in the course of balloon drift is given. Deviations gradiometer measuring base of the vertical due to the action of this factor were carried out using the formula:

$$\mathbf{P} = \frac{\mathrm{SpV}^2}{2\mathrm{g}},$$ where S - the combined area (sail), the frontal surface of the lander part of the device, p - air density, V - the increment of wind speed on the length of the measuring base. Based on the above formula, in [4] shows that deviations do not exceed the base measuring 200 meters at its length equal to 6000 m in summer flights at low (50 km / h) speed of air flow. In winter conditions, the flight velocity is 3-4 times higher, and these deviations from this can be as high as 600 m. However, there is another reason that leads to deviations from the vertical position of the system (the second factor of influence). It is due to the fact that the envelope in balanced air flow and in its motion repeats all the nuances of air flow. Suspension gradiometer, length 6000 m has a period of pendulum vibrations of the order of 150 s, and hence an increment of speed the envelope, the latter outperforms the provisions lowered down containers and lead to the disorder vertical position of the measuring base gradiometer with its subsequent recovery. Position of the axis gradiometer measuring base of the vertical lines in the drift of the balloon was verified experimentally in the most unfavorable, cold season with navigation GPS-receivers. Natural experiment took place on November 3, 2005 In this experiment contained three gradiometer measuring container, evenly spaced vertically within the ~ 5.4 km, each with a magnetic meter and navigation GPS-receiver.

5. CONCLUSION

In the IZMIRAN and the MAI it is created the balloon magnetic gradiometer (BMC), the design of which and how to use the patent of the Russian Federation [1] is taken out. The BMC consists of three instrument containers, in each of which there is scalar nuclear magnetometer, GPS-global positioning system receiver, on-board computers for the collection and packaging of scientific information, satellite data modem "Globalstar" and system of automatic expansion gradiometer at the set height after balloon launch. In implementing the gradiometer solved the problem of stability.

6. REFERENCES

[1] Цветков Ю.П., Брехов О.М., Филиппов С.В., Бондарь Т.Н., Иванов А.А., Крапивный А.В., Николаев Н.С. Экспериментальные оценки погрешности измерений вертикальных геомагнитных градиентов в стратосфере. Геомагнетизм и аэрономия, 2007, том 47, № 4, с. 543-54.

[2] Крапивный А.В., Николаев Н.С., Баранов Я.В., Брехов О.М., Цветков Ю.П., Кириаков В.Х. Аэростатный магнитный градиентометр. Приборы и техника эксперимента, 2007, № 4, с.159-160.

[3] Цветков Ю.П., Бондарь Т.Н., Брехов О.М., Крапивный А.В., Николаев Н.С. Способ получения вертикального градиента аномального магнитного поля Земли на стратосферных высотах. Патент на изобретение № 2310892. 20.11.2007 г. Бюл. № 32.

[4] Николаев Н.С., Крапивный А.В., Баранов Я.В., Брехов О.М., Цветков Ю.П., Пчелкин А.В. Высокоточный аэростатный градиентометр со спутниковыми каналами связи. Датчики и системы. №1, 2008, с. 16-20.

[5] Черников С.П., Цветков Ю.П., Брехов О.М., Крапивный А.В., Николаев Н.С. Компьютерная модель динамики процесса автоматического развертывания аэростатного магнитного градиентометра. Датчики и Системы, 2009.

[6] Yu.P. Tsvetkov, V.D. Kuznetsov, V.P. Golovkov, O.M. Brekhov. A new method for detection of the anomaly Earth's. ISSN 1028 334X, Doklady Earth Sciences, 2011, Vol. 436, Part 1, pp. 117–121. © Pleiades Publishing, Ltd., 2011.

List of participants

Takumi Abe
JAXA
3-1-1, Yoshinodai
252-5210 Sagamihara
Japan
abe.takumi@jaxa.jp

Kolbjorn Adolfsen
Prenessen DT 22
8480 Andenes
Norway
kolbjorn@adolfsen.com

Thor-Arne Agnalt
UiO Norway
Elvestadveien 989
1827 Hobøl
Norway
t.a.agnalt@fys.uio.no

Glauberto Leilson Alves de Albuquerque
Barreira do Inferno Launch Center
Rua Neuza Frache 1938
59082100 Natal/RN
Brasil
glaubertoleilson@gmail.com

Tarjei Antonsen
Stakkeveien 2
9018 Tromsø
Norway
tarjei.antonsen@gmail.com

Nicolas Arnold
FHNW
Alpenstrasse 5
8803 Rüschlikon
Switzerland
nicolas.arnold@fhnw.ch

Joseph Ashkenazy
Soreq
Rojanski 21
76453 Rehovot
Israel
joseph@soreq.gov.il

Cecilia Axelsson
SSC
P.O. Box 4207
SE-171 04 Solna
Sweden
cecilia.axelsson@sscspace.com

Gábor Balassa
BME - HVT
18. Egry József street
1111 Budapest
Hungary
emc2@hotmail.hu

Carsten Baumann
German Aerospace Center
Institute of Atmospheric Physics
Pfundmayerstraße 27
81375 München
Germany
carsten.baumann@dlr.de

Tore André Bekkeng
University of Oslo
P.O.Box 1048 Blindern
316 Oslo
Norway
t.a.bekkeng@fys.uio.no

Evguenia Belova
Glimmervagen 33
98140 Kiruna
Sweden
belova@irf.se

Gwenael Berthet
LPC2E/CNRS University of Orleans
3A Avenue de la recherche scientifique
45071 ORLEANS
France
gwenael.berthet@cnrs-orleans.fr

Andrea Boscaleri
Via A. Stoppani 12
50131 Firenze
Italy
a.boscaleri@ifac.cnr.it

Adam Bourassa
University of Saskatchewan
116 Science Place
Saskatoon S7N 5E2
Canada
adam.bourassa@usask.ca

Oleg Brekhov
Moscow Aviation Institute
Alabyana, 10
125080 Moscow
Russia
obrekhov@mail.ru

Pål Brekke
Norwegian Space Centre
Ostadalsveien 4A
753 Oslo
Norway
paal@spacecentre.no

Natacha Callens
HeSpace for ESA
Keplerlaan 1, PO Box 299
2200 AG Noordwijk
Netherlands
natacha.callens@esa.int

Giuseppe Capuano
TSD Space
via Provinciale Pianura 2
80078 Pozzuoli
Italy

Sandip Chakrabarti
S.N. Bose NationaL Centre for Basic Sciences
JD Block, SalT Lake, Sector-III
700098 Kolkata
India
chakraba@bose.res.in

Jean-Marc Charbonnier
Z Marine
Zi Labal Prioul
31 450 Ayguesvives
France
jean-marc.charbonnier@zodiacmarine.com

Hugo Charrier
Estaca Space Odyssey
34 Rue Victor Hugo
92300 Levallois-Perret
France
hugo.charrier@estaca.eu

Sergey Chernouss
Polaz Geophysical Institute of KSCRAS
26a Academgorodok St.
184209 Apatity
Poland

Lasse Clausen
University of Oslo
Postboks 1048 Blindern
316 Oslo
Norway
lasse.clausen@fys.uio.no

Philippe Cocquerez
CNES
18 avenue Edouard Belin
31401 Toulouse
France
Philippe.Cocquerez@cnes.fr

Augusto Cogoli
Retired
Riedhofstrasse 273
8049 Zurich
Switzerland
augusto.cogoli@zeglit.ch

Flavio de Azevedo Corrêa JR
Instituto de Aeronáutica e Espaço
Pça. Eduardo Gomes,50
S. José dos Campos
Brasil

Gwennou Coupier
CNRS
140 rue de la physique
38400 Saint Martin d'Hères
France
gwennou.coupier@ujf-grenoble.fr

Arne Croell
Universität Freiburg
Sebastian-Kneipp-Str. 14
79104 Freiburg
Germany
arne.croell@krist.uni-freiburg.de

Nico Danneberg
MT Aerospace
Franz-Josef-Strauß-Straße 5
86153 Augsburg
Germany

Kristine Dannenberg
Swedish National Space Board
Solna strandväg 86
171 04 Solna
Sweden
dannenberg@snsb.se

Erik de Schrijver
Sint-Pieterscollege Jette
L.Theodorstraat 167
1090 Brussels
Belgium
eds@sint-pieterscollege.be

Doug Degenstein
University of Saskatchewan
116 Science Place
S7N 5E2 Saskatoon
Cook-Island
doug.degenstein@usask.ca

Voncenzo Della Corte
University of Napoli
Corso Umberto I
80138 Napoli
Italy

Alexis Doerenbecher
Meteo-France
Avenue Coriolis, 42
31057 Toulouse
France
alex.doerenbecher@meteo.fr

Lev Dorman
Tel Aviv University
Gamla 24
12900 Katsrin
Israel
lid@physics.technion.ac.il

Françoise Douchin
CNES
18 avenue Edouard Belin
31 401 Toulouse
France
francoise.douchin@cnes.fr

Petter Dragoey
Andoya Rocket Range
P.O.Box 54
8483 Andenes
Armenia
tone@rocketrange.no

Robin Dufour
Ecole Polytechnique Fédérale de Lausanne
GR-SCI-IAG, Statio 9
1015 lausanne
Switzerland
penelope.leyland@epfl.ch

Cedric Dupont
Bertin Technologies
10 Avenue Ampere
78180 Montigny Le Bretonneux
France
dupont@bertin.fr

Roel Eerkens
T-Minus Engineering
Molengraaffsingel 12/14
2629 JD Delft
Netherlands
r.h.p.eerkens@t-minus.nl

Marcel Egli
Hochschule Luzern
Werftestrasse 4
CH-6052 Hergiswil
Switzerland
marcel.egli@hslu.ch

Yngve Eilertsen
University of Tromso
Dept. of Physics and Technology
9037 Tromso
Norway
yngve.eilertsen@uit.no

Odd Roger Enoksen
Andoya Rocket Range
P.O.Box 54
8483 Andenes
Armenia
tone@rocketrange.no

Svenja Fengler
University of Tübingen
Auf der Morgenstelle 1
72076 Tübingen
Germany
svenja.fengler@uni-tuebingen.de

Sergey Filippov
Russian Academy of Sciences (IZMIRAN)
142092 Troitsk
Moscow Region
Russia

Sebastian Finke
Argus Electronic Gmbh
Joachim- Jungius- Straße 9
18059 Rostock
Germany
diana.gontarz@argus-electronic.de

Gilberto Fisch
IAE/DCTA
Rua Itatiba, 220
12243-200 Sao Jose dos Campos
Brasil
fisch.gilberto@gmail.com

Simey Fisch
IAE/DCTA
Rua Itatiba, 220
12243200 Sao Jose dos Campos
Brasil
fisch.gilberto@gmail.com

Gunnar Florin
SSC
P.O. Box 4207
SE-17104 Solna
Sweden
gunnar.florin@sscspace.com

Martin FRIEDRICH
TU Graz
Inffeldgasse 12
8010 Graz
Austria
martin.friedrich@tugraz.at

Eckart Fuhrmann
ZARM
Sielwall 72
28203 Bremen
Germany
fuhrmann@zarm.uni-bremen.de

Michel Garcia
Ruag Space Switzerland Nyon
Chemin de la Vuarpillière 29
1260 Nyon
Switzerland
michel.garcia@ruag.com

Roberto Gardi
CIRA
Italy

Andreas Gierse
FH Aachen
Hollerallee 14
28209 Bremen
Germany
andreas_gierse@gmx.de

Jeffrey Gram
H.E Space Operations B.V.
Huygensstraat 44-2A
2201 DK Noordwijk Zh
Netherlands
jeffrey.gram1@gmail.com

Jøran Grande
NAROM
Bernhoffs gate 9
8480 Andenes
Norway
joran@rocketrange.no

Veronika Grósz
BME-HVT
Egry József utca 18
1111 Budapest
Switzerland
veronika.grosz@gmail.com

Rüdiger Hampp
Universität Tübingen
Pappelstr. 23
72076 Tübingen
Germany
ruediger.hampp@uni-tuebingen.de

Gudmund Hansen
Andoya Rocket Range
P.O.Box 54
8483 Andenes
Armenia
tone@rocketrange.no

Arne Hjalmar Hansen
NAROM-Norwegian Centre for Space-Related Education
P.O. Box 54
8483 Andenes
Norway
arne-hjalmar@rocketrange.no

Swantje Hauschild
University of Zurich
Winterthurerstr. 190
8057 Zürich
Switzerland
swantje.hauschild@uzh.ch

Ove Havnes
University of Tromsø
Helmer Hansensgate 4
9011 Tromsø
Norway
ove.havnes@uit.no

Kurt Hempe
airborne Systems
537 S Dustin Place
90806 Anaheim
USA
kurt.hempe@airborne-sys.com

Reinhard Hilbig
Universität Hohenheim
Garbenstr. 30
D 70596 Stuttgart
Germany
rhilbig@uni-hohenheim.de

Ylva Houltz
Box 4207
17104 Solna
Sweden
ylva.houltz@sscspace.com

Felix Huber
DLR
Muenchnerstr. 20
82234 Wessling
Germany
felix.huber@dlr.de

Mikael Inga
SSC
P.O: Box 4207
SE-17104 Solna
Sweden
mikael.inga@sscspace.com

Nickolay Ivchenko
KTH
Teknikringen 31
10044 Stockholm
Sweden
nickolay@kth.se

Miranda Jackson
KTH
Broddgatan 3
16969 Solna
Sweden
mirandaj@kth.se

Thomas Jauss
Universität Freiburg
Hermann-Herder-Straße 5
79104 Freiburg
Germany
thomas.jauss@fmf.uni-freiburg.de

Xiujie Jiang
NSSC
No.1 Nanertiao - Zhongguancun
Haidian district Beijing
China

Otfried Joop
DLR
Koenigswinterer Str. 522
53227 Bonn
Germany
Otfried.Joop@dlr.de

Wolfgang Jung
DLR
Münchener Str. 20
82234 Wessling
Germany
wolfgang.jung@dlr.de

Mikhail Khaplanov
Stockholm University
Klippgatan 16 C
17147 Solna
Sweden
misha@misu.su.se

Sheila Kirkwood
Swedish institute of Space Physics
Gronstensvagen 12
98140 Kiruna
Sweden
sheila.kirkwood@irf.se

Alexey Kondyurin
School of Physics
University of Sydney
2006 Sydney
Australia
a.kondyurin@physics.usyd.edu.au

Stefan Krämer
FH Aachen
Weberstrasse 13
52064 Aachen
Germany
stefan.kraemer@me.com

David Krause
NASA - Orbital
Bldg F10 S237
23417 Wallops Island
USA
krause.dave@orbital.com

Rainer Kuhl
DLR
Koenigswinterer Str. 524
53227 Bonn
Germany
rainer.kuhl@dlr.de

Patrick Kühl
Christian-Albrechts Universität Kiel - Institut für Experimentelle und Angewandte Physik - Abteilung Extraterrestrik
Leibnitzstraße 11
24118 Kiel
Germany
kuehl@physik.uni-kiel.de

Thomas Kuhn
Lulea University of Technology
Box 812
98128 Kiruna
Sweden
thkuhn@gmail.com

Miguel Larsen
Clemson University
Physics Department
118 Kinard Lab
29634 Clemson
USA
mlarsen@clemson.edu

Ditte Latteck
Germany

Michel Deroeve
University Hasselt
Martelarenlaan 42
3500 Hasselt
Belgium
michel.deroeve@uhasselt.be

Carole Lecinana
CNRS
9 Av du colonel Roche
31028 Toulouse
France
Carole.Lecinana@irap.omp.eu

Jianning Li
SSC
Solna Strandväg 86
17104 Solna
Sweden
jianning.li@sscspace.com

Geir Lindahl
Andoya Rocket Range
P.O.Box 54
8483 Andenes
Norway
tone@rocketrange.no

Robert Lindberg
Luleå University of Technology
Bromsgatan 2E
98136 Kiruna
Sweden
solar.robert.lindberg@gmail.com

Cheng Liu
NSSC
No.1 Nanertiao - Zhongguancun
Haidian district Beijing
China

Lars Ljunge
RUAG Space AB
Bröderna Ugglas Gata
58111 LINKÖPING
Sweden
lars.ljunge@ruag.com

Christian Lockowandt
SSC
Solna strandväg 86
17104 Solna
Sweden
clo@ssc.se

Jose Mariano Lopez Urdiales
zero2infinity
Masia Nova, Ronda Can Fatjó
8290 Cerdanyola del Valles
Spain
jmlu@inbloon.com

Jose Juan Lopez-Moreno
IAA-CSIC
Glorieta de la Astronomia
18008 Granada
Spain
lopez@iaa.es

Silvia Losch
Leibniz-Institute of Atmospheric Physics e.V. at the University Rostock
Schloßstr. 6
18225 Kühlungsborn
Germany
losch@iap-kborn.de

Kenneth Löth
SSC
Solna Strandväg 86
17104 Solna
Sweden
kenneth.loth@sscspace.com

Emilio Lozano
KTH REXUS team(MUSCAT)
Bygatan 21
17149 Solna
Sweden
emiliolozano13@gmail.com

Franz-Josef Lübken
Leibniz-Institute of Atmospheric Research
Schloss-Str. 6
18225 Kühlungsborn
Germany
luebken@iap-kborn.de

Hitrud Lübken
Germany

Alexey Lykov
Central Aerological Observatory
Prvomayskaya, 3
141700 Dolgoprudny
Russia
alykov@mail.ru

Rolf Maag
Meteolabor AG
Hofstr. 92
8620 Wetzikon
Switzerland
rolf.maag@meteolabor.ch

Siri Magnussen
Andoya Rocket Range
P.O.Box 54
8483 Andenes
Armenia
tone@rocketrange.no

Johannes Marquardt
Christian-Albrechts-Universität zu Kiel
Im Brauereiviertel 13
24118 Kiel
Germany
marquardt@physik.uni-kiel.de

Lebeuf Martin
Canadian Space Agency
6767 route de l'aéroport
J3Y 8Y9 Saint-Hubert
Canada
martin.lebeuf@asc-csa.gc.ca

Tiago Matos de Carvalho
Institute of Aeronautics and Space (IAE)
Praça Marechal Eduardo Gomes, 50
Vila das Acácias
12228-904 Sao Jose dos Campos-SP
Brasil
tiagomatoscarvalho@gmail.com

Tom McElroy
York University
4700 Keele Street
M3J 1P3 Toronto
Canada

Alexis Merlaud
Belgian Institute for Space Aeronomy
Avenue Circulaire 3
1180 Bruxelles
Belgium
alexism@oma.be

Kevin Merrell
Airborne Systems
2555 Main Street Apt 2024
92614 Irvine
USA
kevin.merrell@airborne-sys.com

Wojciech Miloch
Department of Physics, University of Oslo
Postboks 1048 Blindern
317 Oslo
Norway
w.j.miloch@fys.uio.no

Joeran Moen
Univ. of Oslo
Oevre Linneslia 17
3400 Lier
Norway
jmoen@fys.uio.no

Steeve Montminy
Canadian Space Agency
6767 route de l'aeroport
J3Y8Y9 St-Hubert
Canada
steeve.montminy@asc-csa.gc.ca

Francisco Mota
FUNCATE
Av Dr Joao Guilhermino, 429-Sala 94
12210131 Sao Jose dos Campos-SP
Brasil
mota@dca.ufrn.br

Brigitte Müller
FH Aachen
Hohenstaufenallee 6
52064 Aachen
Germany
brigitte.mueller@alumni.fh-aachen.de

Donal Murtagh
Chalmers tekniska högskola
Linnégatan 3, 3tr
41304 göteborg
Sweden
donal.murtagh@chalmers.se

Karl Wieland Naumann
Bayern-Chemie GmbH
Liebigstrasse 17
84544 Aschau am Inn
Germany
karl.naumann@mbda-systems.de

Satoshi Nonaka
JAXA
3-1-1, Yoshinodai, Chuo
2525210 Sagamihara
Japan
nonaka.satoshi@jaxa.jp

Olle Norberg
Swedish National Space Board
Skolvägen 13
19270 Sollentuna
Sweden
olle.norberg@snsb.se

Hermann Oelhaf
KIT
Hermann-von-Helmholtz-Platz 1
76344 Eggenstein-Leopoldshafen
Germany
hermann.oelhaf@kit.edu

Sveinung Olsen
University of Tromso
Dept. of Physics and Technology
9037 Tromso
Norway
sveinung.olsen@uit.no

Guillermo Ortega
ESA
Keplerlaan 1
AG2200 Noordwijk
Netherlands
guillermo.ortega@esa.int

Qinsu Peng
NSSC
No.1 Nanertiao - Zhongguancun
Haidian district Beijing
China

Sylvain Pernon
IPSA
7 rue Maurice Grandcoing
94200 Ivry sur Seine
France
pernon@ipsa.fr

Jean-Pierre Pommereau
CNRS
36 Rue de la Convention
75015 Paris
France
Jean-Pierre.Pommereau@latmos.ipsl.fr

Lennart Poromaa
SSC Esrange
P.O Box 802
98128 Kiruna
Sweden
lennart.poromaa@sscspace.com

Thierry portes
ELTA
14 place marcel dassault
31700 blagnac
France
thierry.portes@areva.com

Anneli Prenta
Luleå University of Technology
Docentvägen 16
97752 Luleå
Sweden
solar.anneli.prenta@gmail.com

Carla Prevoo
Congrex Holland / ESA Conference Bureau
ESA-ESTEC, Keplerlaan 1, PO Box 299
2200 AG Noordwijk
Netherlands
natacha.callens@esa.int

Peng QinSu
CASC
BaQiao,TianWang NO.1 special
710025 Xi'An
China
chbert@yahoo.cn

Tone Raabye
Andoya Rocket Range
P.O.Box 54
8483 Andenes
Armenia
tone@rocketrange.no

William Reid
Royal Institute of Technology
16 Wells Street
2042 Newtown
Australia
will.reid3@gmail.com

Maria Roth
DLR Space Administration
An der Wielermaar 75
51143 Koeln
Germany
maria.roth@dlr.de

Alessandra Rotundi
University of Napoli
Corso Umberto I
80138 Napoli
Italy

Gutemberg Santiago
Federal University of Rio Grande do Norte
R. Gentil Ferreira, 6, Cohabinal
59140-720 Parnamirim
Brasil
gutemberg.santiago@gmail.com

Hiroatsu Sato
DLR / Univ. Oslo
Olav M. Troviksvei 60
864 Oslo
Norway
hiroatsu.sato@fys.uio.no

Elke Schaberger-Zimmermann
Access e. V.
Intzestraße 5
52072 Aachen
Germany
j.dolfen@access.rwth-aachen.de

Enno Scharrenberg
Christian-Albrechts-Universität zu Kiel
Samwerstraße 33
24118 Kiel
Germany
scharrenberg@physik.uni-kiel.de

Marco Scharringhausen
German Aerospace Center
Robert-Hooke-Straße 7
28359 Bremen
Germany
marco.scharringhausen@dlr.de

Francis Schmidlin
2709 N Buck Harbor Ct
Pocomoke City, Maryland 21851
USA
fschmidlin@comcast.net

Burkhard Schmitz
Astrium
Airbus Allee 1
28199 Bremen
Germany
burkhrad.schmitz@astrium.eads.net

Jan Berend Schumacher
University of Rostock
Seidenstr 1
18055 Rostock
Germany
jan-berend.schumacher@uni-rostock.de

Andreas Schütte
Astrium GmbH
Airbus-Allee 1
28199 Bremen
Germany
Andreas.Schuette@astrium.eads.net

Larisa Sidorova
IZMIRAN
142190 Moscow, Troitsk
Russia

Martin Siegl
DLR Bremen
Robert-Hooke-Straße 7
28359 Bremen
Germany
martin.siegl@dlr.de

Andres Spicher
University of Oslo
Cossettes 15
1723 Marly
Switzerland
andres.spicher@gmail.com

Andreas Stamminger
DLR
Oberpfaffenhofen
82234 Wessling
Germany
andreas.stamminger@dlr.de

Christian Steigies
CAU Kiel
Olshausenstr 40
24098 Kiel
Germany
steigies@physik.uni-kiel.de

Helmut Steinau
Astrium GmbH - TEXUS/ MAXUS-Missions
Airbus-Allee 1
D 28199 Bremen
Germany
helmut.steinau@astrium.eads.net

Laszlo Sturz
Access e. V.
Intzestr. 5
52072 Aachen
Germany
j.dolfen@access.rwth-aachen.de

Astrid Sunna
SSC, Esrange Space Center
Postbox 802
S- 981 28 Kiruna
Sweden
astrid.sunna@sscspace.com

Luna Laura Tania
UFRSA
Caraubas
Brasil

Toru Tanimori
Deparment of Physics, Kyoto University
KitashirakawaOiwakecho, Sakyoku
6068502 Kyoto
Japan
tanimori@cr.scphys.kyoto-u.ac.jp

Svantje Tauber
University Zurich
Winterthurerstr. 190
8057 Zurich
Switzerland
svantje.tauber@anatom.uzh.ch

Cora Thiel
Univerity of Zurich
Winterthurerstrasse 190
8057 Zurich
Switzerland
cora.thiel@anatom.uzh.ch

Eivind Thrane
Andoya Rocket Range
P.O.Box 54
8483 Andenes
Armenia
tone@rocketrange.no

Kjell Toften
Andoya Rocket Range
P.O.Box 54
8483 Andenes
Armenia
tone@rocketrange.no

Giovanni Tovo
None
Via C. Battisti 67/a
36078 Valdagno
Italy
supertovo@gmail.com

Johan Tresvig
University of Oslo
Sem Saelandsvei 24
N*-0371 Oslo
Norway
j.l.tresvig@fys.uio.no

Thuy Quynh Trinh
DLR Bremen
Robert-Hokke-Str.7
28359 Bremen
Germany
thuy.trinh@dlr.de

Yury Tsvetkov
IZMIRAN
142190 Moscow
Troitsk
Russia

Peter Turner
DLR
Münchener Str. 20
82234 Wessling
Germany
peter.turner@dlr.de

Jo Urban
Chalmers University of Technology
Department of Earth and Space Sciences
41296 Göteborg
Sweden
joaurb@chalmers.se

Didier Vassaux
CNES
2 place Maurice Quentin
75039 Paris
France
didier.vassaux@cns.fr

Peter von Kampen
ZARM
Sielwall 72
28203 Bremen
Germany
peter.vonKampen@zarm.uni-bremen.de

Kaley Walker
University of Toronto
60 St. George Street
M5S1A7 Toronto
Canada
kwalker@atmosp.physics.utoronto.ca

Wigor Webers
GFZ Potsdam
Charlottenstr. 99
14467 Potsdam
Germany
wigor@gfz-potsdam.de

Hendrik Weihs
DLR
Pfaffenwaldring 38-40
70569 Stuttgart
Germany
hendrik.weihs@dlr.de

Mark Whale
Chalmers
lgh 1084, Gibraltargatan 80
41279 Göteborg
Sweden
whale@chalmers.se

Martina Wiedner
Observatoire de Paris-CNRS
77 avenue Denfert Rochereau
75014 Paris
France
martina.wiedner@obspm.fr

Xuan Yang
NSSC
No.1 Nanertiao - Zhongguancun
Haidian district Beijing
China

Eliot Young
SwRi
2410 Jasper Ct
80304 Boulder
USA
efy@boulder.swri.edu

Vladimir Yushkov
Central Aerological Observatory
Prvomayskaya, 3
141700 Dolgoprudny
Russia

Balazs Zabori
MTA Centre for Energy Research
Konkoly-Thege Miklos street 29-33
H-1121 Budapest
Hungary
zabori.balazs@energia.mta.hu

Bernard Zappoli
CNES
18 avenue Edouard Belin
31401 Toulouse Cedex 4
France
bernard.zappoli@cnes.fr

Martin Zell
European Space Agency
Keplerlaan 1
2201 AZ Noordwijk z/h
Netherlands
martin.zell@esa.int

Kun Zhao
National University of Defense Technology
College 1, Team 5, National University of Defense Technology
410073 Changsha
China
zk198907@qq.com

Gerhard Zimmermann
Access e. V.
Intzstr. 5
52072 Aachen
Germany
welcome@access.rwth-aachen.de